TOHOKU UNIVERSITY

Tenth International Conference on Flow Dynamics

November 25-27, 2013

Sendai International Center, Japan

Institute of Fluid Science Tohoku University

IFS

Proceedings

Institute of Fluid Science, Tohoku University

Preface

We thank you for your participation in the Tenth International Conference on Flow Dynamics ICFD2013, Sendai, Japan.

"Flow Dynamics" is a comprehensive scientific field which deals with the flow and transport phenomena concerning atoms, molecules and nano-scale particle, any fluids, any materials, energy, information, economic activities and so forth. Through the past nine conferences on Flow Dynamics held in Sendai, “Flow Dynamics” has become a major academic discipline deeply related to various difficult issues that the human society is currently facing, such as the global environment, the depletion of energy resources, and future lives on our planet.

We are pleased to hold “Tenth International Conference on Flow Dynamics ICFD2013, aiming to explore new science horizons and cutting edge technologies of Flow Dynamics, and providing young researchers with unique opportunities of experience and self-development in this very attractive and competitive field. We believe that this conference will give us a great opportunity to discuss what we have learned from the disastrous effects, and what we can do to contribute to our society.

The Conference is composed of 3 plenary lectures, 1 General Session, 13 Organized Sessions and 3 Planned Sessions. The number of presentations and participants are more than 450 and 650, respectively. We are glad to see the number of presenters is increasing every year.

This is the first ICFD which is hosted by the Institute of Fluid Science (IFS), Tohoku University, which was an affiliated body of the Global COE Program “World Center of Education and Research for Trans-disciplinary Flow Dynamics” (the GCOE). And also, IFS decides to continue to hold “International Symposium on Advanced Fluid Information (AFI)” in the ICFD.

On behalf of the organizing committee of the Tenth International Conference on Flow Dynamics, we wish you will enjoy fruitful discussions and exchanges of information, and we want you to have the opportunity to strengthen old friendships all over the world.

Toshiyuki Takagi
Professor, Institute of Fluid Science,
Tohoku University and
Jean-Yves Cavaillé
Professor, MATEIS Laboratory,
INSA-Lyon as
General Co-Chair

Tenth International Conference on Flow Dynamics

Hosted by:

- Institute of Fluid Science, Tohoku University

In cooperation with:

- Combustion Society of Japan
- Cryogenics and Superconductivity Society of Japan
- The Electrochemical Society of Japan
- Japan Aerosapce Exploration Agency
- The Japan Society of Aeronautical and Space Sciences
- The Japan Society of Applied Electromagnetics and Mechanics
- Japanese Society of Biorheology
- The Japan Society of Fluid Mechanics
- The Japan Society of Mechanical Engineers
- The International Centre for Heat and Mass Transfer (ICHMT)
- European Society of Minimally Invasive Neurological Therapy (ESMINT)

SCOPE:

Tenth International Conference on Flow Dynamics (ICFD2013), in the annual series, which is hosted by the Institute of Fluid Science, Tohoku University will be held on November 25th through 27th at Sendai International Center, Sendai, Japan. The objectives of this conference are to explore new science horizon by discussing and exchanging information in the most advanced scientific fields and in cutting edge technologies in Flow Dynamics. One of the features of this conference is to provide young researchers and students with unique opportunities of being educated and self-developed through their proactive participation in the conference.

The past nine ICFD conferences were hosted by two Tohoku University COE Programs, "The 21st Century International COE on Fluid Dynamics (21COE, Year 2003 – Year 2007)" and its successor "Global COE Program World Center of Education and Research for Trans-disciplinary Flow Dynamics (the GCOE, Year 2008 – Year 2012)". The conference accomplished remarkable successes each time in research and education in the field of Flow Dynamics at large. ICFD is now recognized by world researchers, engineers and academicians as the biggest and the most important international conference in Flow Dynamics. The Institute of Fluid Science (IFS) had been the principal operating body of both the 21COE and the GCOE, and it is worth noting that the GCOE will end in March 2013.

At the occasion of its 70 years anniversary from its launch, IFS is regenerated as a further powerful research institute, particularly in energy related research: its reorganization leads to the creation of three new flow research divisions and the Innovative Energy Research Center. In this new context, IFS decides to continue to host ICFD, and we promise you to keep ICFD's dynamism and integrity cultivated in the past. We really appreciate for your continuing participation in the ICFD2013.

Flow Dynamics is a comprehensive scientific field which deals with the flow and transport phenomena concerning atoms, molecules and nano-scale particle, any fluid, any material, energy, information, economic activities and so forth. It addresses multiscale and multidisciplinary problems and is involved in all natural phenomena (biochemical processes, corrosion, weather, volcanic eruptions, earth magnetic field and tectonic motions, etc.) and in most of human activities (industrial processes, energy production and saving, transportation, etc.). Through the past successful achievement in ICFDs, Flow Dynamics has became a major academic discipline which is dealing with various difficult tasks that human society is facing at, such as control of nuclear power generators, global warming, energy depletion, diseases, and so on. Flow Dynamics is taking major roles in realization of the future dreams of the people as advanced

medicine and medical treatment, aerospace technology, robotics, IT technology accessible by anybody, anytime, anywhere, and so forth. Scientists and engineers who are working and/or interested in such kind of areas, please come to the ICFD2013 and extend your domains and databases.

We cordially invite you scholars, researchers, educationists, students and planners exploring and studying in the relevant research and development fields of bio-, nano-, material, energy, environmental, planetary and earth sciences and technologies, particularly in the academic field of mechanical engineering, aerospace engineering, nuclear engineering, physics, medical science and engineering, chemistry, chemical engineering and so forth, to join the conference.

About two years have passed since the last East Japan Great Earthquake and Disaster struck the area. In Sendai and the vicinities started the reconstruction works right after, and those are still vigorously going on . Tohoku University activities as well as city lives have recovered quite much to the level they were before, and we feel an air of excitement now in Sendai. We are sure you will enjoy the beautiful scenery and crisp air of Autumn in Sendai in November.

CONFERENCE COMMITTEE:

Executive Committee Members:

Toshiyuki Takagi (ICFD2013 General Co-Chair, Tohoku University)
Jean-Yves Cavaillé (ICFD2013 General Co-Chair, INSA de Lyon)
Toshiyuki Hayase (IFS Director, Tohoku University)

International Scientific Committee Members:

Chair: Shigenao Maruyama (Tohoku University)

Australia
- Masud Behnia (The University of Sydney)
- Gary Rosengarten (RMIT University)

Canada
- Javad Mostaghimi (University of Toronto)

China
- XinGang Liang (Tsinghua University)
- Xing Zhang (Tsinghua University)

France
- Patrick Bourgin (ECL)
- Jean-Yves Cavaillé (INSA de Lyon)
- Philippe Kapsa (ECL)

Germany
- Serge A. Shapiro (Freie University Berlin)

India
- Subhash C. Mishra (Indian Institute of Technology Guwahati)

Italy
- Gian Piero Celata (ENEA)

Japan
- Keisuke Asai (Tohoku University)
- Yu Fukunishi (Tohoku University)
- Masato Furukawa (Kyushu University)
- Toshiyuki Hayase (Tohoku University)
- Nobuhide Kasagi (The University of Tokyo)
- Chisachi Kato (The University of Tokyo)
- Yoichiro Matsumoto (The University of Tokyo)

Junichiro Mizusaki (Tohoku University)
Kazuhiro Nakahashi (Japan Aerospace Exploration Agency)
Masami Nakano (Tohoku University)
Tomohide Niimi (Nagoya University)
Hideya Nishiyama (Tohoku University)
Masaki Sano (The University of Tokyo)
Akihiro Sasoh (Nagoya University)
Masaaki Sato (Tohoku University)
Toshiyuki Takagi (Tohoku University)
Michio Tokuyama (Tohoku University)
Takashi Yabe (Tokyo Institute of Technology)
Satoru Yamamoto (Tohoku University)

Korea
Joon-Hyun Lee (KETEP)
Joon Sik Lee (Seoul National University)
Hyung Jin Sung (Korea Advanced Institute of Science and Technology)

Russia
Mikhail Ivanov (Institute of Theoretical and Applied Mechanics SB RAS)
Oleg P. Solonenko (Insitute of Theoretical and Applied Mechanics SB RAS)
Alexander Vasiliev (Moscow State University)

Sweden
Fredrik Lundell (Royal Institute of Technology)

Switzerland
Bastien Chopard (University of Geneve)
Dimos Poulikakos (ETH Zurich)

Taiwan
Wu-Shung Fu (National Chiao Tung University)

UK
Yiannis Ventikos (University of Oxford)

USA
Louis N. Cattafesta III (University of Florida)
Yiguang Ju (Princeton University)
Ishwar K. Puri (Virginia Tech)
Kozo Saito (Kentucky University)
John P. Sullivan (Purdue University)
Rongia Tao (Temple University)
Satish Udpa (Michigan State University)

Organizing Committee Members:

Atsushi Shirai (Chair), Hideaki Kobayashi, Shigeru Yonemura, Kazushi Miyata, Hiroyuki Shimizu, Fukuo Ohta, Yoshinori Sasaki, Kunihiro Takahashi, Fumio Saito Hisanori Masuda

(Observer) Shigenao Maruyama, Naoto Wada

Administrative Staff

Ruriko Azumi, Natsuko Hatakeyama, Satsuki Kudo, Tomomi Nagayoshi

Plenary Lectures

Fluid Flow in Micron Spaces: Fluid dynamics in Microfluidic Devices

David A. Weitz (Harvard University, USA)
(9:20-10:10, November 25 at TACHIBANA)

Porous Media Combustion – Its Potential Applications in Wide Range of Liquid and Gas Fuelled Cooking Stoves

Subhash C. Mishra (Indian Institute of Technology Guwahati, India)
(10:15-11:05, November 25, at TACHIBANA)

Progress in Panasonic's R&D of Advanced Photovoltaic Technologies

Shigeo Yata (Panasonic Corporation, Japan)
(11:10-12:00, November 25, at TACHIBANA)

Sessions

General Session:

- GS1: General Session

Organized Sessions:

- OS1: Discussion on Hybrid Rocket Propulsion for the Future Space Utilization Demand
  Organizers: T. Shimada (JAXA), K. Sawada (Tohoku University)

- OS2: Next-Generation CFD
  Organizers: K. Nakahashi (JAXA), S. Obayashi, H. Kobayashi, S. Yamamoto (Tohoku University), D. Sasaki (Kanazawa Institute of Technology), K. Yamamoto (JAXA)

- OS3: Heat and Mass Transfer in Materials Processing
  Organizer: P. Bourgin (INSA de Lyon)

- OS4: Corrosion Problems under Flow in Energy Industries
  Organizers: Y. Watanabe (Tohoku University), B. Normand (INSA de Lyon), T. Shoji (Tohoku University)

- OS5: Global / Local Innovations for Next Generation Automobiles
  Organizers: A. Miyamoto (Tohoku University), P. Kapsa (Ecole Central de Lyon)

- OS6: Smart Fluids and Materials, and Their Applications
  Organizers: M. Nakano (Tohoku University), J. Y. Cavaillé (INSA de Lyon), R. Tao (Temple University)

- OS7: Cutting Edge of Thermal Science and Engineering
  Organizers: S. Maruyama, A. Komiya (Tohoku University)

- OS8: International Symposium on Smart Materials and Structures for Energy Saving
  Organizers: T. Takagi, T. Uchimoto (Tohoku University), J. Y. Cavaillé (INSA de Lyon), C. Boller (Fraunhofer Institute for NDT), J. Qiu (Nanjing University of Aeronautics and Astronautics), Hiroyuki Miki (Tohoku University)

- OS9: International Symposium on Innovative Energy Research
  Organizers: S. Samukawa, K. Maruta (Tohoku University)

- OS10: Advanced Physical Stimuli and Biological Responses
  Organizers: T. Sato (Tohoku University), T. Ohashi (Hokkaido University), S. Kawano (Osaka University), R. Shirakashi (The University of Tokyo)

- OS11: Blood Flow for Medical Equipment
  Organizers: T. Nakayama, M. Ohta (Tohoku University)

- OS12: Basic and Applied Research on Membrane Protein for Health Care
  Organizers: N. Tomita, M. Ohta (Tohoku University)

- OS13: Ninth International Students / Young Birds Seminar on Multi-Scale Flow
  Organizer: T. Okabe (Tohoku University)
  Co-Organizers: T. Mabuchi, K. Kanda (Tohoku University)
  Supervisors: Y. Iga, K. Miyata, H. Shimizu, A. Komiya, K. Sato
  (Tohoku University)

Planned Sessions:
- PS1: IFS Collaborative Research Forum

- PS2: Young Researcher Overseas Visits Program Research Forum

- PS3: Fluids Science Research Award Lecture

Special Session:
- Liaison Office Session

General Information

Registration:
The conference registration desk is located in the lobby, 2nd floor.
8:30 - , Monday, November 25, 2013

8:30 - , Tuesday, November 26, 2013

8:30 - , Wednesday, November 27, 2013

Opening: (at TACHIBANA)
9:00-9:20, Monday, November 25, 2013

Students / Young Birds Friendship Night: (at SAKURA 2)
18:00-20:00, Monday, November 25, 2013
All students and young researchers can attend to Students / Young Birds Friendship Night.

Banquet: (at SAKURA)
18:00 – 20:00, Tuesday, November 26, 2013

Internet access corner
All conference attendees may use internet for free. Free Ethernet access will be possible during the conference at 2nd floor. Standard wired hubs (with RJ45 sockets) will be provided for networking.

Coffee service:
Coffee is served in the lobby, 2nd floor.

ICFD2013 Secretariat:
COE Building, Institute of Fluid Science, Tohoku University
2-1-1, Katahira, Aoba, Sendai, 980-8577, Japan
Phone&Fax: +81-22-217-5301 E-mail: icfd2013@fmail.ifs.tohoku.ac.jp

Floor Plan of Sendai International Center

1st floor (ROOM1, ROOM2, ROOM3)

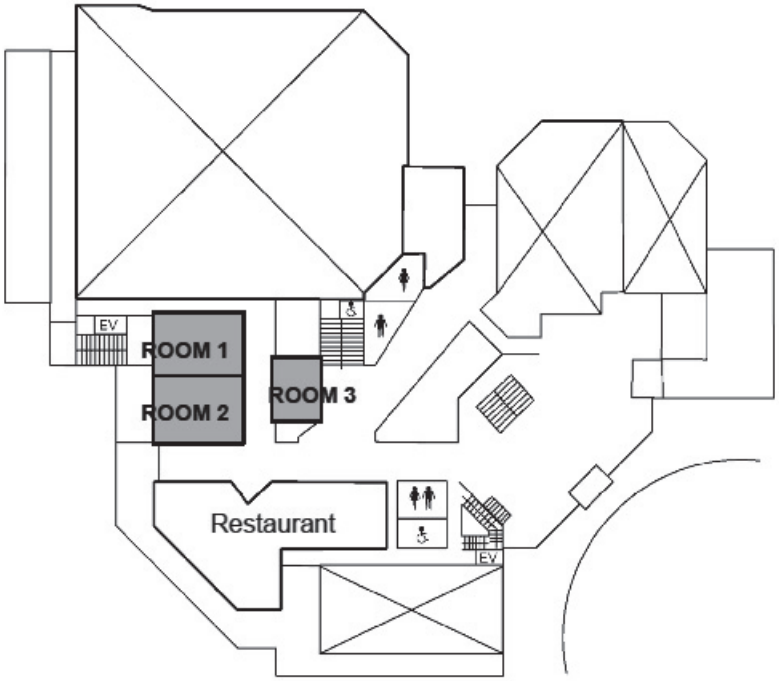

2nd floor (SAKURA, TACHIBANA, HAGI, ROOM4, ROOM5)

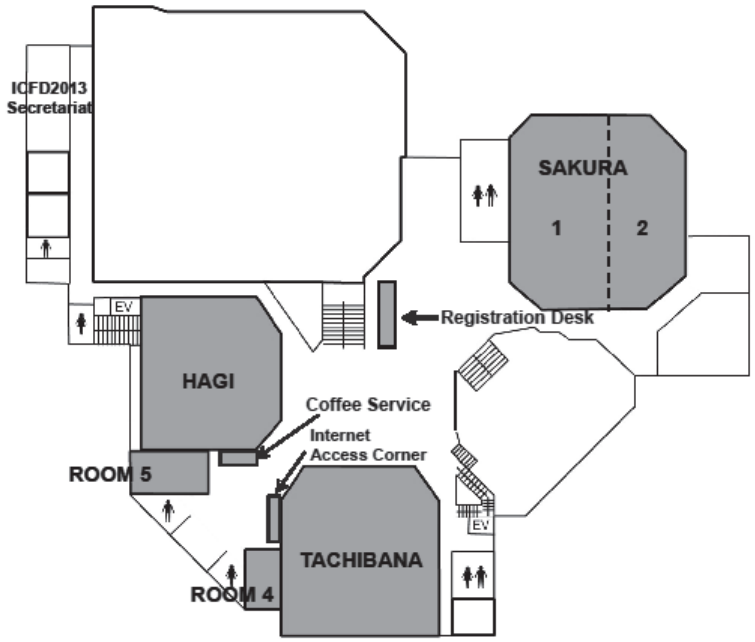

3rd floor (SHIRAKASHI1, SHIRAKASHI2, ROOM6, ROOM7, ROOM8)

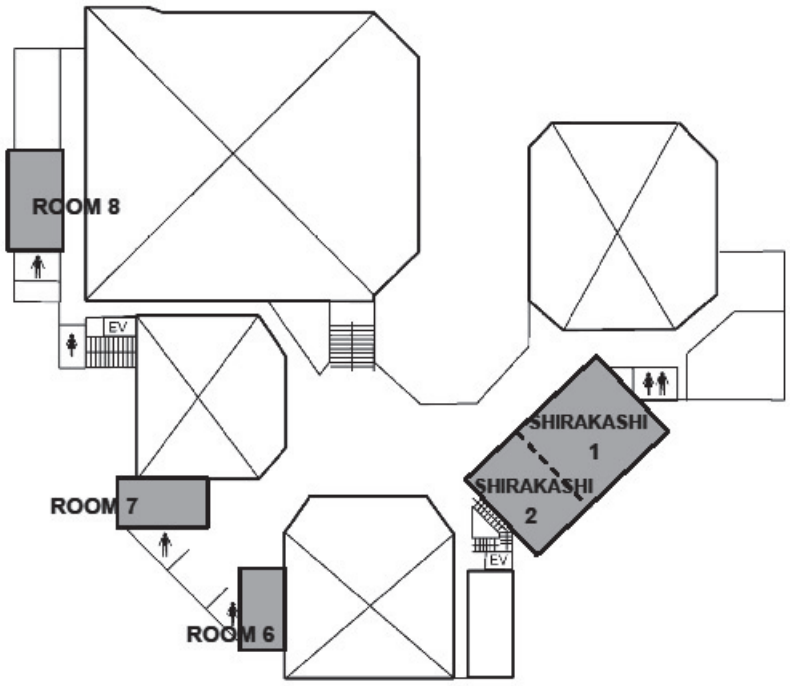

10th ICFD (2013) Time Table

Monday, November 25, 2013

ROOM	SAKURA 2	TACHIBANA	ROOM4	ROOM5	SHIRAKASHI 1	SHIRAKASHI 2	ROOM
Floor	2nd Floor				3rd Floor		Floor
8:00							8:00
9:00	9:00-9:20 **Opening Address** @ TACHIBANA						9:00
9:20	9:20-10:10 **Plenary Lecture** @ TACHIBANA "Fluid Flow in Micron Spaces: Fluid dynamics in Microfluidic Devices" David A. Weitz (Harvard University, USA)						9:20
10:15	BREAK						10:15
	10:15-11:05 **Plenary Lecture** @ TACHIBANA "Porous Media Combustion - Its Potential Applications in Wide Range of Liquid and Gas Fuelled Cooking Stoves" Subhash C. Mishra (Indian Institute of Technology Guwahati, India)						
11:10	BREAK						11:10
	11:10-12:00 **Plenary Lecture** @ TACHIBANA "Progress of Panasonic's R&D on Advanced Photovoltaic Technologies" Shigeo Yata (Panasonic Corporation, Japan)						
12:00							12:00
13:00	OS13: Session 1 13:00-(14:20) OS13-1 - OS13-24 *Short Oral Presentation* (14:20-15:40) OS13-1 - OS13-24 *Poster Presentation*	OS9: Session 1-1 Combustion I 13:00-13:10 Opening Kaoru Maruta 13:10-13:35 OS9-1 Sergey Minaev (Invited) 13:35-14:00 OS9-2 Vladimir Gubernov (Invited) 14:00-14:25 OS9-3 Nichiki Okada (Invited)	OS11: 13:00-13:10 Opening Toshio Nakayama 13:10-13:50 OS11-1 Bastien Chopard (Invited) 13:50-14:10 OS11-2 Canceled 14:10-14:30 OS11-3 Shin-ichiro Sugiyama	GS1: GS-MA 13:00-13:20 GS1-1 Nannan Wu 13:20-13:40 GS1-2 Koji Fukudome 13:40-14:00 GS1-3 Hiroshi Koizumi 14:00-14:20 GS1-4 Koyo Matsuzaki	OS5:Poster room	OS5: 13:00-13:10 Opening Akira Miyamoto and Philipe Kapsa 13:10-13:50 OS5-1 Mark C. Williams 13:50-14:30 OS5-2 Keiji Aoki 14:30-15:10 OS5-3 Kimihiko Nakano	13:00
14:30							14:30
14:40		OS9: Session 1-2 Combusion II 14:40-15:05 OS9-4 Alexander Kirdyashkin (Invited) 15:05-15:30 OS9-5 Aiwu Fan (Invited) 15:30-15:55 OS9-6 Sudarshan Kumar (Invited)	OS11: 14:40-15:20 OS11-4 Takanobu Yagi (Invited) 15:20-15:40 OS11-5 Kenichi Kono 15:40-16:00 OS11-6 Tomo Kinoshita	GS1: GS-MB 14:40-15:00 GS1-5 Masayuki Anyoji 15:00-15:20 GS1-6 Takaaki Tsuchiya 15:20-15:40 GS1-7 Takahiro Makizono 15:40-16:00 GS1-8 Ryota Nakajima	15:10-15:30 BREAK		14:40
16:10					OS5:Poster room	OS5: 15:30-16:10 OS5-4 Katsuhiko Hirose 16:10-16:50 OS5-5 Alexandre Torday 16:50-17:30 OS5-6 Gerd Dobmann 17:30-18:00 OS5-7 Kiyoshi Hasegawa	16:10
16:20		OS9: Session 2-1 Innovative Energy Research I 16:20-16:40 OS9-7 Prashant Nehe 16:40-17:05 OS9-8 Jun Ishimoto (Invited)	OS11: 16:20-17:00 OS11-7 Guy Courbebaisse 17:00-17:15 OS11-8 Sho Matsumoto 17:15-17:35 OS11-9 Kim Hyoung June	GS1: GS-MC 16:20-16:40 GS1-9 Noritaka Yusa 16:40-17:00 GS1-10 Thien Xuan Dinh 17:00-17:20 GS1-11 Kei Fujisawa 17:20-17:40 GS1-12 Sakiko Kitashima			16:20
17:50							17:50
18:00	18:00-20:00 *Studnets / Young Birds Friendship Night*						18:00
20:00							

Tuesday, November 26, 2013

ROOM	ROOM1	ROOM2	SAKURA 2	TACHIBANA	HAGI	ROOM
Floor	1st Floor		2nd Floor			Floor
8:00						
9:00	OS1: 9:00-9:05 Opening Fuel and Combustion 9:05-9:45 OS1-1 Arif Karabeyoglu (Invited) 9:45-10:05 OS1-2 Mario Kobald 10:05-10:25 OS1-3 Ken Terakawa	OS6: 9:00-9:30 OS6-1 Daniel Guyomar (Invited) 9:30-10:00 OS6-2 Jean-Yves Cavaille (Invited) 10:00-10:30 OS6-3 Miklós Zrinyi (Invited)	OS13: Session 2 9:00 - (10:10) OS13-25 - OS13-47 *Short Oral Presentation* (10:10-11:30) OS13-25 - OS13-47 *Poster Presentation*	OS9: Session 2-2 Innovative Energy Research II 9:00-9:25 OS9-9 Tomohiro Kubota (Invited) 9:25-9:50 OS9-10 Yoshinori Mizuno 9:50-10:15 OS9-11 Cheng-Hsun Lin	PS1: 9:00-10:30 CRF-1 - CRF-35 *Short Oral Presentation*	9:00
10:30						10:30
10:40	OS1: Numerical Simulation 10:40-11:00 OS1-4 Guan-Rong Lai 11:00-11:20 OS1-5 Mikiro Motoe 11:20-11:40 OS1-6 Nobuyuki Tsuboi 11:40-12:00 OS1-7 Wei-Hsiang Chao	OS6: 10:40-11:10 OS6-4 Rongjia Tao (Invited) 11:10-11:40 OS6-5 Katsufumi Tanaka (Invited) 11:40-12:00 OS6-6 Masafumi Taniguchi		OS9: Session 3 Energy Nano-Devices (Solar cell, secondary battery, fuel cell, and optimum energy system) 10:40-10:50 Session Opening Seiji Samukawa Energy Nano-Devices 1 - Fuel Cell 10:50-11:20 OS9-12 Shin-ichi Orimo (Invited) 11:20-11:50 OS9-13 Takashi Tokumasu (Invited)	PS1: 10:40-12:10 CRF-36 - CRF-B1 *Short Oral Presentation*	10:40
12:10					PS1: 12:10-13:10 *Lunch and Poster Session*	12:10
13:10	OS1: Conceptual Design 13:10-13:30 OS1-8 Pietro Tadini 13:30-13:50 OS1-9 Yen-Sen Chen 13:50-14:10 OS1-10 Kazuhisa Chiba 14:10-14:30 OS1-11 Fumio Kanamori	OS6: 13:10-13:40 OS6-7 Weihua Li (Invited) 13:40-14:00 OS6-8 Hiroya Abe 14:00-14:20 OS6-9 Ching-Yao Chen 14:20-14:40 OS6-10 Kazuya Takahashi	OS13: Session 3 13:10 - (14:20) OS13-48 - OS13-69 *Short Oral Presentation* (14:20-15:40) OS13-48 - OS13-69 *Poster Presentation*	OS9: Energy Device 2 - Analysis and Secondary Battery 13:10-13:40 OS9-14 Koji Amezawa (Invited) 13:40-14:10 OS9-15 Taro Hitosugi (Invited) 14:10-14:40 OS9-16 Itaru HONMA (Invited)	PS3: 13:10-14:40 *Fluids Science Research Award Lecture* Yasushi Takeda (Swiss Federal Institute of Technology Zurich, Switzerland) Kozo Fujii (Aerosapce Exploration Agency, Japan)	13:10
14:40						14:40
14:50	OS1: Engine Technology 14:50-15:10 OS1-12 Shigeru Aso 15:10-15:30 OS1-13 Yutaka Wada 15:30-15:50 OS1-14 Koki Kitagawa 15:50-16:10 OS1-15 Ando Hideyuki	OS6: 14:50-15:20 OS6-11 Masami Nakano (Invited) 15:20-15:40 OS6-12 Weihua Li 15:40-16:00 OS6-13 Alexander Vasiliev 16:00-16:20 OS6-14 Olga Volkova		OS9: Energy Device 3 - Solar Cell and Optimization Method 14:50-15:20 OS9-17 Seiji Samukawa (Invited) 15:20-15:50 OS9-18 Noritaka Usami (Invited) 15:50-16:20 OS9-19 Shigeru Obayashi (Invited)	PS2: 14:50-15:38 YRF-1 - YRF-6 *Oral Presentation* PS1: 15:40-16:20 CRF-68 - CRF-83 *Short Oral Presentation*	14:50
16:20						16:20
16:30	OS1: HRrWG Activity 16:30-16:50 OS1-16 Toru Shimada 16:50-17:30 *WRAP-UP*			OS8 & OS9 Joint Session 16:30-17:00 OS8-1 Manfred Kohl (Invited) 17:00-17:30 OS8-2 Gerd Dobmann 17:30-18:00 OS8-3 Tomonaga Okabe	PS1: 16:30 - 16:50 CRF-84 - CRF-R3 *Short Oral Presentation* 16:50-18:00 *Poster Session*	16:30
18:00						18:00
	18:00-20:00 Banquet @ SAKURA					
20:00						20:00

ROOM	ROOM4	ROOM5	SHIRAKASHI 1	SHIRAKASHI 2	ROOM6	ROOM8	ROOM
Floor	2nd Floor		3rd Floor				Floor
8:00							
9:00	OS12: 9:00-9:45 OS12-1 Stephan Wilkens (Invited) 9:45-10:30 OS12-2 Keietsu Abe (Invited)	GS1: GS-TA 9:00-9:20 GS1-13 Manish K. Khandelwal 9:20-9:40 GS1-14 Mohd Hazwan bin Yusof 9:40-10:00 GS1-15 Makoto Hirota 10:00-10:20 GS1-16 Yosuke Hirata	OS5: Poster room	OS5: 9:00-12:00 Short Oral Presentations of Poster 3min for Each Academic Presentation (BREAK 10min) 3min for Each Industrial Presentation	OS7: Biological Heat Transfer 9:00-9:20 OS7-1 Koushik Das 9:20-9:40 OS7-2 Miklós Zrínyi 9:40-10:00 OS7-3 Arka Bhowmik 10:00-10:20 OS7-4 Takahiro Okabe		9:00
10:30							10:30
10:40	OS12: 10:40-11:25 OS12-3 Kazushi Kinbara (Invited) 11:25-11:50 OS12-4 Noriko Tomita (Invited) 11:50-12:10 OS12-5 Kenji Etchuya	GS1: GS-TB 10:40-11:00 GS1-17 Fredrik Lundell 11:00-11:20 GS1-18 Yusuke Yamaguchi 11:20-11:40 GS1-19 Takahiro Wako 11:40-12:00 GS1-20 Jong-Wook Lee			OS7: Convective Heat Transfer & Combustion 10:40-11:00 OS7-5 Masaki Hongoh 11:00-11:20 OS7-6 Dmitry Tereshko 11:20-11:40 OS7-7 Shang-Hao Huang 11:40-12:00 OS7-8 Victoria Timchenko		10:40
12:10							12:10
13:10	OS3: 13:10-13:55 OS3-1 Loïc Favergeon (Invited) 13:55-14:40 OS3-2 Oleg P. Solonenko	GS1: GS-TC 13:10-13:30 GS1-21 Ardian B. Gojani 13:30-13:50 GS1-22 Takeshi Osuka 13:50-14:10 GS1-23 Takahiro Imaizumi 14:10-14:30 GS1-24 Yuki Kutsuna	OS5: 13:00-14:30 Poster Presentations	OS5:	OS7: Fluid Dynamics & Measurement 13:10-13:30 OS7-9 Roman Brizitskii 13:30-13:50 OS7-10 Kiran Joy Irimpan, Viren Menezes	Liaison Office Session 13:10-14:40 Chair: Toshiyuki Takagi Toshiya Ueki Alexander Vasiliev Victoria Timchenko Fredrik Lundell Shigenao Maruyama Jeongmin Ahn Marie Pierre Favre Makoto Ohta	13:10
14:40			OS5: Poster room	OS5: 14:30-15:00 OS5-8 Masato Hisatake 15:00-15:40 OS5-9 Erik P. M. Vermeulen 15:40-16:20 OS5-10 Shigeo Kagami			14:40
14:50	OS3: 14:50-15:35 OS3-3 Svetlana N. Sorokova	GS1: GS-TD 14:50-15:10 GS1-25 Ying-Nung Chen 15:10-15:30 GS1-26 Shuang Xia 15:30-15:50 GS1-27 Keiichi Igari 15:50-16:10 GS1-28 Chayut Nuntadusit			OS7: Radiation 14:50-15:10 OS7-11 Adil Al Mahdouri 15:10-15:30 OS7-12 Abid Ustaoglu		14:50
16:20							16:20
16:30		GS1: GS-TE 16:30-16:50 GS1-29 Tomoya Kitamoto 16:50-17:10 GS1-30 Jinuk Kim 17:10-17:30 GS1-31 Kenichi Hoshino 17:30-17:50 GS1-32 Hiromitsu Morita	OS5: Poster room	OS5: 16:30-17:10 OS5-11 Ryuta Kawashima 17:10-17:50 OS5-12 Takeshi Iwatsubo			16:30
18:00							18:00
	18:00-20:00 Banquet @ SAKURA						
20:00							20:00

Wednesday, November 27, 2013

ROOM	ROOM1	ROOM2	ROOM4	ROOM5	SHIRAKASHI 1	SHIRAKASHI 2	ROOM8	ROOM
Floor	1st Floor		2nd Floor		3rd Floor			Floor
8:00								
9:00	OS10: Opening Takehiko Sato 9:00-9:30 OS10-1 Tetsuji Shimizu 9:30-10:00 OS10-2 Toshihiko Shiraishi 10:00-10:30 OS10-3 Makoto Kanzaki	OS2: 9:00-9:15 OS2-1 Pavel Vaschenkov 9:15-9:30 OS2-2 Yen-Sen Chen 9:30-9:45 OS2-3 Cheng-Chin Su 9:45-10:00 OS2-4 Ming-Chung Lo 10:00-10:15 OS2-5 Manuel Diaz 10:15-10:30 OS2-6 Juan-Chen Huang	OS4: 9:30-10:05 OS4-1 Fumio Inada (Invited) 10:05-10:30 OS4-2 Yoichi Utanohara	GS1: GS-WA 9:00-9:20 GS1-33 Hyunmin Choi 9:20-9:40 GS1-34 Chao Man 9:40-10:00 GS1-35 Hidenori Yamada 10:00-10:20 GS1-36 Pavel Vashchenkov	OS5: Poster room	OS5: 9:00-9:30 OS5-13 Noriko Behling 9:30-10:00 OS5-14 Parasuraman Selvam 10:00-10:30 OS5-15 Hiroshi Matsuo	OS8: 9:00-9:30 OS8-4 Alain Combescure (Invited) 9:30-9:50 OS8-5 Jinhao Qiu 9:50-10:10 OS8-6 Masae Kanda 10:10-10:30 OS8-7 Yuta Yamamoto	9:00
10:30								10:30
10:40	OS10: 10:40-11:10 OS10-4 Atsuhiro Nakagawa 11:10-11:40 OS10-5 Hajime Sakakita 11:40-12:10 OS10-6 Toshiro Ohashi	OS2: 10:40-11:25 OS2-7 Jaw-Yen Yang (Invited) 11:25-12:10 OS2-8 Matthias Meinke (Invited)	OS4: 10:40-11:05 OS4-3 Takayuki Yamagata 11:05-11:30 OS4-4 Hiroshi Abe 11:30-11:55 OS4-5 Kengo Saito	GS1: GS-WB 10:40-11:00 GS1-37 Ko-Chun Chiang 11:00-11:20 GS1-38 Hideaki Ogawa 11:20-11:40 GS1-39 Ahmet Berk Kurtulus	OS5: Poster room	OS5: 10:40-11:00 OS5-16 Naruhiko Inayoshi 11:00-11:20 OS5-17 Florian Brémond 11:20-12:00 OS5-18 Reinhard Pfliegl	OS8: 10:40-11:20 OS8-8 Eric Maire (Keynote) 11:20-11:50 OS8-9 Yoshitake Nishi	10:40
12:10								12:10
13:10	OS10: 13:10-13:55 OS10-7 Chwee Teck Lim (Keynote Lecture) 13:55-14:40 OS10-8 Georg Isbary (Keynote Lecture)	OS2: 13:10-13:25 OS2-9 Hiroaki Kobayashi 13:25-13:40 OS2-10 Xinrong Su 13:40-13:55 OS2-11 Chang Luo 13:55-14:10 OS2-12 Shibo Qi 14:10-14:25 OS2-13 Yuma Fukushima 14:25-14:40 OS2-14 Daisuke Sasaki		GS1: GS-WC 13:10-13:30 GS1-40 Tameo Nakanishi 13:30-13:50 GS1-41 Rahul Korah Shaji 13:50-14:10 GS1-42 Masaru Miyashita 14:10-14:30 GS1-43 Koji Abe	OS5: Poster room	OS5: 13:00-13:30 OS5-19 Philipe Kapsa 13:30-14:10 OS5-20 Joachim Knebel 14:10-14:50 OS5-21 Ray Hoemsen	OS8: 13:10-13:40 OS8-10 Fumio Kojima (Invited) 13:40-14:10 OS8-11 Mitsuharu Shiwa 14:10-14:40 OS8-12 Zhenmao Chen	13:10
14:40								14:40
14:50	OS10: 14:50-15:20 OS10-9 Katsuko S Furukawa (Invited) 15:20-15:50 OS10-10 Makoto Ohta (Invited) 15:50-16:05 OS10-11 Osman Omran Osman 16:05-16:20 OS10-12 Kazuhiro Nakamuraya 16:20-16:35 OS10-13 Kentaro Doi	OS2: 14:50-15:05 OS2-15 Keiji Onishi 15:05-15:20 OS2-16 Fang-an Kuo 15:20-15:35 OS2-17 Kun-Rung Huang 15:35-15:50 OS2-18 Ryotaro Sakai 15:50-16:05 OS2-19 Takashi Misaka 16:05-16:20 OS2-20 Kotaro Makino		GS1: GS-WD 14:50-15:10 GS1-44 Bui Vu Hung 15:10-15:30 GS1-45 Saptarshi Basu 15:30-15:50 GS1-46 Hari Krishna Chilukoti 15:50-16:10 GS1-47 Mikael A. Langthjem 16:10-16:30 GS1-48 Visakh Vaikuntanathan	14:50-15:00 BREAK OS5: Poster room	OS5: 15:00-15:20 OS5-22 Neil Cooke 15:20-16:00 OS5-23 Roberto Horowitz Concluding Remarks Akira Miyamoto and Philipe Kapsa	OS8: 14:50-15:20 OS8-13 Yu Fukunishi (Invited) 15:20-15:50 OS8-14 Jun Ishimoto 15:50-16:20 OS8-15 Jinling Zhao	14:50
16:20	Closing Toshiro Ohashi							16:20
16:30		OS2: 16:30-16:45 OS2-21 Takashi Ishida 16:45-17:00 OS2-22 Debasish Biswas 17:00-17:15 OS2-23 Shujie Li					OS8: 16:30-17:00 OS8-16 Hiroyuki Miki (Invited) 17:00-17:30 OS8-17 Julien Fontaine 17:30-18:00 OS8-18 Gábor Vértesy 18:00-18:10 Closing Jean-Yves Cavaillé	16:30
18:00								18:00

Tenth International Conference on Flow Dynamics

Program

Plenary Lectures

TACHIBANA
November 25, 2013

Chair: Rongjia Tao (Temple University, USA)

9:20-10:10 **Fluid Flow in Micron Spaces: Fluid dynamics in Microfluidic Devices** 68
Esther Amstad, David A. Weitz (Harvard University, USA)
(9:20-10:10, November 25 at TACHIBANA)

Chair: Shigenao Maruyama (Tohoku University, Japan)

10:15-11:05 **Porous Media Combustion – Its Potential Applications in Wide Range of Liquid and Gas Fuelled Cooking Stoves** 70
Subhash C. Mishra, P. Muthukumar (Indian Institute of Technology Guwahati, India)
(10:15-11:05, November 25, at TACHIBANA)

Chair: Seiji Samukawa (Tohoku University, Japan)

11:10-12:00 **Progress in Panasonic's R&D of Advanced Photovoltaic Technologies** 72
Shigeo Yata, Akira Terakawa, Masahiro Iseki, Mikio Taguchi, Eiji Maruyama and Makoto Tanaka (Panasonic Corporation, Japan)
(11:10-12:00, November 25, at TACHIBANA)

GS1: General Session

ROOM 5
November 25, 2013

GS-MA
Chair: Atsushi Shirai (Tohoku University, Japan)

14:30-14:40 BREAK

GS-MB
Chair: Daiju Numata (Tohoku University, Japan)

16:10-16:20 BREAK

GS-MC

Chair: Tetsuya Uchimoto (Tohoku University, Japan)

ROOM 5

November 26, 2013

GS-TA

Chair: Fredrik Lundell (Royal Institute of Technology, Sweden)

10:30-10:40 BREAK

GS-TB

Chair: Makoto Hirota (Tohoku University, Japan)

GS1-27 15:30-15:50 **Heat Transfer of Boiling with Magnetically Driving Metallic Powder in Liquid** 128
Keiichi Igari, Yuki Chinone and Naoki Ono (Shibaura Institute of Technology, Japan)

GS1-28 15:50-16:10 **Heat Transfer Characteristics of Impinging Jet from Pipe Nozzle with Vortex Generators** 130
Chayut Nuntadusit, Burin Kaewkraikrong, Konlawat Songkaor and Makatar Wae-hayee (Prince of Songkla University, Thailand)

16:20-16:30 BREAK

GS-TE
Chair: Mingyu Sun (Tohoku University, Japan)

GS1-29 16:30-16:50 **The Added Mass of Three-Dimensional Basic Bodies in Viscous Fluid** 132
Tomoya Kitamoto (Doshisha University, Japan), Hirochika Tanigawa (Maizuru National College of Technology, Japan), Hideki Shimohara (Doshisha International High School, Japan) and Katsuya Hirata (Doshisha University, Japan)

GS1-30 16:50-17:10 **Effect of Near-wall Modeling on Aero-Thermal Characteristics of High Pressure Turbine Nozzle** 134
Jinuk Kim, Jueong Gyu Bak (Hanyang University, Korea), Dong-Ho Rhee (Korea Aerospace Research Institute, Korea), Leesang Cho (Hansung University, Korea) and Jinsoo Cho (Hanyang University, Korea)

GS1-31 17:10-17:30 **Reactive Viscous Fingering Involving Production of Gel** 136
Kenichi Hoshino, Yuichiro Nagatsu (Tokyo University of Agriculture and Technology, Japan)

GS1-32 17:30-17:50 **Estimation of Stagnant Gas Temperature of Cold Spray using Outer Surface Metal Temperature of the Nozzle Throat** 138
Hiromitsu Morita, Hiroshi Katanoda (Kagoshima University, Japan)

ROOM 5
November 27, 2013

GS-WA
Chair: Hideaki Ogawa (RMIT University, Australia)

GS1-33 9:00-9:20 **Aerodynamic Analysis of Blended Wing Body Business Jet** 140
Hyunmin Choi, Seawook Lee and Jinsoo Cho (Hanyang University, Korea)

GS1-34 9:20-9:40 **Numerical Study of the Vehicle Aerodynamic Performance During Acceleration and Deceleration** 142
Chao Man, Chenguang Lai and Kaiping Wen (Chongqing University of Technology, China)

GS1-35 9:40-10:00 **PIV Flowfield Measurements around a Flapping Wing Object with Feathering Motion** 144
Hidenori Yamada, Yuya Fujii, Ryoma Hashiguchi and Wataru Yamazaki (Nagaoka University of Technology, Japan)

GS1-36 **Numerical Study of High-Altitude Aerothermodynamics of the RAM-C II** 146
10:00-10:20 **Hypersonic Flight Experiment**
Pavel Vashchenkov, Yevgeniy Bondar, Alexander Shevyrin (Khristianovich Institute of Theoretical and Applied Mechanics, SB RAS, Russia), Shigeru Yonemura (Tohoku University, Japan) and Mikhail Ivanov (Khristianovich Institute of Theoretical and Applied Mechanics, SB RAS, Russia)

10:30-10:40 BREAK

GS-WB

Chair: Pavel Vashchenkov (Khristianovich Institute of Theoretical and Applied Mechanics, SB RAS, Russia)

GS1-37 **The Study of Asymmetric Flows in Constricted Microchannel with PSP** 148
10:40-11:00 **Technique**
Ko-Chun Chiang, Yuan-Wei Wang, Ying-Hsuan Chen (National Tsing Hua University, Taiwan), Hsiang-Yu Wang (National Cheng Kung University, Taiwan) and Chih-Yung Huang (National Tsing Hua University, Taiwan)

GS1-38 **Numerical Investigation of Mach Reflection Hysteresis in Stunted Busemann** 150
11:00-11:20 **Intakes for Axisymmetric Scramjet Engines**
Hideaki Ogawa (RMIT University, Australia), Sannu Mölder (Ryerson
. University, Canada) and Evgeny V. Timofeev (McGill University, Canada)

GS1-39 **Investigation of Gas Injector Effect on Two-Phase Flow** 152
11:20-11:40 Ahmet Berk Kurtulus (Marmara University, Turkey), Nurdil Eskin and Emrah Deniz (Istanbul Technical University, Turkey)

12:10-13:10 LUNCH

GS-WC

Chair: Chih-Yung Huang (National Tsing Hua University, Taiwan)

GS1-40 **A Novel Pumping Mechanism of Using Ultrasound Induced Pressure and** 154
13:10-13:30 **Cavitations**
Tameo Nakanishi, Yuki Numazawa (Yamagata University, Japan)

GS1-41 **Effect of Relative Drain Port Size on Vortex Formation in Cylindrical Tanks** 156
13:30-13:50 Rahul Korah Shaji, Raghavan Ajith Kumar, Ambattu Raghavan Srikrishnan (AMRITA University, India) and Pulikkotil Joseph Joshy (CUSAT, India)

GS1-42 **Numerical Plasma Simulation for Reactive Plasma Deposition Equipment with** 158
13:50-14:10 **Multi Gun**
Masaru Miyashita, Hisashi Kitami, Toshiyuki Sakemi, Yasushi Aoki and Takanori Kato (SUMITOMO HEAVY Industries, Ltd., Japan)

GS1-43 **Quenching and Absorption of Toluene-LIF by Acetone** 160
14:10-14:30 Koji Abe, Tomoya Maruyama (Tohoku University, Japan), Toshinori Kouchi (Okayama University, Japan), Goro Masuya and Keisuke Asai (Tohoku University, Japan)

14:40-14:50 BREAK

GS-WD

Chair: Koji Fukudome (Ritsumeikan University, Japan)

OS1: Discussion on Hybrid Rocket Propulsion for the Future Space Utilization Demand

ROOM 1
November 26, 2013

9:00-9:05 **Opening**

Fuel and Combustion
Chair: Toru Shimada (Japan Aerospace Exploration Agency, Japan)

10:30-10:40 BREAK

Numerical Simulation
Chair: Shigeru Aso (Kyushu University, Japan)

12:10-13:10 LUNCH

Conceptual Design

Chair: Saburo Yuasa (Tokyo Metropolitan University, Japan)

OS1-8 13:10-13:30 — **Multi-Active Removal of Large Abandoned Rocket Bodies by Hybrid Propulsion Module** — 188

Pietro Tadini (Politecnico di Milano, Italy), Urbano Tancredi (University of Naples "Parthenope", Italy), Michele Grassi (University of Naples "Federico II", Italy), Luciano Anselmo, Carmen Pardini (ISTI-Consiglio Nazionale delle Ricerche, Italy), Francesco Branz, Alessandro Francesconi (University of Padua, Italy), Filippo Maggi, Michèle Lavagna, Luigi T. DeLuca (Politecnico di Milano, Italy), Nicole Viola, Sergio Chiesa (Politecnico di Torino, Italy), Valery Trushlyakov (Omsk State Technical University, Russia) and Toru Shimada (Japan Aerospace Exploration Agency, Japan)

OS1-9 13:30-13:50 — **Suborbital Flight Experiments Using Hybrid Rocket Propulsion** — 190

Yen-Sen Chen (Hsinchu Science Park, Taiwan), Alfred Lai, Tzu-Hao Chou, Jong-Shinn Wu (National Chiao Tung University, Taiwan) and Bill Wu (Hsinchu Science Park, Taiwan)

OS1-10 13:50-14:10 — **Conceptual Design of Single-Stage Hybrid Rocket in View of Implication of Fuels** — 192

Kazuhisa Chiba (Hokkaido Institute of Technology, Japan), Masahiro Kanazaki (Tokyo Metropolitan University, Japan), Masaki Nakamiya (Kyoto University, Japan), Koki Kitagawa and Toru Shimada (Japan Aerospace Exploration Agency, Japan)

OS1-11 14:10-14:30 — **Conceptual Design: Dependence of Parameterization on Design Performance of Three Stage Hybrid Rocket** — 194

Fumio Kanamori, Yosuke Kitagawa (Tokyo Metropolitan University, Japan), Masaki Nakamiya (Kyoto University, Japan), Koki Kitagawa (Japan Aerospace Exploration Agency, Japan), Masahiro Kanazaki (Tokyo Metropolitan University, Japan) and Toru Shimada (Japan Aerospace Exploration Agency, Japan)

14:40-14:50 BREAK

Engine Technology

Chair: Keisuke Sawada (Tohoku University, Japan)

OS1-12 14:50-15:10 — **Enhancement of Higher Regression Rate and Combustion Efficiency of Hybrid Rocket Engines by with Multi-Section Swirl Injection Method** — 196

Shigeru Aso, Yasuhiro Tani, Sho Ohyama, Kentaro Araki, Kengo Ohe, Hiroshi Tada, Kengo Mizuchi, Hiroshi Hirayama (Kyushu University, Japan) and Toru Shimada (Japan Aerospace Exploration Agency, Japan)

OS1-13 15:10-15:30 — **Study on Mechanical Property of Low Melting Temperature Thermoplastic Fuel** — 198

Yutaka Wada, Keisuke Seki (Akita University, Japan), Nobuji Kato (Katazen Corporation, Japan) and Keiichi Hori (Japan Aerospace Exploration Agency, Japan)

OS1-14 15:30-15:50 **Development of GOX Hybrid Rocket Test Engine Facility in Hybrid Rocket Research Working Group** 200

Koki Kitagawa, Toru Shimada, Keiichi Hori, Toshiaki Takemae, Noriko Shiraishi, Toshio Tomizawa, Naohiro Suzuki, Tsuyoshi Yagishita (Japan Aerospace Exploration Agency, Japan), Nobuyuki Oshima, Harunori Nagata, Masashi Wakita (Hokkaido University, Japan), Kazuhisa Chiba (Hokkaido Institute of Technology, Japan), Keisuke Sawada, Hiroki Nagai (Tohoku University, Japan), Yutaka Wada (Akita University, Japan), Saburo Yuasa, Takashi Sakurai, Masahiro Kanazaki (Tokyo Metropolitan University, Japan), Ichiro Nakagawa, Takakazu Morita (Tokai University, Japan), Masaki Nakamiya (Kyoto University, Japan), Shigeru Aso, Yasuhiro Tani (Kyushu University, Japan) and Nobuyuki Tsuboi (Kyushu Institute of Technology, Japan)

OS1-15 15:50-16:10 **Development of a 5 kN-thrust Swirling-Oxidizer-Flow-Type Hybrid Rocket Engine** 202

Ando Hideyuki, Sakurai Takashi, Yuasa Saburo, Hatagaki Sakashi (Tokyo Metropolitan University, Japan), Yui Ryosuke (The University of Tokyo, Japan), Takahashi Shun (Tokyo Metropolitan University, Japan), Shiraishi Noriko, Kitagawa Koki and Shimada Toru (Japan Aerospace Exploration Agency, Japan)

16:20-16:30 BREAK

HRrWG Activity

Chair: Keisuke Sawada (Tohoku University, Japan) & Toru Shimada (Japan Aerospace Exploration Agency, Japan)

OS1-16 16:30-16:50 **Status Summary of FY 2012 Hybrid Rocket Research Working Group** 204

Toru Shimada (Japan Aerospace Exploration Agency, Japan)

16:50-17:30 **【WRAP-UP】**

OS2: Next-Generation CFD

ROOM 2
November 27, 2013

Chair: Shigeru Obayashi (Tohoku University, Japan)

10:30-10:40 BREAK

Chair: Kazuhiro Nakahashi (Japan Aerospace Exploration Agency, Japan)

OS2-7 10:40-11:25 **Computations of Rarefied Gas Flows Using Semi-classical Boltzmann-ES-BGK Equation *(Invited)*** 220
Jaw-Yen Yang, Chin-Yuan Yan, Manuel Diaz (National Taiwan University, Taiwan) and Juan-Chen Huang (National Taiwan Ocean University, Taiwan)

OS2-8 11:25-12:10 **A Hierarchical Data Structure for Multi-Physics Problems *(Invited)*** 222
Matthias Meinke, Gonzalo Brito Gadeschi, Lennart Schneiders and Wolfgang Schröder (RWTH Aachen University, Germany)

12:10-13:10 LUNCH

Chair: Satoru Yamamoto (Tohoku University, Japan)

OS2-9 13:10-13:25 **Design of the Next-Generation Vector Architecture for Postpeta-Scale CFD** 224
Kazuhiko Komatsu, Ryusuke Egawa, Hiroyuki Takizawa (Tohoku University / Japan Science and Technology Agency, Japan), Takashi Soga (NEC System Technologies, Ltd., Japan), Akihiro Musa (NEC Corporation, Japan) and Hiroaki Kobayashi (Tohoku University, Japan)

OS2-10 13:25-13:40 **Extending the Building Cube Method to Curvilinear Mesh with Adaptive Mesh Refinement** 226
Xinrong Su, Satoru Yamamoto (Tohoku University, Japan) and Kazuhiro Nakahashi (Japan Aerospace Exploration Agency, Japan)

OS2-11 13:40-13:55 **Numerical Investigation on Flow Characteristics and Aerodynamic Losses of Compound Angle Film Cooling Jets** 228
Chang Luo, Takashi Misaka, Shigeru Obayashi (Tohoku University, Japan), Takashi Goto and Ruriko Yamawaki (IHI Corporation, Japan)

OS2-12 13:55-14:10 **Numerical Simulation of Supercritical-fluid Flows around Complex Geometry based on SFS+BC** 230
Shibo Qi, Kotaro Makino, Takashi Furusawa and Satoru Yamamoto (Tohoku University, Japan)

OS2-13 14:10-14:25 **Computation of the Forward Fan Noise Shielding by the Building-Cube Method** 232
Yuma Fukushima, Shigeru Obayashi (Tohoku University, Japan), Daisuke Sasaki (Kanazawa Institute of Technology, Japan) and Kazuhiro Nakahashi (Japan Aerospace Exploration Agency, Japan)

OS2-14 14:25-14:40 **Cartesian-based CFD Solver for Low-Reynolds Number Airfoils** 234
Daisuke Sasaki, Yuya Kojima, Tatsuya Kuroda, Takeshi Akasaka, Masato Okamoto (Kanazawa Institute of Technology, Japan), Koji Shimoyama and Shigeru Obayashi (Tohoku University, Japan)

14:40-14:50 BREAK

Chair: Daisuke Sasaki (Kanazawa Institute of Technology, Japan)

OS2-15 14:50-15:05 **Enhancement of Wall Boundary Condition for Dirty CAD on Building Cube Method based Immersed Boundary** 236
Keiji Onishi, Makoto Tsubokura (RIKEN, Japan)

OS3: Heat and Mass Transfer in Materials Processing

ROOM 4
November 26, 2013

Chair: Hidemasa Takana (Tohoku University, Japan)

14:40-14:50 BREAK

Chair: Loïc Favergeon (Ecole Nationale Supérieure des Mines, France)

OS4: Corrosion Problems under Flow in Energy Industries

ROOM 4
November 27, 2013

Chair: Yutaka Watanabe (Tohoku University, Japan)

10:30-10:40 BREAK

Chair: Yoichi Utanohara (Institute of Nuclear Safety System, Inc., Japan)

OS5: Global / Local Innovations for Next Generation Automobiles

SHIRAKASHI 2
November 25, 2013

13:00-13:10	**Opening** Akira Miyamoto and Philipe Kapsa	
OS5-1 13:10-13:50	**Convergence of Transportation and Energy in the Future** Mark C. Williams (URS, USA)	276
OS5-2 13:50-14:30	**Research and development of fully automated vehicles** Keiji Aoki (Japan Automobile Research Institute, Japan)	278
OS5-3 14:30-15:10	**Human Factor Research Using a Driving Simulator** Kimihiko Nakano (The University of Tokyo, Japan)	280
15:10-15:30	BREAK	
OS5-4 15:30-16:10	**Vehicle Innovations Bring Regional Community into the New Age** **Fuel Cell Vehicle and Hydrogen Move to the 2015 Introduction** Katsuhiko Hirose (Toyota Motor Corporation, Japan)	282
OS5-5 16:10-16:50	**Research and Development of Transport Simulation** Alexandre Torday (Transport Simulation Systems, Australia)	
OS5-6 16:50-17:30	**NDT-Innovations In The Automotive Industrial Sector And To Light-Weight Materials** Gerd Dobmann (Fraunhofer-IZFP, Germany)	284
OS5-7 17:30-18:00	**Compact-Sizing of Optical Topography Technology (NIRS)** Kiyoshi Hasegawa (Hitachi Ltd., Japan)	286

SHIRAKASHI 2
November 26, 2013

9:00-12:00	**Short Oral Presentations of Poster** **3min for Each Academic Presentation** (BREAK 10min) **3min for Each Industrial Presentation**
12:00-12:50	**LUNCH**

SHIRAKASHI 1
November 26, 2013

13:00-14:30	**Poster Presentations**	288

SHIRAKASHI 2
November 26, 2013

OS5-8 14:30-15:00	**Understanding the Triple Helix Model and the Finance of Innovation** Masato Hisatake (Tohoku University, Japan)	398
OS5-9 15:00-15:40	**Understanding the Triple Helix Model and the Finance of Innovation** Erik P. M. Vermeulen (Tilburg University, The Netherlands)	400
OS5-10 15:40-16:20	**Innovation, University Entrepreneurship and the Role of Triple Helix** Shigeo Kagami (The University of Tokyo, Japan)	
16:20-16:30	BREAK	
OS5-11 16:30-17:10	**Can Functional Brain Imaging Prompt Innovations in Next-generation Automobiles?** Ryuta Kawashima (Tohoku University, Japan)	402
OS5-12 17:10-17:50	**Alzheimer's disease: from pathology to therapeutics** Takeshi Iwatsubo (The University of Tokyo, Japan)	404

SHIRAKASHI 2
November 27, 2013

OS5-13 9:00-9:30	**Japanese Low Emission Vehicle (LEV) Policy** **A Successful Strategy to Achieve Global Leadership in Next Generation Vehicles (NGV)** Noriko Behling (Author, USA)	406
OS5-14 9:30-10:00	**NH_3-DeNO_x Performance of the Composite [Fe-Beta + Fe(Mn)MCM-48] Catalyst: Combining SCR Activity and NH_3 Oxidation Activity for NH_3 Slip Removal** Alexandr Yu. Stakheev, Dmitry A. Bokarev, Alina I. Mytareva (N. D. Zelinsky Institute of Organic Chemistry, Russia), Rajesh Kumar Parsapur and Parasuraman Selvam (Indian Institute of Technology Madras, India)	408
OS5-15 10:00-10:30	**Li-ion Battery Module for Small Electric Vehicles** Hiroshi Matsuo (Micro Vehicle Lab. Ltd., Japan)	410
10:30-10:40	BREAK	
OS5-16 10:40-11:00	**Research and Development of Tribological Techniques for Automotive Parts** Naruhiko Inayoshi, Keiji Sasaki and Ryoichi Hombo (DENSO Corporation, Japan)	412

OS5-17 11:00-11:20	**Starved Lubrication: Contribution of Laser Surface Micro-Texturing** Florian Brémond (IREIS, France), Denis Mazuyer (Ecole Centrale de Lyon, France), Philippe Maurin-Perrier (IREIS, France) and Juliette Cayer-Barrioz (Ecole Centrale de Lyon, France)	414
OS5-18 11:20-12:00	**Traffic Management Future** Reinhard Pfliegl (A3PS, Austria)	416
12:00-12:50	LUNCH	
OS5-19 13:00-13:30	**Tribology for the Future: Biomimetism and Surface Engineering** Philippe Kapsa (Ecole Centrale de Lyon, Fracne)	418
OS5-20 13:30-14:10	**Synthetic Biofuels From Biomass** Joachim Knebel, Nicolaus Dahmen and Jörg Sauer (Karlsruhe Institute of Technology, Germany)	420
OS5-21 14:10-14:50	**VEHICLE TECHNOLOGY & ENERGY CENTRE** **Canadian Applied Research Experience at Red River College** Ray Hoemsen (Red River College of Applied Arts, Science and Technology, Canada)	422
14:50-15:00	BREAK	
OS5-22 15:00-15:20	**RED RIVER COLLEGE VEHICLE TECHNOLOGY & ENERGY CENTER** **Applied Research Project Selection: "Student & Staff Centered"** Neil Cooke (Red River College of Applied Arts, Science and Technology, Canada)	424
OS5-23 15:20-16:00	**Modeling, Simulation, Analysis and Control of Freeway Traffic Corridors** Roberto Horowitz (University of California, USA)	
	Concluding Remarks Akira Miyamoto and Philipe Kapsa	

OS6: Smart Fluids and Materials, and Their Applications

ROOM 2
November 26, 2013

Chair: Masami Nakano (Tohoku University, Japan)

10:30-10:40 BREAK

Chair: Weihua Li (University of Wollongong, Australia)

12:10-13:10 BREAK

Chair: Rongjia Tao (Temple University, USA)

OS7: Cutting Edge of Thermal Science and Engineering

ROOM 6
November 26, 2013

Biological Heat Transfer
Chair: Victoria Timchenko (The University of New South Wales, Australia)

OS7-1 9:00-9:20 — **Non-Invasive Detection of Breast Tumor using Curve Fitting Technique** — 458
Koushik Das, Subhash C. Mishra (Indian Institute of Technology Guwahati, India)

OS7-2 9:20-9:40 — **Magnetic Hyperthermia and Heat Conduction in Polymer Gels** — 460
Attila Borsos, Rita A. Bauer, Zsófia Varga, Jedlovszky-Hajdú Angéla and Miklós Zrínyi (Semmelweis University, Hungary)

OS7-3 9:40-10:00 — **Thermal Imaging and Screening of Subsurface Cancer during Thermal Recovery after Cold Stress** — 462
Arka Bhowmik, Ramjee Repaka (Indian Institute of Technology Ropar, India) and Subhash C. Mishra (Indian Institute of Technology Guwahati, India)

OS7-4 10:00-10:20 — **An Experimental Comparison between Thermal Diffusivity and Blood Perfusion Rate of Living and Dead Tissue by Inverse Analysis** — 464
Takahiro Okabe, Junnosuke Okajima (Tohoku University, Japan), Yun Luo, Fang Wang (Shanghai Jiao Tong University, China), Atsuki Komiya (Tohoku University, Japan), Ichiro Takahashi (Yamagata University, Japan) and Shigenao Maruyama (Tohoku University, Japan)

10:20-10:40 BREAK

Convective Heat Transfer & Combustion
Chair: Wu-Shung Fu (National Chiao Tung University, Taiwan)

OS7-5 10:40-11:00 — **Large Eddy Simulation of Turbulent Non-premixed Flame Using OpenFOAM** — 466
Masaki Hongoh, Kazui Fukumoto and Yoshifumi Ogami (Ritsumeikan University, Japan)

OS7-6 11:00-11:20 — **Boundary Heat Flux Estimation for the Heat Convection Flow Using the Velocity Field Data** — 468
Gennady Alekseev, Dmitry Tereshko (Institute of Applied Mathematics FEB RAS / Far Eastern Federal University, Russia)

OS7-7 11:20-11:40 — **Natural Convection between Vertical Parallel Plates with Asymmetric Heating** — 470
Shang-Hao Huang, Wu-Shung Fu and Chung-Jen Chen (National Chiao Tung University, Taiwan)

OS7-8 11:40-12:00 — **Synthetic Jets at Low Stokes Number: Numerical and Experimental Approach** — 472
Isaac Ng, Victoria Timchenko, John Reizes (The University of New South Wales, Australia), Zdenek Travnicek, Jozef Kordik, Zuzana Brouckova (Academy of Sciences of the Czech Republic, Czech Republic)

12:10-13:10 LUNCH

Fluid Dynamics & Measurement

Chair: Atsuki Komiya (Tohoku University, Japan)

14:40-14:50 BREAK

Radiation

Chair: Subhash C. Mishra (Indian Institute of Technology Guwahati, India)

OS8: International Symposium on Smart Materials and Structures for Energy Saving

TACHIBANA
November 26, 2013

ROOM 8
November 27, 2013

OS8-10 13:10-13:40	**Reliability Assessment for Pipe Elbows with Local Wall Pinning using Guided Wave Testing *(Invited)*** Fumio Kojima, Jyunko Hioki, Hiroyuki Nakamoto (Kobe University, Japan) and Hideo Nishino (University of Tokushima, Japan)	502
OS8-11 13:40-14:10	**Non-destructive Materials Reliability Evaluation for Cu-alloy of Combustion Chamber** Mitsuharu Shiwa, Donfeng He, Yoshinori Ono, Masao Hayakawa (National Institute for Materials Science, Japan), Hideo Sunakawa, Naoki Nagao, Sinich Moriya Eiichi Sato (Japan Aerospace Exploration Agency, Japan), Tetsuya Uchimoto and Toshiyuki Takagi (Tohoku University, Japan)	504
OS8-12 14:10-14:40	**Evaluation of Cavity Defect in Metallic Foam with DCPD Method** Zhenmao Chen (Xi'an Jiaotong University, China), Shejuan Xie (Tohoku University, Japan), Xiaojuan Wang (Xi'an Jiaotong University, China), Tetsuya Uchimoto and Toshiyuki Takagi (Tohoku University, Japan)	506
14:40-14:50	BREAK	
OS8-13 14:50-15:20	**Flow Control Attempts Using Smart Materials *(Invited)*** Yu Fukunishi, Seiichiro Izawa (Tohoku University, Japan)	508
OS8-14 15:20-15:50	**The Supercomputing of Fluid and Structure Interaction Caused by Natural Disasters** Jun Ishimoto (Tohoku University, Japan)	510
OS8-15 15:50-16:20	**Reconstruction of Stiffness Coefficients in Orthotropic Plates Based on Lamb Waves Phase Velocities using Genetic Algorithm** Jinling Zhao, Jinhao Qiu and Hongli Ji (Nanjing University of Aeronautics and Astronautics, China)	512
16:20-16:30	BREAK	
OS8-16 16:30-17:00	**Development of the Functional Hard Carbon Coating for Machine and Structural Materials *(Invited)*** Hiroyuki Miki, Takanori Takeno, Hiroyuki Kosukegawa and Toshiyuki Takagi (Tohoku University, Japan)	514
OS8-17 17:00-17:30	**Promoting Energy-saving with Diamond-Like Carbon Coatings: Solid Lubrication Processes** Julien Fontaine (Ecole Centrale de Lyon, France), Hiroyuki Miki, Takanori Takeno (Tohoku University, Japan), Thierry Le Mogne, Sandrin Bec, Michel Belin, (Ecole Centrale de Lyon, France), Koshi Adachi and Toshiyuki Takagi (Tohoku University, Japan)	516
OS8-18 17:30-18:00	**Nondestructive characterization of flake graphite cast iron by Magnetic Adaptive Testing** Gábor Vértesy (Institute of Technical Physics and Materials Science, Hungary), Tetsuya Uchimoto, Toshiyuki Takagi (Tohoku University, Japan) and Ivan Tomáš (Academy of Sciences of the Czech Republic, Czech Republic)	518
18:00-18:10	**Closing** J. Y. Cavaillé (INSA Lyon, France)	

OS9: International Symposium on Innovative Energy Research

TACHIBANA
November 25, 2013

Session 1-1 Combustion I
Chair: Kaoru Maruta (IER, IFS, Tohoku University, Japan)

13:00-13:10 **Opening**
Kaoru Maruta (IER, IFS, Tohoku University, Japan)

OS9-1 13:10-13:35 **On the Path to Effective Energy Production by Heat and Mass Return Combustion Technologies *(Invited)*** 522
Sergey Minaev (Far-Eastern Federal University, Russia), Kaoru Maruta (Tohoku University, Japan)

OS9-2 13:35-14:00 **Modelling Hydrogen-Air Flames With Reduced Two-Step Kinetic Mechanisms *(Invited)*** 524
Vladimir Gubernov (P. N. Lebedev Physical Institute of the Russian Academy of Sciences, Russia)

OS9-3 14:00-14:25 **Experimental and Numerical Investigation of CH4/CO2/O2 Laminar Inverse Diffusion Flames *(Invited)*** 526
Nichiki Okada, Shuhei Yoneyama, Tomohiro Yamanaka, Toshihisa Ueda and Takeshi Yokomori (Keio University, Japan)

14:30-14:40 BREAK

Session 1-2 Combustion II
Chair: Hisashi Nakamura (IER, IFS, Tohoku University, Japan)

OS9-4 14:40-15:05 **SHS Materials Radiative Porous Burners *(Invited)*** 528
Alexander Kirdyashkin, Anatoly Maznoy, Alexander Gushin (Tomsk Scientific Center SB RAS, Russia) and Sergey Minaev (Far-Eastern Federal University, Russia)

OS9-5 15:05-15:30 **Flame Stabilization In A Mesoscale Bluff Body Combustor *(Invited)*** 530
Aiwu Fan, Jianlong Wan, Hong Yao and Wei Liu (Huazhong University of Science and Technology, China)

OS9-6 15:30-15:55 **Formation of Spinning Flames in Stepped Tube Combustors *(Invited)*** 532
Upendra W. Taywade, Anil A Deshpance and Sudarshan Kumar (Indina Institute of Technology Bombay Powai, India)

16:10-16:20 BREAK

Session 2-1 Innovative Energy Research I
Chair: Takeshi Yokomori (Keio University, Japan)

OS9-7 16:20-16:40 **Numerical Study of Methanol Reformation from a Single Channel with Cavities Integrated with a Micro-combustor** 534
Prashant Nehe, Sudarshan Kumar (Indian Institute of Technology Bombay, India)

TACHIBANA
November 26, 2013

Session 2-2 Innovative Energy Research Ⅱ
Chair: Jun Ishimoto (IER, IFS, Tohoku University, Japan)

10:30-10:40 BREAK

Session 3 Energy Nano-Devices
(Solar cell, secondary battery, fuel cell, and optimum energy system)

10:40-10:50 **Session Opening**
Activity of Core Technology Consortium for Advanced Energy Devices in Tohoku University
Seiji Samukawa (IFS and WPI-AIMR, Tohoku University, Japan)

Energy Nano-Devices 1 – Fuel Cell
Chair: Takeo Ohno (WPI-AIMR, Tohoku University, Japan)

Energy Device 2 – Analysis and Secondary Battery
Chair: Akio Higo (WPI-AIMR, Tohoku University, Japan)

OS10: Advanced Physical Stimuli and Biological Responses

ROOM 1
November 27, 2013

Opening
Takehiko Sato (Tohoku University, Japan)

Chair: Satoyuki Kawano (Osaka University, Japan)

OS10-1 9:00-9:30 — **Effect on microorganisms by cold atmospheric plasmas** — 562
Tetsuji Shimizu, Julia L. Zimmermann, Gregor E. Morfill (Max-Planck Institute for extraterrestrial physics, Germany), Georg Isbary and Wilhelm Stolz (General Hospital Munich Schwabing, Germany)

OS10-2 9:30-10:00 — **Effects of Mechanical Vibration on Cell Proliferation and Differentiation** — 564
Toshihiko Shiraishi, Shin Morishita (Yokohama National University, Japan)

OS10-3 10:00-10:30 — **Muscle Contractile Activity and Its Beneficial Effects in Type 2 Diabetes** — 566
Makoto Kanzaki (Tohoku University, Japan)

10:30-10:40 BREAK

Chair: Toshihiko Shiraishi (Yokohama National University, Japan)

OS10-4 10:40-11:10 — **Pulsed-Liquid Jet Surgical Device: Evolution from Shock Bubble Interaction to Clinical Application** — 568
Atsuhiro Nakagawa, Kiyonobu Ohtani, Yoshikazu Ogawa, Toshiki Endo, Masaki Iwasaki, Kuniyasu Niizuma (Tohoku University, Japan), Tatsuhiko Arafune (Tokyo Denki University, Japan), Toshikatsu Washio (National Institute of Advanced Industrial Science and Technology, Japan), Takashi Kato (The University of Tokyo, Japan), Daisuke Kudo, Takashi Irinoda, Chikashi Nakanishi, Tadashi Sakurai, Yoshihiro Kamiyama, Chiaki Sato, Masato Yamada, Toru Nakano, Shinichi Yamashita, Tomoyuki Suzuki, Yuji Tanaka, Naoyuki Takagi, Yoshimichi Imai, Yoshihiro Hagiwara, Hiroshi Kunikata, Shunsuke Kawamoto and Teiji Tominaga (Tohoku University, Japan)

OS10-5 11:10-11:40 — **Introduction of Medical Plasma Equipment for the Minimally Invasive Treatment** — 570
Hajime Sakakita (AIST / University of Tsukuba, Japan), Yuzuru Ikehara, Jaeho Kim (AIST, Japan), Nobuyuki Shimizu (Sanno Hospital, Japan), Sanae Ikehara (AIST, Japan), Hayao Nakanishi (Aichi Cancer Center Research Institute, Japan), Hiromasa Yamada, Yusuke Yamagishi (University of Tsukuba, Japan), Satoru Kiyama, Akiko Kubota (AIST, Japan), Masao Ichinose (Wakayama Medical University, Japan) and Toru Niwa (Hashimoto Municipal Hospital, Japan)

OS10-6 11:40-12:10 — **Novel Experimental System for Applying Cyclic Tensile Strain and Fluid Shear Stress to Tenocytes** — 572
Toshiro Ohashi, Yasufumi Hagiwara (Hokkaido University, Japan), James HC Wang (The University of Pittsburgh, USA) and Eijiro Maeda (Hokkaido University, Japan)

Chair: Toshiro Ohashi (Hokkaido University, Japan)

OS10-7 13:10-13:55 **Modes of Collective Cell Migration arising from Physical Constraints *(Keynote Lecture)*** 574
Chwee Teck Lim (National University of Singapore, Singapore)

Chair: Takehiko Sato (Tohoku University, Japan)

OS10-8 13:55-14:40 **Cold Atmospheric Plasmas in Medicine *(Keynote Lecture)*** 576
Georg Isbary (Hospital Schwabing, Germany), Tetsuji Shimizu, Julia Zimmermann, Gregor Morfill (Max Planck Institute for extraterrestrial physics, Germany) and Wilhelm Stolz (Hospital Schwabing, Germany)

14:40-14:50 BREAK

Chair: Makoto Kanzaki (Tohoku University, Japan)

OS10-9 14:50-15:20 **The Scaffold-free Cartilage Tissue by Mechanical Stress Loading for Tissue Engineering *(Invited)*** 578
Katsuko S Furukawa, Masashi Yoshimoto and Takashi Ushida (The University of Tokyo, Japan)

OS10-10 15:20-15:50 **Optimized Stent *(Invited)*** 580
Makoto Ohta, Hitomi Anzai, Toshio Nakayama, Xiaobo Han and Noriko Tomita (Tohoku University, Japan)

Chair: Daisuke Yoshino (Tohoku University, Japan)

OS10-11 15:50-16:05 **Computational Fluid Dynamics Modeling of Micro-Vibrating Flow Pumps** 582
Osman Omran Osman, Satoyuki Kawano (Osaka University, Japan)

OS10-12 16:05-16:20 **Sterilization of Bacterial Spores by Atmospheric Pressure Plasma** 584
Kazuhiro Nakamuraya, Daisuke Yoshino, Tomoki Nakajima and Takehiko Sato (Tohoku University, Japan)

OS10-13 16:20-16:35 **Dynamics and Self-Assembled Pattern Formation of Short DNA Fragments** 586
Kentaro Doi, Ryosuke Nii, Hiroshi Takeuchi and Satoyuki Kawano (Osaka University, Japan)

Closing

Toshiro Ohashi (Hokkaido University, Japan)

OS11: Blood Flow for Medical Equipment

ROOM 4
November 25, 2013

13:00-13:10 **Opening**
Toshio Nakayama (Tohoku University, Japan)

Chair: Toshio Nakayama (Tohoku University, Japan) & Guy Courbebaisse (INSA Lyon, France)

OS11-1 13:10-13:50 **Modeling Thrombosis In Cerebral Aneurysms *(Invited)*** 590
Bastien Chopard, Orestis Malaspinas and Jonas Latt (University of Geneva, Switzerland)

OS11-2 13:50-14:10 **Canceled**

OS11-3 14:10-14:30 **Stagnant Blood Flow in Intracranial Aneurysms: A Possible Association with Atherosclerosis** 592
Shin-ichiro Sugiyama, Toshio Nakayama, Kenichi Funamoto, Daichi Suzuki, Kuniyasu Niizuma, Makoto Ohta and Teiji Tominaga (Tohoku University, Japan)

14:30-14:40 BREAK

Chair: Makoto Ohta (Tohoku University, Japan) & Bastien Chopard (University of Geneva, Switzerland)

OS11-4 14:40-15:20 **Investigation of the relationship between hemodynamics and pathology in cerebral aneurysms *(Invited)*** 594
Takanobu Yagi, Yuki Iwabuchi, Yasutaka Tobe, Mitsuo Umezu (Waseda University, Japan), Yoshifumi Hayashi, Hirota Yoshida, Kazutoshi Nishitani, Yoshifumi Okada and Shigemi Kitahara (Kitahara International Hospital, Japan)

OS11-5 15:20-15:40 **Hemodynamic and Clinical Study of Y-stents for Treatment of Cerebral Aneurysms** 596
Kenichi Kono, Tomoaki Terada (Wakayama Rosai Hospital, Japan)

OS11-6 15:40-16:00 **Development of a new catheter with innovative concepts for selective venous sampling-preliminary study** 598
Tomo Kinoshita, Kazumasa Seiji, Masashi Otake, Makoto Ohta (Tohoku University, Japan) and Kwon Guiryong (Terumo clinical supply Co., Japan)

16:10-16:20 BREAK

Chair: Toshio Nakayama (Tohoku University, Japan) & Takanobu Yagi (Waseda University, Japan)

OS12: Basic and Applied Research on Membrane Protein for Health Care

ROOM 4
November 26, 2013

Chair: Makoto Ohta (Tohoku University, Japan)

10:30-10:40 BREAK

Chair: Noriko Tomita (Tohoku University, Japan)

OS13: The Ninth International Students / Young Birds Seminar on Multi-Scale Flow

SAKURA 2
November 25, 2013

Session 1
13:00-(14:20) **Short Oral Presentation**
3 min for Short Oral Presentation without PC preparation

SAKURA 2
November 26, 2013

Session 2
9:00-(10:10) **Short Oral Presentation**
3min for Short Oral Presentation without PC preparation

PS1: IFS Collaborative Research Forum

HAGI
November 26, 2013

Chair: Kiyonobu Ohtani (Tohoku University, Japan)
9:00-10:30 **Short Oral Presentation**
(2.5 min for Short Oral Presentation)

CRF-1 **Study on Flight Stability of Badminton Shuttlecock for Impulsive Change of Angle of Attack**
Kenichi Nakagawa, Hiroaki Hasegawa (Akita University, Japan), Masahide Murakami (University of Tsukuba, Japan) and Shigeru Obayashi (Tohoku University, Japan)

CRF-2 **Enhancement of the Airfoil Using Active Control of Boundary Layer**
Shuko Ito, Hiroaki Hasegawa, Tetsuya Miyakoshi (Akita University, Japan) and Shigeru Obayashi (Tohoku University, Japan)

CRF-3 **Flow Instabilities of Boiling Nitrogen in a Horizontal Pipe**
Hisatoshi Watanabe, Katsuhide Ohira, Kazushi Miyata, Koichi Takahashi (Tohoku University, Japan), Hiroaki Kobayashi, Hideyuki Taguchi, Motoyuki Hongoh and Takayuki Kojima (Japan Aerospace Exploration Agency, Japan)

CRF-4 **Pressure Drop of Vapor-Liquid Two-Phase Nitrogen Flow in a Corrugated Pipe**
Hisatoshi Watanabe, Katsuhide Ohira, Kazushi Miyata, Koichi Takahashi (Tohoku University, Japan), Hiroaki Kobayashi, Hideyuki Taguchi, Motoyuki Hongo and Takayuki Kojima (Japan Aerospace Exploration Agency, Japan)

CRF-5 **Fundamental Study of Air-Leakage Detection System for Space-Debris Impact using Mechanochromism Metal Complex**
Kakeru Nemoto, Ryo Takahashi, Kiyonobu Ohtani and Kanjuro Makihara (Tohoku University, Japan)

CRF-6 **Toward Numerical Simulation of Jet-Wake Vortex Interaction**
Takashi Misaka, Shigeru Obayashi (Tohoku University, Japan), Anton Stephan, Frank Holzäpfel and Thomas Gerz (Deutsches Zentrum für Luft- und Raumfahrt, Germany)

CRF-7 **Thermal Effects in Bubble Clouds of Cavitation**
Kazuki Niiyama (Kanazawa Institute of Technology, Japan), Yuka Iga (Tohoku University, Japan)

CRF-8 **Unsteady Fluid Dynamic Forces measurements on Airfoils with Heaving and Feathering Oscillations at Very Low Reynolds Number**
Tatsuya Kuroda, Masato Okamoto, Daisuke Sasaki, Takeshi Akasaka (Kanazawa Institute of Technology, Japan), Koji Shimoyama and Shigeru Obayashi (Tohoku University, Japan)

CRF-9 **Numerical Investigation of Ionization and Radiation Processes in Rarefied Reentry Flows**
Alexander Shevyrin, Mikhail Ivanov, Yevgeniy Bondar, Pavel Vashchenkov (Khristianovich Institute of Theoretical and Applied Mechanics SB RAS, Russia) and Shigeru Yonemura (Tohoku University, Japan)

CRF-10 **Shock Tube Measurements of Precursor Radiation ahead of Hypersonic Shock Waves**
Shota Ago, Gouji Yamada, Makoto Setou, Hiromitsu Kawazoe (Tottori University, Japan) and Shigeru Obayashi (Tohoku University, Japan)

CRF-11 **Application of a Sensitivity -Adjustable Three Component Force Balance to a Silent Supersonic Biplane Model**
Singo Imagawa, Katsuyuki Inoue, Gouji Yamada, Hiromitsu Kawazoe (Tottori University, Japan) and Shigeru Obayashi (Tohoku University, Japan)

CRF-12 **Design Exploration for the Next Generation High Wing Aircraft**
Akihiro Hashimoto (Tohoku University, Japan), Shinkyu Jeong (Kyunghee University, Korea) and Shigeru Obayashi (Tohoku University, Japan)

CRF-13 **EVOLVE: A Linked Visualization Environment for Explanatory Variables and Objective Function of Optimization Problems**
Takayuki Itoh, Maki Kubota (Ochanomizu University, Japan), Shigeru Obayashi and Yuriko Takeshima (Tohoku University, Japan)

CRF-14 **Reconstruction of Wall Thinning from Pulsed Eddy Current Testing Signals**
Zhenmao Chen (Xi'an Jiaotong University, China), Shejuan Xie, Tetsuya Uchimoto and Toshiyuki Takagi (Tohoku University, Japan)

CRF-15 **Numerical Simulation Research of External Flow Field on Ahmed Model**
Chenguang Lai, Xun Liu, Chao Man and Yuting Zhou (Chongqing University of Technology, China)

CRF-16 **Simulation analysis on grain boundaries thought relation between Cr depletion distribution and local magnetic properties**
Kenichi Terasima, Suzuki Kenji, Yamaguchi Katsuhiko (Fukushima University, Japan), Tetsuya Uchimoto and Toshiyuki Takagi (Tohoku University, Japan)

CRF-17 **Mass and Heat Diffusion Through Nano-Structured Surfaces**
Gary Rosengarten (Royal Melbourne Institute of Technology University / The University of New South Wales, Australia), Thilaksiri Bandara, Clifford Shum, Mostafa Kahini (Royal Melbourne Institute of Technology University, Australia) and Anggito Tetuko (The University of New South Wales, Australia)

CRF-18 **Numerical Study of Natural Convection in a Tilted Cubical Cavity: Effect of the Prandtl Number on the Stability of the Flow**
Juan F. Torres (Tohoku University, Japan / École Centrale de Lyon, France), Daniel Henry (École Centrale de Lyon, France), Atsuki Komiya, Junnosuke Okajima and Shigenao Maruyama (Tohoku University, Japan)

CRF-19 **Investigation of Subsonic-Supersonic Hybrid-Stabilized Argon-Water Electric Arc With Inhomogeneous Mixing of Plasma Species: Parametric Numerical Study of Turbulence**
Jiří Jeništa (Institute of Plasma Physics AS CR, Czech Republic), Hidemasa Takana, Hideya Nishiyama (Tohoku University, Japan), Milan Hrabovský and Tetyana Kavka (Institute of Plasma Physics AS CR, Czech Republic)

CRF-20 **Kinetics of Excited States and Radicals in a Nanosecond Pulse Discharge and Afterglow in Nitrogen and Air**
Ivan Shkurenkov, David Burnette, Walter R. Lempert, Igor V. Adamovich (The Ohio State University, USA), Hidemasa Takana and Hideya Nishiyama (Tohoku University, Japan)

CRF-21 **Researches on a Sensing-Based Dynamic Forced Ventilation Control of Leaking Hydrogen**
Kazuo Matsuura (Ehime University, Japan), Masami Nakano and Jun Ishimoto (Tohoku University, Japan)

CRF-22 **The Effects of the Unburned-Gas Temperature on the Hydrodynamic Instability of Three-Dimensional Premixed Flames**
Takuto Yanagioka, Wataru Yamazaki (Nagaoka University of Technology, Japan), Hideaki Kobayashi (Tohoku University, Japan) and Satoshi Kadowaki (Nagaoka University of Technology, Japan)

CRF-23 **Ignition Studies of Gaseous Pre-mixtures in Array of Large-scale Vorticities**
Roman Fursenko, Sergey Minaev, Evgeniy Sereshchenko (Far Eastern Federal University / ITAM SB RAS, Russia), Shenqyang Shy (National Central University, Taiwan), Kaoru Maruta and Hisashi Nakamura (Tohoku University, Japan)

CRF-24 **Blast Pressure Mitigation by Water around a Subsurface Magazine**
Tomohiro Tanaka, Akiko Matsuo (Keio University, Japan), Shigeru Obayashi and Kiyonobu Ohtani (Tohoku University, Japan)

CRF-25 **In-situ Measurement of Upward/Downward Radiative Heat Flux in Earth's Atmosphere**
Noboru Yamada, Takanori Yoshida (Nagaoka University of Technology, Japan), Junnosuke Okajima and Shigenao Maruyama (Tohoku University, Japan)

CRF-26 **On Dynamic Processes in Porous Energy Releasing Objects with Partial Closure of the Object's Outlet**
Nickolay A. Lutsenko (IACP FEB RAS / Far Eastern Federal University, Russia)

CRF-27 **Effect of the Pits Size on Nucleate Pool Boiling Heat Transfer and Critical Heat Flux of Liquid Nitrogen on the Surfaces with Small Triangular Pits**
Kazushi Miyata, Katsuhide Ohira (Tohoku University, Japan) and Hideo Mori (Kyushu University, Japan)

CRF-28 **Optimization of Artificial small Islands Arrangement for Tsunami Diminishing using Design Exploration**
Fumiya Togashi (SAIC, USA), Shinkyu Jeong (Tohoku University, Japan) and Rainald Lohner (George Mason University, USA)

CRF-29 **In-depth Investigation of Twinkling Sign: Optical Observation of Ultrasound Radiation Force Driven Oscillation of Glass Particle**
Lei Liu (GE Healthcare Japan Corporation, Japan), Kenichi Funamoto (Tohoku University, Japan), Masayuki Tanabe (Kumamoto University, Japan) and Toshiyuki Hayase (Tohoku University, Japan)

CRF-30 **Cardiac Evaluation of Fetal Mice by ECG and Ultrasound**
Takuya Ito, Kenichi Funamoto, Rika Sugibayashi, Kiyoe Funamoto, Clarissa Velayo, Miyuki Endo, Yupeng Dong, Toshiyuki Hayase and Yoshitaka Kimura (Tohoku University, Japan)

CRF-31 **Numerical simulation of ultrasound imaging for detection of microcalcification in soft tissue**
Masayuki Tanabe, Eiji Tagomori (Kumamoto University, Japan), Lei Liu (GE Healthcare Japan Corporation, Japan), Kenichi Funamoto (Tohoku University, Japan), Masahiko Nishimoto (Kumamoto University, Japan) and Toshiyuki Hayase (Tohoku University, Japan)

CRF-32 **Bactericidal Effect of Plasma Discharge against Biofilm-producing Pseudomonas aeruginosa on Contact Lenses**
Yoshihisa Nakano (Tohoku University, Japan), Shigeru Fujimura (Tohoku University / Tohoku Pharmaceutical University, Japan), Takehiko Sato and Daisuke Yoshino (Tohoku University, Japan)

CRF-33 **Characteristics of Non-equilibrium Plasma Flow for Viral Inactivation**
Yuji Kudo, Michiko Okamoto, Daisuke Yoshino, Takehiko Sato, Akira Suzuki and Hitothi Oshitani(Tohoku University, Japan)

CRF-34 **Endothelial cell orientation under uniform spatial gradient in fluid shear stress**
Daisuke Yoshino (Tohoku University, Japan), Naoya Sakamoto (Kawasaki University of Medical Welfare, Japan) and Masaaki Sato (Tohoku University, Japan)

CRF-35 **Flow Formation in Atmospheric Plasma Discharge between Pin Electrode and Water Surface**
Tetsuji Shimizu, Gregor E. Morfill (Max-Planck Institute for extraterrestrial physics, Germany), Naoya Kishimoto, Masashi Hara, Daisuke Yoshino and Takehiko Sato (Tohoku University, Japan)

10:30-10:40 BREAK

Chair: Hidemasa Takana (Tohoku University, Japan)
10:40-12:10 **Short Oral Presentation**
(2.5 min for Short Oral Presentation)

CRF-36 **Mechanism of Blast-induced Traumatic Brain Injury**
Atsuhiro Nakagawa, Kiyonobu Ohtani (Tohoku University, Japan), Keisuke Goda, Tatsuhiko Arafune (The University of Tokyo, Japan), Toshikatsu Washio (National Institute of Advanced Industrial Science and Technology, Japan), Toshiyuki Hayase and Teiji Tominaga (Tohoku University, Japan)

CRF-37 **Attenuation and Reduction Effect of Underwater Explosion by Porous Materials**
Kazutaka Kitagawa (Aichi Institute of Technology, Japan), Kiyonobu Ohtani (Tohoku University, Japan)

CRF-38 **Biological Actuation with the Magnetic Stimulation**
Hitoshi Mori (IFG Corporation, Japan), Toshiyuki Takagi, Shinichi Izumi, Hiroyasu Kanetaka (Tohoku University, Japan), Kazumi Mori, Kenji Yashima, Risa Sasaki and Toshihiko Abe (IFG Corporation, Japan)

CRF-39 **Research Friction and Drilling on Bio-composite Model**
Makoto Ohta, Kei Ozawa (Tohoku University, Japan), Vincent Fridrici and Philippe Kapsa (École Centrale de Lyon, France)

CRF-40 **Development of a Program for Blood flow and Cell Behaviors Based on LBM Method**
Makoto Ohta (Tohoku University, Japan), Bastien Chopard (Geneva University, Switzerland) and Hitomi Anzai (Tohoku University, Japan)

CRF-41 **Channel Properties of Membrane Proteins on Lipid Bilayers**
Makoto Ohta (Tohoku University, Japan), Liviu Movileanu (Syracuse University, USA) and Noriko Tomita (Tohoku University, Japan)

CRF-42 **Hemodynamic Analysis of Sidewall Type Intracranial Aneurysms**
Shin-ichiro Sugiyama, Toshio Nakayama, Makoto Ohta and Teiji Tominaga (Tohoku University, Japan)

CRF-43 **Evaluation of Intracranial Aneurysm Rupture Using MR-Measurement-Integrated Simulation**
Shin-ichiro Sugiyama (Kohnan Hospital, Japan), Kenichi Funamoto, Daichi Suzuki, Toshiyuki Hayase and Teiji Tominaga (Tohoku University, Japan)

CRF-44 **Toward Development of a Forensic Visualization Lifecycle Management System**
Issei Fujishiro, Kazuhide Ueda (Keio University, Japan), Xiaoyang Mao, Masahiro Toyoura, Atsushi Sugiura (University of Yamanashi, Japan), Yuriko Takeshima and Toshiyuki Hayase (Tohoku University, Japan)

CRF-45 **Observation of Hypoxia Cellular Response by using Microfluidic Devices**
Shuichiro Fukushima, Reiko Maehara (Osaka University, Japan) and Kenichi Funamoto (Tohoku University, Japan)

CRF-46 **Effects of Temporal and Spatial Oxygen Heterogeneity on Cell Processes**
Kenichi Funamoto (Tohoku University, Japan), Ioannis K. Zervantonakis (Harvard Medical School, USA), Kiyoe Funamoto, Takuya Ito, Yoshitaka Kimura (Tohoku University, Japan) and Roger D. Kamm (Massachusetts Institute of Technology, USA)

CRF-47 **Hyperthermia Treatment of Lung Cancer using Laser and Inhalable Nanoparticles**
Rupesh Singh (Indian Institute of Technology Guwahati, India), Junnosuke Okajima (Tohoku University, Japan), Subhash C. Mishra (Indian Institute of Technology Guwahati, India), Shigenao Maruyama (Tohoku University, Japan) and Ujjal Barman (Indian Institute of Technology Guwahati, India)

CRF-48 **Photoconductivity Decay and Carrier Lifetime in Silicon Nanodisk Array Structure Fabricated by Using Bio-templates and Neutral Beam Etching**
Daisuke Ohori, Atsuhiko Fukuyama (University of Miyazaki, Japan), Seiji Samukawa (Tohoku University / Japan Science and Technology Agency, Japan) and Tetsuo Ikari (University of Miyazaki, Japan)

CRF-49 **Intelligent Information Processing Circuits Using Nanodisk Array Structure**
Takashi Morie, Takashi Tohara (Kyushu Institute of Technology, Japan), Kazuhiko Endo (National Institute of Advanced Industrial Science and Technology, Japan), Makoto Igarashi and Seiji Samukawa (Tohoku University, Japan)

CRF-50 **Double-Dot Si Single-Electron Transistor with Tunable Coupling Capacitance**
Takafumi Uchida, Masashi Arita (Hokkaido University, Japan), Akira Fujiwara (NTT Corporation, Japan), Seiji Samukawa (Tohoku University, Japan) and Yasuo Takahashi (Hokkaido University, Japan)

CRF-51 **Fabrication of InAs Qantum Dots on Nitrided GaAs (001) Surface**
Toshiyuki Kaizu, Takashi Kita(Kobe University, Japan)

CRF-52 **Fabrication of Advanced CMOS Transistors**
Kazuhiko Endo (National Institute of Advanced Industrial Science and Technology, Japan), Seiji Samukawa (Tohoku University, Japan)

CRF-53 **Thermal Resistance between Nano-Structured Surfaces and Liquids**
Masahiko Shibahara (Osaka University, Japan), Taku Ohara and Gota Kikugawa (Tohoku University, Japan)

CRF-54 **Computational Study of Bubble Behavior in Semiconductor Cleaning**
Naoya Ochiai, Jun Ishimoto (Tohoku University, Japan) and Jin-Goo Park (Hanyang University, Korea)

CRF-55 **Visualized Propagation Process of Positive Primary Streamers in Water**
Hidemasa Fujita (Tohoku University, Japan), Seiji Kanazawa (Oita University, Japan), Kiyonobu Ohtani, Atsuki Komiya and Takehiko Sato (Tohoku University, Japan)

CRF-56 **Trimming of Silicon Optical Waveguide by Neutral Beam Oxidation**
Jingnan Cai (The University of Tokyo, Japan), Tomohiro Kubota, Seiji Samukawa (Tohoku University, Japan) and Kazumi Wada (The University of Tokyo, Japan)

CRF-57 **Viscosity Effects on Shock Wave Propagation in Microchannels**
Georgy Shoev, Yevgeniy Bondar (Khristianovich Institute of Theoretical and Applied Mechanics, Russia), Kaoru Maruta (Tohoku University, Japan) and Mikhail Ivanov (Khristianovich Institute of Theoretical and Applied Mechanics, Russia)

CRF-58 **Solution Particle Process Using Advanced Hybrid Plasma Flow System**
Juyong Jang, Hidemasa Takana (Tohoku University, Japan), Yasutaka Ando (Ashikaga Institute of Technology, Japan), Oleg P. Solonenko (Khristianovich Institute of Theoretical and Applied Mechanics, SB RAS, Russia) and Hideya Nishiyama (Tohoku University, Japan)

CRF-59 **Effect of Titanium Content Ration on Mechanical properties of Ti/Al Composite Material Formed by Compression Shearing Method at Room Temperature**
Shota Sakagami, Masaomi Horita, Noboru Nakayama (Shinshu University, Japan), Hiroyuki Miki, Toshiyuki Takagi (Tohoku University, Japan) and Hiroyuku Takeishi (Chiba Institute of Technology, Japan)

CRF-60 **Beam Studies of Plasma Surface Interaction**
Kazuhiro Karahashi, Satoshi Hamaguchi (Osaka University, Japan) and Seiji Samukawa (Tohoku University, Japan)

CRF-61 **Study of The Mechanism of Contact Alignment for The Slider Specimen of Tribometer**
Minoru Goto (Ube National College of Technology, Japan), Toshiyuki Takagi (Tohoku University, Japan), Kosuke Ito (Nihon University, Japan), Takanori Takeno and Hiroyuki Miki (Tohoku University, Japan)

CRF-62 **Development of Bio-template Process for Etching Mask of 2D Dispersive Nanoparticle Array**
Ichiro Yamashita (Nara Institute of Science and Technology, Japan), Rikako Tsukamoto (Tohoku University, Japan), Naofumi Okamoto, Ryouta Matsuyama (Nara Institute of Science and Technology, Japan), Yosuke Tamura and Seiji Samukawa (Tohoku University, Japan)

CRF-63 **Construction of Interaction Model for Dissipative Particle Dynamics Method Based on Molecular Dynamics Simulation**
Yuta Yoshimoto, Ikuya Kinefuchi, Toshiki Mima (The University of Tokyo, Japan), Akinori Fukushima, Takashi Tokumasu (Tohoku University, Japan) and Shu Takagi (The University of Tokyo, Japan)

CRF-64 **A Molecular Dynamics Study on the Thermodynamic and Transport Properties of Liquid Hydrogen**
Hiroki Nagashima, Takashi Tokumasu (Tohoku University, Japan), Shin-ichi Tsuda (Shinshu University, Japan), Nobuyuki Tsuboi (Kyushu Institute of Technology, Japan), Mitsuo Koshi (Yokohama National University, Japan) and A. Koichi Hayashi (Aoyama Gakuin University, Japan)

CRF-65 **Quantum Molecular Analysis For The Deposition Process Of SiC Substrate**
Rieko Sudo, Kenichi Kanna (Sagamihara Incubation Center, Japan) and Takashi Tokumasu (Tohoku University, Japan)

CRF-66 **Numerical Study of High-Speed Condensable Vapor Flow with LDI Erosion**
Jun Ishimoto (Tohoku University, Japan), Guanghao Wu (Soft Flow Co., Ltd., Japan) and Kazuo Matsuura (Ehime University, Japan)

CRF-67 **Ultra-High Heat Flux Cooling Characteristics of Cryogenic Micro-Solid Nitrogen Particles**
Jun Ishimoto, Naoya Ochiai (Tohoku University, Japan) and Kozo Saito (University of Kentucky, USA)

CRF-B1 **Frontier Science of Next Generation Reactive Fluid**
Jun Ishimoto, Kaoru Maruta and Takehiko Sato (Tohoku University, Japan)

12:10-13:10 **Lunch and Poster Session**

Chair: Shigeru Yonemura (Tohoku University, Japan)

15:40-16:20 **Short Oral Presentation**
(2.5 min for Short Oral Presentation)

CRF-68 **Transport Phenomena of Substances in Electrolyte of Solid Oxide Fuel Cell**
Takashi Tokumasu (Tohoku University, Japan), Jeongmin Ahn (Syracuse University, USA)

CRF-69 **Momentum Transport Characteristics in a Water Liquid Bridge between Si Surfaces**
Takashi Tokumasu (Tohoku University, Japan), Marie-Helene Meurisse, Nicolas Fillot and Philippe Vergne (INSA-Lyon, France)

CRF-70 **Development and Micro-Channel Flow Evaluation of Electro-Rheological Nano-Suspensions**
Katsufumi Tanaka, Seiya Robson, Wataru Nakano, Haruki Kobayashi, Ryuichi Akiyama (Kyoto Institute of Technology, Japan), Masami Nakano and Atsushi Totsuka (Tohoku University, Japan)

CRF-71 **Development of a Micro-motor for MEMS Utilizing Novel Electroactive Polymer Fabricated by Photolithography**
Miklós Zrínyi, Rita Bauer (Semmelweis University, Hungary), Loránd Kelemen (Hungarian Academy of Sciences, Hungary) and Masami Nakano (Tohoku University, Japan)

CRF-72 **On Hydrogen Generation by the Collapse of Cavitation Bubbles**
Takehiko Sato (Tohoku University, Japan), Marc Tinguely (Swiss Federal Institute of Technology Lausanne, Switzerland), Masanobu Oizumi (Tohoku University, Japan) and Mohamed Farhat (Swiss Federal Institute of Technology Lausanne, Switzerland)

CRF-73 **Analysis of Plasma-generated Bubbles by Electron Microscope**
Takehiko Sato (Tohoku University, Japan), Takashi Miyahara (Shizuoka University, Japan) and Tatsuyuki Nakatani (Toyo Advanced Technologies Co. Ltd., Japan)

CRF-74 **The Continuous Spectrum in the Moore-Saffman-Tsai-Windnall Instability**
Yuji Hattori, Makoto Hirota (Tohoku University, Japan) and Stefan G. Llewellyn Smith (University of California at San Diego, USA)

CRF-75 **A Numerical Study of the Effect of Large Deformations of a Trailing Vortex on Its Breakdown**
Naoya Takahashi (Tokyo Denki University, Japan), Takeshi Miyazaki (University of Electro-Communications, Japan), Nozomu Hatakeyama and Yuji Hattori (Tohoku University, Japan)

CRF-76 **Effects of External Disturbances on Spatial Development of Turbulence and toward the Control of Thermo-Fluid Dynamics (Cases of Boundary Layer and Jets)**
Kouji Nagata, Yasuhiko Sakai (Nagoya University, Japan), Toshiyuki Hayase (Tohoku University, Japan), Osamu Terashima, Nannan Wu, Shuang Xia, Tomoaki Watanabe, Yasumasa Ito, Zhou Yi and Akihiro Sasoh (Nagoya University, Japan)

CRF-77 **Researches on the Suppression Control of Hole Tone Phenomena**
Kazuo Matsuura (Ehime University, Japan), Masami Nakano (Tohoku University, Japan)

CRF-78 **Generation Mechanism of Rising Film Flow along the Rotating Conical Outer Surface and the Subsequent Atomization Characteristics**
Keisuke Matsuda, Takahiro Adachi (Akita University, Japan), Junnosuke Okajima (Tohoku University, Japan) and Takeshi Akinaga (Aston University, UK)

CRF-79 **A View On Kinetic Force Method From Two-Particle Kinetic Equation**
Vladimir Saveliev (National Center of Space Researches and Technologies, Kazakhstan), Svetlana Filko (Zhetysu State University, Kazakhstan) and Shigeru Yonemura (Tohoku University, Japan)

CRF-80 **Numerical and Experimental Research on Active Control of Self-Sustained Flow Oscillations with Sound Interaction**
Mikael A. Langthjem (Yamagata University, Japan), Masami Nakano (Tohoku University, Japan)

CRF-81 **Study on Flow-induced Vibration of Soft Fins**
Akira Rinoshika (Yamagata University, Japan), Masami Nakano (Tohoku University, Japan)

CRF-82 **Modeling of Heat Flow and Entropy Change at Martensitic Transformations in the Framework of Landau Theory**
Anna Kosogor (Institute of Magnetism, Ukraine), Vladimir Khovaylo (National University of Science and Technology "MISiS", Russia), Hiroyuki Miki and Toshiyuki Takagi (Tohoku University, Japan)

CRF-83 **Stability Analysis of Vortices with Axial Flow based on Energetics and its Application**
Yasuhide Fukumoto (Kyushu University, Japan), Yuji Hattori (Tohoku University, Japan)

16:20-16:30 BREAK

Chair: Kennichi Funamoto (Tohoku University, Japan)
16:30-16:50 **Short Oral Presentation**
(2.5 min for Short Oral Presentation)

CRF-84 **Oscillating Flow of Magnetic Fluid between Two Parallel Plates**
Masahide Ito, Seiichi Sudo (Akita Prefectural University, Japan) and Hideya Nishiyama (Tohoku University, Japan)

CRF-85 **Viscoelastic Properties of MR Shear Thickening Fluids**
Weihua Li (University of Wollongong, Australia), Masami Nakano (Tohoku University, Japan)

CRF-86 **Particle structural formations of colloidal MR fluid and their influences on magnetic rheological response**
Hiroya Abe (Osaka University, Japan), Masami Nakano (Tohoku University, Japan)

CRF-R1 **Supercomputing and Scale Modeling of Flotsam Mixed Tsunami**
Jun Ishimoto (Tohoku University, Japan), Kozo Saito (University of Kentucky, USA)

CRF-R2 **Flammability Limits of Low-Lewis-number premixed Flames**
Sergey Minaev (Far Eastern Federal University, Russia), Kaoru Maruta (Tohoku University, Japan), Roman Fursenko (ITAM SB RAS, Russia), Sudarshan Kumar (Indian Institute of Technology, India) and Boris Mazurok (IAE SB RAS, Russia)

CRF-R3 **Electrical Conductivity and Defect Evaluation of Multilayer CFRP Laminates by Eddy Current Testing**
Jun Cheng, Jinhao Qiu, Hongli Ji (Nanjing University of Aeronautics and Astronautics, China), Toshiyuki Takagi, Tetsuya Uchimoto (Tohoku University, Japan) and Ning Hu (Chiba University, Japan)

16:50-18:00 **Poster Session**

PS2: Young Researcher Overseas Visits Program Research Forum

HAGI
November 26, 2013

Chair: Jun Ishimoto (Tohoku University, Japan)
14:50-15:38 **Oral Presentation**
(8 min for Presentation)

YRF-1 **Development of a Microfluidic Device for a Three-Dimensional Cell Culture under a Controlled Hypoxic Environment**
Kenichi Funamoto (Tohoku University, Japan), Ioannis K. Zervantonakis (Harvard Medical School, USA) and Roger D. Kamm (Massachusetts Institute of Technology, USA)

YRF-2 **Combustion Chemistry and Its Experimental Validation for Biofuels and Surrogate Fuels -Collaboration between Quantum Chemistry and Combustion Engineering-**
Hisashi Nakamura (Tohoku University, Japan), Henry Curran (National University of Ireland, Ireland)

YRF-3 **Thermal sprayed coating integrity evaluation using acoustic and electromagnetic methods**
Tetsuya Uchimoto, Toshiyuki Takagi (Tohoku University, Japan), Xiaodong Deng, Thomas Monnier, Joel Courbon, Thierry Douillard and Varlot Masenelli (INSA de Lyon, France)

YRF-4 **Membrane and Hindered Diffusion of Protein -Quantitative Evaluation-**
Atsuki Komiya (Tohoku University, Japan), Jérôme Chevalier, Sébastien Pruvost and Jean-Yves Cavaille (INSA de Lyon, France)

YRF-5 **Analysis of Relationship between Lipid Environment and Protein Nanopore Properties -Toward Creation of Blood Cell Model with Various Membrane Strength-**
Noriko Tomita (Tohoku University, Japan), Stephan Wilkens (SUNY Upstate Medical University, USA), Liviu Movileanu (Syracuse University, USA) and Makoto Ohta (Tohoku University, Japan)

YRF-6 **Crosslinking Effect in Amorphous Polymers on Heat Transfer Characteristics**
Gota Kikugawa (Tohoku University, Japan), Pawel Keblinski (Rensselaer Polytechnic Institute, USA) and Taku Ohara (Tohoku University, Japan)

PS3: Fluids Science Research Award Lecture

HAGI
November 26, 2013

Chair: Toshiyuki Hayase (Tohoku University, Japan)

13:10-13:50 **Ultrasonic Velocity Profiler: How Turbulent is Turbulence?**
Yasushi Takeda (Swiss Federal Institute of Technology Zurich, Switzerland)

13:50-14:30 **CFD in the Merging Period of Practical Engineering and Basic Turbulence Studies –Nonlinear Acoustics and Flow Control as Application Examples–**
Kozo Fujii (Japan Aerospace Exploration Agency, Japan)

Liaison Office Session

ROOM 8
November 26, 2013

13:10-14:40 **Present Status and Future Plan of Liaison Office Activities**

Chair: Toshiyuki Takagi

Tohoku University, Toshiya Ueki (Executive Vice President for General Affairs, International Relations and Academic Affairs) (10min)

Moscow State University, Alexander Vasiliev (8 min)

UNSW and University of Sydney, Victoria Timchenko (8 min)

KTH Royal Institute of Technology, Fredrik Lundell (8 min)

KAIST, Shigenao Maruyama(Tohoku University) (8 min)

Syracuse University, Jeongmin Ahn (8 min)

INSA Lyon, University of Lyon, Marie Pierre Favre (8 min)

IFS, Makoto Ohta(8 min)

Discussion

Plenary Lectures

Tenth International Conference on Flow Dynamics
November 25-27, 2013, Sendai, Miyagi, Japan

Fluid Flow in Micron Spaces: Fluid dynamics in Microfluidic Devices

Esther Amstad and D.A. Weitz.
Department of Physics and School of Engineering and Applied Sciences
Harvard University
29 Oxford St.
Cambridge, MA 02138, USA
weitz@seas.harvard.edu

ABSTRACT

Microfluidic devices provide a simple, convenient means of providing exquisite control over fluid flow at length scales of microns to millimeters. While many microfluidic applications utilize single fluids, it is also possible to produce multiphase fluid flow with microfluidic devices. This can be used to create drops of one fluid in a second, or multiple drop-in-drop structures, thereby creating emulsions or multiple emulsions with a very high degree of control. The key to creating highly monodisperse drops is to exploit an absolute or stationary Rayleugh-Plateau instability. This can be accomplished with many geometries for different applications.

1. Introduction

Microfluidic devices provide a means of producing very highly controlled and very monodisperse drops of one fluid in a second. This can be done a single time to create emulsions, or can be done multiple times to create drops within drops, or multiple emulsions [1,2]. By structuring the microfluidic channels, it is possible to controllably mix a variety of different fluids and to produce a wide range of structures. The key to obtaining very monodisperse drops is to exploit the Rayleigh-Plateau instability in an absolute or stationary geometry, where the velocity of the interface of fluid phase forming the drop is zero [3]. This requires careful control over the geometry and wettability of the microfluidic devices. If this is achieved, a wide range of drop structures can be formed. These have many different potential applications. However, unlike all other emulsion-based or multiple-emulsion-based template structures, the drops are formed one-by-one, and they can remain spatially separated for some period of time, thereby allowing stabilization of their interfaces through delayed coating. In addition, the drops can be further broken by increased flow, which can produce a microfluidic spray drier. This can produce very small drops which can be used to create new classes of nanoparticles.

2. Method

The microfluidic devices used to investigate these phenomena are produced using lithographic techniques and can be made either from the standard poly(methyldisoloxane) (PDMS) or from other, more chemically-robust materials. In addition, devices can be fabricated using capillary microfluidics.

3. Results and Discussion

Drop formation in microfluidic devices typically occurs through the Rayleigh-Plateau instability. As such, it can occur in two distinct regimes, either the 'dripping' mode or the 'jetting' mode [1,2]. The boundary between the regimes occurs when the Capillary number that describes the fluid velocity of the interface between the two fluids is of order unity [2]. At low flow rates, the drop is formed slowly enough that an instability in the thickness of the emitted fluid can lead to full break off of the drop in a time scale shorter than the motion of the instability downstream; this results in dripping [3]. By contrast, if the fluid velocity is sufficiently large, the growing instability is propagated downstream a distance large enough to form a jet. The dripping mode provides the best controlled drop formation and results in the most uniformly-sized drops. It is, therefore, the preferred mode of operation.

The same instability that leads to drop formation with two fluids also can be used to create drops from one fluid in a gas. This has the form of a spray drier, where a fluid is broken into drops by a gas, and the drops are then evaporated. However, to achieve an absolute instability, where the velocity of the interface is zero, becomes more difficult when the outer fluid is a gas, and requires new designs for the geometry of the microfluidic chip. Once achieved, additional channels of air can be used to induce further breakup of the fluid drop into yet smaller drops. These smaller drops then evaporate very rapidly due to their small size and high surface-to-volume ratio.

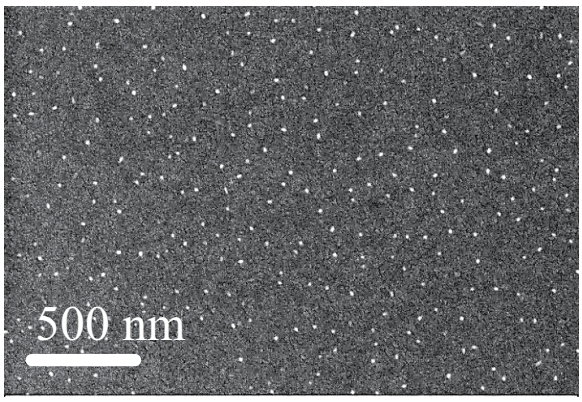

Fig. 1: Amophous $CaCO_3$ nanoparticles produced with a microfluidic spray drier.

The control of drop formation through hydrodynamic instabilities results in fine control over the driving force that creates the drops. As a result, the drops are quite uniform in size.

If the fluid that is used to create the drops also contains some dissolved materials that do not evaporate, these remain as solid particles. Because the size of the drops produced is so small, nanoparticles are produced. Because the drops are quite uniform in size, these nanoparticles are also uniform in size. And, because the drops are so small, and the evaporation is so fast, crystal nucleation can be delayed and crystals do not form during the evaporation. As a result, amorphous nanoparticles are produced. This results solely from the kinetics of the crystallization. Example are shown in Fig. 1.

4. Concluding remarks

The control of the kinetics of the drop formation and fluid evaporation produces amorphous nanoparticles. Because it is only the kinetics that control nanoparticle production, this microfluidic spray drier is a very general technique that can produce amorphous nanoparticles from a very wide range of materials.

References

[1] A. S. Utada, E. Lorenceau, D. R. Link, P. D. Kaplan, H. A. Stone, D. A. Weitz, Science **308**, (2005) 537.
[2] Andrew S. Utada, Alberto Fernandez-Nieves, Howard A. Stone, and David A. Weitz, Phys. Rev. Lett. **99**, (2007) 094502.
[3] Andrew S. Utada, Alberto Fernandez-Nieves, Jose M. Gordillo, and David A. Weitz, Phys. Rev. Lett. **100**, (2008) 014502.

Porous Media Combustion – Its Potential Applications in Wide Range of Liquid and Gas Fuelled Cooking Stoves

Subhash C. Mishra, P. Muthukumar
Department of Mechanical Engineering
IIT Guwahati, Guwahati – 781039, India
scm_iitg@yahoo.com

ABSTRACT

A good number of households throughout the world use liquid and gas fuelled cooking stoves. These cooking stoves, which work on free-flame combustion, have low thermal efficiencies and high CO and NOx emissions. If burners of these cooking stoves employ the principle of porous media combustion, their thermal efficiencies improves and emissions drastically go down. This in one hand saves energy, and on the other hand, minimizes the health hazards. This work briefly highlights the working principle of a cooking stove that utilizes the concept of porous media combustion, and its performance in terms of thermal efficiency and emissions.

1. Introduction

Growing global population combined with improvement in the economic condition of the people, the energy consumption is steadily increasing. Because of the limited reserve of fossil fuels, though, the emphasis is on harnessing various non-conventional sources of energy; their share to the total energy consumption is still minimal. The fossil fuels remain the major source of energy. Apart from its application in thermal power plants, process industries and transport sectors, it finds important application in the domestic sector. In the developed countries like the USA and Japan, the cooking is mainly based on liquefied petroleum gas (LPG) stoves, while in developing counties like China and India, LPG and kerosene stoves are used for cooking in many households.

Thermal efficiencies of LPG and kerosene cooking stoves available in the Indian market range from 55 – 65% [1] and 45 – 55% [2], respectively. From these stoves, CO and NOx emissions are also very high. CO and NOx emissions from LPG cooking stoves are in the 400 - 1050 mg/m^3 and 162 - 216 mg/m^3, respectively.

Low thermal efficiency and high emissions from LPG and kerosene cooking stoves are attributed to the combustion mechanism. These stoves are characterized by free-flame combustion in which the premixed air-fuel mixture burns in the gaseous environment. With combustion in the gaseous environment, heat transport from the narrow combustion zone (CZ) is mainly by convection. For low thermal conductivity and emissivity of the gases, conduction and radiation are low. If low thermal efficiency adds to the cost, the high emissions of CO and NOx are health hazards. Thus, any effort in improving the performance in terms of thermal efficiency and emissions of these stoves is a welcome move.

During the last two decades, combustion in porous media has received great attention [3-6]. In this, unlike the conventional combustion devices, combustion takes place in an inert porous matrix. In a 2-layer porous burner (Fig. 1), the SiC or zirconia solid matrix serves as the combustion zone. Thermal conductivity and emissivity of the porous matrix in the CZ are high. Preheating of air-fuel mixture is advantageous. To realize this, and to avoid flashback, a preheating zone made of low thermal conductivity and emissivity is provided. Normally, alumina is chosen for this. To sustain the combustion, in the combustion zone, the pore size of the porous matrix is higher than the porous matrix in the preheating zone in which the combustion is avoided. This is realized by keeping the modified Pecklet number $Pe = \frac{S_L d_m c_p \rho}{k}$, where S_L, d_m, c_p, ρ and k are the laminar flame speed, critical pore diameter, specific heat, density and thermal conductivity, respectively, more than 65 in the CZ and less than 65 in the preheating zone.

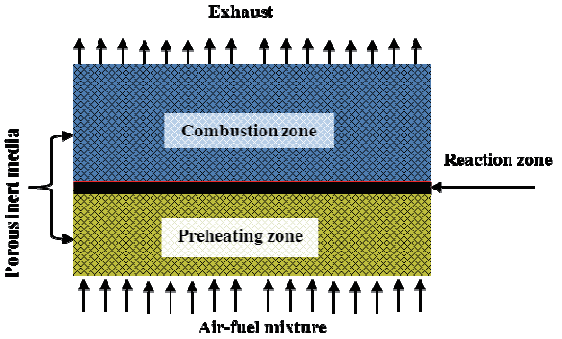

Fig. 1: Schematic of a porous radiant burner.

High thermal conductivity and emissivity of the porous matrix serving as the CZ results in significant conduction and radiation which are almost negligible in conventional cooking stoves working on free-flame combustion. Further, increased surface area to volume ratio improves convective heat transfer. As a whole, better heat transfer in porous matrix leads to improved combustion in terms of thermal efficiency and emissions. In the following, some results on thermal efficiencies and emissions of LPG cooking stoves with porous radiant burners are provided.

2. Measurement of Thermal Efficiency

The water boiling test is employed to measure the thermal efficiencies of the cooking stoves. In India, the Bureau of Indian Standards: 4246:2002 and 10109:2002 are followed for the LPG and kerosene pressure stoves, respectively. With $C_{pw} = 4.1826\,\text{kJ/kg}\cdot\text{K}$ as specific

heat of water, $C_{pv} = 0.8959\,\text{kJ/kg}\cdot\text{K}$ as specific heat of aluminum, $CV = 45780\,\text{kJ/kg}$ as the calorific value of the LPG, m_w, m_v and m_f as the mass of water, the mass of vessel along with the lid and stirrer and the mass of the fuel consumed during the experiment, respectively, for the LPG solve, the % thermal efficiency η is evaluated from the following

$$\eta = \frac{\left(m_w C_{pw} + m_v C_{pv}\right)\left(T_2 - T_1\right)}{m_f \times CV} \times 100 \qquad (1)$$

where T_1 is the initial temperature and $T_2 = 90\,^{\circ}\text{C}$ is the final temperature of water. In measuring the thermal efficiency of kerosene pressure stove, in Eq. (1), for kerosene, $CV = 43890\,\text{kJ/kg}$. Details on experimental procedure for measurements of thermal efficiency and emissions are skipped. The same can be found in [1, 2]. Below we provide some results.

3. Results and Discussion

For a given thermal load, thermal efficiency η of any burner depends on the equivalence ratio. For thermal loads 1.3, 1.5 and 1.7 kW, variations of thermal efficiencies η for the LPG cooking stove with a SiC based porous radiant burner (PRB) are shown in Figs. 2a-c for CZ porosity 80, 85% and 90%, respectively. These results are shown for a 90 mm diameter porous matrix. Alumina matrix in the PZ is 10 mm thick and its porosity is 40%.

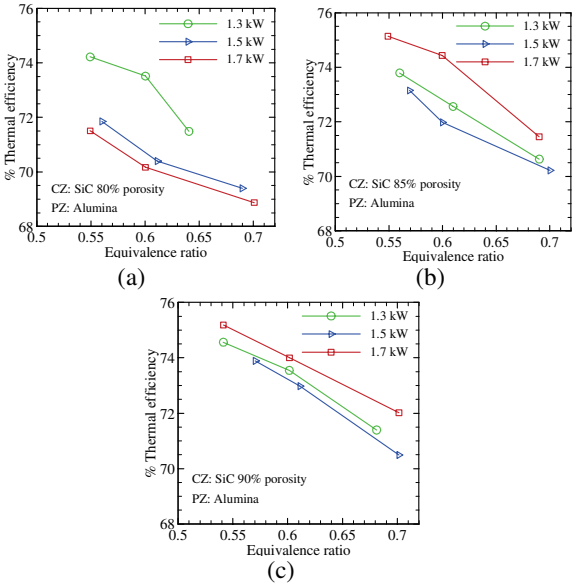

Fig. 2 Variation of thermal efficiency of the SiC-based PRB with equivalence ratio for thermal loads 1.3, 1.5 and 1.7 kW for the porosity (a) 80%, (b) 85% and (c) 90%.

At any thermal load, with increase in the equivalence ratio, thermal efficiency decreases. And, at a given equivalence ratio, thermal efficiency decreases with the increase in thermal load. The maximum thermal efficiency is observed for 90% porosity (Fig. 2c). At any equivalence ratio, for any porosity, efficiency is more than the maximum (≈65%) [5] obtained for the conventional LPG cooking stoves. The corresponding values of CO emissions are shown in Figs. 3a-c, respectively. CO emission increases with increase in thermal load, and for a given thermal load, it decreases with increase in the equivalence ratio. The CO emission is much lower than its conventional counterpart for which it is in the range: 400 - 1050 mg/m^3.

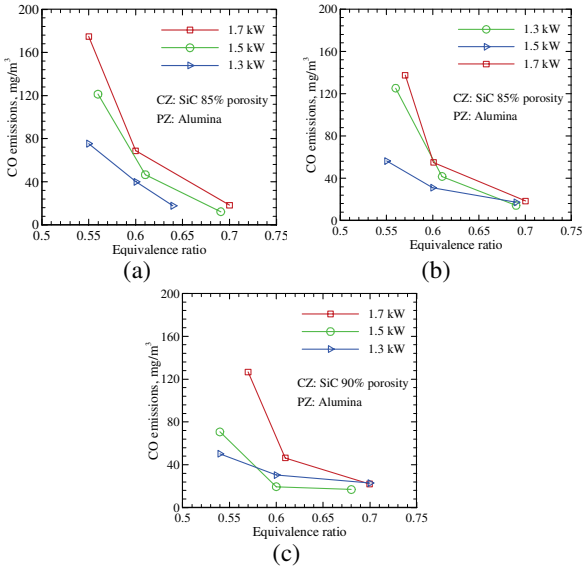

Fig. 3 Variation of CO emissions from the SiC-based PRB with equivalence ratio for thermal loads 1.3, 1.5 and 1.7 kW for the porosity (a) 80%, (b) 85% and (c) 90%.

4. Concluding remarks

Thermal efficiencies of cooking stoves working on the principle of porous media combustion are higher, and emissions of CO and NOx are much lower than the conventional stoves that work on free-flame combustion. Owing to a huge and growing global consumer base, a higher thermal efficiency will lead to huge saving of energy. Enormous reduction of CO and NOx will not affect health of the persons in the kitchen in particular, and will not pollute the environment in general.

References

[1] V.K. Pantangi, S.C. Mishra, P. Muthukumar, R. Reddy, Energy, **36** (2011), 6074-6080.

[2] M. Sharma, S.C. Mishra, P. Mahanta, Int. J. Energy Clean Env. **12** (2011), 79–93.

[3] P. Muthukumar, P.I. Shyamkumar, Fuel **112** (2013), 562-566.

[4] D. Trimis, F. Durst, Combust. Sci. Technol., **121** (1996), 153-168.

[5] V.K Pantangi, S.C Mishra, Adv. Energy Research. **8** (2006), 455-461.

[6] V.K. Pantangi, A.S.S.R. Kumar, S.C. Mishra, N. Sahoo, Int. Energy J., **8** (2007), 139-144.

Tenth International Conference on Flow Dynamics
November 25-27, 2013, Sendai, Miyagi, Japan

Progress in Panasonic's R&D of Advanced Photovoltaic Technologies

Shigeo Yata, Akira Terakawa, Masahiro Iseki, Mikio Taguchi, Eiji Maruyama and Makoto Tanaka
Panasonic Corporation
3-1-1 Yagumo-nakamachi, Moriguchi, 570-8501, Japan
E-mail: yata.shigeo@jp.panasonic.com

ABSTRACT

Panasonic's solar cell business is at present centered on high-efficiency HIT solar cells. In response to intensifying price competition in the solar cell industry, we aim to reduce the cost of HIT solar cells by using thinner (100-μm) Si wafers. We have achieved, at the R&D stage, the world's highest conversion efficiency of 24.7% using a 98-μm Si wafer at a practical size. Another of our strategies to reduce the cost of solar cells has been to develop high-efficiency thin-film Si solar cells and modules. We have achieved stabilized efficiency values of 10.7% for a large module (G5 size) and 12.2% for a small cell (1 cm^2).

1. Introduction

Our research and development of solar cells over the last 35 years yielded the world's first amorphous silicon (a-Si) solar cell, called AMORTON, and more recently the HIT (Heterojunction with Intrinsic Thin-layer) solar cell.

Panasonic's solar cell business centers on HIT solar cells. The HIT structure, which features a very thin intrinsic a-Si layer inserted between a doped a-Si layer and n-type c-Si, realizes very high efficiency.

Growing cost competition in the solar cell industry is driving down solar module prices, forcing every company to face the challenge of further reducing solar cell prices.

This paper reviews recent R&D progress in HIT solar cells with thinner Si wafers and thin-film Si solar cells which have an a-Si/microcrystalline silicon (μc-Si) tandem structure.

2. HIT Solar Cells with Thinner Si Wafers

Figure 1 shows the structure of a HIT solar cell. The HIT solar cell is a structure that we developed, in which an intrinsic (i-type) amorphous silicon (a-Si) layer and a p-type a-Si layer are deposited on a randomly-textured n-type CZ crystalline silicon (c-Si) wafer to form a p/n heterojunction. On the opposite side of the c-Si wafer, i-type and n-type a-Si layers are deposited to obtain a back surface field (BSF) structure. Transparent conductive oxide (TCO) layers and metal grid electrodes are fabricated on both sides of the doped a-Si layers. All of the processes described above are carried out at below 200˚C.

HIT solar cells have the following features: (1) excellent surface passivation which results in high voltage and high efficiency, (2) low-temperature processes (<200˚C) which prevent any degradation of solar-grade CZ c-Si, and (3) an excellent temperature coefficient.

The use of a thinner Si wafer is a very effective strategy for reducing the cost of solar modules, since the Si wafer generally accounts for about 40% of the total production cost of c-Si based solar modules. However, there is a risk that the use of thinner wafers will reduce production yield and output power to below that achieved by conventional processes. Due to its symmetrical structure, though, the HIT structure is ideally suited to the use of thinner wafers.

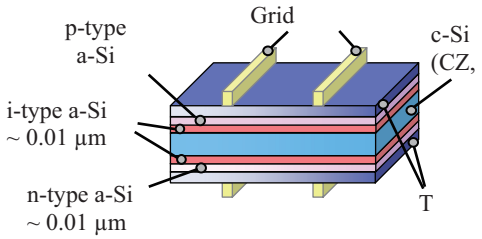

Fig. 1 The structure of a HIT solar cell

Figure 2 shows the gains we have made in the efficiency of HIT solar cells. Although still at the R&D stage, we have successfully applied our high-efficiency processes to very thin Si wafers measuring less than 100 μm thick [1]. We recently achieved a new record efficiency of 24.7% for a practical size (102 cm^2) HIT solar cell (Fig. 3) [2].

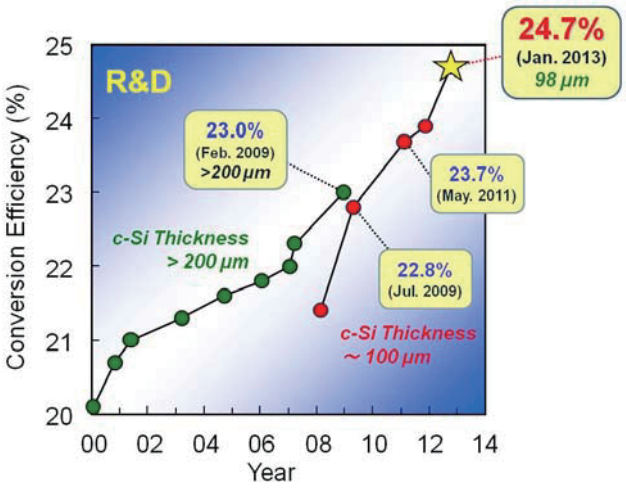

Fig. 2 Progress in the conversion efficiency of HIT cells at the R&D stage

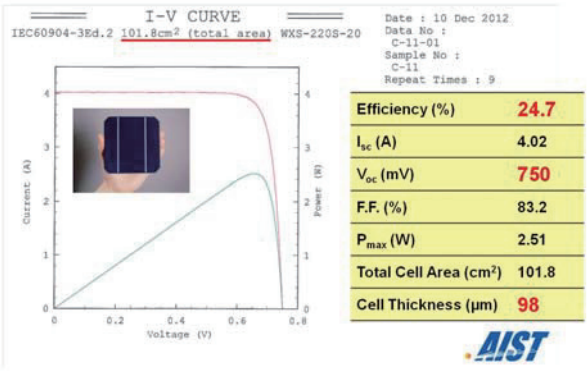

Fig. 3 I-V characteristics of our 98 μm-thick, 24.7% efficiency HIT solar cell at the R&D stage. (Independently certified by Advanced Industrial Science and Technology)

3. Challenges facing Thin-Film Si Solar Cells

In another approach to reducing the cost of solar cells, we have been developing large-area thin-film Si solar modules that have a-Si/μc-Si tandem structure on commercial substrates.

One of the crucial challenges with this type of solar cell is to obtain high conversion efficiency. We have developed a range of techniques that include material design, light management techniques, and laser patterning, which have enabled us to enhance solar cell performance.

Figures 4 and 5 show the appearance and I-V characteristics of an a-Si/μc-Si tandem solar module (G5 size) that has achieved an initial module efficiency of 12.0% and a stabilized module efficiency of 10.7%. We also realized a stabilized cell efficiency of 12.2% for a small cell (1 cm^2). These values for stabilized efficiencies are at the world's highest level for a-Si/μc-Si tandem structures [3-5].

Fig. 4 Large-area (G5 size) a-Si/μc-Si tandem module

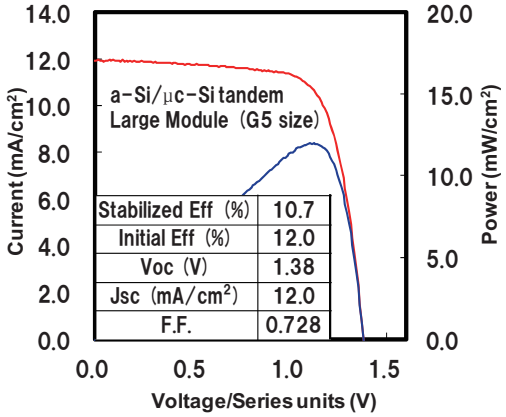

Fig. 5 I-V characteristics of a large-area (G5 size) a-Si/μc-Si solar module measured under AM 1.5, 100 mW/cm^2 light

4. Conclusions

We have successfully applied, at the R&D stage, our high-efficiency processes to silicon solar cells thinner than 100 μm and have achieved the world's highest conversion efficiency of 24.7% in a practical size. These advances also feed through to reducing the cost of HIT solar cells.

In another strategy for reducing the cost of solar cells, we have been developing high-efficiency thin-film silicon solar cells and modules that have a-Si/microcrystalline silicon (μc-Si) tandem structure. Stabilized efficiency values of 10.7% for a large module (G5 size) and 12.2% for a small cell (1 cm^2) have been achieved.

In the near future, in addition to existing HIT solar cells, Panasonic plans to provide truly low-cost, high-performance Si solar cells.

Acknowledgements

This work was supported in part by NEDO under the Ministry of Economy, Trade and Industry.

References

[1] T. Kinoshita, D. Fujishima, A. Yano, A. Ogane, S. Tohoda, K. Matsuyama, Y. Nakamura, N. Tokuoka, H. Kanno, H. Sakata, M. Taguchi and M. Tanaka. Proc. 26th EUPVSEC (Hamburg, 2011) 871.

[2] M Taguchi, A. Yano, S. Tohoda, K. Matsuyama, T. Nishiwaki, K. Fujita, E. Maruyama. To be published in Proc. 39th IEEE PVSC (Tampa, 2013).

[3] A. Terakawa, M. Hishida, S. Yata, W. Shinohara, A. Kitahara, H. Yoneda, Y. Aya, I. Yoshida, M. Iseki and M. Tanaka. Proc. 26th EUPVSEC (Hamburg, 2011) 2362.

[4] S. Yata, D. Kanematsu, K. Kaneko, R. Shimizu, A. Kitahara, M. Hishida, Y. Aya, W. Shinohara, H. Yoneda, A. Terakawa, M. Iseki and M. Tanaka, Technical Digest 21st PVSEC (Fukuoka, 2011) 2A-2O-01.

[5] M. Matsumoto, Y. Aya, M. Hishida, S. Yata, W. Shinohara, I. Yoshida, D. Kanematsu, A. Terakawa, M. Iseki and M. Tanaka. Mater. Res. Soc. Symp. Proc. 1426 (2012) 1117.

GS1: General Session

Reynolds-Number Dependency of Budget of Kinetic Energy and Turbulence Structure in Plane Jet

Nannan Wu[1)], Yasuhiko Sakai[1)], Kouji Nagata[1)], Hiroki Suzuki[2)], Osamu Terashima[1)], and Toshiyuki Hayase[3)]
1) Department of Mechanical Science and Engineering, Nagoya University,Furo-cho, Chikusa-ku, Nagoya, Aichi, 464-8603, Japan 2) Department of Engineering Physics, Electronics and Mechanics, Nagoya Institute of Technology, Gokiso-cho, Showa-ku, Nagoya, Aichi, 466-8555, Japan 3) Institute of Fluid Science, Tohoku University, 1-1-2 Katahira, Aoba-ku, Sendai, Miyagi, 980-8577, Japan
wu.nannan@b.mbox.nagoya-u.ac.jp

ABSTRACT

Based on direct numerical simulation (DNS), the flow characteristics of plane jets with different initial Reynolds numbers are simulated. In the present work, we study the budget of kinetic energy (KE) and the evolution of coherent structure (CS) in the process of jet growth and their relevance. The results reveal the scale and occurrence of CS present obvious Re-dependency and variant features of CS will determine the characteristics of velocity field evolution and KE transport.

1. Introduction

Plane jet as one of prototypical free shear flows has been an important research issue in over 80 years, meanwhile, the research base passed through the change from sole flow experiment to the combination of experiment and numerical simulation. [1,2] The modification and optimization of flow measurement technology (mainly hot wire anemometry, laser doppler velocimetry and particle image velocimetry) and the advancement of the calculation capacity of scientific computer have helped us cognize plane jet better, especially its turbulent characteristics, recently.

Two meaningful study issues of plane jet study are the evolution of vortex structure and budget of kinetic energy (KE) following the flow development, which are helpful to elucidate characteristics of plane jet dynamics, for instance, the laminar-turbulent transition in jet growth. In this paper, DNS based on finite difference method is carried out to study the above aspects of plane jet. The pattern, scale and strength of vortex structure and the transport of mean KE (MKE) and turbulent KE (TKE) are mainly investigated; moreover, we also explore the Reynolds number dependency of plane jet based on three initial conditions.

2. DNS

Code for the present DNS is written based on finite difference scheme, and the fractional step method [3] is used to solve the governing equations which are the continuity equation, the Navier-Stokes equations. We set the three-dimensional nondimensinalized coordinate system in DNS: x' is the streamwise coordinate, y' is the lateral coordinate and z' is the spanwise coordinate. The coordinate origin is placed in the middle of the slit (jet exit). Fig. 1 shows the schematic of computational domain ($14\pi d \times 14\pi d \times 3\pi d$).

The longitudinal mean velocity profile at the inflow is a top-hat profile and the mean lateral and spanwise velocities are initialized as 0 while the pressure is uniform. The typical Reynolds number (Re) for plane jet is defined by the bulk velocity (U_b) and the height of the jet exit (d). Three values of Re (1,000, 2,000, and 3,000) are defined for the initial condition at the jet exit. The variables are located on the staggered grids, the number of grids are set to be $356(x) \times 356(y) \times 80(z)$ for Re=1,000, $556(x) \times 556(y) \times 120(z)$ for Re=2,000 and $756(x) \times 756(y) \times 160(z)$ for Re=3,000.

The Runge-Kutta scheme and the Crank-Nicolson scheme are used for temporal discretization and the central differences are used for spatial discretization. Lateral boundary condition is set as the traction-free boundary condition, the convection outflow condition is applied at the downstream exit and periodic boundary condition is imposed at the spanwise direction.

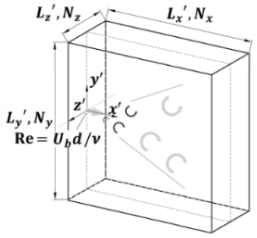

Fig. 1 Schematic of the computational domain

3. Results and Discussion

3.1 Evolution of Flow along Jet Centerline

Figure 2 shows the profiles of mean streamwise velocity (Left) and root-mean-square (rms) velocity (Right) along the jet centerline (i.e. U_C and $u_{i_{crms}}$), normalized by U_j (the mean centerline streamwise velocity at jet exit) and U_C respectively, here i in $u_{i_{crms}}$represents the orientation of velocity.

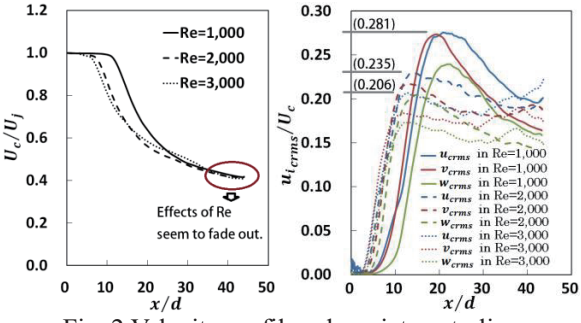

Fig. 2 Velocity profiles along jet centerline

As Re becomes larger, the length of potential core is shorter, which implies that an increase in Re is beneficial to the initial generation of instabilities. Meanwhile, we can find the establishment of spanwise rms velocity (w_{crms}) is posterior to the streamwise and lateral rms velocities (u_{crms} and v_{crms}), which proves

the two dimensional property of initial instabilities. In the interaction region of flow, the decay of mean flow field and the strength of fluctuating flow field are more intense for smaller Re, which related to larger vortex structure, shown in next section. In the later stage of flow evolution, Re dependency of flow is not obviously shown, but we still consider if the jet growth continues, the larger Re should correspond to the larger decay and the stronger fluctuation.

3.2 Coherent Vortex Structure

Based on the local minimum of negative pressure (-0.1 in our study), normalized by $\rho_0 {U_b}^2 (\rho_0$ is the density of flow medium), and the Q-criterion (0.8 in our study), normalized by ${U_b}^2/d^2$, the evolution of coherent vortex structure (CVS) following the jet development is shown by Fig. 3.

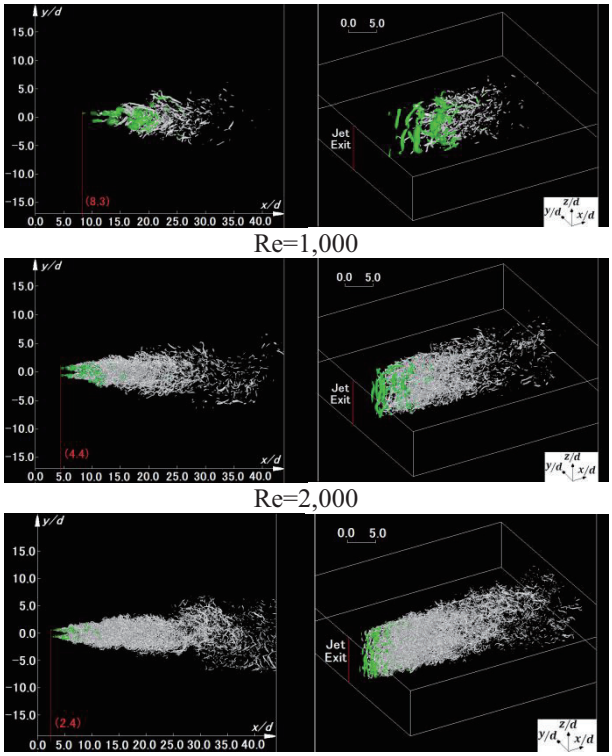

Fig. 3 Coherent vortex (green structures - isosurfaces of pressure; grey structures - isosurfaces of Q)

Figure 3 reveals CVS occurs at the nearer position from jet exit for larger Re, moreover vortices scale is smaller for larger Re. The initial large scale vortices are mainly spanwise and streamwise types; the small scale vortices are more three dimensional.

3.3 Kinetic Energy

Figure 4 shows the variation of MKE and TKE along jet centerline, which are normalized by ${U_b}^2$; The process of viscous dissipation affecting MKE (MVD) and TKE (TVD) and the streamwise convection due to the mean flow acting on MKE (MSC) and TKE (TSC) along jet centerline, normalized by ${U_c}^3/d$, are respectively shown by Fig. 5 and 6. The profiles of MKE and TKE separately present the similar features as the decay of mean streamwise velocity and the evolution of rms velocity; the evolving trend of VD curve is similar for three conditions, but larger Re is more helpful for the turbulence development and the peak values for normalized parameters are smaller, also we can find effects of VD on TKE are more dominant than ones on MKE; The profiles of SC on KE similarly present faster flow transition for larger Re, but the values have not shown the obvious difference for MSC in three conditions, the changeover of TSC sign corresponds to the evolution feature of TKE, e.g. from increase to decrease.

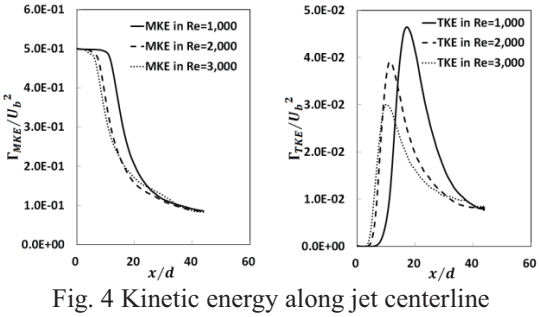

Fig. 4 Kinetic energy along jet centerline

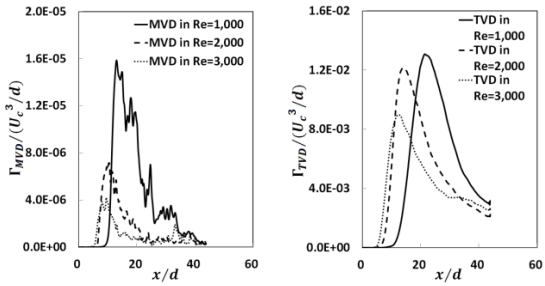

Fig. 5 Viscous dissipation along jet centerline

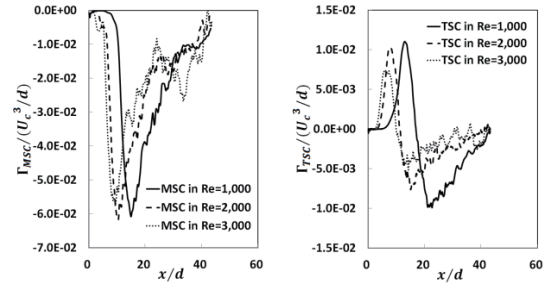

Fig. 6 Streamwise convection along jet centerline

4. Conclusion

The simulation results reveal that Re dependency of plane jet is presented in the evolution of velocity field, the scale of CVS and the transport of KE. The increase of Re will promote the flow transition of plane jet.

Acknowledgements

This study was carried out under the Collaborative Research Project of the Institute of Fluid Science, Tohoku University and supported by Grants-in-Aid (Nos. 25289030, 25289031) from the MEXT in Japan.

References

[1] H. Schlichting, Z. Angew. Math. Mech.,(in German) **13** (1933), 260-263.

[2] E. Gutmark, I. Wygnanski, J. Fluid Mech., **73** (1976), 465-495.

[3] H. Le and P. Moin, Journal of Computational Physics, **92**(1991), 369-379.

Turbulent Structure of the Turbulent-Laminar Patterns in Poiseuille Flow at Low-Reynolds Numbers

Koji Fukudome, Yoshifumi Ogami.
Ritsumeikan University, Nojihigashi 1-1-1, Kusatsu-shi, Shiga, Japan.
fukudome@fc.ritsumei.ac.jp

ABSTRACT

Direct numerical simulations were carried out to study turbulent-laminar patterns in the Poiseuille flow at the transitional regime. The turbulent-laminar pattern consists of turbulent and quasi-laminar regions that are alternately arranged in the streamwise direction and form a striped pattern. Streamwise vortical structures identified by the second invariant of the deformation tensor were detected and conditionally averaged. Asymmetry in numbers of clockwise and counterclockwise vortices occurred in the upwind and downwind turbulent regions. This was due to the existence of the mean spanwise flow in each region.

1. Introduction

Intermittent flow structures appear in various shear flows at the transitional regime. The turbulent-laminar pattern [1] is an intermittent flow structure and has been observed in experiments and numerical simulations of flows bounded by parallel walls at the transitional regime: e.g., the instance Couette flow [1,2], Poiseuille flow [2,3], and Taylor-Couette flow [4]. Recent studies [2,3,5] have identified the flow structure and sustaining mechanism. Duguet and Schlatter [5] indicated that the large-scale flow structure is sustained by contributions from small-scale vortical structures, although the interaction between the large-scale flow structure and small-scale vortical structures is not well-known. Therefore, determining the contribution of small-scale structures is important to understanding the pattern generation mechanism as well as the transition to turbulence. In this study we performed direct numerical simulation of the Poiseuille flow at low Reynolds numbers and clarified the effect of the pattern on the small scale structures.

2. Numerical Procedure

The objective flow is shown in Fig. 1: a Poiseuille flow driven by a constant pressure gradient. The numerical method used in this study was the same as that used by Fukudome and Iida [3]. The governing equations were the incompressible Navier-Stokes equation and continuity. Direct numerical simulation of the equations was carried out by the spectral method using Fourier series in the streamwise x and spanwise z directions and a Chebyshev polynomial expansion in the wall-normal direction y (= x_2). The boundary conditions were periodic for the x (= x_1) and z (= x_3) directions and non-slip at walls. For dealiasing, the 3/2 rule was adapted for both spatial discretizations. Time advancement was carried out by Crank-Nicolson for the viscous terms and second-order Adams-Bashforth for the nonlinear terms. The calculations were carried out at a friction Reynolds number of $Re_\tau = 60$ with a computational domain of $22\pi\delta \times 2\delta \times 10\pi\delta$ and $512 \times 65 \times 288$ grid points in the x-, y-, and z-directions, respectively. Here, the friction Reynolds number was defined by the friction velocity u_τ, channel half width δ, and kinetic viscosity ν. As an initial condition, fully developed flows at higher Reynolds numbers were calculated in advance, and the Reynolds number of the flow was systematically reduced. Hereafter, all parameters are normalized by the u_τ and ν; normalization was represented by the superscript +.

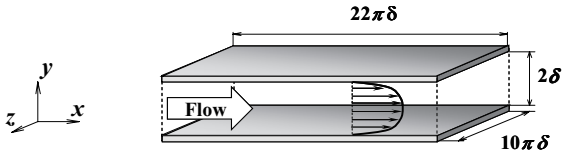

Fig. 1 Computational domain of Poiseuille flow.

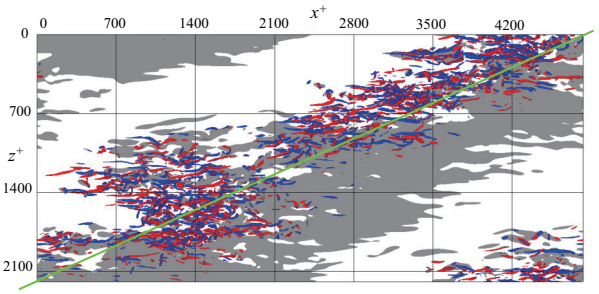

Fig. 2 Instantaneous distributions of quasi-streamwise vortices and low-speed region. Red and blue iso-surfaces represent clockwise and counter-clockwise vortices, respectively, identified by $II^+ = 0.001$. Light gray regions shows $u'^+ < 0$ at channel center. Green line represents boundary between upwind and downwind turbulent regions.

3. Results and Discussion

Fig. 2 shows the instantaneous distribution of the low-speed region and quasi-streamwise vortices over the lower half part of the entire computational domain. The quasi-streamwise vortical structures near the wall were identified by the second invariant of the deformation tensor:

$$II^+ = \frac{1}{2}\frac{\partial u_i'^+}{\partial x_j^+}\frac{\partial u_j'^+}{\partial x_i^+} = 0.5 u_{i,j}'^+ u_{j,i}'^+ . \quad (1)$$

Here, u_i' is the i-th component of the fluctuating velocity vector. The quasi-streamwise vortical structures shown by the red and blue iso-surfaces clustered to form the pattern; this included turbulent and quasi-laminar regions, where the turbulent region consisted of clustered quasi-streamwise vortices and tilted to the

Table 1 Number of the detected vortices.

y^+	Whole region		Upwind region		Downwind region	
	Positive	Negative	Positive	Negative	Positive	Negative
10	13789	13364	7557	8109	6232	4945
15	19073	19412	9923	11637	9150	7775
20	21650	22500	10852	12680	10798	9820
25	22190	23116	10877	12539	11313	10577
30	21958	22823	10552	11972	11406	10851

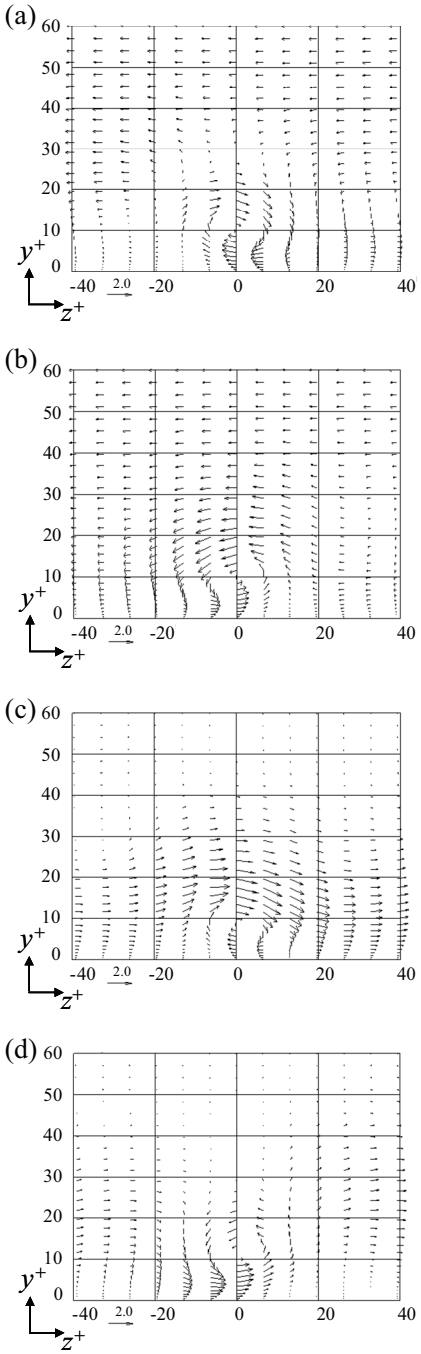

Fig. 3 Conditionally averaged velocity vectors at vortex cores located at y^+=10 in each regions. (a) and (b) represent the clockwise and counterclockwise vortices, respectively, in the upwind turbulent region. (c) and (d) represent the clockwise and counterclockwise vortices, respectively, in the downwind turbulent region.

diagonal direction. However, the pattern was almost steady and kept the shape outline for more than 2400 viscous time units. The turbulent region was flanked by high- and low-speed fluids shown by the white and light gray regions, respectively. We defined the center of the turbulent region, shown by the green line, as the position where the mean value of u_1' at channel center along the line became zero. The high- and low-speed fluids in the upwind and downwind turbulent regions had positive and negative spanwise velocities, respectively, due to the continuity of the flow. Consequently, the circulating flow around the turbulent regions exited on a large scale.

To detect individual vortical structures, the grid points in the vortical structures were connected to traces, and individual vortices were identified to count the number of vortical structures. Table 1 shows the number of detected vortical structures passing each y^+ plane. For the whole region, the number of clockwise vortices was roughly equivalent to the number of counter-clockwise vortices at each location. There were more counterclockwise vortical structures than clockwise vortical structures in the upwind turbulent region, while the opposite was true in the downwind turbulent region. There were much fewer vortices in the downwind turbulent region than in upwind region approaching the wall. Therefore, the wall friction decreased in the downwind turbulent region.

Fig. 3 shows velocity vectors conditionally averaged at the vortex core located at y^+=10. In the upwind turbulent region, the negative spanwise flow exited at y^+>20, which attenuated the clockwise vortices and intensified the counterclockwise vortices. Conversely, the positive spanwise flow exited near the wall in downwind turbulent region, which attenuated the counterclockwise vortices and intensified the clockwise vortices.

4. Concluding Remarks

We studied the turbulent-laminar pattern in the Poiseuille flow and obtained the following result. Asymmetry in the number of clockwise and counterclockwise vortices occurred in both the upwind and downwind turbulent regions. This was due to the existence of the mean spanwise flow in each region.

References

[1] D. Barkley et al., *J. Fluid Mech*., **567** (2007), 109-137.
[2] T. Tsukahara et al, *IUTAM Bookseries*, **18**, Springer, (2010), 421-426.
[3] K. Fukudome et al., *J. Fluid Sci. and Tech.*, 7, 1, (2012), 181-195.
[4] D. Coles, *J. Fluid Mech*., 21 (1965), 385-425.
[5] Y. Duguet et al., *Phys. Rev. Lett.*, **110**(3) (2013), 034502.

Computational Study of Formation of Wing Tip Vortices at Low Reynolds Numbers

Hiroshi Koizumi[1], Yuji Hattori[2]
[1]Department of Applied Information Sciences, Graduate School of Information Science, Tohoku University
Aramaki Aoba 6-3-09, Sendai, Miyagi, 980-8579, Japan
koizumi@dragon.ifs.tohoku.ac.jp
[2]Institute of Fluid Science, Tohoku University

ABSTRACT

The vorticity field of the wing tip vortex has been simulated at the Reynolds numbers between 100 and 1000. The radial profiles of the tangential velocity and the vorticity are compared to the theoretical models of Batchelor[1] and Moore and Saffman[2]. Wing tip vortices are formed at the edge of the wing tip. The vortices decay and dissipate depending on the Reynolds number in the wake region. The numerical results are in good agreement with the theoretical models at the vortex core region, while Moore and Saffman's model fits better than Batchelor's model.

1. Introduction

Wing tip vortices are generated at the edge of wing tips and cause many important phenomena such as induced drag and wake turbulence. To mitigate the induced drag, the formation process of wing tip vortices should be clarified. Recently, winglets which shift the generation point of wing tip vortices are developed and they can reduce the lift-induced drag. On the other hand wake turbulence strongly affects the frequencies of taking off and landing of aircrafts in an airport. Many recent works have investigated the characteristics of wing tip vortices aiming at reduction of the associated hazard. Recent studies are focused on the role of vortex instability on the decay of the wake and its control. However, hydrodynamic stability predictions depend on the precise structure of the vorticity distribution. In this paper we assess the existing theoretical models by comparing them with direct numerical simulation (DNS).

The structure of wing tip vortices has been studied mostly from 1960s and even earlier. The first theoretical model on the structure of trailing vortices was proposed by Batchelor[1]. He took into consideration the axial velocity component. A parallel flow model neglecting the downstream axial variation is called q-vortex which has been used for the base flow of numerical stability analysis of trailing vortices. Moore and Saffman[2] developed Batchelor's theoretical model by taking into account the vortex roll-up process in the formation of trailing vortices. Del Pino et al[3] investigated the trailing vortices by the PIV method and compared the results with these two theoretical models at the Reynolds numbers close to 10000. In this study, we assess these two models at low Reynolds numbers by direct numerical simulation.

2. Method

We solve the three-dimensional incompressible Navier-Stokes equation by Volume Penalization Method (VPM).

$$\frac{\partial \boldsymbol{u}}{\partial t} + (\boldsymbol{u}\cdot\boldsymbol{\nabla})\boldsymbol{u} = -\boldsymbol{\nabla}p + \frac{1}{Re}\boldsymbol{\nabla}^2\boldsymbol{u} - \frac{\chi(x)}{\eta}(\boldsymbol{u}-\boldsymbol{u_b}), \quad (1)$$

$$\boldsymbol{\nabla}\cdot\boldsymbol{u} = 0. \quad (2)$$

The last term of equation (1) is called the VP term which is the key ingredient of VPM. VPM is one of the immersed boundary methods. In VPM, we do not impose the boundary conditions on the surface of the wing using a body-fitted grid system. Instead the boundary conditions are automatically satisfied thanks to the VP term. We discriminate the flow region and the wing region by the mask function χ; $\chi = 0$ in the flow region, and $\chi = 1$ in the wing region.

We simulate the flow past a fixed wing at the Reynolds number between 100 and 1000. The airfoil is NACA0012 and the angle of attack is 8 degree. The length of the cord is $c = 1$ and the aspect ratio is 2.

We set the *x*, *y* and *z* axes as the flow, spanwise and vertical directions, respectively. The origin of the coordinate system is set at the center of the trailing edge. We use the uniform grid in the *y* and *z* directions and non-uniform grid in the *x* direction. In the *x* direction, grid resolution becomes the highest in the wing region to capture precisely the vortex generation process. The grid resolution and the number of grid points are shown in Table 1.

We use the 4th-order Runge-Kutta method for time development. For spatial derivatives the 6th-order compact scheme is used in the *x* direction and the Fourier collocation method is used in the *y* and *z* directions. Batchelor's theoretical model[1] is the axial symmetric model of trailing vortices. This model assumes the steady flow region far downstream from the wing. Moore and Saffman's theoretical model[2] is an improved model of Batchelor's model. They take into account the vortex sheet roll up process shed from the trailing edge.

We use the Levenberg-Marquardt algorithm built in Mathematica for fitting theoretical models with numerical results. Batchelor's model has one fitting parameter and Moore and Saffman model has two fitting parameters.

Table 1. The number of grid pints and the grid resolution

Re	Nx	Ny	Nz	dx	dy	dz
100	750	256	512	0.008	0.004	0.008
200	850	256	512	0.006	0.004	0.008
500	1000	512	1024	0.004	0.002	0.004

1000	1100	512	1024	0.003	0.002	0.004

3. Results and Discussion

We show the vorticity field by the color contour of the magnitude of vorticity at the wing region and the wake region in Fig. 1. At the leading edge, leakage of the flow from the wing surface to the tip region forms the counter vorticity at both sides of the wing surface. In the middle of the wing, flow from pressure side to the suction side is induced by the pressure difference in the wing surfaces. This flow separate at the edge of the wing tip and forms the vortices at the upper edge and the lower edge. These vortices push aside the vortex sheet which is formed at the leading edge, and merge before they reach the trailing edge. Once they are released to the wake region, vortices are dissipated by the viscous effects and are deformed elliptically because of the downwash flow induced by the counter vortices shed from the opposite wing tip.

The radial profile of vorticity is shown in Fig. 2. At the center of the vortex core, vortiicity increases with the Reynolds number. The radial profile of tangential velocity is shown in Fig. 3. The maximum value of the tangential velocity becomes highest at $\mathrm{Re} = 1000$. The value decreases and the vortex core radius increases as the Reynolds numbers decreases. This is due to the viscous diffusion. Viscous effects become larger at the low Reynolds numbers than at the high Reynolds numbers. For this reason, the vortex core radius becomes highest at $\mathrm{Re} = 100$.

Comparison between the numerical results and the theoretical models is shown in Fig. 4. We assess the vorticity distribution at $\mathrm{Re} = 1000$. Moore and Saffman's model shows better fit to the numerical results around the vortex core region. In contrast, Batchelor's model fails to predict the gradient of the profile near the vortex core region. This is because Batchelor's model is constructed under the assumption that it is valid at very far downstream. The two models cannot reproduce the numerical results outside the vortex core region.

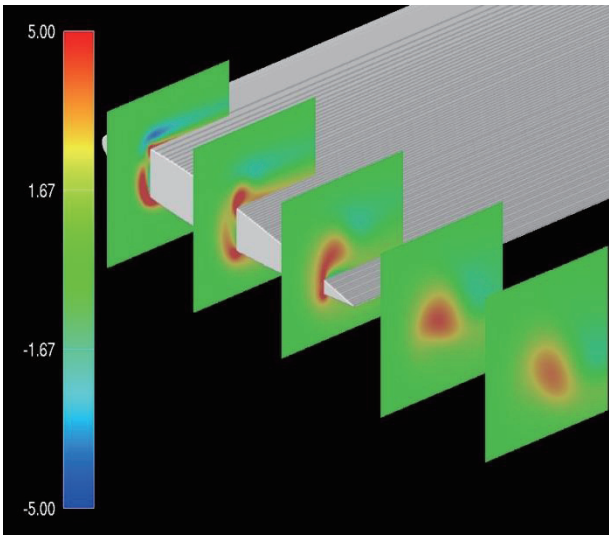

Fig. 1. Contour of the vorticity near the wing region

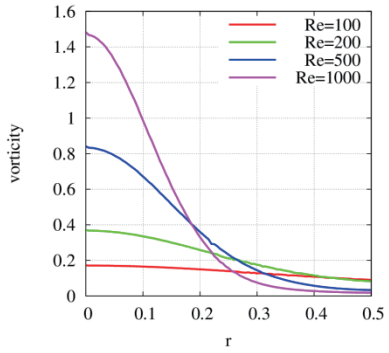

Fig. 2. Radial profile of vorticity at x=5.0.

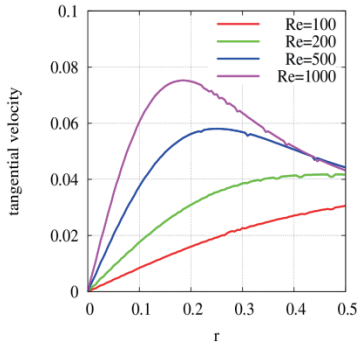

Fig. 3. Radial profile of tangential velocity at x=5.0.

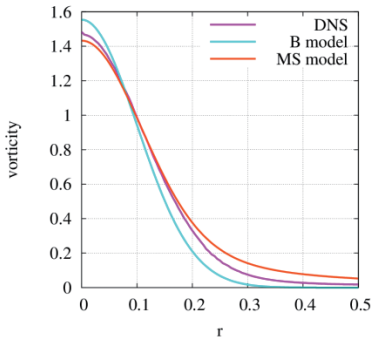

Fig. 4. Radial profile of vorticity compared with theoretical models. DNS: Numerical result at Re=1000, B: Batchelor model, MS: Moore and Saffman model.

4. Concluding remarks

Wing tip vortices are simulated at Reynolds numbers between 100 and 1000 by DNS. Formation process of tip vortices is captured and vorticity and tangential velocity are examined. Viscosity has strong effects on the dissipation of vortices. Moore and Saffman's theoretical model is in good agreement with the numerical results in the vortex core region.

References

[1] G. K. Batchelor, J. Fluid Mech, **20** (1964), pp 645-658

[2] D. W. Moore and P. G. Saffman, Proc. R. Soc. London, Ser. A, **333** (1973)

[3] C. del Pino, L. Parras, M. Felli, and R. Fernandez-Feria, Phys. Fluids, **23** (2011)

Investigation on Aerodynamic Characteristics of Two-Dimensional Airfoils Using High Viscosity Fluid Tank

Koyo Matsuzaki, Hidemasa Saito, Itaru Tamai, Gaku Sasaki,
Takaaki Matsumoto, and Koichi Yonemoto
Kyushu Institute of Technology
1-1 Sensui, Tobata, Kitakyushu,
Fukuoka 804-8550, Japan
n344151k@tobata.isc.kyutech.ac.jp

ABSTRACT

In order to clarify the aerodynamic characteristics in ultra-low Reynolds number flow ($Re<10^4$), the force balance tests of three different two-dimensional airfoils (NACA0012, Flat, and Ishii) were conducted using a high viscosity fluid tank. The results of $Re=10^4$ show that the maximum lift-to-drag ratio of Ishii was the best among the three wings. There is little difference in lift-to-drag ratio of each airfoils for $Re<10^4$, which means that the airfoil effect at ultra-low Reynolds number is small.

1. Introduction

A Mars exploration aircraft is researched by JAXA/ISAS for the new exploration Mars mission [1][2]. Many researchers have studied aerodynamic characteristics of low Reynolds number flow ($Re<10^5$). However, only a few attempts have been done for the ultra-low Reynolds number flow ($Re<10^4$). The ultra-low Reynolds number flow cannot be generated by normal wind tunnels because the measurement force becomes very small and the turbulence gets very large. A towing fluid tank can generate the ultra-low Reynolds number flow using highly viscous fluid. This study clarifies the aerodynamic characteristics of two dimensional wings in ultra-low Reynolds number flow.

2. Experimental Setup

2.1 Towing Fluid Tank

Fig. 1 shows an overall view of the test apparatus. It consists of a fluid tank, a towing device (Fig. 2), and a drive unit with a stepping motor and a ball screw.

The internal dimension of fluid tank is 2000 [mm] in length, 1025 [mm] in width and 600 [mm] in height. In order to study the two dimensional airfoil characteristics, the distance between the wingtip of test models and the end wall is set less than 1 [mm]. The towing distance is 1300 [mm], and the towing speed can be changed from 0.044 to 0.18 [m/s].

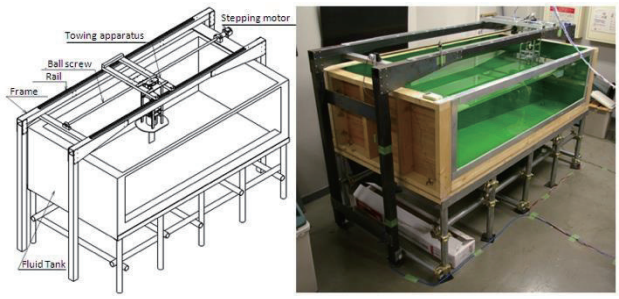

Fig. 1 Towing Fluid Tank

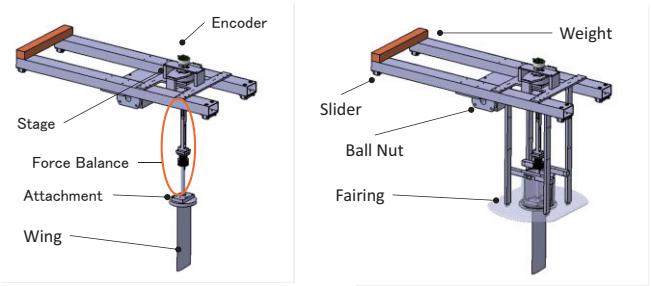

Fig. 2 Towing System Attached with Force Balance and Wing

2.2 Experimental Conditions

Fig. 3 shows the test airfoils (NACA0012, Flat (t/c=2.86 [%]), and Ishii). Ishii was developed by the famous hand launch glider world champion Mr. Ishii for his own competition plane based on his long experience. It has a good aerodynamic performance in low Reynolds number flow, which is almost the same for the Mars flight. The test airfoils has rectangular plan form (70 [mm] in chord length, and 210 [mm] in span). The manufacturing accuracy of all wings was verified by a three-dimensional shape measurement system.

Table 1 shows the experimental conditions. The ultra-low Reynolds number is realized by changing towing speed and fluid viscosity using HPC (Hydroxy Propyl Cellulose). The test Reynolds numbers are 5.0×10^2, 1.0×10^3, 5.0×10^3, and 1.0×10^4. The angle of attack is changed from -10 to 20 [deg.] with the increment of 1 [deg.].

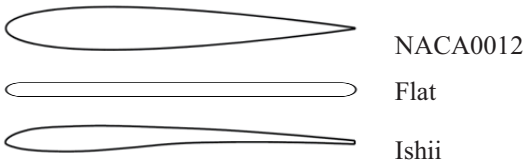

Fig. 3 Test Airfoils

Table 1 Experimental Conditions

Airfoils	Reynolds Number	Angle of Attack [deg.]
NACA0012	5.0×10^2, 1.0×10^3	−10～20
Flat	5.0×10^3, 1.0×10^4	−10～20
Ishii		−10～20

3. Results

The lift coefficient (C_l), drag coefficient (C_d) and pitching moment coefficient (C_m) of three airfoils were measured. The experimental results of NACA0012 are shown in Figs. 4~7. In order to evaluate the validity of the experiment, the results of CFD (Computational Fluid Dynamics) [3] and previous research by Nihon University [4] are also shown.

The figures show that the experimental results are close to those of CFD. There is a difference between the experimental results and those of the previous work. This was seen in the results of other airfoils. But, the difference in the lift-to-drag ratio is relatively small.

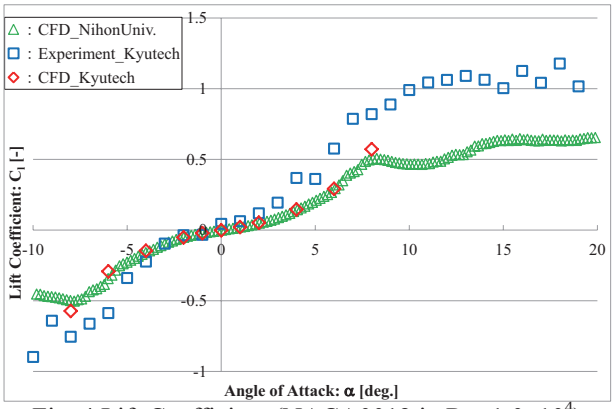

Fig. 4 Lift Coefficient (NACA0012 in $Re=1.0\times10^4$)

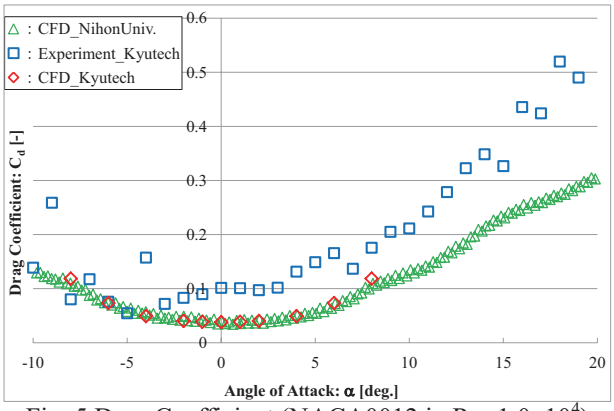

Fig. 5 Drag Coefficient (NACA0012 in $Re=1.0\times10^4$)

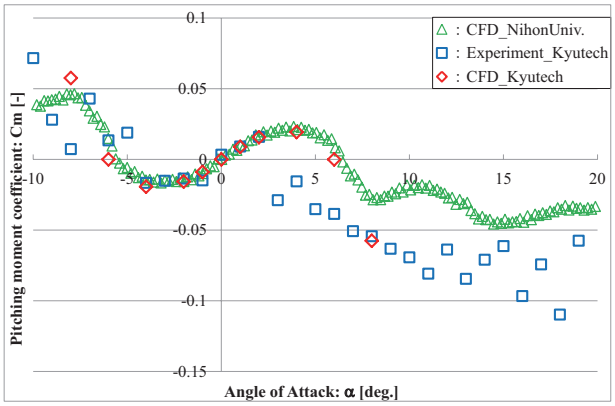

Fig. 6 Pitching Moment Coefficient (NACA0012 in $Re=1.0\times10^4$)

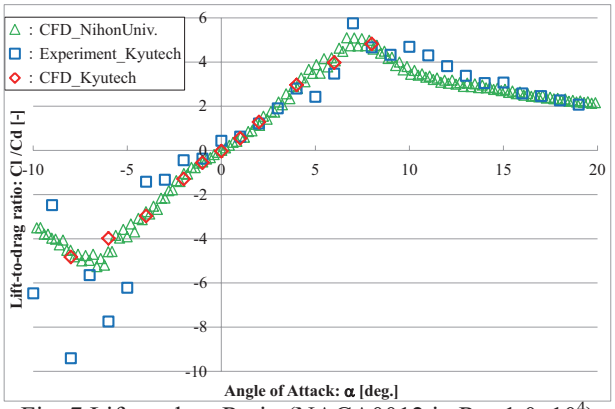

Fig. 7 Lift-to-drag Ratio (NACA0012 in $Re=1.0\times10^4$)

4. Conclusions

In this paper, the two dimensional aerodynamics characteristics of three airfoils were measured using a towing fluid tank. The experiment results were almost the same as the result of CFD, but differ from those of previous work. Further investigation of the discrepancies between the experiment and previous work is the future target.

Acknowledgements

This research was supported by Harada Memorial Foundation, Meisenkai, and Grant-in-Aid for Scientific Research (Grant Number: 24246136).

References

[1] Y. Jimba et al., “Study of the low Reynolds number aerodynamic characteristics for Mars airplane,” 54th Space Science Technology Conference, 2010, 3F05.

[2] H. Saito et al., “Ultra Low Reynolds Number Characteristics of Two-dimensional Wings Using Highly Tow Fluid Tank,” 45th Fluid Dynamics Conference / Aerospace Numerical Simulation Symposium 2013.

[3] K. Nishihara et al., “Numerical Simulation of Ultra Low Reynolds Number Flow around Two-dimensional Wing,” The Japan Society of Mechanical Engineers Kyushu Branch, 2010(63), 185-186.

[4] T. Ohtake et al., “Nonlinearity of the Aerodynamic Characteristics of NACA0012 Aerofoil at Low Reynolds Numbers,” Journal of the Japan Society for Aeronautical and Space Sciences, Vol.55, No.644, pp439-445, 2007.

Control Surface Effectiveness of Low Reynolds Number Flight Vehicles

Masayuki Anyoji[1*], Masato Okamoto[2], Hidenori Hidaka[2], Katsutoshi Kondo[3], Kozo Fujii[1]
[1]Japan Aerospace Exploration Agency, 6-1-1 Yoshinodai, Chuo-ku, Sagamihara, Japan
[2]Kanazawa Institute of Technology, 7-1 Ohgigaoka, Nonoichi, Japan
[3]Tokyo University of Science, 6-3-1 Niijyuku, Katsushika-ku, Tokyo, Japan
[*]Corresponding author: anyoji@flab.isas.jaxa.jp

ABSTRACT

Low-speed wind tunnel tests are carried out to investigate the control surface effectiveness at low Reynolds numbers (Re = 20,000-80,000). A thick airfoil, NACA0012, has a nonlinearity of the control surface effectiveness and also the lift increment with increasing the angle of the control surface is small. However, thin airfoils such as NACA0006 and a 3%c flat plate significantly improves the control surface effectiveness. These differences in the control surface effectiveness are due to the aerodynamic nonlinearity of the airfoils and a separation behavior has a profound effect on the control surface effectiveness.

1. Introduction

Low Reynolds number aerodynamics for low Reynolds number flight vehicles including Mars airplanes[1, 2] and micro air vehicles[3] (MAVs) has become an active area of research. Airfoil characteristics at low Reynolds numbers such as a non-linear lift curve caused by the formation or the burst of a separation bubble have been investigated in many papers[4, 5]. However, aerodynamic performance of control surface effectiveness at low Reynolds numbers has yet to be elucidated fully. We have conducted wind tunnel tests for evaluating aerodynamic performance of a Mars airplane at the Reynolds number of 30,000[6]. Our experiments showed that the horizontal tail with a thick symmetric airfoil had a low impact on the pitching control though a thin symmetric airfoil had beneficial effect on control surface effectiveness.

In this study, we preformed low-speed wind tunnel tests at low Reynolds numbers using three airfoils with a control surface to investigate the airfoil dependency on the control surface effectiveness in detail.

2. Experimental Method

2.1 Low-Speed Wind Tunnel

A low–speed wind tunnel located at Kanazawa Institute of Technology was used. The cross section of the test section is 500 mm × 500 mm and the length is 850 mm. The velocity range is from 2.0 m/s to 35.0 m/s. The turbulence level is 0.3% for the wind velocity of 3 m/s.

2.2 Test Models

The test models with a control surface are shown in Fig. 1. The airfoils are NACA0006, NACA0012 and 3%c flat plate (thickness = 3% of the chord length). Both NACA0006 and NACA0012 are made of rapid prototyping resin and only the 3%c flat plane is made of aluminum. Each airfoil has a chord length of 100 mm and a span of 200 mm. The aft-element of each airfoil (x/c = 0.7-1.0) corresponds to the control surface.

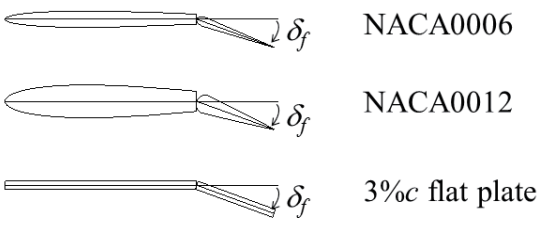

Fig. 1 Test Models with Control Surface

2.3 Experimental Setup

Three component balance (NISSHO ELECTRIC WORKS:LMC-3501-5N) was used for force measurements. End-plates with 3mm thickness were mounted at both ends of airfoil models. The model airfoils were supported by a cantilever connected the balance system. The support strut was covered by a windshield.

2.4 Experimental Conditions

The Reynolds number was changed from 20,000 to 80,000. The angle of attack (α) and the angle of the control surface (δ_f) were varied from -20.7 to 22.5 degrees with 0.9 degrees increments and from 0 to 20 degrees, respectively.

3. Results and Discussion

Figure 2 shows the lift curves for each airfoil with δ_f = 0 degree at Re = 20,000. As shown in Fig. 2, NACA0012 has an obvious non-linear lift curve with a kink point at approximately α = 3 degrees. On the other hand, NACA0006 and the 3%c flat plate have a linear lift slope. The lift for the 3%c flat plate is the highest of

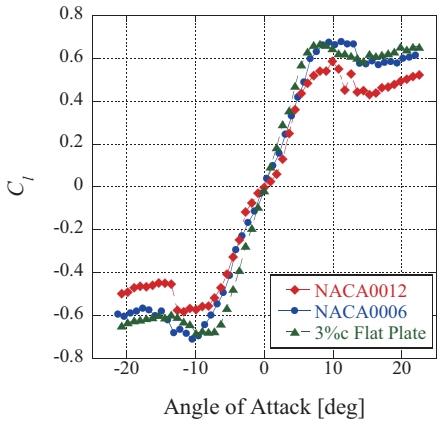

Fig. 2 Lift curves at Re = 20,000 (δ_f = 0 degree)

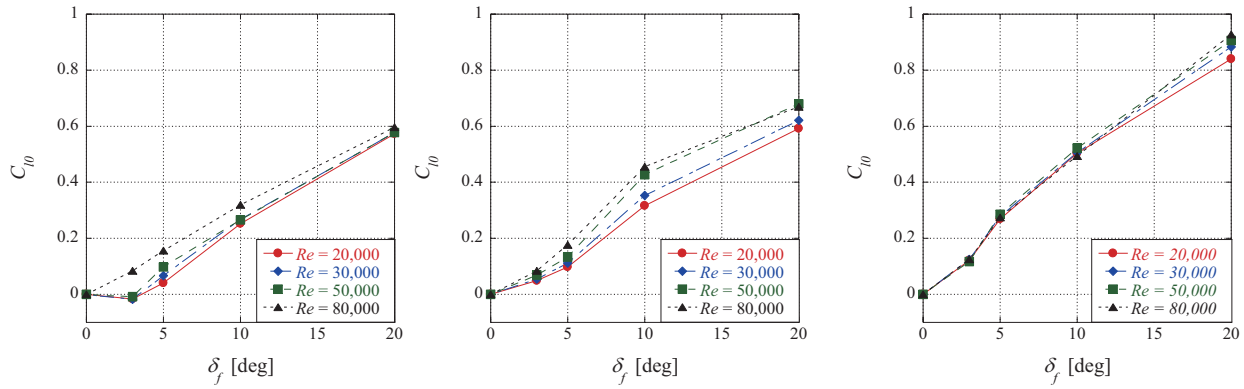

(a) NACA0012 (b) NACA0006 (C) 3%*c* Flat Plate

Fig. 3 Control Surface Effectiveness at Low Reynolds Numbers (C_{l0}: variation of lift coefficient at $\alpha = 0$ degree)

the three airfoils due to the existence of the leading edge separation bubble. A slight non-linearity of the lift curve for NACA0006 between α = 3.75 to 4.5 degrees is observed. Contrary to NACA0012, the flow remains fully attaches up to approximately α = 2.0 degrees and then the trailing edge separation occurs at α > 2.0 degrees. However, the separated shear layer reattaches and the separation bubble forms at around α = 4.0 degrees. Hence, NACA0006 can maintain the comparatively high lift even at the low angle of attacks. As shown in Fig. 2, the shape of airfoils has a profound effect on the aerodynamic performance at such low Reynolds numbers. On the basis of these differences in aerodynamic characteristics of airfoils themselves, the control surface effectiveness is discussed.

Figure 3 shows the Reynolds number effects on the control surface effectiveness for each airfoil. The control surface effectiveness is evaluated by variation of the lift coefficient at $\alpha = 0$ degree (C_{l0}). Variation of the lift coefficient with respect to δ_f for NACA0012 is the lowest among the three airfoils. In particular, the lift coefficient is nearly unchanged from zero lift up to δ_f = 3 degrees. This means the control surface has little effect in enhancing the lift at such low δ_f. The control surface effectiveness of NACA0006 is slightly improved from NACA0012, especially in the low δ_f, but the Reynolds number effect is also observed. By contrast, the 3%*c* flat plate has the largest control surface effectiveness of the three airfoils. Furthermore, it has little Reynolds number effect up to *Re* = 80,000. Consequently, airfoils with linear lift curves such as NACA0006 and the 3%*c* flat plate have high control surface effectiveness. However, the magnitude of the control surface effectiveness for the thick airfoil, NACA0012, with a non-linear lift curve becomes much lower than those of the others.

Considering the flow field around NACA0012 based on CFD results[7] at *Re* = 23,000, the flow separates upstream or its vicinity of the leading edge of the control surface. Therefore, it is believed that the lift is less sensitive to the changes of δ_f because the control surface moves inside the already separated shear layer. The improvement of the control surface effectiveness for NACA0006 and the 3%*c* flat plate would be attributed to an attached or a reattached flow at the leading edge of the control surface. The attached flow for NACA0006 remains at low δ_f and the flow would separate on the control surface. Thus, the lift varies even at the low δ_f. On the other hand, the three-dimensional complex reattached flow due to the leading edge separation bubble on the 3%*c* flat plate covers the control surface. The reattached flow might prevent the flow separation on the control surface by the momentum exchange due to turbulent mixing and contribute the stable control surface effectiveness.

4. Conclusion

The thick airfoil with a non-linearity of the lift curves deteriorates the control surface effectiveness. The thin airfoils with a linear lift curves, especially for the 3%*c* flat plate with a leading edge separation bubble, have high control surface effectiveness.

Acknowledgment

This research was partially supported by KAKENHI (23860076) and (24245136).

References

[1] Robert D. B. and David A. S., "Design of the ARES Mars Airplane and Mission Architecture," *J. Spacecra. Rockets*, Vol.43, No.5, 2006, pp. 1026-1034.

[2] A. Oyama and K. Fuji, "A Study on Airfoil Design for Future Mars Airplane," *AIAA paper*, 2006, 1484.

[3] Muller T. J., et al, "Introduction to the Design of Fixed-Wing Micro air Vehicles Including Three Case Studies," *AIAA,* Reston, 2006, pp. 1-107.

[4] O' Meara M. M. and Mueller, T. J., "Laminar Separation Bubble Characteristics on an Airfoil at Low Reynolds Number," *AIAA Journal*, Vol.25, No.8, Aug. 1987.

[5] Laitone, E.V., "Aerodynamic Lift at Reynolds Number Below 7 x 10 exp 4, " *AIAA Journal*, Vol.34. No.9, 1996, pp. 1941-1942.

[6] M. Anyoji, et al, "Planetary Atmosphere Wind Tunnel Tests on Aerodynamic Characteristics of a Mars Airplane Scale Model", *29th ISTS*, Nagoya, 2013.

[7] R. Kojima, et al, "Large-Eddy Simulation of Low-Reynolds Number Flow Over Thick and Thin NACA Airfoil," *J. Aircraft*, Vol. 50, No. 1, 2013, pp. 187-196.

Tenth International Conference on Flow Dynamics
November 25-27, 2013, Sendai, Miyagi, Japan

Effect of Grid-Generated Disturbances on Aerodynamic Characteristics of an NACA0012 Airfoil at Low Reynolds Numbers

Takaaki Tsuchiya, Daiju Numata and Keisuke Asai
Tohoku University, 6-6-01, Aramaki-Aza-Aoba, Aoba-ku, Sendai 980-8579, JAPAN
Tsuchiya.takaaki@aero.mech.tohoku.ac.jp

ABSTRACT

The objective of this study is to clarify the effect of turbulence intensity on the aerodynamic characteristics of an NACA0012 airfoil at low Reynolds numbers. Turbulence intensity was varied using grids with different mesh arrangements. Aerodynamic force and pressure distributions were measured using a force balance and Pressure-Sensitive Paint. The results show that an increase of turbulence intensity had an effect to improve lift and drag characteristics of the airfoil such as an increase of lift, delay in stall and a decrease of drag. The overall effects of increasing turbulence intensity were similar to those of increasing Reynolds number.

1. Introduction

Aerial vehicles such as airplanes have been considered as a feasible means of exploring the Mars. Flight condition of a "Mars airplane" becomes low Reynolds number condition, mostly below Re = 50,000 because of low pressure and a small size of the vehicle. In this Reynolds number (Re) range, turbulence intensity (TI) has a strong effect on aerodynamic characteristics of wings. In contrast to an airplane on Earth that flies under relatively smooth flow condition, an airplane on Mars is required to fly under relatively turbulent flow condition due to the existence of "dust devil" and "dust storm" that sometimes cover a large area. Thus, in the design of a Mars airplane, the influence of TI on low-Reynolds-number flow on the wing must be considered.

The objective of this study is to clarify the aerodynamic characteristics of an NACA0012 airfoil at low Re under various TI conditions. Aerodynamic force and pressure distributions were measured using a force balance and Pressure-Sensitive Paint (PSP).

2. Experimental method

2-1. Mars Wind Tunnel (MWT)

The MWT, which is located at Tohoku University, is composed of a vacuum chamber, an induction-type wind tunnel and a buffer tank. The induction-type wind tunnel is placed inside the vacuum chamber so that the pressure condition of Martian atmosphere can be simulated by reducing the pressure inside the vacuum chamber. The test gas inside the vacuum chamber, either dry air or carbon dioxide, is available by changing a gas supply line. The turbulence intensity of the test section can be changed by using turbulence grids with different diameters, mesh sizes and cross sections. Currently, the MWT is only being operated at ambient temperature.

2-2. Turbulence intensity control for the MWT

To change the free-stream turbulence intensity of the MWT, turbulence grids were installed between the contraction section and the test section. Three types of turbulence grids were used in this study. These are a wire-mesh grid with a wire diameter of 0.6 mm and a mesh size of 4.23 mm (grid 1) and with a wire diameter of 0.9 mm and a mesh size of 4.23 mm (grid 2) and a mesh grid with a 0.9 mm square cross-section. These turbulence grids were mounted on a 10-mm thick frame. To evaluate the effect of extension of the test section, a frame having no turbulence grid was installed in the same position (called "no grid").

2-3. Two-component Balance System

A two-component balance system was used to measure aerodynamic force. This balance system is composed of two load cells and has sufficient sensibility and accuracy at low pressure.

2-4. Pressure-Sensitive Paint (PSP)

In this study, Pressure-Sensitive Paint (PSP), a coating type sensor consisting of luminescent molecules and binder, was used to obtain pressure distribution on the wing surface. The principle of PSP is based on oxygen quenching. The rate of oxygen quenching depends on local oxygen concentration which is proportional to ambient pressure. Therefore, surface pressure can be calculated from measured luminescent intensity of PSP. For PSP used in this experiment, PdTFPP, poly(TMSP) and toluene were used as luminescent molecule, binder and solvent, respectively.

2-5. Test model

An NACA0012 airfoil was used for this experiment. The test model is made of aluminum alloy. A chord length and a span of this model are 50 mm and 100 mm, respectively.

2-6. Experimental conditions

Experiments were conducted for Re = 11,000 and 25,000 with grids and for Re = 11,000, 15,000, 20,000, 25,000 and 47,000 with no grid. Mach number was fixed at M = 0.2. The angle of attack was changed from -5 deg to 20 deg except for the condition of Reynolds number of 47,000. In this study, TI was controlled from 0.5 % up to 4.2 %.

3. Results and Discussion

3-1. Reynolds number effect

Figure 1 shows the lift and drag curve of the NACA 0012 for Re = 11,000, 15,000, 20,000, 25,000 and 47,000 [1]. The solid line represents the analytical lift curve predicted by the potential theory for a symmetric airfoil. As Re increased, the lift coefficient increased at each angle of attack before the stall angle and the maximum lift coefficient increased. As for the drag curve, the drag coefficient became smaller as Re became larger.

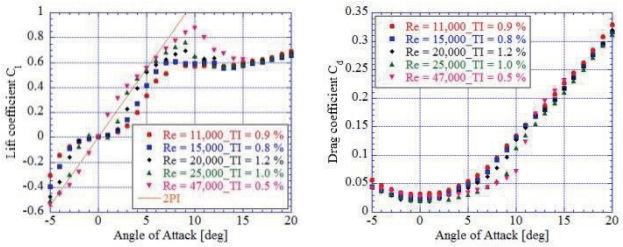

(a) Lift curve (b) Drag curve

Fig.1 Aerodynamic characteristics of an NACA0012 with no grid

3-2. Turbulence intensity effect

Figure 2 shows the aerodynamic characteristics of NACA0012 at Re = 11,000 for four different turbulence intensities. The solid line in Fig.2 (a) represents the lift curve of a symmetric airfoil based on the potential theory. As TI increased, the lift coefficient increased at each angle of attack. Moreover, when TI became larger, a stall angle also became larger although the stall angle at TI = 2.1 % was as the same as that at TI = 4.0 %. As for the drag curve, when TI increased, the drag coefficient increased at low angles of attacks. However, above an angle of attack of 5 or 6 deg, the drag coefficient decreased when TI increased.

Figure 3 shows pressure distribution for four turbulence intensities at α = 4 deg and 9 deg. As shown in both figures, pressure coefficient (C_p) near the leading edge decreased on the upper surface and increased on the lower surface. Therefore, the lift coefficient which corresponds to an area enclosed by C_p curves increased. Generally, the flow with higher turbulence intensity has greater resistance against adverse pressure gradient. From the Fig.3 (b), when turbulence intensity increased, the length of separation bubble shortened at around stall angle of attack. Because of these facts, it is considered that the flow on the surface became much steadier and then the delay in stall happened.

Figure 4 shows the aerodynamic characteristics of NACA0012 for three turbulence intensities at Re = 25,000. As shown in Fig. 4 (a), when TI increased, the lift coefficient at low angles of attack increased and the stall angle increased. As for the drag coefficient, similar trends to the case for Re = 11,000 were observed.

Figure 5 shows pressure distribution for four turbulence intensities at α = 4 deg and 9 deg. At an angle of attack of 4 deg, the area enclosed by C_p curves was almost the same in these three cases. Therefore, the lift coefficient at angle of attack of 4 deg shown in Fig.4 (a) became the same. As for angle of attack of 9 deg, the same trend as the case for Re = 11,000 was observed.

3-3. Effective Reynolds number

Comparing the maximum lift coefficient for each TI only, the lift coefficient for TI = 1.5 % is almost the same as that at Re = 25,000 with no grid. The lift coefficient for TI = 4.0 % is almost the same as that for Re = 47,000 with no grid. These results show that turbulence had an effect to increase Reynolds number even at such low Reynolds number flow conditions.

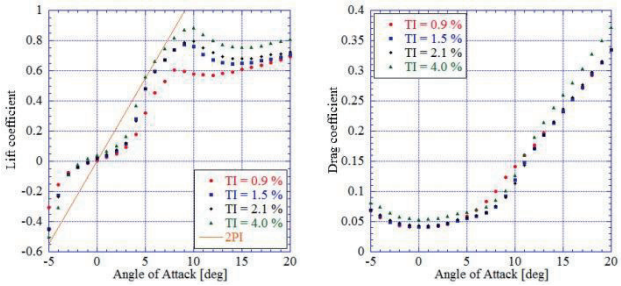

(a) Lift curve (b) Drag curve

Fig.2 Influence of turbulence intensity on aerodynamic characteristics of an NACA0012 at Re = 11,000

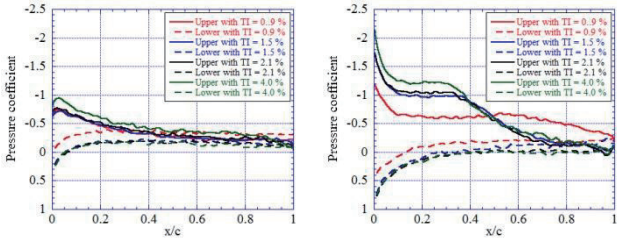

(a) α = 4 deg (b) α = 9 deg

Fig.3 Influence of turbulence intensity on pressure distribution of an NACA0012 at Re = 11,000

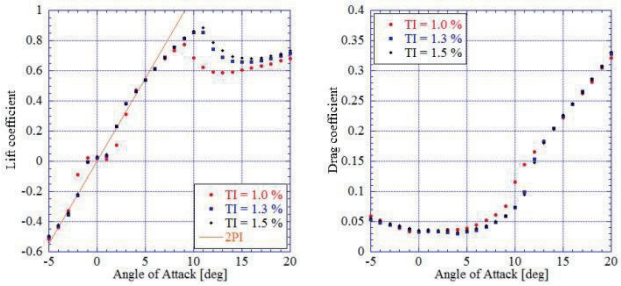

(a) Lift curve (b) Drag curve

Fig.4 Influence of turbulence intensity on aerodynamic characteristics of an NACA0012 at Re = 25,000

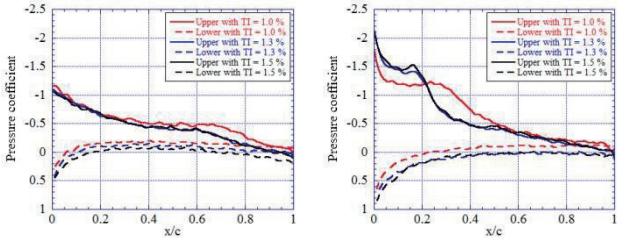

(a) α = 4 deg (b) α = 9 deg

Fig.5 Influence of turbulence intensity on pressure distribution of an NACA0012 at Re = 25,000

References

[1] T. Tsuchiya et al., "Influence of Turbulence Intensity on Aerodynamics Characteristics of an NACA0012 at Low Reynolds Numbers", The 51st AIAA Aerospace Sciences Meeting, AIAA-2013-0065, Grapevine, Texas, 7-11 January 2013

Reynolds Number Effect on Lift and Drag Characteristics of Three-dimensional Wings by Wake Integration Method

Takahiro Makizono[1)], Guku Sasaki[1)], Hiroshi Ochi[2)], Takaaki Matsumoto[1)], and Koichi Yonemoto[1)]
[1)] Department of Mechanical and Control Engineering, Kyushu Institute of Technology
[2)]Department of Mechanical System Engineering, Nishinippon Institute of Technology
yonemoto@mech.kyutech.ac.jp

ABSTRACT

This study aims to clarify the aerodynamic characteristics of three dimensional wings by wake integration method. The wake integration method is an indirect measurement of lift and drag distributions along wing span. It decomposes total drag into profile and induced ones. The results show that the spanwise distributions of lift and profile drag is sensitive to the Reynolds number., but the induced drag is not affected by the Reynolds number. As the conclution, the lower the Reynolds number gets, the more dominant the profile drag becomes.

1. Introduction

The Mars exploration using a small aircraft has been studied by many previous researches. The aerial exploration system enables more precise imaging than orbiters and wider area observation than rovers. But Martian atmospheric density is about 1/100 in comparison with that of the earth. The aircraft has to perform high angle of attack flight at low speed for observation. For these reasons, the order of Mars flight Reynolds number has the range from 10^4 to 10^5. The complicated flow of the low Reynolds number affects the aerodynamics characteristics of a flight on Mars [1].

In this study, aerodynamic characteristic is measured using wake integration method (WIM). Force balance test is commonly used as aerodynamic characteristic measurement in wind tunnel. However, WIM can decompose total drag into profile and induced drags and evaluate lift and drag distributions along wing span. This study aims to clarify the aerodynamic characteristics of three dimensional wings by WIM.

2. Experimental Method

The variable-pressure wind tunnel at Nishinippon Institute of Technology was used. It can decompress the test section pressure to 1/10 of the atmospheric pressure so that low Reynolds number flow can be realized without decreasing flow speed. The specifications of is wind tunnel are shown in Table 1. The test airfoil NACA0012 has the chord length of 70 [mm], and the span of 140, 210 and 280 [mm] (the aspect ratios are 4, 6 and 8, respectively) (Fig. 1). The measurement Reynolds numbers are 2.0×10^4 and 5.0×10^4 (only for the wing of aspect ratio 6). The angle of attack are changed from 0 to 14 [deg.] in increment of 2 [deg.]. Static and total pressures, pitch and yaw flow angles of wake region are measured by a 5 hole pitot tube, which has the tip diameter of 3.0 [mm] and the total length of 210 [mm].

Table 1 Variable-pressure Wind Tunnel Specifications

Test Section	0.5(W) × 0.5(H) × 1.0(L) [m]
Pressure Range	10 [kPa] ~Atmospheric Pressure
Wind Velocity	10~50 [m/s] (at Atmospheric Pressure)
	10~100[m/s] (at 10 [kPa])

Fig. 1 NACA0012 Airfoil

3. Wake Integration Method

The force acting on airfoil can be calculated by the momentum difference between upstream and downstream. The momentum conservation law gives the lift as described by Eq. (1), where subscript ∞ refers to upstream.

$$L = -\iint_S \rho w(\vec{u}\cdot\vec{n})ds - \iint_S (P-P_\infty)n_z ds = \rho_\infty U_\infty \iint_{WA} y\xi ds - \rho_\infty {U_\infty}^2 \iint_{WA} \frac{w}{U_\infty}\frac{\Delta u}{U_\infty} ds + O(\Delta^3) \quad (1)$$

Drag is decomposed as follows:

$$D = \iint_{W_A} P_\infty \frac{\Delta s}{R} dydz + \frac{\rho_\infty}{2}\iint_{W_A}(v^2+w^2)dydz - \iint_{W_A}\frac{P_\infty}{2}\left(\frac{\Delta s}{R}\right)^2 + O(\Delta^3) \quad (2)$$

where the variation of entropy Δs is given by the total pressure P_T loss as follows:

$$\Delta s = R\ln\frac{P_{T_\infty}}{P_T} \quad (3)$$

The first term of Eq. (2) is the profile drag, and the second term is the induced drag. Other terms are negligibly small so that Eq. (2) can be approximated as follows:

$$D \approx D_p + D_i \quad (4)$$

where,

$$D_p = \iint_{W_A} P_\infty \frac{\Delta s}{R} dydz = qSC_{D_P} \quad (5)$$

$$D_i = \frac{\rho_\infty}{2}\iint_{W_A}(v^2+w^2)dydz = qSC_{D_i} \quad (6)$$

where q is the dynamic pressure, and S is the wing reference area.

4. Results

4.1 Spanwise aerodynamic force distribution

The spanwise distributions of lift, profile drag and induced drag coefficients are shown in Fig. 2 to 4. The distribution of lift coefficient except at the wingtip gradually increases as the angle of attack becomes large until stall. On the other hand, the lift coefficient at the wingtip increases even after the stall because the wingtip

vortices suppress flow separation on the wing upper surface. The profile drag also increases as the angle of attack becomes large. The peak of profile drag varies according to the angle of attack. This is attributed to the fact that the flow around the wing is complicated and unsteady. The induced drag is observed at the wingtip and increases with the growth of wingtip vortex.

4.2 The property of profile and induced drag

Fig. 5 shows the comparison of profile and induced drags. The results of Re=1.0×10^5, 2.0×10^5 were measured using the low-speed wind tunnel at Kyushu Institute of Technology [2]. The profile drag increases as the Reynolds number becomes smaller. On the other hand, the effect of Reynolds number to the induced drag is very small. The proportion of profile and induced drag coefficients to total drag coefficient is shown in Fig. 6. The induced drag accounts for about 45 [%] at Re=2.0×10^5. But it decreases approximately by 15 [%] at Re=2.0×10^4. Therefore, the lower the Reynolds number gets, the more dominant the profile drag becomes.

5. Conclusions

In order to investigate the aerodynamic characteristics of three dimensional wings in low Reynolds number flow, WIM was applied to the wing wake measurement. As the result, the following findings are obtained:

1) The profile drag considerably depends on Reynolds number, but the induced drag does not.
2) The profile drag comprises a large percentage of the total drag for the low Reynolds number.

Acknowledgements

This research was supported by Harada Memorial Foundation, Meisenkai, and Grant-in-Aid for Scientific Research (Grant Number: 24246136).

References

[1] Y. Jimba et al., "Study of the low Reynolds number aerodynamic characteristics for Mars airplane," 54th Space Science Technology Conference, 2010, 3F05.

[2] T. Kobayashi et al., "Profile and Induced Drag Decomposition of Low Reynolds Number Flow around Three-dimensional Wing by Wake Survey," 8th International Conference on Flow Dynamics, OS6-7, 2011.

[3] K. Kusunose, "A Wake Integration Method for Airplane Drag Prediction," The 21st Century COE of Flow Dynamics Lecture Series Volume 3, Tohoku University Press, 2005.

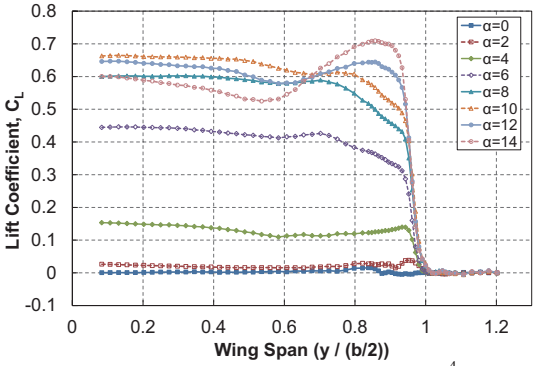

Fig. 2 Spanwise Lift Distribution (Re=2.0×10^4, AR=6)

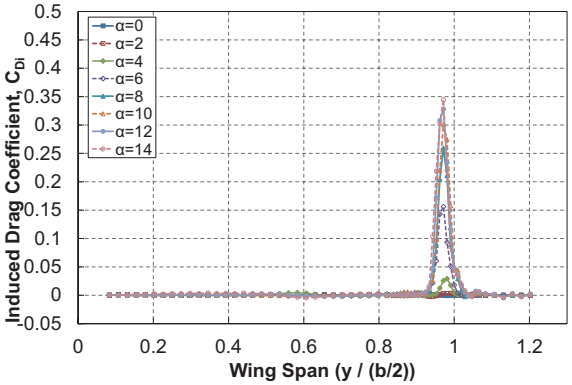

Fig. 3 Spanwise Induced Drag Distribution (Re=2.0×10^4, AR=6)

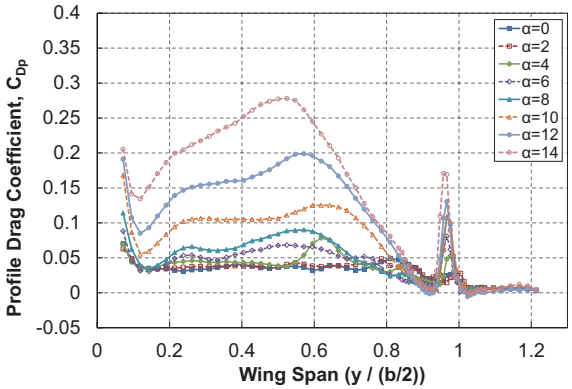

Fig. 4 Spanwise Profile Drag Distribution (Re=2.0×10^4, AR=6)

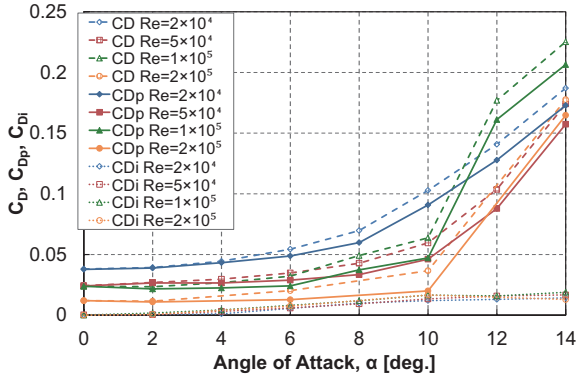

Fig. 5 Comparison of Profile and Induced Drags

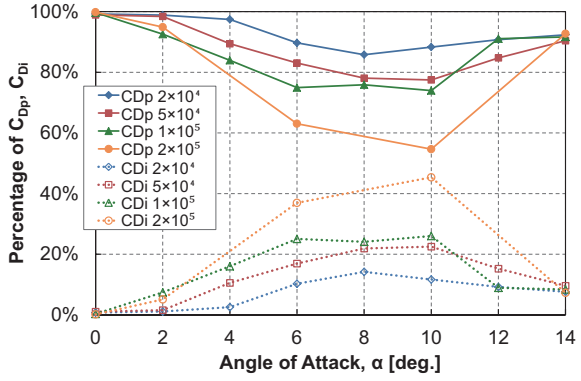

Fig. 6 Proportion of Profile and Induced Drags to Total Drag

Image-Processing Technique for Fluorescence Minituft Method in Dynamic Wind-Tunnel Testing

Ryota Nakajima, Daiju Numata and Keisuke Asai
Department of Aerospace Engineering, Graduate School of Engineering, Tohoku University
6-6-01 Aramaki Aza Aoba, Aoba-ku, Sendai, Miyagi, 980-8579 JAPAN
nakajima.ryota@aero.mech.tohoku.ac.jp

ABSTRACT

To visualize unsteady flow on a model moving in a wind tunnel, an image-processing technique for extracting unsteady regions from fluorescent minituft images has been developed. The index of flow unsteadiness, defined as projected area of minituft, was calculated from processed minituft images. The developed technique has been applied to a slender delta wing undergoing a single-DoF rolling motion. A temporal variation of LEV breakdown was clearly visualized. This study has demonstrated that the present method is an effective experimental means to extract flow features on a moving model.

1. Introduction

Recently, to develop an airplane which has higher flight safety characteristics under various weather conditions have been required. To this purpose, to clarify unsteady and/or nonlinear aerodynamic phenomena on and around the airplane is important. To study nonlinear flight behaviors of an airplane, a demand of Dynamic Wind-Tunnel Testing (DWT) has increased in recent years. In DWT, an airplane model is oscillated or rotated using a robotic manipulator and resulting unsteady force and moment acting on the moving model are measured. In these dynamic tests, it is important to know about unsteady flow fields around a moving model such as hysteresis, vortex breakdown and so on. To this purpose, measurements of force and moment are not sufficient and understanding of the flow field around the model is essential. However, the flow field around a moving model is complicated and varies with time.

Fluorescence minitufts are a promising method to visualize flow field around a dynamically moving model [1]. By applying minitufts on the surface of a model, flow direction and unsteady region on the model surface can be visualized as behavior of tufts. However, the conventional fluorescence minituft method can capture only qualitative features of the flow field because we only estimate the flow field from visual behavior of minitufts. Therefore, it is anticipated to develop a method to analyze the fluorescence minituft images quantitatively.

In this study, we developed a new image-processing technique to extract unsteady regions from surface flow-field images obtained by fluorescence minituft method. The effectiveness of this method has been evaluated in wind-tunnel tests of a slender delta wing performing a single-DoF forced rolling motion. Based on the results obtained in these experiments, the effect of rolling motion on unsteady flow field on surface of the delta wing is discussed.

2. Fluorescence mini-tuft method

The fluorescence minituft method was invented by Dr. J. P. Crowder, scientist at Boeing Company. In this method, extremely thin and light fluorescent monofilaments are used as minitufts. Hundreds of minitufts are glued to the model surface by adhesives. In order to detect thin minituft, the minitufts are dyed with fluorescence material. The minitufts are excited by ultraviolet light and their emission is captured by a video camera. There are three advantages of minitufts; Firstly minitufts have negligible effects of gravitational and inertial forces caused by their own weight. Secondly, minitufts have a negligible effect on aerodynamic force data and thirdly minitufts have a good response to surface flow behavior. With these advantages, the fluorescence minituft method has been applied also to dynamically moving objects.

3. Image processing technique

The sketches in Figure 1 represent three major states of flow for a minituft observed in surface flow visualization [2]. Minituft images can be classified into three types; attached, unsteady and separated flow depending on amplitude of minituft.

In this study, we detect unsteady regions on the model surface by evaluating unsteadiness of local flow as a difference of minituft projected areas. Figure 2 shows a schematic procedure of image processing in this study. Finally, a small circle is drawn at the root position of a minituft. The color of each circle indicates magnitude of the flow unsteadiness index.

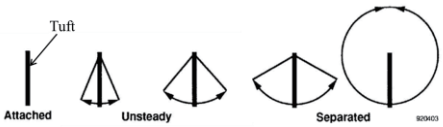

Fig. 1 Flow condition criteria for tufts [2]

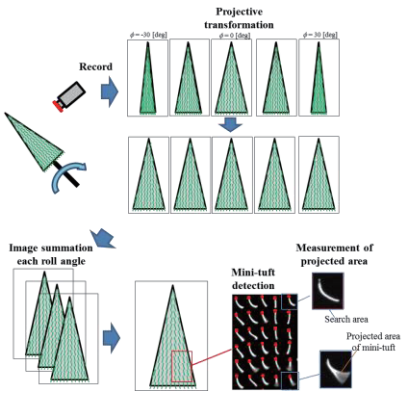

Fig. 2 Procedure of image processing

4. Description of experiment

4.1. Wind Tunnel

Experiments were conducted in the Low-Turbulence Wind Tunnel at Institute of Fluid Science (IFS), Tohoku University. This is a closed circuit wind-tunnel with an open-type octagonal test section with the cross distance of 0.8 m.

4.2. Robotic manipulator

An intelligent serial-type robot manipulator (PA-10, Mitsubishi Heavy Industries, Ltd.) was used to set the model attitude and to produce a rolling motion of the model.

4.3. Test model and minitufts

A test model is a simple flat-plate delta-wing model with sweep angle of 80 degrees. The length (c) is 300 mm and the thickness (h) is 2 mm.

The material of minitufts is polyester monofilament with the diameter of 50 μm. The minitufts were glued on the model surface using fast-acting adhesive. The length and spacing of minitufts was 7 mm.

4.4. Optical system

Two set of UV-LED light sources were used to excite minitufts with 395 nm wavelength. A CMOS high-speed video camera (BASLER acA2000-340 km) was used to record fluorescence images of minitufts. In this experiment, exposure time of the camera was set at 2.5 ms and the shutter speed was at 200 fps.

4.5. Test condition

In this experiment, the actuator forced a single-DoF forced rolling motion of the delta-wing model. The angle of attack (α) of the model was set at 35 degrees. The amplitude of rolling motion ($\Delta\phi$) was 30 degrees and the oscillation frequency (f) was 1 Hz. The free-stream velocity (U) was set at 30 m/s.

Rolling motion of the model was conducted for 22 cycles. The images of fluorescence minitufts were integrated over 20 cycles except those in the first and the last cycles.

5. Results and Discussion

Figure 3 shows an example of image processing procedure. The left figure is raw image, the middle figure summed image of the images transformed using projective transformation, and the right figure the distribution of the flow unsteadiness index. High strength of color indicates the regions showing strong unsteadiness. Seeing the middle image up close, we can detect the unsteady regions. However, it is difficult to understand the flow features from these images intuitively. Meanwhile, the unsteady regions are clearly visualized in right image.

Figure 4 shows the effects of rolling direction on occurrence of leading-edge vortex (LEV) breakdown. It is seen that the flow field on the wing is dependent on the rolling direction and there is time delay between the wing motion and the vortex breakdown. In addition, it is seem that region of vortex breakdown is larger in static than in dynamic.

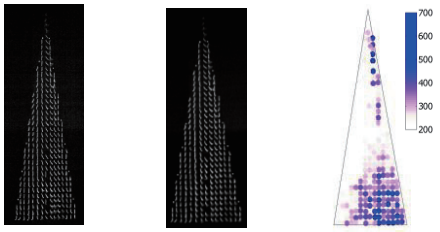

(a) (b) (c)

Fig. 3 Minituft visualization; (a) raw image, (b) image obtained by projective transformation and summation, and (c) processed image (index of flow unsteadiness)

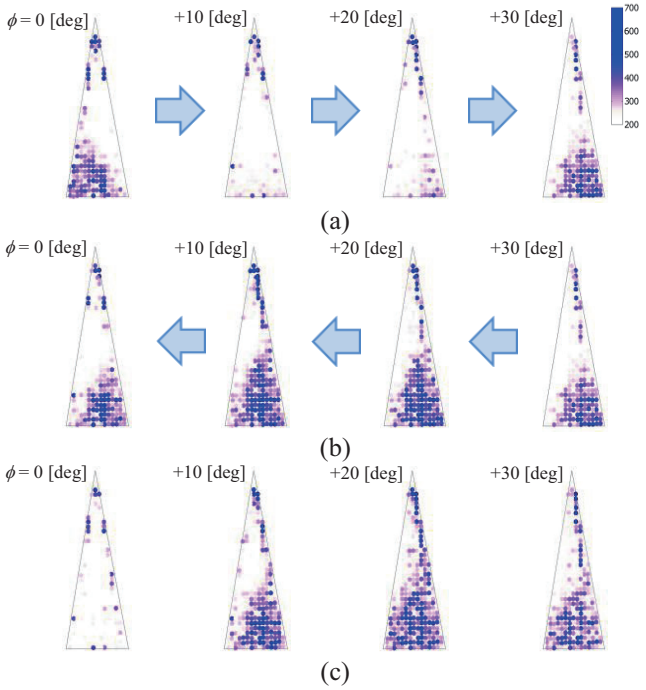

(a)

(b)

(c)

Fig. 4 Effect of rolling direction on the flow; (a) Downward, (b) Upward, and (c) Static

6. Concluding remarks

In order to visualize unsteady flow field on the surface of a model moving in a wind tunnel, an image processing technique to extract the unsteady regions from fluorescent minituft images has been developed. The developed technique has been applied to a slender delta wing undergoing single-DoF rolling motion. A temporal variation of LEV breakdown was clearly visualized. This study has demonstrated that our method can be an effective experimental means to extract unsteady flow features on a moving model.

References

[1] J. P. Crowder, “Add Fluorescent Minitufts to the Aerodynamicist’s Bug of Tricks,”Astron & Aeron., American Institute of Astronautics and Aeronautics, Nov. 1980

[2] John H. Del Frate, John A. Saltzman, “In-Flight Flow Visualization Results From the X-29A Aircraft at High Angles of Attack”, NASA Technical Memorandum 4430, 1992

Tenth International Conference on Flow Dynamics
November 25-27, 2013, Sendai, Miyagi, Japan

Numerical Evaluation of the Effect of the Mode of Microwave Propagating Inside a Pipe on the Detectability of a Microwave Nondestructive Testing Method

Noritaka Yusa, Kota Sasaki, Hidetoshi Hashizume
Department of Quantum Science and Energy Engineering, Graduate School of Engineering, Tohoku University,
6-6-01-2 Aramaki Aza Aoba, Aoba, Sendai, Miyagi, 980-8579 Japan.
noritaka.yusa@qse.tohoku.ac.jp

ABSTRACT

This study evaluates the dependency of a microwave nondestructive testing method to detect and evaluate flaws appearing inner surfaces of a metallic pipe on the mode of the microwave propagating inside the pipe with the aid of finite element simulations. The simulations calculate the reflection of microwave due to a full circumferential wall thinning appearing at the inner wall of an infinitely long straight pipe with an inner diameter of 39 mm. The results of the simulations reveal that the relation between the dependency of the reflection and exciting frequency depends significantly on the mode of the propagation of the microwave.

1. Introduction

Piping systems play an important role in large structures such as plant. However, their deterioration is almost inevitable mainly because of the interaction with fluids flowing inside. Thus it is important to evaluate their integrity with periodical non-destructive testing [1].

A non-destructive method using a microwave has been proposed on the basis of the demands to inspect long and complex piping systems quickly [2]. Its principle is to let microwave propagate inside a piping system, and detect and evaluate flaws appearing inner surfaces of the piping system on the basis of the reflection and transmission of the microwave. Earlier studies have demonstrated that the time-of-flight of the reflection contains the information about the location of a flaw, and the amplitude of the reflection signals can be correlated with the size of the flaw [3]. The studies have also revealed that how microwaves propagate inside a pipe would affect signals due to a flaw [4]. However, studies so far have not discussed the effect of the mode of the microwave propagating inside a pipe on the signals due to a flaw because of the difficulty in controlling the mode.

On the basis of the background above, this study evaluates the dependency of signals of the non-destructive testing method using a microwave with the aid of finite element simulations.

2. Method

This study evaluates the reflection of a microwave due to a flaw appearing the inner surface of a straight pipe with an inner diameter of 39 mm. The simulations excluded a probe that is in reality utilized to convert microwave transmitted inside a coaxial line as TEM mode into circular modes that can propagate inside a pipe. That is, the simulations assumed that a microwave of a given mode was generated at an end of the pipe by imposing suitable boundary condition at the end. Whereas the length of the pipe was 3 m in the simulations, a perfect matching layer [5], which absorbs all electromagnetic fields, was situated at the end of the pipe. This realizes no reflection from the end, and enables to simulate an infinitely long pipe.

Flaws considered in the simulation are full circumferential wall thinning with a rectangular cross section. The depth and the axial length of the wall thinning are 1.9 and 50 mm, respectively. The distance between the end where a microwave starts to propagate and the edge of wall thinning is 1.5 m.

The numerical simulations were carried out using commercial finite element software, Comsol Multiphysics and its RF Module (version 4.3b), in the frequency domain. The governing equation of the simulations is

$$\nabla \times \frac{1}{\mu_r}(\nabla \times \mathbf{E}) - k_0^2 \left\{ \varepsilon_r - \frac{j\sigma}{\omega \varepsilon_0} \right\} \mathbf{E} = 0, \qquad \text{(a)}$$

where $\mathbf{E}$ denotes electric field, and ε_r and μ_r are the relative permittivity and permeability, respectively; σ is the electrical conductivity, and ω is the angular frequency. Imaginary unit is denoted as j, and $k_0^2 = \omega^2 \varepsilon_0 \mu_0$ where ε_0 and μ_0 are permittivity and permeability of vacuum. Since the depth of penetration at frequencies considered in this study is as small as 10 micrometer, the tube wall was dealt as a perfect conductor

The simulations were conducted in an axisymmetric configuration. In order to consider non-axisymmetric electromagnetic fields such as TE_{11} mode, the simulations imposed that azimuthal variation of the field is $\exp(jn\theta)$ where n is the given azimuthal wave number and θ is the azimuthal angle. Consequently, the simulations here assume that the azimuthal variation of the fields is same at anywhere, and thus do not consider the superposition of modes whose azimuthal variations are different.

The simulations used triangular element whose longest edge is assured to be equal to or shorter than 0.75 mm that is shorter than 1/10 of the shortest guide wavelength. Frequencies considered are from 5 to 40 GHz with a step of 0.1 GHz. Cut-off frequencies of several modes considered in the simulations are summarized in Tables 1 and 2.

3. Results and Discussion

The results of the numerical simulations are shown in Figs. 1 and 2. The figures present the relation between the reflection coefficient, which were calculated from S-parameter as $\mathrm{abs}(S_{11})^2$, as a function of exciting

frequency. Reflection coefficients below cut-off frequencies are dealt as zero in the figures.

The results reveal that the reflection coefficient is not constant but has significant dependency on exciting frequency. There are several specific frequencies that provide large reflections. In addition, different propagation modes exhibit different relation between the reflection coefficients and exciting frequency. These imply that mode conversion techniques such as [6] and [7] would be beneficial to obtain clearer signals as well as to extract information needed from measured signals.

Table 1. Cut-off frequencies of TM_{mn} modes

		n				
		1	2	3	4	5
m	0	5.9	13.5	21.2	28.9	36.6
	1	9.4	17.2	24.9	32.6	40.3

Unit: GHz

Table 2. Cut-off frequencies of TE_{mn} modes

		N				
		1	2	3	4	5
m	0	9.4	17.2	24.9	32.6	40.3
	1	4.5	13.1	20.9	28.6	36.4

Unit: GHz

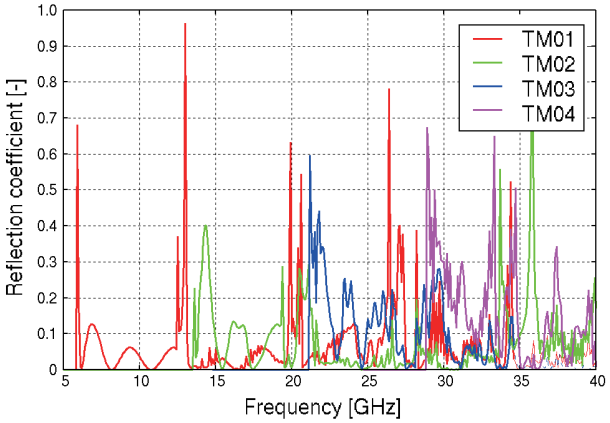

(a) TM_{0x}

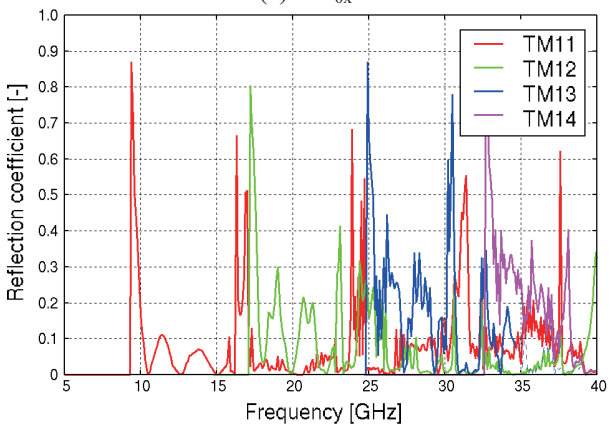

(b) TM_{1x}

Fig. 1 Dependency of reflection coefficient of TM modes on frequency

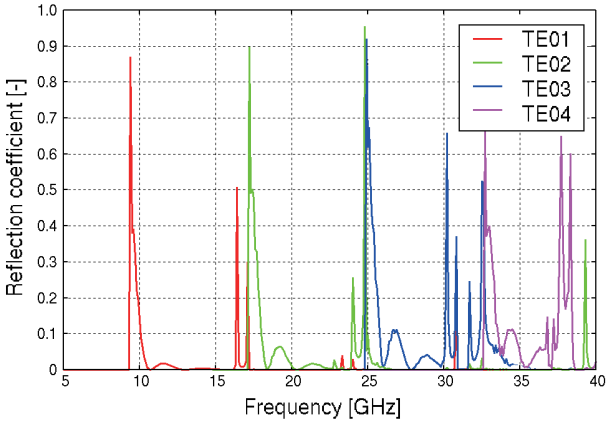

(a) TE_{0x}

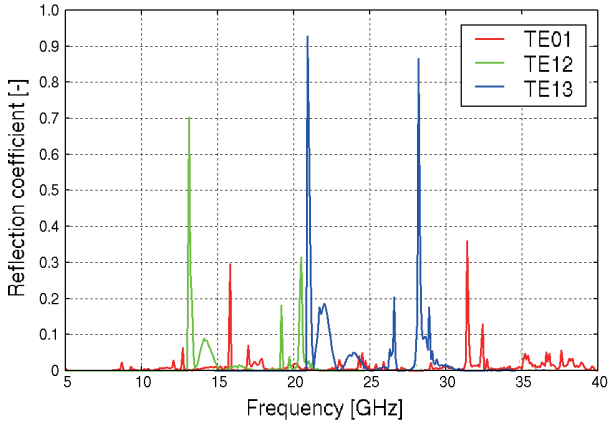

(b) TE_{1x}

Fig. 2 Dependency of reflection coefficient of TE modes on frequency

4. Concluding remarks

This study evaluated the characteristics of a non-destructive testing method using a microwave propagating inside a pipe to evaluate the degradation of the pipe using finite element simulations. The results clearly showed that the characteristics depend on the mode of the microwave significantly. Further studies include evaluating the effect of crack parameters and analyzing the characteristics in time domain.

References

[1] I. Nishiguch et al., E-Journal of Advanced Maintenance, **2** (2010), 14-24.

[2] H. Hashizume, T. Shibata, K. Yuki, Int. J. Appl. Electromag. Mech., **20** (2004), 171-178.

[3] Y. Sakai, N. Yusa, H. Hashizume, Nondestr. Test. Eval, **27** (2012), 171-184.

[4] K. Abbasi, NH. Motlagh, MR. Nematollahi, H. Hashizume, Int. J. PVP., **86** (2009), 764-768.

[5] Comsol Inc., Comsol Multiphysics RF Module Version 4.3b User's Guide (2013).

[6] CW. Yuan et al., IEEE Microw. Wireless Comp. Lett., **15** (2005), 513-515.

[7] RL. Eisenhart, Microwave Symposium Digest, **1** (1998), 249-252.

Development of a Triple-Axis Thermal Acceleration Sensor

Thien Xuan Dinh, Yoshifumi Ogami
Department of Mechanical Engineering, Ritsumeikan University
1-1-1 Nojihigashi, Kusatsu, Shiga, 525-8577 Japan
thien@cfd.ritsumei.ac.jp

ABSTRACT

In this paper, we design and analyze the sensitivity and response of a triple-axis thermal micro-accelerometer. Typically, thermal accelerometers detect acceleration by measuring the deflection of a heat plume on a microcavity. Conventionally, the heat plume is created by a heater at the center of the top of the cavity. In contrast, in our novel design, the heater formed a wide loop rounding the cavity center so that it is able to measure three components of acceleration simultaneously. The cross sensitivities were less than 5% for acceleration up to 10g applied to any directions and frequency bandwidth at 3 dB of 70 Hz was obtained.

1. Introduction

Recently, inertial sensors with multi-axis measurement ability are required since this ability allows lowing energy consumption and high precision. In general, vibratory accelerometers using a suspended proof mass can measure simultaneously three components of acceleration vector because the proof mass can move in three directions [1–2] However, the vibratory accelerometers have the disadvantages such as multi–step and complicated fabrication process. The tiny bridges that are used to hold the proof mass are fragile then cannot suffer a high shock. Furthermore, the efforts to remove the squeeze film effect between the proof mass and accelerometer structure requires a complex package. Alternatively, thermal accelerometers eliminate these drawbacks because they avoid using solid proof mass. Their operation is based on the displacement of a hot air bubble generated by a heated wire in an enclosed chamber under acceleration. Various gas and liquid media have filled in the chamber [3-5] to improve the sensitivity of this type of accelerometers. Nevertheless, the developed thermal accelerometers can measure only two components of acceleration vector. Recently, a principle for a triple–axis accelerometer has been proposed [6]. However, there is no discussion if this principle is efficient or not.

In this study, we design a new structure that can be used as a triple-axis acceleration sensor. The design of the sensor is driven from the thermal fluid analysis. The sensitivity of the sensor is then investigated by computational fluid dynamics. Finally, the response of the sensor under sinusoidal acceleration is analyzed.

2. Design of the Accelerometer

In our new design as shown in Fig. 1(a), the heater is formed a wide ring and therefore the temperature detectors are possible to locate both inside and outside of the heater ring. Figure 1(b) plots ΔT_X and ΔT_Z for $0<x/L<1$. The figure shows that ΔT_X is small and ΔT_Z is large inside the heater ring $0<x/L<\alpha$ where α indicates the location of the heater. In contrast, ΔT_X is large and ΔT_Z is small outside the heater ring, $\alpha<x/L<1$. Therefore, it is obvious that locating Z-detectors inside the heater ring and X-detectors outside the heater ring can reduce significantly the cross talk between X-measurement and Z-measurement. The physics behind this phenomenon is that the buoyancy flow due to a_z in the region just above the cavity center is high when the heater forms a loop, thus temperature here varies sensitively with a_z.

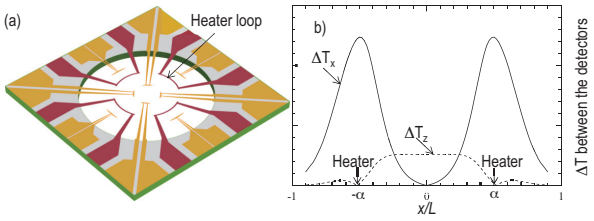

Fig. 1 (a) The configuration of the present sensor. (b) The radial distribution of the difference in temperature between the detectors.

3. Simulation

In order to capture the density–temperature dependence due to large temperature change, the conservative law of mass, momentum, and energy for a compressible fluid are employed to describe the thermo–fluidic phenomena in the accelerometer, which can be expressed as follows:

$$\partial\rho/\partial t+\nabla\cdot(\rho\vec{u})=0 \quad (1)$$

$$\partial\rho\vec{u}/\partial t+\nabla\cdot(\rho\vec{u}\vec{u})=-\nabla p+\nabla\cdot(\mu\nabla\vec{u})+\rho\vec{a} \quad (2)$$

$$\partial\rho c_p T/\partial t+u\cdot\nabla\rho c_p T=\nabla\cdot(\lambda\nabla T) \quad (3)$$

where u, p are velocity and pressure of the fluid flow. ρ, c_p, μ, λ and are density, specific heat, viscosity, and thermal conductivity of the fluid. a is acceleration vector. The term represents the momentum source due to the change of fluid density. To close the equations, we assume that the working fluid obeys the ideal gas law as

$$p=\rho RT/M_w \quad (4)$$

with R is universal gas constant, M_w is gas molecular weight.

The sensor is decomposed into a hexagonal mesh. The flow parameters on this mesh then are obtained by computational fluid dynamics package, Fluent–ANSYS Inc., which uses Volume–Finite Method to discrete the governing equations. The SIMPLEC method was adopted for pressure–velocity coupling and all spatial discretizations were performed using the second–order center scheme. The heaters are simulated as a solid zone with constant heat generation rate.

3. Results and Discussion

We discuss only the measurements of *x* and *z* components of acceleration because of the equivalence between the measurements of *x* and *y* components. To consider the cross effect between the vertical and horizontal measurements, i.e., the effects of a_x to ΔT_z and of a_z to ΔT_x, we simulate for a_x = 0g to 100g and a_z = 1g to 101g in combined manner.

Figure 2 plots the variation of ΔT_x with a_x for different a_z. We observe that ΔT_x varies linearly with a_x up to a_x = 20g with the sensitivity $\Delta T_x/a_x \sim 0.29^0$C/g. The effect of a_z on ΔT_x is within 5% in comparison with ΔT_x at a_z = 1g if a_z is less than 11g.

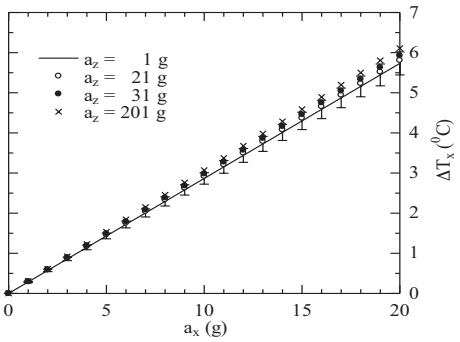

Fig. 2 Variation of ΔT_x with a_x for different a_z. The error bar represents 5% of T_x at a_z = 1 g.

Similar to Fig. 2, Fig. 3 plots the variation of ΔT_Z with a_z for different a_x. It shows that ΔT_z increases linearly with a_z up to a_z = 20g with the sensitivity $T_z/a_z \sim 0.062^0$C/g. The increase in ΔT_Z due to the increasing a_x is less than 5% of ΔT_z at a_x = 0g if a_x is less than 11g.

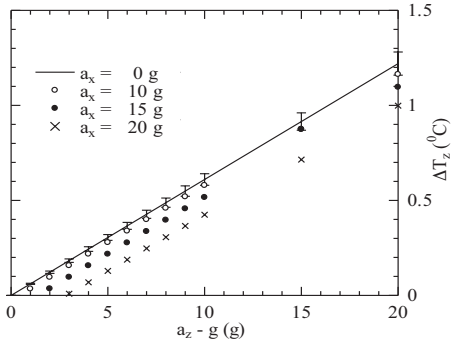

Fig. 3 Variation of ΔT_z with a_z for different a_x. The error bar represents 5% of T_z at a_x = 0 g.

By using linear least square technique, we can formulate the change of ΔT_x and ΔT_z as function of a_x and a_z in the range of 0 g to 10 g as

$$\begin{aligned} \Delta T_x &= 0.29a_x + 0.002(a_z - g) \\ \Delta T_z &= -0.002a_x + 0.062(a_z - g) \end{aligned} \quad (4)$$

Eq. 4 represents the dominant effect and of a_x and neglected effect of a_z on ΔT_x, and in contrast, the significant effect of a_z and neglected effect of a_x on ΔT_z.

The response of the sensor is simulated under a sinusoidal acceleration a_x and a_z as

$$a = A\sin(2\pi ft) \quad (5)$$

Since the detector has typical thermal diffusivity of 1×10^{-4} m2/s and length of 3×10^{-4} m, the response of the detector resistance to the change of its temperature is up to (1×10^5 Hz). In our present study, the sensor is investigated under frequency of (10 Hz). Consequently, the transient response of the sensor is dominated by the fluid response.

The response of the sensor is shown in Fig. 4. The sensor frequency bandwidth at 3 dB is about 70 Hz. This frequency is higher than reported in [5], which is represented by the black dotted line, because the detectors are located a distance above the open surface of the cavity where the air can response easier than at the cavity surface.

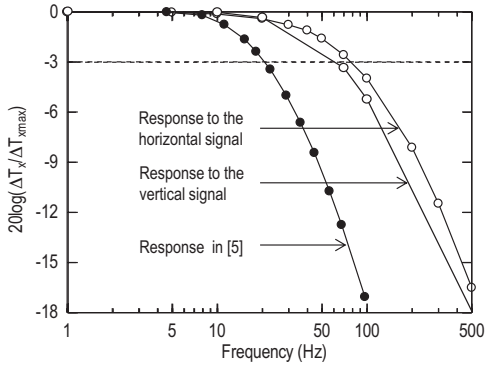

Fig. 4 The response of the sensor

4. Concluding remarks

The sensitivity and response of a triple–axis thermal accelerometer was numerically studied. The sensor was simulated in the state that both vertical and horizontal acceleration are applied simultaneously. Therefore, the mutual effect between the vertical and horizontal measurements was explicitly investigated. The output of the sensor is linear with acceleration with the slope of 0.29^0C/g for horizontal measurement and of 0.062^0C/g for vertical measurement, and cross sensitivities are less than 5%, for acceleration within 10g. Finally, a frequency bandwidth at 3 dB of 70 Hz was obtained with applying a sinusoidal acceleration.

Acknowledgment

This work was partially funded by Grant–in–Aid for Scientific Research (C)–25390047.

References

1. U.A. Dauderstadt, P.M. Sarro and P.J. French: Sens. Actuators A Vol. 66 (1998), p. 244.
2. E. Belloy, A. Sayah and M.A.M. Gijs: Microelectromech. Syst. Vol. 11 (2002), p. 85
3. S. Billat, H. Glosch, M. Kunze, F. Hedrich, J. Frech, J. Auber, H. Sandmaier, W. Wimmer and W Lang: Sens. Actuators A Vol. 97–98 (2002), p. 125
4. K.M. Liao, R. Chen and B.C.S Chou: Sensor Actuator A Vol. 130–131 (2006), p. 282
5. F. Mailly, A. Giani, A. Martinez, R. Bonnot, P. Temple–Boyer and A. Boyer: Sensor Actuator A Vol. 103 (2003), p. 359
6. Y. Hua, L. Jiang, Y. Cai, A. Leung and Y. Zhao: US Patent 0101813 A1 (2007)

Tenth International Conference on Flow Dynamics
November 25-27, 2013, Sendai, Miyagi, Japan

Numerical Study on the Propagation of Ultrasonic Acoustic Sound from a Parametric Array for Application to Underwater Technology

Kei Fujisawa, Youichirou Kawaguchi
University of Tokyo, Graduate School of Interdisciplinary Information Studies, 7-3-1, Hongo, Bunkyo-ku, Tokyo 113-0033 Japan
fujisawa_ocean_eng@yahoo.co.jp

ABSTRACT

This paper presents numerical study on the propagation of ultrasonic acoustic sound generated from a parametric array. To consider the non-linear effect of acoustic sound from the parametric array, the KZK equation is solved numerically for application to the underwater technology. The numerical result shows that the sound pressure level of the emitted sound increases with an increase in the difference frequency in the near field of the parametric array, while the sound pressure level tend to be saturated at higher difference frequency.

1. Introduction

The parametric array is one of effective methods for detecting the concealed structure in the underwater technology. This technique relies on the emission of two different frequencies of ultrasonic acoustic sound from the sound source. Due to the non-linearity of the finite amplitude of the ultrasonic sound propagating through the medium fluid, the difference sound frequency is generated with highly directional acoustic wave and at lower frequency than the emitted acoustic sound. Hence, the parametric array can detect effectively the underwater structure, when the reflected wave is detected by the receiving array. Although the basic idea of parametric array has been studied for application to the underwater technology, the characteristics of the wave propagation of the difference sound in water has not been fully understood due to the non-linear effect of the acoustic sound propagating through the water.

The characteristics of the ultrasonic acoustic sound emitted from a parametric array can be numerically studied by using Khokhlov-Zaboloskya-Kaznetsov (KZK) equation, which is the non-linear wave equation taking into account the influence of non-linear interaction of waves with finite amplitude. This equation was solved numerically by Aanonsen [1], Voronin et al.[2] and Kamakura [3] for the study of parametric array, and the validation of this equation in the underwater technology was experimentally confirmed by Garrett et al. [4] and Saito et al. [5]. However, optimum design performance of the parametric array for application to underwater technology has not been fully understood yet due to the complexity of the non-linear acoustics in water.

The purpose of this research is to study numerically the propagation of the difference sound from a parametric array by solving the non-linear wave equation of KZK for application to the underwater technology.

2. Method

The propagation of acoustic sound in water is governed by the non-linear wave equation, which is called KZK equation;

$$\nabla^2 p - \frac{2}{c_0}\frac{\partial^2 p}{\partial z \partial t} + \frac{b}{\rho_0 {c_0}^4}\frac{\partial^3 p}{\partial t^3} = -\frac{\beta}{\rho_0 {c_0}^4}\frac{\partial^2 p^2}{\partial t^2} \quad 1)$$

$$\left(\nabla^2 = \frac{\partial^2}{\partial x^2} + \frac{\partial^2}{\partial y^2}\right) \quad 2)$$

where b: absorption coefficient, c_0: sound speed, p: pressure, t: delay time, x, y: radial coordinates perpendicular to axial distance, z: axial coordinate, β: non-linear coefficient, ρ_0: density of fluid.

The KZK equation expresses the wave propagation of non-linear acoustic sound, such as higher harmonics wave and the difference sound produced by the interaction of principal acoustic waves from the parametric array. Normally, the difference sound frequency is smaller than 1/3 of the principal sound frequency of the emitted sound from the parametric array. The first term on the left hand side of Eq.(1) represents the wave propagation to radial direction and the second term is the wave propagation to axial direction, and the third is the dissipation, while the right hand side of Eq.(1) shows the non-linear term due to wave interaction.

3. Computational condition

The numerical simulation of the propagation of difference sound from a parametric array in water is carried out for application to the underwater technology. The computational parameters are summarized in Table 1. It should be mentioned that the center frequency of the emitted sound from the parametric array is set to 2MHz and the difference sound frequency was varied from 100kHz to 600kHz. Note that the cylindrical wave is emitted from the parametric array.

The numerical simulation was carried out in the axial distance 2m from the parametric sound source and the radial distance 12m with absorbing cells, which avoids the unexpected numerical noise in the computation.

Table. 1 Parameters of parametric array

Center frequency	2 MHz
Radius of array	1 cm
Pressure amplitude	100 kPa
Absorption coefficient	$25.3 \times 10^{-15} \times f^2$ Np/m
Sound speed	1483.18 m/s
Density of water	998.23 kg/m^3
Nonlinear coefficient	3.5
Temperature	293.15 K
f: frequency [Hz]	

4. Results and Discussion

Figure 1 shows the examples of numerical result of propagation of acoustic sound from a parametric array in water. The variation of sound pressure level of the difference sound is plotted against the distance z from the parametric array for the difference frequencies 200kHz (a) and 600kHz (b) with the central frequency of 2MHz. Generally speaking, the sound pressure level increases in a short distance from the parametric array up to the Rayleigh distance (z=0.42m), where the difference sound pressure level reaches a maximum, while the sound pressure amplitude decreases gradually in the far field. This observation is similarly observed in the previous numerical study [3], which suggests the validity of the present numerical result. On the other hand, the result also shows that the sound pressure amplitude increases with increasing the difference sound frequency. Figure 2 shows the relationship between the sound pressure amplitude and the difference frequency for some distances from the parametric array, which is obtained from the several computations of sound propagation for some difference frequencies of sound from a parametric array. The numerical result indicates that the sound pressure level of the difference sound increases with increasing the difference frequency, which might be due to the improvement in the performance of the difference sound at higher frequency. On the other hand, the improvement in the sound pressure level tends to be saturated at higher difference frequency.

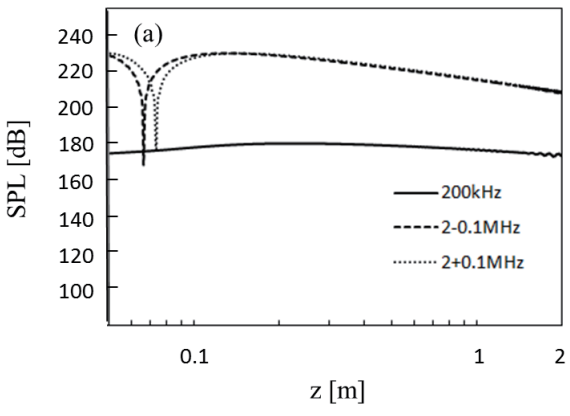

(a) f_d = 200kHz

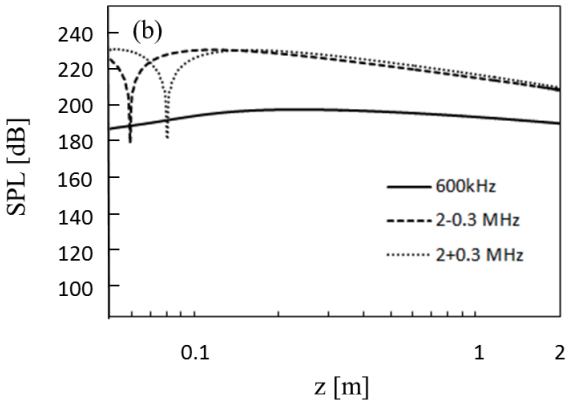

(b) f_d = 600kHz

Fig.1 Propagation of acoustic sound from parametric array (f_d = frequency of difference sound)

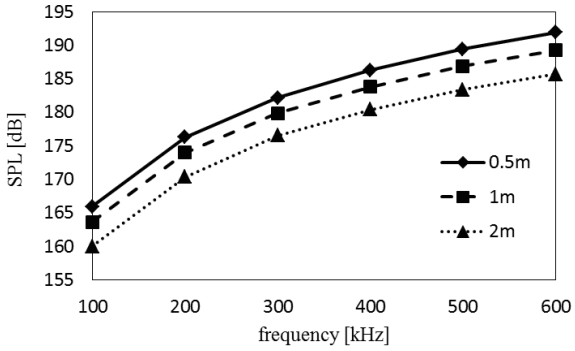

Fig.2 Sound pressure level versus difference sound frequency

4. Concluding remarks

The propagation of the difference sound from a parametric array is numerically studied by solving the KZK equation for application to the underwater technology. The result indicates that the amplitude of the difference sound increases with increasing the difference frequency, while the growth of the sound pressure level tends to be saturated at higher difference frequency. The future work is to study the optimization of the parameters in parametric array.

5. Acknowledgement

The authors would like to thank to Prof. T. Kamakura from The University of Electro-Communications and Prof. A. Asada from University of Tokyo for their helpful suggestion on this research.

References

[1] S. I . Aanonsen, J.N. Tjotta, and S. Tjotta, J. Acoust. Soc. Am. **75** (1984), 749-768.

[2] V.A. Voronin et al., Acoustical Physics, **46** (2000), 838-840.

[3] T. Kamakura, S. Sakai, IEICE Technical Report (2006), US2005-116 EA2005-100.

[4] G.S. Garrett et al., J. Acoust. Soc. Am, **74**(1983) 1013-1020.

[5] S. Saito and T. Tsubono, J. Acoust. Soc. Jpn, **19**(1998), 417-419.

Tenth International Conference on Flow Dynamics
November 25-27, 2013, Sendai, Miyagi, Japan

Characterization of Pressure-Sensitive Paint containing Ceramic Particles

Sakiko Kitashima, Yousuke Sugioka, Daiju Numata, Keisuke Asai
Dept. of Aerospace Engineering, Tohoku University,
6-6-01, Aramaki-Aza-Aoba, Aoba-ku, Sendai, Miyagi 980-8579, JAPAN
kitashima.sakiko@aero.mech.tohoku.ac.jp

ABSTRACT

To understand characteristics of Pressure-Sensitive Paint with ceramic particles, the effects of particle content and thickness of the layer on PSP were studied. In this study, particle content of PSP was changed from 0 to 90%, and static and dynamic properties of each sample were investigated. PSP with mixed dye molecules depends on both particle content and thickness. In contrast, PSP with adsorbed molecules depends only on particle content. By fitting the data measured in dynamic tests to multi-exponential functions, it was found that the time response of PSP was governed by diffusion of O_2 in polymer layer and voids created by particles.

1. Introduction

To study nonlinear flight behaviors of an airplane, a demand of Dynamic Wind-Tunnel Testing (DWT) has increased in recent years. In DWT, the test model is oscillated in the test section by a robotic actuator and the flow on the model is varied with time. As an efficient method to clarify such flow field, Pressure-Sensitive Paint (PSP) has attracted attention of researchers. For example, Hara et al. used PSP to visualize the unsteady pressure field on a rolling delta wing [1].

Hara used Polymer/Ceramic PSP (PC-PSP) that uses a binder composed of high concentration of hard particles and a small amount of polymer. PC-PSP has a good time response on the order of 10 μs, so that it is widely used in unsteady wind-tunnel tests. However, PC-PSP has relatively low pressure sensitivity and high temperature sensitivity that prevents accurate measurement of unsteady pressures in low-speed flow.

In this study, the effects of particle content of PSP binder on static sensitivities to pressure and temperature and dynamic response of PSP were studied to develop a suitable PSP for DWT. Two types of PSP prepared using different dye application techniques were tested and the effects of particle content and binder thickness on the characteristics of each PSP were investigated.

2. Method

2.1. Sample Preparation

In this study, poly(IBM-co-TFEM) (FEM) and TiO_2 (rutile type, $d < 1$ μm) were used as polymer and hard particles, respectively. From these materials, PSP samples were prepared according to Table 1. To evaluate the effect of an application method of dye molecules on PSP characteristics, two types of dye application techniques were employed and compared. One is "mixed-type", in which dye molecules are mixed into binder before splaying, and the other is "adsorbed-type", in which dye molecules dissolved in solvent is applied onto a binder coating splayed on the model beforehand.

2.2. Static Calibration (Sensitivity Measurement)

Both pressure and temperature sensitivities were evaluated by using a calibration chamber. Luminescence from a PSP sample set in the chamber was acquired by using a CCD camera (ORCA II-BT1024). Pressure were controlled from 80 to 120 kPa every 5 kPa, and temperature controlled from 5 to 30 °C every 5 °C.

2.3. Dynamic Calibration (Step Response)

2.3.1. Experimental Method

In this study, a calibration device consisting of a solenoid valve, high-voltage power source and a test cell was developed to create a step change in pressure. Figure 1 shows the experimental set up. First, the cell with a PSP sample inside was evacuated to 80 kPa. Then the cell was quickly opened to the atmosphere by driving the solenoid valve to create a step change in pressure. Over this opening process, luminescence from the PSP sample and pressure inside of the cell were acquired by a photomultiplier tube (PMT, H5784-02) and a pressure transducer (XCL-152-5SG), respectively. The obtained data were recorded by DAQ (USB-6251).

2.3.2. Data Analysis

In this study, two types of analytical procedure were introduced to evaluate the time response of PSP. Both were applied to the data in a step response experiment. The PMT data was transformed to pressure using Stern-Volmer relation, and the rise time was calculated.

The other procedure is a least-square fitting of the measured data to a multi-exponential function (eq. (1)) to determine the factors influencing PSP response.

$$y=1-\{a\exp(-\frac{t}{\tau_1})+b\exp(-\frac{t}{\tau_2})+(1-a-b)\exp(-\frac{t}{\tau_3})\} \quad (1)$$

Table 1. Sample Preparation

Dye application	Solvent of Dye	Thickness	TiO_2 Content[%]							
Mixed		6.3±2.9 μm (thin)	0	10	30	50	70	80	85	90
		9.7±3.5 μm (thick)								
Adsorbed	Toluene	8.0±3.6 μm (thin)		10	30	50	70	80	85	90
		12.0±5.4 μm (thick)								

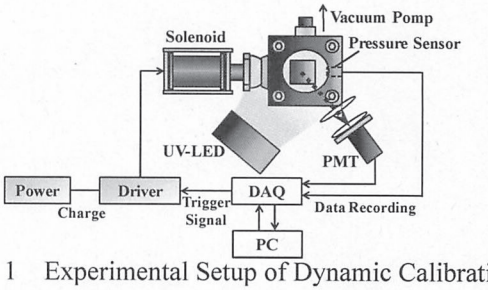

Fig. 1 Experimental Setup of Dynamic Calibration

3. Results and Discussion

3.1. Static Calibration

Figure 2 shows the pressure and temperature sensitivities for "mixed-type" PSP. Both of them tend to become worse when the particle content is above 80 %. The thickness of PSP layer has no significant effect.

Figure 3 shows the pressure and temperature sensitivities for "adsorbed-type" PSP. Both of them get worse as the particle content increases. Similarly to "mixed-type", the thickness of PSP layer has no significant effect on the sensitivities.

The sensitivities of both types of PSPs are similar from a quantitative view point. It is noted that static characteristics of PSP come closer to those of the conventional PC-PSP, as the particle content increases.

3.2.Dynamic Calibration

The rise time of each PSP is shown in Fig. 4. From these results, it is seen that the response time of PSP is improved by addition of particles. The effect on "mixed" PSP is more apparent than that on "adsorbed".

Figures 5 shows the fitting coefficients for "mixed" PSP. It is seen that "mixed" PSPs containing particles up to 80 % have three time-constant components, while the PSPs containing particles more than 85 % have two components. Thickness of PSP layer has no effect on time-constant. Weight coefficients of PSP considerably vary with particle content. The weight coefficient of the fastest time-constant increases as the particle content increases, but the other weight coefficients decrease. Thickness of PSP layer affects contribution of each time coefficient. This is true particularly for two slower time constants.

Figure 6 shows the fitting coefficients for "adsorbed" PSP. It is seen that "adsorbed" PSPs containing particles less than 80 % have two time-constant components, while PSPs containing particles more than 85 % has one component only. Thickness of PSP layer has no effects on time constant and weight coefficient.

4. Concluding remarks

In this study, the effects of particle content of PSP binder on static sensitivities to pressure and temperature and dynamic response of PSP were studied. Also the effects of thickness of PSP layer and application methods of dye were evaluated. Pressure and temperature sensitivities become worse, as particle content increases. Thickness of PSP layer does not influence the sensitivities. The effect of particle content depends on the way of dye application. On the other hand, the time response gets faster as particle content increases. This trend is more remarkable for "mixed" PSP. Also, thickness of PSP layer shows an effect on time response only for "mixed" PSP.

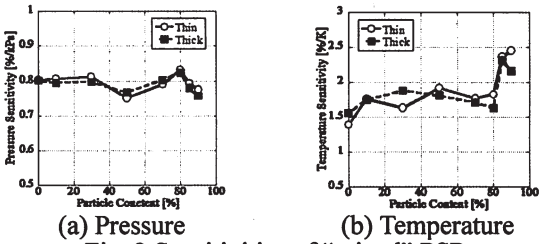

(a) Pressure (b) Temperature

Fig. 2 Sensitivities of "mixed" PSP

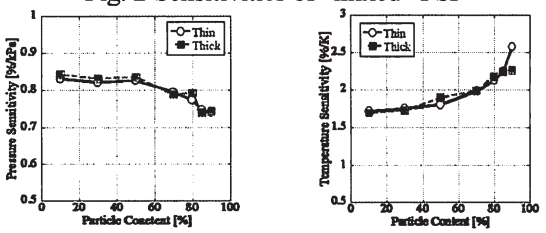

(a) Pressure (b) Temperature

Fig. 3 Sensitivities of "adsorbed" PSP

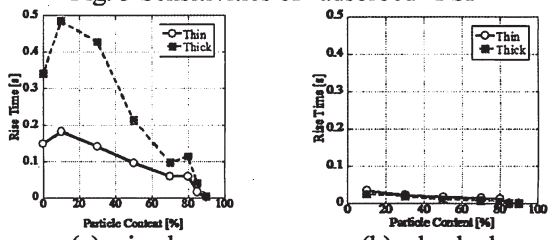

(a) mixed (b) adsorbed

Fig. 4 Comparison of Rise Time

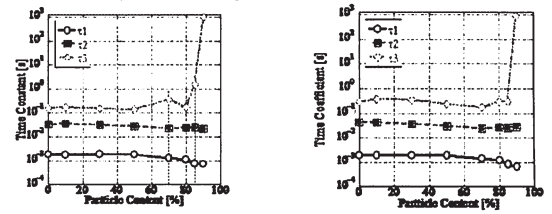

(a)Time Constant (Left: thin, Right: thick)

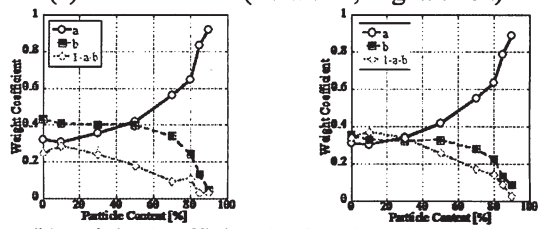

(b)Weight Coefficient(Left: thin, Right: thick)

Fig. 5 Fitting Coefficient (mixed)

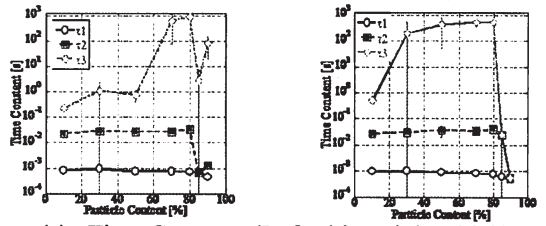

(a) Time Constant (Left: thin, Right: thick)

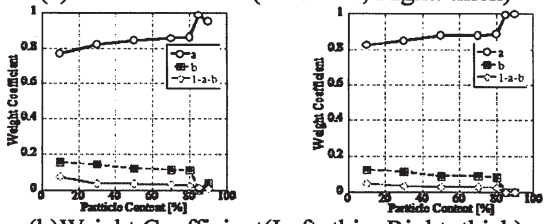

(b)Weight Coefficient(Left: thin, Right: thick)

Fig. 6 Fitting Coefficient (adsorbed)

References

[1]Tatsuya Hara , "Development of Binary Pressure-Sensitive Paint for Dynamic Wind-Tunnel Testing", MC. Dissertation, Tohoku Univ., 2012.

Tenth International Conference on Flow Dynamics
November 25-27, 2013, Sendai, Miyagi, Japan

Combined Influence of Form Drag and Thermal Non-Equilibrium State on the Stability of Mixed Convection in a Vertical Channel

Manish K. Khandelwal[a], Premananda Bera[a], Anupam Chakrabarti[b]
[a]Department of Mathematics, [b]Department of Civil Engineering,
Indian Institute of Technology Roorkee, Roorkee-247667, India
E-mail: mg_khandelwal@yahoo.co.in

ABSTRACT

A numerical study on the linear stability of fully developed mixed-convective flow in a vertical channel filled with saturated porous medium is investigated. The flow is induced by external pressure gradient and buoyancy force under local thermal non-equilibrium (LTNE) hypothesis. The Darcy-Brinkman-Forchheimer-Wooding model is employed. Special attention is given to understand the effect of thermal non- equilibrium parameters: H and γ on instability boundary and transition mechanism in (F, Ra)-plane. Analysis shows that induced form drag in the system stabilizes the flow, which is also characterized by LTNE parameters H and γ .

1. Introduction

Mixed convection in vertical system is a problem of current interest and is encountered in many applications, such as nuclear reactor, heat exchange, electronic equipment and other practical applications. In porous media, when flow strength parameter (Reynolds number) increases, it is expected the nonlinear drag becomes significant. In case of high velocity regime, the inertial effects dominate the flow. Several corrections have been suggested to capture the nonlinear effects. Here the Darcy-Brinkman-Forchheimer-Wooding (DBFW) model is used in momentum equation to capture non-linear effects. Apart from this, the flow mechanics and heat transfer phenomena in porous media also depends on the fluid and solid phases within a porous structure. In most of the studies on stability of mixed convective flow in vertical channel filled with porous medium, the state of local thermal equilibrium (equal temperature of two phases) is profoundly used (e.g. Bera et al. [1], Chen et al. [2], and Kumar et al. [3]). But in case of high Rayleigh number or rapid heat transfer for high speed flow, the temperature of the solid and fluid phase does not remain same and energy transfer between two phases takes place. This state of the medium is known as local thermal non-equilibrium (LTNE) state. Recently, a thermal non-equilibrium perspective on mixed convection in a vertical porous channel is investigated by Khandelwal et al. [4]. They have reported that the impact of LTNE state on basic flow is significant. The literature review shows that, the stability of the mixed convective basic flow under LTNE hypothesis in a vertical channel filled with a porous medium has not been considered yet. Therefore, a study is made to analyze the combined impact of form drag (to capture the non-linear effect) and thermal non-equilibrium state on the stability of mixed convection in a vertical channel.

2. Mathematical Formulation

The problem under consideration is linear stability of mixed convection in vertical channel filled with porous medium. Here flow is induced by external pressure gradient and linear varying temperature ($T_w = T_0 + Cx$, where C is a constant and T_0 is the upstream reference temperature) at the wall of channel (see Figure 1 in [4]). The Brinkman term is needed to satisfy no-slip boundary condition at solid walls. The governing equations are written under assumption of Darcy-Brinkman-Forchheimer model. The detailed governing equations are given in [4]. Stability of steady, unidirectional, fully developed flow is investigated by means of linear theory [6]. Using infinitesimal disturbances on the fully developed laminar base flow, the solution of the problem can be written in the form

$$(V, P, \theta_f, \theta_s) = (U_f(y)\vec{e}_x, P_0(x), \Theta_f, \Theta_s) + (V', P', \theta_f', \theta_s'), \quad (1)$$

The primed quantities denote the infinitesimal disturbances on the corresponding terms and can be represented by $(V', P', \theta_f', \theta_s')^T = e^{i(\alpha x + \beta z - \alpha c t)}(\hat{V}, \hat{P}, \hat{\theta}_f, \hat{\theta}_s)^T$, with α and β being real-valued wave numbers in x and z direction, respectively, and $c = \hat{c}_r + i\hat{c}_i$ is the complex wave speed. The growth and decay of the disturbances depends on $\hat{c}_i$. Three different cases may be distinguished, i.e., stable, neutrally stable or unstable depending on whether $\hat{c}_i < 0$, $\hat{c}_i = 0$ or $\hat{c}_i > 0$, respectively. The disturbance equations for velocity and temperatures are solved by Galerkin method.

In order to validate the results presented in this work, we have compared our results with published results (Chen et al. [5]) for a fluid-filled vertical channel as a particular case (F = 0, Da = 10^6, H = 0, Pr = 0.7 and ε = 1) of our results. The agreement is good (which is not shown here).

3. Results and Discussion

The present study illustrates the influence of form drag as well as thermal non-equilibrium parameters on the flow transition. For all numerical results presented here, Reynolds number (Re), Darcy number (Da), porosity (ε) and heat capacity ratio (σ), always take the values 500, Da^{-2}, 0.9 and 1, respectively. Two different fluids (two different Prandtl number (Pr)), air (Pr=0.7) and water (Pr=7.0), are considered to simulate the stability characteristics. A wide range [1, 10^5] of Forchhemier number (F) and three different values (1, 10, and 100) of inter phase heat transfer coefficient (H) and three different values (0.001, 0.01, and 0.1) of

thermal conductivity ratio (γ) have been considered to investigate the stability characteristic. To examine the combined impact of F and H as well as F and γ on instability characteristics, the stability boundary curves in the (F, Ra)-plane are plotted in Fig. 1 (a)-(c) for above three different values of γ . As can be seen from Fig. 1, for both cases (air (Pr=0.7) and water (Pr=7.0)), and any value of γ taken here, the critical Rayleigh number (Ra) increases on increasing the value of F as well as H. This shows that H and F stabilize the basic flow. Depending on γ there exist a threshold value of F, below which the impact is negligible. In both cases (air and water), for small value of H (=1) the impact of γ is also negligible. However for H=10 and H=100, increase in γ destabilizes the basic flow. It is also important to mention that the relative change of critical Ra on changing γ from 0.001 to 0.1 for H=100 is much more than the same for H=10. For example, in case of air, when F=10000, on changing γ from 0.001 to 0.1 the critical value of Ra changed from 230039 to 23154 for H=100, and from 830 to 594 for H=10.

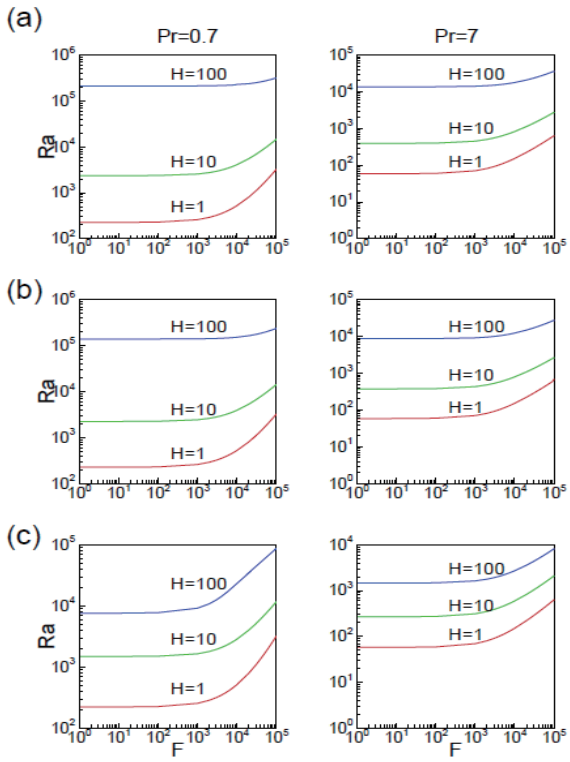

Fig. 1 Variation of critical Rayleigh number as function of F: (a) $\gamma = 0.001$ (b) γ=000 and (c) $\gamma = 0.001$

A qualitative explanation for the physics involved behind above observations can be given by definition of two different LTNE parameters (H and γ). When all other parameters are fixed, increase in H increases the volumetric inter phase heat transfer coefficient. Therefore, the heat transfer will take place from fluid to solid, which will annihilate the disturbance fluctuation. Consequently system will remain stable for relatively higher values of heat source intensity. Similarly, on increasing the value of γ , when all other parameters are fixed, the conductivity of the solid increases. Consequently, heat release from solid to fluid will be enhanced. Therefore, system will be unstable even for relatively lower value of Ra. The variation of secondary flow (disturbed flow) in terms of F at critical level for Pr=0.7, H=10 and γ =0.001 is plotted in Fig. 2. Here, we can see that, there exists a value F_o of F such that the secondary flow is uni-cellular for $F < F_o$ and bi-cellular for $F > F_o$. This shift in pattern is neither sudden nor abrupt. It appears under a continuous development of the flow. In particular, the disturbed flow is uni-cellular upto F=41500, beyond that it is bi-cellular.

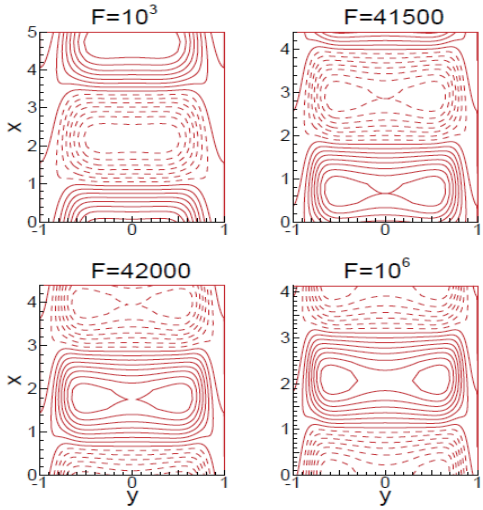

Fig. 2 Secondary flow pattern for different value of F at Pr = 0.7, H = 10 and $\gamma = 0.001$.

4. Conclusions

The following conclusions can be drawn from this study: (1) Form drag and LTNE parameter H stabilize the basic flow, whereas γ acts in reverse way.

(2) For small value of H, the impact of γ is negligible.

(3) The secondary flow pattern continuously shifts from uni-cellular to bi-cellular.

Acknowledgements

Manish K Khandelwal is thankful to the CSIR, India, for supporting financially to carry out this work.

References

[1] P. Bera, A. Khalili, Phys. Fluids, 14 (2002) 1617-1630.

[2] Y.C. Chen, Int. J. Heat and Mass Trans., 47 (2004) 1257-1266.

[3] J. Kumar, P. Bera, A. Khalili, Int. J. Heat Mass Trans. 53 (2010) 5261-5273.

[4] M.K. Khandelwal, P. Bera, Int. J. Thermal Sci., 56 (2012) 23-34.

[5] Y.C. Chen, J.N. Chung, J. Fluid Mech., 325 (1996) 29-51.

[6] P.G. Drazin, W.H. Reid, Cambridge Univ. Press 2004.

Temperature and Pressure Measurements in Cold Flow of Vortex Tube

Mohd Hazwan bin Yusof, Kouhei Moritake, Hiroshi Katanoda
Graduate School of Science and Engineering, Kagoshima University,
1-21-40, Korimoto, Kagoshima City, Kagoshima, 890-8580 Japan.
k1130849@kadai.jp

ABSTRACT

Vortex tube (VT) is a simple mechanical device, which splits compressed room-temperature gas into cold and hot flows. It can produce cold flow to around −30℃and hot flow up to around 130℃. Until now, several researchers have presented the measurement of temperature and pressure inside vortex tube. However, the temperature and pressure of discharged cold flow from VT have not been clarified. In this research, the temperature and pressure of the cold flow were measured, and the structure of the cold flow is discussed.

1. Introduction

Vortex tube is a simple and useful device to obtain cold and hot flows from a compressed gas at room temperature. It has a lot of advantages, such as light, small, no moving parts, no need for maintenance, and instant supply of cold flow. VT has been used mainly as a device to cool, such as electrical pieces, thermal sensors, controlling cabins, cutting tools and spots under thermal stresses [1]. Figure 1 shows the flow pattern and structure of VT. A compressed air enters VT through single or multiple tangential nozzles and produces a high-speed vertical flow in the vortex chamber. A part of the flow rotationally passes alongside the wall towards the opposite end, and the flow exits as a hot flow. The other part of the flow in the core is forced back towards the vortex chamber by a control valve, and exits as a cold flow from a cold exit.

Until now, several theories have been proposed about the thermal separation mechanism inside the VT by several researchers. It is generally accepted from those theories that, the temperature reduction of the cold flow is caused by an adiabatic expansion of a compressed gas. However, details of the physics of the cold flow generation, from the view point of fluid dynamics still remain unclear.

Several researchers had studied experimentally and numerically on the temperature and pressure inside VT [2], [3]. However, the temperature and pressure of the flow discharged from VT have not been studied. In this research, the temperature and pressure of the cold flow discharged from the cold exit were measured, and the structure of the cold flow is discussed.

2. Experimental Setup

Figure 2 shows a schematic diagram of the experimental setup of VT. A compressed air up to 1MPa is supplied to a vortex chamber of the VT through ① mass flow meters, ③ stagnation chamber and ④ pressure control valve. Then, a vertical flow is generated through the inlet tangential nozzles. The cold exit is located near the inlet tangential nozzles. The hot exit is at the other end of the tube. The VT used in this research has a tube inner diameter of D=14mm and a length to inner diameter ratio of L/D=20, a cold exit diameter of d=5mm, and four tangential nozzles. The inlet temperature, inlet pressure, cold flow temperature, and cold flow pressure were measured by a temperature-humidity sensor, total temperature probe, ⑤ digital manometer and ⑧ pressure sensor, respectively. The inlet pressures were varied in the range of 0.2~0.6MPa.

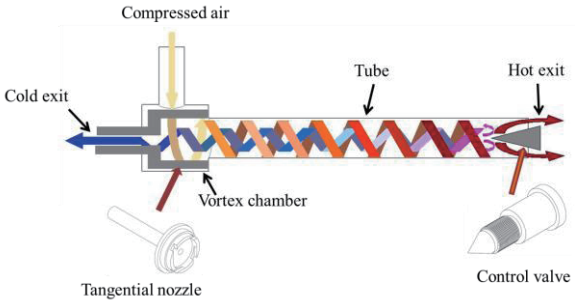

Fig. 1 The flow pattern and structure of Vortex Tube

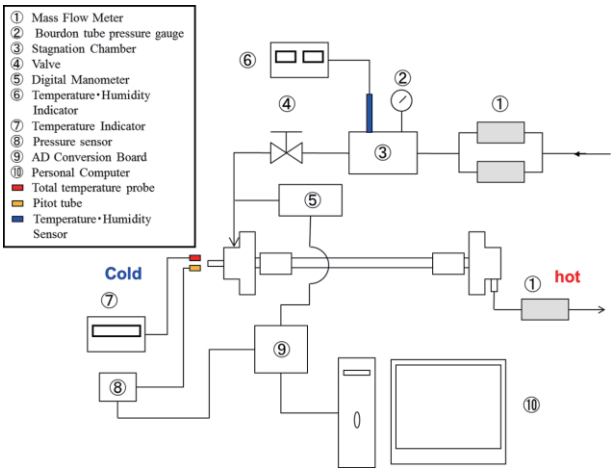

Fig. 2 Schematic diagram of the experimental setup

The temperature and pressure of cold flow were measured along the centerline of cold exit at a distance of 3mm from the exit using a total temperature probe and a Pitot pressure probe, respectively.

The Pitot pressure probe used in this research has inner and outer diameters of 0.13 and 0.31mm at the tip, respectively. The total temperature probe was created by inserting a T-type ϕ0.5 thermocouple into an acrylic rod with inner/outer diameters of 0.6/3.0mm and length of 21.5mm. Around 1mm from the tip of the thermocouple protruded the rod, and the 1mm-tip was covered with sponge to create a stagnation state during measurement.

The ratio of the mass flow rate of cold flow, $\dot{m}_{cold}$, to the inlet mass flow rate, $\dot{m}_{in}$, is called cold fraction, which is defined as;

$$\varepsilon = \frac{\dot{m}_{cold}}{\dot{m}_{in}} \tag{1}$$

The performance of VT is generally determined by the total-temperature difference between the inlet temperature, T_{in}, and the cold flow total temperature, $T_{t.cold}$, as shown in the following equation;

$$\Delta T_{t,cold} = T_{in} - T_{t,cold} \tag{2}$$

3. Results and Discussion

Figure 3 shows a contour map of Pitot pressure, measured at an axial distance of 3mm from the cold exit center, divided by atmospheric pressure, p_i/p_a. The horizontal axis shows the inlet pressure, p_{in}, and the vertical axis shows the cold fraction, ε. From this figure, when the inlet pressure is 0.20MPa, p_i/p_a is larger than 1.0 (positive pressure) for $\varepsilon \geq 0.75$. When the inlet pressure is increased to 0.3MPa, the boundary of positive/negative pressure decreases to $\varepsilon = 0.65$, and this boundary point remains almost constant at $\varepsilon = 0.65$ until p_{in} = 0.6MPa. The existence of p_i/p_a lower than 1.0 (negative pressure) implies the possibility of the occurrence of a reversed flow at the center of the cold flow for $\varepsilon < 0.65$.

Figure 3 shows the contour map of the total-temperature difference of the cold flow at an axial distance of 3mm from the cold exit center. The horizontal and vertical axes are the same as in Fig. 4. It can be seen from this figure that, the total-temperature difference increases when the inlet pressure increases. The total-temperature difference is larger when the inlet pressure is greater for ε smaller than 0.65. By comparing p_i/p_a and the total-temperature difference, the total-temperature difference is larger when p_i/p_a smaller than 1.0. These results clearly show that the pressure at the center of the cold exit is closely related to the amount of decrease in the temperature of the cold flow.

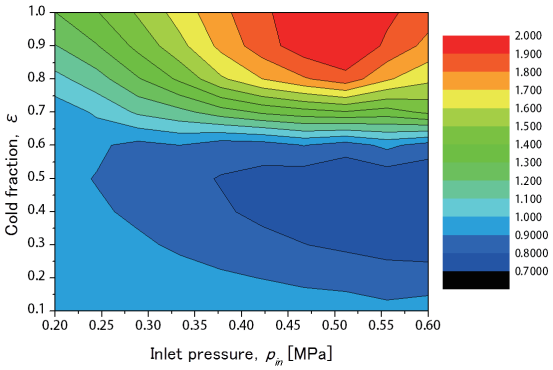

Fig. 3 Contour map of non-dimensionalized Pitot pressure, p_i/p_a, of cold flow

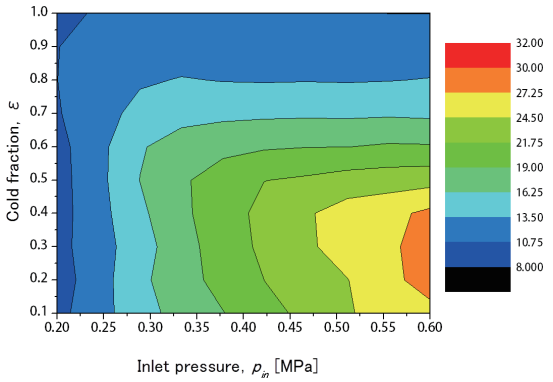

Fig. 4 Contour map of total-temperature difference of cold flow

4. Concluding Remarks

Experimental study of VT was conducted to measure the temperature and pressure of cold flow discharged from the VT. The results are summarized as follows;

The value of ε, where the Pitot pressure at the cold exit center is equal to atmospheric pressure, decreases from 0.75 to 0.65 when p_{in} is increased from 0.2 to 0.3MPa, and remains almost constant at 0.65 for $p_{in} > 0.3$MPa.

1) The Pitot pressure lower than atmospheric pressure at the cold flow exit center implies the possibility of a reversed flow occurring at the cold flow exit center for $\varepsilon < 0.65$.
2) The total-temperature difference increases when the inlet pressure increases for $\varepsilon < 0.65$.
3) The total-temperature difference is larger when the Pitot pressure at the cold exit center is lower.

References

[1] S. Eiamsa-ard, P. Promvonge, Review of Ranque-Hilsch effects in vortex tubes. Renew. Sustain. Energy Rev. 12 (2008), 1822-1842.

[2] Y. Xue, M. Arjomandi, R. Kelso, Experimental study of the flow structure in counter flow Ranque-Hilsch vortex tube, Int. J. Heat Mass Transfer 55 (2012), 5853-5860.

[3] U. Behera, P.J. Paul, K. Dinesh, S. Jacob, Numerical investigations on flow behaviour and energy separation in Ranque-Hilsch vortex tube, Int. J. Heat Mass Transfer 51 (2008), 6077-6089.

Tenth International Conference on Flow Dynamics
November 25-27, 2013, Sendai, Miyagi, Japan

Variational Approach to Necessary and Sufficient Stability Conditions for Inviscid Shear Flow

Makoto Hirota[1], Philip J. Morrison[2], Yuji Hattori[1]
[1]Institute of Fluid Science, Tohoku University, Sendai 980-8577, Japan,
[2]Institute for Fusion Studies, University of Texas at Austin, Austin, TX78712, USA
E-mail of corresponding author: hirota@dragon.ifs.tohoku.ac.jp

ABSTRACT

A necessary and sufficient condition for linear stability of inviscid parallel shear flow is formulated by a novel variational method, where the velocity profile is assumed to be monotonic and analytic. Unstable eigenvalues of the Rayleigh equation are shown to be associated with positive eigenvalues of a certain selfadjoint operator. The stability is therefore simply determined by maximizing a quadratic form, which is theoretically and numerically more tractable than directly solving the Rayleigh equation. This variational approach is based on the Hamiltonian nature of the inviscid fluid and will be applicable to other hydrodynamic stability problems.

1. Introduction

Linear stability conditions for shear flow are generally difficult to derive theoretically, even for the inviscid fluid model. Since the eigenvalue problem for the linearized fluid equation is infinite-dimensional and non-selfadjoint, it is mathematically hard to prove instability for a given equilibrium flow profile (unless the rare analytical solution exists). Although several variational approaches [1-4] have been proposed in the context of Hamiltonian mechanics, it is well-known that they give only sufficient conditions for stability.

The present work revisits the stability of inviscid parallel shear flow and considers the Rayleigh equation [5]. For this classical problem, we show that the variational approach can be improved so as to give a *necessary and sufficient* condition. Restricting our consideration to monotonic and analytic velocity profiles, we present a quadratic form Q whose positive signature indicates the existence of an unstable eigenmode. Instability can be proven by finding some test function that makes Q positive, which is analytically and numerically feasible without knowing the rigorous solution of the equation.

2. Variational stability criterion

Specifically, consider the linear stability of inviscid parallel shear flow $\vec{U}=(0,U(x))$ on a 2D domain $[-L,L]\times[-\infty,\infty]$ bounded by two walls at $x=\pm L$. By introducing the stream function of the disturbance as $\phi(x)e^{ik(y-ct)}+\text{c.c.}$ with a complex phase speed c and a wavenumber $k>0$, the stability is determined by Rayleigh's equation [5];

$$\begin{aligned}&(c-U)(\phi''-k^2\phi)+U''\phi=0,\\&\phi(-L)=\phi(L)=0,\end{aligned}\tag{1}$$

where the prime (') indicates the x derivative. If this equation has a nontrivial solution for c with a positive imaginary part, $\mathrm{Im}\,c>0$, the shear flow is spectrally unstable due to an exponentially growing eigenmode.

Rayleigh's necessary condition for instability [5] is that the velocity profile $U(x)$ must have at least one inflection point; i.e., an $x=x_I$ at which $U''(x_I)=0$. Arnold [1] improved this stability condition by using a variational approach. He showed that the shear flow $U(x)$ is stable if the quadratic form,

$$Q=\int_{-L}^{L}\xi[(U-U_I)+U''G]U''\xi dx.\tag{2}$$

is either positive or negative definite (see [4]), where $U_I=U(x_I)$ and the linear operator G denotes a convolution integral defined by $G^{-1}\phi=-(\phi''-k^2\phi)$. Physically, (2) represents the second variation of the energy with respect to the fluid displacement ξ.

In this work, we further improve this variational criterion by introducing the following assumptions.

Assumption (A1): *the velocity profile $U(x)$ is an analytic, bounded, and strictly monotonic function. Also, if $U''(x_I)=0$ at $x=x_I$, then $U'''(x_I)\neq 0$.*

If $U(x)$ satisfies (A1) and has only one inflection point x_I, then either $U''(U-U_I)\geq 0$ or $U''(U-U_I)\leq 0$ holds for all x. In the former case, the quadratic form (2) is positive definite and the flow is stable, which is also known as Fjortoft's theorem [6].

Thus, our concern is with the latter case, for which we present the following theorem.

Theorem 1. *Let $U(x)$ satisfy (A1) and have one inflection point $x=x_I$. When $U''(U-U_I)\leq 0$ for all x, the shear flow is spectrally stable if and only if the quadratic form (2) is not positive for all $\xi\in \mathrm{L}^2$.*

We can generalize this theorem to the case of multiple infection points as follows.

Theorem 2. *Let $U(x)$ satisfy (A1) and have inflection points x_{In}, $n=1,2,...,N$. The shear flow is spectrally stable if and only if the quadratic form,*

$$Q=\nu\int_{-L}^{L}\xi\prod_{n=1}^{N}\left[(U-U_{In})+U''G\right]U''\xi dx.\tag{3}$$

is not positive for all $\xi\in \mathrm{L}^2$, where $U_{In}=U(x_{In})$ and either $\nu=1$ or $\nu=-1$ is chosen such that

$$\nu U''\prod_{n=1}^{N}(U-U_{In})\leq 0 \quad \textit{for all } x.$$

We remark that the functional space L^2 for ξ may be replaced by other Hilbert spaces satisfying certain conditions. Actually, it is technically convenient to maximize Q with respect to $w = U''\xi \in \mathrm{L}^2$ rather than $\xi \in \mathrm{L}^2$. Then, the number of positive eigenvalues of the selfadjoint operator H, defined by $Q = \int_{-L}^{L} wHw\,d$, corresponds to the number of unstable eigenvalues of the Rayleigh equation.

3. Numerical tests

Here, we exhibit a few numerical results to illustrate how our method works in practice. For each velocity profile $U(x)$, we compare the results of two different numerical codes: one code solves Rayleigh's equation (1) directly to search for complex eigenvalues c, while the other solves for the eigenvalues $\lambda_1, \lambda_2, \ldots$ of the selfadjoint operator H in descending order.

The first example is

$$U(x) = x + 5x^3 + 1.62\tanh[4(x-0.5)] \qquad (4)$$

for $x \in [-1,1]$, which is studied by Balmforth and Morrison [7]. This flow has three inflection points and is unstable only for finite wavenumber $k_3 < k < k_2$, unlike the usual Kelvin-Helmholtz instability. As shown in Fig. 1, the maximum eigenvalue λ_1 (the dashed line) smoothly changes its sign at $k = k_2, k_3$ and becomes positive for $k_3 < k < k_2$.

The second example is

$$U(x) = x - 0.02 + \sin[8(x-0.02)]/16 \qquad (5)$$

for $x \in [-1,1]$, which has five inflection points. As shown in Fig. 2, three unstable eigenvalues emerge at k_1, k_3, k_5 with different phase speeds U_{I1}, U_{I3}, U_{I5}, respectively. The three eigenvalues $\lambda_1, \lambda_2, \lambda_3$ also become positive at these critical wavenumbers.

These numerical results confirm that the signature of Q indeed predicts the existence of unstable eigenvalues ($\mathrm{Im}\, c > 0$).

4. Concluding remarks

We remark that our stability criterion can reproduce the earlier results of the Nyquist method [7] and the perturbation analysis of the neutral modes [8]. Our variational approach is advantageous in that we can prove instability by merely finding a test function (in a certain function space) that makes the quadratic form Q positive. For the purpose of determining stability, the variational problem (i.e., the signature of Q) can be solved more quickly and accurately than the Rayleigh equation (a non-selfadjoint eigenvalue problem with singularity). This variational approach is expected to be applicable to other hydrodynamic stability problems and to be of practical utility in other complicated problems.

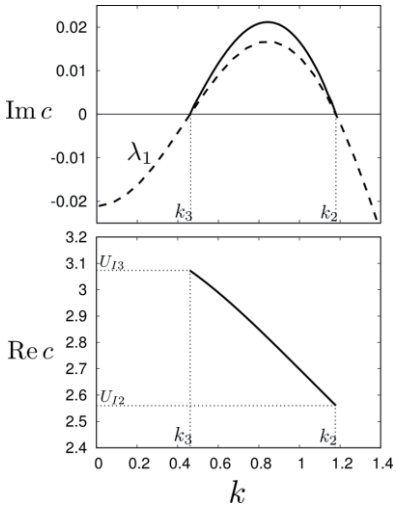

Fig. 1 Growth rate ($\mathrm{Im}\, c$) and phase speed ($\mathrm{Re}\, c$) versus wavenumber k for the shear flow (4).

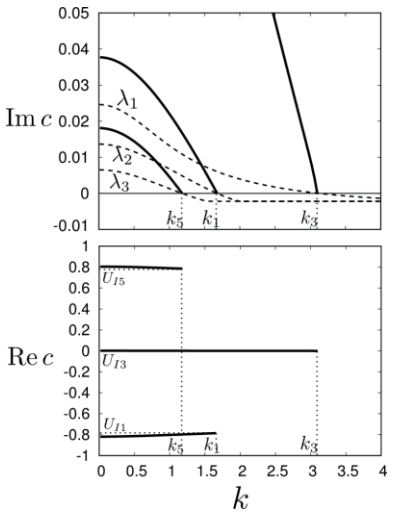

Fig. 2 Growth rate ($\mathrm{Im}\, c$) and phase speed ($\mathrm{Re}\, c$) versus wavenumber k for the shear flow (5).

References

[1] V. I. Arnold, *Mathematical Methods of Classical Mechanics*, Springer, Berlin (1978).
[2] D. D. Holm *et al.*, Phys. Rep. **123** (1985), 1.
[3] P. J. Morrison, Rev. Mod. Phys. **70** (1998), 467.
[4] N. J. Balmforth and P. J. Morrison, *Hamiltonian Description of Shear Flow*, in Large-Scale Atmosphere-Ocean Dynamics II, eds. J. Norbury and I. Roulstone (Cambridge, Cambridge, 2002) , 117.
[5] J. W. S. Rayleigh, Proc. Lond. Math. Soc. **9** (1880), 57.
[6] R. Fjortoft, Geofys. Publ. **17** (1950), 1.
[7] N. J. Balmforth and P. J. Morrison, Stud. Appl. Math. **102** (1999), 309.
[8] W. Tollmien, Nachr. Wiss Fachgruppe, Gottingen, Math. Phys., **1** (1935), 79.

Tenth International Conference on Flow Dynamics
November 25-27, 2013, Sendai, Miyagi, Japan

Statistical Thermodynamic Approach to Droplet Distributions in Entrainment

Yosuke Hirata, Miyuki Akiba
Toshiba Power & Industrial Systems R&D Center
yosuke.hirata@toshiba.co.jp

ABSTRACT

Diameter distribution of droplets is of great concern in analyses of erosion in turbines and pipes, carry-over in moisture separators and dryers, etc. Many experiments have shown that the distribution of droplets can be approximated by Gamma distribution, but no clear reason or mechanism for the distribution to take the form of this function has been reported. This paper is to suggest a Weibull distribution that theoretically maximizes the entropy of droplet distributions. Weibull distributions for types of droplet generation were calculated and compared with reported experiments. Weibull distributions can approximate the experimental distributions well.

1. Introduction

Diameter distribution of droplets is of great concern in analyses of erosion in turbines and pipes, carry-over in moisture separators and dryers, etc. When we use CFD to evaluate behavior of droplets for those components, parameters of droplets such as diameter distribution are required for the input of CFD, but these parameters are not always determined logically.

In two-phase flows with air-water or steam-water mixture in pipes, etc., liquid films develop on the inner surface. Due to the friction between the film and flow, instabilities such as the Kelvin-Helmholtz instability develop. As the instability grows and the surface tension of the wave crest becomes smaller than the shear stress acting on the wave crest, the wave crest starts to be torn off as droplets [1].

Mean diameters of droplets have been obtained experimentally in various fluid conditions. Empirical equations for the mean diameter are usually made based on the mechanism described above [2][3].

As to the distribution of droplet diameters, on the other hand, many papers report that their experimental data can be fitted well with Gamma distributions [4][5][6]. But reasons why Gamma distributions give the best fits have not been clearly discussed. In other papers, log-normal functions or Weibull functions are also used [1].

In the cases where droplet creation is of concern, the flow is most likely to be turbulent. This means that local parameters such as shear stress and surface tension are not constant but statistically changing. The diameter of droplets will be distributed statistically around a mean value.

In the field of meteorology, the distribution of droplets constituting clouds and its theoretical model is of great concern. The droplet distribution is usually approximated by a Gamma, a Weibull or a log-normal distribution. BNL reported that, in the presence of a cloud, the distribution of droplets is so determined as to maximize the entropy of the system and the distribution should be a Weibull distribution [7].

Since the creation of droplets in a pipe with two phase flow accompanies a statistical thermodynamic process, the same approach will be effective. In this paper, we will apply this approach to droplet generation in a two phase pipe flow and compare the obtained distribution with results reported by literature.

2. Method

We use Shannon entropy [8] to evaluate the droplet distribution:

$$H(p_1,\cdots,p_n)=-\int p(E)\log[p(E)]dE\ , \quad (1)$$

where $p(E)$ is a probability density function. The distribution of droplets is so determined as to maximize eq. (1) with the following constraints:

$$\int p(E)dE=1\ , \quad (2)$$

$$\int Ep(E)dE=\overline{E}\ . \quad (3)$$

Here, $\overline{E}$ is the average energy. Using Lagrange multipliers with constraints (2) and (3), the probability function is obtained as

$$p(E)=Ae^{-BE}\ , \quad (4)$$

where A and B are constants.

Major energies related to the droplet diameter, D, are considered as follows:

(a) Latent heat: $\propto D^3$,

(b) Surface tension: $\propto D^2$, and

(c) Gravity: $\propto D^3$.

Latent heat is involved in condensation and this will be a case in which droplet creation occurs with heat transfer, or condensation due to an abrupt pressure drop after an orifice, etc. Surface tension is a case of entrainment from liquid films, or breakup of larger droplets in turbulent fluids, etc. Gravity is negligible since the mass of droplets flowing in fluids is small, and is not considered.

The probability density is then recast as functions of droplet diameter depending on the droplet generation process. Making use of the relation,

$$dE\propto D^2dD\ ,$$

for condensation process, the probability function of droplet distribution will be given by

$$\rho(D)=AD^2e^{-BD^3}\ . \quad (5)$$

This is a Weibull function with a Weibull parameter of 3. In the same analogy, the droplet distribution for entrainment process will be

$$\rho(D)=ADe^{-BD^2} \quad (6)$$

where the Weibull parameter is 2.

In order to confirm these distributions give proper fits for the droplet distribution, we will pick out several experimental results and make comparison. Table 1 shows a list of data taken from literature. Some of the droplet distribution data were taken to investigate erosion. Some were to examine heat transfer with evaporation and condensation.

Table 1 List of data used in comparison.

Data #	Taken by	Taken and digitized from	Number of droplets measured	Note
1	Koizumi, et. al	Fig. 7 of Ref. [6]	410	Heat transfer meas. using R113
2	Koizumi, et. al	Fig. 7 of Ref. [6]	158	Heat transfer meas. using R113
3	Morita	Fig. 11 of Ref. [4]	–	Steam–water experiment
4	Morita	Fig. 11 of Ref. [4]	–	Steam–water experiment
5	Morita	Fig. 11 of Ref. [4]	–	Steam–water experiment
6	Morita	Fig. 6 of Ref. [5]	–	Steam–water experiment
7	Morita	Fig. 6 of Ref. [5]	–	Steam–water experiment
8	Morita	Fig. 6 of Ref. [5]	–	Steam–water experiment
9	Morita	Fig. 6 of Ref. [5]	–	Steam–water experiment

So the former data are likely to be fitted well by Weibull distributions with a Weibull parameter of 2. The latter may be approximated by those with a Weibull parameter of some value between 2 and 3 since droplet generation in this case is through condensation or evaporation as well as entrainment.

3. Results and Discussion

Figure 1 shows droplet distribution data digitized from Fig. 6 of Ref. [5]. In Fig. 1, a Weibull distribution with a Weibull parameter of 2 is also depicted. In this figure the abscissa represents the droplet diameter normalized by the average diameter. This figure shows that a Weibull distribution approximates the data well.

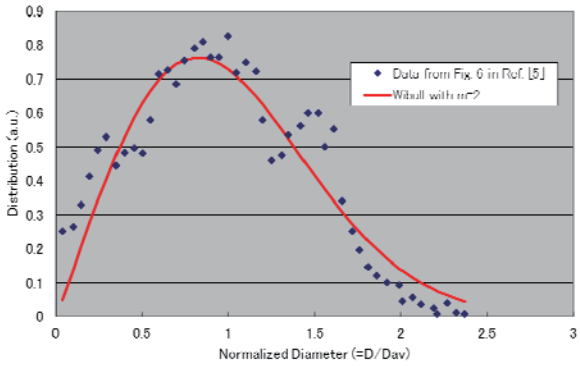

Fig. 1 Data from Fig.6-3 in Ref. [5] and Weibull distribution with a parameter of 2.

Next, regarding each set of data presented in Table 1, Weibull parameters of the best fitted Weibull distributions are shown in Fig. 2. Weibull parameters of most data are between 2 and 3, showing that Weibull distributions with parameters 2 and 3 describe experimental droplet distributions. This also suggests that droplet generation is comprehensible as a process of maximizing the entropy of the system.

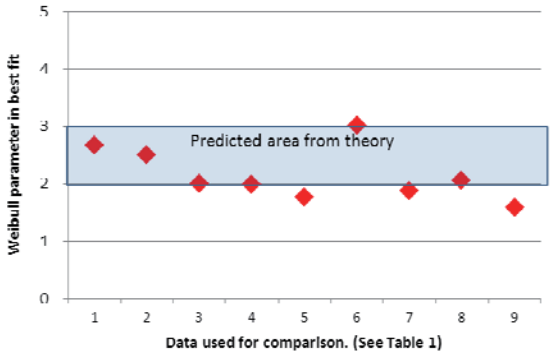

Fig. 2 Weibull parameters for various experiments.

4. Concluding remarks

It has been shown that Weibull distributions have a characteristic of maximizing the entropy of a system with droplet creation. By comparing data from literature, it has been confirmed that Weibull functions with a Weibull parameter of 2 are functions of approximating the droplet distribution entrained from liquid films.

References

[1]Tatterson, et. al., AIChE J., **23** (1977), pp.68-76.
[2]D.J.Azzopardi, Exp. In Fluids **3** (1985), pp. 53-59.
[3]Kataoka, et. al., J. Fluid Eng., **105** (1983), pp. 230-238.
[4]R. Morita, CRIEPI Report, L06008, (2007), in Japanese.
[5]R. Morita, CRIEPI Report, L07016, (2008), in Japanese.
[6]Koizumi, et. al., Trans. Japanese Soc. Mechanical Eng., Vol. **44** (1978), pp. 191-199, in Japanese.
[7]Y. Liu, J. Hallet, "On Size Distributions of Cloud Droplets Growing by Condensation: A New Conceptual Model," J. Atmos. Sci., **35** (1998), 527-536.
[8]E. T. Jaynes, "Probability Theory," Cambridge University Press, 2003.

Flow Manipulation of Nano-Fibrillated Cellulose: a Key Technology for New Bio-based Materials

Karl Håkansson, Fredrik Lundell, Lisa Prahl-Wittberg, Daniel Söderberg
Wallenberg Wood Science Centre and Linné FLOW Centre
KTH Mechanics, Royal Institute of Technology, SE-100 44 Stockholm, Sweden
Fredrik@mech.kth.se

ABSTRACT

Nano-fibrillated cellulose (NFC) is obtained by disintegrating cellulose fibres from paper pulp into fibrils. The fibrils have a thickness of about 20 nm and length around a micron and is a promising commodity for high performance bio-based materials. Here, we show how the nano-structure and fibril alignment of NFC can be manipulated in flow systems. Furthermore, we show how the fibrils can be assembled to a filament with good mechanical properties. The flow and filament is evaluated by x-ray diffraction, polarized light and tensile testing.

1. Introduction

Nano-fibrillar cellulose (NFC) is obtained by disintegrating cellulose fibres extracted from wood (usually used for paper production) into near crystalline nano-fibrils, which have a diamter around 2 nm and a length on the order of a micrometer. The highest reported values of the strength (specific stiffness and ultimate strength) for cellulose fibres extracted from wood are considerably higher than the strength that has been reported for filaments produced by NFC. This could be interpreted so that the full potential of NFC has not been reached yet. Here, an assembly process that combines hydrodynamic alignment of surface-charged nano-fibrils with a controlled dispersion-gel transition. It is demonstrated that the process can produce cellulose filaments from nano-fibrillated cellulose (NFC) with a preferential fibril orientation along the filament direction.

2. Materials and Methods

The filaments are produced in a flow focusing setup (see Fig. 1), where a central flow containing NFC is focused by two outer flows. In this flow setup, the fibrils are aligned and later assembled, so that a thread isformed. After drying, a dry filament is obtained. The process and filament are investigated with small- and wide-angle X-ray scattering (at the P03 beamline at PETRAIII in Hamburg, Germany), tensile testing, polarized light and SEM microscopy.

In addition to experimental determination of fibril alignment, simulations have been performed. The simulations consists of two stages. First, the velocity is determined. The second step is a calculation of fibril orientation in this flowfield by mean of a Smoluchowski equation.

The flowfield is calculated in a 2D geometry designed to capture the key aspects of the channel system. This is obtained in a cylindrical geometry with a central flow and an annular inflow. The velocity along the centerline is used as the basis for the orientation calculation. This velocity shows first a decceleration directly after the beginning of the side injection. This deceleration is followed by a strong acceleration due to the increase of total flow.

The orientation along the central streamline is calculated based on the assumption that there are two mechanisms that affect the orientation. The first is that the fibrils rotate due to the gradients of the flow based on the rotational velocities of inertia free spheroids[1]. The second effect is a diffusion towards an isotropic fibril distribution due to Brownian motion[2]. The magnitude of the latter diffusion has to be fitted to experimental data. Polarized light visualizations have

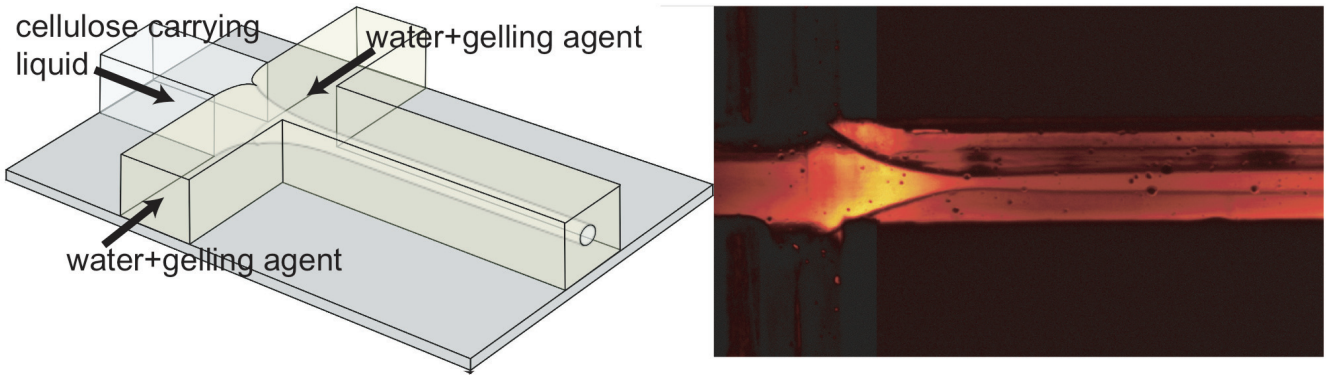

Fig. 1: Flow focusing setup (left) and visualization with polarized light (right). The visualization shows that the fibrils are aligned by the focusing.

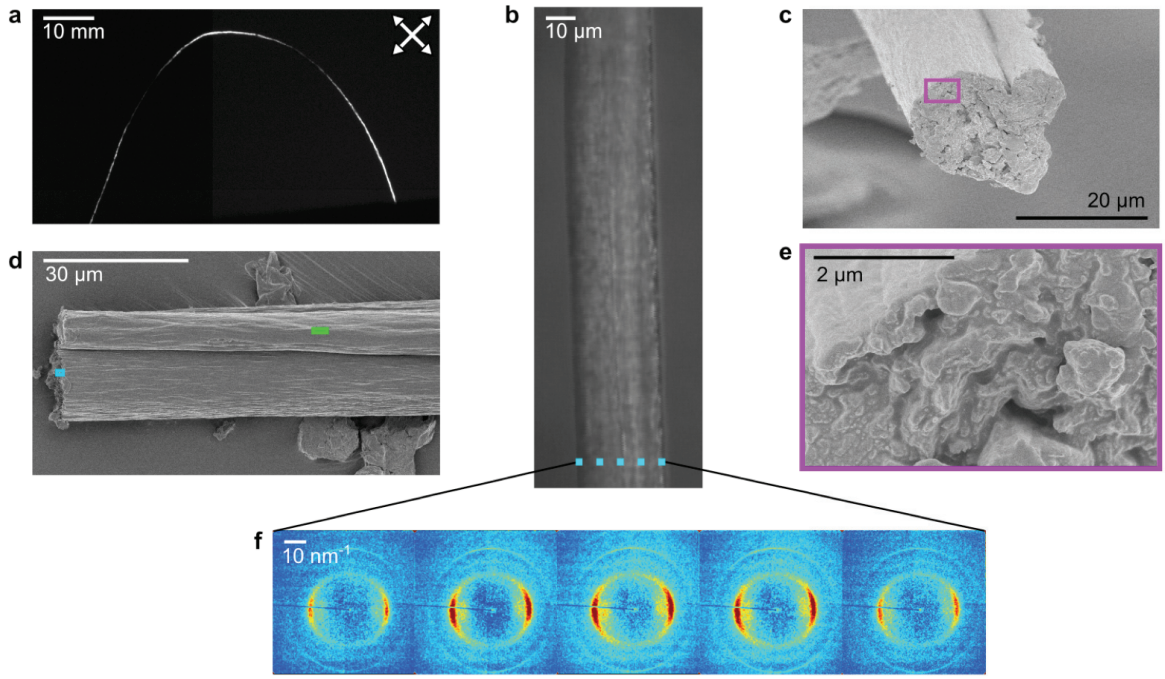

Fig. 2: Picture of the filament in polarized light demonstrating fibril alignment, SEM images of the filament and wide-angle X-ray scattering images showing alignment of Cellulose 1 crystals.

been used for this purpose.

3. Results and Discussion

The filament is shown in Fig. 2. The results show that the specific ultimate strength and stiffness of the filaments are in line with the strongest cellulose pulp fibres extracted from wood with the same degree of fibril alignment. Furthermore, the specific ultimate strength and stiffness of the filaments are considerably higher than previously reported filaments made from NFC as well as regenerated cellulose fibers such as viscose or lyocell. The scattering measurements show that these excellent properties are achieved by creating a controlled nanostructure of free fibrils before the structure is locked. This is achieved in a process that is highly controllable, parallelizable and scalable.

The controllability of the process opens up for reverse engineering of NFC filaments: first, a desired nano-structure is determined by micro-mechanical modelling and analyses. The process would then be tuned a-priori so that this particular nanostructure is created. Thus, the results envisage industrial production of highly specialised filaments made form NFC.

The orientation calculations show decent agreement with the polarized light visualization. They indicate that higher alignment can be achieved as long as hydrodynamic instabilities does not set in and destroy the filament.

4. Conclusions

Homogeneous cellulose filaments with a high degree of fibril alignment have been produced by flow focusing. The alignment is characterized by polarized light and x-ray diffraction. Furthermore, the alignment is modeled with a Smoluchowski equation and agrees well with polarized light visualizations. The process offers a possibility to create filaments with a controllable nano structure.

[1] G. B. Jeffery, Proc. Roy Soc., Serie A **102** (715) pp. 161-179 (1922)
[2] M. Doi & S. Edwards, The theory of polymer dynamics. Oxford University Press (1986)

Tenth International Conference on Flow Dynamics
November 25-27, 2013, Sendai, Miyagi, Japan

Numerical Evaluation of Propulsive Efficiency of Elastic Fin

Yusuke Yamaguchi, Masataka Nakabayshi, Wataru Yamazaki
Department of Mechanical Engineering, Nagaoka University of Technology,
Kamitomioka-machi 1603-1, Nagaoka, Niigata, 940-2188, Japan
s103100@stn.nagaokaut.ac.jp

ABSTRACT

In this research, a water propulsion mechanism of elastic fin, which mimics fish motion mechanisms, is numerically investigated. Since the degree of elasticity is important for efficient propulsion, an elastic fin with dynamic variable effective length spring has been experimentally investigated by one of the present authors. For more detailed investigation, the fluid-structure interaction problem is numerically solved to clarify the characteristics of instantaneous thrust and lateral forces, as well as the propulsion efficiency of the elastic fin.

1. Introduction

Fluid propulsion mechanisms widely used for general ocean vessels are screw propellers. For (micro) unmanned ocean vessels, however, the propulsion mechanism by elastic fin, that mimics fish motions, is watched with keen interests in these days. One of the advantages of the propulsion mechanism of elastic fin is capability of movement without hoisting the garbage of sea bottom. In addition, lower risk to harm water creatures is another major advantage. Motivated by these advantages, a fin with dynamic variable effective length spring that can change its elasticity during oscillation motions has been developed and experimentally investigated by Nakabayashi et. al. [1]

In this research, therefore, the flow field around the elastic fin is numerically discussed by fluid-structure interaction analyses. Furthermore, the possibility to change the elasticity dynamically during the oscillation motion is also considered for more efficient propulsion.

2. Principle of the fin with dynamic variable effective length spring

The principle of the elastic fin is schematically shown in Fig. 1. The elastic portion is made from polyethylene terephthalate (PET), and then the PET plate is sandwiched by rigid plates of brass. By changing the exposed length of the PET plate (H in Fig. 1), the apparent elasticity of fin can be dynamically changed. In this research, the exposed length of the PET plate is changed from 0[mm] (most rigid) to 20[mm] (most elastic).

3. Analysis method

3.1. Analysis model

The fluid-structure interaction analysis of the elastic fin is performed by utilizing ANSYS CFX (for fluid) and ANSYS mechanical (for structure). The two dimensional analysis model is shown in Fig. 2. The computational grids for fluid and for structural deformation are shown in Fig. 3.

At the cases with dynamic change of the elasticity of fin, it is treated by changing the Young's modulus of the PET plate. A standard k-ε turbulence model is utilized in this research. A yawing movement is given on the elastic fin whose maximum oscillation angle $\theta_{\max}$ and its period are respectively set to 30 [deg] and 3[sec].

3.2. Evaluation of propulsive efficiency

In this research, the propulsion efficiency of elastic fins is defined as follows:

$$E = \frac{\overline{F_t}}{\overline{F_p}} = \frac{\overline{F_t}}{M\omega} \qquad (1)$$

where $\overline{F_t}$ and $\overline{F_p}$ are respectively the averaged thrust force and averaged required power among one cycle. M is the moment acting on the center of rotation of the elastic fin. ω is the angular rate of the yawing motion.

4. Results and Discussion

In this paper, three representative results are compared, that are H=0, 20[mm] and a case with dynamic change of the elasticity between 0 and 20[mm]. In the case of the dynamic change, the elasticity of fin is set to H=0[mm] when approaching to the central location, and is set to H=20[mm] when moving away from the central location during the oscillating motion (see the setting shown in Fig.4-5).

Table 1 shows some performance values of the three representative cases. The obtained results are summarized in Fig. 4-8.

When the fin is more rigid, generated thrust force is greater as shown in Fig. 6. As shown in Fig. 7, on the other hand, the propulsive efficiency is higher when the fin is more elastic. Same tendencies have been reported in [1], which indicates the validity of this numerical simulation.

In the case of the dynamic change of elasticity, its thrust force is higher than that of H=0[mm] (most rigid), and its propulsive efficiency is almost comparable with that of H=20[mm] (most elastic). This is because the large thrust force is generated with rigid fin at the phases of ψ=0~90, and 180~270 [deg], and the required power is reduced with elastic fin at the phases of ψ=90~180 and 270~360 [deg]. Larger pressure variation around the rigid fin (which corresponds to larger lateral force / lower required power) is observed in Fig. 8 (a), while that is decreased in Fig. 8 (b)-(c). It can be also observed that the dynamic condition (c) generates larger downstream counterclockwise vortex than the most elastic fin (b), which induces larger thrust force in the dynamic condition. We'll further discuss the setting of the dynamic change of the elasticity for more efficient propulsion.

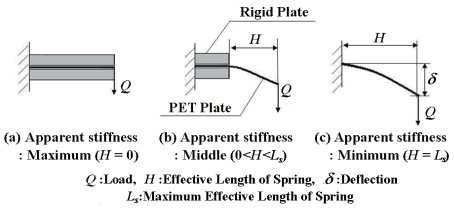

Fig. 1 Principle of elastic fin

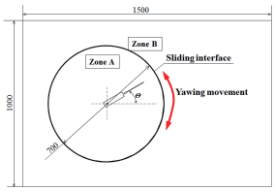

Fig. 2 Analysis model

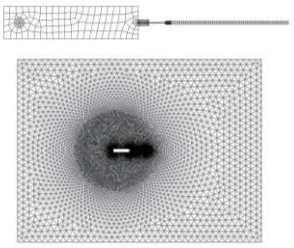

Fig. 3 Computational grids for structural deformation (upper) and for fluid analysis (lower)

Table 1 Averaged thrust force, power and efficiency

Case	$\overline{F_t}$ [N]	$\overline{F_p}$ [W]	E
H=0[mm]	0.286	0.196	1.459
H=20[mm]	0.130	0.049	2.634
Dynamic	0.306	0.119	2.563

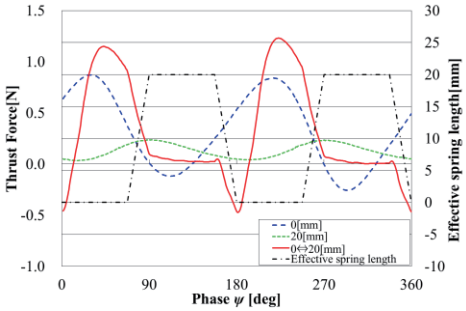

Fig. 4 Instantaneous thrust force distributions, H=0, 20[mm] and dynamic case

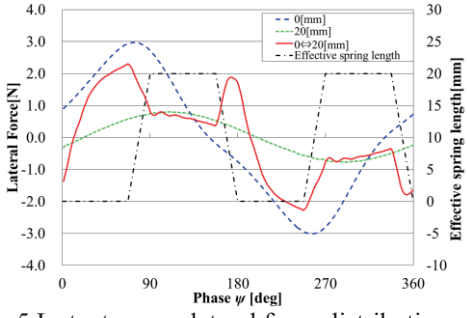

Fig. 5 Instantaneous lateral force distributions, H=0, 20[mm] and dynamic case

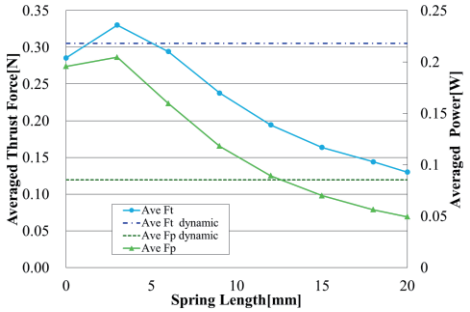

Fig. 6 Averaged thrust force / power in one cycle, H=0~20[mm] and dynamic case

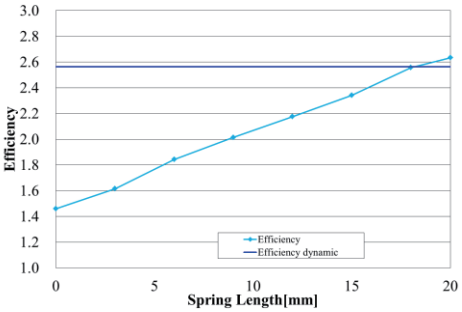

Fig. 7 Comparison of propulsive efficiency

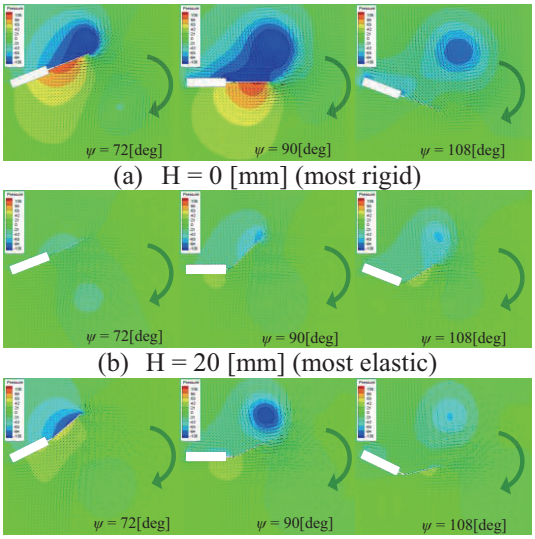

(a) H = 0 [mm] (most rigid)

(b) H = 20 [mm] (most elastic)

(c) Dynamic condition (0[mm]⇔20[mm])

Fig. 8 Flow field at ψ = 72, 90 and 108 [deg] (flow vector and pressure contour)

Reference

[1] Masataka, N., Reiji, K., Shunichi, K., and Hirohisa, M., Propulsion Mechanism in Fluid Using Fin with Dynamic Variable-Effective-Length Spring (Evaluation of Thrust Efficiency and Flow-Visualization Around the Fin), Transactions of the Japan Society of Mechanical Engineers, Series B, Vol.73, No.736(2007-12), pp.115-123

Development and Evaluation of a Mini-tube Multistage Gas Separator Utilizing Soret Effect

Takahiro Wako[1], Aiki Omomo[1], Tomohiro Higurashi[1] Souhei Matsumoto[2] and Naoki Ono[1]
[1]Shibaura Institute of Technology, 3-7-5, Toyosu, Koto-ku, Tokyo, 135-8548, Japan
[2]AIST, 1-2-1, Namiki, Tsukuba, Ibaraki, 305-8564, Japan
naokiono@shibaura-it.ac.jp

ABSTRACT

Soret effect is a phenomenon in which temperature gradient gives rise to concentration gradient. In this study, we attempted simple technique of hydrogen separation from mixture gas. From the result of the single process device, gas separation using Soret effect was confirmed. However, concentration difference by single separation was very small. Therefore, it needs the connection with many channels. However, the total size of the device has to be small even if built with so many channels. Thus, we attempted to build a MEMS device and collected the experimental data for manufacturing the multi process device.

1. Introduction

These days, technology has developed toward the sustainable society where environmental conservation and de-fossil, de-atomic energy are regarded as key issues. Above all, the energy system using hydrogen is expected as a new energy source because it has little environmental load and high energy conversion rate. However, the establishment of the hydrogen production technology is indispensable, but it still has many technical problems. Current main hydrogen manufacturing method is raised-steam reforming method, but this technique emits hydrogen and carbon dioxide. Therefore, technology to separate hydrogen and carbon dioxide is necessary in order to obtain purer hydrogen[1]. Therefore, we had concern to mixed gas separation technology utilizing Soret effect, which can cause concentration difference only due to temperature difference. In addition, setting the difference of temperature could be available if we use exhaust heat that occurred in gas reforming or LNG cold energy. Furthermore, as for the separation by the Soret effect, it is thought that space-saving can greatly contribute to energy saving to be completed within a short time. However, since having passed through one separation process gives a little concentration improvement[2], it is necessary to separate the gas repeatedly. Therefore, using MEMS (Micro Electro Mechanical Systems) technology for device production, we think the devices size will be made miniature and we can increase the separation number of times. We actually built a MEMS device, and performed experiment of gas separation.

2. Theory

The principle of the Soret effect is illustrated in Fig.1. The mass flux is occurred by the temperature gradient when heating temperature T_1 and cooling temperature T_2 are given in domain one or two, respectively. This phenomenon is called Soret effect. A property of this phenomenon is that the concentration gradient increases with the increase of the temperature gradient. On the other hand, the mass flux based on the concentration gradient, i.e. Fick's law influences the gas to relieve concentration gradient when the system has the concentration gradient. In the system of two ingredients (chemical species A and B), Soret effect and Fick's law is expressed to (1) and (2), respectively[3].

$$j_i^{(T)} = -\frac{c^2}{\rho} M_A M_B D_{AB} \frac{k_T}{T} \frac{\Delta T}{L}. \quad (1)$$

$$j_i^{(x)} = -\frac{c^2}{\rho} M_A M_B D_{AB} \frac{\Delta x_i}{L}. \quad (2)$$

In those equations, c and ρ are the molar density and mass density, respectively, M is the molecular weight, D_{AB} is the diffusion coefficient, x is the molar fraction. k_T is the thermal diffusion ratio, T is the temperature, and L is the separation distance. The subscripts i indicates chemical species A and B. When these two mass fluxes are balanced, it is in a condition that species was completed. The separation density difference is expressed as: (3).

$$\Delta x_i = x_{i2} - x_{i1} = k_T \ln \frac{T_2}{T_1}. \quad (3)$$

Between two ingredients, the value of k_T takes a positive value with light molecules and takes a negative value with the heavy molecules. In the system of H_2-CO_2, the value of k_T is 0.0899. This value is detected by Bastick[4].

Therefore, the light molecules move to the high temperature domain, and the heavy molecules move to the low temperature domain, respectively.

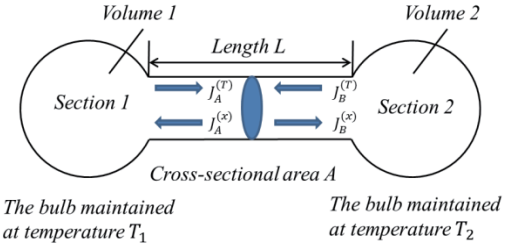

Fig.1 Steady-state binary thermal diffusion

3. The outline of the experiment

3.1 Single process device

In a study until last year, the experiment was conducted in order to investigate about the gas separation by the Soret effect with stainless steel pipe[2]. In addition, the experimental condition is shown in Table 1. In this device, the cooling part was set at the upper part, the heating part was set at the lower part. It was the device for the purpose of improving separation efficiency by producing a sudden temperature gradient just before one of the outlet tube.

We found improvement of the separation efficiency in the low flow rate from the experimental result. Because

the concentration boundary layer was thought to be formed thickly, there was little influence of the re-mixture of the gas. However, concentration difference by one separation was very small, which was 2.0% in the low concentration side and was 1.8% in the high concentration side. Thus, it needs to separate the gas for several times. Therefore, the system would need to connect many channels, but we need to avoid the enlargement of the device. We adopted MEMS technique and made a test MEMS device with silicon substrate and glass plates and performed experiments.

Table1 Experimental Condition

Inside diameter/Outside diameter(Tube)[mm]	2.4/3.0
Flow rate[ml/min]	20~200
Heating/Cooling temperature[℃]	450/0
Inside diameter/Outside diameter (Branch Tube)[mm]	0.7/1.0
H_2:CO_2	48.1:51.9

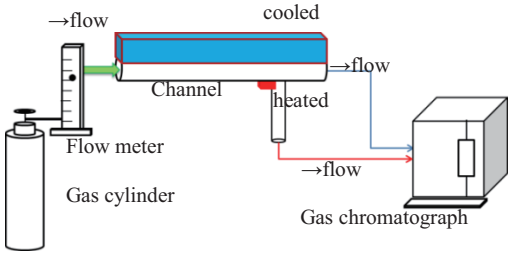

Fig.2 Experimental apparatus

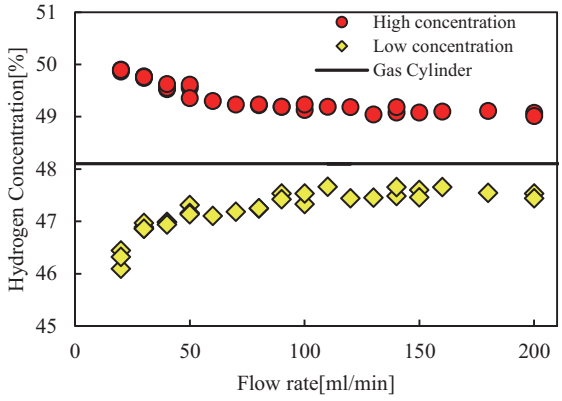

Fig.3 Experimental result(Single process)

3.2 MEMS device(Downsized device)

A manufactured MEMS device is shown in Fig.4. In addition, the experimental condition is shown in Table 2. The reason why a heating temperature was 80℃, was that the heat resistance temperature allowed for the connector which connects the channel and the tube in the inlet and the outlet, was in that low temperature.

Table2 Experimental Condition

Thickness of the channel[mm]	0.2
Width of the channel[mm]	20
Flow rate[ml/min]	20
Heating/Cooling temperature[℃]	80/0
H_2:CO_2	48.7:51.3

The experimental result is shown in Fig.5. The concentration difference of 0.3-0.4% of both of high concentration side and of low concentration side was confirmed by this experiment. According to this result, we found this MEMS device was able to separate the gas using by Soret effect. Both of the results had the errors about ±0.1%, which was caused by the detection error of the gas chromatograph. By giving the bigger temperature difference, we think that concentration difference can be improved in future.

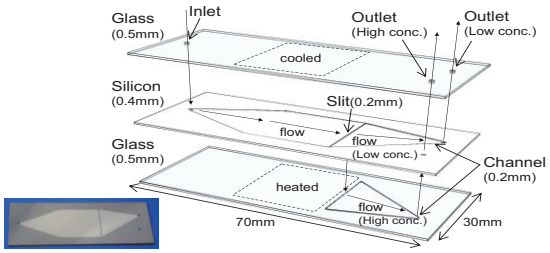

Fig.4 MEMS device

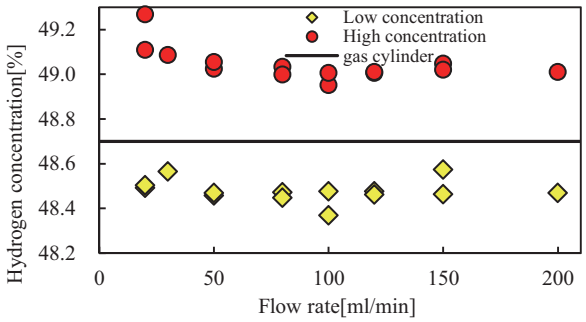

Fig.5 Experimental result(MEMS device)

4. Conclusion

・From the result of the experiment using single process device, we found that the low inflow velocity was more effective than the high velocity. Because of the thick concentration boundary layer was thought to be formed just before branching outlet.

・From the result of the experiment using MEMS device, we confirmed that the gas separation in the small MEMS device utilizing Soret effect was possible.

5. Future plan

We plan to produce the multi process device which the channels are connected. We think that this device can increase concentration difference efficiently.

Acknowledgement

This research was partially supported by the MEXT/JSPS, Grant-in-Aid for Challenging Exploratory Research (No. 24656146).

References

[1] K.Yamaji, Hydrogen Energy Society, JSER, (2008), pp.136-143

[2] T.Wako, graduation thesis, Shibaura Institute of Technology, (2011)

[3] R.Byron Bird, Watten E. Stewart, Edwin N. Lightfoot Transport phenomena , John Wiley & Sons , (1976) , pp.554-575.

[4] R.E.Bastick, H. R. Heath, T. L. Ibbs, The molecular fields of carbon dioxide and nitrous oxide , Proc.Roy.Soc , A173(1939), pp.543-546.

Performance Analysis of Argon Vaporizer for Waste Heat Recovery Applications

Jong-Wook, Lee and Won-Seok, Kim
R&D Centre, BHI, 165-2, Jangji-ri, Gunbuk-myeon, Haman-gun, Gyeongnam, South Korea
wskim@bhi.co.kr

ABSTRACT

The aims of this study are to investigate the recovery of waste heat in a system and to predict the performance of a shell and tube heat exchanger in the light of super low temperature argon application. Conventional argon vaporizer is used using the steam as heat source which is expensive to supply. The vaporizing characteristic of argon vaporizer with water has fixed ice and causes a low efficiency. Enhanced type of argon vaporizer is optimized. The HTRI design program over predicted the performance of Ar vaporizer and the field test shows that parallel configuration using two vaporizers is better than series configuration for reducing pressure drop.

1. Introduction

Recycling waste heat energy is an important for economic development of any country. An example of this is the integration of various factory sections where the waste heat from one section is used in another. This is common practice in the steelmaking industry and not only saves money, but results in better efficiencies. Nonetheless, a large amount of energy is still being lost in the form of heat generated by everyday industrial.

The aims of this study were to investigate the recovery of waste heat in the system and to predict the performance of a shell and tube heat exchanger in the light of super low temperature argon application. The characteristic of argon vaporizer in horizontal tubes with water as heat source has fixed ice and a bad flow pattern for two-phase heat transfer. This characteristic causes a low efficiency in vaporizer. On that reasons, enhanced type of argon vaporizer is optimized through numerical analysis and experiments [1].

2. Design of Argon vaporizer system

The conventional evaporation methods to make the Ar gas using -186℃ of cryogenic liquid argon. It is used a hot water container which is heated by external steam. However, the maintenance of existing system costs high due to hot steam. Therefore, in this study, waste heat from the compressed air can be used for vaporizing the liquid Ar.

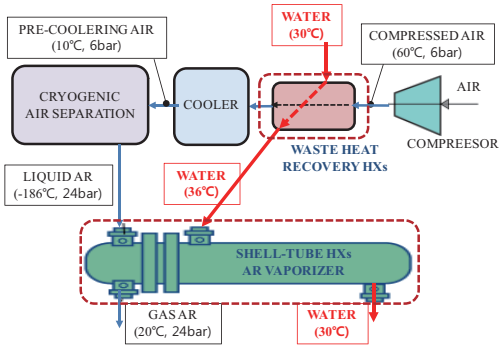

Fig. 1 Modified Ar vaporization system

Figure 1 shows the modified Ar vaporization system for saving energy using waste heat. With the available data from the site, system design was carried out. Two heat exchangers were added; one to generate hot water using waste heat from the compressed air and the other one to generate Ar gas from the cryogenic liquid argon without hot steam as a heat source. Because Ar vaporization system operates at temperature levels much below ambient temperature, the design is concerned with reducing the heat transfer rate to a low value due to water freezing in the shell side and two phase heat transfer in the tube side.

3. Results and Discussion

3.1 Numerical analysis (Freezing water problem)

The cryogenic liquid Ar passes through the tube side and the warm water passes through the shell side. Tubes using a 316L stainless steel as cryogenic structural materials with excellent mechanical properties at cryogenic temperatures are consists of a total of 66 U-tube in the form of plain array. A single type baffles are consists of 27. The commercial code CFX13.0 was used for this work. The SST(Shear Stress Transport) turbulence model was used. Figure 2 shows the different designs of the entrance region of Ar vaporizer to solve the problem of freezing water. The arrangements of the Ar vaporizer for Case1 and Case 2 are the same with original type except the shape of the baffle and the location of the water inlet nozzle.

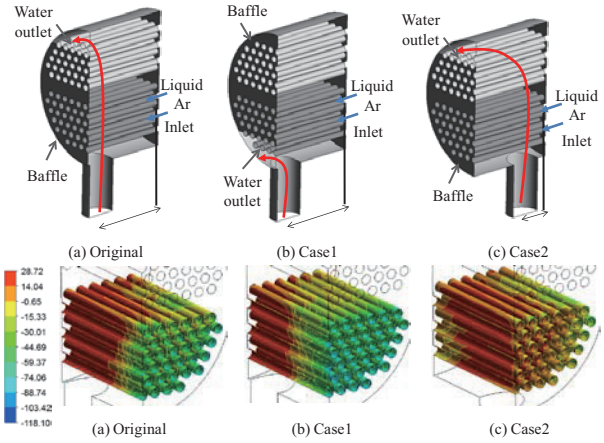

Fig. 2 Temperature distributions in the entrance region of the vaporizer

Figure 2 also shows the temperature contours at shell-side near the entrance of tube. For Case 1, it shows the less mixing of water than original model, because the main stream of water come out through the baffle cut

which is located in the bottom of first baffle directly. For Case 2, according to the change of the location of shell entrance nozzle, the mixing of flow is better than that of the original one in the entrance region of the tube.

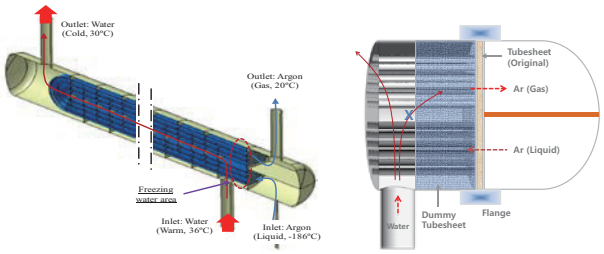

Fig. 3 The Ar vaporizer with a dummy tubesheet

Based on the results, the Ar vaporizer was redesigned using Case 2 model. But there is another problem for water nozzle to move to the entrance because a flange was there. So a dummy tubesheet was used to cover the freezing water region which means it is dead zone for heat transfer. Figure 3 shows the modified vaporizer to avoid the freezing water. Therefore, the vaporizer was extended to cover the dummy tubesheet.

3.2 Field tests (two phase heat transfer problem)

A shell and tube heat exchanger for the Ar vaporizer was designed and installed into the system (Design A, see Fig. 4).

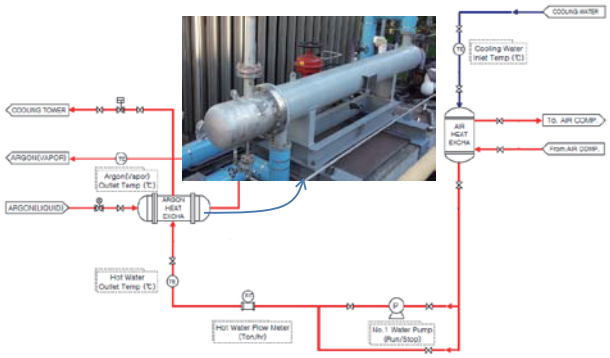

Fig. 4 Schematic diagram of Ar vaporization system

The HTRI was used in the thermal design of Ar vaporizer. Actually the Ar vaporizer was designed for an overall rate of 300 kW to make Ar gas with 2500 Nm3/hr. However, when the overall rate was back calculated from the measured temperatures, it was only 150 kW with 1250 Nm3/hr and 10 ℃ outlet temperature. Thus, with increasing mass flow rate, Ar gas outlet temperature decreases rapidly, which cannot be appropriate in downstream components of the vaporizer system. Apparently, design of two-phase heat exchanger is considered more complicated and interesting than a simple heat exchanger. Ar vaporization is basically a phenomenon where liquids undergo complicated flow patterns. In design, the HTRI was analyzing poor for the performance of Ar vaporizer (over predicted about two times in this case). Actually, it is hard to predict exactly the performance numerically because nonequilibrium conditions are sensitive to droplet size and rate of droplet transport to the wall, while the HTRI programs assume equilibrium conditions. In order to meet the design conditions especially, outlet Ar flowrate and temperature, an additional vaporizer was considered. The size and capacity of the extra vaporizer is same as previous one, because the performance of the first one shows almost half of the designed one. As a result of field test, there was no Ar outlet temperature limit which we had in Design A with increasing flowrate. But in series configuration using two vaporizers (Design B), increasing mass flowrate strongly influences the pressure drop in the vaporizers. Thus, 1900 Nm3/hr was the maximum flowrate which we can use in this design within allowable pressure drop. However, the Ar gas flowrate is still lower (1900 Nm3/hr) than designed one (2500 Nm3/hr). Therefore, it is arranged into parallel configuration to reduce the pressure drop and to increase the Ar gas flowrate (Design C). Figure 5 shows the results of Design C which has the reasonable flowrate, outlet temperature, and pressure drop compared with the previous designs [2].

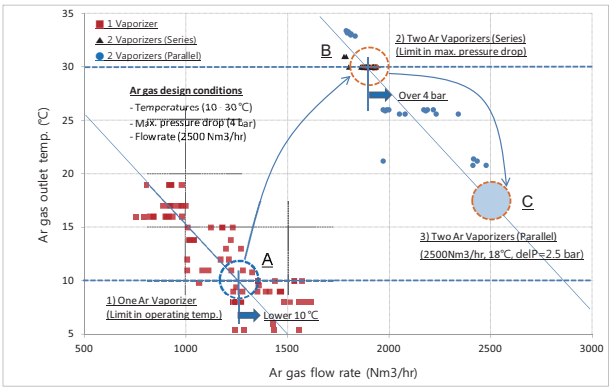

Fig. 5 The results of Ar vaporizaton systems

4. Concluding remarks

The water heat-exchanged from the waste heat of compressed air was used for vaporizing liquid argon in the system. The vaporizing characteristic of argon vaporizer with water as heat source has fixed ice. This characteristic causes a low efficiency in the vaporizer. In order to solve the problem of frozen water, numerical analysis was carried out. The results show clearly that the location of water inlet nozzle is better to move closer to the tube inlet. The HTRI predicted poor for the performance of Ar vaporizer (about 2 times over predicted). The field test shows that the parallel configuration is better than series for reducing pressure drop using the Ar vaporizers.

References

[1] R.F. Barron, Cryogenic heat transfer, Taylor & Francis (1999).
[2] L.D. Huang and T.G. Lestina, Complete vaporization in horizontal tubes, Report BY-35, Heat Transfer Research Inc. (HTRI) (2007).

Tenth International Conference on Flow Dynamics
November 25-27, 2013, Sendai, Miyagi, Japan

Laser Induced Electrostriction in Liquids

Ardian B. Gojani[1], Rasim Bejtullahu[2], and Shigeru Obayashi[1]
[1]Institute of Fluid Science, Tohoku University, 2-1-1 Katahira, Aoba, Sendai 980-8577, Japan
[2]Faculty of Physics, University of Prishtina, Nëna Terezë, 10 000 Prishtina, Kosovo
gojani@edge.ifs.tohoku.ac.jp

ABSTRACT

Electrostriction is the tendency of materials to compress in the presence of a varying electric field. The electrostrictive pressue causes several phenomena, including acoustic waves and tensile stresses. This paper describes these effects, which can play important roles in microfluidics and optomechanics. Also, electrostriction can be applied for the measurement of liquid properties.

1. Introduction

The dielectric constant ε of dielectrics depends weakly on the density ρ, and the application of the electric field $\mathbf{E}$ causes a change in pressure p_s, which is expressed by the Helmholtz-Lippmann equation

$$p_s = -\frac{\varepsilon_0 E^2}{2}\left(\rho\frac{\partial\varepsilon}{\partial\rho}\right)_T, \tag{1}$$

where ε_0 is the permittivity of the vacuum and T is temperature. This pressure, known as electrostrictive pressure [1], has the nature of a force density, that is

$$f = -\nabla p_s, \tag{2}$$

and can cause several effects in the dielectric. Most notably, this force is a source of acoustic waves, of fluid rupture, which leads to cavitation, and can cause deformation or vibrations of inhomogeneities (microdroplets) within the dielectric.

2. Pressure Field from Laser

Induction of these effects is possible only in cases of strong electric fields, which can easily be achieved when laser beam propagates through a dielectric. In the case of liquids, one can distinguish between polar dielectrics, such as water, for which

$$\rho\frac{\partial\varepsilon}{\partial\rho} = \alpha\varepsilon, \tag{3}$$

where $\alpha \leq 1.5$, and nonpolar dielectrics, for which

$$\rho\frac{\partial\varepsilon}{\partial\rho} = \frac{(\varepsilon-1)(\varepsilon+2)}{2}. \tag{4}$$

This means that f in water is approximately an order of magnitude larger than in oils.

The pressure field in the vicinity of the laser beam is calculated by adding the force term from eq. (2) into the equation for the conservation of momentum [2], and the main result is shown in figure 1. Here, the temporal characteristic of the laser is an on-off unit step pulse of duration τ_0 (usually not larger than a few tens of nanoseconds), and the spatial profile is a Gaussian beam with

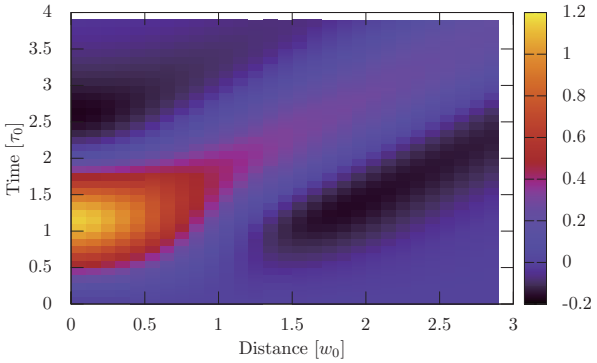

Fig. 1 Electrostrictive pressure field map.

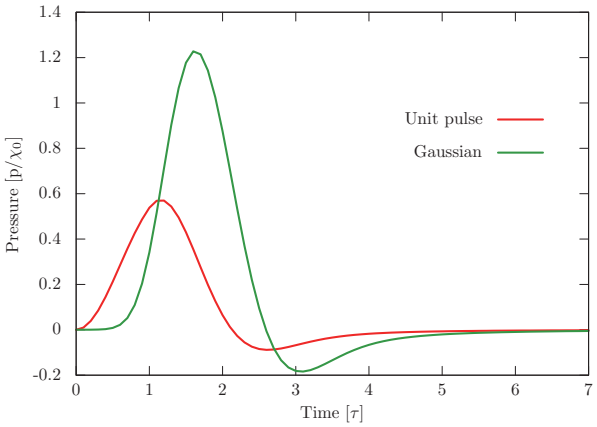

Fig. 2 Electrostrictive pressure evolution.

waist radius w_0 (usually of the order of a few tens of micrometers). The magnitude bar presents the ratio between electrostrictive pressure and the initial pressure of the dielectric, both divided by the corresponding values of susceptibility (for the case without electrostriction, susceptibility is χ_0.)

Two observations can be made:

(i) electrostrictive force may create a zone of negative pressures (tensile stress) in the vicinity of the beam [3], and

(ii) this pressure variation leads to generation of a propagating acoustic wave.

Pressure evolution and the possibility of negative pressures depends on the temporal characteristics (rise-fall

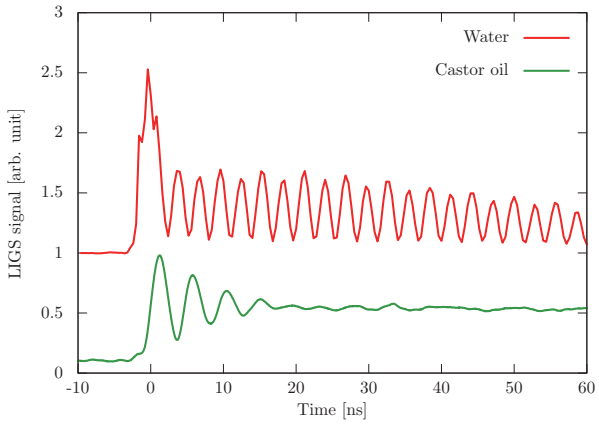

Fig. 3 LIGS signals.

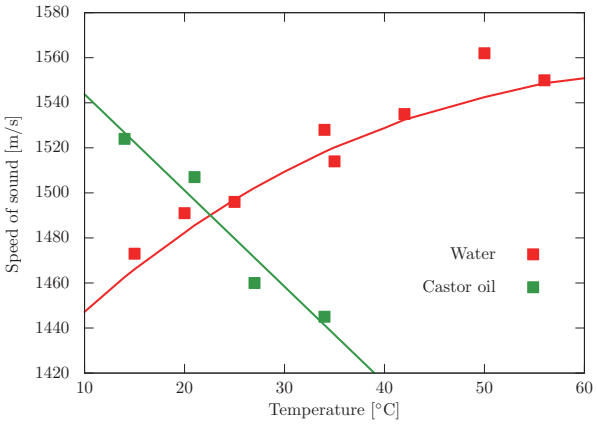

Fig. 4 Temperature vs. speed of sound relationship measured by LIGS.

time) of the laser pulse. When considering only the axis of the laser beam, the pressure evolution can be described by

$$p_s(0,t) = \tau(t) - \tau'(0)F(t) - \int_0^t \tau''(t-s)F(s)ds, \quad (5)$$

where $\tau(t)$ is the function describing temporal behaviour of the pulse and $F(s)$ is the Dawson function. Graphical presentation of eq. (5) for $\tau(t)$ corresponding to an on-off unit step function and a Gaussian function is given in figure 2.

Negative values of the pressure cause tensile stresses that might lead to cavitation. If the temporal variation of the electric field is comparable to the speed of sound of the medium, then the pressure differences are quickly eliminated by the motion of the fluid, thus negative pressures do not appear.

3. Acoustic and Temperature Measurements

On all occasions, electrostriction causes acoustic waves. These have been used for spectroscopic measurements, in particular by observing Brillouin scattering in laser-induced grating spectroscopy (LIGS) [4]. LIGS is realized by crossing two pulsed laser beams (wavelength λ_p, crossing angle θ), so that they generate an interference grating in the medium with fringe periodicity

$$L = \frac{\lambda_p}{2\sin(\theta/2)}. \quad (6)$$

In addition to electrostriction, grating is generated by thermalization, and the latter is in fact the dominant mechanism. Thermalization starts by absorption of laser energy by molecules and its conversion into thermal energy through collisions.

The interference grating can be modeled by the change of the refractive index, which is expressed by

$$\Delta n \propto \exp(-\Gamma_T t) + \exp(-\Gamma_A t)\cos(\nu t), \quad (7)$$

where Γ_T is the thermal grating decay rate determined by thermal diffusion, Γ_A is the acoustic damping coefficient, and ν is the Brillouin frequency.

A probe beam is Bragg diffracted by the grating. Periodicity of the interference grating and its frequency, coupled with the frequency of the diffracted light into the signal, give the fundamental characteristics of the acoustic waves generated by the interference grating. Thus, the speed of sound u in the medium can be calculated from the measurement of the frequency of the diffracted signal ν, by $u = L\nu$.

Examples of LIGS signals for water and castor oil are shown in figure 3. Signal from water clearly shows two frequencies, corresponding to thermalization and electrostriction, while for castor oil the signal due to electrostriction is so weak, that is not detectable ($f_{water} \approx 10 \times f_{oil}$).

If the equation of state of the liquid is also known, then temperature can be estimated, as it is shown in figure 4 for the cases of water and castor oil.

4. Conclusions

Electrostriction plays an important role in the stability and establishment of equilibrium in liquids. The electric field from a laser propagating through a liquid generates a pressure wave that in turn causes acoustic waves and tensile stresses. These disturbances can be used for the measurement of different liquid properties, and an example of temperature vs. speed of sound measurement is given.

References

[1] R. W. Boyd, *Nonlinear Optics*, 3rd ed. (2007), p. 431
[2] S. A. Ellingsen and I. Brevik, Phys. Fluids **23** (2011), 096101
[3] M. N. Shneider and M. Pekker, Phys. Rev. E **87** (2013), 043004
[4] A. B. Gojani, et al., Proc. SPIE **5251** (2004), 313

Tenth International Conference on Flow Dynamics
November 25-27, 2013, Sendai, Miyagi, Japan

Effect of Laser Energy Deposition on Supersonic Aerodynamics

Takeshi Osuka[1], Ryosuke Majima[1], Takahiro Tamba[1], Kiyokazu Yamashita[1], Naoki Hasegawa[1], Akira Iwakawa[1], Akihiro Sasoh[1], Erinc Erdem[2], Konstantinos Kontis[2]
[1]Department of Aerospace Engineering, Nagoya University, Furo-cho Chikusa-ku Nagoya 464-860, Japan
[2]School of MACE, The University of Manchester, M13 9PL, UK
osuka@fuji.nuae.nagoya-u.ac.jp

ABSTRACT

Experimental study of the interaction between the boundary layer and the low density babble generated by the laser energy deposition for lift generation was conducted by using Nose-Cylinder-Flare model and high-repetitive pulsed laser. Asymmetrical asymmetrical flow field, such as compression waves at upper region and the shock wave at lower region. About 0.8N lift force was generated by the asymmetrical flow field.

1. Introduction

One of the major aerodynamic problems to develop next generation supersonic transportation is its poor aerodynamic performance caused by large wave drag. Some methods, such as to attach physical spike in front of the body or to eject the gas to fore direction and the energy deposition into flow, were suggested to solve this problem. Laser energy deposition which doesn't need any mechanical action and can change the flow structure remotely has some advantages [1].

Conventional studies using the laser energy deposition focused on deformation of the shock wave in front of the model caused by interaction with low density babble generated by laser energy deposition. Iwakawa et al. [2] investigated the effect of the residence time of low density babble, and unveiled that the deformation of the flow field has the strongest correlation with it. However, the speed of the supersonic flow makes it difficult to extend the residence time in front of the model. So, in our study, the boundary layer was used as a low speed region to extend the residence time of the low density babble.

Interaction between the low density bubble and the boundary layer was studied by using Nose-Cylinder-Flare model [3]. Fig. 1 shows the schlieren images of the flow field. Compression waves at the flare segment changed to the shock wave by 60 kHz energy deposition (60 kHz ED). Fig. 2 shows the drag result vs. ED frequency. The drag increment was caused by the flow field change from compression waves to the shock wave at the flare segment. From these results, it was considered that asymmetrical energy deposition can generate lift force by forming asymmetrical flow field.

The objective of this paper is to generate a lift force by using asymmetrical laser energy deposition on Nose-Cylinder-Flare model.

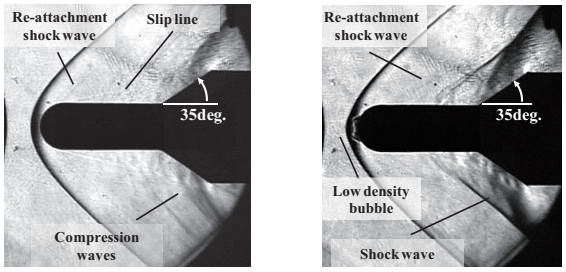

(a) w/o ED (b) w/ 60 kHz ED

Fig. 1 Schlieren images of Nose-Cylinder-Flare model

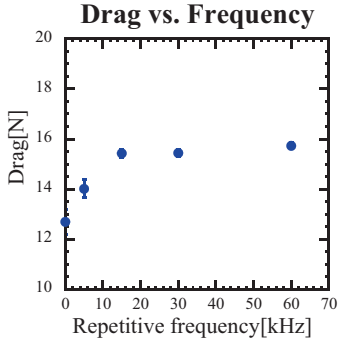

Fig.2 Drag vs. repetitive frequency

2. Experimental Setup

Fig. 3 shows the schematic of the experimental setup. A In-draft supersonic wind tunnel was used for the experiment, the Mach number is 1.92. The test section is 80mm ×80mm square cross section. The available test time of the wind tunnel is 5s. Upper stream is open to atmosphere, and downer stream is connected to the vacuum chamber which has 11.5m^3 volumes. The static pressure and the static temperature during running is 13.8 kPa and 168 K, respectively. A highly-repetitive, Nd:YVO_4 laser [wavelength, 1064nm; repetition frequency, 100kHz maximum; average power, 400W maximum] is used for the energy deposition. The output laser beam with 6mm×6mm square shape is expanded to 15mm×15mm square shape by using a concave and a plane-convex lens, is focused by using a plane-convex lens with 60mm focal length. The Flow field was visualized by framing schlieren visualization with a

high-speed framing camera (HS-106E, NAC Co., 360×410 pixels, 1250000 frame/s maximum, 120 frames)

The Ring force balance system which can measure lift and drag force and moment with small interaction is used for force measurement in small cross section wind tunnel (Fig. 4) [4].

Fig. 5 shows the schematic of asymmetrical energy deposition. The Distance of the energy deposition from the central axis of Nose-Cylinder-Flare model is defined as z. The effect of z is investigated to change from z = 0mm to z = -8mm.

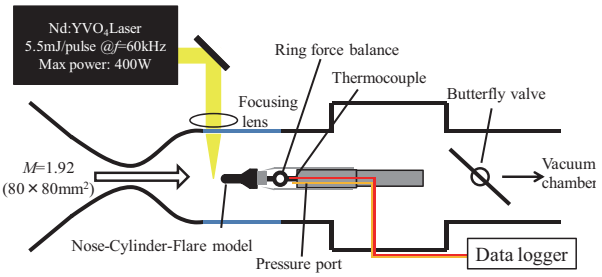

Fig.3 Ring force balance

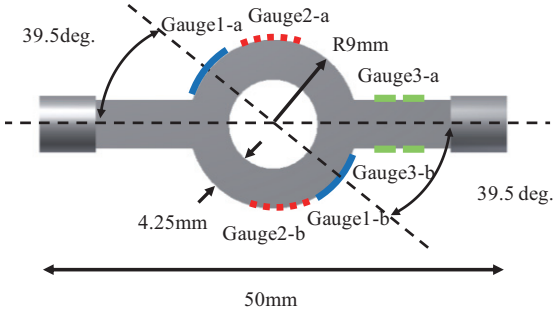

Fig.4 Ring force balance

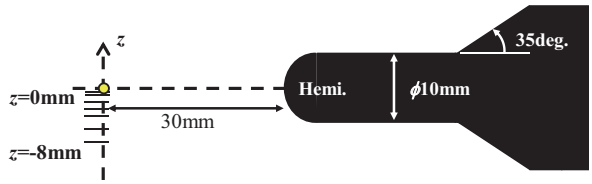

Fig.5 ED position of asymmetrical energy deposition

3. Experimental Result

Fig. 6 shows the schlieren image with z=-2mm energy deposition. We can see the asymmetrical flow field formed by asymmetrical energy deposition. At upper surface, compression waves can be observed at the flare segment. On the other hand, the shock wave is formed by asymmetrical energy deposition. Fig. 7 shows the force time history with the energy deposition. We can see the lift generation and the drag increment. Fig. 8 shows the force vs. energy deposition position. z=-3mm showed the maximum lift approximately 0.8N.

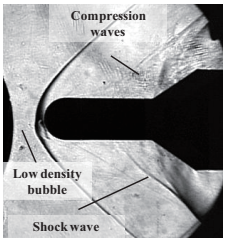

Fig.6 Schlieren images

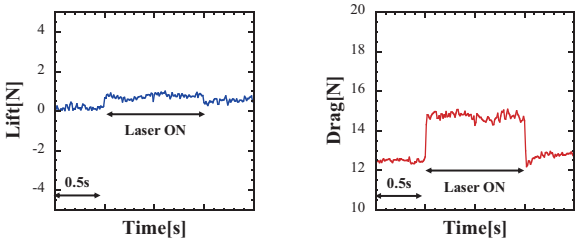

(c) Lift time history (d) Drag time history

Fig.7 Force time history with asymmetrical ED (z=-2mm)

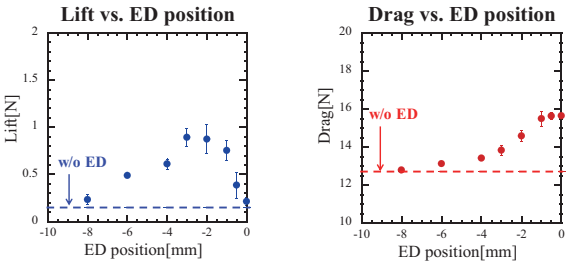

(a) Lift vs. ED position (b) Drag vs. ED position

Fig.8 Force vs. ED position

5. Conclusion

A Lift force generation experiment was conducted by asymmetrical energy deposition on Nose-Cylinder-Flare model. The asymmetrical flow field was generated by asymmetrical energy deposition. It caused generation of shock wave at lower region, and pressure difference between an upper region and a lower region created lift force. Maximum lift approximately 0.8N was generated at z = -3mm energy deposition.

Acknowledgements

The authors would like to thank Messers. K. Yamamoto, Technical Division, Nagoya University for their valuable technical assistances. This research was supported by Japan Society for Promotion of Science as Grant-in-Aid for Scientific Research(S), No. 22226014.

References

[1] D. Knight, *J Prop&Power* 24, (2008), 1153-1167,

[2] A. Iwakawa et al, *Trans. JSASS Aerospace Tech Japan* Vol. 11, (2013), 53-60

[3] T. Osuka et al, *45th Fluid Dynamics Conference/Aerospace Numerical Simulation Symposium*, (2013)

[4] H. Suemura et al, 51th AIRCRAFT SYMPOSIUM, (2012)

Tenth International Conference on Flow Dynamics
November 25-27, 2013, Sendai, Miyagi, Japan

Supersonic Free Flight Experiment of Three-Dimensional Bodies in Aeroballistic Range

Takahiro Imaizumi, Takeshi Ohyama, Atsushi Toyoda and Akihiro Sasoh
Department of Engineering, Nagoya University, Aichi, 464-8603, Japan
takahiro@fuji.nuae.nagoya-u.ac.jp

ABSTRACT

An aeroballistic range is a useful experimental facility for measuring near field pressure signature from an aircraft like model. The aeroballistic range at Nagoya University was installed with some new ideas[1],[2] to launch three dimensional aircraft like model. In order to evaluate this upgraded system, supersonic free flight experiment with AGARD-B calibration model was conducted. Experimentally obtained near field pressure signature and the pressure signature extrapolated from the computational simulation were compared. As a result, it became clear that this aeroballistic range can obtain near field pressure accurately.

1. Introduction

Aeroballistic range is suited facility for measuring a near field pressure around a supersonic free flight model. An aeroballistic range can measure the pressure field which is not affected by a sting, boundary layer and a quality of uniform flow because an experimental model flies freely inside a test chamber. An aeroballistic range also has a disadvantage, which is a control of a flight attitude of an experimental model.

Aeroballistic range at Nagoya University employed Gasdynamics/mechanical hybrid sabot separation method and installed 44 x 20 mm rectangular bore to solve the problem [1][2] .

In this paper the performance of near field pressure measurement around supersonic free flight aircraft like three-dimensional model were investigated by using AGARD-B calibration model.

2. Facility

2.1 Aeroballitic range

Figure 1 expresses aeroballistic range located at Nagoya University. This facility consists of driver gas section (1.6m), launch tube (5.6m) and test section (4m). Launch tube consists of acceleration section (3.2m), ventilation section (0.8m), sabot separation section (1.6m). In addition, dump tank is connected to the ventilation section to vent the high pressure driver gas. This aeroballistic range uses helium gas as a driver gas because acoustic impedance is low. The ventilation tube has 96 holes to release the driver gas into the dump tank. This reduced the pressure behind the sabot which ends the acceleration. Inside the sabot separation tube, gasdynamics sabot separation takes place[3][4]. Fig.2 expresses the equipment in the test chamber. Eight piezo-electric transducers (PCB piezotronics Inc., 113B28) are located 2.8m from the muzzle. Fig. 3 expresses the location of the pressure transducers. Each sensor was placed 150mm from the nominal flight path and distributed evenly around the flight path. This enables eight point simultaneous measurement. In this experiment only two pressure transducers: 360 and 180 in fig.3, were used due to symmetry of model.

2.2 Model and sabot

Figure 4 shows the model and the sabot for the free flight experiment. This model is AGARD Type-B calibration model, which the configuration is defined in the reference 5. The specification of the employed modes are as follows; diameter of cylindrical body is 10 mm; wing span is 40 mm, total length is 85mm. Model was made from aluminum alloy (Al7075), and mass is 10g. The center of gravity is different from the definition since the fuselage was hollowed to lighten the mass. However, this does not matter when evaluating near field pressure. The sabot to seals the high pressure driver gas and to keep the model attitude while accelerating is shown in the right side of Fig. 4. The sabot and the model are separated by the hybrid sabot separation method[2].

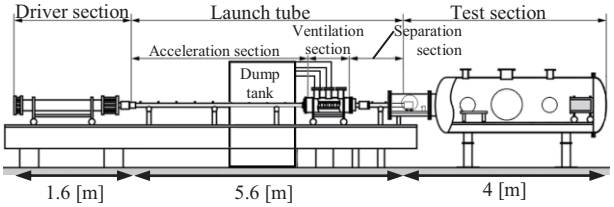

Fig. 1 Aeroballistic Range

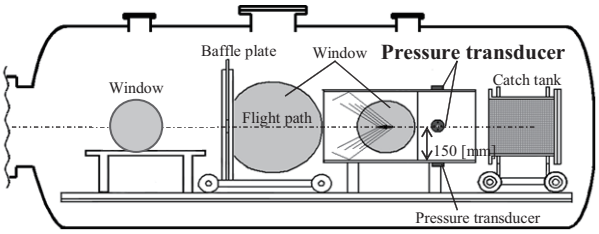

Fig. 2 equipment in test section

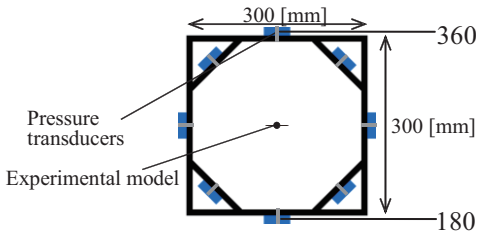

Fig. 3 Section view of the pressure measurement section
360, 180 means sensor location

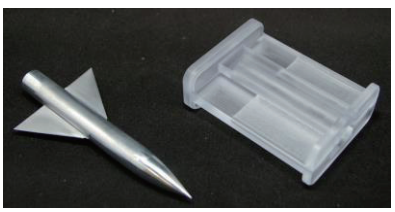

Fig. 4 AGARD-B model (left) and the sabot (right)

3. Results and Discussion

3.1 Ballistic range experiment

Figure 5 is the Schlieren photograph obtained from launching AGARD-B at Mach 1.71. From this image, angle of attack was 0.7 degrees. As shown in this image, four major shock waves were induced from the nose, leading and trailing edges of the wing and the tail.

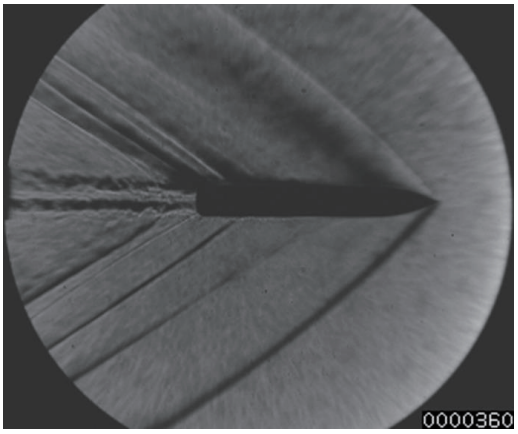

Fig.5 Schlieren photograph of free flight
Mach 1.71, A.o.A.=0.7[deg.]

3.2 Simulation

Figure 6 is the *Cp* contour obtained from the three-dimensional CFD simulation conducted at the same condition as the experiment. The computational grid was generated using Hexa grid[6] and the flow field was solved by the FaSTAR[7]. Numerical simulation is based on the Euler equations and the number of grid point is 6.6 million points.

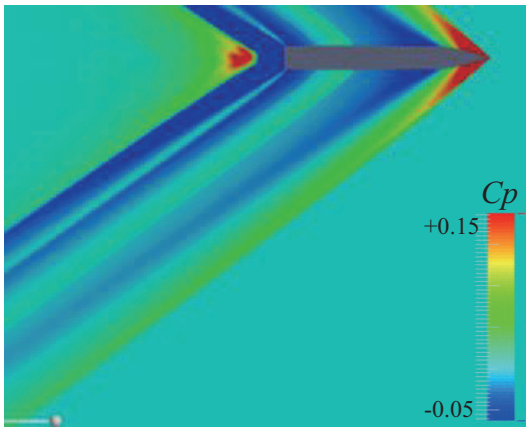

Fig. 6 *Cp* contour obtained from the CFD simulation

3.3 Comparison of experiment with CFD

Figure 7 shows near field pressure which obtained from experiment and simulation.

The red signature is the near field pressure above the model and the blue is near field pressure below the model: *H*/*L*=1.76. Both blue and red lines showed both qualitative and quantitative agreement. The slight difference between them is caused by the angle of attack. The green signature in fig.7 is from the result of the CFD simulation. The experimental pressure signature and the pressure signature from the CFD simulation agrees qualitatively but the overpressure were different.

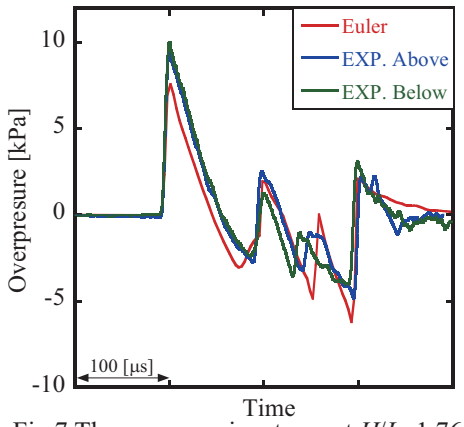

Fig.7 The pressure signatures at *H*/*L*=1.76
360 and 180 means location of pressure transducer
Mach 1.71, A.o.A.=0.7[deg.]

4. Concluding remarks

To evaluate the performance of measuring near field pressure signature from an aircraft like model, AGARD-B model was launched. For comparison, the near field pressure was also simulated by CFD. By comparing with these results, it is cleared that this aeroballistic range at Nagoya University can obtains near field pressure accurately.

Acknowledgements

The authors would like to thank Messrs. K. Yamamoto, N. Shiraki, Y. Masanaka and A. Saito, Technical Division, Nagoya University for their valuable technical assistance. This research was supported by Japan Society for Promotion of Science as Grant-in-Aid for Scientific Research (S), No.22226014.

Reference

[1] A. Toyoda, *et al.*: Near Field Pressure Measurement around Three-Dimensional Free Flight Models, 31st AIAA Applied Aerodynamics Conference, 10.2514/6.2013-2661 (June 24-27, 2013)

[2] T. Imaizumi, *et al.*: Gasdynamics/mechanical hybrid sabot separation method rectangular –bore ballistic range, International Symposium on Shock Waves 29th, 0246-000176 (2013)

[3] Akihiro. S and S. Oshiba: Impact-less, in-tube sabot separation useful for modest-sized supersonic ballistic ranges , Review of Scientific Instruments, 77 (10), 105106-105106-5, (2006)

[4] Sasoh, A, *et al.*: Ballistic-Range Technology, International Journal of Aerospace Innovations, 2 (3) , 147-156, (2010)

[5] Hills. R; *A review of measurements on AGARD* calibration models, AGARDograph, 64.(january, 1961)

[6] Hashimoto, A., *et.al.*, "Lift and Drag Prediction Using Automatic Hexahedra Grid Generation Method," 47th AIAA Aerospace Sciences Meeting, 5-8 January 2009, Orlando, Florida, AIAA 2009-1365.

[7] Hashimoto, *et.al.* , "Toward the Fastest Unstructured CFD Code "FaSTAR"", 50th AIAA Aerospace Sciences Meeting Including the New Horizons Forum and Aerospace Exposition, January 2012, AIAA 2012-1075.

Tenth International Conference on Flow Dynamics
November 25-27, 2013, Sendai, Miyagi, Japan

Optimization of Supersonic Flow Generator Using Genetic Algorithm

Yuki Kutsuna, Akira Todaka, Gaku Sasaki, Takaaki Matsumoto, and Koichi Yonemoto
Kyushu Institute of Technology, 1-1 Sensui, Tobata, Kitakyushu, Fukuoka
n344118y@tobata.isc.kyutech.ac.jp

ABSTRACT

This paper addresses the design and evaluation of a supersonic wind tunnel that can generate desired Mach number and uniform flow speed distribution. The nozzle shape is described by a sextic polynomial and optimized using Genetic Algorithm. A fitness function calculates the distribution of Mach number at the nozzle exit using the method of characteristics. The optimization result shows that the optimum nozzle design excels in the uniformity of Mach number distribution at the test section compared with that of conventional studies.

1. Introduction

Space Systems Laboratory at Kyushu Institute of Technology has started winged rocket project to research and develop a fully reusable space transportation system since 2005. When a spacecraft reenters the earth's atmosphere, aerodynamic heating occurs due to the compression of air around the spacecraft and the kinetic energy conversion into the thermal energy. A Pitot-tube cannot be used because the heating intensifies at the reentry. Therefore, FADS (Flush-type Air Data System), which measures surface pressure distribution using a large number of pressure holes around nosecone, is preferable as an air data system. Fig. 1 shows an image of aerodynamic heating of HYFLEX (HYpersonic FLight EXperiment), which is designed to equip FADS. In order to evaluate FADS, a supersonic wind tunnel is necessary. In this study, a supersonic nozzle shape optimization using Genetic Algorithm is studied.

Fig. 1 Image of HYFLEX Aerodynamic Heating

2. Method

2.1 Supersonic Nozzle Design

The Mach number of a supersonic nozzle depends on the ratio between throat and exit areas. However, the total nozzle slope is also very important because bad shape causes flow separation and shock wave.

Conventional method designs expansion and divergent sections separately, and connects those two smoothly. But the divergent area is not be designed arbitrary so that the conventional method is a deterministic approach.

In this study, in order to find the optimal supersonic nozzle shape, a polynomial function that fully express the nozzle slope is used. The coefficients of polynomial are optimized by a genetic algorithm to find the global best shape which generates desired Mach number and uniform flow speed distribution at test area.

2.2 Optimization Flow

The optimization method of supersonic nozzle shape employs the RCGA (Real-coded Genetic Algorithms). The roulette selection and the blend crossover are used for selection and mutation of Genetic Algorithm. Fig. 2 shows the optimization flow.

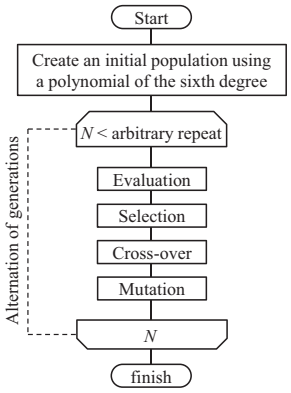

Fig. 2 Optimization Flow

2.3 Individual Generation

The constraints of nozzle shape design are following:

- The nozzle length is 1
- The heights of throat and nozzle exit are given
- The slopes of throat and nozzle are 0
- The nozzle has only one inflection point

In this study, a sextic polynomial Eq. (1) expresses the nozzle shape. Eq. (2), which is the second order derivative of Eq. (1), is used to determine the inflection point. Applying the constraints to Eq. (1) and (2), the number of design variables becomes 3. Fig. 3 shows the initial individuals.

$$f(x) = a_6x^6 + a_5x^5 + a_4x^4 + a_3x^3 + a_2x^2 + a_1x + a_0 \quad (1)$$

$$f''(x) = 30a_6(x-x_1)(x-x_2)(x-x_3)(x-x_4) \quad (2)$$

where a_0~a_6 are the polynomial coefficients, x_1~x_4 are the inflection points and x is the distance from nozzle throat.

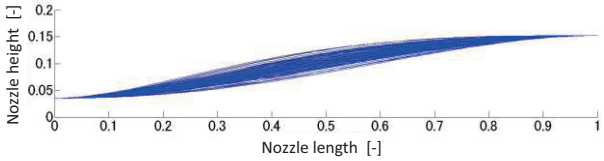

Fig. 3 Initial Individuals

2.4 Evaluation

The Mach number distribution at the test section is calculated for all generated individuals using the method of characteristics. Eq. (3) gives the fitness of each individuals, which is the root-mean-square of error between the target and the test section Mach numbers. The smaller M_{RMS}, the better performance the nozzle shape provides. Fig. 4 shows an example of individual. The fitness is calculated by the Mach number distribution at the test section.

$$M_{RMS} = \sqrt{\frac{1}{N}\sum_{i=1}^{N}\left(M_{set} - M_i\right)^2} \rightarrow \min. \qquad (3)$$

where M_{set} is the target Mach number, M_i is the calculated Mach number at i-th point of the test section, and N is the total number of calculation points at the test section.

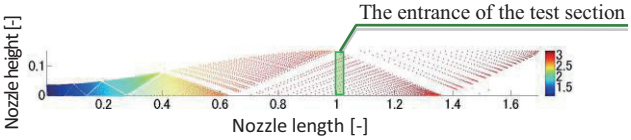

Fig. 4 Flow Speed Calculation Using the Method of Characteristics

3. Results

The calculation conditions are shown in Table 1.

Table 1 Calculation Conditions of GA

Number of Individuals	100
Number of Generations	20
Selection Method	Roulette Selection
Crossover Method	Blende Crossover
Crossover Rate	50 %
Mutation Rate	0 %
Number of Elites	3

Fig. 5 shows the optimized shape of supersonic flow generator and its Mach number distribution at the test section. Fig. 6 and 7 indicate the nozzle shapes and their Mach number distributions of the author's previous research and JAXA's supersonic wind tunnel.

The fitness of this study is 0.007372, while those of author's previous work and JAXA's supersonic wind tunnel are 0.04307 and 0.01936, respectively. This result indicates that the optimized nozzle excels in the uniformity of Mach number distribution.

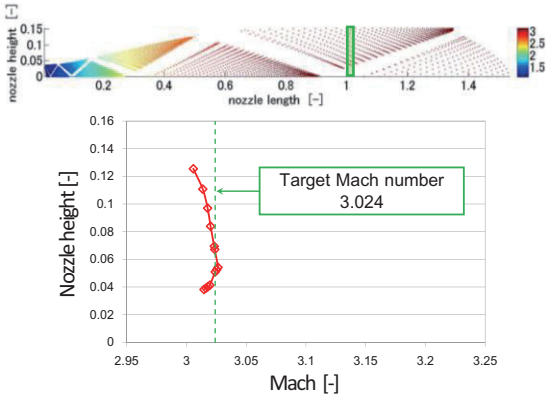

Fig.5 Optimized Mach Number Distribution

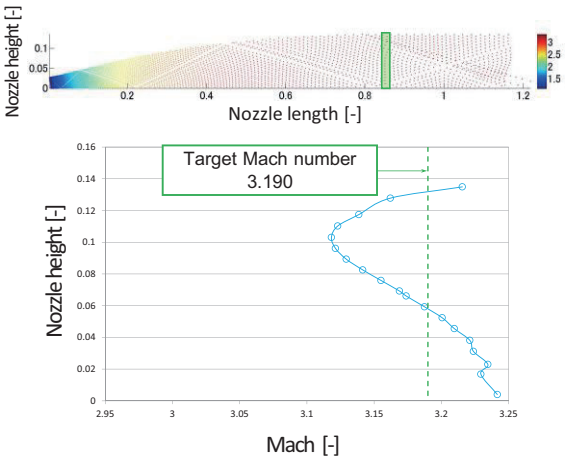

Fig. 6 Nozzle Shape and Mach Number Distribution at Test Section of the Author's Previous Research

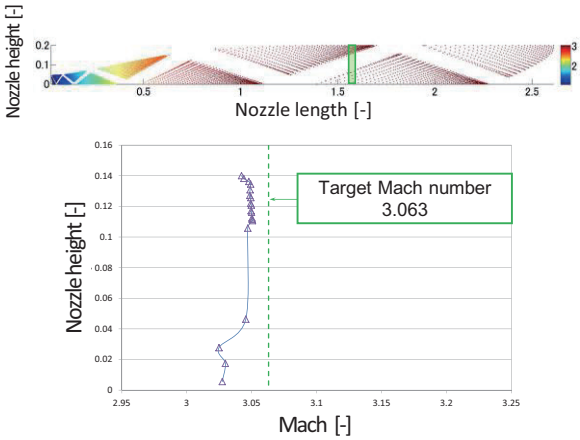

Fig. 7 Nozzle Shape and Mach Number Distribution at Test Section of JAXA's Supersonic Wind Tunnel

4. Conclusions

In this paper, in order to evaluate FADS and build a flow generator that can generate desired Mach number and uniform flow speed distribution, the supersonic nozzle shape was optimized using Genetic Algorithm. The practical performance evaluation of the optimum nozzle is the future target. Using the supersonic flow generator, authors will investigate a FADS of a suborbital spacecraft.

Acknowledgements

This research was supported by Harada Memorial Foundation.

References

[1] A. Todaka, Y. Kutsuna, T. Matsumoto, and K. Yonemoto "Preliminary Research on a Fault Tolerant Flush Airdata Sensing (FADS) System for Supersonic Flight", 56th Conference on Space Science and Technology, 2B10, 2012.

[2] T. Akiyama, "Hybrid Optimal Trajectory Generation Using Genetic Algorithm and Sequential Quadratic Programming", Master's thesis of Kyushu Institute of Technology, 2010.

Tenth International Conference on Flow Dynamics
November 25-27, 2013, Sendai, Miyagi, Japan

The Investigation of Heat Transfer Enhancement in Segmented Microchannel Flow Using Micro-PIV and TSP Techniques

Ying-Nung Chen[1], Jhih-Ren Lin[1], Bo-Han Huang[1], Tong-Miin Liou[1] and Chih-Yung Huang[1]
[1]Department of Power Mechanical Engineering, National Tsing Hua University, Hsinchu, Taiwan
cyhuang@pme.nthu.edu.tw

ABSTRACT

This study aims to investigate the characteristics of heat transfer with segmented flow in PDMS microchannel using micro PIV and TSP techniques. Compared with heat transfer from single phase flow, the two phase segmented flow helps the flow mixing in the liquid segment and enhance the heat transfer. The averaged Nu number of two phase segmented flow is about 30% higher than single phase flow.

1. Introduction

Heat dissipation inside micro devices has been an important issue with the increase power generation inside MEMS devices. There are several research proposed to improve the heat removal performance like designing high aspect ratio, curved and constricted microchannels in micro heat sink. These designs have been demonstrated that they can remove heat effectively, and many researchers have devoted in the design and measurements of such microchannels. However, the flow in the micro heat sink has the limitation of low Reynolds number due to the small characteristic length and lower Nusselt number have been reported compared to the macroscale measurements. Therefore, segmented flow in microchannels has been proposed to improve the heat transfer of micro heat sinks [1, 2]. The recirculation in the fluid section has been observed in the segmented flow and it improves the mixing of fluid [3, 4]. The temperature distribution in segmented flow has also acquired by experimental approaches using thermocouples, liquid crystal thermography and micro laser induced fluorescence [5, 6]. In present study, the characteristics of heat transfer of segmented flow with ethanol/air inside PDMS microchannel has been analyzed by using temperature-sensitive paint (TSP) technique with both fluid and wall temperature measurements. TSP technique has been applied in microscale heat transfer analysis to provide global temperature profiles with detailed resolution [7].

2. Method

To study the characteristics of heat transfer in microscale, a Polydimethylsiloxane (PDMS) microchannel was fabricated by standard soft lithography procedure. Fig. 1 shows the picture of experimental setup in current study and the design of microchannel. The total length of microchannel is 11 cm and the depth of microchannel is 150 μm. Two reservoirs were positioned at microchannel inlets to serve as liquid-inlet and gas-inlet. Segmented flow was successfully produced by using this design after the T-junction and is shown in Fig. 2. At the bottom of the microchannel, an electric heater was used to provide constant heat flux through the bottom of microchannel during the experiment and a copper block was inserted in between the microchannel device and the heater to provide uniform heat flux. Due to the low thermal conductivity of PDMS, this design can deliver one side heating boundary condition. T-type thermocouples were applied to the microchannel device for in-situ calibration before experiments. Tris(bipyridine) ruthenium(II) dichloride ($Ru(bpy)_3$) was selected as the temperature sensor and dissolved in ethanol to measure the fluid temperature. $Ru(bpy)_3$ also dissolved in ethanol and mixed with dope to measure the surface temperature while applied at the bottom of microchannel. 462 nm LEDs were used as excitation source and the luminescence was recorded by a CCD camera with 550 nm long pass optical filter. Micro-PIV measurements were performed using 0.71 μm red polymer particle with a double shutter CCD camera. The details of micro-PIV experimental arrangement can be found in Ref [7]. To create different experimental conditions in the segmental flow, three gas flow rates were used with one liquid flow rate and they were controlled by syringe pumps. The experimental conditions of single phase flow (S-P, Liquid: ethanol) and two phase flow (segmented flow, Liquid: ethanol, Gas: air) are listed in Table 1.

3. Results and Discussion

The segmented flow has been successfully built using ethanol and air with different flow rates, as shown in Fig. 2. Fig. 3 shows the fluid temperature profiles acquired by temperature sensor mixing with ethanol after in-situ calibration. It can be noticed that temperature rises from the inlet through the microchannel. Temperature gradient inside the segments reduces while moving downstream from the entrance. Stronger flow recirculation has been observed as the stream line and velocity profiles acquired at the condition of case 3 using micro-PIV technique, as shown in Fig. 4. This indicates the improved heat transfer to the fluid due to increased flow circulation by higher gas flow rate. The acquired temperature profiles have been analyzed and the calculated Nu numbers at different experimental conditions are presented in Fig. 5. Theoretical calculation with microchannel flow and the

experimental data with single phase flow have also been provided in Fig. 5 for comparison. About 30% Nu number increase are achieved by using segmented flow in microchannel than single phase flow at the same liquid flow rate in low Re number of 11.

4. Concluding remarks

The velocity and fluid temperature profiles in segmented flow inside microchannel device were successfully measured by micro-PIV and TSP techniques, respectively. Due to the circulation in the liquid region in segmented flow, the fluid temperature increases and the Nu number is about 30% higher than the single phase flow. The heat transfer enhancement due to segmented flow has been identified in current study. (This work is supported by NSC project via NSC 101-2221-E-007-057-MY3)

References

[1] M. T. Kreutzer, F. Kapteijn, J. A. Moulijn, J. J. Heiszwolf, Chemical Engineering Science, **60**, (2005) pp. 5895-5916.
[2] A. Gunther, S. A. Khan, M. Thalmann, F. Trachsel, K. F. Jensen, Lab on a Chip, **4**, (2004) pp. 278-286.
[3] A. Asthana, I. Zinovik, C. Weinmueller, D. Poulikakos, International Journal of Heat and Mass Transfer, **54**, (2011) pp. 1456-1464.
[4] U. Miessner, 14th Int Symp on Application of Laser Techniques to Fluid Mechanics (2008).
[5] C. Y. Yang, T. Y. Lin, Experimental Thermal and Fluid Science, **32**, (2007) pp. 432-439.
[6] S.-S. Hsieh, C.-Y. Lin, International Journal of Heat and Mass Transfer, **52**, (2009) pp. 260-270.
[7] C. Y. Huang, T. M. Liou, C. A. Li, M. W. Wang, 15th Int Symp on Flow Vis. (2012).

Table 1 Experimental conditions of flow rate settings

	Case 1	Case 2	Case 3	S-P
Q_L (ml/hr)	10	10	10	10
Q_G (ml/hr)	8	10	14	
Re_L	11	11	11	11

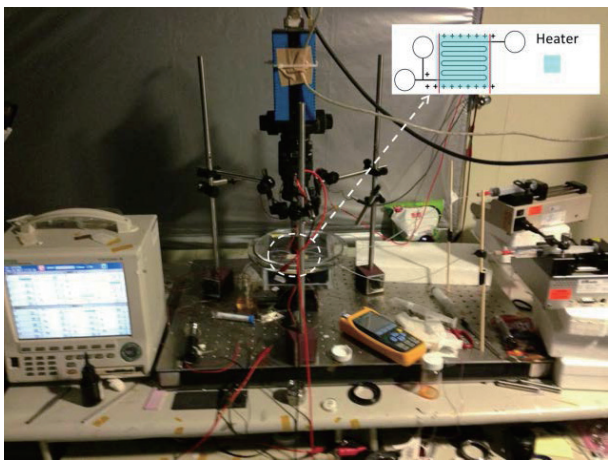

Fig. 1 Experimental setup

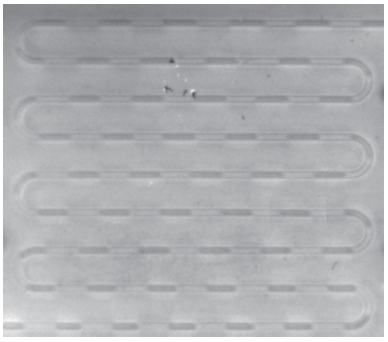

Fig. 2 Raw image of TSP

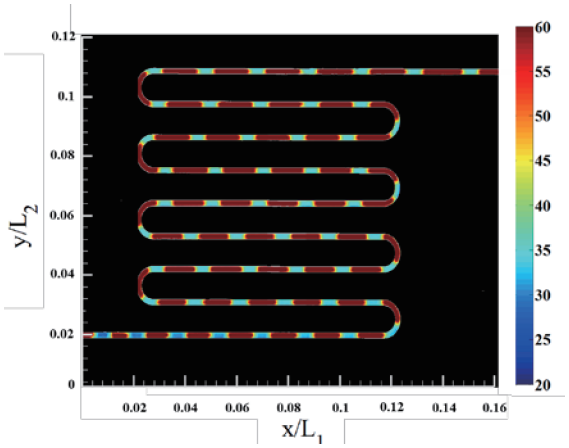

Fig. 3 Fluid temperature profile in the segmented flow

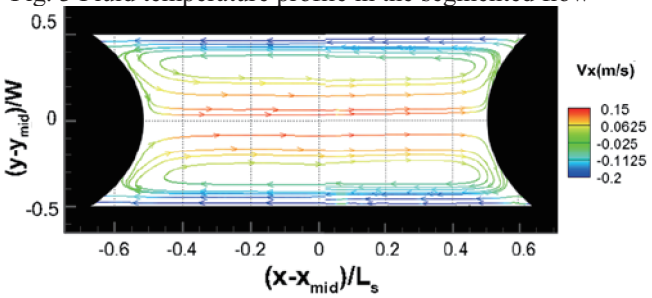

Fig. 4 The velocity distribution inside the segmented flow

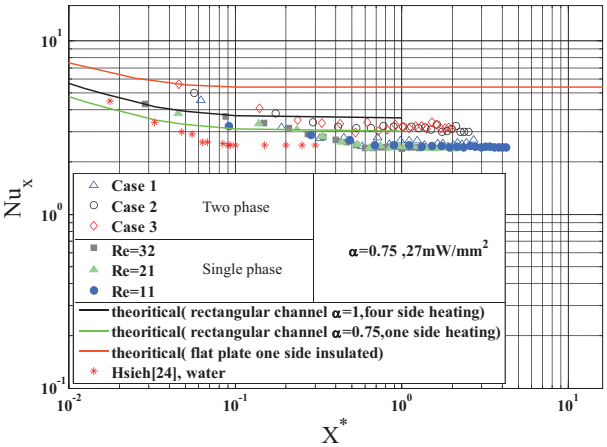

Fig. 5 Nu number comparison with single phase and two phase (segmented flow) experiments

Tenth International Conference on Flow Dynamics
November 25-27, 2013, Sendai, Miyagi, Japan

DNS Study on Boundary Layer with Heat Transfer affected by Disturbances Created by a Grid and Small Cubes

Shuang Xia[1)], Yasumasa Ito [1)], Kouji Nagata[1)], Yasuhiko Sakai[1)], Hiroki Suzuki[2)], Osamu Terashima[1)] and Toshiyuki Hayase[3)]
1) Dept. of Mechanical Science and Engineering, Nagoya University, Nagoya, 464-8603, Japan
2) Dept. of Engineering Phys., Electronics and Mechanics, Nagoya Institute of Technology, Nagoya, 466-8555, Japan
3) Institute of Fluid Science, Tohoku University, Sendai, 980-8577, Japan
E-mail: xia.shuang@f.mbox.nagoya-u.ac.jp

ABSTRACT

Direct numerical simulation (DNS) is carried out to investigate the effects of disturbances created by a grid and tripping object on boundary layer with heat transfer. Related statistics of convective heat transfer in boundary layer are presented and discussed. The results show that the heat transfer is enhanced by the grid-generated turbulence rather than the tripping object. It is also found that the strain contributes to the heat transfer on the wall rather than the rotation.

1. Introduction

Boundary layer over a flat plate is one of the canonical wall-bounded shear flows and heat transfer through the wall is strongly affected by the flow. The details of the flow structure and heat transfer in a pure boundary layer without any disturbance have been investigated over decades [1-4]. However, in practice, they are often affected by external disturbances of the flow or objects on the wall. It is, therefore, of importance to clarify the effects of such disturbances on the boundary layer with heat transfer for the prediction and control.

In this paper, DNSs are performed to investigate the heat transfer mechanism in a boundary layer under the effects of grid-generated turbulence and a tripping object.

2. DNS Method

2.1 Computational domain

Figure 1 shows the schematic of the computational domain. The domain size along with the numerical mesh number is listed in Table 1. Here, H is the height of the computational domain. A turbulence-generating grid with a solidity of 0.36 is numerically installed at a position of $0.4H$ downstream from the inlet. For the case with the tripping object, an array of staggered cubes with a height of $0.02H$ is numerically placed at the same position as the grid. The origin of the coordinate is at the center and bottom end of the grid and tripping object on the wall, and x, y and z denote the streamwise, wall-normal and spanwise coordinate, respectively.

2.2 Boundary conditions

The uniform flow with a $1/7$ power law near the wall region of $L_y \le H/8$ is given as the inflow boundary condition. The convective outflow condition is applied at the exit. The non-slip and constant temperature ($\theta = 0$) conditions are imposed on the wall, while the slip and constant temperature ($\theta = 1$) conditions are applied to the upper boundary. The periodic boundary condition is used in spanwise direction. On the surface of the grid and tripping object, the interpolation method is applied to make the velocity zero.

2.3 Numerical method

The governing equations are the incompressible Navier-Stokes equations, the scalar transfer equation and the continuity equation. The fractional step method is used to solve the governing equations. The 3rd-order Runge-Kutta method and the 2nd-order central difference method are applied for time advancement and spatial discretization, respectively. The Poisson equation for pressure is solved by the Bi-CGstab method [5]. The staggered meshes are applied in the arrangement of velocity and pressure on mesh points to prevent spurious pressure oscillations.

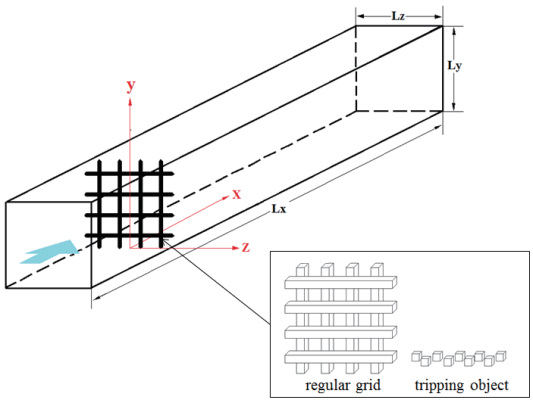

Fig. 1 Schematic of computational domain

Table 1. Computational domain and mesh number

domain size $L_x \times L_y \times L_z$	$6H \times H \times H$
mesh number $N_x \times N_y \times N_z$	$624 \times 200 \times 160$

3. Results and Discussion

3.1 Mean temperature

Figure 2 shows the wall-normal distribution of the mean temperature at $\mathrm{Re}_\theta = 240$ ($x/H = 4$). Here, '+' denotes the value normalized by the wall units. The linear and log law distributions with the same coefficient as that in Kong *et al.*'s study [4] is also included for comparison. It is observed that, in the case with the grid turbulence, the mean temperature profile has the linear and log-law regions as seen in typical pure turbulent thermal boundary layers. On the other hand, in the case

with the tripping object, the mean temperature profile deviates from the log-law distribution, indicating that the boundary layer is in transition.

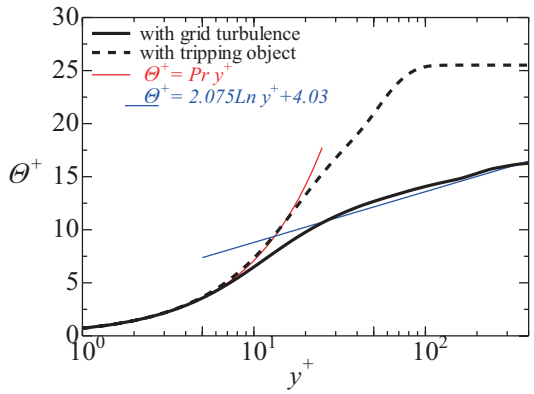

Fig. 2 Mean temperature profile

3.2 Temperature fluctuation

The wall-normal distribution of the root-mean-square (rms) value of temperature fluctuation at $\mathrm{Re}_\theta = 240$ ($x/H = 4$) is shown in Fig. 3. The rms temperature in the case with the grid turbulence is larger than that in the case with the tripping object, especially in the log-law and the outer regions of the boundary layer.

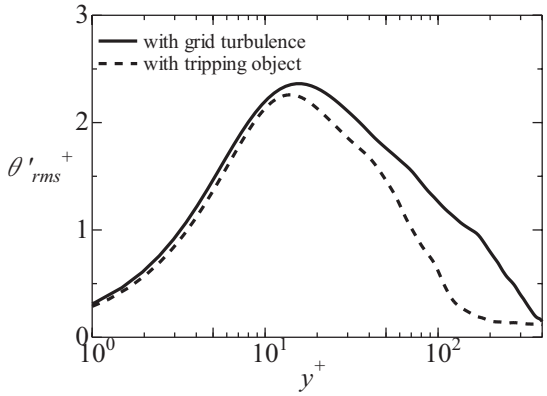

Fig. 3 Rms temperature profile

3.3 Wall-normal heat flux

Figure 4 shows the distribution of the wall-normal heat flux. It is observed that, in the case with the grid turbulence, the wall-normal heat flux is larger than that in the case with the tripping object.

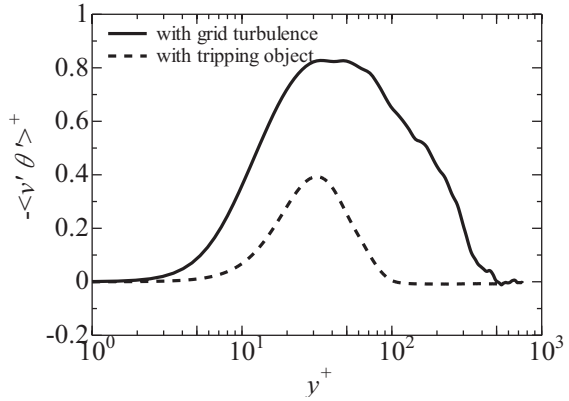

Fig. 4 Wall-normal heat flux

3.4 Heat transfer and vortical motion on the wall

Figures 5 and 6 show the visualized heat transfer coefficient, h, and the second invariant of velocity gradient tensor, Q, on the wall ($y = 0$), respectively. Here, h is calculated from $h = \dfrac{-k(\partial\theta/\partial y)\big|_{y=0}}{\theta_w - \theta_\infty}$ where k denotes the conductivity of the fluid, subscript w and ∞ represent the wall and the free-stream, respectively. It is clearly observed that Q is mostly negative (blue in Fig. 5) in the region where h is high (red in Fig. 6). This indicates that heat transfer is enhanced when the strain dominates over the rotation.

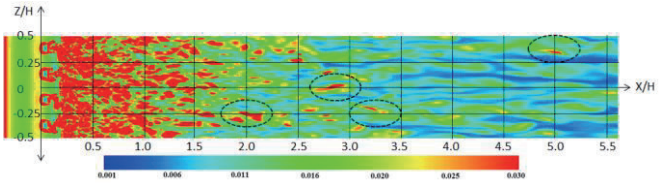

Fig.5 heat transfer coeffcient on the wall

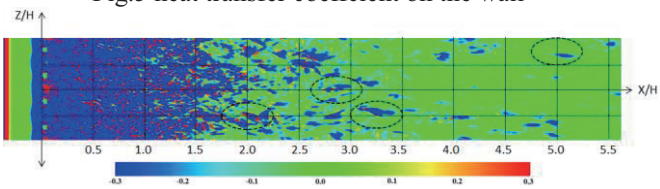

Fig.6 Q on the wall

4. Concluding Remarks

In this paper, heat transfer in a boundary layer under the effects of grid-generated turbulence and tripping object is discussed. The results show that the heat transfer is enhanced by the grid-generated turbulence rather than the tripping object. It is also found that the strain contributes to the heat transfer on the wall rather than the rotation.

Acknowledgements

Part of the work was carried out under the Collaborative Research Project of the Institute of Fluid Science, Tohoku University. Part of this work was supported by Grants-in-Aid (No. 25289030) from the Japanese Ministry of Education, Culture, Sports, Science, and Technology.

References

[1] P. R. Spalart, J. Fluid Mech. **187** (1988), pp. 61-98.
[2] J. H. Lee, H. J. Sung, Int. J. Heat and Fluid Flow, **32** (2011), pp 1-10
[3] H. Hattori, T. Houra and Y. Nagano, Int. J. Heat and Fluid Flow, **28** (2007), pp 1262-1271
[4] H. J. Kong, H. C. Choi, and J. S. Lee, Phys. Fluids, **12** (2000), pp. 2555-2568.
[5] H. A. Van Der Vorst, SIAM J. Sci. Stat. Comp., **13** (1992), pp. 631-644.

Tenth International Conference on Flow Dynamics
November 25-27, 2013, Sendai, Miyagi, Japan

Heat Transfer of Boiling with Magnetically Driving Metallic Powder in Liquid

Keiichi Igari, Yuki Chinone and Naoki Ono
Shibaura Institute of Technology, 3-7-5 Toyosu, Koto-ku, Tokyo 135-8548, Japan
naokiono@sic.shibaura-it.ac.jp

ABSTRACT

This study is basic research about boiling heat transfer aiming to promote miniaturization and detachment of boiling bubbles, and suppression of dryout. In the experiment, the pure water containing metallic powder was used, and the metallic powder was expected to drive the flow by using rotation of magnetic field. Force caused by the metallic powder affected the gas-liquid interface and decreased the size of bubbles. A sudden rise in superheat temperature as seen in normal dryout, was not clearly observed in this study.

1. Introduction

In recent years, as electronic devices have realized downsizing and superior performance with intense heat generation from the devices, the study of the method that can effectively cool the devices has also progressed. As a part of the study, there are ideas using electromagnetism effect in the field of the boiling heat transfer. In this field, some researchers already have attempted to use electric field[1]. However, there are not many previous studies using "magnetic field". In this study, the effective technique to promote the bubble detachment and to improve heat transfer properties at the heated surface by applying magnetic field in semi-three dimensional pool boiling was investigated. The magnetic field was imposed on the test fluid which included some amount of metallic powder in the experimental apparatus, and the state of bubble detachment at the heated surface was observed. In addition, the heat transfer properties were measured.

2. Theory

Various forces such as buoyancy, inertial force, pressure and surface tension act on boiling bubbles leaving from the heated surface. The magnetized metallic powder can cause the external force as described in Eq. (1), if it is placed in the magnetic field. In Eq.(1), B is magnetic flux density (T), μ_0 is vacuum permeability (H/m) and S is surface area of a metallic powder (m^2).

$$F = \frac{B^2 S}{2\mu_0} \tag{1}$$

When it is assumed that the distance between the metallic powders are so far apart as it cannot affect each other, the drag force to act on the metallic powder is given by the external force F (as in Eq.(1)) and the pressure force received from the fluid, as shown in Eq. (2), where M is the mass of a metallic powder (kg), $\boldsymbol{x}$ is position vector at the center of a metallic powder (m), ρ is density of the domain fluid (kg/m^3) and a is average radius of a metallic powder (m).

$$M\boldsymbol{x}'' = F - \frac{2}{3}\pi\rho a^3 \boldsymbol{x}'' \tag{2}$$

It is thought that the same force acts on the fluid in the opposite direction. The force that the fluid receives is proportional to the density of the metallic powder in the fluid per unit volume. It is thought that the force can affect the behavior of the boiling bubbles around the heated surface.

3. Method

As the method for the experiment, the periodic magnetic field change was activated by turning the permanent magnet having 12mm of rotation radius which was put outside the examination fluid. The pivot point of the magnet was placed in the center of the heated surface. Then, by the magnetic field, the metallic powder gave the force to make the fluid move around the heated surface. It is thought that bubble detachment at the heated surface was promoted by the effect. When a static magnetic field was adopted in this experiment system, it was thought that the metallic powder could not act on boiling bubbles effectively due to the pressure force acting on the metallic powder from the fluid as show in Eq.(2). Therefore, rotational magnetic field was used to utilize the drug force from the metallic powder for the heated surface continually. It should be noted that the metallic powder did not necessarily move largely in the rotational magnetic field. In this study, triiron tetraoxide (Fe_3O_4) which is a kind of oxide of iron, and has strong magnetism character, was used as the material of the metallic powder.

The test section (a semi three dimensional device) to be used for the experiment is shown in Fig. 1. As the advantage of adopting the device, the liquid supply to the heated surface was carried out smoothly, and driving the metallic powder by the magnetic field from the outside of the liquid was enabled. This device was constructed with copper sheet as the heated surface, wall surface of polyester putty and two glass boards. The copper sheet was heated by a ceramic heater and a long nose section of 2×3×20mm was established to the copper sheet to measure the heat flux value by the K-type thermocouples glued to the three points in the nose. The magnetic flux density distribution of the magnet in the direction of the thickness of the semi-three dimensional device is shown in Fig. 2. The solution what was mixture of 0.04 g of triiron tetraoxide and 10.8 ml of pure water in addition of 1 wt% of surfactant, was used for the experiment. Types of the solution used in the experiment and the magnetic field condition are shown in Table 1. The type names indicated as Type-1 to Type-4 in Table 1 were used for the explanation of each experimental result and the discussion as follows.

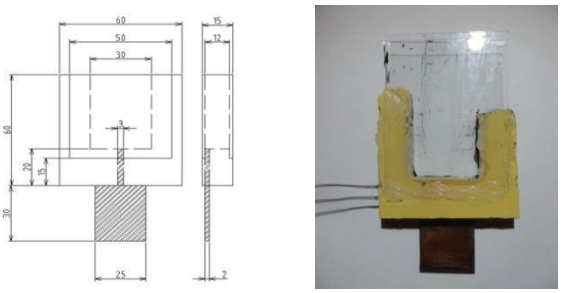

(a) Geometry (b) Photo

Fig.1 The detail of the semi three dimensional pool device

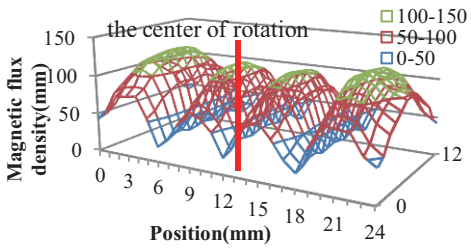

Fig.2 Magnetic flux density distribution in rotating magnetic field

Table 1. Types of solutions and magnetic field condition

Type	Details of the solution and magnetic field condition
Type-1	Pure water + Surfactant (1wt %)
Type-2	Pure water + Surfactant (1wt %) + metallic powder
Type-3	Pure water + Surfactant (1wt %) + metallic powder + Static magnetic field
Type-4	Pure water + Surfactant (1wt %) + metallic powder + Rotational magnetic field

4. Results and Discussion

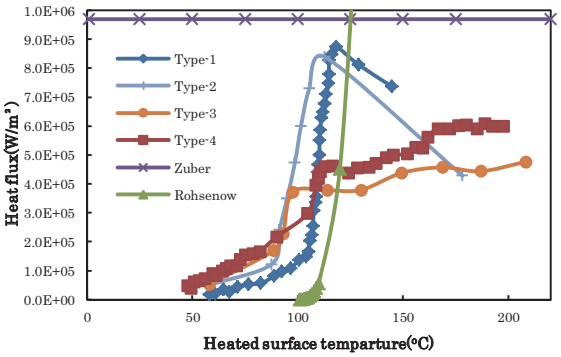

Fig.3 The results for the experiments as the relation between the heated surface temperature and the heat flux value

The relation between the heated surface temperature and the heat flux value in each experiment condition as boiling curves including natural convection region is shown in Fig. 3. This graph shows heat flux in vertical axis without logarithm and heated surface temperature in horizontal axis, and the curves provided by Zuber's equation as the predicted value of the critical heat flux (CHF) in the pool boiling and Rohsenow's equation as the predicted expression of the boiling curve of the Type-1 in the pool boiling are added.

The CHF value appeared at Type-1 and Type-2 conditions without magnetic field, respectively. On the other hand, the CHF points disappeared at Type-3 and Type-4 conditions when adding magnetic field, respectively, in Fig. 3.

The shape of the boiling curve was similar in both Type-1 and Type-2, but the wall surface temperature in the range from the onset of nucleate boiling to the CHF value were lower in Type-2 compared with in Type-1. The difference of effective heat transfer coefficient of the aqueous solutions between Type-1 and Type-2 conditions could be the reason. The effective heat transfer coefficient should have been changed because of the existence of 0.4% of metallic powder, which has about 100 times larger thermal conductivity than that of the fluid. In particular, it should be noted that the heated surface temperature at the onset of nuclear boiling was lower in Type-2. By the comparison of Type-2 and Type-3 conditions, it was confirmed that the heat flux values were higher at Type-3 than at Type-2 in the natural convection region. Because a magnetic field did not rotate in Type-3, there was no change of the magnetic flux and metallic powder having larger thermal conductivity than the fluid formed a layer near the heated surface. However, over the natural convection region, the heat flux values of Type-3 condition had lower value than that of Type-2 because the layered metallic powder interfered with the convection in progress of nuclear boiling. The heat flux value was decreased rapidly after CHF arrival in Type-2. In contrast, in Type-3, the heat flux did not clearly show CHF, but increased gradually even if heating face temperature exceeded 115 degrees. By the comparison of Type-3 and Type-4 conditions, from natural convection region to the early stage of nuclear boiling, both tended to be almost similar. When the heated surface temperature rose from the early stage of nuclear boiling, the heat flux values in Type-4 became higher than that in Type-3. It is thought that the drag caused by the metallic powder near the heated surface driven by the rotational magnetic field, seemingly acted on the surface of the bubbles. The heat flux did not clearly reach CHF, but increased gradually even if heating face temperature exceeded 200 degrees in both conditions.

5. Concluding remarks

In the experiments, the CHF appeared in the conditions without magnetic field, otherwise the value did not clearly appear in the conditions with imposing magnetic field. However, it was yet difficult to fully understand that the results primarily depended on the influence of the magnetic field or the metallic powder in the fluid from those experiment conditions. The heat flux value will be measured in the condition where heated surface temperature is much higher over the heat-resistant temperature of the device. In addition, the relationship of the change of the heat transfer properties between the density of metallic powder in the fluid and the number of revolutions of the rotational magnetic field will be investigated.

References

[1] Tadashi CHIKA, Yuta HIGUCHI and Ichiro KANO, JSME, (2011), J054073

Tenth International Conference on Flow Dynamics
November 25-27, 2013, Sendai, Miyagi, Japan

Heat Transfer Characteristics of Impinging Jet from Pipe Nozzle with Vortex Generators

Chayut Nuntadusit, Burin Kaewkraikrong, Konlawat Songkaor and Makatar Wae-hayee
Department of Mechanical Engineering, Faculty of Engineering, Prince of Songkla University,
Hat Yai, Songkhla, 90112, Thailand
chayut@me.psu.ac.th

ABSTRACT

This study investigated the heat transfer characteristics of impinging jet from pipe nozzle with vortex generators at nozzle exit. The half delta-wing vortex generators were applied into inner pipe with two arrangements of 2 vortex generators placed 180° apart and 4 vortex generators placed 90° apart. The heat transfer characteristics were investigated using Thermochromic liquid crystal sheet. For case of 2 vortex generators, the heat transfer pattern divides in two peaks in jet impingement region. For case of 4 vortex generators, the heat transfer patterns looks like cross mark symbol at small jet-to-plate distance.

1. Introduction

Jet impingement is wildly applied in thermal equipment and processes in industrial applications. It has been used for heating and drying in paper or textile industry and cooling combustor wall and gas turbine blade in gas turbine engine. Since the heat transfer rate is very high at the area where the jet directly impinges. It also provides rapid cooling or heating on local heat transfer area.

Various techniques have been employed to enhance the heat transfer rate on impingement surface by increasing turbulent intensity. Some examples are the modification of the jet orifice configuration [1], using mesh screens [2], and generate a swirling jet [3] or pulsating jet [4]. Delta tabs and delta-wing vortex generators have been wildly used in mixing enhancement in industrial applications. It was also used to increase turbulent intensity in jet flow [5]. However, there are a few researches that concerned adding delta tabs or vortex generators at the jet outlet to increase the heat transfer on impinged surface.

The aim of this research is to study the heat transfer characteristics on the jet impinged surface from pipe nozzle installed half delta-wing vortex generators. The heat transfer enhancement was also compared for case of different attack angles, arrangement of vortex generators and jet-to-plate distance based on constant jet Reynolds number at 29,500.

2. Experimental Apparatus and Method

In this study, the turbulent jet discharges from round pipe with inner diameter of D=28.15 mm, the nozzle wall was mounted at the jet outlet for confining the jet flow. The jet flow was discharged from the round pipe then impinged normal to impinged surface.

The geometry of vortex generator using in this study are shown in Fig. 1. The vortex generator is half delta-wing type with a right triangle. It is made of thin metal plate with thickness of 0.2 mm. The generator has sweep angle of 60o and height of h=0.1D. The attack angle of coming flow from pipe on vortex generator was varied at θ=45° and 60°. For vortex generators arrangement at pipe exit, two arrangements of 2 vortex generators placed 180° apart and 4 vortex generators placed 90° apart are selected for this study. The conventional pipe without tab was also studied to compare the effects of the jet with vortex generators on heat transfer characteristics. The jet mass flow rate was controlled to constant for all experiment. The jet-to-plate distance were varied at H=1D, 2D, 4D, 6D and 8D.

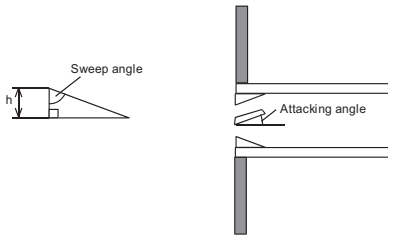

Fig. 1 Geometry of vortex generator

The heat transfer surface was made of stainless steel foil (SUS304) with 30-μm-thicknesses. The stainless steel foil was stretched between couples of copper bus bars. The heat transfer surface was heated by a DC power supply that can supply current up to 50 A through the copper bus bars.

For temperature measurement, Thermochromic Liquid Crystal (TLC) sheet was attached on the rear side of the jet impinged surface. The liquid crystal sheet used in this study changed the color systematically from black, red, yellow, green and blue between 29-36°C. The wall temperature on the impinged surface was measured from the color pattern appearing on the TLC sheet. The CCD camera was used to capture color on the TLC sheet. Images of the color pattern on the TLC were converted from the RGB system to the HSI system. The Hue (H) was used to produce correlation between the color of the TLC and the temperature.

The local Nusselt number was calculated from

$$Nu = \frac{(\dot{q}_{input} - \dot{q}_{losses})D}{(T_w - T_j)k} \quad (1)$$

where T_w is wall temperature, T_j is jet temperature, $\dot{q}_{input}$ is input heat flux from power supply, $\dot{q}_{losses}$ is heat losses from the rear side of TLC and k is thermal conductivity of air jet.

3. Results and Discussion

Figure 2 shows the Nusselt number distribution on impinged surface for revealing the effect of vortex generator orientations and jet-to-plate distance at same Reynolds number.

For conventional case (pipe nozzle without vortex generators), the heat transfer pattern is axis-symmetry for all jet-to-plate distance. The distribution of Nusselt number has a peak at stagnation point and then decreases gradually as going far from stagnation point. It also appears the secondary peak at about 1.5D-2D from the stagnation point for case of small jet-to-plate distance at H=1D, 2D and 4D.

For case of 2 vortex generators placed 180^{o} apart at pipe exit, the heat transfer patterns are not axis-symmetry and become more complex. At small jet-to-plate distance H=1D and 2D, the Nusselt number has peak at the stagnation point, and then decrease rapidly when compare with the conventional case. It appears local low Nusselt number in the wall jet region behind the location of vortex generators. This may due to the blocking effect of jet flow from vortex generators or vortex flow structure generated from vortex generators. For case of large jet-to-plate distance at H=4D, 6D and 8D, there are two peaks of Nusselt number near the stagnation point. This is due the bifurcation phenomena of jet flow from pipe with 2 vortex generators. It is found that the case of attacking angle θ=60^{o} shows more prominent of two peaks than case of attacking angle θ=45^{o}. The distance between these two peaks becomes larger when increasing jet-to-plate distance. However, the Nusselt number in wall jet region decreases rapidly when compare to the conventional case.

For case of 4 vortex generators placed 90^{o} apart at pipe exit, the heat transfer patterns are still complex. At small jet-to-plate distance H=1D, 2D and 4D, heat transfer pattern in the jet impingement region looks like cross mark symbol. This is due to the blocking effect of the vortex generators. The jet flow accelerates through the unblocked area at pipe exit and strongly impinges on the wall. There are 4 regions of local low Nusselt number around the jet impingement region. The heat transfer pattern in wall jet region looks like 45^{o} rotated square for case H=1D and 2D. There are 4 of secondary heat transfer peaks in wall jet region for case of attacking angle θ=60^{o} at H=1D only. At large jet-to-plate distance H=6D and 8D, the peak of Nusselt number at stagnation point become larger as increasing the jet-to-plate distance. The heat transfer patterns are similar with conventional case. However, the Nusselt number decreases rapidly as going far from stagnation point when compare with conventional case.

4. Conclusion

In the present study, the effect of vortex generators attachment on heat transfer characteristic was investigated. The main results show that:

1. The heat transfer on the impinged surface for case of impinging jet with vortex generators is higher than case of conventional impinging jet only for high jet-to-plate distance H=4D, 6D and 8D.

2. The heat transfer patterns are very complex for case of small jet-to-plate distance H=1D and 2D. They appear regions of low Nusselt number in wall jet region due to the effect of vortex generators.

3. For case of 2 vortex generators placed 180^{o} apart, the distribution of Nusselt number in jet impingement region divides in two peaks when jet-to-plate distance H is larger than 4D and the distance between these two peaks increases with increasing the jet-to-plate distance.

4. The heat transfer enhancement overall the impinged surface can be achieved only for case of 4 vortex generators with attacking angle θ=60^{o} at small jet-to-plate distance H=1D, 2D and 4D and for case of 2 vortex generators with attacking angle θ=45^{o} at H=2D and 8D.

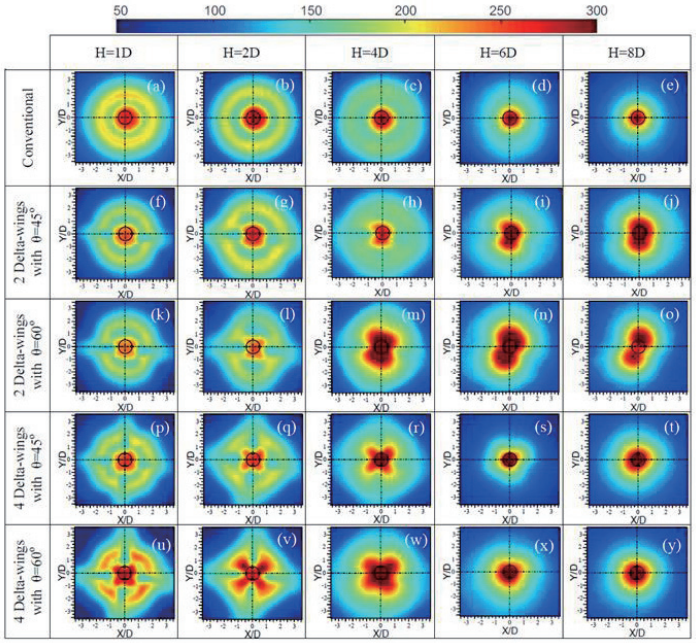

Fig. 2 Nusselt number distribution on impinged surface

Acknowledgements

The authors are grateful for the support of this research by Prince of Songkla University through grant No.ENG540633s.

References

[1] B. P. E. Dano, J.A. Liburdy and K. Kanokjaruvijit, Int. J. Heat and Mass Transfer, **42** (2005), 3919-3926.

[2] D.W. Zhou, S.J. Lee, Int. J. Heat and Mass Transfer, **47** (2004), 2097-2108.

[3] L. Huang, M.S. El-Genk, Int. J. Heat Mass Transfer, **41** (1998), 583–600.

[4] E. C. Mladin, D. A. Zumbrunnen, Int. J. Heat Mass Transfer, **46** (1997), 3305-3321.

[5] J. Mi, G. J. Nathan, Int. J. Heat and Mass Transfer, **42** (1999), 3919-3926.

Tenth International Conference on Flow Dynamics
November 25-27, 2013, Sendai, Miyagi, Japan

The Added Mass of Three-Dimensional Basic Bodies in Viscous Fluid

Tomoya Kitamoto[1], Hirochika Tanigawa[2], Hideki Shimohara[3] and Katsuya Hirata[1]
[1]Department of Mechanical Engineering, Doshisha University, Kyoto 610-0321, Japan
[2]Department of Mechanical Engineering, Maizuru National College of Technology, Kyoto 625-8511, Japan
[3]Doshisha International High School, Kyoto 610-0321, Japan
E-mail: khirata@mail.doshisha.ac.jp

ABSTRACT

In many fluid-structure interaction problems, the added mass is one of important interests. In the present study, we propose a simple and efficient method, to specify the added-mass coefficients of a three-dimensional body in fluid. In this method, we properly modify the three-dimensional full Navier-Stokes equations into linear equations the Brinkman equations. In order to confirm the method's effectivity and validity, we compute bodies with sharp edges such as a circular cylinder and a cube, comparing the computations to theories and experiments.

1. Introduction

In many fluid-structure interaction problems, we often needed to consider the fluid forces caused by arbitrary accelerated motions of fluid and/or structures. Such forces have been understood using the concept of the added mass, or the virtual mass. When acceleration is greater or fluid density is near the whole structure's density, the added mass is one of important and essential interests in various engineering aspects.

Then, due to the importance of the added mass, there have been many previous studies in concern, which are mainly related with two-dimensional flow. Among them, we have considered a simple method to specify the added mass coefficients of arbitrary two-dimensional solid bodies with non-simple cross sections [1], [2]. The solving method is based on a discrete singularity method (referred to as DSM), in which we employ a fundamental solution of the Brinkman equations as a singularity.

However, there have been few researches concerning a three-dimensional (3D) body, despite its importance in various industrial aspects. That is, analytical solutions for the added mass of a sphere in ideal fluid and in viscous fluid were shown by Lamb [3] and Stokes [4], respectively. Experimentally, Patton [5] showed the added masses of various bodies. And Inoue & Sato [6] showed the added masses of a sphere and various circular cylinders.

Therefore, we extended the DSM to 3D bodies [7]. Specifically, with respect to a sphere, we considered the numerical accuracy and property of the application of this method. Furthermore, we compared the DSM's result to theoretical solutions [3], [4] and experiments [6].

However, there are some unknown factors concerning numerical accuracy and stability in the applicability of the presented method to the 3D bodies with non-simple geometries with sharp edges. Then, we now consider two types of fundamental 3D bodies with sharp edges; namely, a circular cylinder and a cube. And, we try to reveal the applicability of the DSM to such bodies.

2. Model and governing parameters

Fig. 1 shows the present model. A 3D body sinusoidally oscillates in stationary and infinite fluid with incompressibility and viscosity. The x axis is parallel to the forced-oscillation direction. Then, the body displacement is given by $x = A\sin(\omega t)$, where t denotes time. Dimensionless governing parameters are kinetic Reynolds number $S \equiv \omega L^2/\nu$, where L and ν denote a characteristic length scale and the viscosity of fluid, respectively.

3. Numerical Procedure

We propose a numerical method of a 3D body based on the DSM. As a fundamental solution of DSM, we employ a solution of the Brinkman equations proposed by Tsai [8], as a singularity in our DSM.

In the DSM, singularities of M and control points of N (= M) are discretely distributed inside and surface of the body, respectively (Fig. 2). Then, we solve the Brinkman equations under the non-slip conditions at control points.

4. Results and Discussion

We apply the DSM to circular cylinder whose aspect ratio is 1.0, and a cube. And, we compare our computations with theories and experiments. The tested range of the kinetic Reynolds number S is 20–4000.

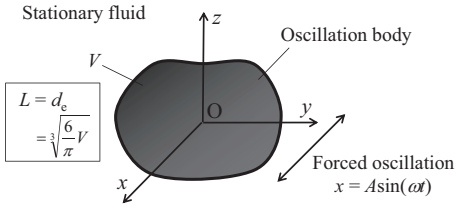

Fig. 1 Model: an oscillating 3D body in stationary fluid.

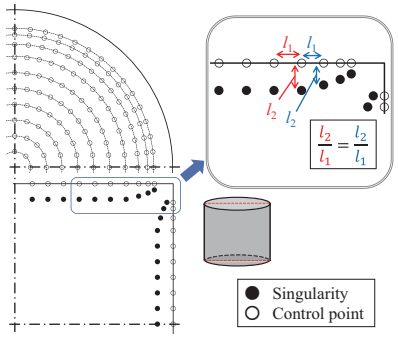

Fig. 2 An analytical model of DSM for a circular cylinder.

4.1 Circular cylinder

First, we see the results at S = 20. Fig. 3 shows Re(H_x) and –Im(H_x) as functions of l_2/l_1 at M = 2450. Re(H_x) and –Im(H_x) are the added mass coefficient and the damping coefficient, respectively. And, l_2 and l_1 are the distance between a singularity and the nearest control point and the distance between neighboring control points, respectively. We can confirm that Re(H_x) and –Im(H_x) converge from diverged values to 2.25 and 2.61, respectively. On the other hand, at l_2/l_1 > 2.5, computations tend to become unstable from the converged values. Then, we can obtain accurate results in a range of l_2/l_1 = 0.9–2.5.

Next, we discuss the influence of M. Fig. 4 shows a relative error e plotted against l_2/l_1 at M = 1470, 1960 and 2450. We define e by

$$e = \frac{\left||H_x| - |H_x|_{M=2450}\right|}{|H_x|_{M=2450}} \qquad (2)$$

where $|H_x|_{M=2450}$ denotes the converged value of $|H_x|$ at M = 2450. In Fig. 4, at l_2/l_1 = 1.0–1.5, we can confirm that e is less than 5 % being independent of M.

Fig. 5 summarises the results for the circular cylinder, where stable values of Re(H_x) and –Im(H_x) are plotted against S in a range of 20–4000. In the figure, experimental result [6] is also shown for comparison. In Fig. 5, we can confirm good agreement between the present computations and the experimental result. Moreover, Re(H_x) and –Im(H_x) of a sphere by DSM [7] are also shown for comparison. The circular cylinder is the same as a sphere from a qualitative view point. However, from a quantitative viewpoint, all the results of the circular cylinder are larger than those for a sphere, being independent of S.

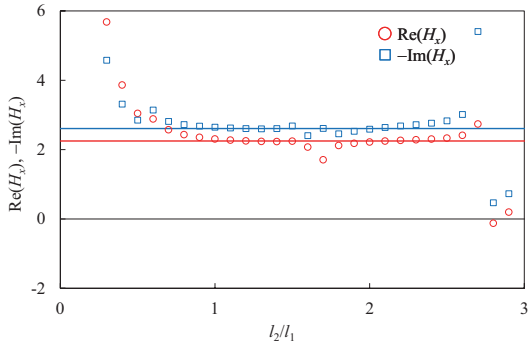

Fig. 3 H_x as a function of l_2/l_1 for a circular cylinder at S = 20 and M (= N) = 2450.

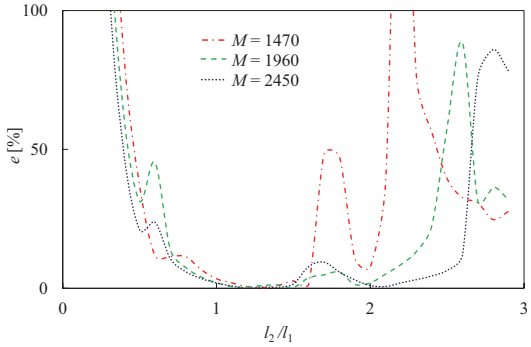

Fig. 4 Relative error e against l_2/l_1 for a circular cylinder at S = 20 and M (= N) = 1470–2450.

4.2 Cube

Fig. 6 summarises the results for a cube as with the circular cylinder. In the figure, the result of a sphere by DSM [7], the results of the circular cylinder (Fig. 5) and experimental result [5] are also shown for comparison. From a qualitative view point, the results of a cube are the same as a sphere and the circular cylinder. However, from a quantitative viewpoint, all the results of a cube are larger than those for a sphere, being independent of S. And, compared with the circular cylinder, Re(H_x) and –Im(H_x) are always the slightly larger values and almost the same values, respectively. Also, in the figure, we can estimate the experiment by Patton [5] is $S \approx 20$.

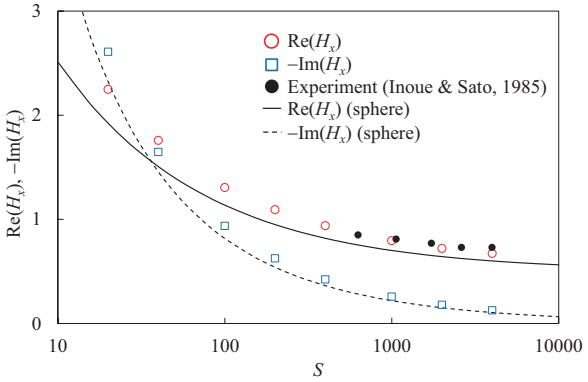

Fig. 5 H_x as a function of S for a circular cylinder.

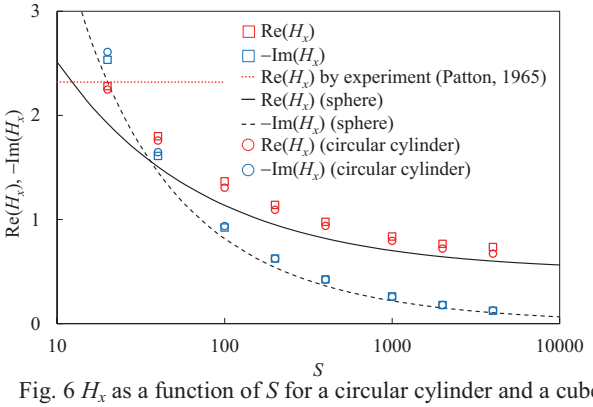

Fig. 6 H_x as a function of S for a circular cylinder and a cube.

References

[1] H. Shimohara and K. Hirata, *Transactions of JSME*, *Ser. B*, Vol. 66, No. 644 (2000), pp. 1061–1066 (in Japanese).

[2] H. Shimohara, S. Kikukawa, M. Yashima, T. Tsuji and K. Hirata, *Transactions of JSME*, *Ser. B*, Vol. 77, No. 782 (2011), pp. 1904–1919 (in Japanese).

[3] H. Lamb, *Hydrodynamics, 6th Ed.*, Dover Publications, New York (1932), p. 738.

[4] G. G. Stokes, *Cambridge Philosophical Transactions*, Vol. IX, pt. 2 (1851), pp. 8–106.

[5] Patton, K. T., *ASME Paper*, No. 65-WA/UNT-2, 1–7 (1965).

[6] S. Inoue and O. Sato, *Bulletin of Japanese Society of Scientific Fisheries*, Vol. 51, No. 12 (1985), pp. 1997–2006 (in Japanese).

[7] H. Shimohara, T. Tsuji, T. Kitamoto, H. Tanigawa and K. Hirata, *Transactions of JSME*, *Ser. C*, in press (in Japanese).

[8] Tsai, C. C., *Int. J. Numer. Method Fluid*, Vol. 56, 927–940 (2008).

Tenth International Conference on Flow Dynamics
November 25-27, 2013, Sendai, Miyagi, Japan

Effect of Near-wall Modeling on Aero-Thermal Characteristics of High Pressure Turbine Nozzle

[1]Jinuk Kim, [1]Jueong Gyu Bak, [2]Dong-Ho Rhee, [3]Leesang Cho, [1]Jinsoo Cho
[1]Department of Mechanical Engineering, Hanyang University, [2]Korea Aerospace Research Institute
[3]Dept. of Mechanical and System Engineering, Hansung University
M-111 Engineering Center, 222 Wangsimni-ro, Seongdong-gu, Seoul, Rep. of Korea
jscho@hanyang.ac.kr

ABSTRACT

In order to investigate the effect of near-wall treatment on aero-thermal characteristics of the high pressure turbine, the numerical simulation was performed using the k-ω based SST turbulence model with different near-wall treatment methods, that is, the wall-function method and the low Reynolds number method. The geometry and conditions for C3X vane were used for this study. The pressure distribution on the nozzle vane surface shows quite good agreements with the experimental results while the temperature distributions are over-estimated for both near-wall treatments.

1. Introduction

The reliable numerical simulation for the high pressure turbine is necessary to predict the flow characteristics at nearby the surface area. Recently the low Reynolds number method using the wall-integration approach is used because of the improvement for the computing power and numerical accuracy. [1, 2, 3] But, the low Reynolds number method is demanded more computational cost and more computational grids for $y^+ \leq 1$ compare with the wall-function method.

In general, the wall-integration method is more accurate than the wall-function method. [1, 4] Jiang et al. [5], however, presented that the wall-function method is more reliable in an uncertain boundary conditions.

The purpose of this study is the investigation for the aero-thermal characteristics of the high pressure turbine with different wall treatment methods, which are the wall-function method and the low Reynolds number method using the wall-integration approach.

2. Numerical Simulation

The simulation was performed using the steady, viscous, three-dimensional RANS code, ANSYS CFX.

The k-ω based Shear Stress Transport (SST) turbulence model, which is developed by Menter [6] was applied in this study. This turbulence model was designed to give very accurate calculations of the onset and amount of flow separation under adverse pressure gradients by the inclusion of transport effects into the formulation of the eddy-viscosity. [7] The k-ω turbulence model was applied in the sublayer of the wall boundary layer and in the wake region of the boundary layer in this study.

In order to compare with the wall-function approach and the wall-integration approach, two grid types were generated. For the wall-function approach with k-ω based SST turbulence model, grids were generated coarse. The wall-function in the CFX solver is automatically turned on for $y^+ \geq 2$. For $2 < y^+ < 30$, a specific blend function is used. And, the log law is applied for $20 < y^+ < 300$. For wall-integration approach, grids were generated fine compare with the wall-function approach. The wall-integration method of the k-ω based SST turbulence model was applied at $y^+ \leq 2$. [8]

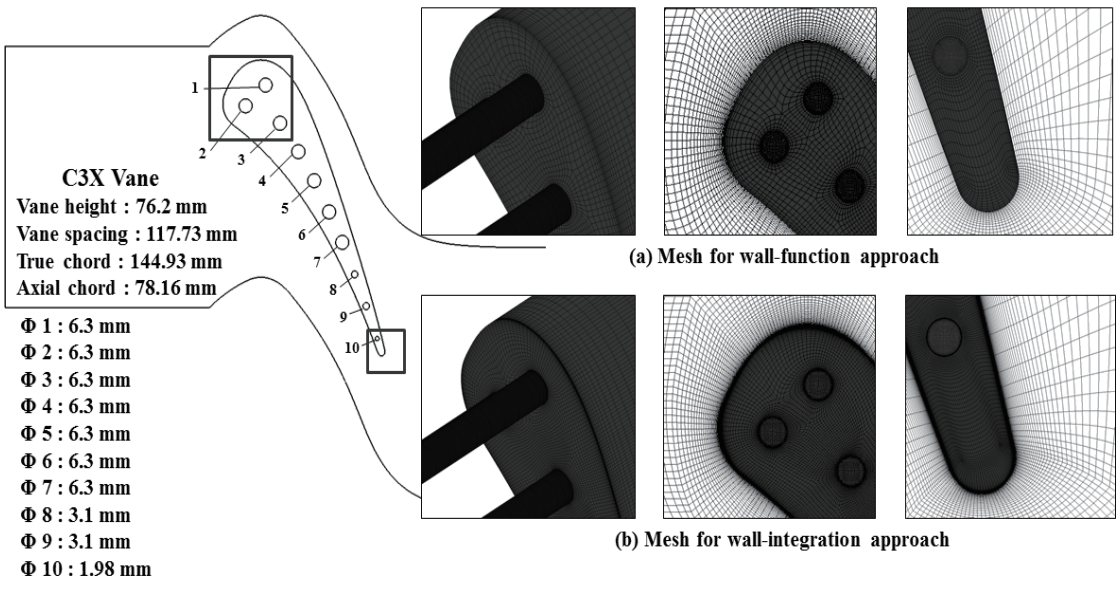

Fig. 1 C3X vane cascade geometry and computational mesh

The C3X vane, which was used in this study, consists of 1 vane and 10 circular channels. This vane designed by Allison Engine Co. has a constant cross-sectional area and without twist. Computational grids consist of 4.5 million cells for wall-function and 8.6 million cells for wall-integration. Fig. 1 shows a view of cascade geometry and computational meshes.

3. Results and Discussion

The static pressure and temperature distributions are measured at the 50% of vane span. Fig. 2 shows that the static pressure distributions using the wall-function method and the low Reynolds number method coincide with experimental results by Hylton et al. [9]. However the trailing edge region of the suction side does not fit with experimental results because this region has very strong unsteadiness.

Figure 3 shows that the temperature distributions on the vane surface. CFD results, which are analyzed by the wall-function method and the low Reynolds number method, are higher than experimental results. However the temperature tendency, which is predicted by the wall-function method, is less correspond with the experimental results than that of the low Reynolds number method because the wall-function method is assumed that the entire boundary layer is the fully turbulent.

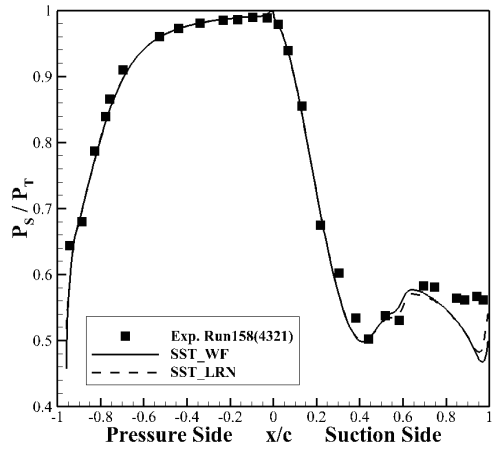

Fig. 2 Static Pressure distributions on the vane surface

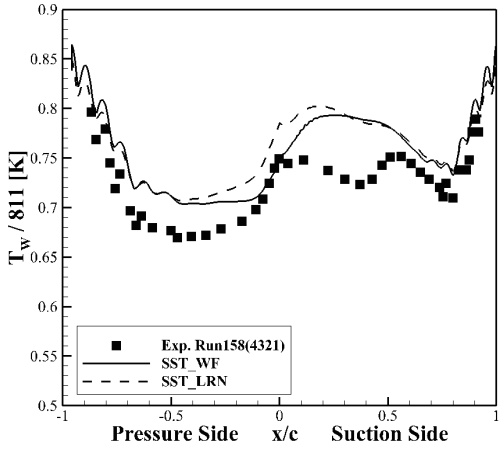

Fig. 3 Static temperature distributions on the vane surface

4. Conclusions

In order to figure out the difference between the wall-function method and the low Reynolds number method, the numerical simulation for the high pressure turbine (C3X vane) was performed.

Static pressure distributions, which are predicted by the wall-function method and the low Reynolds number method, are good matched compare with experimental results. Temperature distributions at the vane surface are analyzed higher compare with experimental results. Temperature tendency, which are predicted by the wall-function method, differ from experimental results. The magnitude of temperature distributions, which are analyzed by the wall function method, are more close to the results of the experiment compare with the low Reynolds number method.

5. Acknowledgements

This study is gratefully supported by the Korea Government, Ministry of Trade, Industry and Energy (KA000157).

References

[1] G.A. Ledezma, G.M. Laskowski and A.K. Toplpa, 2008, “Turbulence Model Assessment for Conjugate Heat Transfer in a High Pressure Turbine Vane Model”, ASME Paper GT2008-50498.

[2] William D. York and James H. Leylek, 2003, “Three-dimensional Conjugate Heat Transfer Simulation of an Internally-cooled Gas Turbine Vane”, ASME Paper GT2003-38551.

[3] Facchini, B. Magi and Greco A.S., 2004, “Conjugate Heat Transfer of a Radially Cooled Gas Turbine Vane”, ASME Paper GT2004-54213

[4] Jiang Luo, Eli H. Razinsky and Hee-Koo Moon, 2013, “Three-Dimensional RANS Prediction of Gas-Side Heat Transfer Coefficients on Turbine Blade and Endwall”, Journal of Turbomachinery, Vol. 135, No. 2, 021005.

[5] Jiang Luo, Eli H. Razinsky and Hee-Koo Moon, 2013, “Three-Dimensional RANS Prediction of Gas-Side Heat Transfer Coefficients on Turbine Blade and Endwall”, Journal of Turbomachinery, Vol. 135, No. 2, 021005.

[6] Menter, F. R., “Two-equation eddy viscosity turbulence models for engineering applications,” AIAA Journal, Vol. 32, No. 8, pp. 1598~1605.

[7] Bardina, J.E., Huang, P.G. and Coakley, T.J.,“Turbulence Modeling Validation Testing and Development”, 1997, NASA Technical Memorandum 110446.

[8] J.T. Tomita, L.M. Silva and D.T. Silva, 2012, “Comparison between Unstructure and Structure Meshes with Different Turbulence Models for a High Pressure Turbine Application”, ASME Paper GT2012-69990

[9] L.D. Hylton, M.S. Mihelc, E.R. Turner, D.A. Nealy and R.E. York, 1983, “Analytical and Experimental Evaluation of the Heat Transfer Distribution Over the Surface of Turbine Vanes”, NACA-CR-168015

Tenth International Conference on Flow Dynamics
November 25-27, 2013, Sendai, Miyagi, Japan

Reactive Viscous Fingering Involving Production of Gel

Kenichi HOSHINO, Yuichiro NAGATSU
Tokyo University of Agriculture and Technology
2-24-16 Nakacho, Koganei, Tokyo, 184-8588, Japan
E-mail: 50013642314@st.tuat.ac.jp

ABSTRACT

We have experimentally investigated viscous fingering with chemical reaction producing gel. Here, two systems were employed. In one system, sodium polyacrylate (SPA) solution and aluminum ion (Al^{3+}) solution were used as the more and less viscous liquids, respectively. In another system, SPA solution and ferric ion (Fe^{3+}) solution were used as the more and less viscous liquids, respectively. In the case of Al^{3+}, displacement efficiency was smaller than that in the non-reactive case, whereas in the case of Fe^{3+}, the displacement efficiency was larger.

1. Introduction

When a more-viscous fluid is displaced by a less-viscous one in porous media and in Hele-Shaw cells, the interface or boundary of the two fluids becomes unstable and forms a finger-like pattern. This phenomenon is referred to as viscous fingering (VF). VF accompanied by chemical reactions is observed in processes such as petroleum recovery, chromatographic and adsorptive separation, polymerization, and the flow of gastric mucus and reactive VF is confirmed as playing an important role to these processes. Therefore, the coupling between hydrodynamics and chemistry in reactive VF has been studied. Here, we have conducted experiments on reactive VF with production of gel. In the present study, we also have tried to make rheological measurements of gel produced by chemical reaction at the liquid-liquid miscible interface. Furthermore, we have investigated the relationship between VF experiments and the rheological measurements.

2. Experiment

We used a more-viscous sodium polyacrylate (SPA, molecular weight $2.2 \times 10^6 \sim 6.0 \times 10^6$) solution and less-viscous aluminum ion (Al^{3+}) and ferric ion (Fe^{3+}) solutions. We used a radial Hele-Shaw cell (Fig. 1) for VF experiments. The concentration of metal ions, C, was varied, while the injection rate, q, the gap of the cell, b, and the concentration of SPA in the more viscous liquid were fixed. The more viscous liquid was dyed blue for visualization of VF.

We used a rheometer (AR-G2 TA instruments) with an interfacial rheology measurement equipment (Double Wall Ring type sensor) (Fig. 2) to measure rheological properties of gel formed by reaction at the liquid-liquid miscible interface.

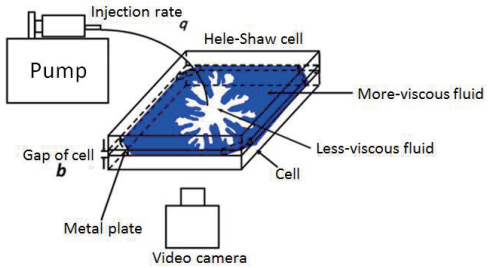

Fig. 1 VF experimental apparatus

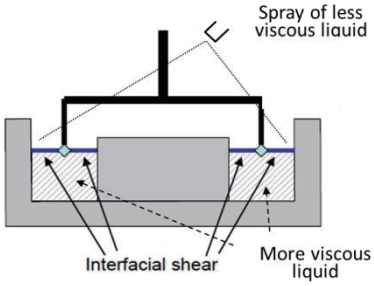

Fig. 2 Schematics of cross section of Double Wall Ring type sensor

3. Results and Discussion

Fig. 3 shows gel produced by SPA and these metal ion solution in a beaker. We show the results of VF experiments in Fig.4. Here, $C = 0.1$ M, $b = 0.5$ mm and $q = 8.21 \times 10^{-9}$ m^3/s. In Fig.4, VF patterns at t_b are shown. Here, t_b is the time until which the longest finger is reached the edge of the measuremt region. In Fig.4, t_b is described at the below to the right.

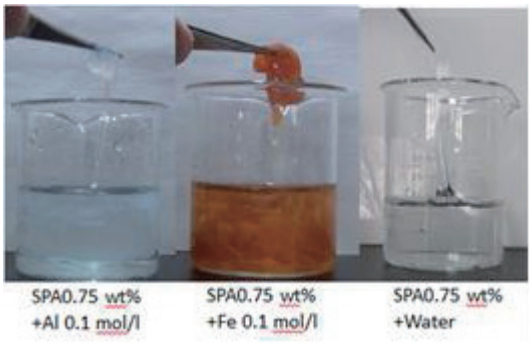

Fig. 3 Gel's photograph

In the case of Al^{3+}, it is shown that the less-viscous fluid's color is light. It means that less-viscosity fluid is not completely displaced in depth direction. Thus, t_b and displacement efficiency get smaller. On the other hand, in the case of Fe^{3+}, the displaced area near the inlet is larger than that in the nonreactive case. Therefore, t_b and the displacement efficiency is larger than those in the nonreactive case. These results suggest that influence of the gels on VF pattern and the displacement efficiency is opposite although the gels are produced in both the Al^{3+}

and Fe^{3+} cases. We consider that the difference is caused by viscoelastic property of the gels. Thus, we measured rheology property of the gel produced at liquid-liquid miscible interface.

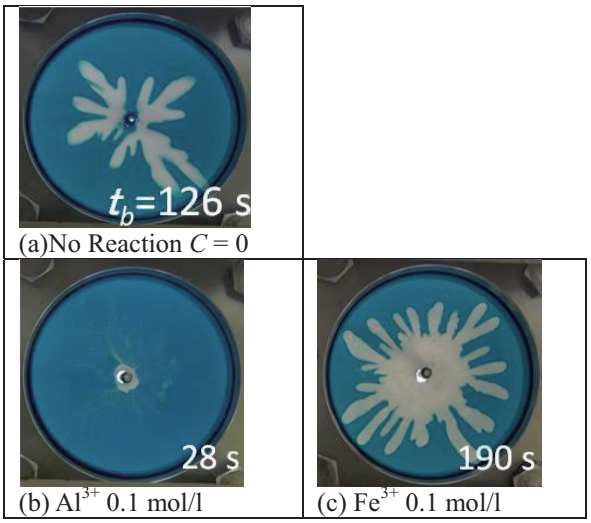

(a)No Reaction $C = 0$

(b) Al^{3+} 0.1 mol/l (c) Fe^{3+} 0.1 mol/l

Fig. 4 Result of VF experiment

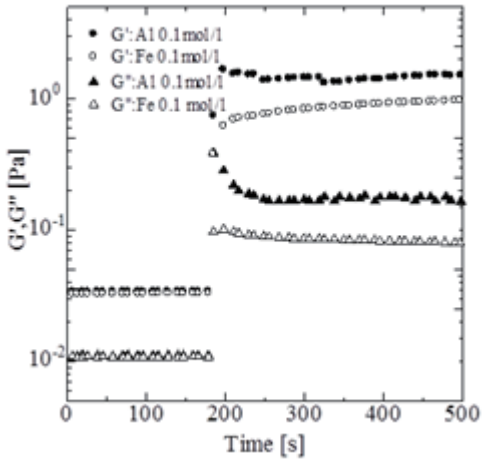

Fig. 5 Result of rheological measurement

Fig. 5 shows the viscoelasticitic measurement results in this experimental condition. Measurement parameter are G', storage modulus (elastic response), G", loss modulus (viscous response). Reaction is started at t = 180 s. We find there is the difference in behavior of G' and G" in the cases of Al^{3+} and Fe^{3+} just after the production of the gels. In the case of Al^{3+}, G" gradually decreased. On the other hand, in the case of Fe^{3+}, G' gradually increased. We consider these differences are responsible for the difference in the influence of the gel on VF pattern.

We consider the physical models on the effects of the gel on VF flow field based on the results of the rheological measurements. There is no difference until the reaction takes place at the miscible interface and the gel is produced. In Al case, after the production of gel, the viscosity is decreased. Thus, Al^{3+} solution can not completely displace SPA in depth direction and flows under the gel (Fig. 6). In Fe^{3+} case, the elasticity was increased. Thus, gel can completely displace SPA solution in depth direction (Fig. 7). Also, on examination of lateral direction, thicker fingers are made to shorten the perimeter of the pattern because of the existence of the viscoelastic gel at the interface (Fig. 8).

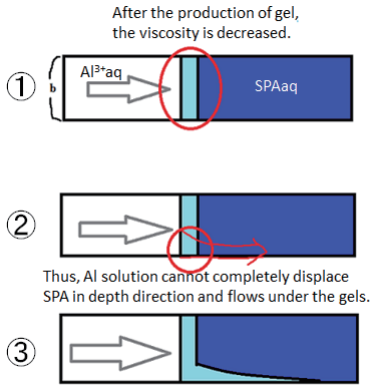

Fig. 6 Physical model (Al^{3+})

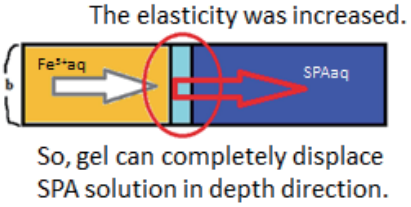

So, gel can completely displace
SPA solution in depth direction.

Fig. 7 Physical model (Fe^{3+})

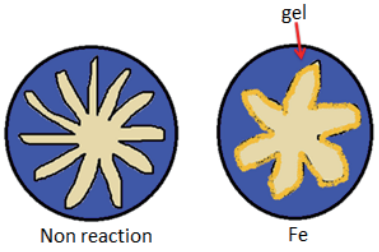

On examination of lateral direction, thicker fingers are made to shorten the perimeter of pattern because of existence of viscoelastic gel at the interface.

Fig. 8 Physical model (Fe^{3+}, lateral)

4. Conclusion

We performed experiments on VF involving production of gel by using two kinds of less viscous liquid. In a particular experiment condition, displacement efficiency is decreased for Al^{3+} case while increased for Fe^{3+} case by production of gel. We performed viscoelastic measurement of the gel produced at the liquid-liquid interface. After formation of gel, viscosity is decreased in case of Al^{3+} while elasticity increased in case of Fe^{3+}. We proposed the physical model that explains difference in the effects of gels on VF pattern based on the viscoelastic measurement.

Reference

[1]Y. Nagatsu et al., J.Fluid Mech, vol. 571, 475 (2007)

Estimation of Stagnant Gas Temperature of Cold Spray using Outer Surface Metal Temperature of the Nozzle Throat

Hiromitsu Morita, Hiroshi Katanoda
1-21-40 Korimoto, Kagoshima, 890-0065 Japan
K1958090@kadai.jp

ABSTRACT

In cold spray, two of the most important spray parameters affecting the mechanical properties of the coatings, are the temperature, and the pressure of the gas, in the stagnation chamber. This paper investigates the possibility of estimating the stagnant gas temperature by measuring the nozzle throat surface metal temperature, and numerically solving the equation of heat transfer of the cold spray gun, along with the boundary conditions of the forced and free convection heat transfer on the inner and outer walls of the gun.

1. Introduction

Cold spray (CS) is a technique to coating a wide variety of mechanical parts by spraying solid particle accelerated through a high-speed gas flow in a converging-diverging nozzle. In CS, two of the most important spray parameters affecting the mechanical properties of the coatings, are the temperature, and the pressure of the gas, in the stagnation chamber (SC). The gas pressure in the SC using a properly calibrated pressure sensor, is easy to measure precisely. However, it is not simple to accurately measure the gas temperature in the SC. In traditional studies, the "gas temperature" as an experimental condition, is the temperature measured at the electric heater exit. However, the gas temperature will decrease after exiting the electric heater, due to convection from the gas to the inner wall of the SC. Although adding a thermocouple to the SC may solve this problem, it causes another problem, that of spray particle hitting and sticking onto the thermocouple. One of the realistic solutions is measuring metal temperature of the outer surface of the gun.

This paper investigates the possibility of estimating the stagnant gas temperature by measuring the nozzle throat surface metal temperature, and numerically solving the equation of heat transfer of the CS gun, along with the boundary conditions of the forced and free convection heat transfer on the inner and outer walls of the gun.

2. Experimental Method

The experimental setup consists of a CS nozzle and SC. The working gas used in this study is compressed dry air. The pressurized dry air stored in an air-tank. The compressed air was supplied to an electric heater. The air was heated a preset temperature ($T_{pre.}$=100, 200, 300, 400℃). The heated air flows into the SC, then the air in the SC accelerates to supersonic speed through the CS nozzle. Then the air was discharged into the atmosphere through a nozzle. A pressure sensor measured the stagnation pressure. A K-type sheathed thermocouple (ϕ0.5) inserted into the SC, measured the total temperature at the SC exit. The surface metal temperature of the nozzle throat was measured using a K-type thermocouple attached to the nozzle surface.

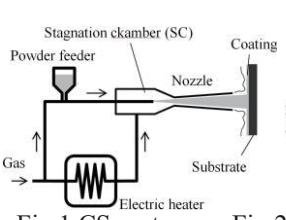

Fig.1 CS system

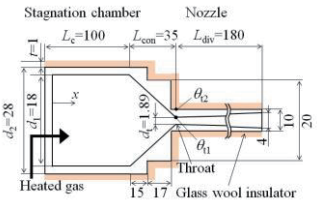

Fig.2 Analytical model of CS gun

3. Numerical method

The schematic diagram of the CS gun analyzed in this study is shown in Fig.2. The gas temperature decreases due to heat transfer from the gas to the inner wall of the CS gun. The major assumptions used in this calculation are; 1) The gas flow is non-frictional and quasi-one-dimensional in the axial direction, 2) The gas follows the perfect gas, 3) Heat transfer is steady and conducted in the radial direction. Based on these assumptions, the gas/metal temperature is calculated as explained in the CS gun, with glass wool insulator. The amount of heat dQ_1 transferred per unit time from the gas moving a small distance between x and $x+dx$ to the inner surface of the gun can be written as;

$$dQ_1 = h_1(T_{aw} - \theta_1)\pi d_1 dx \tag{1}$$

where h_1, T_{aw}, and θ_1 are, the heat transfer coefficient of forced convection, the adiabatic wall temperature and the inner surface temperature, respectively. The adiabatic wall temperature of turbulent flow is calculated as;

$$\frac{T_{aw}}{T} = 1 + r\frac{\gamma - 1}{2}M^2 \tag{2}$$

$$r = P_r^{1/3} = \left(\frac{c_p \mu_g}{k_g}\right)^{1/3} \tag{3}$$

where P_r, c_p, μ_g and k_g are The Prandtl number of the gas flowing in the gun, the specific heat at a constant pressure, the viscous coefficient and thermal conductivity, respectively. The h_1 in Eq.(1) is calculated using the following equations under the assumption of turbulent flow.

$$Nu_1 = \frac{d_1 h_1}{k_g} = 0.023 R_{ed}^{0.8} P_r^{0.4} \tag{4}$$

$$R_{ed} = \frac{\rho_g u_g d_1}{\mu_g} \tag{5}$$

where Nu_1 ,R_{ed}, ρ_g, u_g are The Nusselt number of

forced convection, The Reynolds number, the gas density and gas velocity, respectively. When the compressibility of the gas flow cannot be ignored, the thermodynamic properties such as c_p, μ_g, and k_g, must be evaluated at the following reference temperature, in order to account for the effect of the temperature gradient caused in the boundary layer.

$$\hat{T} = T + 0.5(\theta_1 - T) + 0.22(T_{aw} - T) \tag{6}$$

Developing Eq.(1), the inner surface temperature is

$$\theta_1 = T_{aw} - \frac{dQ_1}{\pi d_1 dx h_1} \tag{7}$$

From the analyzed solution of the cylindrical coordinate heat conduction equation, the outer-surface metal temperature θ_2 is expressed as follows with the radial conductive heat flow rates in metal dQ_{12} and in thermal insulator dQ$_{23}$;

$$\theta_2 = \theta_1 - \frac{dQ_{12}}{2\pi k_{12} dx} \ln \frac{d_2}{d_1} \tag{8}$$

$$\theta_3 = \theta_2 - \frac{dQ_{23}}{2\pi k_{23} dx} \ln \frac{d_3}{d_2} \tag{9}$$

where d_2, d_3, k_{12} and k_{23} are outer diameter of SC, outer diameter of thermal insulator, thermal conductivity of SC material (SUS;16.3W/(m・K)) and thermal conductivity of insulator (0.05W/(m・K)), respectively.

The heat flow rate dQ_3, from the outer surface of the thermal insulator into the atmosphere by free convection and heat radiation is expressed as;

$$dQ_3 = h_3(\theta_3 - T_a)\pi d_3 dx + \sigma\varepsilon_3(\theta_3^4 - T_a^4)\pi d_3 dx \tag{10}$$

where h_3, T_a, σ and ε_3 are the heat transfer coefficient of free convection, atmospheric temperature, The Stefan-Boltsmann constant, and the thermal insulator surface emissivity, respectively. In this calculation, the parameters included in Eq.(10) were set at T_a=300K, ε_3=0.10 and ε_a =0.90. The h_3 for the horizontally placed cylinder (CS gun) is calculated by the following equations under the assumption of laminar flow.

$$Nu_3 = \frac{d_3 h_3}{k_{a,f}} = 0.53(G_r P_r)^{1/4} \tag{11}$$

$$G_r = \frac{g\beta_f |T_a - \theta_3| d_3^3}{(\mu_{a,f}/\rho_{a,f})^2} \tag{12}$$

$$\beta_f = 1/T_f \tag{13}$$

$$T_f = T_a + \theta_3/2 \tag{14}$$

where G_r, g and β are The Grashof number, acceleration of gravity and the volumetric thermal expansion coefficient, respectively. In Eq.(12), $\mu_{a,f}$ and $\rho_{a,f}$ are the viscosity and density of air at film temperature T_f. When considering the steady heat flow,

$$dQ_1 = dQ_{12} = dQ_{23} = dQ_3 \tag{15}$$

All the unknown variables, including dQ_1 can be calculated by solving Eqs.(1) – (15). Then, the total temperature T_0 at an axial location x+dx, can be calculated using an energy conservation law as;

$$T_0(x + dx) = T_0(x) - \frac{dQ_1}{c_p \dot{m}} \tag{16}$$

where $\dot{m}$ is the mass flow rate of process gas.

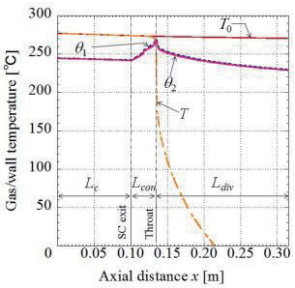

Fig.3 Gas/wall temperature distributions for $T_{pre.}$=300℃

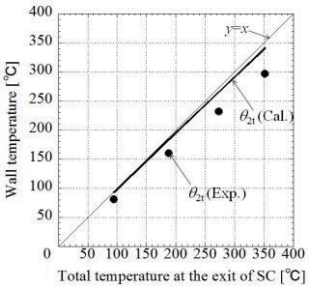

Fig.4 Experimental and calculated result of θ_{2t}

4. Results and Discussion

The axial distribution of total temperature, static temperature T, and inner and outer wall temperature at $T_{pre.}$=300℃ and p_0=1.21MPa are shown in Fig.3. The x-axis is the axial distance measured from the upstream end of SC to the nozzle exit. The total temperature decreases due to heat loss from 277℃ to 269℃ almost linearly from x=0 to 0.315m. The static temperature is almost identical to the total temperature from x=0 to 0.125m, it decreases rapidly when passing the throat. The inner surface temperature θ_1 is 241℃ at x=0, and decreases until the downstream end at SC of x=0.10m. However, it increases at x=0.10m towards the throat, with a maximum value of 257℃ at the throat x=0.135m, it then decrease in the downstream direction. The outer nozzle surface temperature θ_2 is around 1℃ lower than θ_1 in the range of 0.135<x<0.315m.

The experimental and calculated results of the outer surface metal temperature of the nozzle throat θ_{2t} are shown in Fig.4 against the total exit of SC temperature T_{0c}. The thick line is the calculated wall temperature, the solid circle represents the experimental result, and the thin line shows "y=x". Considering the imperfect thermal insulation in the experiment and measurement uncertainty of temperature, the calculated result θ_{2t} (Cal.) reasonably agree with the T_{0c} for the range from T_{0c}=95 to 352℃. However, the temperature difference between θ_{2t} (Cal.) and θ_{2t} (Exp.) increases as T_{0c} increases. The relationship between θ_{2t} (Exp.) and T_{0c} shows the same tendency of θ_{2t} (Cal.) and θ_{2t} (Exp.). The maximum deviation of θ_{2t} (Exp.) from T_{0c} is −55℃ for this calculation.

4. Concluding remarks

The possibility of estimating stagnant gas temperature by measuring the nozzle throat surface metal temperature was studied by numerically solving the equation of heat transfer and the experiment. The result shows that the outer surface metal temperature at throat is closer to the total gas temperature at throat.

References

[1] K. Nishikawa and Y. Fujita, *Dennetsugaku*, Rikogakusya, (1981).
[2] I. Kimura, *Rocket Kougaku*, Yokendo, (1993)

Tenth International Conference on Flow Dynamics
November 25-27, 2013, Sendai, Miyagi, Japan

Aerodynamic Analysis of Blended Wing Body Business Jet

Hyunmin Choi[1], Seawook Lee[1], Jinsoo Cho[2]
[1] Department of Mechanical Engineering, Hanyang University, Seoul, Korea
[2] School of Mechanical Engineering, Hanyang University, Seoul, Korea
jscho@hanyang.ac.kr

ABSTRACT

Aerodynamic analysis of the BWB business jet is performed to analyze the flow field around the aircraft at high subsonic flight speed. Because of the cabin height, center body section is designed relatively thicker than general transonic airfoils. REA 5212 airfoil is selected for wing section. ANSYS Fluent is used for aerodynamic analysis of the BWB business jet. Because of the center body section produces less lift than wing section, strength of local shock on the center body is weaker than wing section. The weaker shock on the center body has advantage of locating the engine intake.

1. Introduction

The global air traffic is growing explosively. And convenient to adjust the flight schedule, demand on the business jet is getting large and the business jet market is growing fast.

The Blended-Wing-Body (BWB) configuration has many advantages for aerodynamic performance. Smaller wetted area reduces surface drag and additional lift of center body increases total lift. High lift to drag ratio is benefit for high fuel efficiency and low emission. And large scale BWB aircrafts have been studied by Boeing and many researchers[1-6].

Harijono and Alvin[7] are carry out conceptual study on the BWB business jet. By applying the BWB configuration to the business jet, not only the small business jet takes advantages of the BWB configuration, but also the advantage of wide cabin space from wide center body is provided. But aerodynamic analysis at high subsonic speed for design the high subsonic BWB business jet is not presented yet.

In this paper, modeling of BWB business jet and the aerodynamic analysis of the BWB business jet are performed to analyze the flow field around the BWB business jet at high subsonic speed.

2. Method

The BWB business jet is modeled with multi-section surfaces. Spline curve is used for smooth leading and trailing edge. For the center body section, arbitrary airfoil section is designed by considering the cabin space and shock strength. For enough cabin height, thickness of 2.5m is selected. And the chord length of 18m are selected for reducing thickness ratio of center body section. REA 5212 transonic airfoil is selected for the wing section. The important design variables are shown in fig. 1. Total span, width of center body, span of wing, the chord length, sweep back angles and incidence angles of each airfoil section are selected as geometric parameter and design variables.

For the aerodynamic analysis, commercial CFD tool, ANSYS Fluent is used and half sphere of computational domain is generated. The radius of computational domain is 20 times of MAC. Computational mash is shown in fig. 2. 8 layers of prism mesh on the aircraft surface and over 2 million tetra mesh are generated. SST k-e turbulent model and pressure far field boundary condition are applied. Free stream Mach number of 0.85 and standard atmosphere condition at altitude of 11km are applied to the boundary condition.

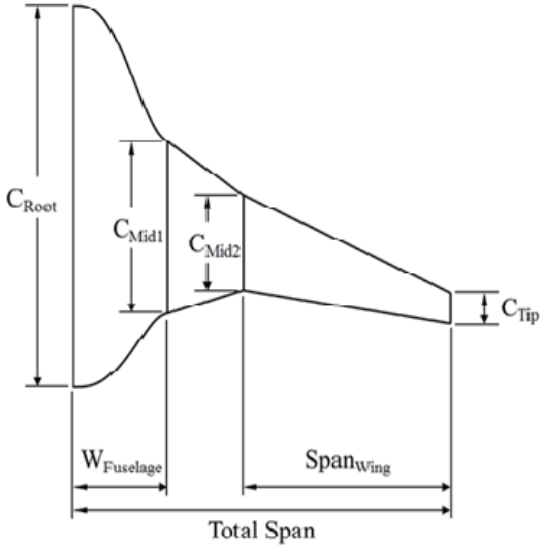

Fig. 1 Design Variables of BWB Business Jet

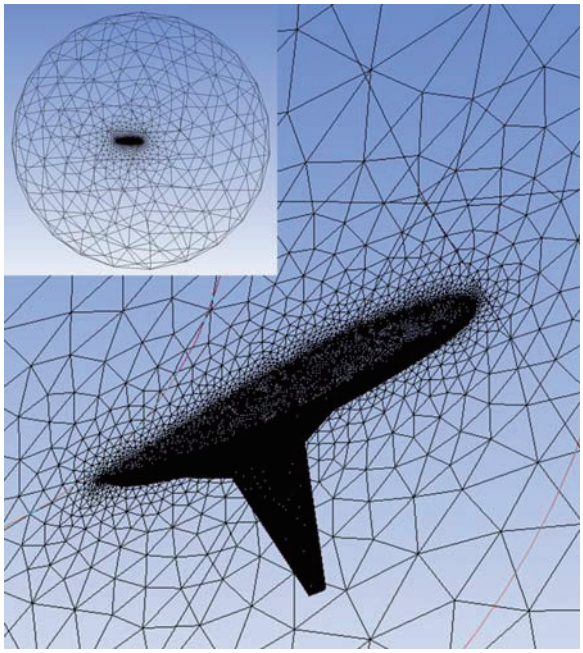

Fig. 2 Computational Mesh on BWB Business Jet

3. Results and Discussion

The contours of pressure coefficient on the BWB business jet is presented at fig. 3. Most of lift is generated by wing section. But the center body section also produces small lift. At the atfbody of center body section produces negative lift to provide positive pitching moment for pitch stability.

The contours of Mach number around the BWB business jet is presented at fig. 4. Weak local shock is generated at center body section and stronger of shock is generated on wing section.

Because of the center body section produces less lift than wing section, strength of local shock on the center body is weaker than wing section. The weaker shock on the center body has advantage of locating the engine intake.

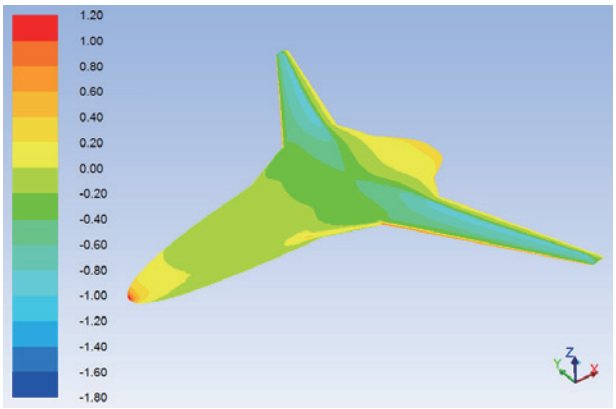

Fig. 3 Contours of Pressure Coefficient on BWB Business Jet

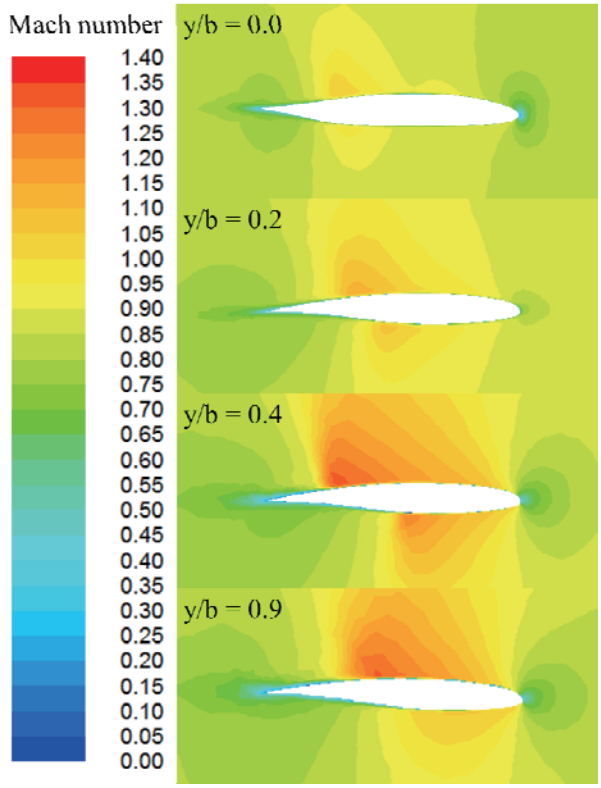

Fig. 4 Contours of Mach number on Sections of BWB Business Jet

4. Concluding remarks

In this paper, the aerodynamic analysis of high subsonic BWB business jet is performed. The analyzed shock characteristics are expected to useful for aerodynamic design of high subsonic BWB business jet.

References

[1] Potsdam, M. A. "Blended wing body analysis and design," AIAA Applied Aerodynamics Conference, 15th. 805 ed., AIAA, Atlanta, GA, 1997, pp 7.

[2] Osterheld, C. M., W. Heinze, and P. Horst. "Preliminary design of a blended wing body configuration using the design tool PrADO." *DGLR BERICHT* Vol. 5, 2001, pp 119-128.

[3] Qin, N., Vavalle, A., Le Moigne, A., Laban, M., Hackett, K., and Weinerfelt, P. "Aerodynamic considerations of blended wing body aircraft," Progress in Aerospace Sciences Vol. 40, No. 6, 2004, pp. 321-343.

[4] Liebeck, Robert H. "Design of the blended wing body subsonic transport." *Journal of Aircraft* Vol. 41, No. 1, 2004, pp10-25.

[5] Hileman, J. I., Spakovszky, Z. S., and Drela, M., "Airframe Design for Silent Aircraft", 45th AIAA Aerospace Science Meeting and Exhibit, 8-11 January 2007, Reno, Nevada.

[6] Felder J., Hyun D. Kim, Brown G., "Turboelectric Distributed Propulsion Engine Cycle Analysis for Hybrid Wing Body Aircraft", 47th AIAA Aerospace Science Meeting, AIAA-2009-1132, 2009.

[7] Harijono Djojodihardjo, and Alvin Kek Leong Wei. "CONCEPTUAL DESIGN AND AERODYNAMIC STUDY OF BLENDED WING BODY BUSINESS JET." ICAS 2012.

Numerical Study of the Vehicle Aerodynamic Performance During Acceleration and Deceleration

Chao Man, Chenguang Lai, and Kaiping Wen
College of Vehicle Engineering, Chongqing University of Technology, Chongqing, China;
E-mail: chenguanglai@cqut.edu.cn

ABSTRACT

In this numerical study, the complex driving conditions of acceleration, constant and then deceleration are reappeared through the User-Defined Function (UDF). The change histories of aerodynamic drag and lift as well as the flow field around the vehicle were obtained after the transient numerical simulation. The result shows that, different from the lift, the drag changes heavily during driving condition changes; while the fluctuation ranges of lift, which are caused by the unsymmetrical rear airflow distribution, are bigger than that of the drag at other times, especially in the process of constant speed motion after acceleration.

1. Introduction

Vehicles would always accelerate or decelerate in the real driving condition, especially on the city road. At present, the study of vehicle aerodynamic performance is mainly under the airfield at constant speed. But for complex driving conditions, boundary condition of speed could not be set directly in the software. And it is difficult to control the acceleration during wind-tunnel test or on-road test. Currently, the research of vehicle aerodynamic performance about acceleration and deceleration could hardly be found. In this paper, the complex driving conditions from acceleration to constant and then to deceleration are reappeared through UDF, and the transient aerodynamic performance is studied.

This study provides a new method for the research of the aerodynamic performance in complex driving conditions. And also supplies important references for the safety control of vehicle.

2. Model and computational domain

The ratio of the model is 1:1 with the passenger vehicle. Simple sizes: length a = 4.1 m, width b = 1.6 m, height c = 1.5 m. The shape is similar to Mira Model except the separated wheels. Computational domain in this case is cuboid. And the sizes are shown in Fig.1. In the computational domain, the relation of the velocity of the wind $v(m/s)$ and the time $t(s)$ is as follows:

$$v=\begin{cases}3*t & (0<t\le 8)\\ 24 & (8<t\le 11)\\ 24-6*(t-11) & (11<t\le 15)\end{cases}$$

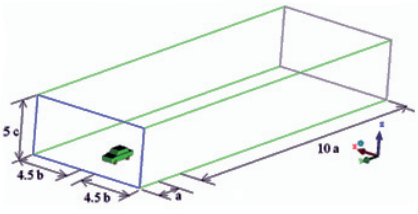

Fig. 1 Computational domain

3. Computing result

As shown in Fig. 2, the drag increases along the time by quadratic because of the increased velocity in the first 8 s. With the driving condition translates from acceleration to constant at 8th second, the drag curve sharply drops and rises. The gradient is as high as -1665 N/s. The basically balanced drag 200 N at the constant speed is smaller than the drag at the end of acceleration of 217 N. While t = 11 s, the driving condition changes from constant to deceleration, the gradient reaches -3330 N/s. This would deteriorate the travelling comfort. During the deceleration process, the drag decreases by quadratic.

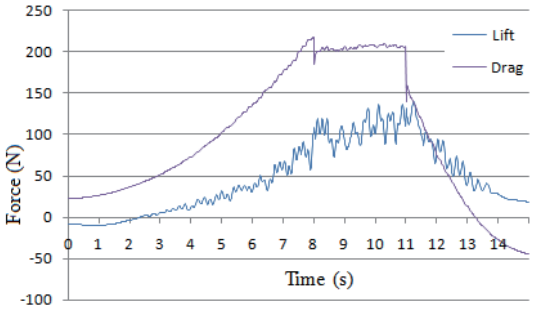

Fig. 2 Drag and lift force curves

The lift curve is undulated all the time. It increases a big step about every 0.6 s since t = 5.5 s. This regular is broken while t = 8 s as the driving condition changes. During constant speed process, the curve also shows obvious periodicity. The amplitude is bigger than that in acceleration, while the period is shorten from 0.6 s to 0.4 s. The ranges at t = 11 s and during the deceleration process are bigger than that of acceleration but smaller than constant motion. Thus, it can be seen, in this complex driving condition, the lift is unsteady, which would threaten the safety of travelling vehicle. Besides, it is more dangerous to accelerate at high speed.

Fig. 3 shows the rear pressure contours of the vehicle

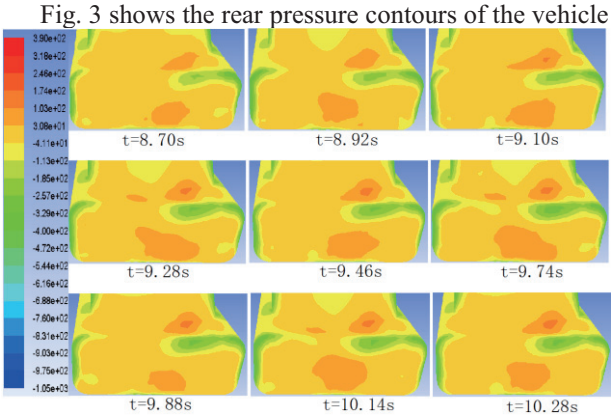

Fig. 3 Rear pressure contours of the vehicle

corresponding to the lift curve's valleys and peaks in

sequence since t = 8.70 s, the first valley of the curve at the constant motion. The result is homologous with that "the unsteady parameters of airflow around Ahmed body with symmetry geometry are not absolute symmetrical" [1]. This figure also suggests that the more symmetrical the contour is, the higher the lift curve would be.

As is known, because of the effect of airflow superposition, the airflow structure at each time would influence the following's, which leads to the unsteady phenomenon. In the study, 8 points, as shown in Fig. 4, are chose to study how the pressure changes along the time.

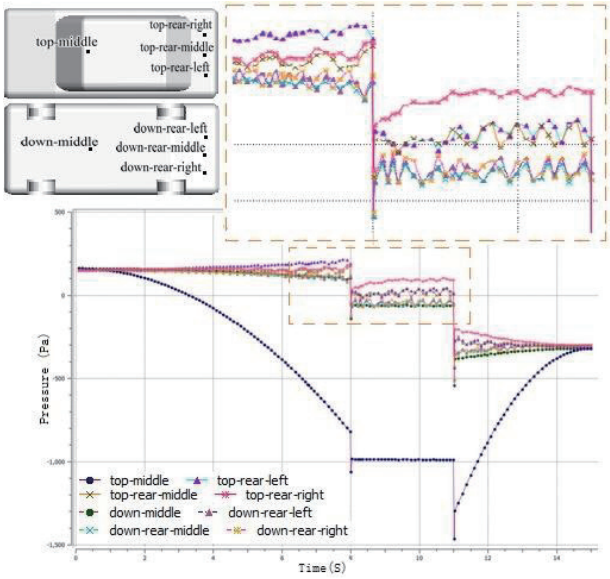

Fig. 4 Points and their pressures

Fig.4 also reveals that the lift is mainly contributed by the pressure difference between top-prism and bottom side. The pressures of rear points wave all the time though their difference values between top side and down side are much smaller. What's more, the pressures of left points are higher than those of the middle and right points during acceleration. The lift on the left side is bigger than that on the right side, which would cause rightward overturning moment. But for the constant speed motion, it is opposite to the acceleration process. Therefore, the safety of travelling vehicle would be deteriorated.

As shown in Fig. 5, the streamlines are smooth when t = 7.3 s and t = 10.1 s because of the acceleration air or the high speed airflow. This would promote the dissipation of vortex. During the process of deceleration, the airflow seems more stagnant, causing the air pile-up against to the rear of the vehicle, which would decrease the pressure difference between the front and rear of the vehicle.

Fig. 6 shows the velocity vector in the section 100mm behind the rear of the vehicle at different driving conditions. In all three cases, the trailing vortices are clear. Below them, so called "lower trailing vortices" [2] are obvious in acceleration case, vague in constant case and hardly to perceive in deceleration case, which means the vortices have been dissipated before reaching this section. It suggests that the vortices would be trailed longer during acceleration.

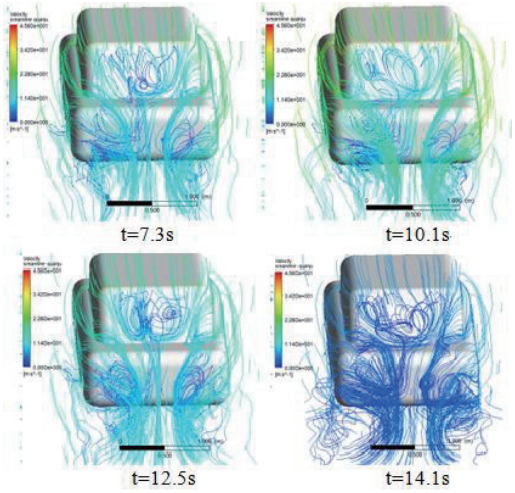

Fig. 5 The rear wake structure of the vehicle

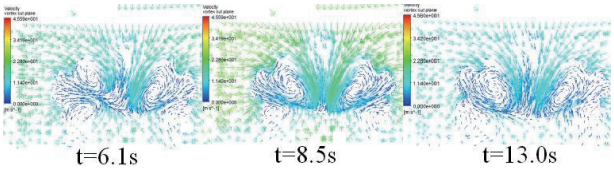

Fig. 6 The velocity vector in the section

4. Conclusions

The following conclusions are made through the numerical study:

(1) The vehicle aerodynamic performance in complex driving condition could be simulated effectively through UDF.

(2) The drag sharply drops and rises when the driving condition changed, and the lift fluctuates all the time and appears obvious periodicity.

(3) The more unsymmetrical the rear pressure is, the lower the lift is, which cause greater overturning moment.

(4) The rear vortices dissipate easier during acceleration while airflow stack occurs during deceleration.

Acknowledgements

This research is supported by Natural Science Foundation Project of CQ CSTC (CSTC, 2011BB6113). Part of the work was carried out under the Collaborative Research Project of the Institute of Fluid Science, Tohoku University, Japan.

References

[1] Hui Zhu, Zhigang Yang: Numerical study of unsteady features of airflow around the Ahmed body. Acta Aerodynamic Sinica, 36(6), 2012.12

[2] Chenguang Lai, et al: Experimental and Numerical Investigations on the Influence of Vehicle Rear Diffuser Angle on Aerodynamic Drag and Wake Structure. International Journal of Automotive Engineering, 2(2), 2011.6

Tenth International Conference on Flow Dynamics
November 25-27, 2013, Sendai, Miyagi, Japan

PIV Flowfield Measurements around a Flapping Wing Object with Feathering Motion

Hidenori Yamada, Yuya Fujii, Ryoma Hashiguchi, Wataru Yamazaki
Department of Mechanical Engineering, Nagaoka University of Technology, Niigata, 940-2188
s103103@stn.nagaokaut.ac.jp

ABSTRACT

In this research, a mechanism for feathering motions is introduced in our flapping wing object and then its flow field is measured by a particle image velocimetry (PIV) approach. The PIV measurements are performed with the ranges of feathering motion of 0, 45 and 90[deg]. The differences of flow field by the feathering motions are discussed by the PIV measurement.

1. Introduction

Flapping wing micro air vehicles (MAV) are watched with keen interests these days since these are promising for advanced unmanned MAV for exploration and observation under risky and ultimate environments. Although the flapping wing flight can be often found in nature, its physical mechanisms are still difficult to understand from the viewpoint of aerodynamics. The fluid mechanics of flapping wing are more difficult than traditional fixed wing due to its complex unsteady fluid physics at low Reynolds numbers. Therefore, we have self-developed a flapping wing object and then started to analyze the flow physics around the flapping wing object by PIV measurements [1-2]. In this research, feathering motions of wing are introduced in the flapping wing object, and then its flowfield is analyzed by the PIV measurements.

2. PIV Measurement around Flapping Wing Object with Feathering Motion

The developed flapping wing object is shown in Fig.1 (Left). By transferring the rotational motion of a D.C. motor into a simple harmonic motion by using gears, the flapping motion can be achieved at 5[Hz] whose flapping amplitude is ±30[deg]. The semi-span length of the wing is 210[mm] and the chord length is 60[mm].

At the PIV measurement around the flapping wing object, a fiber illuminator is utilized as the source of light and its light sheet (thickness~15[mm]) is exposed on the measurement section of 60% semi-span. In closed space including the flapping wing object without uniform flow, smoke is generated by a smoke generator of Power Tiny. The fluid motion is recorded by a high-speed camera of GX-8. Its resolution is 1024×1280[pix] and the frame rate is set to 1000[fps] in this study. In Fig.1 (Right), the schematic sketch of the PIV measurement apparatus is indicated. The flapping angle and phase are defined as Fig.2. Since the flapping motion at 5[Hz] is recorded by the high-speed camera at 1000[fps], there are about 200 frames per cycle. At the 60% semi-span section of the flapping wing, the size of the PIV measurement region is about 264[mm]×380[mm].

Fig. 3 shows the mechanics of feathering motion and the definition of the feathering angle α. Since the wing portion has the degree of rotational freedom along the leading edge beam axis, the feathering angle automatically shifts towards 90[deg] at the upstroke and towards 0[deg] at the downstroke by the effect of aerodynamic force acting on the flapping wing. By limiting the possible range of the feathering angle at a component of wing root location, different feathering motions can be easily realized on the flapping wing object. Three cases are investigated in this research, in which the possible ranges of the feathering angle are respectively set to 0 (no feathering motion), 0<α<45 and 0<α<90[deg].

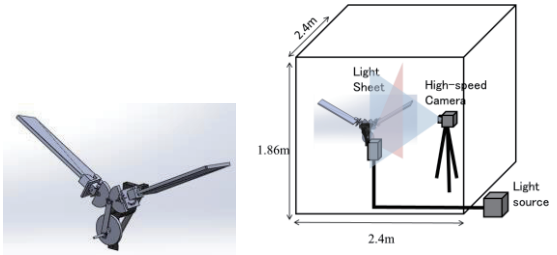

Fig.1 (Left) Flapping Wing Object with Feathering Motion, (Right) PIV Measurement Apparatus

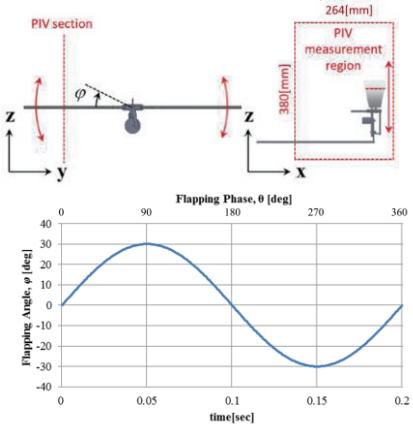

Fig.2 Definition of Flapping Phase and PIV Measurement Region

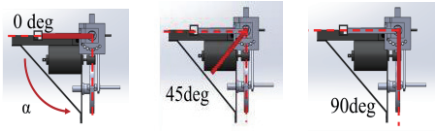

Fig.3 Definition of Feathering Angle, L to R: 0, 45 and 90[deg]

3. Results and Discussion

Fig 4 shows the actual relationship between flapping phase φ and feathering angle α measured by continuous

photographic recordings. By giving the possible ranges of the feathering angle, the feathering angle reaches the specified maximum at the upstroke while the wing is approximately horizontal (0~30[deg]) at the downstroke (90<θ<270[deg]). This result indicates our expected feathering motions are approximated realized by the developed mechanics of feathering motion.

Figs 5-7 show the results of PIV measurements at 60% semi-span section. In the all three cases, leading edge vortex (LEV) and trailing edge vortex (TEV), that are characteristic in various flapping wings, can be observed on the upper surface of wing at the downstroke. At the first case with no feathering motion (Fig.5), LEV and TEV on the lower surface also can be observed at the upstroke. At the second case with the possible range of α of 45[deg] (Fig.6), the fluids at the upper side of wing drift towards the lower/left direction at the beginning of upstroke, which may result in the generation of thrust force. At the third case with the possible range of α of 90[deg] (Fig.7), on the other hand, the fluids at the upper side of wing drift towards the lower direction at the beginning of upstroke, which may result in the generation of lift force. Thus, the differences of vortex structures due to feathering motions can be captured by the PIV measurements.

4. Concluding Remarks

A flapping wing object which achieves feathering motions has been developed in this research. The ranges of the feathering motion were set to 0, 45 and 90[deg], and then the flow fields have been discussed by PIV measurements. The large differences of vortex structures around the flapping wing object can be observed. We'll analyze the differences of vortex structures in more detail by additional PIV measurements at various sections.

Acknowledgment

This research was supported by JSPS KAKENHI (Grant-in-Aid for Young Scientists) Grant Number 24760117.

References

[1] Yamazaki, W., and Yamada, H., "PIV Data Analysis around a Flapping Wing via Proper Orthogonal Decomposition," AIAA Paper 2013-2473, 2013.

[2] Yamada, H., Fujii, Y., Ueta, K.., Yamazaki, W., "PIV Flowfield Measurements around a Flapping Wing," Proceedings of 50th Aircraft symposium of Japan, 2012. (in Japanese)

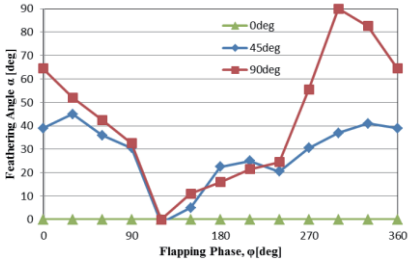

Fig.4 Relationship between Feathering Angle and Flapping Phase

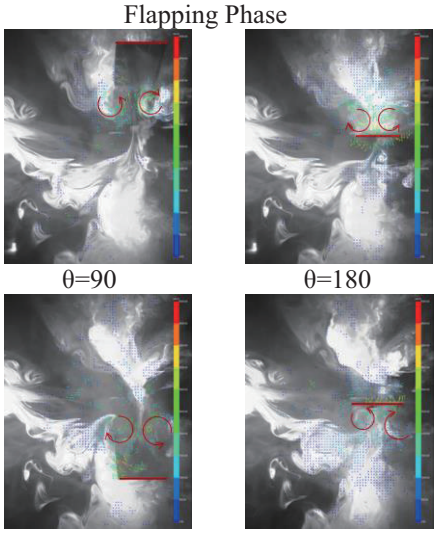

Fig.5 PIV Data without Feathering Motion at 60% Semi-span Location

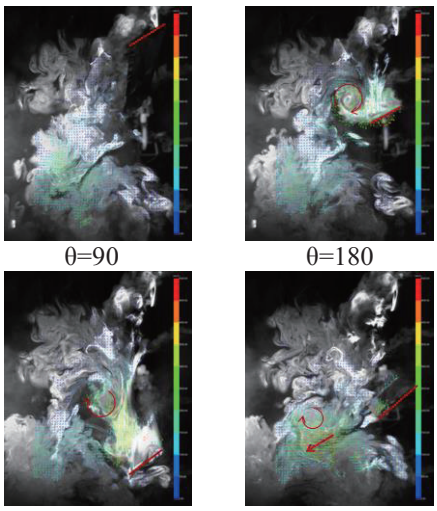

Fig.6 PIV Data with Feathering Motion Possible Range of α = 45[deg]

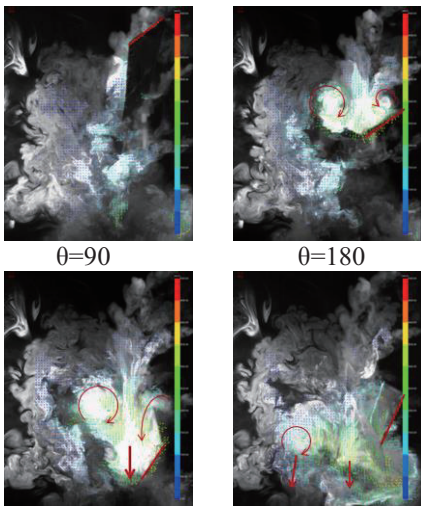

Fig.7 PIV Data with Feathering Motion Possible Range of α = 90[deg]

Numerical Study of High-Altitude Aerothermodynamics of the RAM-C II Hypersonic Flight Experiment

Pavel Vashchenkov[1], Yevgeniy Bondar[1], Alexander Shevyrin[1], Shigeru Yonemura[2], and Mikhail Ivanov[1]
[1] Khristianovich Institute of Theoretical and Applied Mechanics, SB RAS, Russia
[2] Institute of Fluid Science, Tohoku University
vashen@itam.nsc.ru

ABSTRACT

The goal of this work is to study gas ionization during hypersonic motion of bodies. Reentry of a space vehicle at altitudes from 150 to 81 km is simulated. The geometric model and flow parameters correspond to the RAM-C II in-flight experiment. Computations are performed by using the DSMC method

1. Introduction

Reentry of space vehicles from the orbit to the Earth occurs at velocities of the order of 8000 m/s. The vehicle descent is accompanied by substantial heating of air in the bow shock wave and formation of an intensely heated air layer in which ionization and radiation occurs. Though ionization is rather weak when the body moves in the atmosphere with the orbital velocity, it is still sufficient to generate interferences in radio communications between the vehicle and ground-based stations. The well-known communication blackout effect occurs.

The main goal of this work is numerical determination of aerothermodynamic characteristics of the model used in RAM (Radio Attenuation Measurements) experiments, namely, the RAM-C II model [1], at altitudes from 150 to 81 km. Results of this work were used for simulations described in [2].

2. Initial Parameters

The RAM-C II vehicle is an axisymmetric conical body with a spherical nose part. The apex angle of the cone is 9°. The radius of the nose cap is R=0.1524 m, and the total length is 1.3 m. The geometric model of the RAM-C II vehicle is shown in Fig. 1. The sizes are listed in Table 1.

Fig. 1 RAM-C II model

Table 1. RAM-C model

Point	X, m	Y, m
1	0	0
2	0.129	0.151
3	1.3	0.336
4	1.3	0

The atmosphere parameters correspond to altitudes from 150 to 81 km. Standard atmosphere model USSA-76 was used for this. Aerothermodynamic parameters of the vehicle moving with a velocity of 7800 m/s are studied at different angles of attack. The Direct Statistical Monte Carlo (DSMC) method is used for the simulations, which are performed by a SMILE software system [3]. Gas interaction with the vehicle wall obeys the law of diffuse reflection with complete accommodation of energy. The wall temperature is constant and equal to 1500 K. The exchange of internal energy of molecules in intermolecular collisions was modeled in accordance with the Larsen–Borgnakke model. Gas consists of six species: N, N_2, O, O_2, NO, and ions NO^+. Chemical reactions that occur during particle collisions were taken into account: 18 dissociation reactions, 4 exchange reactions and 1 associative ionization reaction. The procedure of simulation of chemical reactions is described in detail in [4]. Up to 256 processors of computational clusters of the Novosibirsk State University and the Siberian Supercomputer Center (Russia) were used in these computations.

3. Results

The aerodynamic characteristics were obtained as functions of the angle of attack for altitudes from 150 to 90 km. The drag and lift force coefficients are shown in Fig. 2.

Fig. 3 shows the surface distributions of the local heat transfer coefficient $C_h = \dfrac{Q}{\rho_\infty V_\infty^3 / 2 \cdot S_\Delta}$, where Q is the amount of heat that arrives on an elementary area, ρ_∞ and V_∞ are the free-stream density and velocity, and S_Δ is the elementary area. The distributions shown in Fig. 3 were obtained at an altitude of 90 km at the angle of attack equal to 0 and 40°. It is seen that the heat fluxes at the stagnation point are almost identical.

There are no differences in the gas temperature distribution along the stagnation line either (see Fig. 4, which shows the distribution at an altitude of 90 km at the angle of attack equal to 0 and 40°).

The calculated thermodynamic characteristics of the capsule at a zero angle of attack are summarized in Table 2: integral heat transfer coefficient for the entire capsule (C_h), integral amount of heat imparted to the

capsule by the heated gas (Q), and local heat transfer coefficient ($C_{h\,stag}$) and heat flux (q_{stag}) at the stagnation point. It is seen that a decrease in flight altitude leads to a decrease in the heat transfer coefficient and to a significant increase in the amount of heat incoming onto the capsule surface.

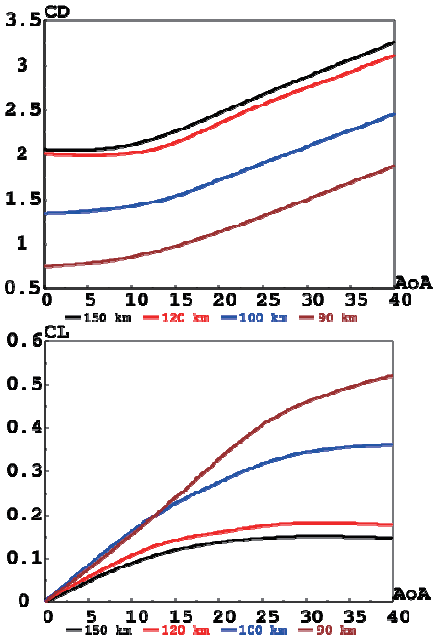

Fig. 2 Drag and lift force coefficients

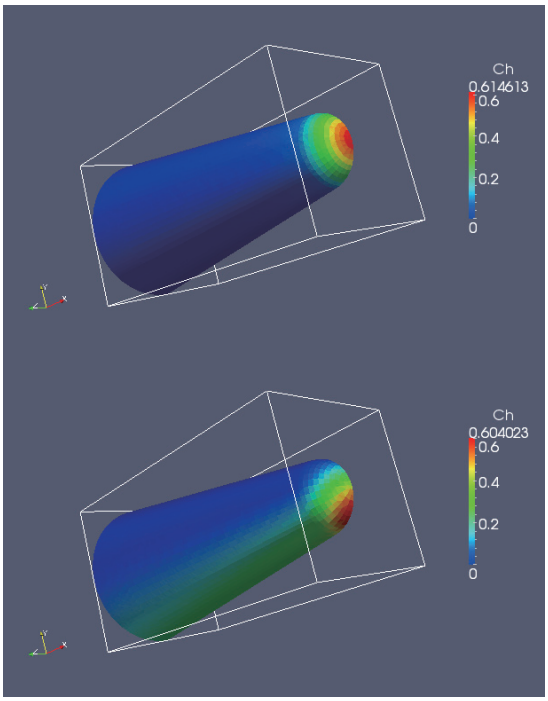

Fig. 3 Surface distribution of the heat transfer coefficient. Altitude 90 km. Angle of attack 0 (top figure) and 40° (bottom figure)

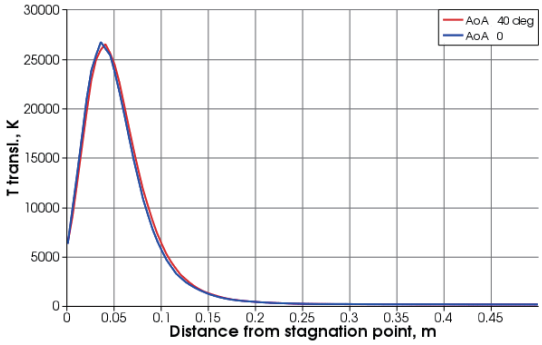

Fig. 4 Distributions of translational temperature along the stagnation line. H=90 km

Table 2 Integral parameters and parameters at the stagnation point

H, km	ρ, kg/m^3	C_h	$C_{h\,stag}$	Q, kW	q_{stag}, kW/m^2
150	2.08e-9	0.97	0.96	0.17	0.47
120	2.22e-8	0.94	0.96	1.76	5.05
100	5.58e-7	0.59	0.79	27.7	104
90	3.40e-6	0.28	0.61	81.4	493
85	8.19e-6	0.17	0.41	120	796
81	1.57e-5	0.13	0.31	168	1147

4. Concluding remarks

Aerothermodynamic characteristics of the RAM-C II capsule descending from 150 to 81 km at angles of attack up to 40° were obtained by the DSMC method. The results on fields of temperature, density, and chemical composition of the gas around the capsule obtained in this work were used for simulating ionization and radiation in [2].

Acknowledgements

This work was supported by the IFS Collaborative Research Project "Numerical investigation of ionization and radiation processes in rarefied reentry flows" and RFBR projects 11-07-00135 and 12-07-00548. This support is gratefully acknowledged.

References

[1] W.L. Grantham, NASA TN D-6062, 1970

[2] A. Shevyrin, M. Ivanov, Ye. Bondar, P. Vashchenkov, S. Yonemura, Numerical investigation of Ionization and radiation processes in rarefied reentry flows, Proc. of ICFD-2013

[3] M.S. Ivanov, G.N. Markelov, S.F. Gimelshein, Statistical simulation of reactive rarefied flows: numerical approach and applications, Proc. 7th Joint Thermophysics and Heat Transfer Conf., 1998

[4] Ye.A. Bondar, A.A. Shevyrin, A.V. Kashkovsky, M.S. Ivanov , Modeling of High-Temperature Weakly Ionized Flows with SMILE++ Software System // Proc. of 5th European Conference for Aeronautics and Space Sciences (EUCASS) - Munich, Germany, July 2013

Tenth International Conference on Flow Dynamics
November 25-27, 2013, Sendai, Miyagi, Japan

The Study of Asymmetric Flows in Constricted Microchannel with PSP Technique

Ko-Chun Chiang[1], Yuan-Wei Wang[1], Ying-Hsuan Chen[1], Hsiang-Yu Wang[2], and Chih-Yung Huang[1]
[1]Department of Power Mechanical Engineering, National Tsing Hua University, Hsinchu, Taiwan.
[2]Department of Chemical Engineering, National Cheng Kung University, Tainan, Taiwan.
cyhuang@pme.nthu.edu.tw

ABSTRACT

This paper presents the application of pressure-sensitive paint technique on microscale pressure measurements to investigate asymmetric flow in constricted PDMS microchannels. The deflected flow pattern behind the constricted structure has been revealed by the pressure map with detailed resolution around 3.7 μm acquired by PSP measurement using microscopy setup. The pressure distributions behind the rib deviates 2.5 kPa at the locations of y=±0.15W at Reynolds number of 279 with constriction ratio 5:1 in the microchannel.

1. Introduction

The microscale physical phenomena have drawn great interest by researchers due to its importance to the development of micro-electromechanical systems (MEMS) [1]. However, it is not easy to measure with conventional experiment techniques developed at macroscale. Microscale temperature and pressure sensors fabricated by MEMS technology have been applied to study the microscale physics but with the limitation of discrete data points [2]. It is difficult to acquire detailed temperature and pressure profiles inside the devices and around the structure where the flow field changes. In order to explore the physics of fluid in MEMS devices, alternative pressure measurement techniques has been adapted from pressure-sensitive paint (PSP) technique which was developed in 1980s for the wind tunnel measurement at macroscale. PSP technique is capable of providing global and detailed pressure profiles on the model surface using non-invasive luminescence measurement [3]. Because of the small size of molecules in PSP sensor, this technique can further apply to microscale measurements [4-6]. Constricted microchannels have been used in micro mixers due to the characteristics of flow behind the constriction structure. Past studies of constricted microchannel flow were limited by the measurement technique using micro sensors prepared by MEMS technique and only one-dimensional pressure distribution and be obtained [2]. Most studies regarding constricted microchannel flow were using simulation [7]. The current study provides detailed pressure profiles behind the constricted structure and reveals the asymmetric flow.

2. Method

In the study of pressure distribution inside the constricted microchannels, the PSP sensor mixed by Pt(II) meso-tetrakis- (pentafluorophenyl) Porphine (PtTFPP) and Polydimethylsiloxane (PDMS) was chosen as the pressure probe and binder for the experiments. PDMS was selected as the binder because of its comparability to microchannel devices, which was fabricated using standard soft lithography with PDMS material. The constricted microchannel device is 1 cm long, 250 μm wide, and the constricted section is in the middle of the channel as a pair of rib with constricted ratio of 5:1. The depth of microchannels is 252 μm. Figure 1 shows the schematic of constricted microchannel devices in current study. In order to improve spatial resolution of acquired pressure profile, a microscopy system was used with a 16 bit CCD camera and a light source using UV LED as excitation. Figure 2 shows the experimental arrangement of current PSP system in the microscale pressure measurements with a microscope. During the experiment, the UV LED illuminated through the optical path in the microscope to provide top-side excitation perpendicularly and a 4X objective lens was used to deliver magnification with around 3.7 μm per pixel resolution. A flow controller was positioned upstream at the inlet of microchannel along with a pressure transducer to control the air flow rate and monitor the pressure. A vacuum system with a vacuum pump and a buffer tank was used to drive the flow in the microchannel device. Another pressure transducer was positioned at the exit to measure the pressure at outlet. The pressure transducers were used as reference pressure during calibration. In-situ calibration and pixel-by-pixel correction were applied to truthfully present the pressure fields [8].

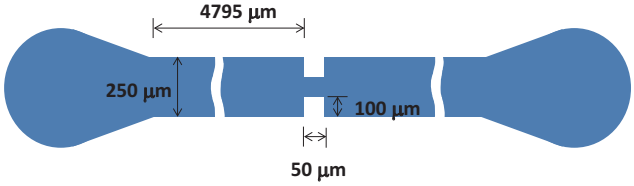

Fig. 1 The schematic of constricted microchannel device

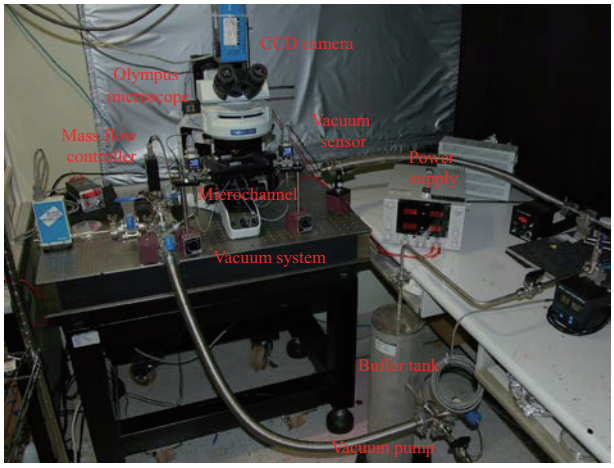

Fig. 2 The experimental setup of PSP measurements with a microscope

3. Results and Discussion

In order to examine the asymmetric flow phenomenon in constricted microchannel, the PSP technique has been utilized to provide detailed pressure profiles around the structure of ribs, as shown in Fig. 3. Around 8% of pressure map from the edge of microchannel have been masked due to the inaccurate pressure data affected from the side wall and shadow. The region measured by PSP technique has been improved to 85% laterally in the microchannel, due to the utilization of microscopy setup with perpendicular lighting. The asymmetric flow pattern is observed at the condition of Reynolds number of 279, as the low pressure region moving toward to the side of channel in the pressure contour. The pressure distributions located at y=±0.15W in the section of x/L=0.4~0.6 are plotted in Fig. 4. The flow stays symmetric before the ribs (the dashed lines at the location x/L =0.5) and immediately deviated behind the structure. About 2.5 kPa pressure difference has been identified between the pressures acquire at locations of y=±0.15W. The flow is recovered to symmetric further downstream at the location x/L=0.56.

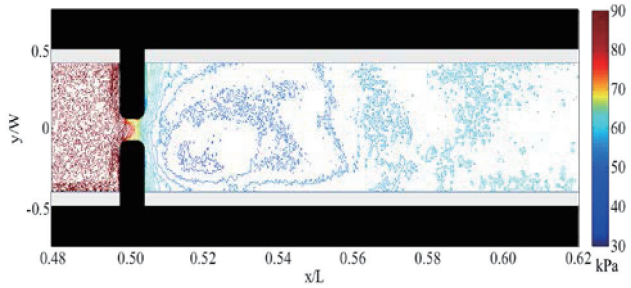

Fig. 3 The pressure profile acquired by PSP technique in constricted microchannel with constrict ratio =54:1 and Re = 279.

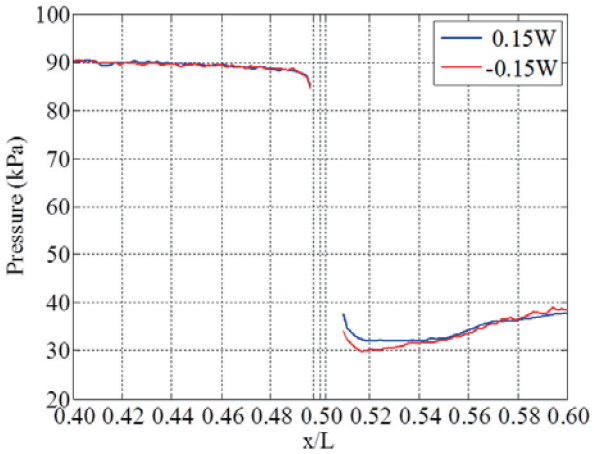

Fig. 4 The pressure distributions plotted at the location of y= ±0.15W in the section of x/L=0.4~0.6.

4. Concluding remarks

In this study, the PSP technique was successfully applied to the investigation of constricted microchannel flow with improved resolution using microscopy setup. In the constricted microchannel with constrict ratio of 5:1 at Reynolds number of 279, the asymmetric flow phenomenon was identified after the constriction region, and the pressure deviates 2.5kPa at the location of y = ±0.15W downstream. The detailed pressure map measured by PSP technique show the flow pattern deflects to the side of microchannel and the pressure distribution behind the rib structure deviates. The flow characteristics presented in current study could benefit the design of micro mixers with improved performance utilizing constriction structure.

Acknowledgements

This work is funded by the National Science Council of Taiwan via NSC100-2221-E-007-107 and NSC 102-2311-B-006 -003 -MY3.

References

[1] C.M. Ho and Y.C. Tai, Ann. Rev. Fluid Mech., pp. 30-579, 1998.

[2] W. Lee, M. Wong, and Y. Zohar, Journal of Microelectromechanical System, **11** (2002), pp. 236-244

[3] T. Liu and J.P. Sullivan, Pressure and Temperature Sensitive Paints, Springer-Verlag (2004)

[4] C.Y. Huang, J.W. Gregory, and J.P. Sullivan, Journal of Microelectromechanical Systems, **16** (2007), pp. 777 – 785

[5] H. Nagai, R. Naraoka, K. Sawada, and K. Asai, AIAA Journal **46** (2008), pp. 215–22

[6] C.Y. Huang, C.M. Lai, Journal of Micromechanics and Microengineering, vol. 22, Jun 2012.

[7] M. S. N. Oliveira, L. E. Rodd, G. H. McKinley, and M. A. Alves, Microfluidics and Nanofluidics, (2008) **5**, pp. 809-826

[8] C.Y. Huang, C.M. Lai, and J.S. Li, Journal of Microelectromechanical Systems, **21** (2012), pp. 1090 – 1097

Numerical Investigation of Mach Reflection Hysteresis in Stunted Busemann Intakes for Axisymmetric Scramjet Engines

Hideaki Ogawa*, Sannu Mölder†, and Evgeny V. Timofeev‡
* School of Aerospace, Mechanical and Manufacturing Engineering
RMIT University, Melbourne, VIC 3083, Australia
† Department of Aerospace Engineering, Ryerson University, Toronto, Ontario, M5B 2K3, Canada
‡ Department of Mechanical Engineering, McGill University, Montreal, Quebec H3A 0C3, Canada
hideaki.ogawa@rmit.edu.au

ABSTRACT

Axisymmetric Busemann intakes can achieve high compression efficiency for hypersonic scramjet propulsion, but inevitably require length reduction to mitigate penalties in weight and friction drag. Stunting (longitudinal contraction) has been examined as a simple shortening method in a preceding study, which observed drastic changes of the Mach reflection structure at the centerline. This paper investigates the shock structure of the Mach reflection and hysteresis of the mode transition in the stunting process by means of numerical simulations. Various characteristics unique to axisymmetric flowfields have been revealed as a consequence.

1. Introduction

Scramjet propulsion is a promising air-breathing technology for reliable and economical access to space and atmospheric transport at hypersonic velocities. The air intake plays a crucial role in scramjet operation, being responsible for the compression of inflow to high pressure and temperature required for combustion, while maintaining high total pressure. In particular, the full Busemann geometry (Fig. 1) enables a highly efficient axisymmetric intake in the inviscid flowfield, attaining a total pressure recovery of 97% with a minimum loss across a conical shock as a single entropy source [1].

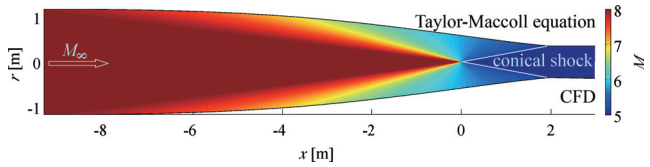

Fig. 1 Full Busemann intake for $M_\infty = 8$ and inviscid flowfields from theory (top) and CFD (bottom)

However, considerable penalties in structural weight and skin friction due to its inherently length invite shortening the intake by leading-edge truncation and axial contraction. In a preceding study [2], marked changes in the flow structure have been observed in the latter (stunting) process, where the shock reflection at the symmetry axis was found to change abruptly between two distinctly different modes. This change has the potential of major impact on the intake performance.

The present research is conducted to investigate the physical mechanism of this flow mode transition. Numerical simulation is performed to gain insights into the underlying physics as well as the duality and hysteresis of the Mach reflection (MR) mode transition as a Busemann intake is progressively shortened by means of longitudinal contraction (stunting).

2. Methods

1. Flow conditions and configurations

The Busemann intake captures a uniform airflow at Mach 8 with a static pressure of 1197 Pa. Stunting is obtained by axially contracting the full Busemann geometry [1]. The degree of stunting is indicated by the shortening factor f_s, defined as the ratio of the length reduction to the full Busemann length. The contraction ratio is 11.2 with the intake entrance radius of 0.335 m.

2. Computational fluid dynamics

The airflow is treated as calorically perfect and inviscid. Intake flowfields on uniform two-dimensional structured grids are computed by solving the Euler equations primarily with a commercial code, CFD++. The stunting and reverse (stretching) processes are simulated by varying the shortening factor f_s by 1% and performing time-accurate computations with a global time step of 0.01 ms by restarting from the previous flowfield. A (quasi-)steady state is reached, typically after 10 ms. An unstructured solver Masterix [5], which has a shock capturing as well as an adaptive mesh capability, is utilized to cross-check the CFD++ results.

3. Results

1. Mach reflection duality and hysteresis

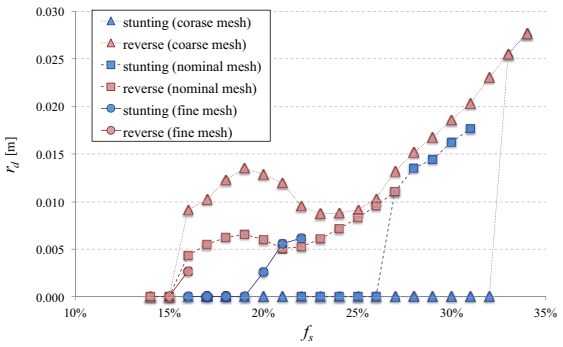

Fig. 2 Variations of Mach stem height in stunting and reverse process with various mesh resolutions

The variations of the Mach disk radius, r_d, are displayed in Fig. 2, as determined by the stunting and reverse processes. The figure shows clearly that two different Mach disk sizes can be obtained at the same shortening factor (duality) and that the change of one size to the other occurs at differing values of the shortening factor (hysteresis). The results are compared for flowfields modeled with structured grids of three resolutions, namely, coarse (275 cells along walls × 200 in the normal direction, as in [2]), nominal (2200 × 200) and fine (4400 × 400) meshes. It can be noted that the

reverse transition from MR type B ($r_d > 0$) to MR type A ($r_d \approx 0$) occurs at shorter lengths than for MR type A→B transition with all tested resolutions[1]. Thus, the results still suggest, as in [2], the possible duality of the MR modes and their hysteresis, however grid convergence is not achieved yet and further studies are warranted[2].

2. Mach reflection characteristics

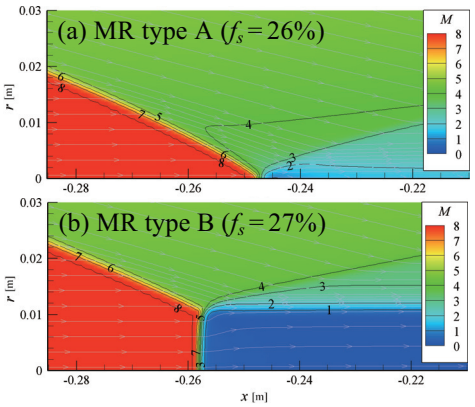

Fig. 3 Comparison of Mach number distributions

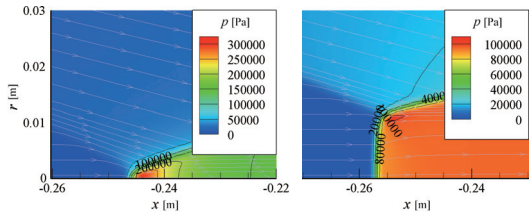

(a) MR type A (f_s = 26%) (b) MR type B (f_s = 27%)

Fig. 4 Comparison of static pressure distributions

The Mach number distributions in the vicinity of the shock reflection points are compared in Fig. 3 for the Mach reflections before and after the MR type A→B transition in the stunting process. Fig. 4 shows the corresponding distributions of the static pressure. Both figures indicate a substantial change in shock structure in a narrow (1%) range of shortening factor change.

Table 1 Flow properties before/after MR transition

f_s	MR type	θ[°] (CFD)	p_3/p_∞ (CFD)	p_3/p_∞ (theory) two shocks weak	two shocks strong	three shocks
26%	A	22.0	254	89.3	**254**	74.5
27%	B	17.9	75.2	60.0	253	**74.5**

Summarized in Table 1 are the pressure ratios, p_3/p_∞, downstream of the reflected shock, measured from the CFD flowfields, compared with those obtained from the oblique (two-shock) and three-shock theories. The flow turning angle, θ, is measured from CFD for each MR type. It is notable that p_3/p_∞ is substantially higher for MR type A than for B, as also seen in Fig. 4.

Shock polars are plotted for the deflection angles measured in CFD for the two MR types, along with the curves for the detachment and von Neumann (vN) criteria from the two and three shock theories, respectively. The pressure ratios p_3/p_∞ tabulated in Table 1 suggest that the mode transition occurs across the vN configuration from (A) Mach reflection akin to planar regular reflection with a strong reflected shock (regular reflection is not possible in axisymmetric flow [3,4]) to (B) Mach reflection featuring an upward deflected shear layer emanating from the triple point and thus a Mach stem that is convex toward the oncoming flow (Fig. 3b). Fig. 6 displays the quasi-steady flowfield obtained at the verge of the reverse MR transition (B→A) at f_s = 16%. A toroidal vortex can be seen behind a highly curved Mach stem, being a unique flow feature of this configuration.

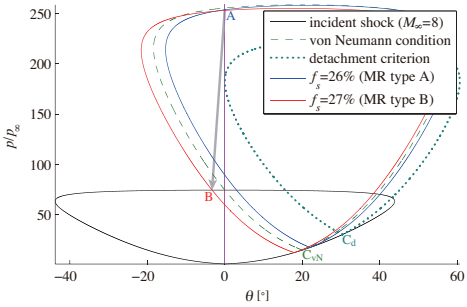

Fig. 5 Shock polar analysis for MR transition

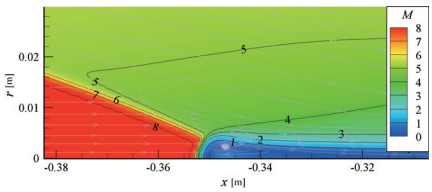

Fig. 6 Toroidal vortex structure (f_s = 16%)

4. Concluding remarks

Numerical calculations have revealed two different flows (duality) in axially stunted and re-stretched Busemann intakes for Mach 8. The two flows are characterized by differing shock structures at the centerline. Stunting-driven transition from one structure to the other appears at different amounts of stunting (hysteresis). The effect of the mesh resolution on duality and hysteresis has been elucidated. Computations and shock polar analysis have revealed various interesting features including: (a) strong regular reflection-like MR before mode transition; (b) MR with a convex (forward) curved Mach stem after mode transition; (c) a toroidal vortex behind the Mach stem before reverse transition. These may be phenomena unique to axisymmetric flows that can occur only in peculiar circumstances [4].

References

[1] Mölder, S. and Szpiro, E. J.: *Journal of Spacecraft*, Vol. 3, No. 8, 1966, pp. 1303-1304

[2] Ogawa, H., Mölder, S., Timofeev, E. V., and Boyce, R. R.: ISSW 0246-000197, 29th ISSW, Madison, WI, Jul 2013

[3] Rylov, A. I.: *Prikl Mat Mekh*, Vol. 54, 1990, pp. 200-203

[4] Mölder, S., Gulamhussein, A., Timofeev, E. V., and Voinovich, P.: ISSW 5601, 21st ISSW, Great Keppel Island, Australia, July 1997

[5] Masterix, *Software Package*, Ver. 3.40.0.3018, RBT Consultants, Toronto, ON, 2010-2013

[1] Note that computations do not cover the entire length range for nominal and fine meshes due to resource limitations.

[2] The discussions in the following sections are based on the results from the nominal mesh resolution.

Tenth International Conference on Flow Dynamics
November 25-27, 2013, Sendai, Miyagi, Japan

Investigation of Gas Injector Effect on Two-Phase Flow

Ahmet Berk Kurtulus[1], Nurdil Eskin[2], Emrah Deniz[2]
[1]Marmara University Faculty of Technology,
[2] Istanbul Technical University Faculty of Mechanical Engineering,
berk.kurtulus@marmara.edu.tr

ABSTRACT

This study has aimed to examine effects of injector design on two-phase flow characteristics such as void fraction and bubble diameter for water-air flow in a horizontal channel having 40 mm inner diameter, experimentally. During the experiments, flow rate for water is kept constant at 3 l/s while that for air is taken as 30, 50 and 60 l/min. Thus volumetric void fraction of the flow is calculated to be between 13.78-25.31 %. Measurements were made locally, via dual optical probe. Experimental data shows that the injector design effect is significant for the upper half of the channel for the flow conditions investigated.

1. Introduction

Multiphase flow involves in the general case as two-phase flow [1]. Multiphase flow is therefore a complex phenomena which can be explained by tough mathematical models validated by experimental studies and an attractive research field for the scientist to work on Some of the studies performed are as follows. A mathematical model for flow of bubbles into liquid slugs is worked by [2]. Gas effects are investigated in the models, in the other study, the gas mixture and air are together. The condition of the experiment are viewed void fraction and bubble size [3]. In some studies, the flow is vertical and structure and bubble characteristics are investigated. This case is important as vertical in nuclear engineering [4]. Meanwhile, the bubble size is necessary to find related to momentum, mass and heat transfer between the phases [5].

In this study, characteristics of gas-liquid flow through horizontal pipe are investigated experimentally. Effects of injector design on the characteristics are determined thanks to the measurements performed by dual optical probe.

2. Method

Water at atmospheric conditions is taken from a tank by a pump. The atmospheric air is compressed to 4 bar absolute pressure. Outlet the compressor the compressed air passes by the particle and the moisture filters. Air flow rate at different values is controlled by a rotameter. Compressed air is then injected to the water flow by an immersed injector at where the two-phase flow is obtained.

Two different injectors are designed to investigate effects of the bubble formation. As design criteria, the total opening area of the injectors is kept constant: The first injector has 16 holes with 2 mm diameter and is named as the circular injector. The second injector titled as inline injector has 32 holes with 1 mm diameter. Air-water flow through the test section is subject to the measurements by means of dual optical probe. Measurement technique of the probe can be found in [6].

Fig. 1 Circular (left) and Inline (right) injector

Test section is given as schematic in Figure 2. It consists of a pipe with prescribed lengths and diameters. Black bars stand for the measurement positions. The measurements were obtained by dual optical probe along the radial direction of the pipe at each measurement positions represented by black bars in the figure.

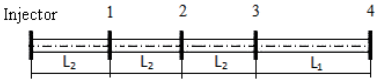

Fig. 2 Schematic diagram of test section

The experimental conditions are given in Table 1.

Table 1. Geometrical and experimental conditions of the study

Pipe diameter	40 [mm]
Pipe length (L_2)	33 [cm]
Pipe length (L_1)	50 [cm]
Water flow rate	3 [l/s]
Air flow rate	30, 50, 60 [l/min]
Acquisition time	90 [s]
Experiment interval in radial direction	2 [mm]

3. Results of Local Void Fraction and Bubble Sizes

Gas volumetric flow rate at the inlet plays important role in distribution along the pipe. The volumetric void fraction ($\beta = \dot{Q}_{air}/\dot{Q}_{total}$) of the cases are estimated to be 13.87 %, 21.74 % and 25.31 %, respectively.

Local void fraction distributions along the pipe diameter for each injector are given in Figure 3 and 4

and measured values of bubble size are shown in Figure 5 and 6.

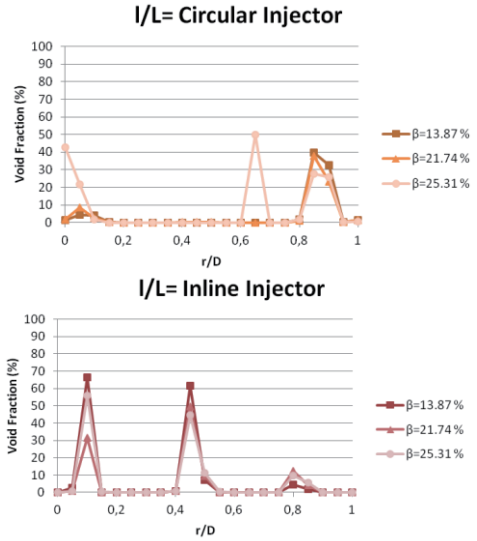

Fig. 3 Void fraction distribution of circular and inline injector outlet

At the circuler injector outlet the bubbles gather in the middle of the pipe and to walls of the pipe. The gas is injected from the holes of the injector and hence the flow involves two phase characteristic in some radial location.

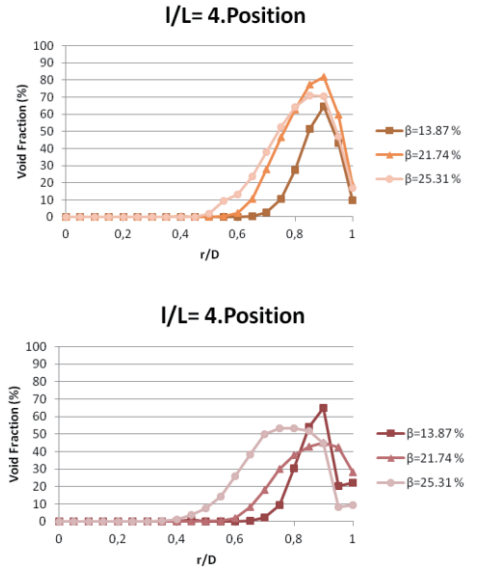

Fig. 4 Void fraction distribution of circular injector at the fourth position

The gas bubbles gather upper part due to the effects of the buoyancy force on the bubbles.

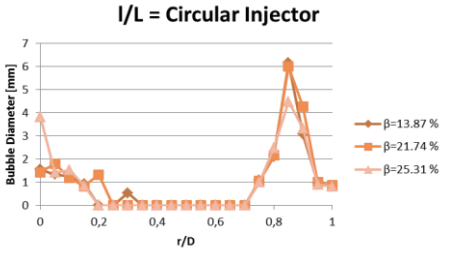

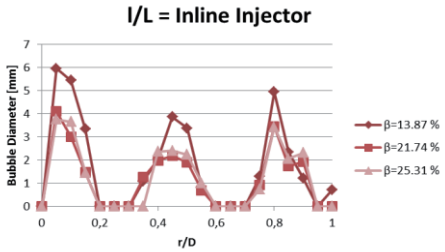

Fig. 5 Bubble diameter profiles at the outlet of circular and inline injectors

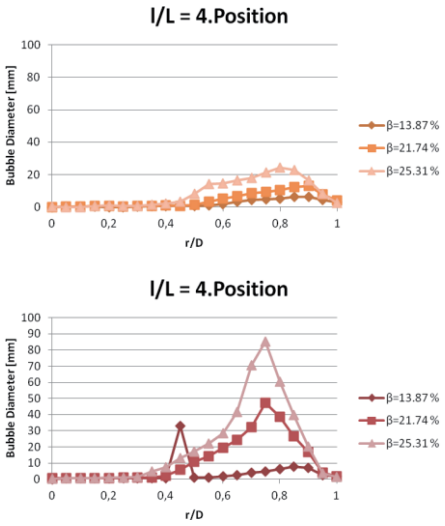

Fig. 6 Bubble diameter profiles of circular and inline injectors at the first position

Bubble sizes are around 1 to 7 mm at the outlet of the injection, as the flow rate increases the bubble diameters gets larger and reaches 90 mm in diameter. The bubble size profile is consistency with the void fraction distributions as expected.

4. Conclusion

Air bubbles injected shows different behavior as they flow along the channel. Because of influence of buoyancy force, bubbles gather at the upper part of the pipe. Void fraction has proportional relation with the two-phase flow rate. Even though the total opening area of the injectors is the same, different nozzle diameter affects the distribution of the bubble especially at increasing of the local void fraction and bubble size.

References

[1] G.B. Wallis, McGraw Hill, 1969.
[2] M. Bonizzi and R.I. Issa, Int. J. of Multiphase Flow, **29**, (2003), 1685-1717.
[3] M.A. Rahman, M. Balzan, T. Heidrick and B.A. Fleck, Int. J. of Multiphase Flow, **38**, (2012), 35-52.
[4] K. Yoneda, A. Yasuo and T. Okawa, Nuclear Eng. and Des., **217**, (2002), 267-281.
[5] R.H.S. Winterton and J.S. Munaweera, Chem. Eng. and Processing, **40**, (2001), 437-447.
[6] F. François, J. Garnier and G. Cubizolles, Measurement Sci. and Tech., **14**, (2003), 929-942.

Tenth International Conference on Flow Dynamics
November 25-27, 2013, Sendai, Miyagi, Japan

A Novel Pumping Mechanism of Using Ultrasound Induced Pressure and Cavitations

Tameo Nakanishi and Yuki Numazawa
Graduate School of Science and Engineering, Yamagata University
4-3-16 Johnan, Yonezawa-shi, Yamagata-ken, Japan
tameo@yz.yamagata-u.ac.jp

ABSTRACT

We report a new pumping method of using ultrasound induced pressure differences and cavitations. An ultrasonic vibrating surface is fabricated at the bottom of a water tank. Standing waves of half wavelength are formed between the vibrating surface and the water surface. A vertical rising pipe of small inner diameter of 0.37mm is inserted in the water in a depth of 1/4 wavelength. Micro-bubble cloud is formed around the rising pipe inlet, which suppresses the negative pressure in the vibrating cycle and results in continuous pumping of water. A pumping pressure of over 22kPa and a maximum flow rate of 10 ml/min were achieved.

1. Introduction

There are two existing approaches to pump fluid using ultrasonic vibration. The first one utilizes MHz frequency ultrasound to generate acoustic streaming [1]. The achievable velocity, however, is of a few cm/s. The converted pressure head is too small to be used in practical applications. The other approach is based on an observation that when a pipe of a small inner diameter vibrating at kHz ultrasonic frequency is dipped into fluid, the fluid can rise a few centimeters. It was reported that a pipe of an inner diameter of 3mm can obtain a pumping pressure of 1kPa. This pressure can be further improved to 20kPa by placing a plate or an alternate vibrating surface very close ($10\,\mu m$) to the pipe [2-4]. This arrangement, however, requires high precision and may cause collision of the pipe inlet with the plate.

We re-investigated the case of pumping fluid using ultrasonic vibration and a small diameter rising pipe, finding that the cyclic sound pressure and formation of micro-bubble cloud (i.e. cavitations) around the rising pipe inlet are critical to achieve an overall pumping pressure. The micro-bubble cloud can suppress the negative pressure of the vibrating cycle, and results in a continuous pumping of water. This effect is maximized when the inner diameter of the rising pipe has a comparable size with the micro-bubbles. Following these considerations, we developed a novel pumping method using ultrasound induced pressure differences and cavitations. A pumping pressure of over 20kPa and flow rate of 10ml/min were achieved by this pumping method.

2. Experimental method and pumping mechanism

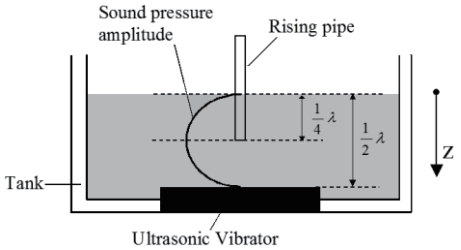

(a) Experiment setup

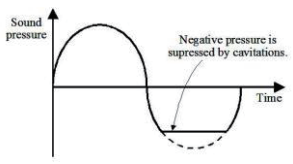

(b) Sound pressure cycle

Fig. 1 Experiment setup

Figure 1 (a) shows the experiment setup applied to investigate the pumping mechanism. A 40kHz ultrasonic vibrator is fabricated at the bottom of the water tank. The water depth to the vibrating surface is maintained at 1/2 ultrasound wavelength (λ). Standing waves are formed between the vibrating surface and the water surface. A rising pipe of a small inner diameter is inserted in the water in a typical depth of $\lambda/4$. Micro-bubble cloud is formed around the rising pipe inlet. Figure 1(b) shows an illustration of the sound pressure during one cycle. The micro-bubble cloud suppresses the negative pressure of the half cycle, resulting in a positive average pressure during one cycle.

The experiment was conducted at room temperature by using tap water and a stainless steel pipe of inner diameter of 0.37mm and outer diameter of 0.55mm as the rising pipe. The ultrasonic vibrator was driven by a sinusoidal wave. The maximum sound pressure amplitude occurs at a depth of $z = \lambda/4$ from the water surface as shown in Fig.1(a). The maximum pumping pressure is expected to be achieved by inserting the rising pipe inlet in this depth. The water depth that can most effectively induce micro-bubble cloud was determined as 0.568λ, which is slightly larger than $\lambda/2$. Three types of measurements were conducted to reveal the fundamental characteristics of the pumping method.

(a) Water heads are measured by changing the depth of the rising pipe inlet while maintaining the same applied voltage. The depth range that obtains large water head is named working depth range.
(b) Water heads are measured by changing the applied voltage while maintaining the rising pipe inlet in a given depth.
(c) The flow rates are measured by changing the water head while maintaining the same applied voltage.

3. Results and discussions

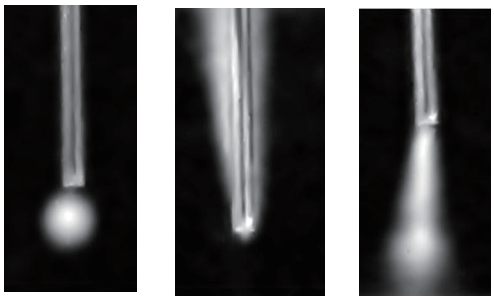

(a) Round type (b) Upward type (c) Downward type

Fig.2 Micro-bubble cloud photos at a shutter speed of 1/4 s

Figure 2 shows micro-bubble cloud photos. Continuous pumping of water takes place when micro-bubble cloud forms around the pipe inlet. The cloud patterns may be classified into (a) round type, (b) upward type and (c) downward type. The cloud pattern changes from type (a) to type (b) and finally to type (c) when the depth of the pipe inlet increases for a given applied voltage. The round type cloud can be seen in a deeper location of the pipe inlet when applying a smaller voltage. Transitional types between the three types were also observed.

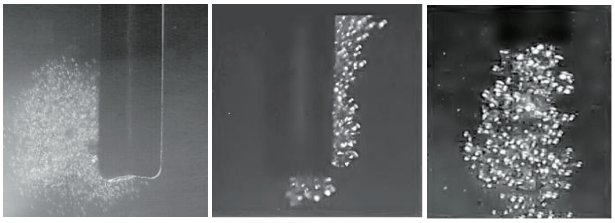

(a) Round type (b) Upward type (c) Downward type

Fig.3 Micro-bubble cloud photos at a shutter speed of 1/100000s

Figure 3 shows micro-bubble cloud photos at a shutter speed of 1/100000 s. The bubbles generated in the round type cloud are considerably smaller than those in the upward and downward type clouds. The reason is considered that at a small applied voltage or a close to the water surface location of the pipe inlet, the negative pressure of the standing waves is not strong enough to create large size bubbles.

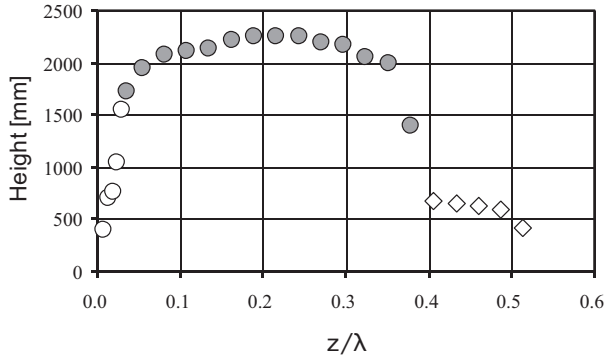

Fig.4 Water head versus normalized depth z/λ at 78 Vpp

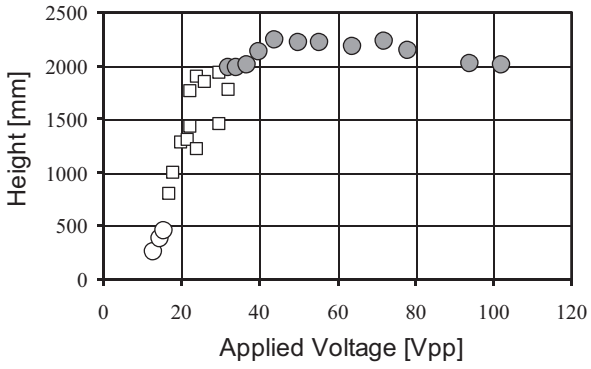

Fig.5 Applied voltage versus maximum water head

The water head versus normalized depth z/λ at 78 Vpp is shown in Fig.4. The cycle, the painted cycle and the diamond indicate respectively round type, upward type and downward type micro-bubble clouds. A positive pumping pressure was measured for z/λ between 0.01 and 0.51. Water heads over 2000mm (20kPa) were obtained for a wide working range of z/λ from 0.08 to 0.35, which is a very preferable feature for practical applications. Stable and intensive upward type micro-bubble cloud can form in this range, which effectively suppresses the negative pressure and results in a large water head.

The water head was measured for different applied voltages by inserting the rising pipe inlet in the normalized depth of $z/\lambda = 0.25$. Figure 5 shows applied voltage versus maximum water head, where the cycle, the square and the painted cycle indicate respectively round type, transitional type and upward type micro-bubble clouds. Water head initially increases as to increasing applied voltage. The micro-bubble cloud takes shape from a round type and then changes into a transitional type. The transitional type cloud is unstable that different values of water head were measured for a given applied voltage. The cloud type switches to an upward one when the applied voltage is greater than 33 Vpp. The maximum water head of 2236 mm was measured at 44 Vpp. The applied voltage beyond this value causes significant oscillations of the water surface and impedes further increase of the water head.

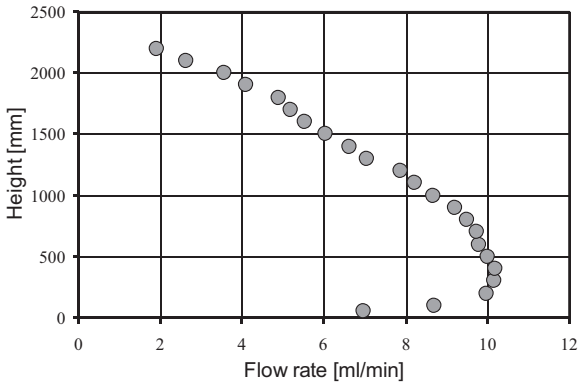

Fig.6. Flow rate versus water head plots at 78 Vpp.

Figure 6 shows flow rate versus water head plots at 78 Vpp. The flow rate increases as to decreasing H when H>400mm, and decreases as to decreasing H when H<400mm. This is an interesting behavior associated with the present pumping method. It may be explained like that water pressure is required to stabilize micro-bubble cloud at the rising pipe inlet.

4. Concluding remarks

We have developed a new pumping method of using ultrasound induced pressure differences and cavitations. The mechanisms and fundamental characteristics have been explored by experimental investigations. A pumping pressure of over 22kPa and a maximum flow rate of 10 ml/min were achieved.

Acknowledgments

This work was supported by JSPS KAKENHI Grant Number 24656151.

References

[1] S. Boluriaan, et. al., Intel. J. Aeroacoustics, **2**(2003), p.255.
[2] S. Nomura, et. al., Jpn. J. Appl. Phys. **44**(2005) p.3161.
[3] C. H. Yun, et. al., Jpn. J. Appl. Phys. **43**(2004) p.2864.
[4] T. Hasegawa, et. al., Jpn. J. Appl. Phys. **44** (2005) p.4658.

Tenth International Conference on Flow Dynamics
November 25-27, 2013, Sendai, Miyagi, Japan

Effect of Relative Drain Port Size on Vortex Formation in Cylindrical Tanks

Rahul Korah Shaji[1], Raghavan Ajith Kumar[1], Ambattu Raghavan Srikrishnan[2], Pulikkotil Joseph Joshy[3]
[1]Department of Mechanical Engineering, AMRITA University, Amritapuri Campus, Kerala, India
[2]Associate Professor, Department of Aerospace Engineering, AMRITA University, Coimbatore Campus, India
[3]Associate Professor, Department of Mechanical Engineering, CUSAT, Kerala, India
amritanjali.ajith@gmail.com

ABSTRACT

Vortex formation is known to reduce discharge flow rate from cylindrical containers. Almost all the studies conducted so far on the suppression of vortex formation suggested the use of external suppression devices like use of baffles, veins or cup-shaped devices. In the present work, the effect of relative port ratio on vortex formation at various values of rotation between 60rpm and 200rpm has been analysed. A limiting value of relative port ratio has been found out at which vortex formation is suppressed which is thought to be the first of its kind in this field of study.

1. Introduction

Many studies have been conducted in the past on the phenomenon of vortex formation (eg. Joshy *et al* (1996)). In the studies reported so far effect of the relative drain port ratio has not been analyzed with adequate focus. The present study primarily addresses this aspect. All the experiments in the present work are conducted using a cylindrical container made of glass of diameter, D=100mm and height, H=400mm. Different drain port diameters (d) were utilised to gather data for a wide range of relative drain port ratios. The initial liquid level in the container is denoted by H_i and H_c represents the height at which vortex formation just begins to occur (Fig.1). A wide range of port ratios (d/D) with values ranging from 0.09 to 0.03 have been considered to obtain a deep insight to the effect of relative port ratio on the phenomenon of vortex formation which is the major objective of the study.

2. Experimental Procedure

Water is filled to the required height in the cylinder (H_i). The stirrer was inserted to a depth of three-fourth the water level. Using the stirrer rotation was provided to the water column with a specified rotational speed for two minutes. Then, the drain port was unplugged and water was allowed to drain. At the same time stirrer was lifted cautiously so that the presence of stirrer in the water doesn't interfere with the vortex formation. Vortex formation with an air-core begins to occur at a certain height, H_c is noted. The same procedure is followed for various rotational speeds.

3. Results and Discussion

3.1 Effect of initial rotation on vortex formation

Certain key observations are made based on the experimental results from the study. Larger the relative port ratio, higher is the value of critical height (H_c) of vortex formation (Fig.2). At a larger port ratio, the tendency of vortex formation increases. Larger the rate of rotation imparted, larger will be the value critical height of vortex formation. Larger the critical height of vortex formation, more will be the tendency of vortex formation and longer will be the time of emptying (Temp) of the tank, i.e. the rate of discharge reduces as the vortex formation occurs (Fig.3). Temp(r)/Temp(nr) Vs stirrer rpm is plotted in Fig.3; Temp(r) is the time of emptying with rotation and Temp(nr) is that without rotation. For port ratios 0.09 and 0.07 the trend of graphs obtained were similar and hence, not shown. For port ratios 0.09 and 0.07, irrespective of the rate of rotation provided to water, vortex formation was observed in all cases. For port ratio of 0.05, no vortex formation occurred in the range of rotational speed between 60rpm and 120rpm (Fig.2). At higher values of rotation, the critical height value of vortex formation remains almost the same. Similarly, for a port ratio of 0.04, no vortex formation was observed till 180 rpm as shown in Fig.3. Similar results were obtained when the experiments were performed at different initial heights of 400mm, 350mm and 300mm.

3.2 Vortex Suppression

When the relative port ratio used was 0.03, irrespective of the rotation provided and initial height of the liquid, vortex formation never occurred. The phenomenon of vortex formation was found to be suppressed in this case. For port ratio just higher than 0.03, vortex formation occurs at higher rotational speeds. So it could be concluded that d/D = 0.03 is the limiting port ratio which provides a vortex suppression in the range of rotations used in the experiments. In the previous studies, external means like dish (Gowda et al (1996)), vanes (Sohn et al(2009)) etc. were suggested for vortex suppression. By maintaining the above mentioned port ratio, vortex suppression can be obtained during draining in the range of rotational speed 60rpm-200rpm. This appears to be a new introduction to the area of vortex suppression never tried before.

3.3 Vortex Intermittency

The phenomenon of intermittency during vortex formation, breaking up of the vortex tip and inconsistency in the dip length has also been noted for certain combinations of rotation and port ratio (Fig.4). It was experimentally seen that, beyond a port ratio of 0.07, the phenomenon of intermittency does not occur.

3.4 Numerical Studies

A numerical analysis was conducted using

the general purpose commercial software ANSYS FLUENT in order to gain further insight into the flow physics of vortex formation. A transient analysis was carried out using the volume of fluid method for multiphase modeling in FLUENT. Numerical results were in excellent agreement with the experimental results with respect to the time of emptying during draining. Formation of a bottom boundary layer and an upward pumping phenomenon have been observed in the numerical analyses which are expected to play an important role in the phenomenon of vortex formation (Fig:5). At present numerical results are being analyzed further from the perspective of vortex suppression.

4. Conclusions

Effect of relative-port ratio on vortex phenomenon has been analyzed in depth. A relative port-ratio of 0.03 for vortex suppression have been found out which is expected to be a new approach to vortex suppression. Phenomenon of vortex intermittency has also been observed for concentric ports.

(The third author acknowledges the support from ANSYS Inc., who provided the research license of their product).

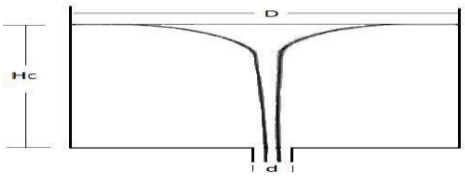

Fig.1 Vortex Formation

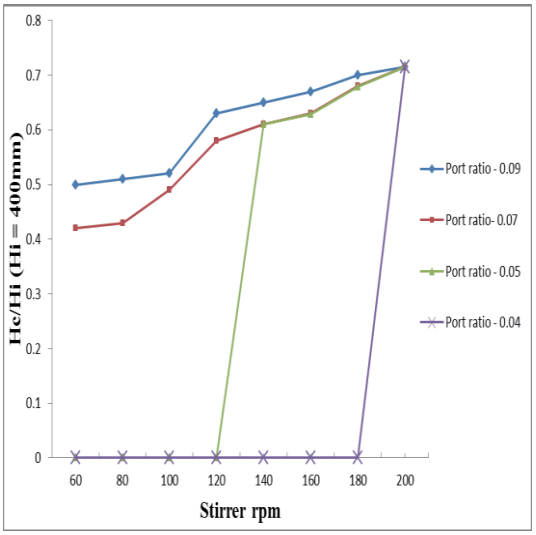

Fig.2 Variation of $\frac{H_c}{H_i}$ with stirrer speed

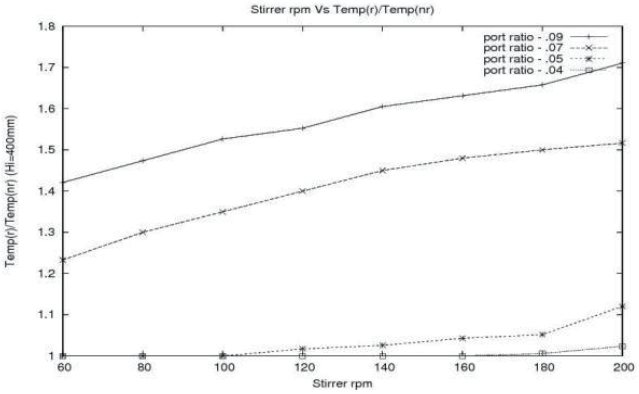

Fig.3 Variation of Temp(r)/Temp(nr) with stirrer speed

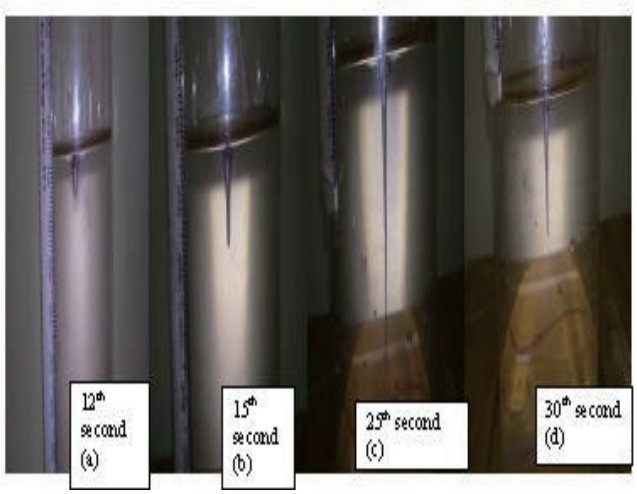

Fig.4 Vortex Dip Length variation with time

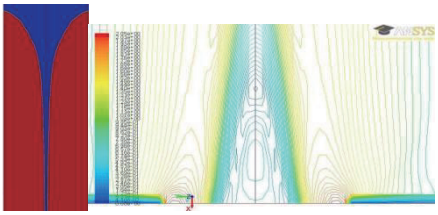

Fig.5 Vortex-air core formation and zoomed-in view of upward fluid pumping region near the drain port from the numerical simulation

References

[1].P.J.Joshy and B.H.Lakshmana.Gowda, 21st National Conference on Fluid Mechanics and Fluid Power (1996).

[2] B.H. Lakshmana Gowda and P.J. Joshy, Journal on Spacecraft (1996)., Vol.33, No.4.

[3] C.H. Sohn, M.G. Ju and B.H. Lakshmana Gowda. Journal Of Visualisation (2009). , Vol.12, No.4, 347-360.

Tenth International Conference on Flow Dynamics
November 25-27, 2013, Sendai, Miyagi, Japan

Numerical Plasma Simulation for Reactive Plasma Deposition Equipment with Multi Gun

Masaru Miyashita, Hisashi Kitami, Toshiyuki Sakemi, Yasushi Aoki, Takanori Kato
SUMITOMO HEAVY Industries, ltd.
19, NATSUSHIMA-CHO, YOKOSUKA-SHI, KANAGAWA 237-8555 JAPAN
Msu_Miyashita@shi.co.jp

ABSTRACT

Numerical simulation code by Hybrid Particle In Cell / Monte Carlo collision (PIC/MCC) method for Reactive Plasma Deposition equipment with multi plasma guns have developed. In this method, behaviors of ions and neutrals are treated with the particle model and characteristics of electron are treated with the fluid model. The electron fluid equations are discretized by Finite Element Method. Algebraic multi grid preconditioned BiCGSTAB method is employed as a liner algebra solver for acceleration. Using the code, simulation of two guns case is calculated in reasonable calculation time and results explain the empirical facts qualitatively.

1. Introduction

The Reactive Plasma Deposition (RPD) equipment manufactured by Sumitomo Heavy Industries is one of ion-plating equipment, which is used to form transparent conductive coatings with high throughput and high quality (low resistance and high transparency) at relatively low temperature (~200°C)[1]. Figure 1 shows the RPD equipment configuration. The plasma gun on the right hand side produces argon plasma. The plasma is delivered to the anode with the guide of magnetic field generated by the steering coil and the plasma beam controller. The anode is made from depositing (evaporation) materials. The plasma heats the anode, and the material is evaporated. The evaporated particles interact with plasma to be ionized and accelerated. At last, some of the particles are deposited on the substrate.

Recently, the RPD equipment which have wide deposition area is desired from transparent conductive market. In order to satisfy the requirement, the RPD equipment which has multi plasma gun has been developing. Accordingly, plasma simulation technique is necessary to calculate in cubic meter size.

The Hybrid PIC/MCC code, in which ions and neutrals were treated with the particle model for getting precise information and electrons were treated with fluid model to reduce calculating time, have been developed [2]. This article shows plasma simulation results by this code for the RPD equipment with 2-gun configuration.

2. Method

The simulation procedure is shown in Fig.3. The calculation flow is divided into two parts. One is a part of particle model calculation, which includes solving motion equation and collision calculation. The other is for fluid calculation, which includes calculation of plasma potential and average electrons energy. The motions of ions and neutrals in plasma are calculated under the plasma condition that is calculated from the electron fluid equation. In this code, the calculation is iterated until convergence is obtained.

In order to calculate the distribution of electric potential (ϕ) and the distribution of average electrons energy (T_e), we use the following conservation laws in terms of momentum, mass and energy of electron fluid,

$$\vec{\Gamma}_e = n_e[\mu_e]\nabla\phi - T_e[\mu_e]\nabla n_e - n_e[\mu_e]\nabla T_e \quad (1)$$

$$\nabla\cdot\vec{\Gamma}_e = \gamma_{ion} \quad (2)$$

$$\frac{5}{2}\nabla\cdot\left(T_e\vec{\Gamma}_e - n_e T_e[\mu_e]\nabla T_e\right) = \vec{\Gamma}_e\cdot\vec{E} - Q \quad (3)$$

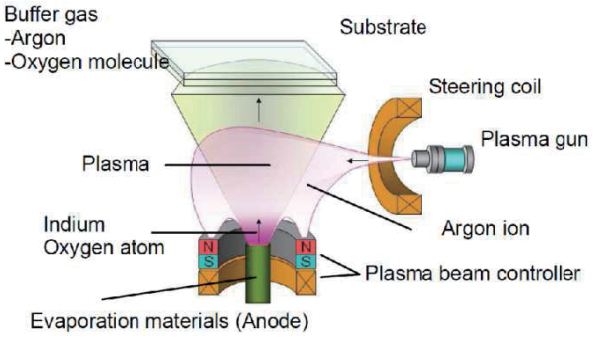

Fig.1 The RPD equipment configuration (1gun)

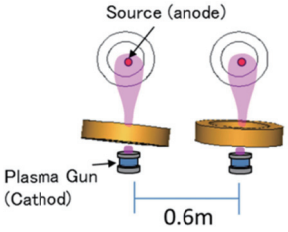

Fig.2 Two guns configuration (Top of view)

where, $\vec{\Gamma}_e$, $[\mu_e]$, γ_{ion}, Q are the electron flux, the electron mobility tensor, the ionization density, the reaction energy, respectively. n_e is the electron density and is supposed equal to ion density.

The boundary condition was assumed that the thermal flux is affected by magnetic field, then, the following equation was used.

$$\vec{\Gamma}_{edge} = \frac{1}{4}n_e\vec{v}_e\vec{b}\cdot\vec{n}\exp\left[-\frac{\delta\phi}{T_e}\right] \quad (4)$$

where, $\vec{v}_e$, $\vec{b}\cdot\vec{n}$ and δϕ are the electron thermal velocity, the inner product of the normalized magnetic vector and the unit normal vector on the wall, and the potential drop between plasma and wall, respectively.

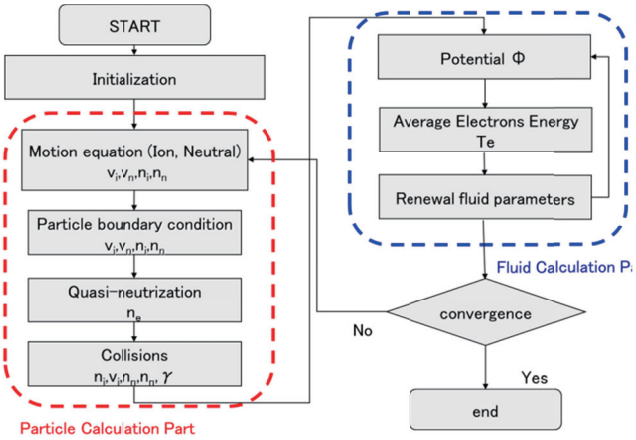

Fig.3 Hybrid PIC procedure

These equations are discretized by finite element method with partial approximation for suppressing numerical vibration [3]. The G-DEP MCL (G-DEP), algebraic multi grid preconditioned Bi-CGSTAB or ICCG method library, is employed as a linear algebra solver [4]. For ions and neutrals, their motions are calculated with the Newton's equation (5) using the fourth-order Runge-Kutta method,

$$m_\alpha \frac{d\vec{v}_\alpha}{dt} = e\left(\vec{E} + \vec{v}_\alpha \times \vec{B}\right) \quad (5)$$

where, $\vec{E} = -\nabla\phi$, $\vec{B}$ is the magnetic field applied by the external coils. m_α, $\vec{v}_\alpha$ are the mass and the velocity of particle α.

The magnetic and the electric fields at each particle position in cell were obtained by interpolation of the neighboring grid values.

The interaction number density of the neutral particles which shows ionization and dissociation events per unit volume are calculated as a function of electrons energy and electron density. The number density is sometimes overestimated in fluid model, partly because electron energy distribution based on the Maxwell distribution. In this study, the (ionization) number density is limited $1\text{x}10^{23}$ [$\text{m}^{-3}\text{s}^{-1}$], such that the calculation divergence due to overestimate in ionization number density does not occur. The collisions between heavy species are calculated by the Direct Simulation Monte Carlo (DSMC) method with weighed algorithm and maximum collision method assuming macro particles.

3. Results and Discussion

Figure 4 shows the electric potential surface distribution calculated by this code for the RPD in two gun configuration case. It was calculated in reasonable time (in a day). In addition, potential dimples were generated near the anodes.

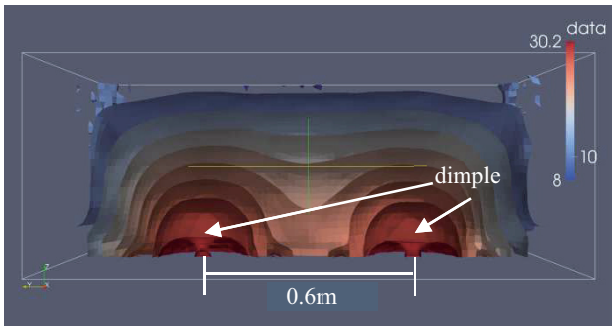

Fig.4 potential's isosurface (cross section)

Figure 5 shows the ion flux distribution on the transverse direction axis. This indicates that the distribution under 20A of plasma beam controller current is wider than that under 30A. Since the potential dimples are changed by magnetic field controlled by the plasma beam controller, the ion trajectories in the plasma should be changed. The simulation results explain the empirical facts qualitatively.

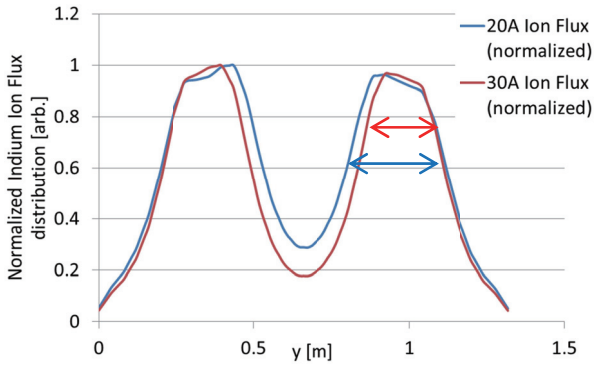

Fig.5 Normalized Indium Ion Flux distributions on substrate

4. Conclusion

A plasma simulation code which is incorporated some sophisticated methods has been developed for the RPD. The experimental result which was previously difficult to reproduce by calculation was successfully simulated on fine grid in reasonable time. Furthermore, the simulation could be performed for the RPD equipment with 2-gun configuration. In future works, adaptive mesh refinement will be introduced into the code for calculating complex-shape and to perform calculation precisely, shortening a calculation time.

References

[1]M.Tanaka, et.al., J.Vac. Soc. Jpn., **44**, (2001) 435-439 (in Japanese)
[2]M.Miyashita, et al. Frontier of Applied Plasma Technology, Vol.5, (2012) 79-82
[3]M.Miyashita, UT Numerical Analysis Seminar 049 (2013) (in Japanese)
[4] http://www.gdep.jp/product/view/63

Tenth International Conference on Flow Dynamics
November 25-27, 2013, Sendai, Miyagi, Japan

Quenching and Absorption of Toluene-LIF by Acetone

Koji Abe[1], Tomoya Maruyama[1], Toshinori Kouchi[2], Goro Masuya[1], and Keisuke Asai[1].
[1] Department of Aerospace Engineering, Tohoku University, Sendai, Japan.
[2] Department of Mechanical and System Engineering, Okayama University, Okayama, Japan.
abe.koji@aero.mech.tohoku.ac.jp

ABSTRACT

Instantaneous data of fuel-air mixing is important to develop supersonic combustor, but they are difficult to measure in the flow-field. Two-color Planar Laser Induced Fluorescence (PLIF) is one of promising methods to measure them in the supersonic flow. In this experimental method, the LIF signals of two seeded tracers have to be detected simultaneously. But composition and concentration of surrounding-gas affects LIF signal intensity. This work presents that LIF signals could be affected by the other tracer for two-color PLIF imaging measurement.

1. Introduction

The fuel injection system for scramjet engines is required to complete fuel/air mixing and combustion process within the order of 1 millisecond in the supersonic flowpath. Many researchers have investigated the mean mole fraction of fuel injected into the supersonic flow because the mole fraction has a significant impact on rapid ignition and combustion. For example, Takahashi et al. [1] applied acetone PLIF imaging to measure averaged mole fraction distribution. However, averaged data are not sufficient to understand the supersonic flow with combustion because it exhibits strong turbulence behavior. Combustion reactions occur not with time-averaged mole fractions but with instantaneous ones. Thus, instantaneous mole fraction data is strongly required to design the efficient fuel injection system.

Koban et al. [2] has developed PLIF measurement using two different tracers that have different fluorescence spectrum to measure the instantaneous mole fraction in the internal combustion engine. In their measurement, they used toluene and 3-pentanone because they can be excited upon single laser excitation. When applying two color PLIF to the supersonic flow, combination of toluene and acetone is more suitable because acetone has sufficiently large vapor pressure to seed into the cold supersonic flow and its fluorescent spectrum is similar to 3-pentanone. Figure 1 shows the fluorescence spectrum of acetone and toluene.

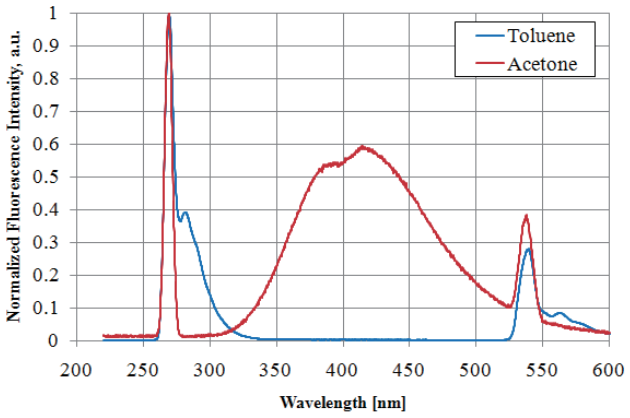

Fig. 1 Fluorescence spectrum of acetone and toluene

The problem is that toluene fluorescence may be absorbed by acetone because toluene fluorescence spectrum and acetone absorption spectrum is overlapped. Furthermore, toluene fluorescence is strongly affected by surrounding composition. Therefore, it is necessary to reveal the effect of acetone on toluene LIF.

2. Method

Figure 2 shows the apparatus of this experiment. Acetone and toluene liquid was injected into the looped plumbing line by a syringe through septum. The volume of injected liquid was controlled. Air was supplied from air cylinder. The fan generated the flow to vaporize the injected liquid and fill the cell and the sampling bag with uniform mixture of air and tracer gas. The tracer concentration in the flow line was measured by a gas detector tube (GASTEC GV-100S). After each measurement, the mixture gas was purged using vacuum tank and air from air cylinder.

Figure 3 shows the optical setup. The cell has two quartz windows for passing the laser and other two for imaging the fluorescence. This cell was located on the guide rail and can be moved perpendicular to the laser sheet with the range of ±10 mm. This device allows the change of optical path length, which are 20 mm, 30 mm and 40 mm. A frequency quadrupled Nd:YAG laser (Continuum Surlite2000) delivered a 266 nm beam to excite the tracer molecules. The beam was expanded into a sheet (25 mm-wide and 5 mm-thick) by two cylindrical lenses.

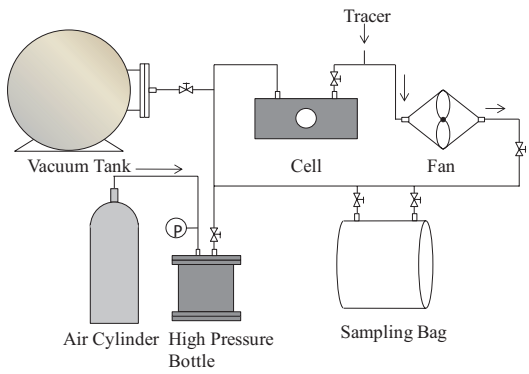

Fig. 2 Experimental apparatus

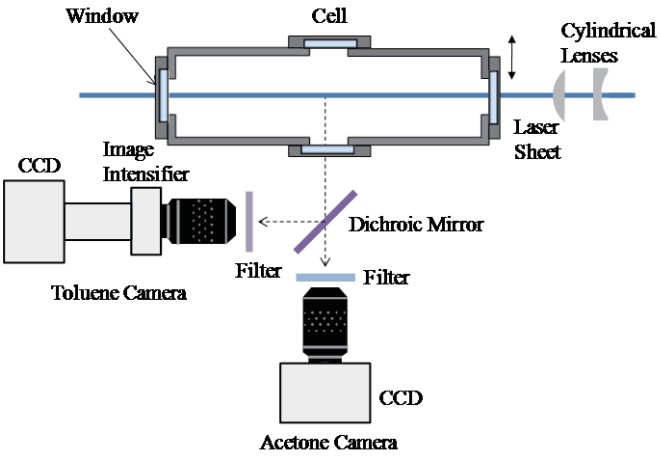

Fig. 3 Optical setup

The toluene fluorescence was separated from acetone fluorescence by a dichroic mirror (Semrock FF310) and recorded by a CCD camera (Hamamatsu Photonics ORCA) with a UV lens (Hamamatsu Photonics 50 mm f/3.5) and an image intensifier unit (Hamamatsu Photonics C9547-04). The UV lens was equipped with a band pass filter to detect the light between 275 nm and 310 nm. Acetone fluorescence passed through the dichroic mirror and recorded by a CCD camera (Hamamatsu Photonics ORCA-R2). This camera equipped with a band pass filter to detect the light between 290 nm and 500 nm. These cameras were synchronized with the laser trigger.

3. Results and Discussion

The effect of absorption of light is expressed by Lambert-Beer law. Lambert-Beer law for toluene LIF intensity is expressed as below:

$$S(C_A, L) = \int_{\lambda_2}^{\lambda_1} 10^{-\frac{\sigma(\lambda) N_A C_A L}{10^4}} S_0(\lambda) T(\lambda) d\lambda \quad (1)$$

where $S(C_AL)$ is toluene LIF signal intensity detected by CCD camera, $\sigma(\lambda)$ acetone absorption cross section, C_A acetone concentration, L optical path length, $S_0(\lambda)$ original toluene LIF signal spectrum, and $T(\lambda)$ all transmittance of dichroic mirror and camera filter.

Figure 4 shows the effect of acetone concentration and optical pass length on toluene LIF intensity. The horizontal axis is (acetone concentration) × (optical path length). This represents C_AL in Equation (1). Circle plots are experimental data and solid line is calculated data by Equation (1) using $S_0(\lambda)$ measured in this study and $\sigma(\lambda)$ from reference [3]. Each data are normalized by the value of C_AL = 0.01 mol/m^2. This result shows Equation (1) is reliable.

Figure 5 shows the effect of acetone concentration on toluene LIF intensity. Circle plots are the experimental raw data. These data are affected by both absorption and quenching. By applying Equation (1) to compensate for absorption effect, we obtain square plots in the same figure representing only the quenching effect. This result shows that toluene LIF signal intensity decay is almost due to the quenching effect of acetone and absorption effect of acetone is negligibly small for this experimental configuration. The Stern-Volmer coefficient of acetone was 2.41×10^{-22}. This value is an order bigger than the Stern-Volmer coefficient of oxygen, which is 1.39×10^{-23}.

4. Conclusion

We experimentally investigate the effect of quenching and absorption on toluene LIF signal by acetone to realize the two color PLIF using toluene and acetone. As a result, we conclude that toluene LIF signal was decayed by acetone and that is mostly due to the effect of quenching.

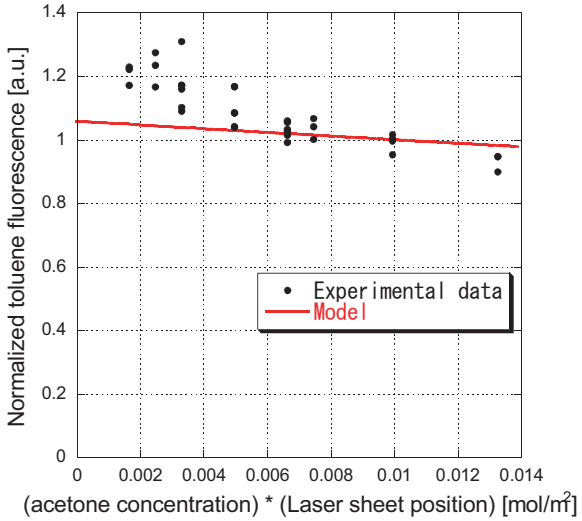

Fig. 4 The effect of acetone concentration and optical path length on toluene LIF intensity

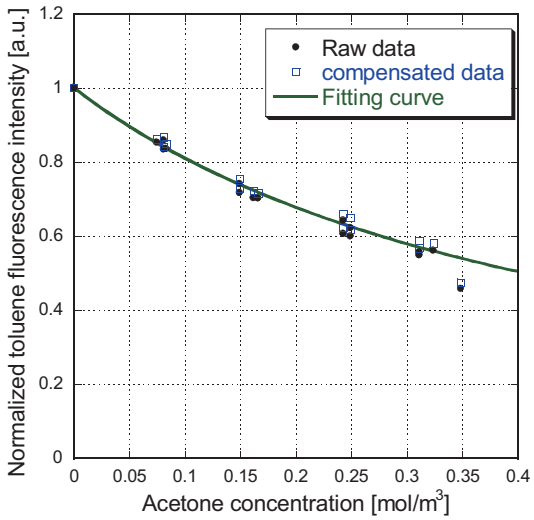

Fig. 5 Stern-Volmer plot of toluene LIF

References

[1] H. Takahashi et al., AIAA Journal, Vol. 46, No 11, pp.2935-2943, 2008.
[2] W. Koban et al., Appl. Phys. B 74, 111–114 (2002).
[3] M. Yujing et al., J. Photochem. Photobiol. A 134 (2000) 31–36.

Simulation of Sound Generated by a Flow over a Circular Cylinder Using the Discrete Vortex Method

Bui Vu Hung, Kazui Fukumoto and Yoshifumi Ogami
Department of Mechanical Engineering, Ritsumeikan University
1-1-1 Nojihigashi, Kusatsu, Shiga, 525-8577 Japan
E-mail: bui@cfd.ritsumei.ac.jp

ABSTRACT

In this study, the aerodynamic sound generated by a flow over a circular cylinder is calculated by combining the source of sound with the wave equation. The vorticity vector is considered to describe the source of the sound obtained when the flow-field of an incompressible fluid with a low Mach number is solved using the vortex panel method. The flow-field is represented as a distribution of discrete vortices. Calculation of the unsteady motion of the flow requires less computing power than the finite element method applied to large eddy simulation. The compact Green's function is used to account the far-field effects of the cylinder on the sound.

1. Introduction

In our daily life, noise is considered to be a type of pollution; our exposure to it is increasing rapidly and it is known to have a negative impacts on human health. Consequently, reducing noise is one of the most important environmental and engineering issues at present. The interactions between fluids and immersed objects such as the surfaces of cars, the pantographs of bullet trains, cooling fans in computers and many domestic and industrial appliances produce a type of noise that is referred to as aerodynamic sound.

Hardin [6] used Howe's method to calculate the sound generated by the Karman vortex street and showed that the important factor for increasing calculation accuracy is having a computational domain that is large enough to contain all shed vortices. However, Takaishi [4] proposed a method by which the accuracy of Hardin's calculation could be improved without the need for a computational domain. Takaishi indicated that the sound pressure could be calculated from properties inside the finite computational domain using an image potential velocity.

In this study, the flow field and the acoustic field were treated separately. The vortex panel method was applied to calculate the characteristics of the flow field of an inviscid incompressible fluid. Therefore, the flow field was represented by the motion of discrete vortices, eliminating the need for a generated grid as well as making it possible to calculate the sound from all of vortices in the fluid domain. The acoustic field was estimated using the method proposed by Howe [1] and the effect of the presence of the circular cylinder was taken into account using the Kirchhoff vector for a solid body. The phenomena of the Karman vortex street in the wake region and the sound pressure levels generated by the flow over the circular cylinder are introduced.

2. Results of Simulation

2.1 Flow-Field Calculation

Shown in Fig. 1 are the two types of vortices used in this study: bound vortices, which represent solid bodies, and free vortices, which are generated and shed into the wake flow. Non-permeable conditions at the locations of control points placed in the middle of each panel and Kelvin's theorem on circulation were employed to calculate the strength Γ_{Bi} of bound vortices.

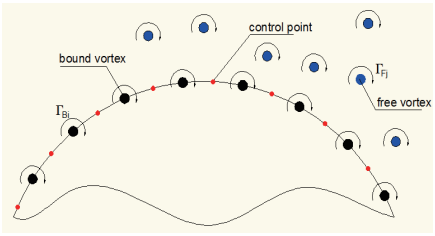

Fig. 1 The discrete solid body

The strengths of free vortices Γ_{Fj} were determined by assuming non-slip conditions on the surface of bodies as follows

$$\Gamma_{Fj} = u_s \Delta s_j \; ; \quad \varepsilon = \frac{2}{\sqrt{\pi}}\sqrt{\nu \Delta t} \tag{1}$$

where u_s is the velocity on the surface at a distance of ε for the surface based on the displacement thickness of Rayleigh boundary layer with time step Δt; Δs_j is the length of panel j, and ν is the dynamic viscosity of the fluid.

The vorticity equation in vector form for incompressible and viscous flows is derived by taking the rotation of the Navier-Stokes equation as follows

$$\frac{D\boldsymbol{\omega}}{Dt} = \frac{\partial \boldsymbol{\omega}}{\partial t} + (\mathbf{u}.\nabla)\boldsymbol{\omega} = (\boldsymbol{\omega}.\nabla)\mathbf{u} + \nu\nabla^2\boldsymbol{\omega} \tag{2}$$

$$\boldsymbol{\omega} = \nabla \times \mathbf{u} \; ; \quad \mathbf{u} = \mathbf{U}_{\mathbf{stream}} + \mathbf{u}_{\mathbf{c}} + \mathbf{u}_{\mathbf{d}}$$

where $\boldsymbol{\omega}$ is the vorticity vector; t is the time; $\mathbf{u}$ is the velocity vector; $\mathbf{U}_{\text{stream}}(U,V)$ is the stream velocity; $\mathbf{u}_c$ is the convection velocity; and $\mathbf{u}_d$ is the diffusion velocity.

The convection velocity $\mathbf{u}_c=(u_c,v_c)$ of a free vortex at $\mathbf{x}(x,y)$ is given by the Biot-Savart law. We assume that a vortex line remains rectilinear when it interacts with the body, and therefore, the two-dimensional potential velocity can be used to compute the convection velocity of a free vortex as follows.

$$u_c = \sum_i \frac{\Gamma_i}{2\pi} \frac{y - y_i}{|\mathbf{x} - \mathbf{y}_\mathbf{i}|^2} \; ; \quad v_c = -\sum_i \frac{\Gamma_i}{2\pi} \frac{x - x_i}{|\mathbf{x} - \mathbf{y}_\mathbf{i}|^2} \tag{3}$$

The diffusion velocity $\mathbf{u}_d=(u_d,v_d)$ of a free vortex at $\mathbf{x}(x,y)$ was computed using the diffusion velocity method proposed by Ogami and Akamatsu [2] as follows.

$$u_d = -\frac{\nu}{\omega}\frac{\partial \omega}{\partial x} \; ; \quad v_d = -\frac{\nu}{\omega}\frac{\partial \omega}{\partial y} \tag{4}$$

$$\omega = \sum_i \exp\left[-\frac{(x - x_i)^2 + (y - y_i)^2}{\sigma_i^2}\right]\frac{\Gamma_i}{\pi\sigma_i^2} \tag{5}$$

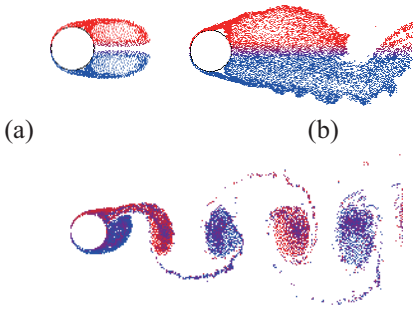

(a) (b)

(c)

Fig. 2 The distribution of free vortices

where ω is the vorticity at $\mathbf{x}(x,y)$ and $\mathbf{x}_i(x_i,y_i)$, Γ_i, σ_i are the position, strength, the core radius of the i^{th} vortex, respectively. Furthermore, it is assumed that the vortex core can be describe using a Gaussian distribution.

Fig. 2 shows the distribution of free vortices with respect to the different dimensionless time $t^* = U \times t/D$. At time ($t^*=0$), there is no free vortex created at the surface of the cylinder. Fig. 2(a) shows that when ($t^*>0$), free vortices are generated and moved by the convection and diffusion velocity. This movement of free vortices creates two initial symmetrical vortex blobs on the upper and lower sides of the cylinder. Fig. 2(b) indicates that when t^* increases the symmetry of these blobs disappears and new blobs are alternately formed and shed into the wake. As a result, the Karman vortex street is formed behind the cylinder as shown in Fig. 2 (c).

2.2. Acoustic-Field Calculation

Howe [1] simplified Lighthill's equation to obtain an equation that governs the production of sound for an incompressible flow at a low Mach number as follows.

$$\left(\frac{1}{c_0^2}\frac{\partial^2}{\partial t^2}-\nabla^2\right)B=\nabla.(\boldsymbol{\omega}\times\mathbf{u})\,;\quad B\equiv\frac{p}{\rho_0}+\frac{1}{2}|\mathbf{u}|^2 \tag{6}$$

where c_0 is the sound velocity; B is the total enthalpy; p is the pressure; ρ_0 is the density of the fluid; and $\mathbf{u}$ is velocity vector.

Since the position of the observer $\mathbf{x}$ is in the far field, the compact condition that the characteristic length of the source region is small compared to the wavelength of sound is applied and the compact Green's function for the wave equation can be given by.

$$\begin{aligned}G(\mathbf{x},\mathbf{y},t-\tau)&=\frac{1}{4\pi|\mathbf{x}-\mathbf{Y}|}\delta\left(t-\tau-\frac{|\mathbf{x}-\mathbf{Y}|}{c_0}\right)\\&=\frac{1}{4\pi|\mathbf{x}|}\delta\left(t-\tau-\frac{|\mathbf{x}|}{c_0}\right)+\frac{x_jY_j}{4\pi c_0|\mathbf{x}|^2}\delta'\left(t-\tau-\frac{|\mathbf{x}|}{c_0}\right)\end{aligned} \tag{7}$$

Here Y_j are the components of the Kirchhoff vector Y which represent the velocity potentials around the body of an imaginary flow with unit speed in the j direction are given as follows.

$$\phi_x=Y_1=x-\sum_{i=1}^{N}\frac{\Gamma_{Bi}^x}{2\pi}\theta_i\,;\quad \phi_y=Y_2=y-\sum_{i=1}^{N}\frac{\Gamma_{Bi}^y}{2\pi}\theta_i \tag{8}$$

where θ_i is the argument of $(z\text{-}z_i)$; $z=z(x,y)$; Γ_{Bi}^x and Γ_{Bi}^y are the strengths of bound vortices for the flow in the x and y directions which are obtained using the panel method.

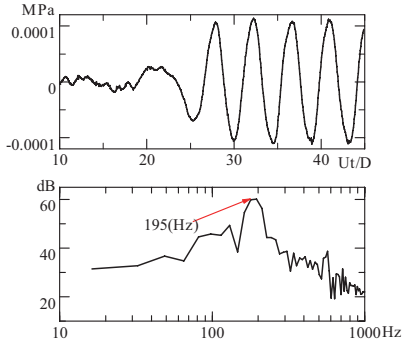

Fig. 3 The acoustic pressure and the sound pressure level at x (0,2m,0)

Green's theorem yields the sound pressure at $\mathbf{x}$ caused by a source of sound at $\mathbf{y}$ in the present of solid body as follows.

$$\begin{aligned}p(\mathbf{x},t)&=-\rho_0\int_V(\boldsymbol{\omega}\times\mathbf{u})(\mathbf{y},\tau).\nabla G(\mathbf{x},\mathbf{y},t-\tau)d^3y d\tau\\&=-\frac{\rho_0 x_j}{4\pi c_0|\mathbf{x}|^2}\frac{\partial}{\partial t}\int_V(\boldsymbol{\omega}\times\mathbf{u})(\mathbf{y},t-\frac{|\mathbf{x}|}{c_0}).\nabla Y_j d^3y\end{aligned} \tag{9}$$

where $\mathbf{u}(u,v)$ is the velocity vector of a free vortex placed at $\mathbf{y}(x,y)$.

The parameters of the flow used in this simulation were chosen as follows: Reynolds number Re =1.1×10^5; the stream velocity U=41.27m/s; the diameter of cylinder D=0.05m and the observer at $\mathbf{x}$ (0,2m,0) in order to compare our result with those of Takaishi [5]. In this simulation, the acoustic pressure was computed by combining Eq. (9) and the sources of sound obtained from the flow-field calculation for a previous section.

Fig. 3 shows that the maximum SPL of 65 Hz is at a frequency of f =195 Hz corresponding to the Strouhal number of St = 0.23. Hence, we found that the sound generated by the fluid flow over a circular cylinder is dominated by the vortex shedding frequency.

3. Conclusion

In this study, the discrete vortex method was used to simulate the sound generated by an incompressible flow over a circular cylinder at a low Mach number. The results obtained by our simulation agreed with the results of previous studies. The Karman vortex street phenomenon was observed in the wake of the cylinder and the sound emitted from the circular cylinder is dominated by the vortex shedding frequency.

References

[1] M.S Howe, Cambridge University Press, ISBN 978-0-521-01223-2, 2003.
[2] Y. Ogami and T. Akamatsu, Computers & Fluids, Vol. 19, No. 3/4, pp. 433-441, 1991.
[3] Y. Ogami and S. Akishita, Fluid Dyn. Res. **42**, 015009, 2010.
[4] T. Takaishi, M. Ikeda and C. Kato, J. Acoust. Soc. Am. 116 (3), September 2004.
[5] T. Takaishi, M. Miyazawa and C. Kato, J. Acoust. Soc. Am. 121 (3), March 2007.
[6] J. C. Hardin and S. L. Lamkin, AIAA J. 22-1, 51-57,1984.

Agglomeration and Crack Propagation Observed through Evaporation of Nano Silica Colloidal Droplets

Apratim Sanyal[1], Unnikrishnan P K[2], Saptarshi Basu[3], Swetaprovo Chaudhuri[4]
[1,2,3] Department of Mechanical Engineering, Indian Institute of Science, Bangalore
[4]Department of Aerospace Engineering, Indian Institute of Science, Bangalore
sbasu@mecheng.iisc.ernet.in.

ABSTRACT

Drops of nano silica aqueous solution have been evaporated and the agglomerate structures have been studied. A deviation from the well known coffee ring structure has been observed as the agglomerate structure is seen to extend upto the drop centre. Apart from this, radial cracks have been observed for lower concentrations and both radial and circumferential cracks for higher concentrations. The primary reason for these patterns is the size of the nano particles as opposed to micron sized particles, the latter being one of the primary reasons for the coffee ring.

1. Introduction

Deposition of agglomerates from evaporating colloidal solution is being studied extensively for its applications in material processing, spray paintings etc. One of the most important observation in this regard has been the coffee ring [1]. An evaporating coffee drop leaves most of the solute as a ring-like deposit at the initial drop periphery and it was shown to occur through outward radial capillary flow. This observation however has been valid mostly for micro particle colloids. Some alternate structures have been reported for nano particle colloids. For example Crivoi and Duan [2] observed branched-like agglomeration with copper nano particles. Jing and Ma [3] have reported the formation of circular and radial crack patterns in drop evaporation of nano silica colloidal solution. What is common to these observations with nano particles is the propagation of these particular structures all the way to the centre of the drying drop and this feature sets it apart from the coffee ring pattern. What we have studied in this current work is the reason for the propagation of the agglomerate structure to the drop centre.

2. Method

Drops of HS40 nano silica colloidal solutions of volume 0.1 µl are dispensed on to clean glass slides and are allowed to evaporate at room temperature. The drying process is recorded using a high speed camera. Various concentrations have been used to observe the variation in the agglomerate structure.

3. Results and Discussion

A distinct observation is the decrease in the number of cracks with increase in concentration of nano silica particles. The pinned contact line is where the evaporation rate is highest. As a result agglomeration initiates from the contact line. Since the contact line is pinned, reduction of the wetted area of the drop becomes impossible. Earlier explanation [1] state that to compensate for the evaporative flux, capillary flow from the drop centre to the periphery is setup. However a current is setup inside the drop and the low inertia of the nano particles allows their transport back to the droplet centre. As the evaporation front (air-water interface) recedes the evaporative flux from the periphery goes up but the agglomeration time scale comes down leading to the rapid formation of the structure towards the centre. With the recession of the evaporating front, the non wetted portion of the deposit comes of the glass surface. The strong inward capillary flow along with the shrinkage of the solid agglomerate induce radial and circumferential stress which lead to crack propagation.

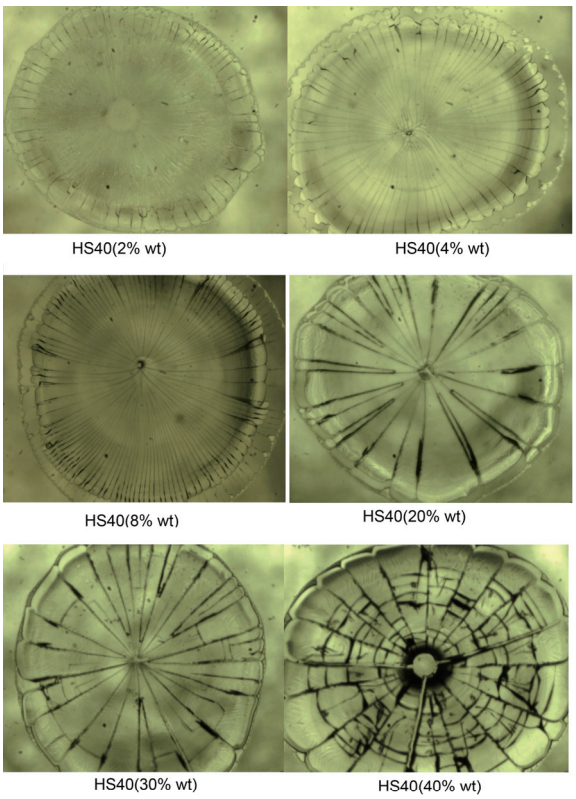

Fig. 1 Final agglomerate structure for various nanosilica concentrations

4. Concluding remarks

The deviation from coffee ring pattern has been observed in evaporating aqueous colloidal solutions having nano particles as the suspension. Instead of majority of the deposition being on the periphery, the agglomerate has been seen to spread to centre. The

reason for this has been identified as the size of the nano particles. The vertical current setup due to the evaporative flux from the droplet cause easier transport of the low inertia particles to the centre leading to a radial structure. Shrinkage of the agglomerates and strong inward capillary flow lead to radial and circumferential cracks and due to the silica particle concentration variation in the number of cracks is seen with varying percentage of solute.

References

[1] R. D. Deegan, O. Bakajin, T.F. Dupont, G. Huber, S. R. Nagel, T.A. Witten, Nature, 389(6653)(1997),827-829.
[2] A. Crivoi, F. Duan. The Journal of Physical Chemistry C 117.15 (2013), 7835-7843.
[3] J. Guangyin, J. Ma. The Journal of Physical Chemistry B 116.21 (2012), 6225-6231.

Tenth International Conference on Flow Dynamics
November 25-27, 2013, Sendai, Miyagi, Japan

Surface Termination Effect on Structure of Decane Liquid in the Vicinity of α-Quartz Surfaces

Hari Krishna Chilukoti[1], Gota Kikugawa[2], Taku Ohara[2]
[1]Graduate School of Engineering, Tohoku University, Japan
[2]Institute of Fluid Science, Tohoku University, Japan
E-mail of corresponding author: chilukoti@microheat.ifs.tohoku.ac.jp.

ABSTRACT

Effect of surface termination group on the structure of liquid decane in the vicinity of the α-quartz substrate terminated with -H and -OH groups to create hydrophobic and hydrophilic surfaces for (001) and (100) crystal planes has been investigated using molecular dynamics (MD) simulations. Layering of decane liquid molecules in the vicinity of the solid wall is not significantly changing with type of termination group for a given crystal plane. Portions of decane liquid molecules are entered into H-terminated side with the molecular orientation in the parallel direction and in the perpendicular direction into the OH-terminated side for (100) crystal plane.

1. Introduction

Examination of liquids adjacent to solid surfaces plays an important role in lubrication, wetting, heterogeneous catalysis, corrosion, and surface modification in a variety of industrial processes. For a wide range of above applications, molecular level understanding of interfaces is important. Molecules show a unique behavior close to interfaces which is different from that in a bulk region. This is related to the difference in interaction between the molecules in the bulk liquid and in the interface region. Structure of liquids close to solid surfaces have great influences on solid-liquid interfacial transport phenomena such as heat and mass transfer.

Silica is an abundantly available compound in the form of α-quartz. Due to its industrial applications α-quartz was extensively studied by many researchers at the molecular level using MD simulations. Liquid alkanes have many industrial applications like lubrication and coating. Interfaces involving alkane and silica substrate attract scientific and engineering interest. For example, study of structural and transport phenomena of alkanes in the vicinity of silica surfaces have applications in the oil production industry and MEMS. Terminations of silica surfaces that are utilized in industry frequently have been simulated in the present study and structure of liquid decane, a typical linear alkane, have been examined. Influence of termination group was studied by comparing the structural quantities near the surface terminations.

2. Simulation Details

To examine the structure of liquid decane in the vicinity of α-quartz surfaces we have performed the MD simulations. In the present work, we modeled the α-quartz wall using the force field of Lopes et al. [1]. The NERD force field [2] parameters were used for decane liquid. Lopes et al. [1] force field is compatible with NERD force field to build the system of α-quartz solid and alkane liquid. The LJ interactions were truncated with a cut-off radius of 16.0 Å.

Periodic boundary conditions were applied in three spatial directions. Computational system consists of a pair of α-quartz solid walls and decane liquid is sandwiched between solid walls. The α-quartz solid wall was created in such a way that required crystal plane was perpendicular to the z-axis. The surface of the left wall was terminated by -OH (silanol) and the right wall by -H (silane), which gives hydrophilic and hydrophobic characteristics, respectively. Initially, liquid density of decane at a given temperature was calculated from bulk liquid simulations. Next, initial configuration was created by placing the required number of molecules randomly in between the two α-quartz solid walls so as to have the saturated liquid pressure in the direction normal to the film. After that, the system temperature was gradually raised to the required temperature and then simulations were performed in the NVT ensemble where the temperature was maintained at constant using Nosé-Hoover thermostat. Equilibrium averages were collected for about 3 ns.

3. Results and Discussion

Structural quantities of decane liquid were obtained after the system reached equilibrium. The density profiles were examined to get a basic insight into the structure in the interface region. Density profiles for liquid decane at 345.6 K near the hydroxylated and hydrogenated surfaces for (001) and (100) crystal planes are shown in Figure 1. As expected, density profiles for all alkane liquids exhibit oscillatory nature in the vicinity of the solid walls. The oscillations in the density

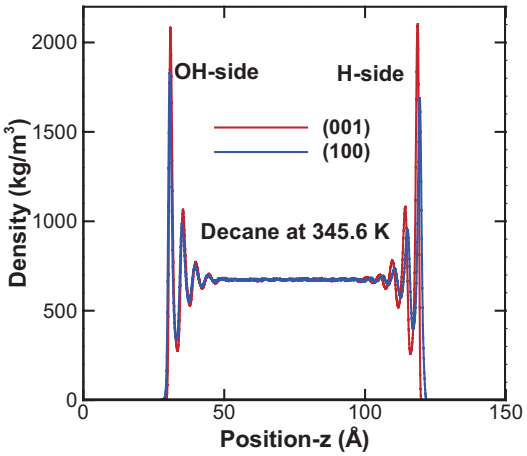

Fig.1. Density profiles for decane at 345.6 K

profile indicate layering of liquid molecules at the interface. For all density profiles oscillations disappear after some distance away from the wall and show a flat region which indicates the bulk liquid region which is free from the influence of solid surfaces. Figure 1 illustrates that for decane, layering caused by the wall disappears approximately at the same distance away from the wall irrespective of the surface termination type and crystal plane. For decane maximum density in the adsorption layer depends on the surface termination type for a particular crystal plane.

Table 1 shows the penetration depths of liquid decane into the solid wall for two crystal planes. Penetration depth is defined as the distance to which liquid molecules reach from the average surface layer of atoms. Maximum density of the liquid entered into the wall was indicated in the bracket. It is observed from the table that for (001) crystal plane more number of liquid molecules intrude into the OH-terminated side than the H-terminated side and opposite for (100) crystal plane. This might be because of different surface termination shapes of the crystal planes. It is also observed that liquid molecules penetrate more deeply into hydrophilic surface than hydrophobic surface for a given crystal plane. opposite

Orientation order parameter can be used to quantify the effect of interface on the chain ordering. A convenient orientation order parameter is defined as follows[3].

$$P(z) = \frac{1}{2}\left\langle 3\cos^2\theta - 1 \right\rangle \qquad (1)$$

where θ is the angle between a vector connecting two carbon atoms which are two units apart in a molecule and interface normal. The average $\langle\ \rangle$ is taken over all vectors and time steps. The range of this parameter is [-0.5, 1]. A positive value indicates preferential alignment normal to the interface. Negative value indicates preferential alignment parallel to the interface. Zero indicates completely random arrangement of molecules.

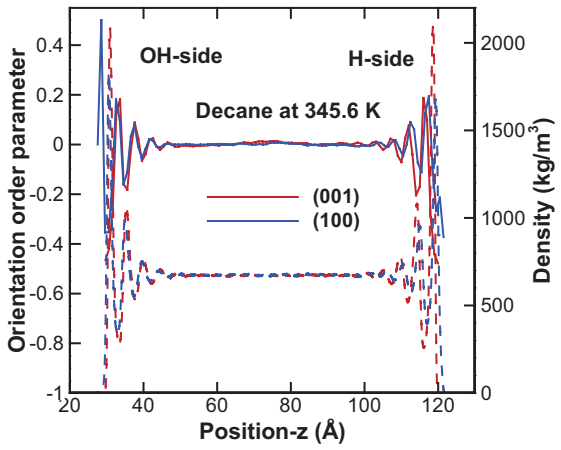

Fig.2. Orientations order distributions along z direction for decane at 345.6 K.

Table 1. Comparison of decane liquid penetration depths into the solid wall for two crystal planes. The numbers in the braket indicate the maximuam local density of liquid intruded into the solid wall.

	(001) crystal plane		(100) crystal plane	
	H- side Å (Kg/m^3)	OH- side Å (Kg/m^3)	H-side Å (Kg/m^3)	OH- side Å (Kg/m^3)
Decane	-- (--)	0.1 (0.0965)	0.9 (119.933)	2.1 (48.9242)

Variation of the Orientation order parameter along z-direction for decane was shown in Figure 2. Density profiles were also shown in the figure. According to the oscillations in the density profile, the orientation order parameter exhibits oscillations between positive and negative values. The value is negative in the layers of molecules located at the peaks of the density, while it is weakly positive between the layers. This indicates that molecules in the layer tend to lie perpendicular to the interface. The positive value between the layers is an indication of the interlayer interdigitation. The amplitude of oscillation of the orientation order parameter is the largest for the (001) surface and smallest for the (100) surface, although it is a slight difference. The difference between H-side and OH-side is very small.

A remarkable feature is observed in the inner side of the first adsorption layer for the OH-terminated side of (100) surface. The orientation order parameter exhibits large positive value. This implies that a few liquid molecules get into the solid surface structure with a perpendicular orientation and the entered portions of molecules are oriented randomly. Whereas the molecules near the H-terminated side intrude into the solid wall in the parallel direction.

4. Concluding Remarks

Structure of decane liquid in the vicinity of α-quartz crystal planes terminated with -H and -OH groups was investigate using MD simulations. It was observed that influence of crystal plane and termination type on layering of molecules is not significant. Liquid molecules penetrated more deeply into solid wall on the OH-terminated side than that on the H-terminated side. The intruded parts of alkane molecules on the OH-terminated side for (100) crystal plane are in perpendicular direction whereas the intruded parts on the H-terminated side are in parallel direction.

References

[1] P. E. M. Lopes, V. Murashov, M. Tazi, E. Demchuk, A. D. Mackerell, J. Phys. Chem. B, **110** (2005), R2782.
[2] S.K. Nath, F.A. Escobedo, J.J. De Pablo, J. Chem. Phys., **108** (1998), R9905.
[3] J.G. Harris, J. Phys. Chem., **96** (1992), R5077.

Tenth International Conference on Flow Dynamics
November 25-27, 2013, Sendai, Miyagi, Japan

Numerical Analysis of Flow-Acoustic Interaction in a Hole Tone System with a Tailpipe

Mikael A. Langthjem[1], Masami Nakano[2]
[1]Graduate School of Science and Engineering, Yamagata University
[2]Institute of Fluid Science, Tohoku University
mikael@yz.yamagata-u.ac.jp

ABSTRACT

This paper is concerned with a mathematical model of a very simple axisymmetric silencer model consisting of a hole tone system equipped with a tailpipe. The unstable shear layer is modeled via a discrete vortex approach, based on axisymmetric vortex rings. The aeroacoustic model, which is described in the present short paper, is based on the Powell-Howe theory of vortex sound. The boundary integrals, which represent the scattering by the end plates are discretized via the boundary element method. The tail pipe is represented by an exact Green' function.

1. Introduction

Expansion chambers are often used in connection with silencers in engine exhaust systems, with the aim of attenuating the energy flow. The gas flow through the chamber may however generate self-excited oscillations, thus becoming a sound generator rather than a sound attenuator. Similar geometries and thus similar problems may be found in, for example, solid propellant rocket motors and heat exchangers.

A related problem is that of flow past a rectangular cavity. This, too, has connections to a number of practical applications, such as the sunroof in an automobile, weapon and landing gear bays of aircraft, and musical instruments. Analytically, the two-dimensionality makes the problem attractive; accordingly is has been extensively studied and a large number of articles are available [1].

The present project is concerned with a mathematical model of a simple axisymmetric silencer model consisting of a expansion chamber followed by a tailpipe. The aim is to contribute to the understanding of the interaction between oscillations of the flow field and the acoustic field.

By oscillations of the flow field we mean the self-sustained oscillations of the jet shear layer. It is unstable and rolls up into a large, coherent vortex (a 'smoke-ring') which is convected downstream with the flow. It cannot pass through the hole in the downstream plate but hits the plate, where it creates a pressure disturbance. The disturbance is thrown back (with the speed of sound) to the upstream plate, where it disturbs the shear layer. This initiates the roll-up of a new coherent vortex. In this way an acoustic feedback loop is formed, making up one type of flow-acoustic interaction.

These so-called hole-tone feedback oscillations may interact with the acoustic axial and radial eigen-oscillations of the cavity and the tailpipe. It is these interactions that we seek to understand.

In the present paper we study the configuration shown in Fig. 1. This is the hole-tone feedback system equipped with a tailpipe.

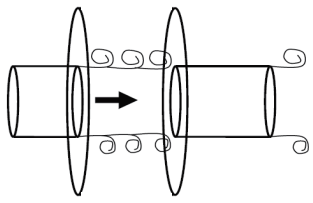

Fig. 1 The hole-tone feedback system with a tailpipe. The arrow indicates the direction of the flow.

The unstable shear layer is modeled via a discrete vortex approach, based on axisymmetric vortex rings. The aeroacoustic model is based on the Powell-Howe theory of vortex sound [1, 2]. The boundary integrals, which represent the scattering by the cavity and the tailpipe, are discretized via the boundary element method.

The present short paper gives a description of the aeroacoustic analysis. A description of the flow analysis (discrete vortex method) has been given in earlier papers [3, 4]. The geometry of the problem facilitates the use of cylindrical polar coordinates (r, θ, z), with the fluid flowing in the positive z-direction. Although it is possible that non-axisymmetric modes may be excited, we will, at this stage, consider only the axisymmetric modes (r, z).

2. Mathematical model

The flow model is based on the discrete vortex method [3]. The acoustic model is based on Howe's equation for vortex sound at low Mach numbers [1]. Let $\mathbf{u}$ denote the flow velocity, $\boldsymbol{\omega} = \nabla \times \mathbf{u}$ the vorticity, c_0 the speed of sound, and ρ the the fluid density. Then the sound pressure $p(\mathbf{x}, t)$ at the position $\mathbf{x} = (z, r)$ and time t is related to the vortex force (Lamb vector) $\mathfrak{L}(\mathbf{x}, t) = \boldsymbol{\omega}(\mathbf{x}, t) \times \mathbf{u}(\mathbf{x}, t)$ via the non-homogeneous wave equation

$$\left(\frac{1}{c_0^2} \frac{\partial^2}{\partial t^2} - \nabla^2 \right) p = \rho \nabla \cdot \mathfrak{L}.$$

This equation is solved by using the Green's function method. The boundary integrals are evaluated by applying the boundary element method. The pipe is however represented by its exact Green's function, and boundary element discretization is thus only used used for the nozzle-plate assembly.

Finally, the flow field and the acoustic field are coupled by evaluating the acoustic particle velocities via the Euler equations, and imposing them on the flow field.

3. Numerical examples

In the numerical examples to follow data have been used. The nozzle-, end plate-hole-, and pipe-diameters are all 50 mm. The mean flow speed is u_0 = 10 m/s. This gives a hole tone sound of main frequency $f_0 = 160$ Hz.

Figure 2 shows a time series for the pressure within a tail pipe of length 1063 mm, at the mid-position. Figure 3 shows the corresponding sound pressure spectrum. It is noted that the resonance frequency is coinciding with the hole tone frequency f_0 = 160 Hz. Note also that the mid-position corresponds to a nodal point for the even modes, so these will not appear in the spectrum.

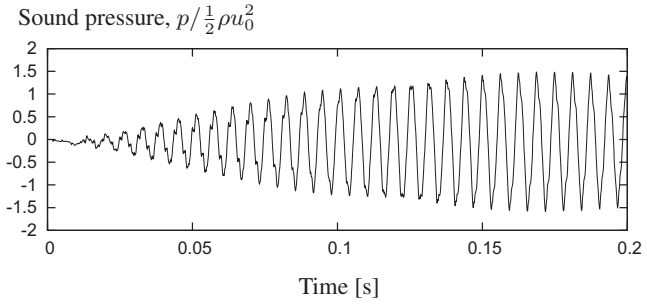

Fig. 2 Time series for the acoustic pressure in the mid-position within a tailpipe of length 1063 mm.

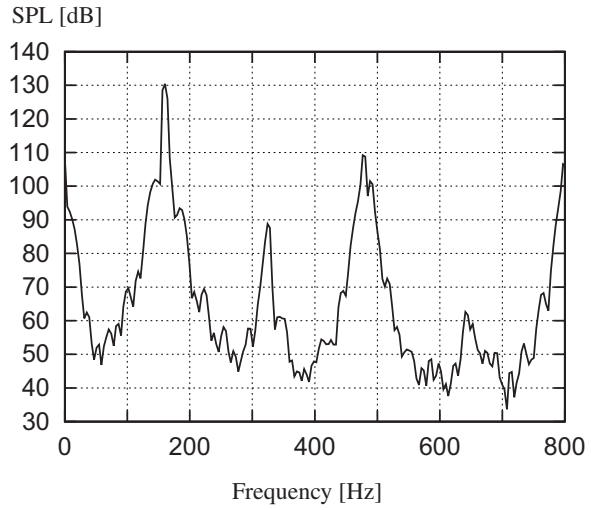

Fig. 3 The corresponding sound pressure spectrum.

Figure 4 and 5 are similar to Figs. 2 and 3, but here the pipe length is 1163 mm, a bit longer. The resonance frequency is now 146 Hz. Interaction with f_0 causes a beat phenomenon, as can be seen from Fig. 4.

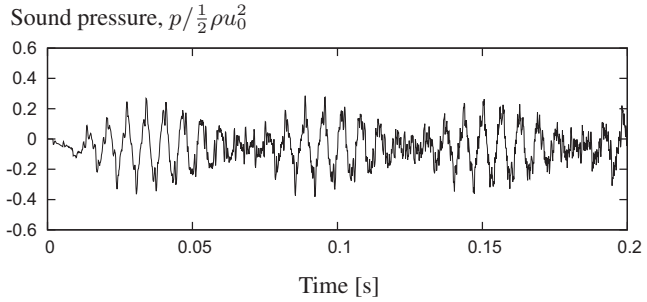

Fig. 4 As Fig. 2, but here the pipe length is 1163 mm.

As the excitation now is away from the pipe resonance frequency the sound pressure level is seen to be significantly lower.

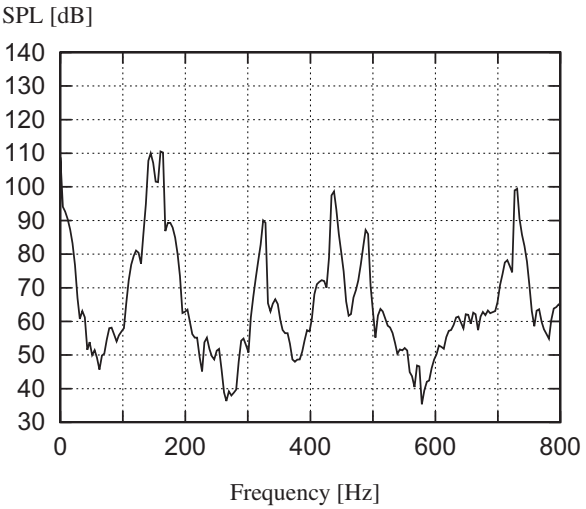

Fig. 5 The corresponding sound pressure spectrum.

3. Summary and concluding remarks

We have derived an aeroacoustic model, based on the theory of vortex sound, to evaluate the sound generation from a simple silencer model. The coupled flow-acoustic analysis includes a model of acoustic feedback. The acoustic particle velocity is coupled with the acoustic pressure through the (linearized) momentum equation. The acoustic velocity field is evaluated by integrating this equation. This velocity is then added to the 'hydrodynamic' velocity of the vortex rings, making up the acoustic feedback.

Acknowledgements. The support of the present project by the Institute of Fluid Science, Tohoku University, via a 'Collaborative Research Project 2013' grant is gratefully acknowledged.

References

[1] M. S. Howe, Acoustics of Fluid-Structure Interactions, Cambridge University Press, Cambridge, 1998.

[2] M. S. Howe, Theory of Vortex Sound, Cambridge University Press, Cambridge, 2003.

[3] M.A. Langthjem, M. Nakano, J. Sound Vibr.,**288** (2005), pp. 133-176.

[4] M.A. Langthjem, M. Nakano, Fluid Dyn. Res., **42** (2010), pp. 1-26.

Morphological Dynamics of a Liquid Drop Impacted on a Superheated Textured Surface

Visakh Vaikuntanathan[1], Sakthikumar Ramachandran [1], Sivakumar Deivandren[1], Hidemasa Takana[2], Hideya Nishiyama[2]
[1] Department of Aerospace Engineering, Indian Institute of Science, Bangalore, INDIA
[2] Institute of Fluid Sciences, Tohoku University, Sendai, JAPAN
dskumar@aero.iisc.ernet.in

ABSTRACT

High speed imaging and analysis of water drop impact on a superheated groove-textured surface, TGS3 were conducted for surface temperatures, T_s ranging from 120^{0}C to 305^{0}C and for drop Weber number, *We* ranging from 10 to 110. From 120^{0}C to 180^{0}C a transition from static to contact boiling is observed on both TGS3 and smooth surface, RS1 for all *We*. In static boiling, the boiling initiation time, t_i which decreases with *We*, is similar on both the surfaces; in contact boiling, t_i is higher on TGS3 than on RS1. At higher T_s qualitative differences are seen in drop morphological dynamics on RS1 and TGS3.

1. Introduction

The interaction of a liquid drop with a heated solid surface is of interest in practical applications such as spray cooling. The typical processes involved in drop impact dynamics on unheated smooth solid surfaces are[1]: spreading of the drop radially outward from the impact point till a maximum spread is achieved (primary spreading); receding of drop front back towards the impact point (primary receding); secondary spreading and receding events; settling down to a final equilibrium configuration on solid surface after the decay of drop liquid-vapor interfacial oscillations. Previous studies have indicated that the presence of surface roughness or texture alters the drop impact process by modifying the surface wetting[1]. Studies have explored drop morphological dynamics on heated smooth surfaces[1,2], effect of average surface roughness on critical heat flux and Leidenfrost point[3], and maximum spreading and contact boiling to Leidenfrost regime transition on post-textured[4] surfaces. The present study focuses on the effect of surface temperature on the morphological dynamics of drop impacted on a groove-textured surface in comparison with that on a smooth surface.

2. Experimental details

The experimental set-up consisted of a micrometer-syringe-needle arrangement to dispense distilled water drops, high speed video acquisition system, and plate heater with thermocouples and temperature controllers to heat (maintain) the target surfaces to (at) a desired temperature, T_s. The height of the needle tip from the target surface could be adjusted so as to vary the drop impact velocity, U_o. Two target surfaces were used: a groove-textured stainless steel surface, TGS3 and a reference smooth (R_a ~ 40 nm) stainless steel surface, RS1. The cross-sectional surface profile superimposed on the SEM top-view image of TGS3 is shown in Fig. 1 highlighting the geometry; groove top width, w = 199 μm, pillar top width, b = 35 μm, and groove depth, d = 141 μm. The experimental drop impact conditions are summarized in Table 1. At each condition, drop impact is conducted three times to ensure repeatability.

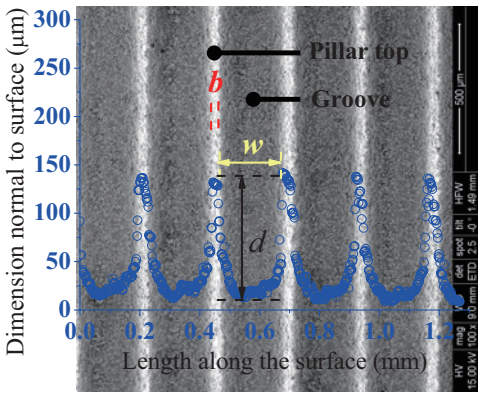

Fig. 1 Optical surface cross-sectional profile (blue circular symbols) superimposed on the top view SEM image of TGS3 highlighting the geometry of groove texture.

Table 1 Experimental drop impact conditions

T_s (^{0}C)	D_o (mm)	U_o (m/s)	$We = \rho U_o^2 D_o / \sigma$ *
120-305	2.59	0.5-1.8	10-110

* ρ and σ are density and surface tension of drop liquid

3. Results and Discussion

From visual observations of high speed images, the drop impact conditions are classified into various regimes depending on the morphological dynamics of drop impacted on target surfaces in response to heat transfer from the target surface. At T_s = 120^{0}C for all *We* on both RS1 and TGS3, it is observed that during the primary spreading and receding processes there is no significant change in drop morphology due to heat transfer from solid surface. Rapid formation of bubbles inside the drop together with continuous drop liquid-vapor interfacial perturbations are seen at a much later time when the drop is almost static on solid surface (*static boiling*). The time lapsed after drop impact when drop morphological changes indicating drop boiling are seen due to continued heat transfer from solid surface, t_i decreases with increase in *We* (squares in Fig. 2(a)). The drop morphology corresponding to t_i for the impact conditions enveloped with black dotted rectangle in Fig. 2(a) are shown in the first column of Fig. 2(b). There is

no significant difference in the drop morphologies on RS1 and TGS3 except for a slight reduction in the drop contact diameter on TGS3. This may be the reason for very similar quantitative behavior of t_i with *We* on both RS1 and TGS3 as seen in Fig. 2(a).

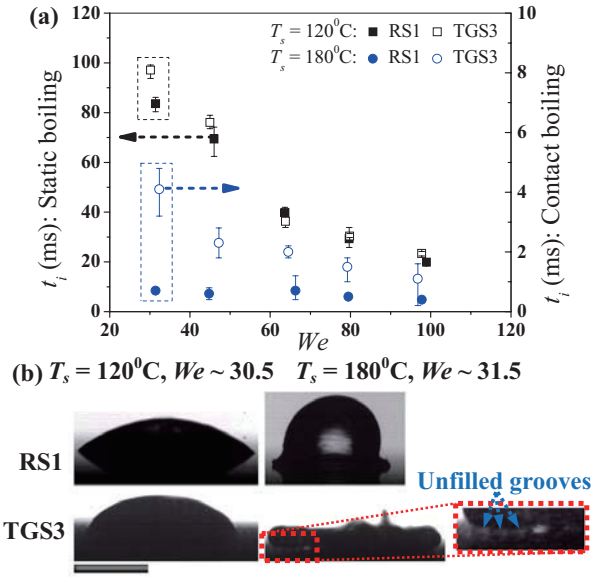

Fig. 2 (a) Variation of boiling initiation time with *We* for drop impact on RS1 and TGS3 in static and contact boiling cases, and (b) the corresponding drop morphologies for one *We*.

When the surface temperature is increased to 180^{0}C, secondary droplet ejection is observed in the initial stages of spreading (*contact boiling*; see second column in Fig. 2(b) corresponding to conditions shown in blue dotted rectangle in Fig. 2(a)). However, there is a significant difference in the drop morphology as well as t_i on RS1 and TGS3. The presence of air pockets underneath the drop away from drop impact location on TGS3 (Fig. 2(b)) leads to a less heat transfer from surface to drop through the small pillar tops thereby increasing t_i. Further, in the case of TGS3 t_i decreases with *We* whereas on RS1 it is almost constant. Boiling initiation time for contact boiling is much less than that for static boiling (Fig. 2(a)). Assuming the heat flux from surface to drop liquid to initiate boiling, q_b is constant, $q_b = h(T_s\text{-}T_o)t_i$ = constant. The convective heat transfer coefficient, h is a function of U_o and $(T_s\text{-}T_o)$ where T_o (~ 25^{0}C) is the drop temperature prior to impact. The constant is a function of drop liquid properties (density, specific heat capacity, and boiling point) which are kept constant here. Performing a simple dimensional analysis on the above relation shows that t_i is inversely proportional to $U_o(T_s\text{-}T_o)$. Hence at a given T_s, t_i decreases with U_o (or, *We*) and for a given U_o (or, *We*) it decreases with increase in T_s. This explains the trends seen in Fig. 2(a).

As T_s is increased to 240^{0}C, a clear qualitative difference in drop morphological dynamics is seen on RS1 and TGS3 (Fig. 3). On RS1, for *We* ranging from 30 to 110 the drop spreads out into a thin lamella (surrounded by thick rim) which boils and evaporates away resulting in a ring-shaped rim with undulations on it. This, further, lifts off from the surface and the undulations break into fragments (*rim fragmentation* in Fig. 3(a)). On TGS3, for the same range of *We* the grooves near the drop impact point being filled by drop liquid due to impact pressure leads to more heat transfer resulting in a central bubble which expands with continued heat transfer from surface. However the outer drop rim remains attached to the surface due to reduced heat transfer from only pillar tops. This creates a *parachute*-like structure (Fig. 3(b)) which may lift-off from the surface or rupture, resulting in many irregular fragments. The only effect of changing *We* is to change the drop dynamics stage at which fragments form.

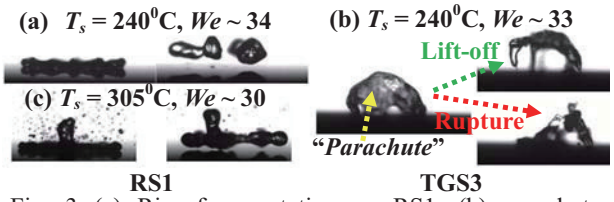

Fig. 3 (a) Rim fragmentation on RS1, (b) parachute formation and lift-off or rupture on TGS3, and (c) central liquid mass formation with rim fragmentation on RS1.

As T_s is increased to 305^{0}C, Leidenfrost drop, characterized by no apparent contact between drop and solid surface due to vapor layer formation, is observed on RS1 at *We* ~ 10; whereas on TGS3 the parachute rupture behavior is observed for *We* in the range 10-100 at T_s = 305^{0}C. On RS1, as *We* is increased beyond 10 up to 100, a central liquid mass formation with rim fragmentation is seen[2] (Fig. 3(c)) due to the rapid boiling of lamella between central downward moving drop mass and outer rim.

4. Concluding remarks

At low T_s, the drop morphological dynamics remains similar on both TGS3 and RS1 due to static boiling nature. As T_s is increased, contact boiling mode shows differences in drop morphology as well boiling initiation time (which decreases with U_o) on TGS3 and RS1. At higher T_s, different morphological dynamics is observed on RS1 and TGS3. Future studies should explore the surface texture effect on boiling initiation time.

References

[1] A. L. Yarin, Annu. Rev. Fluid Mech., **38** (2006), 159-192.
[2] G. E. Cossali, M. Marengo, and M. Santini, Exp. Thermal Fluid Sci., **29** (2005), 937-946.
[3] J. D. Bernardin, C. J. Stebbins, and I. Mudawar, Int. J. Heat Mass Transfer, **40** (1996), 73-88.
[4] T. Tran, H. J. J. Staat, A. S. Arce, T. C. Foertsch, A. van Houselt, H. J. G. E. Gardeniers, A. Prosperetti, D. Lohse, and C. Sun, Soft Matter, **9** (2013), 3272.

OS1: Discussion on Hybrid Rocket Propulsion for the Future Space Utilization Demand

Homologous Series of N-Alkanes as Hybrid Rocket Fuels

Arif Karabeyoglu
KOC University
Istanbul, Turkey
akarabeyoglu@ku.edu.tr

Abstract

The liquid layer hybrid combustion theory which was developed to predict the regression rate behavior of hybrid rocket fuels burning by forming a liquid layer on their surfaces has been improved. In the enhanced version of the theory, the regression rate equations are cast in a non-dimensional format, normalized by the classical regression rate, and a universal law for the non-dimensional regression rate has been derived. Comprehensive prediction methods for the surface temperature have been developed for the subcritical and the supercritical operating conditions for the molten fuel.

1. Introduction

The homologous series of normal alkanes is a group of fully saturated, straight chain hydrocarbons with the chemical formula C_nH_{2n+2}. Each member of the series is identified by the carbon number *n*, which ranges from 1 (methane) all the way up to High Density Polyethylene (HDPE) polymer with very large carbon numbers. The high heat of combustion (due to the high hydrogen to carbon ratio), low cost, availability and chemical inertness characteristics of n-alkanes makes them ideal fuels for combustion systems. A short list of materials that are primarily made out of n-alkanes, that are of interest in propulsion applications, are: methane (*n=1*), pentane (*n=5*), paraffin waxes (*n=16-40*), PE waxes (*n=40-300*) and HDPE polymer (*n>300*). Note that the specified ranges for the carbon numbers of the waxes is arbitrary and they are listed here to give a general idea. We would like to emphasize that a large fraction of the fast burning liquefying hybrid fuels tested to date are also either pure normal alkanes such as pentane or mixtures of n-alkanes such as paraffin waxes.

The purpose of this study is to enhance the liquid layer combustion theory such that it can be used to predict the regression rate performance of a selected fuel and apply it to the homologous series of normal alkanes [1]. We set the problem in a non-dimensional format and derive an approximate closed form solution for the non-dimensional regression rate as a function of the entrainment parameter which is an empirical relation that correlates the entrainment mass transfer to the material properties of the fuel. The surface temperature is an important variable that needs to be determined since the thermophysical properties of the fuel depends strongly on the effective temperature of the melt layer. The surface temperature is dictated by some complex physical and/or chemical phenomena depending on the critical state of the molten fuel under the operating conditions. We have derived formulas for the surface temperature for subcritical and supercritical conditions. For the subcritical case the temperature is determined by a physical process controlled by the phase change (evaporation), whereas for the supercritical case the temperature depends on the chemical process of pyrolysis.

In the next step, we studied the important property prediction methods for the normal alkanes that are needed to calculate the regression rate using the liquid layer combustion theory. Finally the theory is applied to the homologous series of n-alkanes and the theory predictions are compared to the motor test data for various paraffinic fuels.

2. Liquid Layer Combustion Theory

Due to the complexity of the problem, the modeling has been performed in three stages. In the first stage, the requirements for the formation of a melt layer on the fuel grain have been investigated. In the second stage, the linear stability of a thin melt layer under the strong shear of a gas flow has been considered. Later the linear stability results has been linked to the entrainment of liquid droplets with use of some experimental results and some semi-empirical relations developed in the nuclear engineering and film cooling literature. Eventually in the final stage, classical theory has been extended to the case of liquid droplet entrainment.

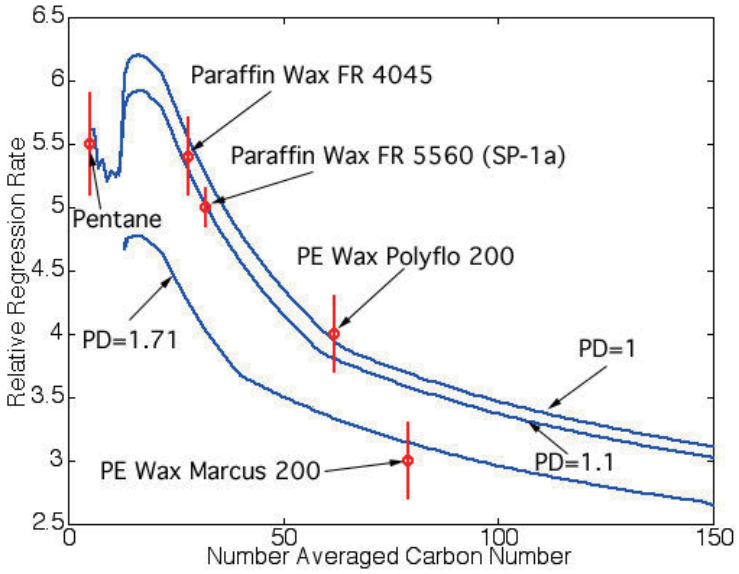

Fig. 1 The regression rates of n-alkanes with respect to the regression rate of the HDPE polymer. Three plots corresponding three different polydipersity values have been produced. The experimental regression rate data for various paraffinic fuel have also been included in the figure. (Data from Ref. 1)

3. Conclusions

The following are the conclusions of the study:

- The liquid layer combustion theory has been improved. The regression rate equations are cast in a non-dimensional format. A non-dimensional universal regression rate law has been developed for liquefying fuels that are characterized by entrainment mass transfer along with vaporization mass transfer. It turns out that the mass flux exponent for the entrainment part of the regression rate is slightly higher than the classical flux exponent, and the length exponent for the entrainment component is approximately zero. Note that the classical theory predicts a negative length exponent of -0.2. The lack of significant dependency on the grain length is in agreement with the results of motor tests conducted at different scales.
- The surface temperature has been estimated for the subcritical and also for the supercritical operating conditions. Even though a large jump in the surface temperature has been observed at the critical carbon number for which the transition takes place, the regression rate prediction is a relatively smooth function of the carbon number. In the supercritical region the effect of chamber pressure on the regression rate is determined to be negligible. This observation is also in very good agreement with the experimental results.
- The improved liquid layer theory has been applied to the homologous series of normal alkanes. The predicted regression rates agree well with the motor test data obtained from several paraffinic fuel formulations covering a wide range of carbon numbers: liquid pentane, paraffin wax 4550, paraffin wax 5560, PE wax Polyflo 200, PE wax Marcus 200 and HDPE polymer. The good agreement between the theory and the test results over a wide range of carbon numbers indicates that the implemented entrainment scaling law is reasonably accurate (see Figure 1). It has also been determined that, especially in the supercritical operation regime, viscosity is the most important variable that dictates the regression rate behavior of a fuel system. Another important outcome of the theory is that the narrow cut mixtures of n-alkanes are most suitable as hybrid rocket fuels, since they present the fastest burning rate for a specified melting temperature.
- The results of this paper show that, for most applications, the paraffin waxes have the best properties as hybrid rocket fuels among the series of n-alkanes due to their fast regression rates at relatively high melting temperatures.
- The theory can easily be applied to the other homologous series such as normal alcohols or normal acids. We believe that the regression rate characteristics for the heavy members of these series will be quite similar to that of the series of n-alkanes since, as the carbon number increases, most properties for different homologous series converge.

References

[1] Karabeyoglu A., Cantwell B. and Stevens J. AIAA/SAE/ASME/ ASEE 41th Joint Propulsion Conference and Exhibit, Tucson, AZ, AIAA Paper No. 2005-3908, July 2005.

Tenth International Conference on Flow Dynamics
November 25-27, 2013, Sendai, Miyagi, Japan

Investigation of different Hybrid Rocket Fuels in a 2D Slab Burner with Optical Techniques

Mario Kobald and Stefan Schlechtriem.
DLR - Institute of Space Propulsion, 74239 Hardthausen, Germany.
Mario.Kobald@dlr.de

ABSTRACT

The combustion behavior of hybrid rocket fuels has been analyzed with high speed video data measurements. Tests have been performed with gaseous oxygen (GOX) as oxidizer in a 2D slab burner with windows on two sides. High regression rate paraffin-based fuels have been tested as well as conventional polymeric fuels like high density polyethylene (HDPE). For the paraffin-based fuels the flame showed wave like behavior. The appearance and dimension of the wave like flames on the surface is related with the inlet configuration of the combustion chamber in front of the fuel.

1. Introduction

The interest in hybrid rocket engines is increasing every year which can be seen in an increasing number of publications during the last years [1]. Hybrid rocket engines do have certain advantages compared to classical solid or liquid propellant rocket engines. They are known to be inherently safe. Considering storage and handling they have zero TNT-equivalent compared to solid propellants. This in combination with their throttling capability makes them attractive for certain applications. Paraffin-based hybrid rocket fuels offer the advantage of a liquid film layer on top of the fuel surface during combustion. Film instabilities induced from the oxidizer gas flow generate a higher fuel mass flow rate by liquid droplet entrainment [2, 3]. This results in a 3-5 times higher fuel mass flow rate compared to conventional fuels.

A limited number of optical tests have been done previously to determine the combustion behavior of liquefying hybrid rocket fuels [4, 5]. Some tests also showed droplet entrainment but no relations to the physical properties of the fuels like viscosity or surface tension could be made.

2. Test campaign

4 different paraffin based fuels from the supplier Sasol Wax have been investigated during the tests; they are listed in table 1. As conventional, non-liquefying fuel, a HDPE sample was used as a reference. A detailed description of the experimental setup can be seen in reference [6, 7].

Table 1. Paraffin based fuel samples

Sasol wax Type	Congealing point [°C]	Viscosity [mm^2/s]
6003	60-62	-
6805	66-70	6-8
0907	83-94	14-18
1276	64-68	880-920

These paraffin waxes have been tested in pure form and also mixed with 2% carbon black (CB) and 10% stearic acid (SA). The reason they have been chosen is due to their different viscosity values. The liquid fuel viscosity is expected to have the biggest influence on the entrainment. For that reason a detailed analysis of the viscous behavior of the different fuels has been done previously [6]. The burning rate tests are done at atmospheric pressure due to the restrictions of the combustion chamber. Ignition is done via a GOX/ gaseous hydrogen torch igniter from the bottom of the chamber which is fired for 0.5 s.

In a first test campaign these fuels have been burned in a configuration with a rearward facing step before the fuel grain [7]. This setup was originally designed to provide flame holding for ramjet applications. Results of these tests showed that droplet entrainment was visible for the low viscosity paraffin samples 6003, 6805 and 0907. An example for that entrainment process is shown in figure 1 for type 0907. Type 1276 showed almost no entrainment. This is obvious also in the measured regression rates that are listed in table 2. These results show that entrainment and regression rate increase for decreasing paraffin fuel liquid layer viscosity.

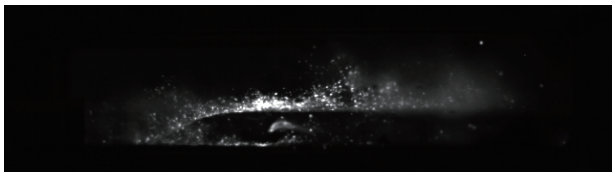

Fig. 1 Test 151, Sasol 0907, t=0.4348 s, rearward step

A wave like flame structure appears on the surface for all paraffin fuel samples. The waves originate periodically from the front end of the fuel grain. These waves are shown in figure 2. Here fewer droplets are seen, mainly because the flame is now fully burning about 2 s after ignition and the flame becomes so bright that it is not possible to achieve better resolution with the current camera settings.

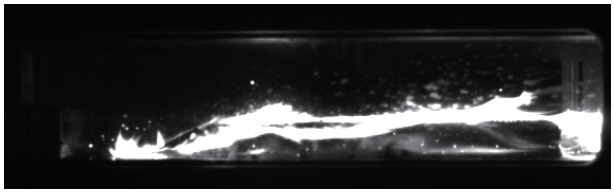

Fig. 2 Test 151, 0907, t=2.102 s, rearward step

From optical analysis it seemed that these large scale structures were released from the recirculation zone after the rearward facing step. Thus in the next test series the step was removed to evaluate its effect on the combustion behavior.

Figure 3 shows test 154 of type 0907+CB+SA without the step. A lot of droplets can be seen which is similar to tests with the step. The differences are the wavelength of the flames on the surface and their amplitude. The time between two waves is shorter and they seem to appear more randomly in this configuration.

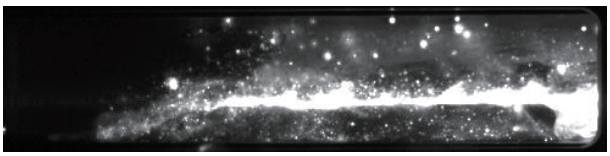

Fig. 3 Test 154, Sasol 0907+CB+SA, t=0.6866s, no step

Figure 4 shows the same test at the time of 2.131 s where the operating conditions are steady-state. Here more droplets can be seen compared to figure 2, because the settings of the camera have been changed slightly.

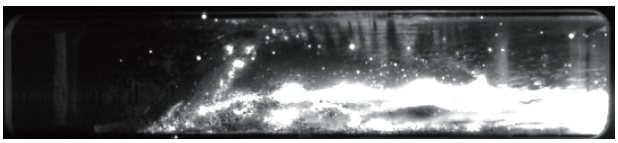

Fig. 4 Test 154, 0907+CB+SA, t=2.131 s, no step

A test with HDPE can be seen in figure 5. Here the flame is smaller which is expected due to the lower burning rate. HDPE is also expected to form a liquid layer but the viscosity is too high for entrainment. No droplets were visible during the tests. Some small waves seem to appear on the surface but they are much smaller in amplitude compared to the paraffin samples.

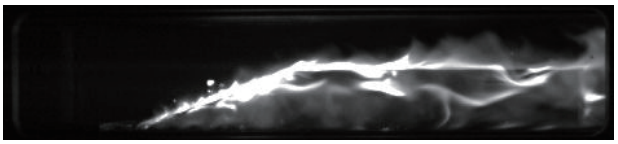

Fig. 5 Test 159, HDPE, t=0.1778 s, no step

Results of the measure regression rates are shown in table 2. An increasing burning rate is observed for a decreasing liquid layer viscosity. This is also in agreement with the optical analysis. There it could be seen that the fuel 1276 with the highest viscosity showed almost no droplet entrainment. This implies that there exists an upper limit for the viscosity of paraffin-based fuels, above which the entrainment mass flow is strongly reduced. The non-liquefying fuel HDPE has a very low average regression rate although the average oxidizer mass flux is higher than for the paraffin tests. The regression rate is about 10 times lower than the fastest burning paraffin type 6003.

Table 2. Fuel regression rates

Sasol wax type	Oxidizer mass flux [g/cm^{2}s]	Regression rate [mm/s]
6003+CB+SA	0.74	0.204
6805+CB+SA	0.74	0.173
0907+CB+SA	0.73	0.154
1276+CB+SA	0.77	0.07
HDPE	2.34	0.02

3. Conclusions

During the tests good flame holding and stable combustion was observed for the rearward facing step as well as for the configuration without step. The flame stays attached at the front end of the fuel grain for the whole burn time. Considering the entrainment process no big changes had been measured during the ignition phase between the configuration with and without rearward facing step. For both cases lots of droplets are visible. But the number and amplitude of the wave like flames changed. With the step, these waves seem to originate from the recirculation zone. They appear with the frequency of that recirculation. Without the step, more waves appear and they become smaller, and somewhat more random.

The values of the liquid layer viscosities are the main difference between the fuels. This affects the droplet entrainment process during combustion and also the regression rates of the fuels. Entrainment and regression rate increase for decreasing fuel liquid layer viscosity.

4. Acknowledgements

The support of the M11 team and the department of propellants is greatly acknowledged.

References

[1] T. Shimada, 9th ICFD, **OS3** (2012).
[2] M. A. Karabeyoglu, D. Altman and B. J. Cantwell, JPP, **vol. 18, no. 3**, (2002), pp. 610–620.
[3] M. A. Karabeyoglu and B. J. Cantwell, JPP, **vol. 18, no. 3**, (2002), pp. 621–630.
[4] I. Nakagawa and S. Hikone, JPP, **vol. 27, no. 6**, (2011), pp. 1276–1279.
[5] A. Chandler, E. Jens, B. J. Cantwell and S. G. Hubbard, 48th AIAA/ASME/SAE/ASEE Joint Propulsion Conference and Exhibit, AIAA 2012-396, (2012).
[6] M. Kobald, E. Toson, H. Ciezki, S. Schlechtriem, S. di Betta, M. Coppola and L. T. De Luca, 5th EUCASS, (2013).
[7] M. Kobald, H. Ciezki and S. Schlechtriem, 49th AIAA/ASME/SAE/ASEE Joint Propulsion Conference and Exhibit, AIAA 2013-3894, (2013).

Investigation of Heat Transfer Mechanism in Solid Fuel – Impinging Oxidizer Jet Diffusion Flame near Stagnation Region

Ken Terakawa[1], Harunori Nagata[1], Tatsuya Saito[1]
1:Hokkaido University Laboratory of Space Systems
nagata@eng.hokudai.ac.jp, k.terakawa@frontier.hokudai.ac.jp

ABSTRACT

A combination of impinging oxidizer jet and solid fuel can be used to create an opposed flow diffusion flame, with applications such as high thrust hybrid rocket motors. In this study, the fuel regression rate for varying oxidizer pressure and Reynolds number was experimentally obtained. Results suggest that under stable combustion, the regression rate can be predicted according to the Reynolds number. A hypothesis for explaining the effect of combustion pressure is also proposed but not quantitatively verified.

1. Introduction

An opposed flow diffusion flame can be created with a solid fuel and gas/liquid oxidizer, using the heat from the flame to vaporize the solid fuel. While similar to a flame spread situation, it is difficult to determine the fuel regression rate since the fuel is provided by the heat from the flame. Previous studies [1] indicate dependencies on oxidizer flow rate, oxidizer ratio and combustion pressure. In this study, experiments were conducted to measure the regression rate under varying O2 mixture ratio, oxidizer flow rate, fuel scale, and combustion pressure. Results were nondimensionalized for comparison amongst different experiment series.

2. Experiment Method

A combustion chamber with variable nozzle width, O2 ratio, oxidizer flow rate and combustion pressure was used to conduct the experiments. A plastic fuel grain is placed directly beneath the nozzle and oxidizer is fed through the nozzle. Combustion is initiated by a Kanthal heat wire, and terminated by purging the chamber with nitrogen gas. The nozzle is replaceable to accept either a cylindrical quasi-one dimensional nozzle or two dimensional slit nozzle of 0.2-4.0mm width. Two types of fuel, Polyethylene and PMMA were used. Pressure senors measure the inlet oxidizer and exhaust pressure. N type thermocouples measure the exhaust gas temperature. The entire chamber and fuel is sandwiched between two 10mm thick VYCOL glass windows, allowing observation by a video camera. For filming the flame, a 430nm±10nm band pass filter is used.

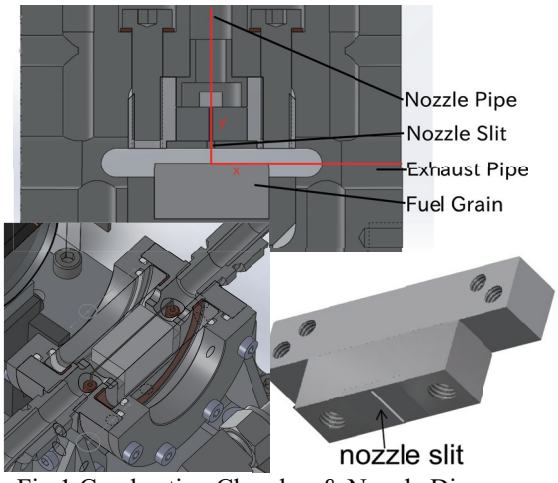

Fig.1 Combustion Chamber & Nozzle Diagram

After combustion, the fuel grain is removed and measured by laser to obtain the surface regression rate. The surface regression rate is nondimensionalized according to Eq.(1) under the premise that the y axis oxidizer velocity gradient a in the vicinity of the fuel surface is proportional to the nozzle exit velocity U_o [2] .This was confirmed in advance by computational analysis. Through dimensional analysis, the "Surface Damkohler number" Ds and "Gas phase Damkohler number" Dd will be defined by Eq.(2) and Eq.(3) respectively. The surface Damkohler number [3] can be interpreted as being the rate of of reaction in which the fuel is heated and evaporates, and is a function of Reynolds number and pressure. The Gas phase Damkohler number [4] is defined using a flame temperature with equilibrium dissociation taken into account, and can be considered as the ratio of diffusion layer thickness to reaction zone thickness. Note that τ_{conv} is proportional to $1/a$ and τ_{chem} is proportional to $\sqrt{p/\rho}$.

$$f_{wo}=\frac{U_{fuel}}{U_o(\mathrm{Re}\,Y_o/2)^{0.5}} \quad (1)$$

$$\mathrm{Ds}=\frac{k_s\exp(-E_s/\mathrm{R}\,T_s)}{(2a\nu_f)^{0.5}} \quad (2)$$

$$\mathrm{Dd}=\frac{\tau_{conv}}{\tau_{chem}}=\frac{Y_o p^{0.5} k_d \exp(-E_d/\mathrm{R}\,T_d)}{a\rho} \quad (3)$$

f_{wo}: nondimensional regression rate
Y_o: oxidizer O2 mass ratio
U_{fuel}: fuel regression y-axis velocity
Re: oxidizer Reynolds number
τ_{conv}, τ_{chem} :characteristic convection and chemical time
p, R: combustion pressure and gas constant
ρ, ν_f: gas ethylene density and kinematic viscosity
s,d: subscripts for Ds and Dd

The kinetic constants E and k are difficult to determine, and is considered to be a function of a reference temperature T_p. From first-order reaction laws, E and k are defined by Eq.(4) and Eq.(5) respectively [5].

$$E=\frac{RT_p^2}{\Delta T} \quad (4) \qquad A=\frac{2\dot{T}}{\Delta T}\exp(E/RT_p) \quad (5)$$

$\dot{T}$ =300 K/min and ΔT =80 K are reference values called heating rate and pyrolysis rage and can be regarded as constant when the fuel thickness is the same. Through measurements of fuel regression rate [1], the kinetic constants were obtained as follows. T_s=470 K, E_s= 45.92 kJ/kmol, T_d=723 K, E_d= 108.66 kJ/kmol for PE. E_s=46 kJ/kmol, E_d=142 kJ/kmol, for PMMA.

3. Results and Discussion

The method of nondimensionalization requires that the regression rate be proportional to √Re. Fig.2 shows that except for near quench and blowoff regions, this assumption is reasonably accurate for all experiments.

The nondimensional regression rate was found to be dependent on Re and Da.. Combustion pressure can be divided by O2 mass flux *Go*, to provide a comparison between constant mass flux or constant pressure case . The function of p/G_o is similar to Ds but of different dimension, and can be used conveniently to express change in oxidizer flow rate and pressure. O2 ratio and scale had no effect, and only the fuel substance influenced the nondimensional regression rate. For the same fuel, this value is expected to remain constant, about 1.1 for PMMA and 1.6 for PE. At first glance at Fig.3, the regression rate seems to decrease with an increasing Ds, however this is a near quench region with oxidizer velocities well under 1m/s, so it can be considered irrelevant of the stable region. When the Damkohler numbers decrease significantly, flame blowoff occurs. The blowoff limit differs by the type of fuel and oxidizer ratio, as well as nozzle width. Further experiments are required to verify the sensitivity of the regression rate against varying Dd or pressure.

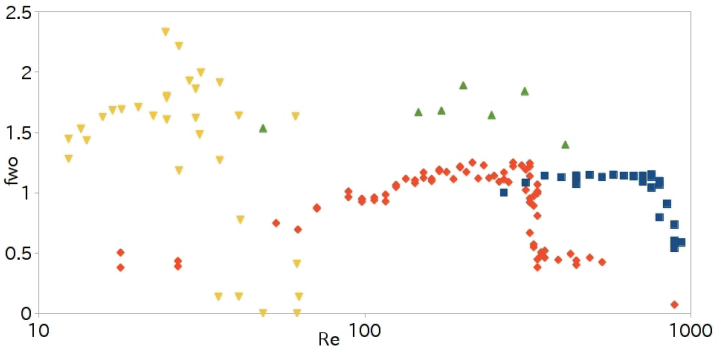

Fig.2 Re – f_{wo} plot

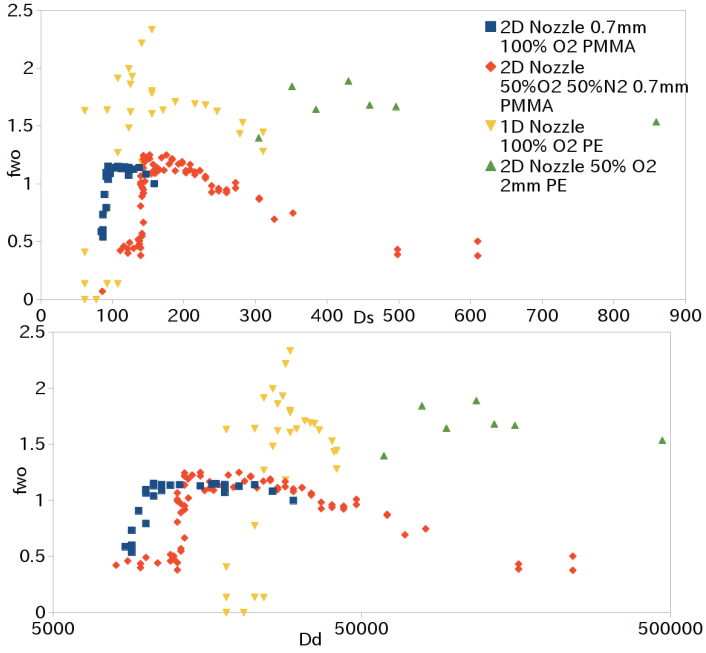

Fig.3 Ds-f_{wo} and Dd-f_{wo} plot for PE and PMMA

Although the relation of regression rate to Re is obvious [2], the sensitivity to pressure may seem unnatural. An increasing combustion pressure should accelerate the reaction process, resulting in faster regression rates; however in this case the opposite trend is observed. This can be hypothesized as a result of reaction zone thickness; the peak temperature indeed decreases at lower pressures, but the temperature distribution becomes widespread, resulting in a higher gaseous temperature at the fuel surface. Fig.4 shows two flames with varying p/G_o values photographed using a filter. A change in reaction thickness is evident.

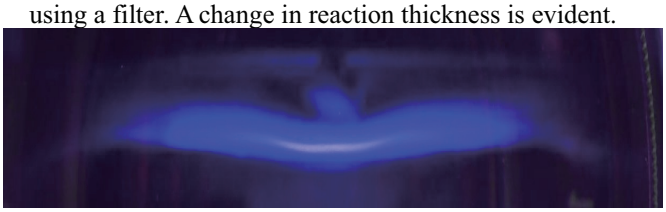

Fig.4(a) 2mm Nozzle 50%N2 1atm 2slm

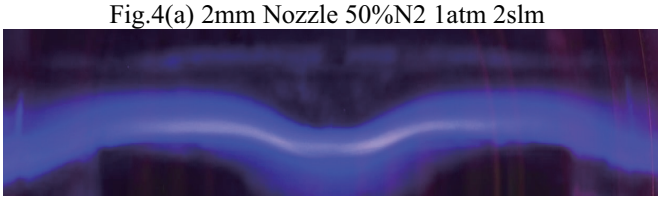

Fig.4(b) 2mm Nozzle 50%N2 1atm 3slm

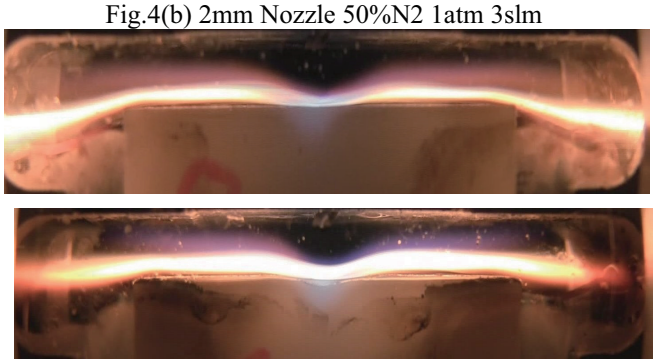

Fig.5 Similar case shown in visible light

4. Conclusions

The experiments have confirmed that the regression rate is dependent on the square root of the Reynolds number, as predicted by convection theory, and can also be affected by varying combustion pressures. Only the blowoff limit is affected by O2 ratio. It can be surmised that this is caused by a varying reaction zone thickness, but this has yet to be tested by further experiments, possibly with infrared imagery or filtering techniques.

References

[1] K.Terakawa, T.Saito, H.Nagata, 50th Japan Combustion Symposium, (2012), m163

[2] H. Tsuji, Prog. Energy Combustion, Sci. Vol.8, (1982) , Vol.8 Issue2 p.93-119

[3] K. Matsui, A. Koyama, K. Uehara, Combustion and Flame 25, (1975), Vol.25 p.57-66

[4] J.S. Wichman, F.A. Williams, I. Glassman, 19th Symposium on Combustion, (1982), Vol.19 issue1 p.835-845

[5]Homer E. Kissinger, Journal of Research of the National Bureau of Standards, (1956), 57-4 p.214

CFD Modeling of Hybrid Combustion in a Dual/Quad Vortical Combustor

Guan-Rong Lai[1], Tzu-Hao Chou[1], Jong-Sin Wu[1]*, Yen-Sen Chen[2] and Gary Cheng[3]
[1]Department of Mechanical Engineer, National Chiao Tung University, Hsinchu, Taiwan
[2]National Space Organization, Hsinchu Science Park, Hsinchu, Taiwan
[3]Department of Mechanical Engineer, University of Alabama, Birmingham, Alabama, USA
*E-mail of corresponding author: chongsin@faculty.nctu.edu.tw

ABSTRACT

In this paper, parallel CFD simulations of hybrid combustion in the very compact dual and quad vortical combustors were performed. Test conditions include different total pressures (30-60 atm), and different types of flame holders (trapezoidal and triangular). Results show that the ISP can reach up to 287 s with the total pressure in the range of 30-50 atm with acceptable fuel lean O/F ratio. In addition, the triangular flame holders perform approximately the same as the trapezoidal ones with the O/F ratio close to the stoichiometric value because of a larger area of higher combustion temperature.

1. Introduction

Hybrid rocket technology has attracted much attention lately mainly because of its safety, simplicity and possibility of thrust profiling as compared to other well-known propulsion technologies such as solid and liquid ones. Among different types of hybrid propulsion technologies, HTPB (hydroxyl-terminated polybutadiene) and nitrous oxide are considered to be a very good combination, considering its simplicity and fairly good ISP. For example, SpaceShip Two of Virgin Galatic has applied the same technology and is expected to send passengers to space for tourism in 2014. One of the key issues in this type of hybrid propulsion is how to increase its mixing for better combustion efficiency but with a compact size, which is one of the major objectives of the current study.

In recent years, we have invented a single-port design with mixing enhancer(s) [1] in which eight blades were clustered in each mixing enhancer in the port region. Results of simulation and static burn test showed that exceeding 250 s of ISP can be obtained with two mixing enhancers installed properly in series [2], which is close to the performance of most advanced solid propellants. Even though the design of single port combustion chamber is very simple, a very large aspect ratio (length to diameter) of the chamber is often required even with mixing enhancers, which is not favored in the rocket design. A compact size of combustion is indeed highly favored from a practical viewpoint.

In this paper, we intend to address this problem as mentioned in the above by proposing and numerically investigating a hybrid combustion chamber with dual/quad vortical sections for HTPB and nitrous oxide using a parallel CFD technique considering finite-rate chemistry with a real-fluid model of nitrous oxide.

2. Numerical Method

In this study, we have applied a multiphysics finite-volume CFD code, the continuity equation, the momentum equations (Navier-Stokes equations), the energy equation, the species continuity equations and the extended k-ε turbulence modeling equations [3]. They are summarized in the following in turn.

$$\frac{\partial \rho}{\partial t}+\frac{\partial}{\partial x_j}\left(\rho u_j\right)=0 \tag{1}$$

$$\frac{\partial \rho \alpha_i}{\partial t}+\frac{\partial}{\partial x_j}\left(\rho u_j \alpha_j\right)=\frac{\partial}{\partial x_j}\left[\left(\rho D+\frac{\mu_t}{\sigma_\alpha}\right)\frac{\partial \alpha_i}{\partial x_j}\right]+\omega_i \tag{2}$$

$$\frac{\partial \rho u_i}{\partial t}+\frac{\partial}{\partial x_j}\left(\rho u_j u_i\right)=-\frac{\partial p}{\partial x_i}+\frac{\partial \tau_{ij}}{\partial x_j} \tag{3}$$

$$\begin{aligned}\frac{\partial \rho H}{\partial t}+\frac{\partial}{\partial x_j}\left(\rho u_j H\right)=&\frac{\partial p}{\partial t}+Q_r+\frac{\partial}{\partial x_j}\left(\left(\frac{K}{C_p}+\frac{\mu_t}{\sigma_H}\right)\nabla H\right)\\&+\frac{\partial}{\partial x_j}\left(\left(\left(\mu+\mu_t\right)-\left(\frac{K}{C_p}+\frac{\mu_t}{\sigma_H}\right)\right)\nabla\left(V^2/2\right)\right)\\&+\frac{\partial}{\partial x_j}\left(\left(\frac{K}{C_p}+\frac{\mu_t}{\sigma_H}\right)\left(u_k\frac{\partial u_j}{\partial x_k}-\frac{2}{3}u_j\frac{\partial u_k}{\partial x_k}\right)\right)\end{aligned} \tag{4}$$

$$\frac{\partial \rho k}{\partial t}+\frac{\partial}{\partial x_j}\left(\rho u_j k\right)=\frac{\partial}{\partial x_j}\left[\left(\mu+\frac{\mu_t}{\sigma_k}\right)\frac{\partial k}{\partial x_j}\right]+\rho\left(\Pi-\varepsilon\right) \tag{5}$$

$$\frac{\partial \rho \varepsilon}{\partial t}+\frac{\partial}{\partial x_j}\left(\rho u_j \varepsilon\right)=\frac{\partial}{\partial x_j}\left[\left(\mu+\frac{\mu_t}{\sigma_\varepsilon}\right)\frac{\partial \varepsilon}{\partial x_j}\right]+\rho\frac{\varepsilon}{k}\left(C_1\Pi-C_2\varepsilon+C_3\Pi^2/\varepsilon\right) \tag{6}$$

An efficient method for treating the real-fluid equations of state and fluid properties is employed herein for liquid propellant reactive flow [4]. Convection terms of the governing equations are discretized with a second-order upwind scheme. Second-order central schemes are applied to the diffusion and source terms. For complete description of the thermal environment in the combustion chamber, a radiative heat transfer model with a finite-volume integration method [5, 6] is also employed in the present model. In the combustion chamber, the main participating species in the radiation model are carbon-dioxide and hot steam. For transient flow computations, an efficient second-order time-marching scheme, which has been validated for vortex shedding and transient start-up nozzle flows [7] is employed in the present study. These numerical models are important for high fidelity simulations of combustion physics. In addition,

3. Results and Discussion

Fig. 1 shows the schematic diagram of proposed the hybrid combustion chamber with dual vortical sections [8]. The oxidizer (nitrous oxide) are injected tangentially into the chamber in each chamber but

counter-rotationally to increase the strain rate of the flow field, which in turn improves mixing between fuel and oxidizer. Apparently, the proposed design of combustion chamber has a very impressively short aspect ratio, as compared to the single-port design with mixing enhancers. Test conditions for the CFD simulations include different total pressures (30-60 atm), and different types of flame holders (trapezoidal and triangular). Several important results are presented next.

Fig. 2 shows the temperature distribution within a dual vortical combustion chamber with trapezoidal flame holders (8 in total) with a total pressure and a total mass flow rate of 40 atm and 3.76 kg/s, respectively. The resulting thrust, chamber pressure, O/F ratio and ISP is 1,080 kgf, 31 atm, 10.3 and 287 s respectively. It is clearly that the combustion temperature is as high as 3400 K and is relatively uniform, which results in a very impressive ISP.

Table 1 summarizes the key results of simulation with various inlet total pressures with four trapezoidal flame holders. Results show that nearly the same ISP (~284-287 s) is obtained in the range of 30-60 atm, except the case of a high total pressure of 60 atm (268 s), in which the O/F ratio is too high for practical application. In addition, it also shows that we can obtain larger O/F ratio and thrust with larger upstream total pressure. This is caused by the smaller residence time at higher injection flow rate of nitrous oxide for the same chamber dimension.

Fig. 3 shows that similar simulation to Figure 2 but with triangular flame holders. Results show that a uniformly higher temperature distribution is obtained as compared to the case with trapezoidal flame holders. Resulting O/F ratio (9.3) is also closer to the stochiometric ratio (7.1), which is more favored for practical applications in rocket propulsion.

4. Conclusion

CFD simulations are performed for modeling hybrid combustion of HTPB and nitrous oxide in a dual vortical chamber in the current study. Results show that ISP close to 290 s can be obtained in the range of total pressures of 30-50 atm. In addition, hybrid combustion with triangular flame holders performs better than that with trapezoidal ones considering O/F ratio. More results will be presented in the conference.

References

[1] U.S. Patent, App. No. 2011/0203256 (2011)

[2] Chou, T.-H., Lin, J.-W., Lai, G.-R., Wu, J.-S., Chen YS and Cheng, G., 29th International Symposium on Space Technology and Science (ISTS), June 2-9, 2013.

[3] Wang, T. and Chen, YS, J. of Prop. & Power, **9** (1993), No. 5, pp. 678-685.

[4] Chen, Y. S., Chou, T. H., Gu, B. R., Wu, J. S., Wu, B., Lian, Y. Y., and Yang, L., Computers & Fluids, **45** (2011), pp. 29-36.

[5] Hainds, F. D. and Keyes, J. W.: Shock Interference in Hypersonic Flows, *AIAA J.*, **10** (1972), pp.1441-1447.

[6] Liu, J. W., Chen, Y. S., Numerical Heat Transfer, Part B, Vol. 36, pp. 115-137, 1999.

[7] Wang, T. S., AIAA Paper 2005-3942, 41st AIAA/ASME/SAE/ASEE Joint Propulsion Conference, Tucson, Arizona, 2005.

[8] Taiwan Patent, App. No. 102119323 (2013)

Table 1. Key simulation results of hybrid dual vortical combustion of HTPB and nitrous oxide with various inlet total pressures (four trapezoidal flame holders).

Total pressure (atm)	60	50	40	30
ISP (s)	268	287	287	284
Mass rate (kg/s)	7.4	4.95	3.76	2.73
O/F ratio	23.6	12.4	10.3	9.5
Thrust (kgf)	1,989	1,423	1,080	776
Comb. pressure (atm)	57.8	40.3	31	22.3

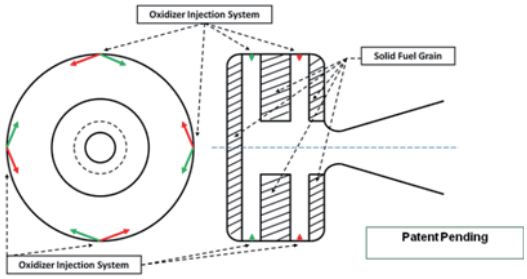

Fig. 1. Sketch for the proposed hybrid combustion chamber with dual vortical sections.

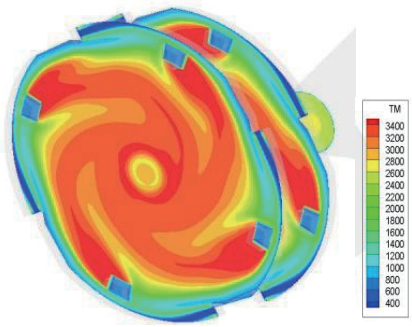

Fig. 2. Temperature distribution in the dual vortical combustion chamber (total pressure: 40 atm, total mass flow rate: 3.76 kg/s, flame holder: trapezoidal).

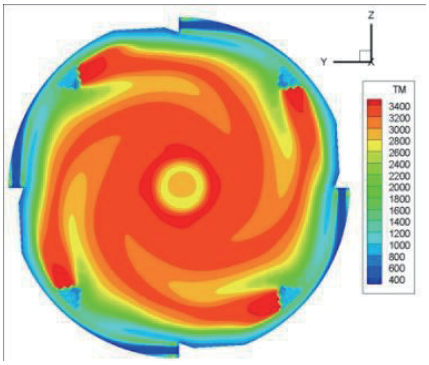

Fig. 3. Temperature distribution in the dual vortical combustion chamber (total pressure: 40 atm; total mass flow rate: 3.76 kg/s, flame holder: triangular).

Numerical Simulations of Combustive Flows in a Swirling-Oxidizer-Flow-Type Hybrid Rocket

Mikiro Motoe*, Toru Shimada**
*Department of Aeronautics and Astronautics, University of Tokyo., Bunkyo, Tokyo, Japan, 113-8656
** Institute of Space and Astronautical Science, Japan Aerospace Exploration Agency, Chuouku, Kanagawa, Japan, 252-5210
8367791179@mail.ecc.u-tokyo.ac.jp

ABSTRACT
Object of this study is to clarify details of inner state of a chamber of the Swirling-Oxidizer-Flow-Type Hybrid Rocket by means of a combustion analysis using LES with Flamelet approach. In this paper, states of the chamber that are structure of the flow field, the flame shape and so on are clarified. After that, characteristics of the chamber are discussed.

1. Introduction

A Swirling-Oxidizer-Flow-Type hybrid rocket [1] is considered as promising alternatives of next-generation hybrid rocket which has improved fuel regression rate and combustion efficiency more than before. Better understandings of details of inner states are required in order to design more sophisticated combustion chamber of hybrid rocket. Therefore, many numerical approaches have been done for the chamber of a hybrid rocket [2-4]. However, because analyses that can estimate characteristics of a Swirling-Oxidizer-Flow-Type hybrid rocket have not been enough, inner states of this type of chamber have not been cleared.

The objective of this study is to clarify inner state of combustion chamber of a Swirling-Oxidizer-Flow-Type hybrid rocket by means of turbulent and combustive analysis using LES and Flamelet approach respectively.

2. Method

In this study, multicomponent compressible Navier-Stokes equations and a transport equation of mixture fraction for Flamelet approach are defined as governing equations, and these are treated as one vector equation. In addition, because turbulent analysis is performed by LES, a spatial filter is applied to the equations.

The governing equation is spatially discretized by finite volume method, and it is temporary discretized by ADI-SGS implicit method with 2nd order dual time method. The numerical flax at cell boundary is calculated by SLAU scheme using primitive variables that are interpolated by WENO-Z 5th order scheme [5]. Flamelet approach is used for combustion modeling [6].

3. Analysis Objects

A sketch of the analysis object is shown in Figure 1. The axial length of it is 0.6 m without the rocket nozzle and the diameter is 0.04 m. The object imitates a lab-scale combustion chamber of a hybrid rocket motor. As the figure shows, the oxidizer is injected tangentially into the chamber with swirling from the head end and the fuel is blowing from the wall placing little distance away from the region of oxidizer injection all the way up to the rocket nozzle. The injector and the fuel blowing are treated as the boundary conditions. The 100% gaseous oxygen and 100 % methane are used as the oxidizer and the fuel, respectively. In actuality, because the fuel is a solid material as plastic, paraffin and so on, the vaporized gas from the fuel is the mixture of a variety size of hydrocarbon. There are no typical chemical species in the gas, and there are not any extreme differences of state of combustion in respect to hydrocarbons. Therefore, in this paper methane, which is the simplest hydrocarbon, is used as the fuel for the simplicity of chemical reaction calculations. The feed rate of the oxidizer is 200 g/s with temperature of 300 K and is constant temporally. The feed rate of fuel is changed by axial direction. From experiment of Hirata et al. [7], as shown in Figure 2, temporal and circumferential averaged local regression rate of fuel grain of Swirling-Oxidizer-Flow-Type Hybrid Rocket is indicate maximum value at leading edge of the grain, which is the closest position to the injector, at 100 mm from the leading edge the value decrease to half of the maximum and they maintain almost same value to trailing edge of the grain. These trends are independent from grain length and pressure of the chamber. From the experimental result, in this paper, distribution of fuel regression rate is set as shown in Figure 3, and then estimated pressure in the chamber is about 20 atm. The feed rate of fuel is obtained from the distribution of the regression rate by means of following formula as blowing speed V_b.

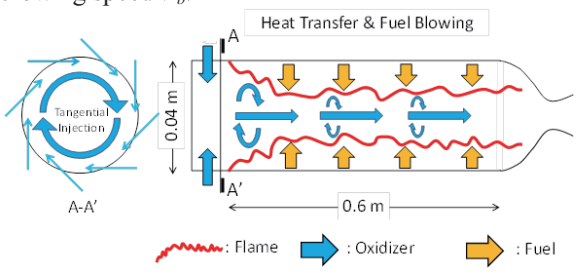

Fig. 1 Numerical set up of main analysis object

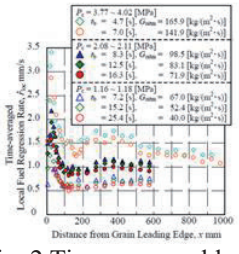

Fig. 2 Time averaged local regression rate [7]

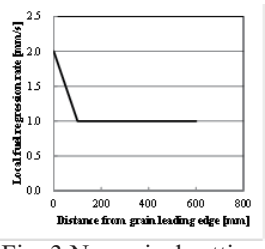

Fig. 3 Numerical setting of local regression rate

$$V_b = \frac{\rho_f \dot{r}_f}{\rho_g} \quad (1)$$

In equation (1), ρ_f is the density of fuel, $\dot{r}_f$ is the regression rate of the fuel and ρ_g s the density of vaporized gas of fuel. In this paper, we set $\rho_f = 950\,\mathrm{kg/m^3}$, and that the value of ρ_g is obtained from equation of state, when the temperature of fuel gas is 600 K. In this situation, the gross equivalence ratio in the chamber becomes 1.55.

The computation is conducted in three dimensions and a 360-degree circumferential numerical mesh is constructed. A grid resolution of 655 cells in axial, 80 cells in radial and 160 cells in circumferential direction result in more than eight million cells.

Flamelet table calculation is performed under the condition that both fuel and oxidizer temperatures are 600 K at 20 atm. GRI-Mech 3.0 is used as Chemical reaction model, and then scalar dissipation rate is set to 2 – 4000 1/s. In this study, flamelet table is obtained by "Flame Master" code which is developed by Pitsch [8].

4. Results and Discussion

Figure 4-7 show contour of temperature, mixture fraction, pressure and axial velocity at cross-section through central axis. From these figures, it can be confirmed that flow field is well disturbed in the chamber. Figure 8 shows iso-volume of Q criteria. This figure indicate that the turbulent eddies invoke disturb in the chamber. Figure 9 shows iso-volume of mixture fraction. Surface of the volume is iso-surface of mixture fraction, and its value is at stoichiometry. In this study, the iso-surface is defined as flame. From this figure, it can be seen that flame is disturbed by turbulent eddies.

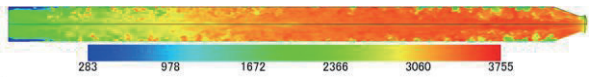

Fig. 4 Contour of temperature

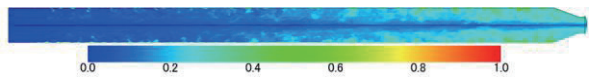

Fig. 5 Contour of mixture fraction

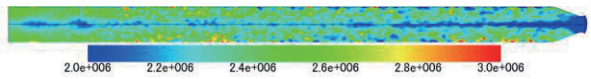

Fig. 6 Contour of pressure

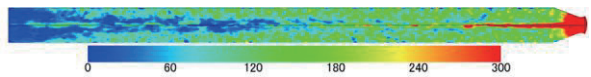

Fig. 7 Contour of axial velocity


Fig. 8 Iso-volume of Q criteria

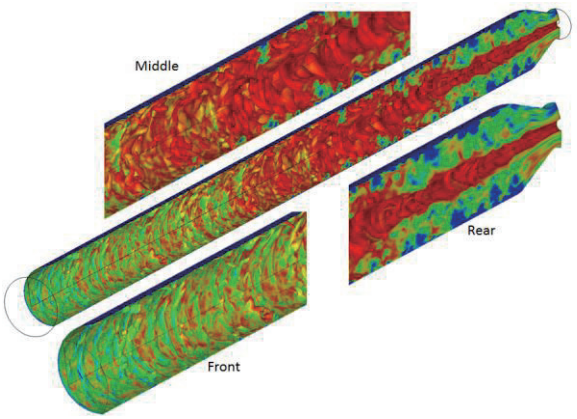

Fig. 9 Visualization of Flame

5. Concluding remarks

In this paper, numerical analysis of combustion chamber which imitates Swirling-Oxidizer-Flow-Type Hybrid Rocket Engine is performed by means of Large Eddy Simulation and Flamelet approach. By performing this analysis, the structure of the flow field and the structure of flame in the combustor have been revealed.

Acknowledgments

This research is supported by the Hybrid Rocket Research Working Group (HRrWG) of Institute of Space and Astronautical Science, Japan Aerospace Exploration Agency. The authors thank members of HRrWG for their helpful discussion.

References

[1] S. Yuasa, at al., AIAA Paper 2001-3537
[2] W. H. Knuth, J. Propul. Power., **18** (2002), pp. 600-609
[3] M. Motoe, et al., AIAA Paper 2009-5025
[4] K. Ishiko, et al., AIAA Paper 2010-6741
[5] R. Borges, et al., J. Comput. Phys.,**277** (2008), pp. 3191-3211
[6] N. Peters, Prog. Energy Comb. Sci.,**10** (1984), pp. 319-339
[7] K. Hirata, et al., AIAA Paper 2011-5677
[8] H. Pitsch, Flame Master, A C++ Computer Program for 0D Combustion and 1D Laminar Flame Calculations

Tenth International Conference on Flow Dynamics
November 25-27, 2013, Sendai, Miyagi, Japan

Numerical Simulation on Unsteady Compressible Low-Speed Flow Using Preconditioning Method: Preconditioning Method Including Multi-Species Mass Conservation Equations

Nobuyuki Tsuboi
Kyushu Institute of Technology, 1-1 Sensui-chou, Tobata-ku, Kitakyushu, Fukuoka, Japan
tsuboi@mech.kyutech.ac.jp.

ABSTRACT

The shock tube problem is simulated by using the time-dependent preconditioned compressible Euler equations with multi-species equations. The numerical flux is calculated by the preconditioned AUSMDV schemes and the time integration adopts the third-order TVD Runge-Kutta method. Four preconditioning matrices Γ are adopted in order to estimate the convergence histories in the pseudo-time domain. The results show that all preconditioning matrices have better convergence except the case of the pressure-temperature type of primitive variable with full matrix.

1. Introduction

The hybrid rocket engine uses a solid fuel and gas oxidizer to become more safety and less expensive than the solid rocket engine because the fuel and oxidizer are separated and solid fuel is typically made of polymer materials. Therefore the hybrid rocket is a candidate for the transportation of the manned space mission.

Although the numerical simulations are necessary for the design of the hybrid rocket motor, common compressible flow solvers are " density-based " schemes, which are impossible to solve incompressible flow lower than free-stream Mach number of 0.1 due to small time step and slow converging rate. This causes a stiffness problem in which the ratio of maximum eigen value to minimum one in inviscid flux is of the order of 100. This stiffness problem also arises in the simulations with chemical reaction. The preconditioned Euler or Navier-Stokes equations [1] , which is control the eigenvalues without stiffness, can be solved for such the low speed as well as high Mach number. However, few researches applied the preconditioning technique on the combustion problems because the preconditioning matrix is arbitrary and becomes complex.

We have recently developed the time-dependent preconditioning Navier-Stokes code to solve such the high *Re* number and low speed flow in order to understand flow mechanism in the hybrid rocket combustion chamber. In the present research, the unsteady preconditioning method is applied to the full Navier-Stokes code with species mass conservation equations[2] in order to simulate the combustion flow under the low-speed and high-Reynolds number effectively. The present paper reports the results of the unsteady shock tube problems in order to understand the various preconditioning matrices by using the simple test case.

2. Numerical Method and Simulation Conditions

The unsteady three-dimensional compressible Navier-Stokes equations including the preconditioning matrix are used. The present simulations do not include the viscous term.

$$\frac{\partial \boldsymbol{Q}}{\partial t} + \Gamma \frac{\partial \boldsymbol{W}}{\partial \tau} + \frac{\partial \boldsymbol{E}}{\partial x} + \frac{\partial \boldsymbol{F}}{\partial y} + \frac{\partial \boldsymbol{G}}{\partial z} = 0 \qquad (1)$$

where t is real time and τ is pseudo time, respectively. The time accuracy assumes second-order and i is the number of sub-iteration, then

$$\left[\Gamma + \frac{3\Delta\tau}{2\Delta t}\frac{\partial \boldsymbol{Q}}{\partial \boldsymbol{W}}\right]\Delta \boldsymbol{W}^{(i)} = -\Delta\tau\left[RHS^{(i-1)} + \frac{3\boldsymbol{Q}^{(i-1)} - 4\boldsymbol{Q}^{n} + \boldsymbol{Q}^{n-1}}{2\Delta t}\right] \qquad (2)$$

where $\boldsymbol{Q} = [\rho, \rho u, \rho v, \rho w, e, \rho_i]^T$ are the conservation variables, $\boldsymbol{E}, \boldsymbol{F}, \boldsymbol{G}$ are the inviscid fluxes, respectively. The above equations are transformed by using the method proposed by Weiss and Smith[1]. Instead of the consevation variables $\boldsymbol{Q}$, the primitive variables $\boldsymbol{W} = [p, u, v, w, T, Y_i]^T$ and the preconditioning matrix Γ are applied to the above equations. There are three sets of primitive variables including the species mass fractions: $\boldsymbol{W}_T = [p, u, v, w, T, Y_i]^T$(pressure-temperature type), $\boldsymbol{W}_{\overline{h}} = [p, u, v, w, \overline{h}, Y_i]^T$(pressure-enthalpy type), and $\boldsymbol{W}_p = [p_i, u, v, w, T]^T$(partial pressure-temperature type). Merkle et al.[3] and Yang et al.[4, 5] adopt $\boldsymbol{W}_T$. Chen et al.[6, 7, 8], Olsen et al.[9], and Yang et al.[11] adopts $\boldsymbol{W}_{\overline{h}}$. Edwards et al.[10, 12, 13] use $\boldsymbol{W}_{p_i} = [p_i, u, v, w, T]^T$. The present study uses first and second sets of the primitive variables. Then the preconditioning matrix Γ is defined by using the primitive variables $\boldsymbol{W}_T$ and $\boldsymbol{W}_{\overline{h}}$. One example is shown here though four preconditioning matrices, which depend on the treatment of $\partial/\partial Y_i$, can be derived. If Y_i is a variable independent of the conservative variables and $\partial/\partial Y_i$ sets zero(for example, $\partial\rho/\partial Y_i = 0$), the

Table 1. Various preconditioning matrices Γ.

Type	Primitive variable	Off-diagonal components for species
$\mathrm{prec_{T0}}(\Gamma_{\mathrm{T_0}})$	T	0
$\mathrm{prec_{T}}(\Gamma_{\mathrm{T}})$	T	cal.
$\mathrm{prec_{h0}}(\Gamma_{\overline{\mathrm{h}}_0})$	$\overline{h}$	0
$\mathrm{prec_{h}}(\Gamma_{\overline{\mathrm{h}}})$	$\overline{h}$	cal.

preconditioning matrix becomes simple one. However, the preconditioning matrix has a complex off-diagonal terms as Y_i is a variable dependent on the conservative variables and $\partial/\partial Y_i \neq 0$. One example of the simple preconditioning matrix by using $\boldsymbol{W}_T$ is shown as follows:

$$\Gamma_{T_0} = \begin{pmatrix} \Theta & 0 & 0 & 0 & \rho_T & 0 & \cdots & 0 \\ \Theta u & \rho & 0 & 0 & \rho_T u & 0 & \cdots & 0 \\ \Theta v & 0 & \rho & 0 & \rho_T v & 0 & \cdots & 0 \\ \Theta w & 0 & 0 & \rho & \rho_T w & 0 & \cdots & 0 \\ \Theta H - 1 & \rho u & \rho v & \rho w & X & 0 & \cdots & 0 \\ \Theta Y_1 & 0 & 0 & 0 & \rho_T Y_1 & \rho & 0 & 0 \\ \vdots & \vdots & \vdots & \vdots & \vdots & 0 & \ddots & 0 \\ \Theta Y_N & 0 & 0 & 0 & \rho_T Y_N & 0 & 0 & \rho \end{pmatrix} \tag{3}$$

where $e = \rho H - p$, $H = \overline{h} + (u^2 + v^2 + w^2)/2$, $h_i = \int C_{p_i} dT$, $\overline{h} = \sum_{i=1}^{N} Y_i h_i$, $\Theta = 1/U_r^2 - 1/c^2 + \rho_p$, $U_r^2 = \min[c^2, \max(|V|^2, K|V_\infty|^2)$, $K = 0.25$, and

$$X = e_T = \rho_T \sum_{i=1}^{N} Y_i h_i + \rho \sum_{i=1}^{N} Y_i C_{p_i} + \frac{1}{2}\rho_T \left(u^2 + v^2 + w^2\right). \tag{4}$$

Table 1 shows the various preconditioning matrices Γ.

The inviscid flux adopts the preconditioning AUSMDV(pAUSMDV)[10]. The second-order MUSCL with van Albada limiter is used and time integration uses third-order TVD Runge-Kutta method.

Initial conditions for the shock tube are as follows: left gas is hydrogen, ρ_L=1.3 kg/m^3, p_L =8 MPa, and T_L =1500 K; right gas is oxygen, ρ_R=1.3 kg/m^3, p_R =0.1 MPa, and T_L =300 K, respectively. The present computational grid is orthogonal system with 401x5x5 and $\Delta x = \Delta y = \Delta z = 25$ mm.

3. Results and Discussions

The results of the shock tube problem with different gas species are discussed. The speed of sound in hydrogen is three times larger than that in oxygen. The effects of the speed of sound are also presented. The number of sub-iteration except for $\mathrm{prec_T}$ sets 40. That of $\mathrm{prec_T}$ is 60 because of the slow convergence. The results of the instantaneous pressure are shown in Fig. 1. The maximum Mach number in this case becomes two. The results of the preconditioning methods agree well with those without the preconditioning method. Figure 2 shows the RMS histories of the present case. The reduction of the two orders magnitude from initial sub-iteration requires 20∼30 of the inner-iteration though $\mathrm{prec_T}$ shows slow convergence.

4. Conclusions

The shock tube problem is simulated by using the time-dependent preconditioned compressible Euler equations with multi-species equations. The results show that all preconditioning matrices have a better convergence except the case of the pressure-temperature type of primitive variables with full matrix(Γ_T). Further simulations such as a hydrogen/oxygen diffusion flow will be carried out in the future.

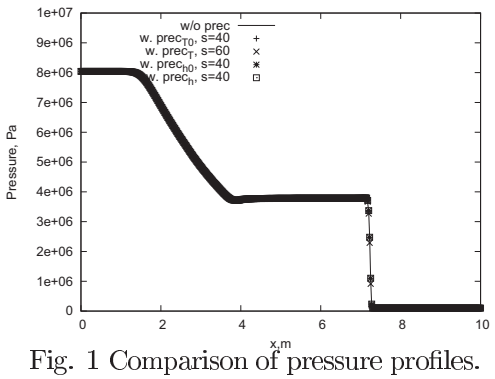

Fig. 1 Comparison of pressure profiles.

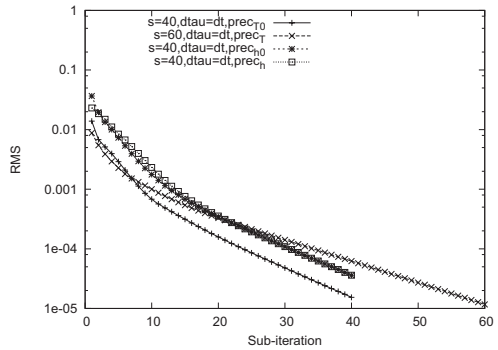

Fig. 2 Comparison of RMS histories.

Acknowledgements

This research is conducted as a contribution to the Hybrid Rocket Research Working Group (HRrWG) with the approval of the Space Engineering Steering Committee of Institute of Space and Astronautical Science, Japan Aerospace Exploration Agency.

This research has also been supported by the Ministry of Education, Science, Sports and Culture, Grant-in-Aid for Scientific Research (B) (No.23360380). The present numerical simulations are collaborated with Cybermedia Center in Osaka University and V system in JAXA supercomputer system.

References

[1] J.M. Weiss and W.A. Smith, AIAA J., **33**, **11**, (1995), 2050.
[2] N. Tsuboi, T. Ito, H. Miyajima, Transactions of The Japan Society for Aeronautical and Space Sciences,Vol.51, No.172, pp.86-92, 2008.
[3] S. Venkateswaran, M. Deshpande, C.L. Merkle, AIAA paper 95-1673, 1995.
[4] N.Zong, V. Yang, Int. J. Computational Fluid Dynamics, Vol.21, No. 5-6, pp.217-230, 2007.
[5] J.C. Oefelein, V. Yang, AIAA paper 96-2880, 1996.
[6] J.S. Shuen, K.H. Chen, Y. Choi, J. Computational Physics, Vol. 106, pp.306-318, 1993.
[7] J.S. Shuen, K.H. Chen, Y.Choi, AIAA paper 92-3639, 2003.
[8] K. Ajmani, K.H. Chen, AIAA paper 2001-0972, 2001.
[9] V. Sankaran, M. Olsen, AIAA paper 2003-3543, 2003.
[10] J.R. Edwards and M.-S. Liou, AIAA J., **36**, **9**, (1998), 1610.
[11] H. Meng, V. Yang, J. Computational Physics, Vol. 189, pp.233-304, 2003.
[12] J.R. Edwards, AIAA paper 96-3129, 1996.
[13] J.R. Edwards, C.J. Christopher, AIAA J. Vol.36, No.2, pp.185-192, 1998.

Film cooling on a wedge surface

Wei-Hsiang Chao, Wu-Shung Fu, Yu-Chih Lai, Shang-Hao Huang
EE306, Department of Mechanical Engineering, 1001 Ta Hsueh Road, Hsinchu, Taiwan
huchihauu.me01g@nctu.edu.tw

ABSTRACT

Film cooling on a wedge surface with multiple cooling holes is studied numerically. This subject is very important in the application of a high efficiency turbine blade. The compressibility and viscosity of working fluid are taken into consideration. Methods of the Roe scheme, preconditioning, and dual time stepping matching with MUSCL are adopted to solve governing equations. Results show that the film cooling effectively protects the surface to get rid of a damage caused by high temperature fluids. Due to the limitation of a single cooling hole, multiple cooling holes are necessary to be used for a long surface.

1. Introduction

In order to improve efficiency of a gas turbine engine, increasing the temperature of the inlet working fluid is a great method. But increasing the temperature of the working fluid means the component of the gas turbine engine to be necessarily operated under hazardous conditions, as a consequence the life of the component will be decreased dramatically. One of the important component is the turbine blade, so in order to protect the turbine blade using film cooling is necessary.

Therefore, a problem of investigation of behaviors of the cooling fluid mentioned above flowing through the gas turbine blade becomes important and worthy investigated deeply.

2. Physical model

A compressible forced convection flow in a three dimensional converging channel is investigates and the model is shown in Fig. 1.

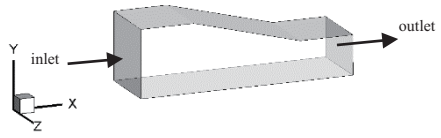

Fig. 1. Physical model

The initial temperature in the channel is the normal atmospheric temperature $T_i = 25^{\circ}C$ and the initial pressure is 1 atm. The boundary of the inlet is forced convection condition, the outlet is the non-reflection condition, and all the other wall is adiabatic. The length, width, and height of the channel are shown in Fig. 2.

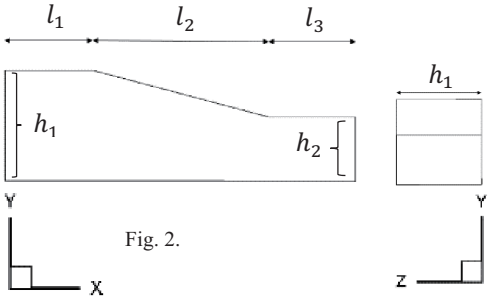

Fig. 2.

The governing equations in which the parameters of viscosity and compressibility of the fluid and gravity are considered simultaneously are shown in the following equations.

$$\frac{\partial U}{\partial t} + \frac{\partial F}{\partial x} + \frac{\partial G}{\partial y} + \frac{\partial H}{\partial z} = S \qquad (1)$$

$$P = \rho RT \qquad (2)$$

3. Method

Schemes of Roe, preconditioning[1] for resolving compressible flow under a low Mach number situation, dual time stepping and MUSCL (Monotonic Upstream-Centered Scheme for Conservation Laws) coordinating LUSGS[2] (Lower-Upper Symmetric Gauss Seidel) are adopted to resolve 3-D Navier–Stokes equations. Methods of algebraic grid generation and a non-reflecting boundary condition are used to execute coordinates transformation and decrease the computational domain, respectively. Furthermore, Boussinesq assumption is no longer used and the compressibility of fluid is considered instead

4. Results and Discussion

In order to compare the difference between single film cooling hole and multiple film cooling holes, two different blowing ratio have been used. Blowing ratios are 0.6 and 0.3 for single and multiple film cooling holes, respectively, so the total mass flow rate of the coolant is the same. Fig 3.1 shows the location of single film cooling hole, and Fig 3.2 for the multiple film cooling holes.

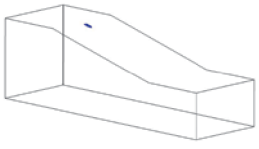

Fig. 3(a). Location of single film cooling hole

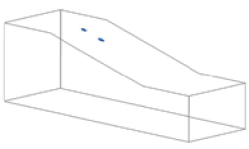

Fig. 3(b). Location of multiple film cooling holes

The mainstream and the coolant inlet boundary condition is forced convection with $U_{mainstream} = 0.5\ ^{m}/_{S}$ (Re= 1.09×10^{3}) and $U_{coolant} = (0.125\sqrt{3}i - 0.125j)\ ^{m}/_{S}$, respectively. The angle of the coolant velocity is 15° to the surface, and the non-reflection boundary condition are used at the outlet to decrease meshes. Fig. 4 shows the velocity field in the central cross section of the channel before the cooling fluid flowing into.

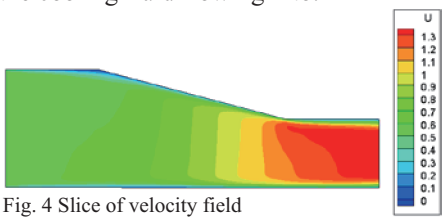

Fig. 4 Slice of velocity field

Fig. 5 and Fig. 6 show the top and side views of the temperature field of single film cooling hole under the blowing ratio of 0.6, Fig. 7 and 8 show the top and side views of the temperature field of the single film cooling hole under the blowing ratio of 0.3, respectively, the larger the blowing ratio is, the larger region affected by the cooling film is observed.

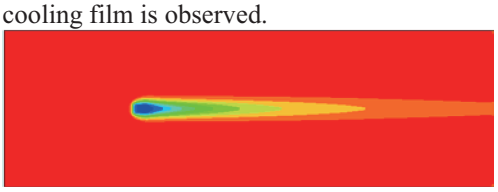
Fig. 5. The top view of the temperature field of single film cooling hole

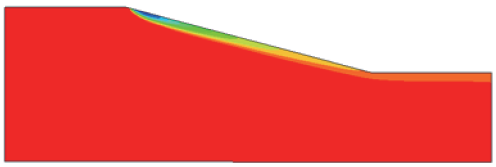
Fig. 6. The side view of the temperature field of single film cooling hole

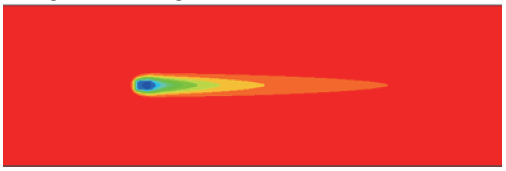
Fig. 7. The top view of the temperature field of multiple film cooling holes with only one coolant inlet opened.

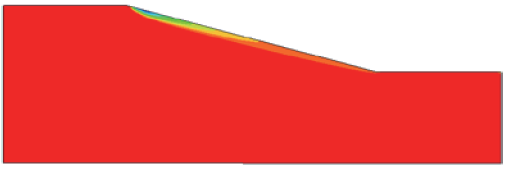
Fig. 8. The side view of the temperature field of multiple film cooling holes with only one coolant inlet opened.

Fig.9 and 10 indicate the top and side views of the temperature field of the multiple film cooling holes, respectively. The criterion of selection of the location of the second hole is the temperature of the location to be 330K. The region affected by the cooling film is apparently larger than that shown in Fig.5.

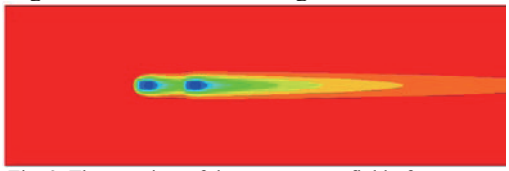
Fig. 9. The top view of the temperature field of multiple film cooling holes.

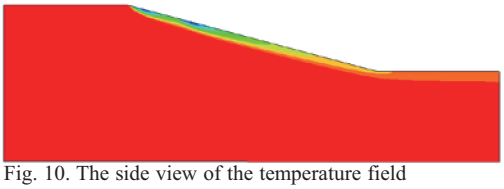
Fig. 10. The side view of the temperature field of multiple film cooling holes.

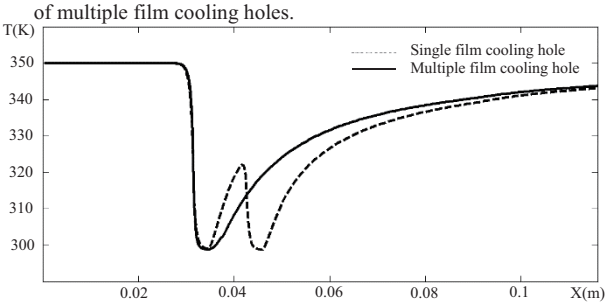

Fig. 11. Temperature field alone the top wall of channel.

Fig.11 indicate temperature distributions on the wedge surface caused by two situations. Although the total blowing ratio of the film cooling of the two situations is the same, the region cooled by the multiple film cooling holes is apparently lower than that of the single film cooling hole. Two reasons are suggested. Firstly, relative to the second film cooling hole, the first film cooling hole is to conduct pre-cooling function to decrease the temperature of the inlet fluid. Secondly, since the heat transfer rate of forced convection is usually huge at the front edge from point views of the first and second holes both holes occupy the location of the front edges of two continuous forced convections. Achievement of the larger heat transfer rate is reasonable.

5. Concluding

The main points may be concluded as follows.

1. With same coolant mass flow rate multiple coolant inlets will better than the single film coolant inlet.
2. The second coolant inlet cooling effect will better than the first one due to the pre-cooled.

6.References

[1] J. M. Weiss and W. A. Smith, AIAA. **33** (1995) 2050-2056
[2] S. Yoon, A. Jameson, AIAA. **26** (1988) 1025-1026.
[3] Rozati, A. and Tafti, D, Int. J. Heat Fluid Flow **29** (2009) 857-873.
[4] H. Schneider , D. von Terzi, H.-J. Bauer, Int. J. Heat Fluid Flow **31** (2010) 767-775
[5] HAN Zhen xing, Kiyoshi Suenaga, LIU Shi, AAAS **25** (2004) 551-555.

Multi-Active Removal of Large Abandoned Rocket Bodies by Hybrid Propulsion Module

Pietro Tadini[1], Urbano Tancredi[2], Michele Grassi[3], Luciano Anselmo[4], Carmen Pardini[4], Francesco Branz[5], Alessandro Francesconi[5], Filippo Maggi[1], Michèle Lavagna[1], Luigi T. DeLuca[1], Nicole Viola[6], Sergio Chiesa[6], Valery Trushlyakov[7] and Toru Shimada[8].
[1]Politecnico di Milano, [2]University of Naples "Parthenope", [3]University of Naples "Federico II",
[4]ISTI-Consiglio Nazionale delle Ricerche, [5]University of Padua, [6]Politecnico di Torino, Italy.
[7]Omsk State Technical University, Omsk, Russia
[8]Institute of Space and Astronautical Science, Japan Space Exploration Agency, Sagamihara, Japan
pietro.tadini@polimi.it

ABSTRACT
The feasibility study of an active removal mission of multiple large abandoned objects from Low Earth Orbit region is presented. A chaser spacecraft, powered by a hybrid rocket engine, achieves contact with two Cosmos-3M second stages and provides for their de-orbiting by means of a hybrid propulsion module. Critical mission aspects and related technologies are investigated, such as an innovative electro-adhesive system for target capture, mechanical systems for the hard docking before the disposal. De-orbiting trajectory simulations and preliminary sizing and mass budget of chaser spacecraft and hybrid rocket engines were performed.

1. Introduction

As of 14 May 2013, 3738 payloads and 1965 rocket bodies orbit the Earth [1]. Taking into account that approximately 1050 spacecraft are operational [1], there are around 4650 intact payloads and rocket bodies abandoned in the circumterrestrial space. In Low Earth Orbit (LEO) there are 1939 payloads and 813 rocket bodies, of which about 2250 are completely abandoned. Large abandoned objects represent a dangerous source of new debris in case of accidental collisions. The active removal of 3-5 large objects per year would be sufficient to prevent the outbreak of the "Kessler Syndrome" in the next 200 years [2], reducing significantly the exponential growing of space debris. The greater cost of a space mission is related to the launcher and the propellant consumption. The possibility of multiple removals with one single launch is the only way to promote the development remediation missions. Hybrid rocket technology for de-orbiting applications [3], despite its poor combustion efficiency and low regression rate, is considered a valuable option due to the high specific impulse obtainable, intrinsic safety, possibility of green propellant use, low cost technology and, especially, re-ignition and thrust throttleability.

2. Target Selection

Presently, the current distribution of abandoned intact spacecraft and upper stages [3], suggests that optimal active debris removal missions should be carried out in seven most populated bands with altitudes between 700 and 1000 km and inclinations between 65° and 99° [3]. Taking into account the LEO distribution of intact objects and the collision risk ranking, a very attractive target for multiple active removal is represented by the Russian Cosmos-3M second stages, with mass of 1400 kg, diameter of 2.4 m and length of 6.5 m, of which 298 are still in orbit mainly concentrated around two inclinations, 74° and 83° [3]. These objects have been catalogued considering a RAAN (Right Ascension of Ascending Node) difference less than 1 degree since one of the main design requirements of a multi-removal mission is to limit the Chaser out-of-plane maneuvers needed for the rendezvous with multiple targets. Around 74° the average altitude of the objects is between 750-780 km, whereas around 83° the average altitude is between 950-990 km. In the latter inclination band several couples with a low RAAN difference are present, while just 8 couples can be found in the former band. The debris couple selected for developing the multi-removal mission concept consists of Cosmos-3M 11112 and Cosmos-3M 22676, respectively at an average altitude of 767.62 km and 777.97 km in the first inclination band.

3. Mission Profile

In the multi-removal mission a Chaser spacecraft, equipped with a Hybrid Rocket Engine (HRE) as primary propulsion, aims at achieving contact with the two selected targets: on the first one a Hybrid Propulsion Module (HPM) is attached, which performs debris de-orbiting and controlled reentry, while the second one is directly de-orbited by the Chaser itself, using the HRE remaining propellant. The HPM is the main component of the de-orbiting kit (called DEO-kit in Figure 1), which also includes a Hard Docking System (~20 kg), for the rigid connection with the debris, and a Reaction Control System (RCS) for the attitude control, as well as the required avionics (~20 kg) for the disposal.

3.1 Rendezvous Strategy

For rendezvous (RV) preliminary analysis it is assumed that the Chaser is injected in a 700-km circular orbit in the same plane of the first target (Cosmos-3M 11112), which is reached with a two-burn Hohmann transfer. For the debris capture and de-orbiting kit installation a duration of 48 hours is assumed. Then the Chaser is detached from the first debris and maneuvered up to the second target, by a three-impulse in-plane Hohmann maneuver, for simultaneous phasing and orbit transfer, plus a plane change to null delta inclination and RAAN. The two RV maneuvers require about 36 m/s and 60 m/s, respectively. The total ΔV needed is thus 96 m/s.

3.2 De-orbiting and Controlled Reentry

Due to the large size and mass of Cosmos-3M, the re-entry shall be controlled and directed to a specific uninhabited location on Earth. To allow an immediate atmospheric capturing and limit the ground impact area, the elliptical transfer orbit must have perigee lower than 60 km and a steep flight path angle (FPA ~1.7°). A ΔV of 200 m/s is required for each target; the disposal is performed with one-burn maneuver of 52 s and 63 s, respectively for the HPM (see Figure 1)and the HRE.

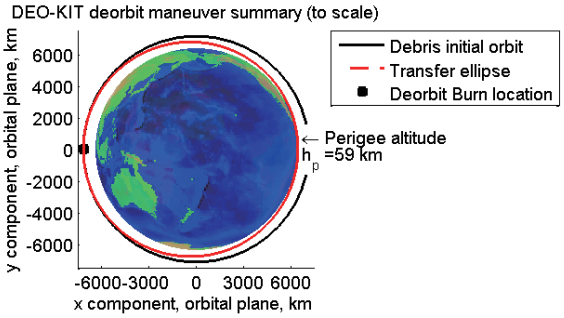

Fig. 1: DEO-Kit de-orbiting maneuver summary.

4. Capture and Mating

The debris capture strategy employs two grasping systems which operate in sequence: the first one (Soft Docking System) is in charge of establishing the initial contact with the object, damping the impact loads and compensating for the residual Chaser-target relative attitude motion at the end of the rendezvous phase; the second one (Hard Docking System) realizes a strong structural connection between the HPM or the Chaser and the Cosmos-3M, in order to withstand the propulsive loads during the de-orbiting maneuver. The Soft Docking System exploits electrostatic adhesion to generate the requested contact forces (10 kPa of attraction pressure normally and 4 kPa in shear) between the target surface and flexible electrodes mounted on a deformable material substrate which guarantees a better adaptability and adhesion between the interfaces [4]. The Hard Docking System, equipped on both Chaser and HPM, consists in a titanium rod with a special corkscrew mechanism [1] which allows to penetrate he Cosmos-3M nozzle throat, the strongest structural element of the target. With the corkscrew system a safe connection to the debris is theoretically possible.

5. Preliminary Sizing and Mass Budget

A hybrid rocket engine typically features the oxidizer in the liquid or gaseous state, while the fuel is in the solid state. Its safety is guaranteed by no-contact between fuel and oxidizer, except during the combustion phase. For the preliminary sizing of the HPM and HRE, HTPB (hydroxyl-terminated polybutadiene) as fuel and H_2O_2(90%) as oxidizers are considered. H_2O_2 catalytic decomposition provides oxygen-rich hot gases up to 1,000 K, ideal for HTPB ignition, allowing the development of a simple and reliable re-ignition system. Moreover, with a single tank of H_2O_2, it is possible to feed both the primary propulsion system and a set of catalytic micro-thrusters for attitude control. The preliminary sizing and mass budget is performed with a zero-dimensional model based on the simplified regression rate Marxman equation [5], experimentally evaluated. Thermo-chemical parameters are estimated with CEA NASA [6] according to combustion conditions, then rocket performance are calculated and velocity increment requirements are checked in an iterative process. Finally, the thrust profile evaluated is used for the trajectory simulation and maneuver feasibility analysis. Two engines were designed: the HPM and the HRE. Because of nozzle losses and low combustion efficiency a margin of 25% on ΔV is applied. The HPM results with a mass of 160 kg, including the propellant mass and the RCS, generating an average thrust of 6.2 kN with an average acceleration on the system (HPM + debris) of 0.42g. The vacuum specific impulse results about 320 s. The external rocket diameter is 21 cm, while the total length (including submerged nozzle) is 136 cm. Four spherical tanks (40 cm dia) with an internal elastomeric membrane for pressurization with gaseous N_2, are placed at the sides of the rocket, thus the total HPM diameter is about 101 cm. The ΔV requirement for HRE includes RV and disposal maneuvers, total ΔV of 370 m/s, 25% margin included. The chaser is composed by the HRE, a RCS for the attitude control, the Chaser bus (845 kg) and one de-orbiting kit (200 kg). The HRE has a mass of 305 kg, including the propellant mass, generating an average thrust of 8.4 kN with an average acceleration on the system of 0.35g during the de-orbiting phase, while, during RV maneuvers, average thrusts of 4.3 kN with average accelerations on the system of 0.37g are estimated. The $I_{s\text{-}vac}$ results about 320 s. The external diameter of HRE is 25 cm, while the total length is 162 cm. The total HRE diameter, with four spherical tanks (51 cm dia) is about 126 cm. Both rocket engines use a conical nozzle made by phenolic material, with an area ratio of 50 to keep small sizes.

6. Conclusion Remarks

Preliminary sizing and mass budget provide a Chaser spacecraft with a mass of 1150 kg and a de-orbiting kit of about 200 kg, for a total mass of 1350 kg. This result agrees with VEGA's payload requirements (1700 kg up to 700 km orbit altitude), making possible the removal of at least 2-3 Cosmos-3M with a single mission.

References

[1] DeLuca L.T. et al. Paper ID 469, EUCASS 2013.

[2] Liou, J.-C., and N.L. Johnson. Acta Astronautica 64:236–243, 2009.

[3] De Luca, L.T. et al. Acta Astronautica 91:20-33, 2013.

[4] Branz, F. et al. IAC-12.D1.2.7, 63rd IAC Congress.

[5] Chiaverini, M.J., and K.K. Kuo. AIAA Progress in Astronautics and Aeronautics, Volume 218, pp. 37-116, 457-485, 2007.

[6] S. Gordon et al. NASA-RP-1311, 1994

Tenth International Conference on Flow Dynamics
November 25-27, 2013, Sendai, Miyagi, Japan

Suborbital Flight Experiments Using Hybrid Rocket Propulsion

Yen-Sen Chen[1], Alfred Lai[2], Tzu-Hao Chou[2], Jong-Shinn Wu[2], Bill Wu[1]
[1]National Space Organization, Hsinchu Science Park, Hsinchu, Taiwan
[2]Department of Mechnical Engineering, National Chiao Tung University, Hsinchu, Taiwan
e-mail: yenchen@nspo.narl.org.tw

ABSTRACT

Sounding rocket with solid propellants has been to be a standard platform for suborbital flight experiments. Hybrid rocket technology developed in recent years is becoming a viable and cost-effective alternative in sounding rocket applications. Due to its safety nature in material handling and combustion processes, and its ability to throttle in flight, hybrid rockets are suitable for low-cost developments of advanced rocket concepts and technology demonstrations. In this paper, the approach and strategies for the overall performance enhancement in hybrid sounding rocket development are described with the future plan outlined.

1. Introduction

Sounding rocket flight experiment is a viable platform in aerospace research activities. It has benefited low-cost developments in the early stages of advanced aerospace design concepts and provided experimental measurements and scientific discoveries in upper-atmosphere research. Sounding rockets have been demonstrated, over the past 60 years, to be particularly useful for flight experiments above 50 km altitude, under which airplanes and balloons are available. Recent survey of the US FAA indicates that over 80 percent of sounding rocket flights are between 100 km to 300 km, and the demand will continue to increase for the next 10 years.

Although it has almost always been motivated by military applications, for many space faring countries, sounding rockets also served as rocket technology research and development platforms for the establishment of their space launch capabilities. Today, sounding rockets are often used for science experiments in atmospheric studies, microgravity environment, advanced aerospace technologies and space components developments and qualifications. And, solid rockets are commonly employed for these applications, which are mostly fabricated by military or well-established aerospace organizations in technically qualified facilities with skilled personnel.

In the recent development of sounding rockets and space launch systems, hybrid rocket propulsion has drawn a lot of attention, especially in the civilian space tourism community, and has been demonstrated to become a viable alternative to the liquid and solid rockets. The hybrid rocket is a combination of both the solid and liquid systems with half of the plumbing of the liquid rockets but retaining the flexibility of operation and avoiding the explosive nature of the solid propulsion [1]. It is therefore suitable for advanced hybrid technology developments in university and research institute environments for advanced technology research and development.

In combining both theoretical and experimental approaches, the hybrid rocket development programs have been demonstrated to be very effective and efficient. For the theoretical approaches, since the early 1980s, computational modeling approaches have been gradually adopted in the aerospace community in the development of flight vehicles, combustion devices and space launch systems. Numerical models using computational fluid dynamics (CFD) methods have been applied to liquid and solid rocket combustion systems with successful results in supporting the technical programs [2-7]. These computational tools are suitable for the design studies of hybrid rocket propulsion, aerodynamics, structural dynamics and flight mechanics, etc. Among these disciplines, rocket propulsion and combustion physics is the key that demands extensive research efforts.

There are many types of hybrid combustion systems, in which fuel is classically a solid and the oxidizer is a liquid or gas. Typical examples of combination of fuel and oxidizer with optimum O/F ratio, specific impulse Isp (184 to 326 sec) and characteristic velocity (1224 to 2118 m/sec) are summarized and discussed in [1]. For material local availability, N_2O-HTPB propulsion system is selected in the present hybrid rocket development. The maximum vacuum Isp demonstrated in pratice so far for the N_2O-HTPB propulsion system is only fair around 250 seconds while its theoretical limit can be as high as 320 seconds. This indicates that it is worthwhile to invest in this research to push the thrust performance closer to the theoretical limit.

Following previous studies [8,9], an energy-balanced surface decomposition model is employed to initiate the complex combustion processes that involve finite-rate chemistry and real-fluid properties. The real-fluid properties affect the overall flow structure in the combustion chamber, especially near the injectors, and affect the combustion processes and heat transfer characteristics, which is the key to the regression rates of the solid grain.

Thrust performance, propellant mass fraction, reliability and cost are the major factors that determine the overall performance of a rocket system. Theoretically, hybrid rocket systems are advantageous among many of these factors as compared to solid and liquid rocket systems. However, the thrust performance aspect of hybrid rockets still need further investigations to improve their combustion efficiency, Isp and stable O/F ratio control, etc.

2. Hybrid Rocket Technology Demonstration

The sounding rocket program of National Space Organization of Taiwan was initiated in 1998 with the

aim to establish a flight test platform for ionosphere studies and space technology developments. The long-term goal of this program is for building up the technical capabilities for designing space launch systems.

In 2009, a hybrid rocket development program was launched with two university research teams selected to bring lab-scale hybrid combustion devices to their maturity that can be integrated into flight-worthy small-scale sounding rocket systems. This technology demonstration program gave the university team research opportunities in extending the results of their fundamental studies to multi-disciplinary systems engineering practices in order to realize the system integration, testing and flight operations. This program is unprecedented in Taiwan's research community and has broadened the views and hands-on experience of the researchers and students involved in the program. As part of the results of the program, successful hybrid rocket flight tests were demonstrated in 2010 and 2011 to altitudes around 10 km.

In this program, two combustion design concepts were employed. They are a N_2O-HTPB system with mixing enhancer of NTCU (National Chiao Tung University) [9] and a N_2O-50%HTPB+50%Paraffin system of NCKU (National Cheng Kung University) [10]. The thrust level (around 300 kgf) and Isp (around 220 seconds) of these two approaches are comparable. The rocket system is completed with carbon fiber composite N_2O pressure tank, flight computer and telemetry data link. During the propulsion system development, hybrid rocket motors with flight specifications and configurations were hot-fire tested in the laboratory to measure the thrust performance, solid grain regression rates, thermal protection environment and nozzle erosion characteristics. In the meantime, a comprehensive numerical model with finite-rate chemistry and real-fluid properties [9,11] was developed and employed by the NCTU team to study the internal ballistics of the hybrid rocket motor and compared with the hot-fire test data.

3. Hybrid Sounding Rocket Development

Based on the successful program of the hybrid technology demonstration, the National Science Council of Taiwan has approved proposals of the two university teams in 2011 for the continuing developments of the sounding rocket technology in the next phase. The main goal of the new program is to develop viable sounding rockets in three years, capable of performing science experiments in altitude above 100 km.

With the mission descriptions of the next-phase sounding rocket using hybrid propulsion one design concept has required that the thrust level for a 600 kg rocket is to be greater than 3,000 kgf. For the new rocket motor development, the comprehensive numerical model is employed in the extensive design analysis work while a hot-fire ground test facility has been completed. A final design of the hybrid motor was selected based on theoretical and experimental studies.

A two-stage hybrid rocket system is resulted based on the system design analysis. The first-stage motor will be similar in design as that used in the previous study with direct scale-up and fine-tuned. For the second-stage motor, a low slenderness form factor design using dual vortical flow concept is proposed. This new design also ends up with higher combustion efficiency based on numerical optimization processes. The new design gives a maximum vacuum Isp of 292 sec, which is one big step closer to the theoretical optimum value for the N_2O-HTPB hybrid system. This new design will be confirmed by hot-fire experiments later during the preliminary design phase of the rocket.

The 8 meter long sounding rocket will carry three nano-size satellite engineering models to be deployed at around 100 km altitude after nose fairing separation. The scientific instruments onboard will conduct ionosphere measurements and send the data to the ground stations through the downlink telemetry system. The second-stage of the rocket is designed to deploy parachute after reentry and splash down the Pacific Ocean about 50 km off the southeast coast of Taiwan. The second-stage, which contains the flight computer and some position and attitude sensors, will be recovered from the ocean. To accomplish the mission, reliable flight computer avionics and telemetry subsystems is critically important for the present hybrid rocket system.

4. Conclusions

The sounding rocket development program of Taiwan using hybrid propulsion has been discussed in this paper. A comprehensive computational model with hot-fire test data validations has played an important role in the development of the N_2O-HTPB hybrid rocket propulsion systems of the present study.

In the future development the hybrid sounding rocket technology, a two-stage rocket has been designed and analyzed using the in-house numerical models and has been validated with experimental data. A new motor has been designed numerically for the second-stage of the rocket that has shown very good Isp improvements.

Acknowledgements

This work is supported by the Sounding Rocket Program of the National Space Organization of the National Applied Research Laboratory of Taiwan. The computational resources and services are provided by the National Center for High-performance Computing of the National Applied Research Laboratory.

References

[1] M.Chiaverini, K.Kuo, Prog. Astro. & Aero, (2007)218.
[2] Y.S. Chen, et al., J.Prop. & Power (1998), 11:4.
[3] P. Liaw, et al., AIAA-94-2780 (1994).
[4] Y.S. Chen, JENNAF 28th Ehaust Plume (2004).
[5] T.S. Wang, et al., J.Prop. & Power (2002) 18:6.
[6] T.S. Wang, J.Prop. & Power, (2005) 22:1.
[7] T.S. Wang, AIAA-2005-3942 (2005).
[8] R.C. Farmer, et al., JANNAF 35th (1998).
[9] Y.S. Chen, et al., Computers & Fluids, (2011)45.
[10] T.S. Lee, et al., 5th Taiwan-Indonesia Wkshp, (2006).
[11] T.S. Wang, Y.S. Chen, J. of Prop. & Power, (1993) 9:5.

Tenth International Conference on Flow Dynamics
November 25-27, 2013, Sendai, Miyagi, Japan

Conceptual Design of Single-Stage Hybrid Rocket in View of Implication of Fuels

Kazuhisa Chiba[1)], Masahiro Kanazaki[2)], Masaki Nakamiya[3)], Koki Kitagawa[4)], and Toru Shimada[4)]
[1)] Hokkaido Institute of Technology, Sapporo, Japan, [2)] Tokyo Metropolitan University, Tokyo, Japan
[3)] Kyoto University, Kyoto, Japan, [4)] Japan Aerospace Exploration Agency, Sagamihara, Japan
kazchiba@hit.ac.jp

ABSTRACT
A single-stage hybrid rocket has been conceptually designed by using design informatics. The primary objective of the design is that the sufficient down range and duration time in the lower thermosphere are achieved for the aurora observation whereas the initial gross weight is held down. The multidisciplinary design optimization and data mining were performed under the conditions that five kinds as solid fuel and liquid oxygen as oxidizer were adopted and that single-time ignition is implemented in sequence. Consequently, the useful design information was obtained.

1. Introduction

Single-stage rockets have been being researched and developed for the scientific observations and the experiments of high-altitude zero-gravity condition, whereas multi-stage rockets have been being also studied for the orbit injection of payload. The Institute of Space and Astronautical Science (ISAS), Japan Aerospace Exploration Agency (JAXA) has been managing K, L, and M series rockets as the representatives of solid rocket in order to contribute to the space scientific research. A next-generation single-stage rocket as well as multi-stage rocket is necessary due to the retirement of M-V in 2008 and in order to promote space scientific research. In fact, E rocket will begin to be operated from August 2013. On the other hand, the launch vehicle with hybrid rocket engine using solid fuel and liquid oxidizer has been being researched and developed as an innovative technology in mainly Europe and United States. The present study will investigate the conceptual design in order to develop a next-generation single-stage launch vehicle with hybrid rocket engine. A hybrid rocket offers the several advantages as higher safety, lower cost, and pollution free flight. In fact, the SpaceShipOne successfully uses a hybrid rocket engine for a private manned space flight. The multi-time ignition is the especial advantage of hybrid rocket engine. On the other hand, the disadvantage of a hybrid rocket engine is in its combustion. As a hybrid rocket engine has low regression rate of solid fuel, the thrust of hybrid rocket engine is less than that of pure solid and pure liquid engines. Multidisciplinary design requirements should be considered in order to surmount the disadvantage of hybrid rocket engine. Moreover, design information will be obtained in order to exhaustively grasp the design space.

In the present study, a single-stage launch vehicle with hybrid rocket engine of solid fuel and liquid oxidizer for the scientific observation of aurora will be conceptually designed by using design informatics approach in order to quantitatively reveal the advantage and in order to discover the fundamental physics regarding hybrid rocket engine.

2. Problem Definition

The conceptual design for a single-stage hybrid rocket, simply composed of a payload chamber, an oxidizer tank, a combustion chamber, and a nozzle, is considered in the present study. A single-stage hybrid rocket for aurora scientific observation will be focused because the rocket for more efficient scientific observation is desired for successfully obtaining new scientific knowledge on the aurora observation by ISAS in 2009.

Three objective functions are defined in the present study. First objective is the maximization of the down range in the lower thermosphere (altitude of 90 to 150km) R_d [km] (obj1). Second is the maximization of the duration time in the lower thermosphere T_d [sec] (obj2). It recently turns out that atmosphere has furious and intricate motion in the lower thermosphere due to the energy injection, which leads aurora, from high altitude. The view of these objective functions are to secure the horizontal distance and time for the competent observation of atmospheric temperature and the wind for the elucidation of atmospheric dynamics and the balance of thermal energy. Third objective is the minimization of the initial gross weight of launch vehicle $M_{\rm tot}(0)$ [kg] (obj3), which is generally the primary proposition for space transportation system.

Seven design variables are used as initial mass flow of oxidizer $\dot{m}_{\rm oxi}(0)$ [kg/sec] (dv1), fuel length $L_{\rm fuel}$ [m] (dv2), initial radius of port $r_{\rm port}(0)$ [m] (dv3), combustion time $t_{\rm burn}$ [sec] (dv4), initial pressure in combustion chamber $P_{\rm cc}(0)$ [MPa] (dv5), aperture ratio of nozzle ϵ [-] (dv6), and elevation at launch time ϕ [deg] (dv7). Note that there is no constraint except the limitations of upper/lower values of each design variable. These upper/lower values are exhaustively covering the region of design space which is physically admitted.

3. Results

3.1 Optimization Result

The population size is set to be 18 and evolutionary computation is performed until 3,000 generations when the evolution is roughly converged. The plots of acquired nondominated solutions reveal that there generates no multimodal and clean convex curved surface.

There is no tradeoff between the down range R_d and the duration time T_d in the lower thermosphere. Also, there are upper limitations of roughly 250[km] for the down range R_d and of roughly 220[sec] for the duration time T_d. Therefore, the projection plots onto two dimension between the down range R_d and the duration time T_d do not converge in one point. In the present study, the initial mass flow of oxidizer $\dot{m}_{\rm oxi}(0)$ (dv1) has the limitation of upper/lower values. Since the regression rate of fuel $\dot{r}_{\rm port}(t)$ as an empirical model uses the mass flow of oxidizer $\dot{m}_{\rm oxi}(t)$, $\dot{r}_{\rm port}(t)$ has constraints. As a result, the limitations are generated for the down range R_d and the duration time T_d.

There is an incomplete tradeoff between the duration time T_d and the initial gross weight $M_{\rm tot}(0)$. The convex nondominated surface to optimum direction with incompleteness is generated due to the limitation of the duration time T_d. In addition, the minimum initial gross weight to reach the limitation of the duration time(roughly 220[sec]) is approximately 700[kg]. And also, the minimum initial gross

weight to attain to the lower thermosphere(altitude of 90[km]) is approximately 350[kg]. As these values are better than those of the solid rockets which are operated at present for scientific observation, it suggests that hybrid rocket has an advantage even when hybrid rocket does not have a sequence of multi-time ignition.

There is a severe tradeoff between the down range R_d and the initial gross weight $M_{\rm tot}(0)$. This figure shows that the maximum down range is roughly 130[km] when the minimum initial gross weight to reach the limitation of the duration time T_d(roughly 700[kg]) is adopted. The initial gross weight $M_{\rm tot}(0)$ should be absolutely increased in order to have more down range R_d(greater than 130[km]) despite no increase of the duration time T_d(remaining roughly 220[sec]). This fact suggests that the design strategies for the maximizations of the down range R_d and the duration time T_d are different.

3.2 Data-Mining Result

As the SOM learning is implicated based on the values of the objective functions as the indicator for the similarity on the neural network, SOMs colored by the objective functions have absolutely gradation.

3.2.1 Acquired Information regarding Relationship among Objective Functions

The comparison of the coloring pattern reveals the tradeoffs among the objective functions. When obj1 is high value, obj2 absolutely becomes high. However, as obj1 does not always become high whenever obj2 is high, this relationship is irreversible. This is because not only the down range R_d (obj1) but also the attained maximum altitude gives the effect on the duration time T_d (obj2). In contrast, when obj2 is low value, obj1 absolutely becomes low. However, as obj2 does not always become low whenever obj1 is low, this relationship is similarly irreversible. Although there is no tradeoff in the global space of the objective functions, there is locally tradeoff. This local tradeoff is caused by the limitation of the duration time T_d(obj2), that is, reaching the maximum value of the duration time T_d(obj2) is easier than achieving the maximum value of the down range R_d(obj1).

Since the initial gross weight $M_{\rm tot}(0)$(obj3) is the minimization function, there are severe tradeoffs among obj3 and the others. It especially reveals the severe problem that the optimum direction of the down range R_d(obj1) and the pessimum direction of the initial gross weight $M_{\rm tot}(0)$(obj3) accord. The structural constraints and the combustion mode should be reconsidered in order to avoid this problem. On the other hand, the optimum region of the duration time T_d(obj2) and the pessimum direction of the initial gross weight $M_{\rm tot}(0)$(obj3) overlap only in part. Therefore, the initial gross weight $M_{\rm tot}(0)$ can become low when the duration time T_d is the primary objective. On the other hand, the minimum initial gross weight is decided by the expected down range when the down range R_d is the primary objective, that is, the minimum initial gross weight depends on the mission requirement as the necessary down range.

3.2.2 Acquired Information regarding Behavior of Design Variables

The SOMs colored by the design variables show their behavior in the design space and also show the influence for the objective functions. Although this design information was revealed, it would be unfortunately omitted in the present abstract due to the rejection regarding the format. All of the figures and the results would like to be shown and explained in the full paper.

3.3 Difference among Fuels

Although there reveals no drastic transformation of the objective functions by the fuels, the implication of each fuel will be compared. The performance of polypropylene will be set as a criterion. The extension of the duration time T_d(obj2) cannot be achieved by any fuels because the limitation is already reached by using polypropylene. The reduction of the initial gross weight $M_{\rm tot}(0)$(obj3) can be carried out by any fuels. When waxes are used, 17% of the weight $M_{\rm tot}(0)$ is reduced. There is no specific difference between waxes FT0070 and PW120. When the compounds between GAP and PEG are used, maximum 40% of the weight $M_{\rm tot}(0)$ is reduced. GAP60PEG40 is better performance than GAP50PEG50 regarding the reduction of the initial gross weight $M_{\rm tot}(0)$(obj3). The performance for the extension of the down range R_d(obj1) is similar between polypropylene and waxes. On the other hand, the compounds between GAP and PEG has the performance of maximum 4%(roughly 10[km]) increase for the down range R_d(obj1). The selection of the compounds between GAP and PEG materializes to hold down the initial gross weight $M_{\rm tot}(0)$(obj3) and to increase the down range R_d(obj1).

4. Conclusions

The next-generation single-stage launch vehicle with the hybrid rocket engine of solid fuel and liquid oxidizer in place of the present pure solid-fuel rockets has been conceptually designed by using design informatics in order to contribute to the low cost launch vehicle system and efficient space scientific observation. The objective functions as the design requirements in the design problem is the maximization of the down range and the duration time in the lower thermosphere as well as the minimization of initial gross weight. The evolutionary hybrid computation between the differential evolution and the genetic algorithm is employed for the efficient exploration in the design space. A self-organizing map is used in order to structurize and visualize the design space. As a result, the design information has been revealed regarding the tradeoffs among the objective functions and the behavior of the design variables in the design space. Consequently, the design strategy for the maximizations of down range and duration time is different because the duration time can easily attain to the limitation rather than the down range. The characteristics as the regression rate of fuel and structure coefficients should be investigated as a next design phase in order to reveal the performance limitation of single-time ignition on hybrid rocket engine. And also, these results indicates that the ascendancy of multi-time ignition as the advantage of hybrid rocket will be quantitatively shown. The results show the quantitative data to compare the performances of solid-fuel rocket in present and hybrid rocket with multi-time ignition.

Tenth International Conference on Flow Dynamics
November 25-27, 2013, Sendai, Miyagi, Japan

Conceptual Design: Dependence of Parameterization on Design Performance of Three Stage Hybrid Rocket

Fumio Kanamori[*], Yosuke Kitagawa[*], Masaki Nakamiya[**], Koki Kitagawa[***],
Masahiro Kanazaki[*] and Toru Shimada[***]
[*]Tokyo Metropolitan University, 6-6 Asahigaoka, Hino-shi, Tokyo, Japan
[**]Kyoto University, Gokasho, Uji-shi, Kyoto, Japan
[***]Institute of Space and Astronautical Science/Japan Aerospace Exploration Agency, 3-1-1 Yoshinodai,Chuo-ku, Sagamihara-shi, Kanagawa, Japan
kanamori-fumio@ed.tmu.ac.jp

ABSTRACT

The design space of a conceptual three-stage launch vehicle hybrid rocket engine was reconsidered based on the results of multi-disciplinary design optimization. The design variables of the nozzles were reconsidered by exploring the design space. Specifically, the nozzle expansion ratio was considered as the ratio of the nozzle exit radius to the body radius. Consequently, the propulsive performance calculated using the new design variables was better.

1. Introduction

A hybrid rocket has the advantages of being safer, cost effective, and environmentally friendly. However, owing to the low fuel regression rate and the difficulty of controlling the fuel flow, it is difficult to design a hybrid rocket that performs better than a conventional liquid/solid rocket. In a previous study[1], we developed a conceptual design methodology for a three-stage hybrid rocket, wherein a multi-objective genetic algorithm is used for thrust evaluation, vehicle sizing, and trajectory analysis. In the previous study, the combustion chamber pressure for the optimum designs tended to be low. Such designs have limitations in terms of flight attitude.

In this study, we modified the design variables to achieve higher performance designs by visualizing the design space.

2. Design Method and Constraints

2.1. Rocket Sizing and Fuel Types

The hybrid rocket of this study comprised a nozzle, a chamber, an oxidizer tank, a pressurized tank with an exterior wall for each stage, and the payload. Fig.1 is a conceptual illustration of the rocket, and the evaluation procedure is shown in Fig.2.

A single port fuel grain is considered here. The regression rate $\dot{r}_{port}(t)$ is expressed as follows:

$$\dot{r}_{port}(t) = \beta a \left[G_o(t)\right]^n \tag{1}$$

The coefficient a and the exponent n are empirical coefficients. The values of a and n used in this study are given in Table 1[2]. β is a design variable used to simulate the swirling effect of the oxidizer, which can increase the value of a. From $\dot{r}_{port}(t)$ and the burning time t_b, which is a design variable, the rocket body radius can be calculated as follows:

$$r_{body} = r_p(0) + \int_0^{t_b} \dot{r}(t)dt \tag{2}$$

2.2. Previous Results and Nozzle Constraint

In our previous study, the radius of the nozzle exit was calculated from the nozzle expansion ratio and the radius of the nozzle throat using the following equation:

$$r_e = \sqrt{\varepsilon} r_t \tag{3}$$

This parameterization produces a nozzle exit radius that is larger than the rocket body radius, and not much promising solutions can be obtained by the optimization process. The nozzle exit radius can also be parameterized as follows:

$$r_e = \kappa r_{body} \tag{4}$$

where κ is the ratio of the radius of the nozzle exit to the radius of the rocket body. κ is a design parameter introduced in this study.

Fig.3(a) shows the solution space of the objective functions obtained by the previous design method, and Fig.4 visualizes the design variables and the objective function. From these figures, it can be seen that the design that has a larger expansion ratio produces a lower chamber or tank pressure. This shows that a lower expansion ratio can be used to reduce the mass of the tank and nozzle. In addition, the design that produces a lower chamber pressure may be optimal when the expansion ratio is smaller.

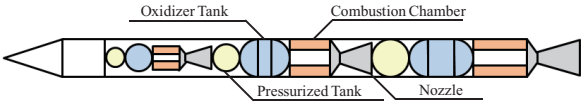

Fig.1 Illustration of conceptual hybrid rocket

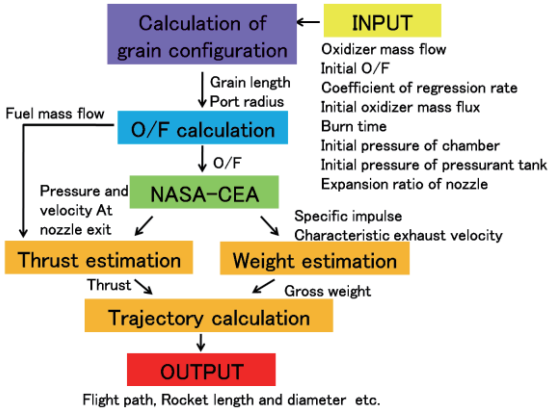

Fig.2 Flow chart of design and evaluation

Table 1. Coefficient of fuel used in this study

Fuel Name	*a* coefficient	*n* exponent
FT0070 (Paraffin)	0.1561	0.3905

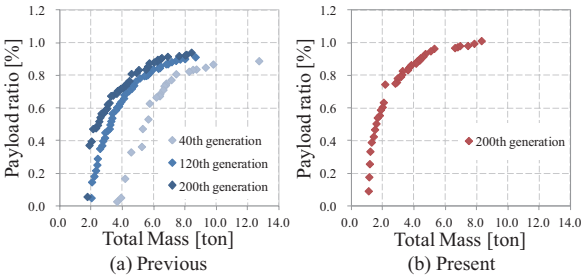

Fig.3 Solution space of objective function

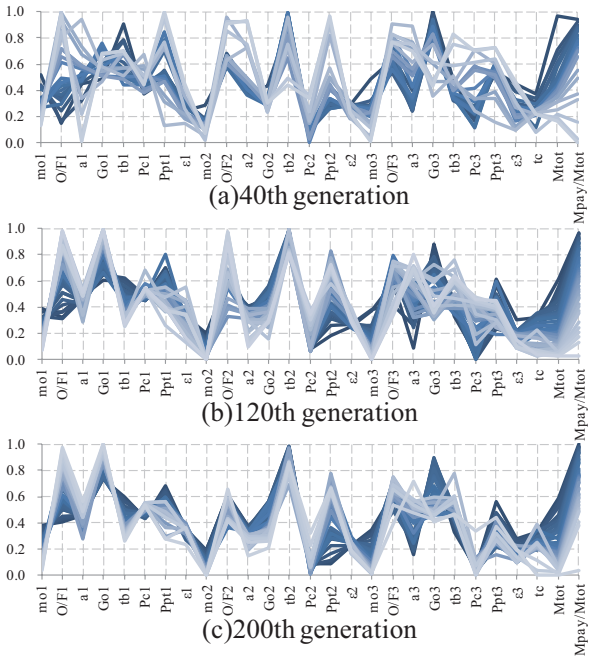

Fig.4 PCP of Pareto calculated using previous method

3. Results Using New Design Variable

Fig.3(b) shows the Pareto solution after the 200th generation obtained by the present parameterization. The Pareto solutions obtained in the present study advanced the optimal direction beyond that of the previous study. The maximum payload ratio is 1.01[%] when the total mass of the rocket is 8.3 [ton], whereas the maximum payload ratio is 0.94[%] when the total mass is almost the same as that in the present study.

Fig.5 shows the PCP obtained in the present study. The equivalent expansion ratio κ is also shown. Based on Fig.4(c) and Fig.5, the design variable obtained from the Pareto solution for the 1st stage is significantly different. The combustion time is particularly longer than the previous one. By changing the nozzle parameterization, the pressure of the combustion chamber and the nozzle expansion ratio were increased compared to those of the previous design. The design with a larger nozzle expansion ratio could be used to achieve a higher combustion chamber pressure. Conversely, the combustion chamber pressures and nozzle expansion ratios for the 2nd and 3rd stages are similar to those of the previous study. The propulsive performances of the rocket for the maximum payload ratios are given in Table 2. Table 2 reveals that the design of this study can be used to achieve higher acceleration and angular momentum *h* compared to that of the previous study. Furthermore, the mass for the 2nd stage in the present study is less than that in the previous study because the pressure of the combustion chamber and the nozzle expansion ratio were lower in the present study.

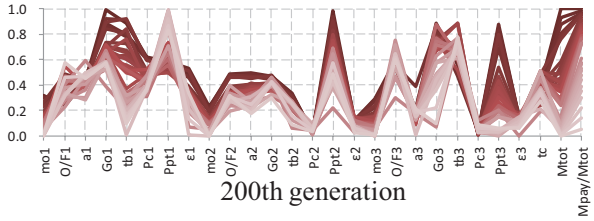

Fig.5 PCP of Pareto calculated using present method

Table 2. Values of propulsive performance

		1st Stage	2nd Stage	3rd Stage
Isp_{ave}[s]	Previous	249.5	299.5	306.4
	Present	257.9	292.5	298.6
t_b[s]	Previous	47.8	129.1	119.4
	Present	56.5	90.2	140.4
ΔV[km/s]	Previous	+1.22	+3.14	+3.76
	Present	+1.41	+3.01	+3.75
h[km^2/s]	Previous	5486.9	27152	52449
	Present	7313.2	27264	52501
M[ton]	Previous	5.340	2.534	0.445
	Present	5.687	2.076	0.453

4. Conclusion

In this study, we considered the parameterization for a conceptual design of a multi-stage launch vehicle hybrid rocket. Based on the findings of our previous study, the relationship between the nozzle and the geometrical constraint of the optimization is a key factor in improving the propulsive performance. In this study, the ratio of the nozzle exit radius to the rocket body radius was introduce as a design variable of the nozzle, and results better than those of the previous study were obtained.

Acknowledgments

We thank members of the hybrid rocket research working group in ISAS/JAXA for giving their experimental data and their valuable advices. This paper and presentation was supported ISAS/JAXA.

References

[1] Y. Kitagawa, K. Kitagawa, M. Nakamiya, M. Kanazaki, T. Shimada, T JSASS, 55(2012), R4

[2] I. Nakagawa, S. Hikone, T. Hasegawa, Proc AJCPP(2010)

Enhancement of Higher Regression Rate and Combustion Efficiency of Hybrid Rocket Engines by with Multi-Section Swirl Injection Method

Shigeru Aso[1], Yasuhiro Tani[1], Sho Ohyama[1], Kentaro Araki[1], Kengo Ohe[1], Hiroshi Tada[1], Kengo Mizuchi[1], Hiroshi Hirayama[1] and Toru Shimada[2]
1 Department of Aeronautics and Astronautics, Kyushu University, Fukuoka 819-0395, Japan
2 ISAS, JAXA, Sagamihara 252-5210, Japan
aso@aero.kyushu-u.ac.jpd.

ABSTRACT

In order to improve fuel regression rate of hybrid rockets, a new method with multi-section swirl injection has been proposed. The new method is to introduce swirling flow within fuel port through multi-section swirl injection holes, which are placed at several locations along the fuel grain. The method is applied for high density polyethylene fuel and paraffin fuel (FT-0070) with pressurized gaseous oxygen. Interactions of injector jets and swirl flow directions are newly investigated.

1. Introduction

Recently, hybrid rocket engine becomes one of the promising space propulsion systems. The advantages of hybrid rocket engines are 1) safety, 2) low cost, 3) throttling of thrust, 4) re-ignition, 5) nontoxic and nonhazardous propellant. However, hybrid rocket engines have low fuel regression rate and low combustion efficiency. In order to overcome those disadvantages, there are several research activities[1-6].

In the present study the new method that can improve the fuel regression rate more than that of conventional methods is proposed. The method is multi-section swirl injection method. In the previous, though the proposed method showed excellent increase of fuel regression rate, the combustion duration was rather short. In the present study longer combustion duration has been established for 8 seconds. The increase of combustion efficiency has been realized.

2. Method

Figure 1 shows the schematic diagram of multi-section swirl injection method. The injection of the oxidizer through a number of injector holes that are set in the fuel grain causes swirling flow.

High density polyethylene fuel and paraffin fuel (FT-0070) are used for the present study. Three different grain length of fuel grain with inside diameter of 35 mm are tested in high density polyethylene fuel and paraffin fuel. Diameter of the injector holes, which inject the oxidizer, are 1 or 2 mm. In the present study four injector holes are located at four cross-sections along the axis of the fuel grain.

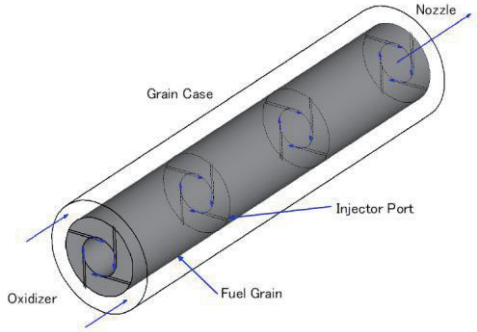

Fig. 1 Schematic diagram of multi-section swirl injection method.

3. Results and Discussion

3.1 High Density Polyethylene Fuel Cases[7]

Figure 2 shows schematic diagram of Grain type A through D of High Density Polyethylene fuel. To reduce the interference of each injector port, the number of injector ports at each cross-sections is decreased from four(Type A) to three(Type B). The injector port diameter was 2.3 mm to conform the total injector port area of previous study. Also, to reduce the interference of each injector port, the number of injector ports at each cross-sections is decreased from four(Type A) to two(Type C). The injector port diameter was 2.8 mm to conform the total injector port area of previous study. In addition to Type C, Type D has two injection ports at only two cross-sections from upper stream.

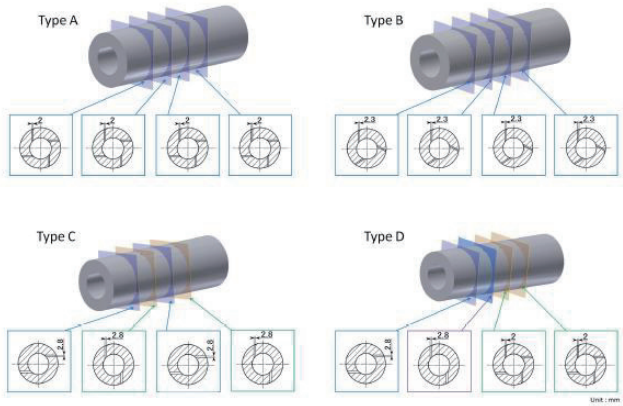

Fig.2 Schematic diagram of Grain type A through D (fuel: High Density Polyethylene)

Case	Case1	Case2	Case3	Case4	Case5	Case6
Grain Type	A	A	B	B	C	D
L[mm]	200					
d_p[mm]	2	2	2.3	2.3	2.8	2.8 & 2
p_c[MPa]	1.1	0.7	1.1	0.7	0.7	0.7
$\bar{r}$[mm/s]	0.52	0.60	0.68	0.60	0.62	0.69
$\overline{G_{ox}}$[g/cm^2·s]	3.61	5.35	3.19	5.22	5.10	5.09
$\overline{O/F}$	3.5	4.5	2.4	4.4	4.2	3.8
c^* Efficiency	0.92	1.00	0.86	1.08	1.06	1.03

Fig.3 Testing conditions and experimental results (fuel: High Density Polyethylene)

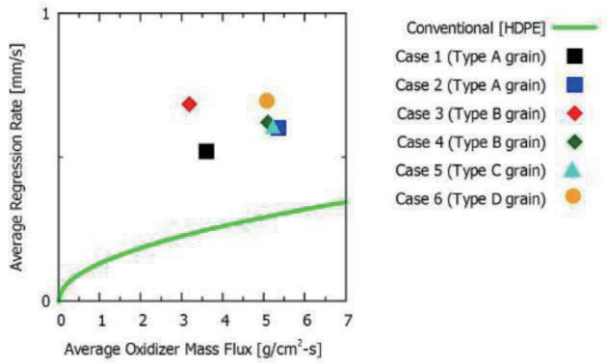

Fig.4 Correlation between average regression rate and average oxidizer mass flux (fuel: High Density Polyethylene)

Testing conditions and experimental results are shown in Figure 3. Also, correlation between average regression rate and average oxidizer mass flux for testing cases are shown in Figure 4. The results show Type B at smaller average oxidizer mass flux suggests higher average regression rate compared with that of Types A, C and D. This results shows interaction between injection gas is decreased by reducing number of injections from 4 to 3 at single cross section. Also Type D shows higher average regression rate compared with that of Type A ,B and C at higher average oxidizer mass flux. The results show two injector ports at upstream section works well to reduce injection jet interaction and four injector ports at downstream section does not cause major injection jet interaction because direction of injection jets at downstream bends downstream and does not interact each other and in this condition four injection jets are quite effective.

3.2 Paraffin Fuel Cases[8]

Figure 5 shows schematic diagram of Grain type A through D of paraffin fuel(FT-0070). To reduce the interference of each injector port, the number of injector ports at each cross-sections is decreased from four(Type A) to three(Type B). Also, to increase turbulent combustion, in Grain Type C the direction of swirl is alternated between clockwise and counterclockwise as shown in unlike Grain Type A. In Grain type D direction of swirl is varied as one anti-clockwise direction and three clockwise directions as shown in Figure 5.

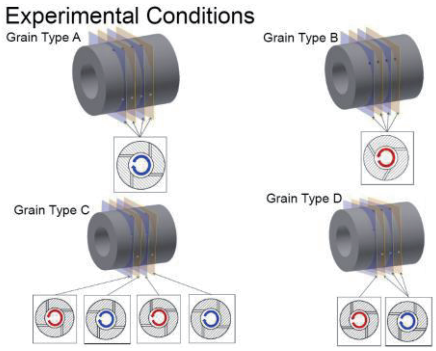

Fig.5 Schematic diagram of Grain type A through D

(fuel: Paraffin fuel: FT-0070)

Grain Type	A	B	C	D
Throat Diameter [mm]	15			
Combustion Pressure [MPa]	0.92	0.88	0.93	0.91
Oxidizer Mass Flow Rate [Kg/s]	0.062	0.056	0.059	0.060
O/F	1.39	1.19	1.58	1.19
c^* efficiency	0.92	1.0	0.98	0.95

Fig.6 Testing conditions and experimental results (fuel: Paraffin fuel: FT-0070)

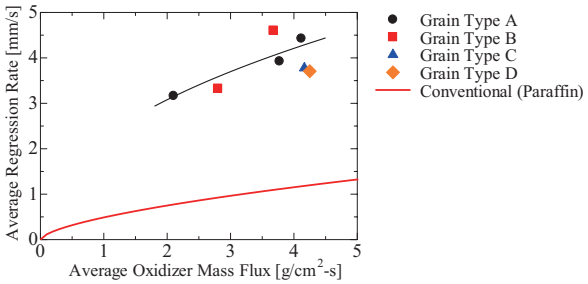

Fig.7 Correlation between average regression rate and average oxidizer mass flux (fuel: Paraffin fuel FT-0070)

Testing conditions and experimental results are shown in Figure 6 Also, correlation between average regression rate and average oxidizer mass flux for testing cases are shown in Figure 7. The results show Type B at larger average oxidizer mass flux suggests higher average regression rate compared with that of Types A, C and D. Also the results show reduction of number of injection jets in same cross section and switching swirl direction of injection jets are effective to increase turbulent combustion.

4. Conclusions

For fuels of high density polyethylene fuel and paraffin fuel, the average regression rate of three injector ports grain type per a cross section at high oxidizer mass flux is higher than that of four injector ports type. This means that average fuel regression rate was increased by reducing the interference of oxidizer injection.

For paraffin fuel, c* efficiency and thrust of grain type with clockwise and counterclockwise swirl is larger than that of only clockwise swirl grain type, because that mixing of paraffin wax and oxidizer is enhanced. Proposed methods might improve c* efficiency and thrust without mixing chamber

References

[1] Nagata, H. et al.: Acta Astronautica, **59 (1-5) (2006)**, 253-258.
[2] Tamura, T. et. al.: AIAA paper 99-2323 (1999).
[3] William, H. et. al.: AIAA paper 99-2318 (1999).
[4] Aso, S. et. al.: AIAA paper 2011-5907 (2011).
[5] Sutton, G.P.: Rocket Propulsion Elements, John Willey & Sons, New York, 6th Edition (1992).
[6] Karabeyoglu, A. et. al.: Journal of Propulsion and Power, **20**, No. 6 (2004), 1037-1045.
[7] Ohyama, S. et. al.: AIAA-2013-4040(2013)
[8] Araki, K. et. al.: AIAA-2013-3634(2013)

Tenth International Conference on Flow Dynamics
November 25-27, 2013, Sendai, Miyagi, Japan

Study on Mechanical Property of Low Melting Temperature Thermoplastic Fuel

Yutaka Wada[1], Keisuke Seki[1], Nobuji Kato[2], Keiichi Hori[3]
[1]Akita University, Akita, Japan [2]Katazen corporation,Aichi, Japan, [3]ISAS/JAXA, Kanagawa, Japan
E-mail:wada@mono.akita-u.ac.jp

ABSTRACT

Hybrid rocket using Low Melting Temperature Thermoplastics (LT) fuel as a solid fuel has been studied. The LT fuel has higher regression rate than classical inert polymer fuel such as a Hydroxyl-Terminated-PolyButadiene (HTPB), and an excellent mechanical property as same as solid propellants. Efforts has been paid successfully to enhance the adhesion property against metallic casing and linear material, and thus, the fuel looks promising for the application to large scale motors. In this paper, the detailed discussion of this investigation of LT fuel mechanical property is presented.

1. Introduction

The hybrid rocket is focused / expected as a next sounding rocket motor and a manned space vehicle engine because of having low cost system and high safety design due to the non-explosive propellant. However, the hybrid rocket system has not established of commercial base as a mainstream the space system. The reason is difficult to generate the large thrust due to the low combustion efficiency, the low fuel regression rate and poor fuel mechanical property of the hybrid rocket.

Therefore, the thermoplastic polymer of the low melting point excellent in the mechanical property is focused in this study. The LT fuels have been developed by Katazen Corporation, and the melting point of the fuels is approximately at 90 degree Celsius. The regression rate characteristics with gaseous oxygen were evaluated in the previous study. Figure 1 shows the results, and the LT fuel has higher regression rate than classical fuel by three to four times because of the similar physical property with paraffin and wax fuels[1].

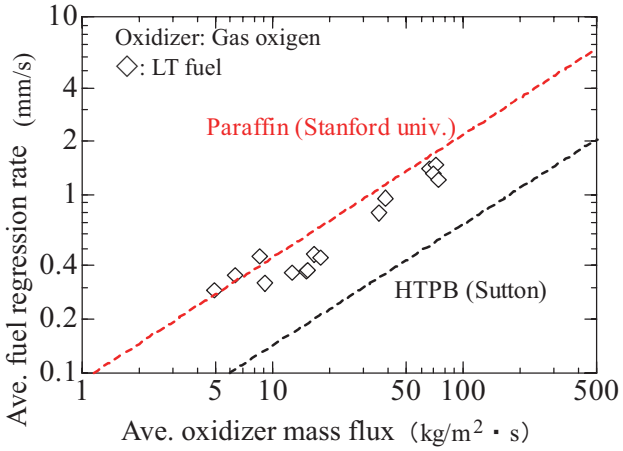

Fig. 1 Comparison of regression rates for LT fuel, HTPB, and paraffin fuel.

The uniaxial tensile test of the LT fuel was carried out and evaluated. The maximum strain is over 300% at the test sample, and they have enough elongation better than the conventional solid motor propellant. Therefore, in this study, several types of LT fuels are evaluated the mechanical property and adhesion property. And both of results are compared and discussed.

2. LT fuel

The LT fuel was composed of several chemicals. Table 1 shows the compositions, mechanical properties, and the regression rate at 50kg/m^2 of averaged oxygen mass flux of four samples. The paraffin oils are the main component at all LT fuels, and the styrene resin is used as the thermoplastic resin. The xylene resin is added to improve the adhesive property. Stearic acid is selected as a solubilizing agent between xylene resins to other components.

The sample #2 has highest regression rate than other samples. The adhesion test of the sample #2 and the sample #4 was carried out and evaluated in this study.

Table 1. Component and mechanical property of LT fuel samples

Component (Mass %)	#1	#2	#3	#4
Styrene resin	10.2	8.7	11.3	13.1
Xylene resin	0	12.5	32.3	31.3
Stearic acid	0	4.2	3.2	6.2
Paraffin oils	89.8	74.6	53.2	49.4
Temp. @2000poise (°C)	Not measure	72.3	92.8	95.7
GOX Regression rate @50kg/m^{2}s (mm/s)	0.85	1.13	0.93	0.83

3. Experimental setup

Tensile test was conducted according to JIS K 6251. More than four measurements were conducted for each sample at the chuck displacement rate of 500±50mm/min. Measurement items are maximum tensile force (N), gauge length of yield point (mm), gauge length at cutting (mm), cutting tensile force (N) and video recording. Black sign in the position of 40mm of gauge length was marked to the test piece.

The LT#2 and #4 fuels were evaluated for adhesive property to EPDM rubber (ethylene propylene diene monomer rubber) using polyolefin-based adhesive. The photograph of an adhesion test sample is shown in Fig. 2. The tensile tester used in adhesion test is 5967 series INSTRON. More than four measurements were conducted for each sample at the chuck displacement rate of 1000±50mm/min. Measurement items are maximum tensile force (N), gauge length of yield point (mm), gauge length at cutting (mm), cutting tensile force (N) and video recording.

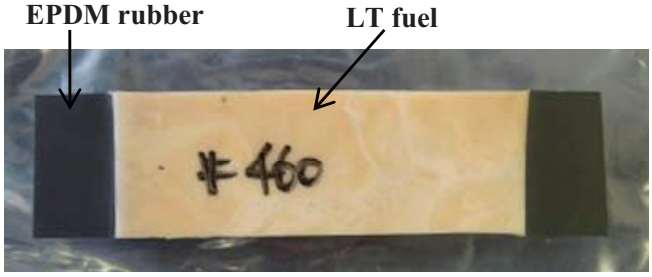

Fig. 2 Adhesion test pieces.

Fig. 3 Test piece of LT#4 during adhesion test.

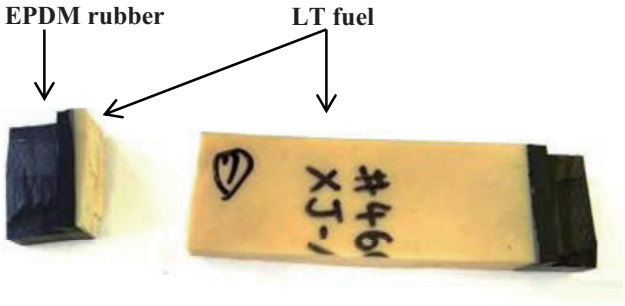

Fig. 4 Test piece of LT fuel result of adhesion test.

4. Experimental results and discussion

All samples were cut from the parallel portion of the distance between black markings, and there was little dispersion in the obtained data. Table 2 shows the results of the tensile test. The maximum strain is over 300% at all the test samples, and they have enough elongation better than the conventional solid motor propellant. The sample #4 has highest Young's modulus and maximum stress, and the sample #4 was selected as fuel of large scale.

Table 2. Component and mechanical property of LT fuel samples

Mechanical Property	#1	#2	#3	#4
Young's modulus (mN/mm2)	22.3	37.7	267.7	617.7
Maximum stress (mN/mm2)	0.06	0.09	0.41	0.58
Elongation (%)	437.4	378.8	344.0	300.2

The photograph of during adhesion test was shown in Fig.3, and the good elongation was observed. The LT#4 fuel was confirmed having excellent adhesive property from observation of cohesion failure shown in Fig.4. However, the LT#2 fuel was observed interfacial failure. The mass ratio of xylene resin is large different between #2 to #4. The results suggested that the xylene resin was worked as tackifier resin.

5. Summary

In this study, LT fuel was focused for high regression rate and excellent mechanical properties and adhesion property. The LT#4 is expected for making large scale motor fuel because of its excellent adhesive property. The LT#2 was selected as small scale motor fuel which does not need strong adhesiveness because of its high regression rate at this study. The detail research about the LT#4 for large scale motor is our near future study.

Acknowledgments

This research is supported by the Hybrid Rocket Research Working Group (HRrWG) of Institute of Space and Astronautical Science, Japan Aerospace Exploration Agency. The authors thank members of HRrWG for their helpful discussion.

References

[1]Y. Wada, M. Jikei, R. Kato, N. Kato, K. Hori, Transactions of JSASS, **10**, (2012), pp1-5.

Development of GOX Hybrid Rocket Test Engine Facility in Hybrid Rocket Research Working Group

Koki Kitagawa[1], Toru Shimada[1], Keiichi Hori[1], Toshiaki Takemae[1], Noriko Shiraishi[1], Toshio Tomizawa[1], Naohiro Suzuki[1], Tsuyoshi Yagishita[1], Nobuyuki Oshima[2], Harunori Nagata[2], Masashi Wakita[2], Kazuhisa Chiba[3], Keisuke Sawada[4], Hiroki Nagai[4], Yutaka Wada[5], Saburo Yuasa[6], Takashi Sakurai[6], Masahiro Kanazaki[6], Ichiro Nakagawa[7], Takakazu Morita[7], Masaki Nakamiya[8], Shigeru Aso[9], Yasuhiro Tani[9], Nobuyuki Tsuboi[10]
[1]Japan Aerospace Exploration Agency, Sagamihara, Kanagawa, 252-5210, Japan
[2]Hokkaido University, Japan, [3]Hokkaido Institute of Technology, Japan, [4]Tohoku University, Japan, [5]Akita University, Japan, [6]Tokyo Metropolitan University, Japan, [7]Tokai University, Japan, [8]Kyoto University, Japan, [9]Kyushu University, Japan, [10]Kyushu Institute of Technology, Japan
kitagawa.koki@jaxa.jp

ABSTRACT

To demonstrate the technologies of the hybrid rocket engine, the hybrid rocket test facility in Akiruno facility, which belongs to JAXA, were designed and reviewed. The low spec GOX feed system include the purge system, the test stand, the measurement system and the control system have been constructed so far. The operability and functionality, such as the GOX mass flow range and the natural frequency of the test stand, were checked. We confirmed that the combustion test at the condition of up to 0.5 kg/s in GOX mass flow rate can be carried out.

1. Introduction

Hybrid Rocket research Working Group (HRrWG) with the approval of the Space Engineering Steering Committee of ISAS/JAXA consists of scientists on hybrid rockets from many Japanese universities and from JAXA in order to research hybrid rockets scientifically. From 2008, basic researches, such as development of new fuel, clarifying hybrid combustion mechanism, development of element technology, development of numerical analysis code and clarifying future concept, are carried out. To some extent, technology for the hybrid rocket engine is matured in HRrWG. It becomes the step of performing demonstration of the technologies at present. We set the target to the thrust of 5 kN.

In 2012, the demonstrators of Hybrid rocket Test Engine (HTE-5-1) and the test facility in Akiruno facility, which belongs to JAXA, were designed preliminary [1]. In 2013, one of the demonstrators [2] and the low spec test facility which can feed low mass flow of GOX were designed and manufactured. In this paper, the outlines of the low spec test facility are introduced.

2. Test facility

The main components of the test facility are a feed system, a test stand, a measurement system and a control system. In our plan, GOX feed system and LOX feed system are constructed eventually. However only the low spec GOX feed system has been constructed so far, because of the budget.

2.1 Feed system

The feed system is schematically represented in Fig.1. Figure 2 shows a photo of the feed system. This system mainly consists of a GOX feed line and a N_2 purge line. About the GOX feed line, it can supply GOX more than 0.5 kg/s for 40 s at the condition of 5 MPa in the injector upper-stream pressure. The oxygen volume flow rate is measured by the turbine flow meter. An oxygen mass flow rate is determined by the volume flow rate and the upper-stream pressure and temperature of the turbine flow meter. The oxygen flow rate is controlled by the choked orifice. The diameter of the chocked orifice is 6.5 mm. Oxygen flow tests were carried out and the flow coefficient of the orifice was measured. The result of the flow coefficient of the orifice shows in Fig. 3. The flow coefficient of the orifice is approximately 0.95.

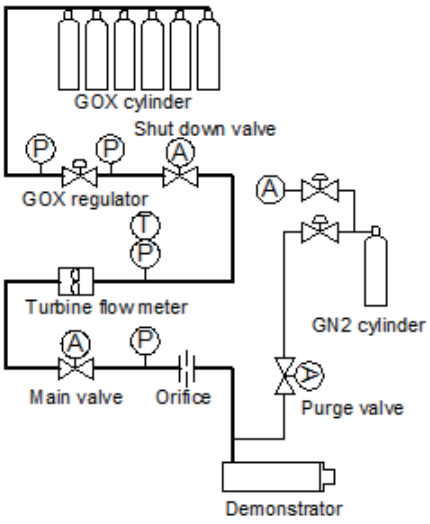

Fig. 1 Schematic of feed system

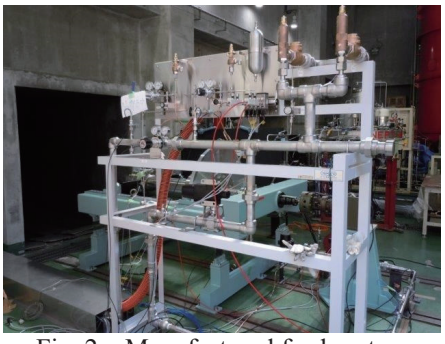

Fig. 2 Manufactured feed system

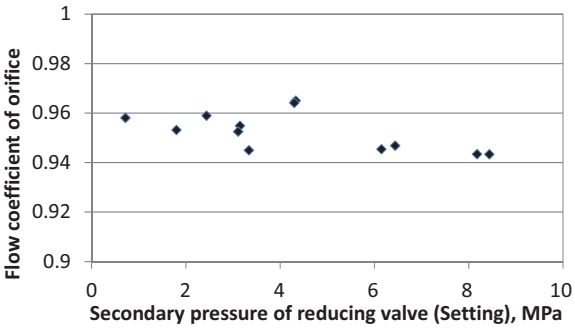

Fig. 3 Flow coefficient of orifice

2.2 Test stand

Figure 4 shows a photo of the test stand. The test stand contains the thrust measurement system. This test stand is a lifting type using plate springs to measure the thrust. The test engine is set inside the u-shaped frame. The permissible size of the test engine is up to 1 m in diameter, up to 1.5 m in length and up to 1.5 t in weight. The thrust can be measured up to 10 kN.

A hammering test was conducted to identify the natural frequency of the test stand with the demonstrator. Figure 5 shows the result of the hammering test. As a result of FFT analysis of this oscillation, it was found that the natural frequency of the test stand with the demonstrator is 23.2 Hz.

Fig. 4 Manufactured test stand

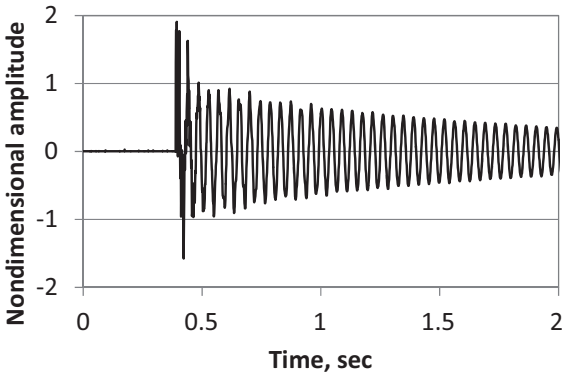

Fig. 5 Result of hammering test

2.3 Measurement system

The main parameters for the measurement are shown in Table 1. LabVIEW (National Instruments) is used for the data logger. The sampling rate is normally up to 10 ms.

Table 1 Measurement parameters

Component	Parameter
Feed system	Primary pressure of GOX reducing valve
	Secondary pressure of GOX reducing valve
	Upper-stream pressure of GOX flow meter
	Upper-stream temp. of GOX flow meter
	GOX volume flow rate
	Upper-stream pressure of orifice
	Primary pressure of purge gas
Demonstrator	Upper-stream pressure of injector
	Combustion pressure (upper)
	Combustion pressure (down)
	Down-stream temperature of injector
	Combustion chamber wall temperature
	Nozzle throat wall temperature
	Upper-stream pressure of rupture Disk
	Thrust

2.4 Control system

LabVIEW is used for the sequencer to control the valves and the ignition. If the start condition of the combustion test is not proper, a system is interlocked. If some pressures or temperatures, such as the combustion pressures or the nozzle throat wall temperature, exceed a limit during the combustion test, two feed valves are shut off and the purge gas is fed. Also, an emergency stop button is equipped. When the combustion test finishes, the purge gas is fed automatically to extinguish the combustion.

3. Summary

To demonstrate the technologies of the hybrid rocket engine, the hybrid rocket test facility in Akiruno facility, which belongs to JAXA, were designed and reviewed. The low spec GOX feed system include the purge system, the test stand, the measurement system and the control system have been constructed so far. The operability and functionality, such as the GOX mass flow range and the natural frequency of the test stand, were checked. We confirmed that the combustion test at the condition of up to 0.5 kg/s in GOX mass flow rate can be carried out.

The combustion tests using the demonstrator in reference [2] have been carried out, so far. These results are introduced in reference [2].

At the next step, the GOX feed system will be improved to the full spec by the end of by the end of this fiscal year. LOX feed line will be constructed after that.

References

[1] K. Kitagawa, et al., 9th ICFD, OS3-26, 2012.
[2] H. Ando, et al., 10th ICFD, ID 5181, 2013.

Tenth International Conference on Flow Dynamics
November 25-27, 2013, Sendai, Miyagi, Japan

Development of a 5 kN-thrust Swirling-Oxidizer-Flow-Type Hybrid Rocket Engine

Ando Hideyuki[1], Sakurai Takashi[1], Yuasa Saburo[1], Hatagaki Sakashi[1], Yui Ryosuke[2], Takahashi Shun[1], Shiraishi Noriko[3], Kitagawa Koki[4], Shimada Toru[4]
1:Tokyo Metropolitan University, Hino City, Tokyo 191-0065, JAPAN
2:University of Tokyo, 3:JAXA, 4:ISAS/JAXA
Mail:ando-hideyuki@ed.tmu.ac.jp

ABSTRACT

In order to verify how increases of the fuel grain size and an oxidizer mass flux influence combustion of a swirling-oxidizer-flow-type hybrid rocket engine, a 5kN-thrust hybrid rocket engine was developed. The engine was designed based on the fuel regression rate behavior with swirling oxidizer flow. As the first step of the demonstration of the engine technology, the burning test of the engine was carried out under the conditions below the design point of the chamber pressure and oxygen mass flow rate. Ignition was smooth, combustion was stable, and some fundamental data for evaluating the engine characteristics was obtained.

Nomencluture

F : Thrust, G_O : Oxidizer mass flux, $\dot{m}_o$: Oxidizer mass flow rate, P_c : Combustion chamber pressure, $\dot{r}$: Fuel regression rate, Sg : Geometrical swirl number, t_b : Burning time, η_{C^*} : C* efficiency, φ : Equivalence ratio, T_C : Combustion chamber temperature

1. Introduction

To actualize practical hybrid rocket engines, the authors have been developing a 5 kN-thrust hybrid rocket engine as a project of Hybrid Rocket research Working Group (HRrWG) of ISAS/JAXA. In this engine, a swirling oxidizer injection at the fuel grain head is applied to increase the fuel regression rate that is a major disadvantage of the hybrid rocket engines [1]. The fundamental burning properties of the engine were predicted considering the fuel regression behavior [2-4]. Based on this prediction, a demonstration 5kN-thrust hybrid rocket engine was designed. In this paper, the authors present the details of the developed engine and the results of the preliminary burning test.

2. Design and manufacturing of the 5 kN-thrust swirling-oxidizer-flow-type hybrid rocket engine

The objective of this study is to evaluate how increases of fuel grain size and oxidizer mass flux comparing with the previous experiment [3,4] influence combustion of the swirling-oxidizer-flow-type hybrid rocket engine. To acquire this knowledge, the HRrWG project established the target specifications of the engine as follows: the averaged thrust is more than 5 kN, the burning time is more than 10 seconds, the fuel regression rate is more than 3 mm/s, the C*efficiency is more than 95%.

A 5 kN-thrust engine was designed by considering the fuel regression rate behavior with swirling oxidizer flow. From the past experiments of the swirling-oxidizer-flow -type hybrid rocket engines, it was found that the local fuel regression rate showed different behavior in the grain front and rear regions [3,4]. Using these regression rates, the fundamental burning properties of the 5 kN-thrust engine were predicted : $\dot{m}_o$=1370 g/s, G_0=250 kg/m^{2}s, $\dot{r}$ =2.25 mm/s, φ=1.32, T_C=3600 K, P_C=4.26 MPa, F=5349 N. These values almost match the required specifications of the project except for the overall fuel regression rate. The fuel regression rate of more than 3 mm/s might be attained by increasing Sg or increasing Go with smaller grain internal diameter. The decided engine configurations were : $\dot{m}_o$=1.37 kg/s, Sg=19.4, the fuel grain is polypropylene (PP), the grain internal diameter of 56 mm and the length of 0.97 m, the nozzle throat diameter of 32 mm and the exit diameter of 82 mm.

The 5kN-thrust swirling-oxidizer-flow-type hybrid rocket engine called HTE-5-1 was manufactured and the schematic is shown in Fig.1. This engine was designed to be adapting to the Akiruno facility of ISAS/JAXA and had the same in configuration used in our previous experiments [3]. The oxidizer was GOx. The engine consisted of a commercial miniature rocket-type igniter, a swirler-type injector with Sg=19.4, a fuel grain (PP) and a graphite nozzle. The graphite was used for the nozzle and for the refractory at the fuel grain front region and at the rupture fitting flange. As an insulator, the rosnaboard was placed around the refractory. Thickness and materials of each engine part were decided to have enough strength for the maximum load of combustion.

In the burning test, the thrust, GOx mass flow rate, upper and rear combustion chamber pressure, and temperatures of the injector wall, insulator wall, burned gas near the rupture disk and nozzle throat wall were measured. The engine system has two safety mechanisms. First, when the temperature or pressure exceeds the limit value, the burning test is immediately aborted by stopping the oxidizer supply and blowing the nitrogen gas. Secondly, the engine has rupture disk which rapidly releases the pressure in the engine when the pressure exceeds the limit value.

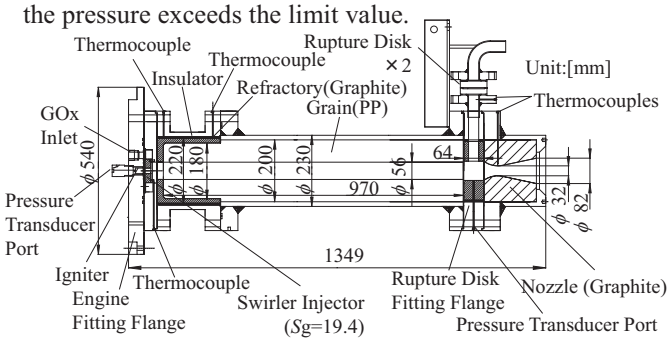

Fig.1 Schematic of 5 kN-thrust swirling-oxidizer-flow-type hybrid rocket engine HTE-5-1

3. Ignition and combustion tests

To verify the engine design and to obtain the combustion characteristics, the ignition and combustion tests were carried out in Akiruno facility. In the ignition test (#1), the target conditions were F=0.5 kN, $\dot{m}_o$=153 g/s, Pc=0.5 MPa, t_b=2 s, whereas in the combustion test (#2) the target condition were F=1.5 kN, $\dot{m}_o$=470 g/s, Pc=1.5 MPa, t_b=5 s. In the tests, we replaced nitrogen purge gas in both the GOx supply line and the engine with oxygen before ignition. Figure 2 shows the thrust history during ignition in the ignition test. Ignition of the igniter started at about -0.2 s and the oxygen main valve opened after some delay. Then, rapid increase of the thrust indicated the ignition of the grain. Ignition occurred smoothly and reliably.

Figure 3 shows time histories of F, P_c and $\dot{m}_o$ of the engine in the combustion test #2. The combustion of the engine was stable as seen in the combustion chamber pressure. However, the thrust indicates large oscillation. From the FFT analysis, it is found that this oscillation occurred by the resonance between the engine and the thrust stand. The GOx mass flow rate gradually decreased against burning time because of the decrease of supply pressure. As a result, the combustion chamber pressure and the thrust slowly decreased during combustion.

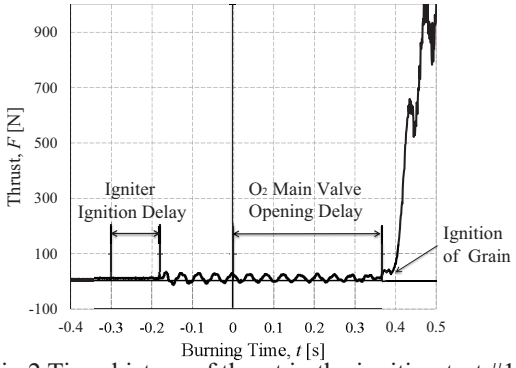

Fig.2 Time-history of thrust in the ignition test #1

4. Engine performance

We carried out twice tests (#1, #2) using the same fuel grain due to the limitation of time. Hence, the engine performance was roughly estimated based on the thrust, combustion chamber pressure, GOx mass flow rate, burning time and whole burning fuel mass. Table 1 shows the estimated engine performance. Because of the lower combustion chamber pressure than the target value of 4 MPa, the C* efficiencies were not good. However, the other engine properties agree well with the prediction and the overall fuel regression rate can be evaluated as shown in Fig.4. Thus, the developed engine keeps the same good characteristics of the swirling-oxidizer-flow type hybrid rocket engine even if the engine scale increases.

5. Concluding remarks

・The 5kN-thrust swirling-oxidizer-flow-type hybrid rocket engine using the GOx/PP propellant was designed and manufactured.

・Ignition and combustion tests were carried out in the Akiruno facility of ISAS/JAXA and the reliable ignition and stable combustion of the engine were attained.

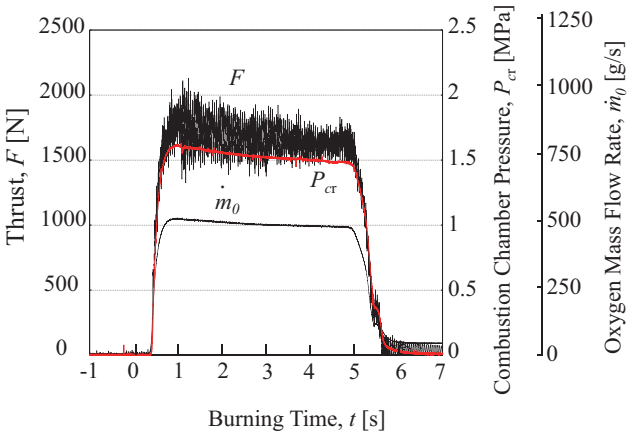

Fig.3 Data of the thrust and combustion chamber pressure and oxygen mass flow rate

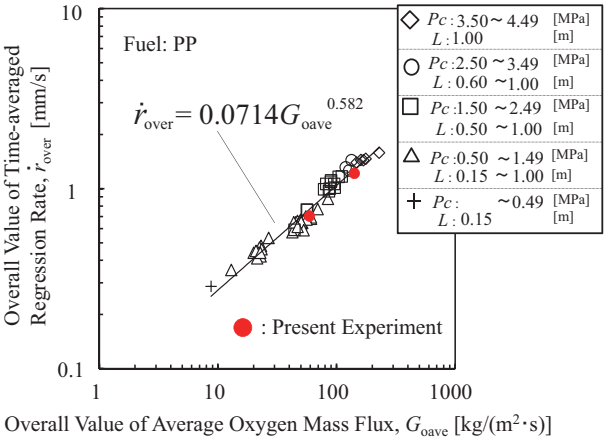

Fig.4 Relation between overall fuel regression rate and time-averaged oxygen flux

Table 1. Engine performances (#1, 2)

Run No.	Measured Values			Estimated Values			
	F [N]	Pc_r [MPa]	$\dot{m}_o$ [g/s]	φ	G_{oave} [kg/m²・s]	$\dot{r}_{ave}$ [mm/s]	η_{C^*}
#1	361	0.413	155	3.27	59.5	0.93	0.621
#2	1660	1.52	501	2.00	155	1.66	0.860

Acknowledgments

This research is supported by the Hybrid Rocket Research Working Group (HRrWG) of Institute of Space and Astronautical Science, Japan Aerospace Exploration Agency. The authors thank Mr. Irie.G., Mr. Tomizawa. T., Mr. Hayashi.D., Mr. Suzuki. N., and Mr. Yasuda. S. for their cooperation in conducting this study.

References

[1]S.Yuasa.,O.Shimada.,T.Imamura.,T.Tamura.,K.Yamamoto., AIAA Paper 99-2322, 1999.

[2] N.Shiraishi.,S.Yuasa., *J.JSASS*, 61(3),71-78,2013.

[3] K.Hirata.,C.Sezaki.,S.Yuasa.,N.Shiraishi.,T.Sakurai., AIAA Paper 2011-5677, 2011.

[4] S.Yuasa.,N.Shiraishi.,K.Hirata.,AIAA Paper 2012-4106, 2012.

Status Summary of FY 2012 Hybrid Rocket Research Working Group

Toru Shimada
Japan Aerospace Exploration Agency, Sagamihara, Kanagawa, 252-5210, Japan
shimada.toru@jaxa.jp

ABSTRACT

In this report, the status summaries of Hybrid Rocket research Working Group (HRrWG) activities of the fiscal year of 2012, especially about the fabrication and tests of Hybrid Test Engine (HTE-5-1) and basic technology R&D, are described.

1. Introduction

In this report, we describe the status of Hybrid Rocket research Working Group (HRrWG) activities in the fiscal year of 2012. With the approval of the Space Engineering Steering Committee of ISAS/JAXA, HRrWG is working for R&D of next-generation hybrid rockets (HR) as an inter-university research activity in Japan.

2. Fabrication and Functional Tests of Hybrid Test Engine (HTE-5-1)

As the first step to demonstrate technologies for next-generation hybrid rockets, we have been working on the development of HTE-5-1 that operates at 5kN thrust for more than 30 s with LOX at above 95% C* efficiency in the Akiruno testing facility of ISAS/JAXA. We have added the goal one constraint that the averaged regression rate is more than 3mm/s.

HTE-5-1 is consisting of a static firing test facility (SFTF) and various test engines and combustors (TEC). As described in FY 2011 status summary [1], we finished preliminary design of feed system, defined a system diagram, and selected high-pressure gas feeding equipment. We defined the system requirement and conducted preliminary design. In addition to those, we defined the outline of measurement system and control system. We defined two sub-goals before reaching the above-mentioned goal. The sub-goal No.1 is to achieve 5kN thrust for more than 10s with GOX at above 95% C* efficiency with average regression rate of 3mm/s. The sub-goal No.2 is to achieve the gasification of LOX, that is, to heat LOX to more than 160K and vaporize it for more than 30s at the flow rate of 1.5kg/s. Preliminary design peer reviews (PDPR) were conducted on proposed 9 TEC's. We confirmed the completion of the PDPR for the two TEC's for the sub-goal No.1 and another two TEC's for the sub-goal No.2.

In FY 2012, we have conducted the detailed design of SFTF and completed the fabrication of plumbing of the gas oxygen line and the nitrogen purge line, which enables firing experiments for the sub-goal No.1.

Next, we have carried out the detailed design of the test engine (HTE-5-1-240202-103, hereafter we refer to as "TEC-1") for the sub-goal No.1 and have conducted the detailed design peer review (CDPR) by the working group members. The detailed design of TEC-1 has been approved and fabrication has been completed. In February 2013, we conducted functional tests of the fabricated SFTF with TEC-1 installed to confirm the soundness of their designed functions, of firing test sequences, and of safety measures for firing tests. At the end of the functional tests, we conducted ignition tests, but ignition was not established at the time. (At this moment of writing this paper, September 2013, the reason of this immature ignition is clarified and static firing experiments have been conducted up to 5 seconds with generation of 1500N thrust.)

3. Technology R&D

In next-generation hybrid rockets, it is expected that innovative technologies will be used to achieve higher fuel regression rate. We conducted studies on the fuel regression characteristics under various conditions described below.

Aso et al. [2] have studied a new method with multi-section swirl injection in which swirling oxidizer flows are generated at several cross-sections in the cavity of the fuel grain. The results show the average regression rate of the proposed method is about 2 to 3 times higher in case of high-density polyethylene fuel and 10 times higher in case of paraffin fuel than that of a conventional no-swirl injection method. Nakagawa et al. [3] have studied regression rate of paraffin-based fuel under swirled oxidizer flow to find that paraffin-based fuel shows about 1.7 times higher regression rate under the conditions of the swirl number of 1.97 to 2.21 than no-swirl oxidizer flow. It is also found that the regression rate of paraffin-based fuel is over 2 times sensitive to oxidizer swirl strength, compared with that of PMMA. Nagata et al. [4] have developed regression formulas for solid fuels in CAMUI type hybrid rockets by considering effect of Reynolds number and flow channel geometry. Wada et al. [5] have studied low melting point thermoplastics (LT) material that is developed by Katazen Corporation as a hybrid rocket fuel to show that the reason for a high regression rate of LT is fuel droplets injection from the melted fuel surface by the experiments done by a double slab motor with an observation window.

We have studied on combustion efficiency of paraffin-based hybrid rockets to evaluate effects of post combustion chambers. Yuasa et al. [6] have studied the effects of post combustion chamber on combustion characteristics of paraffin-fueled swirling oxidizer-flow-type hybrid rocket engine to find that the C*efficiency is increased with increasing the residence time and also that

the effect of the residence time in the main combustion chamber on the C* efficiency is more important than that in the post combustion chamber. The study also shows that the velocity of the swirling oxygen wall jet along the grain and the flame temperature control the fuel regression rates.

We have been developing theoretical and numerical technologies for hybrid engines. Shimada et al. [7-9] have studied several topics on the internal flows and ballistics of hybrid rocket engines. Motoe and Shimada [7] have studied improvement of two-equation turbulence model for swirling flows by introducing anisotropic eddy-viscosity coefficients that can adjust particular direction of these with substantial derivative of vorticity. Funami and Shimada [8] has studied on the validation of their simplified numerical prediction model of hybrid rocket internal ballistics and confirmed that numerical evaluation of time- and space-averaged regression rate agrees well with that in experiments, whereas n-exponent of the regression rate dependence on the oxidizer mas flux deviates from experimentally-determined values. Adachi and Shimada [9] have been investigating numerically liquefied fuel characteristics, especially the liquid film stability under super-critical conditions with using van der Waals equation of state. They have discussed the characteristics of steady-state solutions obtained to serve as the base flow for instability analysis of liquid layer, as well as the numerical scheme appropriateness for the problems concerned.

Morita et al. [10] have presented a theoretical analysis of the low-frequency unstable combustion in hybrid rocket motors with a liquid-fed system by applying a linear stability analysis to the quasi-one-dimensional mass and momentum conservation equations of the gas mixture in hybrid rocket motors. The analysis accommodates the spatial non-uniformities of the physical quantities in the combustion chamber so that it is applicable to large hybrid rocket motors. In addition, it includes the non-steady effects of pre- and post-combustion chambers. Sawada et al. [11] have performed a computation of flow field in a combustion chamber of swirling-oxidizer-type hybrid rocket engine in order to predict local regression rate. Three-dimensional Navier-Stokes equations with thermochemical assumption are solved and the local regression rate is determined from the heat balance on the fuel surface. The computed time-averaged local regression rate along the fuel surface shows a qualitative agreement with the experimental results, whereas the computed regression rate becomes smaller than those for experimental data with similar oxidizer mass flux. Kanazaki et al. [12] have worked on multi-disciplinary conceptual design of multi-stage hybrid rocket.

We also worked on preconditioning methods for unsteady compressible flows, utilization of flamelet model and Large Eddy Simulation for combustive turbulent flow simulation. Preliminary investigations are set out on ignition simulation, parallel swirling flow mixing enhancement, and theoretical stability analysis of hybrid rocket with swirling injection.

4. Summary

The activities of Hybrid Rocket research Working Group of FY 2012 are described. We would like to continue these activities toward the establishment of next-generation rocket technologies that meet the future social demands.

Acknowledgments

The author would like to thank for the support of the members of Hybrid Rocket research Working Group.

References

[1] T. Shimada, Status Summary of FY 2011 Hybrid Rocket Research Working Group, ICFD, 2012.

[2] S. Ohyama, S. Aso, Y. Hirata, K. Araki, K. Oe, Y. Tani, and T. Shimada, A Study of Hybrid Rocket Engine with Multi-Section Swirl Injection Method, AIAA 2012-3905, 2012.

[3] K. Shinohara and I. Nakagawa, Regression Rate Characteristics of Paraffin-Based Fuel under Swirled Oxidizer Flow, AIAA 2012-4104, 2012.

[4] H. Nagata, M. Nohara, R. Kanai, M. Wakita, and T. Totani, Effect of Reynolds Number and Flow Channel Geometry on Fuel Regression Characteristics in CAMUI Type Hybrid Rocket, IAC-12-C4.9.5, 2012.

[5] Y. Wada, Y. Kawabata, R. Kato, N. Kato, and K. Hori, Observation of Hybrid Rocket Boundary Flame using Double Slab Motor with Observation Window, JSASS-2012-4659, 2012.

[6] D. Saito, S. Yuasa, T. Sakurai, and N. Shiraishi, Effects of Post Combustion Chamber on Combustion Characteristics of Paraffin-Fueled Swirling Oxidizer-Flow-Type Hybrid Rocket Engine, JSASS-2012-4657, 2012.

[7] M. Motoe and T. Shimada, Improvement of Two-Equation Turbulence Model with Anisotropic Eddy-Viscosity for Hybrid Rocket Research, ICCFD7-1903, 2012.

[8] Y. Funami and T. Shimada, Validation with Experiments on Simplified Numerical Prediction of Hybrid Rocket Internal Ballistics, ICNPAA 2012.

[9] M. Adachi and T. Shimada, Numerical Investigation of Liquefied Fuel Characteristics in Hybrid Rocket Engine, IAC-12-C4.2.12, 2012.

[10] T. Morita, J. Harada, S. Yuasa, K. Kitagawa, T. Shimada, and S. Yamaguchi, Theoretical Investigation of Hybrid Rocket Combustion Including Time-Delay Systems, JSASS-2012-4652, 2012.

[11] T. Koda, Y. Ogino, and K. Sawada, Flow field Calculation Coupled with Fuel Surface Regression in Combustion Chamber for Swirling-Oxidizer-Type Hybrid Rocket Engine, AIAA 2013-0715, 2013.

[12] M. Kanazaki, Y. Kitagawa, K. Kitagawa, M. Nakamiya, and T. Shimada, Multi-Disciplinary Conceptual Design of Multi-stage Hybrid Rocket using Data Mining Technique, JSASS-2012-4655, 2012.

OS2: Next-Generation CFD

Tenth International Conference on Flow Dynamics
November 25-27, 2013, Sendai, Miyagi, Japan

Parallel Implementation of DSMC Method on Graphic Card for High Altitude Aerothermodynamics of Space Vehicles

Mikhail Ivanov, Alexander Kashkovsky, Pavel Vaschenkov, Anton Shershnev
Khristianovich Institute of Theoretical and Applied Mechanics, SB RAS, Novosibirsk
sasa@itam.nsc.ru

ABSTRACT

The present work was aimed at the development of a high-performance GPU code for modeling rarefied gas flows around 3D models of space vehicles by the DSMC method. The high efficiency of GPUs for high-altitude aerothermodynamic problems is demonstrated.

1. Introduction

The Direct Simulation Monte-Carlo (DSMC) method is the main tool in studying rarefied gas flows and is widely used, in particular, in computational aerodynamics of spacecraft. The DSMC method imposes extremely high requirements to computational resources. The development of a DSMC code with the use of a Graphic Processor Unit (GPU) may substantially increase the computation efficiency.

2. Parallelization of DSMC Method on GPUs

DSMC [1] is a stochastic numerical method of solving the nonlinear kinetic Boltzmann equation, where the gas flow is presented by a large set of model particles moving and colliding with each other similar to gas molecules. The flow is modeled in a computational domain constructed around the examined model. In the simplest case, the computational domain is a parallelepiped divided into sufficiently small cells by a uniform rectangular grid. These cells are used to organize intermolecular collisions and acquire statistical information.

Modeling is performed in time, in discrete intervals Δt, with two major independent stages in each interval:

1. **Moving** of each particle in accordance with its current velocity during the time Δt.
2. Modeling of intermolecular **collisions** in accordance with the majorant collision frequency method [2]. Only particles located in one cell can collide.

The numerical algorithms are designed for applications on heterogeneous computational computers, i.e., those with several multicore computational nodes with several GPUs installed on all nodes. The nodes are connected with each other by a high-speed network. The computations are divided between GPUs by means of **domain decomposition**: the flow domain is divided into subdomains in accordance with the number of GPUs. Each GPU performs computations in cells of the subdomain allocated to it. Each computation step contains an additional **Exchange** stage, which transfers particles located after the **Move** stage in cells of some GPUs to other GPUs. As the global memory is accessible to all threads within one GPU, **data parallelism** is used in each GPU (when each thread performs the same task on different pieces of distributed data). The combination of domain decomposition and data parallelism is named **hybrid parallelization**. Figure 1 illustrates the diagram of computations on two nodes, each having three GPUs.

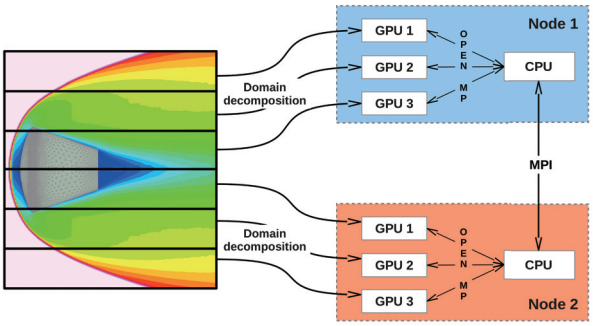

Fig.1 General scheme of hybrid parallelization

Data parallelism implies the use of the shared memory for all threads: any thread has access to all GPU data. At the **move** stage, each GPU thread shifts one particle independent from other threads and then shifts the next "free" particle. At the **collisions** stage, the thread computes collisions on one cell. This scheme ensures sufficiently uniform computational loading of all threads. The details of data parallelism are described in [3]. Independent of [3], a similar algorithm was presented in [4], which allows us to hope that this is an optimal algorithm for GPU calculations.

For correct DSMC simulations of flows, the cell size should be comparable with the local mean free path (MFP). As the MFP in the shock wave at altitudes of 80-90 km is several millimeters and a typical spacecraft size is several meters, it is necessary to use a computational grid with several million cells. A two-level grid is used in this work to reduce the number of cells. Any cell of the initial uniform grid can be divided by a uniform grid of the second level. As the MFP is inversely proportional to density, the criterion for division is the mean number of particles in a cell. As the number of particles increases severalfold, the algorithm tries to decrease the cell volume by the same factor. If the number of second-level cells is identical along each coordinate axis, it is obvious that, for instance, for the 2x2x2 division, the density in the first-level cell should increase by a factor of 8. Owing to this procedure, only significant changes in flow density are tracked. Therefore, the cell size in each coordinate direction is chosen to be proportional to the gradient of the number of particles in this direction. If the density in some axial direction remains almost unchanged, the grid is not refined in this direction. As a result, the grid can be more smoothly adapted to local MFP values.

An important aspect of using the two-level grid is an

almost identical mean number of particles in all cells. Therefore, in modeling collisions, which depend on the number of particles in a cell, the GPU threads are loaded fairly uniformly. In some test cases, the **collisions** stage could be more than twice accelerated owing to the use of a two-level adaptive grid.

As the GPU memory is limited, several graphic cards have to be used for modeling the flow around real spacecraft. In this case, it is important to minimize the exchange of particles between the GPUs and to ensure the load balance. To minimize the exchange of particles, the computations are performed in a flow-fitted coordinate system, where the incoming flow is always directed along the X axis, and the spacecraft model is aligned at specified angles of attack and sideslip. Domain decomposition between the GPUs is performed by layers of cells along the X axis. In this case, the streamlines usually do not go outside the subdomain belonging to on GPU, and particles pass to the neighboring subdomain due to thermal velocity only, and the number of such particles is small.

The exchange of particles between the GPUs can be performed via MPI. In the proposed scheme of parallelization (see Fig.1), the exchange of particles between the GPUs within one node is performed via the CPU memory. As compared to the use of MPI only, the code became more complicated (because it is necessary to use OpenMP for GPU control), but provided substantial reduction of system overhead and the amount of information transferred via MPI, which ensured an 8% speedup of computations.

Uniform loading of all GPUs is ensured by using the dynamic load balance. For this purpose, the cells are periodically redistributed over the GPUs so that the number of cells, including the second-level cells, on each GPU is more or less identical. As there is an approximately identical number of particles in each cell owing to the grid adaptation algorithm, each GPU has an approximately identical number of particles and collisions.

Test computations of various spacecraft models with the use of up to 24 GPUs show that the above-considered algorithms provide the parallelization efficiency of 80-95%.

4. Example of GPU computation

The computations were performed on a 24 GPU Tesla M2090 for a Prospective Piloted Transport System (PPTS) at an altitude of 80 km. For comparison, a similar computation was performed on a 128 CPU Intel Xeon E5420 @ 2.50GHz. Figure 2 shows the Mach number flowfield, and the computer resources used in these computations are listed in Table 1. The CPU computation required a greater amount of memory because some part of information (geometric model, etc.) is duplicated on all processors. The greater number of cells in the GPU computations is caused by the difference in the algorithms of construction of the second-level grid in the CPU code. The use of GPUs provided results within less than eight hours (overnight) instead of two days, and the number of computational devices was five times smaller. Therefore, the number of processor-hours was smaller almost by a factor of 36. Thus, the GPU computations substantially simplify and speed up numerical investigations of high-altitude aerodynamics.

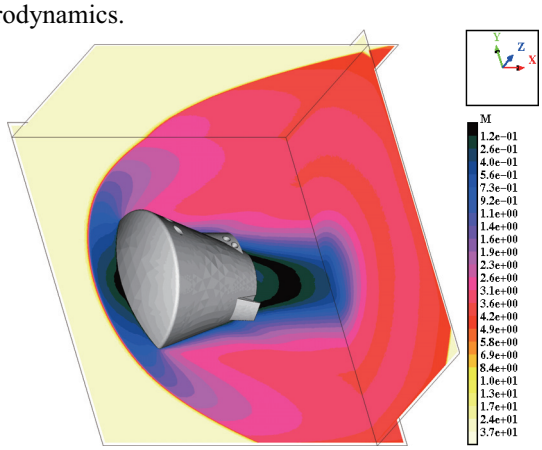

Fig.2 Mach flowfield.

Table 1. Comparison of computer resources

	CPU	GPU	CPU/GPU
Processors	128	24	5.3
Particles, [mln]	215	216	
Cells, [mln]	18	42	
Calculation time, [h]	51	7.75	6.4
Processor-hours	6500	182	35.7
Alloc. memory, [Gb]	175	127	1.4

4. Conclusions

The use of GPUs is a promising direction in high-altitude computational aerodynamics. A smaller number of GPUs makes it possible to reduce the cost of the cluster and energy consumption. To solve moderate-scale problems (<20 CPU processors), a possibility of fast computations on one graphic card built into the office computer is provided. For large-scale problems, it seems easier in the future to find a cluster with 10-20 graphic cards than an MPI cluster with 500 and more processors.

Acknowledgements

This work was supported by the Collaborative Research Project IFS No. J13058, IFS No. J13059, Grant RFBR 11-07-00135

References

[1] G.A. Bird, Molecular Gas Dynamics and the Direct Simulation of Gas Flows, Clarendon Press, Oxford, 1994.

[2] M.S. Ivanov, S.V. Rogazinsky, Analysis of the numerical techniques of the direct simulation Monte Carlo method in the rarefied gas dynamics. Soviet J. Numer. Anal. Math. Modelling, **3**, 453--465 (1988).

[3] A.V. Kashkovsky, A.A. Shershnev, and M.S. Ivanov, Efficient CUDA implementation in the DSMC method, // Rarefied Gas Dynamics: 28th Int. Symp., 2012, pp. 511-518

[4] Su, C.-C.; Smith, M. R.; Kuo, F.-A.; Wu, J.-S.; Hsieh, C.-W.; Tseng, K.-C., Large-scale simulations on multiple Graphics Processing Units (GPUs) for the direct simulation Monte Carlo method.// Journal of Computational Physics, V. 231, I. 23, p. 7932-7958.

Tenth International Conference on Flow Dynamics
November 25-27, 2013, Sendai, Miyagi, Japan

Assessment of Hypersonic Reentry Flow Modeling with Thermal Nonequilibrium Air Chemistry

Heriberto Saldívar Massimi[1], Yen-Sen Chen[2], Y.Y. Lian[3], Cheng-Chin Su[3]
Ming-Chung Lo[3], Chih-Yung Wen[1], Jong-Shinn Wu[3], Y. A. Bondar[4], M. S. Ivanov[4], Shen-Min Liang[5]
[1]Department of Aerospace Engineering, National Cheng Kung University, Tainan, Taiwan
[2]National Space Organization, Hsinchu Science Park, Hsinchu, Taiwan
[3]Department of Mechnical Engineering, National Chiao Tung University, Hsinchu, Taiwan
[4]Khristianovich Institute of Theoretical and Applied Mechanics SB RAS, Novosibirsk, Russia
[5]Department of Computer Application Engineering, Far East University, Tainan, Taiwan
e-mail: yenchen@nspo.narl.org.tw

ABSTRACT

The present work focuses on the problem of aerothermodynamics of blunt bodies on the hypersonic segment of the flight trajectory. Firstly, the in-house Navier-Stokes solver, UNIC-UNS code, with the slip boundary condition is used to simulate flows around a spherical-nosed cylinder at different Knudsen and Mach numbers, in order to validate the code capability in providing accurate predictions of the shock structure. Simulations of thermal-chemical nonequilibrium air flows around blunt bodies are performed at different Mach and Knudsen numbers, and the results are compared with DSMC results and experimental data.

1. Introduction

The development of promising future generation space vehicles require a complete and detailed knowledge of their aerothermodynamics along the complete descent trajectory [1-3]. For this reason, it is necessary to study phenomena associated with rarefaction and thermochemical non-equilibrium of the gases in hypersonic flows. Typical parameters (Mach numbers, Ma, and Knudsen numbers, Kn), of the flow around the space vehicle at high altitudes are very often beyond the capabilities of ground-based facilities; therefore, numerical methods of rarefied gas dynamics have become practically an effective tool for studying these phenomena and vehicle design parameters.

Continuum methods based on solving the Navier-Stokes equations are usually used for studying the flow around space vehicles at lower altitudes [4-5]. The initial rarefaction effects are taken into account with the use of the slip and temperature jump boundary conditions. Continuum methods cannot be used to describe the flow at higher flight altitudes because of strong rarefaction effects. A kinetic description of the flow based on the Boltzmann equation should be used in this case.

The Direct Simulation Monte Carlo (DSMC) method is a widely used numerical method of solving the Boltzmann equation [6-9]. The DSMC method also allows correct simulations of non-equilibrium rarefied flows at lower altitudes, but as the flight altitude decreases (the near-continuum flow regime), the cost of simulations rapidly become extremely expensive. Of particular interest are investigations where the DSMC method is combined with methods of continuum gas dynamics (solving the Navier-Stokes equations in the transitional and near-continuum flow regimes: there is a range of parameters where both the continuum and kinetic approaches can be used. Because of the complicated character of non-equilibrium physical and chemical processes in such flows, the problem of cross validation of the continuum and kinetic approaches for the near-continuum flow regime has not been completely solved yet.

With the increasing success on the development of new thermal protection materials, that offer higher possibilities of developing a space vehicle with a high lift-to-drag ratio, the problem of studying specific features of high-velocity flows in the vicinity of sharp and weakly blunted leading edges has brought renewed attention to the field of hypersonic aerothermo-dynamics. To estimate the applicability of continuum gas dynamics solution methods for studying such flows, it is necessary to determine the range of parameters where those flows can be accurately described by the Navier-Stokes equations, whereas the DSMC method can be used as a reference solution.

First, this work focuses on the validations of our in-house UNIC-UNS [10] code for Mach between 5 and 10, and Kn between 0.06 and 0.5. Then, simulations of blunt body thermal nonequilibrium flows at different Mach and Knudsen numbers are performed and the results are compared with those of DSMC and of Tchuen and Zeitoun [11].

2. Method

The in-house UNIC-UNS code is used for the solutions of the Navier-Stokes descriptions of thermally and chemically non-equilibrium airflow. The SMILE [12] software system is employed for DSMC computations to validate the UNIC-UNS code in the transition to rarefied flow regime.

For transition flow regime with the continuum approach, the wall boundary conditions are modified considering the velocity slip and temperature jump based on near-wall gas kinetics [13]. The wall slip velocity, u_w, is calculated as:

$$u_w \approx \left(\frac{2}{f}-1\right) l \left(\frac{du}{dy}\right)_w, \quad where \quad l = \frac{2}{3}\left(\frac{\tau_w}{\rho a}\right) \tag{1}$$

and the wall temperature jump condition is described by the following relation.

$$T_{gas} - T_w = \left(\frac{2}{\alpha}-1\right)\frac{2\gamma}{(\gamma+1)P_r} l \left(\frac{dT}{dy_w}\right) \tag{2}$$

where $f = 1$ for regular smooth surface, τ_w denotes the

wall shear stress, a is the speed of sound, T_{gas} and T_w are the translational temperature of the gas and the wall temperature respectively. And, α = 1, γ is the ratio of specific heats, and P_r the Prandtl number.

3. Results and Discussion

The free-stream conditions of 13 test cases are shown in Table 1. Argon, nitrogen and dry air (thermochemical nonequilibrium model conditions) are adopted as the test gases. The computed shock standoff distances of the present method for small Kn flows are in good agreements with previous works [14,15].

Table 1 Test cases matrix.

Case	Test Gas	Kn	Type	Ma	p (Pa)	ρ $\left(\frac{kg}{m^3}\right)$	T (K)
1	Ideal Gas (Ar)	0.1	3D	5	5.29	1.142E-4	219.585
2	Ideal Gas (Ar)	0.5	3D	5	5.29	1.142E-4	219.585
3	Ideal Gas (Ar)	0.1	3D	10	5.29	1.142E-4	219.585
4	Ideal Gas (Ar)	0.5	3D	10	5.29	1.142E-4	219.585
5	Ideal Gas (Ar)	0.1	2D	5	5.29	1.142E-4	219.585
6	Ideal Gas (Ar)	0.5	2D	5	5.29	1.142E-4	219.585
7	Ideal Gas (Ar)	0.1	2D	10	5.29	1.142E-4	219.585
8	Ideal Gas (Ar)	0.5	2D	10	5.29	1.142E-4	219.585
9	Non reacting N_2	0.06	2D	20	5.29	8.754E-5	219.585
10	Non reacting N_2	0.006	2D	20	5.29	8.754E-5	219.585
11	Non reacting N_2	0.06	3D	20	5.29	8.754E-5	219.585
12	Non reacting N_2	0.006	3D	20	5.29	8.754E-5	219.585
13	Dry Air	0.0044	3D	18	432.2	8.754E-5	252.000

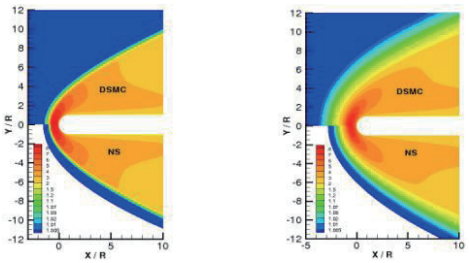

Fig. 1 Temperature fields for cases 5 and 6. M=5: Kn = 0.1 (left) and Kn = 0.5 (right).

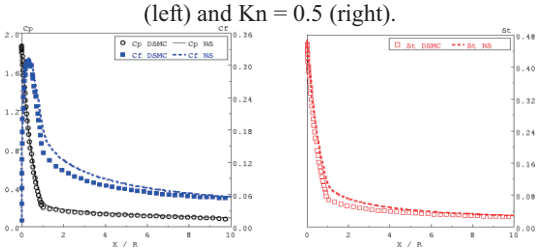

Fig. 2 Surface data for M=5 and KnR = 0.5: pressure and friction coefficients (left) and Stanton number (right).

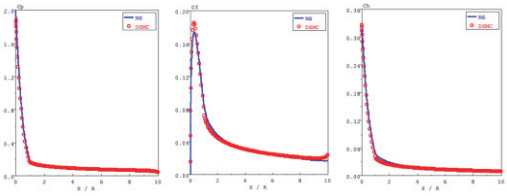

Fig. 3 Surface data for Case 10: pressure coefficients (left), friction coefficients (center) and Stanton number (right).

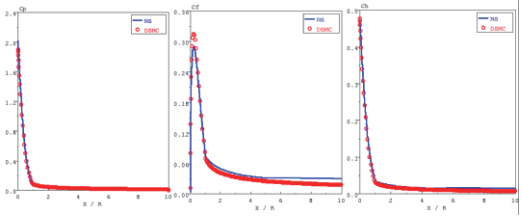

Fig. 4 Surface data for Case 11: pressure coefficients (left), friction coefficients (center) and Stanton number (right).

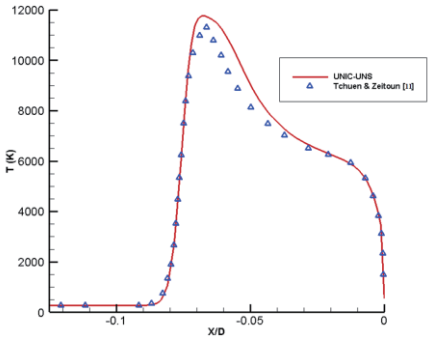

Fig. 5 Temperature profile along the stagnation line for case number 13. M=18

Figure 1 shows comparisons of shock structures between N-S and DSMC solutions [16]. Clearly, the shock thickness differences increase with Kn. The predicted surface data show close correlations in Fig. 2 even for the Kn = 0.5 case. Figures 3 and 4 show surface data comparisons for Mach 20 cases with close comparisons. These results indicate that the N-S solution with slip/jump conditions is applicable to transition flow regimes. A thermochemical nonequilibrium test case of Fig. 5 show good comparisons with data provided by other investigations [11,17].

4. Concluding remarks

The UNIC-UNS code with slip boundary conditions has been developed to simulated hypersonic flows in the transition regime over blunt bodies. This code has been validated using the DSMC baseline solutions. The predicted velocity and temperature profile, skin friction coefficient, Stanton number and pressure distributions show good agreements with the DSMC data. It is also validated for thermochemical non-equilibrium dry air conditions with the data of Tchuen and Zeitoun [11], and Rose and Stankevics [17]. Future research will include complex spacecraft geometries, with flight conditions on realistic descent trajectories.

References

[1] R. Votta, A. Schettino, G. Ranuzzi and S.F.M. Borrelli, J. Spacecraft & Rockets, 46-4, 2009.
[2] S. Di Benedetto, G.C. Rufolo, M. Marini and E. Trifoni, AIAA J., 50-10, 2012.
[3] A. Viviani and G. Pezzella, J. Spacecraft & Rockets, 47- 2, 2010.
[4] T.S. Wang, Y.S. Chen, J. Propulsion & Power, 9, 2013.
[5] Y.S. Chen, AIAA-89-0286.
[6] M. Ivanov, G.N. Markelov, S.F. Gimelshein, AIAA-98-2669.
[7] M. Ivanov, S.V. Rogasinsky, 17th RGD, 1991.
[8] G.N. Markelov, A.V. Kashkovsky and M. Ivanov, J. Spacecraft & Rockets, 38-1, pp. 43-50, 2001.
[9] G.A. Bird, AIAA J., 74, p. 239–255, 1981.
[10] Y.S. Chen, Y.Y. Lian, B. Wu and J.S. Wu, AIAA-2009-5386.
[11] G. Tchuen and D.E. Zeitoun, J. Thermophysics & Heat Transfer, 23, pp 433–442, 2013.
[12] M. Ivanov, A. Kashkovsky, S. Gimelshein, G. Markelov, A. Alexeenko, Y. Bondar, G. Zhukova, S. Nikiforov and P. Vashenkov, 25th RGD, 2006.
[13] F. White, Third Edition, McGraw-Hill.
[14] C.Y. Wen,. and H.G. Hornung, J. Fluid Mech., 299, 1995.
[15] H. Olivier, J. Fluid Mech., 413, pp. 345-353, 2000.
[16] Y. Bondar, A.A. Shershnev, A.N. Kudryavtsev, D.V. Khotyanovsky, S. Yonemura and M. Ivanov, 28th Intl. Sym. Shock Waves, pp 215-220, 2012.
[17] P.H. Rose and J.O. Stankevics, AIAA J., 1-12, 1963.

Tenth International Conference on Flow Dynamics
November 25-27, 2013, Sendai, Miyagi, Japan

A Parallel General-Purpose Direct Simulation Monte Carlo Code (PDSC^{++}) using an Unstructured Grid

Cheng-Chin Su[1], Kun-Chang Tseng[2], Ming-Chung Lo[1], and Jong-Shinn Wu[1*]
[1]Department of Mechanical Engineering, National Chiao Tung University, Hsinchu, Taiwan
[2]National Space Organization, National Applied Research Laboratories, Hsinchu, Taiwan
[*]E-mail of corresponding author: chongsin@faculty.nctu.edu.tw

ABSTRACT

In this study, a new general-purpose parallel 2D/3D DSMC (named PDSC^{++}, hereafter) based on the C++ language using a hybrid unstructured grid is developed and validated. Two key features of the PDSC^{++} code are presented in the study, including a transient adaptive sub-cell (TAS) method [1] and parallel performance of PDSC^{++}. Results show that simulations by using the TAS method can maintain the accuracy of the simulation, and up to 123 times of speedup can be reached using 192 processors. We also have demonstrated the superior capability of PDSC^{++} by simulating a 3-D problem with 1.2 billion simulation particles.

1. Introduction

Rarefied gas dynamics has played an important role in various research disciplines, which include hypersonic fluid dynamics, vacuum pump technology, low-pressure semiconductor related materials processing, and micro- and nano-scale gas dynamics, to name a few. The Boltzmann equation that governs rarefied gas dynamics is generally very difficult to solve. The particle-based method, the direct simulation Monte Carlo (DSMC) method [2], has been considered as the most efficient and accurate numerical method for solving the Boltzmann equation statistically, as long as the number of simulation particle is large enough [3]. However, its computational expense is generally very high, especially in the transitional and near-continuum flow regimes. Thus, parallel processing of the DSMC method to reduce the computational time is necessary for an efficient application of the method in general rarefied gas dynamics.

2. A General-Propose Parallel DSMC Code (PDSC^{++})

In this study, a new general-purpose parallel DSMC (PDSC^{++}) code based on the C++ language and Message Passing Interface (MPI) using a 2-D/3-D hybrid unstructured grid was developed and validated. Some important features of the PDSC^{++} include hybrid unstructured mesh, variable time-step (VTS) scheme [4], transient adaptive sub-cell (TAS) method [1], and parallel processing for load-balancing. Basic idea of the VTS scheme in PDSC^{++} is to enforce the flux conservation (mass, momentum and energy) of moving particle when crossing the interface between two neighboring cells. This strategy can greatly reduce both the number of iterations towards the steady state, and the required number of simulated particles for an acceptable statistical uncertainty. For the TAS method, a dynamically adaptive number of sub-cells, based on the local mean free path or number of simulation particles, is imposed in each cell to ensure the average collision distance is less than the local mean free path.

3. Results and Discussion

Fig. 1 shows a hypersonic flow over a 30° hollow cylinder/flare which has been investigated experimentally by Holden [5] and numerically by Wang [6]. As a further test of TAS for the three-dimensional simulation, PDSC^{++} is used to simulate the flow and compare with results of simulation and experiment. Free-stream conditions for nitrogen gas include a Mach number of 12.4, and a temperature of 95.6 K. The resulting Knudsen number based on the length of the cylinder (L=101.7 mm) is 8.264×10^{-4}. The surface of the cylinder and the flare are modeled as fully diffusive walls at a temperature of 297.2 K. A rotational energy exchange model is used with a constant rotational collision number of 5. Fig. 2 illustrates the present simulated pressure coefficients with TAS are in better agreement with experimental data than those without TAS. However, Fig. 3 shows the present simulated heat transfer coefficients with and without using TAS show a large discrepancy, while the data of the former agree better with the experiments than other simulations. As it can be seen, the simulation with TAS does improve the simulation results even when the cell size is larger than the local mean free path.

Fig. 4 shows the results of parallel performance of PDSC^{++} and it indicates that ~123 times of speedup can be reached using 192 processors for the large scale problems with 40 million particles which was performed at the ALPS cluster of the National Center for High-Performance Computing (NCHC), Taiwan. We expect a better parallel performance could be obtained, should the problem size be larger.

Finally, we demonstrate the superior capability of PDSC^{++} by simulating a Mach 9.9 hypersonic flow with a 10° angle of attack over a sharp double cone, which has an angle of 50 and 130° in the first and second cone respectively. The geometry of the double cone is described in reference [7]. The simulation conditions are air gas flow over a double cone with a diffusive wall at 290 K. The number density, velocity, and temperature in free-stream are 9.4×10^{21} particles/m^3, 1382.6 m/s, and 48.5 K, respectively. Fig 5 shows the distribution of the density and pressure on the surface of the double cone with a cell number of 7 million and the particle number of 1.2 billion using 768 cores of ALPS. The computational time in this simulation is 155 hours for 50,000 time steps.

4. Conclusion

A new general-purpose parallel 2D/3D DSMC (PDSC^{++}) based on the C++ language using a hybrid unstructured grid was developed and validated. The results indicate that up to 123 times of speedup can be reached using 192 processors for a problem of 40 million particles, which is performed at the ALPS cluster of the National Center for High-Performance Computing (NCHC), Taiwan. In addition, we also have demonstrated the powerful capability of the PDSC^{++} code by simulating a three-dimensional problem with 1.2 billion simulation particles using 768 cores of the ALPS cluster.

References

[1] C.-C. Su, K.-C. Tseng, H.M. Cave, J.-S. Wu, Y.-Y. Lain, T.-C. Kuo and M.C. Jermy, Comput. Fluids, **39** (2010), pp. 1136-1145.

[2] G.A. Bird, Molecular Gas Dynamics and the Direct Simulation of Gas Flows, Clarendon Press, Oxford, 1994.

[3] W. Wagner, J. Stat. Phys., **66** (1992), pp. 1011-1044.

[4] J.-S. Wu, K.-C. Tseng and F.-Y. Wu, Comput. Phys. Comm., **162** (2004), pp. 166-187.

[5] M.S. Holden, "Measurement in regions of laminar shock wave/boundary layer interaction in hypersonic flow-code validation", CUBRC report (CD-ROM), 2003.

[6] W.L.Wang, "A hybrid particle/continuum approach for nonequilibrium hypersonic flows", Ph.D. Thesis, University of Michigan, 2004.

[7] J.N. Moss, G.J. LeBeau and C.E. Glass, The 23th International Symposium on Rarefied Gas Dynamics, AIP Conference Proceedings, **663** (2003), pp. 425.

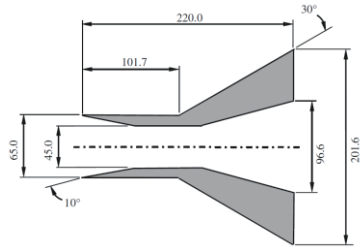

Fig. 1 Sketch for a hypersonic flow over a hollow cylinder/flare (dimension in mm).

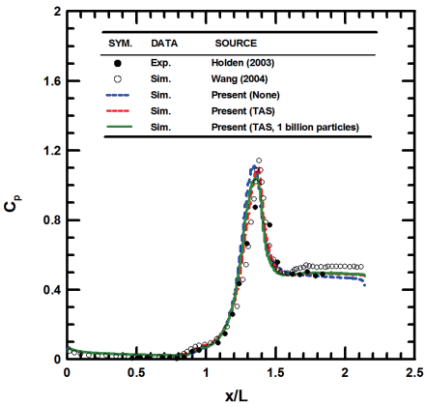

Fig. 2 Comparisons of pressure coefficient along the surface of the cylinder and flare

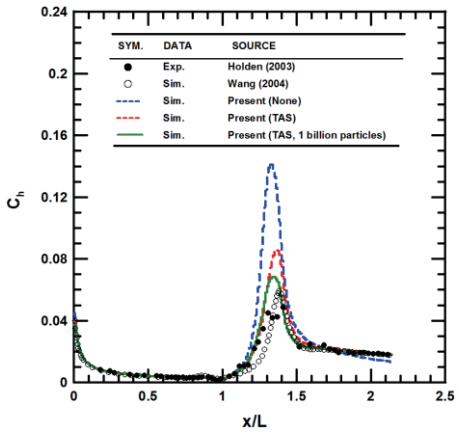

Fig. 3 Comparison of heat transfer coefficient along the surface of the cylinder and flare

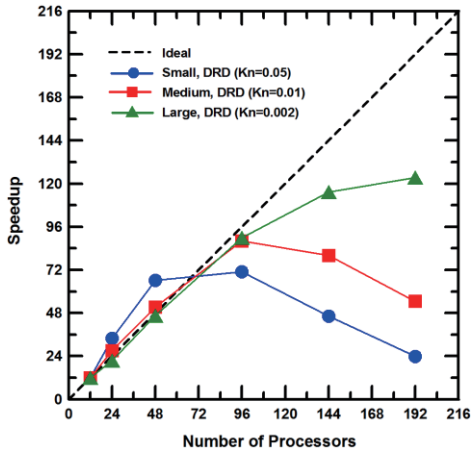

Fig. 4 Parallel performance of the PDSC^{++} code in strong scaling (40 million particles).

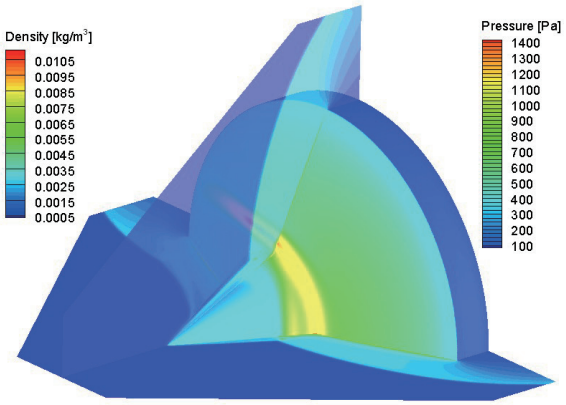

Fig. 5 Distribution of density and pressure on the surface of double cone

Tenth International Conference on Flow Dynamics
November 25-27, 2013, Sendai, Miyagi, Japan

Parallel Direct Simulation Monte Carlo Method using Cut-cell Approach with Graphics Processor Units

Ming-Chung Lo[1], Cheng-Chin Su[1], Fang-An Kuo[1], Jong-Shinn Wu[1]*, Pei-Yuan Tzeng[2]
[1]Department of Mechanical Engineering, National Chiao Tung University, Hsinchu, Taiwan
[2]Department of Mechanical, Energy and Aerospace Engineering, Chung Cheng Institute of Technology, National Defense University, Tahsi, Taoyuan, Taiwan
*E-mail: chongsin@faculty.nctu.edu.tw

ABSTRACT

In the current study, we have developed a parallel Direct Simulation Monte Carlo (DSMC) method using a cut-cell Cartesian structured grid on a single graphics processor unit, which also includes the implementations of transient adaptive sub-cell (TAS) function and variable time-step (VTS) approach to further improve the accuracy and reduce the computational time. Its capability in accurately modeling rarefied gas dynamics considering complex geometry with reduced runtime is demonstrated through several benchmarking problems.

1. Introduction

The direct simulation Monte Carlo (DSMC) method, based on particle collision kinetics, has become a dominant numerical technology for simulating rarefied and non-equilibrium gas dynamics since its invention by Bird [1] half a century ago. Recently, Graphics Processing Units (GPUs) have become an alternative platform for parallelization, employing a Single Instruction on Multiple Data sets (SIMD) parallelization philosophy. A parallel two-dimensional DSMC method using a Cartesian structured grid on multiple GPUs (graphic processor units) for simulating rarefied gas dynamics was proposed and validated [2]. The results presented an impressive capability/price ratio. However, its capability in treating complex geometry is still unexplored. Thus, we would like to further extend its capability for treating objects with complex geometry using cut-cell approach.

In addition, the quality of the DSMC simulation strongly depends upon the merit of collision (i.e., the relative ratio of averaged binary collision distance to the local mean free path), which is required to be much less than unity for a physically correct collision process physically [3]. This leads to the use of TAS (transient adaptive subcell approach) and VTS (variable time-step scheme) combining with the cut-cell approach to further reduce the runtime in the current study.

2. Method

2.1 Parallel DSMC on a single GPU

In this study, an all-device (GPU) computational approach is adopted, in which all major components of the DSMC method, including particle moving, indexing, colliding between particles and sampling, are performed in the GPU. Fig. 1 shows the flowchart of DSMC computation using a single GPU.

2.2 Cut-cell approach

In the cut-cell approach, solid body in the flow domain is cut out of a background Cartesian grid with their boundaries represented by different types of cut cells. There are three kinds of cells in the flow domain, including flow cell, solid cell and cut cell. Further, we consider three basic types of cut cells (A, B and C) which are illustrated in Fig. 2. A special treatment is proposed to properly handle particle interactions with these solid boundaries in the cut cells, which will be presented in detail in the conference.

2.3 VTS algorithm

The VTS algorithm was proposed by enforcing the conservation of fluxes (mass, momentum and kinetic energy) of each moving particle when crossing the interface between two neighboring cells [4]. The main advantage in implementing the VTS is to reduce the total number of simulation particles and thus the simulation time for the same simulation conditions.

2.4 TAS algorithm

The measure of the "collision quality" in a simulation is the ratio of the mean collision spacing (*mcs*) to the local mean free path (*mfp*). The merit of collision (*mcs/mfp* ratio) should be much less than unity for a simulation to be accurate [3]. TAS module was developed to ensure that the merit of collision is enforced everywhere in the computational domain as much as possible.

3. Results and Discussion

To validate the cut-cell approach, a simulation is performed for the two-dimensional hypersonic flow over a compression ramp, and is compared with Wu and Tseng [5] and Moss *et al*. [6]. Fig. 3 provides the density contours and shows that the maximum density is about 14.5 times than the free stream one. Fig. 4 illustrates the pressure and shear stress coefficient distribution, respectively, along the solid wall with a short ramp at three different ramp angles. Detailed simulation conditions and discussion on the physics of the flow field is skipped since it can be found in Wu and Tseng [5]. The simulation results represent that the current parallel DSMC simulation using cut-cell approach is as accurate as previous simulation study with unstructured mesh.

The two-dimensional hypersonic flow past a cylinder for several different flow regimes, from the continuum to a rarefied flow was also investigated for validation. Tables 1 and 2 compare the total drag and the peak heat

transfer predicted by different grid topologies. They proved that the simulation results in the higher *Kn* cases have a good agreement with Lofthouse *et al*. [7]. Fig. 5 and Table 3 illustrate that the use of both TAS and VTS enables replication of the benchmark results with considerably much less computational cost (about 1/14 times in this case).

4. Concluding remarks

In this study, we have proposed and validated a cut-cell approach for treating complex geometry in a recently developed Cartesian-grid DSMC using a single GPU. Running simulations with TAS and VTS results in a great reduction in the computational and memory requirements of the simulation, albeit at the cost of a reduction in the possible sampling resolution of the macroscopic properties, but without sacrificing simulation accuracy.

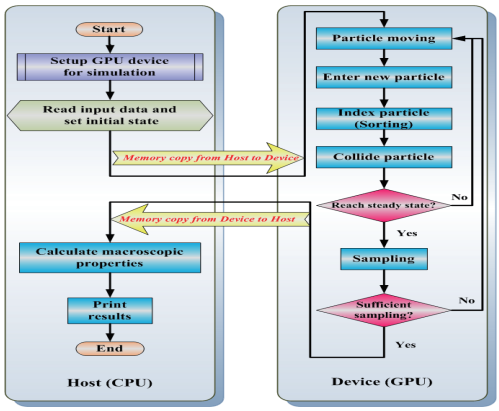

Fig. 1 Flowchart of DSMC on a single GPU

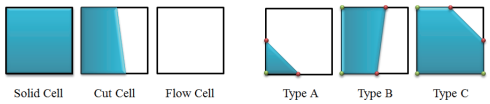

Fig. 2 Cell types (left) and cut-cell types (right)

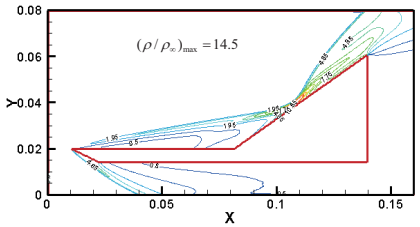

Fig. 3 Density contour of the 2-D hypersonic ramp flow

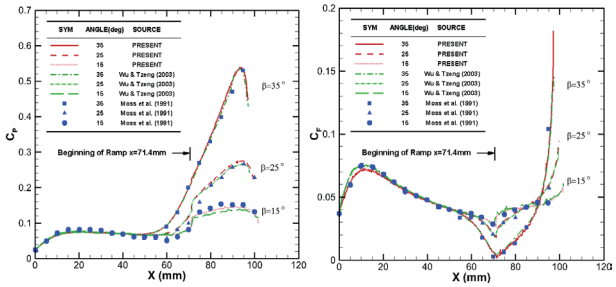

Fig. 4 Distribution of (left) pressure coefficient and (right) shear stress coefficient as a function of the distance along the short ramp at different ramp angles

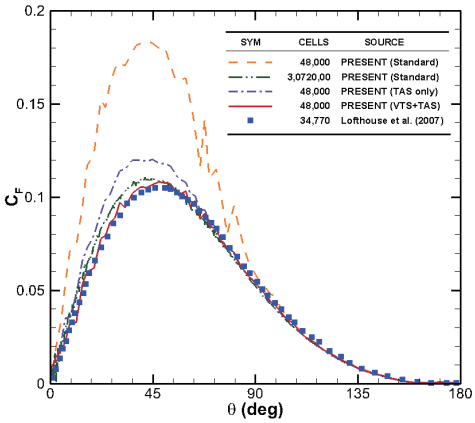

Fig. 5 Distribution of shear stress coefficient as a function of the angle around the cylinder for flow past a cylinder with or without the use of TAS and VTS

Table 1. Total drag for flow past a cylinder with different mesh methods

Kn_∞	Cut-cell	Unstructured*	Difference
0.05	8.90	8.91	0.1%
0.25	2.08	2.08	-

*Developed by Lofthouse *et al*. [7].

Table 2. Peak heat transfer for flow past a cylinder with different mesh methods

Kn_∞	Cut-cell	Unstructured*	Difference
0.05	16770	16667	0.6%
0.25	5901	5984	-1.3%

*Developed by Lofthouse *et al*. [7].

Table 3. Simulation time for flow past a cylinder with or without the use of TAS and VTS while Kn_∞=0.01. (Total time-step=50,000, sample times=20,000)

	Standard	Standard	TAS only	TAS+VTS
Total cells	48,000	3,0720,00	48,000	48,000
Simulation time (s)	1448.6	93823.7	2079.7	6793.4
$(MOC)_{max}$*	11.78	2.62	1.68	1.02

*$(MOC)_{max}$: maximum merit of collision

References

[1] Bird, G. A., Molecular Gas Dynamics and the Direct Simulation of Gas Flows, Oxford Univ. Press, 1994.

[2] Su, C.-C., Smith, M. R., Wu, J.-S., Hsieh, C.-W., Tseng, K.-C. and Kuo, F.-A., Journal of Computational Physics, Vol. 231, pp. 7932-7958, 2012.

[3] Bird, G. A., Sophisticated Versus Simple DSMC, in Proceedings of the 25th International Symposium on Rarefied Gas Dynamics (RGD25), 2006.

[4] Wu, J.-S., Tseng, K.-C., Wu, F.-Y., Journal of Computer Physics Communications, Vol. 162, pp. 166-187, 2004.

[5] Wu, J.-S., and Tseng, K.-C., ASME Journal of Fluids Engineering, Vol. 125, pp. 181-188, 2003.

[6] Moss, J. N., Rault, D. F., and Price, J. M., Rarefied Gas Dynamics: Space Science and Engineering, edited by Shzgal, B. D. and Weave, D. P., 1994.

[7] Lofthouse, A. J., Boyd, I. D., and Wright, J. M., Phys. Fluids, Vol. 19, No. 027105, pp. 1-12, 2007.

Tenth International Conference on Flow Dynamics
November 25-27, 2013, Sendai, Miyagi, Japan

Towards a General Purpose Algorithm for Applications on Rarefied Gas Flows Using Semi-classical Boltzmann-BGK Equation

Jaw-Yen Yang[1,2], Manuel Diaz[1], and Ming-Hung Chen[3]
[1]*Institute of Applied Mechanics, National Taiwan University, Taipei 106, TAIWAN*
[2]*Center of Advanced Study in Theoretical Science, National Taiwan University, Taipei 106, TAIWAN and*
[3]*Department of Mathematics, National Cheng Kung University, Tainan 70101, TAIWAN*
(Dated: July 31, 2013)

We report the current progress on the development of a general purpose algorithm for dealing with applications for rarefied gas dynamics that follows classical and quantum statisticas by using a parallel treatment of the semiclassical Boltzmann ellipsoidad statisitical (ES) BGK equation. Computation of various degrees of rarefaction and Hydrodynamic limits are presented using a numerical method that combines the discrete velocity (or momentum) ordinate method in momentum space and Discontinuous Galerkin-Finite Element Method (DG-FEM) as high resolution methods for shock capturing in physical space.

1. Introduction

Based on the generalization of Uehling and Uhlenbeck [1] for the classical Boltzmann Equation to quantum gases, and the BGK approximation [2]; new classes of classical and semiclassical Boltzmann-BGK solvers have been derived and succesfully tested for dealing with applications near equilibrium [3, 5–7]. In this regard, we further study the implementation in [7] with a class of high resolution shock-capturing scheemes based on dicontinuous Galerkin-finite element method due to have combined advantages of finite element and finite volume methods. In this method one may assume, for different element, shape functions of differente degress. On the other hand, this method have the property of element wise conservation. In the classical rarefied gas flow computation, the implementation of discrete ordinate method to nonlinear model Boltzmann equations has been developed by Yang and Huang [4]. Extension to semiclassical Boltzmann-BGK equation has been reported [7] Also, if the classical limit situations of the same flow problem are considered, then one expects to obtain similar or identical flow structures for the three statistics. Computations of several 2-D Riemann problems [8, 9] have been performed and flows over a *Forward Facing Step*, extensively studied in [10, 11], are used to illustrate the complex rarefied gas dynamics as governed by the semiclassical Boltzmann-ES-BGK equation.

2. Governing Equations in Two Space Dimensions

The semiclassical Boltzmann-UU-BGK equation in two space dimensions can be expressed as

$$\frac{\partial f(\upsilon_x,\upsilon_y,x,y,t)}{\partial t}+\upsilon_x\frac{\partial f(\upsilon_x,\upsilon_y,x,y,t)}{\partial x}+\upsilon_y\frac{\partial f(\upsilon_x,\upsilon_y,x,y,t)}{\partial y}=-\frac{f-f^{ES}_{2d}}{\tau}, \tag{1}$$

where υ_x and υ_y as particle velocity components and the two-dimensional ES equilibrium distribution, f^{ES}_{2d}, is

$$f^{UU}_{2d}(\upsilon_x,\upsilon_y,x,y,t)=\frac{1}{z^{-1}\,exp\left\{\frac{(v_x-u_x)^2+(v_y-u_y)^2}{T}\right\}+\theta} \tag{2}$$

where $\theta=-1,0$, and $+1$ denote the Bose-Einstein (BE), Maxwell-Boltzmann (MB), and the Fermi-Dirac (FD) statistics, respectively.

Once the distribution function is known, the macroscopic quantities, the number density n, number density flux $n\vec{u}$, and energy density ε, the pressure tensor P_{ij} and the heat flux vector Q_i are defined, respectively, by

$$\Phi(\vec{x},t)=\int f(\vec{p},\vec{x},t)\phi(\vec{p})\frac{d\vec{p}}{h^3}, \tag{3}$$

where $\Phi=(n,n\vec{u},\varepsilon)^T$ and $\phi=(1,\vec{\xi},\frac{m}{2}c^2)^T$. Here, $\vec{\xi}=\vec{p}/m$ is the particle velocity and $\vec{c}=\vec{\xi}-\vec{u}$ is the thermal velocity. The gas pressure is defined by $P(\vec{x},t)=[\varepsilon(x,y,t)-\frac{1}{2}n(x,y,t)(u_x^2-u_y^2)](\gamma-1)$. To obtain the new f^{UU}, one needs z this value can and these can be determined through solving,

$$\Psi(z)=2\varepsilon-\frac{\mathscr{Q}_2(z)}{\pi}\frac{n}{\mathscr{Q}_1(z)}-n(u_x^2+u_y^2) \tag{4}$$

Using a suitable root finding algorithm. Multiplying Eq. (1) by $1,\vec{p}$, or $\vec{p}^2/2m$, and integrating the resulting equations over all $\vec{p}$, then one obtains the general hydrodynamical equations

$$\frac{\partial n}{\partial t}+\nabla_{\vec{x}}\cdot(n\vec{u})=0, \tag{5}$$

$$n(\frac{\partial}{\partial t}+\vec{u}\cdot\nabla_{\vec{x}})u_i+\frac{\partial P_{ij}}{\partial x_j}=0, \tag{6}$$

$$\frac{\partial \varepsilon}{\partial t}+\nabla_{\vec{x}}\cdot(\varepsilon\vec{u})+\nabla_{\vec{x}}\cdot\vec{Q}+S_{ij}P_{ij}=0. \tag{7}$$

where $S_{ij}=(\partial u_i/\partial x_j+\partial u_j/\partial x_i)/2$ is the rate of strain tensor.

3. Solution Methods

We first apply the discrete ordinate method to discretize the velocity space and render a set of hyperbolic conservation equation with source term in physical space. Then we implement a class of high resolution shock capturing scheme. This direct solution methods in phase space for the Boltzmann-BGK type equations have been proven to be very accurate and efficient and can simulate wide range of flow parameters such as Reynolds number, Mach number and Knudsen numbers [4, 7].

4. Results and Discussion

We numerically study the two-dimensional Riemann problems and flows over a facing step for rarefied quantum

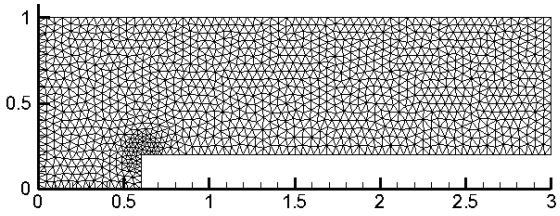

(a) Mesh

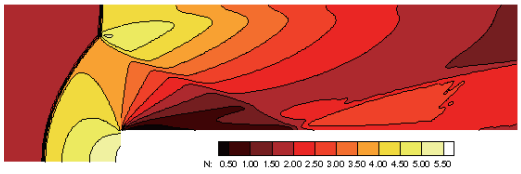

(b) Density

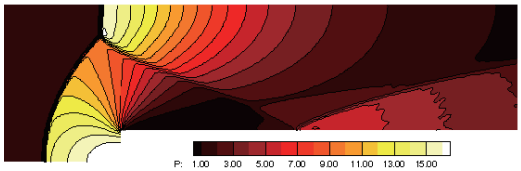

(c) Pressure

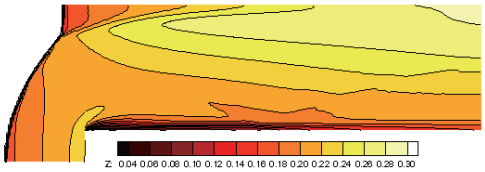

(d) Fugacity

FIG. 1: Hidrodynamic Limit for BE gas over a *Forward Facing step* using DG-FEM method.

gas dynamics for several relaxation times using the present direct solver for the semiclassical Boltzmann-BGK equation. In the $\tau \approx 0$, i.e., $Kn \approx 0$ limit, then $f \approx f^{UU}$, we can recover the ideal gas dynamics governed by the semiclassical Euler solution. Following the works of Lax and Liu [9] and Schultz-Rinne et al. [8], we selected several configurations to be tested among those 19 configurations classified. Each configuration was tested using several relaxation times, and a mesh grid refiment was performed ensure the convergence of the method. Results are consisten with observations in [8, 9]. In Fig. 1, an example of the mesh employed, the number density, pressure and fugacity countours are shown for gas following BE statistics in is hydrodynamic limit are presented. The output time 0.2. No analytical solution is known for this case, but direct comparison shows they are consistent with calculations in [10, 11]. In both case, there are detectable differences among the three statistics although the overall wave patterns are similar. Quantitatively, comparing the same contours for the three statistics, the numerical values of number density and pressure for the Bose-Einstein statistics are the largest among the three statistics and the Maxwell-Boltzmann statistics always lie between the other two as dictated by the θ values.

5. Concluding Remarks

Computations of 2-D rarefied gas flows based on the semiclassical Boltzmann-BGK equation as proposed in [7] have been presented. The computational method treats the governing equation in phase space and employs the discrete ordinate method and high resolution shock capturing schemes. Specifically, we describe the solution method in details for the equation in two space dimensions. A decoding procedure is devised for the semiclassical distribution which is different from that for standard Bose-Einstein or Fermi-Dirac distribution. Computations of two dimensional problems for rarefied gas flows of arbitrary particle statistics are where performed for several order of relaxation times which corresponding to various range of Knudsen numbers. Mesh refinement test for solution convergence has been checked and our results for small Knudsen number (Euler limit) are in good agreement with the calculations in [9][8] and with [10, 11]. These computational examples serve the purpose of exploring the nonlinear manifestation of shock wave, contact line and rarefaction wave and testing the robustness of the present method. All the expected flow profiles comprising shock, rarefaction wave and contact discontinuities of semiclassical ideal gases and their nonlinear interactions can be observed with considerably good detail and are in good agreement with available results. The present work emphasizes on building the unified and parallel framework for treating semiclassical gas dynamics of three statistics.

This work is supported by grants NSC 99-2221-E002-084-MY3 and CASTS Subproject 10R80909-4.

6. References

[1] E. A. Uehling and G. E. Uhlenbeck, Phys. Rev. **43**, (1933) 552.
[2] P. L. Bhatnagar, E. P. Gross and M. Krook, Phys. Rev. **94**, 511 (1954).
[3] W. Lei, J. P Meng, and Yonghao Zhang,Proc. Roy. Soc. A, **468**,(2012), p. 1799.
[4] J. Y. Yang and J. C. Huang, J. Comput. Phys., **120**, (1995) 323-339.
[5] J. Y. Yang,T. Y. Hsieh, Y. H. Shi, Sci. Comput. **29**,(2007) 221-244.
[6] J. Y. Yang and L. H. Hung, Phys Rev. E **79**,(2009), 056708.
[7] J. Y. Yang,B. P. Muljadi, Z. H. Li and H. X. Zhang, Commun. Comput. Phys. **14**, (2013) p. 242-264 .
[8] C. W. Schultz-Rinne, , J. P. Collinsand H. M. Glaz, SIAM J. Sci. Comput. **14**, (1993) 1394-1414.
[9] P. D. Lax and X. D. Liu, SIAM J. Sci. Comput **19**, (1995) 319-340.
[10] B. Cockburn and C. W. Shu, J Comput. Phys. **141**, (1998) p. 199-224.
[11] P. Woodward and P. Colella, J Comput. Phys. **54**, (1984) p. 115-173.

A Direct Solver for Semi-classical Boltzmann-BGK Equation in General Coordinate with Diffusive Wall

Juan-Chen Huang[1], Jaw-Yen Yang[2*] and Man-Chun Lee[1]
[1]Department of Merchant Marine, National Taiwan Ocean University, Keelung 20224, Taiwan
[2]Institute of Applied Mechanics, National Taiwan University, Taipei 10764, Taiwan
[3]Center of Quantum Science and Engineering, National Taiwan University, Taipei 10764, Taiwan
jawyen.yang@gmail.com and jchuang@ntou.edu.tw

ABSTRACT

In present study, following the previous work by J.-Y. Yang [2,3] of developing a direct solver for semi-classical Boltzmann-BGK equation for two space dimensions and implemented on gas particles that obey arbitrary statistics, we extend the method to general coordinate with diffusive wall boundary. Computational examples in two-dimensional initial value problems of rarefied gas flows are presented and the results indicating good resolution of the main flow features can be achieved. Flows of wide range of relaxation times covering different flow regimes are computed to validate the robustness of the method.

1. Introduction

Due to the rapid advancements of micro-technology and nano-technology, the structure characteristic length scales become comparable to the mean free path and the wavelength of energy. Some of the classical continuum transport laws are no longer applicable. The microscopic description of Boltzmann equation (classical and semi-classical) is adequate to treat transport phenomena in the meso-scale range. Different types of carriers (mainly electrons, photons, phonons, and molecules) may involve simultaneously in a single problem. Therefore, it is desirable to have a method that can allow one to treat them in a unified and parallel manner.

With the semi-classical Boltzmann equation [1], it is possible to describe adequately the meso-scale transport of particles of arbitrary statistics. Following the previous work [2,3], which developing an accurate direct solver for the semi-classical Boltzmann-BGK equation, the study extend the algorithm to general coordinate and to diffusive wall Boundary conditions.

2. Method

The Boltzmann-BGK equation for quantum systems with neglect the externally applied field potential is

$$\left(\frac{\partial}{\partial t}+\frac{\mathbf{p}}{m}\cdot\nabla\right)f(\mathbf{p},\mathbf{x},t)=\frac{f^{(0)}-f}{\tau},$$

where m is the particle mass, τ is the relaxation time, and $f(\mathbf{p},\mathbf{x},t)$ is the distribution function which represents the average density of particles with momentum $\mathbf{p}$ at the space-time point $(\mathbf{x},t)$. The equilibrium distribution function for general statistics is expressed as

$$f^{(0)}=\left[z^{-1}\exp\left\{\frac{(\mathbf{p}-m\mathbf{u})^2}{2mk_BT}\right\}+\theta\right]^{-1},$$

where $\mathbf{u}(\mathbf{x},t)$ is the mean velocity, $T(\mathbf{x},t)$ is temperature, k_B is Boltzmann constant $z(\mathbf{x},t)$ is fugacity. θ=+1, -1, 0 denotes the Fermi-Dirac, Bose-Einstein and Maxewll-Boltzmann statistics respectively.

By applying conventional discrete ordinate method to 2D Boltzmann-BGK equation, the distribution function in phase space $f(x,y,v_x,v_y,t)$ can be rendered into a set of hyperbolic equations in general coordinate (ξ,η).

$$\frac{\partial Q_{\sigma,\delta}}{\partial t}+\frac{\partial F^{\xi}_{\sigma,\delta}}{\partial \xi}+\frac{\partial F^{\eta}_{\sigma,\delta}}{\partial \eta}=S_{\sigma,\delta},$$

$$Q_{\sigma,\delta}=f_{\sigma,\delta}/J \qquad F^{\xi}_{\sigma,\delta}=U_{\sigma,\delta}f_{\sigma,\delta}/J$$
$$F^{\eta}_{\sigma,\delta}=V_{\sigma,\delta}f_{\sigma,\delta}/J \qquad S_{\sigma,\delta}=(f^{(0)}_{\sigma,\delta}-f_{\sigma,\delta})/\tau$$

where $f_{\sigma,\delta}(\xi,\eta,v_\sigma,v_\delta,t)$ is the discrete velocity distribution functions and velocity $U_{\sigma,\delta}=\xi_x v_\sigma+\xi_y v_\delta$, and $V_{\sigma,\delta}=\eta_x v_\sigma+\eta_y v_\delta$, where (v_σ,v_δ) is the discrete velocity point in phase space. The metric Jacobian J, and metric terms $\xi_x,\xi_y,\eta_x,\eta_y$. Once the distribution function $f_{\sigma,\delta}$ are solved for every time level, we can update the macroscopic moments in physical space using Gauss- Hermite quadrature rule. To solve fugacity z, which is the root of

$$\Psi_2(z)=2E_t-\frac{\varphi_2}{\pi}\left(\frac{n}{\varphi_1}\right)^2-n(u_x^2+u_y^2)=0,$$

where E_t is the total energy, n is the number density, and φ_1, φ_2 are quantum function defined for Fermi-Dirac and Bose-Einstein statistics respectively as

$$F_\alpha(z)=\frac{1}{\Gamma(\alpha)}\int_0^\infty\frac{x^{\alpha-1}}{z^{-1}e^x+1}dx\approx\sum_{l=1}^{\infty}(-1)^{l-1}\frac{z^l}{l^\alpha}$$

$$B_\alpha(z)=\frac{1}{\Gamma(\alpha)}\int_0^\infty\frac{x^{\alpha-1}}{z^{-1}e^x-1}dx\approx\sum_{l=1}^{\infty}\frac{z^l}{l^\alpha}$$

For diffusive wall condition, it is assumed that molecules reflecting from wall with a equilibrium velocity distribution characterized by the surface temperature T_w. Defining the half range distribution function f^+ and f^- which respect to the outgoing and incoming molecules, and

$$f^+(\xi,\eta,v_x,v_y)=0 \quad for \quad v_n<0,$$
$$f^-(\xi,\eta,v_x,v_y)=0 \quad for \quad v_n>0,$$

where v_n=$\mathbf{v}\cdot\mathbf{n}$ is the velocity component on normal direction. $\mathbf{v}$=(v_x,v_y) is particle velocity vector and $\mathbf{n}$ is the outward unit normal to the wall. On diffusive wall, the half distribution function for outgoing molecules is given by

$$f_w^+=\left[z_w^{-1}\exp\left\{\frac{1}{T_w}\left[(u_{xw}-v_x)^2+(u_{yw}-v_y)^2\right]\right\}+\theta\right]^{-1},$$

if $v_n>0$. The wall temperature T_w and wall velocity u_{xw}, u_{yw} are known, and the fugacity of the molecules

diffusing from the surface, z_w, is not known priori and could be founded by applying the condition of zero mass flux normal to the surface at the wall. That is solving the following equation

$$F(z_w) = \int_{v_n>0} v_n^+ f_w^+ d\mathbf{v} + \int_{v_n<0} v_n^- f_w^- d\mathbf{v} = 0,$$

by Newton's method, where $v_n^+ = (v_n + |v_n|)/2$ and $v_n^- = (v_n - |v_n|)/2$.

3. Results and Discussion

The first testing problem is the lid driven cavity flow with domain length 1. A grid system of 61×61 uniform grid is used for cases of relaxation time τ =0.01 and 0.05, and a uniform fine grid 101×101 is used for case of τ = 0.001 in physical space, and discrete velocity points 15×15 with Gauss-Hermite quadrature formula are used. Results were obtained under an isothermal condition with wall temperature T_w=1 and a velocity of 0.3 for the moving lid. The WENO scheme was employed.

Fig. 1(a)-(c) shows the results of streamline contours calculated with relaxation time τ =0.001, 0.01 and 0.05, respectively. The streamline plots show a large primary vortex near the center of cavity for all three cases, and along with two secondary vortices at the bottom corners for the cases of τ =0.001 and 0.01. The size of the secondary vortex at the right bottom corners is about 0.15 for τ =0.001, and nearly 0.07 for τ =0.01. The secondary vortex were damped in the case of τ =0.05. Fig. 2(a)-(c) depicts, respectively, the results of heat flux streamline contours calculated with τ =0.001, 0.01 and 0.05. From the case of τ =0.05, the heat flux streamline plots the direction of heat flux is found to be from the cold to the hot region in the layer near the driven wall. The gaseous heat transfer direction denotes a counter-gradient heat flux, which implies that thermal energy transfer need not always follow the gradient transport mechanism of Fourier's law for continuum flow. The non-equilibrium expansion and compression of gas flow effects the heat transport significantly.

The second test case is the supersonic flow over circular cylinder with Mach number 1.60, and relaxation time τ =0.001, 0.01, and 0.1. Here, due to symmetry, only half plane on the cylinder is considered and symmetry boundary conditions were employed. A grid system of 91× 121 in physical space, and discrete velocity points 20×20 with Gauss-Hermite quadrature formula are used. The isothermal wall boundary condition was used and T_w equal to free stream temperature. The steady-state solutions are obtained using the implicit LU method. Convergence of a steady-state solution is assumed to have occurred when the L_2 norm of the residual is reduced less than 10^{-4}. Fig. 3(a)-(c) shows the results of pressure contours calculated with relaxation time τ =0.001, 0.01 and 0.1, respectively. The flow structures including the bow shock, the stagnation region, the expansion fan, the shear layer, the near wake, recompression shock, and far wake regions are well captured. By comparing the results, one can observe that most of the flow structures vary with the τ values. The thickening of the front bow shock and no recompression shock are noticeable differences in the more rarefied case. Fig. 4(a)-(c) shows the results of near wake flow structures. For cases of τ =0.001 and 0.01, a recirculation zone is present in the near wake region. On the contrary, recirculation zone was damped by rarefied effects in case of τ =0.01.

4. Concluding remarks

In this work, an accurate direct solver for the semiclassical Boltzmann-BGK equation in general coordinate for diffusion wall condition was developed. Numerical experiments with two-dimensional flow indicate that the present approach is applicable to rarefied gas flows over a wide range of Mach and Knudsen numbers.

Acknowledgments

J.-C. Huang was supported by National Science Council of Taiwan through grant no. NSC 96-2221-E-019-067-MY2.

References

[1]G. Chen, Nanoscale Energy Transport and Conv., Oxford University Press, USA (2005).

[2] J.-Y. Yang, B. P. Muljadi, Z.-H. Li and H.-X. Zhang, Commun. Comput. Phys. (2013), pp. 1242-264.

[3] J.-Y. Yang and B. P. Muljadi, J. Stat. Phys. (2011), pp. 1674-1688.

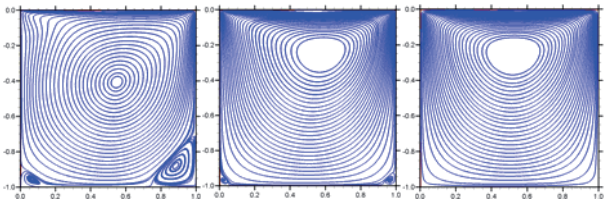

Fig. 1 Streamline contours of cavity flow with (a)τ=0.001, (b)τ=0.01, (c)τ=0.05.

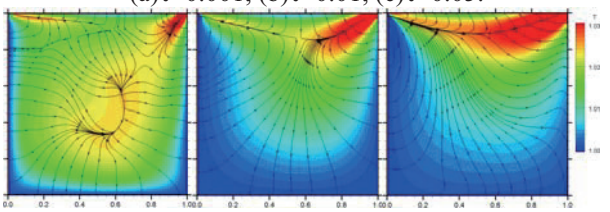

Fig. 2 Heat flux streamline contours of cavity flow with (a)τ=0.001, (b)τ=0.01, (c)τ=0.05.

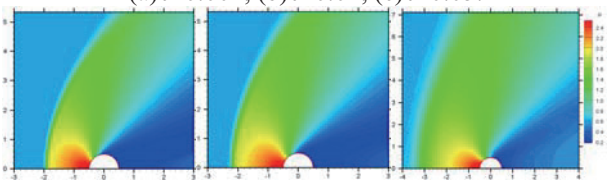

Fig. 3 Pressure contours of cylinder flow with (a)τ=0.001, (b)τ=0.01, (c)τ=0.1.

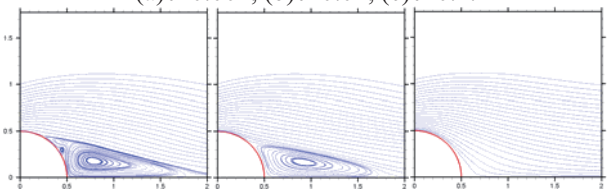

Fig. 4 Near wake flow patten of cylinder flow with (a)τ=0.001, (b)τ=0.01, (c)τ=0.1.

Tenth International Conference on Flow Dynamics
November 25-27, 2013, Sendai, Miyagi, Japan

Computations of Rarefied Gas Flows Using Semi-classical Boltzmann-ES-BGK Equation

Jaw-Yen Yang[1,2*], Chin-Yuan Yan[1], Manuel Diaz[1], and Juan-Chen Huang[3]
[1]Institute of Applied Mechanics, National Taiwan University, Taipei 10764, Taiwan
[2]Center of Quantum Science and Engineering, National Taiwan University, Taipei 10764, Taiwan
[3]Department of Merchant Marine, National Taiwan Ocean University, Keelung 20224, Taiwan
yangjy@ntu.edu.tw

ABSTRACT

Computations of rarefied gas dynamical flows governed by the semi-classical Boltzmann ellipsoidal statistical (ES) BGK equation are presented using an accurate numerical method. The semi-classical anisotropic ES equilibrium distribution differs from the standard Fermi-Dirac or Bose-Einstein distribution. The present numerical method combines the discrete velocity (or momentum) ordinate method in momentum space and high resolution shock capturing method in physical space. Computations of 2-D Riemann problems covering various degree of rarefaction are presented.

1. Introduction

The classical Boltzmann equation has been generalized to quantum gas [1]. The relaxation time approximation is usually applied [2]. Recently, a new semi-classical Boltzmann-ES-BGK equation has been derived [3]. The objectives of this study are two folds. First, we present an accurate numerical method for solving the semi-classical Boltzmann-ES-BGK equation in phase space. Second, we investigate the effect of different range of relaxation times which corresponding to different Knudsen numbers thus different degree of gas rarefaction. The numerical method consists of two parts; one is the discrete ordinate method and the other high resolution shock-capturing methods. In the classical rarefied gas flow computation, the implementation of discrete ordinate method to nonlinear model Boltzmann equations has been developed by Yang and Huang [4]. Extension to semi-classical Boltzmann-BGK equation has been reported [5]. Such a direct method will allow one to examine the same physical flow problems but with different gas of particles. Also, if the classical limit situations of the same flow problem are considered, then one expects to obtain similar or identical flow structures for the three statistics. Computations of several 2-D Riemann problems [6,7] in gas flows of arbitrary statistics for different range of relaxation times are shown to illustrate the complex rarefied gas dynamics as governed by the semi-classical Boltzmann-ES-BGK equation.

2. Governing Equations in Two Space Dimensions

The semi-classical Boltzmann-ES-BGK equation in two space dimensions can be expressed as

$$\frac{\partial f(\upsilon_x,\upsilon_y,x,y,t)}{\partial t}+\upsilon_x\frac{\partial f(\upsilon_x,\upsilon_y,x,y,t)}{\partial x}+\upsilon_y\frac{\partial f(\upsilon_x,\upsilon_y,x,y,t)}{\partial y}=-\frac{f-f_{2d}^{ES}}{\tau}, \tag{1}$$

where v_x and v_y as particle velocity components and the two-dimensional ES equilibrium distribution, f_{2d}^{ES}, is

$$f_{2d}^{ES}(\upsilon_x,\upsilon_y,x,y,t)=\frac{1}{z^{-1}exp\left\{\frac{1}{2\Omega}\left[\lambda_{yy}C_x^2-2\lambda_{xy}C_xC_y+\lambda_{xx}C_y^2\right]\right\}-\theta} \tag{2}$$

where $\Omega=\lambda_{xx}\lambda_{yy}-\lambda_{xy}^2$ and $\theta=-1$, and +1 denote the Fermi-Dirac (FD), Maxwell-Boltzmann (MB), and the Bose-Einstein (BE) statistics, respectively. We also have the gas pressure $p(x,y,t)=(P_{xx}+P_{yy})/2$. The tensor $W_{\alpha\beta}(x,y,t)$ can be obtained through

$$W_{xx}=(1-b)p+bP_{xx}, \tag{3a}$$
$$W_{xy}=bP_{xx}, \tag{3b}$$
$$W_{yy}=(1-b)p+bP_{yy}. \tag{3c}$$

For the conservation of energy, $W_{xx}+W_{yy}=P_{xx}+P_{yy}$ is required. To obtain the new f^{ES}, one needs z and $\lambda_{xx},\lambda_{yy},\lambda_{xy}$ and these can be determined through solving the following equations simultaneously,

$$(\frac{m}{h})^2\sqrt{||2\pi\lambda_{\alpha\beta}||}\mathcal{Q}_1(z)=\frac{\rho}{m} \tag{4a}$$
$$(\frac{m}{h})^2\sqrt{||2\pi\lambda_{\alpha\beta}||}\mathcal{Q}_2(z)\lambda_{\alpha\beta}=\frac{W_{\alpha\beta}}{m}. \tag{4b}$$

Computationally, this requires a root finding procedure and either Newton-Ralphson method or bisector method can be employed. Once the distribution function is known, the macroscopic quantities, the number density n, number density flux $n\vec{u}$, and energy density ε, the pressure tensor P_{ij} and the heat flux vector Q_i are defined, respectively, by

$$\Phi(\vec{x},t)=\int f(\vec{p},\vec{x},t)\phi(\vec{p})\frac{d\vec{p}}{h^3}, \tag{5}$$

where $\Phi=(n,n\vec{u},\varepsilon,P_{ij},Q_i)^T$, $\phi=(1,\vec{\xi},mc^2/2,c_ic_j,mc^2c_i/2)^T$. Here, $\vec{\xi}=\vec{p}/m$ is the particle velocity and $\vec{c}=\vec{\xi}-\vec{u}$ is the thermal velocity. The gas pressure is defined by $P(\vec{x},t)=P_{ii}/3=2\varepsilon/3$. Multiplying Eq. (1) by 1, $\vec{p}$, $\vec{p}^2/2m$, and integrating the resulting equations over all $\vec{p}$, then one obtains the general hydrodynamical equations

$$\frac{\partial n}{\partial t}+\nabla_{\vec{x}}\cdot(n\vec{u})=0, \tag{6}$$
$$n(\frac{\partial}{\partial t}+\vec{u}\cdot\nabla_{\vec{x}})u_i+\frac{\partial P_{ij}}{\partial x_j}=0, \tag{7}$$
$$\frac{\partial\varepsilon}{\partial t}+\nabla_{\vec{x}}\cdot(\varepsilon\vec{u})+\nabla_{\vec{x}}\cdot\vec{Q}+S_{ij}P_{ij}=0. \tag{8}$$

where $S_{ij}=(\partial u_i/\partial x_j+\partial u_j/\partial x_i)/2$ is the rate of strain tensor.

3. Solution Methods

We first apply the discrete ordinate method to discretize the velocity space and render a set of hyperbolic conservation equation with source term in physical space. Then we implement a class of high resolution shock capturing schemes including TVD and WENO methods. This direct solution method in phase space for the Boltzmann-BGK type equations have been proven to be very accurate and efficient and can simulate wide range of flow parameters such as Reynolds number, Mach number and Knudsen numbers [4, 5].

4. Results and Discussion

We numerically study the two-dimensional Riemann problems for rarefied quantum gas dynamics for several relaxation times using the present direct solver for the semi-classical Boltzmann-ES-BGK equation. In the $\tau \approx 0$, i.e., $\mathrm{Kn} \approx 0$ limit, then $f \approx f^{ES}$, we can recover the ideal gas dynamics governed by the semi-classical ES Euler solution. Following the works of Lax and Liu [7] and Schultz-Rinne et al. [6], we selected several configurations to be tested among those 19 configurations classified. We first report the results for the Configuration 5 for three statistics with $\tau = 0.01$ and parameter $b = 0{:}5$. In Fig. 1, the number density and pressure contours are shown for the FD statistics for three different relaxation times. The output time is at about the time instant similar to that reported in [7][6]. From the density and pressure contours, one can identify the interesting and complicated wave patterns. At the right top corner, the two slip lines J_{21} and J_{32} meet the sonic circle of the constant state in the second quadrant and continue as almost straight lines so that a quarter of the sonic circle lies in between. Our results are consistent with calculations in [7][6]. There are detectable differences among the three statistics although the overall wave patterns are similar. Quantitatively, comparing the same contours for the three statistics, the numerical values of number density and pressure for the BE statistics are the largest among the three statistics and the MB statistics always lie between the other two as dictated by the θ values.

5. Concluding Remarks

Computations of 2-D rarefied gas flows based on the semi-classical Boltzmann-ES-BGK equation [3] have been presented. The semi-classical ES model was derived through maximum entropy principle and conserves the mass, momentum and energy but differs from the standard BE or FD distribution. This ES distribution is anisotropic thus it can possess additional high order moments, therefore, its gas dynamical features are not well known. Here, the unsteady rarefied quantum gas dynamical flow features are numerically studied. The numerical method treats the governing equation in phase space and employs the discrete ordinate method and high resolution shock capturing schemes. A decoding procedure is devised for the semi-classical ES distribution which is different from that for standard BE or FD distribution. Computations of 2-D Riemann problems for rarefied gas flows of arbitrary particle statistics are presented for several orders of relaxation times which corresponding to various range of Knudsen numbers. Our results for small Knudsen number (Euler limit) are in good agreement with the calculations in [7][6]. These computational examples serve the purpose of exploring the nonlinear manifestation of shock wave, contact line and rarefaction wave and testing the robustness of the present method. All the expected flow profiles comprising shock, rarefaction wave and contact discontinuities of semi-classical ideal gases and their nonlinear interactions can be observed with considerably good detail and are in good agreement with available results. The present work emphasizes on building the unified and parallel framework for treating semi-classical gas dynamics of three statistics. This work is supported by grants NSC 99-2221-E002-084-MY3 and CASTS Subproject 10R80909-4.

References

[1] E. A. Uehling and G. E. Uhlenbeck, Phys. Rev. 43, (1933) 552.
[2] P. L. Bhatnagar, E. P. Gross and M. Krook, Phys. Rev. 94, (1954) 511.
[3] W. Lei, J. P Meng, and Yonghao Zhang, Proc. Roy. Soc. A, 468 (2012), 1799.
[4] J. Y. Yang and J. C. Huang, J. Comput. Phys., 120, (1995) 323.
[5] J. Y. Yang, B. P. Muljadi, Z. H. Li and H. X. Zhang, Commun. Comput. Phys. 14, (2013) 242.
[6] C. W. Schultz-Rinne, J. P. Collins and H. M. Glaz, SIAM J. Sci. Comput. 14, (1993) 1394..
[7] P. D. Lax and X. D. Liu, SIAM J. Sci. Comput 19, (1995) 319.

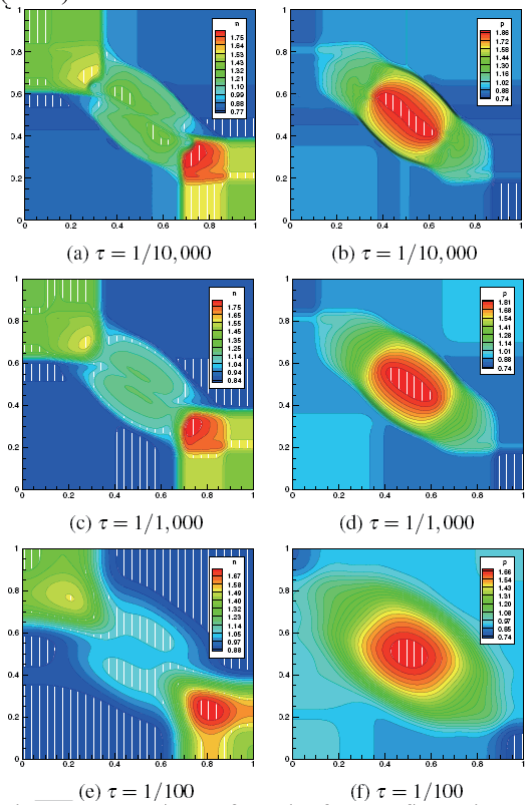

(a) $\tau = 1/10,000$ (b) $\tau = 1/10,000$
(c) $\tau = 1/1,000$ (d) $\tau = 1/1,000$
(e) $\tau = 1/100$ (f) $\tau = 1/100$

Fig. 1: Comparison of results for Configuration 5 for FD gas and three relaxation times with parameter $b = 0.5$ and TVD method.

Tenth International Conference on Flow Dynamics
November 25-27, 2013, Sendai, Miyagi, Japan

A Hierarchical Data Structure for Multi-Physics Problems

Matthias Meinke, Gonzalo Brito Gadeschi, Lennart Schneiders, Wolfgang Schröder
Institute of Aerodynamics, RWTH Aachen University
Wüllnerstr. 5a, 52062 Aachen, Germany.
office@aia.rwth-aachen.de

ABSTRACT

We present a hierarchical data-structure for multiple grids that allow efficient multi-physics simulations for cases with embedded moving objects. This approach is not only ideally suited for e.g. conjugate heat transfer of cold particles in a hot flow but also for any fully coupled multi-physics problem, such as aeroacoustics or aeroelastics as long as hierarchical Cartesian meshes are used for the individual solvers. To demonstrate the proposed approach, we present an interaction of a hot jet with a heat-conducting solid body.

1. Introduction

Solving a multi-physics problem typically involves the solution of two or more different systems of PDEs using adequate numerical methods on grids with an appropriate mesh resolution. The coupling conditions between the different physical zones, require connectivity information between grid cells of the different meshes, which needs to be updated, when the mesh resolution changes, e.g. for solution adaptive methods, or when bodies move within the domain. Hierarchical Cartesian cut-cell methods [1] have been shown to be very efficient in solving flow problems involving complex moving boundaries [2-3] as well as to study acoustic instabilities on premixed flames [4]. In this paper:

- we present a strategy to efficiently store a representation of multiple hierarchical grids suitable for the solution of multi-physics problems that maintains the inter-grid connectivity by imposing restrictions on the mesh topology.
- despite the low memory footprint of this method, the most relevant per node operations can still be performed in O(log N) time or even better.
- demonstrate the feasibility of the approach by showing results of a simple text case where a hot jet interacts with a heat conducting cube.

Multi-physic simulations on multiple grids require efficient closest-neighbor searching. Our approach requires more memory than the approach presented in [5], but allows finding all closest neighbors in O(log N) operations. Our grid compression approach is highly influenced by recent advances in the processing of point clouds resulting of 3D laser scans [5]. To the author's best knowledge, a hierarchical data-structure capable of compressing several grids for multi-physics simulations has not been published in the literature.

2 Method for multi-physics problems

Consider a conjugate heat transfer problem in which the temperature distribution of a solid moving body immersed into a compressible fluid flow should be determined. The problem is fully coupled, i.e. to simulate the fluid flow we need the temperature distribution in the solid and vice-versa. Fig. 1 shows a possible discretization of this model problem. We define two hierarchical Cartesian meshes: the solid mesh and the fluid mesh on which we solve the Navier-Stokes equations for an ideal gas and the heat conduction equation for the solid, respectively.

The cost of storing the mesh connectivity information between the two meshes is of about the number of neighbors per cell. This number can be large if hanging nodes are allowed and/or the diagonal neighbors are also required. It is necessary to allocate extra memory to store the cell data required by the numerical method chosen (e.g. variables at different time steps, derivatives, etc.). Furthermore, the connectivity information between cells of different grids still needs to be determined and stored.

3. Compressed representation of multiple grids

We restrict ourselves to hierarchical Cartesian meshes. The main contribution of this paper is storing all grids into a data structure from which the connectivity information within and between different grids can be efficiently computed.

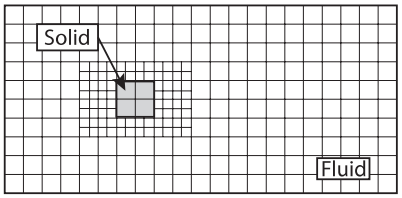

Fig. 1: Solid and fluid meshes.

We proceed as follows: For each solver s, an initial solver domain $D_s(x)$, and some desired grid size distribution $h_s(x)$ are given. First, the whole computational domain $D(x)$ is fit into a single Cartesian cell. In 3D the grid is then generated by subdividing recursively each cell into eight isotropic cells until the grid size distribution $h(x)$ is smaller or equal than the union of each solver's desired cell size distribution. This produces a hierarchical data-structure containing no information about the different multi-physics domains. This is illustrated in Fig, 2 where the black-dots under *topology* represent the tree nodes and the edges between the nodes represent the parent-child relationships. Finally, each solver traverses the grid using breadth-first search to identify those tree nodes located inside their spatial domain $D_s(x)$ that satisfy their grid-size constraint $h_s(x)$. When a node is found, a bidirectional map between the tree node and its corresponding solver-local cell data is created. This bimap is depicted

in Figure 2 with the colors green and blue. One map is stored in the solver-local cell data while its inverse map is stored in the hierarchical data structure. This two-way map allows arbitrary sorting of both data-structures without loosing information.

Each tree node stores two words of information: a pointer to its parent node and a pointer to its first child. The children of node n_i are stored contiguously in memory such that their location encodes their relative positions with respect to their parent node. Furthermore, at most *2S* extra words of memory per node are required to store the bimap between the tree nodes and the solver-local cell data. Although the memory footprint increases linearly with the number of grids, the constant factor of two is small. Note that for hierarchical Cartesian grids, the only spatial information required is the root cell's length and its cell center coordinates.

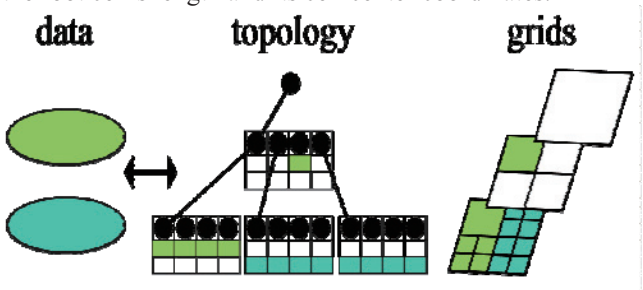

Fig. 2: Solver-local cell data (left), hierarchical data-structure (middle), and hierarchical Cartesian grids (right). Each color denotes a solver and its grid. Under topology, the black dots represent the nodes of the data-structure while the edges represent the parent-child relationship between the nodes.

Let *N* be the number of nodes in the tree. Computing the cell center coordinates of a given node takes O(log N) time. Finding the set of same level neighbors of a given node takes O(log N) time. Testing whether a cell belongs to a given solver takes O(1) time. That is, testing whether a cell is a boundary cell between different solvers as well as finding the connectivity information between the grids can be computed in O(log N) operations. A crucial aspect of the proposed storage concept is that it can be updated without additional overhead, e.g. when the mesh changes due to the movement of immersed bodies and/or solution adaptive strategies.

4. Simple conjugate heat transfer problem

We use the proposed approach to study the interaction between a hot jet and a heat-conducting cube using two different finite-volume solvers and a weakly-coupled partitioned approach. The relevant flow parameters are: Re = 500, Ma = 0.4, Pr = 0.76, ratio of specific heats of 1.4, Sutherland's constant 110.4 K, and the gas constant R = 8134 J / (mol K). The temperature of the hot jet is 1.5 times the free-stream temperature, and the non-dimensional heat conductivity of the solid cube is 4e-3.

Fig. 3 shows the temperature distribution within the solid and the fluid. Solid black lines are streamlines. The dashed black line denotes the solid boundary. The jet impacts the front of the cube heating its surface. A fraction of the heat diffuses into the cube. The hot fluid is transported around the cube, heating it partially from the sides where, simultaneously, the fluid is cooled by the cube. At the body surface, the temperature distributions of the solid and the fluid agree well with each other.

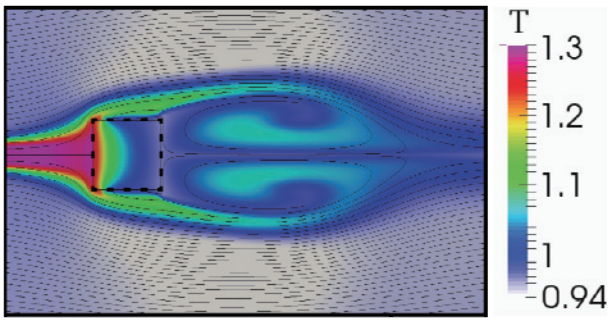

Fig. 3: Temperature distribution in the solid and the fluid at the acoustic time t = 0.14. Streamlines of the flow field are shown in black. The cube boundary is shown in white.

5. Conclusions and future work

We have presented a data-structure for multiple grids that maintains good complexity guarantees for operations typical for multi-physics simulations. The proposed approach relies exclusively on octree-like grid connectivity. That is, the techniques developed here also hold for hierarchical non-Cartesian grids. We demonstrated our approach by showing the interaction of a hot jet with a solid heat-conducting body. Future work will involve a straightforward parallelization of the data-structure for HPC applications as well as applying it to predict the conjugate heat transfer of moving objects in hot turbulent flows.

6. Acknowledgements

The financial support of the research cluster "Fuel production with renewable raw materials" (BrenaRo) at RWTH Aachen University is gratefully acknowledged.

References

[1] D. DeZeeuw, K.G. Powell. An Adaptively Refined Cartesian Mesh Solver for the Euler Equations. Journal of Computational Physics, 104, 56-68, 1993.

[2] M. Meinke, L. Schneiders, C. Günther, W. Schröder. A cut-cell method for sharp moving boundaries in Cartesian grids. Computers & Fluids, 85, 135-142, 2013.

[3] L. Schneiders, D. Hartmann, M. Meinke, W. Schröder. An accurate moving boundary for- mulation in cut-cell methods. Journal of Computational Physics, 235, 786–809, 2013.

[4] D. Hartmann, M. Meinke, W. Schröder. A level-set based adaptive-grid method for premixed combustion. Combustion & Flame, 158, 1318-1339, 2011.

[5] J. Elseberg, D. Borrmann, A. Nüchter. One billion points in the cloud – an octree for efficient processing of 3D laser scans. ISPRS Journal of Photogrammetry and Remote Sensing. 76 (2013) 76–88.

Design of the Next-Generation Vector Architecture for Postpeta-Scale CFD

Kazuhiko Komatsu*¶, Ryusuke Egawa*¶, Hiroyuki Takizawa*¶, Takashi Soga†, Akihiro Musa‡, Hiroaki Kobayashi*
*Tohoku University, Sendai 980-8578, Japan
† NEC System Technologies, Ltd., Osaka 540-8551, Japan
‡ NEC Corporation, Tokyo 108-8001, Japan
¶ Japan Science and Technology Agency, Core Research for Evolutional Science and Technology, Japan
komatsu@isc.tohoku.ac.jp

ABSTRACT

This paper firstly analyses the basic characteristics of a large-scale CFD through the performance evaluations of BCM on various supercomputing systems. Based on the experimental results and the theoretical analyses, this paper clarifies the requirements of a postpeta-scale CFD for designing the next-generation vector architecture. A higher single-node performance is required for a next-generation system, which can avoid inter-node communications by reducing the number of nodes as small as possible. To further enhance the single-node performance, a higher memory bandwidth is essential for postpeta-scale CFD.

1. Introduction

To efficiently perform flow simulations using the CFD methods, there have been high demands for the memory bandwidth rather than computational performance. A vector supercomputing system that is essentially equipped with a high performance memory subsystem is one of the strong candidates to satisfy such demands in the field of CFD. To realize a postpeta-scale simulation, the advancements of the vector architecture toward a next-generation system are necessary.

This paper clarifies the requirements of postpeta-scale CFD for the next-generation vector architecture. By the experimental evaluations of the Building-Cube Method (BCM) on various supercomputing systems, the basic characteristics of a large-scale CFD are analyzed. Based on the basic characteristics of BCM, the system requirements of postpeta-scale CFD for the next-generation vector architecture are clarified.

2. Overview of BCM

BCM has been proposed as a next-generation CFD method to efficiently simulate various fluids on large-scale supercomputing systems. Based on the key aspect that load imbalances drastically affect the sustained performance in large-scale computing, BCM is designed for equalizing load balances by using equally-spaced Cartesian meshes.

BCM decomposes a whole flow domain into sub-domains called *cubes*, and further decomposes each cube into equally-spaced Cartesian meshes called *cells*. As the computational cost and data size are the same for each cube, BCM can balance the computational loads by assigning the equal numbers of cubes into processing elements.

The governing equations of BCM are the incompressible Navier-Stokes equations. In the fractional step method with the finite difference scheme on the staggered arrangement, the field can be classified into a temporal velocity field, a pressure field, and a real velocity field.

The most dominant part is the calculation of the pressure field by solving the Poisson equation that is discretized by the second order central difference scheme. The following equation is expressed for an uniform flow field without any wall boundary.

$$\frac{P_{i+1}-2P_i+P_{i-1}}{(\Delta x)^2}+\frac{P_{j+1}-2P_j+P_{j-1}}{(\Delta y)^2}+\frac{P_{k+1}-2P_k+P_{k-1}}{(\Delta z)^2} = \frac{1}{\Delta t}\left(\frac{u_{i+1}-u_i}{\Delta x}+\frac{v_{j+1}-v_j}{\Delta y}+\frac{w_{j+1}-w_j}{\Delta z}\right),$$

where P_i, P_j, and P_k indicate pressure values at positions i, j, and k in coordinates x, y, and z. u, v, w indicate temporal velocities in each coordinate, respectively. t indicates a time step.

To solve the pressure of each cell using the equation, a seven-point stencil calculation, which requires the pressure data of a cell and its six adjacent cells, is performed. The stencil calculations for all cells in all cubes are repeated until the difference of the calculated field becomes sufficiently small.

The next section analyses the basic characteristics of BCM through the performance evaluations on various supercomputing systems.

3. Evaluations of BCM on supercomputing systems

To analyse the basic characteristics of BCM, the flow simulations around a 200 million-cell model are performed on various supercomputing systems, which are listed in Table 1. Nehalem, FX1, FX10, and SR16K are scalar supercomputers that are equipped with a number of scalar processors in a massively-parallel approach. SX-9 is a vector supercomputer that is equipped with a high performance memory subsystem.

Figure 1 shows the performance of each system for BCM. The x-axis indicates the number of processing elements. The y-axis indicates the sustained performance. These results show that the memory bandwidth of the systems greatly affects the sustained performance of BCM since BCM is a memory-intensive application. The sustained memory bandwidth of each system limits its sustained performance of BCM. As SX-9 has the highest memory bandwidth, it can achieve the best performance among the supercomputing systems.

Table 1. System specifications of the supercomputing systems

System	Peak Tflop/s	Nodes	PEs/node	Cores/PE	Mem. GB/s	On-chip Memory	Network GB/s	B/F
NEC SX-9	26.2	16	16	1	256	256 KB ADB	2x 128GB/s IXS	2.5
Nehalem EX	1.74	6	4	8	34.1	24 MB shared L3	4 GB/s Infiniband	0.47
Fujitsu FX1	5.16	128	1	4	40.0	6 MB shared L2	2 GB/s Infiniband	1.0
Fujitsu FX10	5.68	24	1	16	85	12 MB shared L2	5~50 GB/s Tofu	0.36
Hitachi SR16K	124	128	4	8	128	32MB shared L3	2x 24~96 GB/s custom	0.52

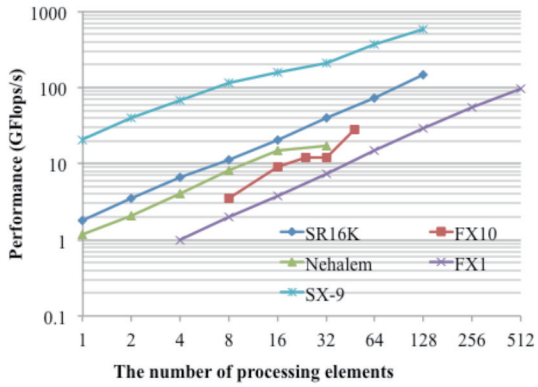

Fig. 1 Sustained performance of BCM.

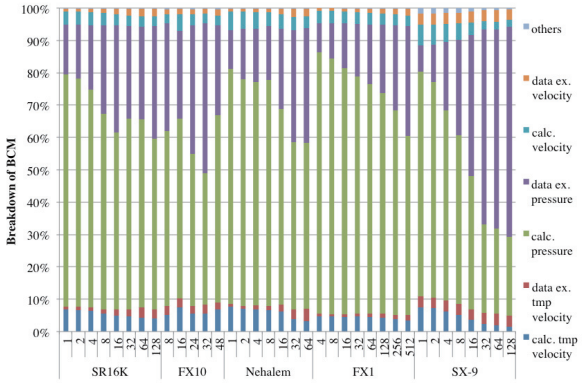

Fig. 2 Breakdown of total execution time of BCM.

Figure 1 also indicates that the performance improvements according to the number of nodes. Most of the systems achieve high scalability due to a large number of parallel tasks and sufficient network bandwidth.

To analyse the bottleneck of BCM, Figure 2 shows the breakdown of the execution time. The x-axis indicates supercomputing systems with changing the number of processing elements. The y-axis indicates the breakdown of the execution time, which includes the calculations and the data exchanges of each field.

These results confirm that solving the pressure field dominates the total execution time on all the supercomputing system with any number of processing elements. Furthermore, these results show that as the number of processing elements increases, the ratio of the data exchanges to the calculations increases, which might lead to performance degradation in a larger-scale system. This is brought by the overhead of data transfers among nodes. As the data transfers to exchange the results of ghost cells are necessary for each iteration, the data transfers may easily become a bottleneck when the numbers of nodes increase.

4. Discussions for the next-generation systems

From the performance evaluations on various supercomputing systems, it is clarified that a higher performance of a single node is required to achieve high scalability on the next-generation system. As the data exchanges are significantly increasing in postpeta-scale CFD, the data exchanges are one of the candidates of bottlenecks. Thus, the number of nodes to execute postpeta-scale CFD should be as small as possible in order to avoid communicating among nodes. Differently from a massively-parallel approach of increasing the number of nodes, the design to enhance the single-node performance is desired for a next-generation system, which can eventually reduce the number of nodes.

In addition to the enhancement of the single-node performance of a next-generation system for postpeta-scale CFD, the memory bandwidth should be improved accordingly, which is clearly shown by the performance evaluation. The importance of a high memory bandwidth can be derived from the theoretical analyses. The ratio of the memory bandwidth to the floating point operations required by the equation in Section 2, which is called the theoretical Bytes/Flop (B/F) ratio, becomes 5.43 since 28 double precision floating point operations and 19 variables are necessary for the pressure calculation. Furthermore, the code B/F ratio derived from the source code of BCM is also investigated as 5.47 by counting the number of memory operations and floating point operations in the object code. The theoretical and code B/F ratios are much higher than the system B/F ratios of the supercomputing systems that are used in the evaluations. These system B/F ratios are from 0.36 to 2.5. In order to satisfy the required high B/F ratio, a novel memory subsystem that realizes a higher sustained memory bandwidth is strongly desired even for the vector architecture.

Based on these requirements that a high memory bandwidth and a single-node performance are necessary, the next-generation vector architecture is under investigation as a future HPC system.

5. Conclusions

Using BCM as an example, this paper analyses the basic characteristics of a large-scale CFD through the performance evaluations on various supercomputing systems. From the experimental results and the theoretical analyses in term of the theoretical and code B/F ratios, it is clarified that the design to enhance single-node performance as well as the memory bandwidth is desired for the next-generation vector architectures to achieve efficient execution of postpeta-scale CFD.

Tenth International Conference on Flow Dynamics
November 25-27, 2013, Sendai, Miyagi, Japan

Extending the Building Cube Method to Curvilinear Mesh with Adaptive Mesh Refinement

Xinrong Su[1], Satoru Yamamoto[1], Kazuhiro Nakahashi[2]
1 Department of Computer and Mathematical Sciences, Tohoku University, Aoba 6-6-01, Sendai, Japan
2 Japan Aerospace Exploration Agency, Chofu Research Center, Tokyo, Japan
su@caero.mech.tohoku.ac.jp

ABSTRACT

Building Cube Method (BCM) adopts block-structured Cartesian mesh and finer resolution can be used where the flow contains detailed flow structures. This paper reports the recent progress in extending the idea of BCM to curvilinear body-fitted mesh with Adaptive Mesh Refinement (AMR). Compared to Cartesian mesh based AMR, body-fitted AMR strategy is more complicated and less studied. In this paper the key components of body-fitted AMR, including curvilinear refinement, complex geometry and implementation are introduced. Numerical example is also given to demonstrate the benefits of current body-fitted AMR strategy.

1. Introduction

Computational Fluid Dynamics (CFD) eventually plays a vital role in both research and industrial communities. Continuous efforts are made towards more accurate results by designing higher accuracy numerical methods and better meshing strategies. Within the BCM framework [1] block-structured Cartesian mesh is used and it enables the use of finite difference with high order and high resolution. Also local mesh resolution can be recursively adapted to the detailed flow structures, without using expensive global mesh refinement which would result in excessive number of mesh points.

Within the BCM framework Cartesian mesh is used and it is not body-fitted. Currently body-fitted mesh still dominates the CFD market and in this work we try to extend the idea of BCM to body-fitted mesh, specifically, multi-block body-fitted mesh. Compared to Cartesian mesh based AMR, for body-fitted mesh the complex geometry has to be considered and as a result the refinement is difficult. For accuracy considerations, several properties like the smoothness and singular features must be preserved. In this work, to preserve the mesh smoothness and grid stretching, cubic interpolation in the parametric space is developed for mesh refinement. Also to preserve the singular geometry features, a boundary patch based sub-block refinement strategy is proposed. Together with high accuracy scheme [2] and efficient solution method, an efficient body-fitted AMR framework is developed. In this paper the key components of this framework are introduced and several numerical examples are also given.

2. Method

In the current framework a body-fitted mesh is first generated and the AMR process is recursively conducted. The flowfield is automatically checked to identify areas requiring finer resolution. A sensor function is used to assess the local mesh density and if the sensor function value exceeds a refinement threshold, the mesh cell is marked for refinement. Then several rectangular regions are generated which fully cover the marked cells and new mesh blocks with finer resolution will be generated.

Targeted at the applications in real-world simulations which are always transonic flows with large Reynolds number, special treatments are required. For turbulent flow computations, in the near wall region mesh cell is stretched with large aspect ratio. A direct and simple method is to generate finer mesh by linear interpolation. However, results show that this method does not preserve the smoothness and stretching in the near wall region, which may adversely affect the efficiency of AMR. Currently the mesh lines are represented by straight lines and if linear refinement is used, after several circles of refinements, there will be obvious acute structures on the solid surface. Result show that in this case visible wiggles can be observed near the solid.

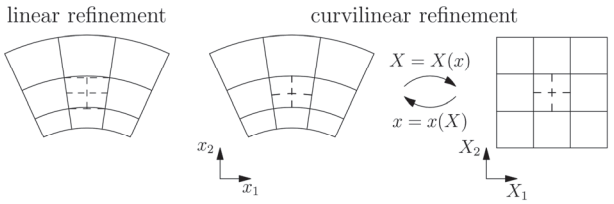

Fig.1 Comparison of linear and curvilinear refinements.

A more complex refinement method is developed. As demonstrated in Fig.1, the body-fitted mesh is first mapped from curvilinear into Cartesian formulation. Denote x be the originate coordinate of the mesh and X be the coordinate in the Cartesian space, the mapping between these two spaces are formulated and denoted as $X=X(x)$. The mesh refinement is conducted in the Cartesian space with linear interpolation and the refinement is mapped back to the curvilinear mesh by the inverse mapping $x=x(X)$. In this work cubic formulations are used for these two mappings. As given in Fig. 1, with this strategy the smoothness and mesh stretching are better preserved.

Another difficulty in the body-fitted AMR is the refinement near singular geometry features, such as sharp corners and trailing edges. During the mesh generation, special cares are needed to preserve these important features and mesh quality. With the cubic refinement, sometimes it would fail to preserve the exact singular feature. What's more, in these regions cubic refinement would possibly result in mesh cells with negative Jacobian. Linear refinement is free of this problem. A solution to this problem would be designing a hybrid strategy which only activates linear refinement near the singular structures. However, with this method

defining the extent of linear refinement region is a trial-and-error process. Also near the singular structures the flow is always complex and preserving the smoothness and stretching is also very important.

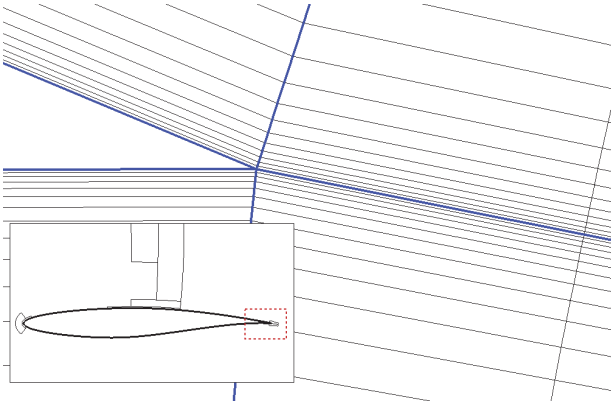

Fig. 2 Boundary patch based refinement within sub-block for singular geometry features.

To solve this problem, a new refinement strategy is developed. As demonstrated in Fig. 2, the mesh block to be refined is further divided into several sub-blocks according the boundary conditions. After the division, singular features exist only on the surfaces between sub-blocks. Then cubic interpolation based refinement is conducted inside every sub-block. In this manner the rigorous requirements of preserving smoothness, stretching and singular features are fully satisfied. In Fig. 2 the cells near the sharp trailing edge have to be refined. With original cubic refinement, there will be mesh tangling in this region. The thick lines in Fig. 2 denote the boundary of sub-blocks and refinement inside every sub-block fully solves this problem.

3. Results and Discussion

Here a two-dimensional turbulent case is given. The flow past NACA-0012 airfoil is simulated and the freestream Mach number is 0.55 and angle-of-attack is 8.34 degrees and the Reynolds number is 9 million.

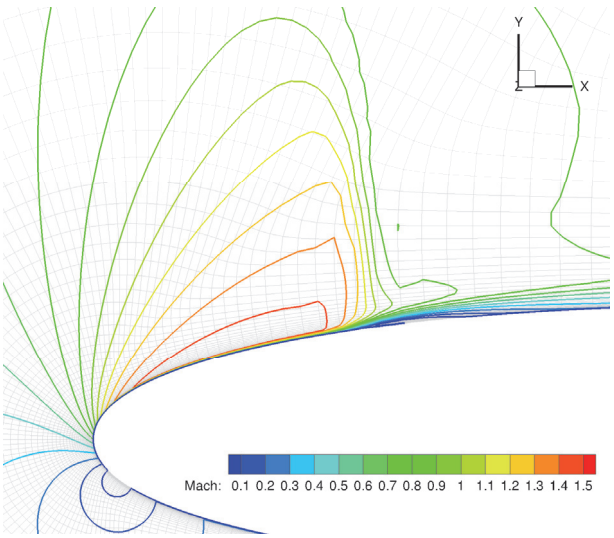

Fig. 3 Mach number obtained with baseline mesh.

Fig. 3 gives the Mach number using the baseline mesh which is optimized for zero angle-of-attack. A small region of supersonic flow exists near the leading edge and the interaction between shock wave and boundary layer is of interest.

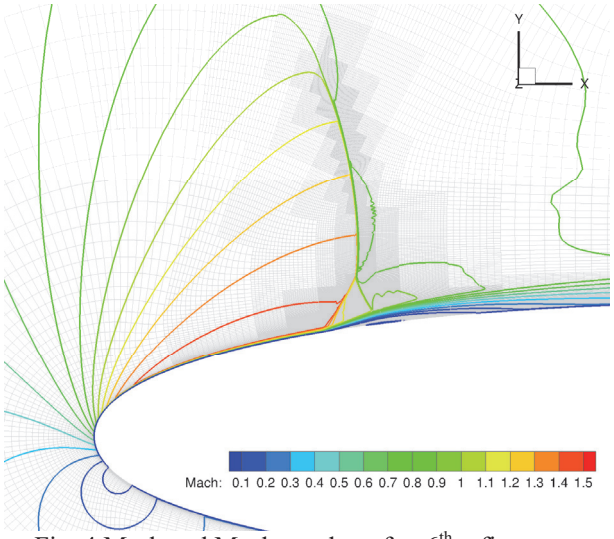

Fig. 4 Mesh and Mach number after 6th refinement.

The mesh and Mach number contours after 6th AMR refinement is given in Fig. 4. The mesh refinement is automatically conducted in the shock wave region. Detailed flow structures about interaction between shock wave and boundary layer are clearly captured. Original mesh is composed of 40k points and refined mesh consists of 175k points. If global mesh refinement is used, about 16 million points are required to obtain similar mesh resolution. It is clear current body-fitted AMR strategy works well and results in vast saving of computing resource.

Here only a two-dimensional case is demonstrated and more three-dimensional cases will be given in the presentation.

4. Concluding remarks

In this work a body-fitted AMR framework is developed, following the idea of BCM. For its applications with complex geometry, several key strategies are developed to implement AMR with body-fitted mesh, including the curvilinear refinement and boundary patch based sub-block refinement. The applicability of current method is numerically verified and works well with complex flow.

Acknowledgement

This work was supported by JSPS KAKENHI (21226018).

References

[1] T. Ishida, S. Kawai, K. Nakahashi, AIAA Paper 2011-1296, 2011.

[2] X. Su, D. Sasaki, K. Nakahashi, Int. J. Numer. Meth. Fluids, **71**(2013), 185-207.

Numerical Investigation on Flow Characteristics and Aerodynamic Losses of Compound Angle Film Cooling Jets

Chang Luo[1], Takashi Misaka[1], Shigeru Obayashi[1], Takashi Goto[2], Ruriko Yamawaki[2]
[1]Institute of Fluid Science, Tohoku University, 2-1-1 Katahira, Aoba-ku, Sendai 980-8577, Japan
[2]IHI Corporation, 229 Tonogaya, Mizuho-machi, Nishitama-gun, Tokyo 190-1297, Japan
luochang33@163.com

ABSTRACT

Flow characteristics and aerodynamic losses of compound angle film cooling jets for three velocity ratios of 0.5, 1.0 and 2.0 are numerically investigated using a three-dimensional Reynolds-Averaged Navier-Stokes (RANS) solution. Flow fields and loss distributions of compound angle film cooling jets in a fixed plane are analyzed. It has been found that the aerodynamic loss tends to increase with the increasing of the orientation angle regardless of the velocity ratio, and the tendency becomes more obvious when the velocity ratio is large.

1. Introduction

Film cooling is one of the most efficient cooling concepts, and is generally more efficient than internal convection cooling. In film cooling, cooling air is injected into the hot gas areas through slots or holes, and forms an isolating layer on the surface. The isolating layer reduces the heat exchange and enhances the cooling of the surface. In order to improve the film cooling effectiveness, various injection arrangements [1-3] have been proposed. Among these arrangements, the compound angle film cooling arrangement is considered as one of the most effective cooling arrangements. The compound angle film cooling jets can obtain higher and more uniform film cooling effectiveness because of the reduced axial momentum and enhanced lateral momentum of the cooling air. Therefore, more comprehending of the flow structure and loss generation associated with compound angle film cooling jets will be very meaningful for optimizing the thermal design of hot components in gas turbine and aero engine.

2. Computational Model and Method

Figure 1 shows the computational model of compound angle film cooling jets. The injection tube attaches at the center of the bottom plate in order to ensure that the injection center always is at the same position regardless of the compound angle variations.

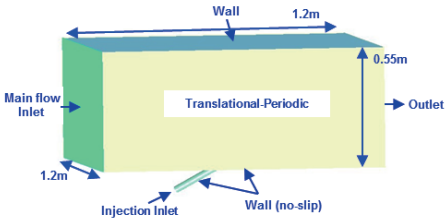

Fig. 1 Computational model

The compound angle is identified by the inclination angle α and the orientation angle β, which are showed in Fig. 2. The inclination angle holds a fixed value of 30 deg, and the orientation angle is varied as in Table 1. At the same time, three velocity ratios ($R=U_j/U_\infty$, R=0.5, 1.0, and 2.0) are simulated for each orientation angle.

The numerical simulations are performed by using the three-dimensional unstructured-mesh CFD solver, parallel TAS-code (Tohoku university Aerodynamic Simulation code). The solutions are obtained by solving the compressible RANS equations in which the cell-vertex finite volume method is used to discretize these equations. Inviscid flux evaluation method is HLLEW [4] and LU-SGS [5] implicit method is used for time integration. The turbulence characteristics of the flow are modeled by the Spalart-Allmaras turbulence model. Each simulation is parallel calculated with 8 CPUs. The number of grid elements is set to be 9,145,533 (see Fig. 3).

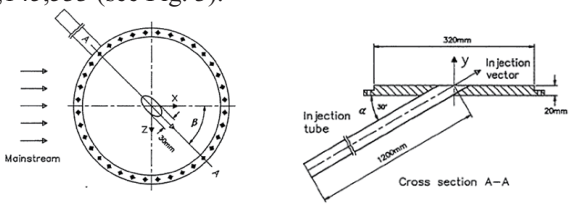

Fig. 2 Compound angle and coordinate system [3]

Table 1. Computational conditions

U_∞ (m/s)	D (mm)	α (deg)	β (deg)	R
15	30	30	30, 60, 90	0.5, 1.0, 2.0

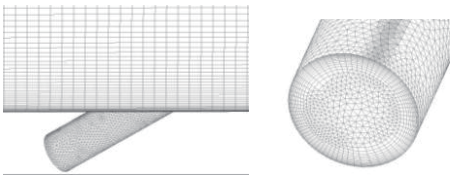

(a) Main flow inlet (b) Injection inlet

Fig. 3 Computational grid

3. Results and Discussion

3.1 Three Dimensional Flow Fields

Figure 4 shows the contours of dimensionless x-directional velocity for β=30, 60 and 90 deg in the case of R=2.0. The below mentioned results are all carried out in y-z plane at x/D=8. As can be seen from this figure, the velocity gradients decrease with the increasing of β, and the velocity deficit appears in the jet core when β=90 deg.

The projection of velocity vectors on y-z plane is presented in Fig. 5. When β increases from 30 deg to 60 deg, the location of vortex center migrates from about 1D to 2D in the z-direction. However, the change of the vortex center is relatively small (0.3D) from 60 deg to

90 deg. It is because the jet of large β loses the z-momentum more easily than that of small β.

Figure 6 gives the contours of dimensionless vorticity in x-direction in the case of R=2.0. The regions of positive and negative vorticities are existed regardless of β (for β=30 and 60 deg, positive vorticities is very close to the wall boundary). The absolute peak value of counter clockwise vortex (negative) is much larger than that of clockwise vortex (positive), and the absolute peak value of counter clockwise vortex increases with the increasing of β.

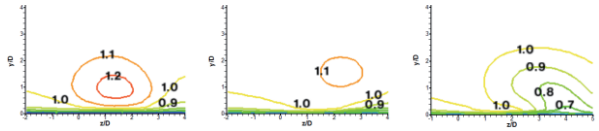

(a) β=30 deg (b) β=60 deg (c) β=90 deg

Fig. 4 Dimensionless x-directional velocity for R=2.0

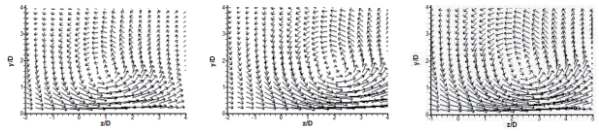

(a) β=30 deg (b) β=60 deg (c) β=90 deg

Fig. 5 Projection of velocity vectors for R=2.0

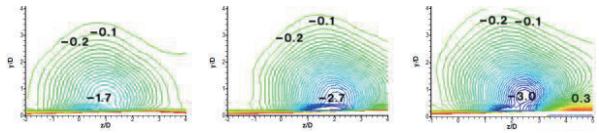

(a) β=30 deg (b) β=60 deg (c) β=90 deg

Fig. 6 Dimensionless vorticity in x-direction for R=2.0

3.2 Aerodynamic Loss Distributions

The aerodynamic loss of film cooling jets consists of the loss due to the jet injection and the total pressure deficit in the boundary layer. The two loss coefficients and the net total pressure loss coefficient are defined as follows,

$$C_{Pt,inj}=\frac{P_{t,\infty}-P_{t,inj}}{\frac{1}{2}\rho U_{\infty}^{2}}, \quad C_{Pt,bas}=\frac{P_{t,\infty}-P_{t,bas}}{\frac{1}{2}\rho U_{\infty}^{2}}, \quad C_{Pt,\mathrm{net}}=C_{Pt,inj}-C_{Pt,bas}$$

Figure 7, 8 and 9 show the contours of net total pressure loss coefficient distributions for R=0.5, 1.0 and 2.0 in turn. As can be seen from Fig. 7, there always exists positive net total pressure loss coefficient all over the planes. The peak value of net total pressure loss coefficient increases with the increasing of β. When R=1.0 (Fig. 8), the region with negative net total pressure loss coefficient can be seen close to the left side of the wall boundary, and the positive net total pressure loss region expands with increasing of β. When R=2.0 (Fig. 9), the positive net total pressure loss region is difficult to be found in the case that β is less than 60 deg. when β is larger than 60 deg, the position loss region appears and tends to spread over the whole jet region.

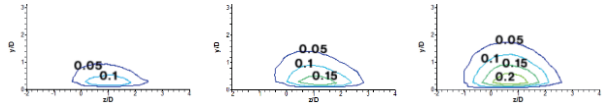

(a) β=30 deg (b) β=60 deg (c) β=90 deg

Fig. 7 Net total pressure loss coefficient for R=0.5

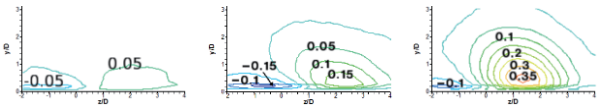

(a) β=30 deg (b) β=60 deg (c) β=90 deg

Fig. 8 Net total pressure loss coefficient for R=1

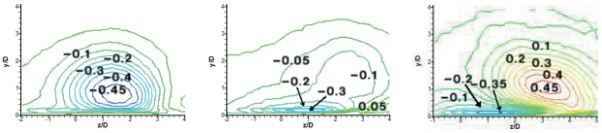

(a) β=30 deg (b) β=60 deg (c) β=90 deg

Fig. 9 Net total pressure loss coefficient for R=2

The mass averaged net total pressure loss coefficients are defined as follows [3],

$$\overline{C}_{Pt,\mathrm{inj}}=\frac{\int_{z^-}^{z^+}\int_{y^-}^{y^+}C_{Pt,\mathrm{inj}}U dydz}{\int_{z^-}^{z^+}\int_{y^-}^{y^+}U dydz}, \quad \overline{C}_{Pt,bas}=\frac{\int_{z^-}^{z^+}\int_{y^-}^{y^+}C_{Pt,bas}U_b dydz}{\int_{z^-}^{z^+}\int_{y^-}^{y^+}U_b dydz}, \quad \overline{C}_{Pt,\mathrm{net}}=\overline{C}_{Pt,\mathrm{inj}}-\overline{C}_{Pt,\mathrm{bas}}$$

The mass averaged net total pressure loss coefficient of the simulation and experiment are presented in Fig. 10. The simulation is good agreed with the experiment except for the case of R=2 for β=90 deg, the net total pressure loss coefficient of which is higher than that of experiment. We also can see from Fig. 10, the net loss coefficient tends to increase with the increasing of β regardless of the velocity ratio. When R is not lager than 1.0, there always exists aerodynamic loss due to the jet injection. When R is larger than 1.0, there exist considerable total pressure surplus for small β.

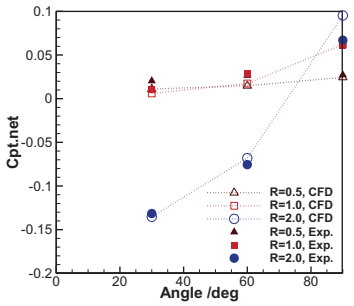

Fig. 10 Mass average net total pressure loss coefficient

4. Conclusions

The detailed flow fields and loss distributions of film cooling jets with three orientation angles (β=30, 60, and 90) for three velocity ratios (R=0.5, 1.0 and 2.0) are illustrated in this study.

For R=0.5 and 1.0, there always exists net total pressure loss due to the jet injection for any β. For R=2.0, large amount of total pressure surplus appear when β is small. However, when β=90, the net total pressure loss is always existed regardless of the velocity ratio.

References

[1] R.J. Goldstein, E.R.G. Eckert, F. Burggraf. Int. J. of Heat Mass Transfer, 177(1974).

[2] D.G. Hyams, J.H. Leylek. ASME Paper 97-GT-271.

[3] S.W. Lee, Y.B. Kim, J.S. Lee. ASME Paper 95-GT-38.

[4] S. Obayashi, G.P. Guruswamy. AIAA J., 33(1995).

[5] D. Sharov, K. Nakahashi. AIAA J., 36(1998).

Tenth International Conference on Flow Dynamics
November 25-27, 2013, Sendai, Miyagi, Japan

Numerical Simulation of Supercritical-fluid Flows around Complex Geometry based on SFS+BC

Shibo Qi, Kotaro Makino, Takashi Furusawa, Satoru Yamamoto
Dept. of Computer and Mathematical Sciences, Tohoku University.
6-6-01 Aramaki Aza Aoba, Aoba-ku, Sendai, Miyagi, 980-8579 Japan
qi@caero.mech.tohoku.ac.jp.

ABSTRACT

Numerical simulation of supercritical water flows is presented. In the present scheme, the preconditioning method developed by the authors is coupled with Building-Cube Method (BCM). An Immersed Boundary (IB) method is applied as wall boundary treatment and mathematical models of thermophysical properties for water programmed in the PROPATH are used for property estimation of fluids. In the paper, flow past an 'E' shape fin is calculated at a low Reynolds number. Local flow structures in the concave-convex part of 'E' shape fin are clearly captured and features of thermophysical properties of supercritical water are shown.

1. Introduction

Generally, substances own their respective thermophysical properties. Accurate prediction of thermophysical properties is absolutely a critical issue for accurate prediction of flow behaviors. It is especially difficult for simulation of supercritical fluid flows since there are sharp variations of physical properties. The supercritical-fluids simulator (SFS) has been developed by our group, which is based on the preconditioning method [1], with all thermophysical properties referred to from PROPATH [2]. For complex geometry configuration problems, grid generation is one of the main difficulties.

The SFS has been coupled with BCM, as to solve supercritical-fluid flow problems with especially complex geometry configurations. Special wall treatment is a critical issue for the whole scheme. Immersed Boundary (IB) method has been proved to be an appropriate choice because of its superior accuracy in solid wall surface definition.

In the paper, supercritical water flows past an 'E' shape fin at a low Reynolds number is calculated. The behaviors of supercritical water flows over complex geometry configurations are shown.

2. Numerical Method

2.1 Governing equation

The governing equation used in the paper is based on the preconditioned two-dimensional compressible Navier-Stokes equations. The vector form equation set in the general curvilinear coordinates is written as

$$\Gamma \frac{\partial \hat{\boldsymbol{Q}}}{\partial t} + \frac{\partial \boldsymbol{F}_i}{\partial \xi_i} + \frac{\partial \boldsymbol{F}_{vi}}{\partial \xi_i} = 0 \qquad (1)$$

The governing equation is solved by a finite-difference scheme. For spatial discretization, preconditioned ROE scheme is used for inviscid flux estimation, and second-order MUSCL scheme is applied for left and right property evaluation. For time-integration process, the preconditioned implicit LU-SGS scheme is used. For thermophysical properties estimation in the present research, all mathematical models are referred to from PROPATH as an external function.

2.2 Building-Cube Method

The Building-Cube Method [3] proposed by Nakahashi et al. is used as the grid generation approach for CFD calculation in the paper. In BCM, the computational domain is firstly divided into a number of basic units called Cube as subdomains for calculation; then same number of equally-spacing Cartesian mesh called Cell is generated in the cubes as calculation grid in subdomains. Since all cubes share a same number of Cartesian meshes, the local resolution is determined by the cube size.

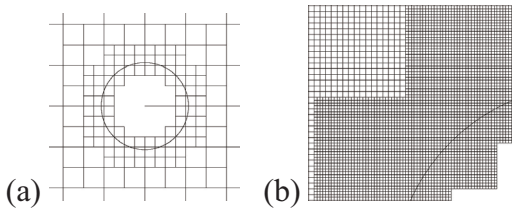

Fig. 1 Mesh configuration and parallel application in BCM
(a) Cube (b) Cell

Overlapping cells are used for data communication of adjacent cubes. Bilinear-interpolation (extrapolation) is used to estimate values of any physical properties at the overlapping cells for data communication of adjacent cubes with a size difference.

2.3 Wall boundary treatment

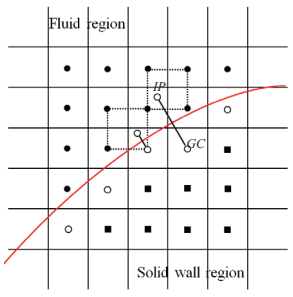

Fig. 2 Schematic of ghost cell settings in IBM

In the present study, ghost-cell based IBM is proposed [4]. Ghost cells are defined as wall cells within stencils of fluid cells, as shown in Fig. 2. First, the body-

intercept point (BI point) in the wall normal direction for ghost-cell node is determined; then the image point (IP) of ghost-cell node is defined as the symmetric point of ghost-cell node with BI point as a reference. Values of any physical properties at the ghost cells are defined by their image points. In the present study, the inversed distance weighted interpolation is used to determine the values at IP with the four stencil nodes in the fluid region.

3. Results and Discussion

Supercritical water flows past an 'E' shape fin is calculated to show the ability of the present scheme for supercritical-fluid flows over complex geometry configuration problems.

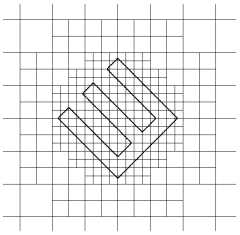

Fig. 3 Schematic of BCM grid (cube) for 'E' shape fin

3.1 Numerical results of conventional settings

First, results of conventional settings are shown. The simulation domain is meshed by BCM with 525 cubes and 16 × 16 cells in each cube, thus the total number of grid points is over 130 thousand. The Reynolds number based on the length of diagonal is set to be 30. The fluid medium is set to be supercritical water at a state of 25.0MPa, 700K.

Figure 4 shows the stream lines past the 'E' shape fin. The symmetric vortices attached to the 'E' shape fin are captured, which shows that the concave-convex effects of solid surface in 'E' shape fin do not affect the symmetrical flow structure significantly. The local flow structures in the 'E' shape fin are also captured. the local flows interact with the main flow and vortices appear at the corner.

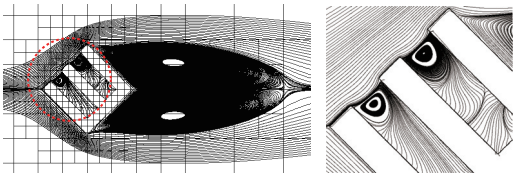

Fig. 4 Streamlines past the 'E' shape fin

3.2 Numerical results of unconventional settings

Then, results of unconventional settings are shown. Temperature difference of 10K is set between solid wall surface and medium fluid (T_{wall}=680K, T_{∞}=670K, P=30.0MPa). The same grid is used and other basic settings are similar with the conventional fluid settings.

Figure 5 shows the comparison of local flow structures for conventional and unconventional settings. The basic features are similar. However, there are still some minor differences observed at the regions close to the upper vortices in the fin.

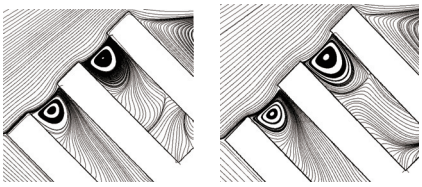

Fig. 5 Comparison of local flow structures for conventional and unconventional settings

Figure 6 shows the temperature contour and isobaric specific heat contour for supercritical water flows past the 'E' shape fin.

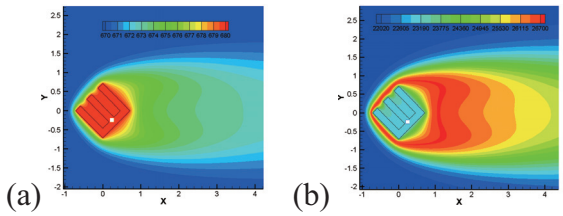

Fig. 6 Temperature contours and and isobaric specific heat contour

The temperature distribution in the concave-convex part of the fin is clearly captured, though not significant. A peak value in the whole domain is observed as expected, since it is known that there is a peak value of isobaric specific heat at the critical point for certain substance.

4. Concluding remarks

In the present scheme, the SFS has been coupled with BCM, and Immersed Boundary (IB) method was applied as wall boundary treatment. Mathematical models of thermophysical properties for water programmed in the PROPATH were used for physical property estimation of fluids.

Numerical simulation of supercritical water flows past an 'E' shape fin was presented in the paper and behaviors of supercritical water were investigated. The present scheme was proved to be applicable to supercritical-fluid flows around complex geometry problems.

References

[1] S. Yamamoto, Journal of Computational Physics (2005), 207(1), 240-260
[2] A program package for thermophysical properties of fluids, Ver. 12.1, PROPATH GROUP.
[3] K. Nakahashi, L-S. Kim, AIAA(2004), 2004-0434
[4] R. Ghias, R. Mittal, H. Dong, Journal of Computational Physics (2007), 225(1), 528-553

Tenth International Conference on Flow Dynamics
November 25-27, 2013, Sendai, Miyagi, Japan

Computation of the Forward Fan Noise Shielding by the Building-Cube Method

Yuma Fukushima[1], Shigeru Obayashi[1], Daisuke Sasaki[2], Kazuhiro Nakahashi[3]
[1]Institute of Fluid Science, Tohoku University, Sendai, 980-8577, Japan
[2]Kanazawa Institute of Technology, Nonoichi, 921-8501, Japan
[3]Japan Aerospace Exploration Agency, Chofu, 182-8522, Japan
E-mail:fukushima@edge.ifs.tohoku.ac.jp

ABSTRACT

The characteristics of shielding effect of forward fan noise are investigated on the Over-the-Wing Nacelle (OWN) configuration. The block-structured Cartesian mesh method named as the Building-Cube Method (BCM) is employed. The results show the qualitative agreement with experiment at the position just below the fuselage. However, there are some discrepancy that are large shielding metric and negative values. The details of shielding metric would be revealed in the future work.

1. Introduction

Noise from aircraft has been reduced with improvements in various components of engines. However, regulations of airport noise are getting strict at the same time, thus the attention is currently focused on the noise analysis for further noise reduction. To achieve the drastic reduction of engine noise, several concepts have been proposed. One of them is the configuration that installs engine nacelles over the main wing named the Over-the-Wing Nacelle (OWN) configuration [1]. This concept intends to shield the engine noise toward the ground by a main wing.

The objective of this study is the numerical investigation of noise shielding effect on the OWN configuration. The noise shielding metric is evaluated and compared with the experiment conducted by Powell [2].

2. Computational methods

As the computational framework, block-structured Cartesian mesh method called Building-Cube Method (BCM) [3] is employed. BCM has several advantages over body-fitted structured or unstructured mesh: (1) quick mesh generation for complicated geometries, (2) easy application of high order scheme, (3) higher computational efficiency, (4) easy parallelization of computational processes. Computational mesh of BCM is generated in the following procedures. First, computational domain is divided into aggregation of square area named “Cube” as the left side in Fig. 1. Next, each Cube is divided by equi-spaced Cartesian mesh named “Cell” as the right side of Fig. 1. Computation is performed in each Cube and all Cubes are parallelized using OpenMP and Message Passing Interface (MPI). One Cube has three Cells overlapped with adjacent Cubes for data exchange.

The governing equation of noise propagation is the Linearized Euler Equation (LEE). The spatial derivation is calculated by fourth-order Dispersion Relation Preserving (DRP) scheme. Time integration is conducted by six-stage fourth-order Low Dissipation and Dispersion Runge-Kutta (LDDRK) scheme. For high accuracy computation, Immersed Boundary Method (IBM) using ghost cell and image point is employed at the wall boundary and third-order Lagrange interpolation is employed for data exchange at the Cube boundary of different size. The outgoing wave is damped by buffer zone boundary conditions using absorbing domain. The details of LEE code are described in Ref. [4].

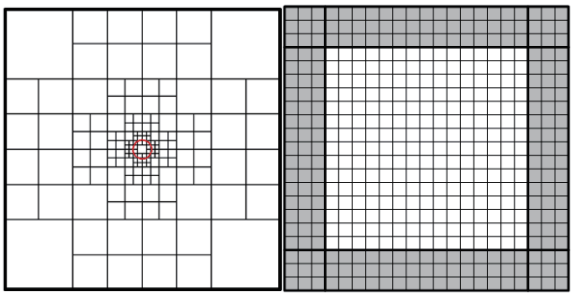

Fig. 1 Computational domain (left) and example of one Cube (15×15, 3 overlap cells) (right)

3. Computational condition and Results

Sound propagation from engine nacelle is computed for the isolated nacelle and for the OWN configuration. Pressure is monitored at the locations where the microphones are placed in the experiment. The ratio of root mean square pressure computed from the both cases defines the noise shielding metric shown in Eq. (1).

$$Metric\ \Delta = 10\log_{10}\left(\frac{\overline{p}_c^2}{\overline{p}_s^2}\right) \tag{1}$$

where p_c is the pressure of the isolated nacelle and p_s is that of the OWN configuration.

Figures 2 and 3 show the top view of the OWN configuration and the relative x and z position of microphones in the experiment. These microphones are located 0.19 m lower than the position of sound source.

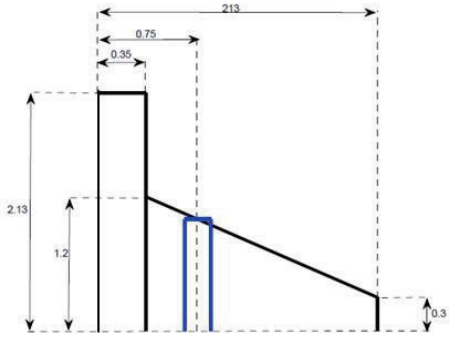

Fig. 2 Top view of the aircraft model

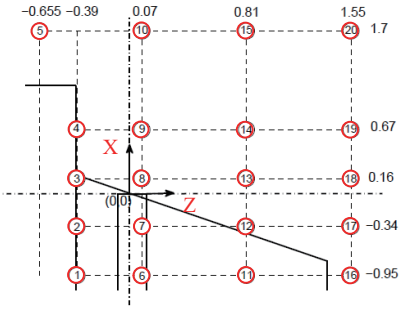

Fig. 3 Relative x and z positions of sampling points (Units in meters)

For this model, computational mesh is generated as shown in Fig. 4 and Table 1. In Fig. 4, the black line show the Cube boundary and the orange region is the buffer zone. Using this minimum cell size, the frequency up to 5kHz can be resolved from the points per wavelength constraint. The sound source is the white noise generated by the normal random number. This source is introduced to the inner region of the nacelle.

Figure 5 shows the instantaneous pressure distribution on the model surface and on the cross-sectional surface at y = -1.285. It is found that the generated noise from the nacelle is effectively shielded by the main wing. Pressure fluctuation at the cross-sectional surface is obviously weakened in the OWN configuration.

Figure 6 shows the noise shielding metric computed by Eq. (1) at the locations of microphones in Fig. 3. The results show the qualitative agreement with the experiment at the positions just below the fuselage as seen in microphones 2,3,4,5,11, and 12. However, the results of microphone 1 have large discrepancy with the experiment. The location of this microphone is almost hidden by the fuselage. Therefore, it is supposed that the generated noise is most shielded as seen in the result of computation. The computational result of microphones 6,9, and 10 shows negative value that means the noise is enhanced. The tendency of diffraction changes depending on frequency of noise. The metric at each frequency is analyzed by the fast Fourier transform in the future work.

4. Conclusions

In this research, the noise shielding effect of the OWN configuration was investigated quantitatively using the noise shielding metric, and it was compared with experiment. In this computation, the noise shielding metrics containing all frequency components are computed. However, a behavior of each frequency component is important for more detailed analysis. The details of shielding metric would be revealed in the future work.

Acknowledgements

This work was supported by JSPS KAKENHI (21226018). The computation in this research was conducted by SGI AltixUV1000 of Institute of Fluid Science, Tohoku University.

References

[1]D. Sasaki and K. Nakahashi, Modeling and Simulation in Engineering, **2011**(2011) 1-13.

[2]S. Powell, A. Sobester, P. Joseph, Journal of Sound and Vibration, **331**(2012) 5054-5068.

[3]K. Nakahashi, Computational Fluid Dynamics, **2**(2003) 77-81.

[4]Y. Fukushima, D. Sasaki, K. Nakahashi, AIAA Paper 2012-0832, 2012.

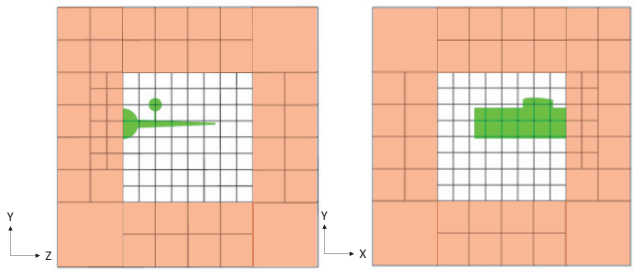

Fig. 4 Computational mesh

Table 1. Mesh information

Min. Cell size	Number of Cube	Number of Cells in one Cube	Total Number of Cells
5.86×10^{-3}	946	64×64×64	2.48×10^{8}

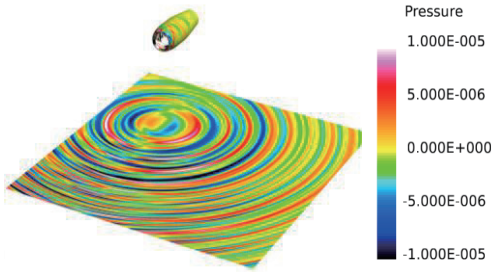

(a) Isolated nacelle

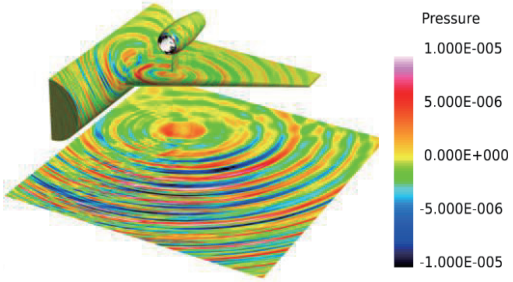

(b) OWN configuration

Fig. 5 Instantaneous pressure distribution of the model and cross-sectional surfaces

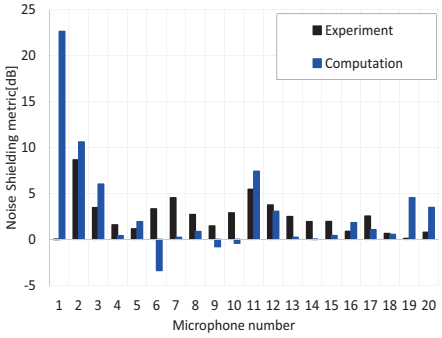

Fig. 6 Noise shielding metric at microphone locations

Tenth International Conference on Flow Dynamics
November 25-27, 2013, Sendai, Miyagi, Japan

Cartesian-based CFD Solver for Low-Reynolds Number Airfoils

Daisuke Sasaki[1)], Yuya Kojima[1)], Tatsuya Kuroda[1)], Takeshi Akasaka[1)], Masato Okamoto[1)],
Koji Shimoyama[2)], Shigeru Obayashi[2)]
[1)] Kanazawa Institute of Technology, Nonoichi 921-8501, Japan
[2)] Institute of Fluid Science, Tohoku University, Sendai 980-8577, Japan
dsasaki@neptune.kanazawa-it.ac.jp

ABSTRACT

The performance of airfoil and wing at low-Reynolds number flows is getting important with regard to the development of UAV/MAV. In this study, Cartesian-based CFD solver has been developed to compute the aerodynamic performance of airfoils. The validation will be conducted to thin flat plate, whose aerodynamic performances were obtained through water channel test. The computational technique will be extended to flapping wings at low Reynolds number flows.

1. Introduction

Many small UAVs (Unmanned Aerial Vehicles) and MAVs (Micro Aerial Vehicles) have been proposed and developed in recent years due to the requirements in various fields. Long endurance operation is one of the important requirements in the mission of surveillance and monitoring. To achieve the goal, aerodynamic performance has to be high, but the suitable airfoil shapes and wing configuration at low Reynolds number flows are still unknown because of the complicated unsteady flow phenomena. Thus, various experimental and computational efforts have been devoted for low-Reynolds number flows these days to understand the complicated flow physics [1].

The aim of the study is to develop efficient CFD (Computational Fluid Dynamic) tools for low-Reynolds number flows to enhance the aerodynamic performance of small UAVs. The suitable airfoil shape can be very thin or corrugated like insect wings, and thus Cartesian-based mesh has large advantages in terms of the efficient mesh generation. This enables the quick aerodynamic evaluation of the new geometry. In addition, Cartesian-based solver can easily employ higher-order schemes, which are required to capture the complicated unsteady flows in low Reynolds number flows regarding vortices. In this study, block-structured Cartesian-based CFD solver, Building-Cube Method (BCM), has been applied to the flows to validate its usefulness to predict the aerodynamic performance and also the flow physics.

2. Building-Cube Method

BCM is based on a multi-block structure of equally-spaced Cartesian meshes to achieve the simplicity in the mesh generation, in the spatially higher-order solution algorithm, and in the post processing [2]. These features of simplicity of the Cartesian mesh for all stages of a flow computation as well as the less memory requirement per node will become more important for large-scale computations on expected near-future high performance computers. The computational mesh consists of many cuboids which include equally-spaced Cartesian mesh as shown in Figs. 1 and 2. They show cube and cell distribution around NACA0012 airfoil. These cuboids in Fig. 1 are called as 'cube', and Cartesian mesh in each cube are called as 'cell' in Fig. 2. Since the number of mesh points is completely same in all the cubes regardless the cube size, high parallel efficiency is accomplished as the computation is parallelized based on cube. The mesh resolution is controlled by each cube size, thus the geometrical size of cube becomes large as the increase of distance from a wall boundary. In the present approach, the body surface is approximated as staircase representation for the simplicity.

Governing equations of the present solver are incompressible Navier-Stokes equations as follows;

$$\frac{\partial \mathbf{u}}{\partial t} + (\mathbf{u}\cdot\nabla)\mathbf{u} = -\nabla p + \frac{1}{\mathrm{Re}}\nabla^2\mathbf{u} \qquad (1)$$

$$div\ \mathbf{u}=0 \qquad (2)$$

The collocated arrangement is employed with finite difference scheme in terms of the spatial accuracy [3]. In this study, the convective term is discretized by Kawamura-Kuwahara scheme based on a third order upwind scheme. The pressure term is obtained by solving pressure Poisson equation, and the diffusion term is discretized by a second order central difference scheme. The time integration uses fractional step method, and the temporal velocity field is solved by second order Adams-Bashforth explicit method. Simple linear interpolation is employed for the data interchange between different size cubes.

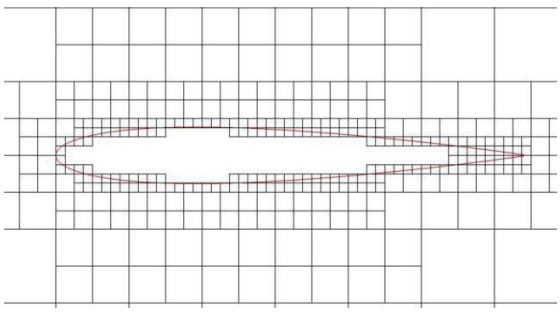

Fig. 1 Cube allocation at BCM structure

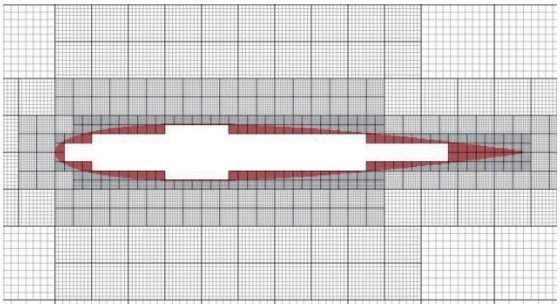

Fig. 2 Cell distribution at BCM structure

3. Results and Discussion

The first step of the research is to validate the prediction of aerodynamic loads of thin flat plate experimented in flow channel test as shown in Fig. 3. Three airfoil shapes (flat plate, circular arc and corrugated geometry) were examined and the obtained aerodynamic loads are plotted in Fig. 4. Incompressible flow solver is applied to flat plate (3.3% thickness) to precisely capture the flow physics at Reynolds number of 2,800.

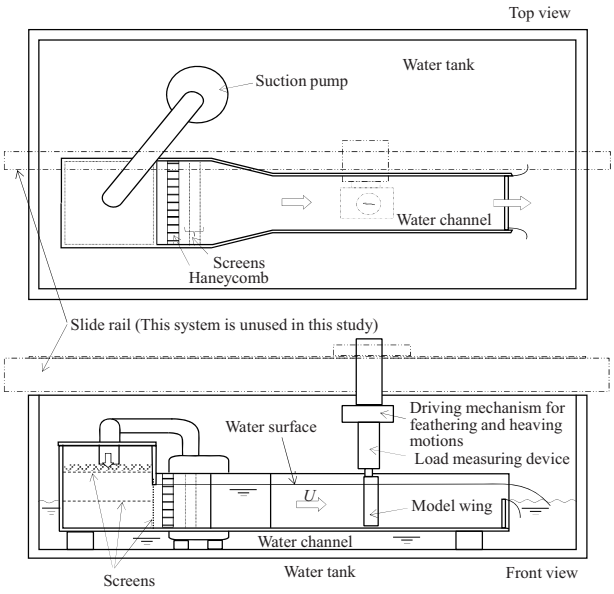

Fig. 3 Schematic view of water channel test

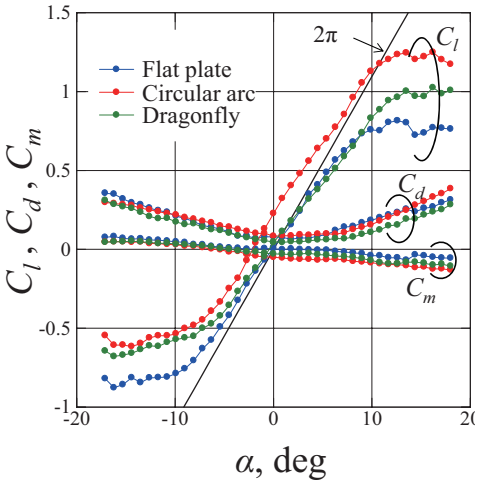

Fig. 4 Steady-state chracteristics of 3 airfoils

The computational set-up for the flat plate is based on the water-tunnel experiments. The overview of the computational mesh is shown in Fig. 5. The flat plate is represented in blue region (wall) in the figure and the rest is fluid region. The aerodynamic loads of the flat plate is computed and compared with the experimental data. The accurate prediction of separation is required at higher angle of attach.

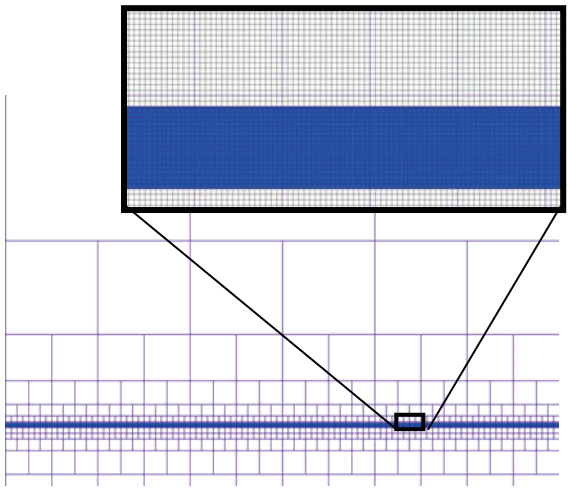

Fig. 5 Computational mesh for flat plate (front view): Cube allocation and cell distributions close to plate

4. Concluding remarks

Block-structured Cartesian mesh-based solver, BCM, has been developed to predict the complicated unsteady flow around the thin flat plate under the very low Reynolds number. When the validation is performed, the approach is extended to the flapping motion (heaving and feathering) of the flat plate. This will then be a useful tool to predict the performance of various small UAVs as well as to enhance the performance.

Acknowledgements

Part of the work was carried out under the Collaborative Research Project of the Institute of Fluid Science, Tohoku University. Part of the computational results in this research was obtained using supercomputing resources at Advanced Fluid Information Research Center, Institute of Fluid Science, Tohoku University.

References

[1] T. Kuroda, et. al., Tenth Int. Conf. on Flow Dynamics, (2013), Sendai, Japan.

[2] K. Nakahashi and L. S. Kim, AIAA Paper 2004-0423, (2004).

[3] R. Sakai, PhD Thesis, Graduate School of Engineering, Tohoku University, (2013).

Tenth International Conference on Flow Dynamics
November 25-27, 2013, Sendai, Miyagi, Japan

Enhancement of Wall Boundary Condition for Dirty CAD on Building Cube Method based Immersed Boundary

Keiji Onishi and Makoto Tsubokura
Advanced Institute for Computational Science, RIKEN, 7-1-26, Minatojima-minami-machi, Chuo-ku
keiji.onishi@riken.jp

ABSTRACT

Methodology is developed to reduce manual work in preparing geometry for simulation when working with dirty computer-aided-design data. A method that uses arbitrary boundary representation is proposed with a dummy-cell technique based on a Cartesian grid and immersed boundary method. The complicated geometry is degenerated into cell-oriented values. The advantage is that the user can handle geometry data that have a gap, overlap or thin wall without any special preprocessing. A calculation example of a full vehicle model provided by an automotive company is presented, and reasonable flow field results are obtained.

1. Introduction

When conducting simulations based on computational fluid dynamics (CFD) in industrial application, there remains a major problem that the user must carry out much work in generating a high-quality grid. It is still necessary to prepare the geometry by reproducing the shape manually or modifying the shape using commercial software for grid generation, although the user uses an unstructured grid or Cartesian grid.

For example, in the simulation of vehicle aerodynamics, it usually takes several days to weeks to prepare the geometry. This is mainly due to gaps and overlaps that are generated in the data conversion process of computer-aided-design (CAD) software. Other causes are the large quantity of surfaces that have zero thickness, unnecessary surfaces inside parts, and tiny parts that have size less than grid size. Such data are called a 'dirty' dataset. This manual workload will increase further in the near future, because faster computers bring higher resolution to CFD analysis, and thus, the amount of operation required for geometry preparation will rise further to modify finer geometries. In other words, the use of a supercomputer does not improve the accuracy of shape representation automatically. And, this heavy workload of geometry preparation strongly hinders the broadening of applications in the industrial CFD field, and as such, it is an important issue to resolve.

2. Numerical Method

In this research, the building cube method (BCM) [1] is employed as the basis of the Cartesian grid approach; the BCM is a computational method with which to calculate the flow field using uniform Cartesian grids in the spatial domain. The space is discretized with cubic units called cubes. Cubes are regularly subdivided, and the smallest unit is called a cell. The algorithm of computation is simple, and it maintains the same number of elements (cells) within each cube. As such, the technique has high efficiency in large-scale parallel computation.

This study employs an incompressible Navier–Stokes equation (Eq. (2))by spatially filtered form of large eddy simulation (LES) with the forcing term (Eq. (3)) of the immersed boundary method (IBM) [2-3] and a continuity equation (Eq. (1)) as a governing equations.

$$\nabla \cdot \overline{\mathbf{u}} = 0 \tag{1}$$

$$\frac{\partial \overline{\mathbf{u}}}{\partial t} + \nabla \cdot (\mathbf{uu}) = -\frac{\nabla \overline{p}}{\rho} + 2\nabla \cdot (\nu + \nu_t)\overline{\mathbf{S}} + \overline{\mathbf{f}} \tag{2}$$

$$\overline{\mathbf{f}}^{\,l+1/2} = \frac{V^{l+1} - \overline{\mathbf{u}}^{\,l}}{\Delta t} - RHS^{l+1/2} \tag{3}$$

To solve an advection term, a QUICK scheme is used. To solve time integration, a second-order Adams–Bashforth explicit scheme is used; the scheme is based on a fractional step approach using an intermediate velocity that is corrected with the pressure gradient obtained from a Poisson equation. The Poisson equation is solved using the red/black ordered successive over-relaxation method. The velocity and pressure variables are defined at the cell center in the collocated grid.

For the wall boundary condition, a method that uses modified immersed boundary representation is adopted with a dummy-cell technique based on a Cartesian grid and IBM. The complicated geometry is degenerated into cell-oriented values, by splitting polygons with the edges of grid lines at the position of intersection between geometry elements and grid lines as shown in Fig. 1. The total area, characteristic gravity center, and characteristic normal vector are obtained as cell-oriented data by summing values for all subdivided polygons within each cell. Thus, the original geometry can be expressed with the simple planes.

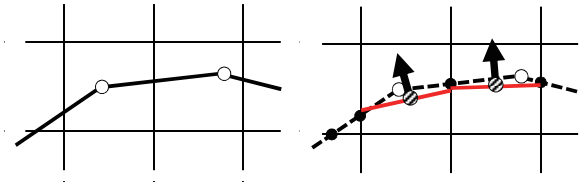

(a) Original surface and grid (b) Representative surface center and normal

Fig. 1 Subdivision of the surface geometry

A virtual cell data structure, called a dummy cell, is employed. In dummy cells, the fluid variables are copied from the background grid, and have arbitrary solid cells due to the position of wall boundary data. The solid cell is treated as ghost cell of IBM. This technique allows the walls to be separated from the front/back side naturally because the solid cell can be placed in arbitrary

position for each cell. This feature allows walls to be treated as having zero thickness. The advantage of this modification is that the user can handle the data that have a gap, overlap or thin wall without any special preprocessing.

The force term of IBM is directly imposed on an arbitrary ghost cell by linear interpolation of the velocity, which is defined according to the distance between the cell-centered position and the crossing point with the grid line as shown in Fig. 2 and Eq. (4), Eq. (5). The intersection point is obtained from the plane equation which is represented with face center and normal.

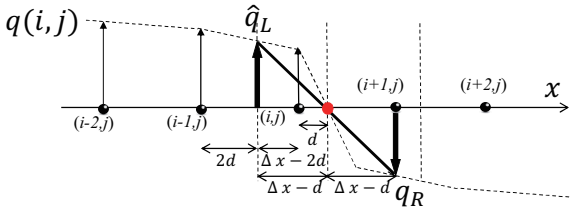

Fig. 2 Definition of direct forcing for the ghost cell

$$\hat{q}_L = \frac{\Delta x - 2d}{\Delta x} q(i-1, j) + \frac{2d}{\Delta x} q(i, j) \quad (4)$$

$$q_R = -\hat{q}_L \quad (5)$$

3. Results and Discussion

A vehicle aerodynamics CFD analysis is conducted using the dirty CAD data as shown in Fig. 3. The computational grid has 26,937 cubes and 110,333,952 cells, and the finest cell resolution is 6.10 mm. The calculation conditions are described in Table 1.

Table 1. Calculation conditions

Term	Value	Unit
Velocity	27.778	m/s
Characteristic Length	1.535	m
Density	1.204	kg/m3
Viscosity	1.820×10^{-5}	Pa•s
Re number	1.838×10^{6}	-

As seen in Fig. 3(a), the geometry data has all vehicle components of the production model except for the interior; e.g., the engine, suspension, brakes, battery, auxiliaries, wire/harnesses inside the engine bay, inner body frames, headlamps and rear lamps, and nuts and bolts. The model is constructed with 12 million triangular elements. The model has more than 1000 errors, gaps, and overlaps as shown in Fig. 3(b) in which the red lines and cyan lines indicate the edges that the geometrical error is existing. The calculation time for grid generation using recently designed desktop PC was about 10 minutes, the calculation time for wall boundary discretization was only 10 minutes using 1024 cores. The calculation is finished about 1 day.

Figure 4 shows the velocity magnitude of the center section of calculation results and Fig. 5(a), (b) shows the magnified views of specific area. The reasonable flow results such as a flow inside engine bay and shear layer around front thin spoiler are obtained despite the many errors in the geometric data.

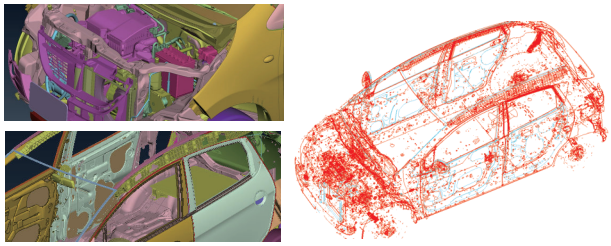

(a) Geometric overview (b) Problems with the geometric data

Fig. 3 Snapshot of the full-vehicle CAD geometry

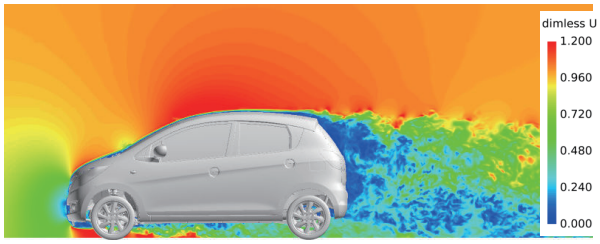

Fig. 4 Results of flow around the full vehicle

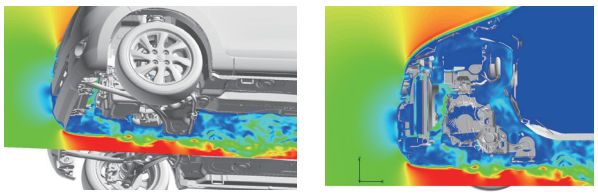

(a) Magnified view of front bottom (b) Magnified view of the engine room

Fig. 5 Velocity magnitude of flow result

4. Concluding remarks

A modified wall boundary condition using in this study with the IBM based on a BCM Cartesian grid approach allows three-dimensional complicated geometries to be handled as they are, without any manual repair of the geometry.

An applicability for the full vehicle geometry was shown, and user could obtain the reasonable flow results within almost 1 day. This has a big impact on the industrial design field because it can reduce significant time to get first result than present. The proposed method has a possibility to become an innovative scheme in industrial CFD to change the design process itself by the advantage of which shows in this research.

References

[1] K. Nakahashi, Comp. Fluid Dyn. 2002 edited by S. Armfield, R. Morgan, K. Srinivas, Springer (2003)
[2] C. S. Peskin, Acta Numeca **11** (2002), pp. 479-517.
[3] E. A. Fadlum, R. Verzicco, P. Orlandi, and J. Mohd-Yusof, J. Comp. Phys., **161** (2000), pp. 35-60.
[4] K. Onishi, S. Obayashi, K. Nakahashi, M. Tsubokura, AIAA-2013-2713 (2013)

Tenth International Conference on Flow Dynamics
November 25-27, 2013, Sendai, Miyagi, Japan

Graphics Processor Unit Accelerated Finite-Volume Solver for Inviscid Euler Equation using a Ghost-cell Immersed Boundary Method

Fang-an Kuo[1,3], Matthew R. Smith[2], Jen-Pao Su[1], Jong-Shinn Wu[1*]
[1]Department of Mechanical Engineering, National Chiao Tung University, Hsinchu, Taiwan
[2]Department of Mechanical Engineering, National Cheng Kung University, Hsinchu, Taiwan
[3]National Center for High-Performance Computing, National Applied Research Laboratories, Hsinchu, Taiwan
*E-mail: chongsin@faculty.nctu.edu.tw

ABSTRACT

In this paper, we propose an explicit cell-centered finite-volume solver for the inviscid Euler equation using a ghost-cell immersed boundary method (GCIBM), which can easily treat objects with complex geometry on a Cartesian structured grid, on multiple graphics processing units (GPUs). The solver was carefully validated against several existing simulations. Parallel performance study shows that the speedup can exceed 100 –on a single GPU (Nvidia Telsa M2070) as compared to a thread of Intel Xeon X5472. In addition, for a problem with 9 million cells, more than 12 times of speedup (> 75 % of parallel efficiency) can be obtained using 16 GPUs as compared to a single GPU.

1. Introduction

In recent years, the large-scale computational fluid dynamics (CFD) has become an inevitable tool in simulating several challenging yet important engineering and science problems. Traditional approaching in performing large-scale CFD simulations is made possible through distributed machines, e.g., PC clusters, using message passing interface (MPI). With the recent introduction of graphics processing unit (GPU), GPU computing has become an active research topic for high-performance computing potentially with a very high capability/performance ratio. In this paper, we intend to present our recent progress in CFD simulations using multiple GPUs.

In this paper, we solve the Euler equation by applying the split Harten-Lax-van Leer (Split HLL or SHLL) scheme [1] for approximating the inviscid flux across the cell interface. It was shown that is highly suitable for GPU computing for general conservation equations because of its high locality of the stencil. In most realistic CFD simulations, generation of a body-fitted grid for the solid objects (fixed, moving or flexible) with complex geometry is often the most tedious and difficult task. In this paper, we resolve this issue by applying a modified ghost-cell based immersed boundary method (GCIBM) on a Cartesian structured grid.

2. Method

There are two key issues in implementing the IBM into a cell-centered finite-volume Euler equation solver. One is how to interpolate the boundary conditions and fluid cell data into ghost cell (or image point) and the other is how to approximate the solid boundary accurately. For the former, we apply bi-linear interpolation function in the two dimensional case, instead of bi-quadratic function, which makes the implementation become complicated without much benefit. For the latter, conventionally either a well-defined function for some special geometry or a polygon for general curved geometry is used for representing the surface contour. In the current study, we employ a cubic-spline curve fitting technique to reconstruct the surface contour, which renders the calculation of surface tangent/normal easier with a higher accuracy. This will be presented later.

Under the framework of inviscid Euler equation, the boundary conditions at solid walls are summarized as follows:

$$\frac{\partial \rho}{\partial \vec{n}} = 0, \quad \frac{\partial \vec{V}}{\partial \vec{n}} = 0, \quad \frac{\partial T}{\partial \vec{n}} = 0 \tag{1}$$

where $\vec{n}$ is the unit normal to the body surface and ρ, $\vec{V}$ and T is the cell-centered density, velocity and temperature of a cell. The corresponding discretized forms of the boundary conditions at solid walls are summarized as follows:

$$\rho_{image} = \rho_{ghost}, \quad \vec{V}_{\vec{n},image} = -\vec{V}_{\vec{n},\text{ghost}}, \quad \vec{V}_{\vec{t},image} = \vec{V}_{\vec{t},\text{ghost}}, \quad T_{image} = T_{ghost} \tag{2}$$

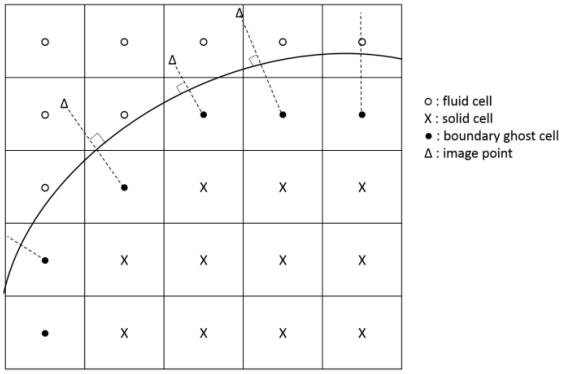

Fig. 1 Illustration of ghost-cell IBM.

Figure 1 illustrates the sketch of cubic-spline GCIBM near a curved solid surface. Firstly, we define a cubic-spline function for each segment to best fit the solid boundary geometry through the interpolation of four surface geometry data points. Secondly, we use the cubic-spline function to identify all the solid cells, fluid cells, boundary cells and ghost cells. Note in the GCIBM, the ghost cells are considered to be the "boundary solid cells" mathematically. Thirdly, we locate each image point

corresponding to the cell center of each ghost cell for all solid boundary cells using the cubic-spline function wherever it is appropriate. Fourthly, we obtain the data at each image point through the data of fluid cells from previous time step around it. Finally, we obtain the data at each ghost cell through the enforcement of boundary conditions, Eq. (2).

Table 1. Performance Benchmarking of supersonic vorticity production by using hybrid MPI and CUDA.

3,000x3,000 (cells)	Flow time = 0.15634 # step = 11,985			CFL # = 0.2		
	1x Telsa M2070	2x Telsa M2070	4x Telsa M2070	8x Telsa M2070	12x Telsa M2070	16x Telsa M2070
Node #	1	1	1	2	3	4
Time (sec.)	2280.1	1205.63	608	329	222.3	187.79
Speedup	1.00	1.89	3.75	6.93	10.26	12.14
Efficiency		94.56%	93.75%	86.63%	85.47%	75.89%

3. Results and Discussion

In the current study, two benchmark problems (supersonic vorticity production and subsonic NACA0012 problems) were used to validate the developed code. Results show that the increase of runtime by adding cubic-spline GCIBM into the SHLL scheme is only 3%, which is negligible in practice.

The supersonic vorticity production problem was used to test parallel performance of the current implementation (Figure 2). Results show that the speedup generally exceeds 100 on a single GPU (Telsa M2070, NVidia) as compared to that on a single thread of an Intel X5472 Xeon CPU with 4 million cells. Table 1 summarizes the test results of multiple GPUs. Results show that more than 12 times of speedup (> 75 % of parallel efficiency) can be obtained using 16 GPUs as compared to a single GPU for a problem having nine million cells.

Figure 3 shows the instantaneous distribution of density at the time of 3.5 seconds for a transonic flow (M=0.8) past a NACA0012 airfoil with an angle of attack of 1.25 degrees. 1,000×1,000 cells are used in the simulation with a CFL number of 0.2. The absolute runtime is about 372 seconds for 48943 time steps. All the important flow features are well captured by the simulation. The results are in excellent agreement with the previous published data [2].

4. Concluding remarks

We have developed an explicit cell-centered finvite-volume code using multiple GPUs. The code was validated by two benchmarking test problems. Parallel performance study shows that very impressive speedup is obtained. More than 100 times of speedup of the code on a single GPU (Nvida Telsa M2070) as compared to a single thread of CPU (Intel Xeon X5472) and >75% of parallel efficiency on 16 GPUs as compared to a single GPU are demonstrated. This shows that the use of multiple GPUs for an explicit scheme with a high-locality stencil is very promising for large-scale CFD simulations in the near future. Extension to 3D and addition of adaptive mesh refinement is currently in progress and will be reported elsewhere in the future.

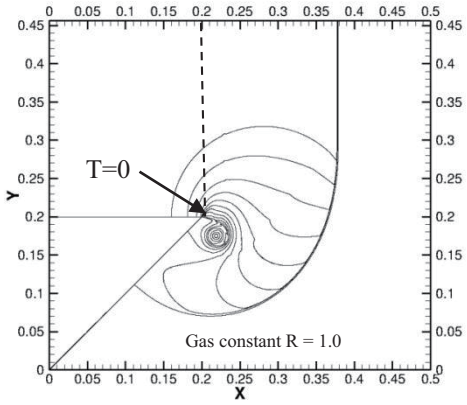

Fig. 2 Instantaneous density distribution of vorticity production problem at T=0.1 seconds (M_s=1.5).

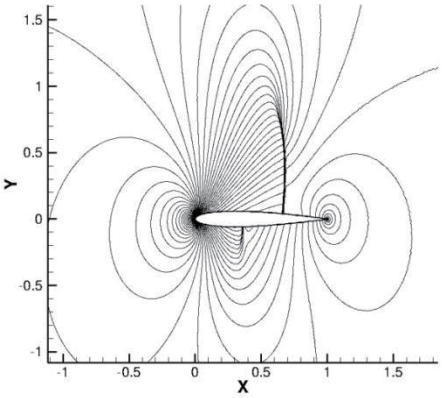

Fig. 3 Pressure contour around NACA0012 (M_∞=0.8, AOA=1.25°, T=3.5 seconds).

References

[1] F.-A. Kuo, M. R. Smith, C.-W. Hsieh, C.-Y. Chou and J.-S. Wu, Computers & Fluids, Volume 45, Issue 1, June 2011, Pages 147–154.

[2] J.-M. Liu, N. Zhao and O. Hu, Advances in Applied Mathematics and Mechanics, Adv. Appl. Math. Mech., Vol. 1, No. 5, pp. 664-682.

An investigation of dissipation effects on a jet propulsion

Kun-Rung Huang (National Chiao Tung University, Hsinchu Taiwan) gibu.me95@nctu.edu.tw; Wu-Shung Fu, (National Chiao Tung University, Hsinchu Taiwan) wsfu@mail.nctu.edu.tw; Wei-Hsiang Wang (National Chiao Tung University, Hsinchu Taiwan) flyman.me98g@g2.nctu.edu.tw; Makoto Tsubokura,(Hokkaido University, Sapporo Japan) (RIKEN, Advanced Institute for Computation Science, Kobe 650-0047, Japan) mtsubo@riken.jp; Chung-Gang Li (RIKEN, Advanced Institute for Computation Science, Kobe 650-0047, Japan) chung-gang.li@riken.jp;

ABSTRACT

An investigation of dissipation effects on a jet propulsion by way of a gaseous discharge from a high pressure vessel is investigated numerically. The compressibility and viscosity of the gas are takes into consideration simultaneously. Methods of the Roe scheme, preconditioning and dual time stepping matching LUSGS method are adopted to solve governing equations. The result shows that became of generation of dissipation caused by the shear stress and temperature difference the thrust produced by the discharged gas is smaller than the reaction produced by the net pressure force.

1. Introduction

Phenomena of a jet propulsion are very important and interesting in applications of aeronautics and aerospace. These phenomena basically include important characteristics in both academic and industrial research. Due to difficulties of definition of a computational domain and treatment of drastic variations of the density, speed and temperature of the working gas, an investigation of a jet propulsion by a numerical simulation is hardly conducted. As a result, detailed mechanisms of the jet propulsion affected by dissipations of a shear stress and temperature difference are not clarified yet.

In the past years researches did the study by means of experimental equipment [1] and the results also had good agreements with actual situation. But it's hard to access the detailed data of the main flow while in the experiment. The researches of numerical simulation of gas release or jet flow became popular in recent years. However, lots of simulation studies focused on outside region the region influenced by main flow. Few researches talked about the inside region affected by storage gas, and no researchers studied both inside and outside regions.

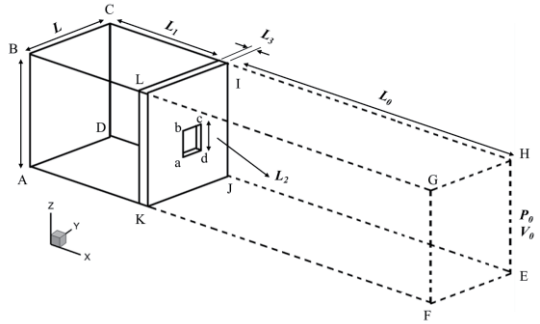

Fig. 1 Physical model of vessel and surroundings

2. Physical model

To simulate the study more appropriately the physical model was divided to two parts: the high pressure vessel and open boundary zone. In the inside region highly compressed gases is filled in the beginning and surrounded by solid wall with a small opening. On the other hand the pressure and temperature at the outside zone is set as 1atm and 298K. The boundary of outside region is open boundary; it means that there are no reflection wave can influence the flow field in the boundary just like real situation which the length of the boundary is infinity. The Fig. 1 is the physical model, the solid lines stand for solid walls and the dashed lines represent open boundaries.

For facilitating analysis, the following assumptions are made.

1. Properties of the working gas follow the equation of state of an ideal gas.
2. Gravity is neglected.
3. The pressure gradient in the normal direction of the solid surface is equal to zero.

The continuity, momentum and energy equations are writing in a general partial form in which the parameters of viscosity and compressibility of the fluid and the force of immersed boundary are considered simultaneously and the governing equations are shown in as following.

$$\frac{\partial U}{\partial t}+.\frac{\partial F}{\partial x}+\frac{\partial G}{\partial y}+\frac{\partial H}{\partial z}=S \tag{1}$$

$$P=\rho RT \tag{2}$$

$$U=(\rho,\rho u,\rho v,\rho w,\rho e)^T \tag{3}$$

$$S=(0,f_x\delta(\overline{X}),f_y\delta(\overline{X}),f_z\delta(\overline{X}),0)^T \tag{4}$$

In which

$e=C_vT\cdot(u^2+v^2+w^2)/2$

f : The reaction force of immersed boundary

$\delta(\overline{X})$: The weighting function

3. Numerical method

Utilizing the Roe scheme to match preconditioning method and applying the coordinate transformation technology [2] solves the equation (5) with Jacobian transformation.

$$\Gamma\frac{\partial U_p}{\partial\tau}+\frac{\partial\widetilde{U}}{\partial t}+\frac{\partial\widetilde{F}}{\partial x}+\frac{\partial\widetilde{G}}{\partial y}+\frac{\partial\widetilde{H}}{\partial z}=S' \tag{5}$$

Then the 3th order MUSCL proposed by Abalakin et al. [3] is used to compute inviscid terms. Viscid terms are solved by a second order central difference. Finally, the LUSGS [4] is used to solve temporal advancements.

4. Result and discussion

The results of two cases (opening of case1: 78.87mm^2, case2: 148.46mm^2) can be divided to three parts and shown as follows:

A. Comparing with experience equation

In this study the results of different cases are

compared with the experience equation [5]. The results are the mass flow rate through the opening and shown in Fig. 2. Both two simulation results have good agreements with the experience equation. The data of mass flow rate accompanied with a little vibration because of the pressure fluctuation at the inside region.

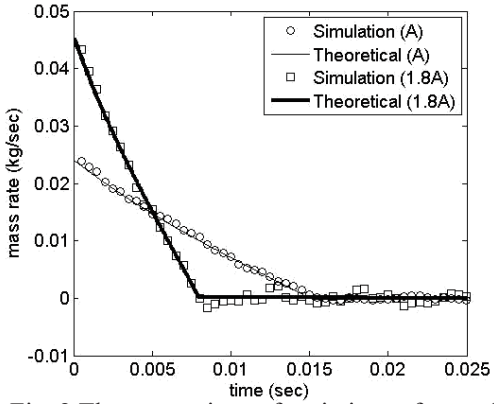

Fig. 2 The comparison of variations of mass flow rates of different cases

B. Rationality verification

The results of the data varying with time are shown in Fig. 3. Both of two cases have the same volume of vessel and same surroundings. Therefore they probably discharged the equal quantity of mass. The pressure decay of the case with the larger opening is faster than the smaller one and the mass flow rate is also higher (see in Fig. 2). During the adiabatic expansion process the temperature of the vessel cool down to minus Celsius suddenly. Consequently the temperature of the released gas at the end of discharge is also lower than a frozen temperature.

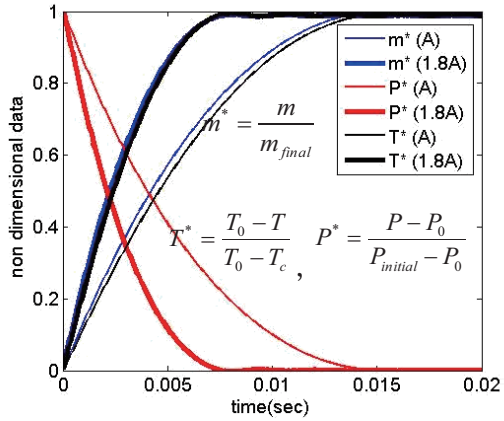

Fig. 3 Variations non dimensional data decay with time

C. Propulsion analysis

The aim of the study to simulate the gaseous discharge process to investigate the dissipation effects on the jet propulsion. The thrust during the gaseous discharge can be calculated by the following equation.

$$F_t = \sum_{1}^{n} (\dot{m} V) \tag{7}$$

$\dot{m}$ and V are mass flow rate and velocity at the grid area of the opening.

The reaction corresponding to the thrust can be calculated by the summation of net pressure forces Δp acting on the where solid walls.

$$F_R = \sum_{A} \Delta p \times \Delta A \tag{8}$$

Usually, the magnitudes of the thrust and reaction ought to be equal and under an equilibrium situation. However, during the gaseous discharge the gas which is viscous and compressible is squeezed from the high pressure vessel and released into the outside region. Then the gas flowing into the outside region processes a high speed and low temperature. Relative to the outside region which is stationary under a normal temperature situation, the difference of the speed and temperature between the released gas and original gas in the outside region easily cause the viscous and thermal entropies to be produced that directly dissipate energy of the released gas. Meanwhile, the variations of the speed and temperature of the inside gas which play an role of the reaction are slights that result in the generation of the entropy of the gas to be a little compared with the released gas in the outside region. Therefore, the magnitude of the reaction is larger than that of the thrust and shown in Fig.4. The ratios of the reaction to the thrust are almost the same in spite of the size of the opening. According with increment of the time, the deviations between the thrust and reaction will decay.

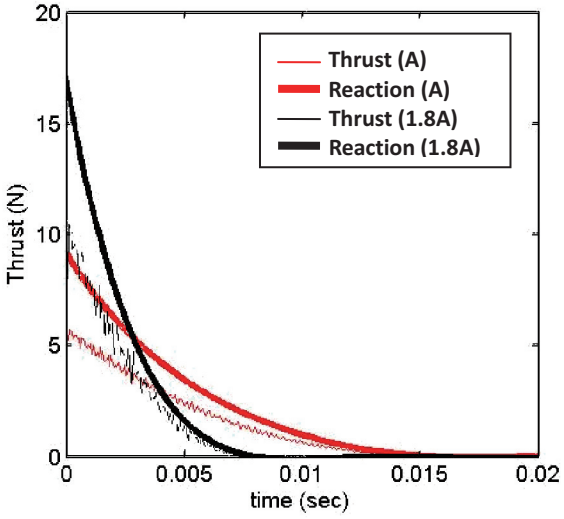

Fig. 4 The comparison of the impulse and thrust

5. Concluding remarks

1. Comparisons of the present results and experimental results have good agreements.
2. Due to the generation of the thermal and viscous entropies of the released gas, the thrust produced by the released gas is smaller than the reaction produced by the gas in the vessel.

References

[1] J. Craig Dutton Int. J. Engng Ed. 13(1997), 123-134.
[2] Upender K.Kaul *NASA Ames Research Center,M/S 258-5, Moffett Field, CA 94035, United States
[3]I. Abalakin, A. Dervieux, T. Kozubskaya, INRIA (2002) No4459.
[4]S. Yoon, A. Jameson, AIAA. 26 (1988) 1025-1026
[5] Perry & Chilton.1973 Chemical engineers handbook 5 edition. Ch. 5, 10-13.
[6] C. L. Iandoli Int. J. of Thermo. (2005) .8, 83-94.

Tenth International Conference on Flow Dynamics
November 25-27, 2013, Sendai, Miyagi, Japan

Wavelet-Based Data Compression Technique for Building-Cube Method

Ryotaro Sakai[1], Shigeru Obayashi[2], Daisuke Sasaki[3], Kazuhiro Nakahashi[4]
[1]Department of Aerospace Engineering, Tohoku University, Sendai, 980-8577, Japan
[2]Institute of Fluid Science, Tohoku University, Sendai, 980-8577, Japan
[3]Department of Aeronautics, Kanazawa Institute of Technology, Nonoichi, 921-8501, Japan
[4]Japan Aerospace Exploration Agency, Chofu, 182-8522, Japan
sakai@edge.ifs.tohoku.ac.jp

ABSTRACT

A data compression method is proposed to solve the data size problem in large-scale simulation by the block-structured Cartesian mesh method named Building-Cube Method. Based on the mesh structure of the Building-Cube Method and flow continuity, four image encoding techniques are employed: discrete wavelet transform, embedded zerotree wavelet encoding, quantization, and entropy encoding. In the compression case for a flow around a sphere, the proposed method effectively reduced data size to less than 5% of the original data, while keeping good data quality in terms of flow visualization and coefficient distribution.

1. Introduction

Although the Building-Cube Method (BCM) as the next-generation CFD method has achieved efficient large-scale flow simulation, it has posed another issue, that is, huge amount of output data. The BCM [1] has designed to make maximum use of recent supercomputers through its simple computational structure. Several large-scale simulations such as the flow past a Formula 1 racing car [2] and the flow around a landing gear [3] have demonstrated high performance computing by the BCM. However, numerical simulation with the large number of mesh points yields huge amount of output data, especially in an unsteady flow analysis. The data size problem should be taken into more consideration because it is not specific in the BCM but potentially inevitable in large-scale simulation.

The objective of this research is to realize efficient post-processing in large-scale simulation by the BCM by introducing a data compression method based on image encoding techniques. So far several compression methods for CFD data have been proposed based on signal processing techniques [4][5]. However, we have found that image encoding techniques are good candidates for data compression method in the BCM due to its mesh structure and an analogy between image and fluid. Here wavelet-based image encoding techniques as well as quantization are employed to construct a data compression method. The present method was applied to the flow field obtained by an incompressible flow solver based on the BCM, and its compression performance was investigated.

2. Building-Cube Method

The BCM employs an isotropic Cartesian mesh and a hierarchical cubic structure covering a computational domain. Figure 1 shows an example of the computational mesh used in the BCM. A computational domain is divided into many cubic blocks named “cube” with different sizes according to their locations. Each cube has an isotropic Cartesian mesh named “cell” inside it. The number of cells in one cube is the same among all cubes. The BCM inherits advantages of Cartesian mesh method, such as robust mesh generation, easy introduction of higher order scheme, and simple algorithm structure. In addition to these advantages, the block structure of the BCM gives other advantages such as easy introduction of adaptive mesh refinement and efficient parallel computation.

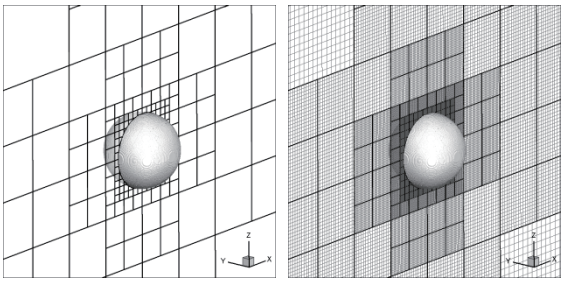

(a) cube (b) cell

Fig. 1 Computational mesh in the BCM

3. Data Compression Method

The present data compression method consists of four image encoding techniques: discrete wavelet transform (DWT), embedded zerotree wavelet (EZW) encoding [6], quantization and entropy encoding. The recursive implementation of the DWT creates hierarchical distribution of the field based on frequency. The EZW encoding reduces data size under the assumption of signal continuity by using the hierarchical structure previously created. In advance of the EZW encoding, quantization is implemented with specific quantization bit rates which vary according to the importance of the flow field. Finally the data size is further reduced by entropy encoding.

The present method is appropriate for flow data compression in the BCM. Due to an analogy between image and fluid in terms of continuity which is utilized to reduce data size, image encoding techniques are considered to be also effective for flow field data. The isotropic voxels of the BCM can be easily processed by the image encoding techniques which receive isotropic image pixels in nature. In addition, thanks to the characteristics that the number of cells is the same in all the coordinate directions, the creation of the balanced hierarchical structure is quite easy in the BCM.

4. Data Compression Results

The present compression method was applied to the flow field obtained by an incompressible flow solver based on the BCM. Here a flow past a sphere has been simulated at the Reynolds number $Re = 1.00 \times 10^4$ based on the uniform flow velocity and sphere diameter. The computational domain consists of 708 cubes, and each cube contains 32^3 cells inside it. The total number of mesh points is about 23.2 million. The size of the original flow data including three velocity components and pressure is about 371 MB.

Figure 2 shows the streamwise velocity distributions around a sphere. The complex flow field including flow separation and vortex shedding is reproduced well from the compressed data. Figure 3 shows the pressure coefficient distribution on the body surface. These two distributions change similarly from the stagnation point ($\theta = 0$) to the backward face ($\theta = 180$) through the flow separation point. These comparisons indicate that the compressed data give comparable results with the original data in terms of flow visualization and coefficient distribution.

Table 1 describes errors arising from the compression and compression rates. All four variables compressed here show the same orders of error in root mean square error (RMSE) and maximum error. They are suppressed to less than 0.1% and 1% of the original data, respectively. The compression rates show that the data size is reduced to less than 5% of the original data in each variable. These results demonstrate effective data compression by the present method with reasonable data quality.

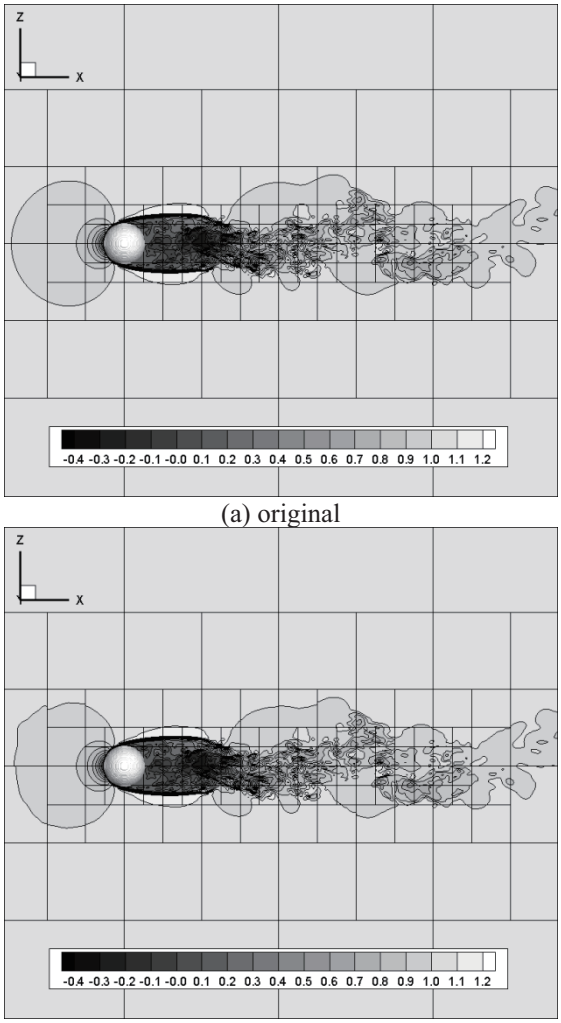

(a) original

(b) compressed

Fig. 2 Streamwise velocity distributions

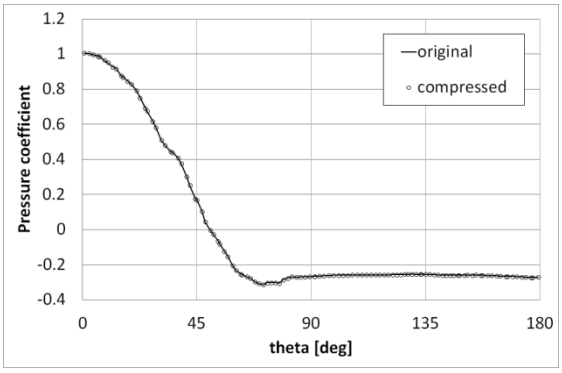

Fig. 3 Pressure coefficient distributions

5. Concluding remarks

A data compression method is proposed for flow simulation data obtained by the BCM. The present method is based on image encoding techniques including DWT, EZW encoding, quantization, and entropy encoding. The compression case of a flow around a sphere shows both good quality of compressed data and efficient data reduction to less than 5% of the original data.

Acknowledgment

The first author would like to thank the support by JSPS Grant-in-Aid for JSPS Fellows Grant Number 24-3800. Computational resources have been provided by Cyberscience Center and Advanced Fluid Information Research Center in Tohoku University.

Table 1 Errors and compression rates

	RMSE [%]	Max. error [%]	Comp. rate [%]
u	0.0234	0.302	3.23
v	0.0255	0.367	3.06
w	0.0277	0.357	3.06
p	0.0320	0.483	1.64

References

[1] K. Nakahashi, AIAA Paper 2005-4876.
[2] S. Takahashi, AIAA Paper 2009-0563.
[3] A. Deguchi, AIAA Paper 2012-0388.
[4] H. Kang, KSME Int. J., **17** (2003), 1784-1792.
[5] LS. Lorente, Aero. Sci. & Tech., **14** (2010), 168-177.
[6] JM. Shapiro, IEEE Trans. on Sig. Proc., **41** (1993), 3445-3462.

Tenth International Conference on Flow Dynamics
November 25-27, 2013, Sendai, Miyagi, Japan

Large Eddy Simulation of Rudimentary Landing Gear based on Building-Cube Method

Takashi Misaka[1], Shigeru Obayashi[2], Keizo Takenaka[3], Kazuhiro Nakahashi[4]
[1]Frontier Research Institute for Interdisciplinary Sciences, Tohoku University
[2]Institute of Fluid Science, Tohoku University
[3]Mitsubishi Heavy Industry
[4]Japan Aerospace Exploration Agency (JAXA)
misaka@edge.ifs.tohoku.ac.jp

ABSTRACT

In this study we consider boundary layer equations in combination with a Cartesian mesh flow solver based on the Building Cube Method to provide appropriate boundary conditions to near wall Cartesian cells in high Reynolds number flows. The approach is applied to a flow around rudimentary landing gear (RLG), which has been used as a benchmark problem for airframe noise computation. The coupling strategy and preliminary results from the RLG model are presented.

1. Introduction

In recent years, aircraft and operation technologies mitigating the impact of aviation on environment have received attention. Airframe noise such as the noise from a landing gear is one of those negative impacts of aviation on environment, therefore, the accurate prediction of unsteady flows causing the airframe noise is required for the design of next generation aircraft.

Our interest in this study is the development of a tool for unsteady flow simulation. As for the target we study an unsteady flow around rudimentary landing gear (RLG), which is a simplified landing gear model for aeroacoustic studies [1]. The unsteady flow simulation such as large-eddy simulation (LES) requires isotropic fine meshes. In this study we employ Building-Cube Method (BCM) which is a multi-level Cartesian meshes adapting local geometry as well as flow structures [2,3]. The BCM also provides an efficient framework for massive parallel computation. Although Cartesian mesh is well suited for unsteady and vortical flows, the treatment of curved surfaces poses a difficulty for handing thin boundary layer in high Reynolds number flows.

In this study we investigate the feasibility of a coupling approach of BCM and boundary layer equations for solving high Reynolds number flows around the RLG model.

2. Method

We employ incompressible Navier-Stokes equations for LES. The pressure term is handled by fractional-step method, while the convection and diffusion terms are discretized by secondo-order central difference scheme. Third-order low-storage Runge-Kutta scheme is used for the time integration. The Lagrangian dynamic model is employed for a sub-grid model. The above schemes are implemented on the framework of the BCM.

The realization of the curved wall boundary in Cartesian mesh is possible in numerous ways. Here we employ immersed boundary method with image points (IPs) in a fluid region as shown in Fig. 1(a). An IP is defined by a wall-normal line segment, which passes cell face center near wall boundary. Based on the interpolated velocity at the IP, the velocity profile toward the wall is defined, which provides approximate boundary conditions for near wall cell faces. Examples of possible velocity profile are shown in Figs. 1(b)-(e). A linear interpolation approach in Fig. 1(b) corresponds to a typical low Reynolds number wall treatment, which is effective if IPs are located at the height of y^+~O(1). It is not the case in practical aerodynamic flows, therefore, high Reynolds number wall treatment, i.e., a wall model, is needed [4,5].

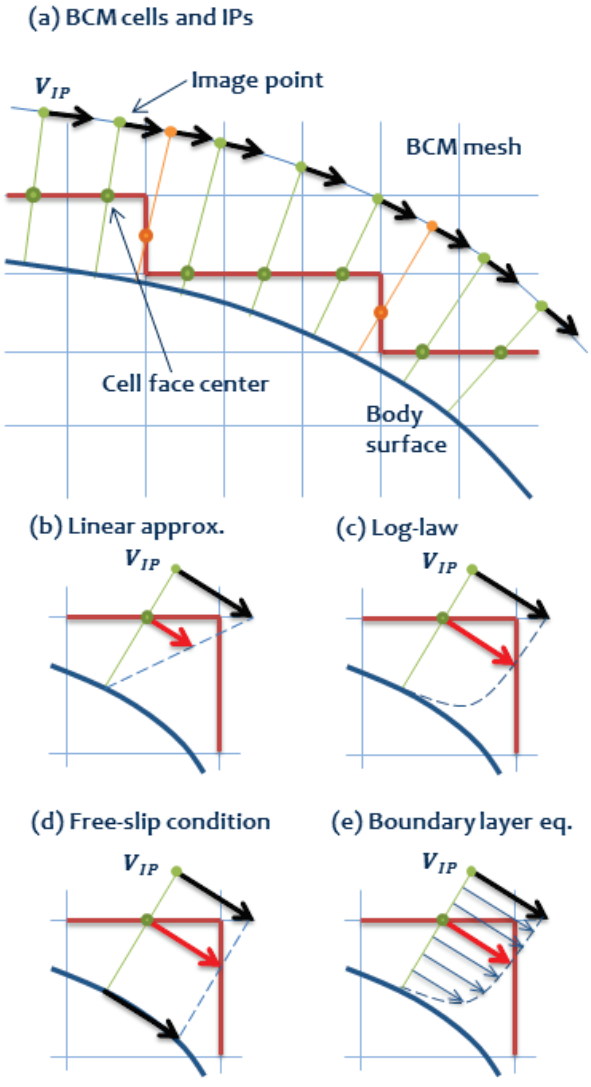

Fig. 1 Treatment of wall boundary conditions in a Cartesian mesh.

For this reason we employ boundary layer equations in combination with the BCM [6,7]. The use of boundary layer equations enables to consider the effect of pressure gradient on the velocity profile, where it is usually ignored in logarithmic law models. The boundary layer equation of a tangential velocity component is solved along a one-dimensional mesh from IP down to the wall with an iterative solution method. Pressure and velocity gradients are taken from the IP position, where the gradients are interpolated from the surrounding cells to the IP. Eddy viscosity appear in the boundary layer equation is provided by a simple mixing length model.

3. Results and Discussion

Figure 2 shows an iso-vorticity surface around RLG colored by pressure. In addition to vortical structures, numerical oscillations due to a central difference scheme are seen near the front wheels. This oscillation is mainly caused by large velocity shear near boundary layer and is alleviated by the use of upwind schemes or spatial filtering. However, too much dumping is not favorable for LES where grid-scale velocity fluctuations need to be revolved. By using high Reynolds wall boundary condition the oscillation due to strong near wall shear was reduced because the present boundary condition works like a free slip boundary condition for inviscid flow.

Figures 3(a) and (b) show velocity vector near wall surface obtained from boundary layer equations on vertical and horizontal cross-sections, respectively. Flow acceleration along the corner the tire's shoulder modifies the velocity profile of the boundary layer as shown in Fig 3(b). Wall shear stress and boundary condition for the near wall cells are provided by the velocity profile.

Figure 4 shows instantaneous pressure distribution on the RLG model with and without boundary layer equation. The linear profile shown in Fig. 1(b) is used for the case without boundary layer equations. Low pressure regions circled by red in the case with boundary layer equations appear lower than those of the case without boundary layer equations. This is related to flow separation behind wheels.

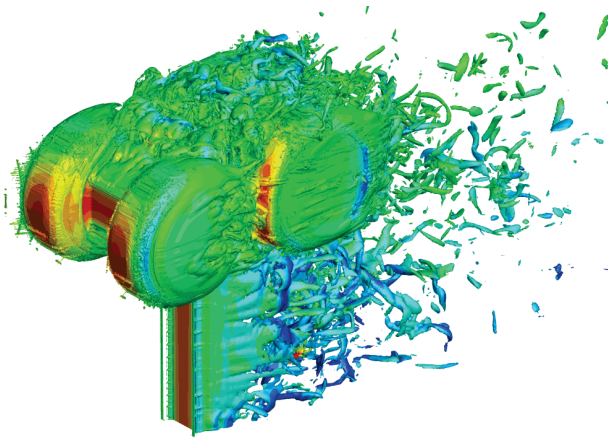

Fig. 2 Iso-vorticity surface around the RLG model colored by pressure.

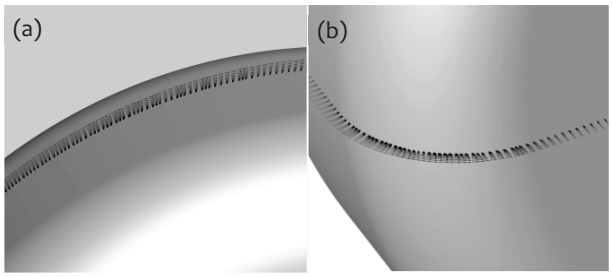

Fig. 3 Velocity vector near wall surface obtained from boundary layer equations, (a) vertical cross-section, (b) horizontal cross-section.

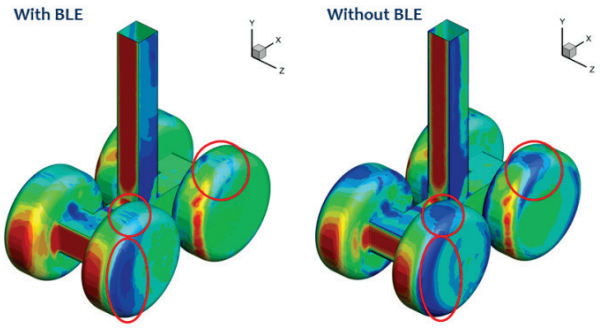

Fig. 4 Instantaneous pressure distributions on the RLG model with and without boundary layer equations.

4. Concluding remarks

In this study we investigated an approach employing boundary layer equations in a Cartesian mesh solver BCM for providing approximate boundary conditions for high Reynolds number flow. In addition a central difference scheme was used for LES to avoid unfavorable damping due to upwind schemes. By using high Reynolds number boundary condition based on boundary layer equations, the time integration was stably conducted without any damping.

Future work includes the sophistication of boundary layer equations regarding the solution efficiency and the fidelity by considering a convective term. Further, we conduct not only the flow field analyses, but also acoustic analyses of sound pressure level and far-field spectrum. The further exploitation of a central difference scheme is of another interest, which is expected to have better characteristics in acoustic spectra, i.e., less dumping of high frequency part if it is used along with an appropriate sub-grid scale model.

References

[1] Spalart P. R., J. Sound and Vibration, **330** (2011), 4180-4195.
[2] Nakahashi, K., AIAA Paper 2005-4876, 2005.
[3] Ishida, T., *et al.*, J. Comput. Sci. and Tech., **2** (2008), 435-446.
[4] Deguchi, A., *et al.*, AIAA Paper 2012-0388, 2012.
[5] Ishida, T., *et al.*, J. Comput. Sci. and Tech., **7** (2013), 33-58.
[6] Wang, M., *et al.*, Phys. Fluids, 14, 2043-2051, 2002.
[7] Capizzano, F., AIAA J., **49** (2011), 2367-2381.

Tenth International Conference on Flow Dynamics
November 25-27, 2013, Sendai, Miyagi, Japan

Numerical Simulation of Internal Flows using 3DSFS+BC

Kotaro Makino, Takashi Furusawa and Satoru Yamamoto
Graduate School of Information Sciences, Tohoku University
Aramaki Aza Aoba 6-6-01, Aoba-ku, Sendai 980-8579, Japan
makino@caero.mech.tohoku.ac.jp

ABSTRACT

Supercritical-fluid Simulator(SFS) is a method developed for solving problems which contain supercritical fluid conditions and the transitions. 3DSFS+BC is proposed as a couple of SFS and Building Cube(BC) method that has advantages in terms of automatic grid generation and massive parallel computation. Simulation of an internal 3D flow in a counter flow reactor is conducted using 3DSFS+BC. The results show that the structure of unsteady asymmetric mixing flow which was not observed in the 2D calculations.

1. Introduction

Supercritical fluid is in a state where the temperature and the pressure are beyond the critical point. It has an intermediate property between gas and liquid. The thermal properties drastically change near the critical point. Due to those remarkable behaviors, supercritical fluids have been applied to various industrial processes. For example in the chemical engineering, organic solvents which have high environmental load can be replaced with supercritical water and carbon dioxide. Therefore supercritical fluid is a key technology to satisfy environmental requirements and to make sustainable society. Likewise, the qualities of equipment used for such applications are improved by the detailed analysis of internal flows of supercritical fluids. Nevertheless, due to the condition under high temperature and high pressure, large costs and errors are unavoidable in experimental analyses. Hence, numerical simulations are desirable. But considering unique thermo-physical change near the critical point is also challenging because this requires a CFD method considering compressible flows with accurate thermo-physical properties.

We proposed a numerical method for simulating supercritical-fluid flows: Supercritical-fluids Simulator (SFS)[1]. In this method, the preconditioning method is coupled with a program package for thermo-physical properties of fluids (PROPATH)[2]. In PROPATH, mathematical models based on a polynomial equation approximating thermo-physical properties are defined in wide range of temperature and pressure. This program package can be adapted for evaluating thermo-physical properties near the critical point. We have alreacy conducted some calculations of high speed flows as well as very slow flows of supercritical fluids, although those were limited in the cases of 2D simple geometries.

On the other hand, real equipments for industrial use of supercritical fluids typically consist of complicated channels. Those complex geometries usually bring 3D flows. In addition, computational cost is an inherent problem in the 3D simulation. Hence, for practical use we applied Building-Cube(BC) method proposed by Nakahashi et al[3]to SFS. By using BC method, grid generation is automatically done in an instance for any kind of bodies. BC method also provides with straight-forward implementation of parallel processing. We developed 2DSFS+BC beforehand and carried out some simulations.

In this study, we developed 3DSFS+BC in the purpose for simulating flows in realistic 3D geometries. Here we present the calculated results of a 3D flow in a counter flow reactor. While the goal of this study is to yield the geometric configurations which maximize the mixing efficiency in liquid-supercritical fluid conditions, this study is at a first step understanding the fundamental flow field.

2. Numerical method

The fundamental equations are based on three-dimensional compressible Navier-Stokes equations in general curvilinear coordinates coupled with BC algorithm and modified by the preconditioning method. The set of equations is written in vector form as

$$\Gamma\frac{\partial\hat{Q}}{\partial t}+\frac{\partial F_i}{\partial\xi_i}+\frac{\partial F_{vi}}{\partial\xi_i}+H=0\quad(i=1,2,3) \tag{1}$$

where

$$\hat{Q}=J\begin{bmatrix}p\\u_1\\u_2\\u_3\\T\end{bmatrix},\ \hat{F}_i=J\begin{bmatrix}\rho U_i\\ \rho u_1U_i+\frac{\partial\xi_i}{\partial x_1}p\\ \rho u_2U_i+\frac{\partial\xi_i}{\partial x_2}p\\ \rho u_3U_i+\frac{\partial\xi_i}{\partial x_3}p\\ (e+p)U_i\end{bmatrix},\ \hat{F}_{vi}=-J\frac{\partial\xi_i}{\partial x_j}\begin{bmatrix}0\\ \tau_{j1}\\ \tau_{j2}\\ \tau_{j3}\\ \tau_{jk}u_k+\kappa\frac{\partial T}{\partial x_i}\end{bmatrix}$$

Eq. (1) is solved by the numerical method based on the preconditioned flux-vector splitting scheme and the preconditioned LU-SGS scheme[4].

Thermophysical properties are calculated from PROPATH. It contains thermophysical properties for 48 substances such as water, carbon dioxide, oxygen, nitrogen and so on, in wide-range pressure and temperature conditions. The properties of gas, liquid and supercritical fluid are defined as a polynomial function of pressure and temperature. For example, the equation of state (EOS) for carbon dioxide was standardized by International Union of Pure and Applied Chemistry (IUPAC).

BC method is used as the grid system. Computational domain is sequentially divided into a number of sub-domains so that sufficient grid resolution is maintained near the body surfaces with a manner of quadtree segmentation. The sub-domain is called as

"cube" and each of them are filled by equally-spaced Cartesian mesh. By using the same number of grid point in all cubes, it is simple to keep load balance among all threads in the use of large scale computers with massively parallel processors. As BC method uses Cartesian mesh, body surface treatment may be properly considered. The simplest way is the black and white style defining each grid cells as fluid cell or wall cell. Considering direct implementation, we apply the black and white style for 3DSFS+BC at first. For advanced boundary treatment, Immersed boundary method with ghost cells has been implemented in 2DSFS+BC. Parallel processing was implemented with OpenMP. All results have been calculated with 16 cores.

3. Numerical results

The calculated results of the 3D flow in a counter flow reactor are presented. Figure 1 shows the geometry of the reactor. The geometry consists of a cross joint pipe and a tinny tube inserted from upper limb of the cross joint pipe. Main stream of cold water comes in through the bottom inlet and mixing flow goes out through the left outlet. Both of the upper limb and the right limb are closed. The BC grid is represented in Fig. 2. The cube outlines and wall cells are drawn as blue lines and grey blocks, respectively. Mixing two fluids is important process for the fabrication of nano-scale metal particles in the reactor. Consequently, the focus is to figure out the structure of the mixing flow near the cross point and tube head. Inflow temperature and pressure are listed in Table 1. This study was carried out in liquid-liquid mixing condition. Adiabatic wall condition was applied. Wall temperature was set to 350[K].

Figure 3 shows the temperature distributions on the cross-section at each time steps. At first, the injected flow sunk down and then reached to near the bottom of cross joint pipe at the time of $t=2t_0$. Subsequently the length of the injected flow was shorten until the time of $t=3t_0$ by the buoyancy effect. Afterwards, the length was remained as approximately half of its maximum. Besides, the mixing flow had complex 3D structure due to the existence of the counter flow. It is also notable that the mixing flow was asymmetric and strongly unsteady. Such behavior was not observed in the 2D calculations. Furthermore, flow stream reaches around the tube. If the heat conduction within the tube wall is considered, the flow temperature may affect the formation of the mixing flow. In addition, as both parts of the upper limb and the right limb were totally dead region, those parts seem not to be so crucial region.

Table 1 calculating condition.

	P [MPa]	T [K]	Flow speed[m/s]
Hot water	0.1013	350	1.3
Cold water	0.1013	300	0.4

Fig. 1 Geometry of the counter flow reactor.

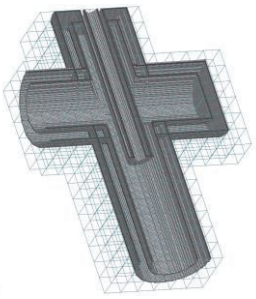

Fig. 2 BCM grid.

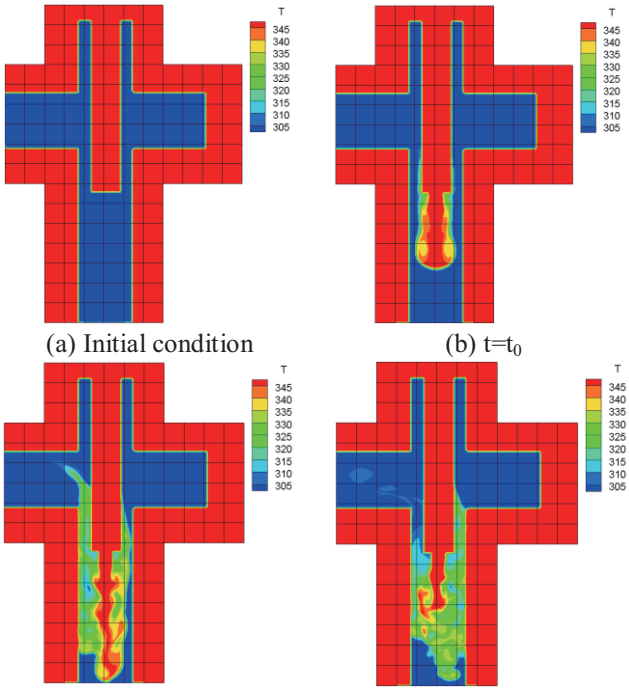

(a) Initial condition (b) $t=t_0$

(c) $t=2t_0$ (d) $t=3t_0$

Fig. 3 Temperature distributions at the cross-section.

4. Concluding remarks

In this study, 3DSFS+BC was developed by coupling SFS with BC method. The calculation of the flow in the counter flow reactor was presented. The results show that unsteady asymmetric mixing flow which is unlikely observed in 2D calculations is formed in the equipment. For future study, we should calculate flows in liquid-supercritical fluids condition and in other tube depth configurations for evaluating the quality of the equipment..

References

[1] S. Yamamoto, T. Furusawa, and R. Matsuzawa, Int. J. Heat and Mass Transfer, 54-4 (2011), pp.774-782.
[2] A PROGRAM PACKAGE FOR THERMO-PHYSICAL PROPERTIES OF FLUIDS by PROPATH group.
[3] K. Nakahashi, AIAA Paper 2005-4876, (2005).
[4] S.Yamamoto, J. Comp. Phys., 207-1 (2005), pp.240-260.

Tenth International Conference on Flow Dynamics
November 25-27, 2013, Sendai, Miyagi, Japan

Unsteady Flow Simulation around Rudimentary Landing Gear by Building-Cube Method

Takashi Ishida, Kazuhiro Imai and Keizo Takenaka
Japan Aerospace Exploration Agency, Chofu 180-0012 Japan
ishida.takashi@jaxa.jp

ABSTRACT

One of the biggest issues of the present Cartesian grid approach is the wall boundary treatment, especially in high-Reynolds number viscous flows. In this paper, Immersed Boundary Method (IBM) and Wall Function (WF) are coupled and the developed method is applied to Building-Cube Method (BCM) to compute high-Reynolds number viscous flows. Rudimentary Landing Gear (RLG) is computed by the present approach and compared with the experimental data and other computational results. The results show reasonable agreement with the experimental data and the reference solution.

1. Introduction

At the beginning stage of CFD research, Cartesian grid method was mainly studied because of its easiness of the algorithms. After that, structured grid method and unstructured grid method were developed for the high-fidelity computation and unstructured grid method has become a popular tool in the CFD community because of its advantage over the conventional approach in treating three-dimensional complex geometry.

These days, Cartesian grid method is being revisited because of the simplicity of the algorithms and the rapid progress in the computer performance. Among various Cartesian grid approaches, Building-Cube Method (BCM) which is proposed by Nakahashi[1][2] aimed for the next generation CFD is attractive and expected to accelerate the product design cycle.

In this paper, we apply BCM to the unsteady flow simulation around Rudimentary Landing Gear (RLG) which is proposed for a standard landing gear model to compute aero acoustics[3][4][5]. Immersed Boundary Method and Wall Function are applied to current BCM to enhance the reliability near the wall boundaries and overcome the defects of current Cartesian grid approach.

2. Numerical Approach

Numerical scheme used in this study is shown in table 1.

Table 1 Numerical scheme.

Governing Eq.	Incompressible NS eq.
Discretization	Collocated, Finite difference
Wall Boundary	IBM+Wall function
Cube Boundary	2nd order Lagrange interpolation
Time Integration	4stage Runge-Kutta
Convective Term	3rd order K-K scheme
Diffusive Term	2nd order central difference
Turbulent Model	Lagrangian Dynamic SGS model

Table 2 Grid information.

Reference length	Tire diameter: D
Far field	100D × 50D × 100D
# of cubes	12408
# of cells/cubes	16^3
Total # of cells	50M
Min. grid spacing	6.0×10^{-3}D
Reynolds number	10^6
Δt	6.1×10^{-4}

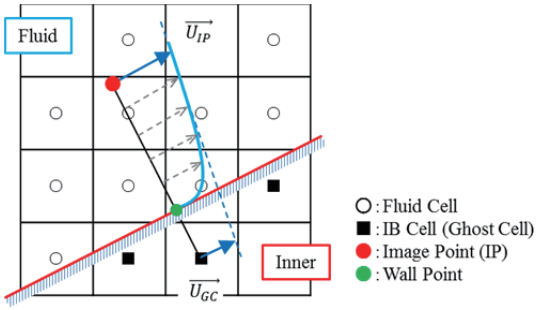

Fig. 1 Immersed boundary treatment at the wall.

Wall boundary treatment used in this study is shown in Fig. 1. In this approach, wall shear stress τ_{wall} is computed by the stream-wise velocity U_{IP} at the Image Point (IP) and the wall function. Following three-layer type wall function is used:

$$F(u_\tau) = \begin{cases} u^+ - y^+ & if\ y^+ < 5 \\ u^+ - 5ln(y^+) + 3.05 & if\ 5 \le y^+ < 30 \\ u^+ - 2.5ln(y^+) - 5.5 & if\ 30 \le y^+ \end{cases} \quad (1)$$

where $y^+ = yu_\tau/\nu, u^+ = U_{IP}/u_\tau$ and $u_\tau = \sqrt{\tau_w/\rho}$. Velocity at the ghost cell is computed by following formula:

$$U_{GC} = U_{IP} - L\frac{dU_{IP}}{dy} \quad (2)$$

where L is the distance from the center of the Ghost Cell (GC) and the Image Point (IP).

Table 2 shows the details of the computational grid and condition. The resulting Y^+ at the wall is approximately 300.

3. Numerical Result

Fig. 2 shows the visualization of the isosurface of the Q-criteria colored by the velocity magnitude. Complex flow field is captured at the wake region.

Fig. 3 shows the comparison of the time-averaged Cp distribution around the front and back wheels. The experimental data and the reference solution computed by UPACS[6] are also plotted. From the comparison of the Cp distribution, the computed results from the present approach show good agreement with the experimental data and the reference solution at the attached flow region. On the other hand, slight

discrepancy is observed at the separated region. One of the reasons of this difference is due to the lack of the effect of the pressure gradient in the present wall function.

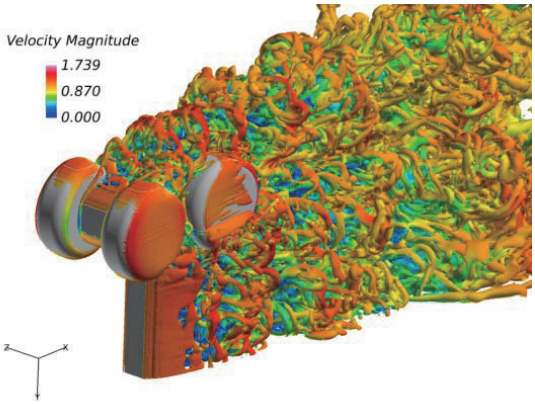

Fig. 2 Q-criteria.

4. Concluding remarks

In this paper, we applied the Immersed Boundary Method coupled with wall function to BCM. Present approach was applied to the unsteady flow computation around RLG. The time averaged data showed good agreement with the experimental data and the reference solution computed by UPACS.

The productivity of the unsteady flow data of RLG computation using 50M grid was 1case/week by SX9(1 node 16 CPUs).

Acknowledgement

This research was supported by the KAKEN S grant. The flow computation in this research was conducted by SX9 at Cyberscience Center in Tohoku University.

References

[1] Nakahashi, K., "Building-Cube Method for Flow Problems with Broadband Characteristic Length," Proceedings of ICCFD2, Computational Fluid Dynamics 2002, edited by S. Armfield, R. Morgan, K. Srinivas, Springer, pp. 77-81, 2003.

[2] Nakahashi, K., "High-Density Mesh Flow Computations with Pre-/Post-Data Compressions," AIAA paper, 2005-4876, 2005.

[3] https://info.aiaa.org/tac/ASG/FDTC/DG/BECAN_files_/BANCII.htm

[4] Konstantin A. Kurbatskii *et al*. "Rudimentary Landing Gear Noise Predictions using Scale-Resolving Simulations: Part 1 – Incompressible Approach", AIAA 2013-0463

[5] Chad M. Winkler et al. "Grid Sensitivity of the Rudimentary Landing Gear Using Unstructured Finite Volume Methods", 18th AIAA/CEAS Aeroacoustics Conference, AIAA 2012-2288

[6] Tanaka et al., "Validation Study of Aeroacoustics Analysis of Rudimentary Landing Gear Using Structured Grid CFD-code UPACS-LES", ANSS 2013

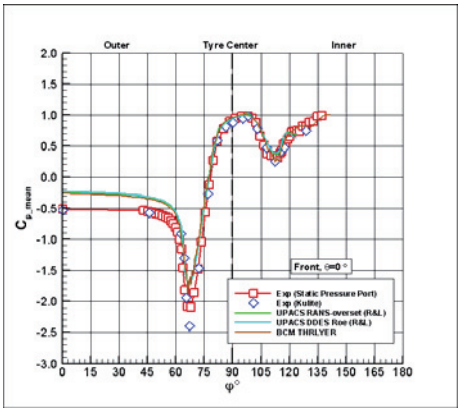

(a) front tire, 0deg.

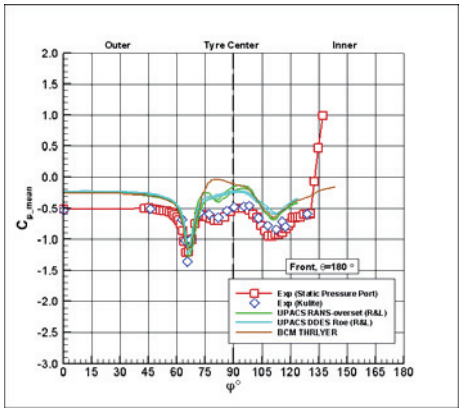

(b) front tire, 180deg.

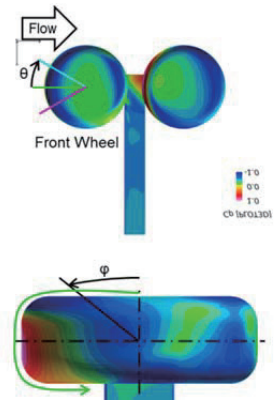

Coordinate of a front tire.

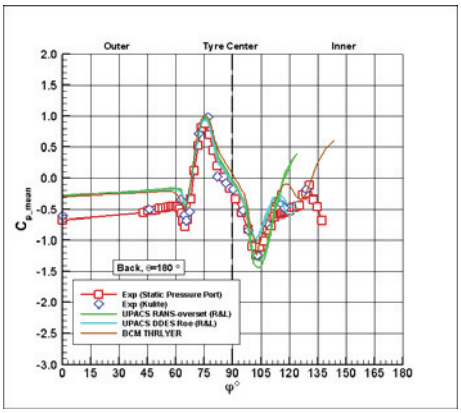

(c) back tire, 180deg.

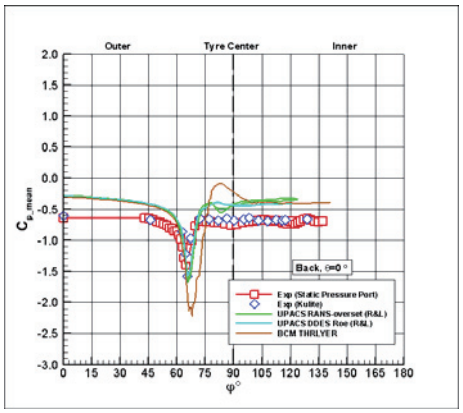

(d) back tire, 0deg.

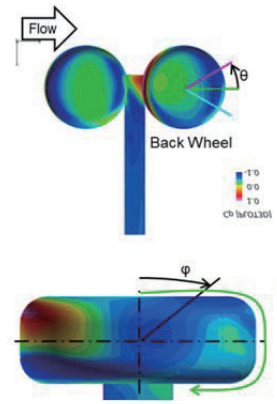

Coordinate of a back tire.

Fig. 3 Cp distribution around wheels.

Tenth International Conference on Flow Dynamics
November 25-27, 2013, Sendai, Miyagi, Japan

Studies of Fluid Plasma Interaction Associated with Gas Blast Characteristics in Thermal Puffer Type GCB Based on High-Order LES Model

Debasish Biswas, Aya Kitoh, and Takeshi Shinkai
Toshiba Corporation, Kawasaki, Japan.
Debasish.biswas@toshiba.co.jp

ABSTRACT

Efficient designing of thermal puffer type gas circuit breaker need the reduction of operating energy to a great extent. In the designing of gas circuit breaker to achieve maximum overall pressure rise by utilizing maximum arc energy and minimum mechanical energy , it is very much necessary to have a good understanding of the transport mechanism of thermal and pressure energy resulted by the fluid plasma interaction associated with the gas blast characteristics. Therefore the main aim of this research is to study the fluid-plasma interaction phenomena in practical gas circuit beaker based on a high-order LES turbulent model.

1. Introduction

Control and protection of power transmission system is carried out by circuit breaker which serves the purpose by interrupting current flowing through the circuit. High voltage power transmission is required to meet the ever increasing demand of electricity. A large current interruption during the accident in addition to usual current opening and shutting is demanded for securing stability in this type of power transmission system. Thermal puffer type SF6 (sulphur-hexafluoride) gas circuit breaker (GCB) are widely being used for large current interruption due to the excellent insulation and current interruption properties of SF6 gas and the simplicity and high reliability of unit structure. Also this type of GCB has the advantage in reducing the operating energy. In circuit breaker, gas blasts are utilized to greatly increase the speed with which the arc follows current changes, and hence to improve the interrupting performance at zero current. In the case of SF6 gas and arc plasma interaction, the arc diameter is greatly reduced due to the increased power removed from the arc column by axial flow of enthalpy of the arc heated gas, and by heat transfer through turbulent mixing from the highly expanded high temperature, low density core gas to the cooler denser surrounding flow. The reduction of arc diameter leads to an increase in arc voltage at a given current, as compared to the free-burning arc. Basically higher current interruption in circuit breaker required higher blast pressure. In the thermal puffer type GCB the blast gas pressure to the arc is increased by utilizing the energy of the arc. Thermal puffer principle is very reasonable because of the fact that higher current interruption needs higher blast pressure. High performance GCBs were successfully developed based on this principle. Presently in power transmission system thermal puffer type GCB having two chambers is used for low operating energy. However, efficient design of this type of GCB needs a detail understanding of the pressure rise mechanism in thermal chamber by utilizing the thermal energy of the hot arc plasma generated by the joule heating in between the electrodes. In this regard sufficient knowledge of the fluid plasma interaction phenomena associated with the gas blast characteristics is very much essential. Several reports on SF6 gas characteristics and thermal puffer type GCB performance are available in the open literature (1)-(2).

2. Method

Basically the flow inside the gas circuit breaker is very complicated in nature and a multi-physics fluid dynamical problem. Flow is highly compressible having flow Mach number in the range of 2 to 3, maximum to exit pressure ratio above 10, maximum arc temperature to surrounding gas temperature ratio of more than 100, chemical reaction associated with arc plasma phenomena, and the movement of the electrode with the compression of gas at the mechanical chamber. In this study emphasis is put to predict fluid plasma interaction phenomena, which is highly unsteady and three-dimensional in nature. In the fluid plasma interaction process, turbulence mixing between the high temperature arc plasma core and the surrounding low temperature dense fluid plays a dominant role. In this work a high-order LES model developed by the first author is used to predict this turbulence mixing characteristics. In this high order LES concept, in a dynamic eddy viscosity model, transfer of information between the sub-grid and large scale eddies is improved by solving an additional transport equation for turbulent kinetic energy in the grid scale level. Here the sub-grid scale turbulent stresses are closed using a dynamic turbulent kinetic energy transport model. The sub-grid scale length scale is represented by the minimum of universal length scale and the grid scale. A test filter is used for the dynamic procedure, which will be applicable to stretched grid near the body surface. The advantages of such model include resolution of interesting scales, simultaneous modeling of high shear region and large scale unsteadiness, and use of stretched grids. In the turbulent kinetic energy transport equation the dissipation of turbulent kinetic energy is defined on the basis of time scale. Three-dimensional compressible turbulent viscous flow analyses using the above mentioned LES model along with the arc plasma model is carried out to study the flow-plasma interaction phenomena. In our work complicated current interruption mechanism in a thermal puffer type GCB is discussed. Designing of this type of GCB to raise required gas blast pressure level is very complicated because it is affected by many parameters. Here the results of three-dimensional analyses using a practical thermal puffer type GCB with moving electrode and

practical arc energy cycle is presented and how the basic physics of compressible flow characteristics explain the blast pressure rise in thermal and mechanical chamber is discussed. A spatially high order accurate upwind-biased WENO finite difference method is used. A 5th order upwind differencing technique is used for convective terms and 4th order central differencing technique is used for viscous diffusion terms. All these equations are solved using a TVD 3rd order Runge-Kutta method. Modeling of arc plasma characteristics in thermal puffer type GCB consists of two main steps: the establishment of the gas pressure under chocking conditions during the steady high current period and the interruption process itself during current zero. In the steady high current region the electrode are separated but the current is still flowing through the circuit and Joule heating result in the formation of high temperature plasma. In zero current, which corresponds to thermal interruption phase, the arc plasma changes into hot gas recovering its dielectric strength. In the computation, experimentally measured arc energy for a complete time cycle of current wave form is specified between the electrodes and thermal arc structure and transport of thermal energy through convection heat transfer and fluid-plasma interaction is computed.

3. Results and Discussion

The thermal puffer type GCB used in our study is shown in Fig.1

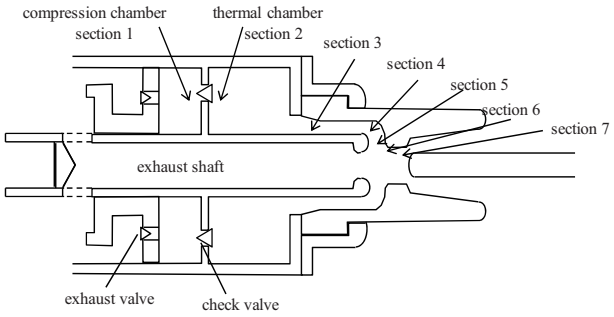

Fig. 1 Schematic view of thermal puffer type GCB

This GCB comprised of two chambers one is thermal chamber and the other is mechanical compression chamber. Zonal grid technique is used in this computation. A total of 7 zones are used to construct the whole configuration. In Fig.2(a) is shown the location of the current level in the current waveform curve. In Fig.2(b) is shown the gas temperature distribution in the respective section during current interruption. Location of the section is indicated in Fig.1. Section number 1 and 2 corresponds to compression and thermal chamber respectively. It can be observed from Fig.2(b) (curve represented by diamond symbol) that a current rising phase corresponds to 1 (40kA) of Fig.2(a) the temperature of throat upstream region (section 6) reached to a value of 18000 K indicating the existence of the hot arc plasma core in that region. At the nozzle throat the temperature is falling a little bit due to interaction of hot arc plasma with surrounding gas. The temperature at the middle of the gas passage still remained low indicating that during this time throat area formed by the electrode and the nozzle outer wall is not chocked yet and the hot gas plasma is located near the junction of the passage duct and the nozzle without inducing pumping of the hot gas through the passage duct. The temperature in the sections 1 to 4 is quite low.

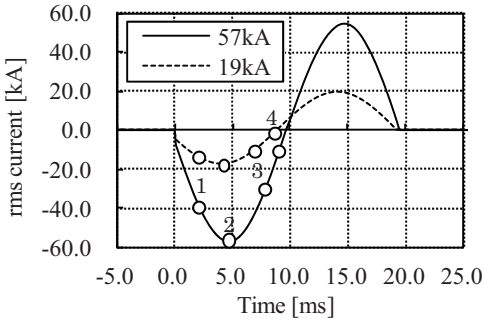

Fig. 2(a) Location on current wave form

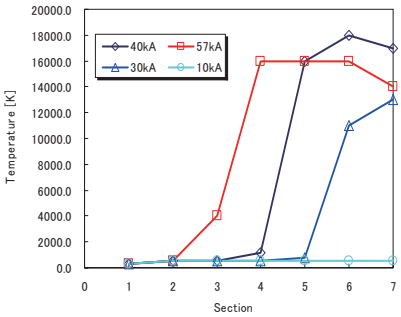

Fig. 2(b) Variation of temperature with section (57kA)

At current rising phase to location 2 (57kA) in Fig.2(a) (peak current of current wave form) results presented in Fig.2(b) (curve represented by square symbol) reveal that the temperature level at 4 to 7 is very high of about 16000 K, at section 3 the temperature level is intermediate of about 4000 K. In this case the very high temperature monitored at section 3 to 5 indicate that during this time the minimum throat area formed by electrode and nozzle outer wall is small and the pressure developed by the compression of the gas inside the exhaust cylinder to accommodate the thermal arc heated expanding hot gas is so large that the minimum throat area can not sustain the flow of such high pressure ratio and the flow at the throat get chocked, resulted in the pumping of hot gas towards the thermal chamber.

4. Concluding remarks

The present computation method along with the physics-based turbulent model could predict the complicated 3-D unsteady multi-physics flow-plasma interaction phenomenon in practical GCB and the related pressure rise and thermal transport characteristics very well.

References

[1] L.S.Frost, R.W.Liebermann, *Proceedings of the IEEE*, 59-4, (1971), pp.474-485.

[2] J.L.Zhang et al., *IEEE Trans. Plasma Sci.*, 30-2, (2002), pp.706-719

A 3D High-order Discontinuous Galerkin Method on Curved Grids with Mixed Elements

Shujie Li
Institute of High Performance Computing (IHPC),
Agency for Science,Technology and Research (A*STAR),
1 Fusionopolis Way, #16-16 Connexis, 138632, Singapore
xpoly.sj@gmail.com

ABSTRACT

A 3D high-order Discontinuous Galerkin solver for high-resolution simulations is presented. The method is based on orthogonal basis functions in physical space of the arbitrary curved elements which has no limitation on element shape . The basis functions are obtained by solving multi-stage linear systems which satisfy the orthogonal properties on general grids. The quadratic Finite Element type of grids are used to represent real local curvature of the wall surfaces. The accuracy and robustness of the resulting solver are validated by several numerical tests.

1. Introduction

The Discontinuous Galerkin (DG) method is a highly compact formulation that provides a method of obtaining high accuracy on unstructured grids. The ability to use unstructured hybrid grids greatly simplifies the largest obstacle in computing the flow around complex geometry. However, the choice of basis function in DG has key affects on the computational cost and robustness. Take non-orthogonal basis functions for example, monomial basis or Taylor basis with full ranked mass matrix could be ill-conditioned on distort grids, especially for complex configures with large curvature or sharp corner. Although the orthogonal basis discretizations based on elemental reference coordinates have made a great success, Lorenzo [1] pointed out that reference frame discretization might suffer from a degradation of *h*-convergence on general meshes with distorted elements.

On the other hand, the curved boundary are reported a significant improvement to the entropy production near solid wall [2]. For achieving high-fidelity simulations, several key aspects mentioned above are considered in this paper. A new procedure of constructing orthogonal basis functions in physical frame with curved boundary elements is proposed.

2. Methodology

The construction of orthogonal basis functions starts from n-th order monomials basis functions:

$$\phi(x,y,z)=(x-x_c)^{\alpha}(y-y_c)^{\beta}(z-z_c)^{\gamma} \quad (1)$$

Where $x_c=\frac{1}{V}\int_v x dv,\ y_c=\frac{1}{V}\int_v y dv,\ z_c=\frac{1}{V}\int_v z dv$ and $\alpha,\beta,\gamma\geq 0, \alpha+\beta+\gamma\leq n$.

The orthogonal basis function has the following general form

$$\hat{\phi}_i(x,y,z)=\phi_i(x,y,z)+\sum_{j=0}^{i-1} a_{i,j}\phi_i(x,y,z) \quad (2)$$

For n-th order DG solution, the total freedom of basis functions is $N=(n+1)(n+2)(n+3)/6$. Algorithm 1 describes the orthogonalization of basis functions.

Algorithm 1 Orthogonalization of Basis Functions

Require:
$\hat{\phi}_0=\phi_0=1;\ \hat{\phi}_1=\phi_1=x-x_c;$
Ensure:
for $m=2$ **to** $N-1$ **do**
Solve $\mathfrak{L}_{m,m}=0$ for $\{A_{m,j},\ 0\leq j\leq m+1\}$
end for
return $\{A_{m,j}\mid 2\leq m\leq N-1,\ 0\leq j\leq m-1\}$

The inner product operator and linear system operator inside the Algorithm 1 are defined as below

$$\langle f,g\rangle=\int_{\Omega} f\,g\,d\mathbf{x}$$

$$\mathfrak{L}_{m,m}=\{\langle\hat{\phi}_i,\ \hat{\phi}_{m+1}\rangle=0,\ 0\leq i\leq m\}$$

The orthogonalization Algorithm 1 has no limitation on cell geometry. So it can be easily applied on curved grids even with arbitrary elements. The quadric finite elements using widely in solid mechanics are adopted for representing the curved surface.

3. Numerical Validations

3.1 Subsonic flow over a sphere

The subsonic flow around a sphere is simulated at Mach=0.3 on two sets of meshes. One set hybrids prism and tetrahedral grids, the other hybrids hexahedral and tetrahedral grids with transitional layers of pyramid elements. In each set of meshes, four cases with serially refined grids are used for accuracy analysis. Results are shown in Table. 1 and Fig. 1.

Table 1. Entropy Error on hybrid grids

Grid size (Log)	Error of Hybird Prism&Tet (Log)	Order
-1.14739E+00	-3.31033E+00	
-1.40800E+00	-4.07801E+00	2.94
-1.70737E+00	-4.98130E+00	3.02
-2.00747E+00	-5.96252E+00	3.27
Grid size (Log)	**Error of Hybird Hex,Pyrmaid&Tet (Log)**	**Order**
-1.12960E+00	-3.09150E+00	
-1.40554E+00	-3.84755E+00	2.74
-1.71150E+00	-4.74242E+00	2.92
-2.01225E+00	-5.69366E+00	3.16

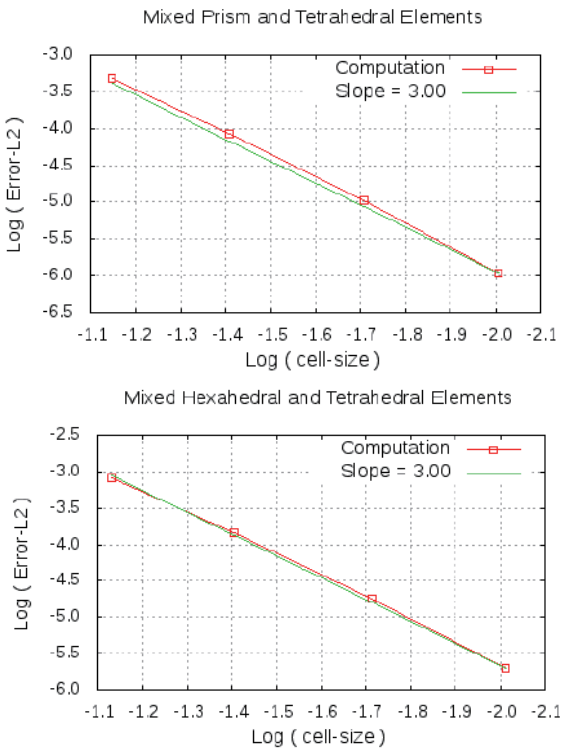

Fig. 1 Error plots

3.2 NACA0012 swept wing

The NACA0012 swept wing is computed at Mach = 0.63, Alpha = 2. The results and comparison with experiments are shown in Fig. 2-3.

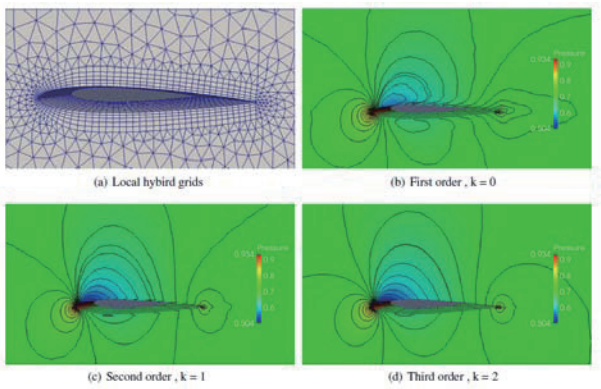

Fig. 2 Pressure isoline of P0~P2 solutions

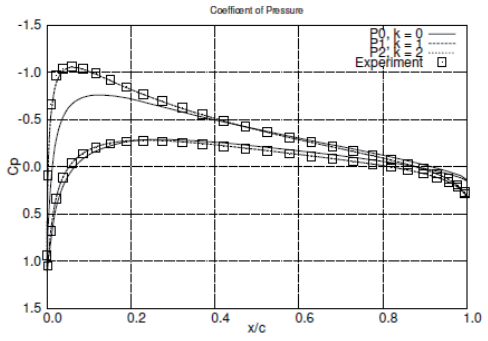

Fig. 3 Comparison of coefficient of pressure

3.3 Common Research Model (DPW-5)

The Common Research Model (CRM) is a wing-body configuration in fifth Drag Prediction Workshop (DPW-5). We take this as a complex geometry test case to show the robustness of the method on mixed elements with curved boundary. The flow condition is Mach = 0.5, Alpha = 0. Fig.4 shows the global pressure contour , close-up views of hybrid grids and showing of curved quadric elements with middle nodes from the top to the bottom.

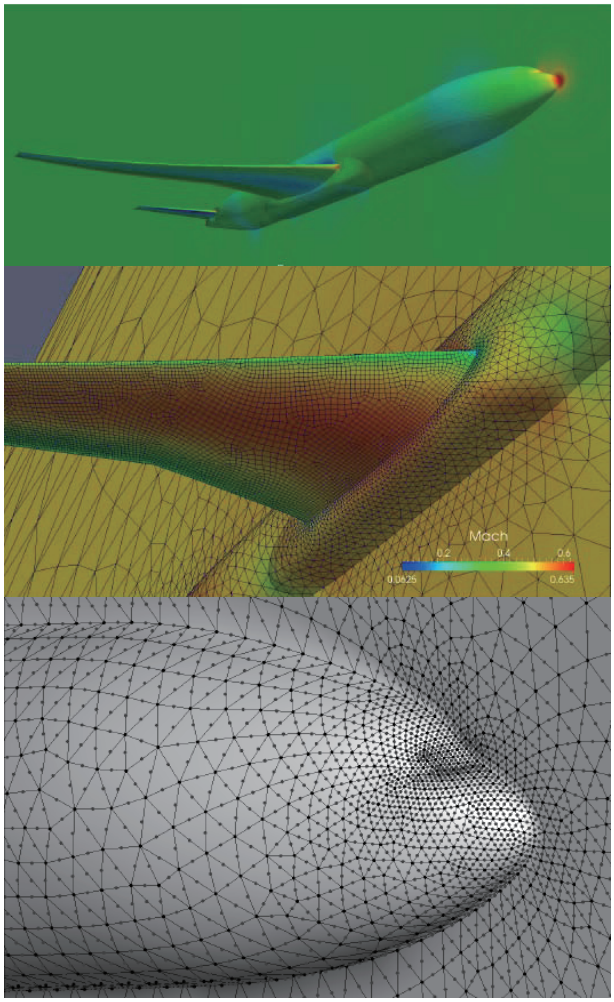

Fig. 4 Coefficient of Pressure Comparison

4. Concluding remarks

In this paper, a 3D high-order Discontinous Galerkin method is proposed which based on orthogonal basis functions on arbitrary grids. The resulting solver shows the design order of accuracy on mixed elements. Further test cases demonstrate the accuracy and reliability for real-world problems.

References

[1] Bott, L. J.Scientific Computing 2012 52, p. 675.
[2] Krivodonova, L., J.C.P 2006 211, p. 492.

OS3: Heat and Mass Transfer in Materials Processing

Tenth International Conference on Flow Dynamics
November 25-27, 2013, Sendai, Miyagi, Japan

Kinetic Modeling Of Solid-Gas Reactions At Reactor Scale: A General Approach

Loïc Favergeon[1], Jacques Morandini[2], Michèle Pijolat[1], Michel Soustelle[1]
[1] Ecole Nationale Supérieure des Mines, SPIN-EMSE, CNRS:UMR5307, LGF, F-42023 Saint-Etienne, France
[2] ASTEK Rhônes-Alpes, F-38130 Echirolles, France
favergeon@emse.fr

ABSTRACT

A rigorous simulation of industrial reactors in the case of solid-gas reacting systems is a complicated task due to several difficulties linked to the kinetic problem at the scale of the solid grains and to the problem of gas and heat transfers within the powder bed. Firstly it requires the knowledge of the kinetic model for the calculation of the speed of reaction in one part of the reactor and for given conditions of temperature and gas composition, and secondly it necessitates solving the material and heat balance equations for the thermohydraulic conditions settled in the reactor.

1. Introduction

Solid-gas reactions are of great interest in many industrial fields such as nuclear, chemistry, metallurgy, CO_2 capture, etc… Industrial reactors where these reactions take place are difficult to understand. Indeed the solid phase is a granular medium through which circulate gaseous reactants and products. The properties of such a medium are modified in space and time due to reactions occurring at a microscopic scale. The thermodynamic conditions are driven not only by the operating conditions but also by the heat and mass transfers in the reactor.

Several models have been developed to account for the complexity of these transformations such as the grain model [1] and the pore model [2] and all their improved derivatives. However most of these models are based on the law of additive reaction times of Sohn [3] which is only valid in some special cases: if the order changes from the gas is equal to one, and for a shrinking core model. In all other cases, it is necessary to consider another approach to understand the kinetics of these reactions.

2. Method

In this goal, we have developed a multi-physic approach combining the resolution of the thermohydraulic equations with kinetic laws describing the heterogeneous reactions, for aggregated or separate particles [4].

Indeed, rather than the restrictive equation

$$\frac{d\alpha}{dt} = A\exp(-\frac{E}{RT})\, f(\alpha) \qquad (1)$$

and with about a tenth of different laws only, depending on the expression of the function f(α), we propose a more general approach for kinetic modeling at microscopic scale, including instantaneous nucleation models, instantaneous growth model, surface-nucleation and growth models (anisotropic or isotropic growth), for the three usual symmetries (spheres, cylinders, planes), and other possible kinetic assumptions depending on where the rate-determining step occurs, and the sense of development of the new phase. This approach is based on the following equations

$$\frac{d\alpha}{dt} = \phi(T, P_i) S_m(t,...) \qquad (2)$$

where $\phi(T,P_i)$ is the areic reactivity of growth and $S_m(t,…)$ is a molar space function. It allows to calculate about 45 various kinetic models (obviously including the classical ones as R3, D3, …) [5].

At macroscopic scale, heat and mass transfer terms entering in the balance equations depend on the kinetics evaluated at the microscopic scale. These equations give the temperature and partial pressure in the reactor, which in turn influence the microscopic kinetic behavior. The various equations corresponding to the thermal model, hydrodynamic and mass transport models can be found in [4].

At microscopic scale, the reaction fractional conversion is followed for a representative population of grains. By finite difference it is possible to evaluate the reaction rate dα/dt. This rate allows to calculate heat and mass sources produced by the reaction. So, using these sources terms, microscopic reactions have an impact on the spatial and temporal evolution of the thermodynamic processes at the reactor scale. Inversely since it modifies the kinetic parameters (areic frequency of nucleation γ and areic reactivity of growth ϕ), thermodynamics influences fractional conversion of the microscopic reaction.

3. Results and Discussion

In order to validate our approach we have chosen to study the dehydroxylation of kaolinite by means of thermogravimetry. Isothermal and isobaric curves were first obtained with about 25 mg of powder (corresponding to a 1 mm height powder bed). During the entire transformation, the sample weight was low enough to prevent any effect of pressure gradients in the powder layer. As expected, the reaction rate increases with temperature and decreases with water vapor pressure.

A second series of experiments was done with various heights of the powder bed. In the same crucible as previously, two distinct TGA experiments were performed at 450°C under a water vapor pressure of 7hPa: the first one with 50 mg of powder corresponding to a powder bed height of 3 mm; the second one with 300 mg corresponding to 10 mm. The kinetic curves and rates curves obtained with both bed heights are presented on Figure 2. One can see that the powder bed

height has an important effect on the kinetic curves since the maximum reaction rate obtained for 3 mm is about twice more that obtained with 10 mm (and is about twice less than that obtained with 1 mm).

In order to interpret the experimental curves obtained with thin powder beds (1 mm height), we used a model involving random nucleation followed by anisotropic growth of the nuclei first proposed by Nahdi et al. [6].

The optimization procedure of CIN4 provided the values of γ (in nb. nuclei m^{-2} s^{-1}) and ϕ (in mol m^{-2} s^{-1}) for each experiment so the laws of variation of these quantities with temperature and water vapor pressure could be expressed.

Concerning the results obtained with thick powder beds, the "macro" part of CIN4 was used in order take into account the heat and mass transfers between all the various places inside the reactor (sample bed, crucible, gas flow). The first step consisted in defining the domains of calculation. The system being axi-symmetric, we used weak forms written in cylindrical coordinates.

Inside the granular medium, heat and mass sources were calculated simulating the reaction phenomena at the microscopic level. Figure 1 shows the gas flow rate obtained as well as temperature and fractional conversion fields at a given time for bed height of 3 mm. Figure 2 presents a comparison of the whole rate of reaction versus fractional conversion between the experimental data and the simulation for both bed heights.

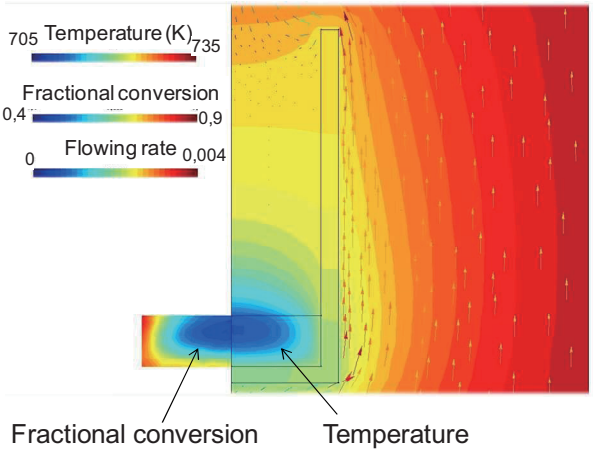

Fig. 1: Representation of the temperature field, the fractional conversion and the flowing rate (arrows) at a given time for 3 mm-height bed.

Figure 2 shows that the CIN4 simulation is able to discriminate the height of the powder bed from 3 to 10 mm. It is important to notice that these results at reactor scale are obtained by means of numerical simulation without any adjustment of parameters. Nevertheless the calculated curves are not perfectly superimposed with the experimental ones. Some improvements should be done in order to get better simulations. For example several points could be improved: at the grains scale ("micro" optimization), the particles size distribution could be taken into account to obtain more precise values of g and f, at the reactor scale, the change in the physical properties of the granular medium (including the porosity) due to the transformation of kaolinite into metakaolinite should be considered using appropriate relationships between the physical properties of the granular medium and fractional conversion.

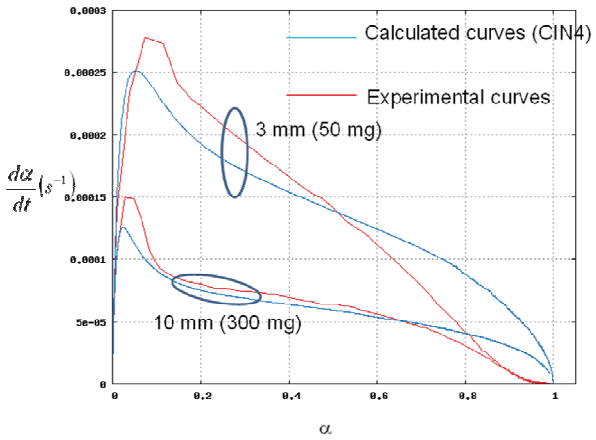

Fig. 2: Reaction rate vs. fractional conversion from the experiment and from the simulation for both powder bed heights.

4. Concluding remarks

CIN4 is a new software tool able to couple kinetics at grains population scale with both heat and mass transfers by means of the finite element method. Kinetic models are based on a general method agreeing with physical reality, offering the possibility to simulate more than 40 models depending on nucleation and growth processes, the shape of the grains, the growth type (isotropic or anisotropic), the development direction of the new phase and the localization of the rate determining step of growth (internal interface, external interface or diffusion volume). Heat and mass transfers are governed by differential equations and solved by a finite element method. Powder beds consisting in separate individual grains (micro and macro scales) or aggregates (micro-meso-macro scales) may be considered. CIN4 allows simulating not only reactions at laboratory scales such as thermobalances, but also industrial reactors.

References

[1] J. Szekely and J.W. Evans, Chem. Eng. Sci., 25 (1970) 1091-1107.
[2] S. Bhatia and D. D. Perlmutter, AIChE J. 26 (1980) 379-386.
[3] H.Y. Sohn, Metall. Trans., 9B (1978) 89-96.
[4] L. Favergeon, J. Morandini, M. Pijolat, M. Soustelle, Oil and Gas Science and Technology, DOI:10.2516/ogst/2012018
[5] M. Pijolat, L. Favergeon, M. Soustelle, Thermochim. Acta 525 (2011) 93-102.
[6] K. Nahdi, S. Perrin, M. Pijolat, F; Rouquerol, Phys. Chem. and Chem. Phys. 4 (2002) 1972.

Scaling of Powder Spheroidization Process Based on Low Power DC-RF Plasma System

Oleg P. Solonenko[1], Hideya Nishiyama[2], Andrey V. Smirnov[1], Hidemasa Takana[2], and Juyong Jang[2]
[1]Khristianovich Institute of Theoretical and Applied Mechanics, SB RAS, Novosibirsk, Russia
[2]Institute of Fluid Science, Tohoku University, Sendai, Japan
solo@itam.nsc.ru

ABSTRACT

Development of the methodical approaches which allow scaling of power-intensive processes based on the experimental data obtained in laboratory environment by their optimization on low power model setups is quite topical. In our previous publications the experimental data on investigation of process of alumina powder spheroidization with use of model DC-RF hybrid plasma flow system with total power of ~ 8 kW (DC plasma torch of ~ 1 kW, RF plasma torch of ~ 7 kW) were presented. In the present paper approach to scaling this process, allowing formulation the requirements to hybrid DC-RF plasma flow systems of considerably higher power and productivity, is proposed.

1. Introduction

At present the energy saving problem at development of specific technologies is almost primary at increase of competitiveness of the final products. Therefore, development of the methodical approaches which allow scaling of power-intensive processes based on the experimental data obtained in laboratory environment by their optimization on low power model setups is quite topical.

It has direct relation to plasma technologies of producing the microspherical powders of metals, alloys, ceramics, etc., which competitiveness in many respects is determined by electric power consumption when obtaining final production unit, that is defined by quantity $\eta_{eff}=P/G$ where P, kWh is total electric power consumption for obtaining of microspherical powder at productivity of process of G, kg/h.

DC-RF hybrid plasma flow systems, which are combined with a radiofrequency inductively coupled plasma (RF-ICP) flow and DC plasma jet, are expected to be one of the next-generation thermal plasma systems, because they have weak backflow, large high-temperature volume, long plasma flow, and high enthalpy [1, 2]. In the DC-RF hybrid plasma flow system, there are many operating parameters to determine the process efficiency because of the complex interactions among RF-ICP discharge, DC plasma jet and in-flight particles [3, 4].

In papers [5-7] experimental data on study and developing of process of alumina powder spheroidization with use of model DC-RF hybrid plasma flow system with total power of P_{total}~8 kW (DC plasma torch of P_{DC} ~1 kW, RF plasma torch of P_{RF} ~7 kW) were presented.

In the present paper approach to scaling this process, allowing formulation of the requirements to hybrid DC-RF plasma flow systems of considerably higher power and productivity, is proposed.

2. Optimization of Process Using Low Power Model DC-RF Hybrid Plasma Flow System

In paper [5], the experimental study was conducted with pure argon gas to obtain the optimum operating flow conditions for in-flight alumina powder processing for particle size and morphology controls using a DC-RF hybrid plasma flow system at constant low operating power based on consideration of correlating plasma flow characteristics. The DC-RF hybrid plasma flow system has been successfully optimized. However, the process efficiency, such as spheroidization ratio of alumina powder remains low because of insufficient operating parameters of DC plasma jet. It has been pointed out [6, 7] that the enhancement of plasma enthalpy with simultaneous decrease of Reynolds number is necessary to improve process efficiency for this system even at the same input power. As a result, it was significantly improved the in-flight alumina powder spheroidization process through the optimization of helium gas mixture percentage and also through the clarification of plasma enthalpy, in-flight powder velocity, and temperature for different DC torch nozzle diameters. The main conclusion which can be made on the basis of carried out investigations: application of DC plasma torches with laminar outflow of jet when processing powder materials by DC-RF hybrid plasma flow systems is very perspective as thus residence time of powder particles, both in plasma jet, and in the field of generation of the high-frequency discharge significantly increases. As a result, it increases competitive ability of DC-RF hybrid plasma flow systems and expands their technological niches.

3. Concept of Scaling

Proceeding from aforesaid, when scaling plasma processes of powder materials spheroidization with use of DC-RF hybrid plasma flow system it is necessary to provide the optimum of efficiency $\eta_{eff}=P/G$, i.e. to find the minimum $\eta_{eff.opt}=\min P/G$. Therefore, of main practical interest are: 1) *power scaling* when it is necessary to determine the minimal electric power of DC-RF hybrid plasma installation providing a given value of productivity on output spherical powder at fixed range of sizes of precursor particles and their size distribution; 2) *productivity scaling* when it is required to provide the maximum productivity of technological process on plasma installation of fixed electric power at preset diapason of initial particles sizes and their size distribution. Thus, even at fixed ratio of DC and RF plasma torches electric power, i.e. $P_{DC}/P_{RF}=const$, scaling of plasma processes of powder materials treatment is a complex multiparameter problem. For its practical solution we offer the approach based on:

1) computer-aided scaling of process by means of program code realizing approved physical and mathematical model [8], which allows carrying out prompt estimations of interphase momentum-, heat- and mass transfer taking into account loading of plasma jet by powder material at given size distribution and possible temperature gradient inside of single particles. The latter is necessary when size of particles to be treated is too big. In these prompt parametrical calculation a family of experimentally measured volt-ampere characteristics and thermal efficiencies of plasma torch are used;
2) use of DC plasma torches with inter-electrode insert (cascade torches), allowing generation of plasma flows in the wide ranges of power and flow rate of working gas that provides different modes of DC plasma jet outflow (quasi-laminar, transient and turbulent);
3) final experimental adjustment of technological process and plasma equipment which provides demanded productivity and quality of final powder product.

4. Scaling DC-RF Hybrid plasma systems

4.1. Scaling DC plasma torches

Brief review of the potential advantages offered to spraying, surface treatment and powder processing by the implementation of cascade plasma torches (CPT) was presented in [9]. It provides evidence that a modular designed single cathode CPT helps eliminate the following major disadvantages of conventional torches: plasma parameters drifting, 1-5 kHz pulsing of plasma flow, as well as excessive erosion of electrodes. More stable plasma results in higher quality, homogeneity and reproducibility of powders treated. CPT offers an extremely wide operating window allowing better control of plasma parameters, particle dwell time and, consequently, particle temperature and velocity within a wide range by generating high enthalpy quasi-laminar plasmas, medium enthalpy transient plasmas and relatively low enthalpy turbulent plasmas. Stable operation, flexibility with plasma gases, as well as wide operating window of CPT, should help significantly improve the existing plasma powder spheroidization processes, and also help develop new advanced technologies based on DC-RF hybrid plasma systems.

4.2. Scaling RF plasma torches

From the point of view of oxide powders spheroidization, in particular α-Al2O3 powder, relatively low-speed zone of high-frequency discharge burning into which rather high-speed two-phase plasma jet "gas - particles" inflows, provides additional heating of processed particles. First of all, it is concerned the particles moving on the periphery of DC plasma jet. It is caused by that its mixing within the discharge chamber of RF plasma torch happens with low-speed high-enthalpy cocurrent flow. Besides, deceleration of particles increases their residence time and extent of their processing in high-enthalpy zone that promotes uniformity of heating and material homogenization in single particles. Therefore, main problem when scaling RF plasma torch is formulation of practical recommendations concerning the required specific thermal power released in RF gas-discharge chamber, its length and diameter, and also flow rate of working gas blown through the burning area of RF discharge. The corresponding estimations can be done using the above-mentioned program code.

5. Concluding remarks

Developed approach to scaling of processes of spheroidization of oxide powders with use of DC-RF hybrid plasma flow systems is briefly described and will be illustrated on the example of powder α-Al_2O_3. Basis of scaling are the results of joint physical and computational experiment obtained on the model low power DC-RF hybrid plasma installation that significantly reduces labor expenditures and power consumptions at working-off of specific technologies. Authors do not raise the questions of designing of DC and RF plasma torches which are rather detailed presented in different known publications.

Acknowledgement

This work was supported in part in the framework of Interdisciplinary Integration Project 98 of Siberian Branch of the RAS for 2012-2014. Part of the work was carried out under Collaborative Research Project J13060 of the Institute of Fluid Science, Tohoku University.

References

[1] T. Yoshida, T. Tani, H. Nishimura, and K. Akashi, J. Appl. Phys., **54**(2) (1983), P. 640-646.
[2] K.S. Kim, J.H. Seo, J.S. Nam, W.T. Ju, and S.H. Hong, IEEE Trans. Plasma Sci., **33**(2) (2005), P.813-823.
[3] J.W. McKelliget and N. El-Kaddah, Metall. Trans. B, **21**(3) (1990), P. 589-598.
[4] J.H. Seo, J.M. Park, and S.H. Hong, Plasma Sources Sci. Technol., **17**(2) (2008), P. 025011.
[5] H. Nishiyama, M. Onodera, J. Igawa, and T. Nakajima, J. Therm. Spray Technol., **18**(4) (2009), P. 593-599.
[6] H. Takana, J. Jang, J. Igawa, T. Nakajima, O.P. Solonenko, and H. Nishiyama, J. of Therm. Spray Techn., **20** (2011), P. 432-439.
[7] J. Jang, H. Takana, O.P. Solonenko, and H. Nishiyama, J. of Fluid Science and Technology, **6** (2011), P. 729-738.
[8] O.P. Solonenko, A.V. Smirnov, A.L. Sorokin, Flow Dynamics: The 2nd Intern. Conf. on Flow Dynamics, American Institute of Physics, Melville, New York, 2006, P. 375-382.
[9] O.P. Solonenko, A.V. Smirnov, Application of cascade non-transfer arc torches for powder plasma spraying, surface treatment and micro-spherical powders production, Proc. of Euro PM2013, 15-18 September 2013, Gothenburg, Sweden (Electronic publication).

Modeling of Additions Nanoparticles on the Dynamics during the Sintering Process Alyumoselikatnoy Ceramics

Svetlana N. Sorokova, Anna G. Knyazeva
National Research Tomsk Polytechnic University,
Russia, 634050, Tomsk, Lenina 30
E-mail: s_sorokova@tpu.ru

In the model proposed and investigated volume sintering the powder compound MgO-Al_2O_3-SiO_2 with the addition of aluminum nanopowder. Nanoparticulate particles comprising reagents were treated as distinct phase having special properties. It was determined the distribution of temperature and element concentrations and compounds in different times for different synthesis conditions.

1. Introduction

Technical ceramics is an independent class of materials and is applied in various branches of engineering and industry. Is of considerable interest cordierite ($2MgO{\cdot}2Al_2O_3{\cdot}5SiO_2$) and alyumomagnezialnaya spinel ($MgAl_2O_4$). Based on them obtained the electrical insulating and heat-resistant ceramics. But the synthesis of ceramic materials based on refractory oxide is energy intensive processes that require long firing at high temperatures. The issue of reducing the temperature, time of synthesis and sintering of ceramic materials is an important and urgent at present. In order to reduce energy use different supplements and different ways of activating the raw material [1-3]. In experimental studies [4-6] have shown the fundamental possibility of activating the synthesis processes. In these works nanosized aluminum powder was prepared by electric explosion of wire.

For the accurately targeted choice of technological modes of synthesis and sintering require detailed theoretical study of the regularities of formation the structure and phase composition of the material. There are numerous mathematical models [7-10] sintering powder compounds and solid phase synthesis. But in the known models explicitly take into account that the processes of synthesis are accompanied by volume changes. They can lead to changes in the kinetic patterns, composition and structure the end product [10-11]. The nanosized particles in the reagents changing both the kinetics of the synthesis process and influence a special way on the physical and mechanical properties of the reactants and products. This leads to additional singularities in the mathematical models.

In this paper we investigate model volume alyumoselikatnoy sintering of ceramics with the addition of nanosized aluminum powder in the initial compacts.

2. Formulation of the problem

Consider compact powders MgO-Al2O3-SiO2 additive aluminum nanopowder as a parallelepiped with dimensions of l1, l2, l3 (size d = 10 mm, h = 10 mm) arranged on the ceramic substrate. Heating of the sample by convection and radiation in the regulated change of temperature furnace walls. In the general case heating process, taking into account physical and chemical phenomena described by the three-dimensional heat conduction problem with the conditions on the surface:

$$-\lambda\frac{\partial T}{\partial \vec{n}} = -\varepsilon\sigma_0\left(T^4 - T_e^4\right) + \alpha(T - T_w);$$

where σ_0 - is the Stefan-Boltzmann, ε - the degree of blackness, α - the coefficient of heat transfer, T_w - the temperature in the chamber. The temperature of the chamber walls T_e - is changed by a given law:

$$T_e = \begin{cases} \upsilon_1 t + T_0, & T \le T_{c1}; \\ T_{c1}, & T > T_{c1}. \end{cases}$$

In assumed that l_k compact small dimensions. Then the temperature field in the system and the concentration distribution of phases can be found from the joint solutions of the equation of heat balance and the problems of chemical kinetics:

$$V_0 c\rho\frac{dT}{dt} = -\varepsilon\sigma\left(T^4 - T_e^4\right)S + \alpha(T - T_w)S + V_0 W,$$

$$\frac{dy_l}{dt} = \phi_l,$$

where T – temperature, $c\rho$ - volumetric heat capacity and density; W - total density of internal heat sources and sinks due to chemical reactions; y_l - molar concentration of reactants and products; S - the entire surface area of the sample; V_0 - its scope.

In accordance with the literature data [5] can write system basic chemical reactions in the compact of powders MgO-Al2O3-SiO2:

$$Al_2O_3 + MgO \rightarrow MgAl_2O_4$$

$$3Al_2O_3 + 2SiO_2 \rightarrow Al_6Si_2O_{13}$$

$$2MgO + 2Al_2O_3 + 5SiO_2 \rightarrow Mg_2Al_4Si_5O_{16}$$

The model assumes that the oxidation of nanophase Al occurred prior to the sintering process the entire compact.

We introduce the notation for the molar concentration of the reactants and reaction products involved in chemical reactions: $y_1 = [Al_2O_3]$, $y_2 = [MgO]$, $y_3 = [SiO_2]$, $y_4 = [MgAl_2O_4]$, $y_5 = [Al_6Si_2O_{13}]$, $y_6 = [Mg_2Al_4Si_5O_{16}]$.

Formal-kinetic equations are written using standard equations of balance. Diffusion - the slow process that takes place at the level of the spatial scale of individual particles and influence the macroscopic patterns. In the mathematical model, this is reflected by the formal

kinetic laws. Therefore, the balance equations explicitly include diffusion terms, and have the form:

$$\rho \frac{dy_l}{dt} = \omega_l$$

where ω_k - the sum of sources and sinks of component *l* in reactions,

$$\omega_k = \sum_{i=1}^{r} m_k \upsilon_{ki} \varphi_i,$$

where φ_i - the rate of reactions

The reaction rates depend on the concentrations in accordance with the law of mass action:

$$\varphi_1 = z_1 y_1 y_2 ; \quad \varphi_2 = z_2 y_1^3 y_2^2 ; \quad \varphi_3 = z_3 y_1^2 y_2^2 y_3^5$$

where [12]:

$$z_i = z_{i0} \exp\left(-\frac{E_{ai}}{RT}\right) \exp(-p_i y) y^{-s_i}, \quad i = 1,\ldots,3$$

$$y = y_4 + y_5 + y_6 -$$

the total share of stationary components (final and intermediate reaction products) impeding the diffusion of the reactants to each other; z_i - the rate constants; *R* - universal gas constant; E_{ai} - the activation energy of reactions. Brake parameters p_i, s_i are either experimentally determined or are of special consideration "micro-tasks", which take into account diffusion through the product layer, reactions at the interface between the individual particles of different sizes, etc. [12]. Can be used the available information in the literature on the range of the braking parameters for the reactions of different types [12].

In the first approximation, we consider nanodispersed particles in the reagents as separate phase having special properties. Suppose that in the initial mixture of the particles are of two varieties, each variety may contain microdispersible phase. Volume fractions of the reactants then respectively

$$y_i = y_{i0} + y_{in} .$$

Volumetric heat capacity of the compact is calculated as the effective properties with the nanophase:

$$c\rho = \sum c_i \rho_i \eta_i + c_p \rho_p (1 - \sum \eta_i),$$

where η_i - the volume fraction of the i-th agent. Also, in the simplest linear approximation accept that

$$p = p_0(1 + \kappa(\eta_{1n} + \eta_{2n})), \quad s = s_0(1 + \kappa(\eta_{1n} + \eta_{2n})).$$

The system of equations is complemented by the terms of the initial time.

3. The numerical solution

The problem is solved numerically using c Runge-Kutta-Merson for the thermal part of the problem and the implicit Euler method for the kinetic part [13]. The results of numerical studies are phase and elemental composition of the sintered sample, depending on the concentrations of elements and phases from time to time for different model parameters responsible for the processing conditions.

All formal kinetic parameters of the model are calculated on the basis of phase diagrams and chemical thermodynamics, using the standard package TERRA [14] and literature data.

4. Concluding remarks

In the paper a detailed mathematical model of the volume powders sintering $MgO\text{-}Al_2O_3\text{-}SiO_2$ with the addition of aluminum nanopowder. The effect of addition of alumina nanoparticles in the final phase structure of corundum (oxide) ceramic.

The work was financially supported by the Ministry of Education and Science of the Russian Federation (GK 11.519.11.3004) .

References

[1] V.A. Vassiliev, V.V. Ipatov, A.N. Alekseev, Proceedings of the Institute of Refractories. V.42. (1971)
[2] E.G. Avakumov, A.A. Gusev, Cordierite - a promising ceramic material. - Novosibirsk: Publishing House of SB RAS. (1999)
[3] A.A. Gusev and etc., Glass and ceramics. №1 (2001)
[4] T.A. Habas, Glass and ceramics. N 12 (2002)
[5] T.A. Habas, Metal nanopowders in the ceramic industry. (2008)
[6] T.A. Habas, O.V. Nevvonen, Chemistry and Chemical Engineering at the turn of the millennium: Materials 2 All -Russian Scientific Conference. Tomsk. (2002)
[7] S.M. Loginov, N.K. Vernigora, D.A. Hyles, Bulletin of the National Technical University "KPI" . Special Issue - 66. (2010)
[8] Physical and metallurgical fundamentals of sintering powders. V.V. Skorokhod, corned beef SM Moscow, Metallurgy, 1984
[9] A.P. Savitsky, The liquid-phase sintering systems with interacting components. (1991)
[10] E. V. Boldyreva, V. V. Boldyrev, (Eds.), Molecular Solid State Series, V. 3 , Wiley: Chichester, 1999
[11] A. G. Knyazeva, Chemistry for Sustainable Development, Vol.10 , № 4 (2002)
[12] A.G. Merzhanov, Theory of gasless combustion. Preprint OIHF, Prunella (1980)
[13] S.N. Sorokova, A. G. Knyazeva, The certificate number 2013611289 on 01/09/13
[14] B.G. Cowards Simulation of chemical and phase equilibria at high temperatures : Computer software / MSTU. NE Bauman ; RosAPO . - State . reg . Number 920054 . - 1992 .

OS4: Corrosion Problems under Flow in Energy Industries

Tenth International Conference on Flow Dynamics
November 25-27, 2013, Sendai, Miyagi, Japan

Technical Basis of Fluid Dynamics Concerning JSME Pipe Wall Thinning Management Rules

Fumio Inada[1], Kimitoshi Yoneda[1], Yutaka Watanabe [2], Akira Nakamura [3]
1 Central Research Institute of Electric Power Industry, 2-11-1, Iwado-kita, Komae-shi, Tokyo 201-8511 Japan
2 Tohoku University, 6-6-01-2, Aoba, Aramaki, Aoba-ku, Sendai 980-8579 Japan
3 Institute of Nuclear Safety System, Inc., 64 Sata,Mihama-cho,Mikata-gun,Fukui 919-1205,Japan
E-mail: inada@criepi. denken.or.jp

ABSTRACT

The Japan Society of Mechanical Engineers established technical rules for pipe wall thinning management of power plants till 2006. Fluid- dynamics is deeply related to these phenomena. The current rules are based on the pipe wall thickness inspection, and the effect of fluid dynamics has been reflected only for the classification of phenomena in the rules. Recently, the clarification of the phenomena from the view point of fluid dynamics is remarkably advanced, which can lead to the revised technical rules in future, by which safety can be improved and reasonable management can be offered.

1. Introduction

Pipe wall thinning is one of the major degradation causes in the piping system of power plants. In 1986, a pipe-rupture accident in a secondary system occurred at Surry Unit 2. In the summer of 2004 in Japan, a large bore carbon steel pipe of a PWR secondary system ruptured in Mihama 3 with some victims. The Japan Society of Mechanical Engineers (JSME) established technical rules for thermal power plants [1], PWRs [2], and BWRs [3], respectively till 2006 to prevent such pipe ruptures, which was requested by the industry as well as the regulatory side.

The pipe wall thinning phenomena managed by these rules are mainly Flow-Accelerated Corrosion (FAC) and Liquid Droplet Impingement Erosion (LDI), and the technical knowledge regarding these phenomena was investigated before establishing the rules. Fluid-dynamics is deeply related to these phenomena. The current rules are based on the pipe wall thickness inspection, and the effect of fluid dynamics has been taken into account a little in the rules.

Recently, the clarification of the phenomena from the view point of fluid dynamics is remarkably advanced, which can lead to the revised technical rules in future, by which safety can be improved and reasonable management can be offered.

In this paper, technical basis of current JSME pipe wall thinning management rules is described in the view point of fluid dynamics at first. Next, recent new technical knowledge related to fluid dynamics, which can enhance the technical rules, is described.

2. Technical Basis Related to Fluid Dynamics for Current JSME Rules[4]

Technical rules provide the processes that enable operators to manage pipe wall thinning by determining pipe wall thickness using ultrasonic testing (UT) techniques and other methods. Specifically, the rules specify the processes for developing an inspection program:

- How to select the piping systems to be inspected
- How to determine the time to implement UT technique
- Performing thickness inspection using UT technique (routine and detailed measurement)
- Evaluating wall thinning rate and remaining period for fit for service
- Determining actions to take (repair or replacement).

This rule was developed based on the basis of the pipe wall thickness inspection data, and the remaining period for fit for service is obtained. The action such as repair or replacement should be conducted before the remaining period for fit for service with the margin defined in rules.

In the current technical rules, the effect of fluid dynamics has been taken into account a little. The most important matter is the classification of the phenomena.

FAC is defined as a phenomenon in which the dissolution of the protective oxide layer into water becomes extremely fast due to turbulent mass transfer. On the other hand, LDI is the phenomenon that liquid droplets accelerated above 100m/sec hit the pipe wall, and a large impulsive force can erode the material.

These phenomena are classified when the fluid force acting on the wall is compared with each other. The wall shear stress due to fluid flow was below 10Pa for a typical condition of FAC in plants. For LDI, impact force of order of several MPa can act on the wall though the impact force can be different depending on the evaluation model. So, the order of the fluid force acting on the wall is different between typical FAC and LDI.

The special feature of FAC is that it can occur at large bore piping of the feed water and condensate lines, and there can be a risk of pipe rupture. On the other hand, the special feature of LDI is that it can occur at relatively low pressure lines such as the pipe connected to condenser, and local thinning can occur, which leads only to pin-hole-leak. The separation of the phenomena led to the separation of piping systems where inspection is required for each phenomenon. The feature of each phenomenon leads to how to conduct the representative inspection and inspection methods.

3. New Technical Knowledge Related to Fluid Dynamics [5]

3.1 FAC

Regarding FAC, fluid dynamic factor is clarified though it is not reflected directly to the management in this stage.

Reference parameter of fluid dynamic factors is

mass transfer coefficient, and it was found that mass transfer can be analogous to turbulent heat transfer. Chilton-Colburn's analogy [6] is simple and can agree with actual mass transfer, which was already reflected into the technical knowledge on which current rules is based. Recently, a concept of effective friction velocity was proposed [7]. Fluctuating velocity near wall surface, obtained by computational fluid dynamics (CFD), was taken into account. Friction velocity at the turbulence promotion parts such as downstream of orifice, elbow, T-junction etc. was obtained as a ratio to friction velocity of straight tube, and mass transfer coefficient was obtained at the turbulence promotion elements. Geometry factor shows the relative wall thinning rate of turbulence promotion elements to fully developed flow of straight tube. Mass transfer coefficient in the downstream of orifice was directly measured experimentally, and the distribution of mass transfer coefficient in the direction of tube axis and the position where the largest value appears was considered [8].

When there was a swirl flow in the upstream of the orifice, flow visualization and CFD analysis showed that jet flow from orifice could become asymmetry, and that the asymmetry of the flow depending on the asymmetry of the orifice could be enhanced [9]. It could lead asymmetric wall thinning. It was suggested from the analogy of mass transfer to momentum transfer that the wall shear stress could well correlate mass transfer, and the tendency was shown in experiment [10].

Regarding FAC prediction model, Uchida & Naito's model [11] and Fujiwara & Yoneda's model [12] were developed in Japan, and the prediction codes were also developed. Above mentioned new knowledge may be integrated into the codes, and the codes can be used in the rules in future for screening of inspection location and evaluation at the change of the environment such as water chemistry change and power uprate.

3.2 LDI

The effect of droplet diameter [13] and attack angle [14] was obtained experimentally. It was shown by CFD analysis that the relaxation effect of impulsive force by the liquid film was important [15][16]. Droplet diameter was measured in high velocity and high quality vapor flow, and a correlation equation was proposed [17]. Though the scattering of the droplet velocity effect and the critical velocity of erosion initiation was one of the most important issues, but unfortunately it is not fully clarified yet. It was suggested to depend on the test methods. In the test of LDI, there are water jet tests, liquid droplet jet tests, rotating disk tests and so on. The droplet diameter, liquid film thickness, and the number of droplet can affect the thinning rate of LDI, and they can also depend on the test methods.

Morita's LDI evaluation system [18] as well as Uchida & Naito's method [19] in which electrochemical model was taken into account were proposed for LDI evaluation code of plant pipe.

Above mentioned new knowledge may be integrated into the codes, and the codes can be used in the rules in future for screening of inspection location and evaluation at the change of the environment such as water chemistry change and power uprate in the same manner as FAC.

References

[1] "Codes for Thermal Power Generation Facilities – Rules on Pipe Wall Thinning Management for Thermal Power Generation Facilities," JSME S TB1-2006.

[2] "Codes for Nuclear Power Generation Facilities – Rules on Pipe Wall Thinning Management for PWR Power Plants," JSME S NG1-2006.

[3] "Codes for Nuclear Power Generation Facilities – Rules on Pipe Wall Thinning Management for BWR Power Plants," JSME S NH1-2006.

[4] N.Sekimura, H. Miyano, I. Nishiguchi, S. Hamada, O. Watanabe, T. Nakamura, J. Hakii, H. Miyaguchi, F. Inada, JSME/ASME ICONE15-10722 (2007).

[5] F. Inada, Y. Watanabe, T. Ohira, A. Nakamura, ICONE21-15184 (2013).

[6] T. H. Chilton and A. P. Colburn, Industrial and Engineering Chemistry, Vol.26, (1934), 1183-1187.

[7] K. Yoneda, T. Ohira, K. Tanji, S. Akiba, K. Niiyama, R. Morita, F. Inada, ASME-PVP2009-77486, Prague (2009).

[8] R. Kojo, Y. Kuroda, M. Kondo and Y. Tsuji, in Proceedings of the 14th International Topical Meeting on Nuclear Reactor Thermalhydraulics, Paper No. NURETH14-542, Toronto, Canada (2011).

[9] T. Takano, T. Yamagata, Y. Ito, N. Fujisawa, Trans. Japan Society of Maintenology, Vol. 10-2 (2011)30-35.

[10] Y. Utanohara, A. Nakamura, Y. Nagaya and M. Murase, in Proceedings of the 14th International Topical Meeting on Nuclear Reactor Thermalhydraulics, Paper No. NURETH14-79, Toronto, Canada (2011).

[11] S. Uchida, M. Naitoh, H. Okada, T. Ohira, S. Koshizuka and D. H. Lister, Power Plant Chemistry, 12 (9), 550 (2010).

[12] K. Yoneda, R. Morita, K. Fujiwara, F. Inada, ASME-PVP2013-97601, Paris (2013).

[13] S. Hattori, R. Nakamura, G. Rin, Trans. JSME Series A, Vol. 77-782 (2011), 1760-1769.

[14] S. Hattori, M. Tsunouchi, R. Nakamura, The 16th National Symp. on Power and Energy System (2011) 317-320.

[15] T. Ikohagi, S. Ebara, N. Fujisawa, H. Hashizume, A. Iwabuchi, M. Satou, M. Uchidate, T. Yamagata and H. Yashiro, International Symposium on the Ageing Management & Maintenance of Nuclear Power Plants(ISaG2010) (2010), 47-57.

[16] T. Ikohagi, The 8th International Conference on Flow Dynamics (ICFD2011), (2011).

[17] R. Morita, The 16thNational Symp. on Power and Energy System (2011), 321-324.

[18] R. Morita, CRIEPI Report No. L09004 (2010).

[19] S. Uchida, M. Naitoh, Y. Uehara, H. Okada, S. Koshizuka and D.H. Lister, Power Plant Chemistry, 11, (2009), 704-717.

Tenth International Conference on Flow Dynamics
November 25-27, 2013, Sendai, Miyagi, Japan

Numerical Evaluations of the Effect of Local Flow Fields on Flow Accelerated Corrosion

Yoichi Utanohara[a], Koichi Kamahori[a], Akira Nakamura[a], Michio Murase[a] and Yukinori Nagaya[b]
[a] Institute of Nuclear Safety System, Inc., 64 Sata, Mihama-cho, Mikata-gun, Fukui 919-1205, JAPAN
[b] The Kansai Electric Power Co., Inc., 13-8 Goichi, Mihama-cho, Mikata-gun, Fukui 919-1141, JAPAN
E-mail of corresponding author: utanohara@inss.co.jp

ABSTRACT

To evaluate the effects of flow field on flow accelerated corrosion (FAC), an orifice flow of the diameter ratio $\beta = 0.41$ was simulated numerically by steady Reynolds-averaged Navier-Stokes (RANS) simulation and the predicted root mean square (RMS) of wall shear stress (WSS) was compared with measured FAC rate. The profile shape of predicted RMS of WSS agreed well with that of FAC thinning rate. The relationship between FAC thinning rate and RMS of WSS was relatively linear in the case of $\beta = 0.41$, while the relationship in the case of $\beta = 0.5$ parabolically decreased with increasing RMS of WSS.

1. Introduction

Flow accelerated corrosion (FAC) is an important issue for aging fossil and nuclear power plants. FAC causes thinning of the pipe wall which occasionally leads to a piping rupture accident. FAC occurs near the pipe geometry where flow is strongly disturbed such as at an orifice.

The authors have studied FAC downstream from an orifice experimentally and numerically [1][2]. The goal of those studies was to develop a numerical method with which the effect of local flow field on FAC can be evaluated. The evaluation parameter employed was the wall shear stress (WSS) based on the analogy between momentum and mass transfer. The profile of the root mean square (RMS) of WSS predicted by numerical simulation had a relatively similar shape of that of experimental data of FAC thinning rate.

In above studies, the orifice diameter ratio $\beta = d / D$ (d, orifice diameter; D, pipe diameter) was set to only $\beta = 0.5$. Hence, the influence of β ratio on FAC thinning rate was investigated experimentally with the orifice of $\beta = 0.41$ and 0.62 [3]. The maximum FAC rate downstream from each orifice increased with decreasing β ratio. However, the influence of β ratio on the distribution of FAC thinning rate was not investigated yet. In the present study, the orifice flow of $\beta = 0.41$ was simulated numerically and the predicted WSS was compared with measured FAC rate. Finally, relationship between the FAC thinning rate and the predicted WSS was compared between $\beta = 0.41$ and 0.5.

2. Experimental methods

The FAC experimental conditions are shown in Table 1. The detailed explanation of the experimental facilities and conditions were described in [1] [3].

The velocity profile downstream from the orifice was also measured using a LDV system (KANOMAX, Smart LDV, Model 8739-S). The number of samplings to obtain the mean velocity by LDV was about 30,000.

Table 1. FAC experimental conditions [3]

Pipe diameter D [mm]	50.0		
Orifice diameter d [mm]	20.5 (β = 0.41)		
Mean cross-sectional velocity U_{ave} [m/s]	3.54	2.83	2.47
Temperature [°C]	149.2 (149.0～149.8)		
Dissolved oxygen [ppb]	about 0.1		
pH	6.3	6.5	6.0
Iron concentration [ppm]	0.06～0.10	0.02～0.09	0.06～0.10

3. Numerical simulations

Steady Reynolds-averaged Navier-Stokes (RANS) simulation of orifice flow of $\beta = 0.41$ was carried out using commercial CFD software FLUENT 14. Details of simulation conditions are shown in Table 2. Simulation conditions were almost same as those of $\beta = 0.5$ described in [4].

Table 2. Calculation conditions

Fluid	Water (150°C, 1.5 MPa)	
	Density, Viscosity	918 kg/m^3, 1.83 x 10^{-4} Pa s
Turbulence model	Steady RANS (Low Re k-ε, AKN model)	
Convection term	2nd order upwind	
Boundary conditions	Inlet	U_{ave} = 0.453 m/s (Re = 1.14×10^5) 1/8th power law profile Turbulence intensity: 5% Turbulent viscosity ratio: 10
	Outlet	Pressure boundary
	Wall	Non-slip ($y^+ < 1$)
Calculation domain	Upstream 4D, downstream 10D	
The number of mesh	6,960,000 (Cross section:16,802)	

4. Results and Discussion

4.1 Predictive performance of numerical simulation

Figure 1 shows axial velocity profiles obtained at 1 mm from the wall along the axial length from the orifice. Though there were slight deviations, the steady RANS predicted LDV data quantitatively.

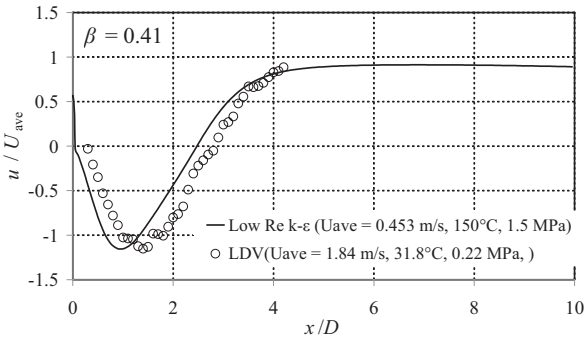

Fig.1 Time-averaged velocity distributions near the wall (1mm) downstream from the orifice

4.2 Evaluation method of root mean square of wall shear stress using steady RANS

Steady RANS can predict only time-averaged values, so that the authors derived an evaluation equation of RMS of WSS $\tau_{w,RMS}$ [4]. The RMS of instantaneous velocity parallel to the wall u_{RMS} is expressed as:

$$u_{RMS} = \sqrt{\overline{u^2}} = \sqrt{\overline{(U_{tave} + u')^2 + v'^2}} = \sqrt{U_{tave}^2 + \overline{u'^2} + \overline{v'^2}} \quad (1)$$

where U_{tave} is time-averaged stream-wise velocity and u', v' are fluctuation velocity parallel to the wall (stream and span-wise component). If isotropic turbulence can be assumed, u' and v' are given from the turbulence kinetic energy k as follows:

$$k = \frac{1}{2}\left(\overline{u'^2} + \overline{v'^2} + \overline{w'^2}\right) \approx \frac{3}{2}\overline{u'^2} \quad (2)$$

From Eqs. (1) and (2),

$$u_{RMS} = \sqrt{U_{tave}^2 + \frac{4}{3}k} \quad (3)$$

The relation between τ_w and u is expressed as Newton's law of viscosity, and if Δy_p, the distance of the first grid node from the wall, is within the viscous sublayer, τ_w, is expressed as follows:

$$\tau_w = \mu \frac{\partial u}{\partial y} = \mu \frac{u}{\Delta y_p} \quad (4)$$

where μ is dynamic viscosity. From Eq. (1) and the RMS of Eq. (4), the evaluation equation of $\tau_{w,RMS}$ can be derived.

$$\tau_{w,RMS} = \frac{\mu}{\Delta y_p}\sqrt{U_{tave}^2 + \frac{4}{3}k} \quad (5)$$

Figure 2 compares the profile of FAC thinning rate [3] and RMS of WSS evaluated by Eq. (5). Each value was normalized by its maximum value to compare only the shape of the respective distributions. The profile shape of RMS of WSS by steady RANS agreed well with that of FAC thinning rate.

Figure 3 shows the relationship between FAC thinning rate [3] and $\tau_{w,RMS}$ derived by the above method. It should be noted that the simulation conditions were different from the experimental conditions, and predicted $\tau_{w,RMS}$ was converted to the those of experimental conditions [2]. There was a relatively linear relationship between FAC thinning rate and $\tau_{w,RMS}$.

Figure 4 shows the influence of β ratio on the relationship between FAC thinning rate and $\tau_{w,RMS}$. Their tendencies were different; in the case of $\beta = 0.41$, the

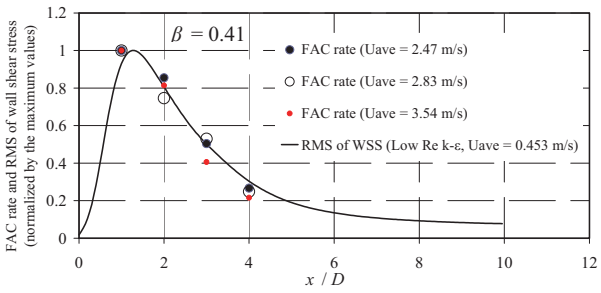

Fig.2 Comparison of the distributions of FAC thinning rate [3] and RMS of WSS

relationship was relatively linear, while in the case of $\beta = 0.5$ FAC rate parabolically decreased with increasing RMS of WSS. The influence of β ratio on the relationship was still not clear yet.

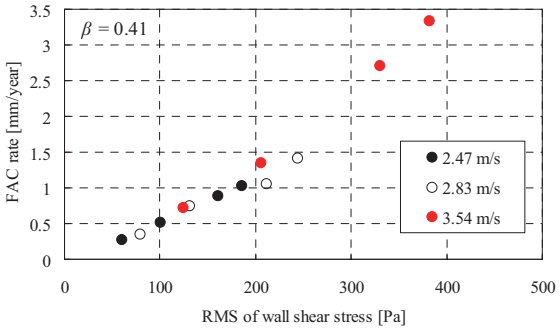

Fig.3 Relationship between FAC thinning rate and RMS of WSS

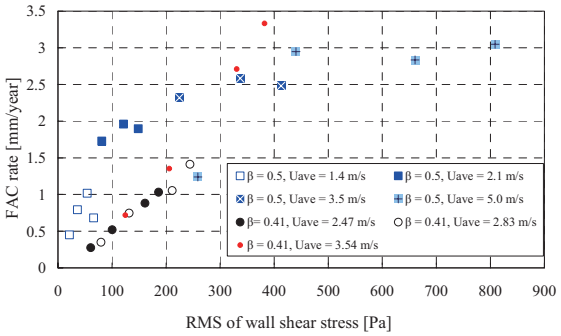

Fig.4 Relationship between FAC thinning rate and RMS of WSS in $\beta = 0.5$ [2] and 0.41

5. Concluding remarks

The orifice flow of $\beta = 0.41$ was simulated numerically and predicted RMS of WSS was compared with measured FAC thinning rate. In addition, relationship between the FAC thinning rate and the predicted RMS of WSS was compared between $\beta = 0.41$ and 0.5.

(1) The profile shape of the RMS of WSS evaluated from steady RANS simulation agreed well with the profile of FAC thinning rate.
(2) There was a relatively linear relationship between FAC thinning rate and $\tau_{w,RMS}$ in the case of $\beta = 0.41$.
(3) Tendencies of the relationship between FAC thinning rate and $\tau_{w,RMS}$ of $\beta = 0.41$ was different from that of $\beta = 0.5$. The influence of β ratio on the relationship was still not clear and more studies are needed.

References

[1] Y. Utanohara, et al., JSME J. Power Energy Syst., **6** (2012), pp. 18-33.
[2] Y. Utanohara, et al., JSME J. Power Energy Syst., (2013), in press.
[3] K. Kamahori, et al., proc. of FAC 2013 (2013), No. 1234.
[4] Y. Utanohara, et al., proc. of NURETH15 (2013), NURETH15-292.

Tenth International Conference on Flow Dynamics
November 25-27, 2013, Sendai, Miyagi, Japan

Numerical Studies on Mass Transfer Characteristics behind an Orifice in a Curved Swirling Flow

Takayuki Yamagata*, Ai Ishizuka*, Tsuyoshi Takano*, Nobuyuki Fujisawa* and Shinji Ebara**
* Visualization Research Center, Niigata University, 8050 Ikarashi 2-Nocho, Nishi-ku, Niigata, Niigata, Japan
** Graduate School of Engineering, Tohoku University, 6-6 Aramaki Aza Aoba, Aoba-ku, Sendai, Miyagi, Japan
E-mail of corresponding author: yamagata@eng.niigata-u.ac.jp

ABSTRACT

Numerical studies are carried out to understand mass transfer characteristics behind an orifice in a curved swirling flow, which is often encountered in pipe-wall thinning due to flow accelerated corrosion in pipelines of nuclear power plants. The numerical prediction method is applied for mass transfer evaluation behind an orifice in the curved swirling flow. The numerical results show the non-axisymmetric flow is produced behind the orifice under the influence of the swirling flow through the elbow. It is also found that the experimental Sherwood number profiles in the axial direction are qualitatively reproduced in the numerical simulation.

1. Introduction

Pipe-wall thinning in pipelines is one of important topics encountered in maintenance and safety management of the pipelines in nuclear/fossil power plants. The mechanism of the wall thinning in the pipelines is known to be caused by the flow accelerated corrosion (FAC), which is the complex physical and chemical phenomenon enhanced by the flow turbulence.

The pipeline rupture accident occurred in Mihama nuclear power plant in 2004, which is known as a typical case caused by the flow accelerated corrosion. Since then, experimental and numerical studies are carried out mainly from the fluid mechanical aspect of a flow behind an orifice [1 – 3]. The most interesting point of Mihama case is the non-axisymmetric wall thinning in the cross-section of the pipe, which results in locally high thinning rate on one side of the pipe. It was also found from the scaled model experiment that the swirling flow was observed in the pipeline [4]. Moreover, there was an elbow upstream of the orifice.

In order to understand the mass transfer characteristics behind the orifice, the numerical simulation has been carried out in literature, and k-ε models of low-Reynolds-number version have been studied [2]. However, the low-Reynolds-number model is difficult to evaluate the influence of the pipe wall roughness, since the model requires detailed computational grids in near wall region. The rough wall is often observed in the actual pipeline and affects pipe wall thinning rate. Therefore, mass transfer modeling from the wall is important to predict pipe wall thinning rate in the pipeline.

In this paper, the mass transfer phenomenon behind an orifice in a curved swirling flow is studied by numerical simulation. The k-ε model of turbulence employing the empirical formula for high Schmidt number flows is examined as a basis of mass transfer modeling to predict pipe wall thinning rate. The availability of the prediction method is validated by comparison with mass transfer experiment.

2. Numerical methods

In order to understand the mass transfer characteristics behind the orifice in a curved swirling flow, numerical simulations are carried out at the same conditions as the mass transfer experiment [3]. In this study, incompressible Reynolds-averaged equations for mass, momentum and concentration are solved with the standard k-ε model of turbulence. These equations are discretized by the finite volume method with the QUICK scheme for the convection term and with the central difference for the other terms, and the equations are solved by the PISO method [5].

The governing equations are solved under the following boundary conditions. Figure 1 shows the schematic image of the flow configuration. Experimental velocity profiles are applied at inlet boundary. The zero gradient condition is employed to all variables at the outlet boundary of the computational domain. The near-wall boundary conditions are employed in the region of logarithmic-law of the wall. The boundary condition for the concentration is given by the following equations [6]:

$$c^+ = \left(\frac{Sc_t}{\kappa}\right)\ln y^+ + \left(3.85Sc^{1/3} - 1.3\right)^2 + 2.12\ln Sc \qquad (1)$$

where $c+$ (= $(c_w\text{-}c)U\tau/J_w$), $y+$ (= $yU\tau/\nu$) are dimensionless variables normalized by the friction velocity $U\tau$, c_w is saturated concentration on wall, c_b is concentration in bulk flow, y is the distance from the wall, ν is the kinetic viscosity and κ (= 0.4) is Karman constant. Note that this empirical formula is applicable in a wide range of Schmidt number Sc of the flow up to 40,000.

The diffusive mass flux J_w is expressed by the following equation:

$$J_w = K(c_w - c_b) \qquad (2)$$

where K is mass transfer coefficient. The mass transfer coefficient is evaluated in terms of the Sherwood number Sh (= Kd/D), where d is the pipe diameter and D is the diffusion coefficient.

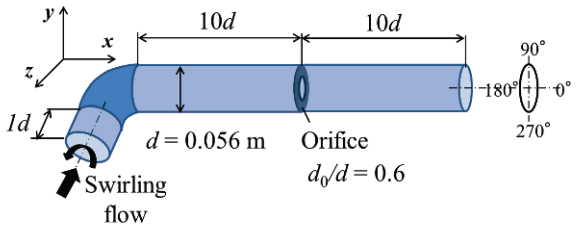

Fig. 1 Flow configuration

3. Results and discussion

Numerical simulation of a curved swirling flow is carried out in order to evaluate mass transfer coefficient behind an orifice. The velocity field and mass transfer for comparison are measured by particle image velocimetry and benzoic acid method [3]. The Reynolds number of the experiment is Re (= ud/ν) = 3.0 × 10^4, where U_0 (= 0.54 m/s) is the bulk velocity and d (= 0.056 m) is the pipe diameter.

Figure 2(a) shows the experimental mean velocity distribution in the cross section behind the orifice at x/d = 1. The result shows that the mean velocity field is non-axisymmetric behind the orifice under the influence of the swirling flow through the elbow. The position of the higher axial velocity is seen on the left side of the cross-section. A secondary flow is observed in the cross-section, and is circulating mainly in counter-clockwise direction around the higher axial velocity region. Figure 2(b) shows the mean velocity distribution of the numerical simulation. Although the complex secondary flow distribution is simplified, the position of the high axial velocity is well reproduced in the simulation.

Figure 3 shows axial distributions of the Sherwood number behind the orifice and compares the results between the experiment and the numerical simulation. The distributions at four different circumferential positions 0, 90, 180, 270 degrees are shown for the curved swirling flow. In the results of the numerical simulation, the maximum Sherwood number distribution of the curved swirling flow is observed at 180 degrees and is larger than that of the straight pipe flow case. This trend qualitatively agrees with the experimental result, although the position of the maximum Sherwood number shifts downstream.

Figure 4 shows the circumferential distributions of the Sherwood number behind the orifice x/d = 1 in the curved swirling flow. The Sherwood number distributions of the numerical simulation indicate that the mass transfer increases on the left side and decreases on the lower side in comparison with the straight pipe flow. On the other hand, the Sherwood number distributions of the experiment decrease on the right side. Although the position of the maximum Sherwood number in the numerical simulation is deviated from that in the experiment, the non-axisymmetric distributions of the Sherwood number are qualitatively

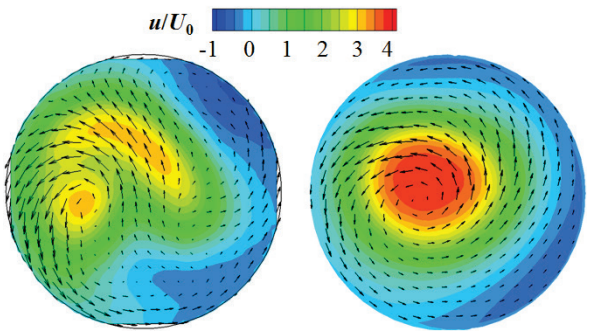

(a) Experiment (b) Simulation

Fig. 2 Velocity fields behind an orifice at x/d = 1

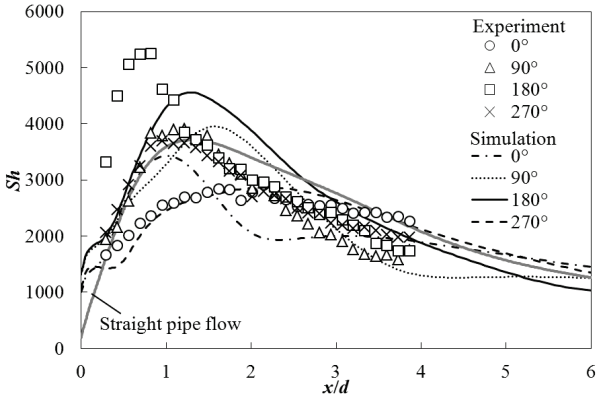

Fig. 3 Axial distributions of Sherwood number behind an orifice

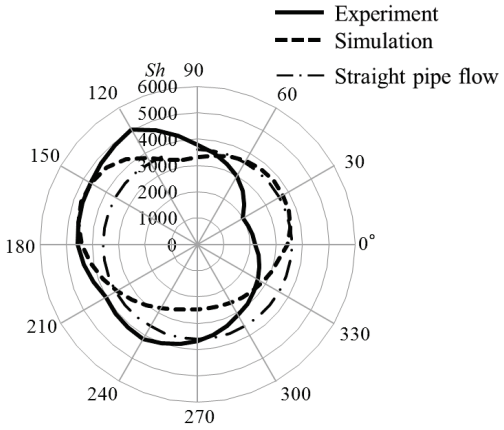

Fig. 4 Circumferential distribution of Sherwood number behind an orifice x/d = 1

reproduced in the numerical simulation with the k-ε turbulence model.

4. Concluding remarks

Numerical studies are carried out to understand mass transfer characteristics behind an orifice in a curved swirling flow. It is found that the experimental Sherwood number profiles and the mean velocity distribution behind the orifice are qualitatively reproduced in the numerical simulation by the k-ε model with the empirical modification of high Schmidt number flows.

References

[1] K. Yoneda and R. Morita, Proc. 15th Int. Conf. Nucl. Eng., Nagoya, (2007), 10200.
[2] J. Xiong et al., Nucl. Eng. Des., **241** (2011), pp. 3190-3200.
[3] T. Takano et al., J. Flow Control Meas. Vis., **1** (2013), pp. 1-5.
[4] NISA, Secondary piping rupture accident at Mihama power station, unit 3, of the Kansai Electric Power Co. Inc., Final Report, (2005).
[5] T. Yamagata et al., Proc. ICONE20-POWER2012, Vancouver, (2012), 54681.
[6] B.A. Kader, Int. J. Heat Mass Transf., **24** (1981), pp. 1541-1544.

Tenth International Conference on Flow Dynamics
November 25-27, 2013, Sendai, Miyagi, Japan

Mechanistic Aspects of Flow-Accelerated Corrosion Suppression by Trace Chromium in Carbon Steels

Hiroshi Abe and Yutaka Watanabe
Graduate School of Engineering, Tohoku University
6-6-01-2 Aoba, Aramaki, Aoba-ku, Sendai, 980-8579 Japan
hiroshi.abe@qse.tohoku.ac.jp

ABSTRACT

Threshold level and time dependency of Cr effect on flow accelerated corrosion (FAC) suppression in carbon steels have been discussed based on the results of FAC experiments. Detailed FAC processes has also been discussed focused on the oxide layer characteristics. No threshold level or time dependency of Cr content for FAC mitigation was observed in the range of Cr content from 0.003 to 1.01 %. Porous outer oxide layer did not affect FAC rate significantly because the thickness of that increased with increasing FAC rate.

1. Introduction

Flow accelerated corrosion (FAC) of pipes made of carbon steels are understood to be chemical or electrochemical dissolution of metal under very fast mass transportation between pipe wall and bulk water, where a number of influencing parameters are involved in chemical, material, and flow dynamics aspects [1, 2]. FAC rate strongly depend on Cr content in steels, and even an impurity level of Cr in steels suppress FAC under the conditions where magnetite (Fe_3O_4) forms [3-5]. The threshold level of Cr (0.04%) on FAC mitigation was proposed [6]. This tendency was reflected in CHECWORKS, and BRT-CICERO [7]. However, mechanistic explanation for the threshold is not clear. Recent experimental results suggest that existence of the other threshold lower than 0.04% [8]. Although the theoretical model as "FAC mitigation by Cr increases with increasing time" was proposed [9], many of experimental results (up to 14,400 h experiment) did not support that motel. Further investigation was needed [8]. While a number of FAC studies have been done, understanding the essential role of Cr content on FAC mitigation is not well known.

In this study, threshold (Ducreux model) and time dependency (Bouchacourt model) of Cr effect on FAC rate have been discussed with comparison to the results of FAC experiments. Detailed FAC processes has also been discussed focused on the oxide layer characteristics.

2. Experimental Details

The steels used in this study were manufactured with tailored Cr content at six levels from 0.003% to 1.01%. The rest of compositions are based on carbon steel JIS G3455 STS "carbon steel pipes for high temperature service". The steels were machined into small plate specimens as big as 9.5mm x 15mm x 2mm thick. FAC tests were performed in low-dissolved oxygen concentration (<1ppb) water at 150 ºC under 1.5MPa pressure. The experimental variables were flow rate (quasi-static, or 3.0 m/s) and test duration (325 or 1100 hrs). FAC rate was evaluated by the weight loss of the specimens. Oxide layer characteristics were investigated using an optical microscope and secondary electron microscope (SEM). In particular, the nanometer-scale oxide properties, e.g. thickness, defect structure, and compositional profile were investigated using transmission electron microscope (TEM) with X-ray analyzer. The thin foils for TEM observation were prepared with focused ion beam technique. The further detailed methods and conditions of FAC experiments and oxide layer characterizations were described in the previous paper [10].

3. Results and Discussion

Relative FAC rate plotted with Ducreux model [6] as a function of Cr content in double logarithmic chart are shown in Fig.1. Cr effect on FAC mitigation increases with increasing flow rate. That tendency corresponds to "Ducreux Model". However, no threshold level of Cr content for FAC mitigation was observed (> 0.003% Cr) in this experiments. Relative FAC rate plotted as a function of Cr content in liner graph are shown in Fig.2. There is no significant difference in relative FAC rate between 325 and 1100h experiments. Cr effect on FAC mitigation did not increase with increasing time. Our findings did not support "Bouchacourt model".

The appearance of specimens tested at 3.0 m/s flow for 1100 hrs are shown in Fig.3. Low Cr content specimens were covered with a great deal of oxide deposit which was easy to break away, on the other hand, high Cr content (~1.01 wt %) specimens covered with relatively compact oxide layer with less oxide deposit. Results of SEM observation of the outer oxide layer formed on the specimen which contain 0.003 % Cr in Fig.3 are shown in Fig.4. Wave-shaped morphology which may be due to the effect of flow was observed on the surface side of oxide. On the other hand, a lot of the grain consists of perlite were observed on the reverse side. It has been considered that porous outer oxide layer did not affect FAC rate significantly because the thickness of that increased with increasing FAC rate.

4. Conclusion

No threshold level or time dependency of Cr content for FAC mitigation was observed in the range of Cr content from 0.003 to 1.01 %. Porous outer oxide layer did not affect FAC rate significantly because the thickness of that increased with increasing FAC rate (decreasing Cr content).

Acknowledgement

Present study includes the result of National Research Project on Ageing Management and Maintenance of Nuclear Power Plant from FY2006 to FY2009 sponsored by Nuclear and Industrial Safety Agency (NISA).

References

[1] Sanchez-Caldera, L.E., Transactions of the ASME, Journal of Engineering for Gas Turbines and Power, 110 (1988), 180-184.

[2] Cragnolino, C., Proc. 3rd Int. Symp. on Environmental Degradation of Materials in Nuclear Power Systems – Water Reactors, TMS/ASM, (1987), 397-406.

[3] H.G. Heitmann, P. Schub, Proc. the Third Meeting on Water Chemistry of Nuclear Reactors, BNES, London, 243, (1983).

[4] T. Tsuruta, et al., Proc. Fontevraud 6 Contribution of Materials Investigations to Improve the Safety and Performance of LWRs, Vol.1, (2006), 181-190

[5] T. Satoh, et al., Proc. 14th Int. Conf. on Environmental Degradation of Materials in Nuclear Systems, (2009).

[6] J. Ducreux, Water chemistry of nuclear reactor systems 3. Proceedings of the British. Nuclear Energy Society, p. 227, London (1983).

[7] T. Knook, et al., "Pipe wall thining management at EDF" E-Journal of Advanced Maintenance, Vol.2, p.1-13, (2010).

[8] E.M. Pavageau and F. Cattant, Residual Chromium Effect on Flow-Accelerated Corrosion of Carbon Steel: Results of an Experimental Program Conducted in EDF's CIROCO Loop. EPRI, Palo Alto, CA and EDF, Moret Sur Loing, France: 2006. 1011837.

[9] B. Chexal et al., Flow Accelerated Corrosion in Power Plants, EPRI, Palo Alto, CA: 1998. TR-106611-R1.

[10] Y. Watanabe, K. Sue, H. Abe, Proc. 2009 ASME Pressure Vessel and Piping Division Conference, No.78126, (2009).

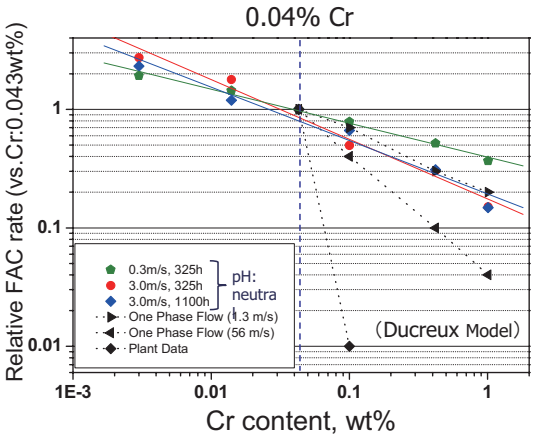

Fig.1 Relative FAC rate plotted with Ducreux model as a function of Cr content of carbon steels.

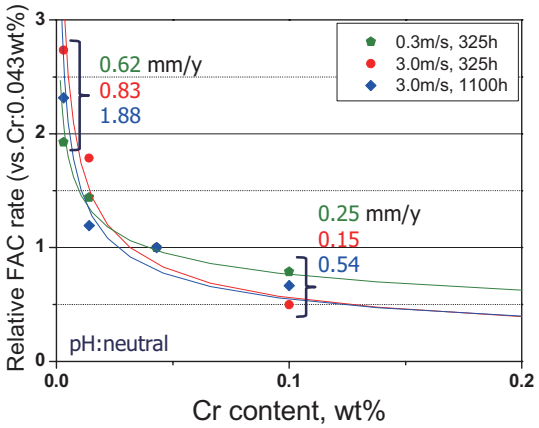

Fig.2 Relative FAC rate plotted as a function of Cr content of carbon steels.

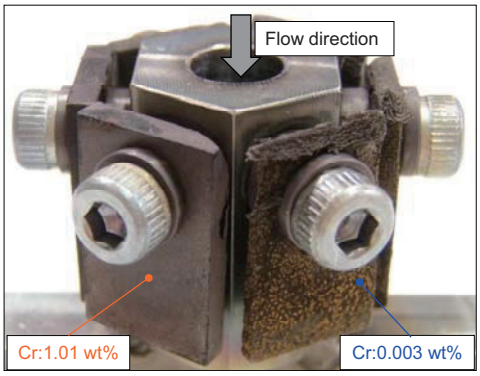

Fig.3 Appearance of specimens after FAC test (3.0m/s, pH:Neutral, DO:<1ppb, 1100h).

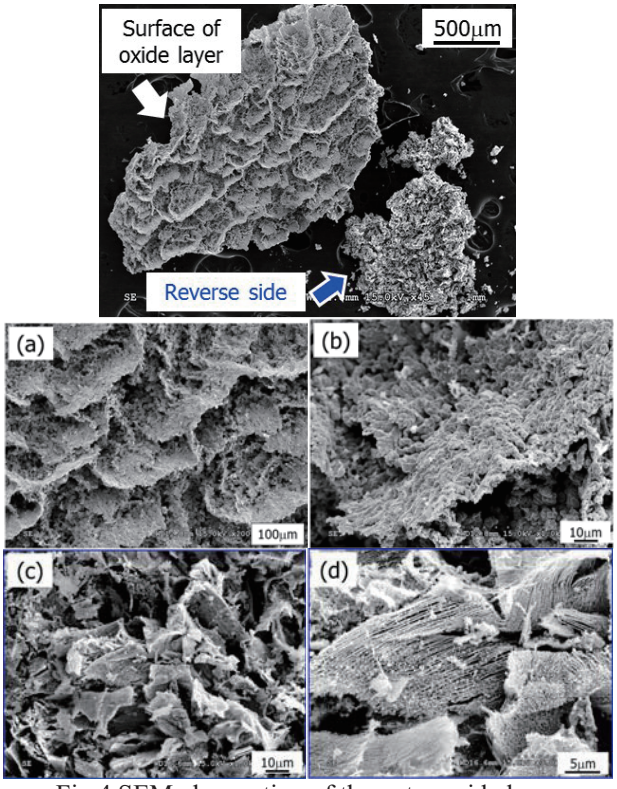

Fig.4 SEM observation of the outer oxide layer (0.003% Cr, pH: Neutral, DO: <1ppb, 1100h) (a), (b): Surface side, (c), (d): Reverse side

Tenth International Conference on Flow Dynamics
November 25-27, 2013, Sendai, Miyagi, Japan

Influence of Material Hardness on Erosion Rate by Liquid Droplet Impingement

Kengo SAITO[1], Takayuki YAMAGATA[1], Nobuyuki FUJISAWA[1], Ryo MORITA[2], Fumio INADA[2]
1 Visualization Research Center, Niigata University,
8050 Ikarashi-2 cho, Nishi-ku, Niigata, Japan, 950-2181
2 Central Research Institute of Electric Power Industry,
2-11-1, Iwatokita, Komae, Tokyo, Japan, 201-8511
E-mail: fujisawa@eng.niigata-u.ac.jp

ABSTRACT

This paper describes the experimental study on the liquid droplet impingement erosion for various metal materials using a spray jet apparatus for droplets with several tens of micrometers in diameter. In order to understand the influence of material hardness on the liquid droplet impingement erosion, the erosion rates for various metal materials, such as aluminum, aluminum alloy, brass and carbon steel, were examined. The resulted erosion rates are well correlated with the droplet velocity and the Vickers hardness.

1. Introduction

When the liquid droplets impinge on a solid wall, the droplet deforms the shape in a very short time, and results in the erosion of metal materials due to the high impact pressure on the surface. This phenomenon appears in the pipelines of nuclear/fossil power plants, and the resulted erosion leads to the leak of the high pressure steam flowing through the pipeline. Therefore, it is important to predict the erosion rate and the remaining life time of the pipeline for the safety management and the maintenance of the power plants.

In order to predict the liquid droplet impingement (LDI) erosion, the erosion model has to be established, which expresses the relationship between the erosion rate and the droplet parameters (velocity, diameter and number of impinging droplets). Since the pioneering work by Heymann [1], there have been several experimental studies on liquid droplet impingement erosion, such as Itoh-Okabe [2], Isomoto-Miyata [3], Hattori-Takinami [4], Fujisawa et al. [5]. However, it is known that these experimental results on the erosion rate are scattering widely in the power index of velocity dependency, which ranges from 5 to 8 [6]. Furthermore, the influence of the material hardness on the erosion rate has not been fully studied yet. Isomoto-Miyata [3] reported that the erosion rate increases in proportional to the droplet velocity to the power of 2 and in proportional to the Vickers hardness to the power of -2.75. However, this power index for Vickers hardness does not match with the theoretical analysis by Ikohagi [7], which suggests the minus half of the power index of velocity dependency. Therefore, there is a need of further study on the relationship among the erosion rate, the droplet velocity and the material hardness.

In the present paper, the influence of the droplet velocity and the material hardness on the liquid droplet impingement erosion is studied to develop the prediction method of the liquid droplet impingement erosion.

2. Experimental Method

The experiments are carried out by using an experimental apparatus for liquid droplet impingement erosion, which consists of high pressure plunger pump (maximum pressure 35 MPa), conical spray nozzle, test specimen and water tank (0.58 m in diameter and 0.84 m in height). Note that the filter is placed in the upstream of the pump to remove the dust in the working fluid of water. The pump pressure is measured by pressure meter located immediately downstream of the pump. The conical spray nozzle used in this experiment consists of a fan type spray and the straight section with a pipe diameter of 3 mm in diameter and 30 mm long. The commercial fan type spray tip is used for this experiment, which has an elliptic exit with a maximum dimension of 0.6 mm (Ikeuchi Co., VNP 1525).

The experiments are conducted for various nozzle pressures ranging from 24 to 34 MPa, which corresponds to the nozzle exit velocity 160 to 190m/s. The standoff distance between the nozzle and the test specimen is set to 150mm. The test specimen is shaped to a cylindrical rod, and one of the circular end-surface is used for the test, while the other end is supported during the experiment. Note that the diameter of the test rod is 1.5mm and the length is 8mm. It should be mentioned that this condition allows the LDI erosion in relatively thin liquid film on the test surface, and a uniform erosion surface was observed on the test specimen. In this experiment, 5 test material are used, that is aluminum (A1070), aluminum alloy (A5056), brass (C3604), carbon steel (SS400, S20C). Note that the hardness of these materials is measured by the standard Vickers' hardness testing machine.

3. Results and Discussion

Figure 1 shows the experimental results of erosion depth E_d in relation to the local volume flux qt for various metal materials, where q: local volume flux, t: time. The erosion depth E_d is measured by the mass loss measurement and the local volume flux q is measured by the sampling probe combined with the mass-flow-rate measurement. It is found that the erosion depth E_d increases almost linearly except for the initial stage of erosion, where the local volume flux qt is small. The gradient of the erosion curve gradually decreases with an increase in the Vickers hardness, which is measured before the erosion test. This result agrees qualitatively with the experimental observation by Isomoto-Miyata [3].

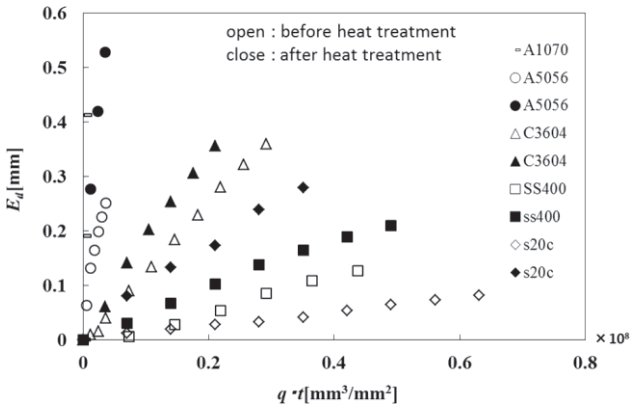

Fig.1 Erosion depth E_d versus local volume flux qt

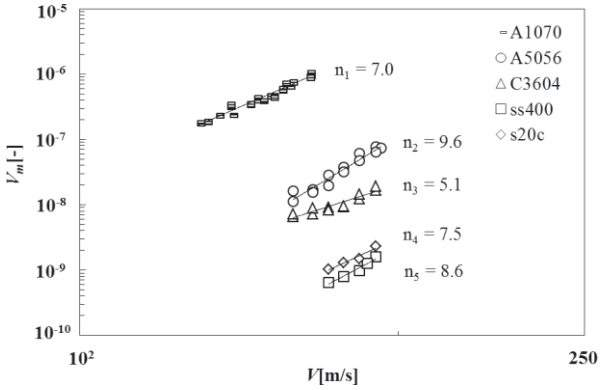

Fig.2 Erosion rate V_m versus droplet velocity V

Figure 2 shows the logarithmic plot of the non-dimensional erosion rate V_m and the droplet velocity V of the present experimental results for various materials, where the non-dimensional erosion rate V_m is defined by the following equation.

$$V_m = \frac{E_d}{qt} \tag{1}$$

The result shows that the non-dimensional erosion rate V_m increases with the droplet velocity V with the power index ranging between 5 to 9, the average value is 7.6, which is in agreement with the previous experiments of liquid droplet impingement erosion [5]. The power index of the velocity dependency is scattering widely with the material hardness.

According to the theoretical analysis by Ikohagi [7], the non-dimensional erosion rate V_m is expressed by the following equation:

$$V_m = c_1 V^n \left(\rho c / p c_s\right)^{n/2} \tag{2}$$

where c: acoustic velocity in liquid, c_s: acoustic velocity of solid, p: material hardness, ρ: density of liquid and c_1 : constant. Eq. (2) is similar to the non-dimensional erosion rate suggested by Sanchez-Caldera [8], but this equation allows the use of arbitrary power index n with respect to the droplet velocity V. It should be mentioned that the non-dimensional erosion rate increases in proportional to the nth power of droplet velocity and the

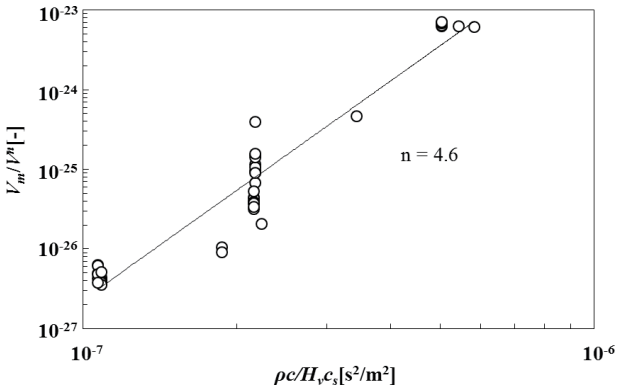

Fig.3 Erosion rate versus Vickers hardness

Vickers hardness to the inverse power of half the velocity dependency, while the c, c_s, ρ are constant.

Figure 3 shows the relation between the erosion rate V_m divided by the power of velocity V^n and the $\rho c/ H_v c_s$,, where H_v is the Vickers hardness measured before the erosion test. The present results indicate that the erosion rate increases in proportional to the power index of 4.6. Therefore, the present results can be summarized by the following equation.

$$V_m = c_1 V^{7.6} (\rho c / Hvc_s)^{4.6} \tag{3}$$

This result implies that the power index derived from the velocity dependency n/2=3.8 approximately agrees with that derived by direct measurement of Vickers hardness 4.6. This result suggests the validity of the theoretical analysis by Ikohagi [7].

4. Concluding remarks

The liquid droplet impingement erosion is experimentally studied using the high-speed spray jet for some metal materials. The results of the erosion rates are summarized by the correlation with the Vickers hardness and the droplet velocity, and the formula is shown.

References

[1] F.J. Heymann, Proc. 5th Int. Conf. Erosion by Liquid and Solid Impact (1979), 20, 1-10.
[2] H. Itoh and N. Okabe, Trans. JSME (A), **59**(1993), 2736-2741
[3] Y. Isomoto and H. Miyata, Zairyo-to-Kankyo, **57**(2008), 146-152
[4] S. Hattori and M. Takinami, Wear, **269** (2010), 310–316.
[5] N. Fujisawa, T. Yamagata, K. Hayashi and T. Takano, Nuclear Engineering Design, 250(2012), 101-107
[6] N. Fujisawa, R. Morita, A. Nakamura and T. Yamagata EJAM, **4** (2010), 79-87
[7] T. Ikohagi, Proc. 8th Int. Conf. Flow Dynamics, 2011, Sendai, 402-403
[8] L.E. Sanchez-Caldera, L.E., Ph.D. thesis, Dep. Mech. Eng., Massachusetts Institute of Technology, 1984

OS5: Global / Local Innovations for Next Generation Automobiles

Tenth International Conference on Flow Dynamics
November 25-27, 2013, Sendai, Miyagi, Japan

Convergence of Transportation and Energy in the Future

Mark C. Williams,
URS, Morgantown, WV USA
Markcwilliams1@frontier.com

ABSTRACT

Energy and transportation are major world industries joined inextricably together. Each available energy source – fossil, nuclear, renewable - has used as used as a transportation fuel. The future of fuel availability is the future of transportation. The existing dominance of fossil fuels can only persist through a transition period. In the future hydrogen, solar, natural gas and other renewable will dominate the transportation. Solar cars, battery vehicles, PHEV, hydrogen fuel cell vehicles, and natural gas vehicles, represent tomorrow's propulsion future.

1. Introduction

Efficient and environmentally sound energy conversion depends on new and improved transportation technology. Reducing energy use, reducing the negative human impact on the environment in a constrained, highly populated state with frequent interactions of unknown consequences is critical to doing as little damage as possible and to intruding as little as possible, in an attempt to extend the transition period so we have time to make right decisions for the future.

2. Oil

The world is rapidly consuming the finite amounts of stored energy, especially petroleum. By way of example, US consumes 20 million BBL/day (7 billion BBL/year) petroleum products. Canada (2-3 million BBL/day - half from tar sands) and Middle East (1.5 million BBL/day) help supply USA petroleum. Canada tar sands contain 300 BBL, one of the world's largest resources ever known, would supply US for only 40 years

3. Natural Gas

We benefit from the chemical energy extracted from sunlight on this planet. As long as there is life and sunlight, we will always have renewable natural gas on this planet in the future. Methane from human (ADG) and plant and animal and plant residues and wastes captured from sunlight are available. Currently, the only natural gas light-duty vehicle manufactured in the U.S. is the Honda Civic GX ($26,000 list price; 24 city/36 hwy/28 combined gasoline equivalent mpg). Only roughly 110,000 of the 12 million CNG vehicles worldwide are in the U.S., including aftermarket conversions. There are roughly 250 million registered passenger vehicles in the US (EIA). The cost to convert vehicles to NG is estimated $12,500 to $22,500 depending on the vehicle, engine, size of CNG tanks needed, and who does the converting (Green Car Journal, 2011**).** Without the development of significant infrastructure, natural gas vehicles cannot be a reality.

4. Hydrogen

Natural gas is currently the principle method to generate hydrogen. Production from renewable energy – wind, solar, geothermal and biomass is possible. Hydrogen fuel cell vehicles will require a hydrogen infrastructure. Fuel cells technology transforms electricity production in stationary and transportation applications because it is the most efficient way to convert chemical energy to electricity. According to some fuel cell cars are decades away from commercialization. While major development has centered on polymer electrolyte fuel cells, solid oxide fuel cells operating on natural gas are a definite possibility.

5. Solar

All the energy stored on the earth comes from the supernova of suns or the Sun itself. With the SEV solar system, the Toyota Prius can operate up to 30 miles per day in electric mode thus improving fuel economy by up to 34-60%. Power from a solar array is limited by the size of the vehicle and area that can be exposed to sunlight. While energy can be accumulated in batteries to lower peak demand on the array and provide operation in sunless conditions, the battery adds weight and cost to the vehicle. The power limit can be mitigated by use of conventional electric cars supplied by solar (or other) power, recharging from the electrical grid. triple hybrid vehicle—the PHEV that has solar panels as well to assist. While sunlight is free, the creation of PV cells to capture that sunlight is expensive. Costs for solar panels are declining.

6. Stationary Power from Coal, Nuclear, Natural Gas, Renewables for Transportation

These fuels will continue to be used until extinct.
While direct propulsion in transportation is limited, the use of this energy for transportation and especially plug-in hybrids is increasing. However, the efficiency of stationary power generation is problematic (Figure 2). Greater use by hybrids will only shorten the life of those fuels. In the nuclear industry, the fuel rods will spend about 3 operational cycles (typically 6 years total now) inside the reactor. Generally until about 3% of their uranium has been fissioned, then they will be moved to a spent fuel pool where the short lived isotopes generated by fission can decay away. After about 5 years in a spent fuel pool the spent fuel is radioactively and thermally cool enough to handle, and it can be moved to dry storage casks or reprocessed. There is no storage facility for nuclear waste in USA. All nuclear waste belongs to the American people. Of course, complete electrification of the transportation through stationary power will eliminate the need to depend on petroleum.

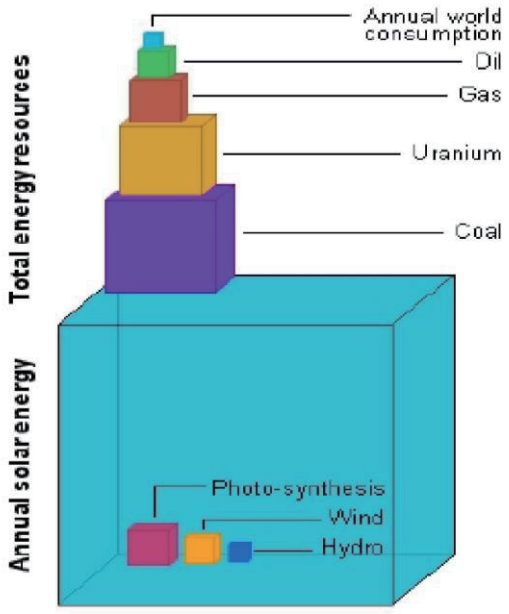

Fig. 1 Energy Consumption, storage energy, and incident energy

7. Battery

The energy for charging batteries must come from some available energy source – fossil, nuclear, renewable. Energy storage costs are falling but batteries remain expensive. The electric car is making great progress (Figure 3).

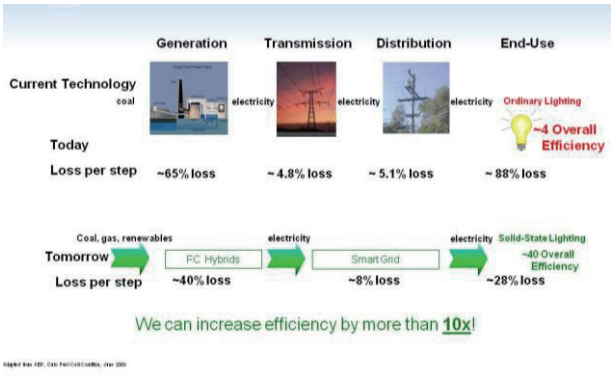

Fig. 2 Energy Efficiency in Stationary Power

8. Concluding remarks

Energy and transportation are major world industries joined inextricably together. The available energy in the future will determine the fuel to be used in transportation. Efficiency of energy conversion will determine when and to what fuel the industry will vector. Technology innovation will help shape this future. Ultimately, solar and renewable natural gas will dominate in the fture.

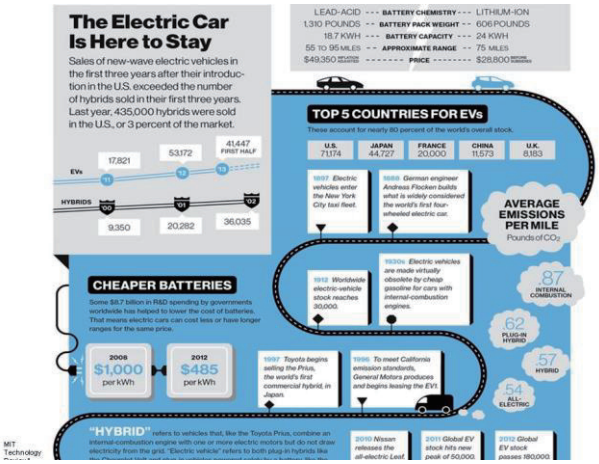

Fig. 3 Status of Battery Cars

References

[1] EIA, 2013.
[2] Green Car Journal, 2011.
[3] Adapted from AEP, Ohio Fuel Cell Coalition, June 2009.
[4] MIT, newsletters@technologyreview.com, August 2, 2013.

Tenth International Conference on Flow Dynamics
November 25-27, 2013, Sendai, Miyagi, Japan

Research and development of fully automated vehicles

Keiji Aoki

ITS Research Division, Japan Automobile Research Institute-1-30,Shibadaimon,Minatoku,Tokyo,Japan
E-mail:kaoki@jari.or.jp;+81-(3)5733-7925

ABSTRACT

Automated truck platoon is focused on being able to improve the fuel economy and operation cost as next freight transportation system. In order to achieve 15 % of CO_2 reduction, an automated platoon system with closed gap distance of 4 m, have been developed. Trucks are equipped with automated steering and speed control system so that vehicles can travel at closed gap distance alone the lane. Automated platoon composed from three heavy duty trucks and one light duty truck has been demonstrated successfully at gap distance of 4 m.

1. Introduction

Automated vehicles being able to improve safety, fuel economy and traffic efficiency which are main issues on automobiles are anticipated as next generation automobiles. Currently, automated vehicles which must become next generation automobiles are being developed in Japan, Europe and United State America. Especially, automated truck platoon is focused on being able to improve the fuel economy and operation cost as next freight transportation system.

In 2008, a national project for reducing CO_2 gas emitted from heavy duty trucks on the highway, called "Energy ITS," was initiated in Japan under the auspices of the New Energy and Industrial Technology Development Organization. The mission of this project is to build an automated platoon system with closed gap distance which will be able to reduce CO_2 gas emission without engine modification. It has been already proven through many studies that the air-drag of each truck can be reduced by the closing of gap distance between trucks, resulting in improvement of fuel consumption. [1] In order to achieve 15 % of CO_2 reduction, an automated platoon system with closed gap distance of 4 m, have been developed and also the automated platoon within three heavy duty trucks have been tested at a speed of 80 km/h on oval test track.

In this paper, automated platoon technologies developed in this project will be described.

2. Concept of Automated Platoon

While it is required for platoon to keep the gap distance closely in order to improve fuel economy by reducing the air-drag, the task of keeping of closed gap distance on mixed traffic within conventional vehicles will be difficult for human drivers because of limited human's physiological response time. Automated vehicle control will be essential for keeping of closed gap distance. Both Lateral and longitudinal control can be made automatically trucks in platoon. Image of platoon is illustrated in Fig.1. The Steering is controlled automatically so that vehicles can keep the lane alone the painted lane line and also the propulsion of engine and the brake is controlled automatically for keeping gap distance between vehicles.

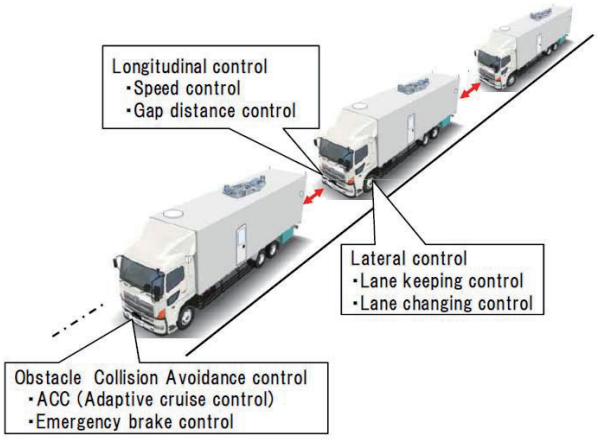

Fig.1 Concept of automated platoon

3. Detail of vehicle control

3.1 Lane keeping control

Block diagram of lane-keeping control system is shown in Figure 2. Nonlinear model based control algorithm was applied to the path following. [2]

The control algorithm consists of feed-back control and feed-forward control module in order to compensate the time lag of sensor and actuator. Feed-back control module can compensate the deviation of the lateral displacement and yaw angle and Feed-forward control module compensates the error due to both the cant and curvature of road.

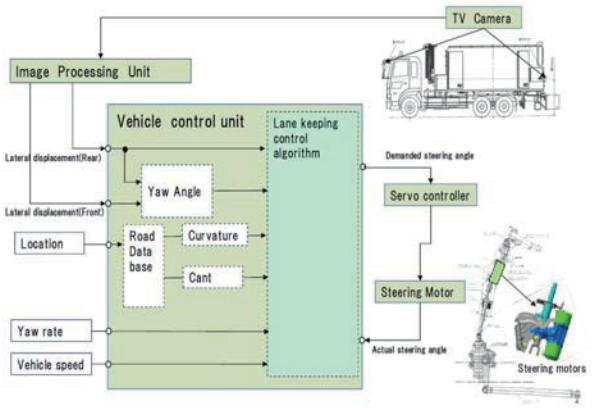

Fig2. Block diagram of lane keeping control system.

The lateral displacement and yaw angle with respect to white lane-marking line is measured by 2 kinds of lane detection sensor which are TV cameras and laser mounted on the left side of a truck. These sensors are mounted on so as to look down road surface in order to prevent the misdetection under the condition of rainy weather or against sun beam. The lateral displacement can be detected by the image processing unit which can recognize the while lane line from the image captured by TV cameras and laser. The yaw angle can be calculated from both lateral displacement of front and rear.

3.2 Longitudinal Control

For longitudinal control, in order to achieve precise controllability under the transient condition such acceleration and deceleration, cooperative distance control algorithm using the vehicle to vehicle (V-V) communication has been developed. The data concerning to vehicle speed, acceleration and deceleration rate of a leading truck is transmitted to following trucks by using V-V communication. Gap distance can be measured by 76GHz mill wave radar and laser radar. The engine propulsion and braking of a truck are controlled to maintain the inter-vehicle distance constantly.

4. Experimental vehicles

Experimental trucks have been developed in order to evaluate lateral and longitudinal controllability and fuel economy.

Figure 3 shows the configuration of experimental trucks. TV cameras and laser sensor are mounted on the top of the cabin and the rear of the cargo compartment on the left side. A mill-wave radar with 76GHz and a LIDAR for distance detection between vehicles are mounted near the front bumper. The steering motors for lane keeping are mounted on steering shaft. Radio-wave based inter-vehicle communication unit with 5.8 GHz and the communication protocol was developed specifically for platoon. HMI unit has been developed for the interface between human driver and automated control system.[3] Mission of human driver during automated control mode is to survey the control state by using display of HMI unit. If control system will be broken, human driver will take over the steering and braking operation.

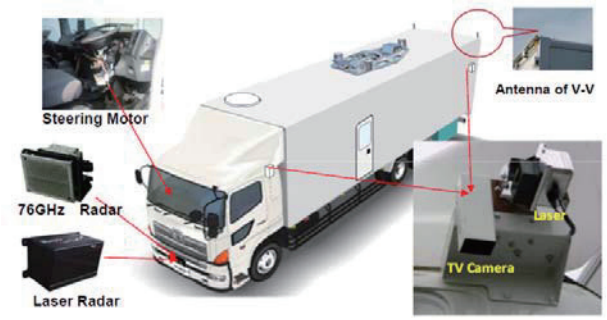

Fig.3 Experimental automated truck

5. Evaluation test result and demonstration

Controllability of lane keeping and gap distance has been evaluated on oval test track and new express-way under the construction. The lateral deviation on lane keeping control is approximately ±0.2 m during the curved road with 180 R. Longitudinal deviation for the Control of gap distance within platoon is approximately ±0.2 m at a constant vehicle speed of 80 km/h and ±1.0 m during the deceleration of 0.4 G.

It has been proven to achieve highly accurate controllability during emergency braking by using V-V communication.

Fuel economy of the platoon composed by tree heavy duty trucks has been evaluated on test track. The saving rate of fuel consumption due to gap distance is shown in Fig. 4. Fuel economy of platoon can be improved up to 15% at the condition of gap distance of 4.5 m compared to the single truck operation.

Finally, automated platoon composed by three heavy duty trucks and one light duty truck has been demonstrated successfully at gap distance of 4 m.

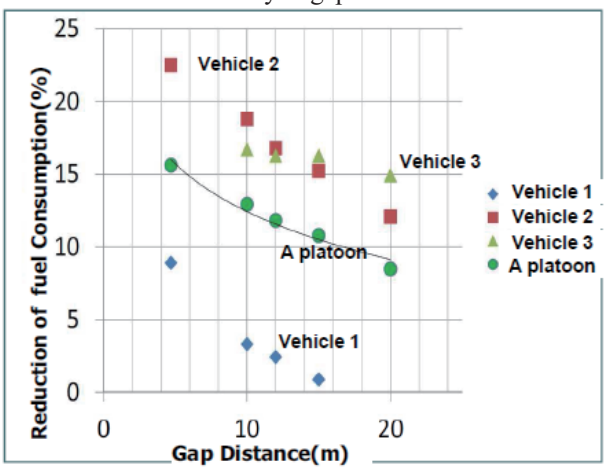

Fig.4 Result of fuel economy by platoon with 3 trucks

6. Conclusion

The automated platoon system with closed gap distance of 4 m, have been developed in order to improve fuel economy and safety on mixed highway traffic. Automated platoon composed from three heavy duty trucks and one light duty truck has been demonstrated successfully at gap distance of 4 m.

However, there are some non-technical issues to be solved so that automated platoon can be implemented to next freight transportation.

References

[1]S. Shladover, "Demonstration of Automated Heavy-Duty Vehicles" Path Report.

[2] T. Fukao," Autonomous Driving of a Truck Based on Path Following Control," 10th International Symposium on Advanced Vehicle Control, 2010

[3] S.Kato, " Human Machine Interface of Platoon Systems " JSAE proceedings, No.7-10,2010, pp.23-28

Tenth International Conference on Flow Dynamics
November 25-27, 2013, Sendai, Miyagi, Japan

Human Factor Research Using a Driving Simulator

Kimihiko Nakano

Interfaculty Initiative in Information Studies, University of Tokyo
E-mail knakano@iis.u-tokyo.ac.jp

ABSTRACT

Two recent topics on human factor research using a driving simulator are introduced. One is evaluation of driving comfort by activity of sternocleidomastoid(SCM) muscle of a passenger, and the other is evaluation of human-machine interface for an automatic platooning truck. To examine human responses, it is essential to carry out experiments since it is hardly possible to make a model of human behavior for numerical simulation. In both researches, driving simulators are utilized to conduct the experiments with safe and ease. The meaningful results are obtained in both researches through the experiments using the driving simulators.

1. Introduction

In the field of automobile engineering, higher importance is placed on human related topics such as comfort, human-machine interface, and safety. It is demanded to carry out human factor researches. As it is difficult to express human behaviors with some mathematical models, we need carry out experiments including humans. Although an experiment using a test car is one of the best methods, it brings risk of accidents. Then a driving simulator is utilized to analyze behaviors and responses of drivers and passengers. Two recent researches on human factor using driving simulators are introduced. The first one is evaluation of driving comfort by activity of sternocleidomastoid (SCM) muscle[1] of a passenger. As SCM is a muscle to keep position of the head, electromyography(EMG) signal of the SCM increases when the unwanted lateral acceleration grows. Usually an automobile having poor driving comfort produces unwanted lateral acceleration when it is steered, thus the comfort can be evaluated with the amplitude of the EMG signal. The effectiveness of the proposed method is examined through experiments using test cars and a driving simulator. The second one is evaluation of human-machine interface for an automatic platooning truck[2]. This research is carried out as a part of project of Development of Energy-saving ITS Technology, financially supported by New Energy and Industrial Technology Development Organization of Japan (NEDO)[3]. Driving environment of a cabin of the truck under automatic platooning control is reproduced on the driving simulator. Then human-machine interface of the controller for the automatic platooning is evaluated on the driving simulator. Through introducing these two research topics, direction of the human factor research on the automobiles and significance of the driving simulator in the research topic are discussed.

2. Evaluation of driving comfort

The possibility to use passenger`s EMG of SCM muscles as an objective evaluation indicator to vehicle dynamics is discussed. The SCM is in the neck, and its main function is keeping the head in the appropriate position. Two same cars are prepared for the experiments. One is the normal car, and the other is the modified car, whose body is reinforced to increase its rigidity. While the test cars were driven at the speed of 65km/h in a slalom course of 30m intervals, the EMGs of 5 subjects were measured as well as the relative acceleration in the car body. Figure 1 show RMS value of EMG signal of SCM muscle of all subjects. The RMS of the EMG in the modified car is significantly smaller than the normal car.

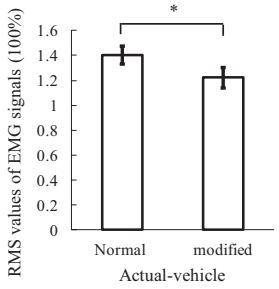

Fig. 1. RMS values of the EMG signals for SCM muscles in the test car experiments (mean ± S.D., and two-sample paired t-test: *P < 0.05 and n = 5).

The motion of the test car in the slalom course is reproduced in the driving simulator (DS), as shown in Fig. 2. Four motions are produced by adding the relative accelerations of the normal car (normal 100%), two times of it (normal 200%), the relative accelerations of the modified car (modified 100%), and two times of it (modified 200%). The EMGs of the SCMs of 10 subjects are measured on the DS. As shown in Fig. 3, RMS value in the modified car significantly lower than the normal car (P < 0.05 and n = 10).

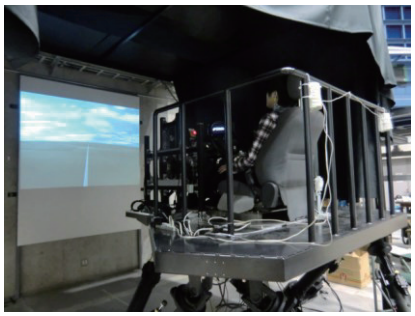

Fig.2 Photograph of the driving simulator.

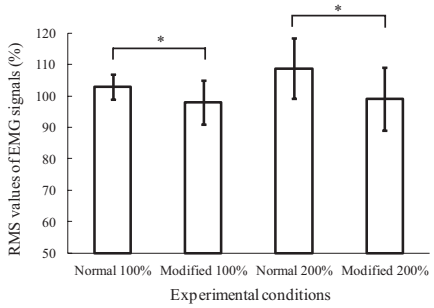

Fig. 3. RMS values of EMG signals in the DS experiments (mean ± S.D., and the two-sample paired t-test: *P < 0.05 and n = 10).

3. Human-machine interface of the controller for the automatic platooning truck

Human factors in automatic platooning are mainly about operations and conditions of driver during the processes of the formation and separation of the automatic platooning. Otherwise, it is also necessary to evaluate human-machine interface for the communication of driver and the system of the automatic platooning. As a novel technology in automobile field, a driving simulator for trucks is used for evaluate automatic platooning driving and its system considering human factors. A truck driving simulator, as shown in Fig. 4, was developed. In whole, a full-scale cabin of a real truck, steering equipment attached a servo-motor, an air seat, a sound generator based on the actual-vehicle driving of truck and control software are integrated into a driving simulator system to improve driver sense in a truck driving. TruckSim software, linked with Simulink, is connected with the host computer of DS using dSPACE. Then the Gap distance control and path following control for automatic platooning and adaptive cruise control (ACC) utilized for the actual platooning trucks, were built in the DS.

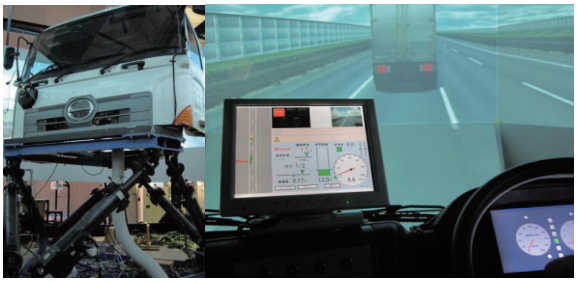

Fig. 4 The DS for the platooning truck.

For the application of the automatic platooning, three types of human-machine interface (HMI) are designed: numeric characters, graphics, and numeric characters & graphics types. Ten full-time truck drivers are cooperated in our study, for evaluation of HMI system. The mean age is 44.3 years old, license experience for truck is 15 years, driving experience of truck is 9.2 years, and driving frequency of truck is 41.2 hours/week. The subjects are asked to rank the three types of HMI system and to evaluate the information provided by the HMI system. The most popular display is that using both numeric characters and graphics, because its contents can be easily understood to master the driving conditions during the automatic platooning. The information items highly rated are control status of own truck by figure, current velocity, current gap distance, target gap distance, and number of trucks in transmission, which are closely related to safety. To the contrary, the drivers paid few attentions to the items of current acceleration, target acceleration, and instantaneous fuel economy.

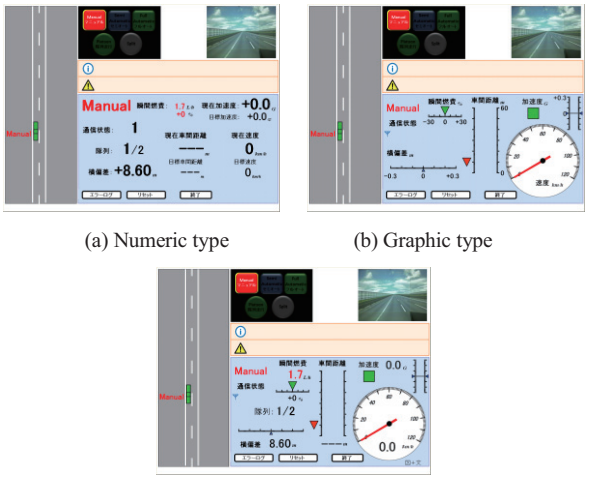

(a) Numeric type (b) Graphic type

(c) Numeric and graphic type

Fig. 5. Three types of HMI; Information is given with numeric characters in (a), graphics in (b), and both numeric characters and graphics in (c).

4. Conclusion

Two research topics are introduced. One is evaluation of driving comfort by activity of sternocleidomastoid(SCM) muscle, the other is evaluation of human-machine interface of the controller for the automatic platooning truck. In both researches meaningful remarks are derived from the DS experiments. The driving simulator will remain important as a tool to examine the human factors in the field of automobile engineering.

References

[1] R. Zheng, K. Nakano, Y. Okamoto, M. Ohori, S. Hori, Y. Suda, Evaluation of Sternocleidomastoid Muscle Activity of a Passenger in Response to a Car's Lateral Acceleration While Slalom Driving, IEEE Trans. Human–Mach. Syst, **43-4** (2013), pp.405-415.

[2] R. Zheng, K. Nakano, S. Kato, T. Ogitsu, S. Yamabe, K. Aoki, Y. Suda, Human-Machine Interface System for Simulation-based Automatic Platooning of Trucks, Proc. of 16th International IEEE Conference on Intelligent Transport Systems, October 6-9, 2013, Hague, The Netherlands, to be presented.

[3] S. Tsugawa, S. Kato, and K. Aoki, An Automated Truck Platoon for Energy Saving, 2011 IEEE/RSJ International Conference on Intelligent Robots and Systems, September 25-30, 2011, San Francisco, USA, pp.4109-4114.

Vehicle Innovations Bring Regional Community into the New Age
Fuel Cell Vehicle and Hydrogen Move to the 2015 Introduction

Katsuhiko Hirose
Project General Manager R&D Management Toyota Motor Corporation
Hirose_katsuhiko_aa@mail.toyota.co.jp

ABSTRACT

Hydrogen fuel cell is the long-waited technology to improve the environment and to alternate the energy to non oil energy source. It takes more than expected but finally commercialization is announced and infrastructure preparation is in progress all over the world. Potential of hydrogen is not only fuel for the automobile but also considered to be an important long time storage media for fluctuated renewable energy. This technology may change the local community to be able to produce and consume and to control by them self rather than import and controlled by the central capital. .

1. Introduction

Mobility is the one of the most basic desire of a human being. And since the invention of automotive the human being obtained the real freedom of moving. Last one and half century automotive itself changed from coal fueled steam to current gasoline fired hybrid vehicle. If you carefully check the fuel and technologies of vehicles, evolution of technologies are also carried out by the environmental restrain. This is very similar to the evolution of life.

Coal is replaced by the liquid fuel because of the limitation of range. Manual transmission is replaced by the automatic transmission because of the comfort and convenience. Next evolution was the introduction of electric drive this was due to the high oil price and brings the hybrid electric vehicle such as TOYOTA Prius to the market.

Next evolution is expected by the sustainability of the earth and brings the new technology “Fuel cell and hydrogen” to the market.

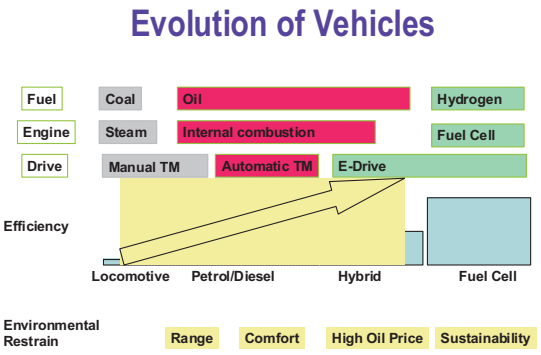

Fig. 1 Material innovation and Society

2. Progress and potential of Fuel Cell Vehicle

Hydrogen fuel cell was once a very expected technology to replace the oil burning vehicles. However engineers faced multiple difficulties to bring into the real road conditions. Day by day efforts of engineers and scientists solve the most of the problems such as durability, volume and range. then finally announced to bring the technology in to the market soon.

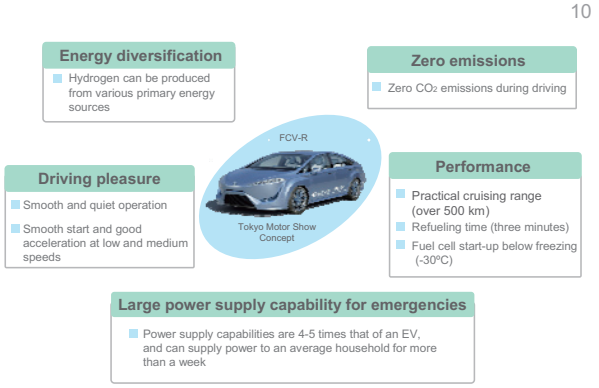

Fig. 2 Advantages of Fuel Cell Vehicle

Advantages of fuel cell vehicle are shown on figure2. In addition to the environmental performance such as zero emission, energy diversification the vehicle performance such as good drivability and slenderness are expected to realize. For the popularization of vehicle continence is very important fuel cell vehicle is now refueled within 3mininutes and is able to travel more than 500km. In addition to the normal performance it is now recognized to be an emergency power source since vehicle has a capability of generating electricity 10kw lever more than few days with stored hydrogen.

There are other zero emission vehicle and environmental friendly vehicle such as Battery Electric Vehicle (BEV) Plug-in Hybrid Vehicle (PHV). We expect those technologies will be segregated by the size and purpose of the mobility shown in figure 3.

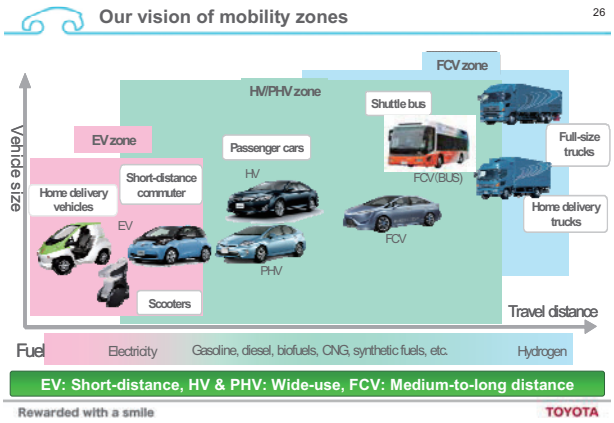

Fig. 3 Vision of Mobility Zone

3. Potential of Hydrogen

Hydrogen is already produced largely in the industry such as petroleum, chemical, fertilizer industries. Potential of those industries to provide hydrogen for early market is more than sufficient.

However recent increase of renewable energy power generation re-recognizes the potential of hydrogen as an energy vector to store the energy of this fluctuating energy source. In northern Europe hydrogen is spot light as a media to transfer the electricity to the south because of the lack of enough grid connection...

Efficiency of hydrogen just for store the electricity is lower than battery or pomp-up hydro. However the hydrogen has a big advantage of long time storage and potential of replacing more expensive/valuable fuel such as gasoline. It is now getting expected to co-grow the renewable electricity and hydrogen to accelerate carbon free world.

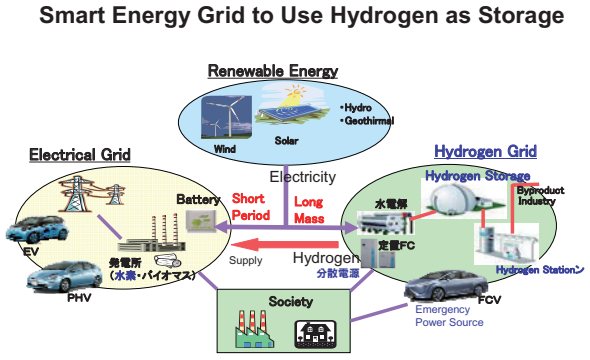

Fig. 4 Smart Grids to Use Hydrogen as Storage

4. Conclusion

Increased hydrogen usage in the society may increase the potential of regional area than ever since use of renewable enhance the regional economic balance to improve. Because of renewable energy is richer in dis centralized area either close to the sea or high mountain area rather than big city. This may lead the preferable economic condition to the local area and bring the area into self sustainable for both energy and fuel for mobility. Cheaper energy and good living condition may attract more industries and people.

5. Concluding remarks

Several car manufacture already announce introduction of fuel cell vehicle into the market, it may be the beginning of new era for the human being to enjoy the mobility of freedom without any deterioration of environment and the regional society going to the center of living life.

References

[1] K. Hirose, Phil. Trans. R. Soc. A 368 (2010) 3365.

Tenth International Conference on Flow Dynamics
November 25-27, 2013, Sendai, Miyagi, Japan

NDT-Innovations In The Automotive Industrial Sector And To Light-Weight Materials

Gerd Dobmann
Fraunhofer-IZFP, Campus E 3 1, 66123 Saarbruecken, Germany
gerd.dobmann@izfp.fraunhofer.de

ABSTRACT

The challenge to produce cars with reduced weight in order to reduce then also fuel consumption and waste was in the last two decades always a driver for innovations in materials design and production. So far new materials were developed or conventional-ones were optimized there was also always the question to answer: Do we have proper NDT-technologies to characterize the quality of the optimized material components and to detect – may be now new type of irregularities – coming-up with the new materials and/or the new production technologies?

1. Introduction

Fraunhofer-IZFP is engaged in 3 industrial sectors where light-weight materials and components, on one hand are produced and on the other hand are consumed, respectively applied. In the 1st group one can find steel and other metal producing industries and the chemical industry producing polymers and polymer-based composites. In the other group we have mainly car manufacturers (automotive industry), aerospace industry and their supplying industry partners.

The here presented contribution is a selection of specific examples of Fraunhofer-IZFP solutions for the above mentioned industries which are introduced in routine practice.

2. Steel Industry

Concerning light-weight materials for car and especially car body developments the progress is by high-strength material allowing to reduce weight and therefore sheet thickness and reducing fuel consumption. This has its benefits also to reduce CO_2 and to contribute therefore against the worldwide green house effect.

2.1 NDT for high-strength steel sheets

In charge of important European steel manufacturers Fraunhofer-IZFP has developed NDT for material characterization technology [1] allowing mechanical property determination in terms of yield strength (Rp0.2), tensile strength (Rm) and texture characteristics r_m and Δr (planar and vertical anisotropy), All of these parameters have to be controlled in a very narrow scattering band concerning the properties along the length of a steel sheet (2.5 km coil length) and the full width.

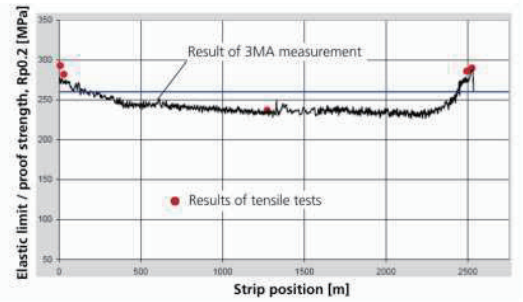

Fig. 1 Yield strength Rp0.2 predicted by micromagnetic NDT [2]

Fig.1, as example, documents the NDT materials property prediction by micromagnetic NDT [2] of which the prediction accuracy is in the range of ~ 10% compared with destructive techniques.

2.2 Cast Iron with lamellar and vermicular graphite

To reduce the weight of the power supply unit the car combustion engines cylinder crankcases can be made of cast iron with vermicular graphite (GJV), because this material in a Diesel engine allows a higher loading pressure even by reduced wall thickness. However, the service live of machining tools is substantially smaller during processing an engine block made from GJV compared with a block from cast iron with lamellar (flake) graphite (GJL) [3].

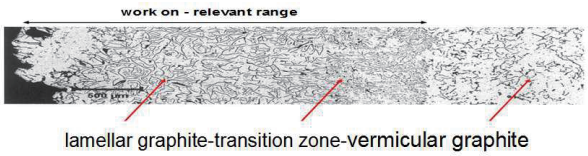

Fig. 2 Microstructure gradient obtained in a cylinder region of a cast engine

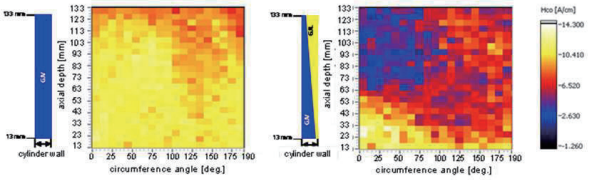

Fig. 3 Gradient of the magnetic coercivity, left hand side GJV cast cylinder block, right hand side GJV/GJL microstructure gradient

This disadvantage can be eliminated by an innovative casting technology that produces a continuous microstructure gradient in the cast iron from lamellar graphite at the inner surface of the cylinders to vermicular graphite in radial direction. By implementing some chemical additives into the core of the mold which can diffuse in the cast iron during the solidification process in the mold the gradient with a continuous transition from lamellar graphite and finally vermicular graphite is obtained. However, the technology can only be used by the casters so far the gradient quality can be characterized and monitored by NDT. Fig.2 documents in a micrograph such a gradient beginning at the left side with cast iron (inner cylinder surface) and lamellar

graphite followed by a transition region and vermicular graphite on the right side.

3MA techniques always cover a certain analyzing depth depending on the magnetizing frequency and geometrical parameters of the magnetization yoke, etc. So far the gradient has different graphite compositions within the analyzing depth, 3MA quantities should be influenced. Based on measurements at an especially designed calibration test specimen set 3MA quantities were selected to image the gradient with optimal contrast. As reference quantity to calibrate 3MA the local thickness of the GJV-layer was evaluated by using micrographs and optimized pattern recognition algorithms in the microscope. A special designed transducer head was developed to scan the cylinder surface by line scans in hoop direction and rotating the head, then shifting the head in axial direction to perform the next line scan. Fig. 3 shows as example the coercivity images derived from the tangential magnetic field strength evaluation (H_{CO}).

3. Carbon Fiber Reinforced Plastics (CFRP)

As CFRP laminates have a complex lamination structure with different fiber directions (0°, 90°, ± 45°) the production process of lamination of the prepregs is complicated and different kind of quality limiting structure irregularities can occur. Therefore NDT after production is a need as well as in aerospace industries in-service inspection of the highly stressed components. As the structures are very often sandwich like where in between two CFRP plates honeycomb structures are embedded the inspection tasks are much more difficult.

However, new developments in NDT have brought progress in the inspection applications.

3.1 Eddy current testing

As CFRP has electrical conductivity the material can be inspected using eddy current (EC) technology [4]. Fig. 4 shows images of the eddy current impedance obtained by an automated scan with an EC-transducer. Frequency range of the equipment is between 10 Hz and 10 MHz. A multi-frequency approach can be performed by time-multiplexing and different typical structural defects can be detected optimal at different frequencies.

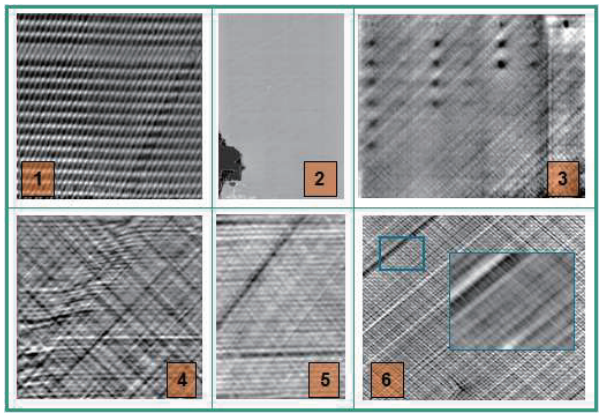

Fig. 4 Defect detection by EC in CFRP

So far direction sensitive transducers are applied angular oriented defects are detected (missing rovings (1, 5, 6), foreign body embedding (here test pieces, fuzzy balls, 3), delaminations (2), and ondulations (4).

3.2 Thermography

Flash pulsed thermography [5] can detect impact damage which by human eye is not detectable. Fig. 5 shows a thermal image of such damage in a CFRP plate

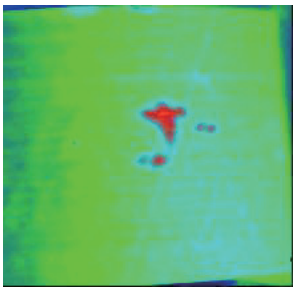
Fig. 5 Impact damage detection by pulsed thermography, field of view 60 mm × 60 mm

4. Conclusions

NDT has developed new technology to inspect light-weight materials. Successful applications were presented to

- high strength steel material property determination
- to the characterization of light-weight steel casting
- to EC and thermal CFRP inspection.

In the oral contribution also results to ultrasonic testing and imaging and X-ray CT will be discussed.

References

[1] G. Dobmann et al., Proceedings of the International Non-Destructive Testing Symposium and Exhibition, 17.-19. 04. 2008, Istanbul University.

[2] G. Dobmann, Proceedings of the 18th European Conference on Fracture, 30. 08.-03. 09. 2010, Dresden.

[3] G. Dobmann, Proceedings of the 10th ECNDT, Moscow, 2010.

[4] http://www.cfk-convention.com/fileadmin/Convention_2013/Referenten/Vortraege/CFK_Conv2013_HEUER.pdf

[5] C. Beine et al., Proceedings of the International Symposium on NDT in Aerospace, Hamburg, 22.-24.11.2010, CD by the German Society for NDT, DGZFP, Berlin.

Compact-Sizing of Optical Topography Technology (NIRS)

Kiyoshi Hasegawa
Hitachi Ltd. Business Incubation Division, Tokyo 101-8608 Japan
kiyoshi.hasegawa.yp@hitachi.com

ABSTRACT

There are several neuro-imaging methods, however, most of them need specialized facilities and high maintenance cost. Recently the need for measuring in the daily-life-like environment is increasing, and Hitachi succeeded to develop compact-sized Optical Topography (OT) units. Compact-sized units will realize the measurement in the various environment efficiently and economically .In this symposium, I will explain the basic technology of NIRS and potential future expansive usage.

1. Introduction

21st century is so called as neurotechnology era, while 20th century is called as physics era. Since the world faces globalization, there is an increasing need to know human itself better. In many case in the past, the way to know how people are feeling and thinking, are the subjective evaluation methods, such as questionnaire sheet or group interview. But recently many noticed that subjective evaluation methods have certain limitation, because it needs a verbal interpretation between the questioner and respondent. For knowing how people feels and think, there are some new solutions created, such as behavior measurements, brain function measurements, and etc.

In the past, in order to measure brain function, it is first necessary to prepare a specialized measuring room which needs a large initial investment as well as maintenance fee. Some measurement tools must fix the examinee's body tight.

What is highly required in the market is the tool measureable in the daily-life-like environment. Hitachi believe that OT technology would be one of the closest and best applicable solution, compared with other brain measurement tools.

2. Method

1) Background of development

OT Technology was developed by Hitachi's Central Research Lab. in 1995, and in 2001, the first medical grade product was introduced by Hitachi Medical Corporation.

Compact-sized product was developed and introduced from 2010, and there are several types of products available now.

2) Basic Principle of OT

OT technology is based on very weak near-infrared light around 800nm, and it can be used safely from neonates to seniors. Measurement system consists of the combination of irradiation sensor and detection sensor. The sensors are designed to be positioned at 3cm distance in square. The irradiated light from the surface of head skin goes inside of the brain and scatters, and a portion of light path, going up to 2 to 2.5cm depth and then come back to the surface of the head (Fig. 1).

The light around 800nm is known as a very good wavelength to measure human body, which goes through the skin, bone, and human tissue, but is absorbed by hemoglobin.

When a part of brain becomes active, it needs more oxygen and glucose. Oxygen is carried by hemoglobin, and when the brain activity becomes higher, the increase in hemoglobin also occurs. The brain activity refers as an increase or decrease of the returned light intensity. When the brain activity becomes higher, the increase in hemoglobin occurs and the decrease of returning light intensity occurs. On contrary, when the brain activity becomes lower, the decrease of hemoglobin occurs and the increase of returning light intensity occurs[1].

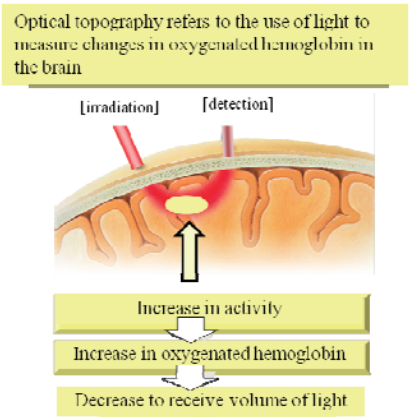

Fig.1 Mechanism of measurement

3) Comparison of measurement technologies

Compared with other measurement technologies, OT has certain merits to be usable in the daily-life-like environment. First, it can be designable as transportable and also wearable. Secondary, it is not affected by the outside radio noises, since the measurement is not electric wave, but near infrared light. The drawback of OT is that it is not possible to measure the deep portion of brain, but the surface of the brain (cerebral cortex part). And also spatial resolution is 3cm, which is wider than fMRI. Nevertheless OT is best fit to measure human's brain activity in cerebral cortex in the daily-life-like environment (Fig.2).

	Signal	Measurable in daily life like condition	Compact Sizing	Simultanous measurement	Realtime measurement	Easiness to wear
EEG	nerve	△	◎	◎	○	○
MEG	nerve	X	×	△	×	×
fMRI	Blood Volume Change(deoxy)	X	×	×	△	×
Optical Topography NIRS	Blood Volume Change	○	◎	◎	○	○

Fig. 2 Comparison of measurement technology

3. Development of Compact-Sized OT

Hitachi has developed 2 types of Compact-Sized OT, which are available commercially in research field. Those 2 models are specialized for forehead measurement.

1) Wearable Optical Topography (WOT series)

WOT's design target is that the unit should be measureable in the daily-life-like environment, so mobility is one of the most important design concept. It employs non-fiber optics ergonomic design, newly developed 2-wave-length built-in laser capsule, rechargeable built-in battery, and wireless LAN for non-cable connection to the host control computer. In addition, new probe design was adopted and soft touch style probe was realized (Fig. 3) [2].

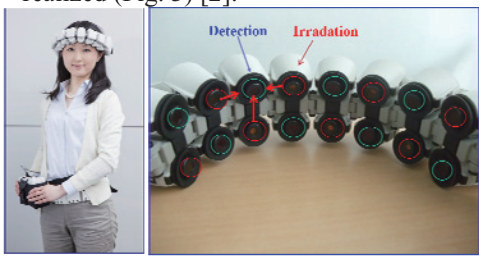

Fig. 3 Wearable form factor and new probe design

Since it employs wireless LAN, Wearable OT's another merit is to measure multiple persons simultaneously. Currently, up to 4 persons measurement becomes possible (Fig. 4), and it is effective to measure people's communications (Fig. 5), interactions, and mass data collection at one time[3].

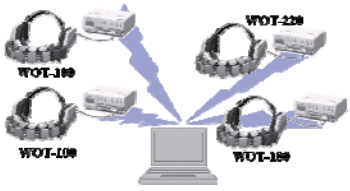

Fig. 4 Wireless System

Fig. 5 Scene of Communication measurement

2) 2 Channel NIRS(HOT121)

Furthermore, the smaller form factor HOT121 was developed to be able to wear headset by examinee itself and start measurement in the very short time. HOT121 measures 2 points of forehead, targeting working memory area (Fig. 6).

Fig. 6 Design of HOT121

Later than HOT121, by the joint research effort with Tohoku University and Hitachi, 1-channel Wireless Proto-Type System was developed (Fig.7). This Proto-Type System enabled up to 20 persons measurement simultaneously at one time.

Fig. 7 Proto-Type System of 1-channel

4. Concluding remarks

By Compact-sized OT hardware, the measurement scene will expand wider.

In the future, by the wireless communication technology, measurement scheme may lead to collect more data and do analysis in almost realtime (Fig. 8).

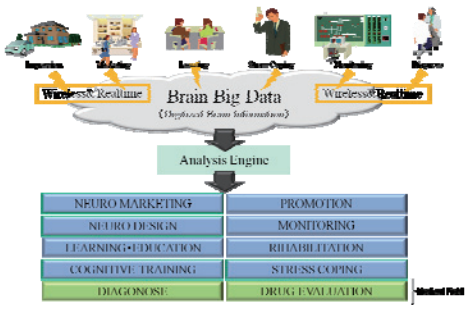

Fig. 8 Future Image

References

[1] A. Maki, Y. Yamashita, Y. Ito, E. Watanabe, Y. Mayanagi, H. Koizumi, *Med. Phys.*, Vol. 22(No. 12), pp. 1997-2005, 1995.

[2] Atsumori H, Kiguchi, M., Obata A, Sato H, Katura T, Funane T, Maki A, Rev Sci Instrum. 80, 043704 (2009).

[3] Kiguchi, M., Atsumori H, Fukasaku I, Kumagai Y, Funane T, Maki A, Kasai Y, Ninomiya A, Rev Sci Instrum. 83, 056101 (2012).

Tenth International Conference on Flow Dynamics
November 25-27, 2013, Sendai, Miyagi, Japan

Solvothermal Synthesis of Ceria Based Metal Oxides for Automotive Catalysts

Qiang Dong, Shu Yin, Tsugio Sato
Institute of Multidisciplinary Research for Advanced Materials, Tohoku University, 2-1-1 Katahira, Aoba-ku Sendai 980-8577, Japan
tsusato@tagen.tohoku.ac.jp

ABSTRACT

Since ceria based oxides possess the oxygen storage capacity (OSC), it has been used as a co-catalyst of the automotive three-way catalyst (TWCs). However, ceria based oxides possessing high surface area tends to fall surface area and consequently, OSC when used at high temperatures. Herein, we describe the preparation of novel ceria based metal oxides of $Ce_{1-x-y}Zr_xM_yO_{2-d}$ (M= Sn, Al, Co, Fe, etc.) supported by Pd-Al_2O_3 by solvothermal method. The as-prepared novel ceria based metal oxides, such as $Ce_{0.5}Zr_{0.5}Sn_{0.1}O_2$/Pd-$Al_2O_3$ have the potential to be used in advanced catalytic converters for automotive TWCs.

1. Introduction

Ceria (CeO_2)-based materials have been recognized as an important component of the three-way catalysts (TWCs) because of their excellent oxygen storage capacity (OSC). The major role of it is to maintain an air/fuel ratio around 14.7 during engine operation, and TWCs have high pollutant conversion efficiency.[1]

Since 1990s, CeO_2-ZrO_2 oxides have gradually replaced pure CeO_2 in the TWCs to reduce the emission of toxic pollutants (CO, NO_x, hydrocarbons, etc.) from auto mobile exhaust, due to their enhanced OSC and improved thermal stability at elevated temperatures. Although CeO_2-ZrO_2 oxides have been studied extensively, there are few reports on the preparation of $Ce_{1-x-y}Zr_xM_yO_{2-d}$ in the literature. We prepared novel oxygen storage materials of $Ce_{1-x-y}Zr_xM_yO_{2-d}$ (M= Sn, Al, Co, Fe, etc.) via a solvothermal route, and found that they showed excellent performance as the co-catalysts of TWCs.[2-5]

In the present study $Ce_{0.5}Zr_{0.5}Sn_{0.1}O_2$/Pd-$Al_2O_3$ (hereafter CZS/P-A) catalyst was selected as a representative ceria based metal oxide to describe in details.

2. Method

The stoichiometric amounts of $(NH_4)_2Ce(NO_3)_6$, $ZrO(NO_3)_2$ and $SnCl_4$•$5H_2O$ were dissolved in 60 ml distilled water. NH_4OH solution was slowly dropped into the above mixed solution, where the pH value was maintained at 9. The yellow mixed solution was introduced in a 100 ml Teflon®-lined autoclave, which was maintained at 200˚C for 24 h, then cooled to room temperature naturally. The obtained products were washed with distilled water and dried in air at 100˚C for 12 h to form the $Ce_{0.5}Zr_{0.4}Sn_{0.1}O_2$. Then, $Ce_{0.5}Zr_{0.5}Sn_{0.1}O_2$/Pd-$Al_2O_3$ catalysts were prepared by mechanically mixing $Ce_{0.5}Zr_{0.4}Sn_{0.1}O_2$ and Pd-Al_2O_3 powder with the weight ratio of $Ce_{0.5}Zr_{0.4}Sn_{0.1}O_2$: Pd-$Al_2O_3$=50:50, where the Pd content in Al_2O_3 was 2 wt %. All samples were finally calcined at 1000˚C for 20 h in air. CeO_2/Pd-Al_2O_3 and $Ce_{0.5}Zr_{0.5}O_2$/Pd-Al_2O_3 ((hereafter C/P-A and CZ/P-A, respectively) were also prepared by the same method.

The morphology and size of the samples were determined by a transmission electron microscopy (JEOL JEM-2010). The specific surface area and pore size were measured using BET analysis (NOVA 4200e).

The OSC of catalysts was determined using a thermogravimetric differential thermal analysis (TG-DTA, Rigaku TAS-200). The mixed gas of CO-N_2 and air was flowed alternatively at 150-600˚C.

The CO oxidation activity of the synthesized sample was evaluated in a fixed-bed flow reactor by passing gas mixtures of 2 vol.% CO in N_2 and 2 vol.% O_2 in N_2 at a rate of 500 cm^3 min^{-1} over 0.15 g sample. The samples were heated at a heating rate of 10˚C min^{-1} from room temperature to 600˚C. A gas FTIR spectrometer (MIDAC Co., IGA-4000) was employed for in situ analysis of gas composition. The conversion of CO was obtained by using the formula X_{CO} = (1-[CO] / $[CO]_0$) ×100 %, where $[CO]_0$ and [CO] are initial and transient concentration of CO, respectively.

3. Results and Discussion

The morphology and crystalline growth of samples were confirmed by TEM images (Fig 1). The crystalline sizes of CZ and CZS on Pd-Al_2O_3 were about 60 and 40 nm, respectively. However, the C/P-A exhibited large particle size of 100-150 nm as shown in Table 1.

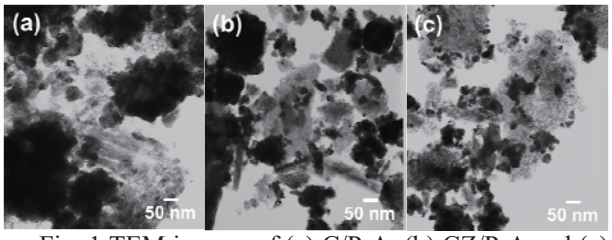

Fig. 1 TEM images of (a) C/P-A, (b) CZ/P-A and (c) CZS/P-A samples

The BET nitrogen adsorption-desorption analysis was undertaken to measure the specific surface area of as-prepared samples. As a result, the CZS/P-A displayed much higher specific surface area (38 m^2 g^{-1}) than C/P-A (22 m^2 g^{-1}) and CZ/P-A (9 m^2 g^{-1}) as shown in Table 1.

Table 1 Characteristics of C/P-A, CZ/P-A and CZS/P-A samples

Chemcial compositon	Particle size (nm)	Surface area (m^2 g^{-1})	OSC (μmol-O g^{-1})
C/P-A	15	9	142
CZ/P-A	18	22	456
CZS/P-A	20	38	621

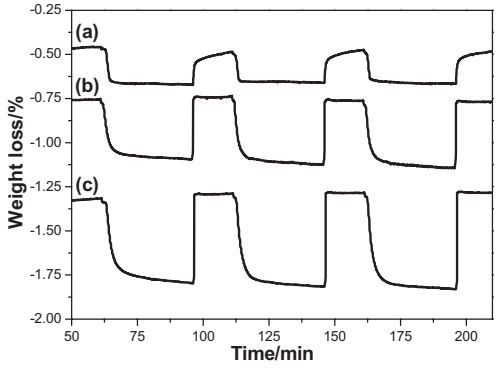

Fig. 2 Oxygen release/storage properties (TG profiles) of (a) C/P-A, (b) CZ/P-A and (c) CZS/P-A samples at 600 ˚C.

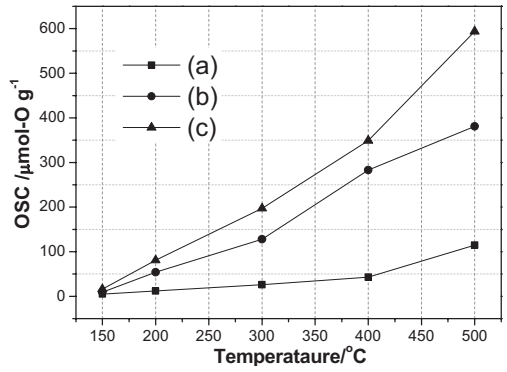

Fig. 3 OSC values of (a) C/P-A, (b) CZ/P-A and (c) CZS/P-A samples at different temperatures

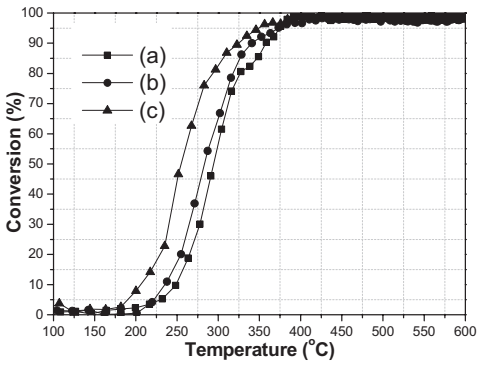

Fig. 4 CO oxidation activity curves of (a) C/P-A, (b) CZ/P-A and (c) CZS/P-A samples

The OSC values of the samples were determined at 600˚C with a continuous flow of CO-N_2 gas and air alternatively. Figure 2 shows the typical oxygen release/storage profiles of the C/P-A, CZ/P-A and CZS/P-A samples at 600˚C with time. CZS/P-A exhibited the highest OSC of 621 μmol-O g^{-1}, when compared with those of C/P-A (142 μmol-O g^{-1}) and CZ/P-A (456 μmol-O g^{-1}) samples (Table 1). Moreover, the temperature-dependent OSC was evaluated by increasing the temperature in a stepwise manner from 150 to 500°C, as shown in Figure 3. It is indicated that the OSC increased with temperature for all samples, and CZS/P-A showed higher OSC than those of CZ/P-A and C/P-A at the same temperature, for example, OSC values of C/P-A, CZ/P-A and CZS/P-A were 12, 54 and 81 μmol-O g^{-1} at 200˚C, respectively.

The activity curves of CO oxidation for all samples are plotted in Figure 4. Comparing with the light-off temperatures of C/P-A (295˚C) and CZ/P-A (283˚C), it can be concluded that CZS/P-A shows the lowest light-off temperature of 245˚C, indicating that CZS/P-A was the most active catalyst. Furthermore, the light-off temperature of CZS/P-A is lower than those of $Pd/Ce_{0.7}Zr_{0.3}O_2$-Al_2O_3 (271˚C) [7] and $Pd/Ce_{0.67}Zr_{0.33}Sr_{0.05}O_{2.05}$ (268˚C) catalysts[8] which were prepared by mechanically mixing of Al_2O_3 with $Pd/Ce_{0.7}Zr_{0.3}O_2$ and $Ce_{0.67}Zr_{0.33}Sr_{0.05}O_{2.05}$ formed by impregnation method.

4. Concluding

A new ceria based metal oxide for automotive catalyst of $Ce_{0.5}Zr_{0.4}Sn_{0.1}O_2/Pd$-$Al_2O_3$ was prepared via a sovlothermal process. $Ce_{0.5}Zr_{0.4}Sn_{0.1}O_2/Pd$-$Al_2O_3$ showed the high OSC even after calcination at 1000˚C for 20 h. Studies using CO oxidation as a model reaction, showed that the high oxidation activity of the sample at low temperatures correlates with their enhanced OSC. The prepared $Ce_{0.5}Zr_{0.4}Sn_{0.1}O_2/Pd$-$Al_2O_3$ has the potential to be a key material in advanced catalytic converters in the design of excellent TWCs.

Acknowledgements

This work was partly supported by Grant-in-Aid for Young Scientists B (25870054) and Grant-in-Aid for Challenging Exploratory Research (24651068) from the Japan Society for the Promotion of Science (JSPS), Rare Metal Substitute Materials Development Project of New Energy and Industrial Technology Development Organization (NEDO), Japan and the Management Expenses Grants for National Universities Corporations and the Grants-in-Aid for Scientific Research Program for Challenging Exploratory Research from the Ministry of Education, Culture, Sports and Science for Technology of Japan (MEXT).

References

[1] J. Kaspar, P. Fornasiero, M. Graziani, Catal. Today, **50** (1999), R285.
[2] Q. Dong, S. Yin, C. S Guo, T. Sato, Catalysis Sci & Tech., **2(12)** (2012), R2521.
[3] Q. Dong, S. Yin, C. S Guo, T. Sato, Nanoscale Res. Lett, **7:542** (2012), R1.
[4] Q. Dong, S. Yin, C. S Guo, T. Sato, RSC Adv., **2** (2012), R12770.
[5] Q. Dong, S. Yin, C. S Guo, X. Y. Wu, T. Kimura, T. Sato, Mate. Res. Bull., in press
[6] M. W. Zhao, M. Q. Shen, J. Wang, J. Catal. **248** (2007), R258.
[7] M. Yang, M. Q. Shen, J. Wang, J. Wen, M. W. Zhao, J. Wang, W. L. Wang, J. Phys. Chem. C, **113** (2009), R12778
[8] M. Q. Shen, J. Q. Wang, J. C. Shang, Y. An, J. Wang, W. L. Wang, J. Phys. Chem. C, **113** (2009), R1543.

Tenth International Conference on Flow Dynamics
November 25-27, 2013, Sendai, Miyagi, Japan

Fine Dry Cleaning Technology Using Supercritical CO_2

Hiroshi Inomata, Yoshiyuki Sato, Masaki Ota, Takumi Ono
Research Center of Supercritical Fluid technology, Graduate School of Engineering, Tohoku University
6-6-11, Aoba, Aramaki, Aoba-ku, Sendai, 980-8579,
inomata@scf.che.tohoku.ac.jp

ABSTRACT

We has developed a supercritical CO2 cleaning system and constructed its equipment based on the thermally-driven solvent circulation, whlch has the advantage of continuously refreshing the cleaning solvent dung operation and allows seamless cleaning and rinsing operations. This article explains our developed equipment and its principle that may be usefu1 in understanding cleaning mechanism, and also shows three applications of the cleaning system; fine precise devices, cloths dry cleaning, ultrafine filter regeneration/recycling.

1. Introduction

Supercritical fluids have been widely used in extraction, purification, and recovery processing mainly because of their capability of controlling physical properties (such as density and viscosity) between those of liquid and gas by manipulating temperature and pressure conditions. Among various fluids, CO_2 can reach its supercritical state easily because of its mild critical point (Tc=31°C and Pc=7.38MPa). In addition, supercritical CO_2 (Sc-CO_2) exhibits high solubility for non-polar substances as well as low surface tension, leading to the recognition that Supercritical CO_2 is an effective solvent in cleaning application.

Sc-CO_2 can dissolve many organic contaminants, penetrate into very narrow gaps/spaces and remove particles through kinetic energy transfer, which are important features in cleaning applications. Use of CO_2 in cleaning can avoid energy intensive drying steps and furthermore prevent re-contamination by residual solvent due to easy evaporation by depressurizing.

We have constructed supercritical cleaning equipment based on the thermally-driven solvent circulation, which has the advantage of continuously refreshing the cleaning solvent during operation and allows seamless cleaning and rinsing operations. Then the developed cleaning system was applied and evaluated its performance for precise devices cleaning, clothes dry cleaning and air filter cleaning.

2. Cleaning Solvent Features

It has been pointed that the roles of solvent in wet cleaning processes are energy transfer of cleaning driving forces to the objectives and stable dispersing of removed dirt component in solution. To attain the roles, the following properties are requested;

- Dissolving capability
- Dispersing capability
- Surface activity
- Chemical reactivity
- Adsorption capability

Sc-CO_2 can provide and smoothly control these required by tuning temperature and pressure, and by adding suitable entrainers. Especially low surface tension is a very nice feature which enables to penetrate into nanometer-scale spaces and not to generate breakage/shrinkage of nano-structured matrix by surface tension.

3. Cleaning System Development

We propose a thermally-driven convection circulation system in which CO_2-transport is induced by density differences in the supercritical region. Since changes in temperature can cause large density differences in the near/supercritical region, the system provides a method to create large solvent fluxes that can be used in practical cleaning systems. Further, the proposed system, which does not require any plunger or piston type pumps to deriver and circulate the solvent, has the possibility for reducing/minimizing particle generation that can be critical to some applications such as precise device cleaning. The flow rates as a function of operating conditions were shown to be suitable for practical applications both by measurement and a simple fluid dynamic simulation.

Based on the above mentioned thermally-driven circulation system, we has designed a supercritical cleaning equipment, which consists of cleaning/washing part, separation part, solvent evaporating part and solvent liquefying part. The outlet stream including dirt components from a cleaning part is depressed to induce vapor/liquid phase separation and transferred to evaporation part where solvent is evaporated to recycle and to remove the dirt component. This evaporation is strongly assisted by solvent condensation in a liquefying part. The liquefying part is located at higher position to allow for liquefied solvent to flow down to the cleaning part in terms of the driving force from gravimetrical potential energy difference. Through these phenomena, the proposed equipment has the advantage of continuously refreshing the cleaning solvent during operation and allows seamless cleaning and rinsing operations.

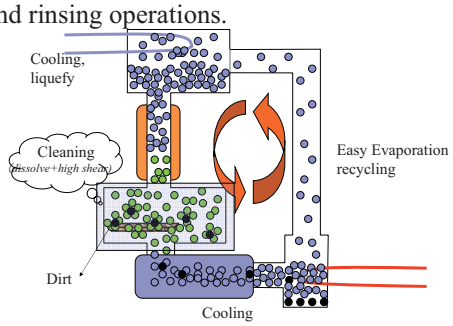

Fig.1 Thermally-driven circulation principle

In fabricating the cleaning equipment, we added expansion pumps to increase the solvent circulation rate for improving cleaning performance. The pump is also thermally operated, where the solvent can be forced to flow with very high velocity from very high pressure difference from high expansion coefficient by heating the liquefied CO2. Therefore it would be noted that the proposed system induces the temperature distribution in the equipment and utilizes the difference of vapor pressure and density, and the coefficient of thermal expansion as driving force.

The developed cleaning equipment is shown in Fig.2, showing from view and also backside view.

Fig.2 Photos of developed claning system.
(Top: Front view, Bottom: Backside View)

4. Applications of Proposed Cleaning System

4.1 Precise Mechanical Devices

Considering the features of the proposed system, we have tried to apply the system to very fine structured metal parts. We prepared test pieces using SUS plate and was as shown in Fig.3.

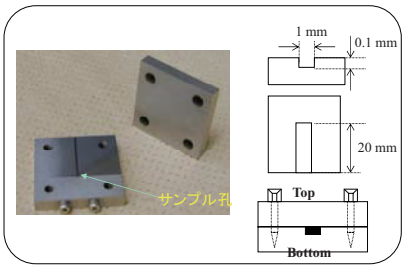

Fig.3 Test pieces

The experiments were carried out for SCF method and also water-solvent cleaning as reference, which used swing to promote cleaning efficiency.

The results shown in Fig.4 clearly indicated that SCF method could remove wax from very fine hole without swing, indicating high penetrating capability of this method. Similar results were obtained for practical devices such as ball bearing, LCD panel, etc.

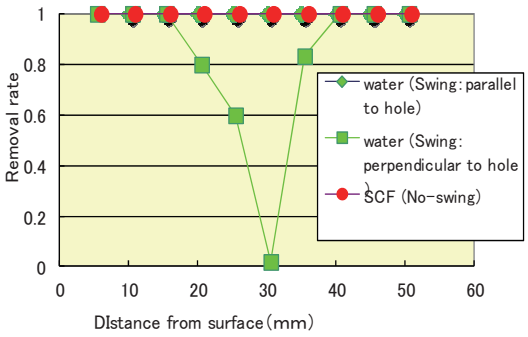

Fig.4 Cleaning results of test pieces

4-2. Cloths Dry Cleaning

We have firstly tested the washing capability of the system by cleaning test samplers made of various kinds of textures, which were artificially dirtied by dyes. The washing rate was evaluated in terms of color change by a brightness measurement. Real cloths were also washed and showed similar good results.

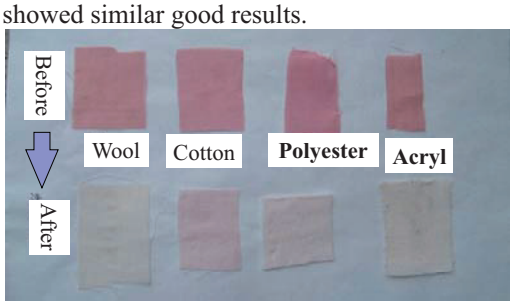

Fig.5 Dry Cleaning of cloth textures

4-3. Filter Cleaning/Recycling

We studied the cleaning of HEPA filters using supercritical CO2. The effects of supercritical CO2 cleaning on filter material and filter performance were experimentally investigated by using model sample filter cleaning. The cleaning performance was assessed by the weight recovery of the filter media as well as by the recoveries of their collection efficiencies and pressure drops. Now this technology has been applied to HEPA and chemical filters of activated carbon.

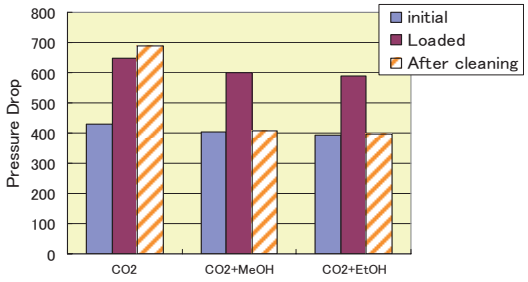

Fig.6 Filter elements cleaning results

5. Concluding remarks

The experimental results revealed that this technology can wash various organic and inorganic materials without adding any detergents with keeping a certain cleaning level, indicating the wide applicability of the CO_2 dry cleaning technology.

Tenth International Conference on Flow Dynamics
November 25-27, 2013, Sendai, Miyagi, Japan

Fabrication and OSC Property of Oriented Fe-based Complex Oxide Grains by Microwave Irradiation

Takumi Nakajima, Yamato Hayashi, Jun Fukushima, Hirotsugu Takizawa
Department of Applied Chemistry, School of Engineering, Tohoku University, 6-6-07 Aoba Aramaki, Aoba-ku, Sendai, 980-8579, Japan
nakajima@aim.che.tohoku.ac.jp

ABSTRACT

We synthesized delafossite-type $CuFeO_2$ by microwave irradiation and applied for oxygen storage materials. The temperature of starting materials rose rapidly by microwave irradiation and we obtain almost single-phase 3R-delafossite-type $CuFeO_2$. $CuFeO_2$ has layered structure and $CuFeO_2$ grains have anisotropically grown in perpendicular to c-axis. It was suggested microwave heating promoted the anisotropic grain growth. From the OSC measurement, anisotropic $CuFeO_2$ synthesized by microwave irradiation shows high OSC value as compared to conventional heating.

1. Introduction

Three-way catalysts (TWCs) have been developed to remove the pollutants such as carbon monoxide (CO), nitrogen oxide (NO_x), and hydro carbon(HC). TWCs consist of noble metal catalyst and promoters supported on carrier. Promoters play important roles in TWCs that suppress the oxidative–reductive compositional fluctuation in exhaust emission. In recent years, cerium-zirconium oxides based materials are widely used as the promoters because of the large oxygen storage capacity (OSC)[1,2]. However, rare earth elements such as Ce become more and more precious and expensive every year, and alternative materials become necessary.

In order to develop an rare earth-free oxygen storage material, we focused on delafossite-type $CuFeO_2$ (at see Figure 1).

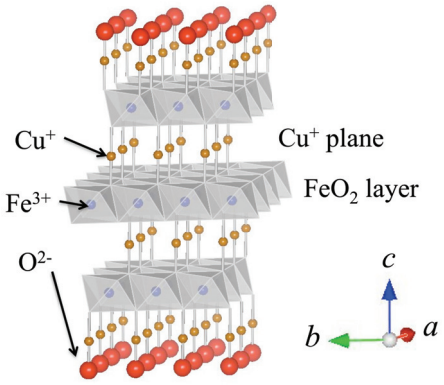

Fig. 1 Crystal structure of delafossite-type $CuFeO_2$

This complex oxide consists of relatively rich elements (Cu, Fe) and exhibits oxygen storage/release behavior at low temperature[3] due to formation of non-stoichiometry $CuFeO_{2+\delta}$. In this compound, FeO_6 octahedra are edge-connected leading to FeO_2 layers, which are stacked along the c axis. This FeO_2 layers are connected together with triangular metallic planes of monovalent Cu. This Cu^+ cation is linearly twofold-coordinate with oxygen of upper and lower FeO_6 layers. There have been reported non-stoiciometric delafossite-type oxides uptake extra oxide ions at the interlayer between FeO_6 octahedra layers[4,5]. In general, it take high temperture and long time to sinter ceramics including delafossite-type $CuFeO_2$ using conventional process as an electric furnace. On the other hand, it is reported that microwave heating techniques were one of the new processing to synthesize materials at short time[6]. We applied microwave heating techniques in order to synthesize $CuFeO_2$ quickly and easily.

Microwave heating techniques have stimulated interest in recent years because of there potential advantages, including significant reduction in manufacturing costs because of energy saving and shorter processing time, development of fine microstructure, and formation of anisotropic grain growth[6]. In microwave heating processing, a material absorbs electromagnetic energy and is internally heated.

In this research, we synthesized delafossite-type $CuFeO_2$ from a powder mixture by 2.45 GHz microwave irradiation in order to improve OSC property. We investigated the microwave effect to morphology of $CuFeO_2$ grain and OSC property.

2. Method

Cu_2O and γ-Fe_2O_3 powders as starting materials were mixed and pressed into a pellet of 15 mm in diameter. We irradiated 2.45 GHz microwaves into this pellet and heated at 500-900 ˚C for 10 min in air. Multimode microwave heating equipment operating at a frequency of 2.45 GHz (Model SMW-105, Shikoku Keisoku Kogyo, Co. Ltd., Kagawa, Japan) was used in this research. For comparison, the same materials were synthesized by conventional solid state reaction using an electric furnace. The samples were characterized by XRD, FE-SEM, and OSC property was investigated.

3. Results and Discussion

Figure 2 shows temperature-time profiles of γ-Fe_2O_3 and Cu_2O powder during microwave irradiation with 300 W output in air. Each powder absorbs microwave energy very well, and temperature rapidly rose to1000 ˚C in air.

Figure 3 shows XRD patterns of the compounds after heating to various temperatures by microwave irradiation. The products were almost single-phase of 3R-delafossite-type $CuFeO_2$. It was observed that all diffraction peak intensities, especially (00*l*) peaks,

became higher in high temperature.

Figure 4 shows SEM images of the sample synthesized by microwave irradiation at in air. It was observed that $CuFeO_2$ grains have layered structure and anisotropic morphology when prepared at high temperature.

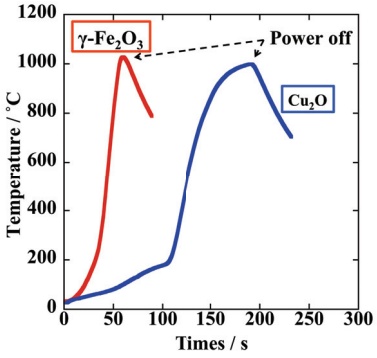

Fig. 2 Temperature-time profiles of starting materials during microwave irradiation with 300 W output in air

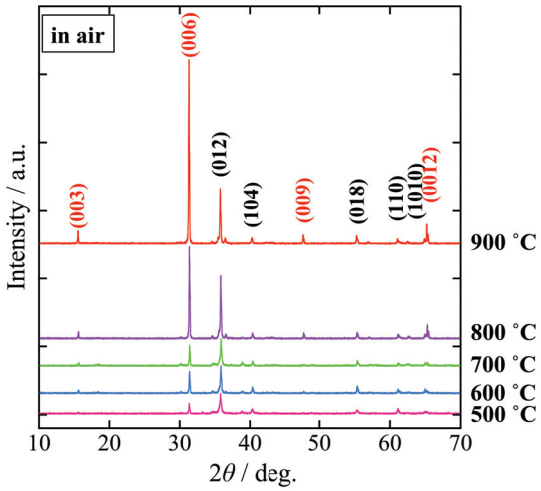

Fig. 3 The XRD patterns of the sample synthesized by microwave irradiation

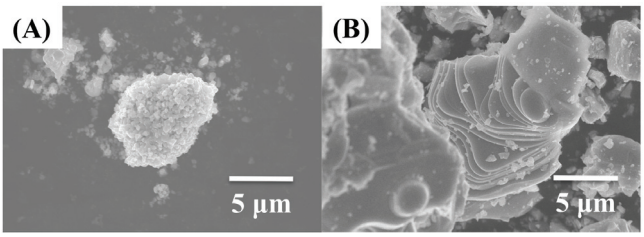

Fig. 4 The SEM images of the sample synthesised by microwave irradiation at (A)500 ˚C, (B)800 ˚C in air.

From the results of XRD patterns and SEM observation, $CuFeO_2$ grains have anisotropically grown in perpendicular to c-axis. In the sample synthesized by microwave irradiation, Lotgering Factor, which is used as an index of the *ab*-plane orientation, was twice as compared to conventional heated one. Therefore, it was indicated microwave heating promoted the formation of the anisotropic grain growth.

Figure 5 shows the OSC value estimated by pulse injection method at 500 ˚C. It was observed that anisotropic $CuFeO_2$ synthesized by microwave irradiation shows high OSC value as compared to conventional heating samples. The maximum OSC value was 466 µmol-O/g at the sample f = 0.71 synthesized by microwave irradiation.

It was considered that the stability of the crystal structures increased during oxygen uptake-release behavior because crystallite was improved when prepared at high temperature. It may be also suggested that (00*l*) plane in delafossite $CuFeO_2$ interacts with oxygen higher than other planes.

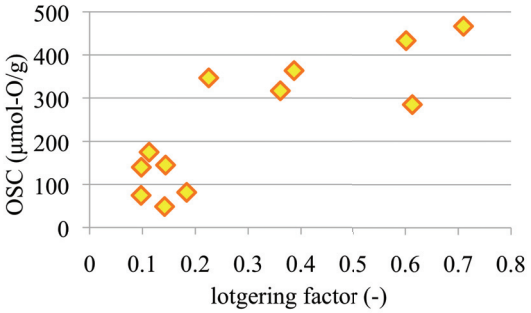

Fig. 5 OSC measurement at 500 ˚C

4. Concluding remarks

In this research, delafossite-type $CuFeO_2$ were synthesized at low temperature and short time by 2.45 GHz microwave irradiation. XRD patterns of microwave samples showed that all diffraction peak intensities, especially (00*l*) peaks, became higher than those of electric furnace samples. From the results of the SEM observation, $CuFeO_2$ grains have anisotropically grown in perpendicular to c-axis. In the samples synthesized by microwave irradiation, Lotgering Factor was twice as compared to conventional one. This result suggested microwave heating promoted the formation of the anisotropic grain growth based on intrinsic layered structure. Microwave processing is effective method for synthesis of anisotropic grain.

From the OSC measurement, anisotropic $CuFeO_2$ synthesized by microwave irradiation shows high OSC value. The stability of the crystal structures increased in oxidative and reductive atmosphere due to the improvement of $CuFeO_2$ crystallite. It may be also suggested that (00*l*) plane in delafossite-type $CuFeO_2$ interacts with oxygen.

References

[1] P. Fornasiero, et al. Journal of catalysis **151** (1995) 168-177
[2] J. Kaspar, et al. Catalysis Today 50 (1999) 285-298
[3] S. Kato, R. Hujimaki, et al. Applied Catalysis B, **89** (2009), 183-186
[4] V. garlea, C. Darie, et al. Solid State Science **8** (2006) 457-461
[5] E.Mugnier, et al. Solid State Ionics **177** (2006) 607-612
[6] W. H. Sutton, et al. Am.Ceram. Soc. Bull. **68** (1989) 376-86

Tenth International Conference on Flow Dynamics
November 25-27, 2013, Sendai, Miyagi, Japan

Creating New Automotive Catalyst without Using Cerium Atom

Tsutomu Aida[a], Yuichiro Wagatsuma[a], Seiichi Takami[b], Tadafumi Adschiri[a, b]
[a] New Industry Creation Hatchery Center, Tohoku University, 6-6-10 Aramaki Aza Aoba, Aoba-ku, Sendai 980-8579, Japan
[b] Institute of Multidisciplinary Research for Advanced Materials, Tohoku University, 2-1-1, Katahira, Aoba-ku, Sendai 980-8577, Japan
E-mail of corresponding author: ajiri@tagen.tohoku.ac.jp

ABSTRACT

Cerium oxide (CeO_2) is usually used as an automotive catalyst. We try to make the new automotive catalyst without using Cerium atom. In this study, we created zirconium - iron oxide nanoparticle catalyst using batch type and flow type reactor. The Oxygen Storage Capacity (OSC) and conversion of exhaust gases of created new catalyst are very higher than conventional CeO_2 catalyst.

1. Introduction

As a well-known metal oxide, and because of its novel properties, Cerium oxide (CeO_2) has been extensively applied in electrochemistry, optics and automotive catalyst. In our laboratory, we can create cubic and octahedral CeO_2 nanoparticles [1, 2]. We have also succeeded in synthesizing CeO_2 nanoparticles with organic modification [3]. In addition, we created and published other nanoparticles such as indium tin oxide (ITO) [4], titanium oxide (TiO2) [5], hafnium oxide (HfO2) [6], barium titanate (BaTiO3) [7], Zinc oxide (ZnO) [8], iron oxide (α-Fe_2O_3, Fe_3O_4) [9], magnesium ferrite ($MgFe_2O_4$) [10] and so on.

In this project, we try to create new automotive catalyst without using Cerium atom. Previous work, we created silicon - iron oxide nanoparticle catalyst. The value of Oxygen Storage Capacity (OSC) at low temperature (300 ^oC) is the same as conventional CeO_2 catalyst. However, the silicon - iron oxide is unstable at high temperature so that the value of OSC was lower than conventional CeO_2 catalyst. In this study, we used zirconium instead of silicon and created zirconium - iron oxide nanoparticle catalyst.

2. Method

We used two type of reactors, batch type and flow type. Firstly, we used batch type reactor because of find good temperature and pressure conditions to create nanoparticle. In batch type experiment, 1.0-2.5 mL of the precursor was transferred to a pressure-resistant SUS316 vessel (inner volume 5 mL). We changed the reaction pressure by precursor volume (10-30MPa). The hydrothermal reaction was performed in the reactor at 400 °C for 10 min and terminated by submerging the reactor in a water bath at room temperature. Secondly, we used the equipment made by company (Momi-cho mini; ITEC CO. LTD.) like Figure 1. The temperature and pressure conditions were used best conditions by batch experiment (400 °C and 30 MPa). The reaction time can be controllable by reaction line length and flow rate (In this study, reaction time was 1-60 sec). Finally, we requested creation of 1 kg of the nanoparticle from the company (ITEC CO. LTD.) because of we get few gram of nanoparticle using Momi-cho mini instrument through the day. The conditions (temperature, pressure and reaction time) were determined by our flow type reaction results.

3. Results and Discussion

The detailed morphology and structure of the products were investigated by TEM (Figure 2). The observed particle sizes determined from the XRD patterns are 20nm.

Figure 3 shows the results of the OSC at several conditions. The conditions were all 400 ^oC and 30 MPa. The concentration of precursor in batch 2 was twice as match as batch 1 and flow experiment. The value of OSC at conventional CeO_2 catalyst is 500. We can find that the values of OSC were very higher than conventional CeO_2 catalyst.

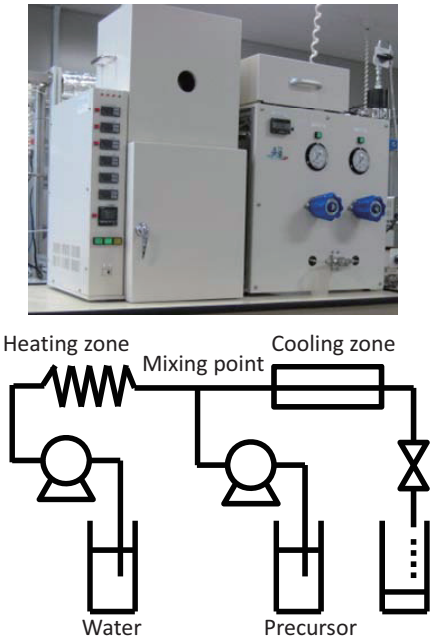

Fig. 1 Flow type experimental instrument (Momi-cho mini)

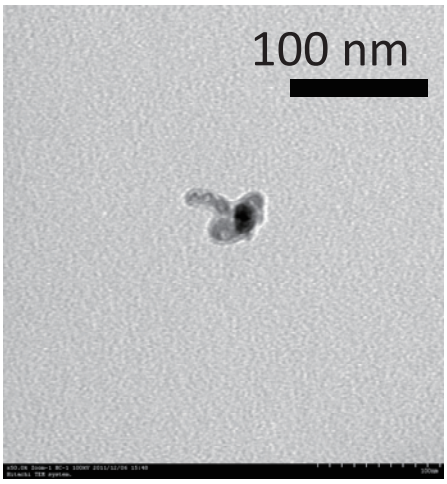

Fig. 2 TEM images of created zirconium - iron oxide nanoparticles

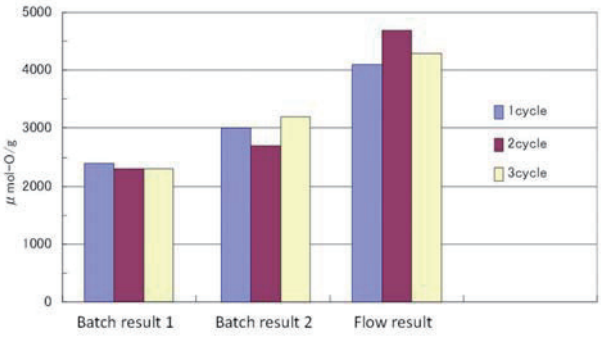

Fig. 3 OSC value of several batch and flow experimental conditions.

The conversion of exhaust gases (NO_X, CO and C_3H_6) by batch result 2 are shown in Figure 4. In fresh results (powder condition), CO and C_3H_6 conversion is similar according to CeO2 conventional catalyst, but NO_X conversion is lower at high temperature conditions. On the other hand at aged results (honeycomb structure), NO_X conversion is higher at high temperature conditions. These results indicated that our new catalyst is useful for automotive catalyst.

Now we try to make silicon - iron oxide nanoparticle by flow reactor.

In the results of OSC at batch experimental (Figure 3), we can see that the value of OSC was changed. We think that there is the optimal experimental condition. If we find good condition to make zirconium - iron oxide nanoparticle and create by flow experiments, we can get large amount of good automotive catalyst.

4. Concluding remarks

We create new automotive catalyst without using Cerium atom. The new automotive catalyst (zirconium - iron oxide nanoparticle) has a good performance for OSC value and conversion of exhaust gases. These values are change at experimental conditions so that we have to find the best experimental condition.

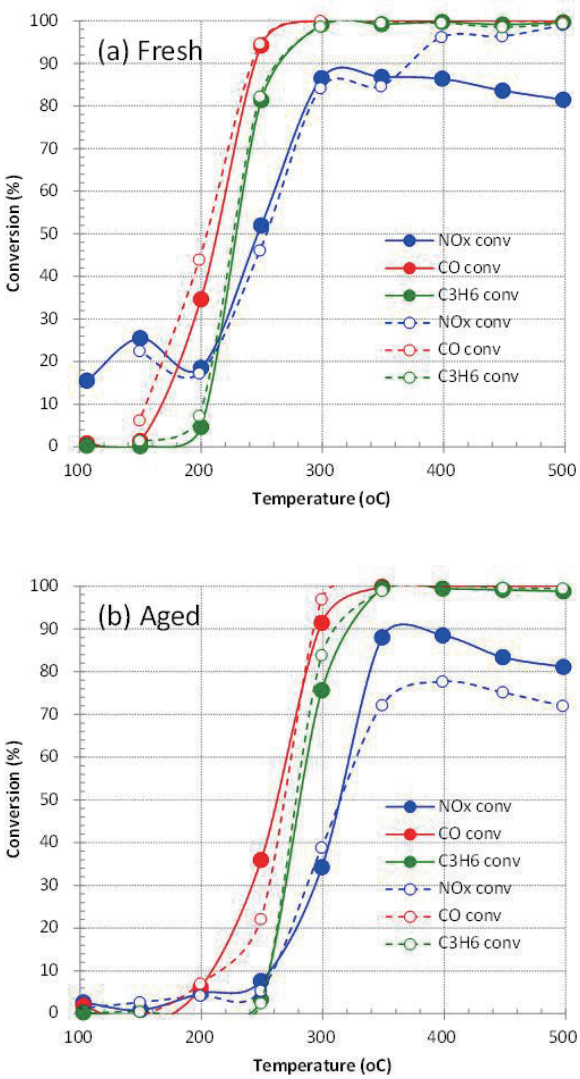

Fig. 4 The conversion of exhaust gases (NO_X, CO and C_3H_6). (a):Fresh (powder) condition, (b): Aged (honeycomb structure) condition.
Filled circle with line: our experimental results, Open circle with dot line: CeO2 conventional catalyst

References

[1] J. Zhang et al., Adv. Mater., **19** (2007) 203-206.
[2] S. Asahina et al., Chem. Cat. Chem., **3** (2011) 1038-1044.
[3] M. Taguchi et al., Cryst. Growth Des., **9** (2009) 5297-5303.
[4] J. Lu et al., Appl.Mater.Interfaces, **4** (2012) 351-354.
[5] T. Arita, Chem. Lett. **39** (2010) 961-963.
[6] A. Sahraneshin, Cryst. Growth Des., **12** (2012) 5219-5326.
[7] M. Atashfaraz, Fluid Phase Equilib., 257 (2007) 233-237.
[8] M. Umetsu et al., Adv. Mater. **17** (2005) 2571-2575.
[9] S. Takami et al., Mater. Lett., **61** (2007) 4769-4772.
[10] T. Sasaki et al., J. Supercritical Fluids, **53** (2010) 92-94.

Tenth International Conference on Flow Dynamics
November 25-27, 2013, Sendai, Miyagi, Japan

Synthesis of Ceria Nanoparticle-Assembled Hollow Mesoporous Silica Composite Particles

Haruyuki Ishii, Saki Ito, Daisuke Nagao, Mikio Konno*
Department of Chemical Engineering, Graduate School of Engineering, Tohoku University
6-6-10, Aoba, Aramaki,Aoba-ku, Sendai 980-8577, Japan
konno@mickey.che.tohoku.ac.jp

ABSTRACT

Mesoporous silica coating is an approach for suppressing nanoparticle aggregation and keeping substrate access to the active site on nanoparticle surface. In the present study, ceria nanoparticles (CeNPs) with a diameter of *ca.* 3 nm were synthesized in aqueous solution of sodium citrate and ammonia, and the mesoporous silica coating of the CeNPs was then performed in the presence of sodium oleate. CeNP-assembled hollow particles with mesoporous silica shell were obtained under weak basic conditions and can be applicable to automotive three-way catalysts.

1. Introduction

Nano-sized catalysts have widely been reported because of their novel catalytic functions and high catalytic activities, called nano-size effect. There is, however, a common problem to be solved in the nano-catalysts, which is reduction of catalytic activity when they aggregate together. Especially, prevention of coalescence between nano-catalysts at high temperature is required for the application to automotive three-way catalysts. Mesoporous silica coating is a method to solve the problem.

Assembling of nanoparticles (NPs) shows novel properties different from NPs itself, which is applicable to drug delivery systems, plasmonic materials, and catalysts. Hollow assemblies of NPs have been reported as catalysts with high activity and thermal stability.

This study present the syntheses of hollow assembly of ceria nanoparticles (CeNPs) with mesoporous silica shell. The composite hollow particles are prepared in two processes, one of which is self-assembly formation in the suspension of ceria nanoparticles (CeNPs) and sodium oleate and the other is the fixation of the self-assembled structures with silica coating. To understand the formation mechanism, the effect of pH on the syntheses is investigated. The particles obtained are further mixed with γ-alumina-supported palladium (Pd) and performance of the mixure as three way catalyst is investigated.

2. Method

CeNPs were synthesized with citrate as a protecting agent [1]. Briefly, ammonia solution was mixed with $(NH_4)_2Ce(NO_3)_6$ and trisodium citrate. The suspension was stirred at 25 ^oC for 30 min and then aged at 80 ^oC for five hours. The concentrations of the ceria source, trisodium citrate, and ammonia were 0.1 M, 0.1 M, and 2.0 M, respectively. To collect CeNPs, an excess of ethanol (80 vol%) was added to the suspension and CeNPs were separated by centrifugation. CeNPs were washed again with ethanol-water mixture (80/20, v/v) and re-dispersed in water.

The preparation of CeNPs-mesoporous silica composite materials was performed typically in the following procedure. The aqueous suspension of CeNPs was mixed with NaOA in the presence of ammonia for controlling solution pH. The mixture was stirred for 30 min. *N*-trimethoxysilyl-propyl-*N*,*N*,*N*-trimethyl-ammonium chloride (TMAPS, 50% in methanol) was then added to the suspension which was stirred for 30 min, followed by the addition of TMOS/ethanol solution, which was stirred for another 30 min. Suspension temperature was maintained at 35 ^oC throughout the procedure. The final concentrations of TMOS, Ce and NaOA were 100, 10 and 10 mM, respectively, in water-ethanol solutions (75/25, v/v) with ammonia at different concentrations. The suspension was heated to 80 ^oC that was kept for more than 5 h under stirring. To remove the anionic surfactant and other organic compounds, sample obtained was calcination at 550 ^oC for 4 h. The calcined samples were mixed with γ-alumina with 2.5 % palladium (Pd) at mixing weight ratio of 1:2 and the mixture was used for three way catalyst with and without aging at 1000 ^oC for 20 h in the presence of 10 % H_2O.

CeNP, CeNPs-silica composite materials, and their suspension were investigated with dynamic light scattering (DLS), scanning transmittance electron microscope (STEM), X-ray diffraction (XRD), and N_2 adsorption-desorption isotherms.

3. Results and Discussion

Fig. 1 shows CeNP aqueous suspension and its size distribution measured with DLS. After the ammonia addition, the color changed to dark brown, which indicated the precipitation of CeNPs. The color was maintained after centrifugation and washing (Fig. 1A).

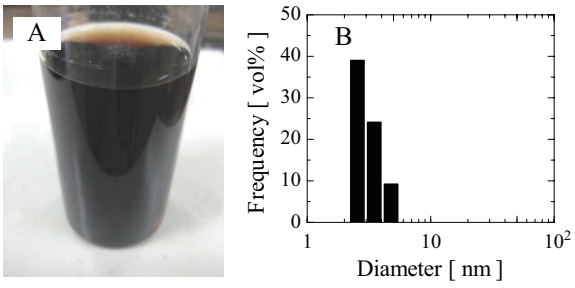

Fig. 1 (A) Photograph of CeNP suspension and (B) its size distribution measured by DLS.

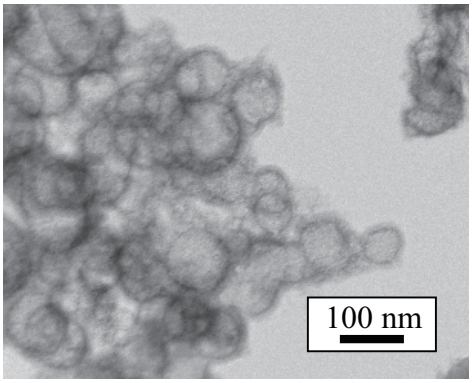

Fig. 2 TEM image of CeNP-assembled particles obtained in CeNP-NaOA suspension at pH 9.9.

The dispersion size was *ca.* 3 nm (Fig. 1B), which shows the high dispersion stability in water. The CeNP was fluorite structure with a crystalline size of 3.2 nm calculated from XRD measurement. The CeNP was also determined as single crystal with fluorite structure with XRD measurement. Although nanoparticle syntheses are difficult at high concentrations of their source, this method yielded CeNPs at 0.1 M ceria source.

CeNPs obtained above were then coated with silica. Fig.2 shows TEM image of the calcined CeNPs-silica composite sample obtained at starting pH 9.9. The calcined sample is sphere with condensed black dots with similar diameter to CeNPs. The structure was hollow CeNP assembly with outer silica shell as evidenced with various STEM modes and energy dispersive X-ray spectroscopy (EDX) analysis. The mesoporous structure was also determined from N_2 desorption/adsorption isotherm. Although the similar spheres to that in Fig. 2 were obtained in the synthesis performed without ammonia, no sphere was observed at starting pH more than 10. Therefore, ceria nanoparticle-assembled hollow mesoporous silica composite particles were obtained below pH 10.

The formation mechanism of the hollow CeNP assembly not highly specified yet. In CeNP-NaOA suspensions at pH values between 9 and 10, structures with dispersion sizes from 30 to 60 nm were observed, which can be a key for the hollow CeNP assembly formation. According to the literature [2], the anionic surfactant, oleate forms vesicles by themselves in aqueous solutions in pH range between 8 and 10. Since the values of starting pH where the mesoporous silica-coated hollow CeNP assemblies formed were in the range, it is reasonable that the oleate self-assemly appears in the CeNP-NaOA suspensions and associates with CeNPs during reaction. The interaction can lead to the formation of the hollow CeNP assembly.

The performance as three-way catalytic reactions was finally investigated by using mixed sample of the CeNP-assembled particles with Pd supported by γ-alumina were then investigated. Fig.3 shows the results of NO conversion catalyzed by the mixture in

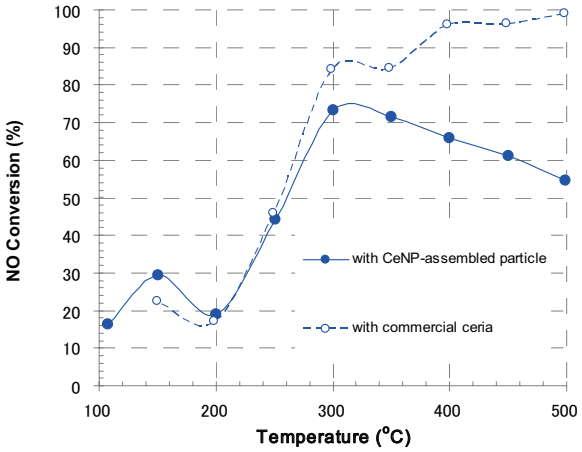

Fig. 3 NO conversion catalyzed by γ-alumina-supported Pd mixed with the CeNP-assembled particles or commercial ceria. Catalytic reactions were performed in the mixed gas with similar compositions to exhaust one.

mixed gas similar composition to exhaust one. In the case of mixed sample without aging, there was first peak of NO conversion (almost 30 %) at 150 °C. Compared with the mixture of the Pd and commercial ceria sample, the values of NO conversion were lower at high temperatures, 300 °C and more. On the other hand, the value is higher at 150 °C. Although similar profile was obtained in the sample with aging at 1000 °C, the first peak appeared at 250 °C

4. Concluding remarks

The present work succeeded in the formation of CeNP-assembled hollow mesoporous silica composite particles in the presence of NaOA by using citrate-protected CeNPs which was highly dispersed in water. Since the hollow particles were obtained at pH values between 9 and 10, the oleate self-assembly that forms at the pH range can be a key for the formation of the hollow CeNP assemblies. As-synthesized particles can be applied to a three way catalyst with high catalytic activity at low temperature.

References

[1] T. Masui, H. Hirai, R. Hamada, N. Imanaka, G. Adachi, T. Sakata and H. Mori, J. Mater. Chem. 13 (2003) 622-627.

[2] K. Morigaki and P. Walde, Curr. Opin. Colloid In. 12 (2007) 75-80.

Tenth International Conference on Flow Dynamics
November 25-27, 2013, Sendai, Miyagi, Japan

Next-Generation Advanced Mobility System

Fumihiko HASEGAWA, Masahiro NISHIZAWA, Kazunori OHNO,
Shigeyuki YAMABE, Yusuke HARA, Hidetoshi MATSUKI
New Industry Creation Hatchery Center, Tohoku University
Aramaki Aoba, Aoba-ku, Sendai, Miyagi 980-8579
hasegawa@niche.tohoku.ac.jp

ABSTRACT

The next-generation advanced mobility and system which composed of integrating various technologies from Tohoku University has the purpose to propose a new concept. We manufactured EVs composed of integrating various technologies and executed demonstration experiments at our campus. As for the emergency such as the disaster occurrence, the social energy request changes from the normal time. The energy management system which is related with the mobility was executed by the traffic simulation.

1. Introduction

Tohoku University plays an important role in academic and educational fields in Sendai City, the center of politics, economics and culture in the Tohoku region. Since the foundation of the university, we have been putting "Research First", emphasizing "Practice-Oriented Research and Education", and creating the highest level of research and education in the world. After the Great East Japan Earthquake, Tohoku University has played a critical role in "Leading the Reconstruction of Tohoku and the Regeneration of Japan", as a member of the affected communities.

The next-generation advanced mobility and system which composed of integrating various technologies from Tohoku University has the purpose to propose a new concept. Our next-generation advanced mobility and system aims to solve various recent social problems such as environmental problems, energy problems, traffic jams, and the aging population, by utilizing our knowledge and cutting-edge technologies, and realizing a better place to live and safer more secure society for citizens.

2. Method

The next-generation advanced mobility was obtained fusing the various integrating technologies. Many laboratories and researchers concern the development of the mobility and the system. The EV is installed in the basis of the mobility. The manufactured EVs were composed of autonomous running technology, wireless charging technology, in-wheel motors and so on.

The energy management system which is related with the mobility was executed by the traffic simulation. By the traffic simulation in the virtual-space, it visualizes an energy analysis result, disaster information, traffic information at the normal time and so on. A driving simulator was used to do the investigation of the driving action which is effective in the energy consumption restraint which is peculiar to the EV.

Our major experiments are executed in driving around a new-campus in Tohoku University. As the developing experiment, it is arranging about the society proof in the earthquake disaster damaged area.

Figure 1 shows the concept of research and demonstration experiment of our mobility and system.

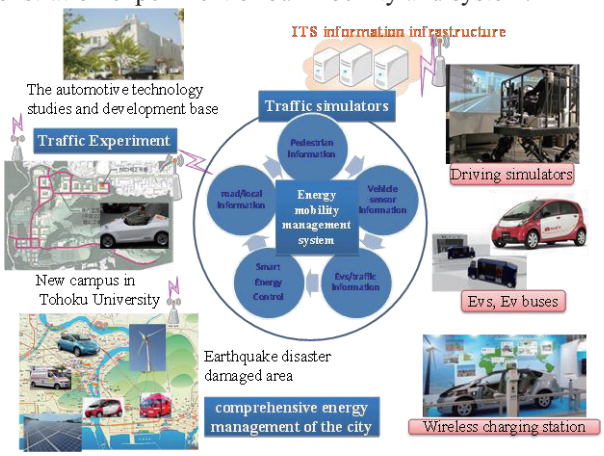

Fig. 1 Concept of research and demonstration experiment of our mobility and system

3. Demonstrations and Discussion

We manufactured EVs composed of integrating various technologies. Figure 2 shows the large EV which had technology such as in-wheel motor control, omnidirectional cameras, wireless charging. Figure 3 shows the small EV which had autonomous vehicle technologies. Moreover, we studied the peripheral technology of the mobility such as robotics, automatic steering control, torque sensing, active safety, tribology, head-up displays, power electronics, switched reluctance motor, vision analysis, battery analysis, traffic simulation.

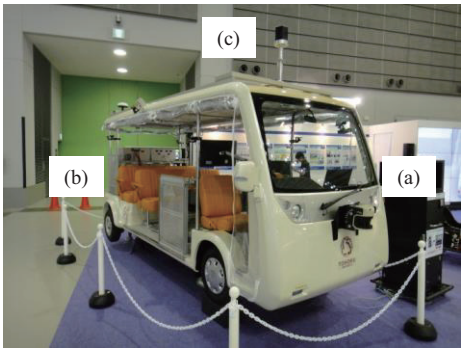

Fig. 2 (a) manufactured large EV, (b) in-wheel motor controller, (c) omnidirectional cameras. Coil for wireless charging is installed under the car.

Fig. 2 Manufactured autonomous vehicles

The energy which the mobility consumes accounts for the high rate in the society. To realize energy saving, the management which optimizes the energy consumption of the movement and the transportation is demanded. The insufficient mileage makes a driver choose the route which always goes via the charging station. The insufficient battery remaining makes a driver head for the charging station. For the energy management, we analyze a best way and predict it by the traffic simulation. Figure 3 shows analysis of electric vehicle users' behavior and desirable allocation of charging station.

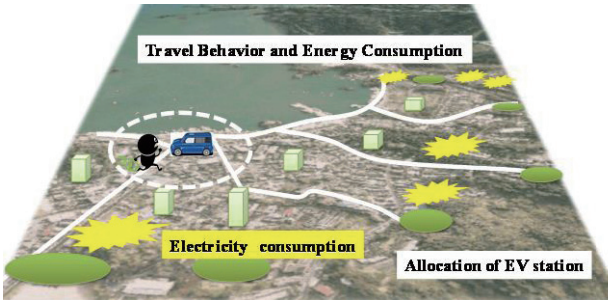

Fig. 3 Analysis of electric vehicle users' behavior and desirable allocation of charging station

As for the emergency such as the disaster occurrence, the social energy request changes from the normal time since rescue operation has higher priority than energy saving. For example, the consumption of the energy must be centered on the rescue support by the management such as the power transmission control. Figure 4 shows concept of the energy management system for the normal time and the emergency.

4. Concluding remarks

Tohoku University proposed new society conceptions after the Great East Japan Earthquake. Our proposal is next-generation advanced mobility. By integration of various technologies such as clean energy, support systems for times of disaster and emergencies, and communication networks, we aim to create smart mobility, a smart campus, and a smart town. We will research, develop and propose valuable things for

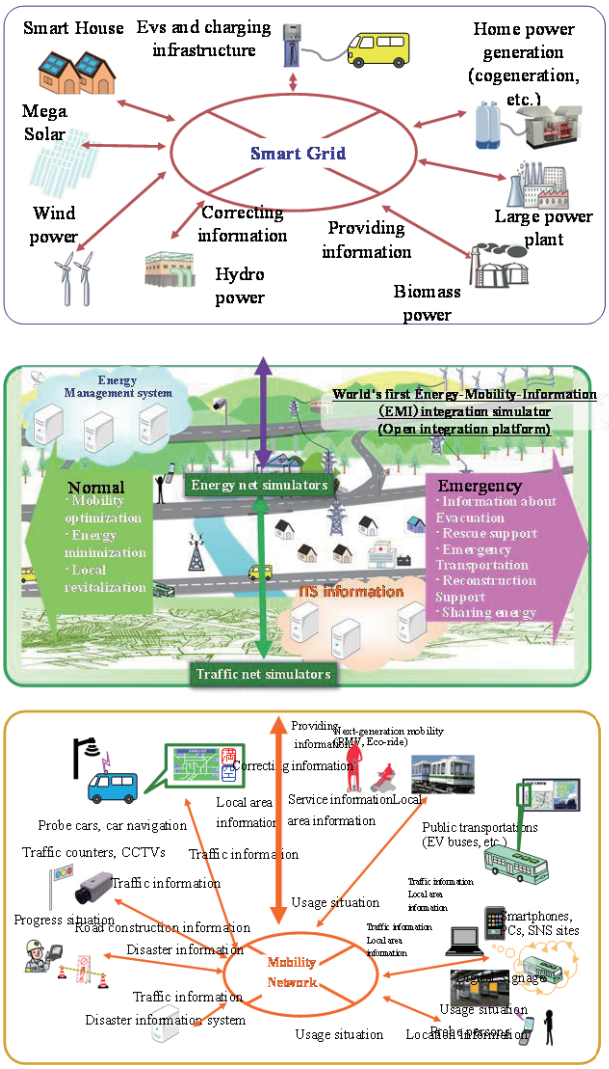

Fig. 4 Concept of the energy management system for the normal time and the emergency

society. In addition, we will carry over our enthusiasm to the next generation for further advancement. We will keep on improving our research for the next generation.

Tenth International Conference on Flow Dynamics
November 25-27, 2013, Sendai, Miyagi, Japan

Motor Technology for Next Generation Automotive

Hiroki Goto, Kenji Nakamura, Osamu Ichinokura
Tohoku University, 6-6-05 Aoba, Aramaki, Aoba-ku, Sendai, Japan
goto@ecei.tohoku.ac.jp

ABSTRACT

In recent years, the spread of Electric Vehicles (EVs) and Hybrid Electric Vehicles (HEVs) began for saving the future. However, permanent magnet (PM) motors made from rare-earth materials, which are used for EV/HEV, are not environmentally friendly. Switched reluctance (SR) motors attract attention as a machine without rare-earth materials. But, torque density of SR motors is smaller than that of PM motors. In the paper, a high torque density SR motor with novel structure is developed for next generation automotive.

1. Introduction

In recent years, environmental problem, such as exhaustion of fossil fuels, global warming and air pollution, become big issue all over the world. For such occasions, the enlargement of Kyoto Protocol is decided. Vehicles, such as car, motorcycle, truck, bus and so on, consume a lot of fuel and put out a lot of emission gas. Improvement in vehicle fuel economy and exhaust emissions must be needed under such circumstances. And so Electric Vehicle (EV) and Hybrid Electric Vehicle (HEV) attract lots of attention and have been developed in recent years. A few hybrid cars and a few electric vehicles are commercialized. But these vehicles have some problems. Almost EVs use Permanent Magnet (PM) motors. PM motors have high torque density and excellent efficiency. However, the cost of magnet materials, such as dysprosium, neodymium and so on, keeps rising in recent years. It seems that this aspect doesn't change.

Because of that, this paper focuses attention on Switched Reluctance (SR) motors for in-wheel direct-drive EVs[1][2]. SR motors are the motor that utilizes the reluctance torque originated in magnetic saliency between stator and rotor poles. SR motors are robust and simple structures because these are made from only steel core and winding wire. SR motors have advantages such as high temperature operation because of no demagnetization of magnet, and low-cost manufacturing. And it has capability of high torque density because the motor can increase its torque even though stator poles are magnetically saturated. In addition, by employing in-wheel drive system, can make car interior space larger, and reduce the mechanical loss such as gear. But SR motors also have disadvantages. One of them is that SR motors torque density is smaller than that of PM motor. On the other hand, its magnetic saliency causes higher torque ripple, noise, and vibration compared to other motors. Torque ripple and so on can measurably get smaller by our proposed control method[3][4]. However, the torque density becomes assignment.

This paper focuses on to increase the torque density of SR motors for in-wheel direct-drive system. In-wheel direct-drive EV that use radial gap SR motors is already investigated as shown in Fig. 1[2]. The volume is very flat because that the wheel space is very thin and to fit in the motor in wheel. So, coil end space and inner diameter are dead spaces as the volume becomes more flat. If can use their spaces, it seems that effective utilization of the available active volume is possible. So this paper also focuses on the axial-gap structure which can use inner bore space and coil end space effectively[5][6].

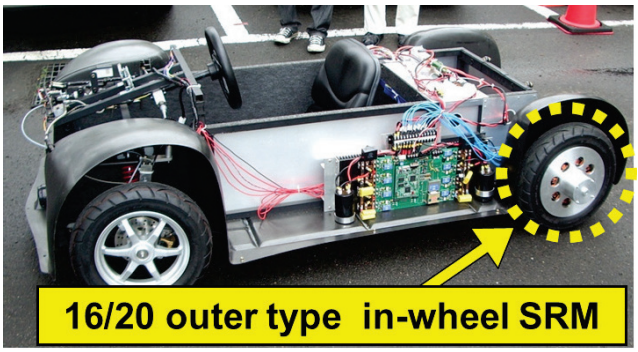

Fig. 1 In-wheel drive EV that mounts SR motors in the rear side.

2. Axial-Gap Switched Reluctance Motor

The torque generation principle of SR motor is shown in Fig. 2. A phase torque of SR motors can be expressed as (1).

$$\tau_k = \frac{1}{2} i_k^2 \frac{dL(\theta)}{d\theta} \tag{1}$$

Where k represent index of phases, i_k is the phase current, θ is the rotor position, and $L(\theta)$ is the phase inductance. Fig. 3 shows the phase inductance L profile versus position θ of the SR motor. Total motor torque can be expressed as

$$\tau = \sum_k \tau_k \tag{2}$$

From (1) and (2), total torque can be improved by increasing inductance changes. The inductance can be increased by increasing gap surface area.

The structures of axial-gap SR motor and radial-gap SR motor are shown in Fig. 3. Axial-gap motors have the gap to axial direction. By this change, dead space of coil end become smaller and inner bore can become smaller as far as the volume allow. Axial-gap structure could reduce the leakage flux from stator to rotor because the flux flow axial direction. And the saturated

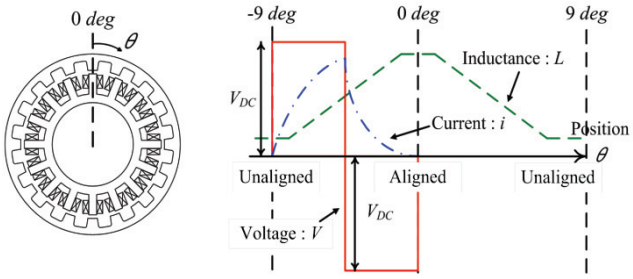

Fig. 2 Inductance L profile versus rotor position θ of the 16/20 SR motor and principle.

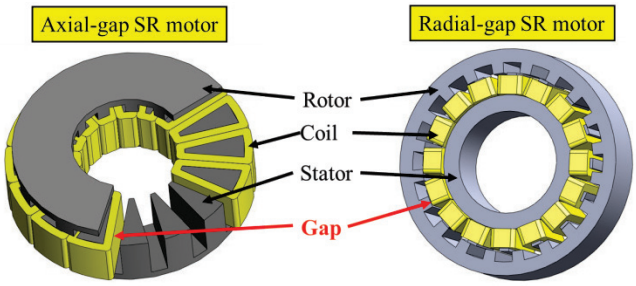

Fig. 3 Structure comparison with Radial-gap SR motor.

magnetic flux can improve. Then the axial-gap SR motors inductance curve become better than the radial-gap SR motors at flat volume. The advantage makes axial-gap SR motors performance better [5].

3. Test of Prototype Machine

This axial-gap In-wheel SR motor is manufactured experimentally. This test machine is shown in Fig. 4. This case is made up of motor, fixed axial length, position sensor and rotational case. The characteristics of this axial-gap In-wheel SR motor test machine is measured. The simulation results and measured experiment characteristics are shown in Fig. 5. The current density limitation is less 22.6 A/mm^2. The maximum torque from simulation is 302 N·m. Experiment results also agree well with the simulation characteristic of current density versus torque.

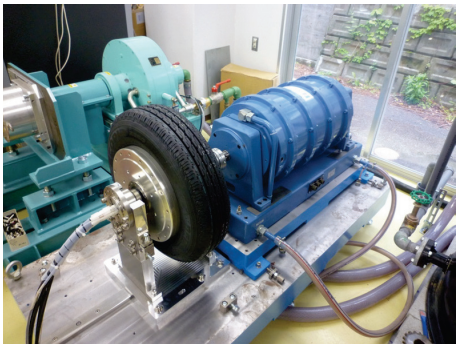

Fig. 4 The view of Axial-gap In-wheel SR motor test machine.

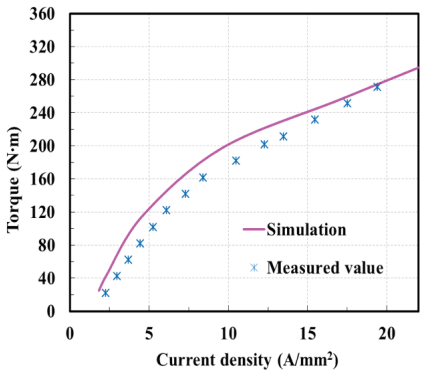

Fig. 5 Currrent density versus torque characteristics.

In the fact, the torque density is 39N・m/L. The value is larger than that of Toyota HEV 3rd generation Prius (35N・m/L).

4. In-wheel direct-drive EV with axial-gap SR motors

The developed in-wheel direct-drive EV with two axial gap SR motors put in rear two wheels is shown in Fig. 6.

The driving test has done successfully. Two axial-gap SR motors move well and smoothly with 8 passengers. The maximum speed of the EV is over the 30 km/h. So, the goal of maxim speed is achieved.

Fig. 6 Electric Bus that mounts axial-gap SR test machines.

References

[1] T. J. E. Miller, Newnes, (2002).
[2] H. Goto, Y. Suzuki, K. Nakamura, T. Watanabe, H. J. Guo, O. Ichinokura, J. of MMM, **290-291**, 1338-1342 (2005).
[3] Ramamurthy, Balda, IEEE Trans. Ind. Applicant., **37**, 1256-1264 (2001).
[4] A. Nishimiya, H. Goto, H. J. Guo, O. Ichinokura, ICEM2008, 1176 (2008).
[5] H. Arihara, K. Akatsu, ECCE2011, 3582-3589 (2011).
[6] T. Shibamoto, H. Goto, K. Nakamura, O. Ichinokura, ICEM2012, FF-001678 (2012).

Tenth International Conference on Flow Dynamics
November 25-27, 2013, Sendai, Miyagi, Japan

Recycling Technologies for End of Life Vehicles

Mitsuru Sato, Takashi Nakamura, Etsuro Shibata, Atsushi Iizuka
Institute of Multidisciplinary Research for Advanced Materials, Tohoku University
E-mail: ntakashi@tagen.tohoku.ac.jp

ABSTRACT

Many materials are used in various components for automobiles, which bring the advanced performance to advanced cars like EHV. Minor rare elements are essential substances for high performance automobiles, while their supply chains have been recently unstable and their price change is strongly intense. Recycling of minor rare elements from the ELVs is one of the good ways to secure their supplies. In our laboratory, several research works on recycling technologies of minor rare elements from ELVs are under research, as well as on recycling of other materials from ELVs.

1. Introduction

As the high technology industries have been developed, the demand of minor rare elements, for example, In, Nd etc., and of PGM (Platinum Group Metals) have been increased, and gap between supply capacity and actual demand of these elements becomes large. Additionally, resources of minor rare elements are unevenly distributed in the world.

Therefore, the minor rare elements recycling from the uses electronic equipment as well as scrapped vehicles should be developed to secure their stable supplies.

In this symposium, the technology on minor rare elements recycling from scrapped vehicles will be presented.

2. Minor Rare elements used in vehicles

The application of minor rare elements to automobiles is shown in Fig.1. Several minor rare elements are contained in materials of the important automobile components.

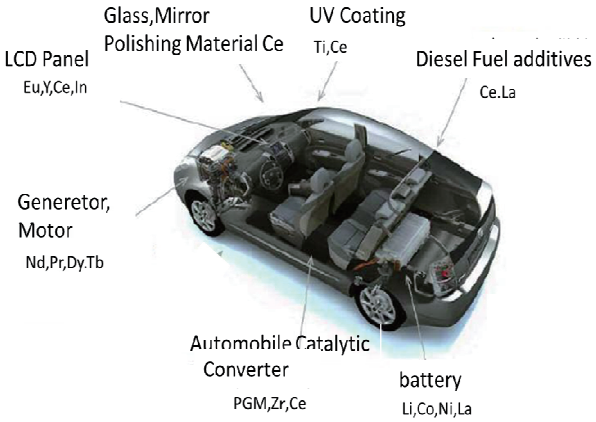

Fig.1 Minor Rare Elements application for Automobiles

The rough price changes of each element is shown in Fig.2. Uneven distribution of minor rare elements resources brings instability of their prices.

The supply and demand forecast of Li, for example, is shown in Table 1. Demand of Li will be rapidly grown, and it is supposed that this rapid demand growth is caused due to growth of electric vehicles. Furthermore, the demand of Li will exceed the supply in 2020.

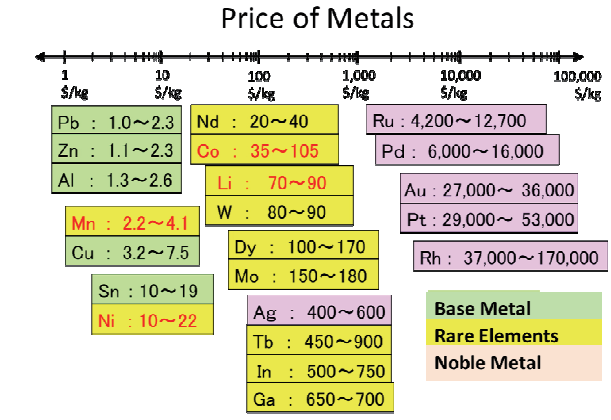

Fig.2 Price of Metals

Table 1. Supply and Demand Forecast of Li

Li Supply and Demand				
	year	2010	2015	2020
Supply (kilo-ton)		137	166	214
Demand (kilo-ton)		90	144	313
	For Automobiles	5	40	186
	For others	85	104	127

* Supply and demand values were estimated from USG, MCS, Jan.2010 and other reports by the Resources and Energy Agency of Japan.
* Li usages for automobiles were assumed to be 1 kg for HEV and 4 kg for EV per unit.
* Demand increasing rate for consumer use was assumed to be 4% per year.
* Lithium amount was converted to Li_2CO_3 amount.

3. Recycling on Automobile Components

In Japan, ELVs are disassembled based on the automobile recycling law, and disassembled components

are reused as used components, or are supplied to material recycling.

Fig. 3 shows the utilization of disassembled components from scrapped vehicles. As shown in Fig.3, a kind of circuit boards is not yet disassembled in more cases, compared with electric motor. This means collecting system and recycling technologies of PCBs from ELVs are not sufficient. We are investigating how to collect them efficiently from car recyclers and how to recover valuable metals from PCBs.

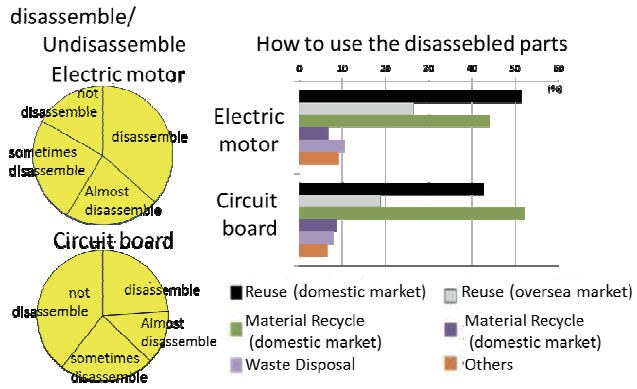

Fig.3 Utilization of Disassembled Components from Scrapped Vehicles

As an example of dismantling of automobile component, dismantling of motor in HEV is shown in Fig.4. In case of magnet recycling from a motor, de-magnetism of magnet is essential. Recycling of Nd and Dy from Neodymium Magnet is at present under research.

Fig.4 Dismantling of Electric Motor in Electric Vehicle

4. Research works on Recycling Technology

At NAKAMURA Laboratory in Institute of Multidisciplinary Research for Advanced Materials, Tohoku University, the following research works on recycle processing technology are at present implemented, in order to accomplish recycling-oriented society.

a. High Efficiency Rare Elements Extraction Technology Area Project
(supported by Ministry of Education, Science and Technology)

In order to recover minor rare elements efficiently from disposed electronics devices, which contains abundant minor rare elements and PGM in electronics parts, physical separation and sorting technology, chemical extraction technology, metallizing technology and process engineering technology are researched and developed in this project.

b. Research on High-Temperature Processing Technology

In order to develop new natural resources of minor rare elements and non-ferrous base metals like copper, fire smelting technology of seafloor hydrothermal deposits is under research.

Also, the environment-friendly refining technology of rare earth metal is developed to reduce the usage of halogenide.

c. Research on Hydrometallurgical Processing Technology

In order to use new resources of minor rare elements and non-ferrous base metals, new mineral dressing and refining technologies are under research. For example, the technology to remove arsenic from copper smelting and to remove boron from waste water generated in Nd-Fe-B magnet recycling are developed.

5. Concluding Remarks

Prof Nanjo, a professor at the Research Institute for Mineral Dressing and Metallurgy which existed at Tohoku University at that time (a forerunner of the current Institute of Multidisciplinary Research for Advanced Material), presented the following comment in 1988 in the journal “the Bulletin of the Research Institute for Mineral Dressing and metallurgy at Tohoku University“. A key to the steady supply of minor rare metal, a scarce resource, is establishment of a system of recycling scraps gathered both domestically and overseas in international cooperation with different countries which produce primary resources. The point is that he was predicting the exact present conditions. He accurately stated that “Minor rare metals are so significant to keep the high-tech industry and that if their supply dried up then this would spell the downfall of Japanese industry.” This sentence could be said about today without changing anything about it at all. This is a concept “Urban Mine”.

Therefore, with Tohoku University at its hub we will establish the 'science of metal cycles’ integrating the knowledge from the areas of the ‘extraction and separation' area, the field of quantum chemistry, as well as reaction analysis, and aim for its application in the collecting and recycling of minor rare metals from urban mines

Basic Research about Contactless Power Station System for Moving Electric Vehicle

Hidetoshi Matsuki, Yuki Ota*, Tetsuya Takura*, Fumihiro Sato*
Graduate School of Biomedical Eng., Tohoku Univ., 6-6-05 Aoba, Aramaki, Aoba-ku, Sendai, Miyagi, 980-8579, Japan
*Graducte School of Engineering, Tohoku Univ., 6-6-05 Aoba, Aramaki, Aoba-ku, Sendai, 980-8579, Japan
matsuki@ecei.tohoku.ac.jp

ABSTRACT

The construction of the charge infrastructure for Electric Vehicle (EV) is indispensable to the spread of EV. We aim at the construction of the wireless charging system for moving EV, from the view point of safety in the handling of the high-power and shortening the stop time by charge. In this system, the electric power for running is transmitted from the power transmission coil which is put on the road to receiving coil which is installed on the underside of EV. This time, we designed one-fifth scale model coil and decided suitable coil shape for this system. And we examined about real EV model from deliberation of scale model.

1. Introduction

Electric vehicles (EVs), which neither use fossil fuels nor emit carbon dioxide when running, have recently drawn attention as a way to mitigate the impact of vehicles on global warming, regional air pollution and energy shortages due to the depletion of oil reserves. However, EVs have two problems: limited range due to insufficient battery capacity and long battery charging time. We propose a technology to resolve these problems: a contactless power supply system that delivers electric power wirelessly from the road to a moving EV. This system employs electromagnetic induction as a method of contactless power supply and aims to supply necessary power to the EV via a pair of coils, a transmission coil installed in the road and a receiver coil mounted in the EV. This study examines the hypothesis that a meander transmission coil embedded in the road (Fig. 1) can supply sufficient energy to an EV in motion. The meander shape of the transmission coil gives it a low leakage flux in areas distant from the transmission coil. Two road lanes had meander transmission coils embedded in them and EVs were tested on these lanes. This technology will enable charging of multiple EVs simultaneously, which will be useful if EVs come into widespread use.

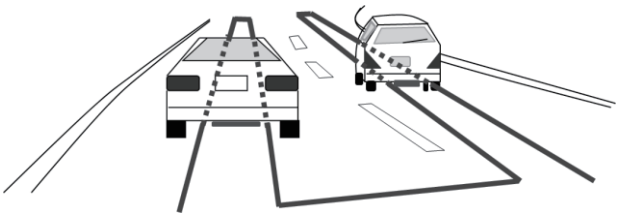

Fig. 1 Wireless charging system for moving EV

2. Circuit architecture of the in-motion power supply system

The circuit architecture of the studied in-motion contactless power supply system is shown in Fig. 2. The transmission coil and receiver coil have substantially different sizes, so the coupling coefficient is low. To compensate for this, an LC resonator with a high Q factor is installed in the receiving vehicle and configured to facilitate load matching.[1]

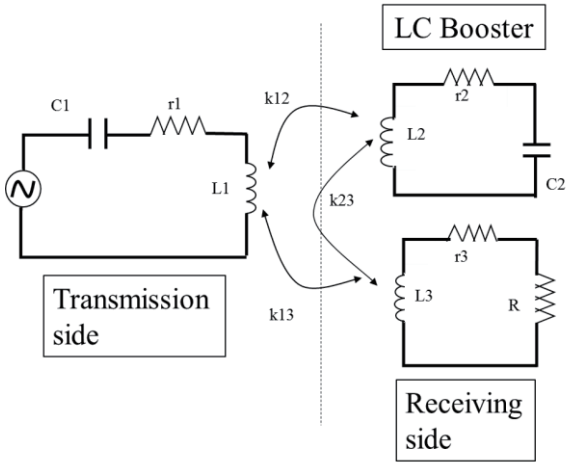

Fig. 2 Circuit for wireless charging system

3. Target transmission efficiency for in-motion power supply

The target efficiency for the proposed vehicle charging system is set by reference to the energy efficiency of gasoline-powered vehicles. The overall efficiency of the system is determined by examining how much fuel, assumed to be petroleum, must be burned per unit distance driven. Conventionally charged EVs have an overall efficiency of 23.3%; thus, if the contactless power transmission system has an efficiency of η%, then the efficiency of the EV travel is 23.3 × η%. The overall efficiency of a gasoline vehicle is 16%. Therefore, the power transmission system must achieve a 68% efficiency to have a total efficiency equivalent to using gasoline in vehicles. Accordingly, the target efficiency was set at 68%.[2]

4. Investigation of a scale model

A 1:5 scale model of the proposed system is shown in Fig. 3. Mn-Zn ferrite has been placed above the receiver coil to increase both the shielding and the coupling coefficient. The pitch interval of the meander coil is 0.3 m; this pitch interval was chosen because it demonstrated the most stable coupling when the LC resonator coil was displaced in the x direction.

An LC resonator and receiver coil were installed on lanes 1 (x: 0.15 m) and lane 2 (x: 0.65 m) respectively, and power transmission was investigated using these two lane models. One LC resonator and one receiver coil were fixed in lane 2 (x: 0.65 m), and the position of the other receiver coil was varied from 0 to 100 mm at 2.5 mm intervals parallel to the x axis. The gap between the coils was set at 40 mm in order to be consistent with the size of an actual vehicle. Power transmission efficiency and output power were measured and analyzed.

The transmission frequency was fixed at 350 kHz and the input current at 7 A. The results are shown in Fig. 4. Values exceeding the target efficiency were obtained at every location, demonstrating that high-efficiency transmission is possible. The model apparatus required transmission power of 15 W or higher, and the system provided sufficient power to both receiver coils at every point. In lane 2, values under changes in the y direction (y: 0, 0.5 and 1 m) were also measured, and the same results were obtained.

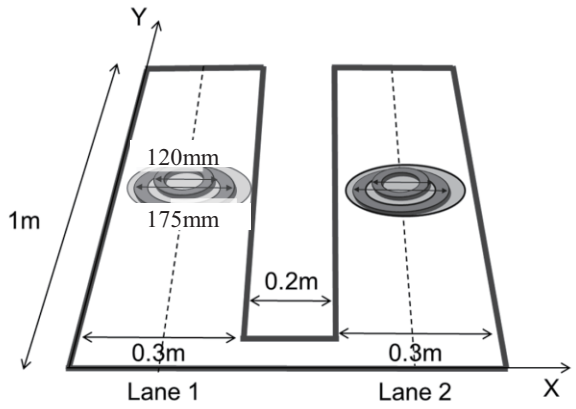

Fig. 3 Coil size of 1:5 scale model

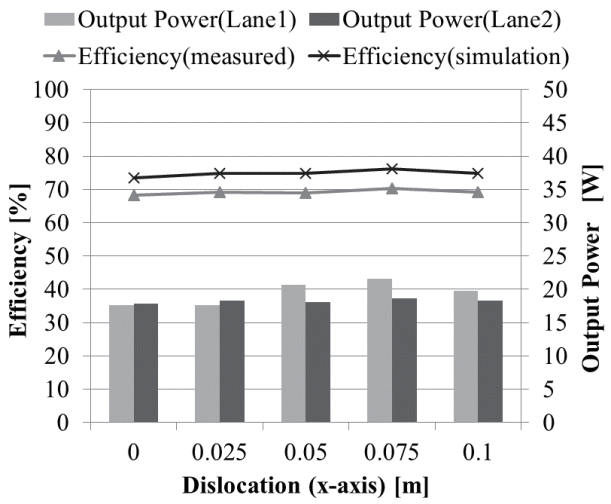

Fig. 4 Multiple wireless power transmission on 1:5 scale model

5. Investigation of a full-scale model

The coil form of a full-scale model was constructed based on the results from the 1:5 scale model: the outer diameter, inner diameter and thickness of the coil were increased by a factor of five and the number of turns was kept the same as in the 1:5 scale model. Coil parameters were estimated and the coils were arranged by the method described in Section 4. The output power and transmission efficiency was analyzed; the results of this analysis are shown in Fig. 5. The target efficiency was exceeded at every location, and the results imply that the maximum power that could be transmitted is 2.7 kW. This level is approximately 1/5 of the power consumed when an EV is traveling.

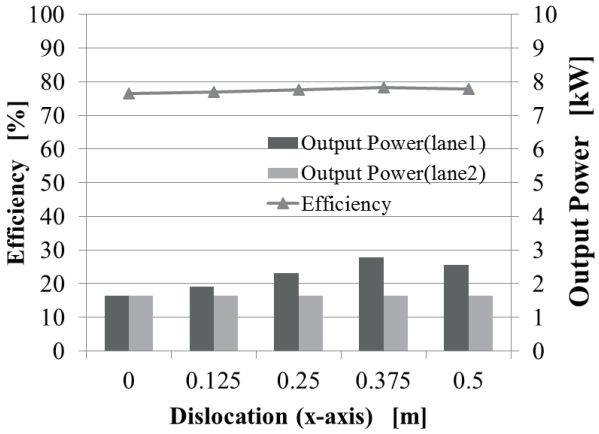

Fig. 5 Multiple wireless power transmission on full scale model

References

[1] T. Takura, Y. Ota, K. Kato, F. Sato, H. Mtauski, T. Sato, T. Nonaka , J. Magn. Soc. Jpn., **35**, 132-135 (2011).

[2] JARI, “Analysis about Total Efficiency and GHG emission” (in Japanese), (2011).

Tenth International Conference on Flow Dynamics
November 25-27, 2013, Sendai, Miyagi, Japan

Development of In Situ Measurement Techniques for Lithium-ion Batteries

Naoaki Kuwata, Yoshiki Iwai, Yasutaka Matsuda, Junichi Kawamura
Institute of Multidisciplinary Research for Advanced Materials, Tohoku University
Katahira 2-1-1, Aoba-ku, Sendai 980-8577, Japan
kuwata@tagen.tohoku.ac.jp

ABSTRACT

We have developed in situ measurement techniques for lithium-ion batteries. In this presentation we will introduce several techniques such as magnetic resonance imaging (MRI), acoustic emission (AE) and micro Raman spectroscopy. In situ measurement techniques are very important tool for lithium ion battery research. Because of the complicated reaction and diffusion dynamics, ex situ experiment gives limited information for the lithium-ion battery system. We also investigate thin-film batteries (TFBs) using thin-film amorphous solid electrolyte. Recently we have applied in situ micro Raman spectroscopy to a thin-film battery. From the in situ Raman spectroscopy, the structural change of a cathode film was observed in the all-solid-state batteries.

1. Introduction

We have developed in situ measurement techniques for lithium-ion batteries. In this presentation we will introduce several techniques such as magnetic resonance imaging (MRI), acoustic emission (AE) and micro Raman spectroscopy. In situ measurement techniques are very important tool for lithium ion battery research. Because of the complicated reaction and diffusion dynamics, ex situ experiment gives limited information for the lithium-ion battery system. We also investigate thin-film batteries (TFBs) using thin-film amorphous solid electrolyte. Recently we have applied in situ micro Raman spectroscopy to a thin-film battery. From the in situ Raman spectroscopy, the structural change of a cathode film was observed in the all-solid-state batteries.

2. Magnetic resonance imaging (MRI)

MRI techniques are powerful tool to provide new aspects from conventional one dimensional NMR spectroscopy. Recently we have performed NMR micro imaging to lithium-ion battery [1]. We have found out that proton (^{1}H) imaging of electrolyte (propylene carbonate: PC) which was located near cathode material ($LiMn_2O_4$) showed characteristic intensity enhancement and distortion. From several considerations as experimental parameters or charge-discharge cycling, we concluded the intensity enhancement and distortion are related to paramagnets in cathode material.

Figure 1 shows the results of in situ ^{1}H MRI measurement of lithium-ion batteries. During charge, the ^{1}H signal around the $LiMn_2O_4$ cathode shows enhancement of intensity. While discharging, the intensity of ^{1}H signal was decreased reversibly. This is due to the magnetism change in the $LiMn_2O_4$ cathode. The manganese ion will be dissolved in liquid electrolyte in the over charge state. The dissolved manganese ions (Mn^{2+}) will have large magnetic moment, which affects the 1H signal of liquid electrolyte. As a result the enhancement of intensity in liquid electrolyte can be observed.

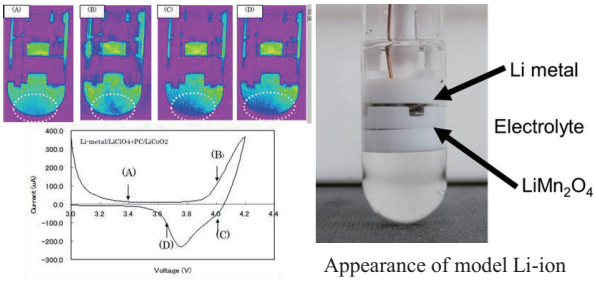

Fig. 1 In situ ^{1}H MRI measurement of model lithium battery. The battery components are Li/ $LiClO_4$+PC/ $LiMn_2O_4$

Recently, we have succeeded in situ MRI measurement using lithium (^{7}Li) nuclei. The ^{7}Li nuclei is a direct probe for reaction and diffusion in the lithium-ion batteries. However, the sensitivity of ^{7}Li is lower than of the proton (^{1}H) nuclei (27%). Due to the low sensitivity, we improved the noise filter and shield. Figure 2 shows the recent advance in ^{7}Li MRI technique. The motion of lithium-ions in the gel electrolyte can be observed by in situ measurement.

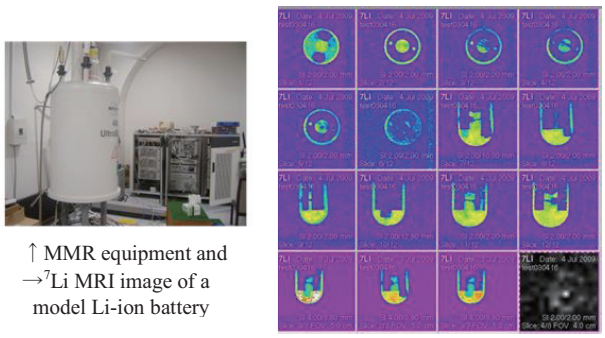

↑ MMR equipment and
→^{7}Li MRI image of a model Li-ion battery

Fig. 2 NMR setup for in situ ^{7}Li MRI measurement of lithium-ion batteries

3. Acoustic emission (AE)

Acoustic Emission (AE) technique is employed to detect degradation events inside of lithium-ion batteries [2]. A commercial battery and model half-cell (Li/organic electrolyte/SnO) are monitored with AE technique during charge and discharge cycles as shown in Fig. 3.

In the model half-cell using SnO anode, AE events are detected during charge and discharge, which can be attributed to the fracture of SnO anode material by phase transition. Many AE events are observed at 0.39 and 0.9 V in discharge process in the 1st cycle. The results suggest that the fractures of SnO electrodes are caused by volume change due to lithium extraction. The AE signals are attributed to the phase transition of Li-Sn alloy.

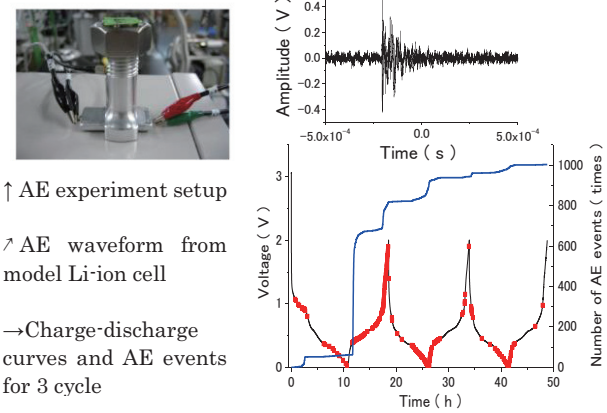

↑ AE experiment setup

↗ AE waveform from model Li-ion cell

→Charge-discharge curves and AE events for 3 cycle

Fig. 3. AE experimental setup for lithium-ion battery, and charge discharge profile with number of AE events for model battery using SnO anode

4. Thin-film lithium batteries

All solid state thin film batteries (TFB) are now developing for the use of micro-batteries, which will be useful for micro IT devices [3]. Figure 4 shows a concept of thin-film lithium batteries. Farmable liquid organic electrolytes can be replaced to inorganic solid electrolytes by thin-film technology. We have developed several thin-film electrolytes [4] and cathode materials [5]. The most reliable battery system is $Li/Li_3PO_4/LiCoO_2$ or $LiMn_2O_4$.

In order to understand the charge-discharge characteristics of the TFB, the *in situ* techniques such as micro Raman spectroscopy should be developed to characterize the structural change of the constituent thin films. In this study, we have applied *in situ* micro Raman spectroscopy to the structural change of $Li_xMn_2O_4$ cathode in the thin-film battery. The change of Raman spectra is related to the electrochemical property.

Figure 5 shows a variation of in situ Raman spectra of the thin-film battery where $LiMn_2O_4$, $Li_{0.5}Mn_2O_4$, λ-MnO_2 and Li_3PO_4 are observed. The λ-MnO_2 shows strong Raman bands of A_{1g} vibrations. The peak intensity and Raman shifts of the $Li_xMn_2O_4$ cathode varies reversibly depend on the battery potential. From these observations, we can discuss the structural change of the cathode film in the all-solid-state batteries.

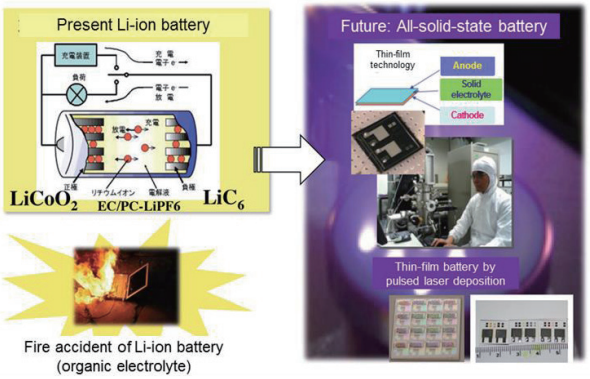

Fig. 4 Concept of thin-film solid-state batteries. Liquid electrolyte can be replaced to solid electrolyte to make all-solid-state batteries

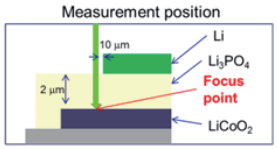

In situ micro Raman spectroscopy of a thin-film $LiMn_2O_4$ cathode in solid-state battery

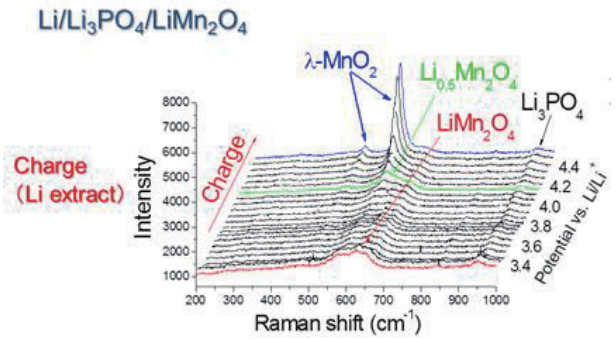

Fig. 5. In situ Raman spectroscopy of thin-film battery. The components of thin-film battery are $Li/Li_3PO_4/LiMn_2O_4$

References

[1] D. Ohno, Y. Iwai, J. Kawamura, Atom Indonesia, **36** (2010), 135-138.

[2] S. Komagata, N. Kuwata, R. Baskaran, J. Kawamura, K. Sato, and J. Mizusaki, ECS Transactions, 25 (33), (2010) 163-167.

[3] N. Kuwata, N. Iwagami, Y. Tanji, Y. Matsuda, J. Kawamura, J. Electrochem. Soc., 157 (4) A521-A527, (2010).

[4] N. Kuwata, N. Iwagami and J. Kawamura, Solid State Ionics 180 (6-8), (2009), 644-648.

[5] N. Kuwata, R. Kumar, K. Toribami, T. Suzuki, T. Hattori, and J. Kawamura, Solid State Ionics, 177, 26-32, (2006), 2827-2832.

Tenth International Conference on Flow Dynamics
November 25-27, 2013, Sendai, Miyagi, Japan

Development of Thermal Barrier Coating for Black Automobiles

Hiroki Gonome[1], Mehdi Baneshi[2], Junnosuke Okajima[3], Atsuki Komiya[3], Shigenao Maruyama[3]
[1] Graduate School of Engineering, Tohoku University, Sendai, Miyagi 980-8579, Japan
[2] School of Mechanical Engineering, Shiraz University, 71936-16548, Iran
[3] Institute of Fluid Science, Tohoku University, Sendai, Miyagi 980-8577, Japan
E-mail of corresponding author: hiroki1006@pixy.ifs.tohoku.ac.jp

ABSTRACT

The thermal barrier coating by the nanoparticle control was developed. The temperature measurement in the solar simulator was conducted in order to evaluate the thermal barrier performance. The coating contains CuO particles and their size was optimized by theoretical analysis. The spectral reflectance of the coating was measured by a spectrometer. The black-colored cool coating with the high near infrared reflectance was achieved. The temperatures of the black-colored cool coating and a typical black-colored coating were compared. The temperature of the cool coating was lower than the that of a typical black-colored coating.

1. Introduction

Automobiles are usually exposed to a great deal of sunlight. In many cases, dark color coatings are used on cars to give them an attractive appearance; however, these dark coatings have high absorptivity of solar irradiation in the visible (VIS) in the wavelength range from 0.38 μm to 0.78 μm and near infrared (NIR) regions in the wavelength range from 0.78 μm to 2.5 μm. Therefore, the interior temperature becomes high and a large cooling load is required [1].

To overcome this problem, a cool pigmented coating that controls nano-scale radiative heat transfer using controlled size submicron particles was proposed [2]. Our desired coating reflects NIR radiation, which accounts for 52% of sunlight energy, while decreases reflectance of VIS light. Baneshi et al. [2, 3] developed the theoretical design method of such coatings. Gonome et al. [4] achieved the cool black coating using CuO particles.

In this study, the objective was to investigate the thermal response of the spectral selective coatings pigmented with CuO particles experimentally. The temperatures of the samples were measured to evaluate their thermal response. The effects of particle size, volume fraction and coating thickness on thermal and esthetic behaviors were discussed.

2. Theoretical optimization

In the previous studies [2-4], the optimization parameter was defined to find the best pigment particles. The performance parameter of pigmented coating for solar reflectance in the solar spectrum region was proposed as

$$\rho_{TSR} = \int_{0.30}^{2.50} \rho(\lambda) I(\lambda) d\lambda \Big/ \int_{0.30}^{2.50} I(\lambda) d\lambda , \qquad (1)$$

where $I(\lambda)$ is the solar irradiation and $\rho(\lambda)$ is the spectral reflectance of the pigmented coating. A parameter which evaluates the aesthetic performance of a pigmented coating by considering spectral human eye sensitivity was defined as follows:

$$\rho_{VIS} = \int_{0.38}^{0.78} \rho(\lambda) \eta(\lambda) I(\lambda) d\lambda \Big/ \int_{0.38}^{0.78} I(\lambda) d\lambda , \qquad (2)$$

where $\eta(\lambda)$ is the normalized standard luminous efficiency. The optimization parameter can be calculated as follows:

$$R = \rho_{TSR} / \rho_{VIS} . \qquad (3)$$

In order to achieve an optimized coating, the parameter R should be maximized. The details of the optimization method are introduced in Ref. [2-4].

3. Experiment

For the experiment, the pigmented coatings were made using CuO powders. To find out the effect of particle size on the reflectivity and temperature, three powders with different nominal sizes (d_p = 0.89, 3.0 and 0.050 μm) were used. 0.89 μm is close to our desired optimum size. The details of the preparation method are introduced in Ref. [4]. The diffuse reflectivity of each sample was measured in the VIS and NIR regions.

The measurement of the temperature for the coating under the solar irradiated condition was performed using a solar simulator (IWASAKI ELECTRIC CO., LTD ESC0436-H134). Figure 1 shows the schematic of the temperature measurement experiment. In the simulator, the wind speed was controlled about 0.5 m/s, the inside temperature was 25 °C and the radiation intensity was about 1000 W/m^2. The T-type thermocouple was attached to the bottom of the coating sample. One of the thermocouples was fixed in the air to measure the inside temperature. The thermal insulation material is laid under the coating sample to avoid the effect of heat conduction with the basement. The pyranometer (Prede Meteorology Instruments PCM-03A) was also set up beside the coating samples to measure the irradiance.

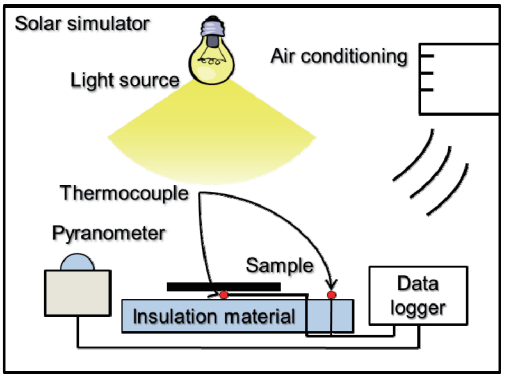

Fig. 1 Schematic of exposure temperature measurement

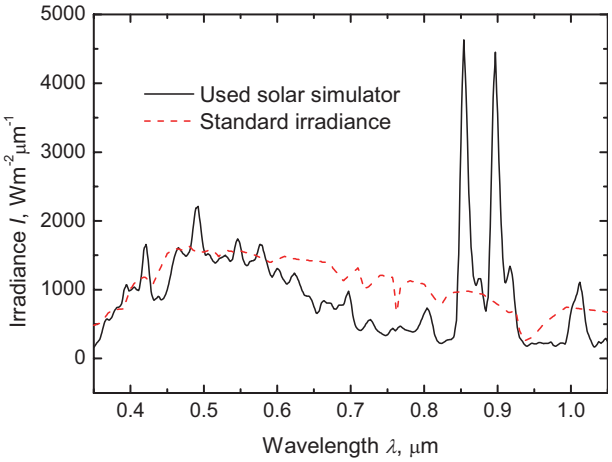

Fig. 2 Spectral irradiance of the used solar simulator and the irradiance standardized in AM1.5G [5]

Spectral irradiance of the used solar simulator and the irradiance standardized in AM1.5G are shown in Fig. 2. This spectral irradiance was provided by the product company [5]. This simulator has the strong peaks of spectral irradiance at 0.85 and 0.9 μm.

4. Results and Discussion

Figure 3 shows the measured spectral reflectances in VIS and NIR regions for the coating samples on black paper. To evaluate the esthetic performance of the cool coating quantitatively, a brightness Y is also calculated. The brightness Y can be evaluated as follows:

$$Y = \frac{100}{k}\int_{0.38}^{0.78} I(\lambda)\rho(\lambda)\bar{y}(\lambda)d\lambda, \qquad (4)$$

where $I(\lambda)$, $\rho(\lambda)$ are spectral sunlight and reflectivity, respectively. $\bar{y}$ is color matching function. k is a normalization factor defined in a way to ensure that an object with uniform reflectivity of 100% gives a brightness Y equal to 100%. The brightnesses Y of all samples are less than 5%. Therefore, they are looked black-color. The VIS reflectances of all samples are almost same. By contrast, their reflectances in NIR region differ. The NIR reflectance of CuO coating with

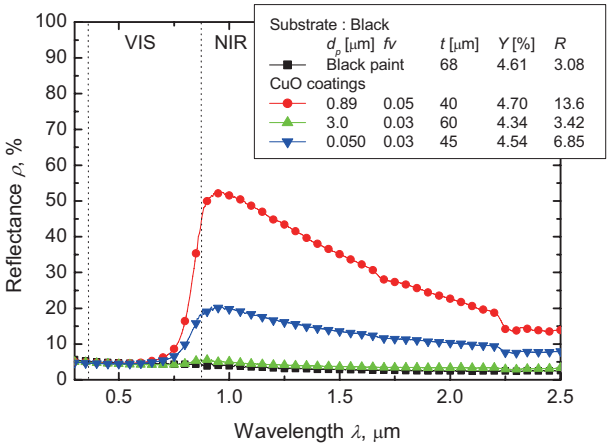

Fig. 3 Variation in the measured spectral reflectivity with particle diameter for CuO-pigmented coating and the typical black paint on black paper

Table 1. Measured temperatures of the coating samples

Sample	Temperature [°C]
Black paint	89.6
CuO (d_p = 0.89 μm)	84.0
CuO (d_p = 3.0 μm)	90.6
CuO (d_p = 0.050 μm)	84.6

d_p = 0.89 μm is highest in all samples. This spectral behavior is almost equivalent to our targeted behavior as the parameter R indicates (R = 13.6). It can be predicted that this coating is coolest in all samples. From this result, the effect of particle size on the coating reflectance can be demonstrated. Much deeper discussion and a fair comparison between analytical and experimental results are written in Ref. [4].

Table 1 shows the measured temperature of the coating samples in the solar simulator. CuO coating with d_p = 0.89 μm is the coolest in all samples as predicted above. The temperature of this coating is 5.6 °C lower than the one of the typical black paint. This result indicates that it is important for the thermal barrier performance to control the particle size. The useful of the coating can be confirmed in the solar simulator and should be examined outside in the future. By using this cool black coating, the interior temperature decreases and the cooling load can be reduced.

5. Concluding remarks

The thermal behavior of cool coatings pigmented with CuO particles was discussed. The temperature of the coating in the solar simulator was measured.

1. By using optimized CuO particles, a cool black coating with high NIR reflectance against solar irradiation can be obtained.
2. The temperature of the CuO coating with the particle size d_p = 0.89 μm, the volume fraction f_v = 0.05 and the coating thickness t = 40 μm is 5.6 °C lower than the one of the typical black paint.
3. By using a cool black coating, the interior temperature decreases and the cooling load can be reduced.

Acknowledgment

This work was supported by Strategic Regional Innovation Support Program by MEXT "Next-Generation Automobiles / Miyagi Area" and Grant-in-Aid for Research Fellowship for Young Scientist.

References

[1] Y. Kondou, Gekkan reform, **10** (2008), 13–17.
[2] M. Baneshi, et al., JQSRT, **112** (2011), 1197–1204.
[3] M. Baneshi, et al., Sol Energy, **86** (2012), 200–207.
[4] H. Gonome, et al., JQSRT, (2013), In Press, *Corrected Proof*.
[5] IWASAKI ELECTRIC CO., LTD., Private communication.

Tenth International Conference on Flow Dynamics
November 25-27, 2013, Sendai, Miyagi, Japan

Development of Novel Hydrogen Storage Materials

Guanqiao Li[1], Motoaki Matsuo[1], Shigeyuki Takagi[1], Shin-ichi Orimo[1,2]
[1]WPI Advanced Institute for Materials Research (WPI-AIMR), Tohoku University, Sendai 980-8577, Japan
[2]Institute for Materials Research (IMR), Tohoku University, Sendai 980-8577, Japan
E-mail: orimo@imr.tohoku.ac.jp

ABSTRACT
Hydrogen in hydrides exhibits various bonding states. We have focused on the transition between the bonding states of hydrogen in the hydrides to develop novel hydrogen storage materials. In this research, kinetics property of the reaction involving this kind of bonding state transition from a metal hydride $YMn_2H_{4.5}$ to a complex hydride YMn_2H_6 was investigated. The time dependence of YMn_2H_6 formation fraction suggests that the kinetics is controlled by random nucleation and nuclei growth. By x-ray absorption fine structure measurement, Mn–H atomic distance in $[MnH_6]^{5-}$ complex anion of YMn_2H_6 was determined to be 1.67±0.05 Å.

1. Introduction

Hydrogen in hydrides exhibits various bonding states depending on the characteristics of and distances and coordination to neighboring atoms; “neutral,” in the case of hydrogen in metal (intermetallic compound) hydrides such as $LaNi_5H_6$, “covalent,” as in complex hydrides such as $LiBH_4$ and “negatively charged,” as in ionic hydrides such as $NaMgH_3$. We have focused on the transition between the bonding states of hydrogen in the hydrides to develop novel hydrogen storage materials.

YMn_2H_6 is a complex hydride with a partially disordered K_2PtCl_6 type structure, as depicted in Fig. 1. In YMn_2H_6, one of the Mn atoms exists as Mn^{2+} cation (Mn1) and the other one covalently binds with hydrogen atoms to form a $[MnH_6]^{5-}$ complex anion (Mn2) [1, 2]. Recently, we experimentally verified that the complex hydride can be synthesized from a metal hydride $YMn_2H_{4.5}$, wherein the hydrogen atoms are located into the interstitial sites, under much lower hydrogen pressure of 5 MPa than the previously reported value of 170 MPa, as predicted by the enthalpy change of -87 kJ/mol H_2 evaluated using first-principles calculations [3]. This transition from metal hydride to complex hydride results in an increased hydrogen density in the hydride and therefore provides us a novel method for designing advanced hydrogen storage materials.

In this research, we have investigated experimentally the formation kinetics and local structure of YMn_2H_6.

2. Method

Intermetallic compound YMn_2 was prepared by arc-melting of pure metal Y and Mn. Metal hydride $YMn_2H_{4.5}$ was synthesized by hydrogenation of YMn_2 at 273 K under 0.1 MPa H_2. YMn_2H_6 was formed after hydrogenation of $YMn_2H_{4.5}$ at 373 K to 448 K under 25 MPa H_2. Formation fraction of YMn_2H_6 was determined by powder x-ray diffraction measurement. The local structure of YMn_2H_6 was investigated by x-ray absorption fine structure (EXAFS) measurement.

3. Results and Discussion

The time dependence of YMn_2H_6 formation fraction after hydrogenation of $YMn_2H_{4.5}$ at each temperature conditions was well fitted by Johnson-Mehl-Avrami equation as shown in Fig. 2 [4]. This result suggests that the formation kinetics is controlled by random nucleation and nuclei growth of YMn_2H_6, and the activation energy was calculated to be 113 kJ/mol H_2.

Mn–H covalent bonding in the $[MnH_6]^{5-}$ complex anion was successfully detected by EXAFS, as shown in Fig. 3, and the Mn–H atomic distance (Mn2-H) in $[MnH_6]^{5-}$ was determined to be 1.67±0.05 Å. Because of the weak scatting intensity of hydrogen, the bonding states associated with hydrogen were seldom observed in EXAFS measurement. The successful observation of the Mn-H bonding is because of as many as six hydrogen atoms binding covalently with Mn and the small Debye-Waller factor due to the weak thermal vibration in the bonding direction in the $[MnH_6]^{5-}$ complex anion.

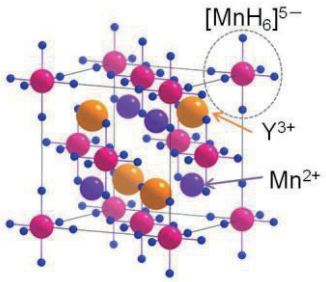

Fig. 1 Crystal structure of complex hydride YMn_2H_6.

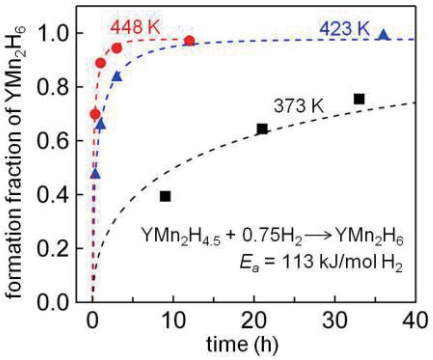

Fig. 2 Time dependence of YMn_2H_6 formation fraction after hydrogenation of $YMn_2H_{4.5}$ and the fitting curve by Johnson-Mehl-Avrami equation is shown.

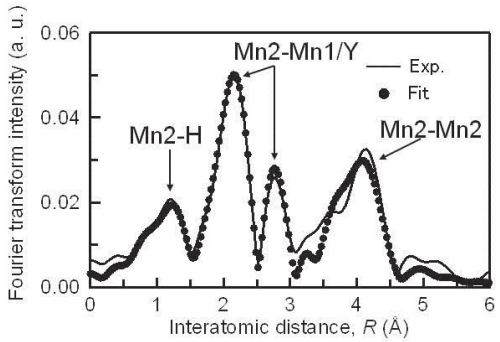

Fig. 3 Fourier transform intensities of k-weighted EXAFS functions $\chi(k)$ of YMn_2H_6.

We have also tried to apply the same method to improve the hydrogen density in the metal hydrides of YFe_2 that has the same C15-type Lave phase structure as YMn_2. Contrary to YMn_2, YFe_2 does not show the transition due to the absence of any stable ionic configurations composed of Y^{3+}, Fe^{3+} and $[FeH_6]^{4-}$. For such systems, we have found that adding of Li is effective to accommodate the charge neutrality, and thus promotes the change in metal-hydrogen bonding, resulting in the formation of complex hydride $YLiFeH_6$ with the ionic configuration of $Y^{3+}Li^{+}[FeH_6]^{4-}$ (Fig. 4) [5].

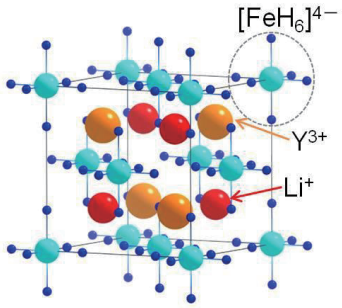

Fig. 4 Crystal structure of complex hydride $YLiFeH_6$.

The Li addition is also effective to modify the metal-hydrogen bonding in transition metal based monohydride NiH. We have synthesized a novel perovskite hydride $LiNiH_3$, in which the hydrogen has a weak covalent character that is totally different from bonding state in NiH, and clarified the formation process of $LiNiH_3$ using *in situ* synchrotron x-ray diffraction measurements [6,7].

4. Concluding remarks

In this study, we focused on the transition between the bonding states of hydrogen in the hydrides of YMn_2. The formation kinetics of the complex hydride YMn_2H_6 consisting of the Y^{3+} and Mn^{2+} cations and the $[MnH_6]^{5-}$ complex anion from the metal hydride $YMn_2H_{4.5}$ was investigated experimentally. The time dependence of the YMn_2H_6 formation fraction after hydrogenation of $YMn_2H_{4.5}$ suggested that the kinetics are controlled by random nucleation and growth with activation energy of 113 kJ/mol H_2. X-ray absorption fine structure analysis successfully detected the Mn–H covalent bonding nature in YMn_2H_6 despite the small x-ray scattering intensity of the H atom. The Mn–H distance was determined to be 1.67±0.05 Å.

In order to promote the transition into complex hydrides of much general metal hydrides, we have introduced a method of adding Li to accommodate the charge neutrality in the hydrides. By this method, the novel complex hydride $YLiFeH_6$ and the perovskite hydride $LiNiH_3$ have been successfully synthesized.

References

[1] S. Takagi, K. Miwa, T. Ikeshoji, M. Matsuo, M. Kano and S. Orimo, *Appl. Phys. Lett.*, **100** (2012) 021908.
[2] M. Kano, T. Ito, M. Matsuo, S. Takagi, S. Semboshi and S. Orimo, *Key Eng. Mater.*, **508** (2012) 310.
[3] M. Matsuo, K. Miwa, S. Semboshi, H.-W. Li, M. Kano and S. Orimo, *Appl. Phys. Lett.*, **98** (2011) 221908.
[4] M. Matsuo, D. Matsumura, Y. Nishihata, G. Li, N. Hiyama, S. Semboshi and S. Orimo, *Appl. Phys. Lett.*, **100** (2012) 044101.
[5] M. Matsuo, H. Saitoh, A. Machida, R. Sato, S. Takagi, K. Miwa, T. Watanuki, Y. Katayama, K. Aokia and S. Orimo, *RSC Adv.*, **3** (2013) 1013.
[6] R. Sato H. Saitoh, N. Endo, S. Takagi, M. Matsuo, K. Aoki and S. Orimo, *Appl. Phys. Lett.*, **102** (2013) 091901.
[7] S. Takagi, H. Saitoh, N. Endo, R. Sato, T. Ikeshoji, M. Matsuo, K. Miwa, K. Aoki and S. Orimo, *Phys. Rev. B.*, **87** (2013) 125134.

Tenth International Conference on Flow Dynamics
November 25-27, 2013, Sendai, Miyagi, Japan

Nanoscale Imaging of Living Cells using Nano-Scanning Electrochemical Microscopy

Yasufumi TAKAHASHI[a], Yoshiharu MATSUMAE[b], Hitoshi SHIKU[b], Kosuke INO[b],
Yuri E. KORCHEV[c], and Tomokazu MATSUE[a,b].
[a]Advanced Institute for Materials Research, Tohoku University, Sendai 980-8577, Japan
[b]Graduate School of Environmental Studies, Tohoku University, Sendai 980-8579, Japan
[c]Division of Medicine, Imperial College London, London, W12 0NN, UK.
E-mail: matsue@bioino.che.tohoku.ac.jp.

ABSTRACT

We describe voltage-switching mode scanning electrochemical microscopy (VSM-SECM), in which a single SECM tip electrode was used to acquire high-quality topographical and electrochemical images of living cells simultaneously. This was achieved by switching the applied voltage so as to change the faradaic current from a hindered diffusion feedback signal (for distance control and topographical imaging) to the electrochemical flux measurement of interest. This imaging method is robust, and a single nanoscale SECM electrode, which is simple to produce, is used for both topography and activity measurements.

1. Introduction

Scanning electrochemical microscopy (SECM) uses an electrode tip for detecting electroactive chemical species and is an effective tool for the investigation of the localized chemical properties of sample surfaces and interfaces. Because SECM has high temporal resolution and can be used under physiological conditions, it is particularly well suited for quantitative measurements of chemicals like neurotransmitters, nitric oxide, reactive oxygen species, and oxygen, which are released/consumed by living cells. In conventional SECM, the probe is often micrometer scale and the probe vertical position is kept at a constant height, a plane, during probe scanning. If the sample topography is not flat, the electrode-sample separation changes during scanning, complicating the SECM measurement and its analysis.

Various methods for SECM electrode miniaturization and control of the electrode-sample separation have been advocated, in order to improve the resolution of SECM imaging. The reliable fabrication of nanoelectrodes with a small ratio of electrode-insulation to active electrode (RG) is of particular importance to improve SECM spatial resolution. In particular, a variety of different approaches have been adopted to create small electrodes with thin insulating coats such as photolithography, chemical vapour deposition, electrodeposited paint methods, laser pulling techniques, and pyrolytic carbon deposition. Photolithography and chemical vapour deposition can be used to make thin insulation layers, but pinholes are often a problem. The laser pulling technique is effective and reproducible, but this method requires special polishing techniques or focused ion beam milling to expose the metal region. On the other hand, pyrolytic carbon deposition inside glass pipettes enables fabrication of nano-sized electrodes with insulation of excellent integrity. This type of electrode has proven powerful for living cell measurements, and we thus use it for the studies herein.

Control of the electrode-sample distance is also critical for electrochemical measurements, free from topographical artifacts but has proved difficult to achieve to date. AFM, shear force, impedance, faradaic current, ion current[1,2], and electrochemical feedback distance-control systems have been developed but many of these required additional probe modifications for distance control. Impedance-feedback and constant-current distance control are effective methods to obtain high resolution topography images because they do not require additional modification of the electrode for distance control. However, the impedance feedback mode has resolution limitations due to the principle of the measurement. The constant-current mode has been shown to be capable of high resolution imaging, but only for topography hitherto.

Here, we report a novel voltage switching mode (VSM)-SECM developed to achieve constant-distance mode measurements and the possibility of (electro)chemical flux measurements at the same location. The imaging protocol involved first translating the tip electrode towards the surface while detecting the distance-dependent current for the hindered diffusion of a redox-active solute to the tip, with the probe potential biased to carry out the cathodic process. When the current diminished compared to bulk solution by a set amount, this indicated that the probe was at a desired distance from the surface or structure of interest. The motion of the probe was arrested and the z-position of the piezoelectric position was registered. By carrying out this process at a number of points over the surface, the topography was mapped out. Additionally, for concomitant flux measurements, when the electrode reached the desired position from the surface, at each tip approach, the applied voltage could be switched positive to permit electrochemical (flux) imaging of the sample surface.

2. Results

Characterisation of the Carbon Electrodes

The topographical resolution in the SECM constant-current mode depends on the size and aspect ratio of the electrode. In this report, we used carbon nanoelectrodes produced by the pyrolytic decomposition of butane gas[3]. Fig. 1 shows field emission-scanning electron microscope (FE-SEM) images of a carbon nanoelectrode produced for these studies. The nanoelectrode is quite sharp (cone angle of the tip is 10) and the radius of the carbon and outer glass was 22 nm.

However, the deposited carbon region is difficult to recognize even when using FE-SEM, and we therefore routinely characterized electrodes using approach curve recordings. Probes radii were estimated from steady-state currents in bulk solution, id assuming disk type electrodes with an RG (glass radius to electrode radius) value of 1.5.

$$i_d = 4.64nFC^*Da$$

where n is the number of electrons transferred in the tip reaction, F is the Faraday constant, $D = 6.5 \times 10^{-6}$ cm^2s^{-1} is the diffusion coefficient of $FcCH_2OH$, of concentration C* in solution. This calculated tip radius (6.4 nm for the data shown in Fig. 1) was used to produce theoretical approach curves for the same tip geometric parameters. The current profiles were fitted to established theoretical curves for simple disk geometry. Good correlation was observed between theory and experiment. Therefore, the pyrolytic carbon nanoelectrode is effectively planar and can be used for high resolution electrochemical microscopy imaging and quantitative analysis of electrochemical species.

Simultaneous Electrochemical and Topographical Imaging in Voltage Switching Mode

We applied VSM-SECM to image epidermal growth factor receptor (EGFR), which is one of the key membrane proteins associated with cancer, on cell surfaces. Epidermal growth factor (EGF) binds to the EGFR, and the activated EGFR initiates the signalling cascades, thereby promoting cell proliferation, differentiation, apoptosis, and migration. The evaluation of EGFR expression levels on cell surfaces is thus important, but extremely difficult to achieve. In previous work, we evaluated EGFR expression level using SECM, but, it was impossible to identify a cell with high EGFR expression from others when the cells were in a confluent stage. The limitation arose because images had to be taken with a relatively large electrode in conventional constant-height mode. In the present study, we used a 650 nm radius carbon electrode for VSM-SECM in HEPES buffer containing 4.7 mM p-aminophenyl phosphate (PAPP). EGFR was labelled with alkaline phosphatase (ALP)-tagged antibody. The ALP-catalysed reaction produces p-aminophenol (PAP) which can be detected by oxidation, giving an electrochemical signal, which indicates the presence of EGFR on the cell surface.

Fig. 2 shows the topography and electrochemical images of A431 cells. The VSM yields highly resolved topographical structures and electrochemical features. From the images, it is evident that EGFR is not evenly distributed on the cell surfaces and also that EGFR distribution is not directly correlated with the microvilli and lamellipodium, which are clearly seen in the topography image. This result demonstrates that the VSM-SECM is potentially promising for nanoscale chemical mapping at biological interfaces.

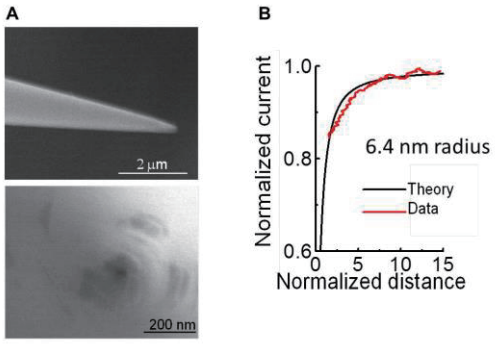

Fig.1 FE-SEM images of side and top view of the carbon nanoelectrode. (B) Approach curves in a 1.0 mM $FcCH_2OH$ (diffusion-limited oxidation) and PBS for electrochemical measurements on insulating substrate. The electrode was held at 500 mV vs. Ag/AgCl. The RG values of the theoretical curves were estimated to be 1.5. The radius of the carbon electrode estimated from steady-state current was6.4 nm (bottom), respectively.

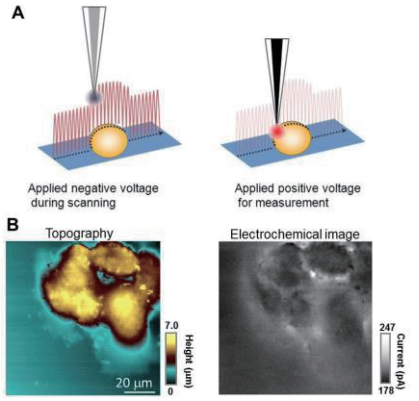

Fig.2 (A) Schematic illustration of voltage switching mode SECM, in which a signal for the hindered diffusion of a mediator, is implemented in hopping mode (probe approach at each pixel) to trace the topography of the surface (left) and at each set point (closest distance) an interfacial flux measurement (electrochemical activity) is made after switching the voltage (right). (B) Topography (left) and electrochemical (right) images of A431 cells. The carbon electrode was held at - 500 mV (topography) and 350 mV (electrochemical activity) vs. Ag/AgCl in HEPES buffer containing 10 mM $Ru(NH_3)_6Cl_3$ and 4.7 mM PAPP. The electrode radius is 721.5 nm.

3. Concluding remarks

We have demonstrated VSM-SECM as a powerful technique for simultaneous topography and electrochemical flux measurements to detect EGFR on A431 cells surface. The method is reliable and does not require special modification of the electrode for distance control. Moreover, because the topography and activity are determine with a single probe, simultaneously-obtained images are co-located. In the future, it would also be interesting to investigate long time or localized intracellular measurement using this electrode.

References

1. Y. Takahashi, A. I. Shevchuk, P. Novak, Y. Murakami, H. Shiku, Y. E. Korchev, T. Matsue, ***J. Am. Chem. Soc***., 2010, 132, 10118-10126.
2. Y. Takahashi, A. I. Shevchuk, P.l Novak, Y. Zhang, N. Ebejer, J. V. Macpherson, P. R. Unwin, A. J. Pollard, D. Roy, C. A. Clifford, H. Shiku, T. Matsue, D. Klenerman, Y. E. Korchev, ***Angew. Chem. Int. Ed.***, 2011, 50, 9638-9642.
3. Y. Takahashi, A. I. Shevchuk, P. Novak, B. Babakinejad, J. V. Macpherson, P. R. Unwin, H. Shiku, J. Gorelik, D. Klenerman, Y. E. Korchev, T. Matsue, ***Proc. Natl. Acad. Sci. USA***, 2012, 109, 11540-11545.

Tenth International Conference on Flow Dynamics
November 25-27, 2013, Sendai, Miyagi, Japan

Development of All-Solid-State Lithium Battery with $LiBH_4$ as a Solid Electrolyte

Xiong Shan, Kuniaki Takahashi and Hitoshi Takamura
Department of Materials Science, Graduate School of Engineering, Tohoku University
E-mail of corresponding author: takamura@material.tohoku.ac.jp

ABSTRACT

All-solid-state lithium batteries using $LiBH_4$ electrolyte and $LiCoO_2$ cathode were prepared and its electrochemical performance and the effect of intermediate layer between $LiBH_4$ and $LiCoO_2$ have been investigated. For the intermediate layer, Li_3PO_4 and Al_2O_3 prepared by pulsed laser deposition, and TiO_2 and ZrO_2 prepared by atomic layer deposition, respectively were utilized. Among them, Li_3PO_4 intermediate layer was found to be the most effective to suppress the interfacial reaction and to improve the capacity retention.

1. Introduction

All-solid-state lithium batteries using a solid electrolyte are a key technology to solve the safety problem resulted from a highly flammable liquid electrolyte in conventional lithium batteries. Our previous work has found that $LiBH_4$, which has a high lithium ion conductivity of 10^{-3} S/cm, chemical compatibility with a lithium metal anode, and good formability, is promising as a solid electrolyte [1]; however, there is a huge interfacial resistance between the electrolyte and a $LiCoO_2$ cathode. To overcome the interfacial problem, intermediate layers, such as Li_3PO_4, have been adapted by using a pulsed laser deposition (PLD) [2]. Material properties required for the intermediate layer are 1) a certain level of lithium ion conductivity, 2) surface coverage as uniform as possible, and 3) thickness as thin as possible. Meanwhile, atomic layer deposition (ALD) has been widely used in semiconductor-research society because of its capability of fabricating an ultra thin film in the thickness of several nm to 100 nm with perfect coverage and smooth surface. The purpose of this study is therefore to fabricate all-solid-state lithium batteries with $LiBH_4$ as a solid electrolyte and $LiCoO_2$ thin-film cathode with intermediate layers prepared by PLD and ALD, and to clarify their electrochemical properties.

2. Experimental procedures

Thin-film $LiCoO_2$ was prepared by PLD on a Pt substrate. Then Li_3PO_4 and Al_2O_3 layers were prepared on the $LiCoO_2$ film by PLD, while TiO_2 and ZrO_2 layers were grown by atomic ALD at 200°C for 750 cycles. The films were evaluated by spectroscopic ellipsometry, XRD, SEM-EDS. The scheme of thin film fabrication is depicted in Fig. 1.

All-solid-state lithium batteries were then fabricated. $LiBH_4$ electrolyte powders were pressed together with the $LiCoO_2$ film having the intermediate layer; Li foil was finally placed on the $LiBH_4$ electrolyte to be an anode followed by tightening screws. This process was carried out in Ar atmosphere. Charge-discharge measurement was performed at 120°C at a constant current density of 0.05 mA (0.065 $mA \cdot cm^{-2}$) in a potential range between 3.0 and 4.2 V using a potentio/galvanostat. Electrochemical impedance spectra were also measured at the same temperature with an ac voltage of 100 mV in the frequency range of 1 MHz to 0.1 Hz.

Fig. 1 Scheme of fabrication procedures

3. Results and Discussion

SEM observation revealed that 25 nm-thick Li_3PO_4 and Al_2O_3 layers were uniformly grown on the columnar $LiCoO_2$ film by PLD. EDX analysis also supported clear element distribution between the layers. The ac impedance analysis was then performed and clarified that the minimum interfacial resistance of 20 Ω was attained for 25 nm-thick Li_3PO_4, which is lower than that for a cell without intermediate layer by 3 orders of magnitude [2]. The resistance turned up to 1500 Ω for Al_2O_3. For Li_3PO_4 showing the best effect, 10–25 nm was found to be an appropriate thickness to minimize the interfacial resistance; on the other hand, for Al_2O_3 intermediate layer, the thickness and the interfacial resistance have linear relationship, suggesting that resistance of the intermediate layer itself reflects the interfacial resistance. In other words, very thin Al_2O_3 layer less than 1 nm might work as an intermediate layer and suppress the interfacial resistance to the sufficient level. In charge-discharge measurement, the cell with 25 nm-thick Li_3PO_4 intermediate layer achieved the best capacity retention of 95% after 30 cycles.

The same analyses were performed for the cell with intermediate layer prepared by ALD. EDS results for the TiO_2-coated $LiCoO_2$ thin film proved that titanium existed after ALD deposition. However the XRD pattern showed no peaks for TiO_2, which indicated the layer was amorphous. The thicknesses of the coated layers were estimated by SEM and spectroscopic ellipsometry. For the ZrO_2 film prepared by ALD, the thickness was estimated to be 100nm.

Figure 2 displays Nyquist plots of the cells. Compared with a previous result for the cell with Al_2O_3 intermediate layer prepared by PLD, interfacial

resistances of the samples with TiO_2 and ZrO_2 layer prepared by ALD were both lower, which implies the smoothness and uniformity of the ALD thin film is hopefully suitable for improving the intermediate properties of all-solid-state lithium battery.

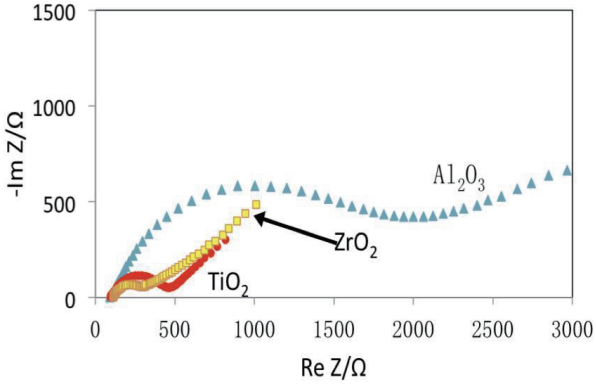

Fig. 2 Nyquist plots for cells with intermediate layers

Figure 3 displays the discharge capacity up to 29 charge-discharge cycles of the four cells with different intermediate layer, which indicated that, except for Li_3PO_4, the cell with TiO_2 intermediate layer had better charge-discharge properties. This might be relevant to a fact that lithium can intercalate into TiO_2.

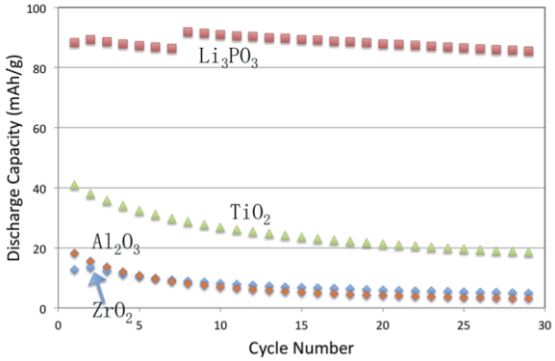

Fig. 3 Charge-discharge performance with cycle number

4. Concluding Remarks

Four materials, Li_3PO_4, Al_2O_3, TiO_2 and ZrO_2 were grown on $LiCoO_2$ thin-film cathodes by either PLD or ALD method to suppress the interfacial resistance between $LiCoO_2$ cathode and $LiBH_4$ electrolyte and the effect of these intermediate layers were investigated. The most effective material for suppression of the interfacial resistance was Li_3PO_4 and the minimum value of 20 Ω was attained for Li_3PO_4 with a thickness of 10-25 nm, which was lower than that for a cell without an intermediate layer by 3 orders of magnitude. For charge-discharge measurement, capacity retention was improved up to 95% after 30 cycles. As for Al_2O_3, because the resistance itself becomes an issue, the thickness should be less than about 1 nm for practical use. Meanwhile, TiO_2 and ZrO_2 intermediate layers prepared by ALD also successfully suppressed the interfacial resistance.

References

[1] M. Matsuo, Y. Nakamori, S. Orimo, H. Maekawa, and H. Takamura, Appl. Phys. Lett., **91** (2007), 224103.

[2] K. Takahashi, K. Hattoria, T. Yamazakia, K. Takadab, M. Matsuoc, S. Orimoc, H. Maekawaa, and H. Takamura, J. Power Sources, **226** (2013), 61.

Tenth International Conference on Flow Dynamics
November 25-27, 2013, Sendai, Miyagi, Japan

Green Nanodevice by Super Low Damage Process

Seiji Samukawa[1,2,3]
[1] Institute of Fluid Science, Tohoku University, 2-1-1 Katahira, Aoba-ku, Sendai 980-8577, Japan
[2] WPI-AIMR, Tohoku University, Japan
[3] Japan Science and Technology Agency (JST), CREST, Japan
samukawa@ifs.tohoku.ac.jp

ABSTRACT

High density and regularly arranged 2-dimensional array of silicon nanodisk, a sub-10nm-silicon-nano-disk (Si-ND) structure, was fabricated using the bio-template (ϕ7-nm-etching-mask) and damage-free chlorine (Cl) neutral beam (NB) etching. In this structure, the controllable band gap energy (from 2.2eV to 1.4eV) and high photon absorption coefficient (>10^5 cm^{-1}) could be obtained at RT. This structure can be used to develop high efficiency and inexpensive silicon quantum dot solar cells.

1. Introduction

Recently, an all-silicon tandem solar cell comprising a quantum dot superlattice (QDSL) has attracted much attention due to its potential to breakthrough the Shockley-Queisser limit.[1,2] One of the advantages of the QDSL is that the required energy band gap for each cell can be engineered by changing the quantum dot size.[3] Reportedly, the maximum conversion efficiency can be improved up to 47.5% for three-cell tandem stacks.[4] However, not only the uniformity and control of QD size but also of the spacing between QDs are equivalently essential to generate the miniband in the QDSL for carrier transport.[5] The ideal spacing between QDs is approximately 2 nm or less in the SiO_2 matrix.[6] The technique widely used to fabricate the Si quantum dot superlattice is depositing alternately multiple layers of amorphous silicon-rich oxide (SiO_x, x<2) and stoichiometric silicon dioxide (SiO_2) by sputtering or plasma-enhanced chemical vapor deposition followed by annealing at a high temperature.[6,7] However, the results showed nonuniform dot size and dot spacing.

To address these problems, we have developed a sub-10nm-silicon-nano-disk (Si-ND) structure using the bio-template (ϕ7-nm-etching-mask) and damage-free chlorine (Cl) neutral beam (NB) etching.[8] The fabricated ND had a quantum effect, i.e. Coulomb staircase, at room temperature (RT). Two geometrical parameters of thickness and diameter in Si-ND can be independently controlled. Interestingly, the quantum effect of a single Si-ND is strongly dependent on its thickness, while almost independent of its diameter.[8] In this study, a 2D Si ND array with a high-density and well-ordered arrangement could be fabricated by using bio-template and an etching process combined with nitrogen trifluoride (NF_3) gas/hydrogen radical treatment (NF_3 treatment) and Cl NB etching. In this structure, the controllable band gap energy (from 2.2eV to 1.4eV) and high photon absorption coefficient (>10^5 cm^{-1}) could be obtained at RT by controlling the Si-ND structure.

2. Fabrication of high-density 2D array of Si-ND

The fabrication of a 2D Si-ND array using the bio-template and damage-free NB etching[8] is schematically shown in Fig. 1(a). The steps are as follows: multilayer films of 1.4-nm SiO_2, several nm-thick poly-Si and 3-nm SiO_2 (the 3-nm SiO_2 was fabricated by our developed neutral beam oxidation at a low temperature of 300 ºC and is called NBO SiO_2 hereafter) were sequentially prepared on a Si wafer as shown in Figs. 1(1), (2), and (3), respectively; (4) a 2D array of ferritin molecules (protein including iron oxide core (Fe-core) in the cavity) was placed through directed selforganization on the surface of NBO SiO_2; (5) ferritin protein shells were removed by heat treatment in oxygen atmosphere to obtain 2D Fe-core as a template; (6) etching was carried out using a NF_3 treatment and Cl NB etching to remove NBO SiO_2 and poly-Si, respectively; (7) and finally 2D Fe core was removed by using hydrochloric solution. The sample underwent NF_3 treatment for 30 min to remove NBO SiO_2 and NB etching for 90 seconds to remove 4-nm poly-Si. Figure 2 shows a SEM image of the top view of the sample after etching. We can see that the 2D Si-ND array has a high-density (>7×10^{11} cm^{-2}) and well-ordered arrangement. The 2D array is what remained after etching, proving that a good-quality 2D Si-ND array was successfully fabricated using the bio-template and Cl NB etching with NF_3 treatment. We performed NF_3 treatment to investigate the controllability of the ND diameter, i.e. the spacing between NDs. When the NF_3 treatment times were 15 and 30 min, the average gaps were about 1 and 3 nm (G_{ii} and G_{iii}), and the diameters were about 10 and 8 nm (D_{ii} and D_{iii}), respectively . These results suggest that the spacing between adjacent NDs can be controlled by changing the NF_3 treatment time, which also indicates that the formation of miniband in a 2D Si-ND array can be controlled. Although the spacing control by NF_3 treatment is accompanied by inevitable changes in diameter, as shown in Fig. 4, the diameter changes do not affect the quantum effect, which was proven in a previous work.[8)]

3. Optical Properties of 2D Si-ND array

The absorption properties of the structure were studied by measuring the transmission for samples by

UV-vis-NIR. The absorption coefficient has been calculated in accordance with the equation below[9]

$$T=e^{-\alpha d} \quad (1)$$

α being the absorption coefficient, d the total thickness of the ND thickness and surface oxide thickness (3-nm thick), and T the transmittance of light passing through the structure. Figure 3(a) shows the results of an absorption coefficient of the structure as a function of ND thickness. We found that the absorption spectra strongly depend on the ND thickness and the absorption edge is blue-shifted when the ND thickness decreases due to the quantum size effect. Additionally, the absorption coefficient (>10^5 cm^{-1}) of 2D Si-ND array is extremely high, and therefore it is possible to obtain sufficient absorption if the NDs can be integrated into the 3rd dimension. To determine the optical band gap energy of the structure, the Tauc formula was used:

$$(\alpha h\nu)^{1/2}=A(h\nu-E_g), \quad (2)$$

where A is a constant, h is Planck's constant, ν is frequency, E_g is the band gap energy, and n is 1/2 in the case of indirect allowed and forbidden electronic transitions. The Tauc formulation as a function of ND thickness is plotted in Fig. 3(b). As the ND thickness changes from 2 to 12 nm, the E_g could be controlled from 2.2 to 1.4eV as shown in Fig. 4. From these results, we found that E_g could be certainly controlled by simply changing ND thickness by thin-film deposition in our proposed fabrication. Based on the processes, all-Si tandem solar cells assembled with 3D ND array fabricated by stacking 2D Si-ND array as schematically shown in Fig. 5 could be constructed.

4. Conclusions

We created a 2D Si-ND array with a high-density and well-ordered arrangement using bio-template and an advanced etching process that included NF_3 treatment and damage-free Cl NB etching. The spacing between Si NDs can be controlled in the structure by changing NF_3 treatment time. The E_g can be easily controlled by changing the ND thickness during thin film deposition. The absorption coefficient of single layer 2D Si-ND is comparable to that of 3D QDSL. Our proposed processes for 2D Si-ND array and stacked ND are very feasible for the all-Si tandem solar cells comprising QDSL.

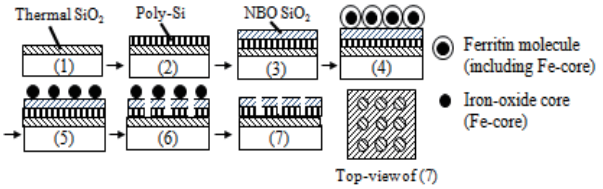

Fig. 1 Fabrication flow of 2 dimensional Si nano-disk array by bio-template and chlorine neutral beam etching.

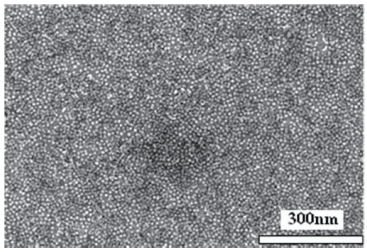

Fig. 2 SEM images of 2 dimensional Si nano-disk array fabricated by Cl neutral beam etching with bio-template.

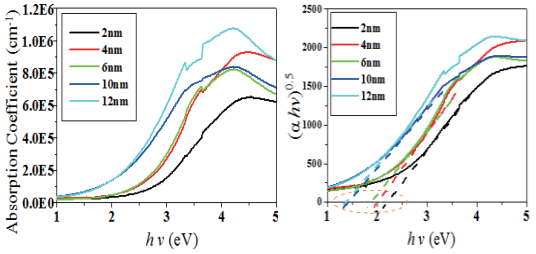

Fig. 3 (a) Absorption coefficient (b) Tauc plot of 2 dimensional Si nano-disk array with different nano-disk thicknesses from 2 nm to 12 nm.

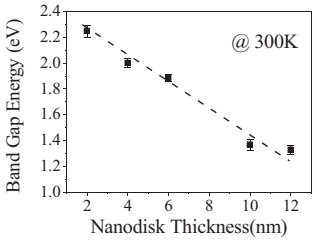

Fig. 4 Band gap energy (E_g) of nano-disk with different Si nano-disk thicknesses by using UV-vis-NIR.

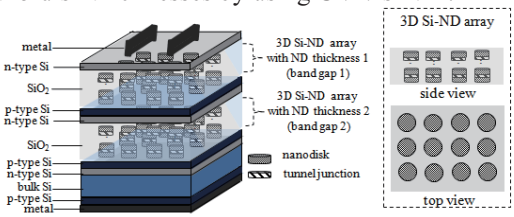

Fig. 5 Scheme of all-silicon tandem solar cell assembled with 3 dimensional Si nano-disk array.

References

[1] W. Shockley and H. J. Queisser, J. Appl. Phys. **32** (1961) 510.

[2] M. A. Green et al, 20th EU-PVSEC (2005), 1AP.1.1.

[3] A. Kongkanand et al., J. Am. Chem. Soc. **130** (2008) 4007.

[4] G. Conibeer et al., Thin Solid Films **516** (2008) 6748.

[5] A. J. Nozik: Physica E **14** (2002) 115.

[6] E. C. Cho et al., Nanotechnology. **19** (2008) 245201.

[7] Y. Kurokawa et al., Jpn. J. Appl. Phys. **45** (2007) L1064.

[8] S. Samukawa et. al., Appl. Phys. Express **1** (2008) 074002.

[9] B. Pejova and I. Grozdanov, Mater. Chem. Phys. **90** (2005) 35.

Tenth International Conference on Flow Dynamics
November 25-27, 2013, Sendai, Miyagi, Japan

Core Technology Consortium for Advanced Energy Devices

Seiji Samukawa[1,2] and Tomohiro Kubota[1]
[1] Institute of Fluid Science, Tohoku University, 2-1-1 Katahira, Aoba-ku, Sendai 980-8577, Japan
[2] WPI-AIMR, Tohoku University, 2-1-1 Katahira, Aoba-ku, Sendai 980-8577, Japan
samukawa@ifs.tohoku.ac.jp

ABSTRACT

Core Technology Consortium for Advanced Energy Devices has been established in February 2013 by rallying core technology on structure control technologies of nano-interface materials of 5 institutes in Tohoku University to develop to develop cutting-edge battery technologies and energy devices, such as ultra-high efficiency and lowcost solar cells, secondary batteries, fuel cells, and their related manufacturing processes, devices, and integrated systems. Our goal is to provide a smart energy supplying system for resilient society and revitalize the Japanese electrical equipment industry, which is currently facing difficult circumstances.

1. Introduction

Since the Great East Japan Earthquake, the development of new clean and renewable energy sources and the realization of efficient and smart stand-alone energy systems using the best mix of energy have been urgently sought. Therefore, we intend to support the reconstruction of the Tohoku area and the renewal of Japan, and to contribute to the establishment of an energy-technology nation, through the realization of state-of-the-art core battery technologies (solar cells, secondary batteries, fuel cells) and their energy optimization integrated systems (Fig. 1). Our efforts will be realized through open innovations in an industry-academia collaboration setting with a vertically-integrated group of companies. The innovations are based on nano-structure interface control technologies, which Tohoku University has been accumulating for many years.

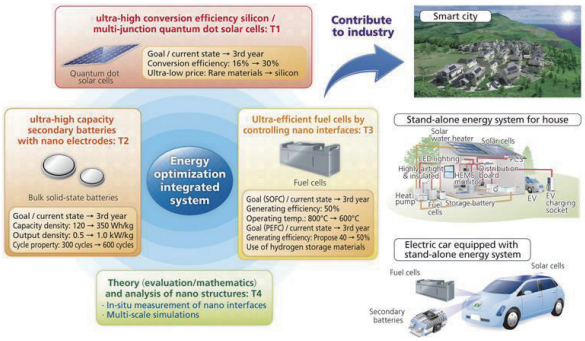

Fig. 1 Research and target of Consortium.

2. Features of the Consortium

Core Technology Consortium for Advanced Energy Devices has the following features:

1. Unique consortium aiming at establishment of optimized nano-energy system created as a fusion of solar cells, secondary batteries, and fuel batteries.

2. Strategic research and development by gathering technologies from vertical integration type firms based on nano-interface material structure control technologies accumulated specifically by the university.

3. Restoration to society, job creation, and national profit increments by strengthening TLO.

4. We propose our own intellectual property strategy of "Patent Marché" for the gathering of technologies. Benefits for firms participating in joint research are following: After individual joint research contract between Tohoku University and firms is concluded, (1) they will be able to obtain non-exclusive rights of the fundamental technology of the university, and (2) as for intellectual property rights related to applied technology, independent management is possible considering the policies of participating firms.

5. For the cultivation of world-class human resources, we propose soulful human resource exchange systems between firms and the university. (Practical cultivation and exchange of human resources).

6. For support of the basis of the battery industry, a facility-sharing system "Coin operated type battery manufacturing device" is constructed based on the Sendai Material Valley.

3. Organization

Figure 2 shows the organization of the Consortium. This consortium has four research teams – solar cell, secondary battery, fuel cell, and analysis & optimization. These researches are based on nano-structure interface control technologies, which Tohoku University has been accumulating for many years. Solar cell research is conducted by Prof. S. Samukawa (Institute of Fluid Science (IFS) and WPI-AIMR), Prof. N. Usami (Nagoya University), and Prof. I. Honma (Institute of Multidisciplinary Research for Advanced Materials (IMRAM)). Secondary battery research is conducted by Prof. I. Honma, Prof. S. Orimo (WPI-AIMR and Institute for Materials Research (IMR)), and Lecturer A. Unemoto (WPI-AIMR). Fuel cell research is conducted by Lecturer M. Matsuo (IMR), Prof. S. Orimo, Researcher T. Ikeshoji (IMR), and Prof. K. Amezawa (IMRAM). Analysis & optimization research is conducted by Assoc. Prof. T. Tokumasu (IFS), Assist. Prof. K. Shimoyama (IFS), Prof. K. Amezawa, and Prof. A. Miyamoto (New Industry Creation Hatchery Center (NICHe)).

Prospective member companies are welcome to apply to the Consortium at any time. A company can be a "Member Company" by concluding Academic Guidance Contract. There are 30 member companies on the end of July 2013. A member company which is

interested in joint research can be a “Joint Research Company” by concluding Joint Research Contract.

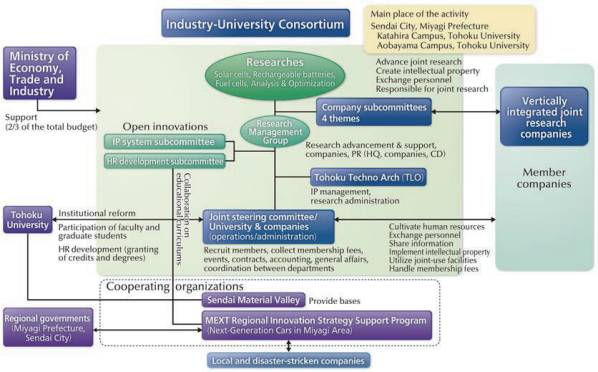

Fig. 2 Organization.

4. Human Resources Cultivation

Human resources cultivation is one of the most important target of the Consortium. We believe mutual and soulful exchange of human resource between companies and university will benefit both. Figure 3 shows the outline of human resource cultivation in the Consortium.

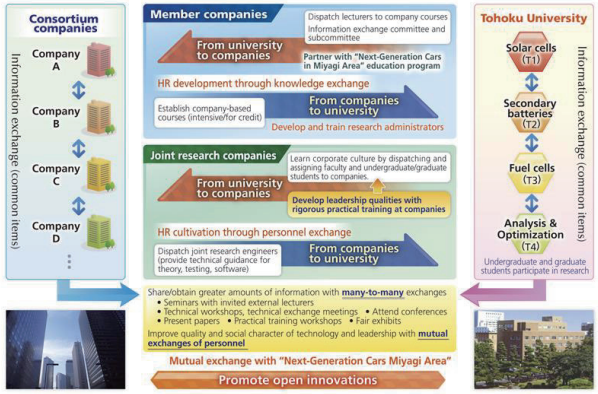

Fig. 3 Human resoure cultivation.

5. Intellectual Property

Figure 4 shows an outline of how intellectual property is handled in our Consortium. To promote strategic R&D using a vertically-integrated group of companies, this project has prepared two sections: Step 1 for consortium companies, and Step 2 for companies participating in joint research. Step 1: consortium companies are qualified to 1) engage in exchanging the newest public knowledge, 2) engage in forming significant human networks, and 3) participate in Step 2. Step 2: joint research participating companies are qualified to participate in “Patent Marché,” the IP management system explained below. Specific strategic R&D activities, which require confidentiality, are managed by a joint research contract between Tohoku University and the participating company.

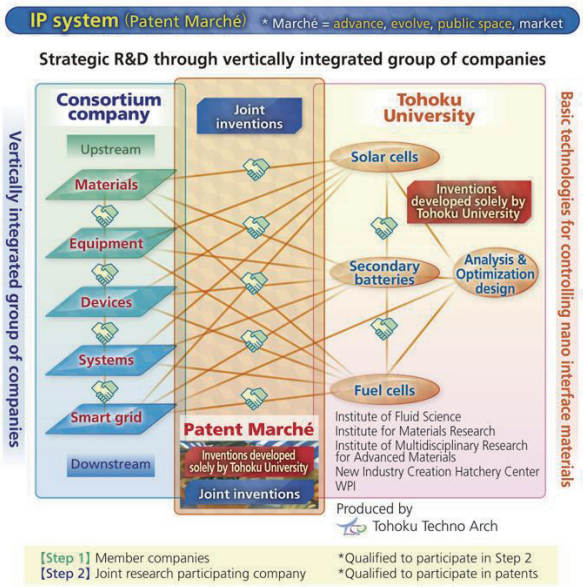

Fig. 4 Vertically integrated group of companies and intellectual property.

6. Research and Development

We have four research teams for solar cell, secondary battery, fuel cell, and analysis & optimization. The goal of solar cell team is to develop a silicon-based inexpensive solar cell with high conversion efficiency of 30 % by combining quantum dot structure fabricated by biotemplate ultimate processing technique and photonic nanostructure. Secondary battery team aims to improve capacity density to 350 Wh/kg, output density to 1.0kW/kg, and cycle property by 600 cycles. Fuel cell team aims to reduce SOFC working temperature to 600 °C with generating efficiency of 50% and to improve PEFC generating efficiency to 50%.

7. Conclusions

Core Technology Consortium for Advanced Energy Devices has been established in February 2013 to realize high performance solar cells, secondary batteries, fuel cells, and their combined energy supplying system for resilient society. The research is based on nano-structure interface control technologies, which Tohoku University has been accumulating for many years. Our efforts will be realized through open innovations in an industry-academia collaboration setting with a vertically-integrated group of companies. Also, to progress industry-academia collaboration, new ideas are included such as effective utilization of TLO, new IP system “Patent Marché”, soulful human resource exchange systems. The Consortium will realize true open innovation by cooperation and combination of organizations, systems, and technologies.

Tenth International Conference on Flow Dynamics
November 25-27, 2013, Sendai, Miyagi, Japan

Science-based New Silicon Technologies Exhibiting Super High Performance due to Radical-reaction-based Semiconductor Manufacturing

Tadahiro Ohmi, Hiroaki Tanaka, Tomoyuki Suwa, Xiang Li*, Rihito Kuroda* and Naoto Miyamoto
New Industry Creation Hatchery Center, Tohoku University, Sendai, Japan
* Graduate school of engineering, Tohoku University, Sendai, Japan
ohmi@fff.niche.tohoku.ac.jp

ABSTRACT

Current silicon (Si) technologies are now facing very severe limitations. This is because very limited capability of the Si crystal can be practically utilized by current Si technologies. In order to utilize the entire capability of the Si crystal, we must establish science-based new silicon technologies to fabricate Large Scale Integrated circuit (LSI) on any crystal orientation Si surface by using three-dimensional structure Metal-Oxide-Semiconductor (MOS) transistors where very high integrity gate insulator films must be formed on any crystal orientation Si surface with the same formation speed, i.e., radical oxidation / nitridation at low temperatures.

1. Introduction

Current silicon (Si) technologies are now faced with very severe limitations such as no more progress on the speed performance of microprocessors from Intel at around a 3-GHz clock rate for more than five years [1], so that the information communication technology cannot be improved any more resulting in the very severe stagnation of the worldwide entire industries.

At present, the semiconductor industry is going to decrease the device dimension less than 45 nm such as 32 nm, 22 nm. But if the target includes improving the speed performance, this is a complete mistake. In case of Cu, mean free path of electrons is about 40 nm, so that Cu wire does not work well below 40nm. Device miniaturization along horizontal direction must be limited larger than the mean free path of electrons in the wire metal. Therefore three-dimensional integrations are essentially required to increase the speed performance.

2. Science-based new silicon technologies exhibiting very high speed performance

Current silicon technologies are now using high temperature oxidation by O_2 molecules and/or H_2O molecules to form SiO_2 films as for the gate insulator films, so that relatively high integrity SiO_2 films can be obtained only on (100) Si surface. Thus, the current silicon technologies can fabricate LSI only on (100) Si surface using two-dimensional structure MOS transistors. We must establish new manufacturing system to fabricate LSI on any crystal orientation Si surface using three-dimensional structure MOS transistors, i.e., radical oxidation and radical nitridation by developing new plasma process equipment completely free from damages and contaminations.

Figure 1 indicates the difference between the radical oxidation at 400 ˚C and the thermal oxidation at 900 ˚C. It is clearly seen that the radical oxidation speed is kept completely the same for the entire substrate surface. If the same integrity oxide film is obtained, the oxidation speed must become the same for the entire substrate surface. Thus, the same integrity oxide films can be obtained for the entire substrate surface by the radical oxidation while completely different integrity oxide films are obtained for the different orientation substrate surface by the current thermal oxidation.

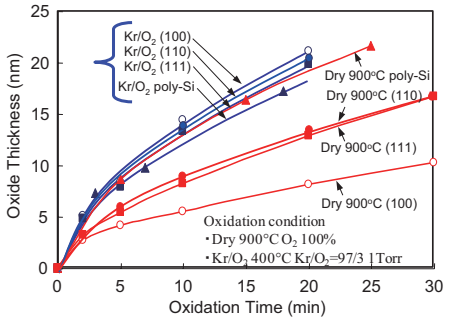

Fig. 1 Oxide film thickness as a function of oxidation time for the radical oxides and the thermal oxides on (100), (110), and (111) and poly-crystalline Si

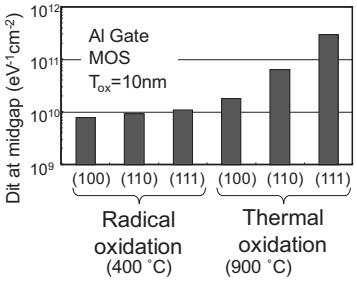

Fig. 2 Interface state density of the radical oxides and the thermal oxides for different crystal orientation Si surfaces

Figure 2 indicates the interface state density (Dit) of the radical oxide and the thermal oxide for different crystal orientation Si surfaces such as (100), (110), and (111). Dit of the radical oxides has been confirmed to be very small for the entire substrate surface while the thermal oxide exhibits relatively small interface state density only for the (100) surface, but not for the other crystal orientation Si surfaces.

The leakage current density through the radical nitride and the radical oxide has been confirmed to decrease down to less than 1/1,000 compared to that of the current thermal oxide on (100) Si surface as shown in Fig. 3.

We have evaluated the Time Dependent Dielectric Breakdown (TDDB) of the thermal oxide and the radical nitride in Fig. 4, where the life time of the radical nitride formed by Xe/NH_3 gas combination has been confirmed to be elongated by a factor of at least 30,000 compared to that of the thermal oxide.

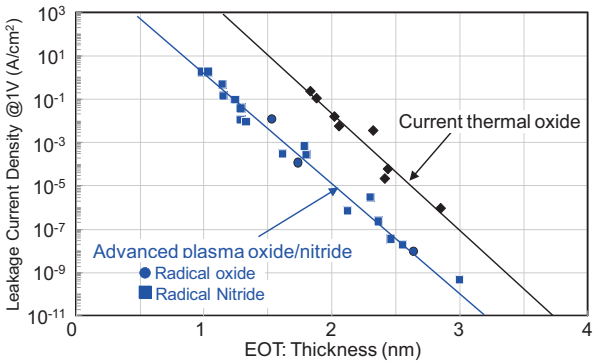

Fig. 3 Leakage current density through the radical nitrides, radical oxides and thermal oxides for the applied voltage of 1V is plotted as a function of the gate insulator film thickness

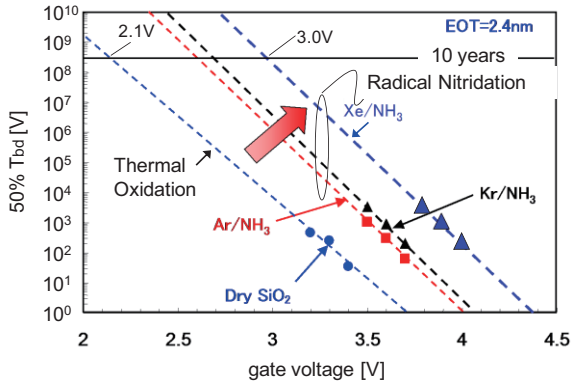

Fig. 4 Leakage current density through the radical nitrides, radical oxides and thermal oxides for the applied voltage of 1V is plotted as a function of the gate insulator film thickness

In order to improve the speed performance of the microprocessors, we are now strongly recommending to introduce the science-based new silicon technologies [2] including the following new technologies such as

1. Radical nitride for the very high integrity gate insulator films,
2. Atomically flat interface of the gate insulator film to silicon substrate,
3. Two orders of magnitude reduction of series resistance of source and drain electrodes by introducing $ErSi_2$ to the n+ region and Pd_2Si to the p+ region,
4. Introduction of accumulation MOS transistors instead of inversion MOS transistors,
5. Introduction of CHx (k=2.8) and CFx (k=1.9) stacked film to the low-k dielectric,
6. (551) surface silicon substrate instead of current (100) surface silicon substrate, where (551) surface is 8 degrees off to <001> direction from (110) surface.

The (551) surface is very excellent surface to maintain the surface smoothness where the wafer surface smoothness is evaluated using 0.3 % NH_4OH solution at the room temperature[3,4]. In case of the existence of the light illumination and the dissolved oxygen 8 ppm from the air, the surface roughness of (100) surface has been confirmed to drastically increase by only 10 min immersion to the 0.3 % NH_4OH solution

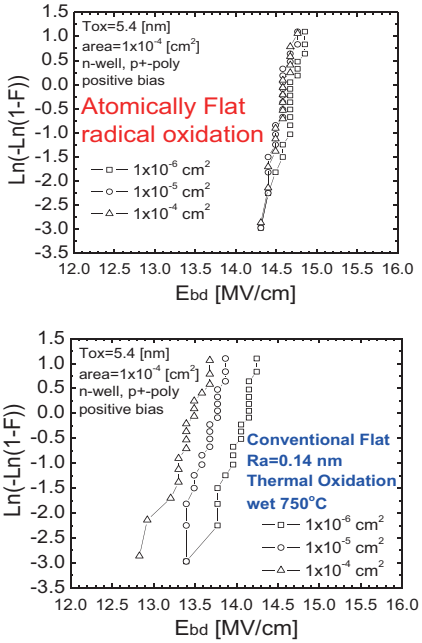

Fig. 5 Breakdown field intensity (E_{bd}) of SiO_2 films formed by (a) the radical oxidation of the atomically flat Si surface and (b) the thermal oxidation of the conventional flat Si surface

at the room temperature. However, the surface smoothness of the (100) surface is completely maintained atomically by eliminating the light illumination and the dissolved oxygen. Even in such situation, the surface roughness of the (110) surface is much roughened in the 0.3 % NH_4OH solution.

The breakdown field intensity (E_{bd}) of SiO_2 films has been evaluated for different fabrication conditions such as (a) the radical oxidation of the atomically flat Si surface and (b) the thermal oxidation of the conventional flat Si surface, each having three different sample areas as shown in Fig. 5. The radical oxides of the atomically flat Si surface exhibit E_{bd} greater than 14.5 MV/cm where no variations and fluctuations exist among three different sample areas. In case of the thermal oxidation of the conventional flat Si surface, E_{bd} is going to gradually decrease with an increase of the sample area.

3. Conclusion

The combination of the radical oxidation / nitridation and the atomically flat Si surface is essentially required to obtain very high integrity gate insulator film on any crystal orientation Si surface having the atomically flat gate insulator film to Si interface in order to eliminate fluctuation and variations of Si devices and improve the reliability. The speed performance of the microprocessors can be improved over 100 GHz clock rate at 45 nm technology node by an introduction of the science-based new silicon technologies.

References

[1] Intel Corp., Microprocessor Quick Reference Guide
[2] T. Ohmi, et al., IEEE Trans. ED **54** (2007), 1471
[3] H. Morinaga, et al., J. Electrochem. Soc. **153**(2006)
[4] T. Ohmi, et al., ECS Trans. **35(2)** (2011), 275

Tenth International Conference on Flow Dynamics
November 25-27, 2013, Sendai, Miyagi, Japan

Development of Al Doped $Ca_3TaGa_3Si_2O_{14}$ Piezoelectric Crystals

Tetsuo Kudo[1], Yuui Yokota[2], Masato Sato[3], Kazushige Tota[3], Ko Onodera[2,3], Shunsuke Kurosawa[1,2], Kei Kamada[1] and Akira Yoshikawa[1,2]

1. Institute for Materials Research (IMR), Tohoku University, Sendai 980-8577
2. New Industry Creation Hatchery Center, Tohoku University, Aoba-yama 6-6-10,Aoba-ku, Sendai, Miyagi, Sendai 980-8579, Japan
3. TDK corporation, Akita 018-0147, Japan

E-mail of corresponding author: t_kudo@imr.tohoku.ac.jp

ABSTRACT

Al doped $Ca_3TaGa_3Si_2O_{14}$ single crystals with various Al concentrations were grown by the micro-pulling-down method and their structural phases and chemical compositions were investigated. $Ca_3Ta(Ga_{1-x}Al_x)_3Si_2O_{14}$ crystals with x = 0, 0.2, 0.4, 0.6, 0.8 and 1 were grown and all crystals indicated a single phase of langasite-type structure in the powder X-ray diffraction measurement. Their lattice parameters, *a*- and *c*-axes lengths, systematically decreased with an increase of Al concentration. By analysis using the EDX, actual Al concentration in the crystals were almost same as the nominal compositions.

1. Introduction

Langasite-type single crystals have been energetically investigated as a piezoelectric element. There is no phase transition up to the melting point and they have the high piezoelectric constant and electromechanical coupling factor at high temperature. For this reason, langasite-type crystals have been expected as various sensor devices at high temperature such as combustion pressure sensor in the engine section of car and ship. $La_3Ga_5SiO_{14}$ (LGS), $La_3Nb_{0.5}GaO_{14}$ (LNG), and $La_3Ta_5Ga_{5.5}O_{14}$ (LTG) have been reported and they indicated relatively high piezoelectric constant and electromechanical coupling factor in a wide temperature range [1-4]. Recently, $Ca_3TaGa_3Si_2O_{14}$ (CTGS), $Ca_3NbGa_3Si_2O_{14}$ (CNGS), $Sr_3TaGa_3Si_2O_{14}$ (STGS) and $Sr_3NbGa_3Si_2O_{14}$ (SNGS) have been developed [5-8] and their crystals showed higher electrical resistivity at high temperature than $La_3Ta_{0.5}Ga_{5.5}O_{14}$ and $La_3Ga_5SiO_{14}$ crystals [9]. Manufacturing cost of these crystals is expected to be lower than that of previous crystals due to the decrease of rare-earth elements in the crystals. However, Ga ion with high cost of raw material is still contained in these crystals. If the amount of Ga ion in the crystal can be decreased, the manufacturing cost of these crystals is expected to be dramatically decreased. In the previous report, Ga ion in $La_3Ga_5SiO_{14}$ crystal could be partially substituted by Al ion [10]. In this study, we grew the Al doped CTGS single crystals with various Al concentrations and their structural phases, chemical compositions, crystallinities were investigated.

2. Method

Al doped $Ca_3TaGa_3Si_2O_{14}$ crystals with various Al concentrations were grown by the μ-PD method using a Pt crucible with a columnar die of 5mm in diameter at the bottom. The mixed powders were prepared using $CaCO_3$, β-Ga_2O_3, α-Al_2O_3, SiO_2 (purity > 4N) and Ta_2O_5 (>3N), as nominal compositions of $Ca_3Ta(Ga_{1-x}Al_x)_3Si_2O_{14}$ [CTGAS], x = 0, 0.2, 0.4, 0.6, 0.8 and 1. The mixed powders were sintered at 1200°C for 12 hours in air three times. The sintered powder was set into the Pt crucible and the crucible was put on a Pt-Rh after heater in the center of a high-frequency induction coil. Alumina insulators and quartz tubes were put around the crucible. The crucible was heated in air up to melting point of the mixed powder by the coil and meniscus on the bottom of the die was pulled down by a LTG seed crystal with *a*-axis along to the growth direction at 0.05 mm/min growth rate. During the crystal growth, the liquid-solid interface was observed by the CCD camera though holes of the after-heater and insulators. Structural phases of the grown crystals were identified by the powder X-ray diffraction (XRD) measurement and their lattice parameters were calculated from the powder XRD patterns using Si powder as an internal standard. Rectangular samples were cut from the as-grown crystals and wide planes were polished for observation of local surface and analysis of chemical compositions. The observation of local surface was performed by the scanning electron microscope (SEM) using back scattering electron (BSE). The chemical compositions were analyzed by the energy dispersive X-ray spectroscopy (EDX).

3. Results and Discussion

Figure 1 is the Al doped CTGS crystals grown by the μ-PD method and their polished crystal cut from the as-grown crystals. As-grown crystals had approximately 5 mm diameter and 3 ~ 4 cm length. Polished crystals indicated insides of the crystals had high transparency. However, there were some clacks in the crystals and they are considered to be generated due to the high temperature gradient during crystal growth.

Powder XRD patterns of the CTGAS crystals were measured after parts of the as-grown crystals were completely ground. Obtained powder XRD patterns are shown in Fig.2. All diffraction peaks of the CTGAS crystals with x = 0 ~ 1 were identified by the langasite-type structure (trigonal, P321) as shown in Fig.2(a) and the result indicates that all grown crystals had a single phase of langasite-type structure. In contrast, the diffraction peaks were systematically

shifted to high angle with an increase of Al concentration (Fig.2(b)). Therefore, their lattice parameters, *a*- and *c*-axes lengths, of the langasite-type phase were calculated by the XRD patterns as it is illustrated in Fig.3. The *a*- and *c*-axes lengths systematically decreased with an increase of Al concentration, *x*. The results suggest that Ga sites in CTGS crystals were substituted by Al ions with smaller ionic radius than Ga ion.

The cross-sectional BSE images of CTGAS crystals showed almost single domain structure in the images. To investigate their chemical compositions of the crystals, the cross-sectional planes were analyzed by EDX. Figure 4 is the Al ions ratio at Ga site of CTGAS in main phase. The result revealed that actual Al concentrations in the CTGAS crystals were almost same as nominal compositions.

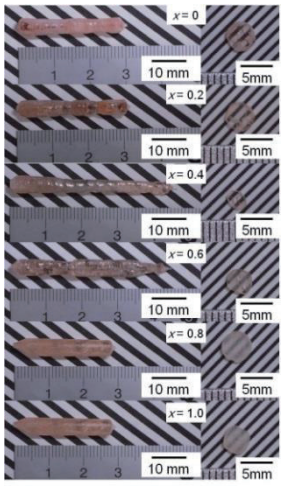

Fig.1 As-grown and polished Al doped CTGS crystals grown by the μ-PD method

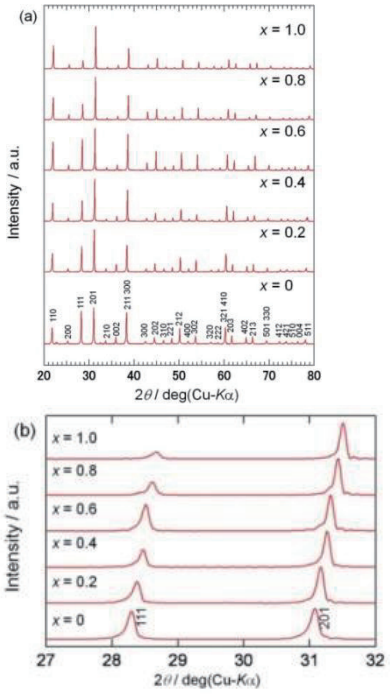

Fig.2 The powder XRD patterns of Al doped CTGS crystals

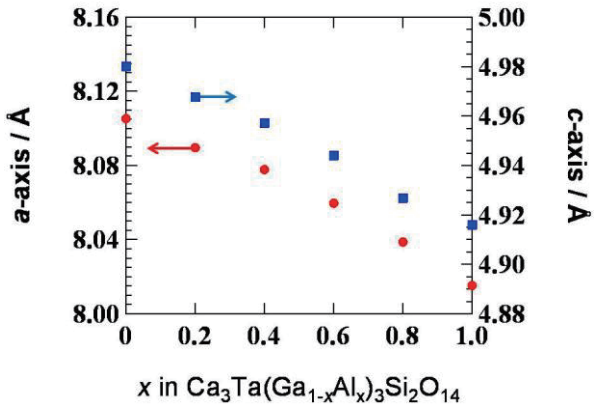

Fig.3 Lattice parameters of $Ca_3Ta(Ga_{1-x}Al_x)_3Si_2O_{14}$ crystals

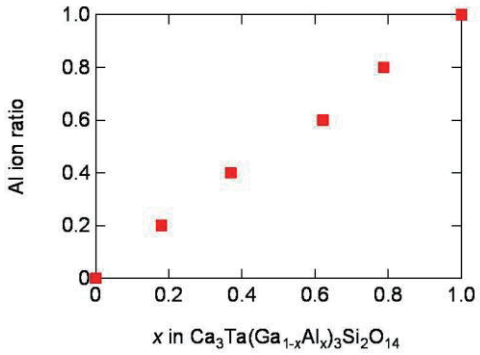

Fig.4 The Al ions ratio at $Ca_3Ta(Ga_{1-x}Al_x)_3Si_2O_{14}$ crystals

4. Concluding remarks

We grew up the $Ca_3Ta(Ga_{1-x}Al_x)_3Si_2O_{14}$ crystals with various Al concentrations *x* by the μ-PD method and investigated the structural phases and chemical composition. The all grown crystals indicated single phase of langasite-type structure. The result means that we could successfully decrease the amount of Ga in the crystals. Their lattice constants systematically decreased with an increase of Al concentration due to the Al substitution to Ga site.

References

[1] H. Takeda, J.Crystal Growth 169 (1996) 503.
[2] Yu.V. Pusarevsky, IEEE Trans. Ultrason. Ferroelectr. Freq. Control 42 (1995) 653.
[3] Yu.V. Pusarevsky, Proceedings of the IEEE International Frequency Contol Symposium, 1998, p. 742.
[4] H. Kavanaka, J. Crystal Grwoth 183 (1998) 274.
[5] H. Takeda, Mater. Res. Bull. 35 (2000) 245.
[6] X. Z. Shi, Solid State Commun. 142 (2007) 173.
[7] T. Karaki, Jpn. J. Appl. Phys., Part 1 43 (2004) 6721.
[8] Z. Wang, J. Cryst. Growth 249 (2003) 240.
[9] S. Zhang, J. Appl. Phys. 105 (2009) 114107.
[10] M. Kumatoriya, J. Cryst. Growth 229 (2001) 289.

Ultra-low Friction Technology Area, Tohoku Innovative Materials Technology Initiatives for Reconstruction (TIMT)

Kazue Kurihara
WPI Advanced Institute for Materials Research (WPI-AIMR) &
Institute of Multidisciplinary Research for Advanced Materials (IMRAM), Tohoku University
kurihara@tagen.tohoku.ac.jp

ABSTRACT

This project aims to elucidate phenomena of friction on oil, water and solid lubrication using nano-technology and science through collaboration of mechanical and material researchers with industrial engineers. They intend to develop ultra-low friction technology based on their studies.

1. About Tohoku Innovative Materials Technology Initiatives for Reconstruction (TIMT)

The Tohoku region excels in the production of electronic components, devices and circuits. Universities in Tohoku are also advanced in material science, optics, and nanotechnology. By taking advantage of the knowledge and strength that universities, public research facilities and industries in the earthquake-affected area have, the Reconstruction Design Council in Response to the Great East Japan Earthquake, a hub will stimulate industrial expansion and create new industries and employment. In nanotechnology and material science, the specialized fields of universities and manufacturing industries in Tohoku, the hub aims to lead the material technology industry through collaborative work on nanotechnology and by developing cutting-edge materials created with the most advanced technology.

The goal of this project (Tohoku Innovative Materials Technology Initiatives for Reconstruction, TIMT) is to promote the development of manufacturing industries in Tohoku and contribute to the reconstruction after the Great East Japan Earthquake. A hub for research and development has been founded at Tohoku University in the fields of nanotechnology and material science, the specialized fields of universities and manufacturing industries in the Tohoku region. This hub is based on the Basic Guidelines for Reconstruction in Response to the Great East Japan Earthquake. With industry-academia-government cooperation, the hub will develop cutting-edge materials using most advanced technology. Ultra-low friction technology is one of the technologies.

2. Ultra-low Friction Technology Area, TIMT

Ultra-low friction technology is the key for energy efficiency, safety and security, not only in the automobile industry but all areas of industry and daily life. Realization of this technology is indispensable towards the achievement of a low-carbon emission society. For instance, 20 % of a total energy loss of vehicle is caused by friction within the engine and transmission, thus research of friction-reducing technology for improving fuel efficiency is a vital task. Actually, fuel efficiency has been improved up to 15 % in the last two decades based on accumulated knowledge obtained through many improving processes.

Economic influences of tribology (study of friction) is about 2 % of GDP [1]. Tribological phenomena (friction/wear that occurs in various industrial products) are found in daily life, as shown in Fig. 1. Friction problems at contact interfaces of machines cause mechanical deterioration, damage and short life. Thus control of friction/wear improves energy efficiency on mechanical systems and guarantee stable quality, high reliability and long life.

In this technology area, practical low-friction technologies for materials and inter face design are developed in collaboration between Tohoku University and private industries by using Tohoku University's cutting-edge advanced science and technology on materials characterization of nano-interface and quantum chemistry simulation.

3. Research Overview

The development of friction-reducing technology has been conducted by private businesses, universities and research institutes in Japan and abroad. Given the dynamic, complex nature of friction in which many factors converge at the interface, it is difficult to fully understand the low-friction mechanisms, so as to draw precise conclusions.

This project aims to develop optimized interfaces on the basis of scientific understanding of nano-interfaces and materials for ultra-low friction. This goal will be achieved by fusion of mechanics, materials and simulation which all contribute to tribology.

Fig. 1 Tribological phenomena in daily life

This project studies: Oil lubrication, which reduces friction losses in engine components such as pistons; Water lubrication, which aims to obtain energy from heat; and Solid lubrication, which is expected to be applied to next-generation vacuum devices.

4. Research Topics

We are developing a guiding principle to interface design for ultra-low friction based on creation of nano-interface, nano-scale measurement and simulation analysis. Figure 2 shows the research diagram. We research three scientific topics listed below.

(1) Development of in-situ analysis systems of friction/wear and optimized design of nano-interfaces realizing ultra-low friction.

(2) Measurement technology for nano-level elucidation of friction & interfacial phenomena

(3) Development of Tribo-Simulator for Analyzing Chemical Reactions on the Interface under Friction

Acknowledgements

Ultra-low Friction Technology Area, Tohoku Innovative Materials Technology Initiatives for Reconstruction (TIMT) is funded by the Ministry of Education, Culture, Sports, Science and Technology (MEXT) and Reconstruction Agency, Japan.

References

[1] Report in Japan Chemical Innovation and Inspection Institute (2002).

Project Webpage

http://www.tohoku-timt.net/tribology/english/index.html

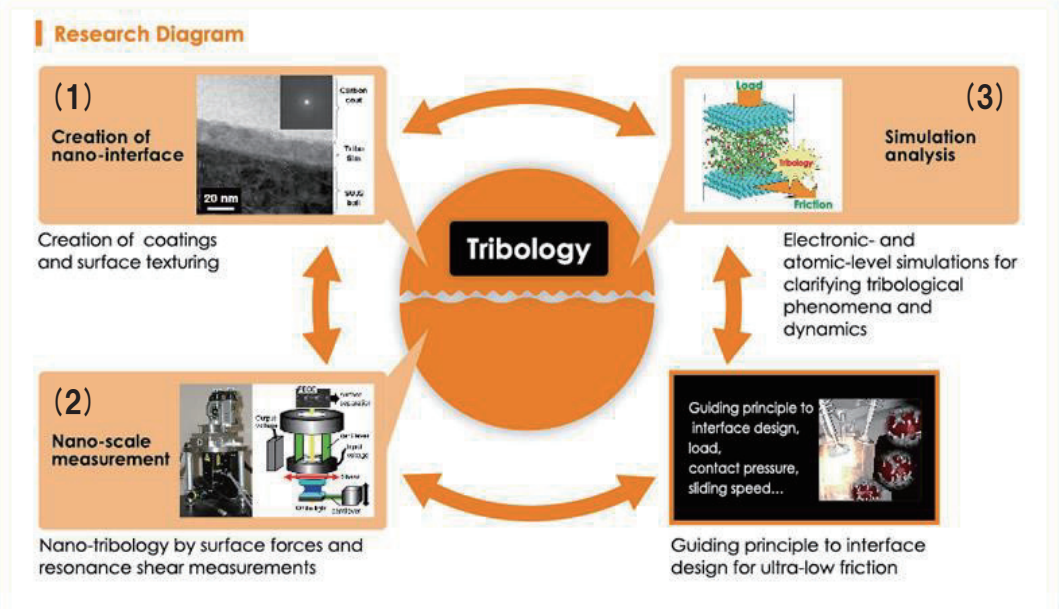

Fig. 2 Research diagram

Tenth International Conference on Flow Dynamics
November 25-27, 2013, Sendai, Miyagi, Japan

Development of Non-destructive Evaluation Technique and Health Monitoring Method of Structures and Understanding of the Functionality and Application to Energy-saving of a Hard Carbon Coating Materials

Toshiyuki Takagi[1], Tetsuya Uchimoto[1], Hiroyuki Miki[2] and Hiroyuki Kosukegawa[1]

[1]Institute of Fluid Science, Tohoku University, 2-1-1 Katahira Aoba-ku, Sendai, Miyagi 980-8577, Japan
[2]Frontier Research Institute for Interdisciplinary Sciences, Tohoku University, 2-1-1 Katahira Aoba-ku, Sendai, Miyagi 980-8577, Japan

Email: takagi@ifs.tohoku.ac.jp

ABSTRACT

System Energy Maintenance Laboratory at Institute of Fluid Science, Tohoku University, is engaged in research and development related to maintenance and energy saving of equipment and systems using material assessment technology targeting large-scale sophisticated systems such as automobiles, energy plants and air planes.

1. Introduction

We investigate the optimization of maintenance methodology using sensing technology, material evaluation technology, etc. for large-scale complicated systems, such as an energy plant. Our activities includes 1) development of nondestructive degradation evaluation method for structural materials, 2) research relating to nondestructive inspection and health monitoring of structures, 3) elucidation of mechanisms of functional materials and application to energy saving technology, and 4) quantification and optimization of maintenance activities.

2. Development of non-destructive evaluation technique and health monitoring method of structures

We propose lifecycle evaluation of materials from pre-service to aging degradation. Our activities include nondestructive evaluations of matrices for various cast irons, susceptibility to stress corrosion cracking, degradation prior to creep damage. In addition, we propose eddy current monitoring to evaluate the crack propagation [1]. Figure 1 shows the directions of our R & D for electromagnetic nondestructive evaluation; we are aiming at improvement of efficiency and reliability of evaluation of artifacts through the lifecycle.

Eddy current testing, one of electromagnetic nondestructive testing method, is well known as an effective tool of surface testing, providing many advantages such as non-contact measurement, rapid inspection, and so on. We have developed a very fast eddy current signal simulator which takes account of eddy current disturbances around cracks. In addition, we succeeded to reconstruct crack shapes from eddy current signals by inverse analysis [2]. Using the numerical computation tools, a multi-coil array probe was developed, and its high capability to detect and evaluate stress corrosion cracks was demonstrated through the testing using large scale specimens as shown in Fig. 2 [3]. Through our activities described above, a novel discipline of “numerical electromagnetic nondestructive evaluation” was established.

As well as the evaluation technique of cracks, we have tackled some research topics on nondestructive evaluation of material properties and degradations. We have established quantitative evaluation method of graphite structures, matrices of various cast irons applying electromagnetic evaluation methods [4]. We are now developing a novel electromagnetic nondestructive method to evaluate creep damage and susceptibility to stress corrosion cracking.

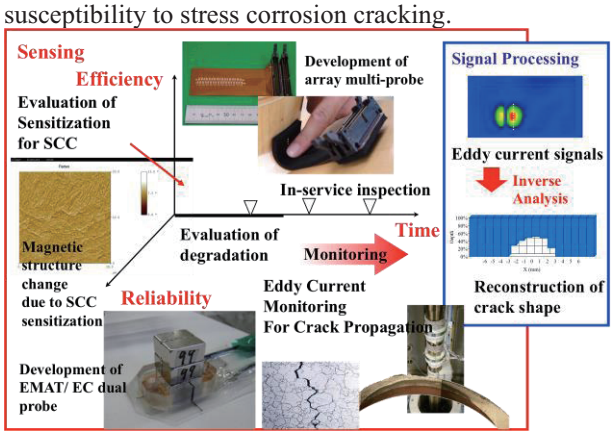

Fig. 1 Electromagnetic nondestructive evaluation for structural materials and components

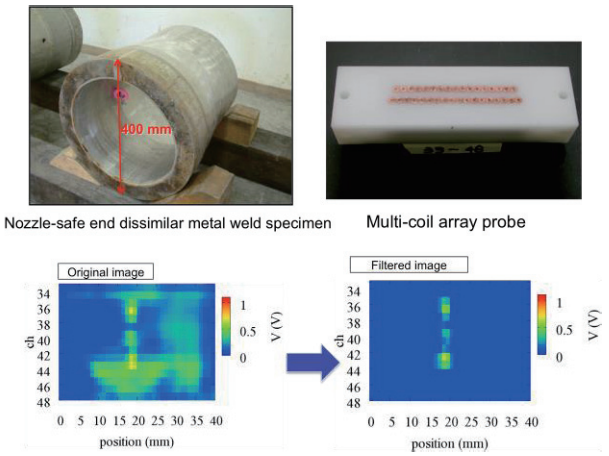

Fig. 2 Testing of large scale specimen by a multi-coil array probe.

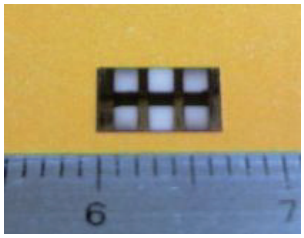

Fig.3 Photo of the Me-DLC fatigue sensor. White part, black part and metallic part correspond to substrate, film and Cu electrodes

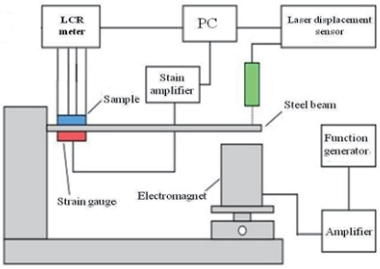

Fig. 4 Experimental setup of vibration test.

3. Functional coatings for mechanical system with a long-life life and energy saving

To make the conventional system highly efficient and also multi-functionalizing, we have proposed functional carbon-based coatings for the solution

The following topics are investigated for the design of the highly efficient machine which is excellent in reliability and durability in order to improve in energy efficiency and conservation of resources: (1) Functional diamond-like carbon films required for the design of "conductivity and contact surface". (2) Polycrystalline diamond based coatings for "super-low friction"

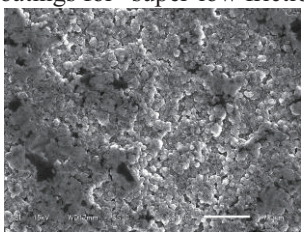

Fig. 5 SEM photograph of polished (Ra = 0.26 μm) CVD diamond film.

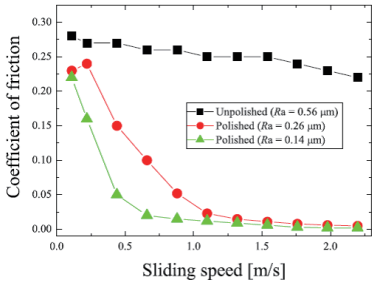

Fig. 6 Sliding speed dependence of friction properties on diamond films against AISI440C pins.

Metal-containing diamond-like carbon (Me-DLC) composite films are attractive as a kind of smart sensors for corrosive environment because of their chemical stability. Recently, we propose the new concept of fatigue sensor using Me-DLC as shown in Fig. 3[5].Vibration fatigue tastings were performed under atmospheric conditions (Fig. 4), and the results indicate the gauge factor decreasing with number of cycles, especially high cyclic region [6]. According to those results, it is suggested the possibility of monitoring sensor using of Me-DLCs.

The partially polished diamond film (Fig. 5) has a good frictional property at high sliding speed [7]. Fig. 6 shows decreasing trend on coefficient of friction (CoF) as sliding speed becomes fast, which is assisted by the lift-off force occurs in the concave part of diamond coated substrate. In this case, the surface geometry of diamond film and lift-off parameters play key role. We investigate this subject both experimental [7, 8] and numerical approach [9].

Acknowledgements

This work was partly supported by a Grant-in-Aid for Scientific Research (A) (23240638), the JSPS Core-to-Core Program, A. Advanced Research Networks, “International research core on smart layered materials and structures for energy saving” and the Promoted Research program from the Frontier research Institute for Interdisciplinary Science, Tohoku University.

References

[1] T. Kasuya, T. Okuyama, N. Sakurai, H. Huang, T. Uchimoto, T. Takagi, Y. Lu and T. Shoji, International Journal of Applied Electromagnetics and Mechanics, **20,** (2004), 163-170.
[2] H. Huang and T. Takagi, IEEE Transactions on Magnetics, **38**, (2002), 1009-1012
[3] T.Yamamoto, T. Takagi, T. Uchimoto, International Journal of Applied Electromagnetics and Mechanics, **33**, (2010), 1179-1184.
[4] T. Uchimoto, T. Takagi, T. Abe, Material Transactions, **51** (2010),1114-1119.
[5] P. Wang, T. Takagi, T. Takeno, H. Miki, Sensors and Actuators, A, **198**, (2013) 46–60.
[6] T. Ohno, T. Takeno, H. Miki, T. Takagi, Diamond and Related Materials, **20,** (2011) 651–654
[7] H. Miki, A. Tsutsui, T. Takeno, T. Takagi, Diamond and Related Materials, **17,** (2009), 868-872.
[8] H.Miki, A.Tsusui, T.Takeno, T.Takagi, Diamond and Related Materials, **24,** (2012), 167-170.
[9] S.Yonemura, M.Yamaguchi, T. Takeno, H. Miki, T.Takagi, AIP Conf. Proc. **1084,** (2008), 1153-1157.

Tenth International Conference on Flow Dynamics
November 25-27, 2013, Sendai, Miyagi, Japan

New Solid-State Joining Processes for Automotive Industry

Hiroyuki Kokawa, Yutaka S. Sato, Hiromichi T. Fujii
Department of Materials Processing, Graduate School of Engineering, Tohoku University, 6-6-02 Aramaki-aza-Aoba, Aoba-ku, Sendai 980-8579, Japan
kokawa@material.tohoku.ac.jp

ABSTRACT

Development of reliable welding processes for newly developed metallic materials or dissimilar combination of the materials is highly required in automotive industry. In our research group, fundamental understanding of metallurgical phenomena during solid-state joining processes, such as welding mechanism, microstructural evolution during welding, relationship between microstructure and property in the welds, has been systematically examined. Some findings of our fundamental researches on friction stir welding and ultrasonic welding will be briefly shown in this paper.

1. Introduction

It is difficult to create highly reliable welds in newly developed metallic materials or dissimilar combination of the materials through conventional fusion welding processes, because melting and solidification, and high thermal-effect during fusion welding frequently result in formation of the weld defect and undesirable microstructure. Solid-state joining processes can alleviate such problems in some cases, so that they have been recently used in some automotive applications. However, fundamental knowledge on solid-state joining processes, such as welding mechanism, microstructural evolution during welding, and microstructure-property relationship in the welds, is still unclear, although they should be academically understood to produce more reliable welds with better properties.

Our research group focuses on friction stir welding and ultrasonic welding as solid-state joining processes for the metallic materials with poor fusion-weldability and dissimilar combination of the materials. One of the research activities is to clarify unclear phenomena during these welding processes based on the materials science, which could provide effective methods to produce reliable welds with good properties in the poor weldable-materials for the automotive industry. Some findings of the fundamental researches will be briefly introduced in this paper.

2. Friction stir welding (FSW)

Basic concept of FSW is remarkably simple. An inconsumable rotating tool consisting of a probe and shoulder is inserted into the material plates to be welded and subsequently traversed along the joint line, as shown in Fig. 1 [1]. Two material plates consolidate well after FSW, and the material stirred by the tool, so-called stir zone, consists of fine equiaxed grain structure. We examined consolidation mechanism during FSW and then obtained the following conclusions. The material flow during FSW can be characterized by simple shear deformation through micro-texture analysis [2]. The shear deformation fragments the oxide layer on the abutting edges, which creates new oxide-free surfaces [3]. Consequently, metallic bond between the oxide-free surfaces is completely achieved during FSW. Schematic illustration of FSW mechanism is shown in Fig. 2.

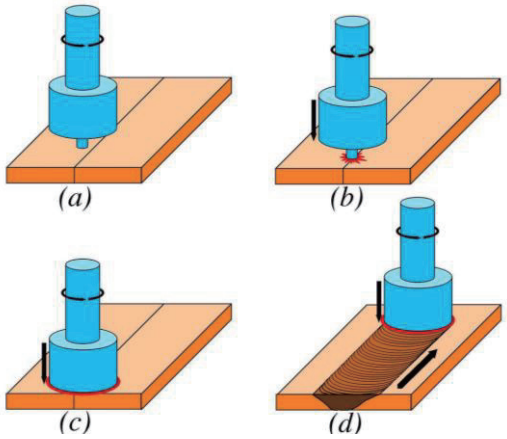

Fig. 1 Principle of FSW. (a) The welding tool is rotated, (b) the tool probe contacts the plate surface, (c) the tool is plunged into the material plate, and (d) the rotating tool traverses along the joint line.

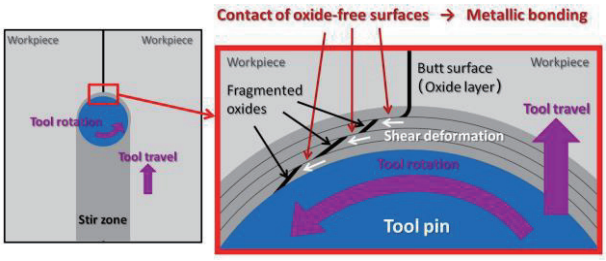

Fig. 2 Schematic illustration of FSW mechanism.

Evolution of fine equiaxed microstructure during FSW is also studied in several metallic materials. Development of the fine grains is mainly driven by continuous recrystallization [4], but some evidences of discontinuous recrystallization can be found in the materials with low stacking fault energy. To expand FSW to high-softening-temperature materials (HSTMs), such as steels and titanium alloys, we develop several kinds of high-temperature materials for the FSW tools of HSTMs. For example, the tool made of new Co-base superalloy exhibits the good performance during FSW of carbon steels and Ti-6Al-4V [5], which suggests that

the tool has a potential as a cost-efficient tool with high reliability.

3. Ultrasonic welding (USW)

USW is a solid state process which can produce a joint between thin metallic materials through ultrasonic vibrating energy and normal clamping force. The USW technique is characterized by a lower energy input, shorter welding time and thinner workpieces than the other spot welding techniques. Ultrasonic vibrations typically of 20 – 100 kHz frequency are locally applied parallel to the metallic sheets or wires through an ultrasonic horn as shown in Fig. 3. Recent publications have revealed that the bond in USW was achieved through various physical phenomena such as dispersion of surface oxides [6], formation of intermetallic compounds [7] and recrystallization due to deformation and heating at the joint interface [8] as shown in Fig. 4. One main motivation of our work on USW is to understand how the bond in USW is achieved through the observation of microstructural evolution around the joint interface. So far, the following findings have been obtained in USW of Al alloys to Cu and steel materials. The fine and equiaxed grains are formed in Al alloy side around the joint interface during USW. The newly formed grains exhibit {111} texture due to the shear deformation of micro-asperities. This deformation is expected to generate high dislocation density in the joint interface region, and thereby providing the stored energy to drive the recrystallization. The recrystallization driven by heat and strain due to ultrasonic vibration is essential to achieve good bonding between metallic workpieces in USW.

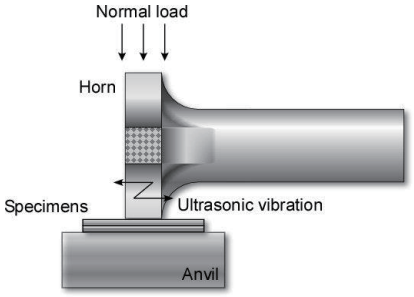

Fig. 3 Schematic showing typical setup used in the ultrasonic metal welding.

The manufacturing technology utilizing ultrasonic metal welding technique has also received attention in recent years. Ultrasonic additive manufacturing (UAM) is a solid state welding process to build complex three dimensional components directly from metallic tapes. A thin metallic tape is initially bonded ultrasonically on a base plate, with additional tapes being subsequently bonded on the previous tape. The majority of our UAM work has been focused on the characterization of microstructure and thermal analysis [9, 10]. The results show that the accumulative effects on microstructure evolution could lead to a gradient in bond quality.

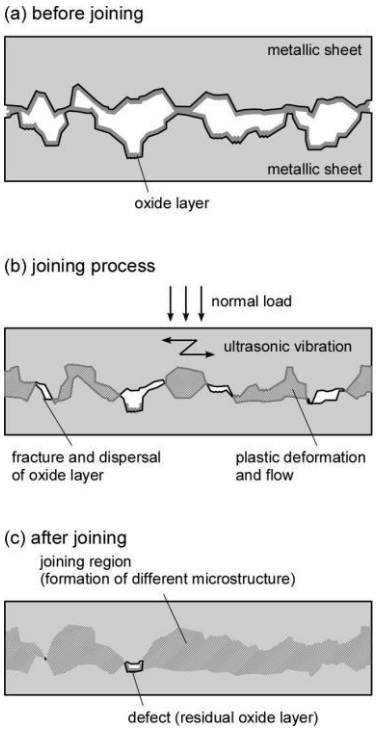

Fig. 4 Schematics of physical phenomena during USW.

4. Concluding remarks

Welding phenomena during solid-state joining processes have been examined based on the materials science, and then some of the fundamental knowledge was obtained, which indirectly contributed to development of the practical applications in automotive industry. To achieve the welding processes for the poor weldable-materials, further studies are ongoing.

References

[1] R.S. Mishra, Z.Y. Ma, Mater. Sci. Eng. R, **50** (2005), 1.
[2] Y.S. Sato, H. Kokawa, K. Ikeada, M. Enomoto, S. Jogan, T. Hashimoto, Metall. Mater. Trans. A, **32A** (2001), 941.
[3] Y.S. Sato, H. Takauchi, S.H.C. Park, H. Kokawa, Mater. Sci. Eng. A, **405** (2005), 333.
[4] S. Mironov, Y.S. Sato, H. Kokawa, Acta Mater., **56** (2008), 2602.
[5] Y.S. Sato, M. Miyake, H. Kokawa, T. Omori, K. Ishida, S. Imano, S.H.C. Park, S. Hirano, Friction Stir Welding VI, TMS, (2011), 3.
[6] D. Bakavos and P. B. Prangnell, Mater. Sci. Eng. A, **527** (2010), 6320.
[7] V.K. Patel, S. D. Bhole and D.L. Chen, Sci. Technol. Weld. Joi., **17** (2012), 202.
[8] N. Murdeshwar and J.E. Krzanowski, Metall. Mater. Trans. A, **28** (1997), 2663.
[9] H.T. Fujii, M.R. Sriraman and S.S. Babu, Metall. Mater. Trans. A, **42A** (2011), 4045.
[10] M.R. Sriraman, M. Gonser, H.T. Fujii, S.S. Babu and M. Bloss, J. Mater. Process. Technol., **211** (2011), 1650.

Tenth International Conference on Flow Dynamics
November 25-27, 2013, Sendai, Miyagi, Japan

Microstructure and High-Temperature Tensile Property of Co–Cr–Mo Alloy Fabricated by Electron-Beam Melting (EBM)

Shi-Hai Sun, Yuichiro Koizumi, Shingo Kurosu, Yun-Ping Li,
Hiroaki Matsumoto and Akihiko Chiba
Institute for Materials Research, Tohoku University, Sendai, 980-0812, Japan
E-mail of corresponding author: a.chiba@imr.tohoku.ac.jp

ABSTRACT

The microstructures and high-temperature tensile properties of a Co–Cr–Mo alloy fabricated by electron-beam melting (EBM) have been investigated. The as-EBM-built samples consisted of face centered cubic (fcc) γ-phase with strong crystallographic texture in which the three <1 0 0> cubic directions are oriented parallel to x-axis, y-axis of electron beam scanning, or the build-direction (z-axis). After aging at 800 ˚C, the γ-phase transformed into hexagonal close packed (hcp) ε-phase forming randomly oriented fine grains structure. The high temperature tensile properties were dramatically improved as a result of the microstructural changes.

1. Introduction

Cobalt-based alloys have been widely used as materials for valve seats in nuclear power plants, aerospace fuel nozzles and engine vanes, as well as orthopedic and dental implant materials because of their strength at high temperature, corrosion resistance, excellent wear resistance, and biocompatibility [1].

Recently, electron beam melting (EBM) has become an established process for additive manufacturing that can create three-dimensional (3D) complex structures from metal powders. In the EBM process, a high-power electron beam is scanned to melt metal powder selectively along a series of two-dimensional (2D) slices of a 3D object repeatedly, layer by layer [2].

The EBM has been applied to Co–26Cr–6Mo–0.2C alloys, and the tensile strength of the EBM-built sample was found to be higher than that of cast or wrought ASTM F75 Co–Cr–Mo (CCM) alloys. However, the microstructures of the CCM alloys fabricated by EBM have not been observed in detail. By clarifying the characteristics of the EBM processed CCM alloys, further improvement of mechanical properties may be possible. In particular, the improvement of high temperature strength will expand the application possibility of CCM significantly

In this study, Co–28Cr–6Mo–0.23C–0.17N alloy rods were fabricated by EBM. The high-temperature tensile properties of the rods with various orientations were investigated, focusing on the effects of directional growth of crystal grains in the EBM process.

2. Method

The raw powder consisted of spherical particles with an average particle size of 64 μm and the chemical composition of the Co–28Cr–6Mo–0.23C–0.17N (wt%), which was within the range of ASTM F75 standards. Rods with the cylindrical axes deviating from the build direction (z-axis) by 0˚, 45˚, 55˚, and 90˚ as in Fig.1 were fabricated on an A_2X EBM system (Arcam AB, Mölndal, Sweden). The rods with the deviation angles of 0˚, 45˚, 55˚, and 90˚ are designated as 0˚-, 45˚-, 55˚-, and 90˚-samples. The rods were 15 mm in the diameter, and 85 mm in the length. Most of the samples were aged at 800 ˚C for 24 h to obtain hexagonal close-packed (hcp) ε- phase [3]. In order to examine the effect of the matrix phase on the high-temperature tensile properties, some of the 90˚-samples were used without the ageing. Tensile specimens with the loading axes parallel to the cylindrical axes were cut from the rods. Tensile tests

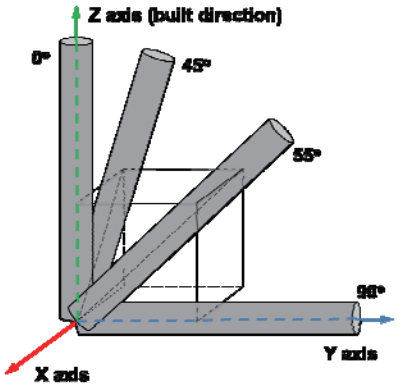

Fig. 1. Schematic of rod-samples fabricated by electron-beam melting (EBM).

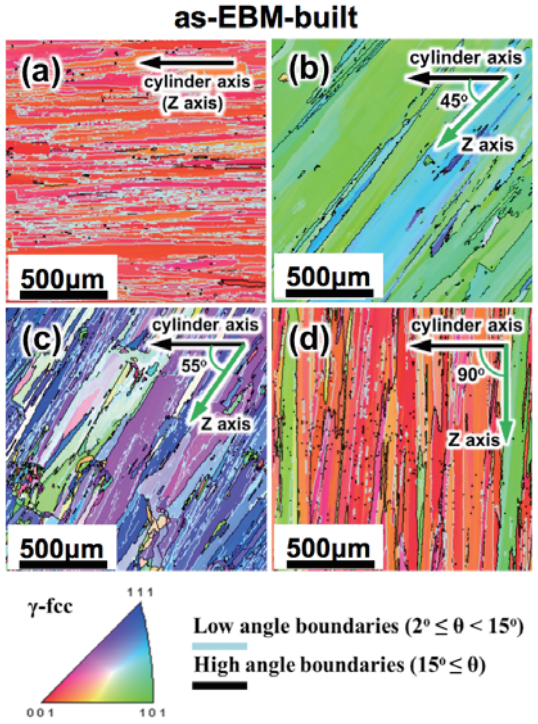

Fig.2. EBSD IPF maps on vertical cross section of as-EBM-built rods; (a) 0˚-sample, (b) 45˚-sample, (c) 55˚-sample and (d) 90˚-sample.

were conducted at 700 ˚C with a strain rate of 1.5×10^{-4} s^{-1}. The microstructures were investigated by scanning electron microscopy (SEM), electron backscatter diffraction (EBSD), and X-ray diffraction (XRD).

3. Results and Discussion

The EBSD-based inverse pole figure (IPF) maps of the as-EBM-built samples are shown in Fig. 2. All the crystal grains were identified as face centered cubic (fcc) γ-phase. The high-angle and low-angle grain boundaries are indicated by black and light blue lines, respectively. The boundaries were mostly seen to be aligned along the *z*-axis. The cylindrical axes directions of the γ phase grains are oriented near [001], [110], [111], and [100] in the 0˚-, 45˚-, 55˚-, and 90˚-samples, respectively. This can be regarded as the result of oriented crystal growth of the γ-fcc phase with the three cubic <0 0 1> direction oriented parallel to x-axis, y-axis of electron beam scanning, or the build-direction (z-axis).

The EBSD-IPF maps of the aged samples are shown in Fig. 3. All of the γ-fcc phase were transformed into the single ε-phase by the aging treatment. Compared with the grains of as-EBM-built samples, the grains are equiaxed, especially in the 0˚-sample. The IPF maps showed the orientations in the direction of the cylindrical axis. No significant preferential orientation was recognized in the ε grains of the aged samples, indicating that the Shoji–Nishiyama (S-N) orientation relationship ($(111)_\gamma$ // $(0001)_\varepsilon$; $[101]_\gamma$//$[11\bar{2}0]_\varepsilon$) was not fully maintained during phase transformation. This suggests that diffusive phase transformation occurred during the aging treatment at 800 ˚C.

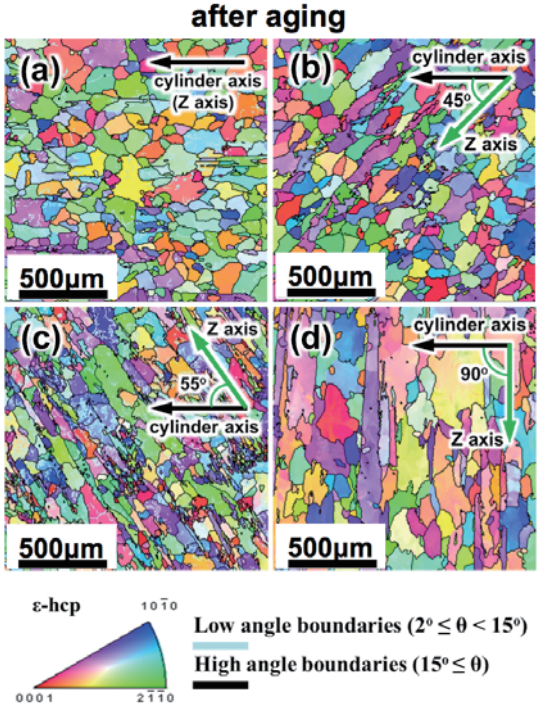

Fig.3. EBSD IPF maps on vertical cross section of as-EBM-built rods; (a) 0˚-sample, (b) 45˚-sample, (c) 55˚-sample and (d) 90˚-sample.

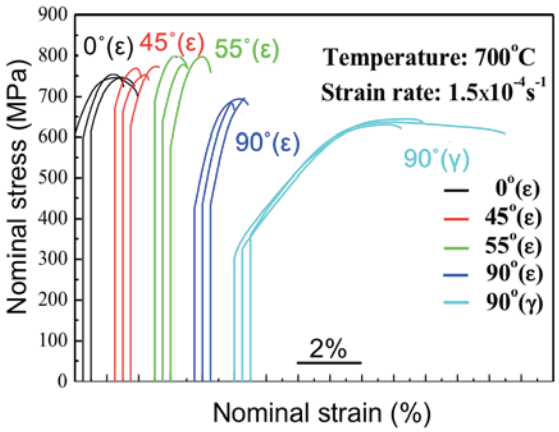

Fig. 4. Stress-strain curves of 0˚-, 45˚-, 55˚-, and 90˚-samples at 700 ˚C with strain rate of 1.5×10^{-4} s^{-1}.

The stress–strain curves of samples after aging treatment are shown in Fig. 4. In order to examine the effect of phase constitution on the tensile properties, the tensile result of the 90˚-sample with the γ phase is also shown together. Higher *UTS* of the aged specimens was obtained in the order of 55˚-, 45˚-, 0˚-, and 90˚-samples. The 0.2% yield stress of the 0˚-, 45˚-, and 55˚-samples were 635 ± 13 MPa, 659 ± 30 MPa, and 684 ± 14 MPa, respectively, while that of the 90˚ sample was as low as 459 ± 4 MPa. The elongation of the 90˚-sample was 2.5 ± 0.7%, which was comparable to those of the 0˚-, 45˚-, and 55˚-samples: 3.1 ± 0.7%, 1.7 ± 0.1%, and 2.0 ± 0.5%, respectively.

4. Concluding remarks

Microstructures and high temperature deformation behaviors of EBM-built CCM alloys have been studied. Strong texture was formed in the EBM-built samples. The cylinder axes were oriented near [001], [011], [111] and [1 0 0] directions in samples whose cylindrical axes were deviated from z axis by 0˚, 45˚, 55˚, and 90˚, respectively. Grains can be equiaxed and randomly oriented after phase transformation from γ-fcc to ε-hcp phase. The 55˚-sample exhibited the highest *UTS* among the samples built in different orientations.

References

[1] A. Chiba, K. Kumagai, N. Nomura, S. Miyakawa, Acta Mater. **55** (2007), 1309–1318.

[2] L.E. Murr, S. M. Gaytan, D.A. Ramirez, E. Martinez, J. Hernandez, K.N. Amato, P.W. Shindo, F.R. Medina and R.B. Wicker, J. Mater. Sci. Technol. **28** (2012), 1.

[3] S. Kurosu, H. Matsumoto, A.Chiba. Mater. Let. **64** (2010), 64.

Tenth International Conference on Flow Dynamics
November 25-27, 2013, Sendai, Miyagi, Japan

Suppression of Crack Initiation of Metallic Materials by Using a Cavitating Jet in Air

Hitoshi Soyama and Osamu Takakuwa
Department of Nanomechanics, Tohoku University
6-6-01Aoba, Aramaki, Aoba-ku 980-8579, Sendai, Japan
soyama@mm.mech.tohoku.ac.jp

ABSTRACT

Cavitation impacts can be utilized to surface modification in the same way of shot peening. The peening method using the cavitation impacts is named as "cavitation peening". In the normal case of cavitation peening, cavitation is produced by injecting a high speed water jet into a water filled chamber, i.e., a cavitating jet in water. A cavitating jet in air was realized by the author, by injecting a high speed water jet into a low speed water jet, which was injecting into air. In the present paper, in order to make clear mechanism of improvement of fatigue strength of metallic materials, the crack propagation rate was investigated experimentally.

1. Introduction

Normally cavitation impact at bubble collapse is harmful phenomena for hydraulic machineries, as cavitation causes severe damage and/or noise in the hydraulic machinery such as pumps, valves, screw propellers and so on. However, the cavitation impact can be utilized to surface modification, e.g., enhancement of fatigue strength of gears, in the same way of shot peening. The peening method using the cavitation impacts is called as "cavitation shotless peening" [1,2] as shots are not required or simply called "cavitation peening"[3-5]. In order to establish cavitation peening, it is necessary to intensify the cavitation impacts and also to make clear the mechanism of enhancement of fatigue strength.

In the case of cavitation peening, cavitation is normally generated by injecting a high speed water jet into a water filled chamber, as cavitation takes place in vortex core of shear layer around the jet. This type of jet was called as a cavitating jet in water in the present paper. A cavitating jet in air was successfully realized by injecting a high speed water jet into a low speed water jet, which was injecting in air by using a concentric nozzle and the injection condition such as injection pressure of the high speed water jet and the low speed water jet [6-8]. Introduced compressive residual stress near subsurface introduced by the optimized cavitating jet in air was larger than that of the cavitating jet in water [6]. Then, in the present paper, the cavitating jet in air was used for cavitation peening to improve fatigue strength.

Mechanism of the improvement of the fatigue strength of surface modified layer can be distinguished to crack initiation and crack propagation. Although test methods to investigate fracture toughness were defined in ASTM and ISO [9,10], that of surface modified layer can not be evaluated, as the purpose of the test methods was the evaluation of bulk metals. In order to investigate effect of peening on crack initiation, a load controlled plate bending fatigue test machine was developed and threshold stress intensity factor range of peened surface was evaluated [11].

In the present paper, in order to make clear the mechanism of improvement of fatigue strength of metallic materials by cavitation peening using the cavitating jet in air, threshold stress intensity factor range was evaluated by the plate bending fatigue test.

2. Experimental Apparatus and Procedures

Figure 1 illustrates schematic diagram of the cavitating jet apparatus. The high speed water was injected into the low speed water jet using the concentric nozzle. The diameter of the nozzle for the high and low speed and water jet was 1 mm and 20 mm, respectively. The injection pressure of the high and low pressure was 20 MPa and 0.05 MPa, respectively. The standoff distance, which was defined by the distance from the nozzle to the specimen surface, was 30 mm.

The tested material was stainless steel Japanese Industrial Standards JIS SUS316L. The processing time per unit length t_p was 0.25, 0.5, 1 and 2 mm/s. After cavitation peening, the notch which was 0.5 mm in width, 5 mm in length and 0.25 mm in depth, was introduced by milling as shown in Fig. 2.

In order to investigate effect of cavitation peeing on crack initiation, the threshold stress intensity factor range ΔK_{th} was evaluated by using the load controlled plate bending fatigue test (see Fig. 3). The crack propagation test was carried out to eliminate plastic

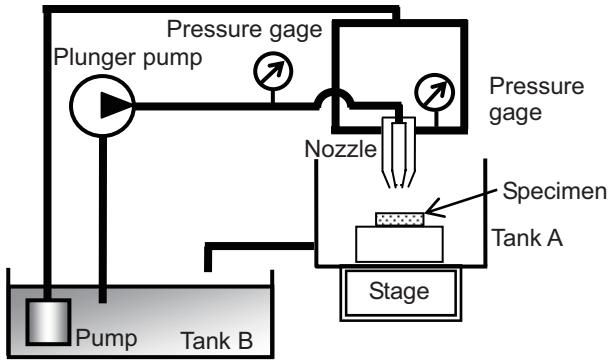

Fig. 1 Cavitation peening apparatus

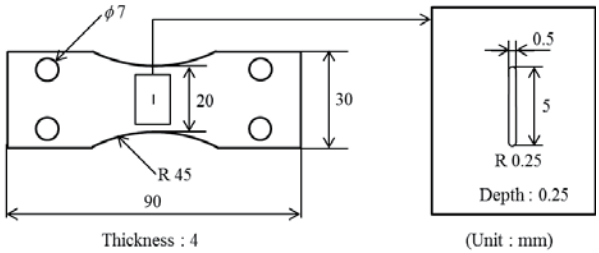

Fig. 2 Geometry of specimen with notch

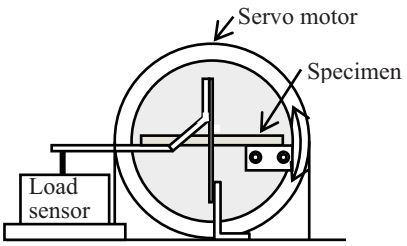

Fig. 3 Schematic illustration of load controlled plate bending fatigue tester.

deformation around the notch introduced by the milling, after the length of fatigue crack 2*a* was 0.4 mm. The ΔK_{th} was defined by ΔK at $da/dN = 1.0 \times 10^{-10}$ m/cycle by the decremental step load test. The residual stress on the surface was also measured by an X-ray diffraction method.

3. Results

Figure 4 illustrates aspect of cavitating jet in air. At optimum injection pressure of the high and low speed water jet, the surface of the low speed water jet formed wavy pattern, as the periodical shedding of the cavitation cloud of the cavitating jet caused pressure wave to affect the low speed water jet.

Figure 5 shows the result of stress intensity factor range ΔK and the crack propagation rate da/dN in decremental step load test using the load controlled plate bending test machine to make clear the mechanism of increase of fatigue strength, as the fatigue strength of stainless steel was improved by cavitation peening using

Fig. 4 Aspect of cavitating jet in air

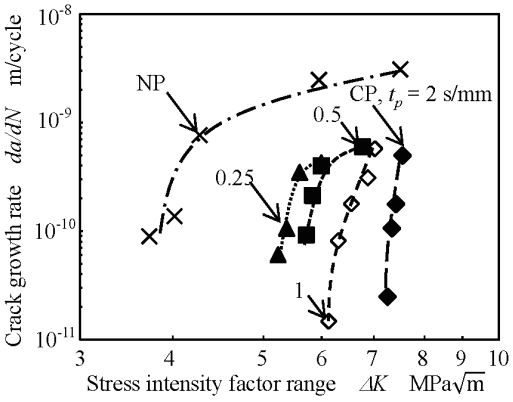

Fig. 5 Relation between ΔK and da/dN in decremental step load test

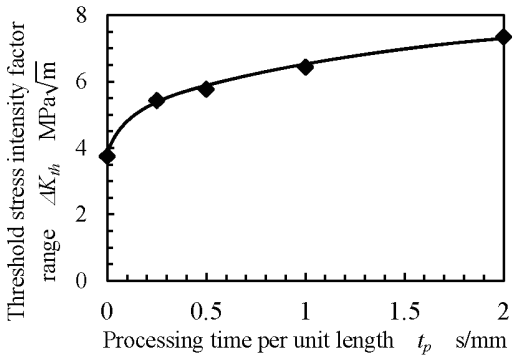

Fig. 6 Increase of ΔK_{th} by cavitation peening

the cavitating jet in air [12]. When da/dN was compared not peened specimen (NP) and cavitation peening specimen (CP) were compared at equivalent ΔK, da/dN of CP was smaller than that of NP. Namely, da/dN was reduced by cavitation peening using the cavitating jet in air.

In order to investigate effect of cavitation peening on the crack initiation, Fig. 6 reveals ΔK_{th} as a function of processing time per unit length. The ΔK_{th} of non peened specimen was 3.75 MPa$\sqrt{m}$ and that of CP at t_p = 2 s/mm was 7.35 MPa$\sqrt{m}$. It can be concluded that cavitation peening reduces the crack initiation.

4. Conclusions

In order to make clear the mechanism of improvement of fatigue strength by cavitation peening, the effect of cavitation peening on crack initiation, the threshold stress intensity factor range was evaluated. It was concluded that the cavitation peening reduced crack propagation but also suppressed the crack initiation.

Acknowledgements

This work was partly by JSPS KAKENHI Grant Number 24360040.

References

[1] H. Soyama, K. Saito and M. Saka, J. Eng. Mater. Technol., Trans. ASME, **124** (2002), 135.
[2] D. Odhiambo and H. Soyama, Inter. J. Fatigue, **25** (2003), 1217.
[3] H. Soyama and Y. Sekine, Inter. J. Sustain. Eng., **3** (2010), 25.
[4] O. Takakuwa, M. Nishikawa and H. Soyama, Mater. Sci. Technol., **27** (2011), 1422.
[5] O. Takakuwa and H. Soyama, Inter. J. Hydrogen Energy, **37** (2012), 5268.
[6] H. Soyama, J. Eng. Mater. Technol., Trans. ASME, **126** (2004), 123.
[7] H. Soyama, J. Fluids Eng., Trans. ASME, **127** (2005), 1095.
[8] H. Soyama, T. Kikuchi, M. Nishikawa and O. Takakuwa, Surf. Coat. Technol., **205** (2011), 3167.
[9] ASTM E399-09, (2009).
[10] ISO 12737:2010, (2010).
[11] O. Takakuwa, K. Sanada and H.Soyama, Proc. 62nd JSMS Annual Meetings, 2013.
[12] H. Soyama, J. Mater. Sci., 42, (2007), 6638.

Ultra Low Power Consumption Display for Next Generation Automotives: Spatially Imaged Iris-plane Head Up Display

Tohru Kawakami, Mutsumi Sasai, Yoshito Suzuki, Tatsuo Uchida*
Tohoku University, Sendai 980-8579, Japan
* Sendai National Colleges of Technology, Sendai 989-3128 Japan
Kawakami@ecei.tohoku.ac.jp

ABSTRACT

Low power consumption display is important for next generation automotives. And so we newly developed a spatially imaged iris-plane head up display (HUD). This HUD successfully achieved ultra low power consumption of 1/10～1/100 times lower than normal liquid crystal displays.

1. Introduction

A conventional display diffuses optical rays from screen or surface of display to free space shown as Fig. 1 (a). But only rays which pass through the pupil of which diameter is 2～8mm of human's eyes are used. The most part of rays are not used. Namely the most energy of displays goes to waste. We omitted this wasted energy and newly developed ultra low power consumption display. A novel concept of this display is that display gathers rays of displayed images near eyes of observer in spatial and angular luminance uniformity shown in Fig. 1 (b). We call this area to which rays gather spatially imaged iris-plane. Only in this area observer can observe displayed image. Therefore the most part of rays are used and ultra high efficiency is achieved.

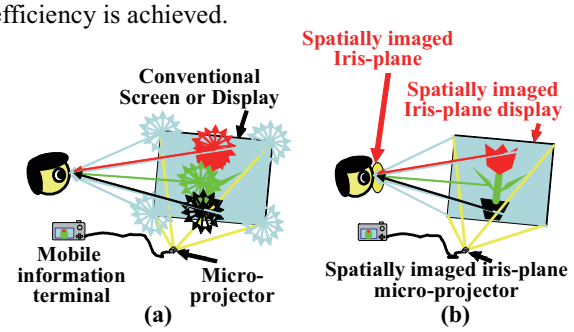

Fig. 1 A concept of spatially imaged iris-plane display
(a) a conventional display (b) a spatially imaged iris-plane display

On the other hand observation area is limited. This trade-off is a dilemma of high efficiency and wide observation area. To solve this dilemma we introduce eye-tracking system. An eye-tracking system detects the position of observer's eyes. According to this detected position of observer' eyes a display changes the direction of rays and shifts spatially imaged iris-plane to the position of observer. When an observer moves a spatially imaged iris-plane tracks observer's eyes. By this method a dilemma of high efficiency and wide observation area is solved.

2. Principles, method and structures of system

Spatially imaged iris-plane display is based on the technology of multi-view display. We have researched on multi-view displays [(1)-(3)]. Fig. 2 shows a structure of our multi-view display using multi spatially imaged iris-plane technology. By this technology the square shaped multi spatially imaged iris-planes are formed side by side in space. There is no overlap and no gap between the adjacent iris-planes. An eye-tracking system detects the position of observer's eyes and selects iris-plane in which observer's eyes exist by selecting multi projectors. Therefore ultra low power consumption display with wide observation area is achieved.

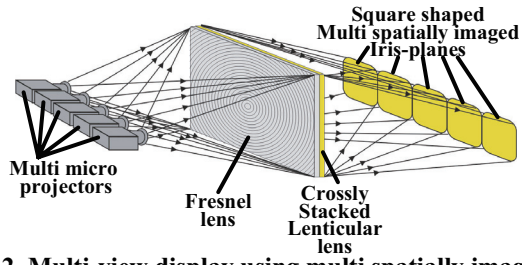

Fig. 2 Multi-view display using multi spatially imaged iris-plane technology

Fig. 3 shows an ultra low power consumption head up display (HUD) by multi spatially imaged iris-planes and eye-tracking system.

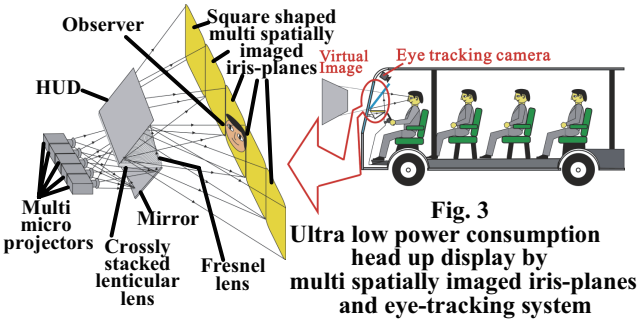

Fig. 3
Ultra low power consumption head up display by multi spatially imaged iris-planes and eye-tracking system

Effect of low power consumption is $(\tan^2\theta)/2$ shown in Fig. 4. where θ is limited diffusion angle. This is a ratio of solid angles. S_1 means a solid angle of all directional uniform diffusion in case of a conventional display or screen. On the other hand S_2 means a solid angle of limited uniform diffusion in case of spatially imaged iris-plane display. Therefore S2/S1 means effect of low power consumption. Our target is 1/10～1/100. Moreover for good see-through HUD our display uses normal glass plate of which a reflective coefficient is 4%. And so in order to realize low power consumption of 1/10 on condition of 4% at a reflective coefficient

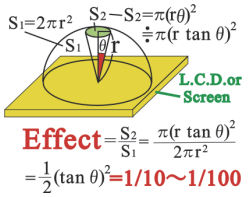

Fig. 4 Effect of low-power -consumption

effect must be needed (1/10)×(1/25)=1/250. On this condition we set diffusion angle 5.1 degrees because of ($\tan^2\theta$)/2=1/250.

3. Experiment and results

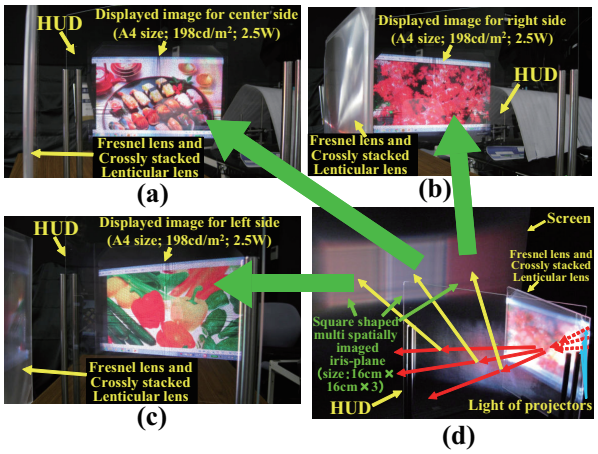

Fig. 5 An experiment and results of ultra low power consumption multi-view HUD
(a) Center side, (b) Right side, (c) Left side, (d) Multi-view HUD

Fig. 5(d) shows an experimental set-up of three-view HUD as shown in Fig. 3. In spatially imaged iris-plane an observation screen is set as shown in the upper side of Fig. 5(d). On this screen three square shaped spatially imaged iris-planes are successfully imaged side by side with no cross-talk and no gap. This is the ideal condition of eye-tracking system. Fig. 5(a), (b) and (c) show observation results of displayed images from within corresponding three spatially imaged iris-planes. It is confirmed that no cross-talk and instantaneous switching of displayed image at boundary between iris-planes. Displayed image size is A4 and luminance is 198cd/m^2. Power consumption of a normal A4 size liquid crystal display is 40W. Compared with this the power consumption of our display is 2.5W. Namely ultra low power consumption of 1/16 is successfully achieved. In case of direct view shown in Fig. 2 ultra low power consumption of 1/400 is successfully achieved.

4. Ultra low power consumption spatially imaged iris-plane HUD and eye-tracking system mounted on an electric vehicle bus (EV-Bus)

Fig. 6 and 7 show our HUD and an eye-tracking system mounted on EV-Bus. This HUD is 5-view HUD shown in Fig. 3 and range of each view is ±5 degrees. Namely total range is ±25 degrees. For practical use this range is enough. Luminance is 412cd/m^2 and power consumption is 2.5W. Ultra low power consumption of 1/16 compared with a normal liquid crystal display is successfully achieved. An eye-tracking system detects the position of observer's eyes at processing speed of 50 frames per second and selects projectors to move spatially imaged iris-plane. Therefore smoothly eye-tracking by spatially imaged iris-plane is successfully achieved as shown in Fig. 7.

5. Conclusions

Low power consumption is more and more important for next generation motives. For this purpose we proposed and developed a spatially imaged iris-plane HUD. By this novel HUD ultra low power consumption of 1/16 compared with a normal liquid crystal display is successfully achieved. Moreover by direct view type ultra low power consumption of 1/400 is successfully achieved. We believe that this display will strongly contribute to realization of ultra low power consumption HUD for next generation automotives.

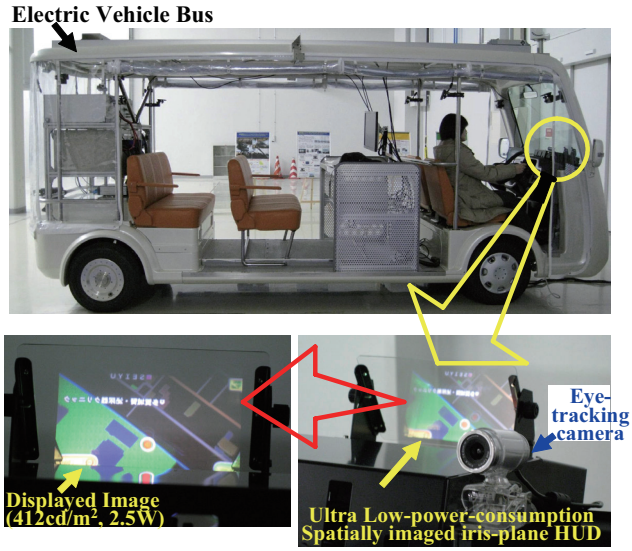

Fig. 6 Ultra Low-power-consumption Spatially imaged iris-plane HUD mounted on Electric Vehicle Bus and Displayed image

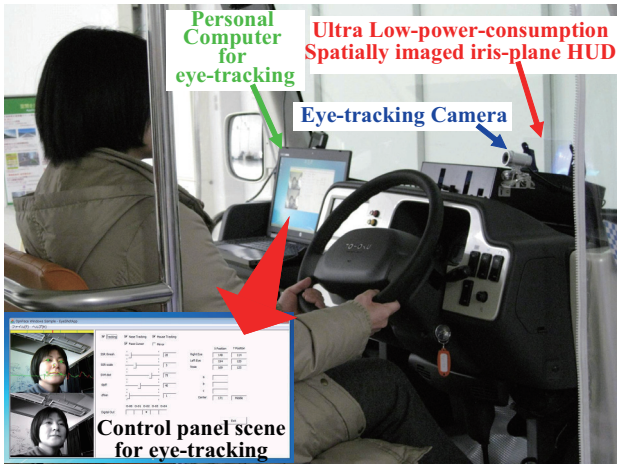

Fig. 7 Ultra Low-power-consumption Spatially imaged iris-plane HUD and Eye-tracking system mounted on Electric Vehicle Bus

References

[1] T. Kawakami, B. Katagiri, T. Ishinabe, T. Uchida "High-Resolution Multi-View Projection Display With a Quantized-Diffusion-Angle Screen" Journal of Display Technology , Vol.8, No.9, p.496-504, September 2012

[2] T. Kawakami, B. Katagiri, T. Ishinabe, T. Uchida, "Multiple Directional Viewing Projection Display Based on the Incident-Angle-Independent, Diffusion-Angle-Quantizing Technology" IEEE IAS annual meeting 2011, 2011-ILDC-382 (2011)

[3] Takahiro Ishinabe, Tohru Kawakami, Noriyuki Takahashi, Tatsuo Uchida "High-resolution autostereoscopic 3-D projection display with a apace-dividing iris-plane shutter" Journal of the Society for Information Display 18/8, 2010 ,pp583-588.

Tenth International Conference on Flow Dynamics
November 25-27, 2013, Sendai, Miyagi, Japan

Establishment of Minimally Invasive Cell Therapy for Diabetes by Introducing Interdisciplinary Approach

Kimiko Watanabe and Masafumi Goto
Graduate School of Medicine & New Industry Creation Hatchery Center, Tohoku University,
1-1 Seiryomachi Aoba-ku, Sendai 980-0872, Japan
E-mail goto@niche.tohoku.ac.jp

ABSTRACT

Arteriovenous malformation (AVM) is appropriately treated with total pancreatectomy (TP) with islet autotransplantation (IAT). We performed this treatment for three AVM patients and had good outcomes in two of the patients. Further optimizations based on a systematic evaluation of clinical experiences are needed to improve the outcome and safety of this promising approach. The roles of Collagenase G (ColG) and Collagenase H (ColH) during pancreatic islet isolation remain controversial, possibly due to the enzyme blends used in the previous studies. We revealed that ColH is crucial, while ColG plays only a supporting role, in rat islet isolation.

1. Introduction

The pancreatic islet transplantation has strong social impact in many of the advanced cell transplant therapies, and is the ideal “minimum invasive” treatment for the severe diabetic patients who are suffering with controlling the blood glucose levels (Fig. 1). However, multiple organ donors are still needed in order to cure a diabetic patient. Therefore, establishment of minimally invasive cell therapy for diabetes by introducing interdisciplinary approach could be necessary to make islet transplantation a standard treatment. Our chief objective is to construct the center of medical cell-engineering therapy as successful examples in Tohoku University.

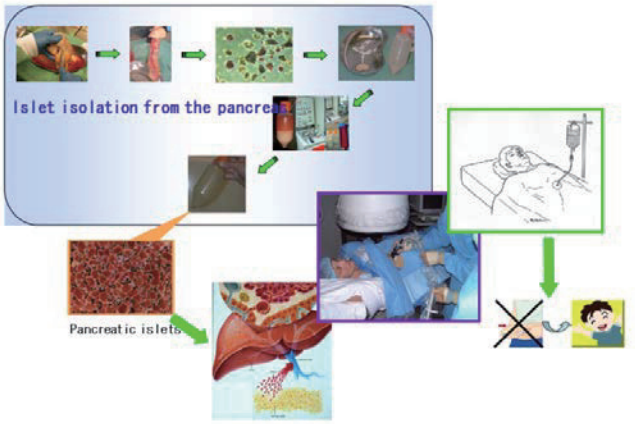

Fig. 1 Islet isolation and transplantation

2. Method

(1) Clinical Experiences in the treatment of pancreatic arteriovenous malformation (AVM) by total pancreatectomy (TP) with islet autotransplantation (IAT)

Most AVM cases have pancreatic bleeding due to portal hypertension and the rupture of abnormal vessels and AVM is thought to correlate with pancreatitis. To prevent diabetes induced by TP, three male AVM patients underwent TP with IAT.

(2) Collagenase H is crucial for isolation of rat pancreatic isles

Rat pancreases were digested using thermolysin, together with collagenase G (ColG), collagenase H (ColH), or ColG/ColH (n=9, respectively). An immunohistochemical analysis, *in-vitro*-collagen digestion assay, and mass spectrometry were also performed to examine the target matrix components of the crucial collagenase subtype.

3. Results and Discussion

(1) Clinical Experiences in the treatment of AVM by TP with IAT

The numbers of isolated islets and total tissue volume were 355,270 islet equivalents (IEQ) and 5.7 mL (patient 1), 244,758 IEQ and 16.0 mL (patient 2), and 310,238 IEQ and 1.0 mL (patient 3). Many larger clusters derived form a cystic lesion were detected in patient 2. Thus, we had to stop patient 2’s transplantation when half of the islets were transplanted. The postoperative courses of the patients. The blood glucose levels were well controlled using low-dose insulin injection in patients 1 and 3. The blood glucose of the recipients was well maintained without hypoglycemia, and a substantial level of fasting C-peptide was observed under a low dose of daily insulin supplementation (1).

(2) Collagenase H is crucial for isolation of rat pancreatic isles

The islet yield in the ColG/ColH group was highest (4,101 ± 460 islet equivalents). A substantial number of functional islets (2,811 ± 581 islet equivalents) were obtained in the ColH group, whereas no islets were retrieved in the ColG group. To examine the role of the collagenase subtypes, ColG and ColH were sequentially injected into the pancreatic duct of rats. An additional injection of ColG following an initial injection of ColH led to a slight increase in the islet yield. On the contrary, no beneficial effects were observed following an additional injection of ColH. Mass spectrometry demonstrated that ColH reacts with collagen-I and III. In the immunohistochemical analysis, both collagen-I and III were located in exocrine tissues, although collagen-III was more pronounced. The collagen digestion assay showed that collagen-III was more effectively digested by ColH than by ColG (2).

4. Concluding remarks

We are convinced that technical innovation though these projects contributes much more to the activation of medical industry based upon cell therapy.

On the other hand, most of us use the motor car and spend amounts of time in a car. In the United State, estimates suggest an additional 42 accidents/year as a result of mild and moderate hypoglycemia in people with insulin-treated diabetes. Therefore, safely driving for people with diabetes requires the development of in-vehicle medical monitoring. Therefore, in the motor car project,

we would like to produce an innovative car in order to reduce the risks of medical mishaps behind the wheel.

References

[1] N. Sakata, M. Goto, F. Motoi, H. Hayashi, K. Nakagawa, M. Mizuma, H. Yamaya, Y. Kasegawa, S. Yamaguchi, S. Sawada, S. Ottomo, T. Okada, K. Fukase, H. Yoshida, T. Ito, M. Hirota, Y. Ishigaki, S. Sekiguchi, T. Rikiyama, Y. Katayose, K. Fujimori, S. Egawa, T. Shimosegawa, H. Katagiri, S. Satomi, and M. Unno, Transplantation, *in press*.

[2] A. Fujio, K. Murayama, Y. Yamagata, K. Watanabe, T. Imura, N., A. Inagaki, N. Ohbayashi, H Shima, S. Sekiguchi, K. Fujimori, K. Igarashi, N. Ohuchi, S. Satomi, and M. Goto, Cell Transplantation, Jun 13, 2013 (Epub ahead of print).

MEMS Based Safety Systems for Automotive

Masayoshi Esashi
The World Premier International Research Center Advanced Institute for Materials Research (WPI-AIMR),
Tohoku University,
519-1176 Aramaki-Aza-Aoba, Aoba-ku, Sendai 980-0845 JAPAN
(Jun-ichi Nishizawa Memorial Research Center)
E-mail: esashi@mems.mech.tohoku.ac.jp

ABSTRACT

MEMS based safety systems have been developed collaborating with automotive companies. Range finder of which principle is a time of flight of laser light uses non-resonant 2D galvanic optical scanner. This enables a zooming function. Another range finder uses a LED pulse and an image intensifier with a high speed shutter. Wireless SAW sensor for tire pressure monitoring was developed for tire pressure monitoring.

1. Introduction

MEMS (Micro Electro Mechanical Systems) is an extended technology of integrated circuit to include not only electronic circuits but also sensors, microstructures and actuators on a Si chip. Since around 1990 MEMS accelerometers have been used as clash sensors for air-bag control systems. MEMS as yaw-rate sensor (gyroscope) have been used in sophisticated sefety systems as "Vehicle stability control" since 2003 [1].

MEMS based safety systems for automotive have been developed in corporation with companies and will be described in the followings.

2. Range finder with zooming function using optical scanner (collaboration with Toyota motor, Toyota Central Research Lab. and Richo)

2D galvanic (electromagnetic) MEMS optical scanners were developed in 1994 [2]. This scanner has a ginbal structure with moving coils and resonates in magnetic field by outer permanent magnet. This has been applied for range finder to obtain 3D image using a time of flight of laser light. The reange finder has been used for safty systems in airport or in railroad station [3].

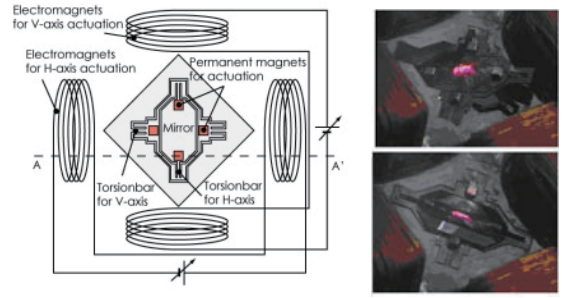

(a) Non-resonant 2D galvanic optical scanner

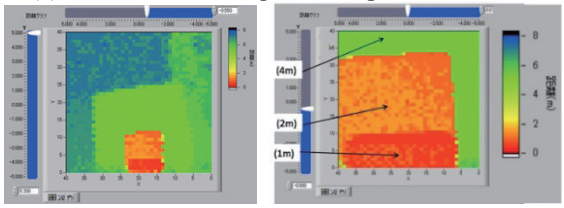

(b) Obtained range image with zooming function

Fig.1 Range finder with zooming function using optical scanner

Newly developed non-resonant 2D galvanic optical scanner is shown in Fig.1 [4]. This has permanent magnets in the moving ginbal structure and deflects in a magnetic field generated by an outer coil. Owing to the non-resonant motion this scanner has a zooming function as shown in Fig.1 (b).

3. Range finder using LED pulse and image intensifier camera with shutter

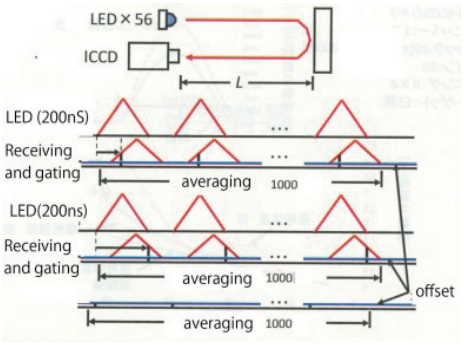

(a) Principle

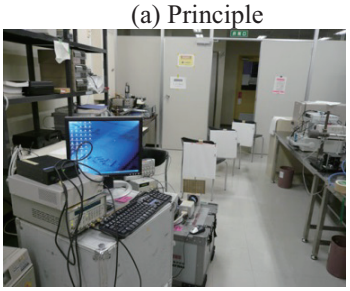

(b) Experimental setup

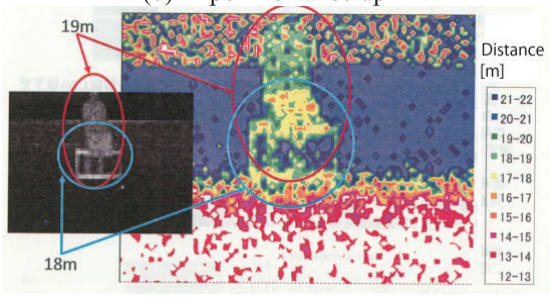

(c) Experimental result

Fig.2 Range finder using LED pulse and image intensifier camera with high speed shutter

Range finder using the time of flight of near infrared LED (Stanley DNK1101) pulse was developed for assisting the awareness during driving in night [5]. The reflected light is received by image intensifier camera with a high speed shutter (Hamamatsu Photonics C10042-02). The principle, the experimental setup and the experimental result are shown in Fig.2.

4. Wireless SAW sensor for tire pressure monitoring (Collaboration with Nissan motor)

2.45 GHz SAW (Surface Acoustic Wave) based passive transponders for wireless sensing have been developed for TPMS (Tire Pressure Measurement System) [6][7]. The principle and the structure are shown in Fig.3 (a)(b). Receiving the 2.45GHz electromagnetic wave, a surface acoustic wave generated by the IDE (Inter Digital Electrode) on a $LiNbO_3$ substrate propagates. It is reflected and a 2.45GHz electromagnetic wave is transmitted back and the sensing can be performed by measuring the delay time. The delay time is modulated by the deformation of the diaphragm by the pressure. Thermal inversion of polarization and the polarization dependent selective etching of the $LiNbO_3$ are used for the fabrication of the diaphragm (Fig.3 (c))[8]. The experimental result and the measurement scheme are shown in Fig.3 (d) and (e).

5. Conclusions

MEMS technology has been successfully applied to safety systems for automobile. The application of accelerometer to crash sensing starts in 1990's for air back systems and that of yaw rate sensor (gyro) to vehicle stability control systems in 2000's. Advanced safety systems as night visions, range imagers for pre-crash safety systems, tire pressure measurement systems (TPMS) are playing important roles for the automotive safety.

References

[1] M.Nagao, H.Watanabe, E.Nakatani, K.Shirai, K.Aoyama and M.Hashimoto, 2004 SAE World Congress, 01-1113 (2004).

[2] N.Asada, H.Matsuki, K.Minami and M.Esashi, IEEE Trans. on Magnetics, **30** (1994) 4647-4649.

[3] T.Ishikawa, H.Inomata, K.Sasagawa, T.Saito and E.Kawasaki, IEEJ Technical Report, TER-11-9, PHS-11-13 (Feb.9, 2011) 41-46 (in Japanese).

[4] W.Makishi, Y.Kawai and M.Esashi, Trans.IEEJ, **130-E** (2010) 135-136.

[5] Y.Nakano, Y.Kawai, N.Ikegami and M.Esashi, 2010 IEEJ Convention, Tokyo, (March 17-19, 2010) 1-116 p.132 (in Japanese).

[6] J.H.Kuypers, L.M.Reidl, S.Tanaka and M.Esashi, IEEE Trans, on Ultrasonics, Ferroelectrics, and Frequency Control, **55** (2008) 1640-1652.

[7] S.Hashimoto, J.H.Kuypers, S.Tanaka and M.Esashi, Trans.IEEJ, **128-E** (2008) 231-234.

[8] A.B.Randles, M.Esashi and S.Tanaka, Jap. J. of Applied Physics, **46** (2007) L1099-L1101.

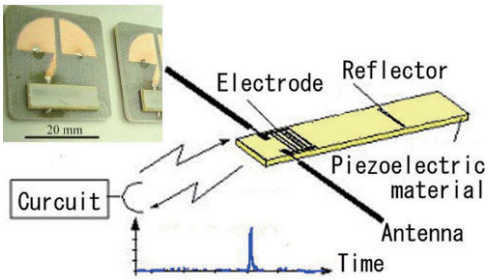

(a) Principle of SAW wireless sensor

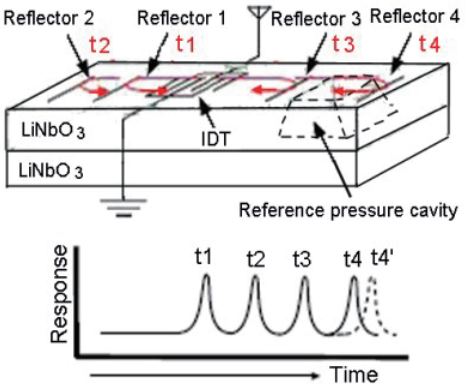

(b) Structure of SAW wireless pressure sensor

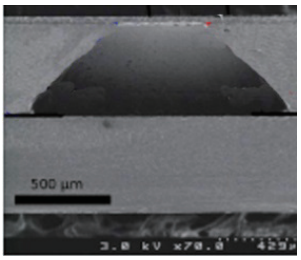

(c) Diaphragm

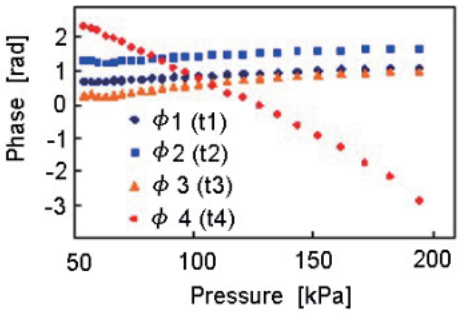

(d) Experimental result of pressure measurement

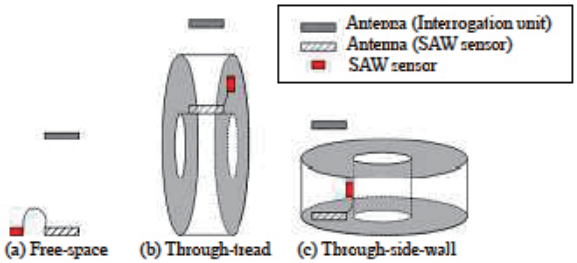

(e) Measurement scheme

Fig.3 Wireless SAW sensor for tire pressure monitoring

High Speed Micro Thermal Imaging System using Temperature Sensitive Paint

Takashiro Tsukamoto, Masayoshi Esashi and Shuji Tanaka
Tohoku University, 6-6-01 Aoba Aza Aramaki Aoba-ku Sendai-shi Miyagi-ken, 980-8579, Japan
t_tsuka@mems.mech.tohoku.ac.jp

ABSTRACT

This paper reports a high-speed, high resolution non-contact thermal imaging method, which uses a temperature sensitive paint (TSP) with europium (III) thenoyltrifluoroacetone ($Eu(TTA)_3$). The TSP was excited by a short UV pulse, thus a temporal resolution as high as 0.2 ms was achieved using a normal CCD camera. By using a high magnification lens, a spatial resolution of about 13 μm was achieved and a temperature resolution of about ±0.2°C was successfully demonstrated.

1. Introduction

Microscale thermal imaging is important for the evaluation of the microdevice such as LSI and MEMS [1, 2]. A non-contact thermal imaging is required due to the quite small heat capacity.. An infrared (IR) thermography is widely used for this purpose. However, the emissivity correction is essential for an accurate measurement. In addition, micro thermal imaging requires a high magnification IR optics, which increases the system cost. In addition, high speed measurement is sometimes required for the evaluation of the device [2]. A temperature sensitive paint (TSP), of which the luminescence is changed by the temperature, is one of the candidates for high speed and non-contact microscale thermal imaging [1]. The response of the luminescence is quite high, which promises a high speed measurement. The micro thermal imaging system can be realized using normal optics, which makes the cost of the system quite low compared with the IR thermal imaging system.

2. Principle of the measurement

Figure 1 shows the principle of our high-speed micro thermal imaging system. When a device under test starts to operate, the temperature of the device changes due to heat generation. A short pulse of ultraviolet (UV) light flashes after a small time delay, Δt, which excites the TSP, then luminescence from the TSP is captured by a CCD camera. The lifetime of luminescence is about 0.2-0.6 ms [3], which promises a high temporal resolution. By changing the Δt, snapshots of a high speed thermal phenomenon is obtained. In this study, we use a normal CCD camera for the measurement, which reduces the system cost compared with a similar system using a high-speed CCD camera [4]. The magnified thermal image can be easily obtained by using a microscope designed for visible light, which has much advantage in cost compared to an IR microscope used in the IR micro thermal imaging system.

3. Experimental result

Figure 2 shows the measurement setup. A Pt/Ti thin film heater deposited on a silicon substrate was used as the device under test. The TSP was consists of 0.03 g of $Eu(TTA)_3$, 0.09 g of polyvinylbutyral and 1.0 mL of methylethylketone. First, $Eu(TTA)_3$ and PVB was mixed in the test tube, then solved into MEK. The prepared

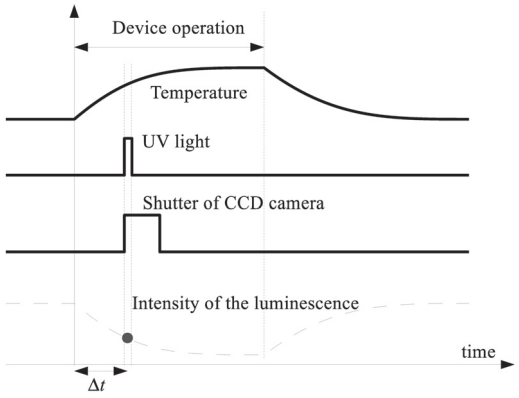

Fig. 1: Principle of the flash thermal imaging method

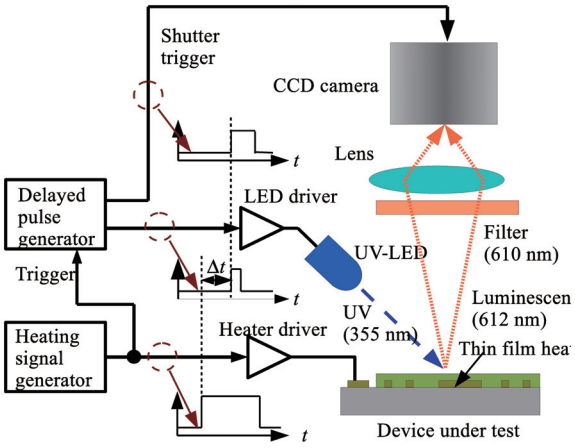

Fig. 2: Measurement setup.

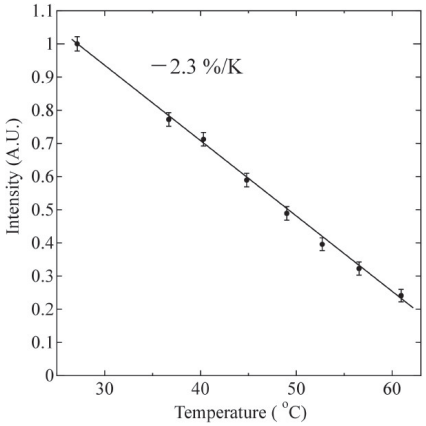

Fig. 3: Temperature dependency of the TSP.

TSP was apin-coated on the device. Figure 3 shows the temeperature dependency of luminescence from the TSP. The intensity linearly decreased with increasing temperature, which is known as thermal quenching. The temperature coefficient of intensitym, S, was about −2.3%/°C. The captured luminescent image was converted to a thermal image as

$$T(x,y) - T_0 = S^{-1}\left(\frac{I(x,y)}{I_0(x,y)} - 1\right)$$

where x, y, I and T are the horizontal and vertical position, intensity of luminescence and temperature, respectively. Subscript "0" indicates the reference condition, i.e. the temperature of the device is uniform and equal to the ambient temperature.

Figure 4 shows the thermal images of the device. The pulsed voltage, of which the duration was 50 ms, was applied to the device. A dotted line in the figure indicates a heating region. The temperature of the device was almost uniform without device operation (Fig. 4(a)). A hot spot at the heating region was successfully observed during the device operation (Fig. 4(a)-(c)), and the hot spot disappeared at the cooling period (Fig. 4(c), (d)). From the images, the spatial resolution was as small as about 13 μ m. Figure 5 shows the measured thermal response at several points near the heating area. The measured thermal response was well consistent with the theoretical results predicted by a finite element analysis (FEA). The time resolution was about 0.2 ms, and the temperature fluctuation was within about ±0.2°C.

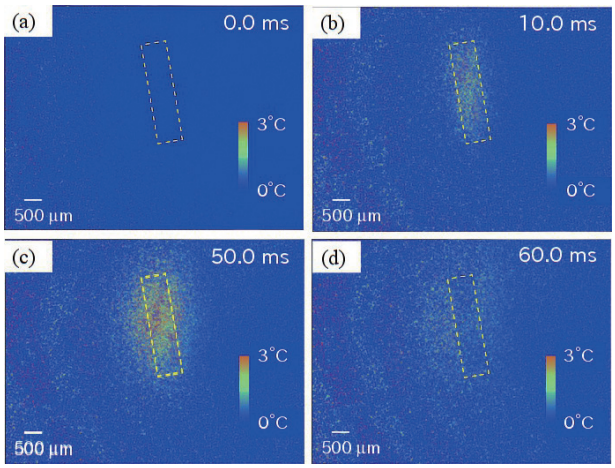

Fig. 4: Thermal images of the micro heater. (a)Initial state, (b) during heating period, (c) end of the heating period and (d) during cooling.

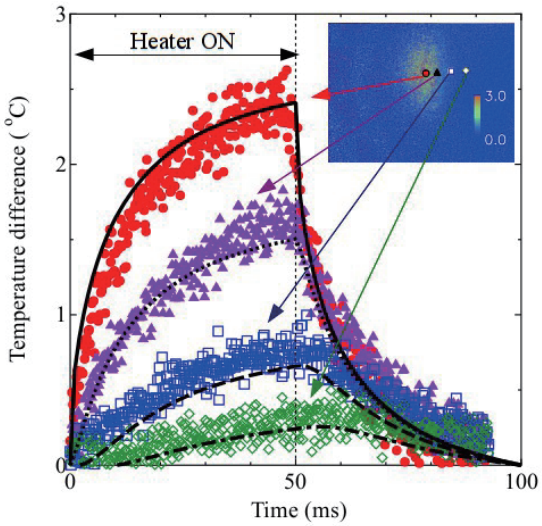

Fig. 5: Thermal response measurement. Each symbol shows the measured data. Lines show the FEA results.

4. Conclusion

We developed a high-speed micro thermal imaging system with quite low cost. The system only needs a TSP easy to prepare, a normal CCD camera and a few optical components. The spatial, temporal and temperature resolutions were 13 μm, 0.2 ms and ±0.2°C, respectively. The method we proposed has much advantages in temporal, spatial and temperature resolution and. This system can be applicable for a wide variety of thermal imaging applications with quite low cost.

Acknowledgement

We thank Sekisui Chemical Co., Ltd. for providing the PVB. This study was partly supported by Creation of Innovation Centers for Advanced Interdisciplinary Research Areas Program and MEXT Regional Innovation Strategy Support Program.

References

[1] Kolodner, P. and Tyson, J. A., "Microscopic fluorescent imaging of surface temperature profiles with 0.01◦ C resolution," Appl. Phys. Lett., Vol. 40, pp. 782–784, 1982.

[2] Kato, F., Kikuchi, K., Nakagawa, H. and Aoyagi, M., "Hot spots suppression by high thermal conductivity film in thin-substrate CMOS ICs for 3D integration," in Proc. 3DIC 2011, Jan. 2012. pp. 326–329.

[3] Basu, B. B. J. and Vasantharajan, N., "Temperature dependence of the luminescence lifetime of a europium complex immobilized in different polymer matrices," J. Lumin., Vol. 128, No. 10, pp. 1701 – 1708, 2008.

[4] Nagai, H., Ohmi, S., Asai, K. and Nakakita, K., "Effect of temperature-sensitive-paint thickness on global heat transfer measurement in hypersonic flow," J. Thermophys. Heat Transfer, Vol. 22, No. 3, pp. 373–381, 2008.

Production of Low-Cost and Highly Functionalized Titanium by Controlling the Light Elements

Takayuki Narushima and Kyosuke Ueda
Department of Materials Processing, Graduate School of Engineering, Tohoku University
6-6-02 Aza Aoba, Aramaki, Aoba-ku, Sendai 980-8579, Japan
narut@material.tohoku.ac.jp

ABSTRACT

Titanium has a high chemical affinity for light elements such as hydrogen, carbon, nitrogen, and oxygen. The solubilities of light elements in solid and liquid titanium are higher than those in other metals such as iron and aluminum. Therefore, light elements are the main impurities in titanium and make the purification of titanium difficult. However, these light elements can be utilized as alloying elements for titanium alloys and can also be used for microstructural control of titanium. In this paper, our research on the interactions between titanium and light elements is presented.

1. Introduction

Much attention has been paid to the interactions between metals and light elements such as hydrogen, carbon, nitrogen, and oxygen, because light elements are easily introduced into metallic materials during production. Figure 1 [1] shows the relationship between the maximum oxygen solubility in a variety of solid metals equilibrated with their respective oxides and the chemical affinities of the solid metals with oxygen. The chemical affinity was evaluated as the standard Gibbs free energy of formation of the oxide at 298 K per mole of oxygen. The metals can be categorized into three groups: "low-solubility and low-affinity," "low-solubility and high-affinity," and "high-solubility and high-affinity" types. Titanium (Ti) is a high-solubility and high-affinity-type metal; oxygen will not only form an oxide layer on a Ti surface but also easily dissolve into Ti at high temperatures.

Ti actively reacts with light elements. Therefore, light elements are the main impurities in Ti that make the purification of Ti difficult, which increases the production cost of Ti [2]. However, these light elements can be utilized as alloying elements for Ti alloys and can also be used for microstructural control of Ti.

In this paper, our research on the interactions between Ti and light elements [3–9] is presented.

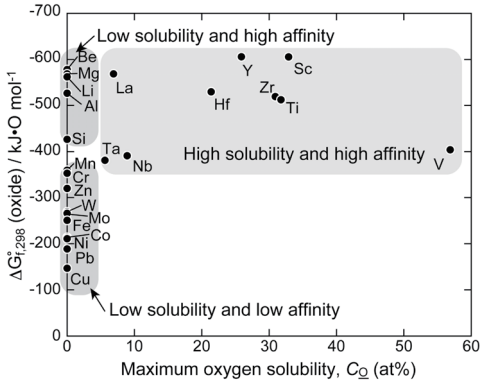

Fig. 1 Relationship between maximum oxygen solubility in solid metals equilibrated with their oxides and standard Gibbs free energy of formation of oxides at 298 K per mole of oxygen.

2. Anatase formation on Ti surface

Thermal oxidation in a gas atmosphere is a simple and low-cost method to synthesize a TiO_2 layer on Ti. The merits of thermal oxidation are (i) the synthesized TiO_2 layer adheres well to Ti substrate and (ii) this method can be used even for Ti substrate with complex geometries. There have been many reports on the formation of a rutile phase by the thermal oxidation of Ti [10]. We propose here a two-step thermal oxidation process (Fig. 2) for the formation of an anatase layer on Ti and its alloys [3,4]. The first step involves the treatment of Ti in an Ar–CO or N_2–CO atmosphere, resulting in the formation of a Ti(C,N,O) phase. Upon treatment in air in the second step, this phase is oxidized to anatase.

Figure 3 summarizes the phases formed at different temperatures in the two steps of the thermal oxidation process for commercially pure (CP) Ti using N_2–CO atmosphere. A single anatase phase was obtained after the second-step treatment conducted at 623 and 673 K.

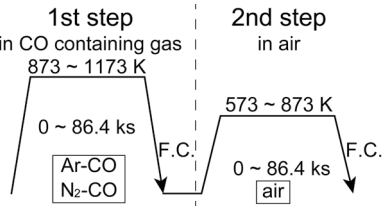

Fig. 2 Heat patterns for two-step thermal oxidation.

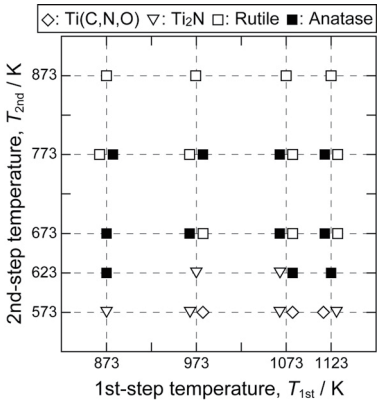

Fig. 3 Phases of the layer formed on CP Ti at different temperatures in the two-step process. The atmosphere in the first step was N_2–1%CO.

3. Surface hardening using CO gas

As compared to other metals, Ti and its alloys are known to have poor wear resistance, which is attributed to their inherent physical and chemical properties [10–13]. Therefore, improvement of wear-resistance in Ti and its alloys is essential when they are used for sliding and rotating parts in machinery, automobiles, or medical implants.

Solid-solution hardening of a Ti surface using carbon, nitrogen, and oxygen is an effective method for improving its wear resistance. Figure 4 [5] shows hardness distribution profiles in CP Ti after heat treatment in Ar–5%CO gas for 21.6 ks at various temperatures. The hardness distribution profile of CP Ti can be estimated primarily by diffusion and the amount of oxygen in the subsurface region because oxygen has a high hardening ability and high solubility in Ti [6]. It was confirmed that this surface-hardening treatment improved the sliding wear properties of CP Ti and Ti-4.5Al-3V-2Fe-2Mo (SP-700) Ti alloy [7].

4. Deoxidation of liquid NiTi alloy using metallic Ba

The removal of solute oxygen in liquid NiTi using metallic Ba was examined [8,9]. Figure 5 shows the change in oxygen content in NiTi alloy melts as a function of holding time (t_H) with and without the addition of Ba [8]. The initial oxygen contents of the Low-O and High-O NiTi alloys were 305 and 615 mass ppm, respectively. The NiTi alloys were melted in a dense CaO crucible at 1673 K for a holding time up to 300 s. Without the addition of Ba, the oxygen content did not significantly change during holding at 1673 K. On the other hand, with the addition of Ba (0.6 g, 1.5mass% relative to the melt), the oxygen content decreased to 130 and 210 mass ppm in the Low-O and High-O alloys, respectively, at t_H = 300 s.

The decrease in oxygen content in the melts resulted from the deoxidation reaction given by Eq. (1), and it demonstrated that Ba deoxidation effectively removed solute oxygen from NiTi alloy melts even with low initial oxygen content.

$$\underline{\mathrm{Ba}} + \underline{\mathrm{O}} = \mathrm{BaO(s)} \qquad (1)$$

The oxygen content decreased to as low as 64 mass ppm after the second addition of Ba.

The Ba content remaining in the melts was less than 10 mass ppm and the Ca content, introduced from the CaO crucible, was 10–15 mass ppm. This result indicates that the deoxidation product (BaO) was removed from the melt.

Acknowledgements

This study was supported by a Grant-in-Aid for Scientific Research from the Ministry of Education, Culture, Sports, Science and Technology (MEXT), Japan, under Contract No. 25249094.

References

[1] T. Narushima, Titanium Jpn., **61** (2013), 126.
[2] T. Takenaka, Titanium Jpn., **60** (2012), 133.
[3] T. Okazumi, K. Ueda, K. Tajima, N. Umetsu and T. Narushima, J. Mater. Sci., **46** (2011), 2998.
[4] N. Umetsu, S. Sado, K. Ueda, K. Tajima and T. Narushima, Mater. Trans., **54** (2013) 1302.
[5] Y.Z. Kim, T. Murakami, T. Narushima, Y. Iguchi and C. Ouchi, ISIJ Int., **46** (2006), 1329.
[6] Y.Z. Kim, T. Konno, T. Murakami, T. Narushima and C. Ouchi, Mater. Trans., **50** (2009), 2763.
[7] Y.Z. Kim, T. Murakami, T. Narushima and C. Ouchi, ISIJ Int., **48** (2008), 89.
[8] D. Ito, N. Nishiwaki, K. Ueda and T. Narushima, J. Mater. Sci., **48** (2013), 359.
[9] S. Miyamoto, M. Watanabe, T. Narushima and Y. Iguchi, Mater. Trans., **49** (2008), 289.
[10] H. Dong and X.Y. Li, Mater. Sci. Eng. A, **280** (2000) 303.
[11] D.H. Buckley and R.L. Johnson, NASA TN D-3235, NASA (1966) 1-16.
[12] D.H. Buckley and K. Miyoshi, Wear, **100** (1984) 333.
[13] R.B. Waterhouse and M.H. Wharton, Industrial Lubrication and Tribology, **26** (1974) 56.

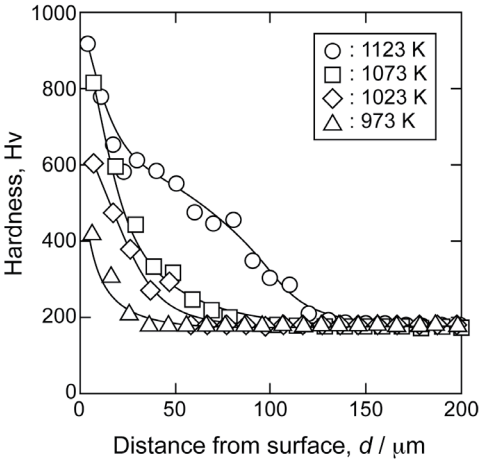

Fig. 4 Variations in hardness distribution profiles at different heating temperatures for CP Ti in Ar–5%CO gas for 21.6 ks.

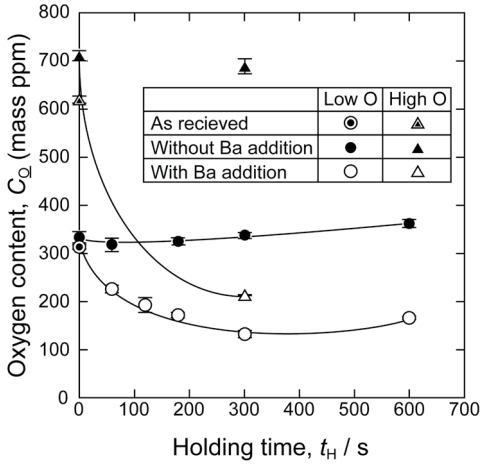

Fig. 5 Change in oxygen content in NiTi alloy melts as a function of holding time (t_H).

Tenth International Conference on Flow Dynamics
November 25-27, 2013, Sendai, Miyagi, Japan

Multiscale, Multiphysics Modeling/Simulation for Next Generation Automobiles: Catalysts, Tribology, and Batteries

Akira Miyamoto, Nozomu Hatakeyama, Ai Suzuki, and Ryuji Miura
New Industry Creation Hatchery Center, Tohoku University, 6-6-10 Aoba, Aramaki, Aoba-ku, Sendai 980-8579, Japan
miyamoto@aki.niche.tohoku.ac.jp

ABSTRACT

Multiscale, Multiphysics computational chemistry methods based on the ultra-accelerated quantum chemical molecular dynamics (UA-QCMD) were developed to realize global/local innovations in a variety of automotive technologies, such as catalysts, tribology, Li-ion battery, fuel cells, and solar cells. It was demonstrated that the UA-QCMD method is effective in performing quantum chemical molecular dynamics calculations of crystals of metals used in various battery systems and their oxides. The method is also useful for calculating local materials properties necessary for the mesoscopic/macroscopic simulations.

1. Introduction

Much attention has been given to innovation in automotive technologies such as catalysts, tribology, Li-ion battery, fuel cells, and solar cells. The design of such systems has provided a variety of technological challenges to experimental researchers. For computational or theoretical chemists also design of such automotive systems has given a variety of theoretical challenges to contribute more from theoretical or computational view points. In collaboration with many experimental/industrial experts, the authors have tried to develop a variety of software for the design of automotive systems[1-3]. The UA-QCMD method is very useful for multiscale. multiphysics simulations of automotive systems because the UA-QCMD method can perform quantum molecular dynamics calculations 10,000,000 times faster than a conventional first principles molecular dynamics method under similar conditions. We have also demonstrated that the UA-QCMD has accuracy as high as that of first-principles or thermodynamics calculations. On the basis of such progress in microscopic, mesoscopic, and macroscopic simulators we have attempted in the present project to develop multiscale, multiphysics simulators for a variety of automotive applications to realize global/local innovations for next generation automobiles..

2. Computational Methods

Details of various simulators including UA-QCMD, mesoscopic simulators, macroscopic catalysts, tribology, batteries, and fuel cells simulators as well as thermal conductivity simulator, electrical conductivity simulator are described in our previous papers

3. Results and discussion

In our previous studies the UA-QCMD method with the first-principles parameterization is 10,000,000 times faster than the conventional first principles molecular dynamics method[4-6]. We also demonstrated that the quantum chemical calculation in UA-QCMD, that is Colors, has high accuracy in comparison with DFT and thermodynamic data. In addition to the high accuracy in binding energy calculations, the UA-QCMD method can quantitatively reproduce the electron configurations of DFT calculations for various compounds. It should also be noted that the UA-QCMD is very effective for

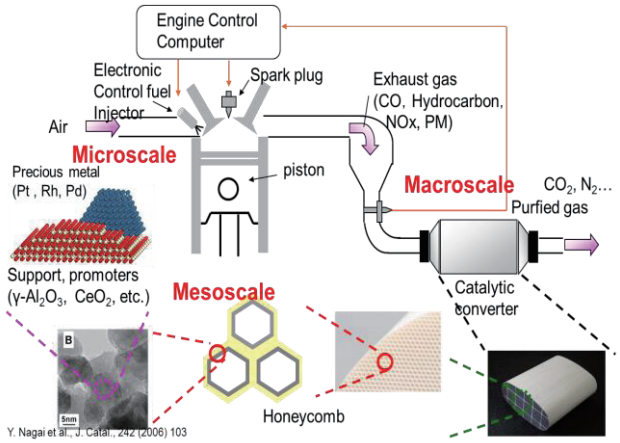

Fig. 1 Multiscale, multiphysics automotive catalysts system simulator based on the UA-QCMD method

electronic calculations of rare earth compounds with f-orbitals, while the DFT method cannot reach divergence easily and thus cannot converge for these compounds. On the basis of high speed and high accuracy the UA-QCMD method has revealed the dynamic structure changes under practical automotive conditions. The validity of the dynamic calculations can be proved by simulating various spectroscopic results coupled with the comparison with experimental measurements. The precise determination of the geometry has determined nanoscale physical properties for mesoscopic and macroscopic simulations. The results of such multiscale, multiphysics simulation agree with various macroscopic measurements.

In the symposium we plan to demonstrate that many important phenomena in automotive catalyst systems(Fig. 1), tribological systems(Fig.2) and PEFC, SOFC, Li-battery, and solar cell systems(Fig. 3) can be simulated with the combination of various software incorporated in the multiscale, multiphysics simulators.

4. Concluding remarks

The most important challenge is to realize global/local innovations in next generation automobiles through various collaborations in the present project.

References

[1] A. Suzuki, K. Nakamura, R. Sato, K. Okushi, H. Tsuboi, N. Hatakeyama, A. Endou, H. Takaba, M. Kubo,

M.C. Williams, and A. Miyamoto, Surf. Sci. **603**, 3049 (2009).
[2] A. Suzuki, R. Sato, K. Nakamura, K. Okushi, H. Tsuboi, N. Hatakeyama, A. Endou, H. Takaba, M. Kubo, M.C. Williams, and A. Miyamoto, SAE Int. J. Fuel and Lub. **2**, 337 (2010).
[3] M.K. Alam, F. Ahmed, K. Nakamura, A. Suzuki, R. Sahnoun, H. Tsuboi, M. Koyama, N. Hatakeyama, A. Endou, H. Takaba, C.A. Del Carpio, M. Kubo, and A. Miyamoto, J. Phys. Chem. C **113**, 7723(2009).
[4] F. Ahmed, M.K. Alam, A. Suzuki, M. Koyama, H. Tsuboi, N. Hatakeyama, A. Endou, H. Takaba, C.A. Del Carpio, M. Kubo, and A. Miyamoto, J. Phys. Chem. C **113**, 15676 (2009).
[5] F. Ahmed, R. Nagumo, R. Miura, A. Suzuki, H. Tsuboi, N. Hatakeyama, H. Takaba and A. Miyamoto, J. Phys. Chem. C **115**, 241123 (2011).
[6] F. Ahmed, R. Miura, N. Hatakeyama, H. Takaba, A. Miyamoto and D. R. Salahub, J. Phys. Chem. C **117**, 5051 (2013).

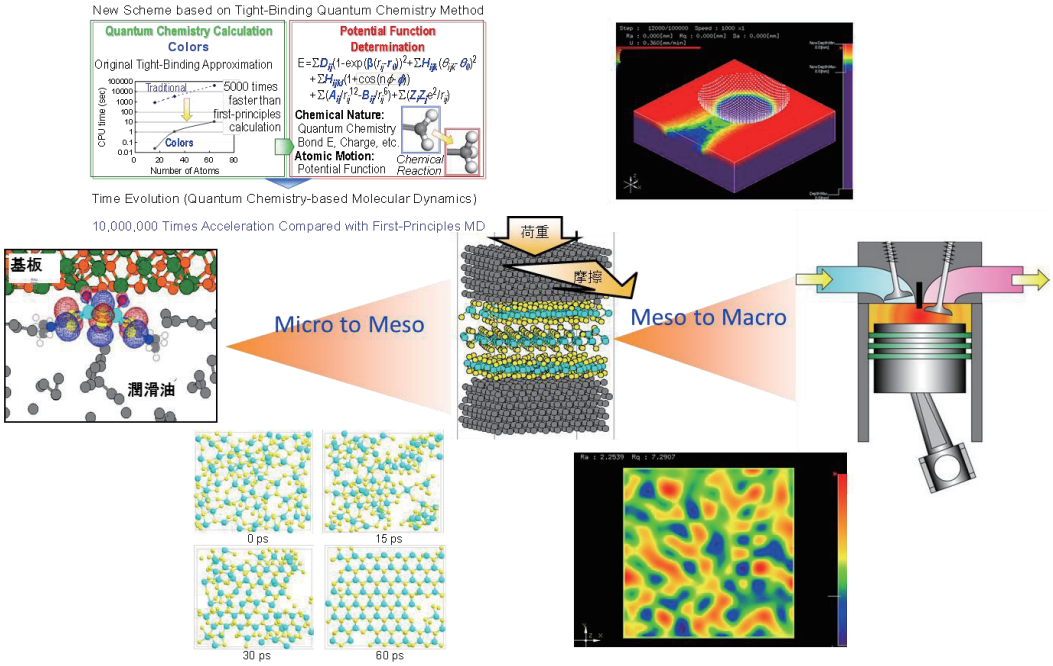

Fig. 2 Multiscale, multiphysics automotive tribological system simulator based on the UA-QCMD method

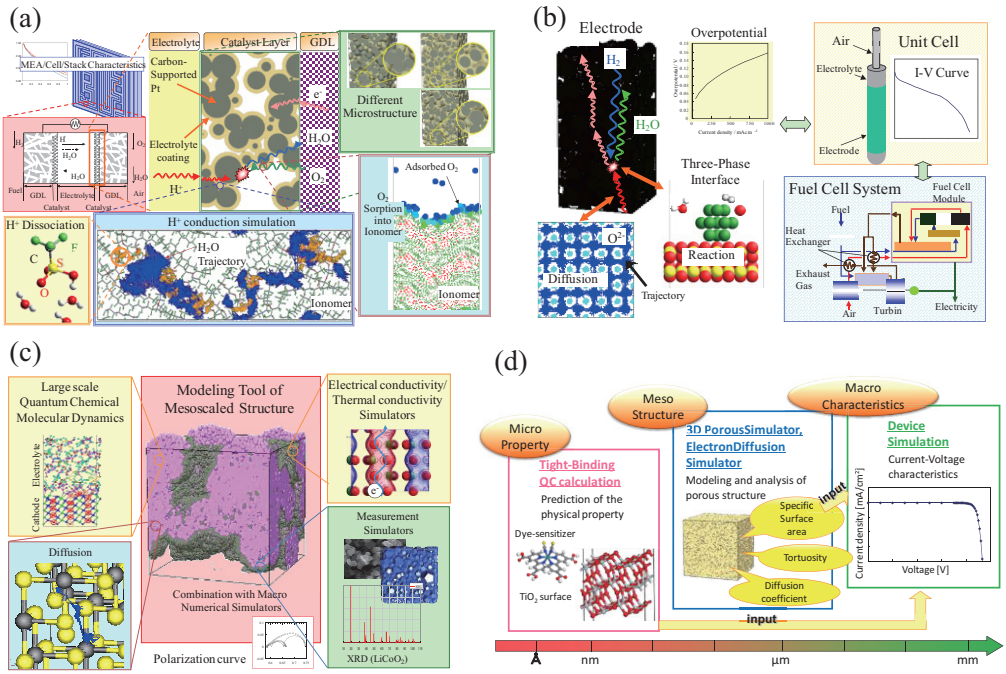

Fig. 3 Multiscale, multiphysics battery technology simulations; (a) PEMFC, (b) SOFC, (c) LiB, (d) DSSC

Tenth International Conference on Flow Dynamics
November 25-27, 2013, Sendai, Miyagi, Japan

Drag Reduction Mechanism of an Automobile with Inside-Fin Tires

Shigenori Hashida[1], Koji Shimoyama[1], Shigeru Obayashi[1], Masataka Koishi[2] and Yuji Kodama[2]
[1]Institute of Fluid Science, Tohoku University, 2-1-1, Katahira, Aoba-ku, Sendai 980-8577, Japan
[2]Yokohama Rubber Co., Ltd., 2-1 Oiwake, Hiratsuka, Kanagawa 254-8601, Japan
hashida@edge.ifs.tohoku.ac.jp

ABSTRACT

The fins installed on tires are expected as an effective device to reduce aerodynamic drag of an automobile without sacrificing other performance. This paper conducted the large eddy simulations (LES) for two different automobile models with normal tires and fin tires, respectively, to clarify the drag reduction mechanism induced by fin tires. These results indicated that the fins induce the flow along the tire rotational direction, and enhance the interaction between the fin-induced flow and under-floor flow. This interaction increases the pressure acting on the front part of the wheelhouse, and thus it reduces the pressure drag of the whole body.

1. Introduction

The increase in fuel efficiency of automobiles is important to prevent the exhaustion of fossil fuels and increase in carbon dioxide. It is effectively done by reducing the aerodynamic drag, which accounts for 50 % of running resistance at 60 km/h. However, it is not desirable to modify the shape of automobile body just to reduce the aerodynamic drag because other performance such as appearance and carrying capacity may be sacrificed.

Therefore, it is getting attention to reduce the aerodynamic drag by modifying the shapes of tires, which does not affect the above performance. Regert *et al*. have conducted experiments and numerical simulations for the flow field around a simplified automobile model where they focused on the effect of vortices around the tire [1]. Based on this, Kimura *et al*. have conducted numerical simulations for the flow field around a simplified automobile model with the tires, which have dimples on the side surfaces, and investigated the interaction between turbulence induced by the dimples and wheelhouse [2]. This result has shown the possibility that aerodynamic drag can be reduced by improving the shapes of tires.

This paper considers fins instead of dimples as the devices for reducing aerodynamic drag. Compared to dimples, fins are expected to be more effective in practical use because they can adjust aerodynamic characteristics more dramatically by modifying the layout such as the number and angle of fins. Hence, our research team has been involved in the drag reduction by fin tires. The previous experiments and numerical simulations have observed the effect of drag reduction but not clarified its detailed mechanism yet.

In this paper, to clarify the drag reduction mechanism induced by fin tires, numerical flow simulations are conducted for two different automobile models with normal (no-fin) tires and fin tires, respectively.

2. Method

In this paper, a flow solver named FrontFlow/red is used to conduct the LES of three-dimensional incompressible turbulent flow field. The Navier-Stokes equations are solved by a cell-vertex finite volume scheme. Spatial discretization is achieved by hybridizing second-order central difference scheme (95 %) and first-order upwind difference scheme (5 %) to suppress numerical oscillations. The effect of subgrid-scale fluid motion is evaluated by the standard Smagorinsky model with the model constant set to 0.15. SMAC method is used for pressure-velocity coupling, and the implicit Euler method is used for time integration.

Figure 1 shows the automobile model. This research conducts numerical simulations for two different automobile models: fin tire model and normal tire model shown in Fig. 2. The former is equipped with fin tires, which put fins on one side surfaces in a circumferential direction. The latter is provided with normal tires, which have no fins. The fin tires are installed to the automobile body so that the fins face the wheelhouses and are not seen from outside. Each model is 1/4 the size of a real automobile. The length, width and height of the model are 1.115 m, 0.438 m and 0.367 m, respectively, and the frontal projected area is 0.1352 m^2. The diameter of the tire models is 0.1583 m. The model is cut in half assuming a symmetric flow condition.

The length, width and height of computational region are set to 15 times, 5 times and 5 times as large as those of the automobile model, respectively, so that the outer boundary conditions may not affect the flow field around the model.

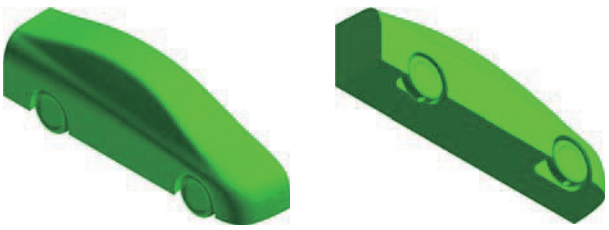

Fig. 1 Automobile model

Normal tire Fin tire

Fig. 2 Tire models

Simulation grid is generated using the commercial software Gridgen. Hexagonal grid is generated around the sliding surfaces (the details are to be mentioned later), prismatic grid is generated near the surfaces of the automobile body and tires, and tetrahedral grid is generated in the other region. The grid for the normal tire model has 5.2 million vertices and 22 million cells, and the grid for the fin tire model has 5.9 million vertices and 24 million cells.

The inlet boundary is set to a uniform flow condition of 20 m/s and the outlet boundary is set to a free outflow condition. The upper and side boundaries are set to a free stream condition, and the median plane is set to a symmetric flow condition. The wall boundary condition is based on a turbulent log-law wall function. To simulate a running situation, the ground surface has a horizontal velocity of 20 m/s equal to the free stream and the tire surfaces have the rotational velocity, which is calculated from the constant angular velocity of 250 rad/s and the distance from the axis of rotation. In addition, to simulate the rotation of the fin array, the grid zone near the fins is separated from the entire stationary grid zone and rotates around the wheel axis. The calculation is individually performed in each zone, and physical quantities are mutually transferred through the sliding surfaces at every time step to connect the flow fields of both zones.

Dynamic viscosity of air is set to be 1.5×10^{-5} m^2/s, and the Reynolds number is 2.1×10^5 based on the diameter of tires.

3. Results and Discussion

Figure 3 shows the pressure distributions and streamlines around the front wheelhouse. In this figure, the streamlines are divided into inflow and outflow, and they are shown in separate images. The pressure distributions confirm that the fin tire model produces higher pressure on the front part of the wheelhouse than the normal tire model. This increases the thrust of the automobile body, and leads to drag reduction. The streamlines show that the flow field in the wheelhouse comes from the tire rotation and the under-floor flow interacting with each other. They also show that the flow goes out of the front part of the wheelhouse after the interaction.

Figure 4 shows the pressure distributions and velocity vectors around the front part of the front wheelhouse from a lateral view. This figure shows that the fin tire model induces the flow along the tire rotational direction. This flow interacts with the under-floor flow and then heads to the front part of the front wheelhouse, where high stagnation pressure is generated. This is a key issue in the drag reduction mechanism induced by fin tires.

4. Conclusions

In this paper, to clarify the drag reduction mechanism induced by fin tires, numerical flow simulations have been conducted for two different automobile models with normal tires and fin tires,

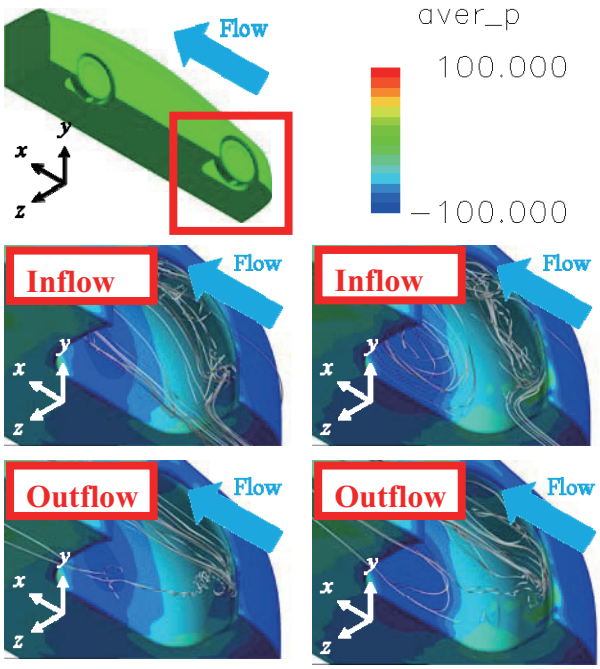

(a) Normal tire model (b) Fin tire model

Fig. 3 Pressure distributions and streamlines around the front wheelhouse

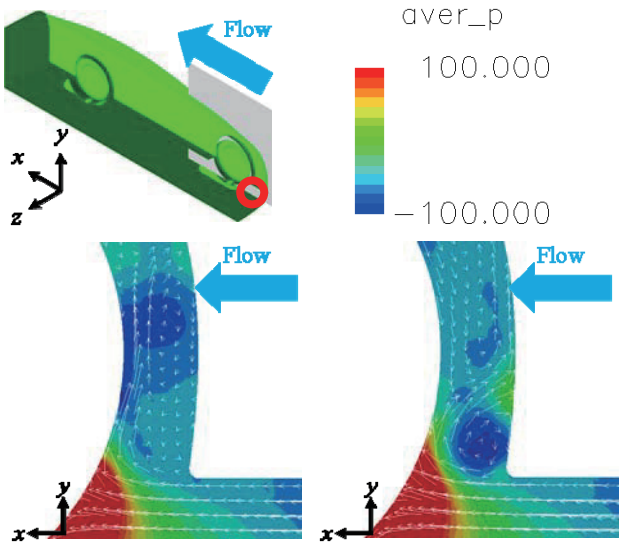

(a) Normal tire model (b) Fin tire model

Fig. 4 Pressure distributions and velocity vectors around the front part of the front wheelhouse

respectively. The results indicated that the fins induce the flow along the tire rotational direction, and enhance the interaction between the fin-induced flow and under-floor flow. This interaction increases the pressure acting on the front part of the wheelhouse, and thus it reduces the pressure drag of the whole body.

References

[1] T. Regert, and T. Lajos, Int. J. Heat and Fluid Flow, **28** (2007), 4, 616-629.

[2] Y. Kimura, M. Suzuki, M. Yamamoto, Y. Kodama, M. Koishi, 25th CFD Symposium (2011) (in Japanese).

A Concept of Automobiles Aerodynamic Testing using the 1-m MSBS in Tohoku University Low Turbulence Wind Tunnel

Yasufumi Konishi, Hideo Sawada, Shigeru Obayashi
Institute of Fluid Science, Tohoku University, Aobaku, Katahira 2-1-1, Sendai, Miyagi, Japan.
konishi@edge.ifs.tohoku.ac.jp

ABSTRACT

The world largest Magnetic Suspension and Balance System (MSBS) is planned to construct in Tohoku University Low Turbulence Wind Tunnel. The large size of the MSBS and the low turbulence intensity of the wind tunnel provide more accurate force measurements. Further, the dynamic aerodynamic test including complex movement, such as pinching with rolling, can simulate a more realistic automobile aerodynamic motion. The 1-m MSBS will play an important role in future automotive development.

1. Introduction

The Magnetic Suspension and Balance System (MSBS) is the model supporting device inside the wind tunnel by the magnetic force without any supporting rod or wire. Thus the interference problem between fluid and a mechanical supporting system is eliminated. This is a major advantage in the wind tunnel testing. Owing to this advantage, several papers were presented in fundamental research of fluid mechanics.[1][2][3][4][5]

MSBS is first developed at ONERA in end of 1950s and several MSBS's were also developed at university level from 1960s to 1980s.[6][7] But these MSBS's were relatively small. In Japan, a research development of 10cm class small MSBS was started in 1980s and they achieved 6-degree of freedom in control including rolling motion in 1992.[8] At the same time, they developed the world largest 60-cm MSBS and have been operating to date.[9]

The new MSBS under construction in Tohoku University's Low Turbulence Wind Tunnel (LTWT) becomes the largest one, which has a regular octagonal cross section of 1 m width. This low turbulence wind tunnel is famous for the lowest turbulence intensity, 0.02 %.[10] Figure 1 shows the comparison of the scale of MSBS. Integrating the largest MSBS to the wind tunnel will enable to achieve new aerodynamic tests.

2. Basic concept of MSBS

A basic concept of the coming MSBS in Tohoku Univ. LTWT is based on 60-cm MSBS in JAXA[9].

The equation of motion for a model suspended by MSBS become as follows

$$\frac{d(m\boldsymbol{v})}{dt} = \boldsymbol{F}_{aero} + \boldsymbol{F}_{gravity} + \boldsymbol{F}_{magnet} \qquad (1)$$

$$\frac{d(\boldsymbol{I}\cdot\boldsymbol{\omega})}{dt} = \boldsymbol{N}_{aero} + \boldsymbol{N}_{gravity} + \boldsymbol{N}_{magnet} \qquad (2)$$

where m is the mass and $\boldsymbol{v}$ is the velocity of its center of mass, and $\boldsymbol{F}$ and $\boldsymbol{N}$ is forces and moments acting the model. $\boldsymbol{I}$ is the inertia tensor of the model and $\boldsymbol{\omega}$ is angular velocity. The subscripts show aerodynamic, gravity, and magnetic forces, respectively. The position is measured by line sensors and the magnetic force is evaluated from the coil currents. Thus, the unknown aerodynamic force can be evaluated from Eq. (1).

The magnetic forces $\boldsymbol{F}$ and $\boldsymbol{N}$ acting on a model can be evaluated from the following expressions.

$$\boldsymbol{F} = (\boldsymbol{M}\cdot\nabla)\boldsymbol{H} \qquad (3)$$

$$\boldsymbol{N} = \boldsymbol{M}\times\boldsymbol{H} \qquad (4)$$

So, to suspend the model at a specified point in the test section, the magnetic moment formed of a magnet in a model and controllable magnetic field around the model is required. The magnetic moment of $\boldsymbol{M}$ is generated by a strong magnet as Neodymium magnet fitted inside a model. And the magnetic field which has intensity $\boldsymbol{H}$ is

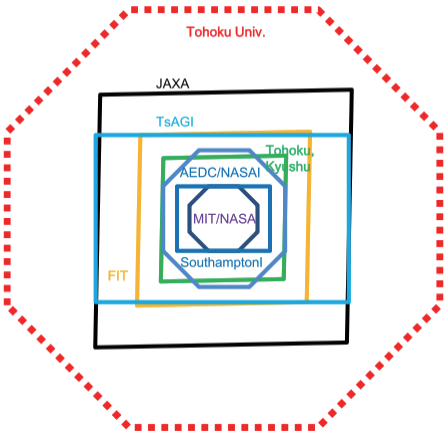

Fig. 1. the comparison of the size of MSBS

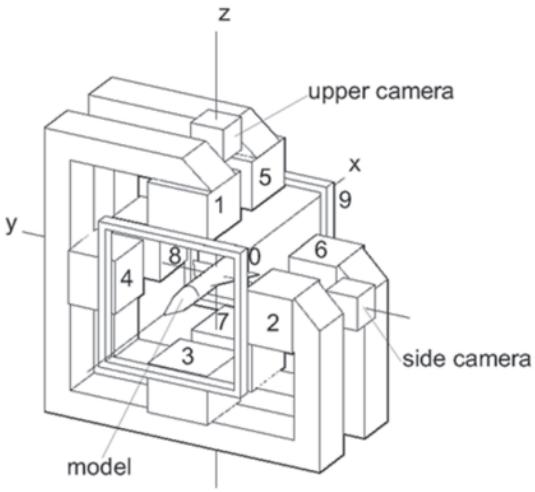

Fig. 2. Coil arrangement of MSBS

generated by coils arranged outside the test section. There are several arrangements to control the magnetic field, we selected the same arrangement of 60-cm MSBS in JAXA as sketched in Fig. 2.

The position of the model is measured by combination of line sensors located at the upper wall and the side wall which count the maker line painted on the model. Line sensors provide a spatial resolution of 0.05 mm and 0.05 degree. To improve the condition of other flow measurements, especially PIV measurement, the color of light source to illuminate the model maker line is separated from green which color commonly used in PIV. e.g. Nd- Yag laser.

To control the position of a model, PI control and a double phase advancer is employed as sketched in Fig. 3. Sampling frequency and control frequency of control system are both faster than 1.0 KHz. This high frequency provides much faster dynamic wind tunnel testing.

The aerodynamic force is limited in 105N, 51N, 91Nm for lifting force, drag force, and pitching moment for a magnet of 1.2 mWbm because of coil current limitation of amplifier. At the same time, a model size is also limited by considering the blockage effect of the closed test section. Thus this is enough force for testing a model.

3. Automobiles aerodynamic testing

A shape of the automobile is classified to a bluff body. The aerodynamic drag reduction is one of a major problem in the aerodynamists of automobile manufacturers. The advantage that there is no support interference can be effective for base drag evaluation or wake measurement and so on. For example, in the case of Ahmed body which is commonly used as fundamental aerodynamic research for automobiles, 48.6% scale model (W189.1 mm × H140 mm × L507.5 mm) has been designed to be tested in 1-m MSBS.[11] Reynolds number based on body length of 1.25×10^6 at wind velocity 40 m/s and blockage ratio of 5.1% for effective uniform flow over a ground plate.

More advantage of the 1-m MSBS appears at dynamic aeroforce measurements. A postural change of the automobile by the road modulation can be simulated by exciting a pitching motion by MSBS. In excitation motion, the left side of the equation of motion (2) cannot be negligible. Thus, we need second deviation of the model position. At low frequency cases, this second deviation can be estimated by the second-order numerical difference and the low-pass filter. In case of the Ahmed body mentioned above, amplitude of 3.6 degree with 10 Hz can be achieved, where Strohal number based on model height 0.14 m is correspond to 0.035. And because of no support needed, the MSBS can make more complex movement, such as a pinching with rolling and so on.

In addition to above force measurements by the 1-m MSBS, PIV and PSP (pressure sensitive paint) measurements can be available. It is not easy to construct an optical system such as PIV in the test

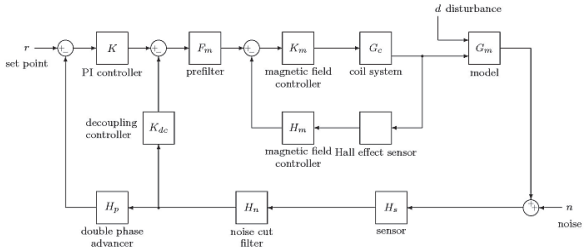

Fig. 1. Control system of MSBS

section equipped with the MSBS like the JAXA 60-cm one because many coils cover the test section. In the test section equipped with the 1-m MSBS, the setup of the optical system becomes easier because of a large number of windows on the test section walls. A change of the photography section was enabled without changing the setup of an optical system, by moving the MSBS forward and backward. Also we are planning to use fiber delivery for laser system.

4. Concluding remarks

A summary of the 1m MSBS in Tohoku Univ. LTWT and advantages in automobile aerodynamic tests are described.

Although the moving belt which is becoming indispensable at the wind tunnel for automobiles is not planned into this MSBS, we think that tests at the LTWT test section equipped with the 1-m MSBS plays an important role in future at automobile aerodynamics.

References

[1] Higuchi, H., Sawada, H. & Kato, H., *J. Fluid Mech*., 596. pp.49-72., 2008.

[2] Sawada, H. and Suda, S., Exp. Fluids, 50, pp. 271-284, 2011.

[3] Asai, M., Inasawa, A., Konishi, Y., et al., *J. Fluid Mech*., 675, pp.574-595, 2011.

[4]Sawada, H., Umezawa, K., Yokozeki, T., Watanabe, A. and Otsu, T., Exp. Fluids, 53, pp.451-466, 2012.

[5]Sawada, H., Mem. Inst. Fluid Sci., Tohoku Univ., Vol. 23, pp.1-11, 2012.

[6]Chrisinger, J. E., Tilton, E.L., et. Al., *J. Royal Aero. Soc*., 67, pp.717-724, 1963.

[7]Tuttle, M.H., Moore, D. L. and Kilgore, R., *NASA TM*-4318, 1991.

[8]Sawada, H., Kanda, H., and Suenaga, H., *AIAA* 91-0397, 1991.

[9]Sawada, H., Kunimatsu, T., *JJSASS* 50(580), pp.188-195., 2002.

[10]Ito, H., Kobayashi, R. et. al., *Mem. Inst. High Speed Mech., Tohoku Univ*. 44, No.395, 1980.

[11] Ahmed, S. R. et al., *SAE paper* 840300, 1984.

Automotive Industry Support using ITIM's Open Equipment

Naoshi Wajima,
Industrial Technology Institute, Miyagi Prefectural Government (ITIM)
2-2 Akedori Izumi-ku Sendai 981-3206, Japan
E-mail: wajima-na374@pref.miyagi.jp.

ABSTRACT

Recently, the advancement of the enterprise related to the automotive industry is increased in Miyagi prefecture and the business dealings expansion with these enterprises is problems in local businesses. ITIM has been provided technical support to local businesses with setting open equipment up for the promotion of the automotive industry. We would like to introduce a part of our action.

1. Introduction

ITIM is a public examination research institution (so-called "kosetsushi") of Miyagi prefectural government; it is a mission to plan local industrial promotion by executing technical support to local businesses. Recently, advance of the automobile-related company to the Miyagi region is progressing. We work giving priority to the auto sector promotion to attempt these enterprises and the dealings expansions with local businesses. We would like to introduce a part of our action.

Fig. 1 Mission of ITIM

2. Example of open equipment for Automotive Industry Support

(1) EMC evaluation for car electrical components

Anechoic chamber and shielded room are open for use by automotive businesses. EMC evaluation based on international standards, shown below, are provided. We also provide electrostatic discharge immunity test.

Fig. 2 CISPR25 radiated emissions

Fig. 3 CISPR25 conducted RF emissions

Fig. 4 Bulk current injection (BCI) test

(2) Shock test machine

Testing more than 1000G of shock with duration of msec is possible. Durability against shock for car electrical and mechanical components is possible to evaluate. Shock direction is changed by altering fixing direction. Simultaneous acceleration measurement is possible by use of 3 sensors. We can give advise about a structure of test jigs.

Fig. 5 Shock test machine

Table 1. Main specifications of Shock test machine

Model	AVEX SM-110-MP
Half-sine Amplitude & duration	30G,18msec～1000G,1msec
Max. shock amplitude	5000G
Max. speed	1.0m/s Peak
Dimensions of test table	W410×D410mm
Max. loading weight	90kg

(3) Catalyst property evaluation

ITIM developed the system that performance evaluated a little catalyst material developed in the laboratory of the university with gas from an engine.

- Small Honeycomb size : D25.4×60mm
- Ion-Molecule Reaction & Electron Impact - Mass Spectrometer enables the simultaneous and synchronous monitoring of NOx, CO, and hydrocarbons (Toluene, Propylene etc.) .
- GC/MS is used to analyze C2 to C11 hydrocarbons (Ethylene, propylene, 1-butene, n-hexane, benzene, toluene, etc.) in automobile exhaust gas.

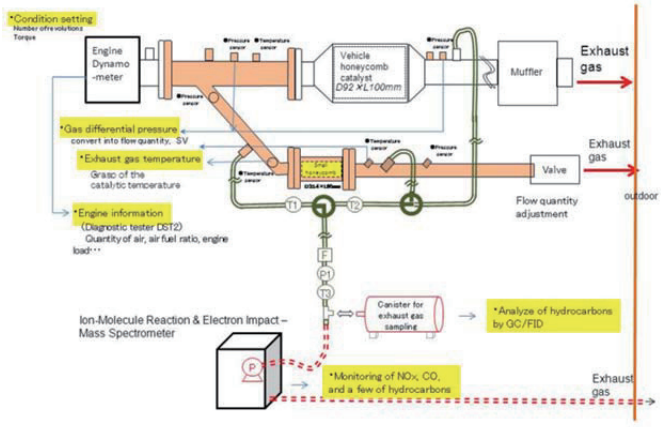

Fig. 6 Constitution of the catalytic evaluation system

Table 2. Component of the system

Component	Maker, model	Main specifications
Engine Dynamo-meter	TOKYO METER CO., LTD. GWE-110/150R	Engine : 1NZ-FE, 1.496 L (which is put on Allion made in Toyota Motor CO., LTD.)
Ion-Molecule Reaction & Electron Impact - Mass Spectrometer	V&F Analyse- und Messtechnik GmbH, AirsenseCompact	Gas consumption : 100ml/min Lower detection limit : ppb Response time :20msec
Gas chromatograph and mass spectroscopy /Headspace Preconcentrator	Entech Instruments Inc., 7100A Agilent Technologies Inc., (GC)7890A(MS)5 975C	3-Stage preconcentrator Detector : MS and two FID(Flame Ionization detector) Lower detection limit : ppt
Exhaust Gas sampling plumbing	NISHIKAWA KEISOKU CO.,LTD.	The Silonite Coated Tubing made in Entech Instruments Inc.
Diagnostic tester	DENSO CO., LTD. DST-2	Trouble diagnostic software for Toyota cars

(4) X-ray CT

This system allows us to inspect the three-dimensional inner structure of automobile parts non-destructively, for example aluminum die-cast products, electronic parts, molding parts etc..

Table 3. Microfocus X-ray CT System

Manufacturer, Model	Comscantecno.Co.Ltd ScanXmate-D225RSS270
X-ray generator	Open tube/Transmission head Voltage 20～225kV (variable) Focal spot size Min, 4μm
Detector	Digital flat panel Pixel size(Pitch) 127μm/254μm Active area 235mm（H）×186mm（V）
Sample size	300dia,×300mm H , weight 15kg

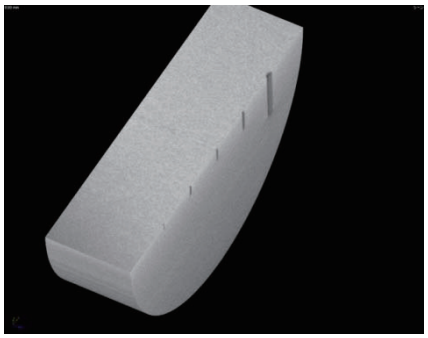

Fig. 7 Aluminum sample size 30×30×10mm

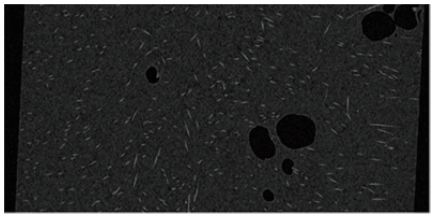

Fig. 8 Carbon-fiber-reinforced plastics fiber dia.10μm, sample size 20×20×10mm

3. Concluding remarks

We introduced an action of the car-related industrial support in ITIM. The contact from anyone who is interested to us is welcomed.

References

[1] ITIM's HP:
http://www.mit.pref.miyagi.jp/index.html
[2] ITIM's HP(English Version):
http://www.mit.pref.miyagi.jp/index_e.html

An Accelerator・Synchrotron・Superconductivity Research Facility High-precision Constant Current Power Supply

Haruo Kudo
Kudo-Denki Co.,Ltd.
3-1-5 Nishitaga, Taihaku-ku, Sendai 982-0034, Japan
E-mail: kudo@kudo-kenki.co.jp

ABSTRACT

Since 1956 to now, our company have been has been related with Tohoku University. Technology has been improved very well from analog generation. From this improved technology, we use this for an elementary particle, accelerator science of radiation, and big science in the field of nuclear fusion. Those technologies use at the research facility in Japan and out of Japan. Moreover, we use these technologies for heavy particle cancer treatment, medical field of MRI etc… And it is also the field of semiconductor ion implantation, too. We established control stability of the DC current and voltage 0.1 ppm, so our next challenge is 0.02 ppm.

1. Introduction

Kudo Electric was established for the purpose of "electronics application development", in 1956. We challenge to find future technique, and we have never ever given up making new stuffs for our future. We have continued to investigate about analogue in strictly over 50 years. We have been related with Tohoku University since it to now. We repeated an analog circuit, a technique of the feedback control while getting instruction of teachers through trial manufacture of the Laboratory Equipment of Tohoku University. We established a control stability of the DC current and voltage 0.1ppm, and Our Next Challenge is 0.02ppm.

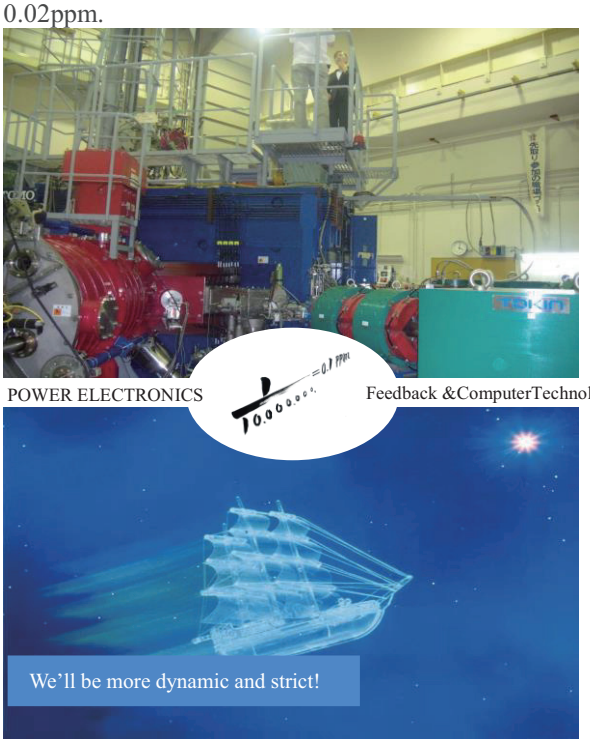

Analog and digital fusion

We challenge to find future technique, and we have never ever given up making new stuffs for our future.

Striving further to improve the quality and performance, we will continue to sail for the future to serve our wider accumulated technologies and to challenge the request of future technology to constant.

2. Development results

Technology has been improved very well from analog generation. From this improved technology, we use this for an elementary particle, accelerator science of radiation, and big science in the field of nuclear fusion. Those technologies use for the research facility in Japan and out of Japan. Moreover, we use these technologies for heavy particle cancer treatment, medical field of MRI etc… And it is also used at the field of semiconductor ion implantation. We established control stability of the DC current and voltage 0.1 ppm, and our next challenge is 0.02 ppm. Typical results are as follows.

Delivering one set （218 units）of Electromagnet power supplies to **" Kyushu synchrotron radiation research center "**in March, 2004.

Ring system large electromagnet and constant current power supply group in
Kyushu synchrotron radiation research facility
Electromagnet

300kw · bending magnet power supply internal

Updating **AVF Cyclotron magnet power supply** of Tohoku University science department was updated with 45 units.

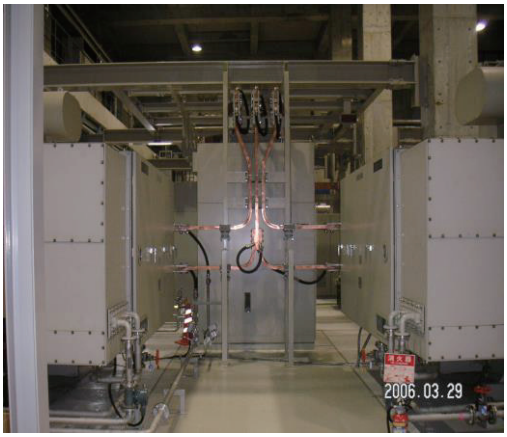

NIMS, 40T strong magnetic field power
Development 16MW, 35KA, current accuracy 10ppm

Delivering Accelerators to **"The power supply in the Gunma heavy ion Center therapy research center"** in 2008.

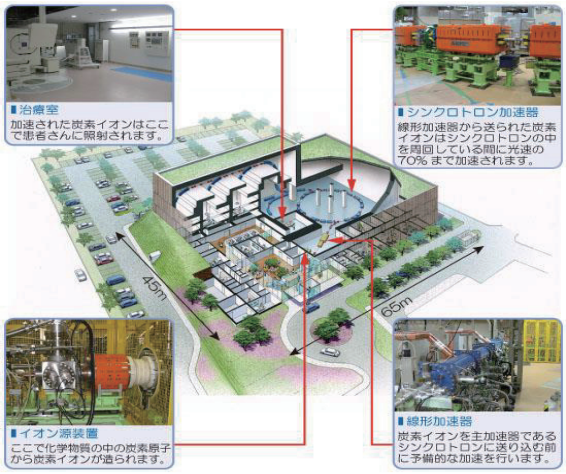

The power supply in the Gunma heavy ion cancer therapy research center

Product Guide is as follows.

SP-series stabilized power supply
≪small high-precision DC switching power≫

0.02-0.001% current stability
Suitable for the electromagnet excitation
1KW～30KW class unit power


2KW

6.6KW


10KW


Honda “Beat” decomposition


In- Wheel Motor


12V50AH 4 battery

3. Conclusions

We challenge to find future technique, and we have never ever given up making new stuffs for our future. Striving further to improve the quality and performance, we will continue to sail for the future to serve our wider accumulated technologies and to challenge the request of future technology to constant.

Industrial labor-saving Machinery・Hikichi Seiko Automatic Machine

Masayoshi Hikichi
Hikichiseiko Co., Ltd.
2-8-28 Fukiage, Iwanuma 989-2436, Japan
E-mail: mh@hikichiseiko.com

ABSTRACT

We help customer's "solution annoyances, production reform &improvement, and efficiency.
The challenge is always to develop new technologies.
Involved from the conceptual design stage of the demand from the customer, will answer to your expectations.

1. Introduction

Our company was established 1979 in Miyagi, have grown in industrial labor- saving machinery, design & manufacture of various devices and tooling, prototype, precision parts processing.

As our strong point, 1. Precision machining design and manufacture of labor-saving equipment, FA equipment, etc. 2. We are the manufacture, design and development of image inspection robot. This robot will grant the wishes of our customers. 3. Perform equipment maintenance such as various types of equipment, the maintenance. (Remodeling, maintenance, overhaul) 4. Precision Machining.

Management policy

The challenge is always to develop new technologies. Involved from the conceptual design stage of the demand from the customer, will answer to your expectations.

Specialty

Up from concept design and manufacturing and material processing line equipment, machinery, fixtures, etc., we will consistently meet your request.

Performs labor saving, efficient and suggestions to customers in manufacturing high quality.

The image inspection robot applications developed in-house design, make your suggestions to lower cost efficiency and high quality of manufacturing.

Utilizing the know-how, design and manufacture of various facilities and equipment, we are remodeling facilities and equipment.

Around for aircraft repair, design and manufacture of peripheral equipment, etc. We also manufacture parts.

2. Section Introduction

Design Division

We receive the specifications for a product from a customer, and create a conceptual drawing. Once we have made the conceptual drawing, we meet with the customer to get his or her approval for the specifics of the design of the product. Then we begin to create detailed drawings of the parts and components of the product. We make all the designs for all parts of assembly lines, self-standing machines, and jigs.

Production Division

Our production division has the necessary equipment to be capable of making every component of an automatic machine so as to be able to produce machines all on its own. We are good at making single products (i. e., high-mix low-volume production). We also have good capability for dealing with orders that allow only short lead-times, and make efforts to reduce costs and improve techniques constantly. Our company has state-of-the-art cutting machines.

Control Division

The control division designs software and hardware products based on PLCs (sequencers). This division is able to use PLCs from many different controller manufacturers. Therefore, we can install, wire, and debug whatever PLCs our customers designate for their

equipment. We can also incorporate single axis or SCARA robots of many different manufacturers.

Assembly Division

The assembly division takes over the work from the design division, and by following the assembly drawings assembles the parts and components into the product. We measure the stacked tolerances of the product as necessary, and send the data to the customer along with the product. We install and adjust the product, and complete the delivery by confirming that it is working properly. At the customer's request, we install our machines anywhere, in Japan or overseas.

Vision Division

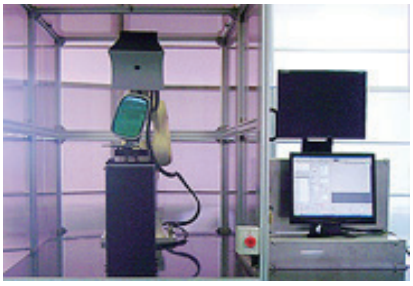

Taking advantage of our accumulated design techniques for conveyance, and our vast experience of creating image verification systems for various works, we can propose the best possible vision systems, from design to installation, for inspecting your product. We have various visual inspection systems, including a visual inspection robot from Denso Wave, so that we are ready to quickly respond to any request. We can also give you advice on what vision system is best for your equipment or facilities, so please do not hesitate to ask us. We have vision system coordinators to take care of your requests.

3. Our product

Inspection robot image processing

Camera moves along the surface, and also taken round products. Regardless of the material such as metal or plastic, can be detected material defects in the mirror that reflects light. The unit can detect flaws in 1/10mm, stuff, and a dent. Robotic inspection saves time, as it is significantly faster than human inspection.

At 2011, we had received certificate from “ Miyagi Sugure MONO” that is award for excellent technology in Miyagi.

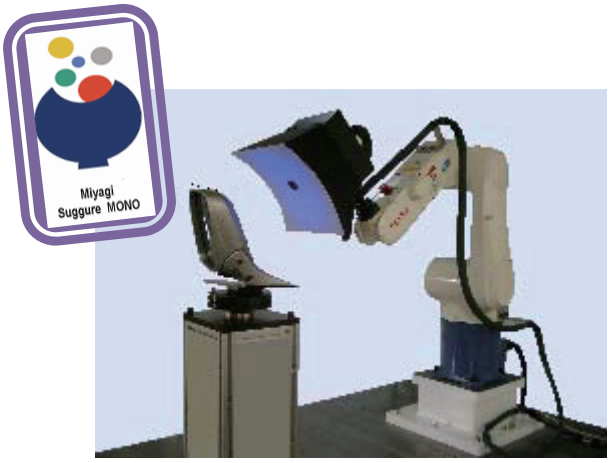

4. Concluding remarks

Our company has been able to improve performance and innovation a steady rate. We appreciate greatly your continued support and guidance.

With our brainpower and technology power we will achieve new developments for limitless future growth. We design and manufacture products all on our own from our customers' perspectives, and further our efforts to maintain our customers' trust.

I hope that with your continued support we will continue to grow and in return help our customers grow also.

Proposal of Diecast Shape in Consideration of The Cost of Quality in the Early Stage of Development

Atsushi Kamada
Iwaki Diecast Co., Ltd.
51-2 Yamazaki Washiashi, Yamamoto cho, Watari gun, Miyagi Japan 989-2204
E-mai: info@iwakidc.co.jp l

ABSTRACT

Iwaki Diecast Co., Ltd. is a comprehensive die-casting company manufacturing high quality high precision aluminum/zinc die-cast products and small products having complex profiles products through the metal injection molding method (MIM Method) (MOLDALLOY). Iwaki Diecast aims to become a manufacturer of a truly comprehensive line of components with the capacity to develop uniquely innovative technologies. We are able to satisfy each and every need of the customer by applying a diverse range of cutting-edge technologies and by handling every production process beginning with the design of dies to the production of finished goods.

1. Introduction

It is start up as a Iwaki Diecast Co.,ltd place in 1968 and it was established Iwaki Diecast Co., Ltd. in 1969. A die making section which is our main businesses was established in 1975, and we started MIM(Metal Injection Molding) production in 1989. We produce the metal injection molding (MIM) of highly precise aluminum, zinc, die-casting product of high quality and the small complicated shape mainly.

2. Half solidification foundry

It is a method to cast after making semi-solidified slurry from molten metal. It makes finely, smooth structure which is less flaws compared to cast from complete molten metal. The method is possible to make product which is high-voltage, high intensity, high tenacity
It is the latest technology which can be expected to be near-net-shape and the substitutes from a forging product.

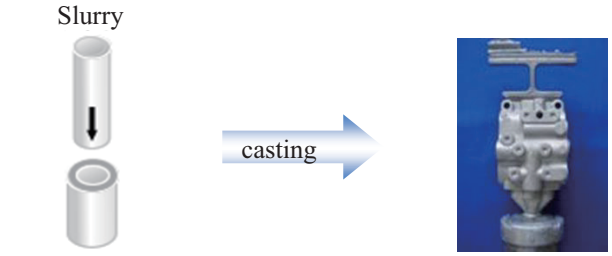

【A use of semi-solid die-casting】

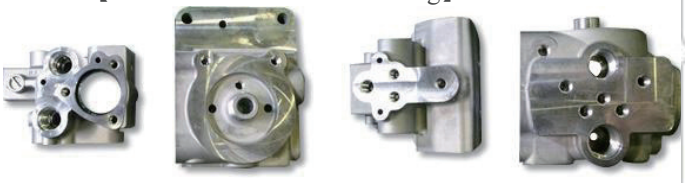

3. MIM(Metal Injection Molding)

MIM is the processing system which is compact and can mass-produce complexity shape parts at highly precise high density which is conventional. It is difficult with precision parts such as iron, the stainless steel is made by the metal powdery injection molding method (MIM).

【A use of MIM**(Metal Injection Molding)**】

【Automobile parts】
Material: Fe -Ni

POS is on in a pipe and it is impossible of production by other manufacturing methods geometrically.

【Clock parts】
Material: SUS -316L

Three folds of ditches of 0.2×0.2×0.2 are structure.

【HDD parts】
Material: SUS -304L

Shape fleshy equally of t=1.5

【Printer parts】
Material: SUS -304L

Mass production is possible in spite of a complicated shape

【Clock parts】
Material: SUS -316L

Approximately 0.4 small slits manufacturing methods geometrically

【Self-acting machine parts】
Material: SUS-630

Approximately 0.4 small slits manufacturing methods geometrically geometrically.

4. Institution equipment guidance is as follows.

Head Office

Performing design and manufacture of a die-casting, die product manufacturing of aluminum die-casting and zinc die-casting squeeze die-casting, and shipment.

Sakamoto Factory

Performing product manufacturing of aluminum die-casting, We have put the solar panel on the roof of the building.

Miyanowaki Factory

Performing from product manufacturing of MIM (Metal Injection Molding) to shipment.

Saitama Factory

Performing from poduct (ultra-hich-speed) and shipment

Tucson Factory in USA**:** performing precision products

5. Results

We would make a sample with 3D printer and perform shape suggestion to clients and design the die having high productivity. We would suggest the best plan by casting flow analytical system.

6. Conclusions

We catch a demand as a professional of the die-castings precisely and cope quickly

References

[1] http://www.iwakidc.co.jp/

Tenth International Conference on Flow Dynamics
November 25-27, 2013, Sendai, Miyagi, Japan

From Yamagata, We Aim to Technological Innovation of Noise Filter Coil

Ryuichi Ueno
Ueno Co., Ltd.
100 Miwa Sekinaka, Tsuruoka, 999-7634, Japan
E-mail: info@uenokk.co.jp

ABSTRACT

Ueno Coil is revolutionize the world of noise filter coil that we developed new.
Noise filter coil, to prevent a malfunction of electrical products, electric components,
which is cut the noise intrusion from power line, is included into the electricity most of the products.
Ueno CO., Ltd. develop and provide the noise-filter coils that are coping with customers' needs by powerful staff members, materials, facilities, such as simple anechoic chamber, and domestic plants of speedy trials.

1. Introduction

Ueno Co., Ltd. is located in the city of Tsuruoka, Yamagata Prefecture and manufactures electronic components called noise suppression coils and noise filter coils, which block signals that cause malfunctions in electronic equipment, from January 1982. We specialize in ring-shaped coils (toroidal coils) and in FY2004 our company was recognized as producing the most toroidal coils in Japan. Although consumers do not directly come into contact with our work, Ueno products are commonly used in items crucial to daily life, including appliances, daily necessities, and goods for receiving information, such as rice cookers, air conditioners, computers, and cars.

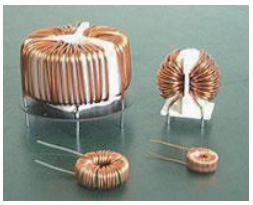

Noise suppression coils (toroidal coils) manufactured by Ueno

Noise suppression coils (toroidal coils)

2. Products developed by Ueno

Ueno's challenge " Toroidal coil automatic winding machine"

We have developed an automated production system of the Troidal coil of the one and only in the world, and has been producing 20 million or more in total in Mikawa plant in Yamagata prefecture. Compared with hand made, characteristics are more stable such as air conditioning. It is used in a variety of areas.

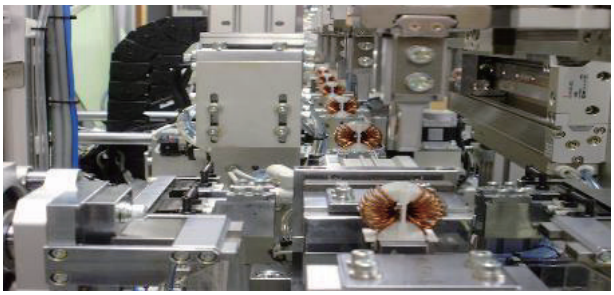

Ueno Coil is groundbreaking products that replace toroidal common mode choke coils.

It has these features that "Exceptional denoising" , "Smaller mounting area than toroidal coils" , "High quality products provided through new development, high-speed automatic winding machines" , "Superior pricing due to reduced utilization of copper wires".

Merit of Ueno Coil

"Winding time is just 10 seconds!!"

Winding in 10 seconds by the high-speed automatic winding. We did the man-hour reduction of about 90% compared with the Toroidal.

"Winding directly to the closed magnetic circuit core"

This is a new method that winding directly to closed magnetic circuit core! Inductance improved about 20 % compared with open magnetic circuit core!

"No short layers!"

Tension of the coil is law at the time of the winding. There are no short layers because of the single- phase winding.

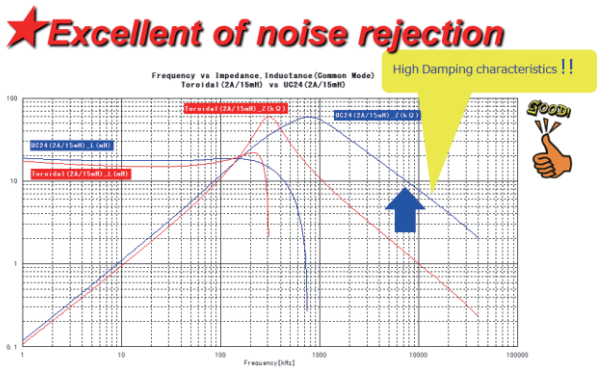

3. What are Ueno products used in?

Noise suppression coils (noise filter coils) are used in all everyday electronic items including, household appliances, OA equipment, cars, and play toys.

Though not directly obvious to the consumer, they used in items crucial to daily life, including appliances, daily necessities, and goods for receiving information.

A noise filter coil used in a computer

The picture below is of the inside of a computer.
Can you see where the noise filter coil is used?

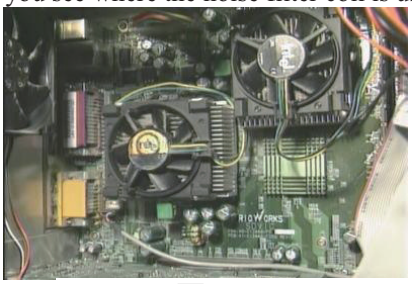

The noise filter coil is circled in red.

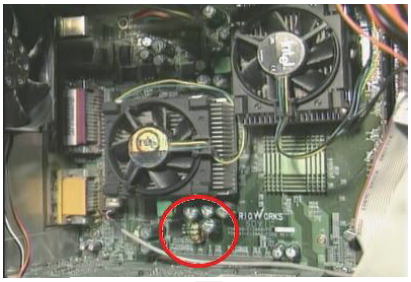

An enlarged image of the noise filter coil.

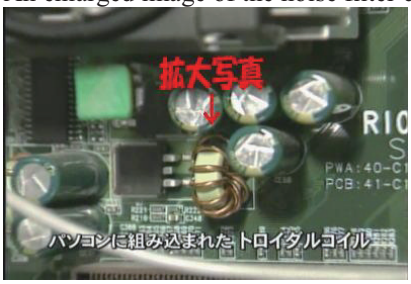

Although not visible to the consumer, Ueno noise filter coils are used in this kind of equipment.

In addition, Ueno coil is also active in the automotive industry. It applies to the electric vehicle, also have helped to parts of the car.

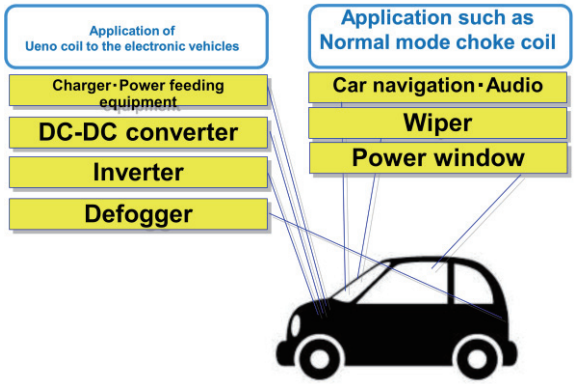

4. Concluding remarks

For many years, noise filter toroidal coils, our company's staple products, were manually wound.
Despite fulfilling the function of eliminating power-supply noise, we were unable to get away from the typical labor-intensive manufacturing of that production method. The primary reasons for not mechanizing that process were an unavoidable rise in costs due to the necessity of considerable investment needed to develop winding machines in relation to the selling price of coils, and the high price of manufacturing winding machines.

Therefore, not only our company, but all companies manufacturing toroidal coils switched production bases in search of low-wage regions.
Although the inconsistency in quality due to manual winding was frequently pointed out by users, the necessity of substantial capital to develop winding machines leads to prohibitively expensive pricing of coils. For this reason, manual winding is still practiced as a compromise between quality and cost.

Our company resolved to break down this barrier inhibiting toroidal coil production, and from 2004 began to develop an automated winding machine. It was a huge challenge and an adventure for a small-to-medium-sized enterprise like ours, but fortunately we received support and cooperation from pertinent organizations in addition to companies that manufacture automated machines who worked diligently with us, and in 2010 the first stage of the project was completed. We continued with our efforts and undertook the second and third stages of the project, and today, in 2012, we have established a goal of mechanizing approximately half of the coils we produce.

For a manufacturing company, 1. stabilization and differentiation of quality, 2. efficient minimization of delivery time, and 3. all-out effort to further reduce costs are important. The third phase of the project will modify the conventional toroidal (ring-shaped) design and greatly strengthen the 3 aforementioned elements of manufacturing.

The year 2012 marks the 30 year since our company's establishment. Though this enterprise began as a sideline, our company foundations are at last being put into place. With this as a turning point, as a manufacturer of noise filter coils, we will strive to win by being a step ahead of the game.

Tenth International Conference on Flow Dynamics
November 25-27, 2013, Sendai, Miyagi, Japan

Development of Industrial & Creative Vitality

Kazuhiko Yashima
Miyagi Industrial Association
Industrial Technology Institute, Miyagi(ITIM) 2-2 Akedori Izumi-ku Sendai 981-3206, Japan
E-mail: yashimak@tiger.odn.ne.jp

ABSTRACT

Miyagi Industry Association aims to contribute to the development and activation of the prefecture industry. We boldly to solve social issues by accurately reflect the trend of the times and support through various business towards the performance improvement of the member companies.
"Miyagi Association human resources network services" and
Outgoing business of *"Miyagi Sugure MONO"* are parts of our business.

1. Introduction

Our company was established at Miyagi in 1986 as the incorporated association. Member is included 421 companies, in it regular member is 356 companies and supporting & special member is 65 companies.

Purpose of establishment is contributed to the vitality and creative sound development of the prefecture industry. This is by that the industry in Miyagi and the people of industrial related industries attempt strengthening the management base, sophistication of the technology and development of new market , through Industries, Scale, Exchange cross-regional, and Promoted diligent study.

2. Method

Activities

Miyagi Industry Association aims to contribute to the development and activation of the prefecture industry. We boldly to solve social issues by accurately reflect the trend of the times and support through various business towards the performance improvement of the member companies.

Promotion of industry-university cooperation

Since its establishment, it has been a very active by providing a forum for technology providers and exchange information with researchers and institutions of many universities in Miyagi Industry Association.

Exchange among personnel in industry

Universities, technical colleges, research institutes, government officials and many people play a industry of Miyagi brings together, industry exchange meetings, which began in order to trigger the industry collaboration, has been held with the participation community of over 300 people twice a year.

Study and research of the Technology Trend

Every year, we introduce the trend of latest technology by inviting lecturers from various fields, and hold workshop participants and instructors can exchange opinions. Also, visited the research organizations and companies inside and outside the prefecture, it continues to provide a forum for study.

Business development and product development from Miyagi

we are recruiting new product development from Miyagi once a year. Organizing the exhibition, review Board and the presentation of the award-winning, it has made support for the expansion project results by business opportunity and providing a field of creation, in addition to the introduction for the national products and technologies of Miyagi development.

Cross-industrial association

Business content of members is very widely as mining, construction, manufacturing, electricity, gas and water supply, transport and telecommunications, wholesale and retail trade, finance and insurance, information and communications industry, service industry at large subject, also it becomes the classification of more than 50 at medium subjects. It also promote inter-regional exchanges, we are back up powerfully aggressive approach in order to build partnerships with companies operating in the Northeast.

Strengthening the management base and awareness of management and management's

What is sought to management and the administrator is the sensitivity to the corresponding ad hoc in addition to rebuilding the strategy of a long-term view from a high place. To grasp the changes of the times, we have to help to strengthen the management foundation and enlightenment of consciousness by implementing seminars and symposiums for the purpose of exercise of strong corporate sentiment and respond appropriately.

Recommendations to the government and Cooperation with related organizations

The cooperation in facility planning of national and prefectural governments for Industry Development, and if necessary, to hold a government-industry meeting with the government officials, it has to reflect the voice of the Association for the administration. Also it seeks to promote regional and training of human resources in conjunction, for example, to carry out various events with related organizations.

Provision of information

We issue on a regular basis, "Miyagi Industry Association report" in order to deepen ties with members. The post event information and guide member companies, we provide the latest information on their website. Also issued a membership list once a year, and we use as a resource of public relations of mutual members. In addition, the report in a timely manner each committee activity, we continue calling for active and Challenge of every members.

3. Results and Discussion

"Miyagi Association human resources network services"

"Miyagi Industry Association Human Resources Network Service" was started as human resources support services for members, in order to survive the turbulent times to strengthen the cooperation between companies of the members of the Miyagi Industry Association, from April 2010.

In this service, it is the purpose that adopt effective excellent human resources and increasing the corporate power to win the competition to the problem and worries about human resources member companies face, by streamlining and centralizing the contact. This network will be able to centralize between companies of personnel relations, than function as a platform of Miyagi Industry Association member's company.

Overview of services

(1) Recruitment Services (mid-career)
(2) re-employment support services
(3) College Recruiting Service

As the three pillars of these, through it supports a full range of recruitment and the introduction of a wide range of human resources, you will be able to tie in to the adoption of excellent regular employees who companies seek.

HUREX Corporation is responsible for secretariat. In cooperation with human resources affiliated companies (As Toyo Work Co., Ltd., Trust Tech Co., Ltd., job station Co., Ltd., etc.) ,we are going to quickly provide information on human resources to member companies.

In the *"Miyagi Association human resources network services"*, by building a system that member companies of all to enjoy this service, we hope that it will lead to acquire new members of Miyagi Industry Association.

Outgoing business of "Miyagi SugureMONO"

We have decided to start the outgoing business "Miyagi Sugure MONO" as a new initiative to identify and develop and promotion to become the industry united the industrial products with excellent. We accredit to "Miyagi Sugure MONO" products that meet strict criteria of 10 categories quality, technology, safety and security, and the environment from the industrial superior products produced in the prefecture. Then the outgoing continuously towards the inside and outside of the prefecture from Miyagi, we hereby declare that they would create a "Miyagi Sugure MONO" towards the customer value creation.

みやぎ
優れMONO

1. We will send out " Sugure MONO" that is superior processes and systems also customer quality is ensured.
1. We will send out "Sugure MONO" that has innovation and novelty also technology that evaluates to a customer is actualized.
1. We will send out " Sugure MONO" that is evaluated commitment to safety and environmental also plays its responsibilities to protect the global environment.

the exhibition, review Board and the presentation of the award-winning

4. Concluding remarks

Currently, there under the harsh conditions, Miyagi Association has come to a turning point. Be realized Industry Association of true independent is urgent state of affairs. Increase in before, the members participating in the activities of the Association actively, we believe that it will change the Industry Association of attractive as "Members, by members, for members".

Now is the time to return to the origin of the Miyagi Industry Association establishment. We are fully aware of the spirit that has claimed the articles of incorporation, to discuss a lot with everybody, the pooled the wisdom, and we would like to work on issues.

Create The Rich And Varied Future Society

Akihiko Oyama
Miyagi Kasei Co., Ltd.
Kitazawa-Hankinzawa15-4, Ichihasama, Kurihara, Miyagi, Japan
E-mail: info@miyagi-kasei.co.jp

ABSTRACT

Miyagi Kasei Co., Ltd. offer Fiber Reinforced Plastics (FRP) products since the establishment. Today, we extend our business to molding, manufacturing, and constructing FRP. We also lease and sell temporary materials. To develop the new technique of noninflammable transparency, Advanced Industrial Science and Technology, and our GFRP try to consist and improve their non-inflammability and transparency by our new combination materials. We aim to be a corporation that can contribute to our society by developing and creating the products.

1. Introduction

Miyagi Kasei Co., Ltd. was established in April, 1987. We offer Fiber Reinforced Plastics (FRP) products since the establishment. Today, we extend our business to molding, manufacturing, and constructing FRP. We also lease and sell temporary materials.

Since FRP is utilized in various areas in the field, we feel that we take great responsibility for the society although we are small and medium-sized businesses. The speed of change in the world becomes more and more quickly in the twenty-first century.

Our Main Facility

Our Mission

・Providing service and valuable products to contribute to the society

・Improving the ability of our staffs by concerning about providing better quality of products and service

2. Method of Molding

There are four kinds of molding FRP.

1. Hand Lay Up Molding: pasting glass and resining into mold by hand

Fig. 1 Hand Lay Up Molding

2. Spray-up Molding: spraying glass and resining by spray molding machine

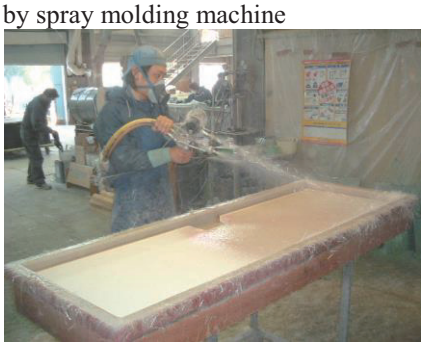

Fig. 2 Spray-up Molding

3. Light RTM Molding: setting glass fiber into rough forming die, and putting resin in it.

Fig. 3 Light RTM Molding

4. Infusion Molding: Setting glass fiber and putting resin by vacuum drawing

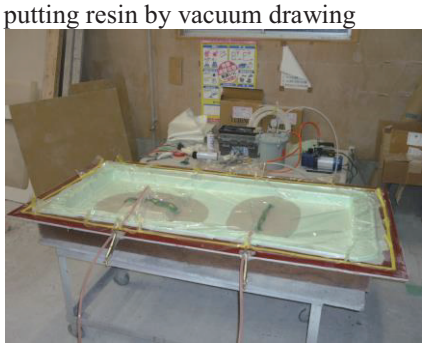

Fig. 4 Infusion Molding

3. Our Effort for New Technique

Miyagi Kasei Co., Ltd. develop the new technique of noninflammable transparency. Noninflammable transparency is utilized in extensive filed such as constructing field, aerospace field, vehicles field, and energy field. Comparing the glasses and plastics, the strength of noninflammable transparency are following:

- Light and irrefrangible
- Noninflammable

Advanced Industrial Science and Technology, and our GFRP try to consist and improve their non-inflammability and transparency by our new combination materials.

It is expected that there will be a lot of need in various field for noninflammable transparency.

Fig. 5 Lighting cover of the bullet train

4. FRP Product

Mitsuoka Mortor Viewt (Frontface, Bonnet, and Trunk)

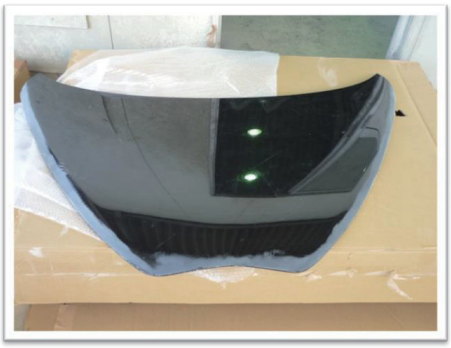

4. Concluding remarks

We consider what could be useful to our customers and society. Then, we aim to be a corporation that can contribute to our society by developing and creating the products.

Tenth International Conference on Flow Dynamics
November 25-27, 2013, Sendai, Miyagi, Japan

Using Electric Vehicle COMS Car-Sharing System

Hiroshi Harusawa
Toyota Tsusho Corporation
2-3-13, Konan, Minato-ku, Tokyo 108-8208 Japan
E-mail: hiroshi_harusawa@toyota-tsusho.com

ABSTRACT

Micro Electric Vehicle (EV) which is more compact and flexible than conventional vehicle, superior environmental performance, has come to draw a lot of attention since the Ministry of Land, Infrastructure, Transport and Tourism (MLIT) had been publicly seeking projects to promote the introduction of micro-sized mobility. Categories for micro-sized mobility are currently being discussed under the initiative of the MLIT in Japan and its regulation will be expected in place in a few years. Toyota Tsusho Corporation sees the big potential on Micro EV market among next-generation mobility products and develops Car Sharing System for EV that is able to estimate the remaining battery charge level and distance that can be traveled.

1. Introduction

Next-generation automobiles such as PHV, EV have been heralded as “eco-cars” which will make energy-efficiency and environmental protection a reality in the transportation industry. Consumers have doubts, however, over the short driving range and high prices compared with conventional automobiles. With the exception of consumers groups with a special interest in the environment, these eco-cars have yet to garner widespread support. The challenge remains to realize an environmentally consciousness mobile society.

How can we make EVs easier to use? To lower the barriers to EV adoption among consumers, we have begun researching car-sharing schemes in which people share the use of an EV. Feasibility studies have begun in four regions around Japan at condominiums where members would typically use shared vehicles. The studies feature the single-occupant micro EV “COMS” produced by Toyota Auto Body Co., Ltd

In Japan, one/ two-passenger vehicle which is more compact and flexible than conventional vehicle, superior environmental performance, and convenient regional transportation has started to draw many people’s attention. Many car manufacturers and venture companies in Japan have started to develop micro-sized short-distance transportation EVs in consideration of the vehicle categories for micro-sized mobility products that are currently being discussed under the initiative of MLIT in Japan. Toyota Tsusho Corporation sees the big potential on Micro EV market among next-generation mobility products and develops Car-Sharing System for EV.

2. Details of system

Large barriers to use EVs for car sharing is managing battery’s state-of-charge(SOC) and downtime during charging. To use EVs without having to worry about the EV driving range and remaining battery level, we have developed a car sharing system which can estimate the remaining battery charge and distance that can be traveled. We have launched a car sharing service using single-occupant Micro EV COMS which is currently only available Micro EV we can drive on public roads without having any special permission.

This newly-developed system is designed to estimate remaining battery level from the accumulated discharge and charge data while driving. The data will be reflected in the reservation system and when reserving one of the car sharing EVs, the system determines whether it is possible for users to reach the destination with the estimated remaining battery level at the time of travel. (Fig.1)

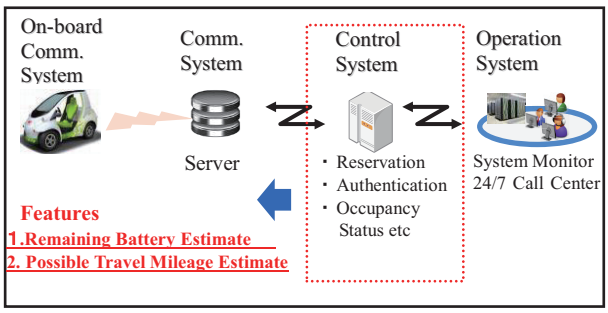

Fig.1 System outline

To explain in more details, we installed on-board data communication module (DCM) and GPS Antenna on the COMS and monitoring battery SOC. The data will be reflected to reservation system and possible travel area at the time of usage will be displayed on the map. Based on possible travel mileage data, users of an EV car sharing service will make a reservation and it makes car sharing service providers to be able to have maximum uses of COMS without having a lot of downtime. Also, this car sharing system only accepts to return cars when user connect COMS to power outlet at the station and that function enables COMS always being charged. (Fig. 2)

Fig. 2 On board sharing system outline

Actual procedure to rent COMS Car-Sharing is as below.

a).Reservation

[1]Access reservation web with given ID and password

[2]Select “Station” users want to use

[3]Select “Day” and “Time(15 minutes increments)” users want to use

[4]Choose available “Vehicle”

Eestimated remaining battery level at the time of rent and possible travel area will be displayed on the web. (Fig.3)

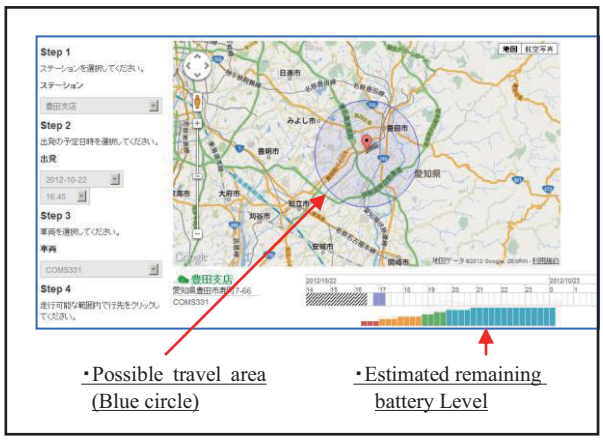

Fig.3 Battery level and estimated driving range on the reservation system

[5]Plot “Destination” users want to go

Maximum 5 stopover places can be set up

[6]System will calculate estimated arrival of time to the destination, travel mileage and show route to the destination.

*If destination is faraway considering remaining battery level, “Retry” message will be displayed.

**Calculation of necessary remaining battery level to the destination will also take into account of slope/grade information on map and drivers’ past driving characteristic.

[7]Select “Return Time”

[8]Completion

b).Car Rent/Return

[1]Tap members card or registered smart phone at the card reader on the car.

[2]Once authentication completes, rear trunk box will be opened electronically.

[3]Take out of key from key box in the rear box and disconnect charging cable

[4]Turn on motor of COMS

* Return procedure is in the reverse order to rent

3. Usage scene of Micro EV as a Car-Sharing

As many reports regarding Micro EV by MLIT indicate, Micro EV sharing can be used for various usages. One of the ideas is to use Micro EV as a personal transportation in the daily life such as going to shopping to the near glossary stores and to clinics. Micro EV sharing can provide convenient rides for users who do not own car in urban areas and cheaper fee compared with Taxi and it is safer than riding motorcycles. The other is to introduce this kind of Micro EV sharing for small lots logistics and small sized delivery.

Currently, we plan to target this electric car-sharing system and service for use in the areas of residents’ car-sharing at condominiums, community car-sharing, company car-sharing and car-sharing at tourist resorts. The system has been launched for practical test use at condominiums in Tokyo and the suburbs of Nagoya. (Fig.4)

Fig. 4 Micro EV car sharing station at condominium

4. Conclusion

The invention of great technologies is meaningless without their wide adoption by society. Some of the key challenges we now face with next-generation automobiles are adapting mobility to fit the unique needs of different communities, and envisioning new lifestyles in which next-generation automobiles can be used. Without solving these challenges, the expansion of next-generation automobiles will be limited. As an example, major car sharing services have generally shunned EVs because of the higher costs. In response, we are evaluating the lower-cost micro EV COMS in field tests to discover how EVs can be used in urban, suburban, tourist, and local community lifestyles. We’re confident that the creation of new business models through this kind of feasibility tests will be critical to the expansion of next-generation automobiles.

If you are interested in working together with us and/or using this EV Car-Sharing System, please contact us at hiroshi_harusawa@toyota-tsusho.com.

Inflection Line Matching Algorithm
-Advanced Defect Detection Technique for Painting on Mirror Surface by Image Processing-

Kumiko Yokojima
By three projects corporation
Chomeigaoka4-15-22,Izumi-Ku,Sendai,Miyagi,Japan
E-mail: sales@x3pro.co.jp

ABSTRACT

We established in March,1987 and the business for Embedded Systems, Measurement & test system development, Operational systems development, Image processing system development, Digital / Analog circuit design, Research & development. We are the member of NATIONAL INSTRUMENTS Alliance. One of the project development results is “Inflection line matching method” is an advanced algorithm to highlight features a more irregular part of the interval and the direction of the curve in the image.

1. Introduction

“Commercialization and development of image processing embedded software for enhancing visual for industrial robot” was an adoption projects for 2010 Strategic Technology Infrastructure Support Sophisticated Business. One of the project development results is “Inflection line matching method”. The method acquired the patent in January, 2013 as “surface inspection method and surface inspection device”. （Patented : No.5182833 ）

2. Distorted due to defects of “Inflection line matching method”

Imprinted slit on the test object and shoot images using organic EL slit lightning. The crowded reflects a slit in the inspection target and shoot the image using organic EL slit illumination the extraction of the defect by the image processing is possible in letting a crooked part rise by a defect with the inflection line matching algorithm.

The image processing by the method：example-1

Input Image

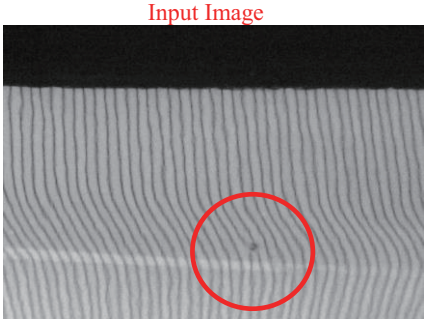

Processed Image

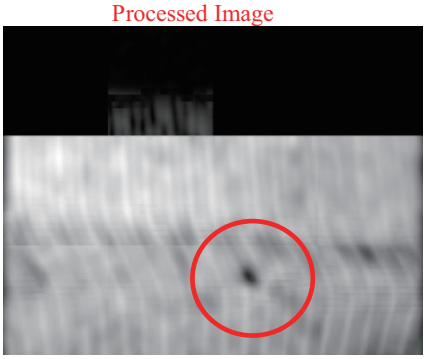

The image processing by the method：example-2

Sample work (Door mirror cover)

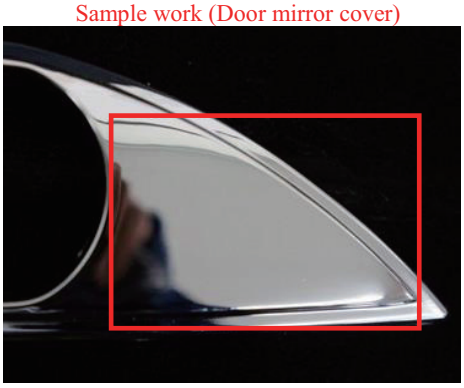

Images were taken using a slit illumination

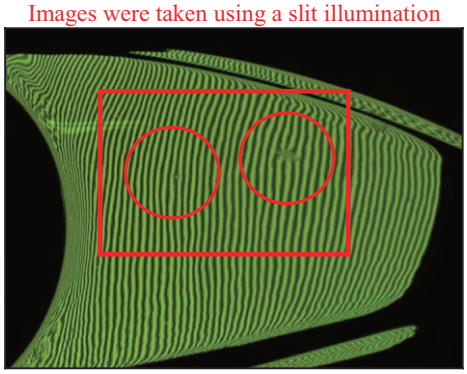

The processed image by the method

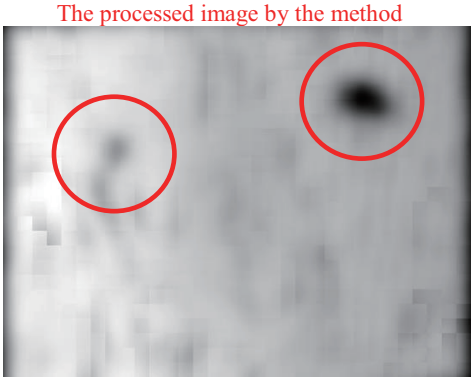

Rad frame: defect

Inspection object

object	Surface condition				
	Citron※1	Minute trace and dirt※2	Mirror surface	gloss	without gloss
paint (including metallic)	×	×	○	○	×
plating	–	×	○	–	–
metal processing	–	×	○	–	–

The shape of the test object and defect

Surface condition	Defect				The shape of the test object				
	cotton wound	dirt dust	gradual irregularities	sharp irregularities	plane	gentle curved surface	curved surface	corner	Complex curved surface
									
Orenge peel	×	×	×	×	×	×	×	×	×
minute trace and dirt	×	–	×	×	×	×	×	×	×
mirror surface	△	○	○	○	○	○	△	×	△
gloss	△	○	○	○	○	○	△	×	△
without gloss	×	×	×	×	×	×	×	×	×

※1 Among those relatively tight ((round) roughness of the coating surface) orange peel enough not to be considered until the defect.

※2 Light things tight polishing marks that arrive when you polish the surface, such as stripes scratches visible colors of the rainbow is diffracted What dirt to loss of surface gloss, with the entire surface inspection.

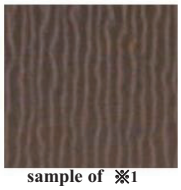

sample of ※1

Achieve automatic defect inspection!

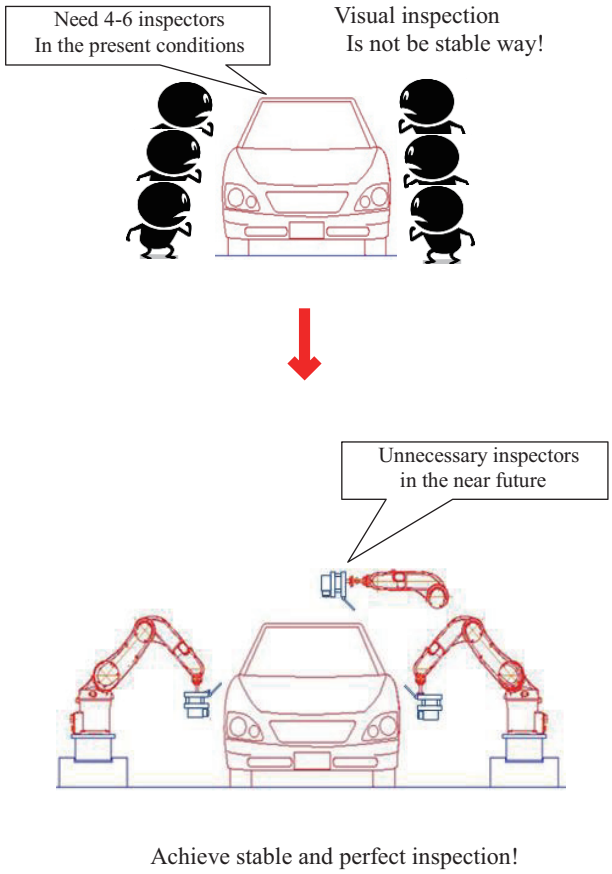

Achieve stable and perfect inspection!

3. Applications examples of “Inflection line matching method”

- Surface defect inspection of the exterior and interior automotive products
- Surface defect inspection of plating painted
- Surface defect inspection of metal processed goods
- Surface defect inspection of plastic products
- Surface defect inspection of resin processed products
- Defect inspection with respect to the surface that has the property of specular reflection to the light.

4. Conclusions

We will be achieving automatic defect inspection to aim of as follows;

- Achieve stable and perfect inspection.
- Prevent defect outflow.
- Save inspection coat.

We'll Provide "New Familiar Hybrid"

Ryuko Obara
My Car Plaza Eco Custom Division Corporation
4-23-1 Kuronuma Ishidoriyacho Hanamaki Iwate
E-mail: info@e-rhs.com.

ABSTRACT

We offer new familiar hybrid car.
The evolution to the "ultimate eco-car" by the RHYBRID of the motor hybrid car is synonymous with eco- friendly cars.
To use of fuel as the "LPG" can make Realistic Ecocustom, that means "Real HYBRID system "
RHYBRID, so called Bi-fuel LPG remodeling is a technique that can be practiced right now.
So it is like dream but active in the nationwide as the vehicle realistic already.

1. Introduction

The Company is developing a new and used car sales / vehicle inspection and various other maintenance / eco custom business in Iwate from 1979. Recently our company has been growing in the field of RHYBRID that is eco custom business.

The evolution to the "ultimate eco-car" by the RHYBRID of the motor hybrid car is synonymous with eco- friendly cars.

The exhibitors participating in RHYBRID Priusα in 2011 Tokyo Motor Show. It was a celebration of next-generation vehicles. Many visitors had to experience abroad to see.

2. Method

Prius series is the flagship model in our company, in order to respond to various needs, we'll continue to expand its corresponding model.

We don't think a technology that requires million people, but at present, it is in the process of evolution of automotive technology, we believe that technology that connects to the next generation.

Know-how and retrofit technology that we have is immediately transferable to bi-fuel of the LNG and CNG. Now, it is a next generation energy issues such as Payload and infrastructure, challenge of widespread use, but when the conditions are in place, it is a technology that can immediately respond.

'LPG' is less environmental burden compared to gasoline so it is ecology and clean fuel. Nano PM and NO× that cause acid rain are plummeted close to zero emissions. By using run as the main fuel LPG turned into RHYBRID, it is working as an environmentally friendly eco-car.

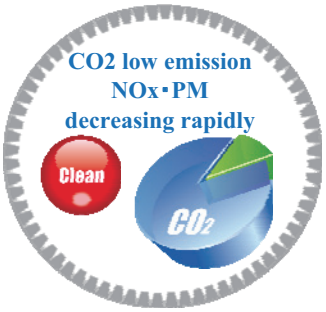

In Japan, the unit price of auto gas to be used for LP gas car, there is also a regional difference, but about 40% more per 1L has remained cheaper than gasoline. It will be more mileage, fuel costs can be reduced only difference worth of fuel.
RHYBRID car is very economic.

* Please check the area of each fuel the actual price.

RHYBRID specification car can leave the original gas tank, to add the LPG tank. That becomes possible to travel with the two fuels. Auto gas (LPG) has become the main fuel, gasoline will be sub fuel. Auto gas station for filling auto gas is present almost in city about 1700 places where taxi runs.

If LPG auto gas runs out, it is all right if gasoline remains. In automatic switching, It will be able to run as fuel gasoline. Distance you can run with the full tank of two fuels, it will be improve drastically approximately 1.5 times to twice normal car.

3. Results and Discussion

RHYBRID, so called Bi-fuel LPG remodeling is a technique that can be practiced right now.
The economic efficiency and excellent environmental performance, a lot of attention from taxi operators around the country, especially in Tokyo metropolitan area, there are more than 400 taxi vehicle active currently.

As a car running daily basis, there is a running truck record of more than 300,000 km after remodeling.
There is also a truck record of introduction as official vehicles of municipal and commercial vehicles.

Adoption in local government, is due to the strong focus on LPG in case of emergency in the earthquake earlier.

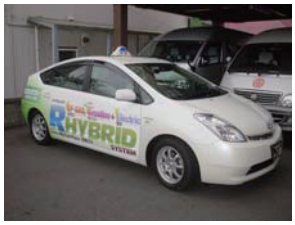

4. Concluding remarks

"Operation and without traveling all the same and ordinary cars, and this device many not be in accident"
"We do not put on the market absolutely until convincing technically"

Feelings that we have for RHYBRID specification care is these two points. Car is to break must be somewhere during using it. However, since it is a customize car, development has been put on the maximum important so that it may not say that it broke.
It is modest as those involved in the special car, but it is the feelings that can not be bent in any way.

Auto industry support through technology seeds

Kazuhiro Matsukura
AKITA Industrial Technology Center
Sanuki4-11, Arayamachi, Akita010-1623, Japan
E-mail: soudanshitu@rdc.pref.akita.jp

ABSTRACT

In this paper, it is described the technology of material development or material processing. One is cobalt Free Material Technology for Cemented Carbide Tool, and another is Electric Field Control Abrasive Technology. These techniques can be utilized for the production of tools or industrial parts. It is described examples of the prototype of cutlery Etc. using the Technologies, by collaborative research between AKITA Industries Technology Center and companies. These techniques are useful in producing a next-generation vehicle.

1. Introduction

Akita Prefectural Government aims to create jobs and increase the amount of product shipment by integrating the industry and industrial development of the region of the measures. Therefore, the government is developing measures the industry support for transport, to enhance the competitiveness of companies in the prefecture. As one of the measures, the region is expanded to enhance the competitiveness of companies in the prefecture by promoting industry support of the transport sector. And it is an organ of Akita prefecture, AKITA Industrial Technology Center has conducted businesses with technical assistance research and development, technical consultation, through technology transfer, human resource development etc..

In this paper, It is described studies which are developing commercialization that were carried out by the center and companies in the prefecture. In particular, it is shown examples of development for (1) Cobalt Free Material for Cemented Carbide Tool, and (2) Electric Field Control Abrasive Technology.

2. Method

2-1. Cobalt Free Material

Tungsten carbide (WC) which is a raw material of cemented carbide, we use it with the addition of silicon carbide (SiC). It is illustrated a manufacturing method in Fig.1.

2-2. Electric Field Control Abrasive

Figure 2 shows Principle of Electric Field Control Abrasive Technology. The technology is a method to control the movement of the polishing abrasive by the AC electric field. This method can make the smooth surface.

Varnish is a liquid, such as diamond powder dispersed in silicone oil. Figure 3 shows behavior of abrasive grain under AC high voltage 2kV.

3. Results and Discussion

3-1. Cobalt Free Material

This material has a high hardness or high fracture toughness feature. Further, since this material is not used cobalt, it is outside the scope of environmental regulations. Based on this feature, we can be applied to tools or parts. In addition, the tools using this material are environmental superior wear-resistant material, because of having cutting oil free, long life and high durability. It is shown in the following application examples.

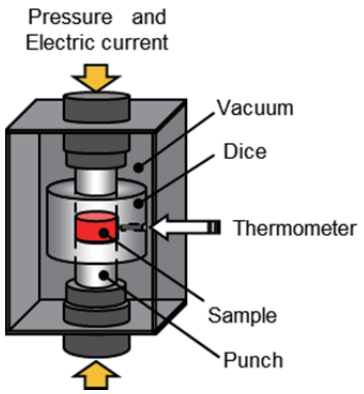

Fig. 1 Manufacturing method for cobalt free material

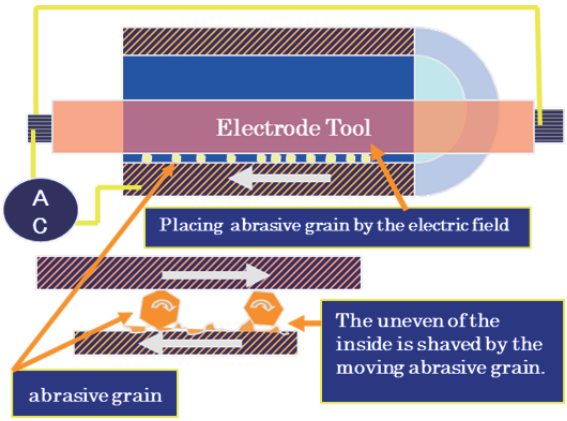

Fig. 2 Principle of electric field control abrasive

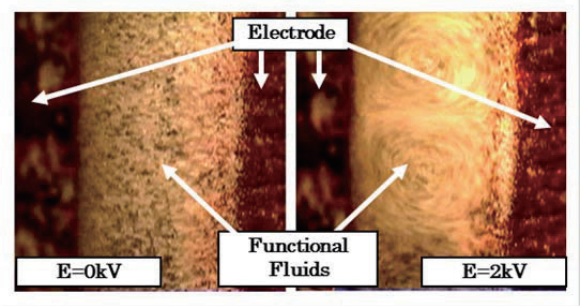

Fig. 3 Behavior of abrasive grain

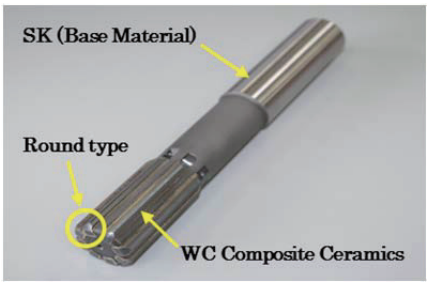

Fig. 4 Prototype for reamers

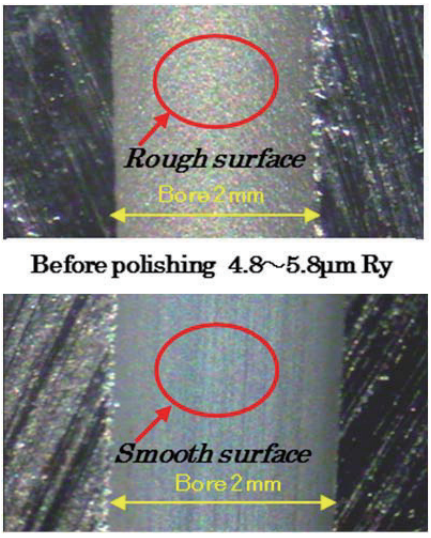

Fig. 5 Surface of small diameter seamless pipe

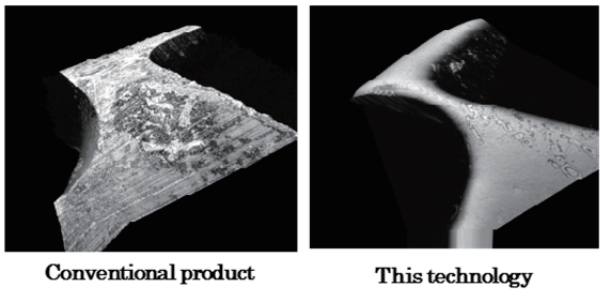

Fig. 6 Surface of ball end mill

Application 1: Reamers

Figure 4 shows the prototype example of reamers. Base material is steel metal material (SK), and the new WC as part of a blade made for brazing banishing reamers that based composite ceramics. The tool has some benefits, such as increase vanishing effect, Anti-chipping (Fine honing), and anti-wear (Tip : Round type).

3-2. Electric Field Control Abrasive

Application 2 : Small diameter seamless pipes

Figure 5 shows the prototype example of prototype for small diameter seamless pipes. The pipes are used as fuel supply of vehicles, and material is ST52NBK, outer 6mm, and bore 2mm. We found that the surface of the pipe is smooth by this technique. The benefits are that it is easy to control the supply of fuel and make improved fuel economy.

Application 3 : Ball end mills

Figure 6 shows the prototype example of prototype for ball end mills. We found that the surface of the tool becomes smooth by this technique. The tool has some benefits, such as doubled tool life versus conventional product, and high precision processing.

4. Concluding remarks

The technology for SiC is a good method that does not use a rare metal, in order to manufacture vehicles low cost. Use the Electric Field Control Abrasive Technology, we attempted to manufacture the pipe with high accuracy. As a result, We have confirmed the usefulness of the technologies.

These techniques enhance the productivity of the production of next-generation vehicles.

References

[1] http://www.rdc.pref.akita.jp/
[2] http://www.rdc.pref.akita.jp/rdc/01/seeds.pdf
[3] http://www.pref.akita.jp/gakujutu/tizai/seeds/seeds-ardc.pdf

” LNG-DDF” , Main Figure in the Shale Gas Revolution

Kazuhiko Kami
Hana Engineering Japan Co.,Ltd.
Haramachi3-1-43,Miyagino-Ku,Sendai983-0841,Japan
E-mail: hanaeng_japan@ybb.ne.jp

ABSTRACT

We provide next generation car. Restraining hazardous exhaust materials, CO2 decrease and fuel efficiency increase. Gas hybrid system, the most practical, becomes the leading role of in the shale gas revolution. We provide the most practical gas hybrid cars that convert petroleum fuel car into high environmentally car as the primacy of post-oil fuel in automobile world.

1. Introduction

Hana Engineering Japan Co.,Ltd. is the company provides gas hybrid car. Our theses are shale gas, DDF, and secondary fuel system.

Company profile

Company name	Hana Engineering Japan Co.,Ltd.
Paid in capital	10,000,000yen
Founded	October 2009
Established	May 2011
President	Kazuhiko Komi

2. Retreat from nuclear power and the shale gas revolution s

We aim to retreat from nuclear power and the shale gas revolution. The new hybrid system of motor and gas not to rely on gasoline protect the global environment, with a thermal power station makes retreat from nuclear possible, and the fuel battery car instead of electric cars.

Nowadays, if the motor hybrid based on gasoline car increase fuel efficiency 40% compared with gasoline car, development of gas hybrid by the shale gas revolution can increase fuel efficiency 30% furthermore.

Therefore, almost hazardous waste will be restrained, and many high environmentally cars exist in the world.

The lowering of price of automobile fuel by the shale gas revolution, automobile fuel efficiency will be able to be halved. So the spread can reduce hazardous wastes from cars.

3. The secondary fuel system not rely on gasoline oil

Though ”hybrid” means to have plural motor in one car, ”Bi-Fuel” means the system combusts dual fuel by switching alternately, we express all of those “hybrid” to understand by general public.

Bi-Fuel is hybrid of gasoline and gas, when warming-up operation it uses gasoline, a few minutes later it switches to gas automatically.

When the Great East Japan Earthquake, gas stations ware filled of crowd, Bi-Fuel car ware able to supply at vacant gas station. Fuel efficiency rise 30 to 35%, and CO2 are cut down above 20%, Nox, PM etc. are able to reduce 50 to 70%. It uses gas: LPG, CNG LNG, HHO. It can utilize almost gas.


Fig.1 Solenoid


Fig.2 LPG Tank valve


Fig.3 Gas filter


Fig.4 Vaporizer

Fig.5 Gas Indicator

Whole Japanese taxies transfer to gas hybrid car from Prius. For several years, Japanese taxi companies have replaced Toyota Prius with LPG auto gas car. And simultaneously, the number of taxi company convert Prius into gas hybrid boosted. Used Bi-Fuel system are occupied almost 100% by our company made.

4. Products and sales items

We deal in Gas hybrid system in general; LPG Bi-Fuel system, CNG Bi-Fuel system and LPG-CNG Bi-Fuel system.

Dealing gas : LPG,CNG,LNG,HHO, oxyhydrogen （OHMASA-GAS） biogas in general.

We make Limousine and adapted vehicles.

Fig.6 Limousine

Fig.7 Adapted vehicles

The ability test strength and stiffness of cars in general.

Operations authorized by Ministry of Land, Infrastructure and Transport and related ministries.

The gas hybrid car's the range per one fuel filling is 10 times as long as electric car. It can reduce CO2 20 to 22% compared with gasoline, reducing hazardous wastes 60 to 90% such as Co, HC, Nox, PM, Sox, fuel efficiency can increase 30 to 40%(compared with gasoline car).

5. Concluding remarks

We contribute to retreat from nuclear with making cars using clean energy liquefied natural gas (LNG).

If you would like to know more information, please contact us. Please send us an e-mail.

hanaeng_japan@ybb.ne.jp
http://www.hanaeng-japan.com

New Ultra Energy Efficient Magnetic Ribbon SENNTIX III

Shoichi Sato
NEC Tokin Corporation
Kohriyama6-7-1, Taihaku-ku, Sendai982-8510, Japan
E-mail: sh-sato@ut.jp.nec.com

ABSTRACT

NEC TOKIN Corporation has developed a new energy efficient magnetic ribbon named "SENNTIX III*" jointly with Professor. Akihiro Makino of the Institute for Materials Research, Tohoku University, based on Prof. Makino's research. This revolutionary new material has the potential to greatly improve the power consumption of motors used in electric cars, and mid-sized and larger transformers used in electric power grids.

1. Introduction

This newly developed magnetic ribbon SENNTIX III enables to minimize the loss generated in the magnetic core (iron loss), which is a cause of loss in devices with high energy consumption, such as motors and transformers. SENNTIX III has been composed with Ubiquitous elements only and its iron proportion exceeds 90%. This makes it an Earth-friendly material that can be supplied stably at low prices.

SENNTIX III is the nanocrystalline micro-structured material (see Fig.1,Fig.2) with extremely low loss characteristic in the range of the saturation magnetic flux density over 1.8T (Tesla) discovered by Prof. Akihiro Makino. NEC TOKIN has conducted joint research with Prof. Makino to commercialize this revolutionary new material.

Over the past few years, there has been rapid growth in development of alternative forms of energy to fossil fuels. While use of solar and wind power has advanced, electric power grids have started being converted into smart grids, and electric vehicles (EVs) equipped with high-capacity batteries have also reached the level where their widespread adoption is possible. Although these technological innovations are effective at reducing emissions of greenhouse gases, which are believed to be a cause of global warming, a major breakthrough is still needed strongly in the effective utilization of energy, or in other words, reducing the energy loss of devices that use electricity.

The global electric-power consumption is currently 19,771 TWh (results from 2007), of which 672 TWh (3.4% of the total power consumption) is wasted as heat energy caused by iron loss** when motors and transformers consume power. Minimizing this loss will make that amount of power consumption unnecessary, which would significantly reduce carbon emissions.

2. Application

Until now, the magnetic-core materials used in large current transformers and motors have required high saturation magnetic flux density and low iron loss, but until now, there had been no material with both of these qualities. For this reason, magnetic silicon steel ribbons would be used if saturation magnetic flux density was prioritized (smaller size), and iron-based amorphous ribbons would be used if low iron loss was prioritized.

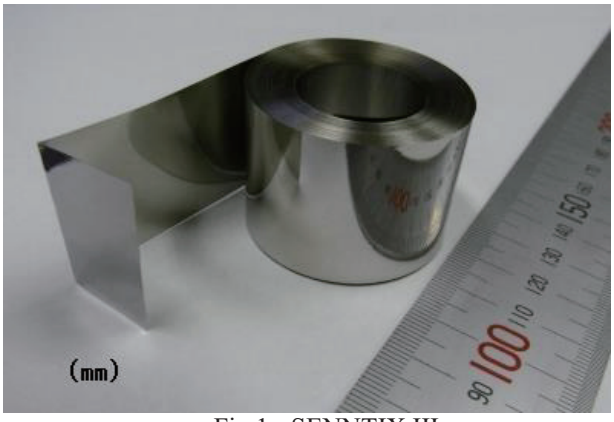

Fig.1 - SENNTIX III
The low-loss nanocrystalline material with high saturation magnetic flux density

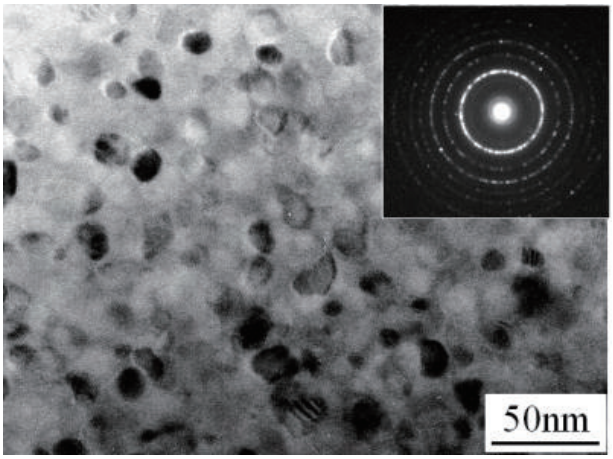

Fig.2 Transmission Electron Microscope (TEM) Image of SENNTIX III, and Electron Diffraction Pattern

SENNTIX III is a revolutionary new magnetic-core material that achieves what no material has been able to do before: deliver both high magnetic flux density and low iron loss. SENNTIX III exhibits significantly lower

loss characteristics than conventional materials such as magnetic steel ribbons and iron-based amorphous ribbons (less than half that of magnetic silicon steel ribbons), while also improving saturation magnetic flux density (a weakness of iron-based amorphous ribbons) by 20%, and achieving high magnetic flux density (as high as that of magnetic silicon steel ribbons) (see Fig.3). This enables electric-power transformers and motors to be made much more energy efficient and smaller.

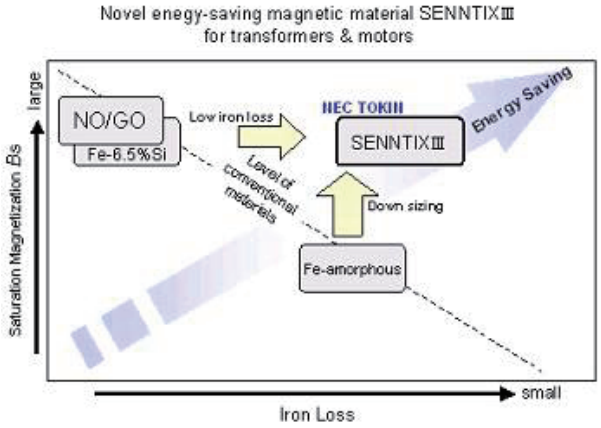

Fig.3 Role of SENNTIX III

Currently, 97% of the cores of transformers and motors are taken up by magnetic steel ribbons, and the rest by iron-based amorphous ribbons. When SENNTIX III is used in the cores of the large transformers used on power-transmission grids, and the cores of motors with high power consumption, the amount of iron loss in the core is reduced greatly. It is estimated that this will save 297ML of petroleum in the world by the year 2020, and 2,829ML by the year 2030, which results in the large reduction of CO2. ***

NEC TOKIN is supplying samples to reactor and coil manufacturers, and will expand the target markets for SENNTIX III. At the same time, it will build a production system, and begin mass production and sales within a few years. The company plans to supply the new material globally. Although initial production will start in Japan, SENNTIX III will be supplied to manufacturers of heavy electric machinery both in Japan and internationally.

Although the markets for both medium and large-sized transformers and motors are considered to be mature, they are expected to grow by about 1 to 5% per year, through improvements in energy efficiency and moves to the use of non-fossil energy. NEC TOKIN will start by expanding its business in the Japanese and international transformer markets, and in the future will enter the motor market as well.

* "SENNTIX III" is the name of a nanocrystalline soft magnetic material with low loss and high saturation magnetic flux density. It is being developed and commercialized jointly by Prof. Makino and NEC TOKIN, based on a revolutionary discovery by Prof. Makino at Tohoku University.

** "Iron loss" is the loss consumed by electromagnetic resistance in magnetic cores when current flows through transformers and motors. Because it is converted into heat, it is a source of electrical loss and heat generation.

*** Calculations compare iron loss in transformers, and iron loss in motors when the operating rate is 50%, to materials currently in use (grain-oriented magnetic steel (GO) for transformers, and iron based amorphous, non-oriented magnetic steel (NO) for motors). This does not take into account the reduction in copper loss that can be expected from a substitute for iron-based amorphous material, and in actual use a larger economic benefit than this can be expected.

Towards a Leading Manufacturer of Next Generation

Nozomi Makita
Ricoh Industry Company, Ltd.
Shinmyodoh3-1, nakanomyo,Shibatamachi, Shibata-Gun, Miyagi989-1695, Japan
E-mail: nozomi_makita@industry.ricoh.co.jp

ABSTRACT

Ricoh Industry Company, Ltd was established as a production company that shoulders Ricoh Group. We aim to create and provide a new value of a product to our customers. We offer printing machines and copiers from the main body and the parts of the products. We perform the concurrent action in close cooperation with design engineers routinely. Therefore, we achieve a quick mass production shift, the achievement of QCDSE, and production capacity maximization. As a production company, we will provide a new value to our clients with our polished technology.

1. Introduction

In April 2013, Ricoh Industry Company, Ltd was established as a production company. Three affiliated domestic companies, Tohoku Ricoh, Ricoh Printing Systems and Ricoh Uni-techno, and a part of production function were integrated into Ricoh Industry Company, Ltd. We create a change by gathering of imagination. We will continue to provide a new value to our customers in the future.

We aim to be an advanced manufacturing company that has technical development for next generation. We also endeavor to be a core company for enforcing the manufacturing power of the Ricoh Group.

< Production items>

- Printing machine
- Copier
- OPC
- Mechanism components sector
- Motor field
- Key parts

2. Method

We offer printing machines and copiers from the main body and the parts of the products. Functions necessary for crafting are gathered in the northeastern branch. We perform the concurrent action in close cooperation with design engineers routinely.

3. Results and Discussion

We achieve a quick mass production shift, the achievement of QCDSE, and production capacity maximization.

<Examples of developed products>

- Copier: Ricoh Pro 1357 (Fig.1)
  Ricoh MPC 8002 (Fig.2)
- Printing machine: Setelio DUO8
  (Degital stencil printing machine, function of printing both side)

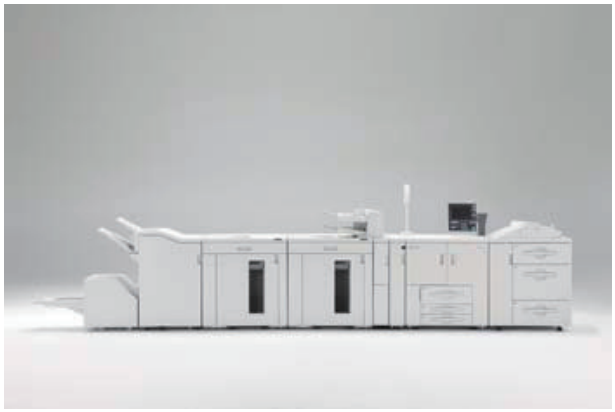

Fig. 1 Ricoh Pro 1357

Fig. 2 Ricoh MPC 8002

4. Concluding remarks

As a production company, Ricoh Industry Company, Ltd will provide a new value to our clients with our polished technology (facility development, production technique, method, research and development, component technology development). (Fig. 3)

Fig. 3

Tenth International Conference on Flow Dynamics
November 25-27, 2013, Sendai, Miyagi, Japan

From Planning, Designing To Manufacturing, Valuation, Servicing Of Electronic Devices

Shinichiro Sato
K Technology Corporation
325 Ganbara, Kami-machi, Kami-gun, Miyagi,
981-4263 Japan
URL:http://www.k-technology.co.jp/
E-mail:info@k-technology.co.jp

ABSTRACT

At K Technology Corporation (K Tech), we understand that not everything can be accomplished through standards alone. For the ultimate customer satisfaction and as part of our operational motto, we ensure that complete support is provided from the pre-production design stage through to the production and post-production stages. We offer each and every customer with a completely tailored service that includes the best possible solution with minimal total cost.

1. Introduction

The K Tech business concept - DMS (Development & Design, Manufacturing, Service & Solution) - is also considered the ultimate keyword in providing additional value to customers.

K Tech aims to provide the best solution through investigating customer circumstances from multiple perspectives. Our scope of activities exceeds that of conventional electronics manufacturing services (EMS).

2. DMS

Having an integrated electronics manufacturing value-chain in house, creating robust designs suitable for Mass Production is our advantage.

- Our design service includes not only mass production, but also design phase services such as product planning and prototype build.
- Our production service is beyond typical EMS. It is backed by highly advanced reliability evaluations and production technologies.
- Our value-adding solution services assure customers of reduced parts procurement costs, product commercialization, and marketing of new ventures over and beyond the usual support services.
- Our engineering expertise enable us to offer independent development of product.

These additional services like above are only possible through the use of DMS.

- Our design services cover all aspects of the design including circuitry, software, circuit boards, and mechanical design.
- We provide solutions for parts selection, surface mounting and product prototyping as well as the ones for all aspects of the production process including development of the production process, reliability evaluation, quotation and procurement of parts.
- Our strength lies in the fact that we provide VE/VA product cost improvements and make technical proposals based on our own product technology, as well as manufacturing of products meeting customer specifications.

■High Density & Reliability Design Flow Chart

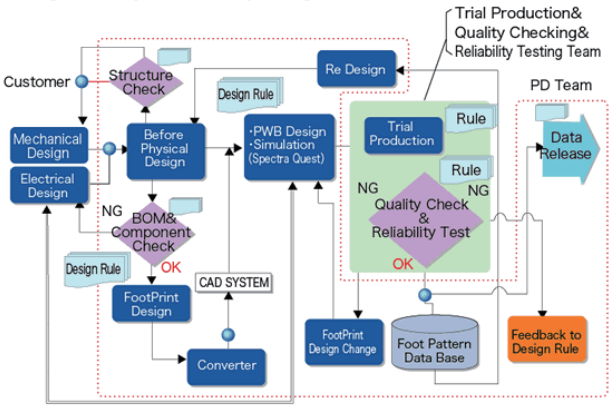

Backed with advanced production technologies and reliability evaluation, our manufacturing section satisfies every sort of customer requirement, from surface mounting to cell production of a high mix / low volume production.

Our technical support includes tester development and on-site production startup support at a customer's factory. And our surface mounting technology has been highly esteemed.

A bonus of using K Tech is that products are manufactured using an environmentally friendly approach, such as the use of lead-free solder and halogen-free material.

As one of the pioneers in the industry who introduced cell production systems, we attained stable product supply, regardless of production quantity and product mix, accommodating highly fluctuating demand.

We provide a range of solutions like below to solve issues that customers may have in design and manufacturing:

- A full range of services related to customer's products, including repairs, reliability evaluation, failure analysis and logistical control.
- New product introduction support including commercialization, marketing, product planning and cost reduction as value-adding service.
- Total production process support such as process control, quality management, production start-up and more that exceed the ones offered by EMS.
- Environmentally friendly product design to avoid the use of hazardous materials.

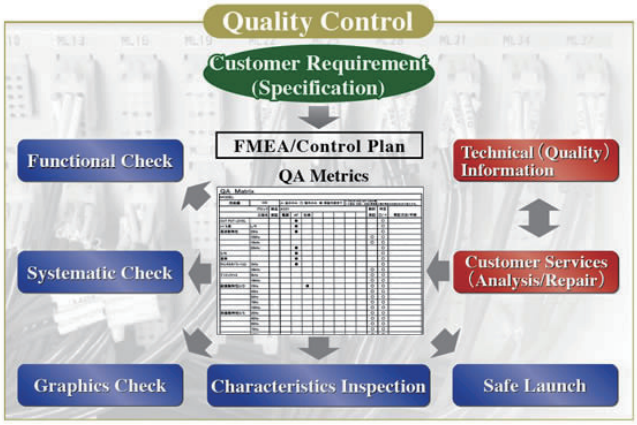

3. Technology

K Tech has produced various products for customers in the past, including audio products, automobile-related products, general information systems, car navigation systems, gaming devices, and digital electronics for consumer market, and printers/plotters, networking devices, and computer motherboards for business market. Items have expanded to include LCD display circuit boards, cellular phone circuit boards, LCD modules, tuner units, signal processors, and other modules and essential units required across various industries. The immense range of K Tech's products is the proof of the flexible and advanced technol1ogies. Our motto, Only One Technology Is What Keeps Us Here, spurs the devotion driving the constant technology development.

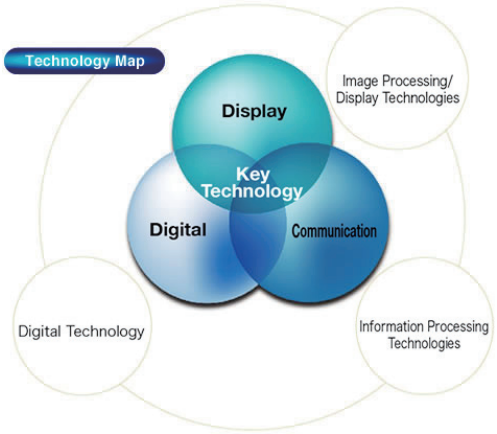

4. Solution

We firmly believe that our range of services based on the DMS concept can provide solutions to any issue that customer may have. “Speed, Challenge, and Creativity” aptly expressed in our action agenda, bring you perfect customer service, while also providing solutions to all of our customers.

Engineer Reservation and Offer of a New Technology Development Project

Masaki Mizuno
Altech Corporation
North Japan operation division Sendai office
Altech Sendai Bill Nagamachi 6th floor, Nagamachi3-7-13, Taihaku-Ku, Sendai982-0011, Japan
E-mail: sendai.tw@alpsgiken.co.jp

ABSTRACT

We are Altech Engineers that provides your company with professional outsourced staff to accomplish your specified technical tasks. Manufacturing companies have now become more motivated to pursue additional business efficiency. They are finding it necessary to limit their own staff resources to their core technology without diminishing their business results. Altech Corporation provides such manufacturing companies with highly trained engineers available for planned or contingent assignments.

1. Introduction

We are Altech Engineers that provides your company with professional outsourced staff to accomplish your specified technical tasks.

Manufacturing companies have now become more motivated to pursue additional business efficiency. They are finding it necessary to limit their own staff resources to their core technology without diminishing their business results. One of their critical success factor is the ability to meet the contemporary needs or wants of their customers at any time. Altech Corporation provides such manufacturing companies with highly trained engineers available for planned or contingent assignments.

Since 1968, Altech Corporation has been expanding in this business. 45 years'or more experience has grown the number of customers of their advanced technology to more than 700 companies. Altech's headquarters, located in Yokohama, directs 19 area business units in Japan and 2 overseas offices with approximately 2,600 total employees. Altech Corp. and 5 affiliate companies constitutes Altech Group. Our company has been listed on the 1st section of the Tokyo Stock Exchange as of December 2004. We promise to continuously support our customers in creating a variety of technical outcomes using the most advanced and diversified methodologies.

2. How Altech can provide ENGINEERS

We Altech provide various engineers to customers (figure 1). All customers can select how to utilize engineers dispatched from our company.

We have the types of utilizing engineers assorted by you subject and period of worker dispatching. For example, spot type that dispatched as a technical expert assignment, team type that dispatched as a working team staff, package type that dispatched as a taskforce group initiative, project type that dispatched as a project assignment contract, and full-time type that dispatched as a full-time engineer assignment.

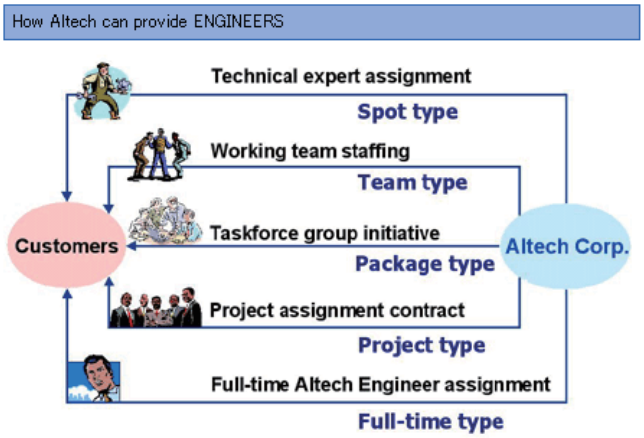

Fig.1

3. What area Altech has a role in-

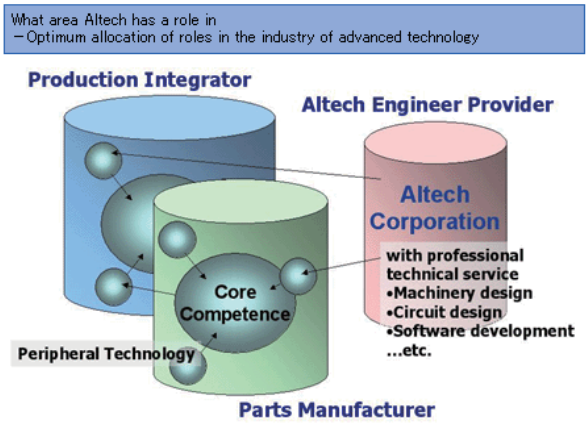

Fig.2

4. Why Altech services are needed

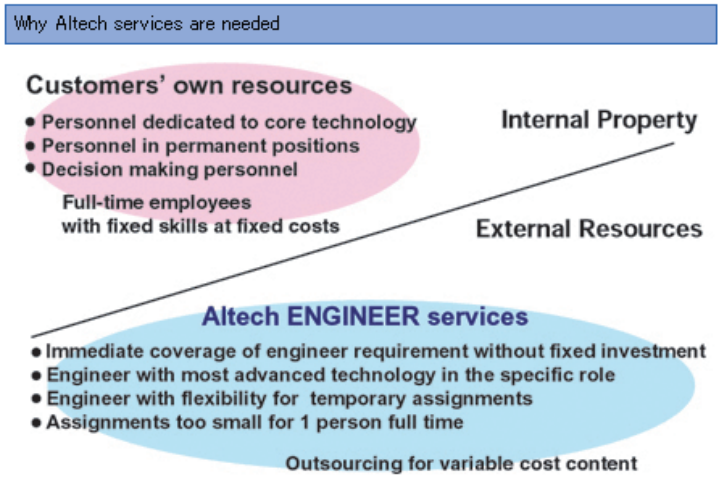

Fig.3

5. How Altech Engineers improve client efficiency

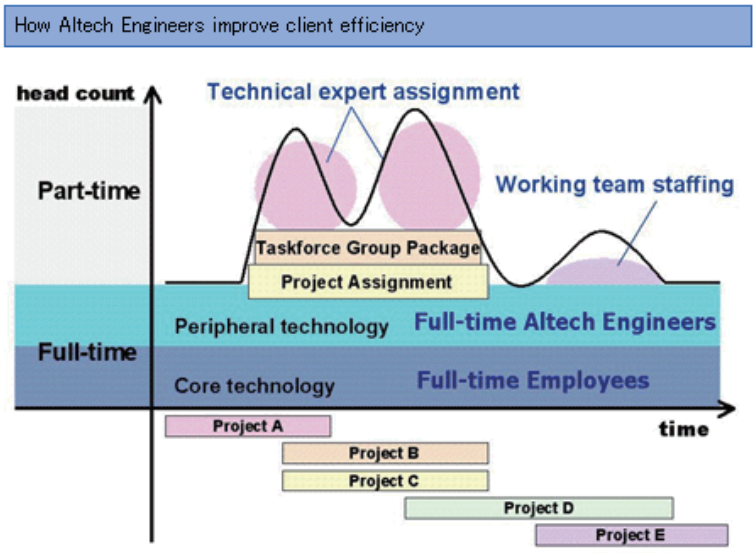

Fig.4

The Goal of "Technology-Oriented Company," We Aim to Meet Precise and Quick to Your Needs a "Manufacturing".

Michio Nakagawa
MG corporation
6-1-8 Shirakashidai Rifu-chou Miyagi-gun Miyagi Japan 981-0134
E-mail:j_watanabe@mg-japan.co.jp
URL: http://www.mg-japan.co.jp/

ABSTRACT

We offer resin and magnetized plastic molding products.
Based on our advanced developing capability, our molding technology led to a number of technologies and products: insert multiplex molding, two-color injection molding, plastic magnets, light-guide plates, digital cameras, cellular telephone chassis, automotive parts, printer parts, writing materials, etc.

1. Introduction

Our company have mainly grown in the field of engineering plastics with development of electronic industry based in forest city Sendai since our company was established 1970, advance to North America and China.

We contribute to the society through our personnel, growth, and creation. We will improve the standard of human life and bring us the joy of getting prospered together. We shall contribute to the company through our personnel, and by growing and creating. We shall improve the lives of everyone and create happiness that fosters affluent growth.

"Technology-Driven Company"what we need consists of "Technology"," Search" and "Customer".

Technology : All the employees regard a technique as important.

Search : Continuing searching for the always most suitable technique.

Customer : We offer an appropriate technique. Become the company pleased with by a visitor.

We have acquired the international standard ISO 90001 for our quality management system.

MG Group Worldwide Network; MG (Main building: Miyagi), MG International (USA),MK Engineering(Hong Kong).

2. Engineering plastic modeling

(1)

Filter device Multiple insert molding

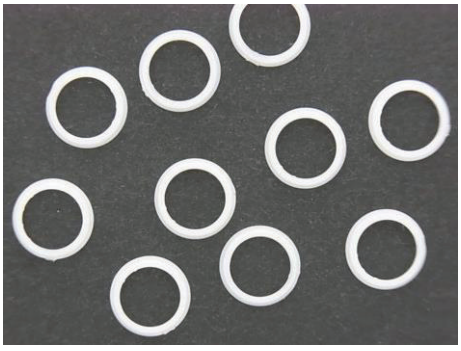

(Assembly process omission adhesion improvement ）

Battery parts
Thin-wall molding and ultra-high cycle molding

Automotive panel unit

From the mold production, integrated production to molding and assembly

Decorative processing technology, such as laser processing

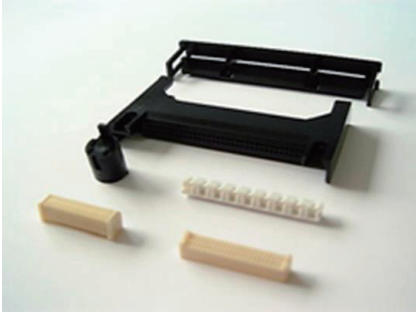

Various connector

3. Forming & plastic magnetized

We offer magnetized plastic parts using double color injection technic with integral molding technologies, including the shaft parts.

We also offer the magnet design and design technology magnetized by magnetic field analysis.

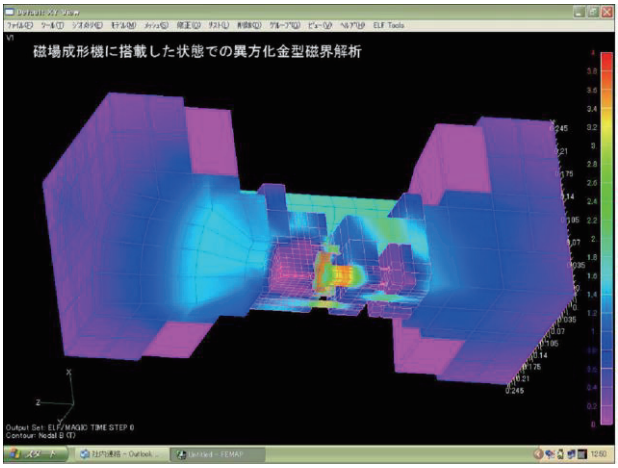

Plastic magnet various

4. Product Development

We perform various research and development as well as processing of plastic.

Solar dimming street light signboard

The power generation by solar, signs will direct the emission of dimming program when it is night. It can be chosen dimming pattern that matches the installation scene, and increase the catch of the eye to the sign. It turns on even at the time of a blackout, and the charge of the cell-phone is a signboard with the publicity possible, too.

5. Concluding remarks

It aims to develop products that make use of advanced injection molding technology, responsible for the rich life of the future.

Furthermore, we have environmental certifications. As a worldwide enterprise, we, MG Co., Ltd, shall continue to work toward preserving the environment for our future development as being placed in the plastics industry.

Analysis/Evaluation, Investigation, And Analysis Technology For Next-generation Automobiles

Tetsuya Mega, Takahiro Inoue , Fumiko Ikebe
JFE Techno-Research Corporation
3rd Floor, Higashi-Nibancho Square-Building,
4-1-25, Ichibancho, Aoba-Ku, Sendai-City, Miyagi-Pref., 980-0811, Japan
E-mail: mega@jfe-tec.co.jp

ABSTRACT

JFE Techno-Research Corporation provides the optimum solutions to problems related to automobile manufacturing in all stages, including research, development, design, production, and inspection. This presentation introduces the following analysis and evaluation technologies:
1. Evaluation of next-generation battery materials, 2. Analysis of nano-region fine structure,
3. Characterization of material properties, 4. Trace and environmental analysis techniques, 5. Evaluation of surface-treated materials,
6. Evaluation of structural performance and dismantled investigation, and 7. Non-destructive testing and numerical analysis.

1. Introduction

JFE Techno-Research Corporation aims to be the client's best partner in solving technical problems related to "monodzukuri" (Japanese–style manufacturing). Our technical staff and experts possess a wealth of experience and are ready to assist clients in solving technical problems in all aspects of manufacturing, such as stabilization of product quality, added functions, and reduction of production costs.

In recent years, stricter requirements have been placed on next-generation automobiles in order to achieve passenger safety, weight reduction for improved fuel economy with the aim of reducing CO_2 emission as a cause of global warming, and zero emissions. In response to these requirements, automakers are increasingly applying new materials such as ultra-high tensile strength steel, power devices, C-FRP, and lithium ion secondary batteries.

In order to solve these technical problems, we provide high reliability analysis and evaluation techniques using state-of-the-art analysis and testing equipment in a wide range of fields from the nano-region to large-scale structures. This presentation introduces some key analysis and evaluation technologies supporting manufacturing of next-generation automobiles.

2. Methods and Results

2.1. Evaluation of next-generation battery materials

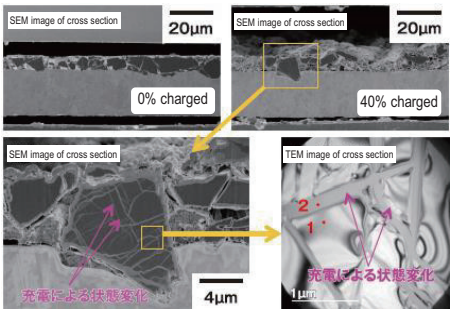

Fig. 1 Cross-sectional views of battery materials

The JFE Techno-Research "Battery Lab" provides full support for R&D and quality control of lithium ion batteries and next-generation batteries utilizing a wide variety of know-how related to material analysis. The Battery Lab provides lithium ion cell prototyping service (coin-type cell and laminate-type cell), charge and discharge performance evaluation, and battery material analyses such as cross-sectional SEM and/or TEM observation (Fig. 1) without exposure to air. Our staff works jointly with customers in investigations of dismantled batteries and deterioration/defect analysis. The Battery Lab also provides consulting services for issues related to battery cases and frames such as strength, corrosion resistance, etc.

2.2. Analysis of nano-region fine structure

We support the development of advanced materials such as power devices, thermoelectric element modules, and catalysts by visualization of their microstructures at the atomic level (Fig. 2). In atomic level observation, it is necessary to use FIB sample processing with a cryo-system in order to obtain excellent images. Rare earth magnets such as Nd-Fe-B compounds are used in auto motor applications. It is possible to visualize the distribution of Dy at grain boundaries by high resolution EBSD analysis and overlapping the grain map on mapping by FE-EPMA (Fig. 3).

Fig. 2 Atomic resolved CS-STEM

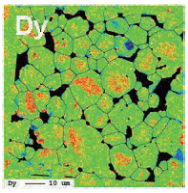

Fig. 3 FE-EPMA grain map and Dy map

2.3. Characterization of material properties

We evaluate material behavior at high strain rates, as well as strength at temperatures from -196°C to 400°C (Fig. 4), fatigue, fracture characteristics, and creep. Other services include corrosion research, anti-corrosion

technology, and magnetic characterization. We can also provide laser and CO_2 welding technologies for dissimilar material joints and evaluations of weldability and joint quality (Fig. 5).

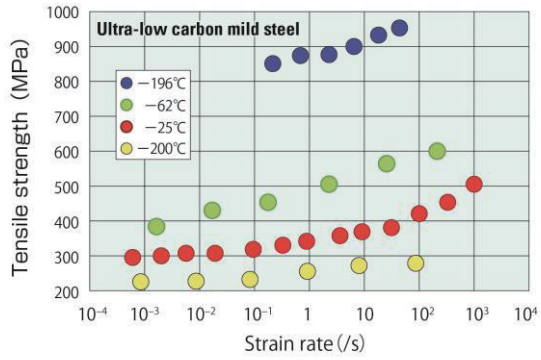

Fig. 4 Effect of strain rate and testing temperature on tensile strength

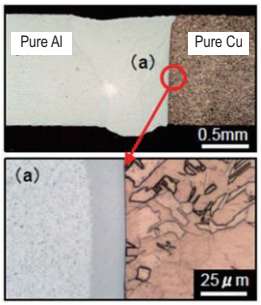

Fig. 5 Cross-sectional observation of Al-Cu dissimilar material joint using laser welding [Joint strength: 80 MPa]

2.4. Trace and environmental analysis techniques

Our analysis capabilities include trace elements in solids and liquids, for example, trace contents of halogen and sulfur in steel. We also provide analysis of environmental hazardous substances under RoHS, REACH, VOC, etc.

2.5. Evaluation of surface-treated materials

We provide evaluations of various characteristics of coated and surface-treated materials, for example, Gravel meter testing, plating film investigation, and measurement of adhesion, thickness, surface roughness, and hardness. (Fig. 6) We also support corrosion resistance evaluation using accelerated corrosion tests such as the gas corrosion test and salt spray test.

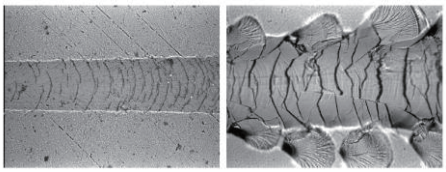

Fig. 6 Adhesion evaluation of film by nano-scratch test

2.6. Evaluation of structural performance and dismantled investigation

We provide investigation services for large-scale automobile structures as-is. Collision performance tests include roof crush test, side impact loading test and crashworthiness test. Falling weight impact test using multi-axial load testing equipment and large-scale (10MN) testing equipment for structures (Fig. 7) is available. Dismantled investigation of automobiles is also possible.

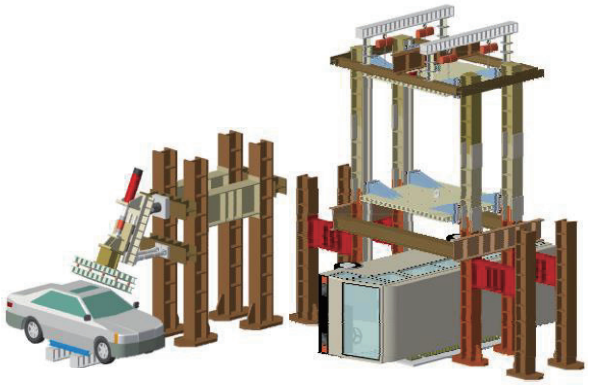

Fig. 7 Roof crush test and large-scale collision test

2.7. Non-destructive testing/numerical analysis.

We provide thermal analysis of magnetic materials and stress distribution measurements of auto parts using high performance infrared camera techniques (Fig. 8), and surface and internal defect detection, such as thin films with different thickness distributions, using the imaging spectrometer and dry ultrasonic spectrometer. These data are combined with numerical simulation analysis for verification between experimental results and numerical analysis (Fig. 9).

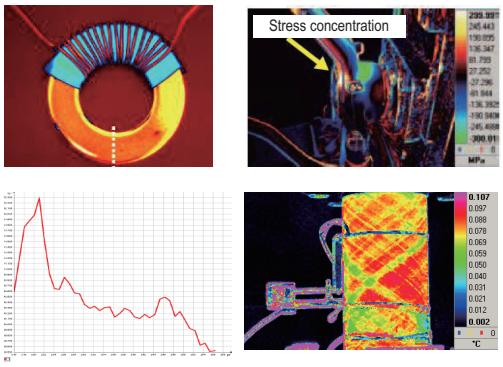

Fig. 8 Results of stress distribution measurement with high performance infrared camera and heat analysis

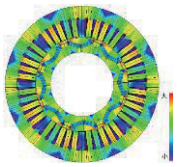

Fig. 9 Result of numerical analysis (magnetic induction) of motor for electric vehicle

3. Concluding remarks

As the "client's best partner," JFE Techno-Research Corporation provides the optimum solutions for manufacturing next-generation automobiles by visualization of the essential nature of the problem in order to develop more accurate and timely solutions and propose solutions from the user's standpoint.

Tenth International Conference on Flow Dynamics
November 25-27, 2013, Sendai, Miyagi, Japan

Efforts To The Automotive Industry Promotion In Akita

Hitoshi　Miura
AKITA Prefecture Department of Industry and Labor
Sanno3-1-1, Akita-Shi, Akita010-8570, Japan
E-mail: induprom@pref.akita.lg.jp

ABSTRACT

Akita is known as an eminent agriculture prefecture, but also the integration of the electronic device industry has progressed in the manufacturing sector, we have set the automotive industry as a pillar of a new industry. We have established the Akita automotive industry promotion plan, it shows the direction of effort by the ALL AKITA.

1. Introduction

We are an organization that support the automotive industry in Akita.

Toyota Motor East Japan,Inc. was established in July 2012, efforts to raise factory fixture and auto parts have been strengthened from Tohoku.

For companies in Tohoku, it is a chance of trade expansion and new entrants.

Recognizing this opportunity, we aim to accelerate the entry into the auto industry by Akita Prefecture companies.

2. Method

2-1 The situation of the Akita manufacturing

The leading industry of Akita prefecture is electronic components and devices industry. Composition ratio of manufactured goods shipments is more than 30%. Composition ratio of national electronic components and devices industry is 6%.

On the other hand, the composition ratio of manufactured goods shipments of transport machinery industry whereas the 19% across the country, the composition ratio in the Akita Prefecture, is a less than 6%. We think that the industry has large growth potential.

Industry Composition of Akita manufacturing[1]

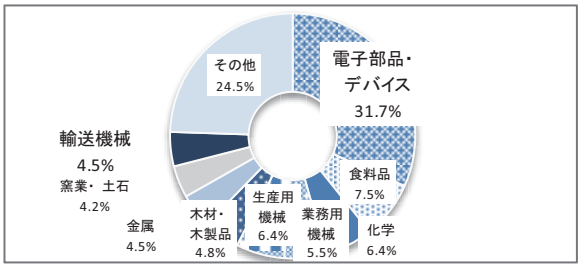

Figure.1

There are attractive car companies in Akita.

- Keep about 50 percent of a share in the semiconductor field of the Toyota group.
- Development and production with the power supply unit of the hybrid car
- The sulfuric acid parent water factory of the separator nonwoven fabric for nickel hydroids batteries only in Japan
- Manufacture O ring　for overseas makers diesels over 30 years
- Top share in the field of a door switch sensor
- Top share in the field of　the car navigation embedded software

Akita is in a readily-accesible location to the main factory in Tohoku.

From Yokote Until Iwate plant of Toyota East about 55 km in distance, time is about 45 minutes.Likewise, from Yokote Until Miyagi Ohira plant about 150 km in distance, time is about 105 minutes.

2-2　Figure to aim at of the Plan

Focusing following six, Akita prefecture aims to become indispensable to car manufacturing in TOHOKU by ALL AKITA.

I　Improvement of QCD
II　Development of human resources
III　Reinforcement of the processing technique
IV　Realization of commercial production by cooperation between companies
V　Development of the new technology by industry, academia, government collaboration
VI　Attraction of enterprises

Six themes tackled by two viewpoints “glowing” and “connecting”

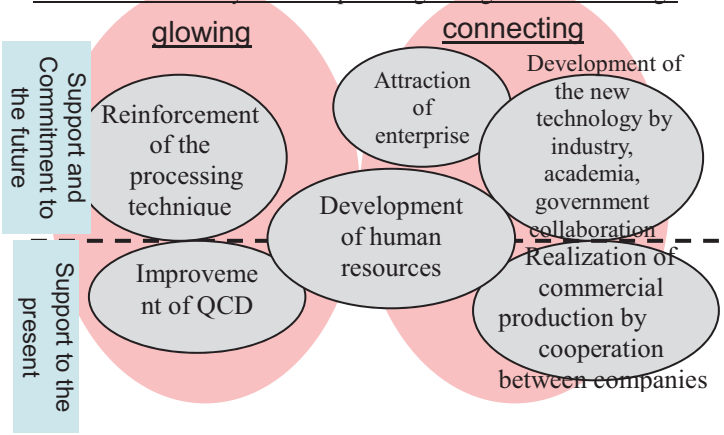

2-3 Main action in the plan

In "Improvement of QCD", we are supporting efforts to improve productivity improvement and production site.

We carry out the guidance by the process improvement adviser intensively and improve the shop floor corresponding to a price reduction, the mass production required for the auto industry.

Guidance by the process improvement adviser

In “Development of human resources” we offered Akita automotive academy.

We are training up the core talented person who can lead problem-solving of quality assurance, price reduction and mass production.

Akita automotive academy

And we hold a seminar to train human resources technical capabilities, production capacity and power management required for auto industry

Guidance of the 2013 training course

Training Course

1. **The cost management**
2. **QC Circle and small group activities**
3. **Process improvement**
4. **Auto parts required performance**
5. **Management**
6. **VE・VA**
7. **Quality management**
8. **Processing technique**

2-4 Permanent exhibition of the AQUA decomposed model

We opened in September last year the decomposition exhibition hall that can study the auto parts.

Car model is Toyota AQUA S grade, all parts are on display. (Number of parts is about 1,000.)

There is no limit to the visitors. Everyone in the company in Tohoku is possible to rent the parts.

Please visit.

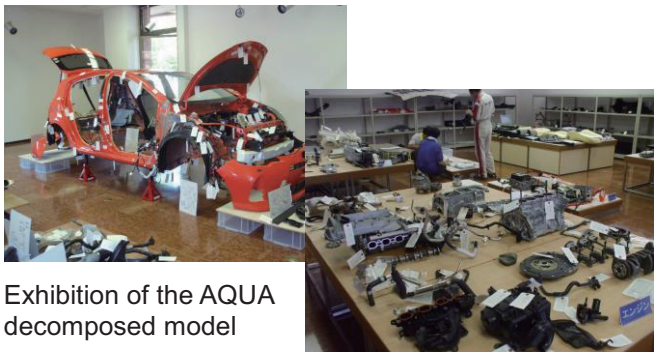

Exhibition of the AQUA decomposed model

3. Concluding remarks

By executing the plan, Akita Prefecture aims to become indispensable to car manufacturing in TOHOKU!

References

[1] Ministry of Economy, Trade and Industry, 2010 Industrial statistics survey (2012)

Tenth International Conference on Flow Dynamics
November 25-27, 2013, Sendai, Miyagi, Japan

Development of High-performance Three-way Catalyst using Novel Heat-resistant Alumina and Special Ceria

Osamu Okada, Nobue Nejo, Akira Hasegawa*
Renaissance Energy Research Corporation,1-7-7-2810, Koraibashi Chuo-ku, Osaka-shi,541-0043, Japan
*Hachinohe National College of Technology, 16-1,Uwanotai Tamonoki Hachinohe-shi, 039-1104, Japan
E-mail: okada@r-energy.com

ABSTRACT

Conventional porous alumina material having a large specific surface area, e.g., γ-alumina, easily undergoes a transition to the α-phase very quickly at temperatures of 1000 °C or higher, but also at lower temperatures over longer periods of time. We succeeded in the development of a high efficiency catalyst that largely reduced ceria and the consumption of noble metals using a novel heat-resistant alumina by the co-precipitation method and special ceria.

1. Introduction

Porous alumina materials having a large specific surface area, e.g., γ-alumina, are useful as catalyst supports or filters. Studies aimed at improving the characteristics of such materials are conducted on an ongoing basis. However, conventional porous alumina materials having a large specific surface area easily undergo transition to the α-phase very quickly at temperatures of 1000 °C or higher, but also at lower temperatures over longer periods of time. Thereafter, the material exhibits a marked drop in specific surface area. Transition to the α-phase tends to be more pronounced in water vapor atmospheres and under higher pressures. As a result, the heat resistance of conventional porous alumina materials is not necessarily sufficient for practical applications. In particular, when the specific surface area in the porous alumina material that is used as a catalyst support drops, catalytic activity is impaired. Accordingly, it is very important in practice that the material exhibits heat resistance such that a large specific surface area is retained even at high temperatures. In this study, we prepared a three-way catalyst using a special ceria developed by Renaissance Energy Research Co. with a new heat-resistant alumina by the co-precipitation method and examined its performance.

2. Method

2.1 Process for the preparation of alumina support

To obtain a uniformly transparent tetraethoxysilane solution, ethanol, hydrochloric acid and water were added to tetraethoxysilane (TEOS). Water was then added to the resulting mixed solution to yield a transparent homogeneous tetraethoxysilane solution. The solution was heated, and aqueous ammonia was added dropwise with stirring until pH 8 was reached. Aluminum hydroxide and a silicon compound co-precipitated as the aqueous ammonia was added. After washing with water, the precipitate was dried in a dryer. Next, the dried precipitate was crushed using a mortar, and was calcined at 1000 °C in air to yield a heat-resistant alumina containing 0.5-10 mass% of SiO_2 with respect to the total mass of SiO_2 plus Al_2O_3.

2.2 Preparation of the three-way catalyst

Ceria and alumina, each carrying Rh and Pd by a liquid phase reduction method, were mixed at a predetermined ratio of Rh/CeO_2 and Pd/Al_2O_3, thereby preparing a three-way catalyst. The performance of the three-way catalyst was evaluated by the purification rate of a simulated exhaust gas.

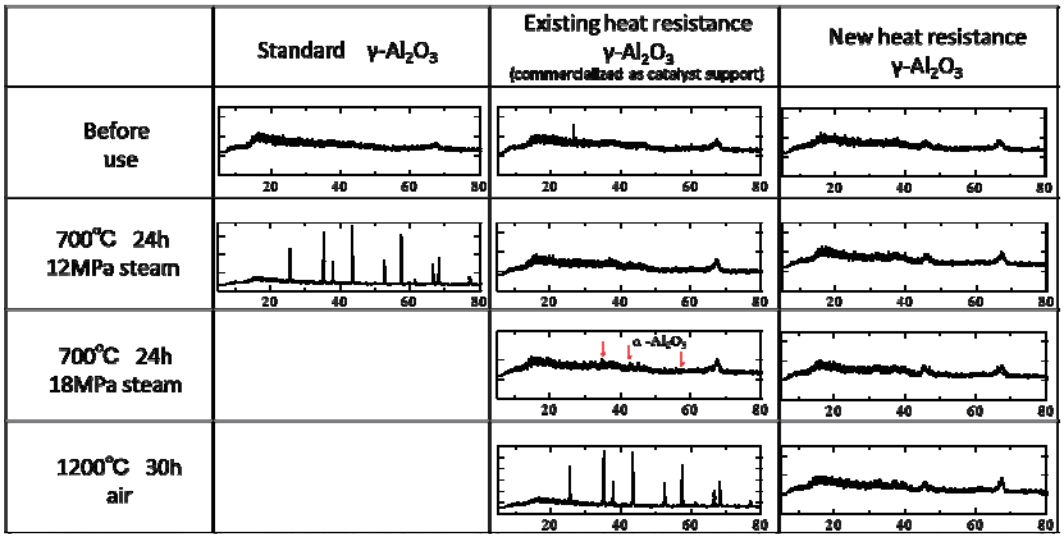

Fig. 1 XRD patterns of alumina aged under various conditions.

3. Results and Discussion

Figure 1 shows the XRD patterns of the novel heat-resistant alumina, standard γ-alumina, and commercial γ-alumina. The sample for comparison having no $Si0_2$ added underwent complete phase transition to α-alumina through calcination for 5 hours at 1200 °C. Standard γ-alumina that did not contain SiO_2 phase transitioned to α-alumina completely in 24 hours at 700 °C in a 12 MPa water vapor atmosphere. The commercial γ-Al_2O_3 comprising SiO_2 phase transitioned to α-alumina completely in 30 hours at 1200 °C. In contrast, in the heat-resistant alumina comprising SiO_2, virtually no peaks were observed derived from the α-phase under any of the calcination conditions. This indicated that the γ or θ-phase was retained.

The samples were subjected to an aging test for a prolonged period of time at 1200 °C. Figure 2 illustrates the relationship between the specific surface area of the heat-resistant alumina and calcination time at 1200 °C. In the comparison sample having no $Si0_2$ added, the specific surface area dropped significantly very early on in the test. In samples where $Si0_2$ was added, the specific surface area dropped initially, but no large drops in specific surface area over long periods were observed from 96 hours onwards. For example, the sample with 5 mass% of SiO_2 exhibited superior heat resistance in that a high specific surface area of about 40 m^2/g was retained even after 700 or more hours of calcination, and α-alumina was not observed.

Figure 3 shows the relationship between SiO_2 concentration and specific surface area of the alumina material aged at 1000 °C for 24 hours in 10% steam atmosphere. It was found that the specific surface area of the heat-resistant alumina tended to increase through addition of SiO_2 for all the calcination conditions.

The three-way catalyst was prepared using a special ceria and novel heat resistance γ-alumina that was modified to improve activity. Figure 4 shows the relationship between the conversion rate of each component and temperature. Despite the fact that reduced amounts of ceria (40%), Pd (30%) and Rh (40%) were present, the catalyst aged at 1000 °C 20 hours under steam atmosphere showed higher conversion rates than the standard catalyst. The specific surface area of standard catalysts after aging was 20 m^2/g. On the other hand, the catalyst with heat-resistant alumina maintained a high specific surface area of 100 m^2/g even after aging, and a higher dispersion of the precious metal than the reference catalyst was found.

4. Concluding remarks

We have succeeded in the preparation of heat-resistant alumina by the co-precipitation method. In the heat-resistant alumina, there was no formation of the α-phase in a steam atmosphere at 1000 °C. Preparation of the three-way catalyst by special ceria and heat-resistant alumina greatly reduced the amount of ceria and noble metal required.

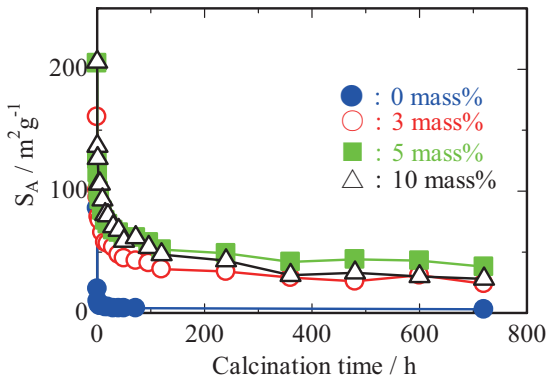

Fig. 2 Relationship between the specific surface area of the heat-resistant alumina and calcination time at 1200 °C.

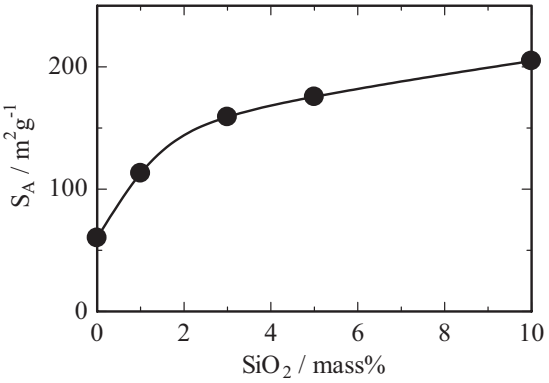

Fig. 3 Relationship between SiO_2 concentration and specific surface area of the alumina aged at 1000 °C for 24 hours under 10% steam atmosphere.

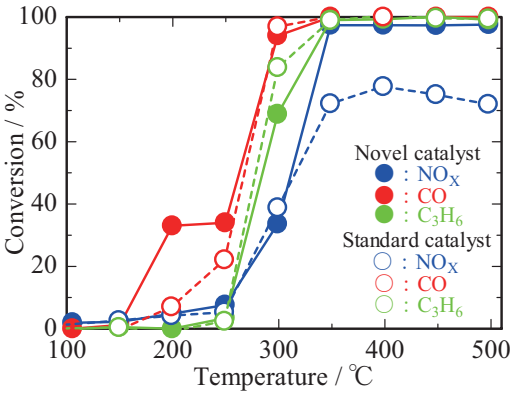

Fig. 4 Conversion curves of C_3H_6, CO and NO_x over the aged catalysts.

We Accept not only Mass-produced Press Working, but also Manufacturing of Secure Device, Mold Design, Labor-saving Design and Product, Manufacturing and Setups

Katsuki Sasaki
Iwanuma-Seiko Co., Ltd.
305-3, Ohmatsubara, Shimonogo, Iwanuma-shi, Miyagi 989-2421, Japan
E-mail: info@iwanuma-sk.co.jp
URL: http://www.iwanuma-sk.co.jp/

ABSTRACT

We contribute to reducing the weight and minimize the medical device by Light press mold and equipment technical fusion. With the high quality facility and technical staff's skill, we offer mass production and planning and manufacturing the metal mold, equipment for labor saving, and sample processing and precision machine.

1. Introduction

Iwanuma-Seiko Co., Ltd. was established in 1974. We deal with mass production press process, precision machine process, mold planning, production, labor saving machine planning, processing, and assembling.

2. Mess production press and planning and manufacturing the metal mold

Below items are correspond to mass production press using press process machine (25t to 110t).

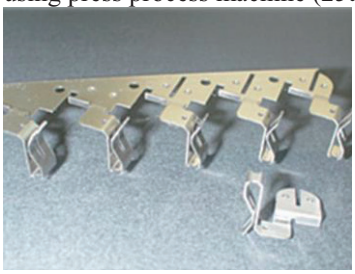

Secondary battery for the tab

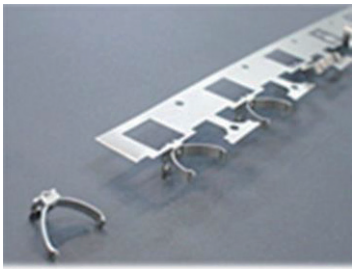

Primary battery for tanshi

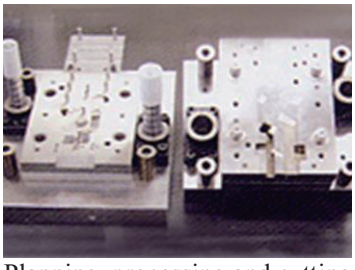

Planning, processing and cutting-in of metal mold

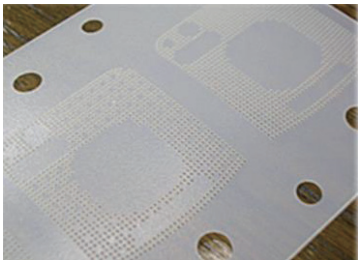

Speaker grill for the mobile phone

3. Equipment for labor saving

We contribute to the energy control by our technique. The below machine can admit the semiconductor which is from a reflow furnace to the magazine.

Equipment

Magazine part (an enlargement of the equipment)

4. Sample processing and precision machine

Laser processing, Wire discharge processing
Machining Center, Processing equipment for CNC lathe

Minute process finishing

Three dimensions process

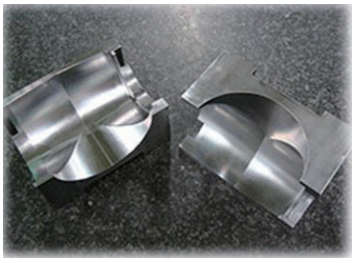

Reflective road sign and metal parts for caulking the ball

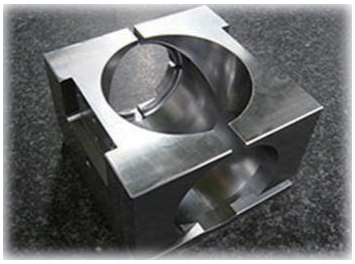

Reflective road sign and metal parts for caulking the ball (after combined)

5. Machine for developing the new product

Press process machine development for miniature pattern precoated metal strip

Metal mold unit for place revision

Using the above machine, print patter (R=0.08mm, Fig. 1) can be print pattern after bending the box (R=0.02mm, Fig. 2) .

Fig. 1

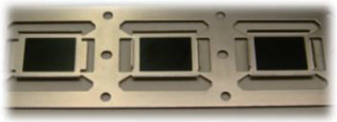

Fig. 2

We also develop a minute process machine. The precision of locating for a whole with steps by front and back discharging process is less than 1 μ m.

minute process machine

6. Concluding remarks

Today, people have different values from what it used to be. We recognize the value and we focus how we make a contribution to the society through our products. As a precision metal company, we are trying to create products not just manufacture products. In order to do that, we master from basic to high-technology skill, and then we improve our product. In the future, we would like to expand our business to the global market with high quality product.

High Thermal Conductivity Silicon Nitride Substrate

Shin Sato
JAPAN FINE CERAMICS CO.,LTD.
Akedohri3-10, Izumi-Ku, Sendai981-3206, Japan
E-mail: satousin@japan-fc.co.jp

ABSTRACT
It succeeded in development of the silicon nitride substrate with high Strength(780Mpa) and high thermal conductivity(100W/m･K) by controlled of the amount of oxygen.

1. Introduction

Recently, a energy problem is significant social issues. And so, high efficiency utilization of electric power energy is a key point. And a power devices is core technology. Expansion of the market, such as home electronics, industrial instrument, automobile, electric train, transmission-transformation of electric energy, electric power is expected.

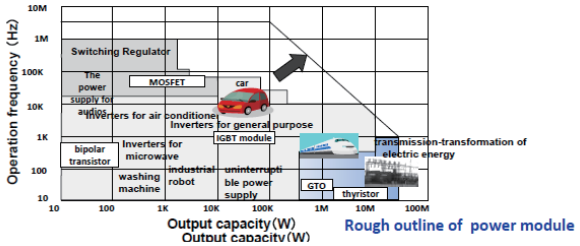

Fig.1

2. Characteristics comparison with each material

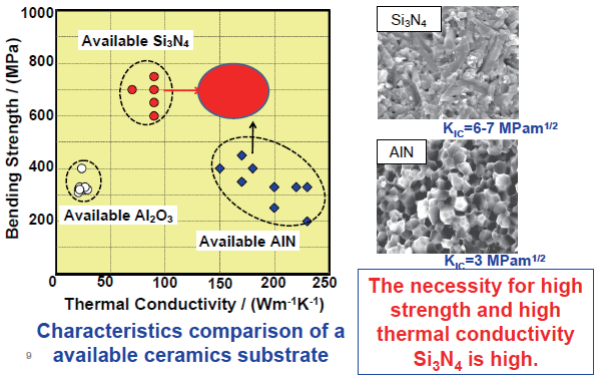

Fig.2

The graph of the thermal conductivity in each material and bending strength is shown. As for Al2O3, thermal conductivity shows a value with 30W/m･K and as low bending strength as 300MPa. Moreover, high thermal conductivity is shown about AlN currently used as a heat dissipation board. However, there is the feature that bending strength is low. On the other hand, available silicon nitride ha thermal conductivity as low as 80W/m･K, although bending strength is as high as 700MPa.

3. Development of high strength and high thermal conductivity

Previous technology, the amount of lattice oxygen content and the grain boundary glassy phase decreased with grain growth by performing prolonged sintered. However, by this technique, bending strength becomes low. Therefore, in this development, the amount of oxygen was controlled and reduction of the lattice oxygen content and a grain boundary glassy phase was aimed at.

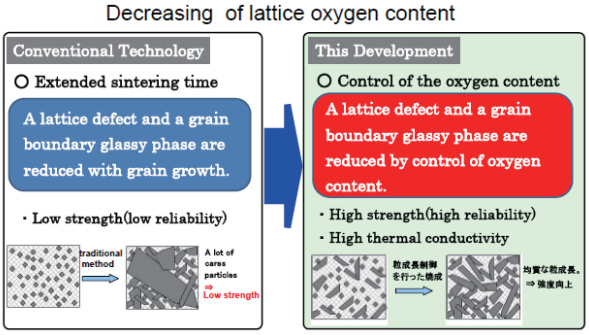

Fig.3

4. Result

In the first, the increase in the amount of oxygen under pulverization was grasped and controlled. The amount of oxygen increased 12% compared with the first stage after 24h pulverization. Since the increase in the amount of oxygen by pulverization was s fixed quantity, pulverization time was fixed 24h. Next, the amount of lattice oxygen content in β -Si3N4 particles was measured. This figure shown relationship thermal conductivity, bending strength and lattice oxygen content. Horizontal axis is lattice oxygen content, vertical axes are thermal conductivity and bebding strength. Red is thermal conductivity, blue is bending strength. The amount of oxygen was controlled by this research. As a result, high thermal conductivity and bending strength were able to be obtained.

Table 1.

1) The oxygen control in pulverization : Relationship between grinding time and Oxygen content

Grinding time [h]	0	6.0	24.0
Amount of oxygen content (0h = 1.0)	1.0	1.01	1.12

2) Dissolution of oxygen in β -Si_3N_4 lattice

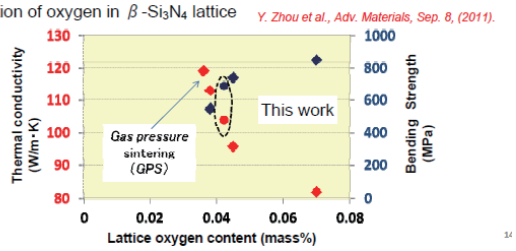

Fig.4

5. Concluding remarks

It succeeded in development of the silicon nitride substrate with high strength (780Mpa) and high thermal conductivity (100W/m･K) by controlled of the amount of oxygen.

Table 2.

Table Properties of Silicon Nitride substrate

Density	[g/cm^3]	3.3
Bending strength	[MPa]	800
Thermal conductivity	[W/m･K]	100
Fluctuate tughness	[MPa･m$^{1/2}$]	8
Coefficient of thermal expansion (R.T~800℃)	[X10^{-6}/K]	3
Poisson's ratio	[-]	0.29
Relative permittivity (25℃ 1MHz)	[-]	7.56
Dielectric loss (25℃ 1MHz)	[X10^{-4}]	22
Dielectric Breakdown Strength (R.T)	[kV/mm]	>20
Volume resistivity value	[Ω･cm]	>10^{13}

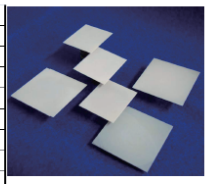

Reinvention of Our Eco-friendly Molding Factory

Masayuki wakiyama
Pla Moul Seiko Co.,Ltd.
Takanomori4-3-5, Tomiyacho, Kurokawa-Gun, Miyagi981-3351, Japan
E-mail: m-wakiyama@plamoul-seiko.co.jp

ABSTRACT

We suggest the Reinvention of our eco-friendly molding factory. Our company is providing accurate electronic parts, low pressure figuration condition, gas-through, and reform of gas influence.Plamoul Seiko is developing the basic human making, makes a company the best reliability merged with the foresight. Our staple products are "Gas Through" a pin with gas vent like ejection pin and/or core pin, and "Air Through" the Air Vent installed to the mold.

1. Introduction

Plamoul Seiko is developing the basic human making, makes a company the best reliability merged with the foresight.

Quality target: Aim at non-defective product by molding machine. To introduce molding model that can form by low pressure.

We specialize in small ultra-precision processing. And we meet the demands of molding shapes to vie with the high precision. Our company's specialty is multi-cavity, so that we are confident in the technique. Please feel free to contact us, for example, if you can't mold 12cavity to 24cavity.

URL:http://www.plamoul-seiko.co.jp/index.html

Fig.1 Head Office

Fig.2 Chinese Factory

We have a relevant factory in Dongguan, Guangdong Province, China.

2. The important thing in molding

The important thing in molding is to keep the conditions in low-pressure molding.

Low-pressure molding can save the resources. It can save electric power and materials.

Low-pressure molding can improve productivity, also. It can cause to rise up utilization of facilities, and reduce maintenance time.

Low-pressure molding can improve quality: Bari, gas burring, warp, deformation.

Do not have an unstable quality in crowded winding of air inside the mold and the gas generated at the time of molding? Let's extinguish manufacturing failure by "Gas Through" and "Air Through".

3. Development Product Introduction

Our products were certified to Miyagi Superior Products in succession for two years.

2012, "Gas Through", Degassing Pin

2013, "Air Through", Air vent devices

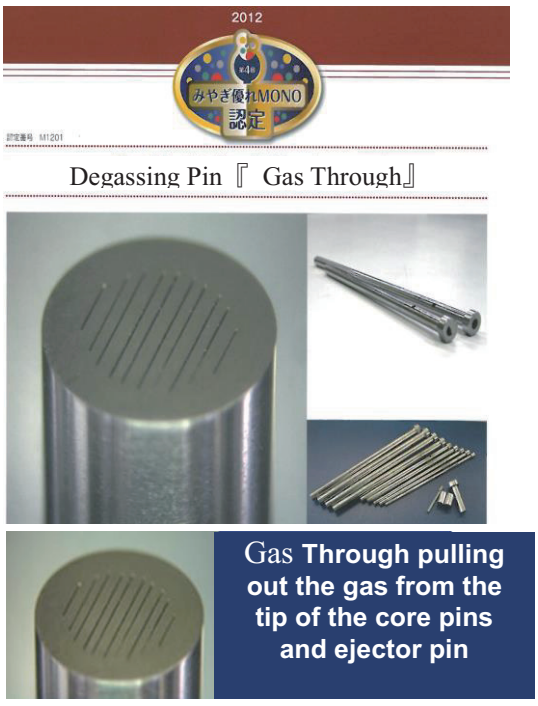

Fig.3"Gas Through "

Gas Through pulls out the gas from the tip of the core pins and ejector pin. According to fluidity of resin, makes sulite wide from 0.005mm to 0.05mm, it is able to be used for wide variety of resins.

Fig.4 “Air Through”

Air Through is the dream apparatus of air vent devices. It can adjust the vent depth by turning its dial (5μm, per 1 scale). It can adjust from 0 to 150μm.

There is lock system installed on the dial.

And we have two types: top face (parting surface) and bottom face (placed on bottom of the product) types.

Fig.5 “Revo Gate” and “Revo Sprue”

Revo Gate can prevent gate convex. By increasing the number of gate holes, we can minimize the diameter of gate, and save the gate from possibility of getting convex.

Revo Sprue is possible to be shorten cooling time for cooling. It makes reality to high cycle molding and cost reduction. Its area of cross surface is small and its surface area is large, the amount of necessary cooling time is reduced.

RevoGate I can prevent gate 凸 off the pin gate Part of 3plate.

4. Concluding remarks

Our products have capacity to shorten production cycle time and improve liquidity at the molding. Production efficiency will be improved, using the mold structure.

Therefore, we frequently have meetings to further improve our products.

We vow to keep our policy “Trust” and “Reliance”. We supply products which make each customer feel safe to use while earning their trust and reliance, and to contribute to the society while each worker must have confidence in products.

The factory tour is held every month. We show you a site where can be continuously molded by Gas Through (The ejector pin that has the function of gas vent). When question and answer time, a company brought a product actually become problem and question about Gas Through with ardor, we received voices that they were able to spend a very worthwhile time.

If you would like to get more information about us, please come to our factories. We hope you will consider participate in.

References

[1] http://www.plamoul-seiko.co.jp/index.html
[2] http://en.nc-net.or.jp/company/74952/

Tenth International Conference on Flow Dynamics
November 25-27, 2013, Sendai, Miyagi, Japan

Challenges to Become a Frontier Company in the Magnetic and Power Transmission Area

Kingo Kuritani
Prospine Co., Ltd.
117 Shinsenkarita, Matsuyama Tsugihashi, Osaki, Miyagi 987-1305, Japan
E-mail: k.kuritani@prospine.co.jp

ABSTRACT

We have proposed the various non-contact power transmissions which are used permanent magnet to the market. I would like to introduce the latest information about a hysteresis brake this time. Control device as a tensioner is one of use applications. Downstream companies had requested us to improve the characteristic of the brake, so we have tackled the problem of it since the last fiscal year. Then, we succeeded in the material development of FCC(Fe-Cr-Co) magnetism material which enables the upgrading of the brake property. Here is the outline of the result. And, downsizing, energy saving, and cost reduction are also expected.

1. Introduction

The hysteresis brakes with a FCC material that is one type of semi-hard magnetic materials have a use in the market of manufacturing equipment for sewing and food markets etc. The market is in expansion late years. However, the hysteresis brakes do not always satisfy the demands of the market in braking characteristic and physical size of products. There are four corporations which are Prospine Co., Ltd., Tohoku University, Industrial Technology Institute-Miyagi Prefectural Government, and Eiwa Co., Ltd. gathered to develop the high performance FCC material, and it delivered a successful result that is about 1.5 to 2 times of braking characteristic with existing FCC materials.

This developed material grows approximately 1.5～2 time better in braking performance as compared to existing FCC materials.

2. Contents

The followings are procedure of the investigation and the development.

1) Survey and measurement of the metal structure for existing FCC materials by EPMA of Institute of Materials Research, Tohoku University.
2) Decision of optimization of heat treatment conditions for FCC materials.
   i) Solution treatment condition
   ii) Aging treatment condition
3) Magnetization measurement by VSM of Industrial Technology Institute-Miyagi Prefectural Government.
4) Mounting of hysteresis electromagnetic brake and its property measurement
5) Finalization of specifications of the FCC material based on the above result of survey analysis.

3. Results

3-1) The results of metallographic analysis of existing and developed products

Resuls as shown in Table 1.

From the result, the development was advanced on the basis of the material No.10 which has high-coercive force and low content of costly V(vicalloy) and Co(cobalt), analyzed by XRD and EPMA of Institute of Materials Research, Tohoku University.

Table1. Metallographic analysis of FCC materials

Samp No.	Alloy	Target	Note
①	Existing vicalloy	Fe-52Co-9V	15Kg Dissolving material
②,⑦	Existing FCC	Fe-26Cr-10Co-1.5Ti	15Kg Dissolving material
④	Upgrading FCC	Fe-21.5Cr-18.5Co-3Mo-1Ti	High coercivity, High flux density
⑤,⑩	Upgrading FCC	Fe-22Cr-15Co-1.5T	Higher coercivity than existing one

3-2) The result of optimization of heat treatment conditions for FCC materials in solution and aging

Heat treatment outline: FCC semi-hard magnet, mono-phase α separates two of FeCo rich-phase and Cr rich-phase in the high-temperature. The coercive force generation of FCC alloy is caused by shape anisotropy of FeCo particulate, and adds higher coercivity by having an age-treatment in the low-temperature and expanding the gap of the compositions.

Generated deposition particle by spinodal decomposition is dependent on differences of temperature between the decomposition temperature and the spinodal curve. The smaller particle has the higher coercivity. Those spinodal decomposition and low-temperature age-treatment are exquisitely sensitive to temperature, and it requires long hours of heat treatments. The magnetic property of FCC materials was controlled by this heat-treating furnace, and the perfect heat treatment conditions for the electromagnetic brake was established. See in Table 2.

Table2. Four types of metallic composition materials and heat treatment conditions & magnetic properties

Samp. No.	Heat treatment condition	Hcj (A/m)	Bs (T)	Brake(mN/m)
Existing material		45000	1.22	12.4
①	Red72 % 600℃ × 1Hr	15000	1.32	16.3
⑦	1200WQ-640-620~500℃	20000	1.45	12.1
④	1200WQ-675-640-620~500℃	19000	1.28	10.1
⑩	1200WQ-690-620~500℃	29000	1.34	15.4

Time program of the optimized heat treatment condition is shown in Fig.1.

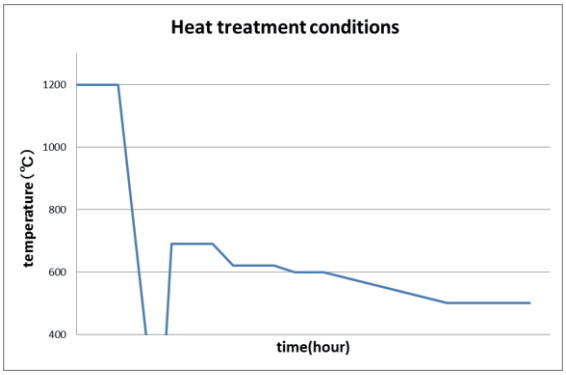

Fig.1 Rough outline of heat treatment conditions (Temp.&Times)

3-3） The observation result of Hysteresis-brake

Structure diagram of the Hysteresis-brake used in the experiment is shown in Fig.2.

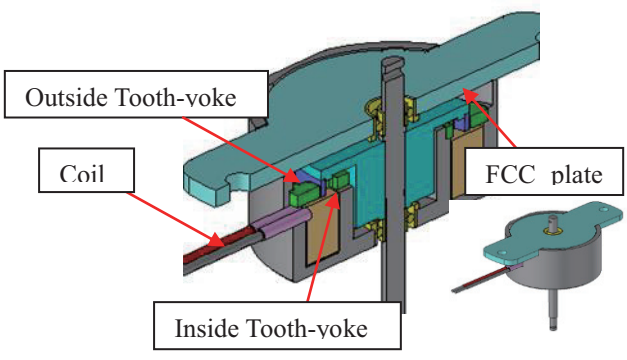

Fig.2 Dia.40 Hysteresis-brake structure

And Braking characteristics for existing and the developed materials are shown in Fig. 3.

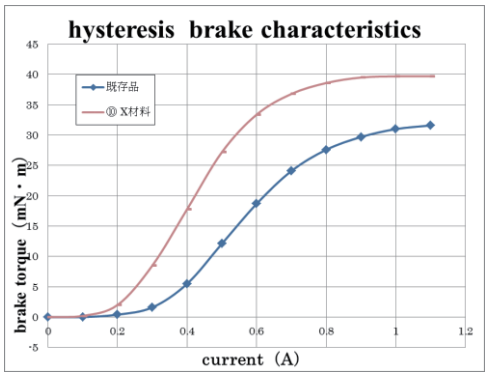

Fig.3 Hysteresis electromagnetic brake and its characteristics

The result of mounting to dia. 40 Hysteresis-brake was that the braking characteristics are 1.5～2 time better as compare with existing materials, when using the developed FCC material made under the following conditions.

FCC material product conditions
1. Metal composition ratio:22Cr-15Co-1.5T
2. Heat treatment conditions
   - Solution treatment: 1200℃ × 1Hr
   - Age- treatment(see in Fig.1)

4. Note

On this development of the above Hysteresis-brake, the simulation was run by magnetic field analysis software, Maxwell Ver.12, and the analysis result was more than 90 percent correlated with its observed value. See Fig. 4 for the comparative graph of the analysis result and its actual measured value.

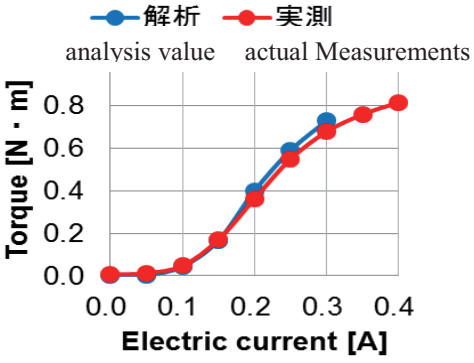

Fig.4 Comparative results of magnetic field analysis & the actual measurement value

Tenth International Conference on Flow Dynamics
November 25-27, 2013, Sendai, Miyagi, Japan

Understanding the Triple Helix Model and the Finance of Innovation

Masato Hisatake and Erik P.M. Vermeulen
Tilburg Law & Economics Center, Tilburg University
Warandelaan 2, Tilburg, The Netherlands
e.p.m.vermeulen@tilburguniversity.edu

ABSTRACT

Governments increasingly partner with corporations, universities and research institutions in an effort to build knowledge-intensive and high tech clusters. These 'triple helix' collaborations generally ignore the importance of financial capital and financially driven incentives. Since the main purpose behind the triple helix approach is to solve economic, social and environmental problems, the policy focus should be on building venture capital ecosystems. New sources of capital, such as joint venture capital funds, crowd funding, online venture capital platforms and partnerships offer new opportunities for governments.

1. Introduction

What should governments and policymakers do to stimulate innovation and entrepreneurship? One way to do it is to encourage the launch and development of start-up companies. But, how should governments support these innovative startup companies? Is there a role for governments in the finance of innovation? There isn't an easy answer. For instance, it has often been argued that governments can only play a very limited role in spurring innovation and entrepreneurship (Lerner, 2009[1]; Hwang and Horowitt, 2012[2]). It is here where the 'venture capital ecosystem' plays a crucial role. Clearly, venture capital (provided by private parties as well as the government) is necessary to support the further growth and development of these companies (Gompers and Lerner, 2001[3]; Mazzucato, 2013[4]).

In order to stimulate innovation, policymakers mainly focus on creating environments in which governments increasingly partner with large corporations, universities and knowledge and research institutions. These triple helix collaborations are, among other things, directed to the establishment of knowledge-intensive service clusters in which the structure and dynamics of interactions among the different actors drive the transfer of knowledge and provide other resources that increase the potential for innovation, growth and value creation. The triple helix approach has proven successful in that it has led to the formation of formal and informal networks of entrepreneurs and other economic actors, thereby increasing the availability of human capital and, more importantly, social capital.

2. Methods

We assess the triple helix model by an analysis of the most innovative regions in the world. Consider Brainport in the Netherlands. Brainport is a business location that is centered around Eindhoven in the Netherlands. it was established as a triple helix cluster. This initiative is considered very successful in terms of R&D spending, the production of patents and job creation. In 2011, companies invested EUR 2.1 billion in research and innovation, which resulted in the production of 42% of the total patents (approximately 1,100 patents) that were registered in the Netherlands. More than 60,000 industry jobs were created in the region. In terms of benchmarking the success of Brainport, the triple helix approach has arguably generated an ecosystem for innovation that belongs to the best in the world. In 2011, the Intelligent Community Forum named Eindhoven the 'Intelligent Community of the Year'. What is perhaps more important is that Forbes Magazine has ranked Eindhoven as the most inventive city in the world (with 22.6 patents for every 10,000 residents) in 2013 (Pentland, 2013[5]). To put this number in perspective, in the second-ranked San Diego, which is considered the world leader in the clean technology economy, this number is 8.9 patents for every 10,000 residents.

Despite the clear benefits of the triple helix model, there is a recognized concern that the Brainport hub may not realize its full potential (European Commission, 2013[6]). Experts increasingly point to a missing fourth helix (and sometimes even fifth helix): the citizens or user communities (also called the 'civil society') and the 'natural environments of society' (Carayannis, Barth and Campbell, 2012[7]). There is something to the quadruple or quintuple helix model. The unique collaboration among academia (research), industry and government focuses on the creation of an engaging and stimulating environment for open innovation and knowledge transfer activities. However, the model does not include the drivers for knowledge production, innovation and growth. This is where the civil society (fourth helix) and natural environment (fifth helix) come into play. It is argued that these elements are necessary to provide incentives to the 'triple helix actors' to drive economic, social and environmental innovations to the market faster and more effectively (Curley and Salmelin, 2013[8]).

Still, there are problems with pushing the quadruple or quintuple helix models too far. First, the extended innovation models prove difficult to implement, because they heavily rely on the actors' willingness and ability to think and act beyond their own functional boundaries (European Commission, 2013[6]). Second, the models arguably put too much emphasis on the interrelations of human capital and social capital in the process of innovation and collaboration, thereby ignoring the importance of financial capital and financially driven incentives (The Economist, 2013[9]). These financial incentives are necessary to accelerate growth and

achieve market leadership. Venture capitalists and other risk capital providers can and must play a crucial role not only in the area of knowledge transfer and innovation, but also as 'social impact' investors that attempt to solve global economic, social and environmental problems, such as global warming and healthy aging (Bennett, 2012[10]; Martin, 2013[11]). This brings us to the challenges that policymakers and governments face in building a venture capital ecosystem.

3. Results and Discussion

The creation of a venture capital ecosystem remains one of the biggest challenges for governments. There are several reasons for this. Most traditionally structured venture capital firms have (with a few notable exceptions) delivered uninspiring returns (Mazzucato, 2013[4]; Mulcahy, 2013[12]). This has not only led to a significant decrease in the number of venture capital funds, but has also moved many of them towards the less risky financing of already profitable later stage companies or companies founded by so-called serial entrepreneurs with considerable track records. Clearly, this development has created an 'investment gap' in the funding of early to mid-stage companies in Europe (see Figure 1). The decreasing number of venture capital funds and their propensity to move to later stages of funding has contributed to the emergence of a 'liquidity gap' in the venture capital ecosystem (see Figure 1). This gap is tied to the significant increase in the time that elapses between the inception of the company, the first involvement of risk capital providers and their ultimate exit.

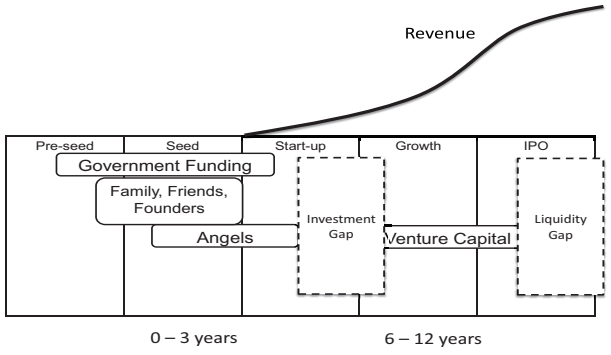

Fig. 1 Gaps in the Venture Capital Ecosystem

Policymakers and governments usually intend to bridge the gaps in the venture capital ecosystem by (a) creating a legal, fiscal and economic environment that is conducive to venture capitalists and (b) providing direct or indirect venture capital in the form of debt and equity. By doing so, governments hope to replicate the success of the world's most successful ecosystem: Silicon Valley. We are all aware of the success stories of entrepreneurs that started their businesses – and developed their innovative ideas with the help of venture capitalists – in garages and basements and built them into global market leaders. The Silicon Valley model, however, is not easily replicated (Hwang and Horowitt, 2012[2]). It appears that providing (access to) venture capital is not sufficient. Policymakers should focus on the specific characteristics of Silicon Valley: the personal interactions among both public and private capital providers that turn innovative ideas into vibrant start-up companies. However, there is good news. Although venture capital has drawn most attention from policymakers in many countries, the venture capital ecosystem is currently evolving. In particular, we observe new breeds of risk capital providers, such as corporate venture capital funds and crowd funding.

4. Concluding remarks

Policymakers have long been committed to create an environment in which high-potential growth companies are able to flourish into large, world-leading companies in a relatively short period of time. Seeing the importance of developing a venture capital ecosystem where innovative firms can prosper, governmental efforts should be geared towards supporting the market-based initiatives that have already emerged to cover the 'gaps' in the venture capital cycle (both in the early and later stages). Again, we will analyze and assess the world's most innovative clusters to get a clearer understanding of the financial and personal factors that drive the venture capital ecosystem.

References

[1] J. Lerner, Boulevard of Broken Dreams, Why Public Effort to Boost Entrepreneurship and Venture Capital Have Failed – and What to Do About It, Princeton University Press (2009).
[2] V.W. Hwang and G. Horowitt, The Rainforest, Regenwald (2012).
[3] P.A. Gompers and J. Lerner, The Money of Invention, How Venture Capital Creates New Wealth, Harvard Business School Press (2001).
[4] M. Mazzucato, The Entrepreneurial State, Debunking Public vs. Private Sector Myths, Anthem Press (2013).
[5] W. Pentland, World's 15 Most Inventive Cities, Forbes Magazine, 9 July 2013.
[6] European Commission, DG Communications Networks, Content and Technology, Open Innovation 2013.
[7] E.G. Carayannis, T.D. Barth and D.F.J. Campbell, The Quintuple Helix Innovation Model: Global Warming As A Challenge and Driver for Innovation, Journal of Innovation and Entrepreneurship (2012).
[8] M. Curley and B. Salmelin, Open Innovation 2.0: A New Paradigm, Conference Paper (2013).
[9] The Economist, Schumpeter, Crazy Daimonds, 20 July 2013.
[10] D. Bennett, Social+Capital, the League of Extraordinarily Rich Gentlemen, Bloomberg Businessweek, 26 July 2012.
[11] M. Martin, Status of the Social Impact Investing Market: A Primer, www.impacteconomy.com (2013).
[12] D. Mulcahy, Myths About Venture Capitalists, Harvard Business Review, May 2013.

Tenth International Conference on Flow Dynamics
November 25-27, 2013, Sendai, Miyagi, Japan

Understanding the Triple Helix Model and the Finance of Innovation

Masato Hisatake and Erik P.M. Vermeulen
Tilburg Law & Economics Center, Tilburg University
Warandelaan 2, Tilburg, The Netherlands
e.p.m.vermeulen@tilburguniversity.edu

ABSTRACT

Governments increasingly partner with corporations, universities and research institutions in an effort to build knowledge-intensive and high tech clusters. These 'triple helix' collaborations generally ignore the importance of financial capital and financially driven incentives. Since the main purpose behind the triple helix approach is to solve economic, social and environmental problems, the policy focus should be on building venture capital ecosystems. New sources of capital, such as joint venture capital funds, crowd funding, online venture capital platforms and partnerships offer new opportunities for governments.

1. Introduction

What should governments and policymakers do to stimulate innovation and entrepreneurship? One way to do it is to encourage the launch and development of start-up companies. But, how should governments support these innovative startup companies? Is there a role for governments in the finance of innovation? There isn't an easy answer. For instance, it has often been argued that governments can only play a very limited role in spurring innovation and entrepreneurship (Lerner, 2009[1]; Hwang and Horowitt, 2012[2]). It is here where the 'venture capital ecosystem' plays a crucial role. Clearly, venture capital (provided by private parties as well as the government) is necessary to support the further growth and development of these companies (Gompers and Lerner, 2001[3]; Mazzucato, 2013[4]).

In order to stimulate innovation, policymakers mainly focus on creating environments in which governments increasingly partner with large corporations, universities and knowledge and research institutions. These triple helix collaborations are, among other things, directed to the establishment of knowledge-intensive service clusters in which the structure and dynamics of interactions among the different actors drive the transfer of knowledge and provide other resources that increase the potential for innovation, growth and value creation. The triple helix approach has proven successful in that it has led to the formation of formal and informal networks of entrepreneurs and other economic actors, thereby increasing the availability of human capital and, more importantly, social capital.

2. Methods

We assess the triple helix model by an analysis of the most innovative regions in the world. Consider Brainport in the Netherlands. Brainport is a business location that is centered around Eindhoven in the Netherlands. it was established as a triple helix cluster. This initiative is considered very successful in terms of R&D spending, the production of patents and job creation. In 2011, companies invested EUR 2.1 billion in research and innovation, which resulted in the production of 42% of the total patents (approximately 1,100 patents) that were registered in the Netherlands. More than 60,000 industry jobs were created in the region. In terms of benchmarking the success of Brainport, the triple helix approach has arguably generated an ecosystem for innovation that belongs to the best in the world. In 2011, the Intelligent Community Forum named Eindhoven the 'Intelligent Community of the Year'. What is perhaps more important is that Forbes Magazine has ranked Eindhoven as the most inventive city in the world (with 22.6 patents for every 10,000 residents) in 2013 (Pentland, 2013[5]). To put this number in perspective, in the second-ranked San Diego, which is considered the world leader in the clean technology economy, this number is 8.9 patents for every 10,000 residents.

Despite the clear benefits of the triple helix model, there is a recognized concern that the Brainport hub may not realize its full potential (European Commission, 2013[6]). Experts increasingly point to a missing fourth helix (and sometimes even fifth helix): the citizens or user communities (also called the 'civil society') and the 'natural environments of society' (Carayannis, Barth and Campbell, 2012[7]). There is something to the quadruple or quintuple helix model. The unique collaboration among academia (research), industry and government focuses on the creation of an engaging and stimulating environment for open innovation and knowledge transfer activities. However, the model does not include the drivers for knowledge production, innovation and growth. This is where the civil society (fourth helix) and natural environment (fifth helix) come into play. It is argued that these elements are necessary to provide incentives to the 'triple helix actors' to drive economic, social and environmental innovations to the market faster and more effectively (Curley and Salmelin, 2013[8]).

Still, there are problems with pushing the quadruple or quintuple helix models too far. First, the extended innovation models prove difficult to implement, because they heavily rely on the actors' willingness and ability to think and act beyond their own functional boundaries (European Commission, 2013[6]). Second, the models arguably put too much emphasis on the interrelations of human capital and social capital in the process of innovation and collaboration, thereby ignoring the importance of financial capital and financially driven incentives (The Economist, 2013[9]). These financial incentives are necessary to accelerate growth and

achieve market leadership. Venture capitalists and other risk capital providers can and must play a crucial role not only in the area of knowledge transfer and innovation, but also as 'social impact' investors that attempt to solve global economic, social and environmental problems, such as global warming and healthy aging (Bennett, 2012[10]; Martin, 2013[11]). This brings us to the challenges that policymakers and governments face in building a venture capital ecosystem.

3. Results and Discussion

The creation of a venture capital ecosystem remains one of the biggest challenges for governments. There are several reasons for this. Most traditionally structured venture capital firms have (with a few notable exceptions) delivered uninspiring returns (Mazzucato, 2013[4]; Mulcahy, 2013[12]). This has not only led to a significant decrease in the number of venture capital funds, but has also moved many of them towards the less risky financing of already profitable later stage companies or companies founded by so-called serial entrepreneurs with considerable track records. Clearly, this development has created an 'investment gap' in the funding of early to mid-stage companies in Europe (see Figure 1). The decreasing number of venture capital funds and their propensity to move to later stages of funding has contributed to the emergence of a 'liquidity gap' in the venture capital ecosystem (see Figure 1). This gap is tied to the significant increase in the time that elapses between the inception of the company, the first involvement of risk capital providers and their ultimate exit.

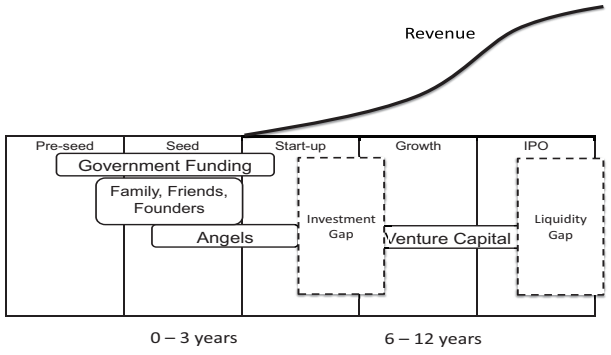

Fig. 1 Gaps in the Venture Capital Ecosystem

Policymakers and governments usually intend to bridge the gaps in the venture capital ecosystem by (a) creating a legal, fiscal and economic environment that is conducive to venture capitalists and (b) providing direct or indirect venture capital in the form of debt and equity. By doing so, governments hope to replicate the success of the world's most successful ecosystem: Silicon Valley. We are all aware of the success stories of entrepreneurs that started their businesses – and developed their innovative ideas with the help of venture capitalists – in garages and basements and built them into global market leaders. The Silicon Valley model, however, is not easily replicated (Hwang and Horowitt, 2012[2]). It appears that providing (access to) venture capital is not sufficient. Policymakers should focus on the specific characteristics of Silicon Valley: the personal interactions among both public and private capital providers that turn innovative ideas into vibrant start-up companies. However, there is good news. Although venture capital has drawn most attention from policymakers in many countries, the venture capital ecosystem is currently evolving. In particular, we observe new breeds of risk capital providers, such as corporate venture capital funds and crowd funding.

4. Concluding remarks

Policymakers have long been committed to create an environment in which high-potential growth companies are able to flourish into large, world-leading companies in a relatively short period of time. Seeing the importance of developing a venture capital ecosystem where innovative firms can prosper, governmental efforts should be geared towards supporting the market-based initiatives that have already emerged to cover the 'gaps' in the venture capital cycle (both in the early and later stages). Again, we will analyze and assess the world's most innovative clusters to get a clearer understanding of the financial and personal factors that drive the venture capital ecosystem.

References

[1] J. Lerner, Boulevard of Broken Dreams, Why Public Effort to Boost Entrepreneurship and Venture Capital Have Failed – and What to Do About It, Princeton University Press (2009).
[2] V.W. Hwang and G. Horowitt, The Rainforest, Regenwald (2012).
[3] P.A. Gompers and J. Lerner, The Money of Invention, How Venture Capital Creates New Wealth, Harvard Business School Press (2001).
[4] M. Mazzucato, The Entrepreneurial State, Debunking Public vs. Private Sector Myths, Anthem Press (2013).
[5] W. Pentland, World's 15 Most Inventive Cities, Forbes Magazine, 9 July 2013.
[6] European Commission, DG Communications Networks, Content and Technology, Open Innovation 2013.
[7] E.G. Carayannis, T.D. Barth and D.F.J. Campbell, The Quintuple Helix Innovation Model: Global Warming As A Challenge and Driver for Innovation, Journal of Innovation and Entrepreneurship (2012).
[8] M. Curley and B. Salmelin, Open Innovation 2.0: A New Paradigm, Conference Paper (2013).
[9] The Economist, Schumpeter, Crazy Daimonds, 20 July 2013.
[10] D. Bennett, Social+Capital, the League of Extraordinarily Rich Gentlemen, Bloomberg Businessweek, 26 July 2012.
[11] M. Martin, Status of the Social Impact Investing Market: A Primer, www.impacteconomy.com (2013).
[12] D. Mulcahy, Myths About Venture Capitalists, Harvard Business Review, May 2013.

Tenth International Conference on Flow Dynamics
November 25-27, 2013, Sendai, Miyagi, Japan

Can Functional Brain Imaging Prompt Innovations in Next-generation Automobiles?

Ryuta Kawashima
Department of Advanced Neuroscience, IDAC, Tohoku University, Sendai 982-8575 Japan
ryuta@idac.tohoku.ac.jp

ABSTRACT

Information about cognitive processing that occurs when an automobile is being driven can be obtained using neuroimaging techniques. Such information will certainly be advantageous in the near future for automobile design, given that automobiles are more than mere tools for transportation; they're a man-machine interface. Therefore, it would be in the best interest of engineers to invest in some knowledge of recent neuroimaging techniques from cognitive neuroscientists, and to at least comprehend the advantages and disadvantages of those techniques. In this symposium, I will discuss the possibility of applying neuroimaging techniques to the R&D of next-generation automobiles.

1. Introduction

Recent advancements in neuroimaging techniques enable us to visualize brain activity during various kinds of cognitive activities. We believe the utilization of information from human cognitive activity is certain to directly contribute to innovations made for the next-generation automobile. Recent automobiles and, of course, those of the future are emphatically acting as a man-machine interface, directly connecting one's intention to move with the mechanical systems of the automobile.

Functional magnetic resonance imaging (fMRI) is one of such techniques which is able to measure changes in brain activity. One of the significant advantages of the fMRI technique is that it can make visualization with relatively high spatial resolution of whole brain networks involved in specific cognitive function(s), and even access those structures located in deeper parts of the brain. However, a few restrictions apply to fMRI experiments. One is that fMRI experiments must be done in a MRI scanner room and the subjects must be put inside a MRI scanner. The MRI system is very large and heavy. Another restriction is that, since the MRI system uses string magnetic power, metals with electrically conductive parts cannot be used within or near the MRI scanner.

Near infrared spectroscopy (NIRS) is another neuroimaging technique. It records activity at the surface of the cerebral cortex by measuring related changes in the concentration of oxygenated hemoglobin (oxy-Hb) and deoxygenated hemoglobin (deoxy-Hb). The advantage of NIRS is that it can be used in daily life situations. For example, it can measure the temporal course of cortical activity while a person actually drives a car. Nevertheless NIRS only can measure the activity of the brain's surface and nothing can be known about what is happening in deeper structures. In addition, its spatial resolution is very low- only several centimeters.

2. An example of an fMRI experiment

As mentioned, one cannot bring metals and electric parts close to the MRI scanner. Nevertheless, one can present any visual and auditory stimuli inside of the MRI scanner through a projector and a pair of MRI compatible headphones. The subject's head must be fixed on a head rest, but he/she is free to move his/her hands and feet during the MRI scans, as long as those movements do not cause any movement of the head.

We previously ran an experiment to measure brain activity when detecting hazardous situations while driving. In this experiment, we placed an accelerator and a brake pedal at the end of the MRI scanner bed and, through the projector, presented several video clips of different driving situations (Fig. 1). Subjects were asked to imagine they were driving their own car and to step on the brake when they came upon a hazardous situation. We then calculated brain activation at the time subjects moved their right foot from the accelerator. In addition, the activity of the activated areas was compared with the subject's score for individual sensitivity to hazard detection, which was measured by psychophysical tests on a different day.

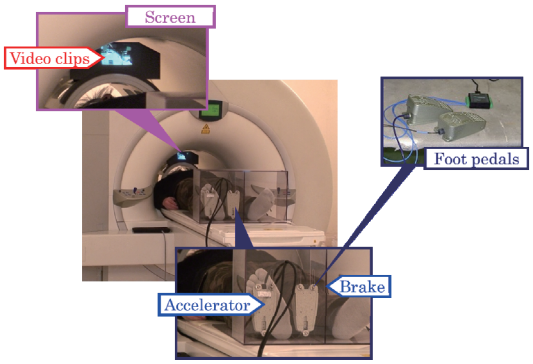

Fig. 1 An example of the experimental set-up for fMRI

The results indicate that a brain network consisting of the premotor cortex of the left hemisphere, the posterior parietal, and the occipital cortices of the bilateral hemispheres are involved in hazard detection. The activity of the left premotor cortex was shown to be related to the sensitivity of one's hazard detection abilities (Fig. 2).

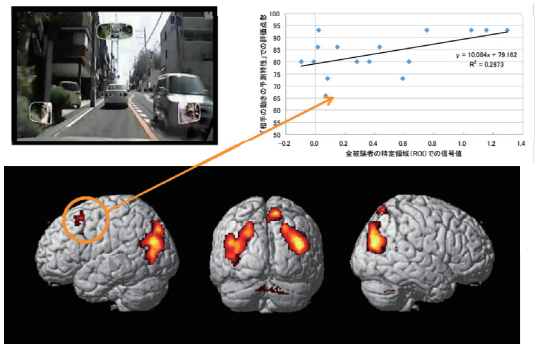

Fig. 2 Brain areas involved in hazard detection

This study gives us the following idea for developments in future automobiles. If we could continuously monitor the brain activity of the left premotor cortex using some device while one is actually driving, we can estimate one's ability to detect hazards as they occur, and then use that information to control the driving system of the automobile.

3. An example of NIRS experiment

We measured the activity of the dorsolateral prefrontal cortex (DLPFC) while cars were being driven using a prototype of the wearable optical topography (WOT) system (Hitachi Ltd., Tokyo, Japan) based on NIRS (Fig. 3). The DLPFC is known to play a key role in cognitive functions directly related to safe driving, such as attention, inhibition, decision making, etc.

A probe unit of the WOT system can be adjusted to fit on the head of a subject, and a processing unit can be strapped to the subject's body. Therefore, we can monitor changes in cortical activities while subjects are driving cars, or even riding motorcycles, in daily life situations.

Fig. 3 A prototype of the wearable optical topography (WOT) system

In our previous preliminary experiments, the activity of the DLPFC in healthy adults was measured while the adults drove cars in a closed driving course using the WOT. While driving cars with manual transmission, only the right DLPFC showed high activation. While driving cars with automatic transmission, the DLPFC of both hemispheres did not show any activation. It is interesting to note that driving a kart activated the bilateral DLPFC.

The left DLPFC showed activation only while a kart was being driven. Activation of the left DLPFC is often related to verbal tasks requiring executive processing. The drivers probably used a logical and/or verbal approach when considering how to handle the kart. In contrast, it has been argued that executive demand increases activity in the right DLPFC for spatial working memory processing. Thus there may be a greater requirement for spatial working memory when driving cars with manual transmission and karts. Cognitive load was relatively low when driving a car with manual transmission.

In general, the rate of age-related decline in measures of cognitive functioning will be less pronounced for people who are more mentally active, or, equivalently, the cognitive differences among people who vary in level of mental activity will be greater with increased age. When we design specific cars for our elderly population, we may have to consider designing cars that lend a hand to those with lower mental activity.

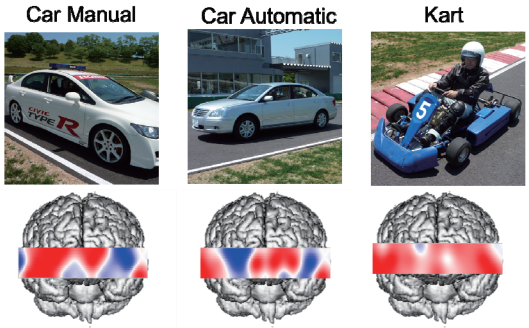

Fig. 4 Typical patterns of cortical activity when driving cars

4. Concluding remarks

We believe that applying what is known about cognitive functions through neuroimaging techniques to the R&D of next-generation automobiles can bring forth a new perspective. Creating a platform for discussion between cognitive neuroscientists and car engineers would surely be fruitful for innovation.

Tenth International Conference on Flow Dynamics
November 25-27, 2013, Sendai, Miyagi, Japan

Alzheimer's disease: from pathology to therapeutics

Takeshi Iwatsubo

Department of Neuropathology, Graduate School of Medicine, The University of Tokyo
iwatsubo@m.u-tokyo.ac.jp

ABSTRACT

Amyloid β peptides are the most characteristic neuropathological protein deposited in the brains of patients with Alzheimer's disease, which is implicated in its pathogenesis and deemed as the prime target for the disease-modifying therapy. In this talk, the molecular pathology of Alzheimer's disease, the most frequent cause of dementia in the elderly and often linked to traffic accidents, will be discussed in relation to the efforts to develop mechanism-based therapeutics for this devastating disease.

Deposition of amyloid β peptides (Aβ) as senile plaques is the most characteristic neuropathological feature of Alzheimer's disease (AD), which is implicated in its pathogenesis and deemed as the prime target for the disease-modifying therapy (DMT) [1] (Figure 1). Aβ deposition is determined by the production and clearance. Aβ is produced by sequential proteolytic cleavages by β- and γ-secretases. γ-Secretase, harboring presenilins (PS) as the catalytic center, forms the C terminus of Aβ that determines its propensity to aggregate: missense mutations in PS genes cause familial AD by altering the preferred γ-secretase cleavage sites in a way to increase production of pathogenic Aβ42 species [2,3]. γ-Secretase forms a hydrophilic pore within the membrane lipid bilayer, which enables the unique mode of intramambrane proteolysis to form Aβ, and inhibitors of β- and γ-secretases with different targets and mode of action are being developed. Aβ immunotherapy facilitates the clearance of Aβ from brain parenchyma through the activities of anti-Aβ antibodies with different characteristics. Efforts to clinically develop the DMTs for AD, including establishment of imaging and fluid biomarkers that surrogate the AD pathology through clinical studies like AD Neuroimaging Initiative (ADNI) and Japanese ADNI are currently underway.

J-ADNI was started in 2008, aiming at conducting a longitudinal workup of standardized neuroimaging, biomarker and clinico-psychological surveys [4] (Figues 2). The research protocol was designed to maximize compatibility with that of US-ADNI, including structural magnetic resonance imaging analysis for the evaluation of brain atrophy, fluorodeoxyglucose and amyloid positron emission tomography, cerebrospinal fluid sampling, *APOE* genotyping, together with a set of clinical and psychometric tests that were prepared to maximize the compatibility to those used in the North America. Japanese ADNI has recruited 545 participants (239 amnestic mild cognitive impairment (MCI), 152 normal aged and 154 early AD). A number of significant results, including the predictive values of amyloid markers (i.e., amyloid PET and CSF Aβ42) for conversion of MCI to AD, are being obtained and analyzed. ADNI activities world-wide will establish the rigorous quantitative descriptions of the natural course of AD in its very early stages. The data, as well as the methodologies and infrastructures, will facilitate the clinical trials of disease-modifying therapies for AD using surrogate biomarkers that will enable the very early treatment of AD, which will further be supported by J-ADNI2 focusing on preclinical AD population as well as early and late MCI.

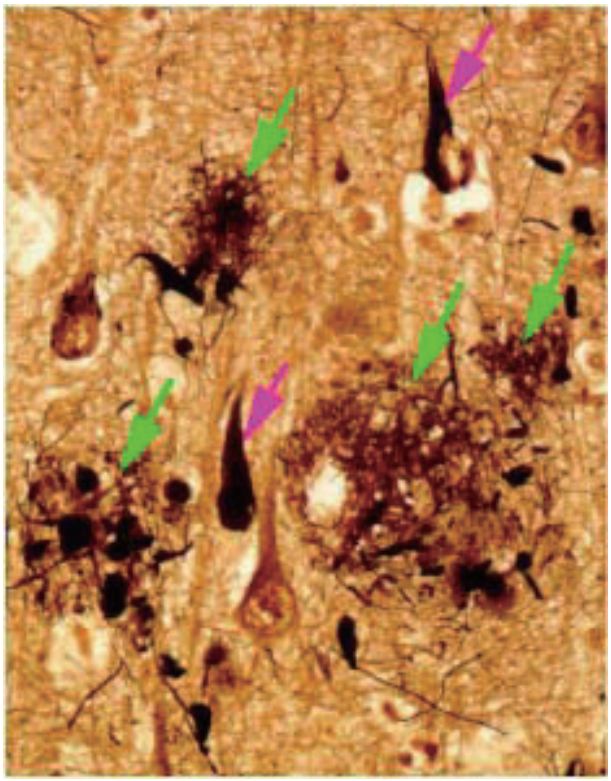

Figure 1. Neuropathology of Alzheimer's disease Green and pink arrows denote senile plaques (amyloid deposits) and neurofibrillary tangles, respectively.

AD and other types of dementias sometimes cause traffic accidents by wrong-way driving. Current status as well as causes of this type of traffic accidents will also be discussed.

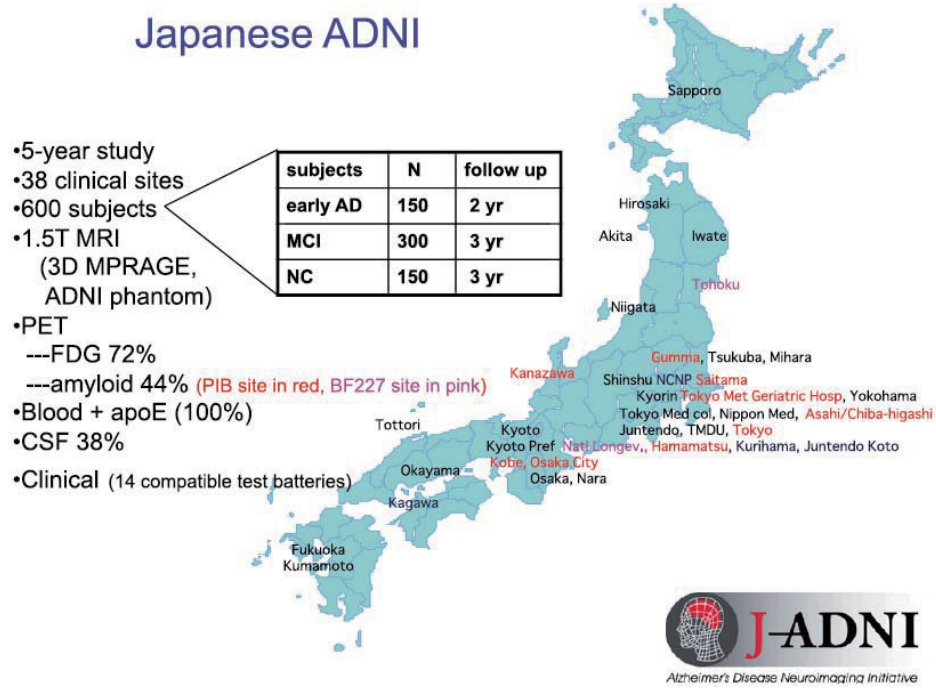

Figure 2. Overview of J-ADNI

References

[1] Iwatsubo T et al. ***Neuron*** (1994) **13**: 45-53
[2] Tomita T et al. ***Proc Natl Acad Sci USA*** (1997) **94**:2025-2030
[3] Takasugi N et al. ***Nature*** (2003) **422**: 438-441
[4] Iwatsubo T ***Alzheimer Dement*** (2010) **6**: 297-299

Tenth International Conference on Flow Dynamics
November 25-27, 2013, Sendai, Miyagi, Japan

Japanese Low Emission Vehicle (LEV) Policy
A Successful Strategy to Achieve Global Leadership in Next Generation Vehicles (NGV)

Noriko Behling
Author
McLean, Virginia
E-mail: behlingn@msn.com

ABSTRACT

Japan has long committed itself to a Low Emission Vehicle (LEV) policy to reduce greenhouse gas emissions as well as to maintain the viability of its automotive industry. For more than ten years, Japan has been implementing a series of programs supported by a multitude of well-designed policy measures. The rapid growth in next generation vehicle sales suggests these efforts are paying off and have led to significant declines in CO_2 emissions within the transport sector. Government implementation of two new action plans will encourage further advances in technologies for next generation vehicles that could obviate the need for fossil fuel engines.

1. Introduction

In early 2000s, Japan started to implement a series of low emission vehicle policies to promote the widespread use of fuel efficient, low emission vehicles (LEVs) in Japan. The government was committed to reduce greenhouse gas emissions and believed that one path toward that goal was to increase the number of high fuel efficient, low emission vehicles on the road. The policy initiatives began when there were relatively few LEVs and fuel supply facilities for serving LEVs were very limited.

- In 2000, the total number of LEVs in use in Japan was only about 600,000 vehicles, and the number of eco-stations was about 230.

2. Implementation of the First Two Low Emission Vehicle Action Plans in 2001 and 2004

Japan implemented "Prime Minister Koizumi's "Low Emission Vehicle Diffusion Action Plan" in 2001 and the "the World's Most Advanced Low Emission Vehicle Society Action Plan" in 2004. Both action plans called for 10 million "low emission vehicles" and 50,000 fuel cell vehicles on the road by the end of FY2010.

- LEVs included low emission gasoline vehicles, CNG vehicles, hybrid vehicles, hydrogen vehicles, methanol vehicles, and fuel cell vehicles.

To promote their plans, Japan deployed a multitude of creative policy measures. For example, Tokyo established a pool of $460 million in incentives to encourage the purchase of LEVs and devised an innovative classification system to determine the level of tax cuts for which a vehicle qualified. Vehicles received one to three stars depending on how much lower the vehicle emission was relative to the current standard, with "three star" vehicles receiving the greatest tax cut. Similarly, vehicles were provided with a certification sticker bearing a percentage number, such as 10, 25, or 50 percent, depending on how much higher the vehicle's fuel efficiency was relative to current and future standards.

This ingenious incentive system effectively shaped both current and future market demand. Tokyo did not need to enforce specific standards, but instead defined a road map that linked future market incentives to increasingly stringent standards. Responding to these incentives, many automakers pledged by 2005 to have 80 to 100 percent of their domestic vehicles qualify for three star emissions standards and bear the highest fuel efficiency ranking certificate. At the same time automakers invested in new technology to meet future standards. Tokyo thus was able to attain higher emission and fuel efficiency standards easily and faster.

Tokyo set vehicle emission and fuel economy goals that far exceeded any standard in the world. Tokyo also compiled a plan for new nitrogen oxide (NOx) and particulate matter (PM) standards for 2005 that were about equal to the Euro IV emission standards placed in force in 2005. Tokyo also has implemented a revised Vehicle NOx/PM Law that would encourage replacement of most trucks, buses, and diesel vehicles, thereby improving the chances for cleaning up NOx and PM pollution in 12 years.

- Incentives included subsidies at the time of vehicle purchase, reduction in the vehicle acquisition tax, and the annual vehicle tax, as well as the reduction in corporate tax and property tax. There were also reverse financial incentives. Owners of older vehicle models paid a greater annual vehicle tax, which created an additional incentive to replace them with new LEVs. Low interest loans were also available for corporate purchasers.

3. Assessment in 2007 Indicated Mixed Results

The two Action Plans triggered a marked increase in gasoline powered LEVs (but did not succeed in reducing CO_2 emissions). The goal of 10 million vehicles on the road was achieved in 2005, five years earlier than planned. Total number of LEVs in use was 16.5 million in 2007, a 26-fold increase since 2000. In 2000, LEVs were less than 1% of the total vehicle fleet but were 13% in 2004 and 22% in 2007.

Hybrid vehicles also increased about 8-fold. Growth

was initially slow but became robust starting in 2004. This outcome pointed to an important lesson, namely that technology advances in vehicles would radically alter buyer behavior. In the case of hybrid LEVs, the increase was triggered by the introduction in 2004 of the more technologically advanced, more fuel efficient 2nd generation Prius.

- The government assessed that the increase in hybrid vehicles was due to its inherent commercial appeal and that government subsidies for the vehicle were no longer necessary. It discontinued subsidies for hybrid vehicles in March 2007.

Sales of other LEVs, such as CNG vehicles, methanol vehicles, hydrogen combustion vehicles, and fuel cell vehicles, were unremarkable. CNG vehicles achieved a modest, 3.7-fold increase but methanol vehicles declined to the point of nearly fading away. Fuel cell vehicles and hydrogen vehicles did not perform well at all. Fuel cell vehicles were too costly and not viable for practical use.

- The government viewed methanol vehicles to be commercially uncompetitive and policy support was discontinued. It appears that the government might have dropped hydrogen combustion vehicles from its policy support as well.

4. Lessons Learned from the Outcome of 2007

The goal of 10 million LEVs was met, and the inventory of LEVs increased. But no significant reduction in CO_2 emissions was achieved.

Gasoline LEVs have a limited ability to cut greenhouse gas emissions because the vehicles still burn fossil fuel. Moreover, efficiency improvements in these vehicles encouraged owners to drive their cars more, undercutting reductions in CO_2 emissions. The government recognized that the key to building a fleet of LEVs that met CO_2 emission reduction goals would require a significant shift away from fossil fuels. It also recognized that R&D on next generation vehicle technology must be promoted because the future vehicle fleet would be based on technology advances derived from non-gasoline LEVs.

5. Implementation of Next Two Action Plans in 2008 and 2010

Japan implemented the "Low Carbon Society Construction Action Plan" in 2008. The Plan called for one out of two new vehicles sold by 2020 to be next generation vehicles (NGVs), which would include hybrid vehicles, electric vehicles, plug-in hybrid vehicles, fuel cell vehicles, clean diesel vehicles, and CNG vehicles. The government aimed to reduce greenhouse gas emissions by 60-80% by 2050. Japan subsequently launched the "Next Generation Automobile Strategy 2010." The Plan stipulated that 20 to 50% on the road should be NGVs by 2020 and 50-70% by 2030. It called for up to 1% of that number to be fuel cell vehicles by 2010 and up to 3% by 2019. Japan continued the same policy measures as before with minor modifications as needed.

6. Outcome as of 2011 Positive

The outcome, as of 2011, shows that the policies have achieved encouraging results. The rate of increase in sales of NGVs is greater than for gasoline LEVs. Sales of gasoline LEVs increased by 40% from 2007 and 2011, but NGVs increased five-fold during the same period.

Electric vehicles and hybrid vehicles both increased substantially. The increase was primarily due to technology advancements. Electric vehicles increased 11-fold due to introduction of two new vehicles, Mitsubishi i-MiEV and Nissan Leaf. Hybrid vehicles increased 5-fold, due to introduction of the 3rd generation Prius in 2009.

- As a result, NGVs comprised 3% of total vehicles in use.

The increase in NGVs in the vehicle inventory notably contributed to a decline in CO_2 emissions. After peaking in 2001, CO_2 emissions in Japan's transport sector steadily declined. It registered 267 million tons in 2001, 245 in 2007 and 230 million tons in 2011—well below the 2010 emissions target for the fourth consecutive year.

7. Challenges Ahead: Japan's Overall CO_2 Emissions Must Be Lowered

While CO_2 emissions in the transport sector have declined, total greenhouse gas emissions in the overall Japanese economy rose to 1,307 million tons in 2011, 3.6% above the 1990 level or 9.6% higher than the target. This is because, following the 2011 earthquake and tsunami, Japan's consumption of fossil fuels increased due to thermal power generation, which outweighed the reductions in emissions from the transport sector and a decline in greenhouse gas emissions from the manufacturing sector caused by decreased production due to the natural disaster. Faced with this challenge, Tokyo is now determined to achieve reductions in emissions that are 6 percent below the 1990 target.

8. Outlook - Japan will Likely Achieve its CO_2 Emission Target as well as Remain the Global Green Car Leader

The past record suggests that Japan's automakers will continue to aggressively reduce emissions and improve fuel efficiency and create breakthrough technology for NGVs, ultimately obviating the need for fossil fuel engines. Consequently, it seems likely that Japan will remain the global green vehicle leader and hold that position as long as it maintains its strong R&D focus on advancing NGV technologies.

NH_3-$DeNO_x$ Performance of the Composite [Fe-Beta + Fe(Mn)MCM-48] Catalyst: Combining SCR Activity and NH_3 Oxidation Activity for NH_3 Slip Removal

Alexandr Yu. Stakheev[a*], Dmitry A. Bokarev[a], Alina I. Mytareva[a]
[a]N.D. Zelinsky Institute of Organic Chemistry, Leninsky prospekt, 47, 119991 Moscow, Russia
Rajesh Kumar Parsapur[b] and Parasuraman Selvam[b*]
[b]National Centre for Catalysis Research and Department of Chemistry,
Indian Institute of Technology-Madras, Chennai 600036, India
E-Mail: st@ioc.ac.ru; selvam@iitm.ac.in

1. Introduction

Diesel engine vehicles are becoming widespread due to their higher fuel efficiency and lower CO_2 emissions compared to gasoline engine vehicles. However, in view of future legislation of efficient NO_x abatement from the diesel exhaust gas becomes a challenging task, which requires more effective methods of exhaust gas purification. In general, NO_x abatement can be achieved by using a catalytic system comprising zeolite-NH_3-DeNOx catalyst (e.g., Fe-Beta or Cu-Beta) followed by NH_3-slip catalyst. The latter usually contains noble metal components such as Pt or Pd, which are quite expensive.[1] In this study, we made an attempt to replace noble-metal catalyst with mesoporous Mn-containing FeMCM-48.

2. Method

2.1. Catalyst preparation

Microporous Fe-Beta catalyst was prepared by incipient wetness impregnation of H-Beta (Si/Al = 12) with an aqueous solution of $Fe(NO_3)_3{\cdot}9H_2O$ followed by calcination at 550°C in flowing air. The estimated Fe content by atomic absorption spectroscopy was found to be ~ 0.7 wt%.

Mesoporous Mn-modified FeMCM-48 catalyst, designated as Fe(Mn)MCM-48 (Si/Fe = 60) was prepared hydrothermally as per the procedure reported earlier[2] with $Fe_2(SO_4)_3{\cdot}H_2O$ having trace amounts of Mn. The nominal iron content of the sample was 1.5 wt%.

Composite [Fe-Beta + Fe(Mn)MCM-48] catalysts were prepared by thorough mechanical mixing of both Fe-Beta and Fe(Mn)-MCM-48 powders in agate mortar followed by pelletization using hydraulic die. The Fe-Beta : Fe(Mn)MCM-48 component ratio was varied from 1 : 1 to 5 : 1.

2.2. Catalyst characterization

The catalysts thus prepared were systematically characterized by various analytical and spectroscopic techniques such as XRD, BET surface area, DRUV-VIS and ESR. The characterization data indicated that Fe cations in Fe-Beta are located in (exchangeable) cationic positions and the amount of iron oxide species is negligible. On the other hand, the characterization data for Fe(Mn)MCM-48 clearly indicate isomorphous substitution of trivalent iron into tetravalent silicon in the framework structure.

2.3. Catalytic tests

Fe-Beta, Fe(Mn)MCM-48, and the composite [Fe-Beta + Fe(Mn)MCM-48] were tested in NH_3-$DeNO_x$ using a fixed-bed reactor with a feed gas containing 600 ppm NO, 700 ppm NH_3, 10 vol% O_2, 6 vol% H_2O, balanced with N_2 at GHSV = 270,000 h^{-1}. An FTIR GASMET-4000 analyzer was used for the reaction product analysis. Note that the reaction was carried out under NH_3 excess (100 ppm above reaction stoichiometry) for evaluation of NH_3-$deNO_x$ and NH_3-slip removal efficiency.

3. Results and Discussion

Fig. 1(A) depicts the XRD of Fe(Mn)MCM-48. The diffraction pattern shows all the reflections characteristic of cubic MCM-48 structure.[2,3]

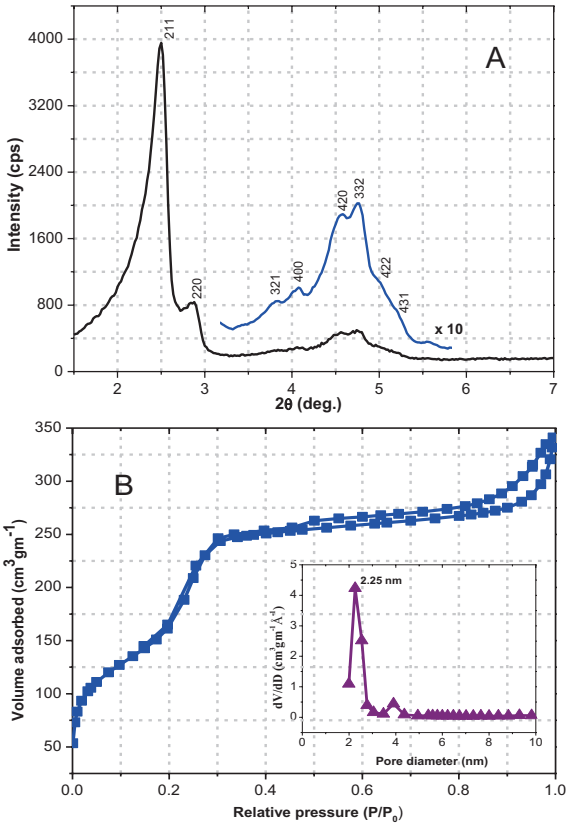

Fig. 1. (A) XRD pattern; (B) N_2 sorption isotherms of Fe(Mn)MCM-48.

Specific surface area and pore-size distribution were obtained respectively by BET and BJH methods. Fig. 1(B) presents the N_2 adsorption–desorption isotherms which show typical type IV pattern with a sharp inflection in the range 0.2–0.3 (P/P_0) corresponds to capillary condensation with uniform mesopores (inset). Further, the isomorphous substitution of trivalent iron in the tetrahedral framework positions was supported by DRUV-VIS and EPR studies (not reproduced here).

Catalytic tests of the plain Fe(Mn)MCM-48 (not shown here) revealed significant activity of the catalyst in NH_3 oxidation, while its activity in NO_x selective catalytic reduction was marginal. It was found that the NH_3 oxidation activity of FeMCM-48 can be additionally boosted by modification with Mn, and hence Mn-modified FeMCM-48 sample, viz., Fe(Mn)MCM-48, was used for the preparation of the composite [Fe-Beta + Fe(Mn)MCM-48].

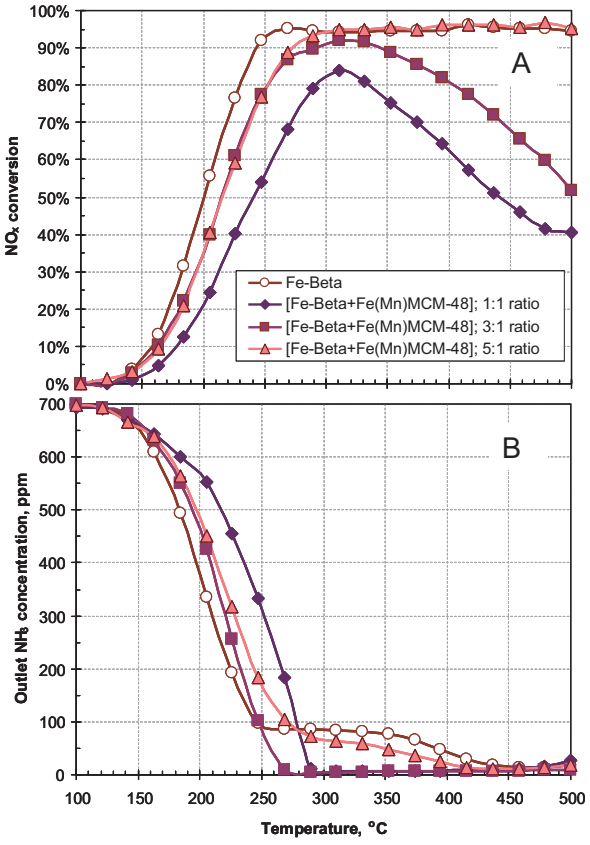

Fig. 2. NH_3-$DeNO_x$ performance of Fe-Beta zeolite and the composites [Fe-Beta + Fe(Mn)MCM-48] with different component ratio. (A) – NO_x conversion; (B) – outlet NH_3 concentration.

NH_3-$DeNO_x$ performance of the composite [Fe-Beta + Fe(Mn)-MCM-48] catalysts having different component ratios are compared in Fig. 2(A). Efficiencies of the catalysts in NH_3 slip removal are compared in Fig. 2(B). [Fe-Beta + Fe(Mn)MCM-48] with 1 : 1 weight component ratio demonstrates efficient NH_3 slip removal, however its oxidation activity appears to be excessive, as indicated by the downward bending of NO_x conversion profile at ~ 300°C. This bending originates from unfavorable NH_3 over-oxidation over Fe(Mn)MCM-48 leading to undesirable NO formation and NH_3 depletion.

Variation of Fe-beta /Fe(Mn)MCM-48 component ratio allows us to minimize the unfavorable NH_3 over-oxidation and to balance activities in NH_3-$DeNO_x$ and NH_3-oxidation. The favorable performance was attained for the composite catalysts with 3 : 1 and 5 : 1 ratios. The data suggest that the performance can be optimized further by careful adjustment of the component ratio.

4. Conclusion

The data on NH_3-$DeNO_x$ performance of the composite [Fe-Beta + Fe(Mn)MCM-48] catalyst indicated that the favorable NO-SCR activity and the efficient NH_3 slip removal can be attained within the wide temperature range. The performance of the composite catalyst can be optimized by variation of Fe-Beta and Fe(Mn)MCM-48 ratio.

References

[1] A. Scheuer et al, Appl. Catal. B, **111-112** (2012) 445.
[2] P. Selvam, S.E. Dapurkar, Catal. Today, **96** (2004) 135.
[3] C.T. Kresge, M.E. Leonowicz, W.J. Roth, J.C. Vartuli, J.C. Beck, Nature, **359** (1992) 710.

Tenth International Conference on Flow Dynamics
November 25-27, 2013, Sendai, Miyagi, Japan

Li-ion Battery Module for Small Electric Vehicles

Hiroshi Matsuo
MICRO VEHICLE LAB.Ltd., 3-3-2-1502 Tosabori Nishi-ku Osaka JAPAN
E-mail: matsuo@mvl.co.jp

ABSTRACT

Li-ion Battery is superior in a characteristic with a high energy density and long cycle life. We try to use these good points and exchange lead acid battery for Li-ion on the small electric vehicles. We report on the development battery module for two kinds of different electric vehicles. As a result, we understand that Li-ion battery influenced the vehicles to be light-weight, and the life of the battery became long.

1. Introduction

The Li-ion battery has been developed as a power supply for a mobile-phone and a small video, notebook-sized personal computer since 1990. It has spread to the most mobile devices recently. A zero-emission design of the State of California atmosphere resources station was announced in the latter half of 1980's, and the development of a fuel cell and the battery car started the application to a movement body, and a car using a lead acid battery and the Ni-MH battery was produced experimentally then. The large-sized Li-ion battery has been developed recently. So, we experimented on the battery exchange to small electric vehicles using the large-sized Li-ion. We report this result.

2. Method

We try to battery exchange from lead acid battery to Li-ion battery on the small electric vehicle. Case-A is use for "COMVOY-88" by MITSUOKA-Motor Company. Case-B is use for "COMOS" by TOYOTA-Body Company. A lead acid battery is used both vehicles. Table 1, 2 shows battery exchange date. Figure 1 is a photo of batteries.

Li-ion cell specification is

Case-A
- Cathode material is Li(Mn/Ni/Co)O2
- Anode material is Carbon
- Rated voltage is 3.6V
- Rated capacity is 15AH
- Weight is 530g
- Dimensions 148x210x6.5mm
- Energy density is 100Wh/kg
- Case is can type

Case-B
- Cathode material is LiMnO2
- Anode material is Carbon
- Rated voltage is 3.7V
- Rated capacity is 10AH
- Weight is 270g
- Dimensions 120x207x6.1mm
- Energy density is 140Wh/kg
- Case is laminating type

Table 1. Case-A "COMVOY-88" battery exchange date

COMVOY-88	Lead Acid	Li-ion
Battery	12V-70Ahx6S	21Sx4P
	72V-70AH	75V-60Ah
Vehicle Weight	236kg	
Battery Weight	129kg	56kg
50km/h run	43.5Ah(62%)	53.0Ah(88%)
	48km	68km
30km/h run	48.8Ah(70%)	58.0Ah(97%)
	67km	102km
Battery cycle life	1.5 years	4years over

Fig. 1 Photo of the Vehicle and Battery in case-A
Lead Acid type (L)/Li-ion type (R)

Table 2. Case-B "COMOS" battery exchange date

COMOS	Lead Acid	Li-ion
Battery	12V-60Ahx6S	21Sx4P
	72AV-60AH	75V-40Ah
Vehicle Weight	284kg	
Battery Weight	126kg	30kg
Battery Capacity	60Ah at 0.2C	40Ah at 0.2C
	43Ah at 1C	39Ah at 1C
Distance per change	50km	55-60km
Battery cycle life	1.5-2.0 years	6years

Fig.2 Lead acid battery in case-B

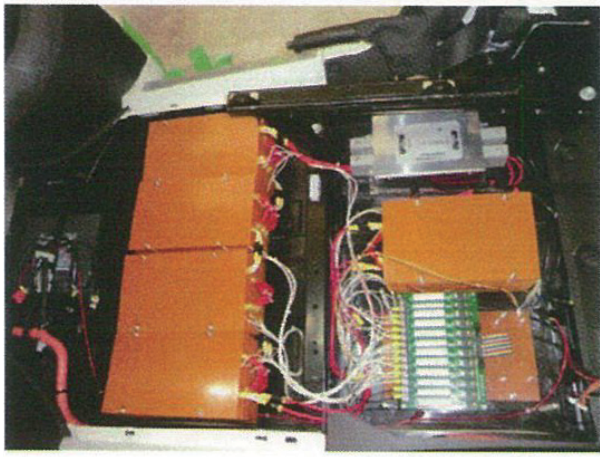

Fig.3 Li-ion battery in case-B

Fig.4 EV " COMS " with Li-ion Battery

3. Results and Discussion

Li-ion battery becomes 25V by 7 series. This voltage is same as two lead acid battery series. It is the same voltage that lead acid battery is 6 years and Li-ion battery is 21 series. The weight energy density of the Li-ion is 3 times of the Lead acid, and large weight loss is possible. In this experiment, light weighting from 70kg to 100kg was possible with small electric vehicles for single passenger.

References

[1] H.Matsuo Large sized Li-ion battery, Mar 2012

Research and Development of Tribological Techniques for Automotive Parts

Naruhiko INAYOSHI, Keiji SASAKI, Ryoichi HOMBO
Material Engineering R&D Division, DENSO CORPORATION, 1-1, Showa-cho, Kariya-shi, Aichi 448-8661, Japan
E-mail of corresponding author: naruhiko_inayoshi@denso.co.jp

ABSTRACT

According to the prevention of global warming and the energy saving policy, the diversification of fuels (bio diesel, ethanol, etc.) for vehicles and the growth of market share of electrical and hybrid vehicles have been increasing. In this paper, a unique in-situ analysis technique and a typical achievement in the fuel tribology related to automotive parts were described as a 1st topic. And as a 2nd topic, tribological and electrical behaviors of a metal containing Diamond-Like Carbon nanocomposite coating deposited on an electrical contact material were discussed.

1. Introduction (topic 1)

As an industrial application, Diamond-Like Carbon (DLC) has been used in various components. Especially, in the automotive application, DLC is used in variety of conditions such as dry, E/G oil and fuel. However, the optimum structure of DLC has not been clarified in each environmental condition.

Recently, we have developed an in-situ system to observe the behavior of lubricant during friction by combining the fast-scan Fourier transform infrared attenuated total reflection (FTIR-ATR) spectrometer with the friction equipment as shown in Figure 1 [1]. In this study, we will report the experimental data of structural changes of DLC in various conditions as measured using the in-situ observation system.

2. Experiment (topic 1)

The infrared spectra were obtained by two experiments, annealing test and in-situ friction test. The annealing test was conducted at 500°C for 2hr. Table 1 shows the test condition for in-situ friction test.

3. Results and Discussion (topic 1)

Figure 2 shows the infrared spectra after annealing at 500°C. We have assigned bands of DLC with some papers (e.g. [2]). The spectra after anneal test shows the large change at ca. 1100 cm-1 which represented the aroma structure and ca. 1600 cm-1 corresponding to sp2 conjugated C=C. It is clarified the graphitization and aromatization are caused by the high temperature.

The intensity of the band at 1600 cm-1 and the friction coefficient obtained by using in-situ observation system are shown in Figure 3. In the running-in region, the intensity of sp2 band obviously increases. The intensity of aroma band also increases during friction. However the behavior of sp1 band intensity is difference between anneal test and friction test. The sp1 band intensity decreases as the temperature rises. In contrast, that intensity increases during friction (Table 2).

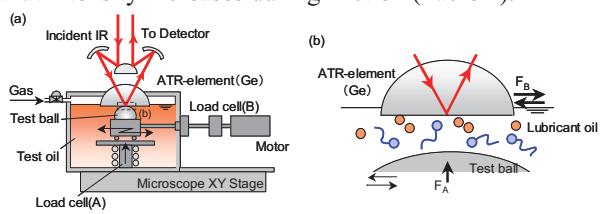

Fig. 1 Schematic diagram of in-situ observation system

Table 1. Experimental conditions

Specimen	a-C:H (on S45C Cylinder)
Speed	0.5mm/s
Load	55N (125MPa)
Time	6hr

Table 2. Structural changes of DLC for each test

	Aroma	sp1C-C	sp2C=C	sp3CH_3
Annealing	+	-	+	-
Friction	+	+	+	-

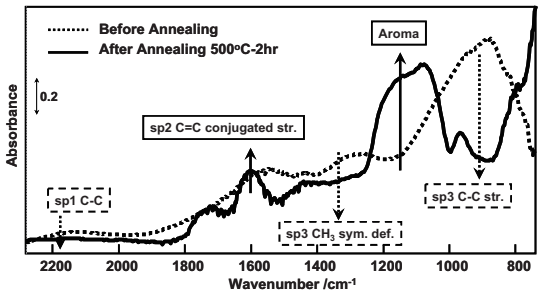

Fig. 2 Infrared spectra after annealing

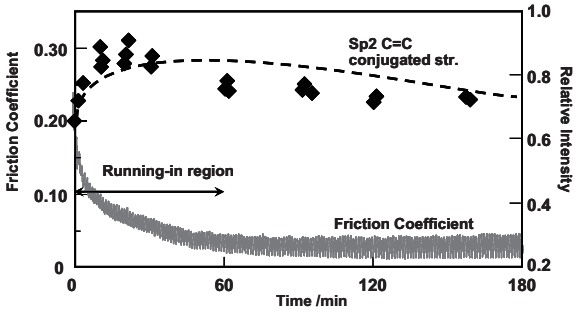

Fig. 3 Time dependence of band intensity and COF

4. Summary (topic 1)

The structural changes of DLC under friction were researched. The experimental results clearly show that friction induces the structural changes of DLC.

5. Introduction (topic 2)

Demands for innovative technology on electrical contacts in vehicles have been increasing with the growth of market share of electrical and hybrid vehicles. Reducing the electrical contact resistance (ECR) and the coefficient of friction (μ) are the major technological issues. In this study, tribological and electrical behavior of a copper containing Diamond-Like Carbon (Cu-DLC) nanocomposite coating deposited on a brass (Copper-Zinc alloy) substrate was investigated.

6. Experiment (topic 2)

Experimental materials and conditions are shown in Table 3. A hybrid deposition process, coupling plasma enhanced chemical vapor deposition and DC magnetron sputtering of a copper target, was used for the deposition of the Cu-DLC [3]. A brass ball was used as the counterpart of the Cu-DLC. The tribological and electrical contact behavior was investigated by using a ball-on-plate linear reciprocating tribometer. The four-terminal method was used for the measurement of ECR between the ball and the plate during the tribo-test. A combination of an uncoated brass plate (the substrate of the Cu-DLC coating) and a brass ball was performed for comparison purpose.

7. Results and Discussion (topic 2)

Figure 4 and Figure 5 show the typical ECR, μ responses of each material combination, respectively.

In the case of the uncoated brass plate, ECR was initially around 50 milliohms but it decreased down to 1.0 to 2.0 milliohms after few cycles. The initial value of μ was approximately 0.3 and it increased rapidly to around 0.8 after few cycles. After, the variations of ECR and μ around these average values were relatively wide.

In the case of the Cu-DLC, while initial value of ECR was hundreds of milliohms, it gradually decreased with cycles and reached 1.5 to 2 milliohms after 600 cycles. μ started below 0.35 and decreased progressively, and stabilized around 0.25, also after 600 cycles. Observation of worn surfaces of the different number of sliding cycles reveals that a tribofilm was built up on the sliding surface of the ball, and it grew as the sliding cycle increased, consisting mainly of copper according to energy dispersive X-ray spectroscopy. The Cu-DLC coating on the plate wore gradually and delamination of the Cu-DLC was observed at 450 cycles. Around this number of cycles, ECR started decreasing, suggesting that such decrease resulted from the delamination of the Cu-DLC coating. After less than 1000 cycles, the Cu-DLC was almost worn out. However, detrimental effects could not be observed either on ECR or on μ. So the tribofilm on the ball should have a key role in achieving and preserving these good electrical and tribological characteristics.

8. Summary (topic 2)

The electrical contact resistance and the coefficient of friction behavior of a Cu-DLC nanocomposite coating deposited on a flat brass substrate with a brass ball combination were investigated. A Cu-rich tribofilm was built up on a brass ball by sliding with a Cu-DLC deposited on a brass substrate. This tribofilm provides the good tribo-electrical characteristics.

Table 3. Experimental materials and conditions

Materials	Ball (φ6.35mm)	Brass	
	Plate (20 x 20 x t0.5mm)	Brass (uncoated)	Cu-DLC (brass substrate)
Conditions	Normal load	1N	3N
	Track length	0.8mm	
	Frequency	0.5Hz	
	Electrical current	0.2Amps	
	Sliding cycles	up to 2000	
	Atmosphere	Ambient air (20-25 °C, 25-35%RH)	

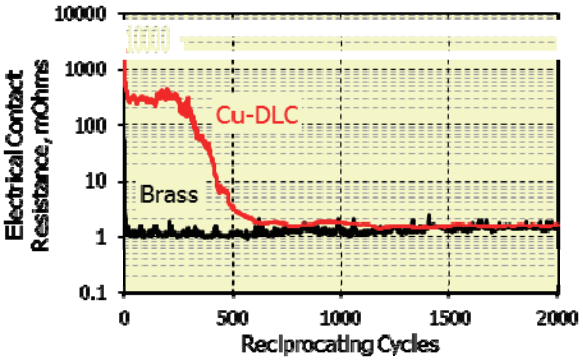

Fig. 4 Electrical contact resistance

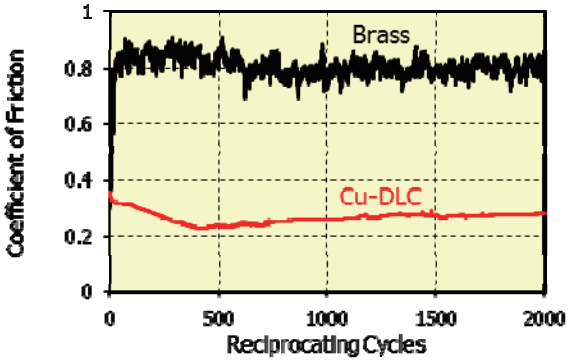

Fig. 5 Coefficient of friction

References

[1] Keiji Sasaki, Naruhiko Inayoshi, Kohji Tashiro, Rev. Sci. Instrum., 79, 2008, 123702.

[2] Thibaut Heitz, Bernard Drévillon, Christian Godet, Jean-Eric BouréeThibaut, Physical Review B, 58, 1998, 13957.

[3] Takanori Takeno, Toshifumi Sugawara, Hiroyuki Miki, Toshiyuki Takagi, Diamond and related materials, 18, 2009, 1023-1027.

Tenth International Conference on Flow Dynamics
November 25-27, 2013, Sendai, Miyagi, Japan

Starved Lubrication: Contribution of Laser Surface Micro-Texturing

Florian Brémond[1)*], Denis Mazuyer[2)] Philippe Maurin-Perrier[1)], Juliette Cayer-Barrioz[2)]
[1)] IREIS, rue Benoît Fourneyron, CS 42077, F-42162 Andrézieux-Bouthéon cedex, France
[*]Corresponding author: fbremond.ireis@hef.fr
[2)] Laboratoire de Tribologie et Dynamique des Systèmes, UMR5513 CNRS, Ecole centrale de Lyon,
36 avenue Guy de Collongue, F-69134 Ecully cedex, France

ABSTRACT

To prevent the occurrence of wear and the increase in friction in case of lubricant starvation between two surfaces in contact, this study demonstrates experimentally the possibility to create oil feeding in the high pressure zone, by controlling the micro-topography of the surfaces. Thanks to a femtosecond laser, micro-cavities are generated on the surface and locally increase the lubricant film thickness.

1. Introduction

The ability of a fluid to separate two surfaces in contact under severe mechanical conditions is outstanding. However, the persistence of this protective film will be challenged in case of inadequate contact feeding in lubricant, that is to say when starvation occurs. Although various experimental [1,2] and numerical [3] studies have focused on starvation and replenishment mechanisms under stationary conditions, only little work has taken into account transient conditions.

The goal of this paper is to evaluate the contribution of a laser micro-textured surface to maintain a lubricating film and to prevent wear. We also analyze the onset of partial starvation based on an effective feeding volume in the convergent zone. The consumption of this volume leads to severe starvation regime.

2. Experimental

In this context, starvation mechanisms in elastohydrodynamic regime were experimentally investigated in pure rolling, in rolling/sliding and also reciprocating conditions for fluid viscosity ranging from 50 to 3000 mPa.s. Thanks to a ball/disk tribometer [4] with an optical interferometric system, the convergent, contact and outlet zones are simultaneously visualized (see Figure 1), and the film thickness distribution and the friction force in the high pressure zone under controlled contact kinematics are measured.

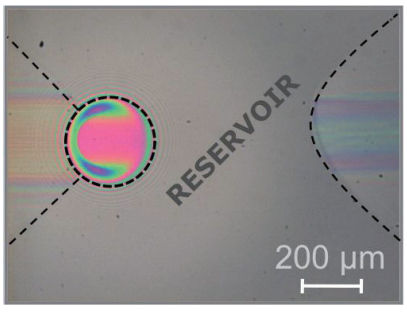

Fig.1 EHL contact. The air/lubricant meniscus is clearly visible in the inlet zone. The flow direction goes from right to left.

Occurrence of starvation will be discussed in terms of film thickness, location of the air/lubricant meniscus and friction.

3. Results and discussion

Severe starvation occurs when an effective volume of lubricant in the convergent zone is consumed: the film thickness decreases and the friction force simultaneously increases. We show that starvation process is function of two time scales. For short time, inferior to 1s, the film thickness and the location L_M of the air/lubricant meniscus are correlated as shown in Figure 2. For longer times, few hundreds of s, a progressive diminution of the film thickness down to few nanometers in the contact zone results from the lubricant deficit induced by the ratio leakage/flow rates. This decrease of the film thickness causes the occurrence of wear in the contact. In presence of a laser micro-textured surface, the shearing of the lubricant entrapped in the micro-geometries is able to provide a local increase of the film thickness, protecting the mating parts. The ability to diminish wear is governed by the density and the depth of micro-texturing.

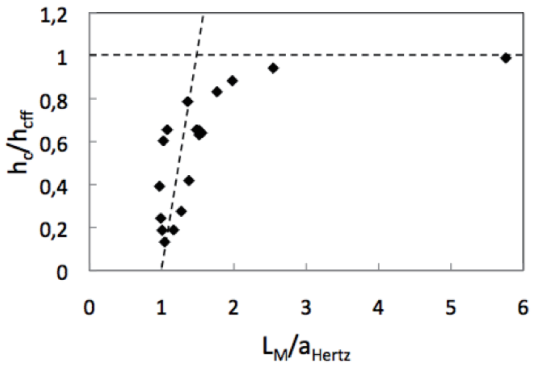

Fig.2 Correlation between the central film thickness h_c and the location of the air/lubricant meniscus L_M.

4. References

[1] Chiu, Y.P., "An analysis and prediction of lubricant film starvation in rolling contact system", ASLE transactions, vol. 17, 22 – 35, 1974.

[2] Guangteng, G. and Can, P.M.E. and Spikes, H.A., "A study of parched lubrication", Wear, vol. 153, 91 – 105, 1992.

[3] Chevalier, F. and Lubrecht, A.A and Cann, P.M.E and Dalmaz, G., “The evolution of lubricant film defects in the starved regime”, Proceedings of the 24th Leeds-Lyon Symposioum of Tribology, vol. 34, Tribology series, 233-242, 1998.
[4] Bou-Chakra, E. et al., “A non-Newtonian model based on Ree–Eyring theory and surface effect to predict friction in elastohydrodynamic lubrication”, Tribology International, 43, 9, 2010, 1674-1682.

Tenth International Conference on Flow Dynamics
November 25-27, 2013, Sendai, Miyagi, Japan

Traffic Management Future

Reinhard Pfliegl
A3PS Austrian Association for alternative Propulsion Systems, Vienna, Austria
reinhard.pfliegl@a3ps.at

ABSTRACT

The economic development in the last 100 years have been mainly enabled by the improved mobility options for persons and goods due to the development of efficient vehicles and provision of transport infrastructure for road, rail, air, maritime and inland waterways. Whilst the number of vehicles today excessively increased beyond one billion adverse effects occurred on safety, efficiency, sustainable use of natural resources, environment and economy. The development of new technologies mainly will allow new regimes in traffic management will to reduce the negative impacts towards a more sustainable mobility of persons and goods.

1. Introduction

Mobility supported by engines has started around 200 years ago with development of steam driven locomotives for transportation of persons and goods. Around 50 years later Maritime transportation changes from wind driven vehicles towards engine driven with similar propulsion principles. Again 50 years later a new generation of engines with ignition principle could be built much smaller and less weight applicable for road vehicles and finally about 30 years later this type of engine have been applicable also for a new generation of aircrafts. In parallel to the development of vehicles it was also necessary to develop a dedicated transportation infrastructure for rail, road, maritime and air transportation (Rail tracks, dedicated roads for road vehicles, ports and air ports). This (technological) development has built the basis for the economic development globally but also was building the basis for the motorized armed forces where the mankind has suffered dramatically in the last 100 years also globally.

2. Technological Development

The technological development induced the production of a huge number of vehicles – specifically in the last five decades-we now can see around the globe. Today we account about 1bn road vehicles, about 180mio rail vehicles, about 80mio ships all sizes and more than 10mio aircrafts requiring an adequate infrastructure to be operated. The investment on transport infrastructure in the last 5 decades has been enormous in all countries and is expected to grow even further due to aging of infrastructure and the demand to extend their capacity to balance the demand. Beside all financial effort we experience a decreased efficiency in transportation and still a much too high number of fatalities and injuries due to accidents in transportation. The European Commission counts the economic loss due to inefficient traffic (traffic jams, loss of workforce by delays, etc.) to about 120bn€ annually and economic loss on social level due to fatalities and injured person to about another 130bn€ annually. Similar figures have been reported from the USA on their economy. Today's most urgent demand beside the significant reduction of GHG emission induced by transport is to increase efficiency and safety in transportation on short notice.

Therefor the organisation of transport (generally addressed as traffic management) on all modes need to be carefully analysed and measures to be identified to improve safety and efficiency specifically in view of the most recent technologies emerged in the last 2 decades.

3. Advances in Traffic Management

Analysing the principles in organizing traffic on the different mode in a general manner one can easily conclude two diverse regimes.

1., A strictly centralised regime as for rail and air traffic – 'the vehicle is only allowed to move with dedicated (individual) advise from a central management point (via signal or message) and

2., A so-called 'decentralized' regime, as there is only an indirect way to impact vehicle movement (e.g. via traffic lights, road side signs, etc.) – 'the vehicle move on the command of the driver more or less independent from centralized advise only steered by some general rules (not addressing each vehicle individually)'.

The first regime applies for rail traffic management and air traffic management, the second regime applies for road traffic management and for maritime and inland waterway traffic management.

In view of the most recent technological developments on all transport mode - the so called 'co-operative systems' - one can see a significant change in organizing traffic for the near and long term future. The key enabler for this 'co-operative systems' in transport are the automated exchange of messages between vehicles (V2V) and between vehicle and infrastructure (V2I). Based on the experience we have made so far in the developments of the last decade globally we will need an additional element to organize traffic in a safe and efficient manner. This element is the 'autonomous function' to allow the vehicle to drive automatically within a limited sphere.

4. Summary

Due to the increasing technological capability of electronic systems based on efficient data capture by sensors, fast processing of mass data and automated data/message exchange between vehicles and infrastructure (e.g. DSRC, GNNS, digital maps, etc.) new ways to 'organise' traffic can be developed. Introducing the 3 elements (V2V, V2I, and autonomous function) will consequently influence the above

mentioned divers ‘traffic management regimes’ to a new harmonised single approach on traffic management equally applicable to all mode of transport (road, rail, air traffic, maritime and inland waterway traffic). This will allow manage traffic in an integrated way across all modes without traffic jam and respect to utmost utilisation of infrastructure capacity while increasing safety of transportation with the goal for zero accidents on road, rail, air and waterways maritime transportation.

Tenth International Conference on Flow Dynamics
November 25-27, 2013, Sendai, Miyagi, Japan

Tribology for the Future: Biomimetism and Surface Engineering

Philippe KAPSA
Laboratoire de Tribologie et Dynamique des Systèmes, UMR 5513 CNRS ECL ENISE, Ecole Centrale de Lyon, Bât. H10, 36 avenue Guy de Collongue 69134 Ecully cedex, France
Philippe.kapsa@ec-lyon.fr

ABSTRACT

While Mechanics can be considered as the science permitting the solids to support forces by contacts, Triblogy is the science, which permit the motion of solids. Tribological processes are always dissipative; a friction force is opposed to the motion and then creating an energy loss. As a consequence, engineers are always trying to lower the friction force in order to decrease the energy losses. This objectives associated to a search of increasing the lifetime of mechanical systems are in fact a challenge for the future Tribologists. Considering some systems from the nature can help to find some interesting ideas for surface engineering.

1. Introduction

The word Tribology was defined in 1968 but the "tribology" fact is very old. As soon as men for their daily activities used the contact between solids and motion, the tribological problems were present: friction force and wear, with their negative consequences.

At first, Tribology was not considered as a problem but people optimize the tribological systems step by step by performing simple dedicated experiments. An example is shown Fig. 1.

Fig. 1 Already at the Egyptian time lubrication was used to decrease the friction force. (transporting the statue of Ti – from a tomb at Saqqara – 2400 B.C.)

Then, people realize that contact between solids and friction exists and that friction and wear is a consequence of the interaction between the surfaces of matting solids. More sophisticated experiments where then developed in order to have information on friction and wear.

After that, the society was more and more developed for mechanical systems and tribological problems were more and more studied. It was then considered that material nature is important for the behavior and performances of tribological systems.

Surfaces appear after this period to be also a determinant factor… and then scientists were studying more and more the surfaces in order to find some way to improve their behavior (Fig. 2).

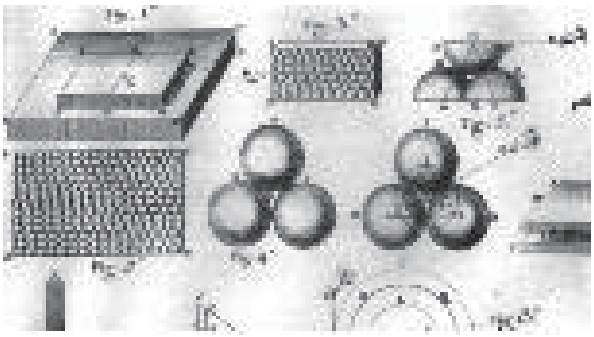

Fig. 2 In 1737 Tribologists begin to consider that the surface topography is an important parameter for friction processes. Belidor, a French scientist, represented the surface geometry using some ideal spheres.

The more simple was first to develop surface treatments in order to modify their mechanical properties; then various surface heat treatments were invented to form at the surface of metals some ompound with higher mechanical properties than the substrate. After, more complex strategies were developed to protect a solid surface by a coating with particular nature, structure and properties (see an example Fig. 3). Consequently, the tribological behavior is considered to be related to the behavior of coated surfaces. Of course, the adherence of the coatings appeared to be very important. In this period, very numerous coatings were investigated: hard coatings, soft coatings, multilayer coatings, composites coatings… always now, this strategy of protecting a sliding surface by a coating is under investigation in order to develop new and high-performence solutions.

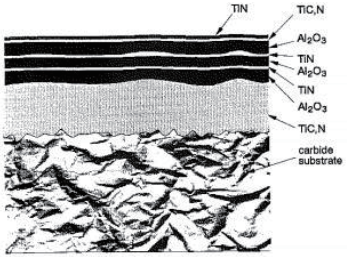

Fig. 3 An example of a multilayer coating for protecting cutting tools (cross section observed with a SEM).

More recently, surface topography was a parameter becoming of the first interest. Studies are trying to understand the relationships between surface topography and friction force and surface damage (Fig. 4). Machining surfaces with conventional machines was investigated: it becomes important to know what is the effect of machining parameters on the characteristics of the machined surface. Particular surface treatments such as sand blasting where used to modify the surfaces.

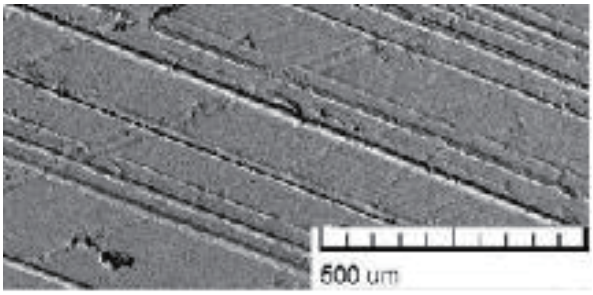

Fig. 4 Surface topography used for the sliding internal surface of diesel engine liners. Scratches with various sizes, which can act as lubricant reservoir and wear particles retainer, compose the particular roughness, manufactured by Honing.

With the development of machining technologies, scientists try to manufacture textured surfaces at a scale being smaller and smaller. Currently, the femto second laser can be considered as one of the most sophisticated machine tool for modifying surfaces; it can be used to create networks of very small holes in order to improve the behavior of surfaces in lubricated conditions (Fig. 5).

In a parallel way, the nature was in fact also optimizing the things in order to adapt them to a function. The structure, the materials and the surfaces are naturally designed in order to present the desired function: adherence, friction noise, mechanical resistance, wettability, colors, … many examples can be considered for this (Fig. 6).

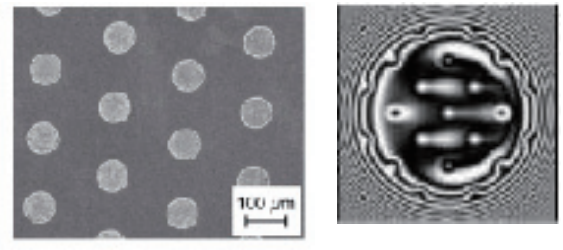

Fig. 5 Laser texturing can be used for tribology: creation of small dimple on a surface (left). This particular topography modifies the lubricant film formation in the case of elastohydrodynamic lubrication (right: result of modeling the film thickness).

(PhD of L Mourier, ECL - 2006)

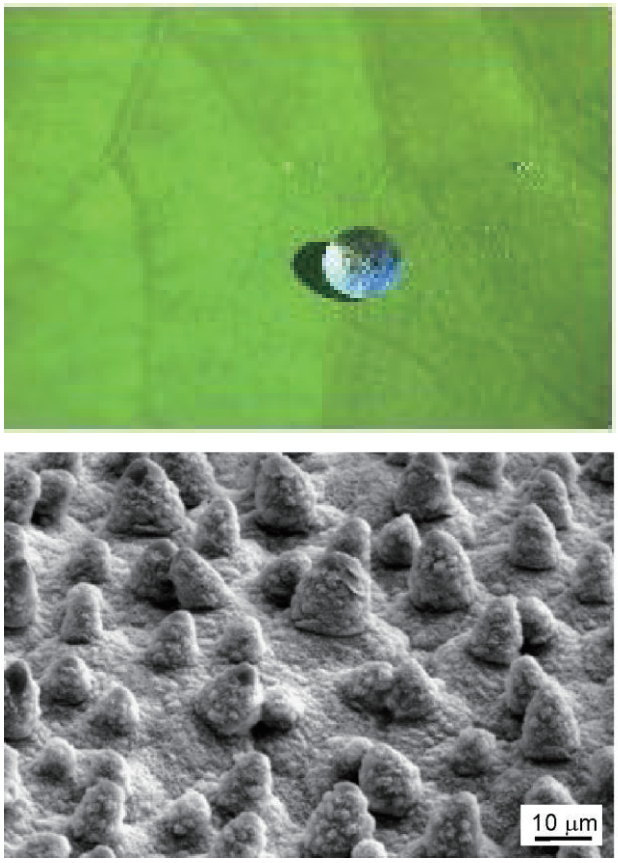

Fig. 6 Observation of a water drop on a Lotus leave (top) showing the super hydrophobicity created by the roughness and nature of surface (SEM picture, bottom).

Then, scientists and tribologists considered the idea of biomimetism. They try in fact to imitate the nature to have some particular function. But now, it is very important to think about the real challenges in the field of Tribology.

2. Future Trends in Tribology

Nowadays, Tribologists have developed a lot of effort to understand tribological processes with the use of high-performent equipements and complex modeling. Predictions are then more and more present but it is always necessary to continue theses efforts.

The present challenges are to develop mechanical systems with high output (low friction losses) and long lifetime. In the field of automotive industry, this challenge has also to be completed by considerations on production costs, recyclability and ecology.

With these aims, surface modifications represent a very attractive strategy. The development of new surface coatings and new surface topography is always a key problem for the future. We have for this to consider not only scientific progress in the field of surface science but may be interesting ides can be found in the nature to optimize a surface for a given purpose.

Tenth International Conference on Flow Dynamics
November 25-27, 2013, Sendai, Miyagi, Japan

Synthetic Biofuels From Biomass

Joachim Knebel[1], Nicolaus Dahmen[2], Jörg Sauer[2]
Karlsruhe Institute of Technology (KIT)
Chief Science Officer (CSO)[1], Institute for Catalysis Research and Technology (IKFT)[2]
Hermann-von-Helmholtz Platz 1 – 76344 Eggenstein-Leopoldshafen – FR Germany
joachim.knebel @ kit.edu

ABSTRACT

The importance of biofuels is growing rapidly in Germany and world-wide. This is reflected in steadily increasing research activities in both academia and industry, as well as in an increasing number of joint ventures comprising several institutions. Thus, not only the extent of publications on this highly dynamic topic is strongly increasing but also the public interest due to its obvious socioeconomic relevance. First generation biofuels such as bioethanol and biodiesel are state of the art today. However it is obvious that neither the quantity nor the quality are sufficient to meet the production potential and the standards expected. The second generation currently under development aims at the use of lignocellulosic feedstocks by-produced in agriculture and forestry. Third generation biofuels are issued in diverse research activities ranging from microbial fuels or algal fuels.

1. Introduction

The bioliq® project at the Karlsruhe Institute of Technology (KIT) aims at large scale production of synthetic second generation biofuels from biomass (BTL, biomass to liquids). The bioliq process concept has been designed to overcome scientific challenges and engineering problems, which arise when low grade, residual biomass shall be used to a large extent in a BTL process. Biomass such as straw, hay or residual wood usually exhibit on the one hand low energetic densities, thus limiting collection area and transportation distances. On the other hand, the production of synthetic fuels requires large scale production facilities in accordance with economy of scale considerations. In the bioliq process, biomass is pre-treated in regionally distributed fast pyrolysis plants for energy densification. The products, being pyrolysis char and liquid condensates, are mixed to form stable, transportable and pumpable slurries also referred to as biosyncrude. Biomass is thus energetically concentrated allowing economic transport also over long distances. In industrial plants of reasonable size, the biosyncrude is gasified in an entrained flow gasifier at a pressure slightly above that of the following fuel synthesis. In the bioliq pilot plant synthetic fuels are produced via methanol as an intermediate. The process requires a gasification pressure of up to 80 bar.

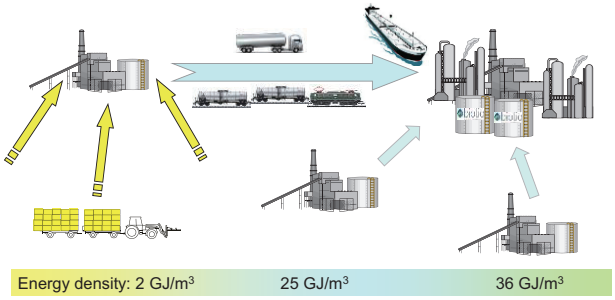

Fig. 1 bioliq concept

On site of KIT, a pilot plant is constructed for process demonstration, to obtain reliable mass and energy balances, for gaining practical experience, and to allow for reasonable cost estimates. The fast pyrolysis plant, already in operation, has a biomass feed capacity of 500 kg/h (2 MW(th)). A twin-screw reactor, equipped with a pneumatic heat carrier loop with sand as the heat carrier medium is the main technical feature of the plant. The biosyncrude is prepared in a specially designed colloidal mixer and stored in stirred container tanks. To prevent from potential sedimentation, the content of the tanks is continuously circulated.

The further process steps have been mechanical completed and commissioned separately in 2013. The high-pressure entrained flow gasifier is designed for 5 MW_{th} (ca. 1 t/h) slurry feed and can be operated at up to 80 bar. The burner is equipped with a twin fluid injection nozzle using oxygen and steam as atomization and gasification media. A 1 MW_{th} burner fed with natural gas is used for process stabilization, e.g. when using low calorific fuels or slurries with a wide and varying specification range. The pumps are designed to feed suspensions with up of 5 Pas viscosity, the burner nozzle is designed for a maximum viscosity of 1 Pas. The gasifier is specifically designed for lower fuel calorific values in the range of 13 - 25 MJ/kg. For adjustment of viscosity the biosyncrude can be heated up to 120 °C in the feed line to the burner nozzle. The gasifier is operated in slagging mode and is equipped with an internal cooling screen, particularly suited for conversion of ash rich feeds and fast start up and shut down procedures. Ethylene glycol slurries with char can be used as model fuel for scientific research. Ash and flux can be added to the fuel feed flow in order to adjust slag melting behavior.

The raw synthesis gas is purified and conditioned by a high pressure hot gas cleaning system, consisting of a hot gas filter with ceramic filter elements, a fixed bed adsorption for HCl and H_2S removal and a catalytic converter for decomposition of nitrogen and sulphur containing trace compounds. Afterwards, CO_2 and water

are separated. The purified synthesis gas is then converted to dimethylether in a one-step synthesis process, which is converted in a subsequently following reaction into gasoline. A ZSM-5 zeolite-type of catalyst is used here. In all reactors, a new heat pipe based system is used for heat exchange, providing nearly isothermal conditions in the catalyst bed and improving process control.

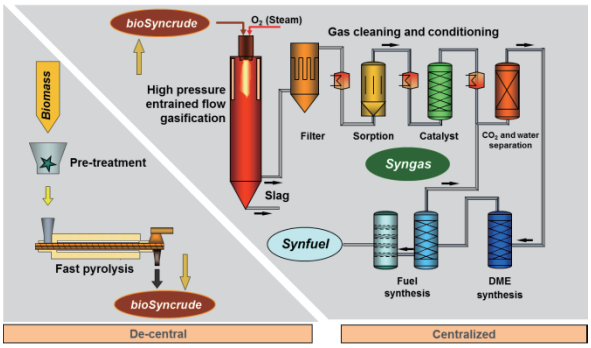

Fig. 1 bioliq process scheme.

Based on mass- and energy balances, an economic analysis of the whole process chain has been performed and will be worked out in more detail when experimental data from the pilot plant become available. Depending on the plant configuration and the selected production scenario and synthesis concept, overall process energy efficiencies from biomass to fuel between 34% and 42% have been estimated.

The process development is embedded into a coherent R&D framework, allowing for scientifically based operation and further development. Process development units for pyrolysis, gasification, gas cleaning and synthesis are utilized to increase the fundamental understanding of the underlying processes, to obtain representative product materials and process data, to develop technical improvements and new process variants, which then can be tested in the pilot plant.

Fig. 2 bioliq pilot plant at KIT.

Acknowledgements

The bioliq pilot plant is constructed and operated in cooperation with partners from chemical engineering and plant construction industries: Lurgi GmbH (Frankfurt), MAT Mischtechnik GmbH (Immenstadt) MUT advanced heating GmbH (Jena), and Chemieanlagenbau Chemnitz GmbH (Chemnitz). Financial support is provided by the Germany Ministry of Agriculture, Food, and Consumer Protection (BMELV) and the state Baden-Württemberg und the European Development Fund.

References

[1] E. Dinjus, U. Arnold, N. Dahmen, R. Höfer, W. Wach; Green Fuels – Sustainable Solutions for Transportation, in: RCS Green Chemistry No. 4: Sustainable solutions for modern economies, R. Höfer (Hrgb.), S. 125-163, RCS Publishing, London, 2009.

[2] N. Dahmen, E. Henrich, D. Dinjus, F. Weirich
The bioliq bioslurry gasification process for the production of biosynfuels, organic chemicals, and energy, Energy, Sustainability and Society 2:3 (2012) Springer Open Journal
(www.energysustainsoc.com/content2/1/3), 44 pages

Tenth International Conference on Flow Dynamics
November 25-27, 2013, Sendai, Miyagi, Japan

VEHICLE TECHNOLOGY & ENERGY CENTRE
Canadian Applied Research Experience at Red River College

Ray Hoemsen, M.Sc., FEC, P. Eng.
Director, Applied Research & Commercialization
Red River College of Applied Arts, Science and Technology
Winnipeg Manitoba CANADA
RHoemsen@rrc.ca

ABSTRACT

Red River College, a recognized Canadian college leader in applied research, has demonstrated capabilities and expertise in vehicle technology and the use of renewable fuels – with an emphasis on performance in extreme climates, especially cold. Local, national and international partners have collaborated on vehicle-related product and prototype development, fleet demonstrations, testing and evaluation, and the use of renewable or zero/low emission fuels (such as biodiesel, hydrogen, and electric/hybrid technologies). A case study will illustrate the College's integrated research, education and training approach to *Mobility from "Green Energy"*.

1. Introduction

Red River College's integrated approach to research, education and training approach for *Mobility from "Green Energy"* has resulted in extensive experience in advanced transportation and energy-related applied research over the last decade.

In close proximity to the geographic centre of North America, the College's main campus is in Winnipeg, Manitoba, Canada (on approximately the 50th parallel) and can experience extreme temperatures in both the summer (35ºC) and winter (-35ºC). The opportunity to evaluate fuels and technologies in a cold climate environment has encouraged research on vehicles which use renewable and alternate fuels.

Cold climate and/or renewable fuels are often key elements in many applied research activities [1] such as the Red River Raycer (solar car); Hybrid Hydrogen Internal Combustion Engine and Hydrogen Fuel Cell bus demonstrations; Plug-in Hybrid Electric (passenger) Vehicle fleet conversion, demonstration and evaluation; diesel highway coach prototypes to meet new emission requirements; Compressed Natural Gas heavy vehicle winter performance evaluation; and development, demonstration and evaluation of an all-electric battery transit bus prototype. These projects complement the $2,400,000 (CDN) investment by the Government of Canada in vehicle technology research infrastructure.

In 2011, the Province of Manitoba provided $645,000 to establish the Electric Vehicle Technology & Energy Centre. EVTEC is a virtual centre which complements and supports provincial policy [2] concerning sustainable transportation. EVTEC serves to test and demonstrate electric vehicle technologies, while allowing the College to enhance applied research, education and training, as well as to raise public awareness of electric vehicle (EV) technology. EVTEC's startup was catalysed by a three-year, $3,000,000 international collaboration to develop an all-electric transit bus and charging system. Subsequent initiatives have led resulted in a $10,000,000 investment for a five vehicle, four-season, four-year demonstration under regular urban transit system operating conditions.

2. Discussion

Nearly 98% of Manitoba's electricity is generated from renewable hydro power, which is a key driver to pursue EV technology. In late 2010 Manitoba and Mitsubishi Heavy Industries of Japan signed a Memorandum of Understanding with the objective of exploring renewable energy development opportunities; including the electrification of transportation and recharging infrastructure, as well as battery-storage technologies.

An international consortia was created and brought together the Province of Manitoba, Manitoba Hydro, Mitsubishi Heavy Industries (MHI), New Flyer Industries (NFI) and Red River College to undertake the development of an all-electric battery transit bus, including the related charging infrastructure, with the ensuing research to be carried out through EVTEC. Anticipated benefits of the "Zero Emissions" bus are:

- only two tonnes of greenhouse gas emissions (from a renewable supply), compared to 108 tonnes for a diesel-electric hybrid and 162 tonnes for conventional diesel;
- assurance of a long-term renewable fuel supply;
- overall energy efficiency improvements, including electrification of ancillary accessories and improved drive train efficiency; and
- longer life and lower maintenance requirements due to reduced maintenance when compared to conventional engines, transmissions and accessories, coupled with longer drivetrain life.

Within one year, the prototype "Zero Emissions" bus (Figure 1), which integrates lithium ion battery packs from MHI in a NFI Xcelsior chassis, was operational. The batteries provide direct current power to a nominal 650-volt system, using an air-cooled 120 kWh battery which is ultimately targeted to be a comparable weight range as the engine and fuel on a diesel bus. The prototype has a range of 80 kms/four hours in typical stop-and-go transit operation, and is the first of its kind in Canada. The prototype has near zero emissions, although a bio-diesel heater is required in winter operation to heat the interior of the bus.

.

Fig. 1 Electric battery transit bus prototype – June 2012

Manitoba Hydro has completed installation of a first generation On Route Rapid DC charger with a dual module output design which is targeting 300 to 500 kW.

Initial validation and testing of the prototype vehicle over a two-year period in Winnipeg has begun, operating primarily on a private route shuttling Manitoba Hydro employees between its current and former head office locations. [3] Initial in-field prototype operating performance test results indicate:

- an overall average energy consumption of 133.kWh/100km;
- HVAC consumption of 32 to 45 kWh/100 km at 35°C ambient; and
- sound (noise) output ranging from 50 dBa at idle (all systems operational) to 61 dBa when at full-throttle acceleration.

The additional energy requirement for winter heating of the interior when using electric heating will drive energy consumption to over 300 kWh/100 km. This high consumption limits available range and increases charging frequency, which in turn limits battery life and increases costs. An alternative is catalytic diesel or bio-diesel heaters with 85 to 90% thermal efficiency.

In late October, 2012 New Flyer Industries was awarded $3.4 million by Sustainable Development Technology Canada to work with the other members of the consortium, as well as Winnipeg Transit; to develop and deploy four additional prototypes and a high capacity charging system by the end of 2013. A four-year evaluation period, while in revenue service, will follow to assess the high capacity charging station, battery capacity and component life and reliability. Red River College is working directly with Mitsubishi Heavy Industries and New Flyer Industries on the integration of the battery packs for two bus prototypes.

In summary, through the combined efforts of the consortium partners, one prototype has been completed and four others are under development. Validation testing of the first prototype has completed its first year. A rapid DC charger for on route use has been deployed. NFI has demonstrated the prototype across North America; and was awarded a contract by the Chicago Transit Authority for two battery electric buses, as well as electric hybrids to other properties.

3. Conclusions

Initiatives such as EVTEC directly complement and support Province of Manitoba policy concerning sustainable transportation; and enable electric vehicle applied research and innovation amongst Manitoba's transportation sector; enhance electric vehicle education at the College and in the region; and increase public awareness of EV technology. [4] Opportunities for future study include the repurposing of ground vehicle batteries for stationary applications, determination of appropriate business models, and the availability of commercial-grade, high-capacity, fast-charging infrastructure, and passenger EV end-of-life.

With a strong industry network and a history of partnering with to conduct practical applied research projects, the College is applying its successful model of supporting innovation to enhance and improve vehicle performance, reduce emissions and integrate the use of renewable and/or alternate fuels. The pursuit of *Mobility from "Green Energy*" has advanced vehicle technology and renewable energy research, development, testing and manufacturing capabilities in Manitoba.

4. Acknowledgements

Red River College greatly appreciates the generous support provided by the Government of Canada (including the Department of Foreign Affairs and International Trade, the Natural Sciences and Engineering Research Council of Canada, the National Research Council of Canada and Western Economic Diversification), the Province of Manitoba (the Council on Post-Secondary Education, Manitoba Innovation Energy and Mines, and Manitoba Entrepreneurship Training and Trade) and local, national and international industry partners such as Atomic Energy of Canada Limited, the Centre for Emerging Renewable Energy, Kraus Global Industries, Manitoba Hydro, the Manitoba Vehicle Technology Centre, Motor Coach Industries, Mitsubishi Heavy Industries, the Natural Gas Vehicle Alliance of Canada, New Flyer Industries, Persentech, the University of Manitoba and the City of Winnipeg. The dedication and effort of the faculty, staff and students at Red River College enable these partnerships.

5. References

[1] R. Hoemsen and K. Webb, Advanced Transportation & Energy, Presentation to the Standing Senate Committee (of Canada) on Energy, the Environment and Natural Resources, Winnipeg Manitoba, 2012.

[2] Province of Manitoba (EV Road Map etc.), http://www.manitoba.ca/iem/energy/transportation/index.html, accessed January 2013.

[3] R. Hoemsen and D. Friesen, Moving Forward with a Green Economy Through the Development & Integration of Electric Vehicles, Second Annual Electric Vehicle Infrastructure Summit, Toronto Ontario, 2013.

[4] R.V. Parsons and R. Hoemsen, Advancing Electric Vehicle Adoption: Insights from Manitoba Experience, EV2012VÉ, Montreal Quebec, 2012.

RED RIVER COLLEGE VEHICLE TECHNOLOGY & ENERGY CENTER
Applied Research Project Selection: "Student & Staff Centered"

Neil Cooke, B. Sc. Tech Ed, CAE, Voc. Ed Diploma, I.P. HDM
Chair, Transportation Heavy Apprenticeship Trades (THAT)
School of Transportation, Aviation & Manufacturing (TAM)
Red River College of Applied Arts, Science and Technology
Winnipeg Manitoba CANADA
ncooke@rrc.ca

ABSTRACT

Red River College has become an identifiable forerunner in applied research activities within the motive power field. With the focus upon development of technicians for the future, Red River College and its staff have been actively involved in the integration of applied research activities to enhance current curriculum content. Through selective project involvement, Red River College has seen the learning activity within the programs expand and more proactive thinkers return in subsequent apprenticeship training levels.

1. Introduction

There has been a conscious effort to structure an integrated approach to applied research activities within the various programs delivered within the Transportation Heavy Apprenticeship Trades division (THAT) of Red River College (RRC). This approach has allowed for the enhancement of learning opportunities for both students and staff that previously weren't available to them.

Beginning in 2006 THAT division of RRC; has been actively involved in applied research activities with the support of the Applied Research & Commercialization (AR&C) department of RRC and a wide variety of industry and government stakeholders. The division has been focused on three major themes of research activity.

- Cold Weather Testing
- Alternative Fuel Vehicles
- Emission Testing

Within these areas the division has been successfully able to expose both students and staff to new technologies and involve all parties in using the research as an active component of the student's studies and for staff development.

With a student centered approach to project selection, we have found that this selective process has had a major effect on the students ability to become better prepared for the technological change they will be exposed to when in industry. From the staff perspective, it has been found that the willingness to pursue expanded research activities internally has also grown such as that of the original bio-diesel project (fig. 1). Case in point; is the current Bio-diesel reactor that is nearing completion and is a joint venture between five separate departments within the college (fig. 2). The interest has spilled beyond the divisions preverbal borders and has other areas of the college now seeking to become involved in applied research. As a group that is made up of technicians and technologies, the desire to expand ones knowledge base comes natural to most staff.

Fig. 1 Original bio-diesel reactor from Red Deer College

Fig. 2 New high capacity PLC equipped reactor (June2013)

2. Discussion

Situated near the geographic center of North America, Manitoba has for many years played host to manufacturers when testing the performance of their vehicle in a region of extreme temperature ranges. With temperatures that will vary seasonally from $+35^0$C to -35^0C and at times beyond both of these values, the climate facilitates data acquisition that may not be achievable in a real world situation anywhere else.

As a result, the applied research that occurs here is very often focused on out three themes of research activity preferences. The College and THAT division has fast become a recognizable institution that provides opportunities for its students and industry partners (Mongeon, 2008).

The division has found that while cold weather has been the catalyst to bring in a project, most projects are based upon validating alternative fuels or propulsion systems. These two areas are closely tied to the fundamental business of the institutions training mandate. As such, the projects fit the criterion for project selection in almost every case. The projects we have been involved with or are currently involved with are varied. Our current list of applied research activities that have been completed or are in progress are as follows:

- EPA Certification for engine and induction system installation for Bus Transportation industry (2007 standards).
- Hydrogen Hybrid cold weather testing.
- Hydrogen production and distribution.
- Hydrogen Fuel Cell Bus project.
- PHEV conversion and service.
- Power Generation Unit assembly project for use in arctic environment.
- Electric bus battery assembly project.
- Electric bus battery design and assembly project.
- EPA Certification for engine and induction system installation for Bus Transportation industry (2010 standards).
- CNG cold weather testing and report submission for Transport Canada.
- Bio-diesel production and vehicle testing.
- Bio-diesel reactor design and commissioning

All of these projects have been well received by the students and staff with no shortage of volunteers to participate in almost every project. It is important to mention that many of these projects are done when faculty are instructing with students (to enhance the learning) or in their non-contact period. When staff participates in their non-contact hours they do so on a purely voluntary basis.

3. Conclusions

With the numerous projects that the division has had the opportunity to be involved in, we have all gained a tremendous amount value from our participation. The support that the college administration, supporting departments such as AR&C, the Province of Manitoba, the Government of Canada and Industry stakeholders and participants from both Canada and abroad, have all given immeasurable opportunities to our students. The growth that the division has experienced to date is only to be out shadowed by our future growth potential. The applied research activity that we have been exposed to has had a major impact on the culture of the division and has become contagious. With the support of AR&C I would expect continued opportunities for our students and staff and future technicians.

4. Acknowledgements

Red River College greatly appreciates the generous support provided by the Government of Canada (including the Department of Foreign Affairs and International Trade, the Natural Sciences and Engineering Research Council of Canada, the National Research Council of Canada and Western Economic Diversification), the Province of Manitoba (the Council on Post-Secondary Education, Manitoba Innovation Energy and Mines, and Manitoba Entrepreneurship Training and Trade) and local, national and international industry partners such as The Centre for Emerging Renewable Energy, Kraus Global Industries, Manitoba Hydro, the Manitoba Vehicle Technology Centre, Motor Coach Industries, Mitsubishi Heavy Industries, the Natural Gas Vehicle Alliance of Canada, New Flyer Industries, Persentech, the University of Manitoba and the City of Winnipeg.

5. References

Mongeon, C. (2008). *High Value University-Industry Interactiions: "A study of 20 interactions".* Electronically published in Canada (ed. 1,20090909).

OS6: Smart Fluids and Materials, and Their Applications

Improved Smart Actuators And Energy Harvesters

Authors names: JF Capsal, M Lallart, PJ Cottinet, J Galineau, D Guyomar
Affiliation and address: Univ Lyon, INSA Lyon, LGEF EA 682, F-69621 Villeurbanne, France.
E-mail: Daniel.guyomar@insa-lyon.fr

1. Introduction

The current trend in electronics is its integration in day to day devices or portable equipments in order to extend the number of functions and to improve their reliability. Moreover, considering the recent progresses in ultralow-power electronics, powering complex systems on ambient energy becomes more and more realistic.

2. Method

This paper addresses the problem of the electrical to mechanical energy conversion in electroactive materials in a general manner and more specifically on ferroelectric materials and electrostrictive polymers that can be used to design energy harvesters.

The ferroelectric are brittle difficult to machine, heavy and contain lead for most of them. Oppositely the electrostrictive polymers are lightweight, flexible, available in large surfaces, conformable to any smooth shape, eco-friendly and their materials properties can be tuned by introducing nano-particles in the polymer matrix.

These polymer composites exhibit a good capability to convert elastic energy into electrical energy once a DC electrical field is applied.

3. Results and Discussion

The proposed energy conversion improvement is an extension, to polymer materials, of the so-called “non-linear voltage processing, or “SSHI” previously developed for ferroelectric materials. The non-linear voltage processing basically consists in switching the voltage, for a short period, when the voltage reaches a maximum or a minimum, resulting in a large enhancement of the conversion as well as 1000% increase of the harvesting capability. The technique is fully adaptive and, thus does not require any frequency tuning.

Due to the bias field, a direct extension of the SSHI techniques is not feasible. The needed adaptations will be discussed as well as the different trade-offs between the mechanical and electrical characteristics that the system must meet to maximize the converted energy.

The paper will present and discuss experimental and theoretical data on the characterization of electrostrictive polymer, the effect of the nano-fillers, the conversion improvement and energy harvesting performances resulting from the switching approach. We also developed a new polymer by adding up phthalate in the terpolymère matrix P(VDF-TrFE-CFE) resulting in plasticization of the terpolymer and a huge increase of the strain performances at low electrical field.

Other effects due to the plasticization are presented in the table below

4. Concluding remarks

- Plasticization of P(VDF-TrFE-CFE) terpolymer decrease the Young modulus without affecting the mechanical strength of the polymer.

- DEHP plasticizer reduces the thermal stability of the crystalline phase without significant modification of the heterogeneity of the crystalline phase.

- The increase of the molecular mobility induce an increase of charges trapped at the heterogeneities of the semi-crystalline polymer inducing very large MWS polarization.

- Below are the permittivity curves (Fig.1, Fig.2)

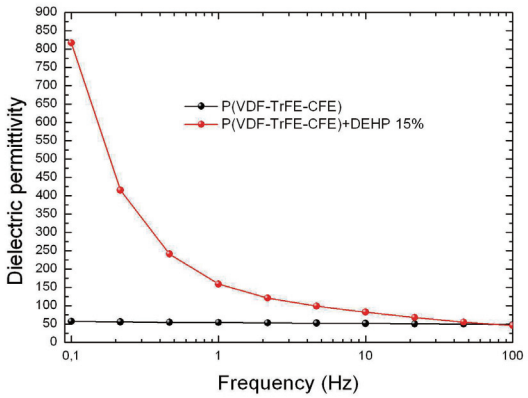

Fig.1 Permittivity versus frequency

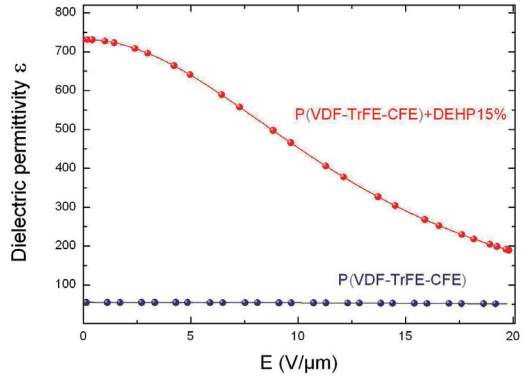

Fig.2 Permittivity versus electrical field

- Longitudinal strain under electric field has been increased by 20 times compared to pure P(VDF-TrFE-CFE) terpolymer (Fig.3)

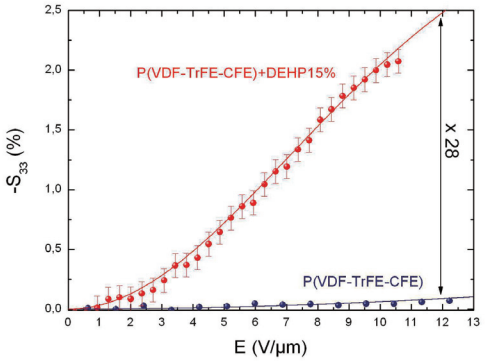

Fig.3 Strain versus electrical field

- Correlation between strain and electrical measurements shows that pure Maxwell Strain/Stress effect governed the electrostictive effect of CMFT.

- The Young modulus varies as indicated on the graph (Fig.4)

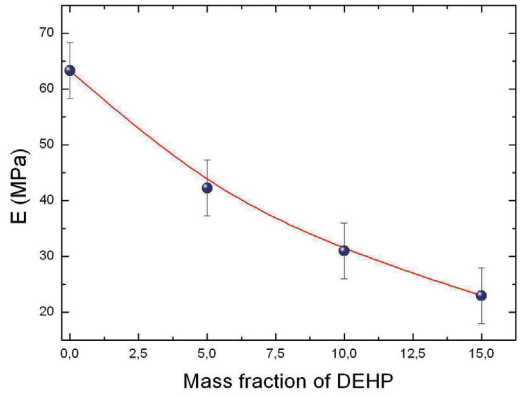

Fig.4 Young modulus versus DEHP mass fraction

- Mechanical energy density has been increased by 140 times compared to pure P(VDF-TrFE-CFE) terpolymer.

References

[1] Cottinet PJ; Guyomar D; Lallart M; Electrostrictive polymer harvesting using a nonlinear approach; Sensors and Actuators A-Physical, Vo172; I2; pp497-503; DOI: 10.1016/j.sna.2011.09.021; DEC 2011.

[2] Lallart M; Cottinet PJ; Guyomar D and al; Electrostrictive polymers for mechanical energy harvesting; Journal of Polymer Science Part B-Polymer Physics; V50; I8; pp523-535; DOI: 10.1002/polb; APR 2012.

[3] Cottinet PJ; Guyomar D; Galineau G and al; Electro-thermo-elastomers for artificial muscles; Sensors and Actuators A-Pysical; V180; pp105-112; DOI:10.1016/j.sna.2012.04.016; JUN 2012

[4] Guyomar D; Cottinet PJ; Lebrun L and al; The compressive electrical field electrostrictive coefficient M33 of electroactive polymer composites and its saturation versus electrical field, polymer thickness, frequency, and fillers; Polymers For Advanced Technologies; V23; I6; pp946-950; DOI: 10.1002/pat.1993; JUN 2012

[5] Lallart M; Capsal JF; Mossi Idrissa AK and al; Actuation abilities of multiphasic electroactive polymeric systems; Journal of Applied Physics; V112; I9; Art: 094108; DOI: 10.1063/1.4764337; NOV 1 2012

Physical Modeling of the Effect of Conductive Fillers on Electro-active Polymers used as Actuators

Gildas DIGUET[1], Jean-Marc CHENAL[2] and Jean-Yves CAVAILLE[2]
[1] Department of Physics, University of Johannesburg
[2] Materials Science and Engineering (MATEIS), INSA-Lyon CNRS
jean-yves.cavaille@insa-lyon.fr.

ABSTRACT

Some polymers have shown their ability as efficient actuators when they are submitted to an electric field. In order to increase this electro-activity, several authors proposed to introduce electrically conducting nanoparticles within the polymer host. It appears that this improvement is not as efficient as expected for matrices like polyurethane often chosen for their high activity. This paper deals with the comparison between experimental data from the literature and predicted data from a model recently developed. Such particles play in fact the same role as heterogeneities at the origin of the strong electrostriction reported for some co-polyurethane.

1. Introduction

Polymers are more and more used to design actuators based on electromechanical coupling. Most of devices are in fact capacitors consisting in 2 electrodes separated by a soft polymer (elastomer).

Since several years, many attempts were made to increase their efficiency. Among them, the introduction of electrically conducting particles within elastomeric matrices are widely used [1,2].

Basically, 3 main mechanisms are considered, namely (i) electrostatic compressive stress due to the applied voltage on the electrodes, (ii) forces due the interaction of the applied electric field on free electrical charges inside the polymer and (iii) intrinsic deformation of the polymer induced by the electric field.

The first one is known as the Maxwell effect, and the strain S is a quadratic function of the electric field, E, such as:

$$S_M = M_M E^2, \text{ avec } M_M = \frac{\varepsilon_0 \varepsilon_r}{Y} \quad (1)$$

where ε_0 refers as to the vacuum permittivity, ε_r, to the average dielectric constant of the material, Y its average Young modulus. M_M is the Maxwell electromechanical coefficient.

The forces due to the free electrical charges is proportional to their density and to E. It can be neglected in pure nonionic polymers.

The third contribution is intrinsic of the material.

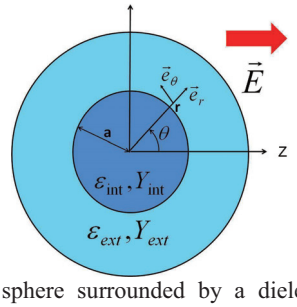

Fig.1 Dielectric sphere surrounded by a dielectric medium placed in an electric field. ε_{int} and ε_{ext} refer to the phase dielectric constants, while Y_{int} and Y_{ext} refer to their Young modulus. This assembly is the representative cell used in the theoretical model [4].

In a recent work [3,4], we have shown that heterogeneities of composition inside a block copolymer, enhanced by the very poor miscibility of macromolecules should lead in gradient of stiffness and of dielectric constant. This in turn, leads to electric field gradients. In the case of spherical inclusions having a larger dielectric constant and a higher stiffness than the matrix, the interaction between dipoles of the matrix and field gradient induces a compressive stress, much stronger that the above mentioned Maxwell effect.

A general expression was derived, which corresponds to the strain induced by intrinsic electrostriction corresponding to packing of composite spheres as displayed in Fig.1. Here, we consider spherical hard domains with a radius a having a permittivity ε_{int} higher than ε_{ext} of the soft matrix. In fact, we have shown that at a distance a from hard domain surface, the gradient and in turn the induced force is close to zero.

$$M_{EC} = -2\frac{(\varepsilon_{ext} - \varepsilon_0)}{Y}\left[A^2 - 0.8A\right](\varepsilon_r + 2)^2 \quad (2)$$

where A is defined as:

$$A = \frac{\varepsilon_{ext} - \varepsilon_{\text{int}}}{2\varepsilon_{ext} + \varepsilon_{\text{int}}} \quad (3)$$

A reflects the dielectric contrast between the two phases, which is responsible for the filed gradient. Y is the Young modulus of the soft phase.

This corresponds roughly to a volume fraction of stiff particles around 15%. Though a more precise calculation should be performed, for lower volume fraction, (dilute dispersion), the electrostriction coefficient M_E is obtained through the following relationship:

$$M_E = \frac{M_{EC}}{0.15}\phi \quad (4)$$

where $\phi < 0.15$ is the volume fraction of stiff polar domains. For higher volume fraction, field gradients partly superimpose which decreases their amplitudes, and so the electrostriction efficiency. On the other hand, above this fraction and for randomly dispersed spherical domains percolation phenomenon may also reinforce the stiffness decreasing also the deformation. Thus, an optimum of the stiff domain volume fraction is expected around 0.15.

It is worthy to notice that nanocomposite materials

containing electrically conducting particles dispersed in a matrix, is a particular case where ε_{int} becomes infinite, and so A= -1.

2. Results from the literature

Several works were done to increase electrostriction by mixing carbon black (CB), or carbon nanotubes (CNT) or even metallic particles, etc. A typical result is given in Table 1 for a block copolymer polyurethane (PU) filled with CB particles. It is worthy to notice that even without fillers, this polymer is strongly electroactive, which has been explained by its heterogeneous microstructure. This microstructure results from the phase separation between soft and stiff blocks, which occurs during its processing [5]. Thus, the improvement of its electro-activity is not as much as it could be expected, though the dielectric constant increases efficiently (from 7 to 30) when CB content increases from 0 to 1%.

Table 1. Main parameters of filled PU [6]

CB /vol%	0	0.1	0.5	1
$M_{Exp}/10^{-15}$	-3	-5	-6	-6
Y/MPa	36	41	42	43
ε_r	7	8	12	30

To analyze the dependence of M with the volume fraction, it is important to recall that CB is made of nanometric spherical particles (around 10nm) which form aggregates more or less ellipsoidal but with a very low CB volume fraction. At increasing volume fraction, the dispersion is more difficult to achieve during the process and larger aggregates remain. We can consider those aggregates as isopotential pseudo particles which occupy a much larger volume fraction than the CB content. The previous calculation has shown that the distance over which the field gradient appears is of the order of the particle radius. The larger the aggregate, the larger the volume of matrix is involved. Thus, for small amount of CB, the probability to have very small particles (10 nm) is higher and the associated field gradients will mainly act over short distances, and forces will act on soft domains with a low stiffness (around 0.1 MPa, see ref [6]. On the contrary, at higher CB contents, a large amount of aggregates with dimension in the order of µm will induce forces over similar distances, which mean that they will act on a composite materials with higher modulus as given in Table 1.

If we apply Eq.(2) & (3) for diluted situations, then the contribution to the electrostriction due to CB should be around the values reported in Table 2, where M_{ECB} refers to the contribution of CB particles.

Table 2. Contribution of CB on electrostriction behavior

CB /vol%	0	0.1	0.5	1
$M_{Exp}/10^{-15}$	-3	-5	-6	-6
$M_{ECB}/10^{-15}$	0	-0.3	-3	30

It seems from these rough calculations that we underestimate the contribution at low CB contents, but overestimate it at high contents.

3. Discussion and Conclusion

In fact, there is a lack in the microstructure knowledge for these materials. It is known that CB particles modify the phase separation process which can induce changes in M_{Exp} which in turn do not come directly from the dielectric contribution of CB. For 0.5%, it is shown that the CB contribution is of the same order of magnitude that the contribution of pure PU. On the contrary, at higher contents, it is possible that the CB contribution be screened by the appearance of large aggregates which are close each other's (percolation threshold is around 1.25%) which limits the contribution of field gradient introduced by CB (see above). Furthermore, the stiffness of domains involved in the deformation process may be much larger than for individual nanoscopic particles.

It is clear that the prediction of electroactive properties of this kind of rather complex materials requires further developments.

References

[1] B. Guiffard , L. Seveyrat, G. Sebald, D. Guyomar *J Phys D Appl Phys* 2006;39:3053–7.

[2] B. Guiffard, D. Guyomar, L. Seveyrat, Y. Chowanek, M. Bechelany, D. Cornu, *J Phys D Appl Phys* 2009;42:055503–6.

[3] JY Cavaillé, Physical Modeling of the Electro-mechanical Behavior of unfilled Polymers, *8th International Conference on Fluid Science (ICFD)*, November 7-9, 2011, Sendai, Japan

[4] G. Diguet, A. Bogner, JM Chenal, and JY Cavaille, *J. Appl. Phys.* 112, 114905 (2012)

[5] Z. S. Petrovic and J. Ferguson, *Prog. Polym. Sci.*, **16** (1991) 695-836

[6] K. Wongtimnoi, B. Guiffard, A. Bogner-Van de Moortele, L. Seveyrat, C. Gauthier, J.Y. Cavaille, *Comp Sci Tech* 71(2011) 885-892

Novel Electroactive Polymer for Micro-motor Development

Miklós Zrínyi [1], Rita Bauer[1], Loránd Kelemen[2] and Masami Nakano[3]
[1]Department of Biophysics and Radiation Biology, Semmelweis University
H-1089 Budapest, Nagyvarad ter 4, HUNGARY.
[2]Biological Research Centre, Hungarian Academy of Sciences
H-6726 Szeged, Temesvári krt. 62 HUNGARY.
[3]Intelligent Fluid Control Systems Laboratory, Institute of Fluid Science, Tohoku University
2-1-1 Katahira, Aoba-ku, Sendai, 980-8577, JAPAN.
E-mail of corresponding author: mikloszrinyi@gmail.com, m-nakano@fmail.ifs.tohoku.ac.jp

ABSTRACT

Epoxy based polymer has been developed for novel electric micro-motor construction. Polymer disks and hollow cylinders were prepared in few micrometer dimensions as rotors. Electrorotation of these micro tools was studied under uniform DC electric field. The effect of shape, size and thickness were investigated. Here, we present the first experimental observation, that novel epoxy based micro devices show intensive spinning in uniform DC electric field. The rotational speed of micron-sized polymer rotors can be conveniently tuned in wide range (between 300 – 2000 rpm) by the electric field intensity.

1. Introduction

Electrorotation (Quincke rotation) is the circular movement of an electrically polarized micron sized particle or material [1, 2]. Controllable rotation of small materials and devices is of relevance to a range of practical applications, for example in micro-motors. In our previous work, we have reported development of micron-sized polymer composites disks that showed electrorotation in uniform DC and AC electric field [3-5].

In the present work, we report the development of novel epoxy based polymer that shows spinning in uniform DC electric field. Our main intention is to fabricate rotors, which could be used as main building blocks of micro-motors.

2. Materials and Method

We have used epoxy based photoresists designed for micromachining and other microelectronic and MEMS applications. The polymer hardens in a pre-defined 3D shape upon illumination with focused laser light. Disks and hollow cylinders as rotors, were prepared with variable diameter and thickness. The diameter was varied between 100 to 500 microns with heights of 20 - 40 microns. Figure1 shows the photos of two main rotor forms.

Electrorotation was studied in oil mixture. Figure 2 shows an experimental device to apply electric field to the disk shaped polymer rotor. The gap distance between the electrodes was 3 mm. The space between the electrodes was filled up with special oil which contains substantial amount of triglicerid of oleic-, palmitic-, and linoleic acids, with conductivity of $\sigma_1 = 9.56 \cdot 10^{-10}$ S/m and relative permittivity of $\varepsilon_1 = 3.32$, respectively. The electric field was supplied by a high voltage DC power supply (TREC, USA). We have increased the electric field intensity step by step up to 2.2 kV/mm. Uniform DC electric field was applied perpendicularly to the axis of the disk. The rotation was followed by optical microscope (OLYMPUS, Japan) equipped by a high speed camera (Photron, Japan). In order to visualize the rotation and to determine the angular frequency, a visible sign close to the edge of the disk was used (see Fig.1). The angular frequency of the rotation was determined by recording the spinning motion of the disk.

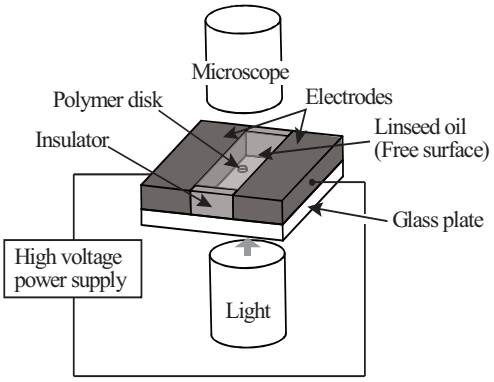

Fig.2 Experimental device to apply electric field to polymer disk

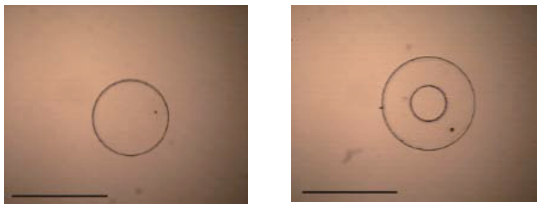

(a) Polymer disk (b) Hollow cylinder

Fig.1 Polymer rotor prepared from epoxy based polymer. The bar indicates 500 microns. The dot close to the edge of the micro tools was used to determine the speed of rotation.

3. Results and Discussion

We have presented the first experimental observation of DC electric field induced rotational motion of this epoxy based polymer micro tools. In DC field above a critical value of electric field intensity which was found to be 0.6 kV/mm, the polymer rotors perform spinning at a constant rate. This rate is sensitive to the electric

field intensity. With increasing field intensities, the angular velocity of rotating polymers increases as shown in Fig.3.

3.1 Electrorotation of polymer disk

The dependence of rotational speed on the electric field intensity for a disk shaped polymer rotors is shown in Fig.3. The dependence indicates that there is a significant size effect on the speed of rotation. At the same electric field intensity, the smaller disk (100 micron) performs the most intensive rotary motion.

We have studied the influence of disk thickness on the rotational speed - electric field dependence as shown in Fig.4. At the same electric field intensity, the thicker disk (38 micron) performs more intensive rotary motion.

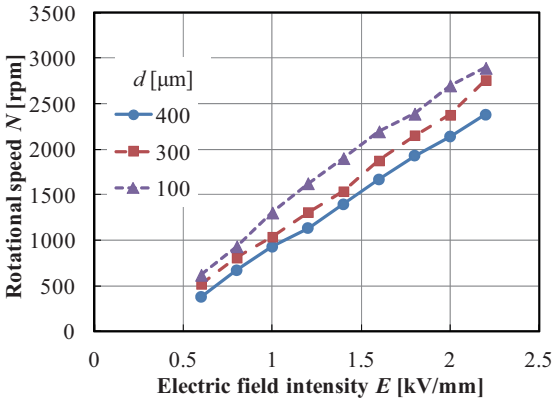

Fig.3 Dependence of rotational speed N of polymer disks as a function of electric field intensity E (t=38 μm). The solid line is guide for eyes. The diameter d of the disks is indicated in the Figure.

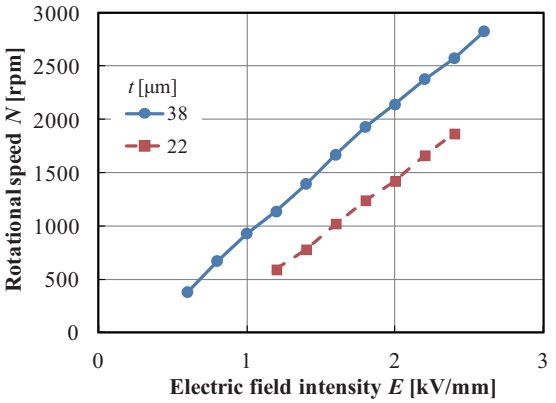

Fig.4 The influence of thickness t of polymer disk on the speed of rotation N (d=400 μm).

3.2 Electrorotation of hollow cylinder

We have studied the rotation phenomena of hollow cylinder. The inner d_2 and outer d_1 diameters were varied in a constant hollow rate of 16%. Figure 5 shows the effects of hollow cylinder shape on the rotational speed N as a function of the applied electric field intensity E. At the same electric field intensity, the smaller hollow cylinder (400/160 micron) performs more intensive rotary motion as well as the polymer disk as shown in Fig.3.

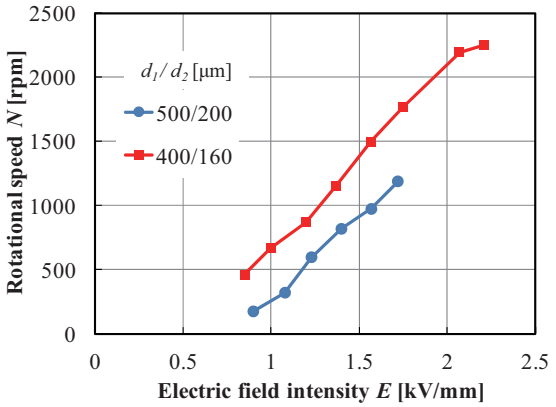

Fig.5 Effect of hollow cylinder shape on the speed of rotation (t=38 μm). The outer d_1 and inner d_2 diameters are indicated in the Figure.

4. Concluding remarks

We have presented the first direct observation of DC electric field induced rotation of epoxy based chemically crosslinked polymer rotors. Polymer disks and hollow cylinders of different size perform very intensive rotation in uniform DC electric field. It was found that above a critical value of electric field intensity the rotors begin to rotate at constant rate. This rate is sensitive to the field intensity. With increasing field intensities the angular velocity of rotating disk increases. This increase can be approximated by linear dependence. The size and shape of the rotors as well as the strength of electric field intensity determines the electro-mechanical performance of the rotors.

Acknowledgements

This research was performed under the Collaborative Research Project of Institute of Fluid Science, Tohoku University and in the frame of Cooperation Agreement between Institute of Fluid Science, Tohoku University and, Department of Biophysics and Radiation Biology, Semmelweis University. The financial support of OTKA Foundation (Grant number: NK 101704) is gratefully acknowledged.

References

[1]G. Quincke, Ann. Phys. Chem., **59**, (1896) 417.

[2]T.B. Jones, Electromechanics of Particles, Cambridge University Press, New York, (1995).

[3] M. Antal, G. Filipcsei, M. Zrínyi, Direct observation of Quincke rotation of disk shaped polymer composites in a uniform DC electric field, Composites Science and Technology, **67**-13, (2007) 2884-2885.

[4]T. Okumura, M. Nakano, M Zrinyi, Micro-Motor Utilizing Electric Field-Responsive Polymer Composites, Proc. of the Eighth International Conference on Flow Dynamics, Sendai, Japan, (2011-11) 634-635.

[5]M.Zrinyi, M.Nakano, T.Tsujita, Electrorotation of novel electroactive polymer composites in Uniform DC and AC electric field, Smart Mater. Struct. **21**, Paper No. 065022, (2012) 1-6.

Tenth International Conference on Flow Dynamics
November 25-27, 2013, Sendai, Miyagi, Japan

Suppressing Turbulence and Enhancing the Liquid Suspension Flow in Pipeline with Electromagnetic Fields

Rongjia Tao
Department of Physics, Temple University, Philadelphia, PA 19122, USA
rtao@temple.edu

ABSTRACT

Flows through pipes and channels are the most common and important transportation of fluids. To enhance the flow output requires reducing viscosity and suppressing turbulence. This can be achieved by application of a strong electromagnetic field in the flow direction at a small section of the pipeline. The field makes the suspended particles polarized and aggregated into short chains in the flow direction The symmetry is broken. In the flow direction, the viscosity is significantly reduced; in the directions perpendicular to the flow, the viscosity is substantially increased. All these suppress the turbulence and enhance the flow.

1. Introduction

Flows through pipes and channels are the most common and important transportation of fluids. To enhance the flow output in pipeline requires reducing the fluid viscosity and suppressing turbulence [1,2].

Let's take crude oil pipeline as an example. Typically, when the Reynolds number $N_R = \rho v D/\eta \le 2300$, the flow in pipeline is laminar (Fig.1). Here D is the diameter of the pipeline, v is the average flow velocity, ρ and η are the fluid's density and viscosity respectively.

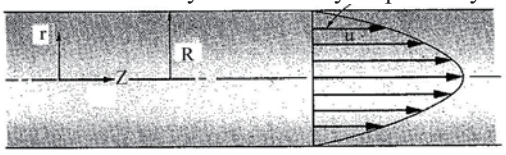

Fig.1 Laminar flow inside the pipeline

The friction factor for laminar flow is $f = 64/N_R$. As $\Delta P/L = \frac{1}{2}\rho v^2 f/D$ we have the relationship between the flow rate Q and pressure drop,

$$Q = \pi D^4 \eta^{-1} (\Delta P/L)/128, \qquad (1)$$

were L is the length of the pipeline. For most crude oil pipelines, the flow is turbulent when $N_R > 2300$ (Fig.2). For a turbulent flow with $2300 < N_R < 100000$, the friction factor is given by the Blasius relation [3] $f = 0.3164/(N_R)^{1/4}$. The flow rate is then given by

$$Q = 2.2526 D^{19/7} \rho^{-3/7} \eta^{-1/7} (\Delta P/L)^{4/7} \qquad (2)$$

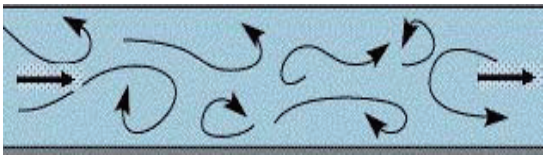

Fig.2 Turbulent flow inside the pipeline.

Equations (1) and (2) illustrate that the transfer of fluids via laminar flow is energetically far more efficient than that via turbulent flow. For example, to increase the flow rate by 30% we only need to increase the pressure by 30% for laminar flow, but for a turbulence flow we need to increase the pressure by 58.3%.

Unfortunately, the widely used heating method reduces the fluid viscosity, but increases the Reynolds number, making the turbulent flow more irregular. Adding polymer chains to the fluid suppresses the turbulence, but has no effect on laminar flows because it increases the fluid's effective viscosity.

Here we show that application of a strong electromagnetic field along the flow direction in a small section of pipeline can accomplish both goals: reducing the viscosity and suppressing the turbulence [4, 5].

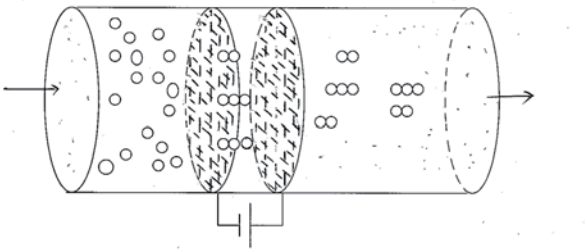

Fig.3 As the flow passes a strong electric field, the suspended particles aggregate along the field direction, and the effective viscosity becomes anisotropic.

2. Method

We will use electric field and crude oil as our example while the principle applies to magnetic field and other liquid suspensions as well. The base liquid of crude oil, gasoline, has very low viscosity. The oil's high viscosity is due to randomly suspended paraffin, asphalt, and other particles in the base liquid. As shown in Fig.3, a strong electric field is applied along the flow direction in a small section of the pipeline. Because the suspended particles and the base liquid have different dielectric constants, the suspended particles are polarized. As the dipolar interaction is stronger than the Brownian motion, the particles aggregate along the field direction to form short chains or ellipsoids. Hence, the symmetry is broken. Under such a condition, similar to flow of nematic liquid crystal with its molecule alignment in one direction, the viscosity is no longer isotropic [6]. Based on the neutron scattering information [7], we can approximate the short chain by a prolate spheroid with its rotational axis along the flow direction,

$$(x^2 + y^2)/b^2 + z^2/a^2 = 1 \qquad (3)$$

For such spheroid, the intrinsic viscosity along the z-axis ν_z is much smaller than that of the intrinsic viscosity along the other direction, $\nu_\perp$. If *(a-b)/a=0.9,* for example, we have $\nu_z = 2.01$ while $\nu_\perp = 4.48$ [8]. From the Krieger-Dougherty equation [9],

$$\eta_i / \eta_0 = (1 - \phi / \phi_{\max})^{-\nu_i \phi_{\max}} \quad (4)$$

where η_0 is the viscosity of base liquid and $\phi_{\max}$ is the maximum volume fraction for randomly packing the particles. Recent work finds that $\phi_{\max}$ strongly depends on the particle shape. For spheres, $\phi_{sphere} = 0.64$ and for spheroids $\phi_{spheroid} \geq 0.72$, higher than that for spheres [10]. If $\phi = 0.5$, the original viscosity is $\eta / \eta_0 = 11.38$; after the electric field is applied, the viscosity along the flow direction is reduced to $\eta_z / \eta_0 = 5.56$, down 51.1%, while the viscosity perpendicular to the flow is increased to $\eta_\perp / \eta_0 = 45.80$, up 302%. As the viscosity in the directions other than the flow direction is increased substantially, the turbulence is suppressed because the vortices in turbulence must have the fluid moving in the direction transversal to the pipeline axis. Meanwhile, the significantly reduced viscosity along the axial direction enhances the flow output.

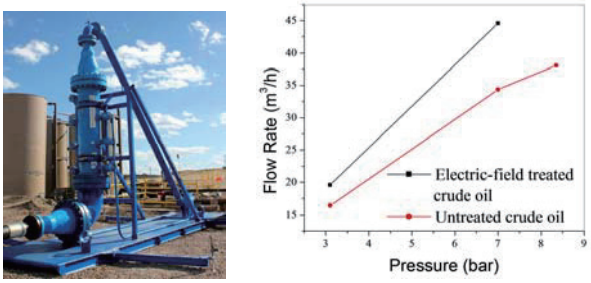

Fig.4 (a) The viscosity reduction device. (b) The flow rate versus pressure indicates that the electric field treated oil flow remains laminar when the Reynolds number reaches 6000. The untreated oil flow becomes turbulent when the Reynolds number >2300.

3. Results and Discussion

Recently we conducted a field test at Daqing oil field in China with our viscosity reduction device (Fig. 4(a)). The Daqing crude oil is paraffin based and has a pour point around 32^0C, below which the oil is frozen inside the pipeline. Heating is currently crucial to transport the oil via pipeline. The oil was typically heated to 55^0C -72^0C at one heating station and flowed through a pipeline of 15-20km to another heating station to be heated again. The pipeline has inner diameter 14.5cm.

Before our device was operated, we confirmed that the oil flow was turbulent. For example, when the oil is heated to 55.6^0C, its kinetic viscosity was 20.36cSt. Under a pressure of 7.0bar, the flow rate was 34.46 m^3/h and $N_R = 4128.3$. When the oil was heated to 71.1^0C, the oil viscosity was down to 14.92cSt, but the flow rate was only increased to 36.0m^3/h, close to the estimation from Eq.(2), $34.46*(20.36/14.92)^{1/7} = 36.02$ m^3/h. If the flow were laminar, the flow rate should be 47.02 m^3/h. On the other hand, at 55.6^0C, if we increased the pressure to 8.35bar, the flow rate increased to 38.1 m^3/h, close to $34.46*(8.35/7)^{4/7} = 38.11$, the estimation from the the Blusiu's formula.

To test our device, we started with a laminar flow. At 55.6^0C and under 3.1bar pressure, the flow rate was 16.4 m^3/h and $N_R = 1964.7$. Then we turned on our device, producing an electric field 16kV/cm to treat the oil. Its viscosity along the flow direction was down to 17.02 cSt. When the pressure was remaining the same, the flow rate was gradually increased to 19.6 m^3/h, close to $16.4*(20.36/17.02) = 19.62$ m^3/h, as the treated oil filled the pipeline. This indicates that the flow remained laminar while N_R was increased to 2808.9.

In order to test the situation at much higher Reynolds number, we increased the pump pressure to 7.0 bar while maintaining the electric field at 16kV/cm. The flow rate was increased to 44.6 m^3/h. This indicated that the flow remained laminar because the flow rate was close to $19.6*(7.0/3.1) = 44.25$ m^3/h. If the flow were turbulent, the flow rate could be only about $19.6*(7/3.1)^{4/7} = 31.2$ m^3/h. The Reynolds number $N_R = 6391.7$. These results are plotted in Fig.4(b).

Naturally, there is a question: How long can such anisotropic viscosity hold after one treatment? As stated before, such anisotropic viscosity is the result of the broken symmetry. When the aggregated short chains are dissembled, the viscosity reduction along the flow direction disappears and the effect to suppress turbulence also diminishes. At our recent field test on pipeline, we have found that the viscosity reduction actually lasts about 11 hours. Therefore, we expect that the effect to suppress turbulence should also last about 11 hours.

4. Conclusion Remarks

The above finding fully confirms that application of a strong electric field can reduce the viscosity and suppress turbulence for flow of liquid suspensions in pipeline. The basic physics here is general. If the suspended particles are sensitive to magnetic field, we can employ magnetic field [11].

This work was supported in part by STWA.

References

[1] K. Avila, et al Science, **V333**, Issue 6039 (2011) 192..
[2]. B. Hof, et al, Science, **V327**, Issue 5972 (2010), 1491.
[3] P. R. H. Blasius, Flüssigkeiten. *Forschungsheft* 131**,** 1-41 (1913).
[4] R. Tao and X. Xu, Energy & Fuels, **20** (2006)**,** 2046.
[5]R. Tao, J. of Intelligent Material Systems and Structure, **V22** (2011) 1667-1671.
[6] M. Miesowicz, *Nature* **158**, 27 (1946).
[7] R. Tao, E. Du, H. Tang & X. Xu, (to be published).
[8] G. B. Jefferry, Proceedings of the Royal Society of London Series A, **V.102**, Issue 715 (1922), 161.
[9] I. M. Krieger & T. J. Dougherty, *Tans. Soc. Rheol*. **3** (1959), 137.
[10] W. Man, *et al*, *Phys Rev Lett*, 94, 198001 1-4 (2005).
[11] R. Tao & K. Huang, Physical Review E, **84** (2011), 011905.

Tenth International Conference on Flow Dynamics
November 25-27, 2013, Sendai, Miyagi, Japan

Electro-Rheological Behavior of Nano-Suspensions based on Titanium Dioxide Nano-Particles

Katsufumi Tanaka[*1], Haruki Kobayashi[*1], and Masami Nakano[*2]
[*1]Department of Macromolecular Science and Engineering, Kyoto Institute of Technology,
Matsugasaki, Kyoto 606-8585, Japan
[*2]Institute of Fluid Science, Tohoku University, Katahira, Sendai 980-8577, Japan
E-mail of corresponding author: ktanaka@kit.ac.jp

ABSTRACT

Flow behavior and microstructure were discussed for electro-rheological (ER) nano-suspensions based on titanium dioxide nano-particles with particle diameter on the order of 100 nm. The ER effect was also discussed in relation to the microstructure developed between parallel plates of the rheometer.

1. Introduction

A suspension composed of micro-particles and insulating oil is known to show the electro-rheological (ER) effect [1]. The flow of the ER micro-suspension under no electric fields is generally assumed to be the Newtonian flow. Under an electric field, the flow is well assumed to be the Bingham flow. In such a micro-suspension, a chain-like microstructure along the electric field is induced, the ground state of which was found to be a body-centered tetragonal (bct) lattice [2]. A ring-like microstructure was also observed under shear and electric fields [3]. Because a characteristic response time of the ER micro-suspension is on the order of milliseconds [4, 5], there are expectations for applications [6], such as dampers, clutches, valves, robotics, force display devices, and so on.

For practical applications, however, there are still demands for the ER fluid to be improved. Although a much higher yield stress has been a major demand, stability in the ER effect would also be a demand. Recently, a suspension based on rutile titanium dioxide (TiO_2) nano-particles with diameter of primary particles around 15 nm has been reported [7]. The suspended secondary particles were remarkably stable against sedimentation and electrical breakdown. The nano-suspension showed a good fluidity within a narrow gap, while it showed a plateau stress at the lower shear rates under no electric fields.

In a previous paper, the effect of particle diameter was discussed, and a candidate for ER nano-suspensions was reported based on the silicone oil of 0.05 Pa·s, and (anatase) titanium dioxide with particle diameter around 300 nm and particle volume fraction of 8.8 vol% [8]. Furthermore, the effects of the continuous phase of suspending oils on the stress under no electric fields and the ER effect were reported for nano-suspensions of 8.8 vol% based on the nano-particles of 300 nm [9]. Under no electric fields, the apparent yield stress of the nano-suspension of 8.8 vol% based on a chemically-modified silicone oil of 0.1 Pa·s was lower than that based on the silicone oil of 0.05 Pa·s. The ER response measured at a given strength of the electric field for the nano-suspension based on the chemically-modified silicone oil was effectively induced by the electric field, and it was slightly larger than that of the nano-suspension based on the silicone oil.

In the present paper, another candidate for ER nano-suspensions based on (rutile) titanium dioxide with particle diameter around 400 nm will be reported, and the effects of the continuous phase will also be discussed. Furthermore, the effects of particle volume fraction will be reported for the nano-suspensions, since a nano-suspension with the higher volume fraction of the particles is expected to show the higher stress induced by the electric field.

2. Experimental

Nano-particles of rutile titanium dioxide with particle diameter ($2a$) around 400 nm were suspended in a chemically-modified silicone oil with a viscosity η_c of 0.1 Pa·s. The volume fractions of the particles were 8.8 and 12 vol%. As reference samples, anatase TiO_2 nano-particles with $2a$ around 300 nm were also suspended in a silicone oil with η_c of 0.05 Pa·s. The volume fractions of the particles were 8.8 and 12 vol%. In the present paper, a nano-suspension will be coded for convenience based on the viscosity of suspending oils, η_c, a typical particle diameter of $2a$ and/or particle volume fraction of ϕ. The rheological measurements were performed at room temperature using rotational rheometers with fixtures of parallel plates. A typical gap between the parallel plates was 50 μm. Particle behavior was observed using an optical microscope equipped with a CCD camera. Furthermore, the effect of shearing time on the ER responses was also investigated.

3. Results and Discussion

Figure 1 shows the shear stress under no electric fields plotted logarithmically against the shear rate for the modified silicone oil based nano-suspensions with $2a$ = 400 nm, and ϕ = 8.8 and 12 vol%. The data for the silicone oil based nano-suspensions with $2a$ = 300 nm, and ϕ = 8.8 and 12 vol% are also plotted in the figure. For the silicone oil based nano-suspensions, the nano-suspension of 12 vol% shows a plateau stress at lower shear rates, the plateau stress of which is one order higher than that of the silicone oil based nano-suspension of 8.8 vol%, and the flow was somewhat unstable, especially at higher shear rates. For the silicone oil based nano-suspension of 300 nm and 8.8 vol%, a plateau stress around 5 Pa is found in Fig.1 at the lower shear rates.

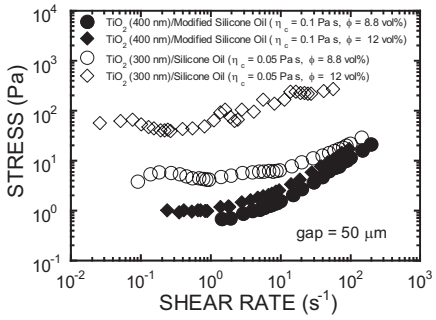

Fig. 1 Shear stress under no electric fields plotted logarithmically against shear rate for the silicone oil and the modified silicone oil based nano-suspensions.

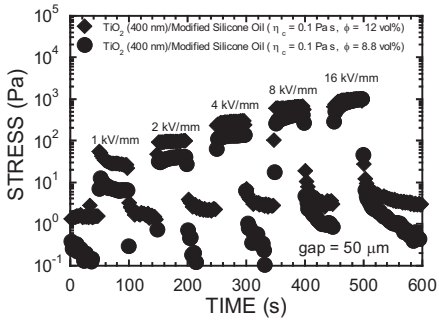

Fig. 2 ER responses for the modified silicone oil based nano-suspensions.

On the other hand, it is noteworthy for the modified silicone oil based nano-suspensions of 400 nm that plateau stresses are also seen but both the plateau stresses are much lower than that of the silicone oil based nano-suspension of 8.8 vol%. The plateau stress of the modified silicone oil based nano-suspension of 400 nm and 12 vol% is around 1 Pa, and that of 8.8 vol% is lower than 1 Pa, the value of which is two orders lower than that of the silicone oil based nano-suspension of 300 nm and 12 vol%, one order lower than the silicone oil based nano-suspension of 15 nm and 8.8 vol%, around 10 Pa [7], and slightly lower than the modified silicone oil based nano-suspensions of 300 nm and 8.8 vol% [9]. These results of the plateau stress are closely related to microstructures of the nano-particles developed in the nano-suspensions.

In the micrograph for the silicone oil based nano-suspension, a microstructure was densely developed across the imaging field of view. On the other hand, a slightly less developed microstructure was found for the modified silicone oil based nano-suspension. Such differences of the secondary particles were also observed in the micrographs for the diluted nano-suspensions with a particle volume fraction of 1.2 vol%.

Figure 2 shows responses of shear stress to the dc electric field measured at a shear rate of 1.88 s^{-1} for the modified silicone oil based nano-suspensions of 8.8 and 12 vol%. In Fig.2, the ER effect for the nano-suspension of 12 vol% is effectively induced by the lower strengths of the electric field. Furthermore, the flow was stable even under the electric field. As discussed in Fig.1, the stresses under no electric fields were relatively low for the modified silicone oil based nano-suspensions. On the other hand, the ER responses for the modified silicone oil based nano-suspensions of 8.8 and 12 vol% were comparable to those observed for the silicone oil based nano-suspension of 8.8 vol%. In addition, a chain-like microstructure induced by the electric field was also observed in the quiescent state for the nano-suspensions studied here.

Finally, the stable flow with a much higher induced stress is expected for the nano-suspension with a much higher volume fraction of the particles, and preliminary measurements have been made. Further study is now in progress to evaluate the micro-gap flow behavior and microstructure of the ER nano-suspension.

4. Conclusions

Plateau stresses under no electric fields for the nano-suspensions based on a chemically-modified silicone oil with particle volume fractions of 8.8 and 12 vol% were much lower than the plateau stress of the nano-suspension based on a silicone oil with a particle volume fraction of 8.8 vol%. The ER responses for the modified silicone oil based nano-suspensions of 8.8 and 12 vol% were comparable to those observed for the silicone oil based nano-suspension of 8.8 vol%. These results were closely related to the microstructure of the nano-suspensions.

Acknowledgement

This work was partially supported by the Cooperative Research Program of the Institute of Fluid Science, Tohoku University.

References

[1] W. M. Winslow, J. Appl. Phys., **20** (1949), 1137.

[2] R. Tao, and J. M. Sun, Phys. Rev. Lett., **67** (1991), 398.

[3] S. Henley, and F. E. Filisko, J. Rheol., **43** (1999), 1323.

[4] A. Hosseini-Sianaki, W. A. Bullough, R. Firoozian, J. Makin, and R. C. Tozer, Int. J. Mod. Phys. B, **6** (1992), 2667.

[5] K. Tanaka, A. Sahashi, R. Akiyama, and K. Koyama, Phys. Rev. E, **52** (1995), R3325.

[6] M. Nakano, and K. Koyama (eds.), Proc. of 6th Int. Conf. on ER Fluids, MR Suspensions and Their Applications (World Scientific, Singapore, 1998).

[7] K. Tanaka, T. Wakayasu, A. Kubono, and R. Akiyama, Sensors and Actuators A, **112** (2004), 376.

[8] K. Tanaka, T. Hira, R. Fukui, N. Nakagawa, R. Akiyama, M. Nakano, K. Yoshida, and T. Tsujita, Colloid Polym. Sci., **289** (2011), 855.

[9] K. Tanaka, T. Hira, R. Fukui, H. Kobayashi, R. Akiyama, M. Nakano, S. Enami, and A. Totsuka, Colloid Polym. Sci., **291** (2013), 1279.

Tenth International Conference on Flow Dynamics
November 25-27, 2013, Sendai, Miyagi, Japan

Creation of a Smart Fluid and its Application by Using Blend Polymer Solution

Masafumi Taniguchi, Yuichiro Nagastu
Department of Chemical Engineering, Tokyo University of Agriculture and Technology
2-24-16 Naka-cho, Koganei, Tokyo, 184-8588, Japan
E-mail: 50013642310@st.tuat.ac.jp

ABSTRACT

In recent years, attention is paid to the concept of chemical control of flows in which flows are controlled by changes in fluid properties (viscosity, elasticity) induced by chemical reactions. We use an aqueous blend polymer solution that contains sodium polyacrylate (SPA) and polyethylene oxide (PEO). We find that gel was formed instantaneously on contact interface when added HCl solution. Furthermore, we perform flow experiments by using blend polymer solution and HCl solution on a radial Hele-Shaw cell, called Viscous Fingering (VF). We find minimization of VF.

1. Introduction

Viscous fingering (VF) is a hydrodynamic instability that typically occurs when a more viscous fluid is displaced by a less viscous one in a porous medium or a Hele-Shaw cell [1]. The interface between the two fluids becomes unstable undergoing finger-like patterns. This situation is commonly encountered in oil recovery [2]. The displaced interface becoming finger pattern causes a decrease in oil recovery when heavy oil in oil reservoir is swept by water (Figure 1). In recent years, some studies have reported how to minimize VF [3] to prevent a decreased in production in process of oil recovery.

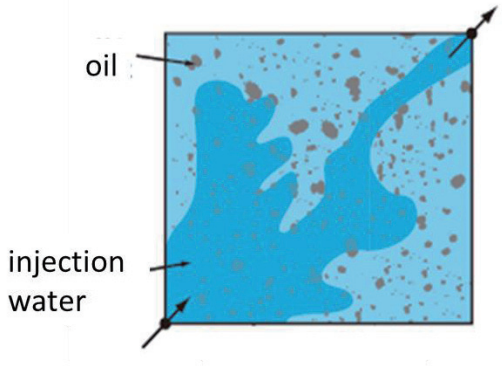

Fig 1, VF appeared when oil is swept by injected water in oil reservoir

In the present study, we challenge the problem by using an aqueous blend polymer solution that contains sodium polyacrylate (SPA) and polyethylene oxide (PEO). We clarify how rheological properties of the aqueous blend polymer solution change when a metal ion and acid are added to the blend polymer solutions. As mentioned below, we find that gel is formed instantaneously at contact interface when HCl solution is added. Therefore, we measure rheological properties of the gel produced by chemical reaction at contact interface. Furthermore, we investigate the effects on the flow field of VF. On the basis of the obtained results, we show that the effect can be applicated in the industry.

2. Experiment

We first prepared two kinds of aqueous polymer solutions. The one is 0.125 wt% SPA (whose molecular weight is 2-6 millions) solution. The other is 0.125 wt% PEO (whose molecular weight is 5 millions) solution. The blend polymer solution was obtained by mixing equal amount of these polymer solutions.

We measured mixing torque by a rotational viscometer (BLOOKFIELD, LVDV 2+P) when 1M potassium chloride (KCl) solutions was added to these polymer solutions. Furthermore, we added 0.1 M hydrochloric acid (HCl) solution to these polymer solutions. And we added HCl to the blend polymer solution containing 1M KCl. Gel was formed instantaneously at contact interface when HCl solution was added.

We measured rheological properties of the gel by a rheometer (TA instrument, AR-G2, with double wall ring (DWR) sensor).

Our Hele-Shaw cell is formed by two transparent glass plates of 140 mm × 140 mm × 10 mm thickness with a constant gap width, b. The gap width, b, was set as b = 0.3 mm by placing four metal triangular plates at four corners between the two glass plates. For liquid injection, the upper glass plate has a small hole of 4 mm in diameter in the center. A syringe pump was used to inject the liquids. The viscous fingering formed in the Hele-Shaw cell was videotaped by a CCD camera mounted below the cell. In this experiment, the less viscous fluid was the blend polymer solutions with 1M KCl colored by addition of 0.1 wt% trypan blue and more viscous fluid was 95 wt% glycerin solution which containing 0.1M HCl. The flow rate, q, was set as $q = 2660 \times 10^{-9}$ m^3/s .

3. Results and Discussion

Figures 2 and 3 show the results of the torque measurement when 1M KCl and 0.1M HCl is added respectively to each solution at t = 180 sec. When we added KCl solution to each polymer solutions, the viscosity was decreased. On the other hand, when we added HCl solution to each polymer solutions, viscosities of SPA and PEO solutions were decreased while that of the blend polymer solution was increased sharply. This phenomenon was caused by that gel was formed instantaneously at contact interface. It is worth noting

that this gel is formed for the blend polymer solution which contains 1M KCl. Thus, functionality of that gel was maintained while viscosity was decrease by KCl.

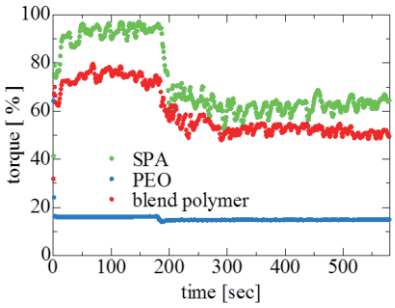

Fig 2, Transient response to KCl

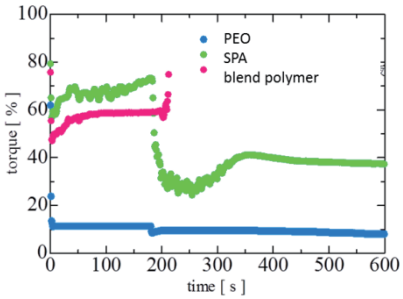

Fig 3, Transient response to HCl

Figure 4 shows measured rheological properties of the gel when 0.1M HCl solution is added after 180 sec. Parameter shown here is $tan\ \delta = G'' / G'$, where G' is storage modulus that represents elastic response , and G'' is loss modulus that represents viscous response in the oscillatory measurement. $tan\ \delta$ is dropped and reaches the fixed value, which shows gel is formed instantaneously at contact interface.

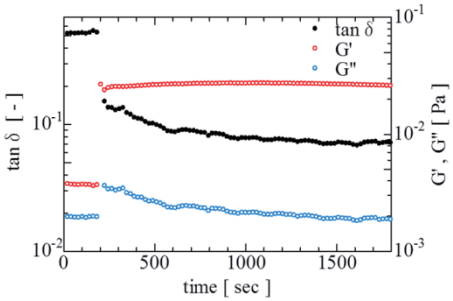

Fig 4, Transient response of the aqueous blend polymer solution to 0.001M KCl

Figures 5 and 6 are images of non-reactive and reactive VF pattern. In the non-reactive system, the more viscous fluid was 95 wt% glycerin solution. In the reactive system, the more viscous fluid was 95 wt% glycerin solution containing 0.1M HCl. In the case of non-reactive system, we observed VF. Displacement efficiency was smaller. But in the case of reactive system, minimization of VF was observed as a result of gel was instantaneous formation at contact interface. Displacement efficiency was larger than that in the non-reactive system. In the periphery, slight VF was observed. It is considered that flow rate of contact interface was lower in the periphery. And q was smaller, the area of VF minimization was smaller (those explanations is not included here) Thus, minimization of VF is more effective as the flow rate is higher.

Fig 5, Non-reactive system

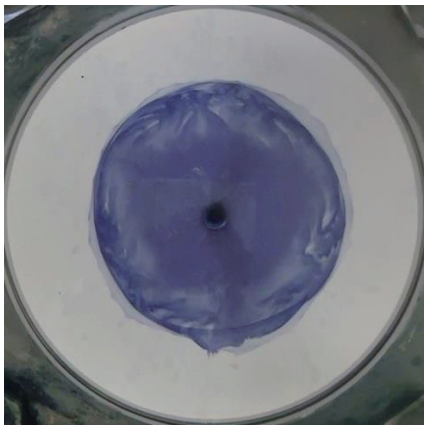

Fig 6, Reactive system

4. Conclusion

We measure how rheological property of the aqueous blend polymer solution (SPA+PEO) changes when some chemical species are added to the polymer solution. We find the aqueous blend polymer solution with KCl responds to H^+, and gel is formed at contact interface. On the flow field, this fluid has an effect of VF minimization. Thus, the displacement efficiency is larger than that in the non-reactive system. This functionality agrees with requirement for EOR.

Reference

[1] G. M. Homsy, 1987 Annu. Rev. Fluid Mech. **19**, 271-311.

[2] S. B. Gorell and G. M. Homsy, 1983 SIAM J. Appl. Math. **43**, 79

[3] E. O. Dias, E. A. Lacalle, M. S. Carvalho, and J. A. Miranda, 2012 Phys. Rev. Lett. **109**, 144502

Tenth International Conference on Flow Dynamics
November 25-27, 2013, Sendai, Miyagi, Japan

Design and Evaluation of a Linear Damper Working with MR Shear Thickening Fluids

Tongfei Tian[1], Weihua Li[1], and Masami Nakano[2]
[1]School of Mechanical, Materials and Mechatronic Engineering, University of Wollongong, Wollongong, NSW 2522, Australia
[2]Intelligent Fluid Control Laboratory, Institute of Fluid Science, Tohoku University, 2-1-1 Katahira, Aoba-ku, Sendai, 980-8577, Japan
weihuali@uow.edu.au

ABSTRACT

Magnetorheological (MR) materials and shear thickening fluids are both smart material and their combination could offer both MR and ST effects. This study looks at the properties and behaviour of magnetorheological shear thickening fluid (MRSTF) in particular whilst applied as a semi-active energy absorber. A device with two forms of varying vibration control has been created and measured. The result shows that this MRSTF filled damper showed both MR and properties.

1. Introduction

Vibration control, a field devoted purely to the absorption of impact energy, has seen vast advancements over time with the implementation of fluid filled shock absorptive dampers [1]. More recently, semi-active devices operating with media possessing varying fluidity properties have been greatly studied [2-5] as their working modes can be adjusted.

Magnetorheological (MR) materials are examples of these variable flow rate or force characteristic mediums [5]. Applying an external magnetic field to these intelligent materials alters the rheological properties of the body. This alteration is completely reversible and a transition from a liquid to a near solid state occurs very quickly (milliseconds) [3].

Shear thickening fluid (STF) is a similar type of 'quasi-Newtonian' substance; it possesses a low viscosity until the transition of the critical shear rate where it increases dramatically [2]. STF's are defined by Zhang et al [6] as 'concentrated colloidal suspensions composed of non-aggregating solid particles suspended in fluids.' The same as MR substances the change in flow properties is completely reversible; however, unlike MRFs, STFs do not require the application of an external field.

In this paper, the result of combining the advantages of MR and ST fluids in vibration control is illustrated. The prepared MRSTF, 'smart fluids,' rheological properties are tested and illustrated with the experimental performance of the fluid in a prototype damper.

2. Method

A kind of shear thickening fluid (STF) was fabricated with the purpose of serving as the base for the tested fluid medium. The STF consists of ethylene glycol solvent in which fumed silica particles (14 nm primary particles) were suspended at a weight fraction of 25% in the entire fluid body. Micron sized carbonyl iron particles, at a 20% weight fraction, were immersed amongst the STF and thoroughly mixed under a high shear condition to introduce the ability to produce the Magnetorheological effect. A vacuum chamber removed air bubbles excited in the mixture and the desired MRSTF is ready to be tested [7,8] and its rheological properties are shown in Fig. 1.

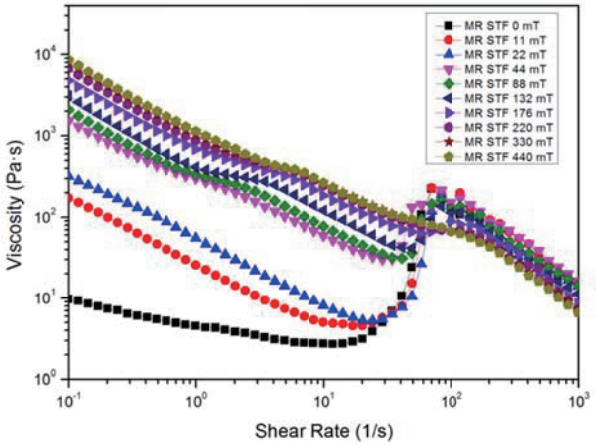

Fig. 1 Rheological properties of MR STF with various magnetic flux

The MRSTF filled damper was designed as shown in Fig. 2. Inside the piston head there is a coil which can generate electromagnetic field and affect the MRSTF's mechanical properties. This damper mainly consisted of piston head, tube, caps, and spring and its magnetic flux field was analysed by finite element analysis software package Flux. This result is shown in Fig. 3.

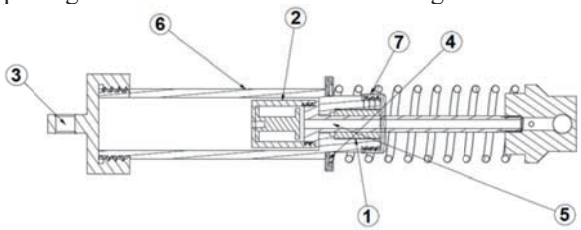

Fig. 2 Damper design. 1, Bearing; 2, Piston head; 3, Screwable cap; 4, Spring seat; 5, Piston rod; 6, Tube; 7, Tube cap.

3. Results and Discussion

The prototype damper was clamped within an MTS Landmark test system, between two coaxially mounted Linear-variable Displacement Transducer (LVDT) load cells. The MTS Landmark operates by servo hydraulic system capable of exerting large axial loads on the test

specimen. The damper test system provides harmonic excitation to the damper and records signals taken through the load cells. The signals were saved to a computer via a data acquisition (DAQ) board measuring various feedback data series, these being time, axial displacement and axial force.

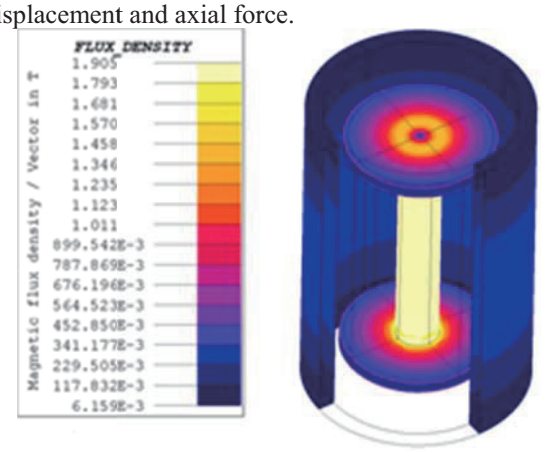

Fig. 3 Flux density of Electromagnetic component

The damper performance was tested under different testing conditions; the simple harmonic motion (sine function) used had its frequency varied, whilst altering applied magnetic field to test its MR effect. In this experimental study, excitation frequencies of 0.5, 1 and 2 Hz were used. Fluctuating the current output from an external power supply (from 0 to 1 A with 0.1 A step and 1 to 3 A with 1 A step) for each test means the internal electromagnets field will increase. Fig. 4 and 5 display the performance of the MRSTF filled damper.

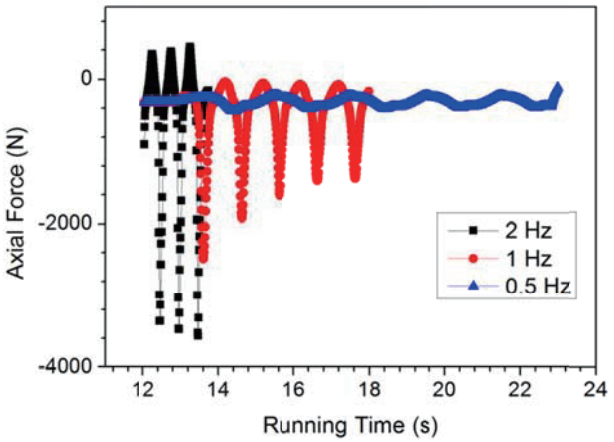

Fig. 4 Force versus time with various frequencies

Fig. 4 presents applied axial force versus time for three different frequency sets. Comparing each plot it is clear that shear thickening is occurring at the fluid piston interface due to the size of force spike for each displacement with the greatest force required to achieve the initial compression location. Each of the three fluids are in neutral state, that is to say, no current is applied to the electromagnet. The representation is reliant completely on speed activation.

Fig. 5 shows the first cycle of compression and extension for 6 runs at a constant frequency of 1 Hz stepping the current in 0.5 A intervals. It is noted that the curves are not perfect ellipses and this damper showed an opposite properties of usually MRF dampers. What is meant by this is that as increasing the applied current to the damper coil, the measured damping force decreases and this also proves that the damper has shear thickening and magnetorheological properties at the same time.

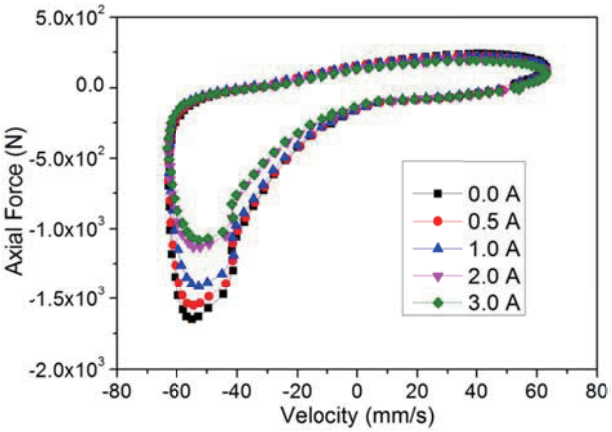

Fig. 5 Axial force versus velocity with various currents

4. Concluding remarks

In this study, an MRSTF consisting of nano sized silica particles suspended in an ethylene glycol, solvent, mixed with carbonyl iron particles was fabricated. The dynamic property of the fluid was tested by a rheometer. Initial findings from the rheometrical testing were extracted and similar trends prevailed when the fluid was applied to MTS damper testing.

A prototype internal electromagnet semi-active damper was designed and fabricated based on research made into similarly performing devices. A secondary element in vibration control is provided as the system exhibits the ability to not only analyse a stiffness coefficient but also a variable damping coefficient. The axially compressing MTS test procedure produced a series of outputs measuring the response of the damper under various loading conditions. Analysing this data series displays the MRSTF to behave as a quasi-Newtonian fluid over a large range of dynamic shear rates with varying magnetic flux densities.

References

[1] H. P. Gavin, C. Alhan and N. Oka, J. Struct. Eng., **129** (2003)
[2] X. Zhu, X. Jing and L. Cheng, J. Intel. Mat. Syst. Str., **23** (2012).
[3] S. B. Choi, H. S. Lee and Y. P. Park, Vehicle Syst. Dyn., 38 (2002).
[4] M. R. Jolly *et al*., J. Intel. Mat. Syst. Str., **10** (1999).
[5] X. Z. Zhang, W. H. Li and X. L.Gong, Smart Mater. Struct., **17** (2008), 035027
[6] X. Z. Zhang, W. H. Li and X. L.Gong, Smart Mater. Struct., **17** (2008), 015051
[7] H. M. Laun, R. Bung and F. Schmidt, J. Rheol., **35** (1991).
[8] J. de Vincente, D. J. Klingenberg, R. Hidalgo-Alvarez, Soft matter, **7** (2010).

Synthesis and Magnetorheology of Iron-based Bidisperse Fluids

Hiroya Abe[1] and Masami Nakano[2]
[1] Joining and welding research institute, Osaka Univ., 11-1 Mihogaoka, Ibaraki, Osaka, Japan
[2]Institute of Fluid Science, Tohoku Univ., 2-1-1 Katahira, Aoba-ku, Sendai, Japan
h-abe@jwri.osaka-u.ac.jp

ABSTRACT

The spherical Fe nanopowder and micropowder were used for preparing the bidisperse MR suspensions. The steady MR responses of the bidisperse suspensions changed significantly as a function of solid fraction of nanopowder. In particular, field-induced yield stress enhanced when the solid fraction of nanopowder was 25%. The field-induced macroscopic structure was visualized and it was revealed that the enhancement of the yield stress can be attributed to the formation of distinct and wide chains. On the other hand, MR effect decreased when the nanopowder was mixed with solidi fraction of 50% or more.

1. Introduction

Magnetorheological (MR) fluids are a class of smart materials whose rheological behavior can be reversibly controlled from a fluid-like to a solid-like state according to magnitude of applied magnetic field. Currently, they are suspensions of micron-sized iron particles dispersed in a non-magnetic liquid such as silicon and mineral oils [1]. The mechanism responsible for the MR effect is the attractive interactions between the induced dipoles which cause the suspended particles to form chain-structures aligned roughly parallel to the applied magnetic field. A finite stress must be developed to yield these chain-structures. The yield stress is continuously controlled and this controllability has been attracted for their use in smart systems [1].

The MR fluids unfortunately exhibit some shortcoming, in particular particle sedimentation. Although an improvement can be made by adding various thixotropic agents such as silica nanoparticles and organoclay particles [2], the yield stress becomes usually smaller. To address this trade-off relation, a bidisperse fluid containing a mixture of both Fe nanopowder and micropowder has been considerable interests [3]. To our knowledge, however, there are few efforts to probe the effect of the nanopowder with high saturation magnetization on MR response of the bidisperse fluids.

Herein, we report the steady MR responses of Fe based bidisperse suspensions. The bidisperse fluids were prepared by mixing carbonyl iron particles (CIPs) and Fe nanopowder synthesized by arc-plasma method. It has been known that the arc-plasma method can synthesize spherical Fe nanopowder with high saturation magnetization (~190emu/g) [4], but the Fe nanopowder has yet to be applied for bidisperse suspensions. In this study, the effects of solid fraction of the nanopowder on the MR responses were examined.

2. Method

The micron-sized Fe powder (CIP CS, D_{50}=6.6μm) was purchased from BASF Japan Ltd. The Fe nanopowder, which was synthesized by arc plasma method, was supplied from Kurimoto Ltd. (Japan). The specific surface area of the nanopowder was measured to be 6.8m^2/g by nitrogen gas adsorption method, and the corresponding diameter was calculated to be about 110nm. The saturation magnetization of the Fe nanopowder was measured to be about 190emu/g at room temperature using a vibrating sample magnetometer [4], which is comparable to that of the micron-sized Fe powder.

To prepare the bidisperse suspensions, silicone oil (KF96-50cs, Shin-Etsu chemical, Japan) was chosen as a carrier fluid. The both Fe powders were dispersed into the silicone oil. The total volume fraction of the solid loading was 10vol%. No surfactant was employed. The solid fraction of the nanopowder in the bidisperse suspensions was varied.

MR responses of the bidisperse suspensions were measured at 293 K using a magnetic field applicable parallel-disk sensor with an electromagnetic system (MR-101N, EKO Instruments, Japan) attached to the high precision rheometer (RheoStress RS-150, HAAKE, Germany).

3. Results and Discussion

The steady-shear flows of bidisperse suspensions containing 0, 25 and 50% nanopowder were investigated in the presence and absence of an applied magnetic flux density. In Fig.1, the shear stress is plotted as a function of shear rate at several flux densities. The range of shear rate tested was swept from 1 to 1000 s^{-1} via log-log scale. For all fluids, the shear stress grows with increasing with magnetic field strength over the entire range of applied shear rate, implying that the chain-like structures constructed within the suspension under applied magnetic fields. However, they differ from one another in MR effect (yield stress), off-state flow behavior (B=0) and shear rate dependency.

For the suspension with 0% nanopowder (100% micropowder), the shear stress depended slightly on shear rate. Extrapolating the shear stress value to the zero shear rate can estimate the dynamic yield stress τ_y [5], and τ_y of 6.1kPa was obtained at 0.31T. These characteristics are similar to those reported in the literature [6].

For the bidisperse suspensions, the steady-state MR response enhanced or decreased, depending on solid fraction of nanopowder. When the solid fraction was 25%, interestingly, τ_y increased significantly (see Fig.2). For example, τ_y at 0.3T increased by ~10% (6.8kPa). The off-state flow behavior is not influenced (see Fig.1 (b)). In addition, the shear stress of this bidisperse fluid had the

larger shear rate dependency compared to the fluid with 100% micropowder. It is thus proven that the bidisperse fluid exhibit a larger field-induced yield stress than monodisperse suspensions when the solid fraction of nanopowder is controlled to be 25%.

In contract, τ_y decreased drastically when mixing 50% nanopowder (4.5kP at 0.3T). The off-state flow behavior becomes quite similar to that of the fluid with 100% nanopowder, i.e., the suspension became agglomerated. When the solid fraction of nanopowder was increased to be 75% (not shown here), τ_y decreased more (3.4kPa at 0.3T). As observed, the steady-state MR response decreased when the solid fraction of the nanopowder is 50% or more. Similar to the suspension with 100% nanopowder, the disorder introduced by the non-magnetic aggregation would become predominant in these bidisperse suspensions, resulting in negative contribution to MR response.

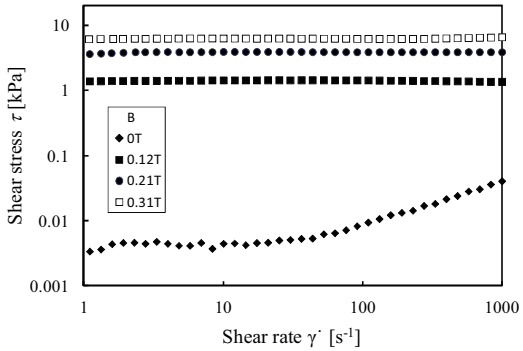

(a) 0% nanopowder (100% micropowder)

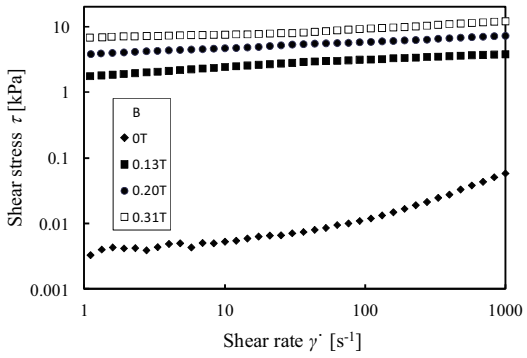

(b) 25% nanopowder

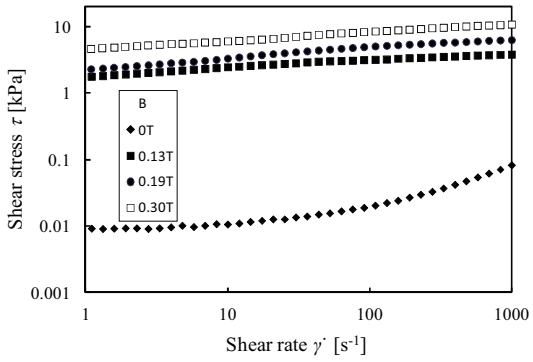

(c) 50% nanopowder

Fig.1 Shear stress curves as a function of shear rate for the four bidisperse fluids containing nanopowder of (a) 0%, (b) 25% (c) and 50%.

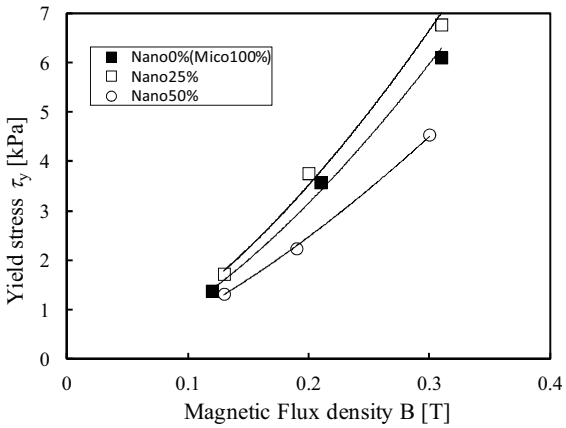

Fig.2 Yield stress as a function of applied magnetic flux density for the four bidisperse suspensions

We have also investigated the magnetic field-induced particle structure associated with the solid fraction of nanopowder (presenting at session "PS1"). It was revealed that the enhancement of the yield stress for the bidisperse fluid (25%) can be attributed to the formation of distinct and wide chains.

4. Concluding remarks

The spherical Fe nanopowder (110nm) and micro powder (6.6μm) were employed for preparing the bidisperse suspensions. The MR responses changed significantly as a function of solid fraction of nanopowder. The bidisperse fluid containing 25% nanopowder provided a substantial increase in the yield stress without an increase in the viscosity of the mixture in the absence of a magnetic field.

ACKNOWLEDGEMENT

Part of the work was carried out under the Collaborative Research Project of the Institute of Fluid Science, Tohoku University.

References

[1] J. D. Carlson and M. R. Jolly, *Mechatronics*, **10** (2000) 555-569.

[2] M. T. Lopez-Lopez, A. G. Ramirez, J. D. G. Duran and F. G. Cabllero, *Langmuir*, **24** (2008) 7076.

[3] N. M. Wereley, A. Chaudhuri, J. –H. Yoo, S. John, S. Kotha, A. Suggs, R. Radhakrishnan, B. J. Love and T. S. Sudarshan, Journal of Intelligent Material System and Structures, **17** (2006) 393

[4] J. Noma et al., J. Magn. Magn. Mater., **322** (2010), 1868.

[5] I. B. Jang, H. B. Kim, J. Y. Lee, H. J. Choi, M. S. Jhon, *Journal of Applied Physics*, **97** (2005) pp. 10Q912.

[6] P. J. Rankin, A. T. Horvath, *Rheological Acta*, **38** (1999) 471

Tenth International Conference on Flow Dynamics
November 25-27, 2013, Sendai, Miyagi, Japan

Double Rotations of a Ferrodrop Array in a Rotating Magnetic Field

Ching-Yao Chen, He-Chin Lin, Hao-Chung Hsueh
Department of Mechanical Engineering, National Chiao Tung University, Taiwan R.O.C.
E-mail of corresponding author: chingyao@mail.nctu.edu.tw

ABSTRACT

We experimentally investigate the motion of a ferrodrop array in a rotating magnetic field. The ferrodrops undergo interesting dual rotations, such as the local self-spins of individual drops and the global revolution of the drop array. While the drops spin nearly synchronized with the overall external field, the revolution always lags behind the field and appears a forth and back movement. Significance of the net revolutionary movement depends on the uniformity of the overall field distribution. In general, a more uniform rotating field leads to a more prominent global revolution of the array.

1. Introduction and Experimental Setups

The dynamics of slender magnetic structures in a dynamical field, such as a chain consisted of magnetic beads in a rotating or an oscillating field, have been intensively studied in recent years [1-4]. A close resemblance is forming such a slender device by arraying ferrofluid drops, instead of chaining superparamagnetic beads. It is also interesting to notice that dynamics of a single ferrofluid drop had been subjects of thorough studies, e.g. in a rotating [5] field. Nevertheless, motion of multiple drops aligned as an array has not yet drawn much attention. The interactions between the magnetized fluid drops might lead to new phenomena. This study intends to realize the motion of such a deformable drop array subjected to a rotating field. An interesting phenomenon of dual rotation, including the local self-spin and the global revolution, is reported.

Two identical sinusoidal field components along the x- and y-axis are generated by the coils associated with a frequency of f=1 Hz. The overall external field ($\boldsymbol{H}$) composed by the two dynamical components is given by $\boldsymbol{H}=H_m\sin(2\pi ft+\triangle\theta_H)\boldsymbol{i}+H_m\sin(2\pi ft)\boldsymbol{j}$, where $\triangle\theta_H$ is the phase difference between $\boldsymbol{H}_x$ and $\boldsymbol{H}_y$. H_m is the reference field strength. Under such a setup, an ideal rotating field with a constant angular speed and uniform field strength can be obtained if the phase difference is taken as $\triangle\theta_H=90^o$. Otherwise a wavering overall field is generated associated with variant angular speed, even the field still rotates periodically. In the study, light mineral oil ferrofluid drops surrounded by distilled water are experimented.

2. Results and Discussion

Motions of a single ferrofluid drop in a rotating field with various phase differences, such as $\triangle\theta_H=50^o$ and 90^o, as shown in Fig. 1 It is known that a initially circular ferrofluid drop would be stretched to the shapes of ellipsoid along the orientation of the external field first, and an equilibrium state would be reached by the balance between the magnetic energy and the surface energy. In the meantime, the stretched ellipsoid is driven to rotate [5], referred to as the self-spin of drop therein. It is noticed that the drop spins almost synchronized with the external field in the present condition. Another interesting but not unexpected observation is that, while the elliptical shape of the self-spinning drop remains nearly unchanged for the case of an ideal rotating field, e.g. $\triangle\theta_H= 90^o$, the prominence of elongation varies during the self-spinning process in the field configuration of $\triangle\theta_H= 50^o$.

A question arises if multiple drops are placed in an array and subjected to the same field condition. Under such a condition, the interactions between magnetized drops would expect to play an important role. Shown in Fig. 2 are the snapshots of a three-drop array under field configurations of $\triangle\theta_H=50^o$, 70^o and 90^o. Similar to the case of a single drop, all the drops undergo local motions of self-spins. Nevertheless, an interesting global phenomenon of array revolution can also be identified. Contrary to the local self-spins which appear almost synchronized with the rotating field, this global revolutionary motion of the array does not follow the orientation of external field consistently. The drop array in a uniform rotating field of $\triangle\theta_H=90^o$ undergoes an apparent overall revolution with the external field, i.e. counter-clockwise, but lagging behind greatly. On the other hand, the drop array in a strongly non-uniform rotating field of $\triangle\theta_H=50^o$ merely shows a local oscillation. For the condition in a milder non-uniform rotating field of $\triangle\theta_H=70^o$, the array appears forth and back with a net counter-clockwise revolutionary movement within the period.

According to the experimental observations described in the above paragraph, a ferrodrop array driven by a rotating field undergoes an interesting motion of dual rotation, such as the local self-spin of individual drops and the global revolution of the array. Understandings of the local self-spins are straightforward. On the other hand, the global revolution of the drop array is attributed by the interactions between the magnetized fluids, whose mechanism can be analogized to the magnetic bead chain subjected to a dynamical field [1-4]. Based on the assumption of point dipoles, the torque (T) generated by the external field to the magnetized chain or array can be approximated as $T \sim \sin(2\triangle\theta_L)$, where $\triangle\theta_L$ stands for the simultaneous phase difference between the external field and the alignment of drop array. This torque is driving source to the global revolution. To further understand this driving force, the trajectories of both the overall fields and drop arrays within one period of rotation for three field

configurations are demonstrated in Fig. 3. For a uniform rotating field of $\triangle\theta_H$=90°, the angular speed of the field is constant, so that the field trajectory is a straight line as shown in the figure. On the contrary, for the configurations of non-uniform fields, their trajectories appear wavering with variant angular speeds within rotation. At an earlier time stage, the fields move well ahead of the arrays for all three conditions and generate effective torques toward the orientations of the rotating fields, i.e. counter-clockwise, so that the arrays are driven to undergo global revolutions. Nevertheless, due to the significant hydrodynamic drags to resist the revolutionary motion, the phase lags ($\triangle\theta_L$) continue to grow. At a certain extent, the phase lags would exceed a critical value of $\triangle\theta_L$ > 90°, and leads to a sign change of torque. Similar phenomenon had also been reported in a superparamegnatic chain, and was referred to as trajectory shift [4]. Then, the revolutionary movement of the drop array would be reversed. This reversed revolution would proceed till the direction of torque is changed again at $\triangle\theta_L$ > 180°. Similar scenarios would proceed continuously afterward at the times when the phase lag exceeds the multiples of 90°. The continuous alternation of torques explains the forth and back motion of the global revolutions. In addition, it is realized that the simultaneous angular speed of the external field at an early stage is the greatest for the most non-uniform rotating field of $\triangle\theta_H$=50°, as shown in Fig. 3, so that a largest phase lag is resulted at the early time interval. As a result, the first reversed revolution occurs the earliest for $\triangle\theta_H$=50°, as the vertical line marked by A1 shown in Fig.3. By the same token, the first reversed revolutions for $\triangle\theta_H$=70 ° and 90°, marked by B1 and C1 respectively, will happen at later times subsequently. Fig. 3 shows that the trajectory of array has been shifted 4 times, e.g. A1~A4, for $\triangle\theta_H$=50°, while there are only 3 shifts for $\triangle\theta_H$=70 ° and 90°, e.g. B1~B3 and C1~C3, respectively. The later and fewer occurrences of the reversed revolutions for more uniform rotating field conditions are the reasons of greater net revolutionary movements.

3. Concluding remarks

Driven by a rotating field, an interesting phenomenon of dual rotations is identified in arrayed ferrofluid drops, including a local self-spin of individual drops and the global revolution of the array. Because of the simultaneous realignments of the induced poles in the magnetized ferrofluids, the ferrodrops and spin nearly synchronized to the field. On the other hand, the global revolution of the drop array is resulted by the interactions between the magnetized drops, and might undergo a wave-like forth and back movement. The wavering behaviors of array revolutions are realized by the alternative magnetic torques acting to the array, which change sign when the phase lag between the orientations of the external field and the alignment of the array reaches multiples of π/2. Prominence of the net revolutionary movement is affected by the uniformity of the overall field distribution.

Support by the NSC 102-2221-E-009-051-MY3 is acknowledged.

References

[1] Biswal, Gast, Phys. Rev. E 69, 041406 (2004).
[2] Cebers , Javaitis, Phys. Rev. E 69, 021404 (2004).
[3] Li, Chen, Sheu,Pai, Microfluid Nanofluid 13, 579 (2012).
[4] Li, Lin,Chen, Microfluid Nanofluid, 14, 831 (2013).
[5] Lebedev, Engel, Morozov, auke, *New J. Phys.* 5, 57 (2003).

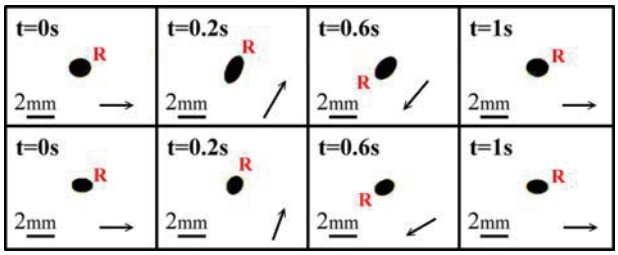

Fig. 1: Motion of a drop subjected to an overall field strength of H_m = 47 Oe and (top) $\triangle\theta_H$=50°; (bottom) $\triangle\theta_H$=90°. The directions and the lengths of arrows represent the simultaneous orientations and magnitudes of the overall field, respectively.

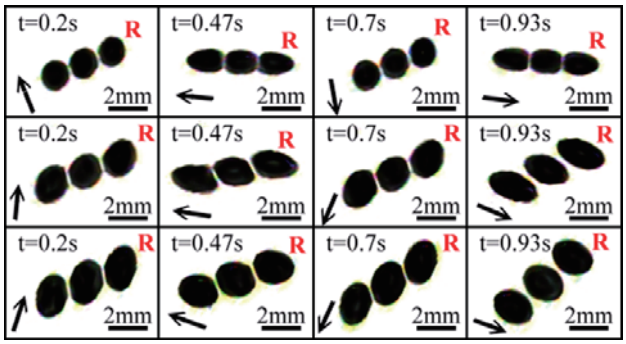

Fig. 2: Motion of a three-drop array subjected to an overall field strength of H_m = 47 Oe and (top) $\triangle\theta_H$=50° ; (middle) $\triangle\theta_H$=70° ; (bottom) $\triangle\theta_H$=90°. The drop on the right is marked by letter "R" to demonstrate the global revolution of the array.

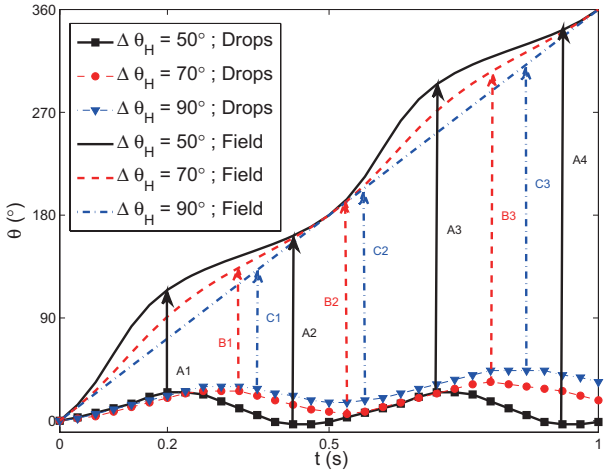

Fig. 3: Corresponding phase trajectories of the external fields and the drop arrays shown in Fig. 2.

Tenth International Conference on Flow Dynamics
November 25-27, 2013, Sendai, Miyagi, Japan

On the Breakup of Magnetic Fluid Bridge

Kazuya Takahashi[1], Seiichi Sudo[1], Hideya Nishiyama[2]
[1]Akita Prefectural University, Ebinokuchi 84-4, Yurihonjo 015-0055, Japan
[2]Tohoku University, Katahira 2-1-1, Aoba-ku, Sendai 980-8577, Japan
E-mail : sudo@akita-pu.ac.jp

ABSTRACT

Experimental study on the breakup of a magnetic fluid bridge formed between two needle-like permanent magnets in alternating magnetic field is described. The surface phenomena of the magnetic fluid bridge were observed using high-speed video camera system. Breakup processes of magnetic fluid bridge were studied. For certain external alternating magnetic field conditions, the liquid bridge disintegration and satellite droplet formation were observed sometimes. Breakup duration in magnetic fluid bridge disintegration was measured.

1. Introduction

With the development of space technology, stable colloidal suspensions (magnetic fluid) of solid magnetic particles of subdomain size dispersed in a nonmagnetic carrier liquid were developed [1]. The fluids respond to magnetic fields and have a magnetization. In our previous papers, authors proposed novel micro electromechanical actuators using a permanent magnet and magnetic fluid [2-5]. In these magnetic fluid devices, various interfacial phenomena on the magnetic fluid surface were observed [3,5]. On the other hand, extensive investigations on the problem of droplet generation and breakup of the liquid jet have been conducted, because it is related to the basic science and technology [6]. Although extensive investigations on the capillary instability of liquid bridges have been conducted, no study has been published on the periodic thinning and breakup of a magnetic fluid bridge under the magnetic fields.

In this paper, the breakup phenomena of a magnetic fluid bridge formed between two permanent magnets subjected to external alternating magnetic fields were studied.

2. Experimental apparatus and procedures

The experimental apparatus is composed of the test magnetic fluid bridge system, alternating magnetic field generation system, and high-speed video camera system. A schematic block diagram of the experimental apparatus to study the breakup phenomena of magnetic fluid bridge under the alternating magnetic fluid is shown in Fig.1. The test magnetic fluid bridge system is consists of thin cylindrical NdFeB permanent magnets and magnetic fluid. The diameter of the cylindrical magnet is 1 mm, and the length is 5mm. The magnetic flux density of permanent magnet is B = 198 mT at the surface. The magnetic fluid bridge is formed between two permanent magnets. Sample magnetic fluid used in the experiment is synthetic hydrocarbon MSG P50. The volume of magnetic fluid was measured by the precision micropipette. The alternating magnetic field was generated by applying alternating voltage to the Helmholtz coil. In the experiment, the applied voltage was given in the sinusoidal form. In the direction of the external alternating magnetic field, two direction in parallel and perpendicular to the gravity were examined.

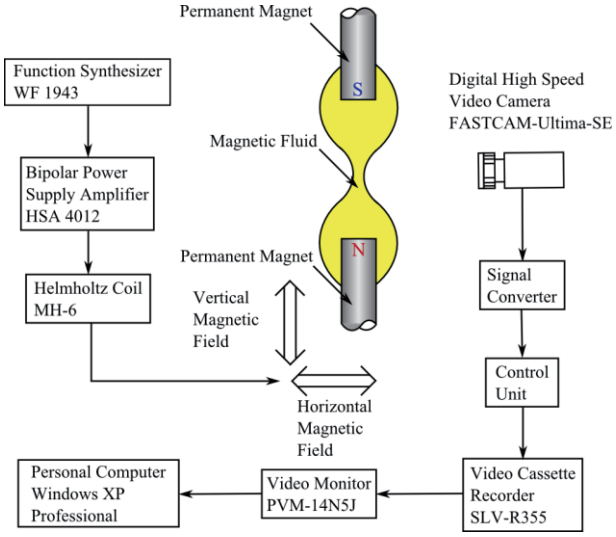

Fig. 1 A schematic diagram of experimental apparatus

The saturation magnetization of the magnetic fluid is M_s = 50.0 mT. The surface tension of magnetic fluid was 0.032 N/m. The magnetic fluid of a prescribed volume (V_m = 10 μl) was injected into the permanent magnet gap. The experiment performed under the condition of room temperature.

3. Experimental results and discussion

3.1 Responses of magnetic fluid bridge

When alternating magnetic field was applied to the magnetic fluid bridge, the shape vibration on the liquid bridge surface occurred. In the experiment, two directions of external magnetic field were examined as shown in Fig. 1. The vertical magnetic field in Fig. 1 is parallel and anti-parallel to the gravity. In this case, the neck diameter of liquid bridge showed thinning and thickening according to the magnetic field directions. The diameter of liquid bridge was contracted when the direction of alternating magnetic field was anti-parallel to the static magnetic field. The horizontal magnetic field in Fig. 1 is perpendicular to the gravity and the magnetic field produced by the permanent magnets. In this case, the magnetic fluid bridge showed a tilt

vibration of the liquid bridge axis.

3.2 Response to vertical alternating field

Liquid bridge disintegration depended on the external alternating magnetic field. When the amplitude of alternating field exceeded the critical value, the breakup of the liquid bridge was observed. Fig. 2 shows an example of such liquid bridge breakup. In Fig. 2, E_0 is the total amplitude of applied voltage, and f_0 is the frequency. In Fig. 2, the breakup of liquid bridge is observed at t = 13.3 ms. Generally, breakup is caused by the stretch flow [6]. Fig. 3 shows the details of the liquid bridge breakup. The neck diameter of liquid bridge, d_{min}, decreases gradually, and liquid bridge is broken up at t = 12.9 ms. The thinner speed of liquid bridge is approximately constant $| d(d_{min}) / dt | \fallingdotseq 0.2$ m/s. In this case, the breakup duration is t_b = 0.44 ms. The breakup duration t_b depends on the frequency of alternating field at the condition of constant E_0. Fig. 4 shows the relation between t_b and f_0 at constant E_0. The breakup duration decreases with the increase of frequency, and t_b reaches 0 at f_0 = 70 Hz.

3.3 Response to horizontal magnetic field

Liquid bridge disintegration in the horizontal alternating magnetic field also observed at larger amplitudes of alternating magnetic field. Fig. 5 shows a sequence of selected frames from high speed movie showing the magnetic fluid bridge breakup produced by the horizontal alternating magnetic field at E_0 = 60V and f_0 = 140Hz. Magnetic torque to act on the liquid bridge causes the breakup.

4. Conclusions

The breakup phenomena of the magnetic fluid bridge formed between two permanent magnets subject to external alternating magnetic fields were studied. The results obtained are summarized as follows;

(1) The breakup of magnetic fluid bridge in vertical alternating field may occur at larger amplitude of external field.
(2) The breakup duration decreases with the increase of alternating field frequency at constant E_0.
(3) Liquid bridge disintegration in the horizontal alternating magnetic field may occur by the magnetic torque.

References

[1] R.E. Rosensweig, Ferrohydrodynamic (Cambridge Univ. Press, Cambridge, 1985).
[2] S. Sudo, H. Takayanagi, S. Kamiyama, J. Magn. Magn. Mater., **323** (2011) 1348.
[3] S.Sudo, D. Asano, and H. Nishiyama, J. Magn. Magn. Mater., **323** (2011), 1314.
[4] S. Sudo, Y. Takaki, Y. Hashiguchi, H. Nishiyama, JSME Int. J., **48**- 3 (2005), 464.
[5] S. Sudo, T. Yano, M. Futamura, H. Takana, H. Nishiyama, J. Solid Mech. Mater. Engn., **6**-6 (2012), 555.
[6] J. Eggers, and E. Villermaux, Rep. Prog. Phys., **71** (2008), 036601.

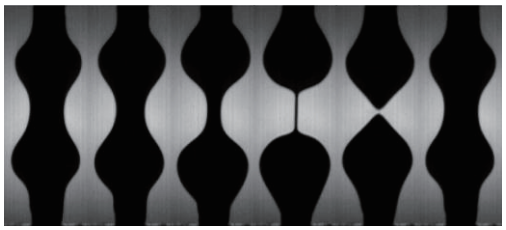

t = 0 ms 3.3 ms 6.7 ms 10.0 ms 13.3 ms 16.7ms

f_0 = 60 Hz, E_0 = 60 V, V_m = 10×10^{-9} m^3, S = 3.8 mm

Fig. 2 Breakup process in vertical magnetic field

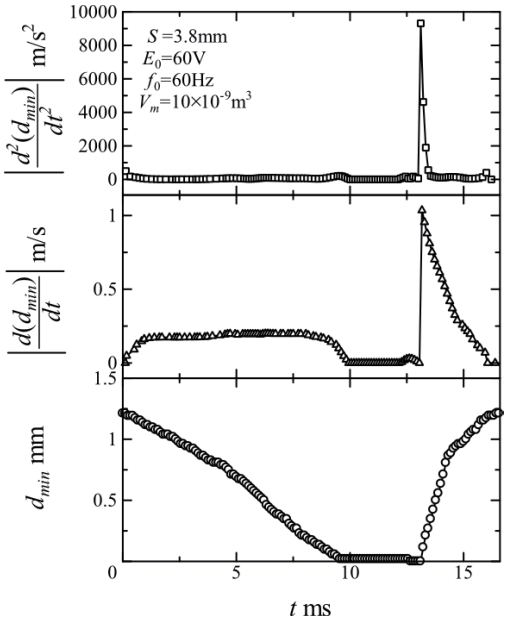

Fig. 3 Breakup details of in vertical magnetic field

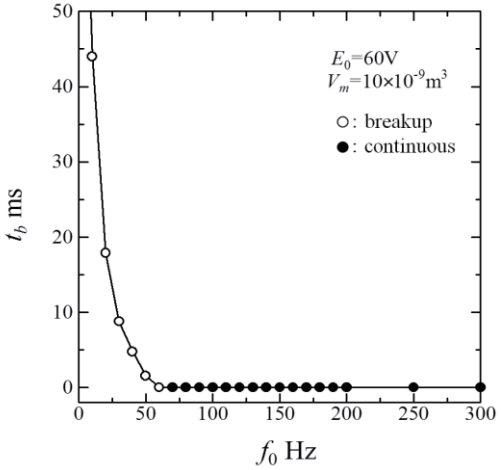

Fig. 4 Relation between t_b and f_0

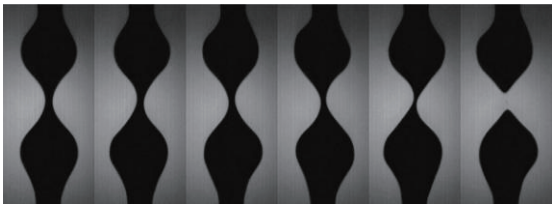

t = 0 ms 2.5 ms 5.0 ms 7.5 ms 10.0 ms 12.5 ms

f_0 = 140 Hz, E_0 = 60 V, V_m = 10×10^{-9} m^3, S = 4.7 mm

Fig. 5 Breakup process in horizontal magnetic field

Tenth International Conference on Flow Dynamics
November 25-27, 2013, Sendai, Miyagi, Japan

Design and Evaluation of Linear Seismic Damper Using MR Fluid Composite Rotary Brake

Masami Nakano[1], Tomoaki Inaba[1], Atsushi Totsuka[1] and Akira Fukukita[2]
[1]Intelligent Fluid Control Systems Laboratory, Institute of Fluid Science, Tohoku University
2-1-1 Katahira, Aoba-ku, Sendai, 980-8577, JAPAN
[2]Institute of Technology, Shimizu Corporation
3-4-17 Etyujima, Koto-ku, Tokyo, 135-8530, JAPAN
m-nakano@fmail.ifs.tohoku.ac.jp

ABSTRACT

In the applications of MR(Magnetorheological) fluid dampers to seismic isolation and suppression technologies for buildings, one of serious problems is the particle sedimentation of MR fluids in the off-working state. To solve this problem, "MR fluid porous composite" made of porous materials pregnant with an MR fluid has been fabricated. And, a seismic linear motion MR damper consisting of a ball screw and a rotary MR brake using the MR fluid porous composite has been designed and developed. The damping properties of the developed seismic MR damper have been investigated experimentally.

1. Introduction

MR(Magnetorheological) fluids are the suspensions with micron-sized ferromagnetic particles dispersed into carrier oil, and are one of smart fluids which can be changed their rheological properties in reversible manner by applying magnetic field [1]. So far, many types of high-performance seismic MR dampers with variable damping force have been developed to isolate and suppress seismic vibration of building systems [2], and however, have not yet resulted in extensive spread because the sedimentation of ferromagnetic particles dispersed into the MR fluid in off-working state poses practical problems such as reliability.

In this study, in order to solve this problem and to make fluid-seals unnecessary, "MR fluid porous composite" made of porous materials impregnated with MR fluid has been fabricated, and it was found that the use of nonwovens intertwined with thinner fibers closely as porous materials was much effective to enhance the MR effects [3]. And then, we have developed a linear motion MR damper of 20 kN class for seismic isolation and suppression of building system which consists of a rotary brake using the MR fluid porous composites and a ball screw for translating linear motion to high-speed rotational motion. In this paper, we present MR properties of the MR fluid porous composite used in the developed MR damper, and describe the design and the damping properties of the developed MR damper using the rotary brake with MR fluid porous composites.

2. MR fluid porous composite and MR properties

As shown in Fig.1, two species of nonwoven (NAMIKEN make) with different internal structures were tested as porous materials. One is KN-60-3 (thickness t_0=0.8 mm, shear modulus G=11.2 kPa) and the other is TRF-50H (t_0=0.5 mm, G=26.5 kPa). The commercial MR fluid (MRF-132DG, Lord Co.) is sufficiently impregnated into the nonwovens to fabricate the MR fluid porous composites. The MR properties were measured in oscillatory shear mode using the double gap-sliding plate oscillatory rheometer with an electromagnet developed at our laboratory. Figure 2 shows the changes of the obtained maximum shear stress with applied magnetic flux density B for two species of nonwoven and sliding plate. The maximum shear stress in the post-yield region increases with increasing B. The shear stress for the iron plate is more than twice of that for the aluminum plate. And also, from the fact that the MR fluid composite of TRF-50H induces higher shear stress than that of KN-60-3, it can be concluded that an MR composite made of nonwovens with closely intertwined thinner fibers and higher G shows the higher MR effects. As mentioned above, it is decided to use the MR fluid composite of TRF-50H for the developed MR damper.

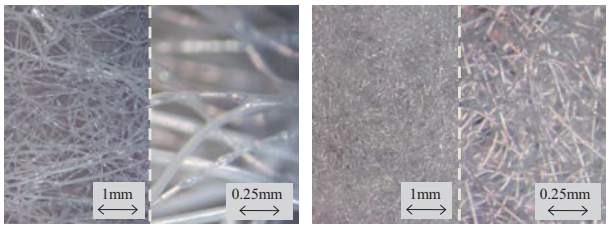

(a) KN-60-3, t_0=0.8mm (b) TRF-50H, t_0=0.5mm

Fig.1 Enlarged pictures of tested nonwovens（×82, ×328）

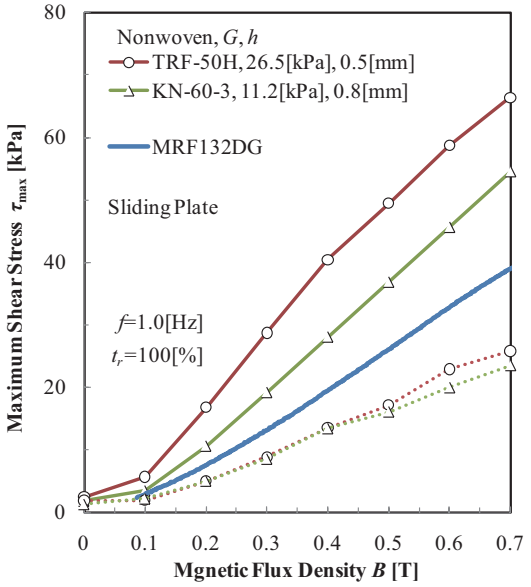

Fig.2 Changes of maximum shear stress with B for two species of nonwoven and sliding plate

3. Developed seismic linear motion MR damper

As shown in Fig.3, the developed linear motion MR damper consists of three main components such as a ball screw mechanism (lead length; 0.03mm) for translating linear motion of the MR damper to high-speed rotational motion, a linear guide mechanism for a ball screw spindle and a rotary MR fluid composite brake connected to a ball screw rotary nut. The damper size is 800 mm in full length, 240 mm in width, the stroke is ± 100mm and the designed damping force is 20 kN. The rotary MR brake shown in Fig.4 has four rotary disks of which MR fluid composites sheets glued to fixed disks lie in both sides and an electromagnet (N=1300 turns, R=59 Ω) for applying magnetic field to the MR composites. The MR fluid composites induce variable shear stress to the rotary disks, resulting in braking torque to the brake shaft.

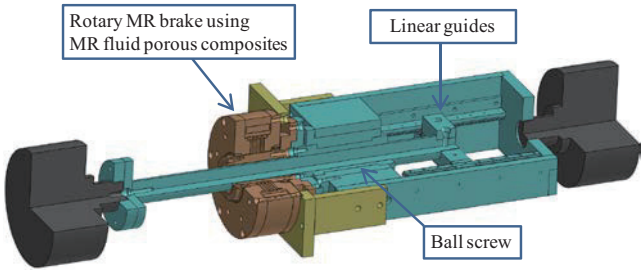

Fig.3 Seismic linear MR damper using rotary MR brake

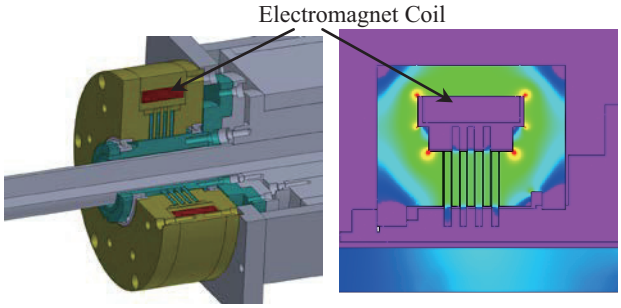

Fig.4 Rotary MR brake using MR fluid porous composite

4. Damping force of MR damper

The damping force of the MR damper was measured under sinusoidal excitations by using a hydraulic fatigue testing machine (Servo Pulser: EHF-UV30, Shimazu). Figure 5 and 6 show the changes of the hysteresis loops of displacement x-damping force F with the applied electric current I and the sinusoidal excitation amplitude x_a, respectively. The loops look like a rectangle. The maximum damping force increases with increasing I and reaches to the designed 20 kN at I=0.5 A, showing slight viscous effect depending on the damper speed. As seen in Fig.6, the increase of excitation amplitude x_a extends an area within the loop, leading to a tendency to a little increase of the maximum damping force.

The transient responses of the damping force F and the coil current I were measured under constant damper speeds when a step input of desired coil current was applied to a servo amplifier with a feedback control of the coil current. As shown in Fig.7, the F begins to

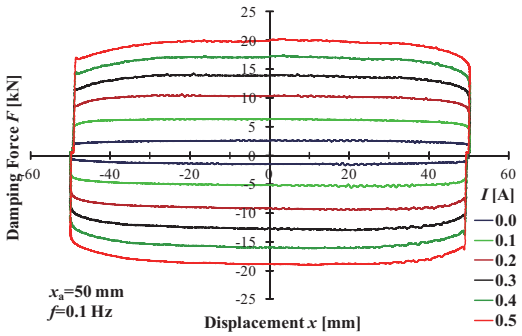

Fig.5 Changes of x-F hysteresis loops with coil current I

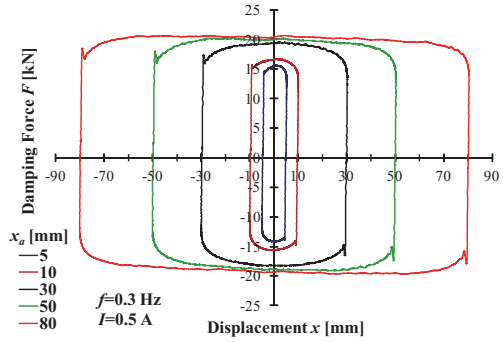

Fig.6 Changes of x-F hysteresis loops with amplitude x_a

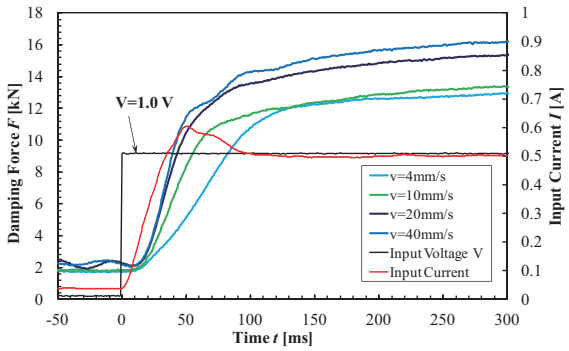

Fig.7 Step responses of damping force

gradually increase at about t=20ms, although the I rises simultaneously. This step response of F can be approximated by a first order lag element plus pure time delay. The dead time L of the pure time delay is 20 ms independent of the damper speed. While, the time constant T of the first order lag element is shortened as the damper speed v becomes higher. In the case of v=40mm/s, the T is 37 ms.

5. Concluding remarks

The developed seismic MR damper had the damping properties similar to that of a variable friction damper, due to the MR effects of the MR fluid composite. The designed damping force of 20 kN was performed at I =0.5 A. The damping properties were clarified in detail.

References

[1] M. Nakano, et al., Int. J. of Modern Physics B, **13-14, 15&16** (1999), 2068-2076.
[2] B.F. Spencer, S. Nagarajaiah, J. of Struct. Eng., **129**-7 (2003), 845-856.
[3] M. Nakano, Fluid Power System, JFPS, **42**-1 (2011), 41-45.

Tenth International Conference on Flow Dynamics
November 25-27, 2013, Sendai, Miyagi, Japan

Development of an Adaptive Structure with MR Elastomers

Miao Guo, Weihua Li
School of Mechanical, Materials and Mechatronic Engineering, University of Wollongong,
Wollongong, NSW 2522, Australia
E-mail: weihuali@uow.edu.au

ABSTRACT

This paper presents the development of a positive-negative stiffness isolator. The isolator used magnetorheological (MR) elastomer and magnetic force to achieve a variable stiffness. A prototype of the positive-negative stiffness was fabricated. The test rig was setup and the transmissibility of the system under different current intensities was tested. The dynamic characteristics of developed isolator under different current intensities were simulated and verified with experimental study.

1. Introduction

Magnetorheological elastomer (MRE) is a smart material because its mechanical modulus can be controlled by an external magnetic field. This characteristic has inquired a number of engineering application areas. The first one is on the sound and vibration control, especially on the vehicle applications, including dynamic vibration absorber and isolator. The second one is on the controllable stiffness change and deformation, such as roll in papermaking machine and releasable fastener system. The third one is on the sensor and actuators. There are still some studies which make use of controllable stiffness and other unique characteristics of these elastomers, such as adaptive tuned vibration absorbers, variable impedance surfaces, tunable stiffness suspensions and mounts [1,2].

While researchers have applied MREs to tunable vibration absorbers (TVAs), little work has been done using MREs in isolation systems [3]. Particularly, there are few reports studying the negative stiffness of vibration isolator to broaden the effective working frequencies ranges of vibration isolator. This work presents the development of a positive-negative stiffness isolator. The isolator uses an MR elastomer and magnetic force to achieve a variable stiffness. The variable stiffness isolator is able to work over a relatively wide range of excited frequencies. A mathematical model of the isolator was derived, and a prototype of the positive-negative stiffness has been fabricated. The test rig was setup and the transmissibility of the system under different current intensities was tested. The dynamic characteristics of this isolator under different current intensities were simulated with Matlab. Both the experimental and simulated results show that the system's natural frequency increases when a positive current is applied, and decreases when a negative current is applied. The simulation results also demonstrated that the positive-negative isolator can efficiently suppress vibration after tuning the current of coils. The goal of this study is to show that MREs have potential to be used as isolation systems over a relatively wide frequency range. This study is also expected to provide good guidance to develop MRE-based devices.

2. Method

The schematic of the proposed positive-negative stiffness vibration isolator is shown in Figure 1. The vibration isolator consists of a top mass, a middle mass, a base, three electromagnets, two MREs, two connecting plates, eight ball bearings, and four guide pins. The base plate, which is made of aluminium, is connected to a shaker. The magnetic field applied to the MRE is generated by electromagnet (EM) 3, which the stiffness can increase. The middle mass is connected to the top mass through a connecting plate. Four guide pins are used to make sure that the top mass and middle mass move smoothly in a vertical direction.

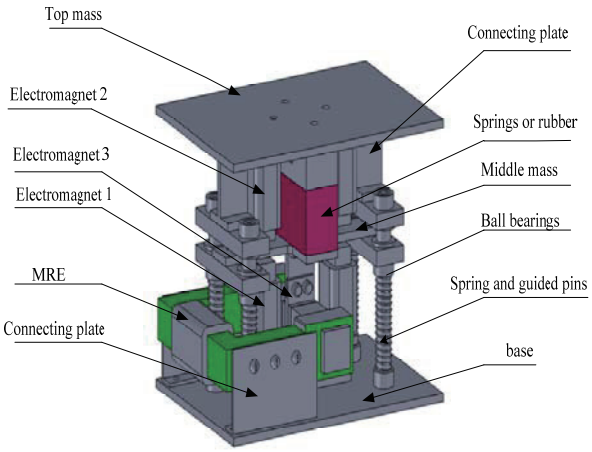

Fig. 1 Schematic of the adaptive MRE structure.

The dynamic performance of the proposed MRE isolator will be characterized with a vibration testing system including a shaker, DAQ board, sensors, power supply, and LabVIEW software for data acquisition and processing. The testing program was designed in LabVIEW. The essential part of this system is the vibration package, which was used to generate the swept sine signals and display and record the test results for the analysis of the isolator. The program measures the frequency response of the device with a swept sine. The start frequency and stop frequency determine the frequency range of the measurement.

In this experiment, the start frequency was 0.2 Hz and the stop frequency was 20 Hz. The number of steps was set as 100, which determines the total number of test frequencies. The current intensity in the coil 1 is ranged from 0 to 3A, while in coils 2 and 3 it changed

from 0 to 2A.

3. Results and Discussion

In order to get the simulation results, a Simulink model was built according to the equation of motion of the isolator. The chirp signal was set as the vibration input of the base with an initial frequency of 0Hz, a target time of 20s, and the frequency at target time of 20Hz. After the Fast Fourier Transform of the input of the base and output of the top mass, the transmissibility of the isolator was obtained at different frequencies. Different parameters were set when a positive current I+ and negative current I- were applied.

Using a control method, the smallest level of vibration can be obtained. When the positive current intensity I+ is applied, the transmissibility peak occurs at a high frequency which is denoted as f_h. When a negative current intensity I- is applied, the transmissibility peak occurs at a relatively low frequency denoted as f_l. When the excited frequency is greater than f_h, the current intensity I should be 0. When the excited frequency is less than f_l, the positive current intensity I+ should be applied. When the excited frequency is between f_l and f_h, the vibration level of isolator should be tuned by the EM based on the transmissibility curve.

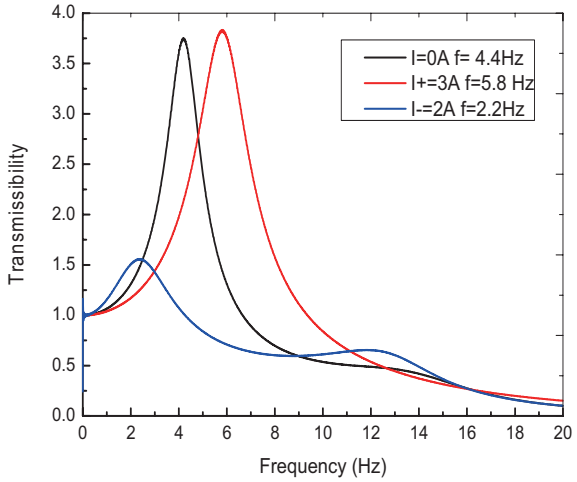

Fig. 2 Simulate results of transmissibility of the proposed MRE isolator.

The simulated transmissibility of the isolator based on the equation of motion under different current intensities is shown in Figure 2. As can be seen, the natural frequency increased from 4.4 Hz to 5.8Hz when the current intensity in electromagnet 3 changed from 0 A to 3 A, and the current intensity in both EM 1 and 2 was 0 A. However, the natural frequency decreased from 4.4 Hz to 2.2 Hz when the current intensity in both EM 1 and 2 was 2A, which in EM 3 was 0 A .

Figure 3 shows the experimental and simulated transmissibility of the positive-negative stiffness vibration isolator at various current intensities. From these figures, the natural frequency of the isolator changed from 2.6Hz, when the current intensity in coil 2 and 3 was 2A respectively, to 5.2 Hz when the current intensity was 3 A in coil 1 (apply magnetic field strength to MRE). The relative change in frequency of this isolator was about 100% when the stiffness changed from a negative state to a positive state. This shows that the experimental results agreed relatively with the simulated results.

The peak transmissibility of the isolator, when there was no external current intensity applied between the experimental and simulated results were slightly different because the vibration isolator proposed is a two level model (two degrees of freedom model) so the transmissibility is related to many parameters, which can be seen from the equations of motion of the vibration isolator. During the experiment, there were probably some factors that affected the results. For example, It was hard to enable get the vibration isolator to move in a vertical direction, and moreover, the amplitude of force from the shaker may have been influenced and friction between the different parts of the vibration isolator probably affected the test results as well.

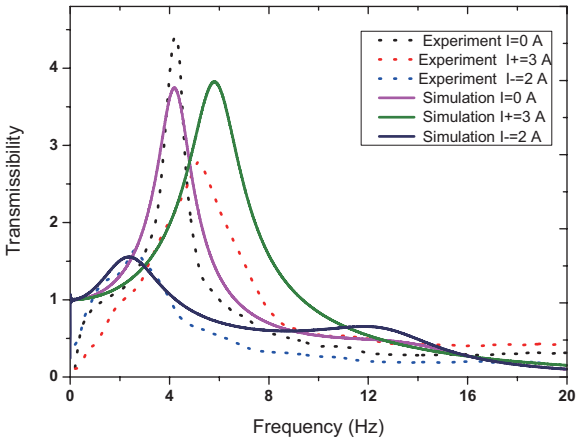

Fig. 3 Storage modulus, loss modulus and loss factor as a function of frequency at magnetic fields of 0.2T and 0.5T respectively.

4. Conclusions

By using different weight fraction ratio of carbonyl iron particle and STF base, four MRSTF samples were fabricated and their viscoelastic properties were characterized. These samples show clear MR effect where both shear moduli and loss moduli increase steadily with magnetic field. However, the shear thickening effect was not observed with the dynamic testing. Compared with conventional MR fluid, the MRSTF material has overcome the particle settling problem without sacrificing MR effect.

References

[1] J. M. Ginder et al., Int J Mod Phys B, **16** (2002), 2447.
[2] H. X. Deng, et al., Smart Mater. Struct., **15** (2006), N111.
[3] Y. C. Li et al., Smart Mater. Struct., **22** (2013) 035005.

Tenth International Conference on Flow Dynamics
November 25-27, 2013, Sendai, Miyagi, Japan

Halloysite Nanotubule Clay for Efficient Water Purification

Alexander Vasiliev[1,2] and Yuri Lvov[3]
[1]Physics Department, M. Lomonosov Moscow State University, Leninskie Gory 1, Moscow 119991, Russia
[2]Institute of Physics and Technology, Ural Federal University, Mira Str., 21, Ekaterinburg, 620002, Russia
[3]Institute for Micromanufacturing, Louisiana Tech University, 911 Hergot Avenue, Ruston, LA 71272, United States
vasil@lt.phys.msu.ru

ABSTRACT

Halloysite clay has chemical structure similar to kaolinite but it is rolled in tubes with diameter of 50 nm and length of ca. 1000 nm. Halloysite exhibits higher adsorption capacity for both cationic and anionic dyes because it has negative SiO_2 outermost and positive Al_2O_3 inner lumen surface; therefore, these clay nanotubes have efficient bivalent adsorbancy. An adsorption study using cationic Rhodamine 6G and anionic Chrome azurol S has shown approximately two times better dye removal for halloysite as compared to kaolin. Halloysite filters have been effectively regenerated up to 50 times by burning the adsorbed dyes.

1. Introduction

Dyes and pigments from textiles, printing, paper, plastics, leather and pulp productions are often toxic and environmentally unsafe, and discharge of colored effluents from these industries wastewater is needed. Precipitation, coagulation, membrane separation, photo-degradation, ion exchange and adsorption have been extensively exploited for dyes-contaminated wastewater treatment. Among them, adsorption has received increasing attention due to high efficiency, environmental friendliness, low cost, easy operation, insensitivity to toxic substances and the possibility of the materials recycling. Many low-cost mesoporous adsorbents have been tested including zeolites, kaolinite and montmorillonite clays, banana peel, saw dust, fly ash, and other materials. However, none of the above materials show high adsorption capacity for both positive and negative dyes. Recently, halloysite nanotubes, economically viable clay mineral, attracted a great interest due to their hollow tubular structure, high surface area and unique surface properties. Halloysite is a naturally occurring 1:1 dioctahedral aluminosilicate clay mineral chemically similar to kaolinite. Halloysite nanotubes with ca. 50 nm diameter, 10 nm lumen and 1 μm length are formed by rolling kaolinite sheets during natural hydrothermal process. Halloysite tubes have multilayer walls with negatively charged Si–OH on the outer surface and positively charged Al–OH on the inner surface (at pH between 4 and 9) and does not require exfoliation, contrary to the kaolinite plate-like morphology. This unique bivalent morphology with spatially separated negative and positive surfaces makes halloysite tube a promising adsorbent for variety of pollutants, both positive and negative. The adsorption properties of halloysite with cationic dyes and heavy metal ions were reported, but anionic dye adsorption was not studied though it may be specifically controlled with its positively charged lumen. We present here the halloysite adsorption study of cationic dye Rhodamine 6G and anionic dye Chrome azurol S and its comparison with kaolinite clay adsorption [1].

2. Method

The batch experiments were carried out in 2 mL centrifuge tubes containing 1 mL of dye solutions and 2 mg adsorbent clay. The tubes were left at 20–60 C to reach equilibrium on dye adsorption. Then tubes were centrifuged for 5 min at 14,000 rpm and the concentration of supernatant was determined using UV–Vis Spectrophotometer (Agilent, 8453). The removal efficiency (R, %) and the amount of dyes adsorbed at equilibrium (q_e, mg/g) were calculated by using the following equations:

$$R = \frac{100(C_0 - C_e)}{C_0} \quad (1)$$

$$q_e = \frac{1000(C_0 - C_e)V}{M} \quad (2)$$

where C_0 and C_e (mg/L) are the initial and equilibrium concentrations of dyes solution; V (L) is the volume of dyes solution and M (mg) is the weight of adsorbents. Strong UV adsorption of dyes allows determination of their concentration at ranges down to ppm levels and hence provides very precise determination of the removal efficiency (up to three decimal points).

The water filter system was set up as follows. One gram of adsorbent clay was added to the water filter and cellucotton was used to block the adsorbent powder. The system was kept at 20 C. 300 mg/L Rhodamine 6G and Chrome azurol S dyes solution were studied in the system and dyes concentration were determined after filtration, respectively. In order to study the reusability of halloysite, the used adsorbents were dried under 60 C in the oven and burned at 300 C. After that, the burned samples were reused as adsorbents in the water filter system and dyes concentration was measured again after filtration. The adsorption-burning-adsorption cycle were repeated for five times.

3. Results and discussion

Adsorption behaviors of positively charged dye – Rhodamine 6G and negatively charged dye – Chrome azurol S were studied with halloysite and kaolinite powders using aqueous dyes of 0–0.05 wt%.

Langmuir and Freundlich models were applied to describe the adsorption process. The correlation coefficients of Langmuir fitting were all above 0.94 and higher than that of the Freundlich model, indicating that

Langmuir model describes our process better than Freundlich. The maximum adsorption capacity calculated from Langmuir model is 43.6 mg/g for Rhodamine 6G and 38.7 mg/g for Chrome azurol S onto halloysite, and 21.4 mg/g for Rhodamine 6G and 36.7 mg/g for Chrome azurol S onto kaolinite. All R_L values fall between 0 and 1, which indicates favorable adsorption process. The values of 1/n are all smaller than 1, representing the favorable removal conditions. It was observed that halloysite has better adsorption for both of the dyes as compared to kaolinite. The larger surface area of halloysite gives more sites for dye adsorption. Besides, both negative outer surface and positive inner surface of the halloysite are exposed to the solution, allowing adsorption of both positive and negative molecules. Recent review on halloysite provides comprehensive data on adsorption of various positively and negatively charged molecules on halloysite external and inner faces [2].

Intermediate layers of both halloysite and kaolinite are blocked by strong hydrogen bonds and dyes cannot readily penetrate there. Due to the dual electrostatic attraction between charged dyes and halloysite nanotubes external/internal surfaces, it efficiently removes both positive dye and negative dye. Similar observation was made on a comparative study of HDTMA and naphthalene adsorption on halloysite and kaolinite. This was ascribed to the higher cation exchange capacity of halloysite as well as clustering and aggregation of adsorbed molecules on clay surface. Maximum adsorption efficiency – q_m is the most important parameter governing efficient dye removal. For halloysite this value varied in the range of 45 ± 5 mg/g, which is superior than most of the conventional adsorbents. q_m values of 12 mg/g were reported for activated carbon obtained from Acacia nilotica leaves with cationic dye – Rhodamine B. Similar study on cationic methylene blue revealed q_m value of 8.53 mg/g. Maximum adsorption of anionic dye – Orange 51 was determined as 8.45 mg/g on activated bleaching earth. Besides, due to its thermal stability, halloysite sorbent can be regenerated and reused by burning the adsorbed organics on fire.

Water filters were prepared using raw halloysite and kaolinite clays. Filtration efficiency was tested by passing 30 mL of 300 mg/L dye solution. Chrome azurol S was completely removed from contaminated water by halloysite, as it is clearly evident from UV spectra of the filtered liquid samples. In spite of having similar chemical structure, kaolinite was shown to be poor filter. Probably this is associated with nanoporous structure of the halloysite. Small pores of ca. 5–10 nm diameter efficiently adsorb dyes from the solution before it passes from the filter. Similar tendency was observed for the case of Rhodamine 6G as well; over 99% of the dye was removed by the halloysite filter. Mixture of dyes passed reasonably well from both the filters, though halloysite was still better than kaolinite. This is associated with formation of precipitate by interaction of positive and negatively charged dyes. Minor quantities of the dye were left over in the filtered sample, indicating the necessary for the additional improvement by surface modifications. Better understanding of the dye adsorption mechanism will be beneficial for further improvements of the filtration system.

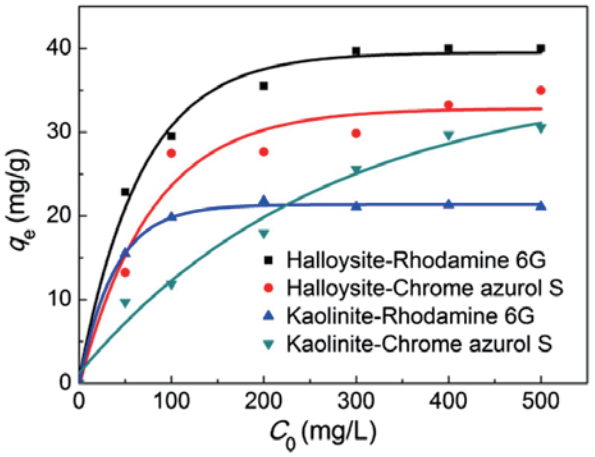

Fig. 1. Adsoption of Rhodamine 6G and Chrome Azurol S onto halloysite and kaolinite.

4. Concluding remarks

Natural halloysite nanoclay was studied as an efficient adsorbent both for cationic and anionic aqueous dyes. Tubular morphology of halloysite favors dye removal, as compared with chemically similar platy kaolin multilayer stacks. The influence of temperature, pH, ionic strength and adsorbent amount of cationic Rhodamine 6G and anionic Chrome azurol S revealed molecular details involved in the adsorption process. Ionic interaction is the major force in Rhodamine 6G adsorption on halloysite, while hydrogen bonding was the most essential for Chrome azurol S adsorption. Halloysite is novel nano-material which can be used in water filter system. The removal efficiency of halloysite is higher than most of conventional adsorbents. Besides, halloysite can be regenerated by burning after adsorption and be reused. Dye removal efficiency exceeded 99.9% after five reuse cycles for negative Chrome azurol S and 95% for positive Rhodamine 6G. Optimal pH for Rhodamine 6G adsorption was in the range of 8 and 9 while acidic solutions were favorable for Chrome azurol S adsorption. Higher temperatures favor Rhodamine 6G adsorption, indicating the endothermic nature of the adsorption. On the other hand, Chrome azurol S adsorption has a negative enthalpy of 28.3 kJ/mol, indicating hydrogen bond was formed.

Acknowledgements

We are thankful for support by the Ministry of Education and Science of Russian Federation, project#8647 and to Applied Minerals Inc., USA.

References

[1] Y. Zhao, E. Abdullaev, A. Vasiliev, Y. Lvov, Journal of Colloid and Interface Science, **406** (2013), 121.

[2] E. Abdullaev, Y. Lvov, J. Mater. Chem. B (in press).

Tenth International Conference on Flow Dynamics
November 25-27, 2013, Sendai, Miyagi, Japan

Interfacial Modification of Clay Nanotubes for the Sustained Release of Corrosion Inhibitors

Olga Volkova[1,2] and Yuri Lvov[3]
[1]Physics Department, M. Lomonosov Moscow State University, Leninskie Gory, Moscow 119991, Russia
[2]Institute of Physics and Technology, Ural Federal University, Mira Str., 21, Ekaterinburg, 620002, Russia
[3]Institute for Micromanufacturing, Louisiana Tech University, 911 Hergot Avenue, Ruston, LA 71272, United States
volkova@lt.phys.msu.ru

ABSTRACT

Long-lasting anticorrosive coatings for steel have been developed on the basis of halloysite nanotubes loaded with three corrosion inhibitors: benzotriazole, mercaptobenzothiazole, and mercaptobenzimidazole. The inhibitors' loaded tubes were admixed at 5−10 wt % to oil-based alkyd paint providing sustained agent release and corrosion healing in the coating defects. The slow release of the inhibitors at defect points caused a remarkable improvement in the anticorrosion efficiency of the coatings. Further time expansion of anticorrosion agent release has been achieved by the formation of release stoppers at nanotube ends.

1. Introduction

Common methods used for the anticorrosion protection of metals include the use of chromate-based pigments; however, their use is limited because of their toxicity. Polymer coatings have been developed for corrosion protection; the coating forms a barrier against strong corrosive species such as O_2 and H+. The metals are easily corroded in the presence of aggressive anionic species such as chloride ions, which are detrimental to the metallic surface. The metals surface can be efficiently protected by the introduction of organic corrosion inhibitors to the coatings system together with a primer. Once the coating is damaged, the inhibitors interact with released metal ions and form a protective barrier on the surface.

Organic corrosion inhibitors are efficient and not harmful to the environment. However, the direct addition of the inhibitor to the coatings is not efficient because of the interaction of inhibitor with other components of the coatings, the poor distribution of low solubility inhibitors within paint, and inhibitors leaching from the coating. All of these lead to the necessity of effective micro/nanoencapsulation of corrosion inhibitors before being mixed with paint. These encapsulated inhibitors leak from coating defects upon the formation of microcracks on the surface in a controllable fashion and heal paint damage by forming thin films on exposed metal surfaces. Clay nanotubes are naturally available, low-cost capsules with an advantage of being easily processed with many polymeric materials and provide a sufficiently high loading efficiency of active agents (up to 30% by weight) as well as the possibility of controlled release through the synthesis of caps at tube endings [1].

Halloysite is a naturally occurring alumina silicate with biocompatible properties. It has been used as a nanocontainer for different chemical agents including corrosion inhibitors, biocides, antifouling agents, and drugs. We have introduced naturally abundant halloysite clay nanotubes to encapsulate triazole-based corrosion inhibitors, and we have dipped these nanotubes into an acrylic coating for enhanced steel corrosion protection. Halloysite nanotubes loaded with inhibitors at 15−20 wt % were kept in a dry paint layer for a long time and released in the defects to suppress the development of corrosion spots.

2. Methods

Halloysite clay nanotubes were obtained from Applied Minerals Inc. (NY). Benzotriazole (BTA), 2-mercaptobenzothiazole (MBT), and 2-mercaptobenzimidazole (MBI) were from Sigma-Aldrich (USA). Oil-based blue alkyd paint (PDS-33) was purchased from Krylon Co.

Saturated solutions of corrosion inhibitors in acetone were mixed with a dry halloysite powder and sonicated for 15 min. The samples were transferred to a vacuum jar, which was then evacuated using a vacuum pump. Slight fizzing indicated the removal of air from the lumens of the halloysite nanotubes, which was replaced with the saturated solution of the inhibitors. The process was repeated three times for the most efficient loading. After loading, the samples were separated from the solution by centrifugation, washed with acetone and water, and then air dried.

All release experiments were performed in water at pH 6−7 and room temperature. The samples were stirred and the supernatants were collected periodically. A typical release time experiment was 15−20 h. Concentrations of released inhibitors were determined using UV−vis spectrophotometry. At the end of the released study, high-power sonication was performed to ensure the complete release of loaded corrosion inhibitors and to calculate the loading efficiency.

Tube Encapsulation with Urea−Formaldehyde was organized as follows. Corrosion inhibitor-loaded halloysite samples were exposed to 0.5 mL of urea−formaldehyde prepolymer solution for 10 min. Then sulfuric acid, which acts as a cross-linking agent, was added dropwise. After 5 min, the sample was centrifuged and the supernatant was discarded. Tube end-stopper formation was done with copper ion treatment. Corrosion-inhibitor-loaded halloysite samples were exposed for 1 min to the bulk aqueous solution containing 0.08 M $CuSO_4$. This suspension was constantly stirred with a magnetic stirrer. Then processed nanotubes were separated from the solution by centrifugation. Halloysite loaded with corrosion

inhibitors was added to the paint at 10 wt %. Paint composites with halloysite loaded with BTA and encapsulated by Cu stoppers and UF stoppers were also prepared.

3. Results and discussion

Halloysite is a naturally occurring tubule clay made of layered aluminosilicate tubes with a 1:1 SiO/AlO ratio and is chemically similar to kaolin. Halloysite tubes are formed by rolling 15−20 alumosilicate sheets with interlayer spacing of 0.72 nm. The tube internal lumen has a diameter of 10−15 nm, and the external diameter is ~ 50 nm. The length of the halloysite nanotube ranges from 0.5 to 1.5 μm.

The hollow tubular structure of the halloysite clay nanotube allows the encapsulation of corrosion inhibitors and other active chemical agents, making it useful as a nanocontainer to store and relase anticorrosion agents in a sustained fashion. The formation of self-healing coatings consists in the doping the paint with corosion-inhibitor-loaded halloysite clay nanotubes. First, the halloysites are loaded with a corrosion inhibitor, dried, and mixed with paint at 5−10 wt %. The paint is then applied to a metal surface. The loaded material stays inside the halloysite lumen for months until defects (cracks, scratches) occur in a paint layer, initiating anticorrosion agent release and healing the metal surface exposed to the environment. When a paint is dissipated, the loaded material gets leaked into the corrosive media and forms a protective layer on the open metal surface through chelation with Fe(II) ions. Current work emphasizes a self-healing approach using nanotube-encapsulated corrosion inhibitors.

Benzotriazole (BTA), 2-mercaptobenzothiazole (MBT), and 2-mercaptobenzimidazole (MBI) were used as corrosion inhibitors for the protection of the metals. Halloysites tubes were loaded with corrosion inhibitors by using saturated solutions in acetone and applying vacuum suction. Vacuum suction helps to remove air bubbles within halloysite lumen. Acetone was the optimal solvent for inhibitor loading for the following reasons: (1) All the corrosion inhibitors have a higher solubility in acetone; therefore, their saturated solutions of about 15−20 wt % can be prepared, whereas for water 0.5 wt % is the highest solubility. (2) Acetone has a lower viscosity than most of the other solvents and allows for faster diffusion of the inhibitors into halloysite pores. (3) Under vacuum, solvent evaporation results in the inhibitor's concentration initiating its precipitation and solidification of the tube lumen.

The release of loaded corrosion inhibitors was studied in deionized water under magnetic stirring. A comparison of the microcrystal (no encapsulation) inhibitor dissolution with the release from halloysite lumen shows that the release became considerably slower in the latter case, allowing anticorrosion agent to be supplied for 20−30 h. Corrosion inhibitors BTA and MBT were released from halloysite in two stages, and MBI release took place in one stage. The first stage is associated with the fast release of externally adsorbed inhibitors, and the second slow stage is the release of the inhibitor encapsulated in the halloysite lumen. Such a dual-stage release mechanism was also reported for tetracycline release from halloysite. One-stage exponential release of MBI shows that there was no essential amount of inhibitor adsorbed at the tube external surface.

It was shown that stoppers are effective at extending the release time of corrosion inhibitors and drugs. The sustained release of corrosion inhibitors was obtained by the tube coating and partial capping of tube ends. The first approach is based on the formation of urea-formaldehyde (UF) polymer plugs at tube endings and the coating on the halloysite surface. Halloysite tubes were exposed to urea-formaldehyde prepolymer solution. Because of its abundant N−H functional groups, prepolymer adsorbs on a halloysite external surface via hydrogen bonding and with enhanced adsorption at the lumen ends. Rapid cross-linking of the prepolymer causes the formation of a thin polymer shell that also plugs tube endings. In the second approach, an extending inhibitor release was based on the formation of copper-inhibitor clogs because of the chelation of Cu(II) ions by released inhibitors (predominantly at tube endings). Corrosion inhibitors form 2D polymer films that covers entire halloysite surface and effectively seal tube endings and other leakage defects. Halloysites were rinsed with 0.08 M $CuSO_4$ solution for about 30 s.

4. Concluding remarks

Natural halloysite nanotubes were employed as inexpensive containers offering essential benefits for the entrapment of corrosion inhibitors in metal coatings. The improvement using the inhibitor-loaded halloysite/polymer coating was demonstrated with ASTM A366 mild steel (alloy 1008) by direct exposure of the coated metal strips to highly corrosive sodium chloride solution. Corrosion was retarded in the initial stage because of the inhibiting action of benzotriazole, mercaptobenzothiazole, and mercaptobenzimidazole slowly released from halloysite pores in response to paint coating defects. Minimal undercoat corrosion and the best paint adhesion were obtained for mercaptobenzimidazole−halloysite embedded coatings. An in-depth analysis of the corrosion inhibitor release kinetics revealed that the slower release of mercaptobenzimidazole (compared to that of other inhibitors used) was responsible for the best performance.

Acknowledgements

We are thankful for support by the Ministry of Education and Science of Russian Federation, project 8647 and grant of Russian Federation President MK-7138.2013.2 and to Applied Minerals Inc., USA for providing halloysite samples.

References

[1] A. Joshi, E. Abdullayev, A. Vasiliev, O. Volkova, and Y. Lvov, Langmuir **29** (2013), 7439.

OS7: Cutting Edge of Thermal Science and Engineering

Non-Invasive Detection of Breast Tumor using Curve Fitting Technique

Koushik Das and Subhash C. Mishra
Dept. of Mechanical Engineering
Indian Institute of Technology Guwahati, India – 781039
scm_iit@yahoo.com

ABSTRACT

Pennes' bioheat equation is solved for a breast tissue with a tumor. With a tumor, the spatial distribution of skin surface temperature is a Gaussian one. Using various parameters of a Gaussian profile, an inverse analysis of the surface temperature is carried out to estimate the size and location of a tumor. Finite volume method is used in direct method to generate temperature profiles.

1. Introduction

Breast cancer in women is the cause of high mortality rate. As per World Cancer Report- 2008 by WHO, breast cancer accounts for 12.7% of the total cancer related death of women. An early diagnosis helps in better treatment and even proves to be a life saver. Though, it is true with all types of cancers, but it is more so with the breast cancer.

A human body is a thermal system, due to its ability to generate and convect heat through various metabolic activities. In 1948, Pennes proposed the first bioheat model to numerically predict heat transfer in a blood perfused tissue. The model is a modified form of heat conduction equation with a temperature dependent volumetric heat generation term, which is a function of two thermo physical properties viz., blood perfusion rate and metabolic heat generation rate. These properties are tissue specific, and these change with change in physiological and pathological conditions of the tissue. An inhomogeneity in a tissue alters thermal profile of the tissue. Through an accurate measurement and analyses of these thermal signals, it may be possible to predict the kind of inhomogeneity the tissue has. The method may prove to be a potential way to detect a cancerous tumor in a tissue.

In the present work, an effort has been made to estimate the size and location of a tumor in 2-D breast tissue with the measured surface temperature distribution.

2. Formulation

Consideration is given to a 2-D tissue of size $2L\times L$ (Fig. 1) with a centrally located tumor of size $L_t\times L_t$. The top surface of the tissue is subjected to convective boundary condition, while the left and right boundaries are adiabatic, and the bottom boundary is isothermal at core body temperature. The Pennes' bioheat equation for the geometry of tissue can be written as [1],

$$\rho C_p \frac{\partial T}{\partial t} = k\left(\frac{\partial^2 T}{\partial x^2}+\frac{\partial^2 T}{\partial y^2}\right)+\eta_b\rho_b C_{pb}(T_a-T)+Q_m+Q_s \qquad (1)$$

where $t, T, k, \rho, c_p, \rho_b, c_{pb}, \eta_b, Q_m, Q_s$ and T_a are time, temperature, thermal conductivity, density of tissue, specific heat of the tissue, density of blood, specific heat of the blood, blood perfusion rate, metabolic heat generation rate of the tissue, distributed volumetric heat source due to spatial heating and temperature of the artery, respectively.

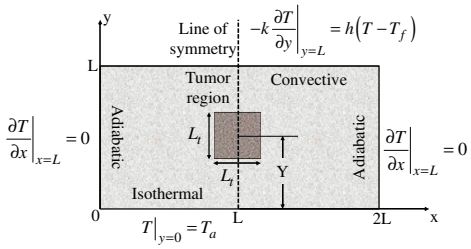

Fig.1: Schematic of the 2-D planar tissue.

In the present work, analysis is done using the finite volume method (FVM). With reference (Fig. 2), in the FVM approach, the discretized form of the Pennes' bioheat equation is written as:

$$\begin{aligned} T_P^{n+1} &= T_P^n + \frac{\Delta t\, k}{\rho c_p \Delta x}\left(T_E^n - 2T_P^n + T_W^n\right) \\ &+ \frac{\Delta t\, k}{\rho c_p \Delta y}\left(T_N^n - 2T_P^n + T_S^n\right) \\ &+ \frac{\Delta t}{\rho c_p}\left[\eta_b \rho c_{Pb}\left(T_a^n - T_P^n\right) + Q_m + Q_s\right] \end{aligned} \qquad (2)$$

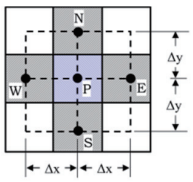

Fig.2: Schematic of the 2-D FVM control volume.

In the present work, with a tumor, the spatial distribution of the surface temperature of a 2-D tissue has been found to have Gaussian one. Spatial distribution and magnitude have been found to depend on tumor size and location. And, through a curve fitting technique, from the knowledge of the temperature profile, the size and location of the tumor, are estimated.

3. Results and Discussion

In a previous work of the authors [1], surface temperature profile for the tissue with a centrally

located tumor has been validated with those available in the literature.

For any tissue with a tumor on its axis of symmetry, (Fig. 1), the resultant surface temperature profile shows Gaussian nature; while a normal tissue shows uniform temperature. It is true for a breast tissue too. For a breast tissue, with properties, $k = 0.42\ {}^{\mathrm{W}}/_{\mathrm{m\cdot K}}$, $\rho = 920\ {}^{\mathrm{kg}}/_{\mathrm{m}^3}$, $c_p = 3000\ {}^{\mathrm{J}}/_{\mathrm{kg\cdot K}}$, and $T_a = 37\ ^{\circ}\mathrm{C}$, surface temperature of the tissue with a tumor of size L_t = 2 cm and L_t = 5 cm at various Y locations is shown in Fig 3. For a normal breast tissue, the value of Q_m and η_b are $450\ \mathrm{W\cdot m^{-3}}$ [2] and $0.92\times10^{-3}\ \mathrm{s^{-1}}$ [3], while in cancerous condition, the values considered are $29000\ \mathrm{W\cdot m^{-3}}$ [2] and $1.22\times10^{-3} - 14.5\times10^{-3}\ \mathrm{s^{-1}}$, respectively [3].

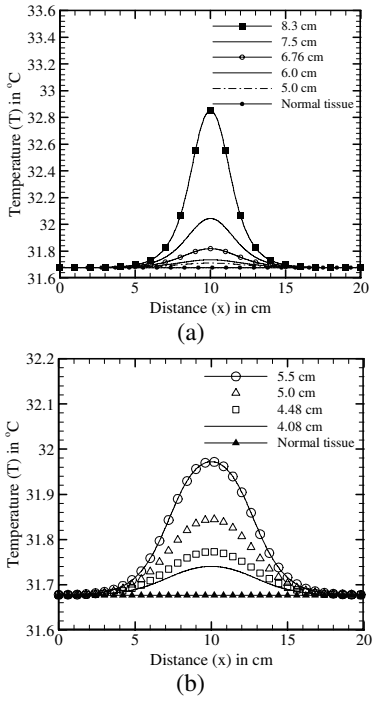

Fig. 3: Steady-state surface temperature plots of breast tissue with a tumor of size (a) 2 cm and (b) 5 cm at different Y along the line of symmetry.

A Gaussian function is an exponential function governed by its general form of equation:

$$y = y_o + Ae^{-(x-x_c)^2/2w^2} \qquad (5)$$

where y_o, x_c, A and w are the offset, the center, the amplitude and the width of the profile, respectively. FWHM is the full width at half maximum of the general Gaussian profile as shown in Fig. 4. For a particular condition of a tissue with tumor of different sizes at different locations, the Gaussian parameters like amplitude *A* and area under the curve shows particular value and it remains unique for that condition.

In the present study in order to estimate the size and the location of the tumor for a breast tissue, a database of *A* vs. location and area vs. location is maintained for different sizes of the tumor. The obtained surface temperature profile has to be fitted with a curve fitting tool using a Gaussian fit. Amplitude *A* and area under the curve obtained, has to be searched from the stored database. Any unavailable data can be interpolated between known values. Table 1 shows estimation for some cases along with the error analysis. The obtained error is within acceptable accuracy.

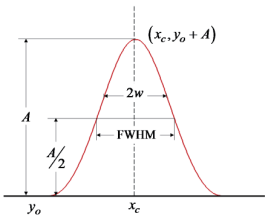

Fig. 4: A general Gaussian profile

Table 1. Estimated value of size and location of tumor

Cases	Actual		Estimated		Error (%)	
	Y (cm)	L_t (cm)	Y (cm)	L_t (cm)	Y	L_t
1	3.35	2.00	3.34	2.00	0.2001	0.0
	2.50	1.00	2.50	1.00	0.0452	0.0
2	4.50	0.50	4.50	0.50	0.0093	0.0
	1.75	2.00	1.74	2.00	0.2940	0.0
3	8.00	0.50	8.00	0.50	0.0249	0.0
	7.50	1.00	7.50	1.00	0.0023	0.0

For all cases in the Table 1, the blood perfusion rate η_b is selected in random, and these are 1.4e-3, 2.9e-3 and 4.8e-3 $\mathrm{s^{-1}}$ for case 1, 2 and 3, respectively. As the value of η_b for breast tissue is very small, the effect of its change for a particular size and location of the tumor is observed to be negligible. Hence, even without the knowledge of blood perfusion rate, the size and location (Y) of the tumor in a breast tissue can be estimated very accurately.

Conclusions

Various cases in breast tissue with different sizes, locations and blood perfusion rates are analyzed. Due to very low blood perfusion rate of breast tissue and a tumor, it shows negligible effect on the temperature profile. Hence, Pennes' bioheat equation for breast tissue takes the form of a general heat conduction equation with volumetric heat generation rate. It further reduces the complexity while estimating the location and size of the tumor using the technique of curve fitting, which is the main advantage of the proposed method.

References

[1] K. Das, S.C. Mishra, J. Therm Biol **38** (2013) 311-317.

[2] F.J. Gonz´alez, Rev Mex Fis **53** (2007) 323–326.

[3] D.A. Mankoff, L.K. Dunnwald, J.R Gralow, G.K Ellis, A. Charlop, T.J Lawton, E.K Schubert, J. Tseng, R.B Livingston, J. Nucl. Med.**43** (2002) 500–509.

Tenth International Conference on Flow Dynamics
November 25-27, 2013, Sendai, Miyagi, Japan

Magnetic Hyperthermia and Heat Conduction in Polymer Gels

Attila Borsos, Rita A. Bauer, Zsófia Varga, Jedlovszky-Hajdú Angéla and Miklós Zrinyi
Semmelweis University, Department of Biophysics and Radiation Biology
H-1089 Budapest, Nagyvarad ter 4, HUNGARY,
E-mail of corresponding author: mikloszrinyi@gmail.com

ABSTRACT

The localization of the heat has an important role in hyperthermia treatment for cancer therapy. We investigate the heat transfer using outer alternating magnetic field, magnetite nanoparticles (Fe_3O_4) and poly(*N*-isopropyl-acrylamide) (pNIPAm) smart gel as a model medium of human tissue. The heat transfer can be visually detected due to the Lower Critical Solution Temperature of the pNIPAm. When the temperature exceeds a critical temperature value, T_{LCST} = 35 °C, the transparent gel becomes opaque and the phase transition temperature front moves forward in the gel.

1. Introduction

In the clinical practice the heating therapy has a significant rule especially in the cancer treatments. Magnetic hyperthermia [1] is the most effective way to heat certain organs, specified tissues or group of cells inside the human body. A critical point of the hyperthermal treatment is to localize the tissue area where the heat treatment will be used. This is important because the healthy cells are also damage due to the increase of the temperature. To achieve the death of the degenerate cells locally, magnetic (magnetizable) nanoparticles (MNP) [2] and outer magnetic source can be used. In our experiment we modeled the tissue with intelligent gel by using poly(*N*-isopropyl-acrylamide) (abbreviated as pNIPAm) gel which has a Lower Critical Solution Temperature (LCST) at 35 °C.

We are able to visualize the phase transition temperature front that moves forward in the opposite direction to temperature gradient. When the temperature exceeds a critical value T_{LCST} = 35 °C, the originally transparent gel becomes opaque. This opacity which is separated from the clear gel phase with a sharp interface boundary makes us possible to follow the evolution of 35 °C temperature front during the heat transfer experiment.

If the experiment is achieved in a cross-linked polymer gel, then the convective motion of fluid is hindered by the presence of network chains and the only mechanism is heat conduction.

2. Method

Magnetite nanoparticles (Fe_3O_4) dispersed in distilled water were used as magnetic 'fluid'. The concentration of the magnetite was 10 g particle/100 mL solution.

The pNIPAm gel with the crosslink density of r=100 (every hundred monomer crosslinked by *N*,*N*' methylene-bisacrylamide, BIS) were used. At the top of the gel were placed the solution with the magnetite nanoparticles creating direct connection between the gel and the magnetic particles. The area of contact interface between the two phases is about 79 mm^2.

The alternating current magnetic field (AC) was produced by electric device connected to an outer magnetic coil (Fig. 1.). The sample was placed in the middle of the coli horizontally and vertically, respectively. The measurements were carried out in function of the voltage power in the range of 40-70 V. The applied frequency was constant 88 kHz. Heating jacket connected to a circulating thermostate was used to eliminate the effect of heat transfer coming from the selfheating of the coil.

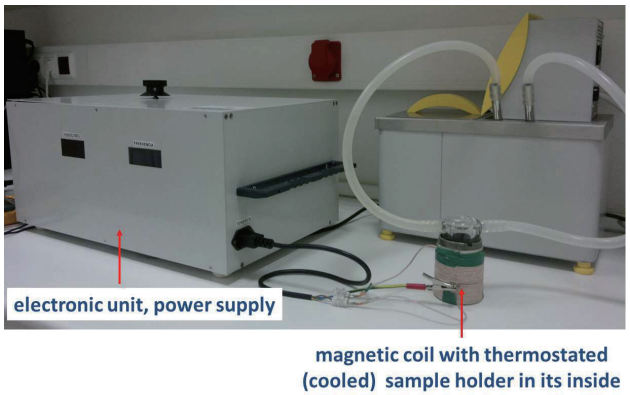

Fig.1. Experimental setup for heat transfer measurements.

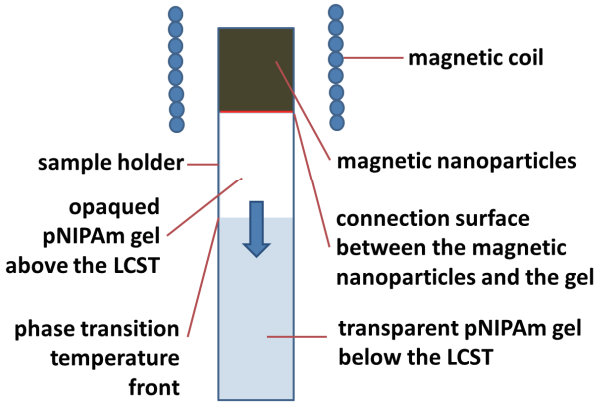

Fig.2. A cylindrical vessel was filled with the poly(*N*-isopropyl-acrylamide) gel and placed the magnetite solution at the top of the gel. The arrow shows the phase transition (and the heat transfer) through the pNIPAm gel.

3. Results and Discussion

Fig.3. shows the development of the heat transfer front in the pNIPAm gel.

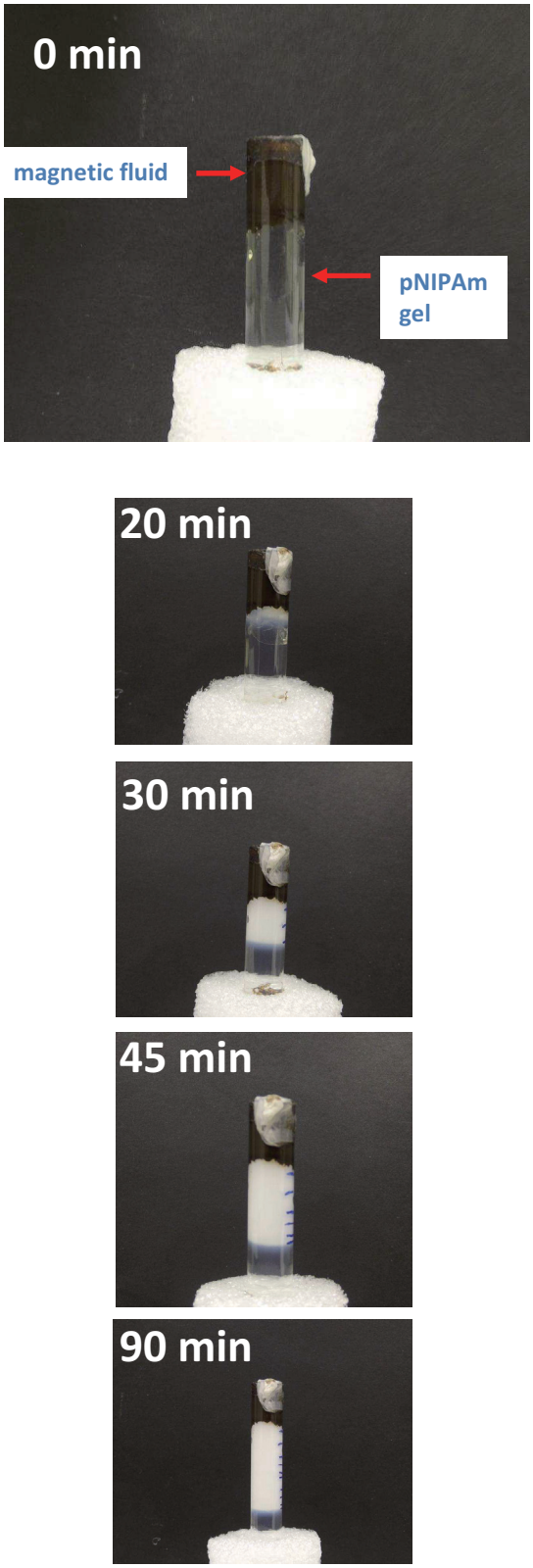

Fig.3. Propagation of the heat through the pNIPAm gel at 40 V.

Fig.4. shows the measured distance between the contact interface of the magnetic nanoparticles/pNIPAm gel and the phase transition temperature front in function of the time at different voltage values in the range of 40-70 V in 10 V steps.

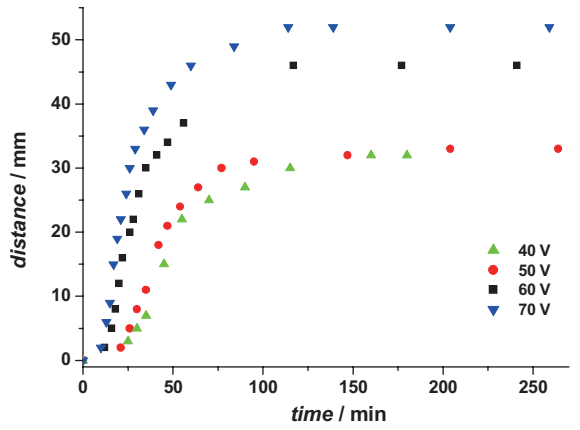

Fig.4. The measured distance between the contact interface and the phase transition temperature front in function of the time at different voltage values.

The experimental results show that the heat transfer caused by the magnetite nanoparticles can be visually detected due to the phase transition of the pNIPAm gel. The shape of the curves is the same independently from the applied voltage: the distance-time functions start from the origo because the beginning of the heating process the magnetite fluid requires time to heating over the LCST of the pNIPAm. This time range (which is approximately 10-20 minutes) is wider at lower voltage and narrower at higher voltage. After this accumulation time the curves are significantly accelerates and tends to a level off depending on the applied voltage. The speed of the acceleration and the available limit distance value increases with increasing voltage, respectively.

4. Concluding remarks

The heat transfer of the magnetic fluid containing magnetite nanoparticles can be followed by using pNIPAm smart gel. This method allows us to detect the heat transfer visually. The results show that after an accumulation time the distance-time functions significantly accelerate until reach a limit distance value. This value is increase with increasing voltage.

Acknowledgement

This research was supported by OTKA Foundation (Grant number: NK 101704), as well as the Molecular Biophysical Research Group, Subsidised Research Units, Hungarian Academy of Science.

References

[1]A.K. Gupta, M. Gupta, Biomaterials, **26** (2005) p.3995.

[2]R.V. Ramanujan and L.L. Lao, Proc. First Intl. Bioengg. Conf., Singapore (2004) p.69

Thermal Imaging and Screening of Subsurface Cancer during Thermal Recovery after Cold Stress

Arka Bhowmik[1*], Ramjee Repaka[1], Subhash C. Mishra[2]
Department of Mechanical Engineering
[1]Indian Institute of Technology Ropar, Punjab, India
[2]Indian Institute of Technology Guwahati, Guwahati, India
[*] Corresponding author: arkabhowmik@yahoo.co.uk

ABSTRACT

This study pertains to thermal imaging and screening of subsurface skin cancer during thermal recovery from cold stress. Based on thermal properties and anatomical details available in the literature, we model the three dimensional skin using a finite element based software package. The staging of harmful skin melanoma has been modelled based on the guidelines provided by American Joint Committee of Cancer staging. The thermal maps and contrast at the surface are further processed in MATLAB using correlated image contrast approach, which has improved the test surface resolution significantly compared to that of the magnitude images.

1. Introduction

A significant number of people throughout the world are affected with skin cancers. According to World Health Organization, approximately 2-3 million cases of non-melanoma and 1,32,000 cases of melanoma type of skin cancers occur every year globally. One of the most important protocols widely recommended is the early detection, which ascertains better treatment and survival. Early detection of skin cancer relies on two types of examinations: (a) self-examination followed by microscopic study, and (b) non-invasive examination using certain tools. Detection using non-invasive tools has the ability to trace the early signs before cancer appears at the surface of the skin [1]. Among the conventional non-invasive methods, infra-red (IR) imaging techniques are quiet useful for pre- and post-clinical diagnosis as well as prognosis because these are faster and can be used repetitively for longer duration without any risk of radiation exposure.

The advancement in bio-optics, digital manipulation, image processing, and deeper understanding of thermography based on human physiological features has made the present thermography quite capable technique to determine associated sub-surface anomalies accurately both in time and space frame non-invasively. The variation of lesion property and depth of penetration within the skin for a given thermal condition leads to identifiable thermal contrast at the surface of the skin. In order to detect and characterize the subsurface cancer, this article uses the concept of thermal mapping and screening of different stages of human skin cancer at the surface during thermal recovery from cold stress.

2. Mathematical Formulation and Numerical Study

The biological heat transfer in a vascularized tissue is given by [1]

$$\frac{\partial T}{\partial t} = \alpha_t \nabla T - \frac{\omega_b \rho_b c_b}{\rho_t c_t}\left(T - T_a\right) + \frac{Q'''_m}{\rho_t c_t} \qquad (1)$$

where T is the tissue temperature, α_t is the thermal diffusivity ($=k_t/\rho_t c_t$), ω_b is the blood perfusion, ρ is the density, c is the specific heat, T_a is the temperature of arterial blood, Q_m is the metabolic heat generation, and the subscripts t and b are for tissue and blood, respectively. In this work, initially the surface of the skin (Fig. 1) with melanoma at different stages is exposed to convective heat transfer with convective heat transfer coefficient h_{conv} = 10 W/m^2·K and the ambient air temperature T_{inf} = 22.4 ^{0}C. In this study, the thermal recovery from cold stress takes almost 20-60 min. During the thermal recovery phase, the dynamic variation of thermal pattern at the surface has been mapped for post-processing. The maximum wavelength at which the emission from the skin surface takes place has been determined using the Wien's-displacement law.

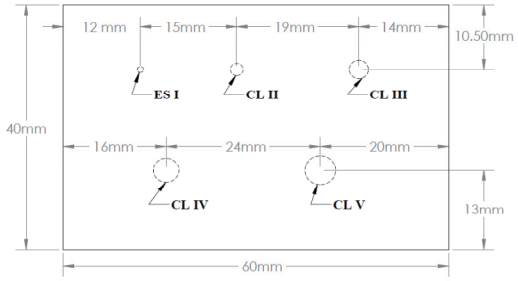

Lesion	Radius, r (mm)	Height, h (mm)	Depth from surface (mm)
ES I	0.5	0.2	0.1
CL II	1 .0	0.44	0.1
CL III	1.5	0.8	0.1
CL IV	2.0	1.2	0.1
CL V	2.4	1.5	0.1

Fig. 1: Schematic of a 3-D multilayered skin with cancerous lesion at different stages.

The 3-D skin is modeled based on the anatomical details available in the literature [1]. The staging of skin melanoma within the normal skin is modeled based on the guidelines provided by American Joint Committee for Cancer Staging [2]. Based on the anatomical invasion of thin T1 melanoma in the skin, the four subcategories of melanoma, viz. Clark level II, III, IV and V have been considered for present investigation [2],

and the melanoma during its early stage before Clark levels is abbreviated as ES I. After solving Eq. (1), the surface thermal map has been processed in MATLAB to obtain normalized thermal contrast image. This allows us to individuate the early cancerous lesion as well as different stages of cancer. In order to represent the variation in a single field of view, all the lesion stages are modeled in a single tissue domain. In this study melanoma during its early stage has no volumetric metabolic heat generation rate for ES I, i.e., $Q_m''' = 0.0$ W/m^3. The arterial blood temperature, T_a is 37 ^{0}C, the density of the blood, ρ_b is 1060 kg m^{-3} and the specific heat of the blood, c_b is 3770 Jkg^{-1}K^{-1}, and cold stress of T_s = 13 ^{0}C is applied on the skin surface for about 1 min.

3. Results and Discussion

The thermophysical properties of tissue depend on associated physiological and patho-physiological conditions. The change in thermal and geometric configuration leads to the identifiable thermal contrast in the thermogram.

Figure 2 depicts the (a) typical surface temperature profile of skin melanoma stages and (b) the surface temperature distribution for a particular case of melanoma. It is observed from the insert in Fig. 2(a) that, with the increase in lesion volume, $\pi r^2 h$ (which is the best predicator of stage and prognosis of melanoma), the magnitude of thermal signals also increases. We observe that during dynamic thermography, during transient stages, difference in the thermal signals persists. As can be seen from Fig. 2(a), the changes are almost negligible at the end of recovery (after reaching the steady-state). The typical surface temperature distribution (STD) due to CL II is shown in Fig. 2(b). Based on Wien's displacement law, we found that the wavelength at which skin emission takes place lies within 9-10 µm (Far-IR). In general, we found that the STD is independent of the irregular/occasional protrusion of lesion geometry. It primarily depends on the volume and average diameter of the lesion. We have also performed sensitivity study in which the effects of various thermophysical and geometric parameters have been studied. We found that apart from blood perfusion and lesion thickness, all other parameters incur negligible variation in STD.

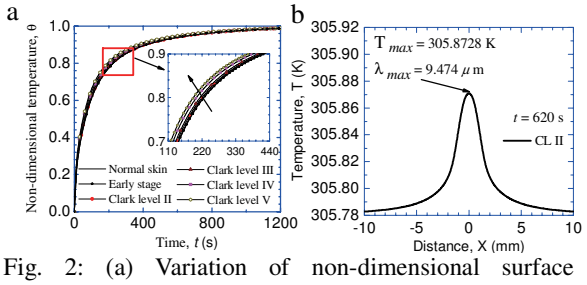

Fig. 2: (a) Variation of non-dimensional surface temperature with time for the case of normal and malignant lesion of different grades, and (b) typical surface temperature distribution for the case of CL II.

For different stages of skin melanoma, temporal variations in the magnitude images of the thermal maps of skin surface are shown in Fig. 3. Figures 4(a) and (b) depicts the 2-D and 3-D plots of correlated contrast image at the end of the recovery time, respectively.

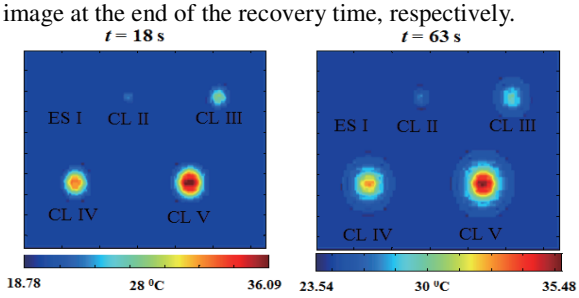

Fig. 3: Temporal variation in the magnitude images of the thermal maps.

It has been found from Fig. 3 that, the melanoma at early stage (ES I with no metabolic heat generation) is hardly visible in the magnitude images. CL II has ting appearance in these images without clear boundaries. On the other hand, the normalized correlated contrast images allow us to clearly individuate the different stages of cancer. The normalized correlated contrast values are defined by Maldague and Marinetti [3].

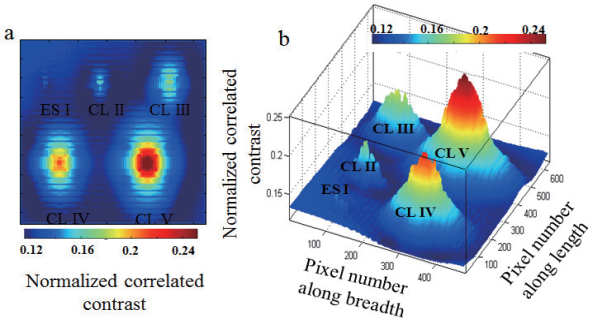

Fig. 4: The variation of normalized contrast for different cancer grades; (a) two dimensional image, and (b) three dimensional image.

4. Conclusions

The study suggests that contrast based non-invasive thermal image processing technique has the inherent ability to individuate the early traces of cancer and is capable to provide better image contrast, which was otherwise not visible in the magnitude images. Further, it has been found that thermal imaging during thermal recovery from cold stress can reveal more qualitative information and warrants further scientific endeavors.

References

[1] M.P. Çetingül, C. Herman, Int. J. Therm. Sci., **50** (2011), 421.

[2] F.L. Greene, C.C. Compton, A.G. Fritz, J.P. Shah, D.P. Winchester, Melanoma of the Skin, AJCC Cancer Staging Atlas Part V. Springer, New York, USA, (2006).

[3] X. Maldague, S. Marinetti, J. Appl. Phys., **79**(1996).

Tenth International Conference on Flow Dynamics
November 25-27, 2013, Sendai, Miyagi, Japan

An Experimental Comparison between Thermal Diffusivity and Blood Perfusion Rate of Living and Dead Tissue by Inverse Analysis

Takahiro Okabe[1], Junnosuke Okajima[2], Yun Luo[3], Fang Wang[4], Atsuki Komiya[2],
Ichiro Takahashi[5] and Shigenao Maruyama[2]
[1] Graduate School of Engineering, Tohoku University, Sendai, Miyagi 980-8579, Japan
[2] Institute of Fluid Science, Tohoku University, Sendai, Miyagi 980-8577, Japan
[3] School of Mech. Eng., Shanghai Jiao Tong Univ., Dong Chuan Rd., Shanghai, 200240, China
[4] Shanghai First People's Hosp., Shanghai Jiao Tong Univ., Haining Rd., Shanghai, 200080, China
[5] Graduate School of Science and Engineering, Yamagata University, Yonezawa, 992-8510, Japan
okabe@pixy.ifs.tohoku.ac.jp

ABSTRACT

This paper describes a fast, non-invasive, and in-situ method for simultaneously estimating the local thermal diffusivity and blood perfusion rate of human skin of the forearm by and inverse analysis. To consider the effect of blood flow and metabolism, the Pennes's bioheat transfer equation was used as the governing equation. The clinical experiments with 9 human objects were conducted in the laboratory. In addition, the experiments with human dead tissue were also conducted to compare with the living tissue. It was found that the both thermal diffusivity and blood perfusion rate could be estimated reasonably.

1. Introduction

Recently, the treatments utilizing the heat transfer phenomena such as laser therapy[1] and cryosurgery[2] are being attention, because these are less invasive and more cost effective than the other ones. The thermophysical properties of human tissue such as thermal conductivity, thermal diffusivity and blood perfusion rate play an important role in the quantitative evaluation of these treatments. However, it is difficult to measure the thermophysical properties of human tissue *in-vivo*, because of the effect of blood flow, metabolism, non-uniformity of the tissue and individual difference. Moreover, the blood perfusion rate varies greatly in various physiological conditions and among different tissues of even the same species. Therefore, there is a growing interest in fast, reliable, non-invasive, and *in-situ* measurements of the thermophysical properties including the blood perfusion rate in the field of bioheat transfer.

We focused on a thermophysical handy tester[3], and have developed an inverse method for estimating the local thermal diffusivity of biomaterials such as pork and beef which has no blood flow and metabolism[4]. This method was validated by measuring the thermophysical properties of known materials such as water. However, this method was still not applied to the living tissue which has the blood flow and metabolism.

The purposes of this study are to conduct a clinical experiment with human skin of the forearm to simultaneously estimate the thermal diffusivity and blood perfusion rate, and to compare them with human dead tissue's results which have no the physiological response.

2. Estimation method

In a proposed method, the thermophysical properties can be determined by the comparison between the measured temperature response by a thermophysical handy tester and calculated temperature response by a heat conduction model proposed in this study.

In the measurements, the thermal probe with a sheathed thermocouple in a thermophysical handy tester is heated at a constant temperature which is higher than that of the human skin, and is placed on the skin surface so that only the exposed junction of the probe tip is in point contact. A tensioned polyimide film is introduced between the probe tip and skin surface to stabilize the contact condition. Then, temperature response of the probe tip is detected non-invasively for 10 seconds.

Figure 1 shows the one dimensional and one dimensional spherically-symmetric numerical model. The probe tip of a thermophysical handy tester makes contact with the human skin through the polyimide film which is used to stabilize the contact condition. This model assumes that the heat conduction processes in the probe and in the sample are one dimensional and one dimensional spherically-symmetric, respectively. The effect of the difference in the heat conduction near the contact point from the real one is considered as the apparatus constant determined by a calibration experiment.

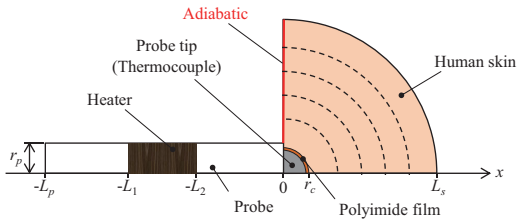

Fig. 1 1D & 1D spherically-symmetric numerical model

To consider the effect of blood flow and metabolism, the Pennes's bioheat transfer equation[5] is used in human skin as follows:

$$A_s\frac{\partial T}{\partial t}=\frac{\partial}{\partial x}\left(A_s\alpha_s\frac{\partial T}{\partial x}\right)+\frac{\rho_b c_b \omega_b A_s}{\rho_s c_s}\left(T_a-T\right)+\frac{A_s\cdot\dot{q}_{met}}{\rho_s c_s}, \qquad (1)$$

where t [s], T[C^o], α [m^2/s], ρ [kg/m^3], c [J/(kg・K)], ω_b [1/s] and $\dot{q}_{met}$ [W/m^3] are time, temperature, thermal diffusivity, density, specific heat, blood perfusion rate and metabolic heat generation, respectively. The subscript s and b are sample and blood, respectively. In

the event of other parts and dead tissue, the common heat transfer equation was used. To consider the three-dimensional heat transfer in human skin, the area A_i at each position is changed as follows:

$$A_p = \pi r_p^{\,2}, (-L_p \le x \le 0), \tag{2}$$

$$A_s = 2\pi x^2, (r_c \le x), \tag{3}$$

where L_p and r_c are the length of the probe and the contact radius between the probe tip and the sample, respectively.

The objective function in this study, φ, is defined as the integration value of the difference between the experimental and the calculated temperature response of the probe tip, and is expressed as follows:

$$\varphi(\boldsymbol{r}) = \int_0^{t_e} \left| T_{\mathrm{exp}} - T_{\mathrm{calc}}(\boldsymbol{r}) \right| d\tau, \tag{4}$$

where $\boldsymbol{r}$, T_{exp} and T_{calc} are the variable vector, measured temperature by a thermophysical handy tester, and calculated temperature, respectively. The variable vector in this study consists of three parameters that affect the temperature responses, and is expressed as follows:

$$\boldsymbol{r} = (r_c, \alpha_s, \omega_b). \tag{5}$$

A Real-coded Genetic Algorithm was selected as the minimization method of the objective function.

The clinical experiments with 9 human subjects (A-I) were conducted in the laboratory. We applied to the ethics board in Tohoku University, and then were approved before the experiments. In addition, the experiment with human dead tissue was also conducted to compare with the living tissue's results, as the international collaborative research at Shanghai First People's Hospital, China. Measurements on the forearm skin were conducted 5 times at same position in the living human subject and at three positions in case of dead tissue.

3. Results and Discussion

Figure 2 shows the estimated thermal diffusivity of human skin of the forearm. In spite of the presence or absence of the physiological response, the results of the living and dead tissue shows the similar value of thermal diffusivity, and show a good agreement with the previous study (α = 0.82-1.20 × 10^{-7} m^2/s)[6]. Therefore, the effect of blood flow and metabolism could be detected by an inverse analysis proposed in this study.

Figure 3 shows the estimated blood perfusion rate of human skin of the forearm. In case of dead tissue, the blood perfusion rate is regarded as zero. The estimated results varied more widely than the estimated results of thermal diffusivity, because the blood perfusion rate is more sensitive to a change in the temperature response. The order of estimated values were similar to the previous study (ω_b = 0.5 – 2.3 × 10^{-3} 1/s)[7][8]. Thus, a proposed method has a possibility to estimate the blood perfusion rate *in-situ*.

4. Concluding remarks

In this study, the clinical experiments with the living and dead human skin were conducted.

(1) In spite of the presence or absence of the physiological response, the results of the living and dead tissue shows the similar value of thermal diffusivity, and show a good agreement with the previous study.

(2) The proposed method has a possibility to estimate the thermal diffusivity and blood perfusion rate of human skin simultaneously.

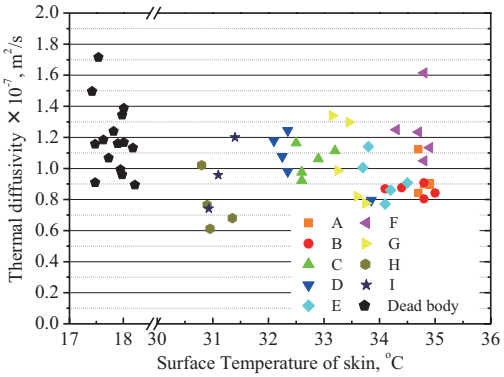

Fig. 2 Estimated thermal diffusivity of forearm skin.

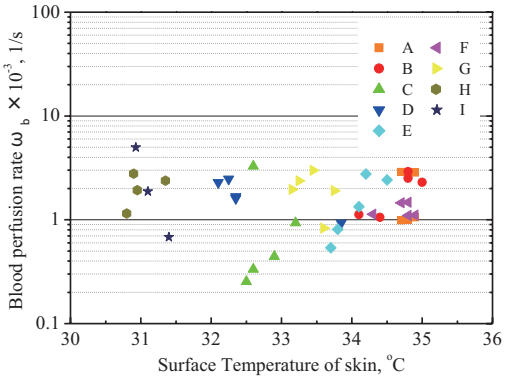

Fig. 3 Estimated blood perfusion rate of forearm skin.

Acknowledgment

This work was supported by Grant-in-Aid for JSPS fellows from the Japan Society for the Promotion of Science.

References

[1] S. Maruyama, Y. Sato, A. Sakurai, J. Okajima, M. Baneshi and A. Komiya, Proc. 8th ICFD, (2011), pp. 534-535.

[2] J. Okajima, A. Komiya and S. Maruyama, IJHFF, **31** (2010), pp. 1012-1018.

[3] I. Takahashi and M. Emori, HTAR, **32** (2003), pp. 202-211.

[4] T. Okabe, J. Okajima, A. Komiya, Y. Luo, I. Takahashi and S. Maruyama, JTST, **8** (2) (2013), pp. 395-406.

[5] H. H. Pennes, J. Appl. Physiol., **1**(1948), pp. 93-122.

[6] Japan Soc. Thermophys. Properties, Thermophysical Properties Handbook, (2008), Yokendo.

[7] E. P. Scott, P. S. Robinson and T. E. Diller, Meas. Sci. Techno., **9** (1998), pp. 888-897.

[8] J. Okajima, S. Takashima, T. Okabe, A. Komiya and S. Maruyama, Proc. JSME Annual Meeting, (2012), J024043.

Large Eddy Simulation of Turbulent Non-premixed Flame Using OpenFOAM

Masaki Hongoh, Kazui Fukumoto, Yoshifumi Ogami
Department of Mechanical Engineering, Ritsumeikan University
1-1-1 Noji-higashi, Kusatsu, Shiga 525-8577, Japan
hongoh@cfd.ritsumei.ac.jp

ABSTRACT

This article describes the large eddy simulation (LES) of a turbulent non-premixed flame. In this study, we developed an OpenFOAM-based computational code and a look-up table approach for analyzing turbulent combustion. The code was validated through an unsteady simulation using an LES model of a non-premixed CH_4-H_2-N_2 jet flame. The results obtained using the developed code were compared with experimental data, and it was found that both datasets are in good agreement with each other.

1. Introduction

Turbulent combustion is dominant in general combustors. Therefore, it is important to predict the combustion state and elucidate complex turbulent combustion behavior. For gathering combustion phenomena related data, including ignition and local extinction, with greater accuracy than possible currently, the calculations involved should consider detailed chemical equations and unsteady simulation using the LES model.

A combustion simulation that considers detailed chemical mechanisms requires significant computation time because the reaction related calculations involves n-dimensional ordinary differential equations that must be solved based on the number of chemical species present. For reducing the computation time, a simulation technique based on the lookup table approach [1] has been proposed.

In this paper, we have developed an OpenFOAM[2] -based computational code and a look-up table approach for analyzing turbulent combustion.

2. Method

The conservation equations for turbulent combustion flow are as follows:

Continuity equation

$$\frac{\partial \bar{\rho}}{\partial t} + \nabla \cdot \left(\bar{\rho} \tilde{U} \right) = 0 \tag{1}$$

Momentum equations

$$\frac{\partial \left(\bar{\rho} \tilde{U} \right)}{\partial t} + \nabla \cdot \left(\bar{\rho} \tilde{U} \tilde{U} \right) = -\nabla \bar{p} + \nabla \cdot \left(\widetilde{\tau_{eff}} \right) \tag{2}$$

Sensible enthalpy equation

$$\frac{\partial \left(\bar{\rho} \tilde{h}_s \right)}{\partial t} + \nabla \cdot \left(\bar{\rho} \tilde{U} \tilde{h}_s \right) = \nabla \cdot \left(\alpha_{eff} \nabla \tilde{h}_s \right) + \sum_J \Delta h_f \bar{R}_J \tag{3}$$

Species transport equation

$$\frac{\partial \left(\bar{\rho} \tilde{Y}_J \right)}{\partial t} + \nabla \cdot \left(\bar{\rho} \tilde{U} \tilde{Y}_J \right) = \nabla \cdot \left(\mu_{eff} \nabla \tilde{Y}_J \right) + \bar{R}_J \tag{4}$$

where $\bar{\rho}$ denotes density, t denotes time, $\tilde{U}$ denotes the velocity vector, $\bar{p}$ denotes the pressure, h_s denotes the sensible enthalpy, Y_J denotes the mass fraction of chemical species J, and R_J is the fuel consumption rate matrix. The tilde and the bar indicate the density-weighted average and time average.

The effective stress tensor of Eq. (2), τ_{eff} represents the summation of viscous and turbulent stresses. The effective thermal flux of Eq. (3), α_{eff}, and the species flux of Eq. (4), μ_{eff}, are calculated as the summation of the viscous and turbulent fluxes. The solver assumes that the laminar and turbulent Prandtl numbers, Schmidt numbers and Lewis numbers of each species are unity. Therefore, the effective thermal flux and species flux are calculated as follows:

$$\alpha_{eff} = \alpha + \mu_{SGS} \tag{5}$$

$$\mu_{eff} = \mu + \mu_{SGS} \tag{6}$$

$$\mu_{SGS} = \rho L_S C_k \sqrt{k_{SGS}} \tag{7}$$

$$k_{SGS} = \left(\left(-b + \sqrt{b^2 + 4ac} \right) / 2a \right)^2 \tag{8}$$

$$a = C_e / L_S \tag{9}$$

$$b = \frac{2}{3} tr(D) \tag{10}$$

$$c = 2 C_k L_S (dev(D) : D) \tag{11}$$

$$D = symm(\nabla U) \tag{12}$$

where α denotes the dynamic thermal diffusivity, μ denotes the dynamic viscosity and μ_{SGS} denotes the sub grid scale (SGS) turbulent viscosity, k_{SGS} denotes the SGS kinetic energy, C_e = 1.05, C_k = 0.07, L_S denotes the filter width, and D denotes the deformation gradient tensor.

In this study, the eddy dissipation concept (EDC) model was used as the combustion model. In this model, it is assumed that combustion occurs in the fine structure of the turbulent flow. The fine structure is considered a perfectly stirred reactor, and the following equations are solved at steady state under the initial conditions obtained from the current mass fractions, density, and temperatures in each computational cell:

$$\frac{dY_J^*}{dt} = \frac{w_J^*}{\bar{\rho}} + \frac{Y_J^0 - Y_J^*}{\tau} \tag{13}$$

$$\tilde{Y}_J = \xi^{*3} Y_J^* + \left(1.0 - \xi^{*3} \right) Y_J^0 \tag{14}$$

where Y_J^* and Y_J^0 indicate the mass fractions of chemical species J in the fine structure and surrounding gas, respectively. w_J^* denotes the reaction rate of chemical species J in the fine structure, τ^* denotes the reaction time scale, and ξ^* denotes the fine structure length. ξ^* is computed as follows:

$$\xi^* = C_\xi \left(\frac{\mu\varepsilon}{\bar{\rho} k^2} \right)^{\frac{1}{4}} \tag{15}$$

where C_ξ = 2.1377, μ denotes the viscosity, ε denotes the turbulent dissipation rate, and k denotes the turbulent kinetic energy. τ^* is given as follows:

$$\tau^* = C_\tau \left(\frac{\mu}{\bar{\rho}\varepsilon} \right)^{\frac{1}{2}} \tag{16}$$

where C_τ = 0.408. The mean reaction rate $\bar{w}_J$ of chemical species J is computed as follows:

$$\bar{w}_J = \frac{\bar{\rho}\varepsilon^{*2}}{\tau^* \left(1 - \xi^{*3}\right)} \left(Y_J^* - \tilde{Y}_J \right) \tag{17}$$

To reduce the computational cost, the look-up table approach [1] was applied to the EDC model.

3. Numerical Conditions

A CH_4-H_2-N_2 turbulent non-premixed flame was simulated for verifying the accuracy of the proposed technique. The numerical conditions were based on Sandia National Laboratories DLR_A [3]. Figure 1 shows a sketch of the computational domain used in this study. The computational domain was constructed based on the three-dimensional, body-fitted curvilinear coordinate system. The mass fractions of CH_4, H_2, and N_2 in the fuel were 0.212, 0.04, and 0.748, respectively. In ambient air, the mass fractions of O_2, N_2, and H_2O were 0.234, 0.005, and 0.761, respectively. Fuel was injected from a nozzle having a radius of 4.0 mm. The velocities of fuel and ambient air were 42.2 and 3.0 m/s, respectively. The temperature of the fuel as well as ambient air was considered to be 292.0 K. The computational domain was discretized to about 600,000 quadrilateral grid cells. The Smagorinsky model was selected as the turbulence model. Kee's mechanism [4] was used for computing the reaction rates.

4. Results and Discussion

Figure 2 shows the radial mean mass fraction and temperature profiles at three different axial positions. In this figure, x, r, and d denote the axial distance, radial distance, and nozzle diameter, respectively. The computational results obtained using our simulation show good agreement with the experimental data. However, at x/d = 40, the calculated mass fraction of H_2O and temperature near the centerline were slightly different from the experimental data, while show the peaks at similar positions on the radial. This is because the average values did not stabilize given that the time for measuring the average values was insufficient. The computation time of our code was about two-thirds compared with the original code.

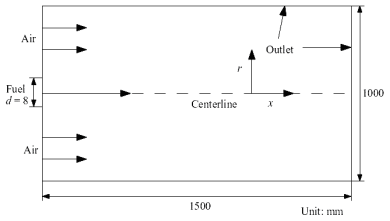

Fig. 1 Computational domain.

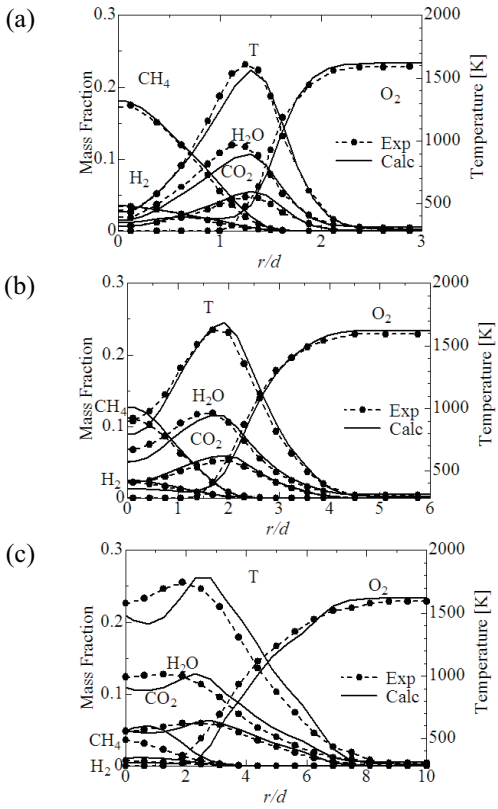

Fig. 2 Radial mean mass fraction and temperature at different axial positions. (a) x/d = 10, (b) x/d = 20, (c) x/d = 40.

5. Concluding remarks

In this paper, we developed an OpenFOAM-based computational code coupled with the look-up table approach, and conducted an unsteady simulation using LES model for validating the prediction accuracy of our code. The computational results were compared with the experimental data. It was found that the predicted values were close to the experimental data.

References

[1] K. Fukumoto, Y. Ogami, Simulation of CO-H2-Air Turbulent Nonpremixed Flame Using the Eddy Dissi -pation Concept Model with Lookup Table Approach, Journal of Combustion, Volume 2012, Article ID 496460, 2012.

[2] OpenFOAM, http://www.openfoam.com

[3] CH4/H2/N2 Jet Flames, http://www.sandia.gov/TNF /DataArch/DLRflames.html

[4] T. Peeters. Numerical Modeling of Turbulence Natural-Gas Diffusion Flames. PhD thesis, Delft Technical University, Delft, The Netherlands, 1995.

Boundary Heat Flux Estimation for the Heat Convection Flow Using the Velocity Field Data

Gennady Alekseev, Dmitry Tereshko
Institute of Applied Mathematics FEB RAS, 7, Radio St., Vladivostok, 690041, Russia
Far Eastern Federal University, 8, Sukhanova St., Vladivostok, 690950, Russia
alekseev@iam.dvo.ru

ABSTRACT

This work is concerned with a numerical solution of inverse extremum problem for the heat convection model. In this problem the heat flux on some part of the boundary is used to minimize a cost functional depending on the velocity. Optimality system describing the first-order necessary optimality conditions is deduced and analyzed. Based on results of this theoretical analysis we propose numerical algorithm for solution of boundary control problem and discuss some results of numerical experiments.

1. Introduction

One of the important problems of thermal convection is the estimation of distributed or boundary heat sources using the data of measurements. The interest to these problems is connected with a large number of applications in science and engineering. Because we don't know the source functions but have some information about the state, we can consider such problems as inverse problems. From a mathematical point of view inverse problems are usually ill-posed therefore regularization methods and special algorithms are required for the numerical solution of these problems. In our work we reduce inverse problems to corresponding minimization problems by choosing a suitable cost functional that adequately describes the given data. Then inverse problems can be analyzed and solved by applying a unified approach based on the constrained optimization theory in Hilbert or Banach spaces [1-4].

Let Ω be a bounded domain in the space $\boldsymbol{R}^m$, $m=2, 3$ with Lipschitz boundary Γ. As a mathematical model we consider the initial boundary value problem for the Oberbeck-Boussinesq equations

$$\mathbf{u}_t - \nu\Delta\mathbf{u} + (\mathbf{u}\cdot\nabla)\mathbf{u} + \nabla p = -\beta T\mathbf{G} \text{ in } \Omega\times(0,t_1), \quad (1)$$

$$\operatorname{div}\mathbf{u} = 0 \text{ in } \Omega\times(0,t_1), \quad \mathbf{u} = \mathbf{g} \text{ on } \Gamma\times(0,t_1), \quad (2)$$

$$T_t - \lambda\Delta T + \mathbf{u}\cdot\nabla T = f \text{ in } \Omega\times(0,t_1), \quad (3)$$

$$T = \psi \text{ on } \Gamma_D\times(0,t_1), \quad \lambda\partial T/\partial n = \chi \text{ on } \Gamma_N\times(0,t_1), \quad (4)$$

$$\mathbf{u}\big|_{t=0} = \mathbf{u}_0 \text{ in } \Omega, \quad T\big|_{t=0} = T_0 \text{ in } \Omega \quad (5)$$

which describes the flow of viscous incompressible heat-conducting fluid in the domain Ω on the time interval $(0,t_1)$. Here $\mathbf{u}$, p and T denote the velocity, pressure and temperature fields respectively, ν is the kinematic viscosity coefficient, $\mathbf{G}$ is the gravitational acceleration vector, β is the volumetric thermal expansion coefficient, λ is the thermal diffusivity coefficient, $\mathbf{g}$ is a given vector-function on Γ, ψ is a given function on a part Γ_D of Γ, χ is a function given on another part Γ_N of Γ, $\mathbf{n}$ is the unit outer normal.

2. Constrained Minimization Problems

Our goal is the theoretical and numerical study of the inverse extremum problems for the model under consideration. The problems consist in minimization of certain cost functional depending on the velocity and control. We assume that the heat flux control χ vary in some closed convex set $K \subset L^2(\Gamma_N)$. The mathematical statement of the constrained minimization problem is as follows: find $(\mathbf{u},p,T,\chi)$ such that $F(\mathbf{u},p,T,\chi)=0$ and

$$J(\mathbf{u},\chi) = J_i(\mathbf{u}) + \frac{\mu}{2}\int_0^{t_1}\int_{\Gamma_N}\chi^2 d\Gamma\, dt \to \inf \quad . (6)$$

Here $F(\mathbf{u},p,T,\chi)=0$ is the operator constraint in the form of the weak formulation of problem (1)-(5); μ is a positive constant, $J_i(\mathbf{u})$ is a cost functional. In the considered heat flux estimation problem the possible cost functionals are defined as

$$J_1(\mathbf{u}) = \frac{1}{2}\int_0^{t_1}\int_{\Omega_d}|\mathbf{u}-\mathbf{u}_d|^2 d\Omega\, dt,$$
$$J_2(\mathbf{u}) = \frac{1}{2}\int_0^{t_1}\int_{\Gamma_d}|\mathbf{u}-\mathbf{u}_d|^2 d\Gamma\, dt \quad (7)$$

in the cases where the velocity field data $\mathbf{u}_d$ in some subdomain Ω_d or on some curve Γ_d are given.

Optimality system describing first-order necessary optimality conditions was derived and analyzed.

3. Numerical Experiments

A numerical algorithm, based on the solution of the nonlinear optimality system applying Newton's method, was proposed. The open source software freeFEM++ (www.freefem.org) was used for the discretization and solution of initial boundary value problems by the finite element method.

The main goal of the computational experiments is to determine the dependence of the solution accuracy on the choice of the problem parameters. For example, the regularization parameter μ in (6) has a great influence on the accuracy and stability of the numerical solutions.

Following example is connected with the 2D viscous incompressible heat-conducting fluid flow in the square cavity $\Omega=\{(x,y)$: $-0.5 < x,y < 0.5\}$ with the heating on the right boundary. The original uncontrolled flow is the solution of the Oberbeck-Boussinesq equations on time interval $(0,1)$ with no-slip boundary conditions $\mathbf{u}=\mathbf{0}$ for the velocity, the Dirichlet boundary condition $T=0$ for temperature on the left, top and bottom boundaries and

the Neumann boundary condition $\partial T/\partial n=\chi_d$ on the right boundary. We assume that distributed heat source $f=0$ and the original heat flux χ_d is defined by the formula

$$\chi_d(y,t)=\begin{cases}\dfrac{t}{2}[1+\cos(10\pi y)], & y\in(-0.1,0.1),\\ 0, & y\notin(-0.1,0.1).\end{cases} \quad (8)$$

The problem (1)-(5) is solved in dimensionless form for the Reynolds number Re=1, Prandtl number Pr=7 and Raleigh number $\mathrm{Ra}=10^4$. The numerical solution to this initial boundary value problem is denoted as $(\mathbf{u}_d, p_d, T_d)$. Then we use the velocity field data $\mathbf{u}_d$ for numerical estimation of the corresponding heat flux χ.

In following examples we solve the minimization problem (6) with the cost functional $J_2(\mathbf{u})$. The vertical line $\Gamma_d=\{(x,y)\colon x=0,\ -0.5<y<0.5\}$ divides the domain Ω into two equal parts. The original heat flux χ_d and the numerical solution χ for the regularization parameter $\mu=10^{-5}$ at $t=0.5$ are shown in Figure 1.

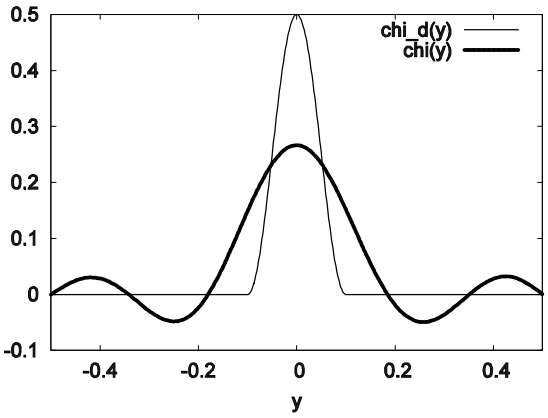

Fig. 1 Heat fluxes χ_d and χ for $\mu=10^{-5}$ at $t=0.5$

The same functions for the case when $\mu=10^{-9}$ are shown in Figure 2.

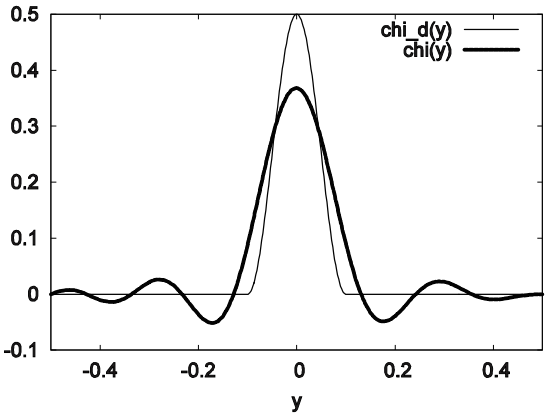

Fig. 2 Heat fluxes χ_d and χ for $\mu=10^{-9}$ at $t=0.5$

Since we do not know in advance that the heat flux is zero on some parts of the boundary, we are looking for a solution on the entire interval (-0.5,0.5) and obtain the graph of the other form. It is clearly seen that in the second case we have a more accurate solution. In the next example we choose the regularization parameter $\mu=10^{-13}$. The original heat flux χ_d and the numerical solution χ for this value are shown in Figure 3.

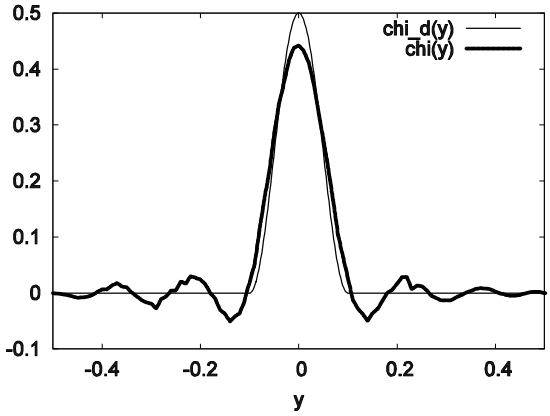

Fig. 3 Heat fluxes χ_d and χ for $\mu=10^{-13}$ at $t=0.5$

Analyzing the graphs of numerical solutions in Figures 1-3, we can conclude that the smaller values of the regularization parameter μ provide more accurate solutions for the heat flux χ. But these solutions are less stable as can be seen in Figure 3. Therefore the correct choice of the regularization parameter μ is a very important question. For different problems we have to find the appropriate balance between accuracy and stability. Let us also note that we could obtain a more accurate solution if we had a priori information that the heat flux is zero for $y\in(-0.5,0.1)$ and $y\in(0.1,0.5)$.

When we use the cost functional $J_1(\mathbf{u})$, solution becomes more accurate with increasing size of subdomain $\Omega_d\subseteq\Omega$. We could obtain a more accurate solution for the heat flux χ if we used the temperature field data T_d instead of the velocity data $\mathbf{u}_d$. Some results of numerical experiments for stationary inverse and control problems can be found in [2-4].

Acknowledgments

This work was supported by the Russian Foundation for Basic Research (project no. 13-01-00313-a), the Far Eastern Branch of the Russian Academy of Sciences (project no. 12-I-P17-03) and the Ministry of Education and Science of Russia (project no. 14.A18.21.0353).

References

[1] M.D. Gunzburger, Perspectives in flow control and optimization. SIAM, (2003).

[2] G.V. Alekseev and D.A. Tereshko, Analysis and optimization in hydrodynamics of viscous fluid. Dalnauka, (2008).

[3] G.V. Alekseev and D.A. Tereshko, J. Appl. Mech. Tech. Phys., **51** (2010), 510-520.

[4] G.V. Alekseev and D.A. Tereshko, Comp. Math. Math Phys., **51** (2011), 1539-1557.

Natural Convection between Vertical Parallel Plates with Asymmetric Heating

Shang-Hao Huang, Wu-Shung Fu, Chung-Jen Chen (National Chiao Tung University, Taiwan)
1001 Ta Hsueh Road, Hsinchu, Taiwan
shhuang.me98g@g2.nctu.edu.tw

ABSTRACT

Natural convection between vertical parallel plates with asymmetric heating is investigated numerically. Numerical methods of the Roe scheme, preconditioning and dual time stepping are adopted for solving governing equations of a low speed compressible flow. The results show that in all cases, the boundary layer flow is found along the heated surface and the reverse flow is formed on the opposite side from the outlet of the channel. However, thermal and flow fields incline to a steady or unsteady situation that is connected with Rayleigh number and aspect ratio. In the low modified Rayleigh number situation, the shear force is dominant, and then the recirculation cell length decreases. Oppositely, the recirculation cell length increases and thermal and flow fields incline to a unsteady situation.

1. Introduction

Natural convection between vertical parallel plates with asymmetric heating is a very important subject in both academic and industrial research. In practical applications, this subject can be observed in much thermal equipment, such as the chimney, the solar panel and the liquid crystal growth chamber. A low-speed compressible fluid flow is taken into consideration instead of Boussinesq assumption in high temperature difference [1]. In those past studies, the effect of distance between vertical parallel plates that is very important and the phenomena of natural convection varying from a steady to an unsteady situation in a heating process are hardly studied. Therefore, the aim of this study investigates of natural convection between vertical parallel plates with asymmetric heating numerically.

2. Physical Model

A physical model of three dimensional vertical parallel plates is indicated in Fig.1. The length, height and width are h, b and w, respectively. The temperature of the heated surface is $T_h(400K)$, and the other regions are adiabatic. The gravity is downward and the temperature and pressure of the surroundings are $T_0(298K)$ and $P_0(101300Pa)$, respectively.

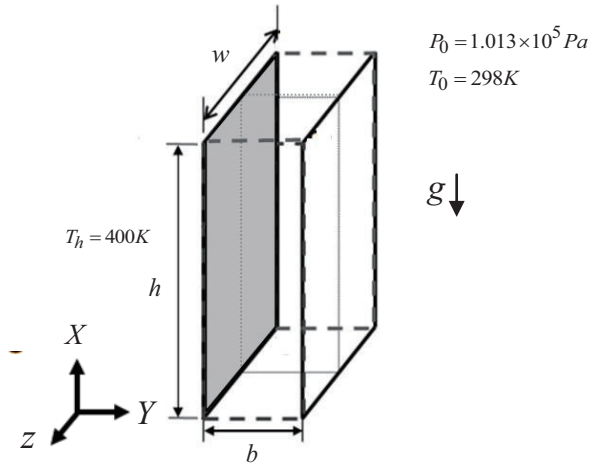

Fig. 1 Physical model

3. Numerical Method

For the investigation of the heat transfer with high temperature difference, the numerical method of compressible flow without Boussinesq assumption is considered. The governing equations of a compressible flow can be divided into two parts. One is the inviscid term and the other is the viscous term. The Roe scheme with $3rd$ order MUSCL proposed by Abalakin et al. [5] are used to compute the inviscid terms. The method of dual time stepping is added to calculate the transient state. And a second order central difference method is adopted to calculate the magnitudes of the viscous terms. Finally, the LUSGS was modified by [6] to suitable for preconditioning in solving temporal term. The non-reflecting boundary conditions are used at the apertures of the vertical parallel plates in order to avoid a low speed compressible flow to be polluted by the reflections of acoustic waves. And both sides of the width are periodic conditions.

And governing equations can be obtained.

$$\Gamma\frac{\partial U_p}{\partial \tau}+\frac{\partial U}{\partial t}+\frac{\partial F}{\partial x}+\frac{\partial G}{\partial y}+\frac{\partial H}{\partial z}=S \qquad (1)$$

where τ is the artificial time, t is the physical time . Γ is a preconditioning matrix proposed by Weiss and Smith[7]

4. Results and Discussion

In Fig.2, thermal fields and streamlines are indicated under the $Ra=1.31\times10^6$ situation. In the thermal field, the heated fluids with light density exerted by the buoyancy force ascend to the aperture. And then ascending fluids along the heated wall continuously accumulate and start to form rotation behaviors. In the flow field, the reverse flow from the outlet forms an eight-shaped structure with two main recirculation cells. The flow field of the top half region begins to swing unsteadily.

In Fig.3, in both cases, the boundary layer flow is found along the heated surface and the reverse flow is formed on the opposite side from the outlet of the channel. However, thermal and flow fields incline to a steady or unsteady situation that is connected with Rayleigh number and aspect ratio ($Ra(b/h)$). In the

low modify Rayleigh number situation, the shear force is dominant, and then recirculation cell length l decreases. Oppositely, recirculation cell length l increases and thermal and flow fields incline to a unsteady situation.

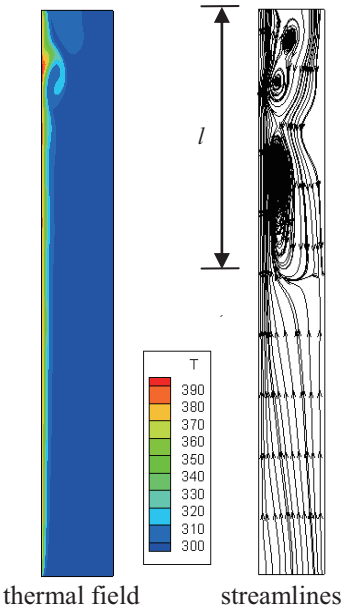

Fig. 2 thermal field and streamlines under $Ra = 1.31\times10^{6}$ at $t = 11.4s$

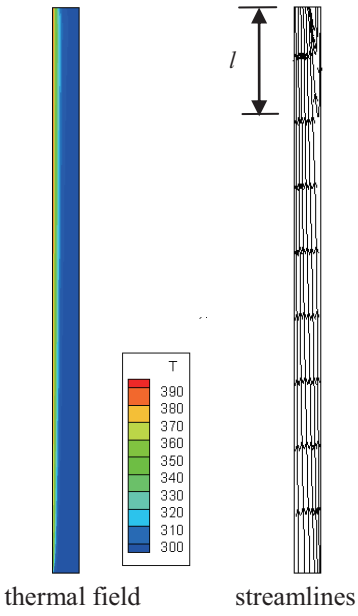

Fig. 3 thermal field and streamlines under $Ra = 8.35\times10^{4}$ at $t = 11.4s$

In Fig. 5, the distributions of variations of area average Nusselt numbers with time under different Rayleigh numbers are shown. For the case of $Ra = 8.35\times10^{4}$, the average Nusselt numbers fluctuates within $t = 2s$, and then stabilizes after 3s. But for the case of $Ra = 1.31\times10^{6}$, the average Nusselt numbers with time oscillates and never becomes a steady state.

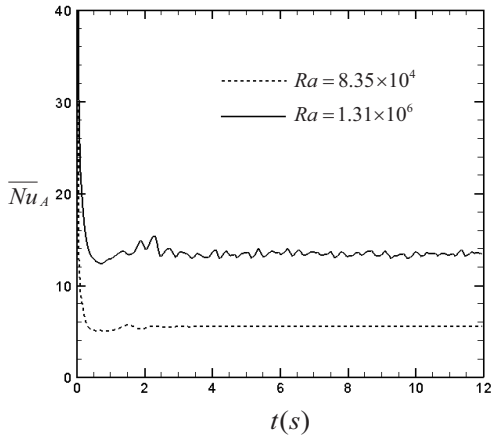

Fig. 4 Distributions of variations of area average Nusselt numbers with time under different Rayleigh numbers.

Comparison of average Nusselt numbers of present results and existing results [2] in Fig. 5. Both results have good agreement between experimental and numerical data.

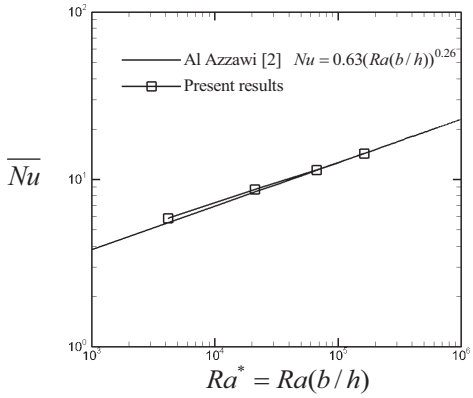

Fig. 5 Comparison of averag Nusselt numbers of present results and existing results [2]

5. Concluding remarks

Several conclusions are summarized as follows.

1. Thermal and flow fields incline to a steady or unsteady situation that is connected with Rayleigh number and aspect ratio.
2. The shear force is dominant, and then the recirculation cell length decreases.

References

[1] D.D. Gray, A. Giorigini, Int. J. Heat Mass Transfer, **19** (1976) 545-551.

[2] A.R.H. Al-Azzawi, PhD thesis, University of Strathclyde, (1987).

[3] T. Yilmaz, S.M. Fraser, Int. J. Heat Mass Transfer, 50 (2007), pp. 2612–2623.

[4] W.S. Fu, C.G. Li, C.P. Huang, J.C. Huang, Int. J. Heat Mass Transfer 52 (2009), pp. 2571–2580

[5] I. Abalakin, A. Dervieux, T. Kozubskaya, INRIA (2002) No4459.

[6] W. S. Fu, C. G. Li, W. F. Lin and Y. H. Chen, Int. J. Nume. Meth. Fluids (2008).

[7] J. M. Weiss and W. A. Smith, AIAA. **33** (1995) 2050-2056

Synthetic Jets at Low Stokes Number: Numerical and Experimental Approach

Isaac Ng[1], Victoria Timchenko[1], John Reizes[1], Zdenek Travnicek[2], Jozef Kordik[2], Zuzana Brouckova[2]
[1]The University of NSW, School of Mechanical Engineering, UNSW, Sydney, 2052 NSW, Australia
[2]Institute of Thermomechanics, Academy of Sciences of the Czech Republic, Prague, Czech Republic
E-mail of corresponding author: v.timchenko@unsw.edu.au

ABSTRACT
A synthetic jet actuator is a zero net mass flux device in which a sustainable jet directed away from the orifice can be generated under the appropriate conditions. A criterion is required to determine the onset of a sustainable jet which is investigated in this paper for low Stokes numbers.

1. Introduction

Synthetic jets (SJ) are zero-net-mass-flux jets that are generated by fluids oscillating through a nozzle. The actuator is a sealed cavity with a nozzle and a diaphragm oscillating at various frequencies. Thus, a flow out of the nozzle and sequentially a negative flow (back into the actuator) will occur. At the expulsion stage a vortex ring is formed and if the vortex ring's velocity is sufficiently high, it will not be re-ingested into the actuator cavity during suction [1]. Advantages of SJs are in the application of active flow control and have been applied in external and internal aerodynamics to improve lift, maneuverability, prevent stalls and reduce noise [1] and also in microelectromechanical systems (MEMS) [2].

The aim of this paper is to study numerically and experimentally the formation of SJs at low Stokes numbers so as to determine the minimum Reynolds number at which a synthetic jet is sustained throughout a diaphragm cycle.

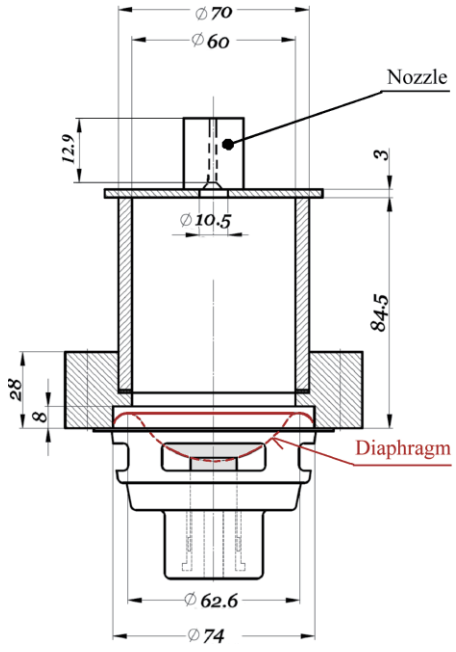

Fig. 1 Sketch of experimental rig.

2. Experimental Apparatus and Methodology

A sketch and leading dimensions of the experimental apparatus are presented in Fig 1. In the experiments the nozzle was shaped as an orifice of the diameter and length D_{or}=1.6mm and 12.9 mm, respectively. An orifice edge in cavity is beveled 2mm x 45°, while the outlet to the surroundings is sharp edged – see Fig. 1. Two flow visualization methods were used depending on the jet flow velocity. The first method was the smoke-wire technique and the second method, useful for small velocities, adopted cold water fog produced by an ultrasonic piezoelectric nebulizer (Mini Nebler) [3].

3. Numerical Method

Similar to the method used by Timchenko et al [4] the complete three-dimensional geometry representing experimental set-up shown in Fig. 1 was simplified to an axisymmetric arrangement as shown in Fig. 2 with the outer boundary of the calculation domain outside the cavity having diameter, $D = 42D_{or}$ and height, $h = 40D_{or}$ respectively, in which D_{or} is the orifice diameter.

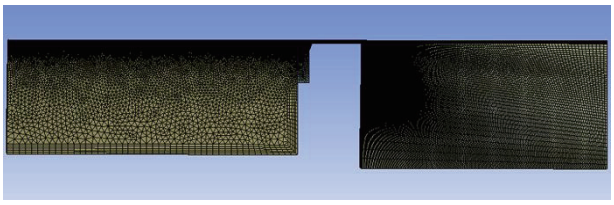

Fig. 2 Axisymmetric model.

A mesh of 382509 elements with a high resolution structured around the axis of rotation and orifice exit has been constructed to simulate incompressible flow of air with constant properties.

Atmospheric pressure was set at the outer boundaries whilst the diaphragm was simulated using a "plug model" velocity inlet with the inlet velocity U_d specified at the diaphragm to model the sinusoidal in time volumetric displacement of the piston as

$$U_d = U_{max} \sin(2\pi ft) \qquad (1)$$

U_{max} was calculated as $U_{max} = (D_{or} / D_d)^2 \pi * U_0$ where U_0 is the time-mean velocity at the orifice defined using the slug flow model [1] as

$$U_0 = \frac{1}{T}\int_0^{T_E} u_0(r=0,t)\,dt \qquad (2)$$

Here $u_0(r=0,t)$ is the orifice centerline velocity at the axis (r=0), T is the time period (T=1/f, where f is frequency), T_E is the extrusion time (e.g., T_E=T/2 at a sinusoidal waveform described by Eq. (1)).

The numerical results were obtained using a second order upwind differencing scheme for the advective terms and second order backward Euler differencing scheme for time derivative [4]. The time step size was 1/200f in agreement with Timchenko and her co-workers [4, 5]. The flow had stabilized after four cycles and the presented results are from the 5th cycle.

Following Timchenko et al [4] a sustained jet is said to exist if anywhere on the centerline outside the orifice there is a velocity, U_{min}, at all times in the cycle directed away from the orifice, such that $U_{\min}/\bar{U} \geq 0.05\%$ where $\bar{U}$ is the time-spatial average velocity over expulsion stage [4]. Note that for parabolic velocity profile at the exit from the orifice $\bar{U} = U_0$.

4. Results and Discussion

The numerical results were obtained for the range of Reynolds numbers, $\mathrm{Re} = D_{or}\bar{U}/\nu$, and Stokes numbers used in the experiments as shown in Table 1. The Stokes number is defined as $S = \sqrt{Re\,St}$, where the Strouhal number, St, can be expressed in terms of the angular frequency ω=2πf as $St = \omega D_{or}/\bar{U}$. For the slug flow model and the sinusoidal waveform of the velocity cycle in the orifice, $St = \pi D_{or}/L_0$ where the "stroke length" L_0=U_0T.

Table 1. Numerical and experimental results.

S	Re	$U_{\min}/\bar{U}$	Experimental observation
1.76	21.9	0.267	No
1.76	76.6	0.505	Yes
2.49	22.8	0.422	No
3.52	25	0.633	No
4.98	13.7	0.228	No
6.97	86	1.921	Yes
9.86	45	1.644	Yes

It should be noted that the present numerical results indicate that there were sustained SJ in all cases shown in Table 1, but only three, viz, for Re=76.6, 86 and 45, have been shown to have sustainable SJs experimentally. As all the present numerical results in Table 1 fall above the threshold developed in [4], the present numerical results are in agreement with the threshold results found in [4] and presented in Fig 3. Because the U_{min} values were too small to be detected for the three Re values for which no jet was found experimentally, it is obvious that criterion used in [4] represents the very minimum threshold for a sustained SJ. For comparison, experimental results obtained from visualization study [3] specifying the threshold of a sustainable SJ without vortex roll up as well as the results of Holman et al. [6] are shown in Fig. 3. Also presented in Fig. 3 are the borders for SJ formation and propagation with vortex rollup (solid line) and without vortex rollup (dashed line) according to Zhou et al. [7].

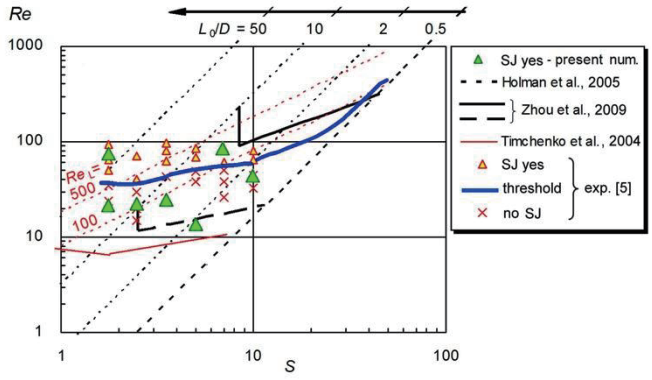

Fig. 3 Re-S parameter map for the SJ formation

5. Concluding remarks

Since the numerical results for the threshold of a sustainable jet using the criterion proposed in [2], lead to velocities well below those able to be detected experimentally, the proposed threshold developed from numerical results is the "absolute floor" and below the minimum level of experimentally obtained thresholds for the existence of a sustained synthetic jet. Future experimental and numerical investigations are planned to study in the thresholds for different regimes and nozzle geometries of synthetic jets.

6. References

[1] Travnicek Z, Brouckova Z and Kordik J. AIAA Journal, Vol. 50, No. 9, September 2012.

[2] Travnicek Z, Dancova P, Lam J, Timchenko V and Reizes J., Experimental Fluid Mechanics, pp 460-467, 2011.

[3] Travnicek Z., Brouckova Z. and Kordik J. The 12th International Symposium on Fluid Control, Measurement and Visualization FLUCOME2013. November 18-23, 2013, Nara, Japan (accepted).

[4] Timchenko V, Reizes J, Leonardi E and de Vahl Davis G. ASME International Mechanical Engineering Congress, Anaheim, California USA, IMECE2004-61374, 2004.

[5] Timchenko V, Reizes J and Leonardi E. 5th Pacific Symposium on Flow Visualisation and Image Processing, Australia, PSFVIP-5, 2005.

[6] Holman, R., Utturkar, Y., Mittal, R., Smith B.L., and Cattafesta, L., AIAA Journal, 43, pp. 2110–2116, 2005.

[7] Zhou, J., Tang, H., and Zhong, S., AIAA Journal, Vol. 47, No. 5, 2009, pp. 1252–1262. doi: 10.2514/1.40602.

.

Tenth International Conference on Flow Dynamics
November 25-27, 2013, Sendai, Miyagi, Japan

Solvability of the Stationary MHD Equations under Mixed Boundary Conditions for Magnetic Field

Roman Brizitskii
Institute of Applied Mathematics FEB RAS, 7, Radio St., Vladivostok, 690041, Russia
Far Eastern Federal University, 8, Sukhanova St., Vladivostok, 690950, Russia
mlnwizard@mail.ru

ABSTRACT

We proved the global solvability of the stationary magnetohydrodynamics equations of a viscous incompressible fluid under mixed boundary conditions for the magnetic field. For this magnetohydrodynamics model we also studied a some optimal control problems.

1. Introduction. Statement of the Boundary-Value Problem

Comparative analysis of engineering and mathematical references on electromagnetism show that mathematical results are not always consistent requirements of technical applications. For example, modeling the real magnetic devices, one of the fragments of the device may be a dielectric, and the other is an ideal conductor. This leads to the necessity of statement the mixed boundary conditions a magnetic or electric field (see [1]), and in the mathematical literature usually avoid their consideration.

In [1] for the first time the solvability of magnetostatic problems with mixed boundary conditions for the magnetic field was proved. Mixed boundary conditions correspond to situation where one part of the boundary is given the tangential component of the magnetic field while the other part is given by the normal component of the magnetic field. Homogeneous conditions of this type just describe the situation where one part of the boundary is a perfect conductor while the other part is a perfect insulator. It is not anticipated that the open parts of the boundary with different boundary conditions can not have a common boundary. These simplifying assumptions is not in our work. In [1] the similar electrostatic problem are studied. However, the results of [1] can not directly apply for the study of mixed boundary value problems of magnetohydrodynamics (MHD) in the nonlinearity of the latter.

In this paper we essentially use the results of [2,3] on additional smoothness of special Sobolev spaces with mixed boundary conditions. In [3] also obtained a stronger coercive inequality allowing find for the magnetic field in the corresponding subspace of space $\mathbf{H}^1(\Omega)$. Note that in contrast to the [1] the results of [2,3] are valid only for domains with smooth boundaries. In [2,3] also obtained the orthogonal decompositions of $\mathbf{L}^2(\Omega)$ similar to the results of [1] and generalizing well known orthogonal decompositions [4]. Using this result,we have proved the correctness of the weak formulation of the problem 1

In the present work we study boundary value-problem for the stationary MHD equations of a viscous incompressible fluid

$$-\nu\,\Delta\mathbf{u}+(\mathbf{u}\cdot\nabla)\mathbf{u}+\nabla p-\kappa\,\mathrm{rot}\,\mathbf{H}\times\mathbf{H}=\mathbf{f},\quad \mathrm{div}\,\mathbf{u}=0, \tag{1}$$

$$\nu_1\,\mathrm{rot}\,\mathbf{H}-\rho_0^{-1}\,\mathbf{E}+\kappa\,\mathbf{H}\times\mathbf{u}=\upsilon_1\mathbf{j},\ \mathrm{div}\,\mathbf{H}=0,\ \mathrm{rot}\,\mathbf{H}=0, \tag{2}$$

considering in domain Ω under following boundary conditions:

$$\mathbf{u}=\mathbf{g}\ \text{on}\ \Gamma,\quad \mathbf{H}\cdot\mathbf{n}=0\ \text{on}\ \Gamma_N,\quad \mathbf{H}\times\mathbf{n}=0\ \text{on}\ \Gamma_T,$$
$$\text{and}\ \ \mathbf{E}\times\mathbf{n}=\mathbf{k}\ \ \text{on}\ \ \Gamma_N \tag{3}$$

Here $\Omega\in\mathbf{R}^3$ is a bounded domain with boundary Γ, consisting of two parts: Γ_N and Γ_T, $\mathbf{u}$ is the velocity vector; $\mathbf{H}$ and $\mathbf{E}$ are the magnetic and electric field intensity vectors, respectively; $p=P/\rho_0$ where P is the pressure, ρ_0=const is a density, $\mathbf{j}$ is the external current density vector, $\mathbf{g}$ and $\mathbf{k}$ are given functions on Γ and Γ_N. We shall refer to problem (1)-(3) as Problem 1.

As far as we know, the MHD equations were not previously considered under the boundary conditions (3). It should be noted that some of the previously studied boundary value problems are special cases of problem 1. For example, articles [5] proved the global solvability stationary MHD equations in the case when the entire boundary is defined the normal component of the magnetic field and the tangential component of the electric field. In [6] similar results were obtained by setting the tangential component of magnetic field across the all boundary. These boundary value problems are considered under Dirichlet problem for the velocity Assuming in turn $\Gamma_N=\varnothing$ and $\Gamma_T=\varnothing$ we can reduce the problem to the one given boundary value problems In [7] the stationary MHD equations under mixed boundary conditions for the velocity are studied.

Our main result is a global solvability of Problem 1. We also proved a local uniqueness of solution of Problem1.

2. Optimal Control Problems

The development of new technologies in engineering fluid mechanics leads to new statements of problems in theoretical hydrodynamics and magnetohydrodynamics. Optimal control problems for the Navier–Stokes and magnetohydrodynamics equations can serve as examples of such problems. On the control problems for MHD equations and MHD equation of heat-conducting viscous fluid see [5,8-12].

Below we mainly pay attention to the analysis of the uniqueness and stability of solutions of extremum

problems for the model (1)-(3) on the basis of new a priori estimates of solutions of the boundary value problem (1)–(3) and an auxiliary theorem on properties of the difference of solutions of the original control problem and a perturbed control problem obtained by a perturbation of the original performance functional. The resulting stability estimates are cumbersome. However, by using specially introduced dimensionless parameters, which are analogs of the Reynolds, Hartmann, and Prandtl numbers used in hydrodynamics, we represent these estimates in a fairly concise and clear form. A typical extremum problem for the considered MHD model is to find one or several functional parameters (controls) occurring in weak formulation of Problem 1 and its solution (**u**,p,**H**) from the minimum condition for a certain performance functional. In what follows, we consider an extremum problem in which the performance functional depends either only on the velocity or only on the pressure and the function **j** occurring in the right-hand side of equation (2) is used as a control. We assume that the control **j** can vary over a set K, where $K \subset \mathbf{L}^2(\Omega)$ is a nonempty convex closed set.

The mathematical statement of the optimal control problem is as follows: find a pair (**x**,**j**), where $\mathbf{x}=(\mathbf{u},H,p) \in X$, and $\mathbf{j} \in K$ such that

$$J(\mathbf{x},\mathbf{j}) = I_i(\mathbf{u},p) + \frac{\mu_1}{2}\|\mathbf{j}\|^2 \to \inf \cdot$$

$$F(\mathbf{x},\mathbf{j}) = 0,\ \mathbf{x} \in X,\ \mathbf{j} \in K \qquad (4)$$

Here F(x,**j**)=0 is the operators form of the weak formulation of Problem 1 (see [ ]); μ_1 is nonnegative parameter, $I_i(\mathbf{u},p)$ is a cost functional. The possible cost functionals are usually defined as

$$I_1(\mathbf{v}) = \|\mathbf{v}-\mathbf{v}_\mathbf{d}\|_Q^2,\ \ I_2(\mathbf{v}) = \|\mathbf{v}-\mathbf{v}_\mathbf{d}\|_{1,Q}^2$$

$$I_3(\mathbf{v}) = \|\mathrm{rot}\,\mathbf{v}-\eta_\mathbf{d}\|_Q^2,\ \ I_4(p) = \|p-p_\mathbf{d}\|_Q^2 \qquad (5)$$

Here Q is a some subset of domain Ω, $\mathbf{v}_\mathrm{d} \in \mathbf{L}^2(\mathrm{Q})$ (or $\mathbf{v}_\mathrm{d} \in \mathbf{H}^1(\mathrm{Q})$) is function, which simulates a given distribution of the velocity field in Q. Functions $\eta_\mathrm{d} \in \mathbf{L}^2(\mathrm{Q})$ and $p_\mathrm{d} \in L^2(\mathrm{Q})$ have a similar sense.

We show further the stability estimates of solutions of concrete control problem:

$$J(\mathbf{v},\mathbf{j}) \equiv \frac{\mu_0}{2}\|\mathbf{v}-\mathbf{v}_\mathbf{d}\|_Q^2 + \frac{\mu_1}{2}\|\mathbf{j}\|^2 \to \inf,$$

$$F(\mathbf{x},\mathbf{j},\mathbf{g}) = 0,\ \mathbf{x} \in X,\ \mathbf{j} \in K, \qquad (6)$$

corresponding to the cost functional $I_1(\mathbf{v})$. Let us assume below that the boundary function **g** in (6) can change in some bounded set $G \subset \mathbf{H}_\mathbf{T}^{1/2}(\Gamma)$. Denote by $(\mathbf{x}_1,\mathbf{j}_1) \equiv (\mathbf{u}_1,\mathbf{H}_1,p_1,\mathbf{j}_1)$ a solution to problem (6) that corresponds to given functions $\mathbf{v}_d \equiv \mathbf{u}_d^{(1)} \in \mathbf{L}^2(Q)$ and $\mathbf{g} = \mathbf{g}_1 \in G$. By $(\mathbf{x}_2,\mathbf{j}_2) \equiv (\mathbf{u}_2,\mathbf{H}_2,p_2,\mathbf{j}_2)$ we denote a solution to problem (6) that corresponds to perturbed functions $\mathbf{v}_d \equiv \mathbf{u}_d^{(2)} \in \mathbf{L}^2(Q)$ and $\mathbf{g} = \mathbf{g}_2 \in G$.

Denote by

$$\Delta \equiv \|\mathbf{u}_d^{(1)} - \mathbf{u}_d^{(2)}\|_Q + (a\|\mathbf{g}_1 - \mathbf{g}_2\|_{1/2,\Gamma} + b\|\mathbf{g}_1 - \mathbf{g}_2\|_{1/2,\Gamma}^2)^{1/2}.$$

We obtained local stability estimates for the solutions of problem (6):

$$\|\mathbf{u}_1 - \mathbf{u}_2\|_{\mathbf{H}^1(\Omega)} \le M_\mathbf{u}\Delta,\ \ \|\mathbf{H}_1 - \mathbf{H}_2\|_{\mathbf{H}^1(\Omega)} \le M_\mathbf{H}\Delta,$$

$$\|p_1 - p_2\| \le M_p\Delta,\ \ \|\mathbf{j}_1 - \mathbf{j}_2\| \le M_\mathbf{j}\Delta, \qquad (7)$$

where a, b, $M_\mathbf{u}$, $M_\mathbf{H}$, M_p and $M_\mathbf{j}$ are not decreasing functions of norms of the initial data of Problem 1.

It is interesting to note that the control problems (4) and (6) are the so-called problems of mixed type. In the sense that "hydrodynamic" cost functionals correspond to the electromagnetic control **j**.

Note we can use also so-called "hydrodynamic" boundary control **g** under mixed boundary condition for the magnetic field. It is hoped that we have found a more effective control mechanism to work with the "hydrodynamic" cost functionals (5) in contrast to the electromagnetic distributed control **j**. Feature of the Problem 1 is the ability to set a non-zero normal velocity components, however, only in some parts of the boundary. In contrast to the boundary conditions for the electromagnetic field in [5,7]. The global solvability of boundary value problem of this type was proved firstly in [5] under condition: $\mathbf{g}\cdot\mathbf{n}=0$ on Γ (normal component of velocity vector is zero on boundary Γ).

Acknowledgments

This work was supported by the Russian Foundation for Basic Research (projects no. 13-01-00313-a and 12-01-31288), the Far Eastern Branch of the Russian Academy of Sciences (project no. 12-I-P17-03) and the Ministry of Education and Science of Russia (project no. 14.A18.21.0353).

References

[1] P. Fernandes, G. Gilardi, Math. Mod. Meth. Appl. Sci., **7** (1997), 957-991.

[2] G. Auchmuty, J.S. Alexander, Quarterly of applied mathematics, **64** (2006), 335-357.

[3] G. Auchmuty, Methods in Appl. Sciences, **14** (2004), 79-103.

[4] A. Valli, Orthogonal decompositions of $\mathbf{L}^2(\Omega)$, Preprint UTM 493, Department of Mathematics. University of Toronto. Galamen (1995).

[5] G. Alekseev, Sibirsk. Mat. Zh., **45** (2004), 243–262.

[6] G. Alekseev, R. Brizitskii, Dalnevost. Math. J., **3** (2002), 285-301.

[7] R. Brizitskii and D. Tereshko, Differrential Equations, **43 (**2007**),** 1-13.

[8] G.VAlekseev, R. Brizitskii, J. Comp. Math. Math. Physics, **45** (2005), 2049–2065.

[9] G. Alekseev, D. Tereshko, J. Comp. Math. Math. Physics, **49** (2009), 1717–1732.

[10] G. Alekseev and R. Brizitskii, Differrential Equations, **48 (**2012**),** 397-409.

[11] M. Gunzburger, J. Peterson and C. Trenchea, Int. J. Pure Appl. Math., **42** (2008), 289–296.

[12] R. Brizitskii, D. Tereshko, Applied Mechanics and Materials, **249-250** (2013), 812-817.

Tenth International Conference on Flow Dynamics
November 25-27, 2013, Sendai, Miyagi, Japan

Development and Validation of Fast Response Thermocouples for Shock Tunnel Applications

Kiran Joy Irimpan and Viren Menezes
Department of Aerospace Engineering, Indian Institute of Technology Bombay, Powai, Mumbai 400076, India.
E-mail:kiran@aero.iitb.ac.in

ABSTRACT

The surface heat flux is a critical parameter that dictates the design of a thermal protection system in hypersonic missions. Analytical and computational studies of surface heat transfer at hypersonic speeds are often difficult owing to the complex flow features. E-type coaxial thermocouples to measure surface heat flux on test models in ultra-short duration impulse facilities like shock tunnels were designed and developed, and the output was validated. The coaxial thermocouples were found apt for use in shock tunnels, in terms of response time, sensitivity, robustness and reliability.

1. Introduction

Capturing the transient temperature rise accurately over the model surface is a paramount part of all heat flux gauges used in impulse facilities. In such a facility, the equilibrium temperature is never achieved owing to its short test duration, making thermal survival possible without complex model design and high-temperature -withstanding materials.

Various thin film sensors were employed to sense the transient temperatures on the model surface from the dawn of the first shock tubes because of their rapid response and ease of construction. Out of the various metals used in thin film construction, platinum thin films stood apart due to their high temperature coefficient of resistance and low self-heating errors [1]. Platinum thin films are essentially metal depositions over an insulator substrate, which are susceptible to wear and tear when subjected to harsh environments like a Mach 8 flow in the shock tunnel. The shearing away of the platinum depositions required frequent maintenance and replacement, making heat flux determination cumbersome. A heat flux sensor developed for ruggedness and repeatability without any compromise in the response time is the exposed junction coaxial thermocouple. The sensing junction in a coaxial thermocouple is formed by abrasion resulting in plastic deformation of one element on to the other, bridging over the insulator separating them.

Objective of the present work was to calibrate and validate the in-house-developed E-type coaxial thermocouples against a standard platinum thin film sensor and a well-known analytical formulation postulated by Fay and Riddell [2] for stagnation point heat flux on a hemispherical body.

2. Method

The coaxial thermocouple developed at IITB has a chromel tube (OD: 3.25 mm and ID: 1.3 mm) and a constantan rod (OD: 1.25 mm) as elements placed concentrically, with an insulator (araldite) in between as described in Fig. 1 [3]. This particular combination results in an E-type thermocouple which has the maximum sensitivity (63 μV/^{0}C) of all the conventional thermocouples. The sensing junction is formed by plastic deformation caused by filing the surface using files or grit papers. The lengths of the elements are determined after taking into account the assumptions involved in the semi-infinite slab theory for heat conduction. The cables used in the thermocouple construction were of Omega (U. K.) make and had a sensitivity of 63.6 μV/^{0}C.

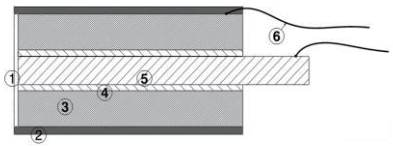

1) Thermocouple junction
2) Teflon casing
3) Chromel tube
4) Araldite layer
5) Constantan rod
6) Extension cable

Fig. 1. Schematic of the coaxial thermocouple.

The coaxial thermocouple was tested in IITB−ST, a standard shock tunnel, working in the reflected mode of operation. A 1.2 mm thick aluminum diaphragm separates the driver and the driven sections (both ID: 50mm) of the shock tube. The rupture of the diaphragm results in a shock wave which moves into the driven section, shocking the test gas (air). As the incident shock wave hits the end flange of the shock tube next to the nozzle, a second shockwave is reflected into the already shocked test gas, increasing its temperature and the pressure further and reducing its velocity to zero. This twice-shocked test gas acts as a temporary reservoir and expands through a converging–diverging Mach 8 nozzle with an exit diameter of 300mm. The free stream conditions for the present set of experiments are listed in Table 1.

The convective flux from the hot shock layer results in heat conduction into the model resulting in its temperature rise. A simplified expression for 1-D heat conduction rate with certain assumptions given by Hollis [4] is as follows.

$$Q(t) = \frac{\beta}{\sqrt{\pi}}\left[\frac{T(t)}{\sqrt{t}} + \frac{1}{2}\int_0^t \frac{T(t)-T(\tau)}{(t-\tau)^{3/2}}\,d\tau\right] \qquad (1),$$

where, $Q(t)$, $T(t)$, t, τ, β are the heat transfer rate per unit area, the time dependent temperature, the time, time variable and the material property of the thermocouple sensing junction, respectively. Beta (β), the thermal product ($\sqrt{k\rho c_p}$, where k, ρ and c_p are the thermal conductivity, density and specific heat at constant pressure at working temperature, respectively) is a measure of the thermal inertia of the substrate material.

Under the assumption that equal number of junctions are formed over both the elements, an average value of β (8457 $Jm^{-2}K^{-1}s^{-1/2}$ @ 30 ^{0}C) of both chromel and constantan has been taken for heat flux integration from the temperature time history.

Validations of E-type thermocouples against platinum thin film gauges were carried out by comparing the deduced heat fluxes after subjecting both the sensors to the same free-stream conditions in the shock tunnel. The thin film sensor, thermocouple and the pitot tube were mounted at the stagnation points of three hemispherical blunt bodies with 24.4±0.2 mm diameters, spaced appropriately on a rake. The pitot sensor recorded the pressure traces behind the shock from which Mach no of the flow and the steady test time could be calculated. The thermocouple was connected to INA128 instrumentation amplifier with a fixed gain of 500 and the thin film sensor was equipped with a differential amplifier with a gain of 50. The Predicted heat flux is based on the simplified Fay and Riddell [2] stagnation point heat transfer equation described below:

$$Q(t) = 0.943(\rho_e \mu_e)^{0.5} \left\{\frac{du_e}{dS}\right\}^{0.5} \left[C_p(T_0 - T_w)\right] \qquad (2),$$

where, $\frac{du_e}{dS} = \frac{1}{R_n}\left\{\sqrt{\frac{2(P_e - P_\infty)}{\rho_e}}\right\}$ is the velocity gradient at the edge of boundary layer as given by the Newtonian theory.

Table 1. Freestream conditions for the thermocouple validation tests against thin film sensor.

Shot no.	Mach no.	P_∞ (Pa)	T_∞ (K)	Enthalpy (MJ/kg)	Re/m
1001	8.2	144.4	81.93	1.20	1.58×10^6
1003	8.15	116.53	73.25	1.06	1.52×10^6

3. Results and Discussion

Figures 2 and 3 represent the typical outputs from the coaxial thermocouple and platinum thin film sensors. As the platinum thin film sensor has a lower effective

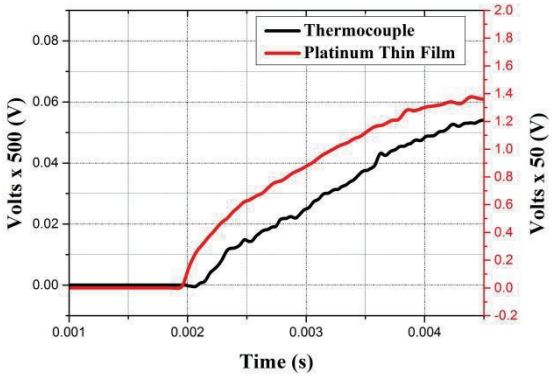

Fig. 2. Representative temperature time histories of thermocouple and platinum thin film.

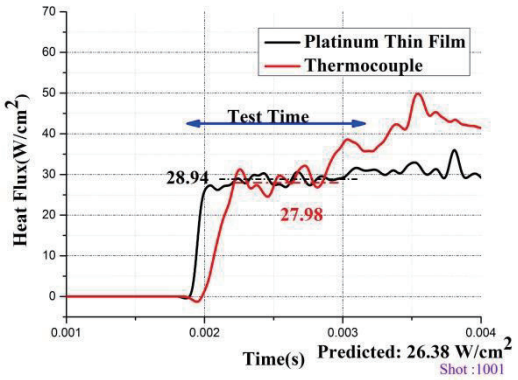

Fig. 3. Representative heat flux signals of platinum thin film and thermocouple.

thermal product (β=1700 $Jm^{-2}K^{-1}s^{-1/2}$), the surface temperature rise recorded by the thin film sensor is higher when compared to the output of the thermocouple. Even though the output of the coaxial thermocouple was feeble, a properly filtered temperature time history yielded a good comparison with the thin film sensor and Fay & Riddell prediction as indicated in Table 2. The disadvantages associated with thin films, such as errors due to self-heating and wear-out due to friction, make the thermocouples preferred sensors for such measurements despite their feeble output.

Table 2. Comparison of measured and predicted (Fay & Riddell) heat flux.

Shot no:	Predicted Q(t), W/cm^2)	Thin Film Q(t), (W/cm^2)	Thermocouple Q(t), (W/cm^2)
1001	26.38	28.94	27.98
1003	19.75	20.7	19.01

4. Concluding remarks

The above study indicates that the coaxial thermocouple is a durable, apt and a low cost alternative to a more complex platinum thin film technology. The integrated heat flux values obtained from both the sensors differ only by a negligible amount for the same test conditions. The E-type coaxial thermocouple is a suitable instrument to measure surface heat flux on models in ultra-short duration, ground-based, hypersonic test facilities.

Acknowledgement: This work was funded by the Grant-in-aid No. 12ARDB008 of the Aeronautical Research and Development Board (AR&DB), New Delhi, India.

References

[1] D.L.Schultz and T.V.Jones, AGARDograph, **165** (1973).
[2] J. A. Fay and F. R. Riddell, J. Aeronaut, Sci. **25** (1958).
[3] V.Menezes and S.Bhat, Rev. of Sci. Inst., **81** (2010).
[4] B. R. Hollis, NASA Contractor Report No. **4691**, (1995).

Tenth International Conference on Flow Dynamics
November 25-27, 2013, Sendai, Miyagi, Japan

Seasonal Thermal Performance of Different Greenhouse Covering Materials

Adil Al Mahdouri[1], Hiroki Gonome[1], Junnosuke Okajima[2], Shigenao Maruyama[2]

[1] Department of Mechanical System and Design, Graduate School of Engineering, Tohoku University, 6-6 Aramaki Aza Aoba, Aoba-ku, Sendai, Miyagi, Japan, 980-8579

[2] Institute of Fluid Science, Tohoku University, 2-1-1, Katahira, Aoba-ku, Sendai, Japan, 980-8577
almahdory@pixy.ifs.tohoku.ac.jp

ABSTRACT

A non-gray rigorous model was constructed to study the radiative heat transfer through greenhouse covering materials by using Radiative Element Method by Ray Emission Model (REM^2). This model was applied to find the difference in thermal performance between silica glass, polyvinylchloride (PVC) and low density polyethylene (LDPE) covering materials. In addition, two outdoor experiments were conducted in summer and winter to measure the thermal performances of three rectangular enclosures covered by the mentioned claddings. The calculated enclosures inside air, ground surface and cover temperatures using the rigorous model showed a good agreement with the experimental measurements.

1. Introduction

Greenhouse covering material plays a key role in providing optimum environmental conditions for growing plants and producing fruits and vegetables. The greenhouses are mainly covered by solar transparent materials such as plastics and glass sheets. However, it varies in term of thermal performance due to absorption/reflection of infrared radiation reemitted from the hot soil. Therefore, in the present study, a rigorous non-gray radiative heat transfer analysis was conducted. An investigation on the temporal thermal performance of rectangular enclosures covered with different greenhouse such as materials, silica glass, Polyvinylchloride (PVC) and Low Density Polyethylene (LDPE), were theoretically investigated. In a similar way, two experiments were conducted to evaluate the heating efficiency of covering materials on rectangular enclosures in summer and winter.

2. Theoretical Method:

In order to evaluate a thermal performance of greenhouses subjected to solar irradiation, a rigorous approach using the Radiation Element Method by Ray Emission Model (REM^2) was modeled. The REM^2 is a generalized method for calculating radiative heat transfer in absorbing, emitting and scattering anisotropic media. The spectral radiative intensity through a medium could be determined by solving Radiative Transfer Equation, Eq. (1),

$$\mu \frac{\partial I_\lambda(x,\mu)}{\partial x} = \beta_\lambda \left[-I_\lambda(x,\mu) + (1-\omega_\lambda) I_{b,\lambda}(T) + \frac{\omega_\lambda}{2} \int_{-1}^{1} I_\lambda(x,\mu')\phi(\mu')d\mu' \right] \quad (1)$$

where $I_{b,\lambda}$, β_λ, ω_λ, $\phi(\mu')$ are spectral value of blackbody intensity[W/m^2.sr], extinction coefficient[1/m], single scattering albedo[-] and scattering phase function of the media [sr^{-1}], respectively. Figure 1 shows 1D model plane-parallel model for greenhouse system. The covering material was considered as a non-gray participating medium and the emission /absorption within cover layer was taken into account. The cover has specular surfaces and it is discretized into 100 participating elements of equal thicknesses and subjected to collimated and diffused solar irradiations.

Directional reflectivity and refraction have been resolved from generalized Fresnel formulae and Snell's Law. The amount of absorption, extincted and diffusely scattered view factors between two participating elements were found using Ray Tracing method.

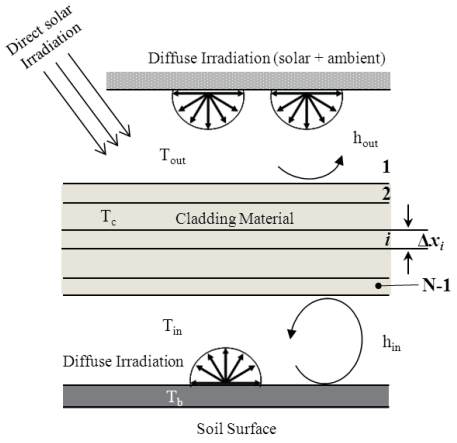

Fig. 1 One-dimensional plane-parallel analysis model

Three greenhouse systems were covered by silica glass, PVC and LDPE. The spectral indices of refraction, in the range from ultraviolet to mid-infrared (0.22-25 μm), were previously obtained using Kramers-Kronig method and the inverse calculation of transmission and reflection measurements applied by REM^2 [2]. The total radiative heat flux through each element i is obtained by integration of all monochromatic radiative heat flux $q_{r,\lambda}(i)$. The radiation heat transfer through the covering material was coupled with inside and outside convective heat transfer of the greenhouse system.

Finally, quasi-steady temperatures of soil surface, inside air and covering material can be determined when the energy balance on the soil surface and covering material were satisfied.

3. Experimental Method:

Two outdoor experiments were conducted in winter (2013/01/10) and summer (2013/06/24) to measure the

heating efficiency of silica glass (1 mm in thickness), PVC (50 μm) and LDP (50 μm) on rectangular enclosures. As shown in Figure 2, the proposed greenhouse system composites of three identical enclosures which are made by using insulation material. Each enclosure has a square surface with length (L) of 100 mm and height (H) of 20 mm. The bottom surface of each enclosure is covered with an aluminum plate having thickness of 0.3 mm and painted by black paint with emissivity of 0.94.

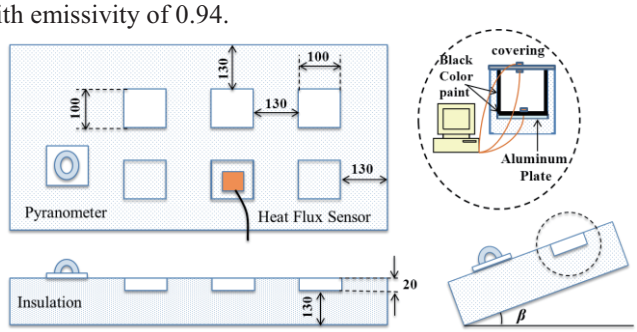

Fig. 2 : greenhouse experimental system

Three thermocouples were attached to the top surface of the aluminum plate, the inside and outside surfaces of the covering material. The system was tilted with angle of 30°. In the interest of global radiation and outer convective heat transfer, a pyranometer and a heat flux (HF) sensor were attached to the inclined system.

4. Results and Discussion

As a representative example, Fig. 3 and 4 show the comparison between temporal values of the measured and theoretically obtained temperatures, ground surface T_p , inside air T_{in} and cover T_c temperatures, for the PVC enclosure in winter. There was a satisfactory similarity between the measured temperatures in both experiments.

In comparison to summer experiment showed in Fig. 4, the air temperature T_{in} inside the enclosure during winter experiment was lower than 50°C and it has dramatically reduced through the day. This was due to three main reasons which are: the higher incidence angle, the lower measured outside ambient temperature (4.0°C) compared to summer (29.5°C) and higher the wind speed and outer convective heat loss.

Figure 5 shows the comparison of calculated air temperature inside enclosures for enclosures covered with different materials. Highest temperature T_{in} was observed for enclosure that was covered by the silica glass. On the other hand, LDPE has the lowest values of about 42.2°C and 74.2°C for winter and summer, respectively. This was due to the high absorptivity of PVC and glass to infrared radiation.

5. Concluding Remarks:

In the present study, a non-gray rigorous model was established to precisely estimate the radiative heat transfer into a greenhouse and differences in thermal performances between the LDPE, PVC and glass were examined.

Summer and winter experiments were conducted to measure greenhouse temperatures for different enclosures. A good agreement was found between the measured temperatures and the ones obtained by the rigorous model.

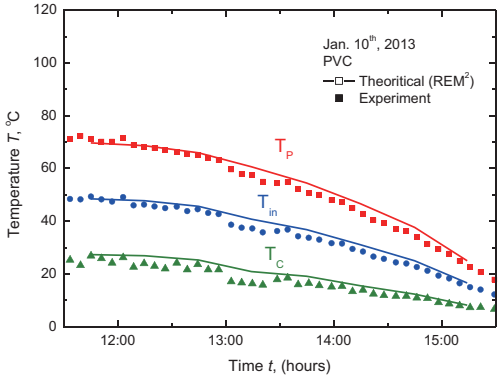

Fig. 3: Comparison between theoretical and experimental results in winter [3].

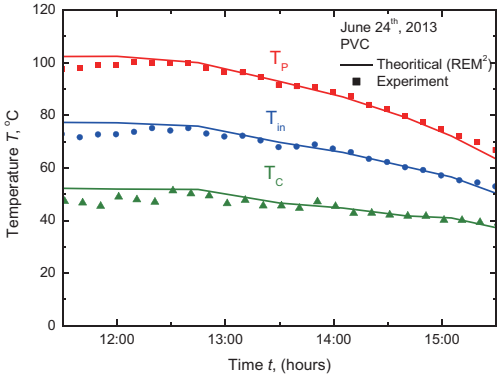

Fig. 4: Comparison between theoretical and experimental results in summer

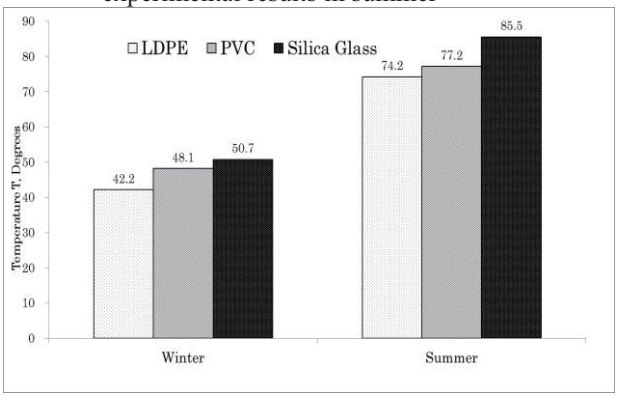

Fig. 5: Comparison in seasonal thermal performance of different GH covering materials.

References

[1] S. Maruyama, Light Energy Engineering, (2004), Yokendo , Tokyo

[2] A. Al-Mahdouri et al., Solar Energy, 96 (2013), pp.21-32

[3] A. Al-Mahdouri et al., *submitted* to Solar Energy.

Comparison of Seasonal Performance of the Combined Involute and Compound Parabolic Solar Concentrator in Single and Dual Forms

Abid Ustaoglu[1], Junnosuke Okajima[2],Xin-Rong(Ron.) Zhang[3], Shigenao Maruyama[2]
[1]Graduate School of Engineering, Tohoku University, Sendai, 980-8577, Japan
[2]Institute of Fluid Science, Tohoku University, Sendai, 980-8577, Japan
[3]Department of Energy and Resources Engineering, Peking University, Beijing 100871, China
E-mail:abid@pixy.ifs.tohoku.ac.jp

ABSTRACT

A combined involute and compound parabolic concentrator with enhanced thermal performance and no the convective heat loss by using an evacuated glass tube has been designed and its thermal and optical efficiencies investigated. Dual form of concentrator is evaluated by comparing with single for in terms of daily and seasonal performance. The performed results show that dual concentrator has significantly higher than single one. In summer, either concentrator can utilize the sun longer compare to winter day. Additionally, incident angle is very important parameter in terms of seasonal performance, so a little seasonal adjustment can prolong the utilization time from solar irradiance in winter.

1. Introduction

Compound parabolic concentrator (CPC) are of interest for design of non-tracking solar concentrators, because they can utilize diffuse and direct solar irradiation, and can approach the maximum possible concentration [1].

Many studies were conducted to improve the efficiency by changing the design of CPC. Rabl et al. [2] compared the modified concentrator designs, in which the tubular absorber surrounded by glass envelope. However, the heat loss significantly exceeds by using glass cover, because of permitting gaps between the reflector and absorber. Thus, some rays pass through the gap and reflect back to the ambient.

Some problems in solar collectors affect the performance. Efficiency decreases due to the heat losses and environmental factors. Other issues are additional expense for using of sun tracking system and some difficulties in the maintenance of solar systems because of inappropriate concentrator geometry.

In order to overcome these problems, a combined involute and compound parabolic reflector in an evacuated glass cover was designed [3]. To obtain higher solar ray acceptance, the ratio of the aperture area of reflector to diameter of glass cover should be increased. Therefore, a dual concentrator was proposed [4]. In the previous studies, the performances of these concentrators were evaluated with arbitrary sun altitude. However, the performance considering the daily or seasonal sun trajectory should be important. In this study the concentrator is compared to the dual concentrator for seasonal performance by assumption of infinite length absorber.

2. Geometry of proposed concentrator

The design of the concentrator is mainly based on the exploitation of the uniform distribution of temperature on absorber and approaching to highest possible concentrator by reflectors. These are achieved by using involute reflector with tubular absorber configuration and compound parabolic reflector. In order to eliminate the convective and conductive heat losses, the configuration is covered by an evacuated tube [3].

The cross section of single concentrator with the concentrator ratio of 2.51 is shown in Fig.1a [3]. In order to utilize as much as possible solar irradiance, the ratio of aperture area to glass cover diameter should be increased. Moreover, the ratio of height to width of concentrator should be close to 1 to obtain optimum size of reflector. In this respect, dual form of concentrator can be one of the best candidates because of its proper size (Fig. 1b) [4]. Although two combined reflectors were used in the dual concentrator, slightly oversizing of 28% occurred on the circumference of the glass cover.

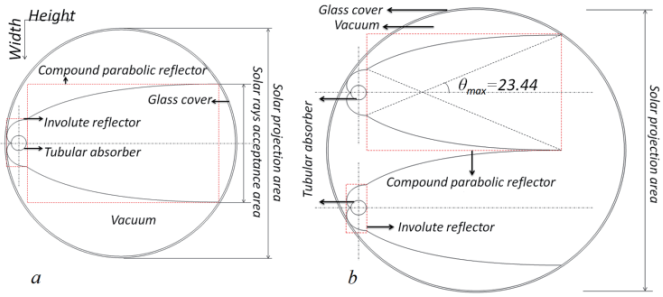

Fig. 1. Single (*a*) and dual (*b*) concentrator

3. Calculation method

The ray is traced numerically according to following cases. When the ray hits glass cover or reflector, intensity of ray is reduced depending on transmissivity or reflectivity, and then, the ray is traced again. When the ray hits absorber surface, all intensity of the ray is absorbed and the position of the hit point is memorized.

The concentrator was orientated with its long axis throughout east-west direction and its azimuth angle to aperture surface was zero. When the solar azimuth angle assumes to be zero, time indicates 12:00 p.m. Thus, the ray tracing can be calculated in two-dimensional geometry. However, incident angle changes both east-west and north-south direction in a day. In order to calculate daily and seasonal efficiency, three-dimensional ray-tracing is required. However, by assuming that the concentrator has infinite length, three dimensional effects can be included in two dimensional calculations.

In Fig. 2, the directional vector *r'* indicates the projection of vector *r* into the 2D surface. Incident angle

on 2D surface $\theta_{\text{inc,2D}}$ can be calculated by

$$(\theta_{inc})_{2D} = \arctan(\tan(\theta_{inc})_{3D} \sin\gamma_s) \quad (1)$$

where $(\theta_{inc})_{3D}$ and γ_s denote incident angle and solar azimuth angle, respectively. Additionally, solar radiation intensity is also modified in the projection from 3D to 2D. The corrected radiation intensity is expressed as,

$$q_s = I_{in} \cos\theta \quad (2)$$

By using Eq. (1) and (2), two-dimensional ray-tracing can include the three dimensional effect.

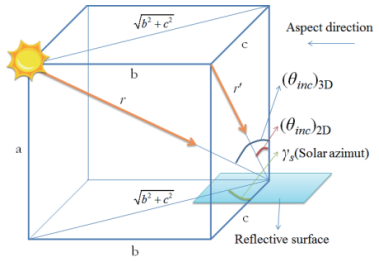

Fig. 2. Positional relationship between the concentrator and the sun with arbitrary azimuth angle

The intensity of solar irradiation I_{in} is assumed as 1000 W/m^2. The ambient temperature T_{amb} and the absorber temperature T_a were assumed to be 293 K, 373 K, respectively. Transmissivity of glass tube, solar absorptance of receiver and reflectivity of reflector were assumed to be 0.9, 0.95 and 0.9, respectively, and all which were independent from incidence angle. Tubular absorber was coated by selective coating with thermal emissivity of 0.07

.

4. Results

In order to compare the concentrators, thermal efficiencies were evaluated in different seasons. In Fig.3, hourly thermal efficiencies and incident angle in 2D surface were shown for a winter day (Feb 16) and a summer day (Aug 16). These days are selected in the last month of winter and summer season and are also characteristic days of the months [5].

Dual concentrator shows significantly better thermal performance compare to single one because of its higher ray acceptance. The either concentrators can generate heat between 10:00 and 14:00 for the day in winter. On the other side, in the summer day, concentrators can utilize the sun from 6:00 to 18:00. This difference in the operating time arises from the different day-time characteristic. In other words, the summer day is close to the longest day and the winter day close to the shortest day. Another reason is that when the concentrator can generate heat, incident angle of rays is within the maximum acceptance angle (23.44º), as it is shown in Fig. 3. Therefore, concentrator would operate with different period of time depends on incident angle in the winter and the summer days. The highest thermal efficiency is obtained around 12:00 in winter, because the solar intensity is highest at this time regarding to orientation of concentrator and incident angle. The incident angle is 12.9º. It is notably close to the incident angle in which the efficiency reaches highest value (12.7º) [3]. In the summer day, the concentrators would operate with better efficiency at 8:00 and 16:00, in that incident angle is approximately 14º. The best efficiency is obtained at 12:00 with the incident angle of 13º in the summer day because of the highest solar intensity and closer value of incident angle to 12.7º.

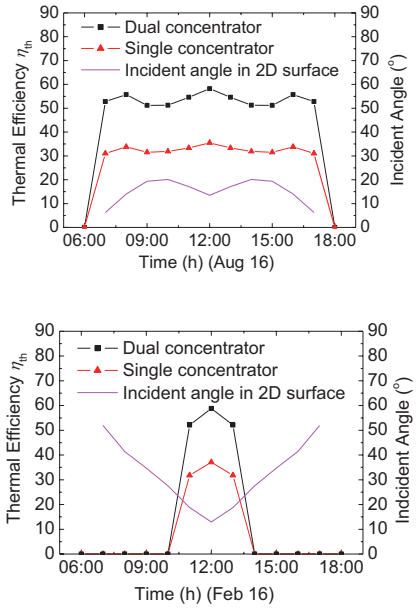

Fig. 3. Thermal efficiency for typical days of month

5. Conclusions

The proposed concentrator was evaluated seasonally in the cases of dual and single ones for the certain days in winter and summer. The analysis was conducted modifying 2D ray tracing model and it was implemented by assuming of infinite length absorber. Following results are obtained:

1. The performed results showed that the design of the dual concentrator leads to better thermal efficiency in seasonal performance because of higher ray acceptance.
2. In summer time, the concentrator can utilize the solar irradiance for longer time, as the best efficiency is at 8:00 and 16:00 for the certain days depending on incident angle.
3. Incident angle is very important parameter in terms of performance of concentrator. A little seasonal adjustment is needed in orientation of concentrator for longer solar energy utilization

References

[1] D. Suresh, J. O'Gallagher, R. Winston, Sol. Energy, **44-5**, (1990), 257-270.

[2]A. Rabl, N.B. Goodman, R. Winston, Sol. Energy, **22**(1978), 373-381.

[3] A. Ustaoglu, J. Okajima, X. Zhang, S. Maruyama, Proc. 9th Int. Con. Flow Dynamics, (2012), pp580-581.

[4] A. Ustaoglu, J. Okajima, X. Zhang, S. Maruyama, 7th Int. Symp. Rad. Trans. Book of Abstracts, RAD-13, (2013), pp67-69,

[5] J.R. Howell, R.B. Bannerot, G.C. Vliet,. Sol-Th. Energ. Syst. Analy. Design, McGraw-hill, (1982), pp63.

OS8: International Symposium on Smart Materials and Structures for Energy Saving

Tenth International Conference on Flow Dynamics
November 25-27, 2013, Sendai, Miyagi, Japan

Smart Microdevices Based on Ferromagnetic Shape Memory Alloys

Manfred Kohl[1], Marcel Gueltig[1], Makoto Ohtsuka[2], Hiroyuki Miki[2], and Ruizhi Yin[1]
[1]Karlsruhe Institute of Technology, IMT, P.O. Box 3640, 76021 Karlsruhe, Germany
[2]Tohoku University, IMRAM, Sendai 980-8577, Japan
E-mail of corresponding author: manfred.kohl@kit.edu

ABSTRACT

This paper presents recent developments of ferromagnetic shape memory (FSMA) microdevices for actuation, sensing and energy harvesting. The layout, fabrication and performance of first demonstrators are discussed. Examples include an optical FSMA microscanner for object detection, a thermal FSMA microgenerator and a vibrational FSMA energy harvesting device allowing for broadband non-resonant operation.

1. Introduction

Novel miniature actuation and energy harvesting devices are currently being developed in order to meet the requirements of low energy consumption in future mobile, wearable and implantable systems [1,2]. A promising approach is the combination of smart materials and microtechnologies (smart MEMS). Smart materials, such as ferromagnetic shape memory alloys (FSMAs), show multiple coupling effects of their physical properties. Due to diffusion-less first order phase transformation they exhibit large abrupt changes of strain and magnetization [3]. The introduction of smart materials in MEMS has been a major challenge due to incompatibilities of standard MEMS technologies and the fabrication technologies of FSMA films requiring thermo-mechanical treatment at high temperature. In recent years, these barriers have been overcome by establishing novel micromachining and transfer bonding processes on the wafer scale [4].

In the following, selected examples of FSMA microdevices will be presented to highlight recent achievements and to demonstrate the application potential of smart MEMS.

2. Bi-directional FSMA film actuation

Bi-directional microactuators make use of thermo-elastic and thermomagnetic coupling [5]. As sketched in Fig. 1, a Ni-Mn-Ga cantilever is mounted on a substrate having a freely movable end. A permanent magnet is placed above the cantilever. A double-beam design of the cantilever allows applying an electrical current for direct Joule heating. At low current, the cantilever is in martensitic and ferromagnetic state. Thus, the magneto-static attraction force dominates and causes an out-of-plane motion of the cantilever towards the magnet. Above a critical current, both, the martensite-austenite reverse transformation and the ferromagnetic transition are induced. The magnetic attraction force strongly decreases, while at the same time the shape recovery force occurs. Therefore, the cantilever bends in opposite direction.

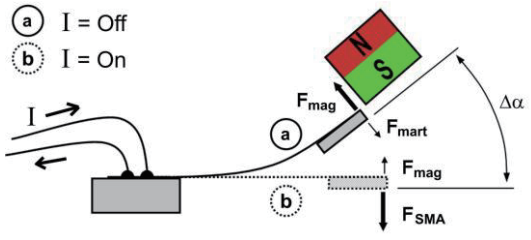

Fig. 1 Operation principle of the FSMA microactuator. Legend: N,S - north and south pole of a permanent magnet; F_{mag} - magnetic force, F_{SMA} - shape recovery force, F_{mart} - force in martensitic condition, Δα - mechanical scanning angle

3. Optical microscanning

The bi-directional actuation can be used to generate an oscillatory motion. The corresponding actuation stroke can be very large as only one of the counteracting forces is active at a given time. In addition, rapid cooling is possible due to heat conduction and forced convection during oscillatory motion.

This actuation mechanism has been implemented in optical microscanners for sensing of unknown environments, see Fig. 2 [6]. Fabrication of the device comprises Ni-Mn-Ga film deposition and optical lithography. The chemical composition of the Ni-Mn-Ga film is adjusted to show the martensitic phase transformation close to the ferromagnetic transition temperature, which is about 90 °C in the present example. Due to the non-resonant nature of actuation, scanning frequencies can be tuned in a wide range up to the thermal cut-off frequency. Applications are, e.g., in monitoring systems, in portable and mobile systems including object detection and driving assistance.

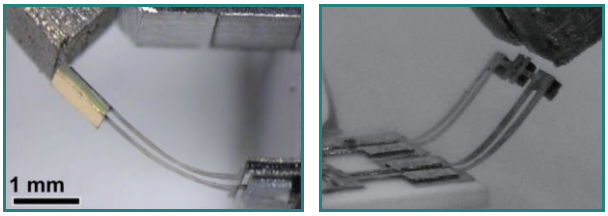

Fig. 2 Demonstrators of 1D (left) and 2D (right) FSMA microscanners [6]

4. Thermal energy harvesting

Based on bidirectional actuation of a FSMA cantilever, a new principle of harvesting thermal energy has been developed [7]. Fig. 3a shows a schematic layout of a demonstrator consisting of a beam cantilever, a miniature heat source, a permanent magnet and a pick-up coil. At

the end of the cantilever, a FSMA tip is attached to tune the mechanical and thermal mass. In this case, reverse martensitic transformation and ferromagnetic transition are induced by an external heat source. A pick-up coil is used to convert the momentum-induced and temperature-dependent changes of magnetization of the magnetic tip during actuator motion into electrical power. Typical time-resolved deflection signals are shown in Fig. 3b. The periods of zero deflection of about 100 ms occur, while the cantilever is in contact to the heater. After heating to the paramagnetic and austenitic state, a strong oscillation occurs for about 400 ms.

Even though periodic heating and cooling occurs at a frequency of about 2 Hz, the cantilever operates close to the eigenfrequency of about 90 Hz. This frequency up-conversion effect and the large oscillation amplitudes are very beneficial for energy harvesting. Due to the large temperature-dependent change of magnetization, this harvesting principle is particularly suitable for exploiting small temperature changes in the order of 10 K. Similar performance is achieved for heater temperatures between 110 and 150 °C. So far, maximum achieved power densities are in the order of 1 μW/cm^3.

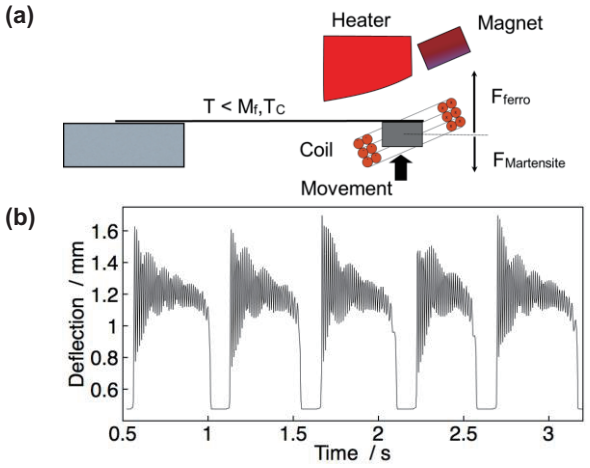

Fig. 3a Operation principle of thermal energy harvesting. 3b Time-dependent deflection of cantilever tip for a heater temperature of 130° C [7].

5. Vibration energy harvesting

Ferromagnetic shape memory alloys also offer mechano-magnetical coupling through the inverse magnetic shape memory effect. Starting material is a Ni-Mn-Ga single crystal of 0.3x2x2 mm³ size that is cut along the (100) direction. At room temperature, the material is martensitic showing a tetragonal crystal structure. Due to magnetic anisotropy, magnetic moments preferentially align along the short c-axis. As sketched in Fig. 4a, uniaxial compressive loading causes the formation of a single variant martensitic state with the magnetic easy axis being aligned along the compression direction. In the presence of a biasing magnetic field B_1 applied in perpendicular direction, unloading results in reorientation of the martensite variants as the magnetic moments preferentially align along the field direction. The corresponding change in orientation of magnetic moments is used in a magnetic circuit to generate a change of magnetic flux and, thus, to generate a voltage in a pick-up coil [8].

Fig. 4b shows experimental characteristics of induced voltage versus time. Optimum performance occurs at a biasing magnetic field of 0.4 T, which is not corrected for demagnetization. When applying periodic mechanical impulses of 4 ms duration, the maximum induced voltage is 120 mV. For a vibration frequency of 50 Hz, the average power density generated by the energy harvesting device is determined to be about 2.5 mWcm^{-3}.

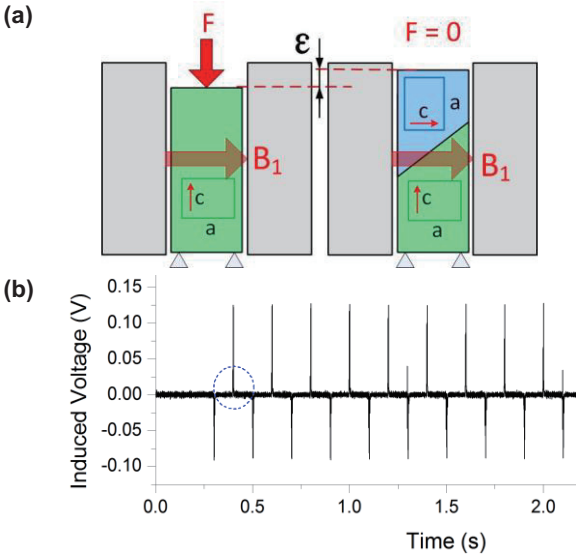

Fig. 4a Operation principle of vibration energy harvesting. 4b Time dependence of induced voltage for a pick-up coil of 2000 turns [8].

6. Conclusions

The multiple coupling effects inherent to FSMA materials are highly beneficial to develop compact multifunctional devices. The large changes of strain and magnetization open up a large application potential in actuation, sensing and energy harvesting.

References

[1] R. Vullers, R. Schaijk, H. Visser, J. Penders, and C. Hoof, IEEE Solid-State Circuits Mag. **2** (2010) 29.

[2] X. Zhang, et al., IEEE Trans. Biomed. Circuits Syst. **4** (2010) 11-18.

[3] A. Planes, L. Manosa and M. Acet, Topical review, J. Phys.: Condens. Matter **21** (2009) 233201 (29pp).

[4] T. Grund, R. Guerre, M. Despont and M. Kohl, Eur. Phys. J. Special Topics **158** (2008) 237-242.

[5] M. Kohl, D. Brugger, M. Ohtsuka and T. Takagi, Sensors and Actuators **114**/2-3 (2004) 445-450.

[6] D. Brugger, M. Kohl, U. Hollenbach, A. Kapp and C. Stiller, Int. J. of Appl. Electromagnetics and Mechanics **23** (2006) 107-112.

[7] M. Gueltig, B. Haefner, M. Ohtsuka, and M. Kohl, Proc Transducers'13, Barcelona, Spain (2013) 2803-2806.

[8] M. Kohl, R. Yin, V. Pinneker, Y. Ezer and A. Sozinov, Mat. Sci. Forum **738-739** (2013) 411-415.

Fatigue Monitoring Of CFRP In The VHCF Regime

Gerd Dobmann and Christian Boller Fraunhofer-IZFP, Campus E 3 1, Saarbruecken, Germany
Dietmar Eifler, WKK, Technical University, Kaiserserslautern; Germany
Gerd.dobmann@izfp.fraunhofer.de

ABSTRACT

Linear and nonlinear ultrasonic methods are convenient covering materials characterization, defect and damage detection, monitoring and evaluation of ageing phenomena (fatigue) and failure prediction. In order to investigate fatigue of CFRP in the VHCF regime under 10^8 cycles or more, in a collaborative project with the Institute of Materials Science and Engineering (WKK), University of Kaiserslautern, Germany, a three point bending ultrasonic fatigue testing system combined with online process monitoring was developed.

1. Introduction

In industrial applications, lightweight materials as carbon fiber reinforced plastics (CFRP) become more and more important entailing the request for nondestructive testing (NDT) techniques for quality assurance of CFRP components during production and in service.

2. Testing Environment

The three point bending ultrasonic fatigue testing system of WKK combined with online process monitoring operates at a frequency of 20 kHz and is simultaneously used as input for ultrasonic monitoring techniques [1].

As so far with existing commercial fatigue systems the VHCF regime (Very High Cycle Fatigue, 10^8 load cycles and more) in realistic testing times cannot be investigated (Fig. 1) WKK has developed an ultrasonic-based 3-point bending system shown in detail in Fig. 2.

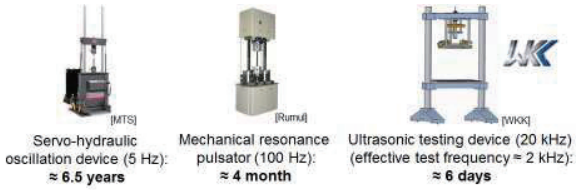

Fig. 1 Testing times in the VHCF regime for 10^9 cycles with commercially available fatigue systems and the new system of the Technical University, Kaiserslautern, WKK

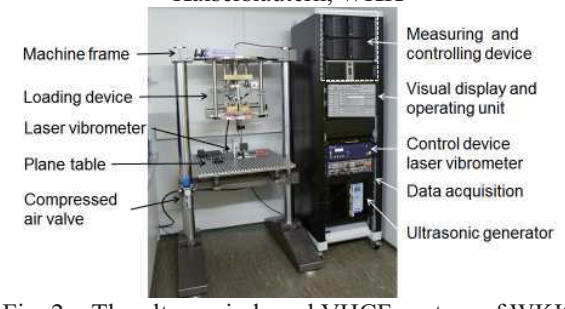

Fig. 2 The ultrasonic-based VHCF-system of WKK

In order to monitor and control the fatigue process the heat development in the fatigue specimens has to be measured which is performed by an infrared camera. As the specimens should not be damaged by the temperature cycles, temperature rise is observed and limited by stopping the cycling process, i.e. limiting the pulse length of the ultrasound (Fig. 3).

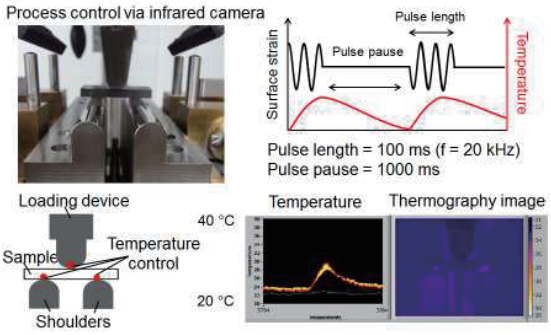

Fig. 3 Ultrasonic setup

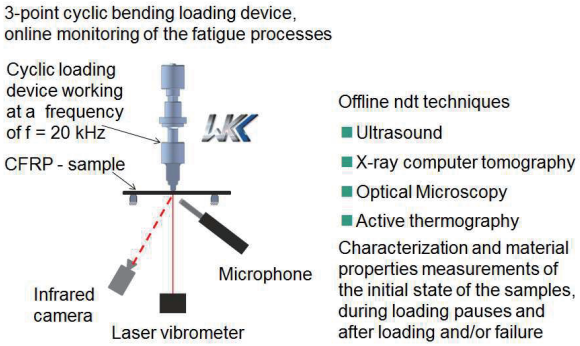

Fig. 4 Online monitoring of the ultrasonic fatigue process

Vibrations of small CFRP plates and their sound irradiation into the air during cyclic loading are recorded due to both, by a laser vibrometer and a microphone, respectively (Fig. 4). The time signals are evaluated by signal processing procedures [2].

Furthermore, the samples are characterized offline by ultrasonic NDT techniques, X-ray-Computer Tomography, optical microscopy, and active thermography in their pristine state, during loading pauses along the fatigue process, and after failure. Changes in the vibration signals and in the material properties with progressive ageing are discussed. For this purpose, linear and nonlinear ultrasonic methods are convenient covering materials characterization, defect and damage detection, monitoring and evaluation of ageing phenomena (fatigue) and failure prediction.

3. Materials

The material under investigation is Tepex® dynalite 207-C22/50 % (CS-PPS), Bond Laminates with orthotropic fiber fabric layout (200g/m^3), Polyphenylensulfide (PPS) matrix, a thermoplast with density of ρ_{PPS} = 1.35 g/cm^3. Glass transition and melting temperature are: Tg = 90°C, TM = 285°C. The advantage of the material is its accordance to a commercial standard which guarantees a restricted scatter in the properties of the "as delivered" material.

4. Monitoring results

Fig. 5 documents the time signals obtained by the Laser Vibrometer and the air-coupled microphone, the process steps, pulse start, constant amplitude fatiguing, active damping due to temperature control, and dying amplitude can be clearly separated. By applying a stepwise time-resolved FFT (Fig. 6) higher harmonics of the fundamental exciting frequency are observed and the increase of the nonlinearity can be documented by calculating a distortion factor K [%] (Fig. 7).

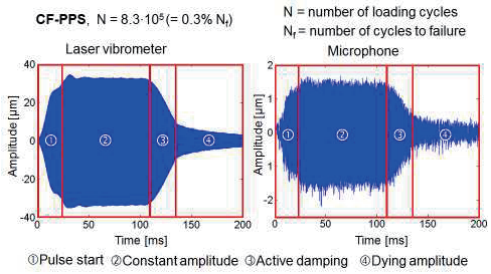

Fig.5 Sample vibration and radiation time signals during ultrasonic fatigue

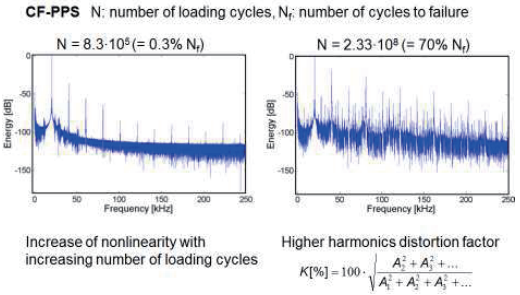

Fig. 6. Fast Fourier Transform of Laser vibrometer time signals

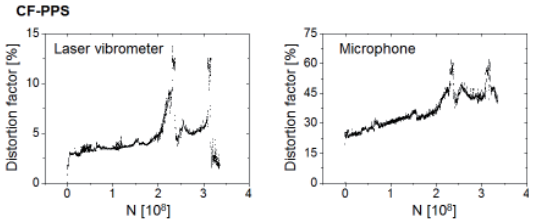

Fig. 7 Distortion factor K[%] versus the number of cycles N[10^8]

One can detect:

- a moderate increase of the distortion factor K with increasing number of cycles in the beginning
- then a strong increase followed by a step-like decrease
- a higher nonlinearity (K-values) in the microphone signal compared with the vibrometer information.

According to the state of progress in the project one can state the reproducibility of these results. However, the reason of the signal behavior is to clarify in the next steps. A hypothesis is:

- crack generation and clapping of kissing bonds in the 1st fatigue phase
- irreversible opening of delamination in the 2nd phase.

In Fig. 8 one example to NDT is shown applying ultrasonic testing in water immersion technique by using compression waves (5MHz B- and C-scan, A/D-conversion with 50 MS/s) comparing the material macrostructure at the beginning (virgin state, cycle number N = 0) with the state after failure (N = 3.3×10^8, N_f number of cycles to failure , N/N_f = 1).

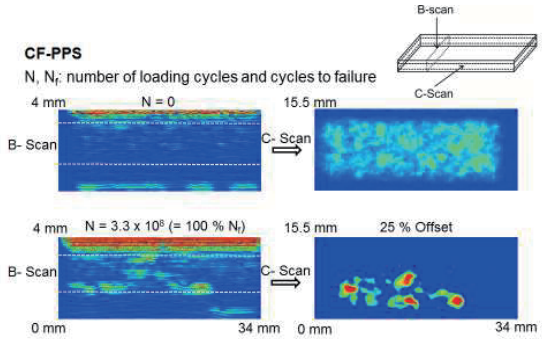

Fig.8 Fiber-matrix structure, delaminations

The delamination is clearly detected and this result is confirmed by optical microscopy.

5. Conclusions

Online monitoring of the fatigue process in the VHCF regime is reliable by:

- temperature measurement for process monitoring and control
- ultrasonic energy and signal pick-up from the specimen online by use of Laser vibrometer and an air-coupled microphone

6. Acknowledgements

The authors very much acknowledge the collaboration in their project teams. The work of S. Hirsekorn, T.B. Helfen, M. Weikert, U. Rabe, D. Backe, and F. Balle is to indicate and to be pointed out.

The financial support from the German Science Foundation (DFG) within the Priority Program 1466: Life∞ is acknowledged.

References

[1] D. Backe et al., The Minerals, Metals & Materials Society (2012), pp 855-863.

[2] U. Rabe et al., 2012, http://asadl.org/poma/resource/1/pmarcw

Tenth International Conference on Flow Dynamics
November 25-27, 2013, Sendai, Miyagi, Japan

Quantitative Detection of Fatigue Damage in Holed Composite Laminates using an Embedded FBG Sensor

Tomonaga OKABE[1], Shigeki Yashiro[2]
1. Department of Aerospace engineering, Tohoku University
2. Department of Mechanical Engineering, Shizuoka University
okabe@plum.mech.tohoku.ac.jp

ABSTRACT

This paper introduces our recent approach of damage detection in CFRP laminate using an embedded fiber Bragg grating (FBG) sensor (T. Okabe, S. Yashiro, Composites Part A, (2012), 388). In order to detect the damage extension in the CFRP laminate, the change in the spectrum shape was measured using an embedded FBG sensor and was compared with that obtained by numerical simulation. The shape of the reflection spectrum did not change during the cyclic loading test; but, it did change with increased strain in the static loading test, due to damage around the hole.

1. Introduction

CFRPs are frequently applied in structural components because of their mechanical properties. Mechanical damage is generally generated around the stress-concentration region in composite components due to static or cyclic loading. Thus, it is essential to monitor the damage extension to ensure structural safety.

This paper introduces our recent quantitative approach for the detection of static and fatigue damage extension in holed CFRP laminates using embedded FBG sensors and describes the limitation or controversial point [1]. First, static load tests were conducted for a holed CFRP cross-ply laminate with an embedded FBG sensor. Second, the cyclic load tests were conducted. The damage pattern near the hole and the reflection spectrum of the FBG sensor were then observed in detail. We found that debonding of the optical fiber increased as the number of cycles of cyclic loading increased. This may limit the monitoring period in the application of the FBG sensor to the health monitoring of composite structures.

2. Experiments

In this study, CFRP T700S/#2521R (Toray Industries, Inc.) cross-ply laminates were used as specimens, and their stacking sequence was [02/902]s. Each specimen was 240mm long and 30mm wide (Fig. 1). A hole was made at the center of the specimen. The diameter of the hole is 5mm. The hole was made using a drilling machine with the specimen pressed between clear plastic plates. Each layer was 0.1mm thick. To detect damage near the hole, an optical fiber with an apodized FBG sensor (Broptics Technology, Inc.), which had a 12.5mm-long gauge section, was embedded into the 0° ply near the 90° ply. The surface of the optical fiber was coated with polyimide resin with a coating diameter of 150μm. The gauge section was set near the hole, with one end positioned closest to the hole's edge. Before drilling the hole, we observed the position of the FBG sensor using soft X-ray and marked a drilling point to make a hole at the correct position. The distance between the hole and FBG sensors is about 1.5 mm. GFRP tabs were attached to both ends of the specimen in order to avoid grip failure.

Quasi-static tensile tests were conducted by an electrohydraulic testing system (INSTRON 8800, Instron Corp.) at a cross-head speed of 0.25mm/min. Tensile strain was obtained by a strain gauge attached away from the hole. The tensile load was measured simultaneously using a load cell. For the specimen with an FBG sensor, the optical fiber was illuminated by a broadband light source (AQ4315A, Ando Electric), and the spectrum of the light reflected from the gauge section was measured by an optical spectrum analyzer (AQ6319, Ando Electric). Figure 2 presents the observed X-ray photographs of damage states in the specimen at applied strain 0.8% with the simulated results proposed in Ref. 2. As indicated in previous studies [2], three main types of damage are visible in those photos: splits in 0° plies, transverse cracks in 90° plies, and delamination at the 0°/90° interfaces. As the load increased, the damage was extended (Fig. 2).

The initial full-width at half-maximum was 0.24nm before the FBG sensor was embedded into the specimen, and it became slightly broader after embedding. This broad spectrum might represent the birefringence effect due to thermal residual strain. Figure 3 illustrates the measured spectra of the light reflected from the FBG sensor embedded near the hole in the tensile test with the simulated results proposed in Ref. 2. The spectrum shape was broad due to the damage state. It changed drastically when splits and delamination appeared near the sensor section. The FBG sensor broke when the applied strain exceeded 0.9%.

Cyclic load tests were also conducted by the same testing system with a maximum stress of 260MPa, a stress ratio of 0.1, and a cyclic frequency of 5Hz. The strain at the maximum stress (0.4%) was much lower than the maximum strain (0.9%) used in the static load tests. The test was stopped after a given number of cycles. After the tests, damage near the hole was observed with soft X-ray radiography.

Figure 4 depicts the damage patterns observed in the cyclic load test with the simulated results proposed in our previous work [3]. Splits in 0° ply, transverse cracks in 90° ply, and delamination were observed in the soft X-ray photographs. With fewer cycles, short splits and transverse cracks were generated near the hole. The splits extended in the fiber direction, and the number of

transverse cracks increased with an increasing number of cycles. The transverse cracks propagated in the width direction due to cyclic loading, and finally reached the edge of the specimen. After both transverse cracks and splits grew sufficiently near the hole, delamination was generated in the 1/4 ellipse shape (Fig. 4).

Next, the reflection spectrum of the FBG sensor was measured at mean stress in Fig. 5. The spectrum shape barely changed during the test, although damage was generated. This result was quite different from the spectrum change observed under static loading. After the tests, the interface between the optical fiber and the composites was observed using an optical microscope (Fig. 6). Debonding, which was not observed in the static load test, propagated along the interface. Therefore, it can be concluded that debonding is the reason for the spectrum's insensitivity to damage near the hole. As illustrated in Fig. 7, the debonding connects with the delamination between the 0/90 interface. Thus, the driving force of the debonding is expected to be the delamination between the 0/90 interface. Therefore, we expect that the debonding growth is related to the splits through the delamination. The strain level of the cyclic load test was lower than that of the static load test; thus, debonding gradually increased as the number of cycles increased. One of reasons for the debondings may be the quality of the coatings. The coatings of FBG sensors used in this study were apparently not uniform. Their diameters varied within a range of 20μm.

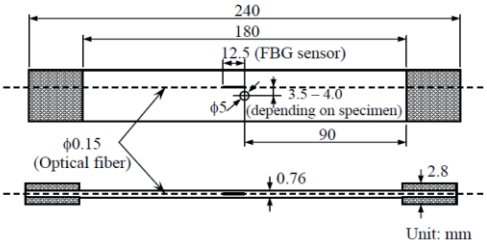

Fig. 1 Schematic figure of test specimens [1]

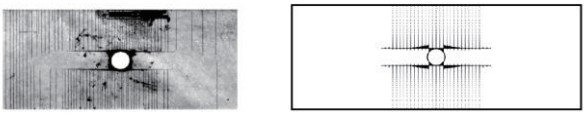

Fig. 2 Soft X-image and simulated results [1]

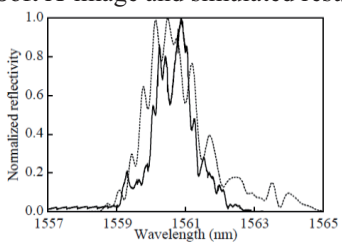

Fig. 3 Measured (broken) and simulated (solid) spectrum under the static test [1]

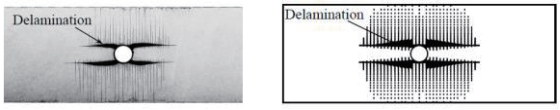

Fig. 4 Soft X-image and simulated results [1]

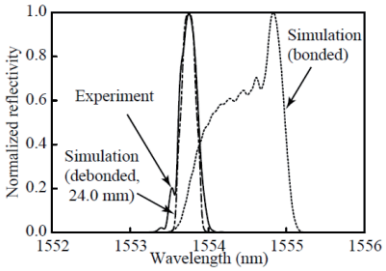

Fig. 5 Measured (broken) and simulated (solid) spectrum under the cyclic loading [1]

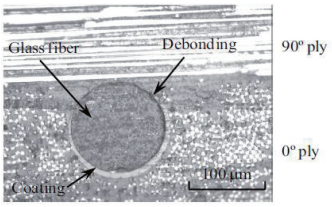

Fig. 6 Photograph of cross section of optical fiber [1]

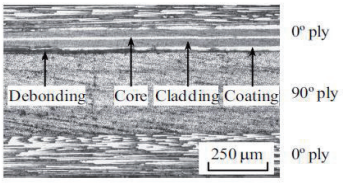

Fig. 7 Photograph of cross section parallel to optical fiber [1]

3. Concluding remarks

This study introduce our recent detection approach of static and fatigue damage extension in holed CFRP laminates by using embedded FBG sensors [1]. Static and cyclic load tests were conducted for a holed CFRP cross-ply laminate into which an FBG sensor was embedded. The shape of the reflection spectrum did not change during the cyclic load test; however, it did change with increased strain in the static load test, due to damage around the hole. To clarify this difference, the polished surface of the cross section of the specimen was analyzed, and debonding between the optical fiber and matrix, which occurred during the cyclic load test, was observed. These results lead us to conclude that fatigue damage around a hole in a composite laminate may not be detected with an FBG sensor, even if it can be detected at a higher strain in a static loading test.

References

[1] T. Okabe, S. Yashiro, Composites Part A,(2012), 388
[2] S. Yashiro, N. Takeda, T. Okabe, H. Sekine, Compos. Sci. Technol. (2005), 659
[3] T. Okabe, S. Yashiro, J. Solid Mech. Mater. Eng. (2009), 1202.

Tenth International Conference on Flow Dynamics
November 25-27, 2013, Sendai, Miyagi, Japan

Generic Elastic and Elasto Plastic Macroscopic Properties of a Closed Cell Polymer Foam

Alain Combescure, Carine Barbier, Dominique Baillis
LaMCoS UMR CNRS 5259 Insa Lyon Université de Lyon 69621 Villeurbanne Cedex (France).
alain.combescure@insa-lyon.fr.

ABSTRACT

This paper is devoted to the proposition of an homogenized material property which gives the macroscopic properties taking into account the relative density, the disorder parameter as well as a normalized yield strain of the base material.

1. Introduction

The design of the architecture of a material like a closed cell polymer foam which has "good" macroscopic non-linear properties remains a heavy and costly procedure because one has to do a large experimental testing program to try to find an appropriate architecture (call shapes and geometries). The aim of this presentation is first to present a virtual design method to assess the macroscopic properties from a choice of geometry of the microstructure and the known non-linear properties of the bulk material. The method consists to build a non-linear finite element model containing a sufficient number of elementary cells, to compute the nonlinear response of this model and to deduce the macroscopic properties from the simulated results. This virtual design method permits to do a systematic analysis of the influence on the predicted macroscopic properties of bulk material properties as well as choice of geometries. Hence one can understand better how does such an architecture responds to the loadings. Once a set of "good" architectures has been found by this virtual prototyping, these geometries can be fabricated, tested and checked with the virtual design: this leads to a more efficient and robust material architecture design. In a second stage this method gives access to the choice of the appropriate macroscopic non-linear model which avoids the detailed micro scale computations and hence opens the possibility to use these materials to perform real 3D structural response computations.

2. The model studied

The method followed here consists to mesh a sufficient number of foam cells with different geometries. The cell geometries are fabricated using a specific program which builds a Voronoi 3D tessellation of the elementary volume [1]. The basic cells are polyhedral with flat faces which may have hexagonal pentagonal or quadrilateral faces. The structure can be repetitive and regular or may be distorted. The distortion (or disorder) is quantified by a parameter denoted α, which is 0 for regular ones. Let us denote Δ the typical size of a foam bubble. The representative volume element (RVE) is meshed with S3R shell element (with 5 points across the thickness to catch the plastic bending effects) and computation done with ABAQUS 6.9 finite element code used in explicit with mass scaling option to be able to easily compute complex post buckling of the compressed faces. A typical mesh has about 100000 elements. Each face of the foam cell is meshed with about 100 elements. This choice allows a good representation of bending and buckling of the faces. The computational results with periodicity conditions have been shown independent of the discretization if the size of the computed specimen is larger than 6Δ. A typical mesh is displayed in figure 1 for 2 different values of α.

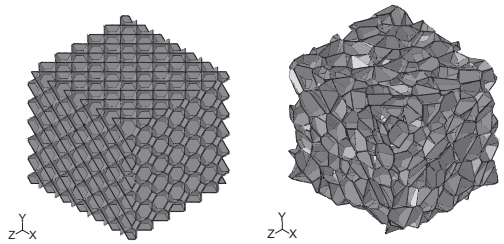

Fig. 1 Meshes of two cases α=0 (left regular material) α =2 (right: most disordered cells)

The material is law is perfect plasticity. It is hence characterized by its Young's modulus and its yield strain. This paper is devoted to the study of a polymer material.

The specimens are submitted either to axial traction or compression or to shear. The global stress strain law is searched for each load case and a general homogenized behavior is searched. The global results are analyzed using the "observations" of the computation at micro scale.

3. Results and Discussion

The main results are the following:

1) this type of material is elastically isotropic.
2) the homogenized Young's modulus is the same for any loading. It is proportional to the homogenized density and does not depend of disorder parameter α
3) The compression and traction macroscopic yield stress are different and the compressive one strongly depends on the disorder parameter α. This is not very surprising because the non linear behavior results from the plastic buckling of the cells which is very different in macroscopic tensile and compression mode. The tensile proportional Yield stress does not depend

on the disorder and is also proportional to the homogenized density and to the bulk Yield stress. The compressive Yield stress is also proportional to the bulk yield stress but it depends of the disorder and of the relative density. A polynomial fit will be presented.

4) The macroscopic elastoplastic model has to include first and second invariant of stress: it is of the Drucker-Prager family.

4. Concluding remarks

The work will be completed by the proposition of a model for unloading for impact loads.

References

[1] J. Radrianalisoa, R. Coqaurd, D. Baillis, J of Porous media, 2013 in press

[2] O. Cathy, E. Maire, S. Youssef, R. Bouchet, Acta materiala, **50** (2008), pp 5524-5534

[3] L. Gibson, M. Ashby, Cellular Solids, Structure and properties, (1997) Cambridge university press.

Tenth International Conference on Flow Dynamics
November 25-27, 2013, Sendai, Miyagi, Japan

Structural Health Monitoring and Non-Destructive Evaluation

Jinhao Qiu, Chao Zhang, Jun Cheng, Hongli Ji
State Key Lab. of Mechanics and Control for Mechanical Structures, Nanjing Univ. of Aeronautics & Astronautics
#29 Yudao Street, Nanjing, Jiangsu 210016, China
E-mail: qiu@nuaa.edu.cn

ABSTRACT

Structural health monitoring is an important function of smart structure and an important technology for future aerospace structures. In this article, some research activities in structural health monitoring and non-destructive evaluation at NUAA, including impact and damage localization using piezoelectric fibers with metal core, identification of multi-site damages on a composite structure using guided wave, identification of damage using laser ultrasonic technology, and non-destructive testing method of composite structure based on eddy current, are introduced.

1. Introduction

The supporting technologies of smart structures include sensor, actuator, signal processing, control theory and system integration, etc. and the functions of smart structures include structural health monitoring, vibration and noise suppression, morphing and flow control, etc. Structural health monitoring is an important function of smart structure and an important technology for aerospace structures. In this article, some research activities in structural health monitoring and non-destructive evaluation at NUAA, including impact and damage localization using metal-core piezoelectric fibers (MPF), identification of multi-site damages on a composite structure using guided wave, identification of damage using laser ultrasonic technology, and non-destructive testing method of composite structure based on eddy current, are introduced.

2. Identification of damage based on MPF

Metal-core piezoelectric fibers (MPF) are the piezo-electric ceramic fibers of 250-400 μm in diameter with a metal core of 50 μm in diameter at the center [1]. Since the response of MPFs is mainly affected by the strain in the axial direction, their sensitivity is highly directional. They are most sensitive to the elastic waves propagating in the length direction, and theoretically they do not respond to the waves propagating in the direction perpendicular to the fiber. If the sensitivity of a fiber to the strain of elastic wave is P, the amplitude of the output voltage can expressed as:

$$\overline{V} = P\overline{S} \tag{1}$$

where $\overline{S}$ is amplitude of strain. The sensitivity factor P for antisymmetric Lamb waves is:

$$P = \frac{2M\cos\theta}{l\xi}\sin(\frac{l\xi}{2}\cos\theta) \approx M\cos^2\theta \tag{2}$$

where M is an constant. As shown in Eq. (2), the sensitivity is a function of θ, which is the angle between length direction of the fiber and the direction of wave propagation.

Based on Eq. (2), MPF rosettes as shown in the left low corner of Figure 1 were proposed. Using the same principle as that used in the strain rosette, the MPF rosette can be used to determine the principal direction of dynamic strain induced by Lamb wave. Hence, impact localization can be realized by using two MPF rosettes.

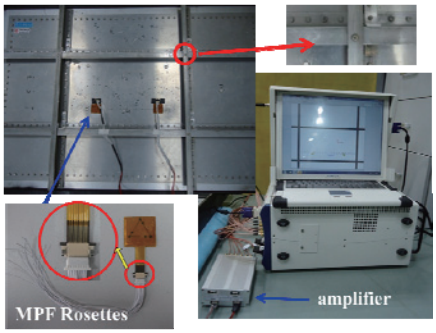

Fig. 1 Experimental setup based on MPF

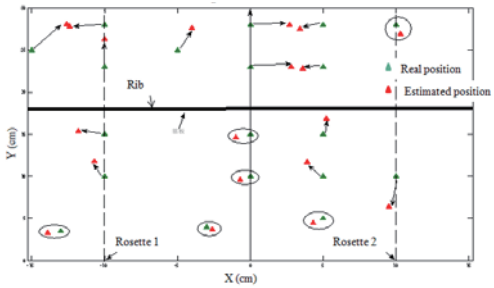

Fig. 2 Results of impact localization

Figure 1 shows the experimental setup for impact localization of a stiffened panel based on MPF rosettes. Figure 2 shows the result of the location tests. Relatively high precision of localization was achieved when the impacts were applied in the same area as the rosettes were bonded. When the impacts were applied in the area beyond a rib, the precision deteriorated, but they were still acceptable for engineering purposes.

3. Multi-damage identification in CFRP structure

In the following section, multi-site damage detection in CFRP stiffened panel is the main focus in the research. Taking the attenuation property of Lamb wave in the specific material as well as the geometric shape of the CFPR stiffened panel into consideration, PZT sensors are aligned to divide the monitoring area into several subareas. Figure 3 shows the experiment set-up.

Then, each subarea is detected in turn by the rectangle sensor array to obtain the damage information

including damage degree and local damage image. Artificial damages which have the same effect as actual damages on scattering the propagation of Lamb wave are introduced to save cost. To identify the damage occurrence in the specific subarea, a damage degree is defined which is proved to be quite valid in the detection process. Damages are located using the proposed optimized delay-and-sum algorithm with the information provided by the scattering signals.

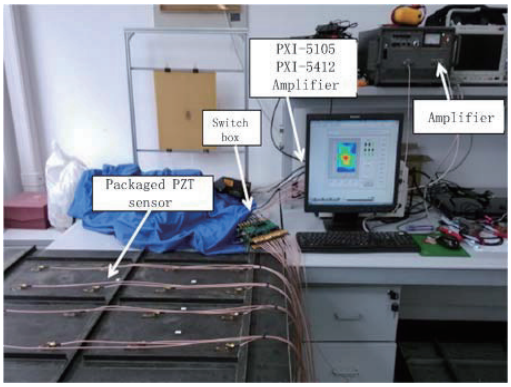

Fig.3 Experiment set-up

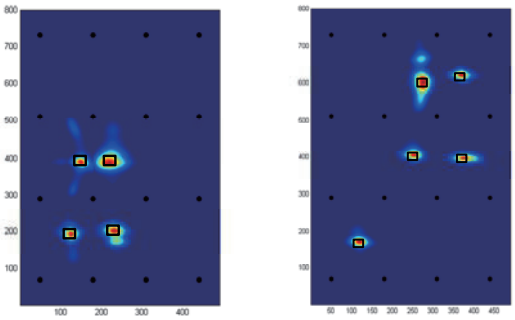

Fig.4 Multi-site damage results in two situations

Afterwards, the damage images of the whole monitoring area are pieced together which comes with the final result. Two specific damage situations are shown in Fig.4, where the symbol "□" represents the actual damage position.

4. Laser ultrasonic technique in anomalous guided wave imaging

Laser ultrasonic system is shown in Fig.5. The wavelength of laser is 532 nm. And the galvano-motorized LMS is used to deflect laser pulses toward a target structure. The pitch of the scanning grid is constant in both directions of the V- and H-axes, in this paper, it is 2mm.

Figure 6 is the wave field images of 40 us. The damage locates in (170, 50). Although the scattered wave due to the interaction of the propagating wave with the damage is not clear, they can still be detected. In order to separate damage-reflected wave, the method based on frequency-wavenumber domain filtering is used to suppress the incident wave and Fig.7(a) is the result corresponding to Fig.6. However, since the inspection error cannot be avoided, the wave in the frequency- wavenumber domain cannot be completely understood which brings in imperfect result.

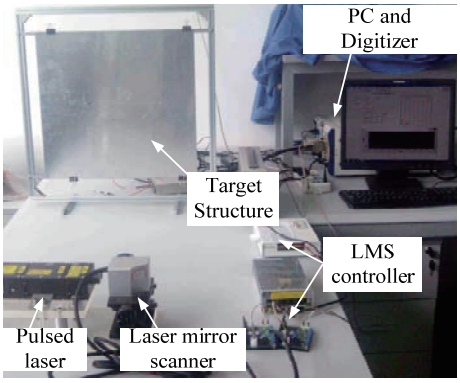

Fig.5 Experiment set-up of Laser ultrasonic system

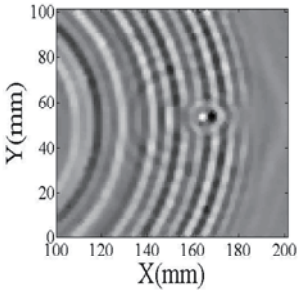

Fig.6 Wave field images of 40us

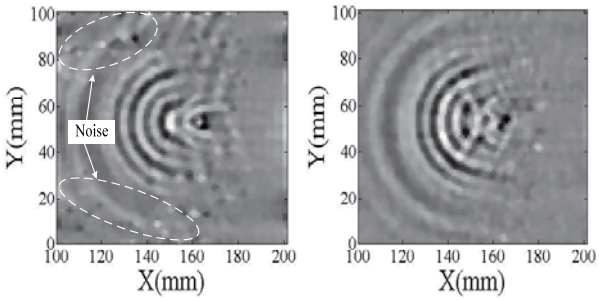

(a) (b)

Fig.7 Wave field images of the filtered wave

In order to improve the visibility of the damage-reflected wave, the adjacent wave subtraction after arrival time matching is used to weaken the incident wave before using the frequency-wavenumber domain filtering, and Fig.6 is the final result. Compared with Fig.7(b), the signal-to-noise rate (SNR) of the wave field image of damage- reflected wave has been increased and the visibility of the reflected has also been improved.

5. Concluding

A structural health monitoring method based on the directional property of metal-core piezoelectric fibers has been introduced. A new effective method for identification of multi-site damages on a composite structure using guided wave has been proposed. The method of damage identification using laser ultrasonic technology has also been introduced.

References

[1] J. Qiu, H. Ji, Frontier Mechanical Engineering, 6(2011), 99–117.

Tenth International Conference on Flow Dynamics
November 25-27, 2013, Sendai, Miyagi, Japan

Preparation of Electrostrictive Polyurethane

Masae Kanda[1], Kaori Yuse[2], Daniel Guyomar[2], Yoshitake Nishi[1]
[1] Department of Materials Science, Tokai University, 4-1-1 Kitakaname, 259-1292, JAPAN
[2] LGEF, INSA Lyon, Bat. Gustave Ferrié, 69621, Villeurbanne Cedex, FRANCE
km616737@tsc.u-tokai.ac.jp

ABSTRACT

To get the large strain at low electric field, a dependence of the solidification condition on electrostriction was investigated for pure polyurethane (PU) films. The starting point of the convergence occurred at a lower electric field for the solidification condition to get thick film with 150 μm thickness as opposed to for the optimum condition to obtain the thin film with 19 μm thickness. Based on the prediction and experimental results, the electrostriction of PU films depended on its solidification condition.

1. Introduction

Electroactive strain up to 380 % has even been obtained when a silicone rubber is utilized as the matrix material [1]. Although such extraordinary results have drastically increased the potential of EAPs, it should be noted that these data were obtained under quite high values of the driving electric field, i.e., 120 MV/m. This limits the use of EAPs since few portable electric components can stand to be used together at such high electrical input. A reduction of the required energy is thus desired for a widespread use of EAPs.

Dielectric EAPs are able to generate a large electroactive strain (> 30 %) while requiring only a low electric field (< 20 MV/m) [2]. Polyurethane (PU) is one of the most versatile materials in the world today. Their many uses range from flexible foam in upholstered furniture, to rigid foam as insulation in walls, roofs and appliances to thermoplastic pure PU used in medical devices and footwear, to coatings, adhesives, sealants and elastomers used on floors and automotive interiors. Over the last two decades, the field of electrically controllable polymer actuators has developed significantly because their performances are comparable to those of natural muscles. However, their experimental errors can be observed. Pure PU elastomers are one of the most important class of polymers due to some remarkable electromechanical characteristics such as large electric field induced strain, high specific energy and fast speed of response [3]. This makes the material very attractive for many electromechanical applications. Many electroactive strain properties of the PU were investigated but the fundamental mechanisms which are responsible for the electrostriction have not been yet well understood [4].

The thermal absorption on melting of differential scanning calorimetry (DSC) analysis was often found to correspond to data of electrostriction [5]. Volume fraction of crystalline with high polarization may contribute to the electrostriction. When the volume fraction of surface crystallization on solidification is controlled by solidification thickness, the high electrostriction can be expected. Therefore, the purpose of the present paper is to report the influence of solidification controlling on electrostriction of the pure PU films.

2. Method

PU film was prepared by a simple solution cast method [5-7]. One gram of PU granules (Noveon Estane 58888 NAT021, USA) was dissolved in approximately 20 ml of N,N-dimethylformamide (DMF) at 85 ºC for 45 min. The solution was poured onto a glass plate and dried at 60 ºC at atmospheric pressure for 1 day. The obtained films were removed from the plate with ethanol. Subsequently, they were placed in a ventilated oven at 130 ºC for 4 h in order to eliminate residual solvent. The thicknesses of the films varied from 19 to 150 μm. For the electromechanical characterization measurements, metal electrodes were placed on both sides of disc-shaped specimens (25 mm in diameter).

The field-induced thickness strain was measured by a laser interferometer (Agilent 5519A) with a precision on the order of 5 nm. The induced electric field was a sawtooth wave for 2-cycles at 0.1 Hz. Its maximum was varied with an upper limit at 20 MV/m. The film samples were placed on a horizontal brass disc (20 mm in diameter) in order to avoid measuring a parasitic flexural motion, and a second brass disc placed on the upper side of the film rendered it possible to apply a bipolar electric field. A function generator (Agilent 33220A) delivered the corresponding bipolar voltage amplified by a factor of 1000 through a high-voltage lock-in amplifier (Trek 10/10B). The ground current between the sample holder and the ground was measured using a current amplifier (Stanford Research Systems SR570).

3. Results and Discussion

The starting point of the convergence occurred at a lower electric field for the thick films as opposed to for the thin films. Optimum solidified thin film with 19 μm thickness does not have convergence until 20 MV/m. Although the thin film shows the high strain value, the strain saturation can not be found until 20 MV/m. The thin film with 19 μm thickness enhances the strain at high electric field, although the thick film with 150 μm thickness exhibits the lower strain at high electric field. On the contrary, thinning the films reduce the electrostriction at low electric field, whereas thick films apparently exhibited the higher electrostriction of low electric field. Namely, thinning the films remarkably enhance the large strain more than 27% at high electric field of 20 MV/m, whereas thick films apparently

exhibit the higher electrostriction at low electric field of less than 4 MV/m. The strain saturation occurs at low electric field for thick sample. We conclude that thinning the PU thickness is a useful tool to obtain the large electrostriction at low electric field.

DSC analysis was used to confirm the volume fraction of crystalline of pure PU films with different thicknesses. The endothermic heat is usually generated by transformation from crystal to liquid on melting. It corresponds thus to volume fraction of crystalline form in material. The fusion enthalpy values were obtained by area of endothermic peak. DSC analysis was carried out to see the fusion enthalpy value of thin and thick films. Endothermic heat from crystal to liquid on melting of thick pure PU film is smaller than that of thin pure PU film. The fusion enthalpy value of thin pure PU film with 28 μm thickness is 1.24 times higher than that of thick pure PU film with 140 μm thickness [5]. The thin pure PU film shows high strain at 20 MV/m. The results show that the strain of films depends on thickness. Thus, it is clear that the high electrostriction of pure PU thin films can be contributed by high volume fraction of surface crystalline. Although the crystalline volume fraction strongly contributes to the electrostriction, the large change in electrostriction quantitatively cannot correspond to the volume fraction. Thus, the crystalline periodicity should be considered.

X-ray diffraction (XRD) is used to confirm the internal structures of periodicity of pure PU films with different thicknesses. The peak width corresponds to the periodicity perfection. Most of the sharp peaks are related to thin pure PU film, whereas the broad peak is related to the thick pure PU film. The big broad peaks from 12 to 29 degree for thick film and from 16 to 26 degree for thin film are found at about 20 degree for soft segments [8]. The sharpness with intensity and width of the peak corresponds to an enhancement of the crystalline periodicity. An additive effect to compressive electrostriction can be gotten, when the periodicity enhancement raises the polarizability. Namely, the angle width of thin pure PU film is smaller than the thick one. The angle width corresponds to the periodicity of soft segments. In addition, remarkable sharp peaks at 28.7 and 26.7 deg of hard segments are found in thin films, whereas they are not observed in thick film [9, 10]. Thus, it is possible that thin film enhances the molar volume and/or their preferred orientation ratio of hard segments and probably enhances the polarizability, resulting in an additive effect to compressive electrostriction.

The pure PU (thin and thick) films show effects of solidification thickness on electrostriction. Furthermore crystallized volume fraction and crystal perfection are confirmed to have changed by thickness difference. In other terns, we can say that constituting thin film presents same differences to the material of thick film. These films are fabricated by solution cast method. The films were solidified on a clean surface. After the films are removed from the glass plate, they are dried again in high temperature. Two surfaces are in contact with heated air at that time. Explanation can be given. One is the thermal conductivity in material and the other is the oxidation from the surfaces. It is possible that formation of a crystal starts from the surfaces due to the thermal gradients. A property gradient takes place (For instance ratio soft/hard segment). Outside of film can have different morphology to the inside one. In other terms, film can have skins. Neither DSC nor XRD can see the different of layers in material, but the results do not against to this hypothesis. The crystallized volume fraction and crystalline periodicity of thin film are higher than those of thick film.

4. Conclusion

To obtain the large strain at low electric field, a dependence of the solidification thickness on electrostriction was investigated for pure polyurethane films. Optimum solidified thin film with 19 μm thickness remarkably enhanced the strain at high electric field at 20 MV/m. Thick films with 150 μm thickness apparently exhibited the higher strain at low electric field of less than 4 MV/m. The starting point of the convergence occurred at a lower electric field for the thick films as opposed to for the thin film, which does not have convergence until 20 MV/m. Based on results of crystalline volume fraction and crystalline periodicity, the solidification thickness dependent electrostriction was explained.

Acknowledgement

Authors would like to thank Profs. L. Lebrun, Dr. L. Seveyrat of INSA Lyon in France and Mr. Yasuo Miyamoto of Tokai University in Japan for their helps.

References

[1] R. E. Pelrine, R. D. Kornbluh and J. P. Joseph, Sensors and Actuators, A **64** (1998) 77-85.
[2] L. Lebrun, D. Guyomar, B. Guiffard, P.-J. Cottinet, C. Putson, Sensors and Actuators, A **153** (2009) 251-257.
[3] Q. M. Zhang, J. Su, C. H. Kim, R. Ting and R. Capps, J. Appl. Phys., **81** (1997) 2770-2776.
[4] I. Diaconu, D.-O. Dorohoi, C. Ciobanu, Rom. Journ. Phys., **53** (2008) 91-97.
[5] M. Kanda, K. Yuse, B. Guiffard, L. Lebrun, Y. Nishi and D. Guyomar, Materials Transactions **53** (2012) 1806-1809.
[6] K. Yuse, D. Guyomar, M. Kanda, L. Seveyrat and B. Guiffard, Sensors and Actuators A **165** (2011) 147-154.
[7] D. Guyomar, K. Yuse, P.-J. Cottinet, M. Kanda, L. Lebrun, J. Appl. Phys., **108** (2010) 114910.
[8] R. C. R. Nunes, R. A. Pereira, J. L. C. Fonseca and M.R. Pereira, Polymer Testing, **20** (2001) 707-712.
[9] Li-Fen Wang, Polymer, **48** (2007) 7414-7418.
[10] Samy A. Madbouly and Joshua U. Otaigbe, Progress in Polymer Science, **34** (2009) 1283-1332.

Tenth International Conference on Flow Dynamics
November 25-27, 2013, Sendai, Miyagi, Japan

Smart Energy Harvester using Digitally Autonomous Device

Yuta Yamamoto and Kanjuro Makihara
Tohoku University Department of Aerospace Engineering, Japan
E-mail: yamamoto@ssl.mech.tohoku.ac.jp

ABSTRACT

This paper presents a smart vibration energy harvester, which is controlled by a built-in digital processor. The built-in processor regulates the harvester circuit as a control authority, so that this harvester can achieve effective power generation. We conducted experiments that supplies harvested energy to various resistive loads and measures the energy consumption of the resistors. The experiments revealed the maximum supply power of the smart harvester and peculiar characteristics depending on electrical loads.

1. Introduction

The space is an environment lacking in energy sources. Not limited to the space, there are many energy lacking environments on the earth, such as moving vehicles, airplanes, auto mobiles and long bridges. The technology of energy harvesting makes a significant contribution in those environments. Energy harvesting generates electrical energy from various energy sources, for example solar light, wind power, radio wave and structural vibration. Solar power generation is a prominent source of an effective energy harvesting. However, the solar power generation cannot be used at night and at the place that sunlight does not reach. So far other ways of energy harvesting have been required. Vibration energy harvesting is one of them, and vibration is a ubiquitous energy source. A lot of machineries such as motors and engines are often accompanied by mechanical vibrations. Bridges are always excited vibrations by car traffic and wind. Therefore, the application of vibration-based harvesting is extremely rangy. Vibration energy harvesting that uses piezoelectric materials has been investigated intensively.

We present a smart vibration energy harvester that is controlled by a built-in digital processor. The harvester is designed in conformity to synchronized switching harvesting on inductor (SSHI). SSHI was proposed by Badel *et al* [1]. This method inverts the piezoelectric charge synchronizing with structural vibration, which is caused by an inductor and regulated switches. The piezoelectric charge inversion encourages energy transfer from vibration energy to electrical energy, which causes piezoelectric voltage amplification. Voltage inversion has a great possibility to improve the energy generation of piezoelectric vibration harvesting. However, the method requires a control authority both to obtain the vibration displacement data from structures and to regulate switches in the circuit. Previous reports[2] did not deal with the control authority. We build a digital processor for the SSHI energy harvester as a built-in control authority. The processor needs electrical energy that is supplied with harvested energy. Consequently, the smart vibration energy harvester does not require any management and energy supply from outsides.

This paper demonstrates the generation efficiency of the smart vibration energy harvester in experiment. The efficiency of our vibration-based harvester is clearly described to show its potential.

2. Smart energy harvester

We build a digital processor into the vibration energy harvester. Figure 1 shows the conceptual system diagram of the smart vibration energy harvester. The digital processor drives with a part of harvested energy that controls the circuit switches according to SSHI. This system is composed of self-powered device that is reported in our previous paper[3]. Short explanations of the harvester behavior and processor operation are presented.

At first, when vibration happens to structures, a piezoelectric transducer generates alternating voltage between two terminals. The alternating voltage is rectified through a diode bridge, which is stored in a storage capacitor. This mechanism is similar to a conventional standard harvester. The stored voltage increases gradually due to the structural vibration. When enough voltage is stored, a DC/DC converter drives and starts to generate steady constant voltage. Then, the digital processor starts to drive.

The digital processor obtains structural displacement data from a piezoelectric sensor that is installed on the host structure. It generates voltage according to the strain, which does not need any power source. The processor calculates the regulating timing that the on/off switch has to change. Then, the processor starts to output control signals.

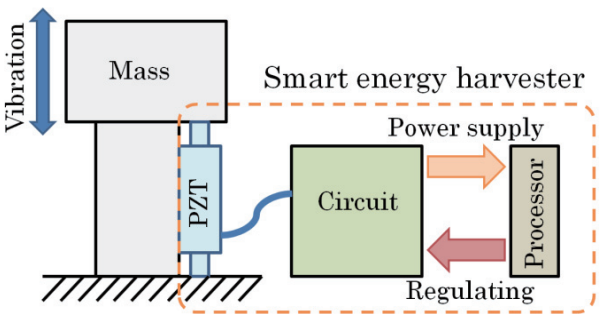

Fig. 1 Smart vibration energy harvester

In this way, we achieve high efficiency of energy harvesting completely without any power supply and control management from the outsides. The smart vibration energy harvester does not require any control and energy supply. It is digitally controlled by the processor, so that it can be applied to advanced and

rewriteable control schemes.

3. Experimental setup

The harvesting experiment was performed under the sinusoidal vibration excitation with the structural resonant frequency. The natural frequency at constant electric charge was 23.1 Hz.

We investigated the harvesting performance with various load resistances. We conducted harvesting experiments with the measurement of resistor consumption. Since the consumption of resistors indicated harvesting capability, this experiment vividly demonstrated the harvesting performance of our smart energy harvester. The electrical power flows through the resistors via the diode-bridge.

4. Experimental results with resistor consumption

Figure 2 shows the energy consumptions at the connected resistors. The energy consumption equals to the electrical power supply for resistors. In Fig. 2, the optimal value of resistance can be seen. This resistance value, approximately 35 kΩ, is able to provide the most effective harvesting as an electrical load. The maximum power supply of our harvester was 4.87 mW at 35 kΩ.

Within the value of 18 kΩ, electrical power of harvesting is drastically low, because the processor is not capable to drive, due to insufficient amount of electrical power sent to the processor. The phenomenon indicates that the smart energy harvester possesses the driving limit of the electric load value.

Piezoelectric transducer generates voltage in proportion to vibration amplitude, so that large vibration amplitude causes high voltage, which also causes large electrical power generation. On the other hand, piezoelectric transducer induces mechanical force in proportion to the voltage. The mechanical force can be regarded as counter force of vibration excitations, which reduces vibration amplitude of the host structure. This means that the vibration amplitude of the host structure is subject to energy transfer by means of energy harvesting. In this experiment, as the resistance became large, the piezoelectric voltage becomes high and the vibration amplitude becomes small. However, when host structures are large as airplanes, moving vehicles, space station and long bridges, the piezoelectric force does not affect the vibration amplitude at all. Thus, we normalized the resistor consumption by the vibration amplitude. The normalized value is plotted in Fig. 3. The maximum normalized power of our harvester was 26.1 mW/mm at 40 kΩ. Comparing with Fig. 2, the most effective electrical load differed from un-normalized one. Even at the higher resistance, the slope of consumption decline is slower than un-normalized. This results shows that the harvesting efficiency probably becomes more effective at high resistance if the vibrating structure is large as airplanes, moving vehicles, space station and long bridges.

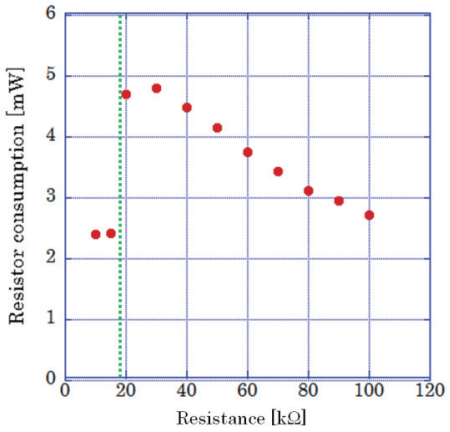

Fig. 2 Resistor energy consumption
(Green dotted line is stands for driving limit of processor.)

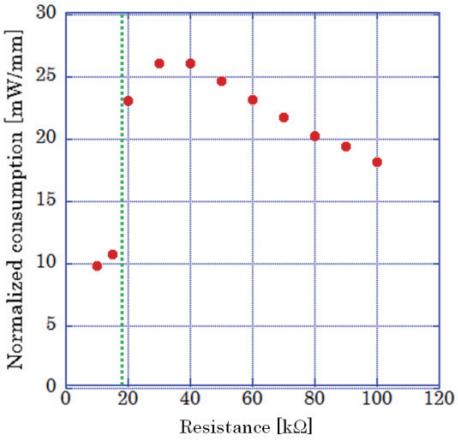

Fig. 3 Normalized energy consumption
(Green dotted line is stands for driving limit of processor.)

5. Conclusion

This paper presents a smart vibration energy harvester that employs a digital processor, which performs well without power-supply. The harvester enhances energy conversion and supply amount of energy to the loads. We carried out an experiment to supply harvested energy to various resistors, which revealed that the maximum normalized power of the harvester is 26.1 mW/mm. The smart energy harvester has the driving limit of electric load value with low resistance. The harvesting efficiency probably becomes more effective at high resistance if the vibrating structure is large.

References

[1] A. Badel, D. Guyomar, E. Lefeuvre, and C. Richard, Journal of Intelligent Material Systems and Structures, **16** (2005), pp.889-901.
[2] K. Makihara, S. Takeuchi, S. Shimose, and J. Onoda, Transactions of the JSASS Aerospace Technology Japan, **10**(2012), pp.13-18.
[3] K. Makihara, S. Takeuchi, S. Shimose, and J. Onoda, AIAA Journal, **50**(9)(2012), 2004-2011

Tenth International Conference on Flow Dynamics
November 25-27, 2013, Sendai, Miyagi, Japan

Fabrication, 3D Characterization and Simulation of Porous Metals for Energy Saving

Eric Maire, Loic Courtois, Jérôme Adrien, Michel Perez, Damien Fabrègue, Sandrine Cottrino
Université de Lyon,CNRS, INSA-Lyon, MATEIS UMR5510, 69621 Villeurbanne, France
E-mail of corresponding author: eric.maire@insa-lyon.fr

ABSTRACT

This paper will present the X-Ray tomography technique and how it can improve our understanding of the structure of porous metals. In situ experiments in tomography will also be reported because they help understanding the deformation modes. Post processing of these 3D images of eventually deformed structures will also be described. This will namely report to 3D image processing, digital volume correlation and Finite or Discrete Element simulation. Examples in the field of energy saving will be used all through the paper to support the argument.

1. Introduction

Porous metals have potential applications in many domains able to lead to energy saving. Porous materials in general exhibit good specific mechanical properties such as specific strength ($\sigma e/\rho$) and specific stiffness (E/ρ). They also have a unique ability to absorb a high amount of mechanical energy by deforming enormously at constant load. In some cases porous materials can also intrinsically absorb mechanical vibrations. This has promoted the use of these materials in general in the field of transport applications as strengtheners, stiffeners and vibration or energy absorbers. In this field they allow for lighter structures to be designed, hence leading to fewer energy consumption for vehicles. Metallic porous materials are more specifically used when toughness and heat resistance are required. Some porous materials also present an open porous volume, accessible to fluids. This has pushed for applications in the chemical industry such as filters but also as core components for heat exchangers. In this domain again a more efficient heat transfer promotes energy saving. Porous metals have also potential applications in the field of Energy in a general way (for both production and storage of energy). Their wider use and efficiency improvement would lead to substantial energy savings in this context. The first of these applications is as electricity collectors in the emerging field of electricity storage for Electric Vehicle batteries, that would lead a substantial reduction of gas consumption. Possible use are also emerging as current collectors in fuel cells electrodes.

The prediction of the combined properties of this rather new class of materials is still a widely open question because the macroscopic properties depend on the structure at different levels, the most important one being the so called “3D architecture”, i.e. the spatial arrangement of the solid and gaseous phases. In this field, X-Ray tomography is now a well established technique allowing the analysis of the 3D architecture of porous materials in a non destructive way. X-ray tomography is now recognized to be superior to standard microscopy for this particular application. The wider availability of X-Ray tomographs has lead to an explosion of the 3D non destructive imaging possibilities of these materials.

This paper will present the X-Ray tomography technique and how it can improve our understanding of the structure of porous metals. In situ experiments in tomography will also be reported because they help understanding the deformation modes. Post processing of these 3D images of eventually deformed structures will also be described. This will namely report to 3D image processing, digital volume correlation and Finite or Discrete Element simulation. Examples in the field of energy saving will be used all through the paper to support the argument.

2. Method

X-ray tomography is the name used in materials science for a more widely know device in medical science: the X-ray scanner. Although anyone in developed countries has heard the name, only few know the interest of this technique (ie 3D non destructive inspection of a sample) and even fewer know the principle. In an X-ray scanner, attenuation radiographs are recorded for many values of the angular position of the sample in the scanner. These radiographs are recorded on a computer outside the scanner and these are subsequently used to calculate the 3D map of the attenuation coefficient of the samples. These reconstructed maps, also names scans or tomograms are 3D images picturing faithfully the internal microstructure of interest. The current trend in X-ray imaging is to go the very high resolution (voxel size = 20 nm) available at synchrotron sources.

These images can firstly be analyzed to obtain a very detailed quantification of the microstructure of a material. For porous materials, one can nowadays precisely measure the amount, distribution, connectivity, shape, size of the two phases (solid and gas).

In materials science, many in situ experiments have been developed for tomography and some examples will be given in the presentation related to porous metals and their application in energy saving. Some of these experiments are reviewed in [1]. These include monotonous or cyclic tension/compression, hydrostatic pressure, double torsion, heating, cooling... In some cases, the dynamic nature of the loading applied imply that the tomograms are acquired rapidly (in minutes or even seconds depending on the time evolution of the phenomenon at play). This requires specific acquisition developments available at synchrotron sources only [2].

These in situ experiments in tomography deliver successive tomograms picturing the evolution of the microstructure. 3D strain fields can be measured by pair digital volume correlation of these tomograms.

These strain fields can finally be compared to predictions obtained from micro-structurally faithful models of the microstructure. This new family of modeling methods consists in using the tomograms as a direct input to produce a faithful finite element (or discrete element) mesh of the internal microstructure of the sample.

3. Results and Discussion

Figure 1 illustrates a classical results that one can obtain when combining 3D non destructive imaging with a cyclic mechanical loading of the sample. One clearly sees by comparing the initial and the fatigued state that the sample damages by fracture of the hollow spheres.

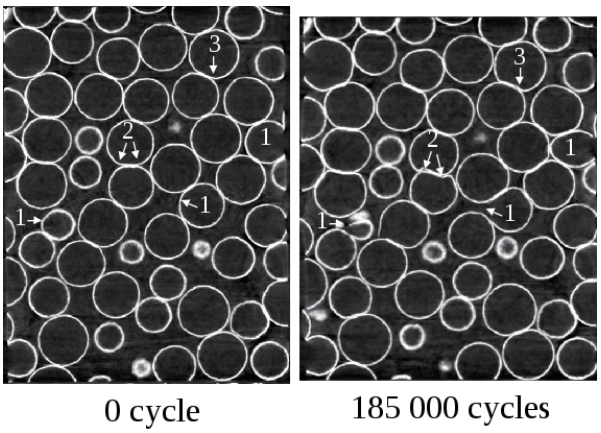

Fig. 1 X-Ray tomography reconstructed slices of a Metal Hollow Sphere Structure (304 steel) before (left and after (right) cyclic mechanical loading. Damage occurs by fracture of the spheres

Figure 2 shows a microstructurally faithful FE mesh of the same sample as this in Figure 1. The figure shows a contour plot of the local values of the von Mises stress calculated from the model.

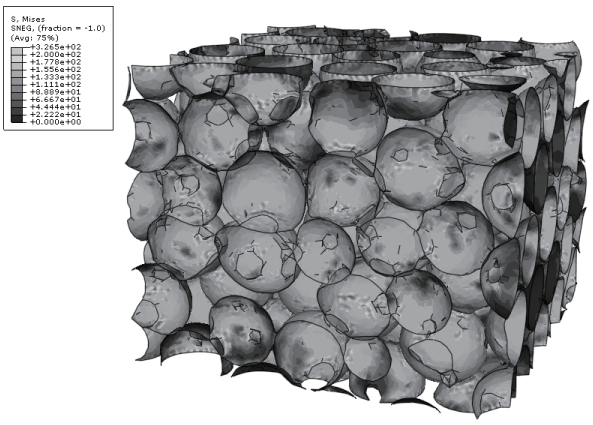

Fig. 2 FE calculation of the local von mises stress inside the sample. The mesh is faithful to the actual microstructure

References

[1] J.Y. Buffière·et al. Experimental Mechanics **50** (2010), p 289-305

[2] S Deville et al. Acta materialia **61** (2013), p 2077-2086.

Tenth International Conference on Flow Dynamics
November 25-27, 2013, Sendai, Miyagi, Japan

High Strength of Prestressed CFRP Inspired by Reinforced Concrete Innovated by Great French Engineer

Yoshitake Nishi, Takumi Okada
Department of Materials Science, School of Engineering, Tokai University, Kitakaname4-1-1, Hiratsuka, Japan
am026429@keyaki.cc.u-tokai.ac.jp

ABSTRACT

Effects of a pre-stressing at 4, 8 and 12 MPa on mechanical properties had been investigated. 4 and 8 MPa pre-stressing remarkably enhanced the as well as Charpy impact value, energy of CFRP with 4 and 50 vol% carbon fibers. They probably depend on the residual compressive stress induced by the pre-stressing in CFRP. Consequently, the pre-stressing apparently improved the fracture toughness and then remarkably enhanced the reliability. They could be explained by the residual compressive stress in matrix among carbon fibers.

1. Introduction

CFRP constructed with carbon fiber and epoxy polymers has been applied to airplaines [1,2]. However the further strengthening with small experimental errors has been required to develop light structural materials with safety and reliability as well as light, high strength and high energy conservation. Although new strengthening methods of CFRP have not been found, the reinforcement by 100 keV class electron beam irradiation has been innovated [3-5]. However the effective depth is generally less than 200 μm from surface [6]. To strengthen the practical bulk CFRP with more than 200 μm thick, a pre-stressing, which generates a compressive stress to enhance the tensile strength of the concrete by inserting pre-stressed piano steel has been suggested. It is inspired by a pre-stressed concrete which was innovated by Eugéne Freyssinet, a French Civil Engineer, on 1928. This method is generally utilized for current huge architectures [7-10]. The tensile strength of carbon fibers is extreamely higher than that of piano steel wire, whereas the stiffness of epoxy matrix in CFRP is smaller than that of concrete. When the pre-stressing of carbon fiber can be also loaded to epoxy resin, the compressive stress occurs in matrix. Since improvements of the elasticity, fracture strain and fracture toughness of CFRP can be expected, the purpose of the present work is to investigate to clear the effect of volume fraction of carbon fibers on the mechanical properties of pre-stressed the CFRP samples.

2. Method

CFRP (carbon fiber reinforced epoxy polymers) has been applied to mover machines [1,2]. However the further strengthening with small experimental errors has been required to develop light structural materials with safety and reliability as well as light, high strength and high energy conservation. Although new strengthening methods of CFRP have not been found, the reinforcement by 100 keV class electron beam irradiation has been innovated [3-5]. However the effective depth is generally less than 200 μm from surface [6]. Thus, the strengthening methods of practical bulk CFRP with more than 200 μm thick have been expected.

A pre-stressing, which generates a compressive stress to enhance the tensile strength of the concrete by inserting pre-stressed piano steel. Eugéne Freyssinet, a French Civil Engineer, has innovated a pre-stressed concrete on 1928, and also innovate the practical post tension method, current PC Engi., by using special jack innovated on 1939. This method is generally utilized for current huge architectures [7-10]. The tensile strength of carbon fibers is extreamely higher than that of piano steel wire, whereas the stiffness of epoxy matrix in CFRP is smaller than that of concrete. When the pre-stressing of carbon fiber can be also loaded to epoxy resin, the compressive stress occurs in matrix. Since improvements of the elasticity, fracture strain and fracture toughness of CFRP can be expected, the purpose of the present work is to investigate to clear the effect of volume fraction of carbon fibers on the mechanical properties of the prestressed CFRP samples

In order to evaluate bending and tensile properties, the three point bending and tensile test used for the Autograph and Instron machine (Instron, 3367) type, were performed with strain rate of one mm/min and $5.56\times10^{-4}s^{-1}$, respectively. Based on Japanese Industrial Standards (JIS-K7074 and JIS-K7113), the sample size were 100 and 105 mm length, 10 and 6 (18) mm width at middle point (holding part), 30 and 60 mm effective length and 2 and 2 mm thickness, respectively.

In order to evaluate the impact fracture toughness, the Charpy impact values of the CFRPs with and without pre-stressing were measured using a standard Charpy impact fracture energy measurement system (Fujisiken Seisakusyo FC3002) (JIS K 7077) [11]. The CFRTP sample, which sizes were 80 mm length, 10 mm width and 2.0 mm thickness. The impact fracture energy (E) was expressed as functions of E, W, R, β, αand α', which were impact fracture energy (kJ), hammer mass (kg), length (m) of hammer weight point from rolling center, start angle before impact (141.5 degree), the maximum angle after impact and the maximum angle of the blank test, respectively. The Charpy impact value (a_{uc}: kJm^{-2}) was expressed by the equation ($a_{uc} = E / (b\, t)$), where E, b (= 10 ± 0.2 mm) and t (= 2.00 ± 0.15 mm) were impact fracture energy (J), sample width (mm) and span distance (sample thickness, mm), respectively. The distance between supporting points was 40 mm.

3. Results and Discussion

Figs. 1-(a) and 1-(b) exhibit effects of pre-stressing at 4, 8 and 12 MPa on reduced mechanical properties of CFRP with 50 and 3 vol% carbon fibers prestressed at 4, 8 and 12 MPa, respectively. Effects of a pre-stressing at 4,

8 and 12 MPa on mechanical properties have been investigated.

4 and 8 MPa pre-stressing remarkably enhances the reduced deformation energy (E_f) and fracture strain (ε_f) as well as Charpy impact values (a_{uc}) of CFRPs with both 4 and 50 vol% carbon fibers.

They probably depend on the residual compressive stress induced by the pre-stressing in CFRP. Consequently, the pre-stressing apparently improved the fracture toughness and then remarkably enhanced the reliability. They could be explained by the residual compressive stress in matrix among carbon fibers.

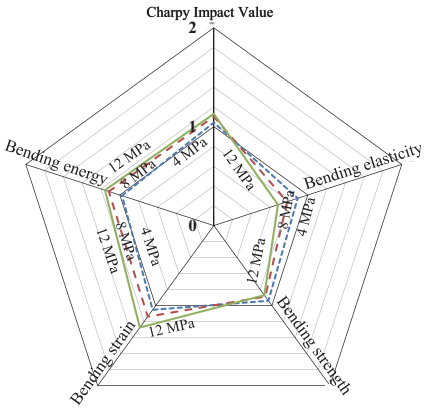

(a)

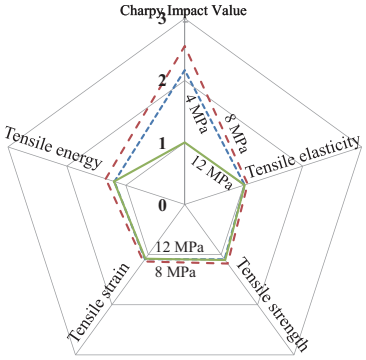

(b)

Fig. 1 Reduced mechanical properties of CFRP with 50 (a) and 3 vol% carbon fibers (b) prestressed at 4, 8 and 12 MPa.

12 MPa pre-stressing enhances the a_{uc}, E_f and ε_f of CFRPs with 50 vol% carbon fibers, whereas it decreases them of CFRPs with 4 vol% carbon fibers. When changes in pre-stress from 8 to 12 MPa are induced by the interface slip between carbon fiber and epoxy matrix, the a_{uc} drop induced by 12 MPa pre-stressing of CFRPs with 4 vol% carbon fibers can be explained.

Pre-stressing enhances the tensile elasticity ($d\sigma/d\varepsilon$) and strength (σ_f) of CFRPs with 4 vol% carbon fibers, whereas it decreases the bending ($d\sigma/d\varepsilon$) and σ_f of CFRPs with 50 vol% carbon fibers.

Furthermore, the a_{uc} drop induced by pre-stressing of CFRPs with 50 vol% carbon fibers can be explained by the low strengthening limit of its epoxy resin matrix, although pre-stressing tremendously loads the compressive stress in epoxy resin matrix of CFRPs with 4 vol% carbon fibers.

4. Concluding remarks

Effects of a pre-stressing at 4, 8 and 12 MPa on mechanical properties had been investigated. 4 and 8 MPa pre-stressing remarkably enhanced the as well as Charpy impact value, energy of CFRP with 4 and 50 vol% carbon fibers. They probably depend on the residual compressive stress induced by the pre-stressing in CFRP. Consequently, the pre-stressing apparently improved the fracture toughness and then remarkably enhanced the reliability. They could be explained by the residual compressive stress in matrix among carbon fibers.

When changes in pre-stress from 8 to 12 MPa are induced by the interface slip between carbon fiber and epoxy matrix, the drops of a_{uc}, E_f and ε_f induced by 12 MPa pre-stressing of CFRPs with 4 vol% carbon fibers can be explained.

Furthermore, the drops of bending ($d\sigma/d\varepsilon$) and σ_f induced by pre-stressing of CFRPs with 50 vol% carbon fibers can be explained by the low strengthening limit of its epoxy resin matrix, although pre-stressing tremendously loads the compressive stress in epoxy resin matrix of CFRPs with 4 vol% carbon fibers.

5. Acknowledgements

Authors would like to thank Mr. N. Hironaka, K. Takada, T. Yamamoto, M. Hirano, K. Kutaraki, Y. Harada, K. Tanaka of Graduate school of Tokai University for their useful helps.

References

[1] J. D. Brooks and G. H. Taylor, Carbon, 3 (1965), 185.
[2] T. Chang and A. Okura, Trans. ISIJ, 27 (1987), 229.
[3] Y. Nishi, T. Toriyama, K. Oguri, A. Tonegawa and K. Takayama, J. Mater. Res., 16 (2001), 1632.
[4] Y. Nishi, A. Mizutani, A. Kimura, T. Toriyama, K. Oguri and A. Tonegawa, J. Mater. Sci., 38 (2003), 89.
[5] A. Mizutani and Y. Nishi, Mater. Trans., 44 (2003), 1857.
[6] H. Takei, K. Iwata, M. Salvia, A. Vautrin and Y. Nishi, Mater. Trans., 51 (2010), 2259.
[7] M. Tezuka, R. Sato, K. Yamamoto and S.Tottori, J.Materials, Concrete Structure, Pavements, 613 (1999), 43.
[8] S. Shirahana, A. Hattori and T. Miyagawa, J. Materials, Concrete Structure, Pavements, 669 (2001), 85.
[9] M.Khin, T. Idemitsu, K. Takewaka and S. Matsumoto, J. Materials, Concrete Structure, Pavements, 526 (1995), 121.
[10] H. Sakai, Y. Hamada, M. Hayashida, A. Hattori and T. Miyagawa, J.Materials, Concrete Stracture, Pavements, 641 (2000), 1173.
[11] K. Kutaragi, Y. Harada, K. Tanaka and Y. Nishi, J. Japan inst. Metals, 71 (2007), 598.

Reliability Assessment for Pipe Elbows with Local Wall Pinning using Guided Wave Testing

Fumio Kojima[1], Jyunko Hioki[2], Hiroyuki Nakamoto[2], and Hideo Nishino[3]
[1]Organization of Advanced Science and Technology, Kobe University
[2]Graduate School of System Informatics, Kobe University
[3]Institute of Technology and Science, University of Tokushima
E-mail of corresponding author: kojima@koala.kobe-u.ac.jp

ABSTRACT

Evaluation of reliability of NDI plays an essential role in keeping the safety of piping system. This paper is concerned with a reliability assessment of guided wave testing (GWT) for pipe wall pinning. An event model is defined by denoting the preliminary assigned threshold value associated with the amplitude of the receiving signals by GWT. In order to evaluate the probability of detection, the received test signals are collected for pipe elbows with local wall thinning using GWT. The proposed method is effectively determined based on the contribution from the defect locations and from the applied frequency rates.

1. Introduction

In the application of NDE studies, there are so many cases that can influence whether or not the inspection will result in the correct decision as to the existence of flaw damages. Such inspection capability is to evaluate through probability of detection (POD) performed prior to the when the inspection system being deployed [1].

In this paper, a reliability assessment of guided wave testing (GWT) can be performed using hit/miss approach. Our focus in the reliability analysis is devoted to the detectability of pipe wall pinning in pipe elbows. In GWT, the inspection process involves randomness due to variability in inspection conditions, including inspection strategies. Taking into account these factors, POD is evaluated from contributions for the flaw damage location and inspection method.

2. Event model for Hit/Miss

2.1 Experimental Setup

In the experiments, elbow test pipes (50A JIS long elbow) were employed as specimens. The outer diameter and wall thickness of aluminum (Al) pipes used in the experiments were 60.5 and 4mm, respectively. A ring-shaped piezoelectric transducer system was used and set on the specimens. The transducer system consists of two sets of eight piezoelectric shear elements. All the eight piezoelectric shear elements of each set were connected in parallel and simultaneously driven for the preferential transduction of the fundamental torsional T(0,1) mode guided wave. Gaussian-modulated tone-burst signals of 30, 40, and 50 kHz center frequency were generated and amplified to 120 V peak-to-peak and fed into the transmitter to generate the T(0,1) mode guided waves. A digital oscilloscope was used to observe and store the signals. A 300 averaging sequence was used to improve the signal-to-noise ratio (S/N). Artificial wall pinning was performed using an abrasive stone having 10 mm diameter. The maximum depth to which the wall was artificially thinned was gradually increased to 2.0 mm in 0.05 mm steps to evaluate the sensitivity of the test signals. The axial position at which the wall was artificially thinned was set as shown in Fig. 1.

2.2 Collection of Data Set

The wavelet transformation with the Gabor function as a mother wavelet was used to obtain enveloped signals. Figure 2 depicts an example of enveloped time domain signals of a no defect and the incremental seven defects. To demonstrate the performance of the GWT, we collect data set for flaw variations with nine pinning depth including no defect at thirteen locations and for three measurement strategies with the driven frequencies (30, 40, and 50 kHz). Then the event model for detecting the local wall pinning is described by

$$d^e = \begin{cases} 0 & \text{if } s < s^{trs} \\ 1 & \text{otherwise} \end{cases} \qquad (1)$$

where s^{trs} denotes the threshold value for the signal amplitude which is preliminary assigned. Table 1 presents an example of hit/miss summary data of hit/miss analysis.

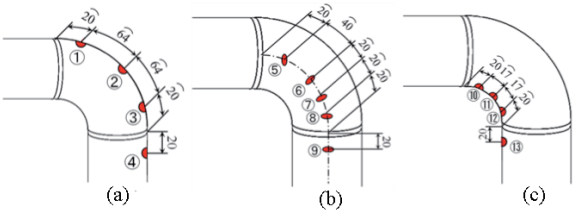

Fig. 1 Defects locations for (a) inner- (b) horizontal-, and (c) outer-side defects

3. Computation of POD

The detection process is conventionally modeled using a probability of detection curve, which describes the probability of detecting a pipe wall pinning with a specific size. In the sequel, POD curve is characterized by the Palmberg equation. It specifies the probability of detecting a pinning size *t* as:

$$P_d(t) = \frac{(t/t_m)^\alpha}{1 + (t/t_m)^\alpha} \qquad (2)$$

where t_m is the pinning size corresponding to 50% probability of detection. When the exponent a increases, the most pinning larger than t_m will be detected and smaller ones will be missed. To generate the Palmberg equation from the experimental data, we use the probability of detection based on summary data of hit/miss analysis [2]. Then the two Palmberg parameters t_m and α can be determined by minimizing the discrepancy as shown in Table 1, e.g.

$$P_e^j = N_{det}^j/3 \tag{3}$$

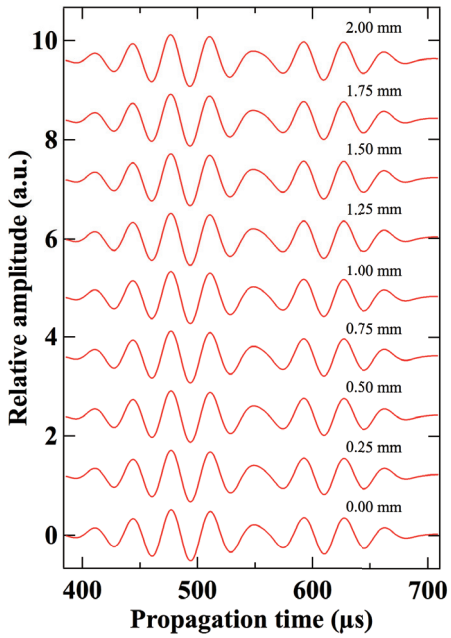

Fig. 2 Enveloped Time Domain Signals

Table 1. Example of Summary Data

Location	Depth of Pinning	Frequencies [kHz]		
		30	40	50
1	0.25	0	1	0
	0.50	1	0	0
	0.75	1	1	1
2	0.25	0	1	1
	0.50	1	1	0
	0.75	1	1	1
3	0.25	0	0	1
	0.50	0	0	1
	0.75	1	1	1
4	0.25	1	0	0
	0.50	1	1	0
	0.75	1	1	1
5	0.25	0	0	1
	0.50	1	0	1
	0.75	1	1	1

where N_{det}^j denotes the number of hits that detect the *j*-th pinning. Then the two Palmberg parameters t_m and α can be determined by minimizing the discrepancy:

$$\min_{t_m,\alpha} \sum_{k=1}^{9} \sum_{i=1}^{13} \left| P_d(t_k) - P_e^{k,i} \right| \tag{4}$$

In our calculations, we obtain

$$t_m = 0.5173[mm] \quad \alpha = 20.4043 \tag{5}$$

Figure 3 shows the POD curves as function of pinning size.

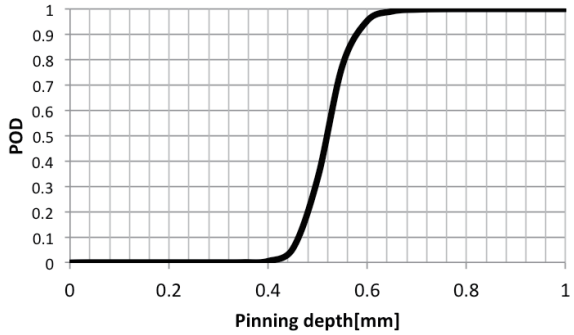

Fig. 3 POD Curve using Palmberg Equation

4. Concluding Remarks

A reliability assessment of guided wave testing (GWT) was applied to the detectability of pipe wall pinning. The probability of detection based on hit/miss approach was evaluated based on the contribution from the defect locations and from the applied frequency rates. The detection of pinning locations and the choice of inspection strategies are strongly correlated for the reliability of the nondestructive evaluatuon. The feasible choice of the threshold value for the event model is currently under study.

Acknowledgement

This work has been performed as a part of the National Research Project for Enhancement of Measures against the Ageing of Nuclear Power Plants sponsored by the Nuclear Regulation Agency (NRA) in Japan.

References

[1] A.P. Berence, NDE Reliability Data Analysis, Metals Handbook (9th Edition), Nondestructive Evaluation and Quality Control, American Society for Metals, **17**(1989), 689-701.

[2] B. Palmberg, A.F. Blom, and S. Eggwertz, Probabilistic Fracture Mechanics and Reliability, Dordrecht:M. Nijhoff, 1987.

Tenth International Conference on Flow Dynamics
November 25-27, 2013, Sendai, Miyagi, Japan

Non-destructive Materials Reliability Evaluation for Cu-alloy of Combustion Chamber

Mitsuharu Shiwa, Donfeng He, Yoshinori Ono, Masao Hayakawa[1], Hideo Sunakawa, Naoki Nagao, Sinich Moriya, Eiichi Sato[2], Tetsuya Uchimoto, Toshiyuki Takakagi[3]
[1]National Institute for Materials Science, Sengen 1-2-1, Tsukuba, Japan
[2]Japan Aerospace Exploration Agency, Yoshinodai 3-1-1, Chuo-ku, Sagamihara, Kanagawa, Japan
[3]Tohoku University, Katahira 2-1-1, Aoba-ku, Sendai, Japan
E-mail of Mitsuharu Shiwa: SHIWA.Mitsuharu@nims.go.jp

ABSTRACT

The aim of this research is to evaluate high temperature damage of combustion chamber material, which is made of Cu-Cr-Zr alloy by using eddy current testing (ECT) analysis techniques based on AMR sensor. The cracks in a simulated combustion chamber can be detected by multi-frequency ECT technique. Also the relative conductivity value of damaged copper alloy specimens both at room temperature during tensile testing and at high temperature of fatigue and creep testing were related to the applied damage with micro cracks.

1. Introduction

The combustion chamber of liquid fuel rocket is made of Cu-Cr-Zr copper alloy. Inside of the combustion chamber is the ultra high temperature gas of about 3000 K. Cooling grooves are made in the wall of the combustion chamber and liquid hydrogen (20 K) flow in them for the cooling. Due to the big thermal gradient, small cracks and material degradation may be happened in the wall of the combustion chamber. For the recycling and safety checking of the combustion chamber of rocket engine, it is necessary to develop nondestructive techniques to do the damage evaluation before and after using.

We have two purposes in the research project. One is to detect the small cracks happened in the combustion chamber using eddy current testing (ECT) method; and another is to do material evaluation or lifetime estimation of copper alloy by electromagnetic (EM) method. We once developed high sensitive AMR (anisotropic magneto resistive) sensor and used it in ECT system [1]. With the AMR-based ECT system, we successfully detected the artificial defects in plate type specimens [2-4].

In this report, we will illustrate the experimental results of crack detection of a chamber type specimen and the evaluation of copper alloy specimens after fatigue and creep testing.

2. Crack Detection and Results

Fig.1 shows the schematic block diagram of dual frequency ECT system with AMR sensor for the crack detection. AMR sensor of HMC1001 was used [5]. Two lock-in amplifiers and two frequencies were used in this ECT system. For high frequency f2, the penetration depth is small, surface condition and lift-off information were detected. For low frequency f1, the penetration depth is big. Both the inside and surface properties of the material can be detected. By subtracting the two output signals, the lift off related noise can be successfully reduced.

A chamber type specimen made of copper alloy was fabricated to simulate the combustion chamber of liquid rocket. Fig.2 shows it. Grooves were made on it to simulate the cooling grooves of the combustion chamber. From the bottom of the grooves, the wall thickness was about 1 mm. 12 artificial slits with different length and depth were made under the bottom of some grooves to simulate the defects. The width of the slits was about 0.2 mm. The lengths were 2 mm, 5 mm, and 10 mm; and the left thickness of the wall at the positions of the slits were 0 mm (through), 0.2 mm, 0.4 mm, and 0.6 mm.

Fig.3 shows the scanning results for the slits with the left thickness of 0.4 mm and 0.6 mm. For the high excitation frequency of 20 kHz, due to the small penetration depth, no slit signals could be observed. For the low excitation frequency of 2 kHz, both the slit defect signals and the lift off related signals were observed. After the subtraction of the two outputs V1 and V2, the line became flat. This proved that the dual frequency method was effective to reduce the influence of the variance of lift off.

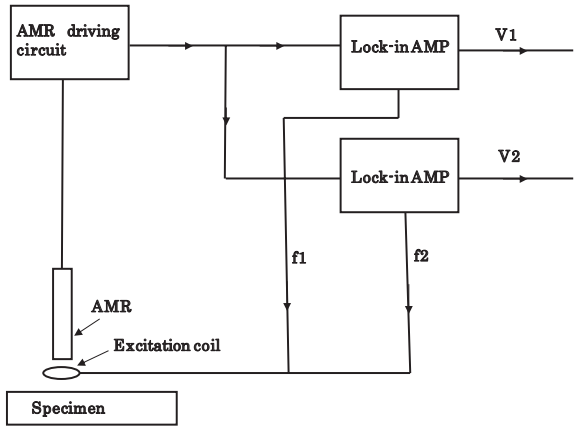

Fig.1 chematic ECT block diagram with AMR sensor.

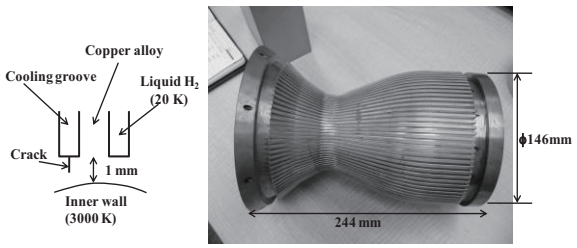

Fig.2 Chamber type specimen to simulate the combustion chamber of liquid rocket.

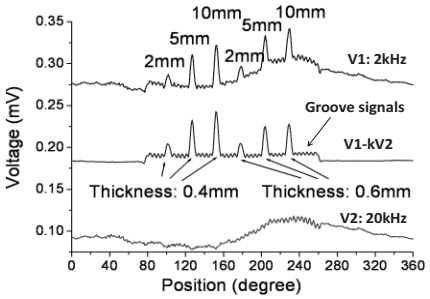

Fig.3 Scanning results for the slits with the left thickness of 0.4 mm and 0.6 mm.

3. Measurement of conductivity and the Evaluation of Copper Alloy

Fig.4(a) shows the configuration of conductivity measurement using ECT with AMR sensor and Fig.4(b) shows the equivalent circuit. Using a simple model, we got formula (1) to express the relation between the conductivity, the frequency and the X, Y signal of ECT.

$$\frac{\Delta X}{\Delta Y} = \frac{a\sqrt{f}}{\sqrt{f} + b/\sqrt{\sigma}} \qquad (1)$$

Where, $\triangle X$ and $\triangle Y$ are ECT signals, f is the excitation frequency, σ is the conductivity of the material. The constants a and b are determined by the size of the excitation coil, the lift off and other experimental conditions. Fig.5 shows the experimental data and the simulation result for an aluminum plate. The tendencies are similar.

Fig.6 shows the specimen of copper alloy. Using the ECT with the AMR sensor, we measured the conductivities of point P1 and point P2, which were 5 mm from the two ends of the specimen respectively. P1 was close to the aging end and P2 was close to the broken end.

Table I shows the copper alloy specimens with different creep and fatigue testing conditions and the measured conductivities at P1 and P2.

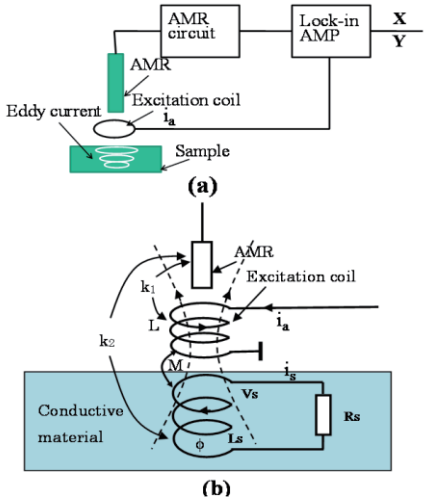

Fig.4 (a) Configuration of ECT with AMR sensor. (b) Equivalent circuit of ECT.

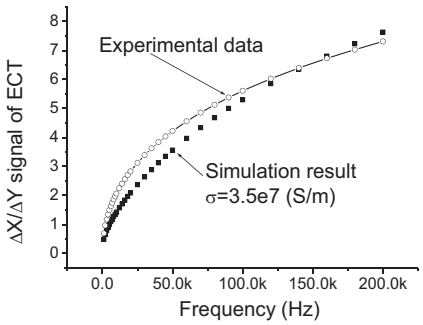

Fig.5 Experimental data and simulation result.

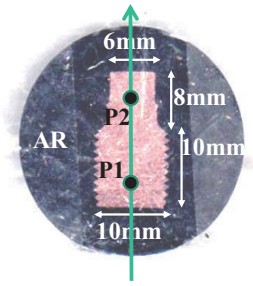

Fig.6 Specimen of copper alloy.

Table I. Specimens and the conducitivities at two ends.

Sample No.	Specimen type	Temp. (°C)	Time (s)	Cycle (N)	σ (10^7S/m) Aging (P1)	σ (10^7S/m) Broken (P2)
1	As-received	20	0	0	4.94	4.56
2	Creep	480	60000	0	5.29	4.81
3	Creep-Fatigue	480	8000	20	5.04	4.51
4	Creep-Fatigue	530	6000	15	4.30	4.94
5	Creep-Fatigue	430	22000	50	4.96	4.53
6	Creep-Fatigue	480	12400	31	5.00	4.20

4. Concluding remarks

Using ECT with AMR sensor, we successfully detected the artificial crack defect in a simulated combustion chamber. We also measured the conductivity of copper alloy specimens with different creep and fatigue testing conditions and observed the differences of the conductivities. We are planning to do real time ECT monitoring to observe the happening and progress of micro cracks during fatigue testing, which may has relation with the degradation of copper alloy.

References

[1] D.F. He, M. Tachiki, and H. Itozaki, Rev. Sci. Instru., **80** (2009), 036102.
[2] D.F. He, M. Shiwa, H. Yamawaki, M. Tachiki, H. Itozaki, S. Moria, T. Masuoka, and I. Uetake, Journal of JSNDI, **59** (2010), 510.
[3] D.F. He, M. Shiwa, J.P. Jia, J. Takatsubo, and S. Moriya, NDT & E International, **44** (2011), 438.
[4] D.F. He, M. Shiwa, J. Takatsubo, and S. Moriya, PIERS proceeding, (2011), 540.
[5] Data sheet of HMC1001, Honeywell.

Tenth International Conference on Flow Dynamics
November 25-27, 2013, Sendai, Miyagi, Japan

Evaluation of Cavity Defect in Metallic Foam with DCPD Method

Zhenmao Chen[1], Shejuan Xie[2], Xiaojuan Wang[1], Tetsuya Uchimoto[2], Toshiyuki Takagi[2]
[1] State Key Lab for Strength and Vibration of Mechanical Structures, Xi'an Jiaotong University, Xi'an, 710049, China
[2] Institute of Fluid Science, Tohoku University, Sendai, 980-8577, Japan
E-mail: chenzm@mail.xjtu.edu.cn

ABSTRACT

To predict the profile of a cavity defect in Metallic Foam (MF) material, the database type fast forward scheme is upgraded by introducing a kind of multi-medium finite element (MME) for the efficient simulation of DC potential drop (DCPD) signals of MF with volumetric defect of complicated shape. In addition, a code of the hybrid inversion strategy combining the neural network and the conjugate gradient optimization method is developed and validated to evaluate the size and position parameters of the cavity defect in a MF block.

1. Introduction

Metallic foam has potential applications in many engineering fields owing to its features such as super light, high specific strength etc. However, cavity defect of size exceeding permission may significantly weaken the MF material and structures. Quantitative nondestructive testing (QNDT) tools are necessary to guarantee the integrity of MF structures. DC potential drop (DCPD) method is considered as an important NDT technique for the quality assessment of MF material[1, 2]. To enhance the detectability of the DCPD for cavity defect in MF, efficient forward and inverse analysis of DCPD signal are very important.

In this work, the conventional fast forward scheme developed by authors [3] is updated based on the multi-medium finite element (MME) [4] to make it suitable for the DCPD signal simulation of MF with volumetric cavity defect, which in turn, is applied to the reconstruction of cavity defect of complicated shape. In addition, a hybrid inversion method combining neural network (NN) and conjugate gradient (CG) method [5, 6] is implemented for the reconstruction of cavity defect from the DCPD signals. Both verifications with numerical and experimental signals are conducted.

2. Numerical Methods

2.1 Upgrade of the fast scheme for DCPD problem

To deal with the signal simulation for MF with defect of complicated boundary by using a regular finite element mesh, a new kind of finite element covering different material zones, i.e., the MME, is introduced. As there is no local electric charge exists in the defect surface for the DCPD problem, this kind of element is suitable for the FEM simulation of DCPD signals.

A MME covers both air and base material (conductor) regions separated by the defect boundary. To efficiently calculate the element matrix $[K]_e$ of MME, an algorithm based on the classification of the gauss points is proposed. $[K]_e$ of MME can be calculated by summing up the values at the gauss points of defect region with

$$[K]_e = \sum_i \sigma(\mathbf{r}_i)\nabla N^T \cdot \nabla N, \qquad (1)$$

where $\mathbf{r}_i$ is the location vector of *i-th* Gauss point, $\sigma(\mathbf{r}_i)$ is the conductivity of the local material at the *i-th* Gauss point, N is the shape function. The summation is only conducted for the Gauss points in the defect region. Based on MME, a simulation code is developed to cope with the 3D defect of arbitrary shape.

For inverse analysis, lots of forward simulations are unavoidable, and a fast and accurate forward simulation tool is very necessary. For this purpose, the database type fast forward scheme is upgraded in this work by introducing MME to treat complicated defect.

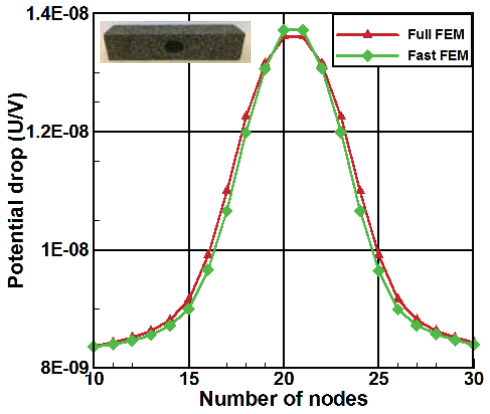

Fig. 1 Simulated signals of a MF block with a hole

The final discretized governing equations of the fast scheme for the DCPD signal simulation are

$$\{\varphi_{1f}\} = [H_{12}K'_{22}]\{\varphi_{20} + \varphi_{2f}\}, \qquad (2)$$

$$[I - [H_{22}K'_{22}]]\{\varphi_{2f}\} = [H_{22}K'_{22}]\{\varphi_{20}\}, \qquad (3)$$

where, the variables with subscript *'0'* represent the quantities of the unflawed field, and those with subscript *'f'* represent the perturbations due to defect, subscripts *1, 2* represent that the corresponding unknowns are of nodes related to the measure surface and the flaw regions respectively, $[H_{12}]$, $[H_{22}]$ are sub-matrixes of the inverse matrix $[H]$ ($[K_0]^{-1}$), $[K'_{22}]$ is the sub-matrix of $[K]$-$[K_0]$, where $[K]$ is the global coefficient matrix of the flawed structure. Once calculated $\{\varphi_{2f}\}$ with Eq.(3), $\{\varphi_{1f}\}$, the potential related to the measure surface, can be easily obtained with Eq.(2). In Eq.(2), (3), $[K_0]$, $[H]$, and $\{\varphi_0\}$ are independent of defect, and can be

pre-calculated and stored as databases, which enable a great reduction of numerical burden. Fig.1 shows an example of fast simulation code for a defect in MF block, which gives a good demonstration of the validity of the fast simulation method.

2.2 Hybrid inverse strategy with NN and CG

Taking advantages and drawbacks of both the deterministic optimization method and the stochastic method into consideration, the hybrid inverse strategy of the NN and the CG-based method is adopted to reconstruct the location and size parameters of cavity defect from DCPD signals. The NN method is adopted to reconstruct the location parameters, and an initial solution is selected for the CG method based on its results. In this way, the NN code is docked to the updated CG code to reconstruct the final defect profile.

1) Artificial Neural Network

A feed forward neural network is adopted to predict the location of the cavity defect. The input of the NN consists of feature parameters of the DCPD signals calculated with the updated fast scheme. The outputs are the location parameters of defect causing the corresponding DCPD signals. The feed forward NN contains a single hidden layer. The training process starts with only one hidden node, and for each training epoch a new node is created respectively. The PCA is also carried to concentrate the input information.

2) Hybrid Inverse Strategy

The hybrid scheme consists of the NN method and the improved CG-based deterministic method. In simulation, vector of the defect profile is denoted as $\{b\}=\{b_l,b_s\}$, with $\{b_l\}$ being the location, and $\{b_s\}$ being the parameter vector corresponding to the defect size. The reconstructed result of NN method is denoted as $\{b_{lNN}^*\}$ and is used as part of the initial solution for CG method as it may not be close to the true solution due to the feature of NN itself. In this way, the initial solution selected for CG method is $\{b^0\} = \{b_{lNN}^*, b_s^0\}$.

For the defect sizing, the first step has to establish the input and output data sets for network training. The data sets are established by calculating the DCPD signals due to defects of randomly selected locations and sizes. Once the input and output data sets of NN method are created, the hybrid inverse scheme can be realized with the following steps

(1) Reconstruct $\{b_{lNN}^*\}$ from $\{u^{exp}\}$ with NN method;
(2) Select the initial solution as $\{b^0\}=\{b_{lNN}^*, b_s^0\}$;
(3) Run the updated CG routine to get the final defect profile solution $\{b^*\}$.

3. Numerical Results

Case studies are conducted to investigate the numerical performance of the hybrid inverse scheme. Reconstructed results of the improved CG-based method with initial solutions randomly chosen or set based on the results of NN method are compared. For cases given here, the physical dimensions and mesh divisions of the modeled MF are 100 mm (20 elements) in both the x and y direction, 50 mm (10 elements) in z direction, and the location parameter vector is chosen as $\{b_l\}=\{x_0,y_0\}$. The results suggest that a better initial solution based on the result of NN method can help the CG method to find a better solution with less iteration.

Table 1 Reconstruction of Ellipsoid

		CG	NN-CG
Initial	x_0,y_0	0.0,0.0	5.0,15.0
	rx,ry,rz	5.0,5.0,5.0	5.0,5.0,5.0
Final	x_0,y_0	11.3,11.5	5.0,15.0
	rx,ry,rz	15.0,15.0,15.	15.0,14.5,13.1
Iterations		12	4

For an ellipsoidal defect located in the $z=0$ plane with $\{x_0,y_0\}=\{5.0,12.5\}$ and size $\{rx,ry,rz\}=\{12.0,15.0,12.5\}$, the result of NN method is $\{b_{lNN*}\}=\{5.,15.\}$. The reconstructed results of the improved CG-based method with and without the help of NN method are shown in Table 1. The results of the hybrid inversion method are better than that of the conventional CG method. In addition, the convergent speed of the hybrid code is also much faster than the conventional one. From these results, one can see how important an appropriate initial solution is for the CG method to solve the multi-valued optimization problem, i.e., hybrid method is efficient.

4. Concluding Remarks

In this paper, a DCPD sizing scheme for complex shaped cavity defect in MF is studied. At first, the database type fast forward scheme is updated by introducing MME for efficient calculation of the DCPD signals due to a complex-shaped defect, Secondly, the hybrid inverse scheme combining the NN method and the CG method is applied to the reconstruction of cavity defect in MF. The methods are validated with both the simulated and the experimental signals. The results suggest that the hybrid inverse method has better accuracy and can save simulation time.

Acknowledgements

The authors would like to thank the National Magnetic Confinement Fusion Program of China (2013GB113005), the NSFC (51277139, 11021202) and the 973 Program of China (2011CB610303) for funding this study. This work is also partially supported by the JSPS Core-to-Core Program, A. Advanced Research Networks, “International research core on smart layered materials and structures for energy saving”.

References

[1] S. Xie, T.Takagi, IJAEM, **33**(2010), 1253-1260.
[2] J.Zhang,Z.Chen,IEEE Trans. Mag,**48**(2012), 375-78.
[3] S. Xie,T.Takagi, IJAEM, **36**(2011), 339-353.
[4] X. Wang, Z.Chen, COMPEL, **23**(2014), in press.
[5] Z. Badics. ,J. NDE, **17**(1998), 67-78.
[6] S.Xie,T.Takagi,IEEE Trans. Mag,**49**(2013), 1653-56.

Tenth International Conference on Flow Dynamics
November 25-27, 2013, Sendai, Miyagi, Japan

Flow Control Attempts Using Smart Materials

Yu Fukunishi, Seiichiro Izawa
Mechanical Systems and Design, Graduate School of Engineering,
Tohoku University
fushi@fluid.mech.tohoku.ac.jp

ABSTRACT

This study reviews our recent work on flow controlling attempts using piezo-ceramic devices. Two flow fields are chosen as a target. One is the laminar/turbulent separating flows over a cavity and the other is the transitional boundary layer. In both cases, we try to control the flow fields using less energy as much as possible by making the use of flow characteristics such as the receptivity and the instability. Piezo actuators have the capability of controlling these flows; however there are some difficulties associated with the controlling attempt.

1. Introduction

Piezoelectricity is the electric charge that accumulates in certain materials in response to applied mechanical stress. Piezo actuators use this effect to convert electrical energy into mechanical energy such as force or displacement. We have used them to control flows aiming at suppressing the aerodynamic noise generated from a cavity and delaying the growth of instability waves in a transitional boundary layer. The both flows have been a subject of many investigations.

For the effective control of the flow fields, it is important to understand the characteristics of the target flows. For instance, the receptivity of cavity flows is very high at the separation point. Yokokawa et al.[1] succeeded to suppress the cavity noise by activating the actuators attached on the upstream edge of the cavity with the alternately different phases along the spanwise direction. Thus, the generated sound waves canceled each other in the far field. Okawa et al.[2] investigated the generation mechanism of velocity fluctuations near the piezo actuator attached on the wall in detail. They demonstrated that the incoming instability waves could be suppressed by the active feedforward control with a semi-automatic algorithm adjusting the control parameters. This study reviews our recent efforts of flow controlling attempts using piezo actuators.

2. Cavity Flow Control

All experiments were carried out in the closed circuit low-turbulence wind tunnels at the Institute of Fluid Science (IFS), Tohoku University. Figure 1 shows the cavity model used in the experiment. The model consists of a flat plate and a cavity. Incoming boundary layer was made turbulent using a tripping wire (ϕ = 0.6) and a sandpaper #80 attached to the surface. The velocity fields were measured by a hot-wire probe and the acoustic measurement were made using a 1/2-inch condenser microphone, placed 1m above the cavity. The thickness of turbulent boundary layer was approximately 7.5mm at the upstream edge of the cavity.

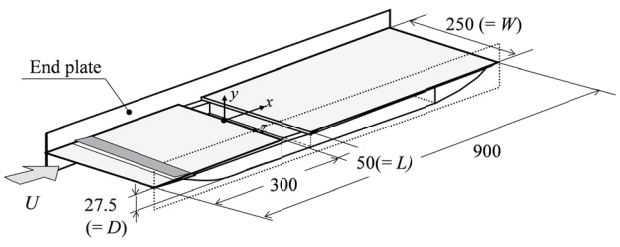

Fig. 1 Experimental setup (cavity flow)

An array of bimorph-type piezo actuators of 30mm in width, 25mm in depth and 0.5mm in thickness were installed inside the cavity, aligned in the spanwise direction, where the upper side of each actuator could move in the streamwise direction in a flapping motion because only the lower side half was fixed. The frequency of operating signals was chosen as the fundamental frequency of cavity flows, 532Hz at U = 30m/s. Several operating modes were tested: mode 1, 4 and 8 (single phase). Where, the mode number represents the number of neighboring actuators driven by the same signals. For example, in mode 1, the neighboring pair of pieces was manipulated 180 degrees out of phase.

Figure 2 shows the contour maps of velocity fluctuations in xz plane at y = 0. The data were obtained by the conditional-sampling and ensemble-averaging technique, where the sound signal was used as the reference signal. The broken lines in the figures indicate the boundaries of the actuator groups operated under the same signal. A two-dimensional fluctuation patterns

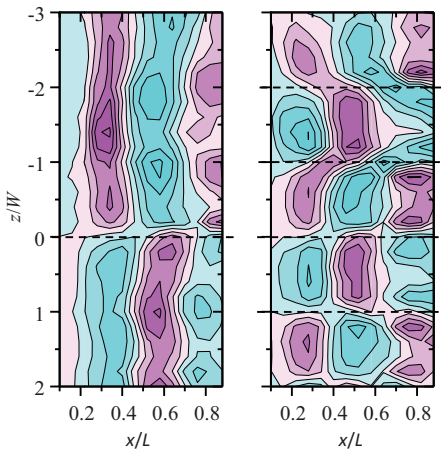

(a) Mode 1 (b) Mode 4

Fig. 2 Contour maps of u' in xz plane at y = 0. Contour interval is 0.03U.

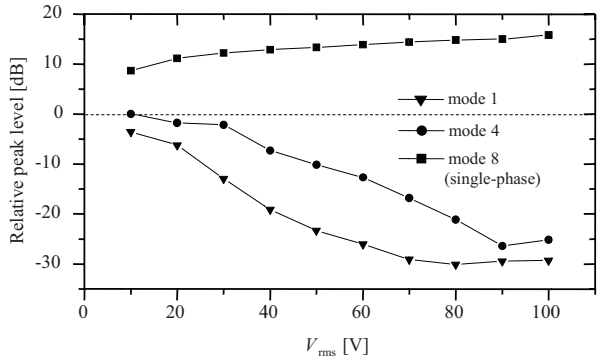

Fig. 3 Cavity noise suppression effect.

above the cavity can be clearly observed in the figure, whose signs alternately change in both the spanwise and the spanwise directions. This is because the timings of rolling up process are in phase with the actuators' motions.

The noise suppression effects of each mode are shown in Fig. 3. The horizontal axis is the rms value of voltage supplied to the actuators and the vertical axis is the peak level of the cavity noise relative to the case where there is no control. The cavity noise decreases in all modes, except for mode 8 (single mode). It is because in mode 8, all the actuators are moving in phase, enhancing the two-dimensionality. The maximum noise suppression effect was obtained when the spanwise scale is the shortest. Conclusion is that piezo actuators are surely useful as a control tool. However, they were not so effective in suppressing noise in a higher Reynolds number experiment.[3] The ratio between the relative moving distance of the actuators and the boundary layer thickness may be important.

3. Transition Control

Figure 4 shows the schematic views of the experimental setup for the transition control. A flat plate mounted in the middle of the test section had a leading edge of 36:1 ellipse to reduce receptivity there. The target instability wave was generated by a combination of a loudspeaker and a roughness element attached on the plate. The loudspeaker was operated at 77Hz, which was within the unstable regain of the neutral stability curve. The control device consisted of an array of hot-wire sensors upstream and piezo actuators downstream. When the sensors detected a wave, the driving signals for the actuators, optimized in amplitude and phase, were calculated and sent to the actuators. The sampling time was 12.6ms. The thickness of the device was 2mm. A piece of actuators had the dimension of 80×0.3×20mm. Each actuator was independently wire and could be controlled separately.

The control results are presented in Fig. 5. Strong stripe pattern is the target T-S wave. In the figure, the pattern becomes much weaker by the actuators. Through this feed-forward control, the maximum peak of the velocity fluctuations could be reduced by 75% measured

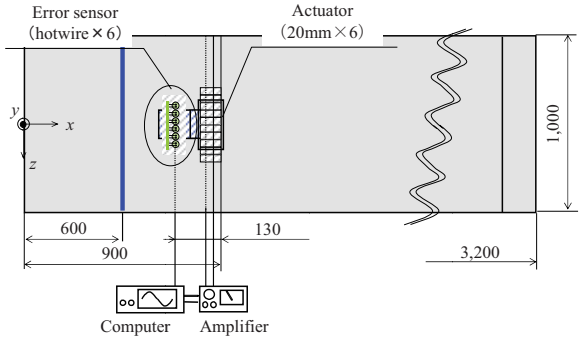

Fig. 4 Experimental setup (transition control)

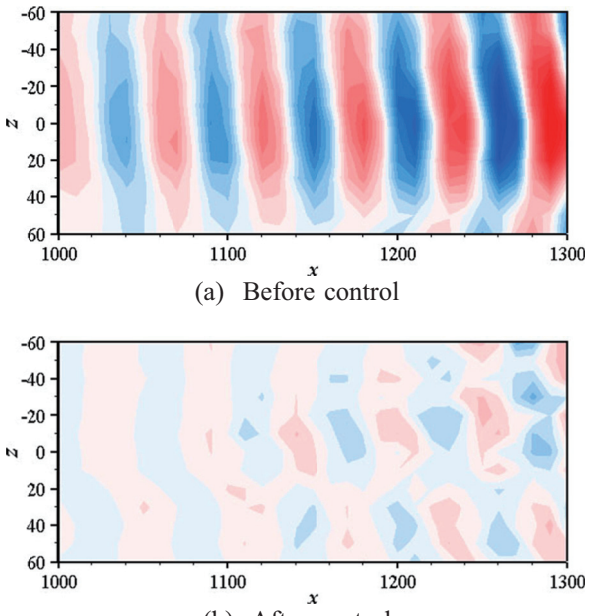

(a) Before control

(b) After control

Fig. 5 Ensemble averaged velocity fluctuation u'_{rms}.

at x = 1,000mm and z = -10mm. In the present method, the output timing of driving signals for the actuators had to be manually adjusted using the data of the preliminary experiment. And, the noise in the signals from the sensors caused serious trouble, especially against a target wave of multiple frequencies. Thus, the noise filtering is very important.

4. Concluding remarks

Two examples of the active flow control using piezo actuators were shown and problems were presented. The smart materials are very useful and promising tools for flow control, and there is still plenty of room for advancement in effectiveness and efficiency.

References

[1] Y. Yokokawa and Y. Fukunishi, Theor. Appl. Mech., **50** (2001), pp.281-287.
[2] H. Okawa et al., Proc. ASME-JSME-KSME Joint Fluid Eng. Conf. (2011), pp. 1-7.
[3] A. Izawa et al., Proc. JSME Ann. meeting, **8** (2003), pp. 140-142. (in Japanese)

Tenth International Conference on Flow Dynamics
November 25-27, 2013, Sendai, Miyagi, Japan

The Supercomputing of Fluid and Structure Interaction Caused by Natural Disasters

Jun Ishimoto
Institute of Fluid Science, Tohoku University, 2-1-1, Katahira, Aoba-ku, Sendai 980-8577, Japan
E-mail: ishimotojun@ieee.org

ABSTRACT

The fundamental characteristics of flotsam mixed tsunami are investigated by a new type of integrated super computation using ALE method (Arbitrary Lagrangian-Eulerian Method) and SPH method (Smoothed Particle Hydrodynamics Method). The fully hydrodynamic governing equations without shallow-water theory were used to calculate tsunami characteristics of water flow with flotsam and debris. Our ALE model predicted the effect of fluid-solid coupled interaction in a limited region, and the model predictions were favorably compared with the scale modeling analysis.

1. Introduction

The magnitude 9.0 earthquake (The Great East Coast Earthquake) hit off the Sendai coast area in Japan, March 11, 2011 and created a huge tsunami which claimed more than 20,000 lives. This high casualty number was partly caused by the enhanced destructive forces of the tsunami that contained floating debris and flotsam. This mixed effect of water and floating debris has not been accurately estimated by any currently existing conventional tsunami simulation models because they only estimate the impact force of single-phase water [1-3]. Our current model clearly showed that the destructive force was significantly enhanced by the leading wave and the outflow of flotsam as compared to a normal tsunami without floating debris and flotsams. To that end, we created a fully hydrodynamic approach model without shallow-water approximation to compute the flow characteristics of the mixed tsunami accompanied with flotsam and debris. In addition, we calculated the impact forces of the mixed tsunami acting on structures by the leading wave and the outflow by backwash of the flotsam against an ideal geometric structure placement. We are focusing on a relatively limited region to be analyzed, such as power plants and industrial plants, taking into account the interaction of the structure and the tsunami, fracture behavior and structural deformation. We are also developing a simultaneous simulation method for the flotsam mixed tsunami behavior of its interface causing deformation when in collision with structures. In addition, the scale modeling analysis for flotsam mixed tsunami is conducted and compared with numerical results.

2. Coupled computation (ALE-FEM)

For the first computation, the ALE method (Arbitrary Lagrangian-Eulerian Method) in application to the tsunami simulation with the FEM vehicle model for hydraulic collision analysis was used. Figure 1 (a) shows the schematic of computational model and vehicle FEM model. In the present computation, the Euler element is applied to analyze the hydrodynamic behavior of the tsunami getting over the breakwater, and FEM vehicle model is applied to analyze the collision behavior between vehicles and tsunami or between two vehicles. For the numerical condition, the height of the breakwater was 2.0 m and the initial velocity of tsunami was 5.0 m/s.

Figure 1 (b) shows the computational result of the tsunami behavior getting over the breakwater, and its attacking behavior of the two vehicles. The hydrodynamic impact behavior of the tsunami on the vehicles is reasonable simulated by the drifting behavior of the vehicles. It was found that the vehicles were covered by tsunami and were washed by the tsunami's inertia.

3. Tsunami behavior by SPH method

We constructed the SPH method to investigate the interaction between a tsunami and structures, and also to investigate the damage of a flotsam mixed tsunami on land structures. For the numerical modeling, we assumed the following mixed tsunami flow conditions.

- A flotsam or obstacle was carried away by the backwash of the first wave of the tsunami, and then pushed by a second wave of the tsunami.
- The flotsam went onto the shore and collided with the land structure.

To analyze these phenomena, we used the computational geometry which demonstrates two small tanks impacting a large tank. The tsunami wave was assumed to break down within collapsing rectangular water column as it collided with the small tank and began to move the small tank because of the impact force of the tsunami. These small tanks in the tsunami wave then collide with the large tank which is fixed to the ground. The small cylindrical tanks were assumed to be filled with oil, and were regarded as obstacles or flotsam within the tsunami with a slip boundary condition relative to the ground. The large cylindrical tank was fixed to the ground, and was assumed to be hollow (empty) with a shell thickness of 20 mm.

Figure 2 shows the SPH numerical results of the flotsam mixed tsunami. The flow characteristics and behavior of its interface deformation and collision with the land structures were clearly simulated.

Conclusion

Two different supercomputing approaches, including the ALE method (Arbitrary Lagrangian-Eulerian Method) and SPH method (Smoothed Particle Hydrodynamics

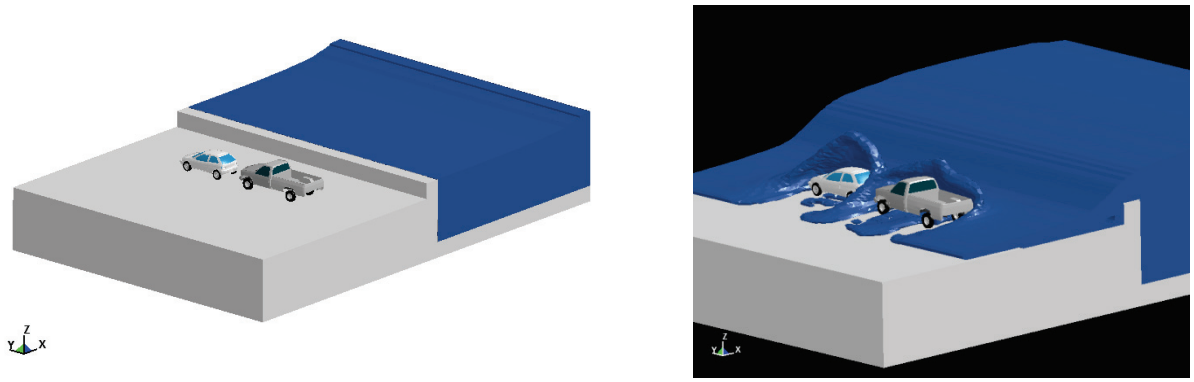

(a) Computational geometry and domain　　(b) Computational results

Fig. 1　Schematic of computational domain. Computational results of the tsunami behavior getting over the breakwater, and its attacking behavior on two vehicles (ALE method).

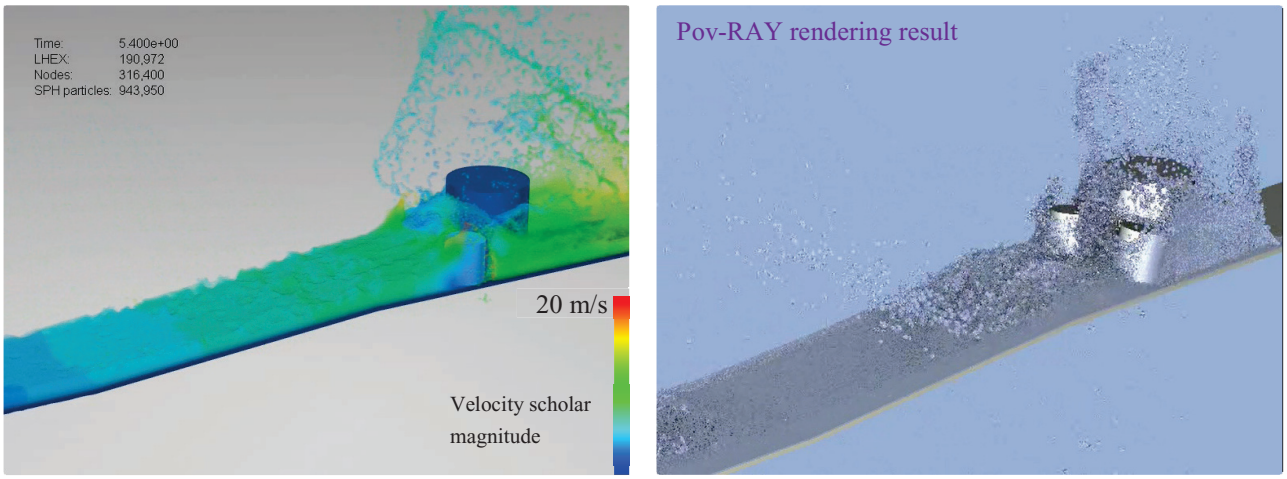

Fig. 2　Flotsam mixed tsunami flow characteristics, and behavior of its interface deformation and collision with a land structure by SPH method.

Method), were used to investigate flow characteristics of a flotsam mixed tsunami. The flotsam mixed tsunami behavior associated with interface deformation and collision with land structures was reasonably reproduced by the supercomputing methods.

References

[1] Goto, K., Takahashi, J., Oie, T., Imamura, F., ``Remarkable bathymetric change in the nearshore zone by the 2004 Indian Ocean tsunami: Kirinda Harbor, Sri Lanka,'' Geomorphology 127 (1–2): 107–116 (2011).

[2] Violeau, D, Fluid Mechanics and the SPH Method: Theory and Applications, Oxford Univ. Pr., Oxford, UK, 2012.

[3] K. Saito edited., Progress in Scale Modeling: Summary of the First International Symposium on Scale Modeling (ISSM in 1988) and Selected Papers from subsequent Symposia (ISSM II in 1997 through ISSM V in 2006), Springer, 2008.

Tenth International Conference on Flow Dynamics
November 25-27, 2013, Sendai, Miyagi, Japan

Reconstruction of Stiffness Coefficients in Orthotropic Plates Based on Lamb Waves Phase Velocities using Genetic Algorithm

Jinling Zhao, Jinhao Qiu* and Hongli Ji
State Key Laboratory of Mechanics and Control of Mechanical Structures,
Nanjing University of Aeronautics and Astronautics, Nanjing, 210016, China
E-mail: qiu@nuaa.edu.cn

ABSTRACT

In this paper, the reconstruction of all nine unknown stiffness coefficients of a unidirectional orthotropic plate is accomplished based on Lamb waves phase velocities using genetic algorithm. Laser-generation based imaging method is utilized to measure phase velocities accurately. In genetic algorithm, the forward problem of calculating phase velocities with given stiffness coefficients is programmed by higher-order plate theory. The reconstructed nine stiffness coefficients are utilized in a commercial FEM software, and the FEM nephograms of Lamb waves propagation turn out to be close to the experimental imaging results.

1. Introduction

There are different methods of measuring the elastic properties of materials. Conventional techniques like tensile, compressive and shear tests are destructive in nature. Ultrasonic techniques are qualified for nondestructive measurement of stiffness coefficients [1]. As with ultrasonic techniques, Lamb wave methods [2] are more advantageous than bulk wave methods [3] because bulk wave methods need separate samples while the Lamb wave methods are *in situ*.

Laser-generation based imaging (LGBI) method [4] is utilized to measure phase velocities based on the Reciprocity theorem. The laser scanning has higher spatial resolution than conventional transducer and makes experimental snapshots of high quality.

The second-order plate theory is much faster than 3-D elasticity theory [5] which gives the exact solutions and much more accurate than lower-order plate theories [6]. In this paper, the forward problem of calculating phase velocities with given stiffness coefficients is programmed with second-order plate theory.

The inversion is carried out through a genetic algorithm (GA) by minimizing the error function. A GA has been extensively used in reconstructing elastic moduli [7]. The reconstructed nine stiffness coefficients are substituted into commercial FEM software, and the FEM nephograms of Lamb waves propagation are close to the experimental imaging snapshots.

2. Method

Evolutionary computation techniques such as a GA are search algorithms based on the mechanism of natural selection. They are robust, conceptually simple and can be used in situations where the search space is complex to use traditional techniques.

An error function was defined as the square of the difference of the velocities that were measured and reconstructed (with assumed values of the stiffness coefficients):

$$Minimize \quad err(C)=\sum_{i=1}^{i=90}[v_i^r-v_i^m]^2 \tag{1}$$

where v^r is the calculated velocity, v^m is the experimentally measured velocity, and i is the index specifying the propagation direction.

The forward problem of calculating v^r with given stiffness coefficients is solved with a higher-order plate theory [8] with a displacement field as

$$\begin{cases} u=u_0(x,y,t)+z\varphi_x(x,y,t)+z^2\phi_x(x,y,t) \\ v=v_0(x,y,t)+z\varphi_y(x,y,t)+z^2\phi_y(x,y,t) \\ w=w_0(x,y,t)+z\varphi_z(x,y,t) \end{cases} \tag{2}$$

The displacement field in (2) depicts three anti-symmetric modes and five symmetric modes. The equations of motion of the higher-order theory can be derived using the principle of virtual displacement of Hamilton's principle. Substituting the displacement fields into the equations of motion leads to a characteristic equation, solution of which gives the phase velocity-frequency curves.

LGBI method is used to visualize Lamb wave propagation and measure experimental phase velocity v^m. Figure 1 shows a schematic illustration of the experimental apparatus for the LGBI method.

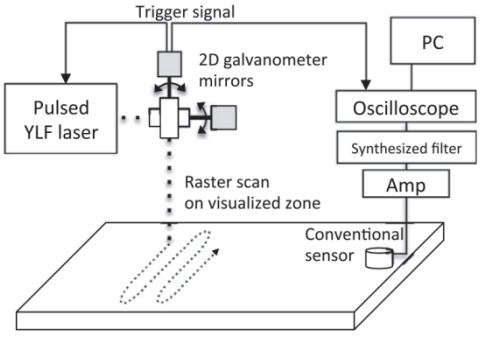

Fig. 1 Experimental apparatus for LGBI method

A pulsed YLF laser (λ=1053nm) was used for Lamb wave generation. The beam spot diameter on the surface is about 2 mm. A promising AE transducer positioned at the center of the scanning circle is used for detection. According to the Reciprocity theorem, the snapshot is identical to the waveform propagating from the transducer.

To obtain the phase velocities in the LGBI method, a position-time diagram is utilized by combing the time series of the snapshot data along a line across the transducer.

3. Results and Discussion

Figure 2 shows the position-time diagrams at 0.44MHz-mm of two different propagation directions in a unidirectional plate. It was clearly confirmed that two different Lamb waves exist. By applying least squares fitting (LSF) to the series of phase peaks, the phase velocities of the signals can be simply obtained as the slopes of the fitting lines.

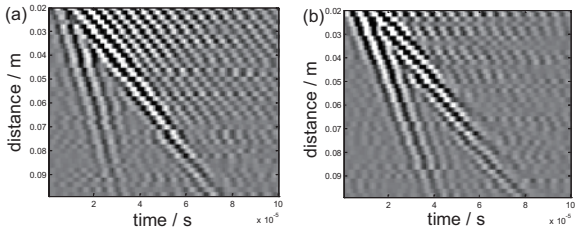

Fig. 2 The position-time diagram at 0.44MHz-mm: (a) propagation direction of 30°; (b) propagation direction of 90°.

The measured phase velocities of the unidirectional plate at 0.44MHz-mm are listed in Table 1. These velocities are substituted into (1) as v^m. And the reconstructed stiffness coefficients are shown in Table 2.

In order to prove the accuracy of the reconstructed stiffness coefficients, the experimental results are compared with the FEM results visually. In FEM simulation module, the stiffness coefficients of Table 2 are regarded as the inputted elastic properties and the receiving signals when laser scanned the center of circle (where the AE transducer is pasted) are imported as the load condition, as shown in Fig.3. The simulation nephograms and the experimental snapshots based on LGBI share similar wave fronts as in Fig. 4.

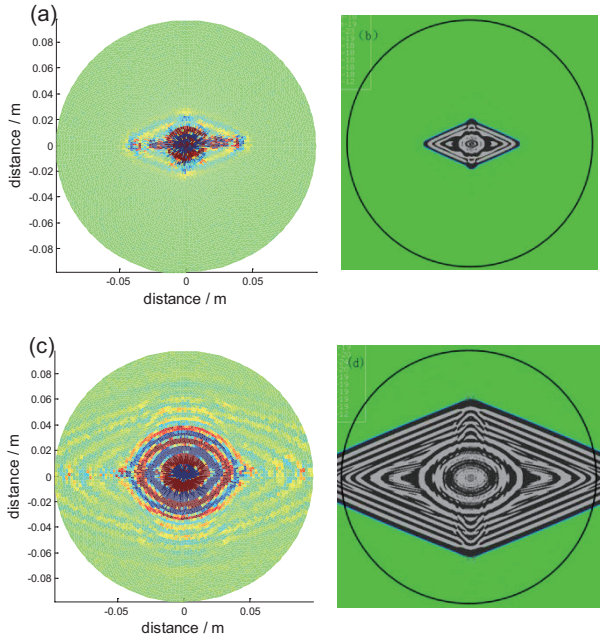

Fig. 4 The snapshots of Lamb waves propagation: (a) experimental snapshot at 10μs; (b) simulation snapshot at 10μs; (c) experimental snapshot at 30μs; (b) simulation snapshot at 30μs.

Table 1. Measured phase velocities of the unidirectional plate at 0.44MHz-mm

Angle/° v^m/(m/s)	0	10	20	30	40
A_0	1465	1366	1275	1190	1151
S_0	5885	5447	4158	3313	2827
Angle/° v^m/(m/s)	50	60	70	80	90
A_0	1033	1021	966	988	973
S_0	2249	2344	2767	2604	2507

Table 2. Reconstructed stiffness coefficients of the unidirectional plate (unit: GPa)

C_{11}	C_{12}	C_{13}	C_{22}	C_{23}	C_{33}	C_{44}	C_{55}	C_{66}
34.7	0.415	0.659	6.97	1.76	16.8	1.79	3.18	0.947

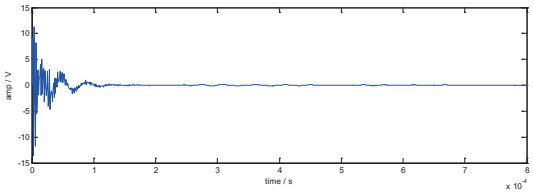

Fig. 3 The receiving signals of the center of circle (where the AE transducer is pasted).

4. Concluding remarks

GA based reconstruction of the nine stiffness coefficients of an orthotropic unidirectional plate is achieved using the exactly measured Lamb waves phase velocities based on LGBI method. FEM nephograms according to the reconstructed stiffness coefficients are similar to the experimental snapshots, which proves the reconstructed results are accurate.

Acknowlegements

We gratefully acknowledge support in this work from Funding of Jiangsu Innovation Program for Graduate Education (No. CXLX13_135) and the Fundamental Research Funds for the Central Universities. This work is also supported by PAPD.

References

[1]Nayfeh A H, Amsterdam: Elsevier (1995) .

[2]Staszewski W J, Lee B C, Mallet L and Scrapa F, Smart Mater. Struct.**13**(2004), R251.

[3]Castagnede B, Kwang Y K and Sachse W, J. Appl. Phys. **70**(1991), R150.

[4]J. Lee, J. Takatsubo, N. Toyama,Smart Mater. Struct. **16**(2007) ,R1025.

[5]Jinling Zhao, Jinhao Qiu and Hongli Ji, J. Intel. Mat. Syst. Str., Accepted(2013).

[6]Jinling Zhao, Jinhao Qiu and Hongli Ji, mart Mater. Struct., Submitted(2013).

[7]J Vishnuvardhan, C V Krishnamurthy and Krishnan Balasubramaniam, Smart Mater. Struct. **16** (2007), R 1639.

[8] Whitney JM and Sun CT, J. Sound Vib. **30** (1973) , R85.

Tenth International Conference on Flow Dynamics
November 25-27, 2013, Sendai, Miyagi, Japan

Development of the Functional Hard Carbon Coating for Machine and Structural Materials

Hiroyuki Miki[1], Takanori Takeno[2], Hiroyuki Kosukegawa[3], Toshiyuki Takagi[3]
[1]Frontier Research Institute for Interdisciplinary Sciences, Tohoku University, 6-3 Aramaki aza Aoba, Aoba-ku, Sendai, 980-8578, Japan
[2]Graduate School of Engineering, Tohoku University, Aoba 6-6-1, Aramaki, Aoba-ku, Sendai 980-8579, Japan
[3]Institute of Fluid Science, Tohoku University, 2-1-1 Katahira Aoba-ku, Sendai, Miyagi 980-8577, Japan
miki@fris.tohoku.ac.jp

ABSTRACT

In the design of a machine element and a system, control of friction and wear is a crucial issue to take into consideration. Lubrication using carbon-based hard films, such as Diamond-like Carbon (DLC) and diamond, has attracted attention as a method for novel lubricating technique. Recently many attempts have been made to fabricate functional coatings with good mechanical property using hard carbon coatings. In this paper, brief review of surface modification technique is presented and a novel concept of metal containing DLC as a functional coating and partly polished diamond films for dry friction coating are proposed.

1. Introduction

A present machine and system device are asked for achievement of saving resources, a simple system, and energy saving. It is also one of the purposes that these demands reduce the time, effort and cost of not only effective use of resources but maintenance management. Especially, the demand concerning maintenance management is increasing every year, and the part has turned into the social problem. We have previously answered to these by producing novel material and machine. As a result, they were enlarged and complicated, but this process has got into the relation of the trade-off to the actual purpose, such as a saving resources, a simple system, and energy saving.

As compared with this, "highly-efficiency" and "multi-functionalization" of the conventional system have been widely proposed as an important key in recent years. It is also important to improve the reliability and stability as a system. Consequently, development of the material which improves energy efficiency and reduces operation cost or the material which brings about the life of a mechanical system and improvement in reliability is important.

We are taking notice of the novel material producing method using the surface modification by thin film deposition. In this method, material surface is modified by a certain technique, but the performance of material improves without losing the characteristic of a base material. For example, the novel excellent surface property, such as low friction, abrasion proof, baking-proof, heat resistance, and corrosion-proof, is realized. As an example of surface modification, the method of the chemical reaction by certain gas and physical deposition of the metal, polymer and carbon, etc. is known widely.

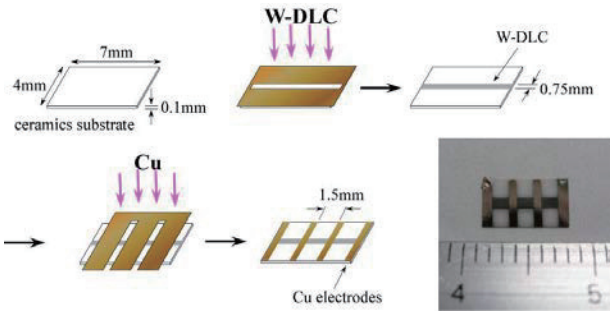

Fig. 1 Sensor module preparation procedure of MeDLC.

Hard carbon films or hard carbon coatings are a kind of those surface modification technique. These are actively investigated as the technology which makes the surface which has low friction and wear, and high durability.

In this paper, we present two latest researches which are related to the topics of "highly-efficiency" and "multi-functionalization" on hard carbon films.

1. Functional development of the Diamond-like Carbon containing a metallic cluster.

2. Development of low and the super-low friction under dry sliding on partially polished polycrystalline diamond

2. Functional development of the Diamond-like Carbon containing a metallic cluster.

Diamond-like Carbon containing (DLC) is amorphous carbon film, and there are some kinds, such as amorphous carbon (a-C), hydrogenated amorphous carbon (a-C:H) and tetrahedral amorphous carbon (ta-C). Wear resistance and low friction are the greatest features of DLC, and are used as surface finishing of a machine part or a tool.

In our research group, amorphous carbon coating containing nanocluster metal (Me-DLC) has been developed aiming at the functional improvement in DLC. The chemical vapor deposition (CVD) and DC magnetron sputtering are combined with the deposition processing on Me-DLC. Although a Me-DLC film is originally an insulator, the electrical resistance appears on Me-DLC from several mΩ/cm to kΩ/cm by adjusting the amount of additional metal. We have reported that Me-DLC can realize the low friction in a DLC/W-DLC multilayer [1] and good dynamic electrical contact with low friction in an Ir-DLC monolayer [2].

In addition, the sensing function of conductive Me-DLCs has received widespread attention not only because they have the ability to directly measure the

base material to change in electrical characteristics, but because they improve the above-mentioned mechanical properties in the host materials.

Recently, we proposed Molybdenum-containing DLC (Mo-DLC) as a fatigue sensor [3-6]. Fig. 1 shows the preparation procedure of a sensor module. As electric resistance on Mo-DLC increases in accordance with fatigue frequency, especially in high cyclic region [7], Me-DLC coating realizes the dynamic monitoring of a contact surface and static condition monitoring.

3. Development of low and the super-low friction under dry sliding on partially polished polycrystalline diamond

It is well known that a diamond film with a rough surface shows a high friction coefficient, and excessively wears the counter material. To reduce the friction and wear, it is necessary to polish the diamond surface or to deposit diamond with a smooth surface.

We have proposed a technique for obtaining a film with low friction and wear by partially polishing polycrystalline diamond (Fig. 2) [8, 9]. We clarify the dry low friction characteristic [10] and the phenomenon in which a coefficient of friction will fall rapidly if sliding speed becomes fast [11]. In the research, we have succeeded in acquiring the excellent sliding characteristic by making a specular surface part and fine asperity intermingled by polishing. In the sliding of a polishing diamond, mixture to fluid lubrication transition phenomenon is occurred by the dilute air flow between diamond with fine asperity and counter material. Friction is reduced by the lift force induced by the gas molecules flowing through a gap, resulted from numerical calculation by a direct simulation Monte Carlo (DSMC) method [12, 13].

4. Concluding remarks

The advanced features of two hard carbon films as the kinds of surface modification technique which improves durability and wear resistance are reported. One is functional development in Me-DLC aiming at the novel functionality by conductivity, and another is development of the polished polycrystalline diamond which aimed at the large improvement in the friction wear characteristic under dry condition.

These are multifunctional coating which have the features, such as a simple structure and low cost, and fully have the practical applicability.

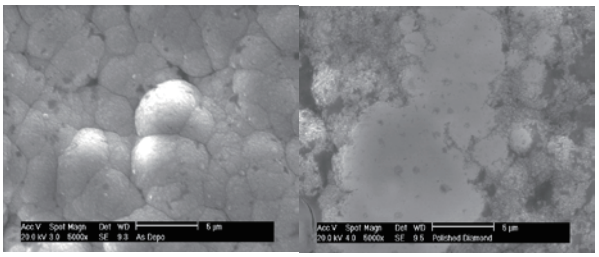

Fig. 2 SEM images of (left) as-deposited micro crystalline diamond film and (right) partly polished diamond film (Ra= 0.2μm).

Acknowledgements

This work was partly supported by a Grant-in-Aid for Scientific Research (A) (23240638), the JSPS Core-to-Core Program, A. Advanced Research Networks, “International research core on smart layered materials and structures for energy saving” and Grant-in-Aid for Challenging Exploratory Research (23656113, 25630032), the Promoted Research program from the Frontier research Institute for Interdisciplinary Science, Tohoku University and the Asahi Glass Foundation in Japan. Authors are thankful to Mr. Takeshi Sato from the Institute of Fluid Science, Tohoku University, Japan, for his technical assistance.

References

[1] H. Miki, T. Takeno, T. Takagi, Thin Solid Films, **516** (2008), pp. 5414-5418.

[2] H. Miki, K. Ito, T. Sugawara, J. Fontaine, T. Takeno, M. Ruet, M. Belin, K. Adachi, T. Takagi, Tribology Online, **4** (2009), pp. 60-65.

[3] T. Takeno, H. Miki, T. Sugawara, Y. Hoshi, T. Takagi, Diamond and Related Materials, **17** (2008), pp. 713-716.

[4] T. Takagi, T. Takeno, H. Miki, Materials Science Forum, **638-642** (2010), pp. 2103-2108.

[5] T. Ohno, T. Takeno, H. Miki, T. Takagi, International Journal of Applied Electromagnetics and Mechanics, **33** (2010), pp. 665–671.

[6] T. Ohno, T. Takeno, H. Miki, T. Takagi, Diamond & Related Materials, **20** (2011), pp. 651–654.

[7] P. Wang, T. Takagi, T. Takeno, H. Miki, Sensors and Actuators A, **198** (2013), pp. 46-60.

[8] T. Abe, T. Takagi, Z.M. Sun, T. Uchimoto, J. Makino, H. Hashimoto, Diamond and Related Materials, **13** (2004) pp. 819-822.

[9] S. Konoplyuk, T. Abe, T. Takagi, T. Uchimoto, Diamond and Related Materials, **16** (2007), pp. 609-615.

[10] H. Miki, N. Yoshida, K. Bando, T. Takeno, T. Abe, T. Takagi, Diamond and Related Materilas, **17** (2008), pp. 868–872.

[11] H. Miki, A. Tsutsui, T. Takeno, T. Takagi, Diamond and Related Materials, **24** (2012), pp. 167–170.

[12] I. Nakamori, T. Takagi, T. Takeno, T. Abe, T. Uchimoto, Y. Kohama, Diamond and Related Materilas, 14 (2005) pp. 2122-2126.

[13] S. Yonemura, M. Yamaguchi, T. Takeno, H. Miki, T. Takagi, AIP Conf. Proc, **1084** (2008), p. 1153-1157.

Promoting Energy-saving with Diamond-Like Carbon Coatings: Solid Lubrication Processes

Julien Fontaine[1)], Hiroyuki Miki[2)], Takanori Takeno[3)], Thierry Le Mogne[1)], Sandrin Bec[1)], Michel Belin[1)], Koshi Adachi[3)], Toshiyuki Takagi[4)]
1) Laboratoire de Tribologie et Dynamique des Systèmes, CNRS UMR 5513, Ecole Centrale de Lyon, 36 Avenue Guy de Collongue, 69134 Ecully Cedex, France
2) Frontier Research Institute for Interdisciplinary Sciences, Tohoku University, 6-3 Aramaki aza Aoba, Aoba-ku, Sendai, 980-8578, Japan
3) Graduate School of Engineering, Tohoku University, Aramaki asa Aoba 6-6, Aoba-ku, Sendai, 980-8579, Japan.
4) Institute of Fluid Science, Tohoku University, 2-1-1 Katahira, Aoba-ku, Sendai, 980-8577, Japan.
Julien.Fontaine@ec-lyon.fr

ABSTRACT

Metal-containing diamond-like carbon films are proposed as a novel coating. Cu-DLC was deposited and characterized for optimization. The mechanical and tribological behaviors of the films were investigated in various conditions, and good electrical conductivity, low friction and wear, and high durability were verified. It is quite similar to the one of silver- or iridium-containing amorphous carbon coatings, tibofilm buildup of metal-containing amorphous carbon coatings could be a key to achieve low friction.

1. Introduction

Friction has large influence on machine performance, durability and energy efficiency. At the point, friction reduction is important technique indispensable to a mechanical system.

Lubricating oil is generally used for friction reduction of a sliding system. Although oil lubricating system is simple and stable, the problem is recently pointed out in the field of high-performance machine. In the case of a micromachine, the viscosity of lubricating oil is resisting to a drive portion, and leads to performance decrement. Because of the lubricating oil evaporation, oil lubrication to an aerospace instrument is also restricted. For that reason, the material which has sufficient lubricity in solid form is required.

Among solid lubricants, Diamond-like Carbon (DLC) coatings are currently very popular; thanks to low friction and good wear resistance in various environments. However, they exhibit unfavorable characteristics such as very low electrical conductivity, high sensitivity of friction coefficient to the sliding environment, and so on. In order to further extend the capabilities of DLC coatings, development of so-called "doped DLC" has been achieved, thanks to the versatility of DLC deposition techniques. In this study, innovative metal-DLC (Me-DLC) nanocomposite coatings are developed, and their tribological behavior is investigated under various environments and contact conditions.

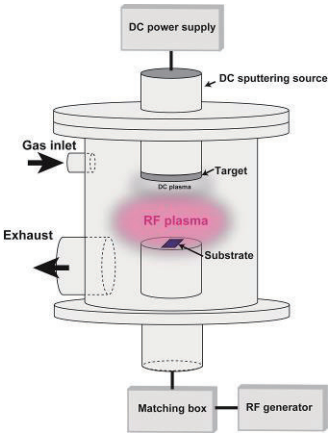

Fig. 1: Schematic view of combination of CVD and sputtering deposition system.

Several metals are considered in earlier study: tungsten [1,2], iridium [3], platinum, silver [4]… Nevertheless, Cu-DLC have been more extensively studied: it has been shown that not only a relatively low and stable friction of 0.15-0.2 could be achieved, but also that such friction coefficient was relatively insensitive to environment (ambient air or ultra-high vacuum) and to initial theoretical contact pressure (0.5 and 1.4 GPa). It has been also evidenced previously that a copper-rich tribofilm was formed on the contacting surfaces. The understanding of the unusual tribological behavior of Cu-DLC requires the study of the growth and the evolution of such tribofilm, and especially of its mechanical properties.

2. Method

Me-DLC nanocomposite coatings are deposited by a hybrid process, combining radio-frequency plasma enhanced chemical vapor deposition (RF-PECVD) for the DLC matrix and magnetron sputtering for the metal inclusions (Fig. 1). Acetylene (C_2H_2) gas was used as a precursor gas for amorphous carbon matrix. The

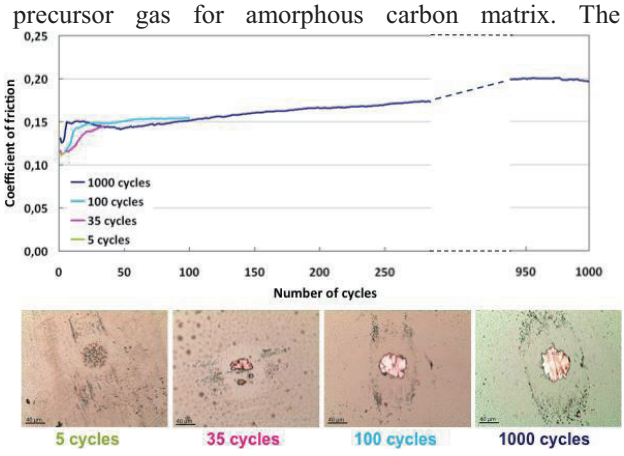

Fig. 2: Evolution of coefficient of friction for a Cu-DLC coating and optical observations of the tribofilms formed on the ball counterface for 5, 35, 100 and 1000 sliding cycles.

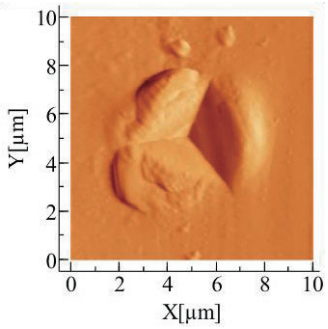

Fig. 3: Error signal by AFM on an indent on 1000 cycles tribofilm, revealing large pile-up phenomenon.

deposition of Cu-DLC coating has been performed with a power of 50 W on sputtering Cu target, and the C_2H_2 precursor gas flow rate at 0.7 sccm.

This Cu-DLC coating was then studied on an ambient air tribometer with reciprocating motion of 3 mm at a sliding speed of 2 mm/s. 52100 bearing steel balls (diameter: 6 mm) were used under a normal load of 1 N corresponding to a theoretical maximum contact pressure of about 0.6 GPa. The rubbed surfaces were then studied by nanoindentation with a berkovich diamond tip and by Atomic Force Microscopy (AFM).

3. Results and Discussion

The evolution of friction coefficient for experiments stopped at 5, 35, 100 and 1000 cycles is plotted on figure 2, with optical images of the corresponding tribofilms formed on the ball counterface in inset. For less than 50 sliding cycles, the friction coefficient increases from about 0.12 to 0.15. Although a tribofilm can indeed be observed as early as 5 cycles, it is not covering the entire contact area. However, after about 50 sliding cycles, the evolution of the friction coefficient is rather slow and increasing very slowly from 0.15 to 0.2. The tribofilms after 100 and 1000 cycles look both smooth and continuous, covering the entire apparent contact area.

Nanoindentation experiments were then conducted on the tribofilms obtained after 100 and 1000 cycles. In order to improve the processing of the load-displacement curves, AFM was also performed on the tribofilm, in an attempt to evaluate the tribofilm thickness and in order to measure piling-up around the indents. Indeed, it is paramount to check the contact area between the berkovich indenter and the probed material to properly compute Hardness and Young's modulus.

Table 1: Material constants by nanoindentation on an indent on 100 and 1000 cycles tribofilm.

	Cu-DLC coating	Tribofilm 100 cycles	Tribofilm 1000 cycles
Thickness	400 nm	400 nm	200 nm
Young's modulus	50 GPa	55 GPa	55 GPa
Hardness	3.5 GPa	1.3 GPa	1.8 GPa

Nanoindentation results are gathered in the table 1. As the tribofilms consist mostly of copper, it is not surprising that their hardness is lower than the nanocomposite Cu-DLC itself. Nevertheless, the hardness measured on the tribofilms is 3 to 4 times larger than the value expected for pure copper, which would be about 0.4 GPa. Interestingly, the tribofilm after 100 cycles is thicker than after 1000 cycles, while its hardness is significantly lower. Such increase in hardness could thus account for the increase in friction, and could be explained by shear-induced hardening.

4. Concluding remarks

The tribological behavior of Me-DLC strongly depends on the growth and evolution of a metal-rich tribofilm formed on the counterface. In the case of Cu-DLC, an unusually hard copper-rich tribofilm is found on the counterface. Its hardness evolution seems correlated with the friction evolution.

Acknowledgement

This work was partly supported by a Grant-in-Aid for Scientific Research (A) (23240638), the JSPS Core-to-Core Program, A. Advanced Research Networks, "International research core on smart layered materials and structures for energy saving" and the Promoted Research program from the Frontier research Institute for Interdisciplinary Science, Tohoku University. Authors are thankful to Mr. Takeshi Sato from the Institute of Fluid Science, Tohoku University, Japan, for his technical assistance.

References

[1] H. Miki, T. Takeno, T. Takagi, Thin Solid Films, **516** (2008), pp. 5414-5418.

[2] T. Takeno, T. Sugawara, H. Miki, T. Takagi, Diamond & Related Materials, **18** (2009), pp.1023-1027,.

[3] H. Miki, K. Ito, T. Sugawara, J. Fontaine, T. Takeno, M. Ruet, M. Belin, K. Adachi, T. Takagi, Tribology Online **4** (2009) , pp. 60-65.

[4] T. Takeno, H. Saito, M. Goto, J. Fontaine, H. Miki, M. Belin, T. Takagi, K. Adachi, Diamond & Related Materials **39** (2013), pp. 20–26.

Nondestructive characterization of flake graphite cast iron by Magnetic Adaptive Testing

Gábor Vértesy[1], Tetsuya Uchimoto[2], Toshiyuki Takagi[2] Ivan Tomáš[3]
[1]Research Centre for Natural Sciences, Institute of Technical Physics and Materials Science,
Budapest, H-1525 Budapest, P.O.B. 49, Hungary
[2]Institute of Fluid Science, Tohoku University, 2-1-1 Katahira, Aoba-ku, Sendai, 980-8577, Japan
[3]Institute of Physics, Academy of Sciences of the Czech Republic, Na Slovance 2, 18221 Praha, Czech Republic
E-mail of corresponding author: vertesy.gabor@ttk.mta.hu.

ABSTRACT

Three series of flake graphite cast iron samples were investigated by the method of Magnetic Adaptive Testing. The flat samples were magnetized by an attached yoke, and sensitive descriptors were obtained from the proper evaluation, based on the measurements of series of magnetic minor hysteresis loops, without magnetic saturation of the samples. Results of the non-destructive magnetic tests were compared with the destructive mechanical measurements of Brinell hardness and linear correlation was found between them.

1. Introduction

Cast iron is one of the most frequently used industrial construction materials. Low cost of production, good machinability, and excellent possibilities of shaping the details by casting attract an intense interest of industry. The mechanical properties are fundamentally dependent both on the matrix and on the graphite, its shape, size and density [1]. One of the types of cast iron, flake graphite cast iron, is an ideal material for automobile brake disks since it has excellent damping properties just because of the flaky graphite.

A nondestructive inspection of construction materials made of cast iron is highly desirable. Several methods exist for this purpose, e.g. ultrasonic technique, eddy current testing, measurement of electromagnetic properties such as conductivity and permeability. An alternative, sensitive and experimentally friendly approach to this topic has been considered recently, based on magnetic minor loops measurement. The survey of this technique can be found in [2]. The method, called Magnetic Adaptive Testing (MAT) was presented, which introduced general magnetic descriptors to diverse variations in non-magnetic properties of ferromagnetic materials, optimally adapted to the just investigated property and material. MAT was successfully applied for characterization of material degradation in different specimens and it seems to be an effective tool e.g. for replacement of the destructive hardness measurements.

In our previous works [3-5] magnetic characteristic parameters of a system of minor loops, measured on a series of ductile cast iron samples, were analyzed, and their sensitivity was evaluated. The flat samples were magnetized by an attached yoke and sensitive parameters were obtained from the series of minor loops, without magnetic saturation of the samples, which characterize well the samples' structure. The purpose of the present work is to investigate flake graphite cast iron samples by MAT, and to find correlation between nondestructively measured magnetic parameters and destructively determined Brinell hardness

2. Samples

Three flake graphite cast iron materials with chemical compositions listed in Table 1 were prepared.

Table 1. Chemical composition of the flake graphite cast iron samples (values in wt%)

Sample	Chemical composition							CE
	C	Si	Mn	P	S	Cr	Ti	(%)
CE4.7	3.77	2.78	0.78	0.025	0.015	0.029	0.015	4.71
CE4.1	3.36	2.15	0.69	0.018	0.010	0.014	0.011	4.08
CE3.7	3.13	1.66	0.72	0.017	0.020	0.038	0.010	3.69

Their carbon equivalent (CE) values were defined by:

$$CE = \text{mass }\%\text{C} + \frac{1}{3}(\text{mass }\%\text{Si} + \text{mass }\%\text{P})$$

and were controlled to produce various graphite shapes and sizes. These metals were designated as CE4.7, CE4.1 and CE3.7 based on their targeted CE values. Pig iron (4.09%C, 0.89%Si, 0.07%Mn, 0.019%P, 0.012%S, 0.016%Cr, 0.003%Ti), ferrosilicon (Fe-75%Si), electrolytic iron and electrolytic manganese were used as raw materials and were melted using a high frequency induction melting furnace at 1743 K. Ferrosilicon (Fe-75%Si) was also used as an inoculant. The melts were poured into moulds made by the CO_2 gas process to produce the columnar bars with a length of 60 mm and a diameter of 46 mm. Later each bar was cut into disks of 10 mm thick. The disks were subjected to two kinds of heat treatments: annealing (AN) to obtain a ferrite based matrix and normalizing (NR) to obtain a pearlite-based matrix. The annealed and normalized disks were heated at 850°C in a furnace for one hour and then either cooled in the furnace or in air for AN or NR, respectively. The as-cast, normalized and annealed materials were designated AS, NR and AN, respectively. We thus produced 9 flake graphite cast iron materials with various matrices and graphite shapes as shown in Table 2. After grinding the specimen surfaces, their Brinell hardness HB (HBW 10/3000) was measured and it is listed in Table 2. These hardness values indicate that the normalizing and annealing treatments were successful in producing the pearlitic and ferritic matrices, respectively.

3. Results and Discussion

MAT degradation functions of all the investigated samples were evaluated and those, optimized for

description of the studied dependences, were considered as functions of Brinell hardness. The results for the three different materials are given in Fig. 1. Here each graph within the same figure represents one composition (CE4.7, CE4.1 and CE3.7) and the type of heat treatment (as cast - AS, furnace cooling - AN, air cooling - NR) is also indicated. In every case the MAT parameters are normalized by the corresponding value of the sample within the same series, which has the lowest HBW value.

Table 2. Schedules of heat treatment and Brinell hardness (HBW)

Material	Base metal	Heat treatment	HBW
CE4.7AS	CE4.7	NA (As-cast)	100
CE4.7AN	CE4.7	850°C×1h, furnace cooling	89
CE4.7NR	CE4.7	850°C ×1h, air cooling	130
CE4.1AS	CE4.1	NA (As-cast)	183
CE4.1AN	CE4.1	850°C ×1h, furnace cooling	110
CE4.1NR	CE4.1	850°C ×1h, air cooling	209
CE3.7AS	CE3.7	NA (As-cast)	207
CE3.7AN	CE3.7	850°C ×1h, furnace cooling	130
CE3.7NR	CE3.7	850°C ×1h, air cooling	221

The three graphs in Fig. 1 show the connection between magnetic parameters and Brinell hardness within the same series (the same chemical composition) of the samples. Different heat treatments result in different values of hardness.

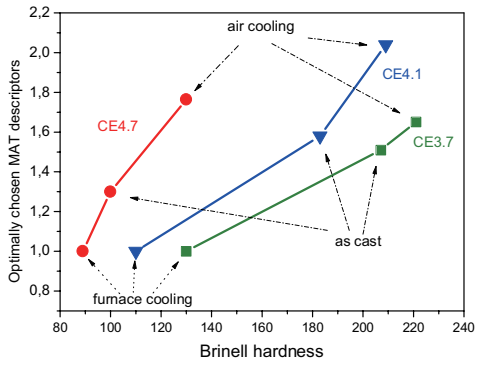

Fig. 1 Optimally chosen MAT degradation functions of the three sample series vs. Brinell hardness.

However, the hardness (and simultaneously the magnetic parameters) are also modified depending on chemical composition, if the samples are made by the same procedure. The best MAT degradation functions vs. Brinell hardnes, optimized for the as cast samples, are shown in Fig. 2.

As it is seen in the figures, closely linear correlation was found between the optimized MAT degradation functions and Brinell hardness in all the investigated cases. It was applicable if the influence of heat treatment was investigated within the same series of the samples (the same chemical composition) – Fig. 1, and also, if the influence of chemical composition was studied for different as cast samples – Fig. 2. This confirms the fact that magnetic hardening follows the mechanical hardening very well and that Magnetic Adaptive Testing is a powerful tool for the nondestructive determination of this hardening.

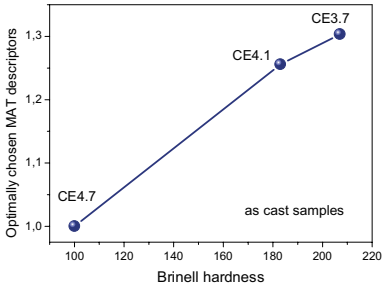

Fig. 2 Optimally chosen MAT degradation functions for the as cast samples vs. Brinell hardness.

4. Concluding Remarks and Acknowledgements

MAT was applied for three series of flake graphite cast iron, where different heat treatments were applied within the series. Close-to-linear correlation was found between the MAT parameters and the mechanical hardness. As a consequence, Magnetic Adaptive Testing proved to be an experimentally friendly and sensitive method for nondestructive tests of the cast iron structure.

One of the co-authors (I.T.) appreciates financial support by the project No.TA02011179 of the Technical Agency of the Czech Republic.

References

[1] C.F. Walton and T.J. Opar (Eds.), Iron casting handbook, Iron Casting Society, Inc., New York, 1981.

[2] I.Tomáš, G.Vértesy, „Magnetic *Adaptive Testing*“, in Nondestructive Testing Methods and New Applications, M.Omar (Ed.), ISBN: 978-953-51-0108-6, (2012), InTech: http://www.intechopen.com/articles/show/title/magnetic-adaptive-testing.

[3] G. Vértesy, T. Uchimoto, T. Takagi, I. Tomáš, O. Stupakov, I. Meszaros, J. Pavo, Physica B, 372 (2006), 156

[4] G. Vértesy, T. Uchimoto, I. Tomáš, T. Takagi, „Nondestructive characterization of ductile cast iron by Magnetic Adaptive Testing“, J.Magn.Magn. Mater. 322 (2010) 3117-3121.

[5] I. Tomáš and O. Perevertov, “Permeameter for Preisach approach to materials testing”, *JSAEM Studies in Applied Electromagnetics and Mechanics 9*, ed. T.Takagi and M.Ueasaka, IOS Press, Amsterdam, p. 5., 2001.

OS9: International Symposium on Innovative Energy Research

Tenth International Conference on Flow Dynamics
November 25-27, 2013, Sendai, Miyagi, Japan

On the Path to Effective Energy Production by Heat and Mass Return Combustion Technologies

Sergey Minaev[1], Kaoru Maruta[2],
[1]FEFU, School of Engineering Sciences, Vladivostok, Russia
[2]Institute of Fluid Science, Tohoku University, Sendai, Japan
E-mail of corresponding author: minaevss@yahoo.com

ABSTRACT

Development of eco-friendly and effective hydrocarbon fuels burning methods for material production of renewable power engineering is vitally important in transition period from traditional to renewable power energy. The main goals of the combustion research in Far-Eastern Federal University and in IFS Tohoku University are to develop clean and efficient energy conversion technologies and to train highly qualified specialists in this field. The research activities are concentrated on fundamental development of effective and ecofriendly methods of hydrocarbon fuels burning and co-production combustion technologies based on direct use of combustion heat in production of power consuming materials and other applications. Three main research directions on the vital up-to-date problems are outlined.

1. Introduction

Future energy needs will be associated with a paradigm shift from the current economy of large scales to the economy of modularity, increased safety, and convenience. This diversified and decentralized power production may have better economic prospects with the collateral benefit of improved national security in case of a disaster. The solution of this problem is possible through:

- development of effective eco-friendly small-scale power engineering;
- raise of the over-all efficiency of energy sector by co-production of heat, electricity and commercial products;
- decrease of energy consumption in the industries through application of effective methods of gas burning;
- development of new methods of burning low caloric fuels and lean gases.

Besides, there is a demand for micro-chemical system such as on-board hydrogen reactors, micro scale effective sources of electricity on the basis of combustion that are lighter, and longer lasting than existing battery, small-sized heat sources with combustion, production of new materials for the energy sector, for example new SHS (Self propagating High temperature Synthesis) porous materials, as well as materials for hydrocarbon fuel reforming and purification. Three main research directions on the vital up-to-date problems are outlined.

2. Flammability limits in systems with heat and mass recirculation

New clean-energy technologies reducing greenhouse effect may be based on controlled burning of lean gas mixtures, hydrogen or bio-fuels in the “excess enthalpy” combustors [1]. In particular, the lack of knowledge on combustion mechanisms and flame stabilization in the systems with heat and mass recirculation hampers the progress in further developments of “mild” or HiCOT, high temperature oxygen combustion technologies that allow reduction CO_2 emission and increasing efficiency of industrial power plants. This leads to the further requirements of fundamental studies on the combustion with a large amount of CO_2 and the absence of nitrogen at elevated temperature and pressure. Theoretical and experimental study (including experiments in microgravity conditions) of these processes would fill a gap in our knowledge about reduced chemical reactions kinetic mechanism, transport processes, radiative heat losses and dynamics of the self-fragmented (or sporadic) combustion waves [2]. Developed models of dynamical behavior of combustion waves in meso- and microchambers, sporadic and “flameless” regime combustion waves as well as reduced kinetic models of gas combustion will facilitate developing of efficient engineering computations. Numerical simulation of combustion processes in practical devices is faced considerable difficulties due to a big variety of physical parameters, a large range of spatial and temporal scales involved, and a complexity of chemical reactions kinetic mechanism, transport processes and structure of reacting gas flow. Solution of these problems requires a significant computational cost, and in many cases, these tasks can be solved only by the next generation of computers. At the same time, the calculation using the hierarchy of relatively simple models based on the reduced kinetics and transport processes enables qualitatively description of the phenomena in the wide range of problem parameters with appropriate accuracy.

3. Micro combustion technologies

The second research direction (micro combustion technologies) constitutes investigations related with micro combustion and co-production combustion technologies based on the direct use of combustion heat in production of power consuming materials, fuel reforming, food industry and other applications omitting electric power generation stage. Nowadays creation of small sized, light and cheap power sources for energy supplying in portable and autonomous communications devices such as control equipment for oil- or gas- pipe lines, transmitters, see beacons, etc. is actual task [3]. The advantage of micro combustion sources of electricity using direct heat to electricity conversion and operating with cheap fossil fuels, would be manifested in their fast charge, running on various hydrocarbon fuels regardless their quality and in the use of mass production techniques for its assemblage. Another

applications of micro combustion technique are micro reactors for hydrocarbons reforming producing hydrogen [4,5], micro burners heat sources. Development of heat sources with adjustable thermal and power characteristics will allow replacing electrical heaters by cheaper gas heaters in industry, for instance, in production of power consuming materials, and in other industrial and domestic applications. In addition to the high efficiency these heat sources have to possess good environmental characteristics, in particular, low NO_x emission and absence of open flame. Burning of ultra lean mixtures and admissible from ecological point of view content of combustion products make possible indoor safety use of such sources. While heat of combustion is extensively used in large scale industrial applications for heat sources, it is difficult to utilize combustion-based heaters for middle or much smaller scale heating purposes since combustion is unstable in nature at smaller scales due to large surface-to-volume ratio. Instead, huge numbers of electric heaters are used in various industrial fields. Swiss roll micro combustor heater with ±1 K temperature controllability created by group of Prof. K. Maruta [6] is an example of possible overcoming of these difficulties.

The systems for technical diagnostics of hydrocarbon fuels may be based on micro channel technologies. New diagnostic techniques will be applied to determine the chemical reaction mechanisms of combustion of fuels extracted from biomaterials and biomass thermal conversion as well as biodiesel fuels surrogates. The diagnostic is based on the spatial structure analysis of the combustion wave stabilizing in the micro channel with a controlled temperature gradient of the walls under ultra low flow rate conditions. This combustion regime was first predicted theoretically [7] and then experimentally verified [8] by authors of the paper. Based on this diagnostic compact and inexpensive on-board sensors determining fuel octane number, fuel quality sensors, devices for determining the self-ignition temperature, etc. may be created.

4. Energy release dynamics in porous media

The third direction (energy release dynamics in porous media) is dedicated to development of clean combustion technologies on the basis of safe to handle and effective radiation burners, new porous material on the basis of SHS (self-propagating high-temperature synthesis) for advanced combustion technologies and hydrocarbon fuels reforming, development of methods for prevention and elimination of natural and man-caused disasters, associated with appearance of combustion and other energy-release sources in porous objects of different origin and configuration. For example, high efficiency as well as combustion management, control and pollutants reduction may be realized in the burners made of new porous SHS materials (http://dsm.tomsk.ru/working/).

The problem of gas combustion in porous media using a discrete representation of the porous medium as a set of individual channels coupled to each other by heat and mass transfer can be regarded as an extension of problems of combustion in micro channels. At the same time, the gas combustion in inert porous medium has its own peculiarities associated with the collective interaction of flames inside the porous carcass and with the effects of the radiative heat transfer and flow features. Currently there are no sufficiently developed models of flame stabilization under the surface of the porous body and on the border of two different porous media, models of radiation heat transfer and its effect on the flame structure in the novel high porosity and fine cellular porous media, models describing thermal stress and deformation of porous bodies induced by gas combustion, models of thermo acoustic phenomena under the filtration gas combustion, nonlinear models of combustion instability in the porous media and formation of spatially localized combustion spots.

5. Concluding remarks

For realization of outlined research plan the efforts of international research teams focused at the solution of joint problems are needed. The research teams would be able to produce synergy effect needed for such complex tasks.

Our research teams have a more than 10 years history of successful research collaboration and we believe that such way of collaboration allows development of new ecologically safe methods of energy production and give out a fundamental knowledge.

Acknowledgements

This work was supported by IFS Collaborative Research Program, and FEFU's Research program № 13-06-0222.

References

[1] Lloyd S.A. and Weinberg F.J., **257**, Nature (1975), 367.
[2] Fursenko R., et al., Proc. Combust. Inst. **34** (2013), 981.
[3] Fernandez-Pello A.C., **29**, Proc. Combust. Inst., (2002), 883.
[4] Kim N.I., K. Maruta K. et al., **141** Combustion Flame (2005) 78.
[5] Schoegl I., J. Ellzey J., **32** Proc. Comb. Inst.(2009) 3223.
[6] Maruta K., **33** Proc. Combust. Inst. (2011) 125.
[7] Maruta K., J. K. Park J.K., Oh K.C., Fujimori T., Minaev S., Fursenko R., Combust. Explosion and Shock Waves, **40** (2004), 516.
[8] Maruta K., Kataoka T., Kim N.I., Minaev S. and Fursenko R., Proc. Combust. Inst. **30** (2005), 2429.

Modelling Hydrogen-Air Flames With Reduced Two-Step Kinetic Mechanisms

Vladimir Gubernov
P.N.Lebedev Physical Institute of the Russian Academy of Sciences
E-mail vvg@spmlab.phys.msu.su

ABSTRACT

In this work we investigate the speed and structure of laminar combustion wave propagating in the rich-hydrogen air mixture. The two-step reduced kinetic mechanisms are employed in order to model the reaction of hydrogen oxidation in air. The analysis is based on numerical calculations employing both the constant and variable density models with the use of either own numerical algorithms or FlameMaster code. The results are compared with the data from the detailed kinetic calculations. It is demonstrated that the two-step reduced kinetic models are capable to reasonably well predict the speed and structure of hydrogen-air flames.

1. Introduction

Although, to date there is a good understanding of the hydrogen oxidation chemistry [1, 2]. there is still a lack of short reduced mechanisms for modeling the problems with multi time and length scales. One of the first models [3] of the H_2-O_2 combustion included the deficient component, O_2, and H as the only radical involved. In [4] the steady-state approximation for O, OH and HO_2 was adopted and a similar model was derived and investigated for rich hydrogen-oxygen flames. In [5] the two-step reaction mechanism was further developed and tested against numerical calculations with detailed mechanism. The inclusion of HO_2 radical results in the two-step model introduced by Linan as reported in [6]. In a number of papers [7-11] the detailed kinetic mechanism was also used to numerically investigate the premixed hydrogen flame propagation near the rich flammability limit.

In this work we employ the two-step reduced kinetic mechanism in order to model rich hydrogen-air flames. The results of our numerical calculations are compared with available experimental and numerical data obtained with the detailed kinetic calculations.

2. Method

We consider adiabatic model for freely propagating rich H_2-air flame that includes 2 steps: chain branching $3H_2+O_2 \rightarrow 2H_2O+2H$ and recombination $H+H+M \rightarrow H_2+M$. According to [6, 8] when the burning temperature is not too high the concentrations of O, OH, and HO_2 are small, the elementary reaction related to them can be considered to be in steady states. The steady state equations are then used in order to obtain the rates of the gross branching and recombination reactions ω_I and ω_{II}. The conservation equations for mass fraction of species, Y_i, and temperature, T, can be written as

$$\mu \frac{dY_i}{dx} - \frac{d}{dx}\left(\frac{\lambda}{c_p L_i} \frac{dY_i}{dx} \right) = m_i$$

$$\mu c_p \frac{dT_i}{dx} - \frac{d}{dx}\left(\lambda \frac{dT}{dx} \right) = q_I \omega_I + q_{II} \omega_{II} \quad ($$

where μ is mass flow, λ, and c_p is the thermal conductivity and specific heat, L_i is the Lewis number.

The governing equations with appropriate boundary conditions are solved numerically using the shooting and relaxation methods. The results are then compared with the data obtained form the detailed kinetic calculations conducted with the FlameMaster code as well as available data from literature.

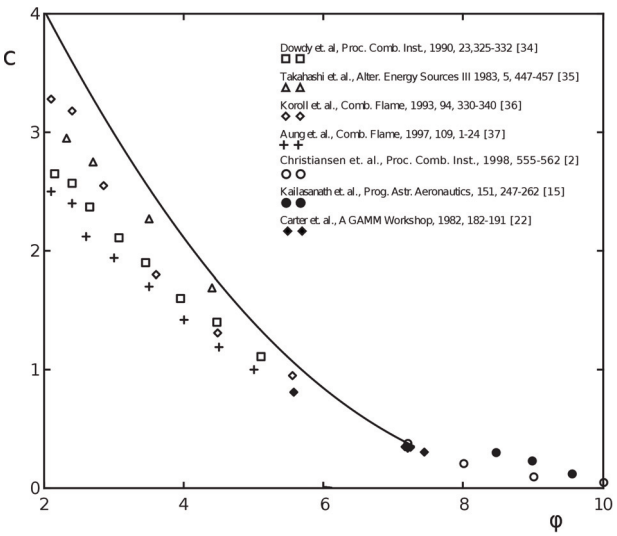

Fig. 1. Dependence of the speed, c, in m/s of the combustion wave on the equivalence ratio.

3. Results and Discussion

The governing equations are solved numerically. The results of the analysis are presented in figure 1 where the dependence of the flame speed, c, on the equivalence ratio of the mixture is plotted. The symbols in figure 1 correspond to data from the literature as referred in figure inlet. As seen in figure the calculated prediction for the flame speed agrees with the data obtained earlier and cited in the figure.

The structure of the combustion wave is also investigated both with the use of the reduced model and detailed kinetics calculations. It is demonstrated that the distribution of H radicals, temperature and O_2 are well approximated by the reduced model.

We also investigate how the variation of initial temperature and pressure of the mixture affects the propagation velocity. Results of both approaches argee well.

4. Concluding remarks

To summarize, our investigation of the reduced

models shows that they are suitable for the analysis of the combustion wave propagation in the rich hydrogen air mixtures in the laminar flow conditions. We plan to further verify the model against different pressure conditions in our future investigations.

References

[1] P. Saxena, F. A. Williams, Combust. Flame 145 (2006) 316–323.
[2] M. O. Conaire, H. J. Curran, J. M. Simmie, W. J. Pitz, C. K. Westbrook, Int. J. Chem. Kin. 36 (2004) 603–622.
[3] Y. B. Zeldovich, Kinetika i kataliz 2 (1961) 305–318.
[4] G. Dixon-Lewis, Proc. R. Soc. A 298 (1967) 495–513.
[5] F. Mauss, N. Peters, B. Rogg, F. A. Williams, in: N. Peters & B. Rogg (Ed.), Lecture Notes in Physics, Berlin Springer Verlag, 1993, volume 15 of Lecture Notes in Physics, Berlin Springer Verlag, pp. 29–43.
[6] P. Clavin, Prog. Energy Combust. Sci. 11 (1985) 1–59.
[7] E. Christiansen, C. Sung, C. Law, Proc. Combust. Inst. 27 (1998) 555 – 562.
[8] L. He, P. Clavin, Combust. Flame 93 (1993) 391–407.
[9] K. Kailasanath, K. Ganguly, G. Patnaik, in: Prog. in Astronautics and Aeronautics, vol. 151, AIAA, Washington DC, 1993, pp. 247–262.
[10] G. Goyal, U. Maas, J. Warnatz, Combust. Sci. and Tech. 105 (1995) 183–193.
[11] N. R. Carter, M. A. Cherian, G. Dixon-Lewis, in: N. Peters, J. Warnatz (Eds.), Numerical methods in Laminar Flame Propagation: A GAMM Workshop, Vieweg, 1982, pp. 182–191.

Tenth International Conference on Flow Dynamics
November 25-27, 2013, Sendai, Miyagi, Japan

Experimental and Numerical Investigation of CH4/CO2/O2 Laminar Inverse Diffusion Flames

Nichiki Okada, Shuhei Yoneyama, Tomohiro Yamanaka, Toshihisa Ueda and Takeshi Yokomori
School of Science for Open and Environmental Systems, Keio University,
3-14-1 Hiyoshi, Kohoku-ku, Yokohama-shi, Kanagawa-ken, 223-8522, Japan
noble_sun@a8.keio.jp

ABSTRACT

Laminar inverse diffusion flames in CO_2 and N_2 atmosphere were investigated experimentally and numerically. Chemiluminescence and soot radiation were weakened both in CO_2 and N_2. However, CO_2* luminosity was much higher in CO_2. This result implies that some reaction roots and intermediate species related to CO_2 were significantly affected in CO_2. It is also found that CO and H_2 were produced mainly in the downstream region of the reaction zone due to the thermal decomposition. In this area, more CO was generated with increasing the fuel concentration because the thermal decomposition was easily occurred in this situation.

1. Introduction

CO_2 recirculated oxy-fuel combustion is one of the key technologies to reduce the levels of CO_2 emissions from the combustion. In this combustion, the mixture of pure oxygen and CO_2 is used as an oxidizer, so that the flue gas is composed only CO_2 and water vapor without N_2. This makes it possible to capture and sequestrate CO_2 easily. Although some authors reported that the abundant presence of CO_2 instead of N_2 affects the combustion characteristics such as the flame temperature and chemical reactions, there have been a few fundamental studies of them [1].

So far, the turbulent combustion has mostly used in the industrial scenes, and it will be also applied to CO_2 recirculated oxy-fuel combustion. However, the effects of CO_2 in the turbulent combustion are difficult to be studied directly, because of their complicated behaviors such as the wrinkled flame shape and the unsteady motion. The study of simple laminar flames which modeled local conditions of turbulent flames provides a better opportunity to explore the turbulent combustion. In this study, therefore, we adopted the co-flowing laminar inverse diffusion flames (IDFs) which corresponded to one of segments of the turbulent flame, where oxidizer is surrounded by fuel (Fig. 1) [2].

From the above, we experimentally and numerically investigate the chemiluminescence, soot radiation and distributions of temperature and incomplete combustion species mole fractions of laminar IDFs in CO_2 and N_2.

2. Experimental and Numerical Methods

The co-annular IDF burner which consisted of inner and outer tubes with 10 mm and 30 mm in diameter was used in this study (Fig. 2). Oxygen and methane were used as oxidizer and fuel, and they were diluted with CO_2 or N_2. The concentrations of diluted oxygen and fuel, x_o and x_f, were varied from 0 to 100 %. Their mean flow velocities, V_o and V_f, were fixed at 0.2 m/s.

To measure the chemiluminescence and soot radiation, the flame emissions were corrected with a collimating lens (Ocean Optics; 74-UV) and it was guided to a spectroscope (Ocean Optics; USB2000+) with an optical fiber (P400-2-UV/VIS). The distribution of the soot radiation was taken by CCD video camera with 680 nm long-pass filter.

The numerical simulations of two-dimensional axisymmetric IDFs in CO_2 were performed with ANSYS Fluent version 14.5. GRI-Mech 3.0 without N reactions (36 species, 217 reactions) was used for methane oxidation [3]. In addition, we added CO_2*, CH_2O* and OH* chemiluminescence reactions (49 reactions), thermodynamic and transport data to the GRI-Mech reaction mechanism [4, 5, 6].

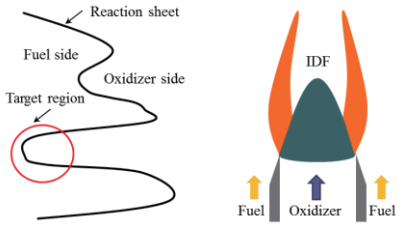

Fig. 1 Schematic of Flames (a) wrinkled turbulent reaction sheet, (b) inverse diffusion flame.

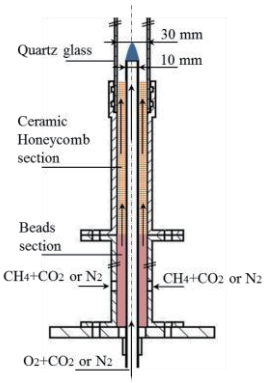

Fig. 2 Schematic of inverse diffusion flame burner.

3. Results and Discussion

Flame emission spectra at the flame tip measured by spectroscope for various x_f diluted with CO_2 and N_2 are shown in Fig. 3. In this figure, all emission spectra are standardized by OH* emission peak (306 nm) observed at the condition of x_o, x_f = 50 % in CO_2. There exists a peculiar broad band emission from 450 to 800 nm, which is from CO_2* (340 - 650 nm) [7] and soot (350 - 800 nm) [8]. This emission indicates the difference of IDFs between CO_2 and N_2. In the case of N_2, especially x_f =70 and 90 %, the peak can be observed near 650 nm, while CO_2, especially x_f =50 and 70 %, the peak cannot be observed near 650 nm but can be observed near 490

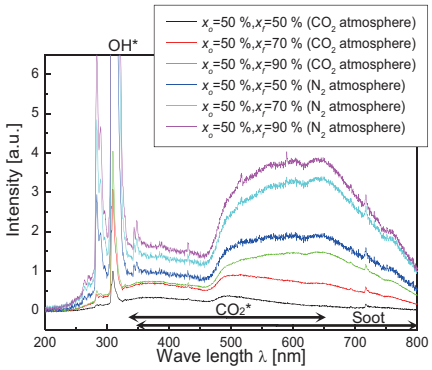

Fig. 3 Flame emission spectra at the tip of IDFs.

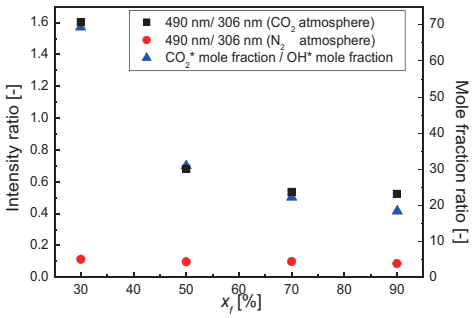

Fig. 4 Emission intensity ratio and mole fraction ratio between CO_2* and OH*, obtained from the experiment and the numerical simulation, respectively.

nm. The former peak corresponds to the soot radiation and the latter corresponds to CO_2* chemiluminescence [7, 8]. In CO_2 atmosphere, both emissions were weakened. This supposes that the flame temperature was decreased and the reaction became weakened in CO_2 because CO_2 has high specific heat and radiation emissivity. However, abundant presence of CO_2 supposed to produce much CO_2* so that its luminosity was relatively higher than soot radiation and made a peak near 490 nm. This tendency is also found in Fig. 4, which shows the intensity ratio of the peak CO_2* luminosity (490 nm) to OH* luminosity (306 nm). From the figure, the ratio was much higher in CO_2 atmosphere than in N_2. Since OH* chemiluminescence could be one of indexes of reaction strength, this result implies that some reaction roots and intermediate species related to CO_2 were significantly affected in CO2 atmosphere.

Figure 4 also shows the mole fraction ratio between CO_2* and OH* in CO_2 obtained from the numerical simulation. The trend qualitatively agrees well with the emission intensity ratio measured in the experiment, so that this result supports the above explanation.

Figure 5 shows the temperature and the mole fraction distributions at $x_o = x_f = 50$ % diluted with CO_2 obtained from the numerical simulation. From the figure, CO and H_2 were produced mainly in the downstream region of the reaction zone (the dotted line indicates the reaction zone height). These results indicate that most of generated CO and H_2 do not pass through the reaction zone and they are exhausted as they are, in the IDFs. This area is called a dark zone [2]. In this area, the thermal decomposition was occurred and a large amount

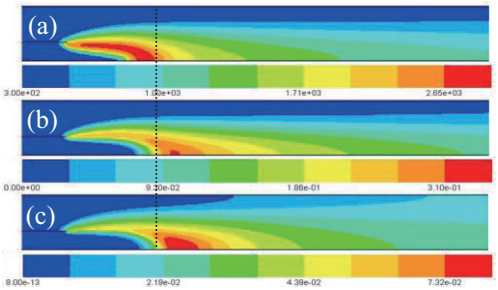

Fig. 5 Distributions of (a) temperature, (b) CO and (c) H_2 mole fractions.

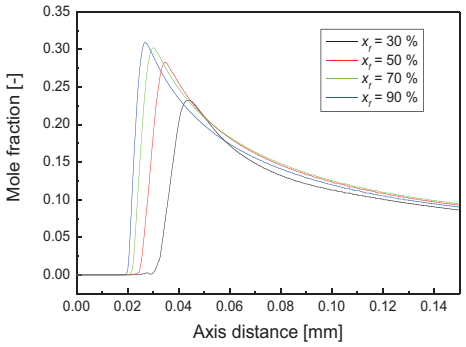

Fig. 6 CO mole fraction distributions at the burner axis.

of incomplete combustion species were exhausted. Figure 6 shows CO mole fraction profiles on the burner axis. From the figure, more CO was produced when x_f became higher. With increasing x_f, the flame temperature was increased and the flame height was decreased. In this situation, the fuel gas was highly heated and the thermal decomposition was easily occurred.

In this paper, the numerical results were showed only in CO_2 atmosphere. The difference of the characteristics between CO_2 and N_2 atmospheres is still investigating and it will be showed in the near future.

4. Concluding remarks

CO_2* chemiluminescence was much higher in CO_2 than in N_2 due to the abundant presence of CO_2. This indicates that CO_2 influenced some chemical reactions and changed them. CO and H_2 were produced mainly in the downstream of the flame zone and much CO was produced with increasing the fuel concentration in CO_2.

References

[1] S. Seepana, S. Jayanti, Fuel, **93** (2012) pp.52-58.
[2] K.T. Wu, et al., Proc. Combust. Inst, **12** (1984) pp.1925-1932.
[3] T. Lu, et al., Progress in Energy and Combust. Science, **35** (2009) pp. 192-215.
[4] M. Kopp, et al., Appl. Phys. B, **107** (2012) pp.529-538.
[5] J.M. Hall, et al., Int. J. Chem. Kinet, **38** (2006) pp.714-724.
[6] E. Goos, et al., Report ANL 05/20 TAE 960 (2011).
[7] S.B. Gupta, et al., Proc. Combust. Inst. **33** (2011) pp.3131-3139.
[8] Y. Ikeda, et al., Proc. Combust. Inst. **30** (2005) pp.391-398.

Tenth International Conference on Flow Dynamics
November 25-27, 2013, Sendai, Miyagi, Japan

SHS Materials Radiative Porous Burners

Alexander Kirdyashkin[1], Anatoly Maznoy[1], Alexander Gushin[1], Sergey Minaev[2]
[1]Department of Structural Macro kinetics Tomsk Scientific Center SB RAS, Tomsk, Russia
[2]FEFU, School of Engineering Sciences, Vladivostok, Russia
E-mail of corresponding author: maznoy_a@mail.ru

ABSTRACT

Nowadays the development of eco-friendly and effective hydrocarbon fuels burning methods is vitally important. The solution of this problem is possible through development of clean combustion technologies on the basis of new SHS (self-propagating high-temperature synthesis) porous material for advanced combustion technologies and hydrocarbon fuels reforming. For example, high efficiency as well as combustion management, control and pollutants reduction may be realized in the burners made of new porous SHS materials. Method of self-propagating high-temperature synthesis was applied for production of porous penetrable materials. The organization of filtrational gas combustion inside of the porous SHS materials allows design effective radiative burners.

1. Introduction

Filtrational gas combustion method is characterized by high ecological compatibility and simplicity of applying for heat-and-power engineering systems. The method uses premixed air/fuel gas combustion inside inert porous medium (converter).

During combustion the converter' outlet surface warms up over 1300 K, which creates intensive infrared radiation (Fig. 1). This method of heat conversion into radiation requires materials with outstanding properties. Porous materials composed of intermetallic, metal-oxide and nonoxide compounds obtain outstanding properties such as strength, high-temperature and corrosive wear resistance, high thermal and electro conductivities etc.

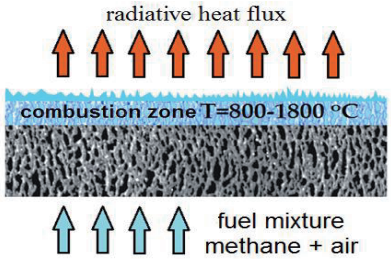

Fig. 1. Scheme of filtrational gas combustion method

New technologies for advanced porous material production have been developed in Tomsk Scientific Centre, Siberian Branch Russian Academy of Science. All technologies are based on the method of self-propagating high-temperature synthesis (also known as «combustion synthesis», SHS).

2. SHS-method and SHS porous materials properties

The SHS-method is based on the use of combustion processes for the production of inorganic materials. In the course of SHS a high-temperature combustion wave propagates through specially manufactured powder sample. The wave converts initial powder mixture into products without external energy consumption. A wide range of intermetallic, ceramic, cermet products with specified chemical composition, structure, porosity, size and shape can be synthesized by the SHS-method.

Technological advantages of the SHS method are the following:

1. high rate of processing,
2. simplicity and cheapness of equipment used,
3. significant reduction of energy consumption in comparison to conventional sintering in high-temperature furnaces.
4. method ensures high ecological parameters in the course of materials' production.

Change of the combustion synthesis conditions (such as addition of nano-size components, fixation of nonequilibrium phase, variation of metal-oxide composites etc.) allows to obtain materials with different phase compositions and porous structures (anisotropic, gradient, periodic etc.), which are not achievable by conventional methods of production (Fig. 2).

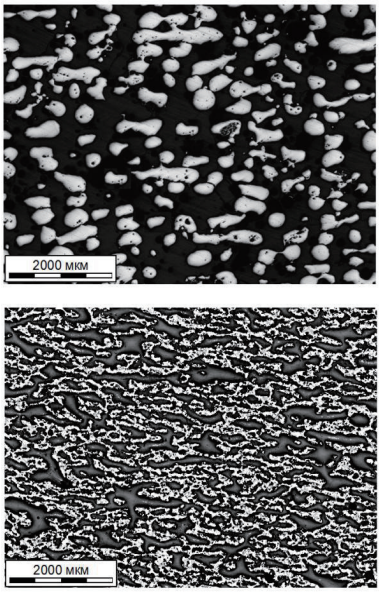

Fig. 2. Cross sections of porous SHS materials.

Due to such features of the method as fast chemical and physical processes, high rate of self-heating, high thermal gradient in the wave and others, the SHS-method allows to synthesize products with unique

structural properties (table 1, Fig.3). In particular, the conducted investigations of SHS combustion wave instability and peculiarities of nonstationary SHS regimes, such as spin or "scintillation" regimes, allows design porous media with variable porosity and structures of micro channels.

Table 1. Properties of porous SHS materials for radiating burners

Porous SHS materials for radiating burners		
Nonoxide compounds and compositions		Ni-Al, Ni-Ti, Ti-C, Mo-Si etc.
Metall-oxide compositions		Al_2O_3-Fe-Ti-Si-C
Porosity		40-70%
Size of porous channel		10-1000 μm
Compressive strength		Up to 30 MPa
high-temperature stability		Up to 1300 K
Geometrical parameters of synthesized items:		
Plate	thickness	Up to 40 mm
	length, width	Up to 500 mm
Pipe	diameter	Up to 400 mm
	length	Up to 1500 mm
Sphere	diameter	Up to 200 mm

3. Radiative porous burners

The developed SHS materials radiative porous burners have the following characteristics:

1. The intensive radiation flux can reach up to 50 W/cm^2
2. The heat power can be raged from 3 kW to 3 MW. Up to 70 % of combustion energy can be converted into infrared radiation flux.
3. Reduction in fuel consumption per unit of radiant energy is up to 30-40%.
4. Low NO_x emission in the combustion products is detected (less than 36-33 mg/m^3).
5. There is possibility of power control within wide range (0.05-100% from maximal thermal power).
6. SHS porous materials have good resistance to thermal shock and thermal cycling.
7. The burning of low calorific fuels, such as biogas, syngas, landfill gas etc., is possible.
8. The use of porous burners allows dramatically decrease steel intensity of power systems by reducing the furnace volume and the convection heat exchanger.

The advantages of new radiative porous over traditional porous burners are elevated temperature of the porous carcass resulting in very intensive radiative flux [1]-[3]. Porous burners made of SHS materials can be used in energy companies, shipbuilding and aviation companies (heating metal structures). The prototypes of infrared radiation sources were created through the use of gas combustion in metal-ceramic porous media with variable porosity. A sample of effective 2MW radiation burner on the basis of SHS materials was developed. (see Fig.3). (http://dsm.tomsk.ru/working/). Along with the study of filtrational gas combustion in porous SHS materials, the methods of new SHS materials synthesizing are developing too. These materials will find applications as gas and liquid media filters, heat regenerators in "flameless" burners and others. Potential applications of the new type of radiative porous burners are metal constructions contactless heating, production hardening, heating before stamping, heat sources in living quarters and food industry, etc.

Fig. 3. 2MW radiative burner on the base of SHS materials.

4. Concluding remarks

In TSC SB RAS have been developed advanced radiating burners on the base of porous SHS-converters, which can be used for heating, warming up, drying in many devises such as boilers, infrared heaters, vapor generators, drying chamber etc. Further development of SHS materials porous burners needs in fundamental knowledge about filtrational gas combustion in porous media with radiative heat transfer and mechanisms of flame stabilization under surface of porous body. Optimization of porous burners requires deep understanding of flame dynamics in microchannels system considering as model of porous media. Along with fundamental investigations of combustion processes and radiation heat transfer in porous burners the development of new porous SHS materials are important problem too.

Acknowledgements

This work was partially supported by FEFU's scientific research programs.

References

[1] Orlovsky V.M., Kirdyashkin A.I., Maximov Yu.M., Baev V.K., Gushin A.N., **25**, Atmospheric and Oceanic Optics (2012), 273.

[2] Palessky F.S., Minaev S.S., Fursenko R.V., Baev V.K., Kirdyashkin A.I., Orlovsky V.M., **48**, Combust. Expl. Shock Waves (2012), 21.

[3] Kirdyashkin A.I., Orlovsky V.M., Sosnin E.A., Tarasenko V.F., Gushin A.N., Panarin V.A., **46**, Combust. Expl. Shock Waves (2010), 37.

Flame Stabilization In A Mesoscale Bluff Body Combustor

Aiwu Fan, Jianlong Wan, Hong Yao, Wei Liu
Huazhong University of Science and Technology, Wuhan 430074, China
E-mail of corresponding author: faw@hust.edu.cn

ABSTRACT

The flame stability of CH4/air mixture in a mesoscale bluff body combustor was investigated experimentally. The results show that the symmetric stable flame appears under most conditions in the bluff body combustor, which is hardly observed in the straight channel without a bluff body. This demonstrates that the bluff body has a strong ability of flame stabilization for the small combustor. Moreover, the blow-off limit increases with the increase of the bluff body dimension and equivalence ratio of the mixture. In addition, some flame dynamics including pulsating flames with large noise emission were also noticed in the mesoscale bluff body combustor.

1. Introduction

With the emerging of various MEMS devices, the combustion under micro- and meso-scales has attracted much attention in the past decade [1, 2]. However, it is challenging to stabilize the flame in small combustors due to the increased heat loss. Tremendous efforts have been made to improve flame stability in micro- and meso-scale combustors. Heat recirculation, such as the "Swiss Roll" structure [3, 4], porous media combustion [5], is a frequently adopted method in the design of small combustors. Catalytic combustion has been demonstrated to be viable in micro channels because the catalyst can accelerate reaction and suppress radical depletion on the walls [6]. Another way to anchor flame in micro-combustors is to form a flow recirculation zone [7-11]. For example, Wan *et al.* [9-11] developed a micro bluff body combustor. The experimental results showed that the blow-off limit of premixed H_2/air flame was extended by 3-5 times as compared with that of the straight channel. In the present paper, we report our latest experimental results of premixed CH4/air flames in a mesoscale bluff body combustor.

2. Experimental setup and method

The geometric diagram of the planar mesoscale bluff body combustor is schematically shown in Fig. 1. The total length (L_0) is 40 mm and the thickness of combustor wall (W_1) is 2 mm. The width (W_0) and height (W) of the combustor chamber are 20 mm and 4 mm, respectively. The cross section of the bluff body is an equilateral triangle with a side length (W_2) of 2 mm. The ratio W_2/W_1 is defined as blockage ratio ζ. The bluff body is symmetrically located with respect to the upper and lower walls of the combustor, and the distance from its vertical surface to the combustor inlet (L_1) is 4 mm. Both of combustor walls and bluff body are made of quartz glass which can endure a very high temperature.

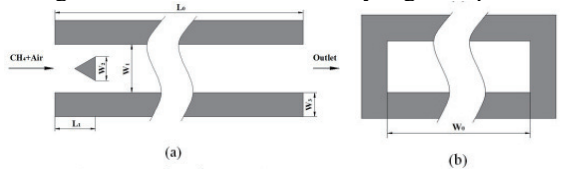

Fig. 1 Schematic diagram of the mesoscale combustor with a bluff body: (a) longitudinal cross-section of the combustor, (b) combustor exit.

Methane and air of atmospheric pressure were fully mixed in a mixer before entering the combustor. Their mass-flow rates were adjusted by electric-mass-flow meters with an accuracy of 1% over the full range. A digital camera was used to take flame pictures. At the beginning of the combustion experiment, the fresh mixture was ignited by an electric spark igniter at an enough low inlet velocity and flame can be anchored behind the bluff body. Then, the inlet velocity was increased with a step of 0.1 m/s, until the flame was blown out of the micro-combustor.

3. Results and Discussion

3.1 Flame dynamics in the straight channel

We first describe the flame dynamics observed in the combustor without a bluff body. Symmetric stable flames were not observed in this combustor and all the stable flames are inclined ones from the top viewpoint. This fact has also been reported by other researchers [12]. Figure 2 presents some photographs of the inclined stable flame taken at the inlet velocity of 0.4 m/s with different equivalence ratios. It can be seen from Fig. 2 that the inclined flames are slightly curved and their directions are stochastic. Furthermore, it is noted that the luminosity of inclined flames goes up with the increase of equivalence ratio for the lean mixture.

When the inlet velocity is increased to relatively high, the inclined stable flame loses its stability and starts to pulsate. Figure 3 illustrates a cycle of the inclined pulsating flame in the mesoscale combustor without a bluff body under the condition of V_{in} = 0.6 m/s, ϕ = 0.9. From Fig. 3 it is seen that the inclined unstable flame pulsates with small amplitude and low frequency. With a further increase of the inlet velocity, the unstable flame is pushed out of the channel.

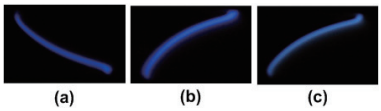

Fig. 2 Photographs of inclined stable flames in the straight channel at V_{in} = 0.4 m/s: (a) ϕ = 0.8; (b) ϕ = 0.9; (c) ϕ = 1.0. The inlet of the combustor is on the left side.

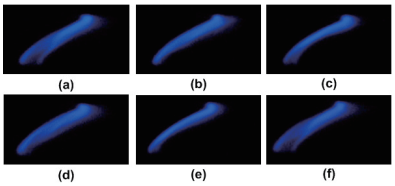

Fig. 3 A cycle of the inclined pulsating flame in the straight channel at V_{in} = 0.6 m/s, ϕ = 0.9.

3.2 Flame dynamics in the bluff body combustor

In contrast, stable planar flames appear under low velocity conditions in the bluff body combustor, as shown in Figure 4(a). It is also seen from Fig. 4(b) that the side view of the flame is like a ball.

Fig. 4 Planar stable flame at ζ=0.4, ϕ=0.9, V_{in} = 0.4 m/s: (a) Top view, (b) Side view

With the increase of the inlet velocity, the flame starts to pulsate with noise emission. Figure 5 shows some direct photographs of the pulsating flames at ζ=0.6 and ϕ= 1.0 but different V_{in}. It is noted from this figure that the flame thickness increases with the inlet velocity, which indicates that the pulsating amplitude increases with the inlet velocity.

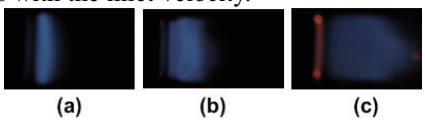

Fig. 5 Pulsating flames: (a) small amplitude at V_{in} = 0.8 m/s; (b) moderate amplitude at V_{in} = 1.8 m/s; (c) large amplitude at V_{in} = 4.8 m/s

In addition, other interesting flame dynamics were observed near the blow-off limit for lower equivalence ratios (i.e., ϕ = 0.7 and 0.8). For example, periodic transitions between the inclined flame and tulip-like flame occurred under the condition of ζ=0.5, ϕ = 0.8, V_{in} = 0.7 m/s, as shown in Fig. 6; while dynamics of the inclined flame were captured under the condition of ζ=0.5, ϕ = 0.7, V_{in} = 0.5 m/s, as depicted in Fig. 7. These two dynamic processes demonstrate that the flame front is prone to be blown from the sidewalls when the equivalence ratio is low, and soon after its departure, the flame strives to reattach to the sidewall.

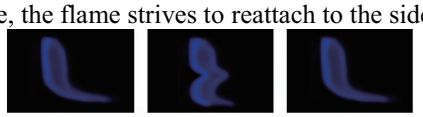

Fig. 6 Dynamics between the inclined flame and tulip flame in the mesoscale bluff body combustor under the condition of ζ = 0.5, V_{in} = 0.7 m/s, ϕ = 0.8.

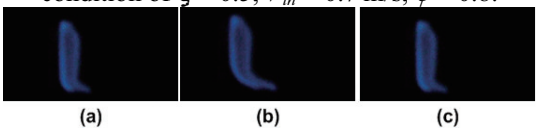

Fig. 7 Dynamics of the inclined flame in the mesoscale bluff body combustor under the condition of ζ = 0.5, V_{in} = 0.5 m/s, ϕ = 0.7.

3.3 Blow-off limit of the bluff body combustor

The blow-off limits of the bluff body combustors with different dimension were given in Fig. 8. This figure shows that the blow-off limit of the case with ζ = 0.4 is much less than that with ζ=0.5 and 0.6. This suggests that blockage ratio of bluff body combustor should be large than 0.4 to obtain a good performance of flame stabilization. Moreover, it is also seen from Fig. 8 that for the cases with ζ=0.5 and 0.6, the blow-off limit increases very slowly when ϕ = 0.7 and 0.8; however, when the equivalence ratio increases from 0.8 to 0.9, the blow-off limit goes up sharply. In addition, for the case with ζ=0.4, the blow-off limit rises linearly, although the values are very small.

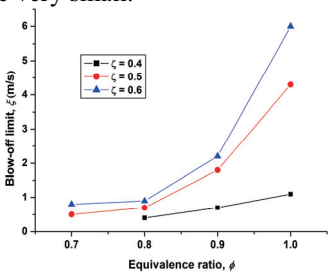

Fig. 8 Blow-off limits of the mesoscale bluff body combustors with different blockage ratios.

4. Concluding remarks

Combustion behaviors of CH4/air mixture in planar mesoscale channels w/o a bluff body were experimentally investigated. The results show that flame stability is greatly improved with the addition of the bluff body and stable planar flame can be anchored behind it. In addition, pulsating flame with noise emission occurs at relatively high inlet velocity and equivalence ratio. Moreover, some interesting flame dynamics appear near blow-off limit at low equivalence ratios. Furthermore, the bluff body significantly extends the blow-off limit of the mesoscale combustor. The blow-off limit increases with the increase of the blockage ratio and the equivalence ratio.

Acknowledgments

This work was supported by the Natural Science Foundation of China (Grant Nos.51076054 and 51276073).

References

[1] Y.G. Ju, K. Maruta, Prog. Energy Combust. Sci. **37**(2011)669–715.
[2] K. Maruta, Proc. Combust. Inst. **33**(2011)125–150.
[3] N.I. Kim, S. Aizumi, T. Yokomori, S. Kato, T. Fujimori, K. Maruta, Proc. Combust. Inst. **31**(2007)3243–3250.
[4] C.H. Kuo, P.D. Ronney, Proc. Combust. Inst. **31**(2007)3277–84.
[5] J. Li, S.K. Chou, Z.W. Li, W.M. Yang, Fuel **89**(2010)708–715.
[6] G.B. Chen, C.P. Chen, C.Y. Wu, Y.C. Chao, Appl Catal A Gen **332**(2007)89–97.
[7] W.M. Yang, S.K. Chou, C. Shu, Z.W. Li, H. Xue, Appl. Therm. Eng. **22**(2002)1777–1787.
[8] B. Khandelwal, G.P.S. Sahota, S. Kumar, J. Micromech. Microengin. **20**(2010)095030.
[9] J.L. Wan, A.W. Fan, K. Maruta, H. Yao, W. Liu, Int. J. Hydrogen Energy **37**(2012)19190–19197.
[10] A.W. Fan, J.L. Wan, Yi Liu, B.M. Pi, H. Yao, K. Maruta, W. Liu, Int. J. Hydrogen Energy **38**(2013)11438–11445.
[11] A.W. Fan, J.L. Wan, K. Maruta, H. Yao, W. Liu, Int. J. Heat Mass transfer **66**(2013)72–79.
[12] U. Dogwiler, J. Mantzaras, P. Benz, B. Kaeppeli, R. Bombach, A. Arnold, Proc. 27th Int. Sympos. on Combust. 2275–2282, 1998.

Tenth International Conference on Flow Dynamics
November 25-27, 2013, Sendai, Miyagi, Japan

Formation of Spinning Flames in Stepped Tube Combustors

Upendra W. Taywade, Anil A Deshpance, Sudarshan Kumar*
Department of Aerospace Engineering, Indian Institute of Technology Bombay Powai Mumbai India 400 076
E-mail of corresponding author: sudar@aero.iitb.ac.in

ABSTRACT

In the present work, formation of spinning flames is experimentally investigated in a three step micro combustors of various aspect ratios to understand their effect on the formation of flame stabilization mode using LPG-air mixtures. Three step backward facing micro combustors made of quartz are selected with different L/D ratio of third step. Experimental results have shown that the combustor with least L/D ratio has wider spinning flame limits than other combustors and its spinning frequency ranges from 40 Hz to 150 Hz. The maximum temperature of combustor wall corresponds to the maximum value of spinning flame frequency.

1. Introduction

Batteries are the tradional source of portable electric power and intensive progress is underway to increase the capacity of existing batteries and develop new energy conversion devices [1]. The high energy density of hydrocarbon fuels with competitive efficiency provides a better opportunity to develop combustion based micro-power generation systems to meet increasing demands for portable power devices as compared to electrochemical batteries [2]. The study was carried out on the formation of stable spinning X shape flame limits in quartz micro combustors with three different L/D ratios of third step to see the future prospects of spinning flame based micro combustors for efficient combustion.

Kwon et al. [3] and Kurata [4] has observed X-shaped spinning flames in sudden expansion tubes and coaxial burner with premixed methane-air mixtures. Xu and Ju [5] have also observed similar spinning flames in mesoscale diverging tubes for both lean and rich methane and propane–air mixtures for a broad range of equivalence ratios. Rotating spiral flame patterns and radial propagation modes were observed by Kumar et al. [6-7] when premixed methane-air mixtures were introduced at the centre of the two parallel circular quartz plates.

2. Experimental Set -up

Figure 1 shows the micro-combustor configuration for a 3-step configuration with major dimensions. Henceforth, the combustors with L/D ratio of third step, 0.9, 1.6, 2.3 are referred as L0.9, L1.6 and L2.3 respectively. The minimum diameter used in all combustors is close to quenching diameter, 2 mm at the inlet to fuel-air mixture. Figure 2 shows the schematic arrangement of the experimental set-up. Fuel and air from high pressure tanks are passed through pressure reducing valves where its pressure is maintained at 2 bar. From low pressure lines fuel and air are passed through precise electric MFCs and premixture is prepared in another chamber. Predetermined mass flow rates of fuel and air were supplied using different flow range electric mass flow controllers (AALBORG-GFC). These electric mass flow controllers were controlled through a computer to which command module is connected. Accuracy of the measured mass flow rates is ±1% of the full scale. To measure the temperatures on the outer wall of the combustor, K-type thermocouples are used. The spinning frequency of flames was measured using Photodiode in FFT mode.

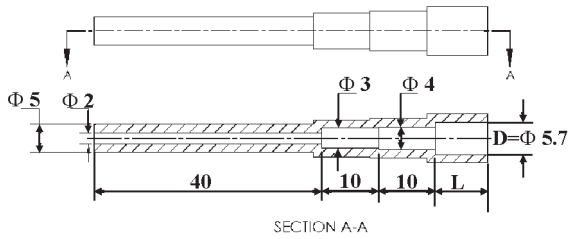

No.	L/D
1	0.9
2	1.6
3	2.3

All dimensions in mm
Material: Quartz

Fig. 1 Dimensions details for 3-step micro combustor

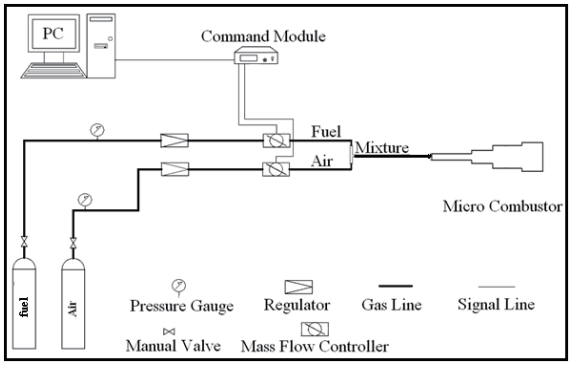

Fig. 2 Schematic arrangement of the experimental setup

3. Results and Discussion

X shaped spinning flames were observed at Φ = 1 in three different combustors as shown in Fig. 3. Observations were made for different inlet flow velocities and range of mixture equivalence ratios. The limits of formation of X-shaped flame in combustors with different L/D ratios are plotted in Fig. 4.

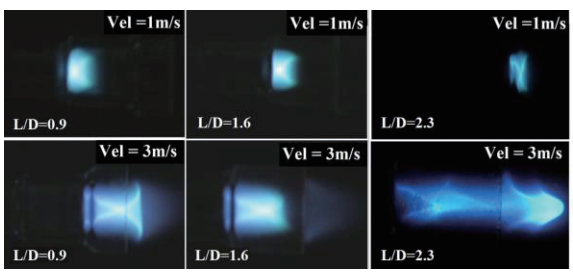

Fig. 3 Spinning flames observed at Φ=1 in combustors

Maximum limits of X flame are observed at Φ = 1.1. Area under the upper and lower limits of X flame shows that combustor L0.9 has wider X limits than combustor L1.6 and L2.3. This may be due to stronger thermal coupling between the flame and wall for the combustor L0.9 than L1.6 and L2.3 combustors.

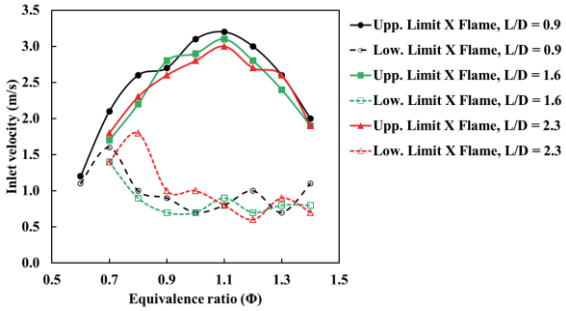

Fig. 4 X flame limits of micro-combustor with different L/D ratio

Fig. 5 shows the spinning frequency of X flames at different equivalence ratio for two velocities. Maximum spinning frequency is observed for Φ = 0.9 for all the combustors. Spinning frequency is maximum for combustor L0.9 as compare to combustors L1.6 and L2.3. Frequency increases with equivalence ratio till 0.9 then decreases for all combustors. At lower velocities and lower equivalence ratios (Φ <1.1), spinning flames are dominant in second step region and anchored to second step.

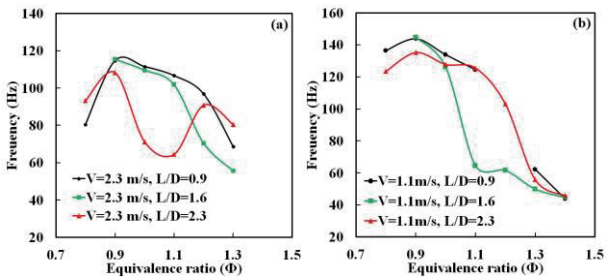

Fig. 5 Variation of spinning frequency with Φ

Figure 6 shows that with the increase in the inlet velocity, frequency of spinning flame increases and reaches the maximum value at velocity 2.5 m/s and 2.1 m/s for Φ = 1 and 1.2 respectively in combustor L0.9 and L1.6, and flame is anchored to third step. Similar trends are seen for all combustors at Φ = 1, when the X flame is anchored to second step.

Figure 7 shows that as the equivalence ratio increases, temperature of all the combustors increases and reaches maximum at equivalence ratio 1 at both lower and higher velocities. At velocity 2.1m/s position of the flame is at third step for all the three combustors except at equivalence ratio 1.1, where the position of the flame is at second step for combustor L2.3 and the temperature at this position is observed to be maximum. Also, at velocity 2.1m/s, mode of flame is X shaped in all the combustors. At a lower velocity (1.1m/s) and higher equivalence ratio, 0.8< Φ < 1.1, X flame is positioned at second step for all three combustors.

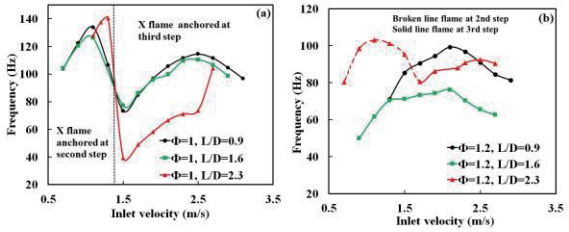

Fig. 6 Frequencies of X flames wrt velocity

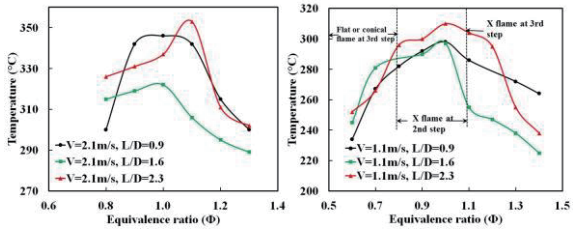

Fig. 7 External wall temperature of combustors wrt equivalence ratio

4. Concluding remarks

It is observed that required quantity of preheating of combustor is necessary to form the spinning flames indicating the strong role of flame-wall thermal coupling. Experimental results have shown that combustor with least L/D ratio has wider spinning X flame limits than other combustors. The maximum temperature of combustor wall corresponds to the maximum spinning frequency of the flame. The spinning frequency of these flames ranges from 40 Hz to 150 Hz depending on the mixture flow velocities, equivalence ratio and the position of flame stabilization (second step or third step). X shape flame is the most suitable mode of flame for power generation because of uniform temperature distribution over a large area of the combustor.

References

[1] P.V.D. Bossche, Journal of Power Sources 80 (1999) 213–216

[2] A.C. Fernandez-Pello, Proc. Combust. Inst. 29 (2002) 883-899

[3] M.J. Kwon, B.J. Lee, S.H. Chung, , Combustion and Flame, 105 (1996) 180–188.

[4] O. Kurata, Combustion and Flame 152 (2008) 206–217

[5] B. Xu, Y. Ju, Proceedings of the Combustion Institute 31 (2007) 3285–3292

[6] S. Kumar, K. Maruta, S. Minaev, R. Fursenko, Physics of Fluids, 20 (2008) 024101

[7] S. Kumar, K. Maruta and S. Minaev, Physical Review-E 75, (2007) 016208

Tenth International Conference on Flow Dynamics
November 25-27, 2013, Sendai, Miyagi, Japan

Numerical Study of Methanol Reformation from a Single Channel with Cavities Integrated with a Micro-combustor

Prashant Nehe, Sudarshan Kumar
Department of Aerospace Engineering, Indian Institute of Technology Bombay, Mumbai, 400076, India
Phone: +91 22 2576 7124; fax: +91 22 2572 2602
E-mail: sudar@aero.iitb.ac.in

ABSTRACT

A numerical study of methanol reformation from a single channel with cavities integrated with a micro-combustor is presented in this paper. Velocity and flow fields are computed to study the effects of variation in the relative cavity depth and cavity spacing on local structure of the flow, heat transfer characteristics and methanol conversion. The results show that higher methanol conversion rates can be achieved within a shorter channel length with cavities. Due to enhanced heat transfer and faster reactions, the length of the channel is reduced by 20 % as compared to a plain channel for similar conversion.

1. Introduction

There are many advances in semi-conductors and micro-machining technologies which ensure the feasibility of producing small scale devices at micro scales. Moreover, the demand for designing and production of systems such as micro-portable machines, micro-robots, small scale aerospace systems and micro power generation devices which are able to generate enormous energy in small dimensions is increasing considerably [1]. For the activation of a methanol steam reforming reaction in the microreformers for producing hydrogen gas to power fuels cells, energy must be supplied from an external heat source because it is an endothermic reaction. Therefore, heat transfer plays an important role in the reforming process [2]. Modeling and numerical simulations are frequently used to obtain a better understanding of the effect of geometric parameters and thermo-fluid processes on the performance of methanol microreformers. Several numerical models report the methanol conversion and the heat and mass transport phenomena which explicates the effects of various flow configurations on the performance of the microreformers [3, 4]. Recently, some numerical and experimental investigations have been performed on steam reforming of methanol with a stepped parallel plate combustor as the heat source [5-7].

This paper describes a numerical study of a single channel based microreformer configuration with multiple cavities integrated with a micro-combustor. The influence of variation in the relative cavity depth, cavity spacing and the flow field on heat transfer enhancement from a micro-combustor and methanol conversion is investigated.

2. Channel Geometry and Numerical Method

Figure 1 represents a two-dimensional geometry and physical model of the microreformer configuration consisting of two parallel plates with symmetrically opposing multiple cavities. The heat for endothermic methanol-steam reforming reaction is supplied by the micro-combustor integrated on the outer side of the microreformer plates. Microreformer plates are coated with CuO/Al_2O_3 catalyst is used to sustain catalytic reaction in the microreformer. The center-to-center spacing between adjacent cavities (s) and the cavity depth (d) are the variables used in this study. A parameter called 'relative cavity depth' is defined as cavity depth to channel height (H) ratio, $d^* = d/H$. The cavity geometric parameters are defined relative to the channel height and the relative cavity depth range is taken as 50-250 % H for this study. Table 1 summarizes the different cases of relative cavity depth and cavity spacing considered for the study.

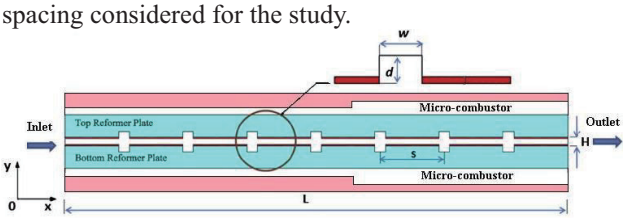

Fig. 1 Schematic diagram of the physical model

Table 1 Summary of the various cavity configurations

Relative cavity depth d^*	0.5, 1,2, 2.5
Cavity spacing s/H	5.62, 2.81, 1.87
Cavity width w/H	0.67

The governing equations are conservations of mass, momentum, energy and chemical species. The flow is studied under the assumptions of laminar, incompressible, and steady state. At the inlet, flow velocity, temperature and chemical composition are specified. At the wall boundaries, no-slip condition is used for velocity. Adiabatic boundary condition is assumed for the top and bottom walls of the microcombustor and the pressure outlet condition is used at the channels outlet.

The governing equations are solved numerically using a general purpose CFD code Fluent 6.3 which is a finite-volume based code and the pressure velocity coupling is attained by using the SIMPLE algorithm. Grid points are distributed in a non-uniform manner with a higher concentration near the walls due to higher variable gradients. The solution is assumed to be converged when the scaled residuals are less than 10^{-6}.

3. Results and Discussion

The dimensionless velocity profile along the midline of a single cavity in a channel is shown in Fig. 2. In cavity area, pressure increases because the slip velocity decreases. The flow entrapment in the cavities is

particulalry useful for applications in microreformers since this will reduce the acceleration caused by the expansion due to heating of the gas mixture.

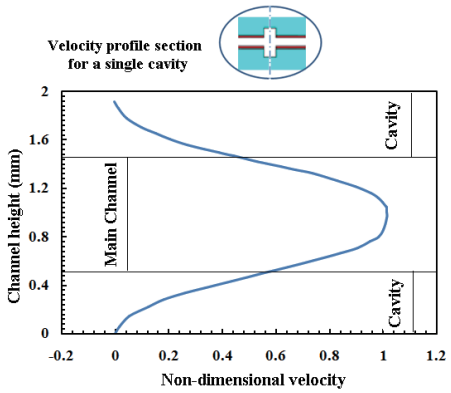

Fig. 2 Non-dimensional velocity variation along the midline of cavities.

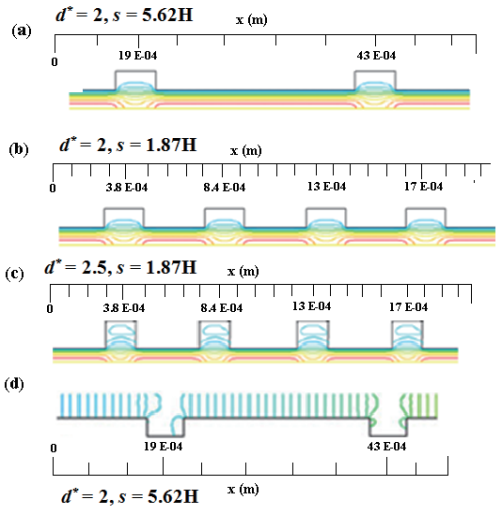

Fig. 3 (a), (b) and (c) Streamline contours for channels with different cavity configurations, (d) pressure contours for channels with cavities.

Flow streamlines pattern and pressure contours for channels with different relative cavity depths and spacing are shown in Fig. 3. As seen from Fig. 3, the presence of cavities noticeably perturbs the local flow near the channel wall. For a channel with large cavity spacing (Fig. 3(a)), there is almost no recirculating region in the cavities. As the spacing between the cavities is reduced, the recirculation zone starts appearing in the cavities and grows for larger cavity depths (Fig. 3(b)). Figure 3(c) shows that the pressure has a sharp drop near the cavity entrance. Along the surface of the channel, the pressure gradient is not monotonically negative like a plain channel and it has some local variations due to presence of cavities. At the inlet of the channel, there is a boundary layer and the flow is not fully developed. Consequently this pressure variation and local expansion of the fluid leads to the formation of recirculation zones. There is sudden expansion and contraction in this area of the channel. The gas is compressed in the narrower space and expanded in the wider space. This indicates that the cavities exert a notable surface friction effect on the gas flow field and enhance the lateral mixing by disrupting the shear layer. Such an effect also enhances the heat transfer characteristics much to the advantage of the microreformers.

Figure 4 shows the distribution of methanol mole fraction and hydrogen mole fraction along the centreline of the channels for different values of d^*. There is a drop of 13% in methanol conversion for the case of zero cavity depth case. This case is equivalent to a plain channel case. Therefore, methanol conversion decreases with a decrease in cavity depths. The faster conversion can be attributed to the presence of cavities in the reformer channel. Due to these faster reactions, the length of the channel is reduced by 20% as compared to a plain channel for similar conversion.

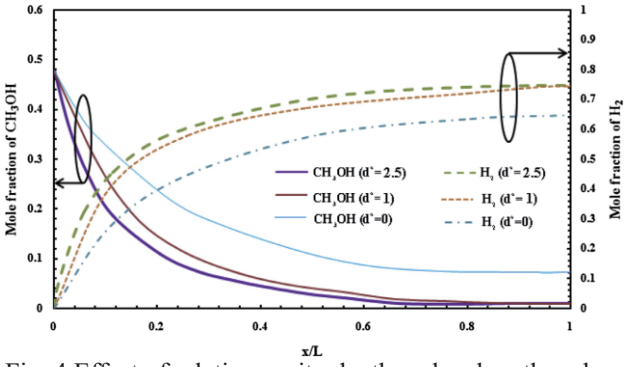

Fig. 4 Effect of relative cavity depth on local methanol and hydrogen mole fraction along the channel

4. Conclusions

A numerical study of a single channel plate type microreformer with cavities integrated with a micro-combustor is carried out. Cavities exert a surface friction effect on the gas flow field in the channel and therefore enhance the heat transfer characteristics, much to the advantage of the microreformers. The rate of methanol conversion is higher within a shorter channel length with cavities.

References

[1] L. Chuan Chia, B. Feng, J Power Sources, 165 (2007) 455-80.
[2] S. Nagano, H. Miyagawa et al., Energy Convers Manag. 42 (2001) 1817-29.
[3] T. Kim, S. Kwon, J Micromech Microeng, 16 (2006) 1760-68.
[4] A.V. Pattekar, M.V. Kothare, J Power Sources, 147 (2005) 116-27.
[5] Khandelwal B., Deshpande A. A. Kumar S., App. Thermal Eng. 58 (2013) 363-8.
[6] Deshpande A.A., Kumar S., App. Thermal Eng., 51 (2013) 91-101.
[7] Khandelwal B., Sahota GPS., Kumar S., J. Micromech. Microeng. 20 (2010) 095030.

Tenth International Conference on Flow Dynamics
November 25-27, 2013, Sendai, Miyagi, Japan

Multiphase High Density Hydrogen Energy and its Risk Assessment

Jun Ishimoto
Institute of Fluid Science, Tohoku University, 2-1-1, Katahira, Aoba-ku, Sendai 980-8577, Japan
E-mail: ishimotojun@ieee.org

ABSTRACT

Comprehensive studies on cost effective production, storage, transportation and distribution, physical characteristics and safety measures and management of "high density multi-phase hydrogen source" are to be carried out. Simulation techniques such as OpenFOAM and other advanced CFD codes are efficiently applied. Such multiphase high density hydrogen contribute to small volumetric storage, carries high enthalpy, i.e. high energy, and suitable for efficient transportation and distribution of energy.

1. Introduction

For hydrogen under the atmospheric pressure, energy generation rate per volume is less than that of fossil fuel such as gasoline. Therefore, it is necessary to develop the technique that high compression method of hydrogen to the high density fuel, and to develop the high density pressure vessels, high rate absorption method to metallic alloys for hydrogen storage [1]. The following studies are made using mainly advanced supercomputing techniques. This research aims to develop and provide useful information to produce, store, transport/distribute, use and manage hydrogen as an important energy vector. Therefore, we propose a new type of high density energy storage and high enthalpy transfer system making use of multiphase hydrogen forms. Based on this strategy, the production technique of several types of highly compressed hydrogen (CH_2), subcooled liquid hydrogen (LH_2), and solid hydrogen (SH_2) production would be developed. Especially, fine solid particulate form of hydrogen is characterized by a higher density and cooling enthalpy than the liquid hydrogen at the boiling point. These characteristics has the advantage for application in low volumetric storage, small space for vehicles, however, it requires effective production method to product finer SH_2 particles continuously. To realize high density hydrogen production, development of continuous finer SH_2 particle production method is in focus. Furthermore, multiphase leakage of compressed hydrogen during liquid to vapour phase change, and related chemical reactions including explosion phenomena will be accurately modelled by means of a suitable development and application of the advances computational code.

2. Next generation strategy for high density multiphase hydrogen energy system

New energy system for multiphase high density hydrogen production, storage, high enthalpy transport method, and hydrogen safety risk management system would be developed.

The future construction of a multiphase high-density hydrogen energy systems from an transdisciplinary energy cycle process is expected in which 1) micro-solid hydrogen collected after cleaning semiconductors is reused as a cyclical high-enthalpy fluid for fuel cell power generation by 2) micro-solid hydrogen used for next-generation processor cooling, glass freezing of human induced pluripotent stem (iPS) cells, and furthermore in cooling 3) that passes through a recovery system that uses hydrogen storage alloys of multiphase type hydrogen. In particular, the application to a semiconductor cleaning process has the feature of using the kinematical properties of the cryogenic solid particles and the ultra-high heat flux effect to perform removal of the resist without performing the current plasma ashing treatment, and can be considered to be a significant contribution to shortening of the semiconductor manufacturing process. Furthermore, the implementation of superconductiong cable cooling system and ultra-high heat flux electronics cooling system will facilitate the drastic downsizing of hydrogen storage, and downsizing of cooling systems for large-scale superconducting devices, supercomputers and contribute to reducing costs. Multiphase compressed hydrogen related application is particularly expected in MEMS microchannels as a low viscosity dissipation, low pressure loss and high-efficiency cryogenic MEMS cooling system by utilizing the extremely low viscosity of the working fluid.

3. High density hydrogen production and computational approach

As a compromise between experimental facility safety and similarity of physical properties, we chose to use nitrogen as a working cryogen for analysis alternative to hydrogen. Namely, solid hydrogen (SH_2) particle production phenomena can be reproduced by solid nitrogen (SN_2) particle production phenomena almost in the same manner.

Figure 1 shows the computational result of the SN_2-phase volume fraction profile through the Laval nozzle. Figure 2 shows the produced SN_2 particle by developed super adiabatic Laval nozzle in the present experiment. It is numerically found that the atomization of LN_2 droplet is induced by shear flow between LN_2 and gaseous nitrogen (GN_2) flow. Sequentially, liquid to solid phase change is enhanced and SN_2 particle is continuously created by LN_2 droplet freezing. This physical process is due to the latent heat release based on the adiabatic expansion of subcooled GN_2-LN_2 subsonic two-phase flow just downstream of Laval nozzle throat section.

Figure 3 shows the instantaneous iso-surface of the

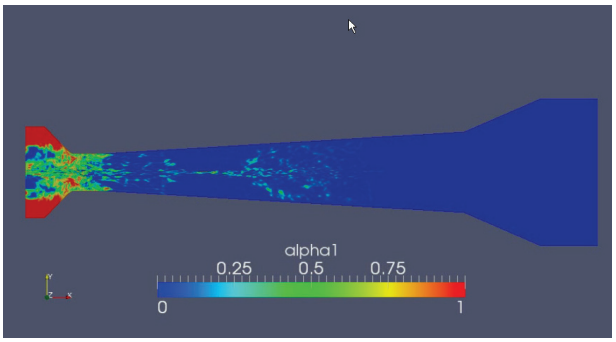

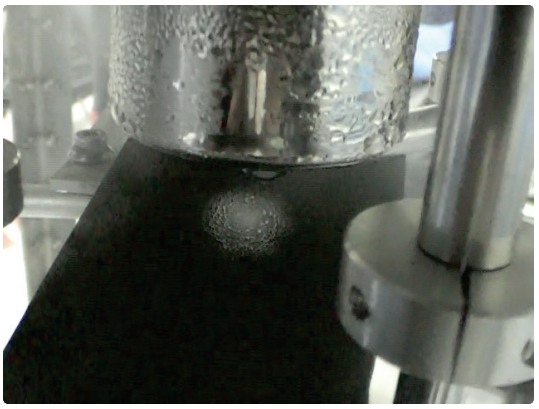

Fig. 2 Produced SN_2 particle by developed Laval nozzle in the present experiment

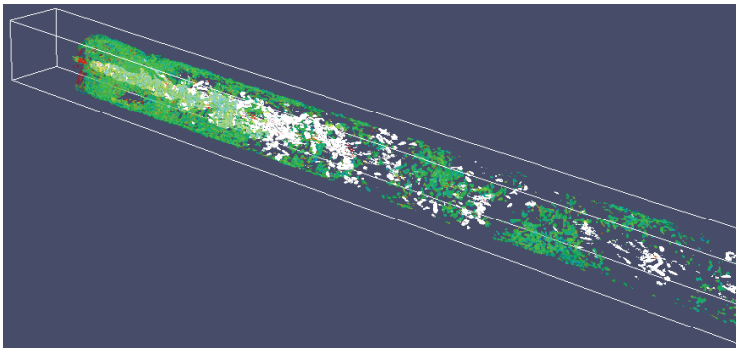

Fig. 3 Instantaneous iso-surface of the atomizing subcooled LH_2 volume fraction with enstrophy profiles

atomizing subcooled liquid hydrogen (LH_2) volume fraction with enstrophy profiles. As the surface tension

of subcooled LH_2 is large, the metastable proportion of atomized droplet group increases, the cryogenic temperature diffusion is promoted due to the enhancement of the liquid column breakup.

References

[1] Katsuhiko Hirose in "Handbook of Hydrogen Storage", ed. by Michael Hirscher, Wiley-VCH Verlag GmbH & Co. KGaA, Weinheim, 2010.

Fig. 1 Computational result of the SN_2-phase volume fraction profile through the Laval nozzle

Tenth International Conference on Flow Dynamics
November 25-27, 2013, Sendai, Miyagi, Japan

On-wafer Monitoring Technique for Highly Efficient Fabrication Process of Nano Energy Devices

Tomohiro Kubota[1] and Seiji Samukawa[1,2]
Institute of Fluid Science, Tohoku University, 2-1-1 Katahira, Aoba-ku, Sendai 980-8577, Japan
WPI-AIMR, Tohoku University, 2-1-1 Katahira, Aoba-ku, Sendai 980-8577, Japan
samukawa@ifs.tohoku.ac.jp

ABSTRACT

A system for predicting distortion of a profile during plasma etching was developed by combination a combination of measurement and simulation. The sensor has numerous small electrodes for measuring sheath potential and saturation ion-current density, from which sheath thickness can be calculated successfully. Based on the measured parameters, distortion of etched structure around arbitrary 3-dimensional structure was predicted by computer simulation. The prediction could successfully explain the experimentally observed distortion in etching of structure with 3-dimensional structure.

1. Introduction

Plasma etching is widely used for fabrication of semiconductor devices, because it can perform anisotropic or vertical etching. This feature is based on an "ion sheath" that is generated at the interface between the plasma and the substrate surface. The ions in the plasma are accelerated vertically by the electric field in the ion sheath and vertical etching is realized by plasma. However, when the substrate has a large-scale three-dimensional (3D) structure with height comparable or larger than the thickness of the ion sheath, which may occur in fabrication process of microelectromechanical systems (MEMS), the ion sheath will not be flat anymore, as schematically shown in Fig. 1.

Distortion of ion trajectory around a large-scale 3D structure has been investigated by calculating the distribution of ion-sheath potential. [1,2] However, these studies did not quantitatively compare the simulation results with experimental result of plasma measurement.

We have been developing "on-wafer" sensors, namely, sensors embedded in a silicon wafer and fabricated by standard microfabrication technology, for measuring plasma parameters on a sample stage of plasma equipment. [3,4] In the present research, we have developed a system to predict etching-profile distortion caused by ion-sheath distortion due to a large-scale 3D structure, by combining an on-wafer sensor (for measuring the condition of the ion sheath of plasma) and prediction software. The sensor can measure the ion-sheath condition at the stage surface. Since radio-frequency (RF) bias is usually applied to the stage to effectively accelerate ions in the plasma toward the samples on the stage, it is indispensable to measure the ion-sheath condition at the stage position. The software can predict the etching-profile distortion based on the on-wafer sensor measurement and given 3D structure. We demonstrated the system could successfully predict the experimental result of silicon trench etching using chlorine inductively coupled plasma (ICP).

2. Experimental procedure

An "on-wafer sheath-shape sensor" for measuring electric potential and saturation-ion-current density was developed. The structure of the developed sheath-shape sensor is shown in Fig. 2.

Then measurement was performed using the developed sensor as shown in Fig. 3. The developed sensor was placed on a silicon wafer on a sample stage of a plasma-etching system. A three-turn spiral-type ICP source was used to generate a high-density plasma. 40 sccm of chlorine gas was introduced into the vacuum chamber, and the chamber pressure was adjusted to 5 – 20 mTorr. An ICP was generated by applying a 13.56-MHz RF power of 500 – 1500 W to the spiral antenna. A 1-MHz bias power of 10 – 40 W was applied to the sample stage. Current-voltage (*I-V*) characteristic and floating potential were measured. Sheath potential can be obtained by measuring the voltage at the electrode, and current-voltage characteristic can be obtained by applying a voltage to the electrode and measuring the current. Sheath thickness can be calculated as:

$$s = \frac{2V_0^{3/4}}{3}\sqrt{\frac{\varepsilon_0}{J_0}}\left(\frac{2e}{m_i}\right)^{1/4}, \qquad (1)$$

where V_0 is the sheath potential, J_0 is the saturation ion current density, m_i is the mass of the ion, e is the unit charge, and ε_0 is the permittivity of vacuum.

Prediction of etching profile was performed based on a calculation of electric field and ion trajectory in the ion-sheath region around a 3D structure. Here, the substrate was assumed to have a vertical step with height of 725μm. Electric potential was then calculated by using the Poisson equation. Next, electron density distribution was calculated by using Boltzmann's distribution. Ion density distribution was obtained by a trajectory (Monte-Carlo) calculation. These calculations are iterated until convergence.

To confirm the validity of the prediction, plasma etching of silicon samples with trench patterns and a large 3D step was performed under the same plasma conditions as those used for the sensor measurements. A silicon sample with a trench-pattern mask and a high vertical step was used. The step height was 725 μm, and a SiO_2 hard mask was used.

3. Results and discussion

Figure 4 shows an example of results of the sensor measurement. It was shown that the sensor can

successfully measure the sheath condition.

Figure 5 shows SEM images of the etched sample. It is clearly shown that the sidewall of the etching profile is distorted near the 3D structure. The distortion angle θ was about 20 degree near at maximum when the distance x from the vertical step was about zero. And θ decreases when the distance x increases. This indicates that the distortion is caused by distortion of the ion sheath around the large vertical step.

Measurement was performed under the plasma condition same as the above etching. Sheath voltage was 365 V, and saturation ion-current density was 27 A/m^2. Sheath thickness was calculated as 1300 µm. Then the simulation was performed as shown in Fig. 6. In the figure, comparison between the prediction and the experimental result was also shown. It is clearly shown that the prediction could reproduce the experimental result, which indicates the prediction system was successfully established.

In conclusion, the constructed prediction system could successfully predict the distorted etching profile. It would thus be useful for designing devices with large-scale 3D structures such as those in MEMS and determining the appropriate etching condition for obtaining the desired profiles.

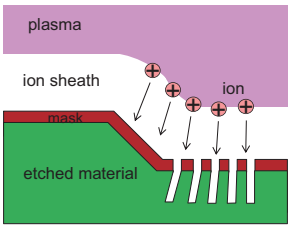

Fig. 1 Schematic illustration of distortion of ion sheath and ion trajectory around a large-scale three-dimensional structure.

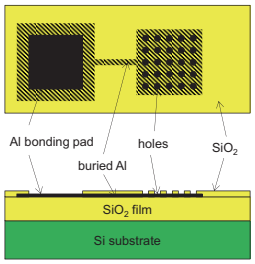

Fig. 2 Structure of on-wafer sheath-shape sensor.

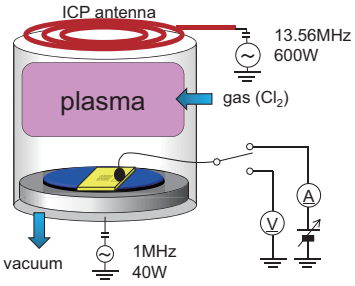

Fig. 3 Experimental setup for measurements of ion-sheath parameters using on-wafer sheath shape sensor.

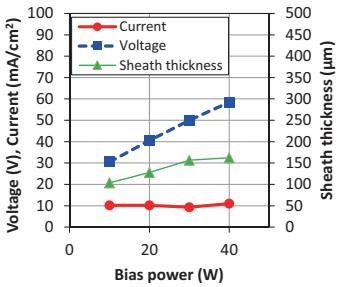

Fig. 4 Sheath voltage and saturation-ion-current density measured by on-wafer sheath-shape sensor and sheath thickness calculated from the measured values.

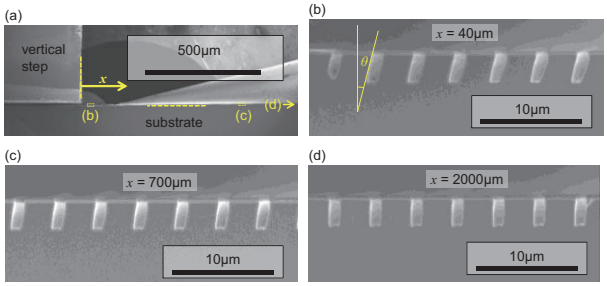

Fig. 5 Cross-sectional SEM images of etched sample: (a) low-magnification image with flat surface and vertical step; (b), (c), and (d) high-magnification images at the surface at distance x of (b) 40 µm, (c) 700 µm, and (d) 2000 µm from the vertical step.

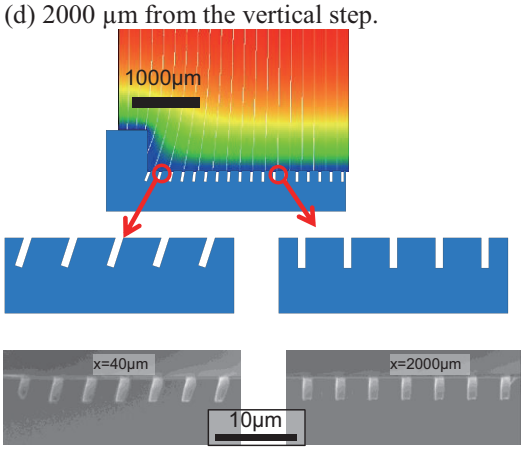

Fig. 6 Result of prediction of potential distribution and ion trajectory based on measurement and comparison with etching results.

References

[1] D. Kim and D. J. Economou, IEEE Trans. Plasma Sci., **30**, 2048 (2002).

[2] F. Hamaoka, T. Yagisawa, and T. Makabe, IEEE Trans. Plasma Sci., **35**, 1350 (2007).

[3] B. Jinnai, T. Orita, M. Konishi, J. Hashimoto, Y. Ichihashi, A. Nishitani, S. Kadomura, H.Ohtake, and S. Samukawa, J. Vac. Sci. and Tech. B **25**, 1808 (2007).

[4] Y. Ishikawa, Y. Katoh, M. Okigawa, and S. Samukawa, J. Vac. Sci. Tech. A, **23**, 1509 (2005).

Tenth International Conference on Flow Dynamics
November 25-27, 2013, Sendai, Miyagi, Japan

Basic Study on Flow Control by Using DC Corona Discharge

[1]Yoshinori Mizuno, [2]Marius Blajan, and [2]Shimizu Kazuo
[1]Graduate School of Engineering, Shizuoka University. Hamamatsu, Johoku, 3-5-1, Japan
[2]Organization for Innovation and Social Collaboration, Shizuoka University. Hamamatsu, Johoku, 3-5-1, Japan
yoshinori7tcybes@gmail.com

ABSTRACT
Gas discharge plasma for active flow control under atmospheric pressure has been developed using low discharge voltage. A corona discharge electrode setup was designed to provide the airflow on a flat plate. The electrode configuration consisted of sharply high voltage energized pin electrode and a grounded plate electrode. The discharge induced an airflow called EHD wind whose velocity was measured with a hot wire velocity meter (up to 2 m/s). It was observed an increasing flow velocity by increasing corona discharge voltage. Saturation of the flow velocity occurred by increasing discharge voltage.

1. Introduction

DC corona discharge for active flow control under atmospheric pressure has been studied. It can generate an air flow with no moving parts, simple structure, and has a fast response due to electrostatic force [1]. Generally, the corona discharge energized is by more than 10 kV [2]. Such high voltage is hard to insulate or requires a large size power supply.

The aim of this study is to investigate a corona discharge that could be driven by a small size power supply with output voltages less than 5 kV. We aim to generate about 1 m/s EHD flow velocity, even corona discharge can generate several m/s EHD flow [3].

2. Method

Geometry of corona electrode in our set of experiments is shown in Fig. 1. A Pin's diameter was 0.35 mmϕ stainless steel wire. Discharge gap was about 5.7 mm. A Pin was energized by a DC high voltage, and corona discharge was generated at edge of this pin. Collector was frame type made of stainless steel wire 0.35 mmϕ.

When a high voltage was applied to the pin and collector, a high electric field ionized the air nearby the pin electrode. Ions (positive corona: positive ions, negative corona: negative ions) are drifted from the pin electrode to the collector by the Coulomb force. While traveling through the air, ions collide with neutral gas molecules and transfer their momentum to neutral particles induced EHD flow. This means the direction of EHD flow is from a pin to collector for both positive and negative polarities.

The x-y-z coordinate system for measuring EHD flow distribution and the electrode geometry is shown in Fig. 1.

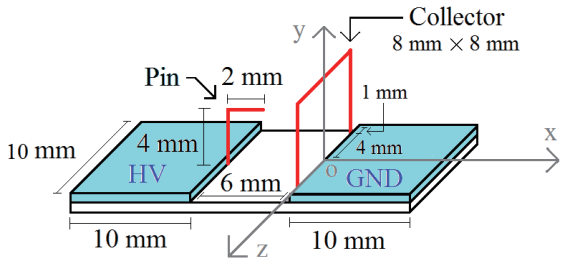

Fig. 1. A Geometry of electrode System.

The experimental setup is shown in Fig. 2. DC corona discharge electrode was set on a flat plate and measurement of EHD flow distribution was carried out. Flow velocity was measured by using a hot wire velocity monitor and a probe. A digital oscilloscope and a high-voltage probe were used to measure the discharge voltage and corresponding discharge current.

A DC high voltage source was used to energize electrode at about 5 kV. A 10 MΩ resistor was used to limit the discharge current thus the discharge current was calculated using Ohm's law and the voltage drop on the resistor.

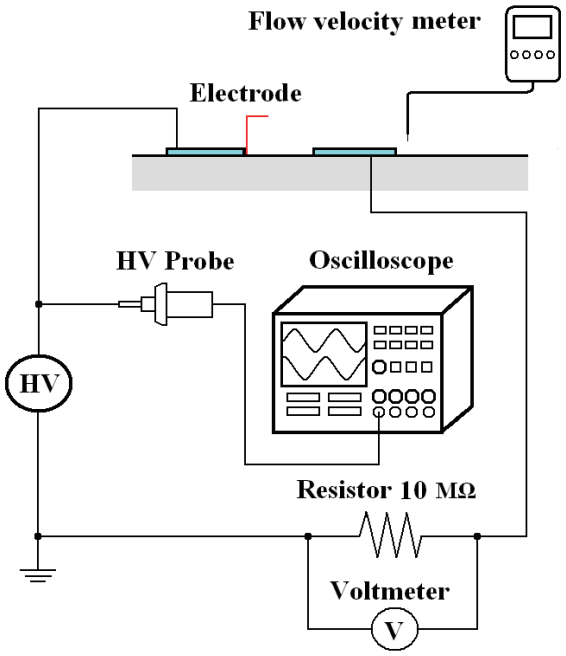

Fig. 2. An experimental setup for measuring EHD flow.

3. Results and Discussion

Fig. 3 shows the characteristics of DC corona discharge voltage and corresponding discharge current and power. Discharge current increased with the increase of the discharge voltage. In this study negative corona current was about 4 times higher than the positive one. A maximum discharge current of 0.22 μA was measured at a negative voltage of 5.5 kV. The discharge power was calculated from the product of

discharge voltage and discharge current. Negative corona power was about 4 times higher than the positive one, similar to the current case. The discharge power of 0.12 W was obtained at a negative voltage of 5.5 kV.

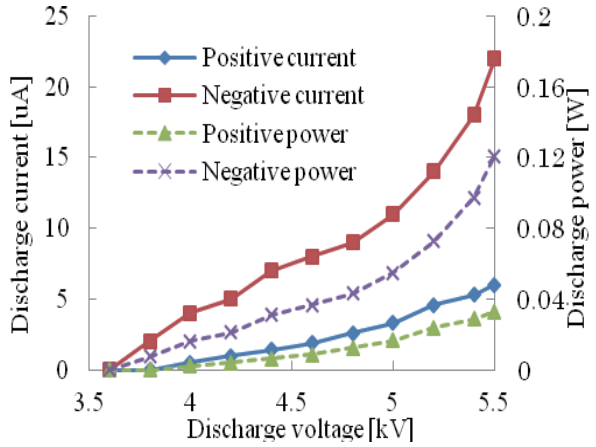

Fig. 3. Discharge current and power versus discharge voltage characteristics at a temperature of 20℃ and humidity 45 %.

Fig. 4 shows discharge voltage and corresponding EHD flow velocity at (x, y, z) = (5 mm, 1 mm, 0 mm). Flow velocity increases with increasing discharge voltage.

Negative corona generated about 2 times faster EHD flow than the positive one at the same discharge voltage. This trend was same as observed for the values of discharge current and power. Flow velocity was saturated by increasing discharge voltage in the case of negative corona unlike the discharge current or power. EHD flow velocity produced by corona discharge is proportional to the square root of product of discharge gap and discharge current [4]. Increasing discharge voltage caused corona discharge to extend from pin to collector electrode. As a result effective discharge gap was narrowed by increasing discharge voltage, and flow velocity tends to saturate.

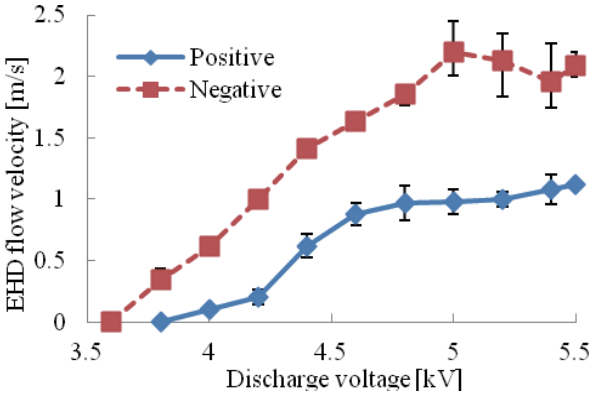

Fig. 4. EHD flow velocity versus discharge voltage temperature 20℃, humidity 45 %.

Fig. 5 shows the flow characteristics along x axis (for y = 1mm and z = 0 mm). Flow velocity decayed exponentially with the increase of x value. It decreased by half every 70 mm away from corona electrode.

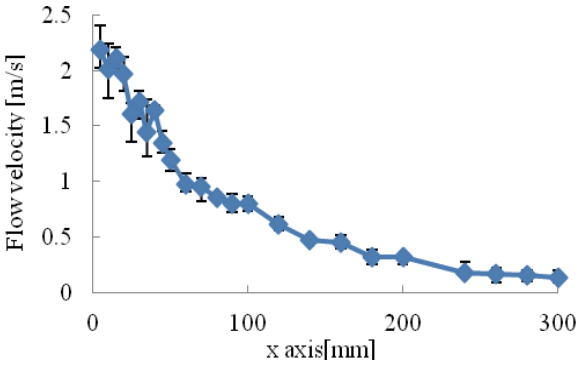

Fig. 5. Flow velocity versus x axis characteristics with y = 1mm and z= 0 mm, temperature 20℃, humidity 45 %.

4. Conclusion

In this study, a low cost, low power and small size corona electrode system and EHD flow was investigated. The following conclusions were obtained by the series of experiment.

1) Discharge current and power increased with the increasing discharge voltage. Negative corona current was about 4 times higher than positive corona discharge current at the same discharge voltage. The highest current of 22μA and a power consumption of 0.12 W were obtained at negative 5.5 kV discharge voltage.
2) Generated EHD flow velocity by driving corona electrode increased with the increase of the discharge voltage. EHD flow velocity values produced by negative corona were about 2 times higher than EHD flow velocity values generated by positive corona at the same discharge voltage.
3) Flow velocity was saturated by increasing discharge voltage. This saturation could occur due to the narrowing of effective discharge gap due to the extending corona discharge. EHD flow velocity reached 2.19 m/s when corona discharge was generated at 5 kV negative polarity.
4) Flow velocity decayed exponentially with the increasing x value. It decreased by half every 70 mm away from electrode.

Acknowledgement

The authors would like to thank Prof. Sanada of Shizuoka University for the fruitful discussions

Reference

[1]H. Kawamoto, H. Yasuda, S. Umezu, J. Electrostat., Vol. 64, pp. 400-407, 2006.

[2]E. Moreau, L. Le´ger, G. Touchard, J. Electrostat., Vo. 64, pp. 215-225, 2006.

[3] P. Magnier, D. Hong, A. L. Chesneau, J. M. Pouvesle, J. Hureau, J. Electrostat., Vol. 65, pp. 655-659, 2007.

[4] R. Karami, B. Kamkari, K. Kashefi, World Academy of Science, Engineering and Technology, ISSUE 58, pp. 527-533, 2011.

Tenth International Conference on Flow Dynamics
November 25-27, 2013, Sendai, Miyagi, Japan

Investigation of Applying Laminar Flow-based Microfluidic Microbial Fuel Cell on The Screening of Carbon Sources for Electricity Generation.

Cheng-Hsun Lin [1], Hsiang-Yu Wang[1-3]
[1]Department of Chemical Engineering, National Cheng Kung University, Tainan, Taiwan
No.1, Daxue Rd., East Dist., Tainan City 70101, Taiwan (R.O.C.)
[2]Research Center for Energy Technology and Strategy, National Cheng Kung University, Tainan, Taiwan
[3]Center for Micro/Nano Science and Technology, National Cheng Kung University, Tainan, Taiwan
ufo26604266@gmail.com, hywang@mail.ncku.edu.tw

ABSTRACT

A laminar flow-based microfluidic microbial fuel cell (LF-μMFC) for rapid-screening of nutrient sources is developed in this study. The LF-μMFC has been applied to examine the effects of different carbon sources: glucose, sucrose, sodium acetate and galactose, on the electricity generation from a mixed-culture microorganism. The results show that sucrose was suitable for our mixed-culture microorganisms for generating electricity generation and the OCV was 40% higher than those from other carbon sources.

1. Introduction

The lab-scale MFC is commonly applied to identify microbes for electricity generation and considered a reliable method; however, they require incubation time between days to weeks [1]. Moreover, the electricity output of the lab-scale MFC reflects the electron recovery efficiency of the whole setup, which is affected by the electrode material, external resistance, and proton exchange membrane. Therefore, it is challenging to identify the contribution of microorganism electro-activity on the electricity output.

In this study, a laminar flow-based microfluidic microbial fuel cell (LF-μMFC) is developed to resolve the abovementioned issues and accurately identify the electro-activity of microorganism. The LF-μMFC has been proven for its ability in identifying the electro-activity of microorganism within 30 min and the obtained results are independent of solution composition, making it a great tool for field application [2]. This study further applies the LF-μMFC to investigate the effects of carbon sources on the electro-activity of a mixed-culture microorganism obtained from the seacoast of Taiwan.

2. Method

The laminar flow-based microfluidic MFC includes a Y-shaped flow channel made of PDMS and two flat gold microelectrodes fabricated by E-beam evaporation and wet etching (Fig. 1). Due to the small scale, the two flow stream injected from the cathode and anode sides remained well separated after joining in the main channel. The flow rate of each flow is 30 ml/hr for keeping Re = 16.78 and Pe = 14326 to obtain the highest open circuit voltage (OCV). The anodal and cathodal electrodes were connected to a common multimeter to measure the OCV. Two samples were used to obtain the difference in OCV that represents the electro-activity of cells: active sample was harvested from culture tank without any treatment while inactive sample was exposed to UV light for 90 sec. Different carbon sources including glucose, sucrose, sodium acetate and galactose, were used to seek suitable nutrients for electricity generation.

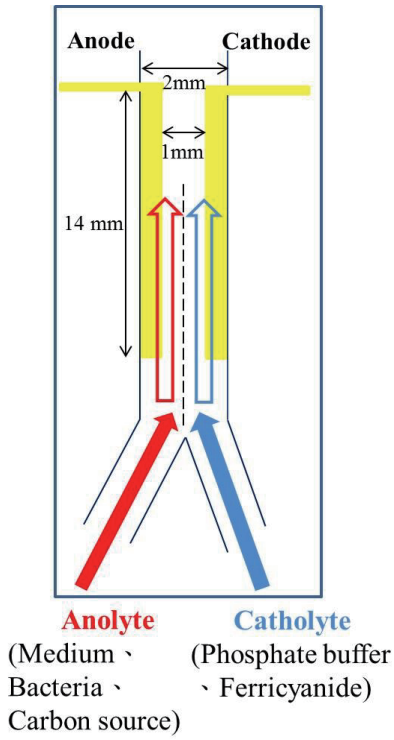

Fig. 1 The laminar flow-based microfluidic microbial fuel cell device.

3. Results and Discussion

Fig. 2 shows the OCV generated by active and inactive samples when the carbon source was sodium acetate. Since the composition of solution was identical in these two samples except for the viability of microorganism, the difference between these two OCVs can truly reflect the potential difference generated by the electroactivity of cells. The figure also shows that the device achieves steady state in 5 min since the OCV of inactive sample was stable after this time point. The OCV of active sample kept increasing because of the constituent metabolism of microorganisms. The result also shows that it is possible to use the device for

examine the impact of carbon source on electricity generation by subtracting the OCV of active by that of inactive sample.

Fig. 3 shows the difference of OCVs between active and inactive samples when different carbon sources were used. The amount of sugar residue was kept identical to the mole number of acetate. According to Fig. 2, the LF-μMFC required 5 min to start up; however, and OCV still increased/decreased after this period. This is possibly due to the different efficiencies of usage between these carbon sources by the mixed-culture microorganism. OCV generated by sucrose kept increasing after 5 min while the OCV generated by galactose showed a delay between 5 to 10 min. This indicates the mixed-culture microorganism accommodate to sucrose more rapidly. After reaching steady-state, sucrose resulted in the highest OCV, which was about 120 mV. Other carbon sources generated similar OCVs about 50 – 70 mV. The OCVs generated by these sugars are higher than sodium acetate. According to these results, sucrose is a better carbon source for the mixed-culture microorganisms to produce electricity.

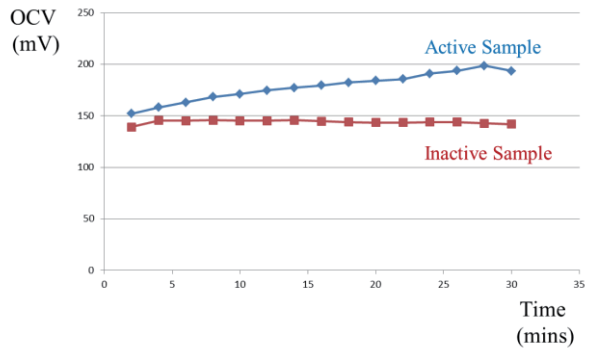

Fig. 2 The OCV generated by the active and inactive sample (exposed to UV) when the carbon source is sodium acetate.

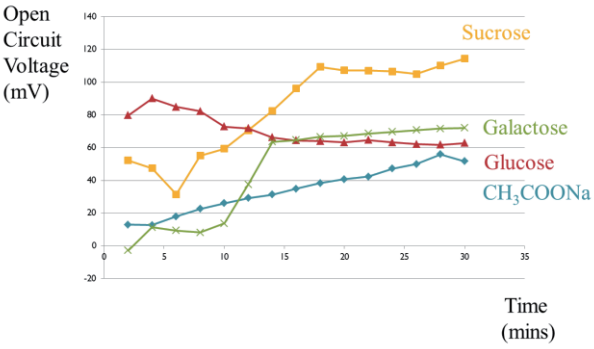

Fig. 3 The OCV generated by different carbon sources in the laminar flow-based microfluidic MFC. The amount of sugar residue was kept identical to the mole number of acetate.

4. Concluding remarks

The LF-μMFC successfully identified the suitable carbon source for the mixed-culture microorganism to generate electricity. The whole detection process can be accomplished in one hour. Applying similar principles, the LF-μMFC can also be applied to screening of other cultivation parameters for improving the performance of large scale MFCs. It can also be applied to find microorganisms that are able to digest industrial or agricultural waste to alleviate pollutions.

5.Acknowledgement

This work is funded by the National Science Council of Taiwan via NSC 102-2311-B-006 -003 -MY3 and by the Ministry of Education, Taiwan, R.O.C. via The Aim for the Top University Project to the National Cheng Kung University (NCKU).

References

[1] H. Y. Wang, A. Bernarda, C. Y. Huang, D. J. Lee and J. S. Chang, Bioresource Technology, 102, 235-243 (2011)

[2] Hsiang-Yu Wang, Jian-Yu Su, Membraneless microfluidic microbial fuel cell for rapid detection of electrochemical activity of microorganism, Bioresource Technology, January/2013, DOI: 10.1016/j.biortech.2013.01.014

Tenth International Conference on Flow Dynamics
November 25-27, 2013, Sendai, Miyagi, Japan

Complex Hydrides for Hydrogen- and Electrochemical-Energy Storage

Shin-ichi Orimo[1,2]
[1]WPI Advanced Institute for Materials Research (WPI-AIMR), Tohoku University, Sendai 980-8577, Japan
[2]Institute for Materials Research (IMR), Tohoku University, Sendai 980-8577, Japan
E-mail: orimo@imr.tohoku.ac.jp

ABSTRACT
Complex hydrides composed of complex anion(s) and counter-cation(s) have been attracting great interest as candidates of high-density hydrogen storage materials for fuel cell applications and also of fast-ionic conductors for rechargeable battery applications. In the presentation, recent progresses on the related researches will be introduced.

1. Hydrogen Energy Storage

For designing high-density hydrogen storage materials that can safely store hydrogen as hydrides at high gravimetric and volumetric densities, we are focusing on the "transition" from metal hydrides to complex hydrides. An example was recently found in YMn_2 hydride, that is, the hydride showed the continuous transformation from the metal hydride $YMn_2H_{3\sim4.5}$ to the complex hydride YMn_2H_6 with $[MnH_6]^{5-}$ complex anion with higher hydrogen density [1]. Some computational [2] and experimental studies including EXAFS [3] have been carried out in order to extend this novel property. Also, a new, reliable and convenient method for the synthesis of novel complex hydrides from metal hydrides by using additional Li as an electron donor [4] was developed. (see; Figs. 1 and 2)

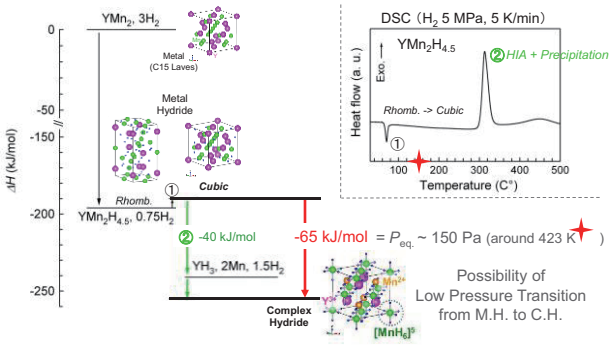

Fig. 1 Thermodynamic prediction and measurement of YMn_2H_6.

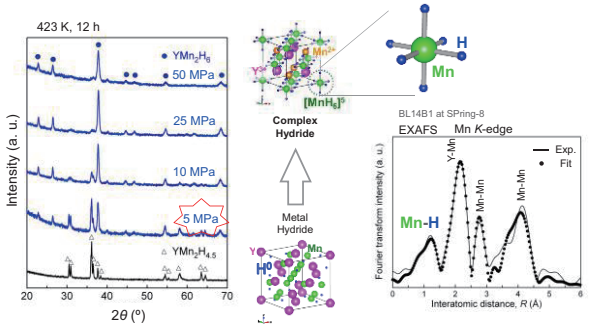

Fig. 2 X-ray Diffraction and XAFS profiles of YMn_2H_6.

2. Electrochemical Energy Storage

We have also reported the fast-ionic conduction of complex hydrides [5, 6]; suggesting that complex hydrides can be a potential candidate of new solid-electrolytes for rechargeable battery applications. The previous study on lithium fast-ionic conduction of complex hydrides will be reviewed; introducing the fast-ionic conduction in $LiBH_4$, and then discussing both the mechanism of the conduction, and the conceptual developments as solid-electrolytes in $LiBH_4$-based [7-13], $LiNH_2$-based [13-14], and $LiAlH_4$-based [15] complex hydrides. The recent progress of the sodium fast-ionic conduction [16, 17], and studies as actual solid-electrolytes for all-solid-state lithium ion rechargeable batteries [18-20] are also to be presented. (see; Figs. 3 and 4)

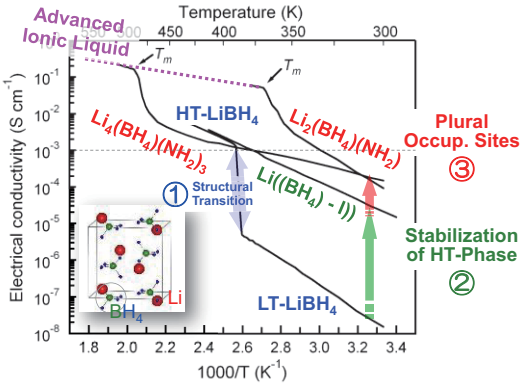

Fig. 3 Lithium fast-ionic conduction of $LiBH_4$-based complex hydrides.

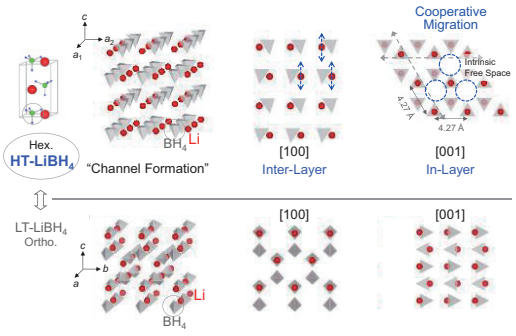

Fig. 4 Migration and conduction mechanism of lithium in $LiBH_4$.

References

[1] M. Matsuo, K. Miwa, S. Semboshi, H.-W. Li, M. Kano, S. Orimo, *Appl. Phys. Lett.*, **98** (2011) 221908.

[2] S. Takagi, K. Miwa, T. Ikeshoji, M. Matsuo, M. Kano, S. Orimo, *Appl. Phys. Lett*., **100** (2012) 021908.

[3] M. Matsuo, D. Matsumura, Y. Nishihata, G. Li, N. Hiyama, S. Semboshi, S. Orimo, *Appl. Phys. Lett.*, **100** (2012) 044101.

[4] M. Matsuo, H. Saitoh, A. Machida, R. Sato, S. Takagi, K. Miwa, T. Watanuki, Y. Katayama, K. Aoki, S. Orimo, *RSC Advances*, **3** (2013) 1013.

[5] M. Matsuo, Y. Nakamori, S. Orimo, H. Maekawa, H. Takamura, *Appl. Phys. Lett.*, **91** (2007) 224103.

[6] M. Matsuo and S. Orimo, *Adv. Energy Mater.*, **1** (2011) 161.

[7] H. Maekawa, M. Matsuo, H. Takamura, M. Ando, Y. Noda, T. Karahashi, S. Orimo, *J. Am. Chem. Soc.*, **131** (2009) 894.

[8] M. Matsuo, H. Takamura, H. Maekawa, H.-W. Li, S. Orimo, *Appl. Phys. Lett.*, **94** (2009) 084103.

[9] H. Oguchi, M. Matsuo, J.S. Hummelshøj, T. Vegge, J.K. Nørskov, T. Sato, Y. Miura, H. Takamura, H. Maekawa, S. Orimo, *Appl. Phys. Lett.*, **94** (2009) 141912.

[10] T. Ikeshoji, E. Tsuchida, K. Ikeda, M. Matsuo, H.-W. Li, Y. Kawazoe, S. Orimo, *Appl. Phys. Lett.*, **95** (2009) 221901.

[11] A. Borgschulte, R. Gremaud, S. Kato, N. Stadie, A. Remhof, A. Züttel, M. Matsuo, S. Orimo, *Appl. Phys. Lett.*, **97** (2010) 031916.

[12] T. Ikeshoji, E. Tsuchida, T. Morishita, K. Ikeda, M. Matsuo, Y. Kawazoe, S. Orimo, *Phys. Rev. B*, **83** (2011) 144301.

[13] M. Matsuo, A. Remhof, P. Martelli, R. Caputo, M. Ernst, Y. Miura, T. Sato, H. Oguchi, H. Maekawa, H. Takamura, A. Borgschulte, A. Züttel, S. Orimo, *J. Am. Chem. Soc.*, **131** (2009) 16389.

[14] M. Matsuo, T. Sato, Y. Miura, H. Oguchi, Y. Zhou, H. Maekawa, H. Takamura, S. Orimo, *Chem. Mater.*, **22** (2010) 2702.

[15] H. Oguchi, M. Matsuo, T. Sato, H. Takamura, H. Maekawa, H. Kuwano, S. Orimo, *J. Appl. Phys.*, **107** (2010) 096104.

[16] H. Oguchi, M. Matsuo, S. Kuromoto, H. Kuwano, S. Orimo, *J. Appl. Phys.*, **111** (2012) 036102.

[17] M. Matsuo, S. Kuromoto, T. Sato, H. Oguchi, H. Maekawa, H. Takamura, S. Orimo, *Appl. Phys. Lett.*, **100** (2012) 203904.

[18] K. Takahashi, K. Hattori, T. Yamazaki, K. Takada, M. Matsuo, S. Orimo, H. Maekawa, H. Takamura, *J. Power Sources*, **226** (2013) 61.

[19] T. Ikeshoji et al., *Appl. Phys. Lett.*, in press.

[20] A. Unemoto et al., *Adv. Functional Mater.*, invited.

Tenth International Conference on Flow Dynamics
November 25-27, 2013, Sendai, Miyagi, Japan

Molecular Scale Analyses of Transport Phenomena in Polymer Electrolyte Fuel Cell

Takashi Tokumasu[1], Akinori Fukushima[1], Hironori Sakai[1], Takuya Mabuchi[2], Yuta Sugaya[2]
[1]Institute of Fluid Science, Tohoku University, 2-1-1, katahira, Aoba-ku, Sendai, Miyagi, 980-8577, JAPAN
[2]Graduate School of Engineering, Tohoku University, 2-1-1, katahira, Aoba-ku, Sendai, Miyagi, 980-8577, JAPAN
tokumasu@ifs.tohoku.ac.jp

ABSTRACT

In this paper, we analyzed the nanoscale transport phenomena in membrane electrode assembly (MEA) of polymer electrolyte fuel cell (PEFC) by large scale molecular dynamics (MD) simulations. Especially, transport phenomena of proton and water in polymer electrolyte membrane (PEM), oxygen permeability of ionomer in catalyst layer (CL), and transport phenomena of water droplet in a nano pore were simulated, and the nanoscale transport characteristics were analyzed in detail to achieve the design of new concept of MEA for next generation PEFC.

1. Introduction

These days Polymer Electrolyte Fuel Cell (PEFC) is expected to be the next-generation power supply system. It is necessary to grasp the transport phenomena of proton, oxygen and water in PEFC to develop its performance and efficiency. Computational Fluid Dynamics (CFD) based on macroscopic transport equation is often used as a conventional numerical analysis. A Membrane Electrode Assembly (MEA) of PEFC, however, consists of Gas Diffusion Layer (GDL), Micro Porous Layer (MPL), Catalyst Layer (CL), and Polymer Electrolyte Membrane (PEM), in which there are many nanoscale structures. Therefore the characteristics of flow phenomena in MEA cannot be analyzed at the macroscopic point of view. Molecular simulation is suitable for analyzing these phenomena.

In this study we have analyzed these nanoscale flow phenomena by Moleclar Dynamics (MD) method. Especially, mechanism of proton transfer in PEM, oxygen permeability of ionomer in catalyst layer, and transport of water droplet in a nano pore were simulated, and the flow characteristics were analyzed in detail. In the analysis of proton transfer in PEM, we considered not only Vehicle mechanism but also Grotthus mechanism and the diffusivity of proton at various water content was estimated. The structure of water molecule in a PEM was evaluated, and the results were compared with those data obtained by experiment. With regards to the oxygen permeability of ionomer, we estimated the dependence of water content. With regards to the transport mechanism of water droplet in a nano pore, we focus on the difference of this mechanism from the macroscopic equations.

2. Proton transfer in PEM

In this study, a revised empirical valence bond (EVB) model is developed based on the the previous study of EVB model reported by Walbran et al.[1] in order to improve the description of proton mobility in both aqueous and Nafion environments. The new EVB model shows a larger proton diffusion coefficient than previous models of multistate EVB which is 0.72 ± 0.05 $Å^2/ps$. In addition, We have applied the new EVB model to Nafion system and performed an atomistic analysis of the transport of hydronium ions and water molecules in the nanostructure of hydrated Nafion membrane by systematically changing the hydration level using classical molecular dynamics simulations. After annealing procedure, the simulated density agreement with experiment is within 1.3 % for various water contents and the trends that density decreases with increasing hydration level are reproduced. A snapshot of water aggregation in Nafion membrane in our simulation is shown in Fig. 1. Using this simulation method, the diffusivity and its relation with the structure of water cluster was analyzed in detail.

3. Oxygen permeation in ionomer

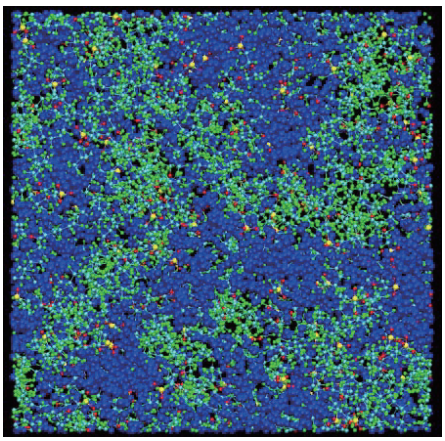

Fig. 1 The schematic diagram of simulation of proton diffusivity in PEM

In this research, the oxygen permeation of ionomer in CLs of the cathode side was simulated by molecular dynamics simulation. This system includes Pt wall, hydrocarbon or fluorocarbon membrane, water, oxonium ion and oxygen molecule. The schematic diagram of the simulation is shown in Fig. 2. In this simulation, the platinum surface was placed at the bottom of simulation box and ionomer which was composed of hydrated hydrocarbon or fluorocarbon molecules were placed on the surface. The number of oxygen molecule was set at the number that is in the gas space corresponds to 1MPa. The number of oxygen in the gas space was constant to keep the pressure in the gas space constant and permeated molecules were returned to gas space. By this procedure, we made the constant oxygen mass flux in

the ionomer. From these simulations we found that the hydrocarbon gathers toward the catalyst surface rather than fluorocarbon membrane. This phenomenon occurs because Pt strongly attracts the other molecules. Moreover, many water molecules distribute on high density hydrocarbon which are attracted by Pt. The density of water molecules on Pt surface is very low. Moreover, the oxygen permeability of fluorocarbon ionomer decreases with the increase in water content, which is an opposite tendency of bulk membrane.

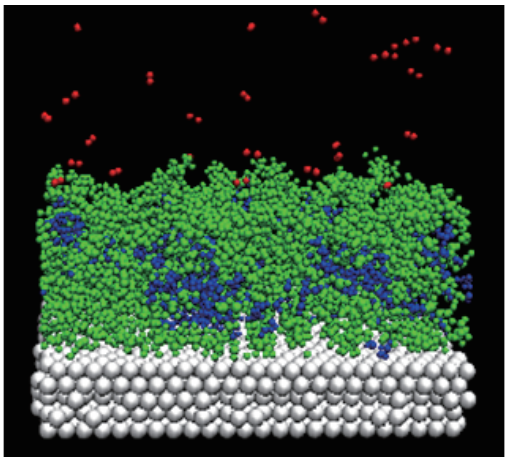

Fig. 2 Schematic diagram of simulation of oxygen permeation of ionomer inCL.

4. Transport of water droplet in a nano pore

In this study, molecular dynamics simulations are performed to evaluate the friction force between water droplet and solid walls, and the dependence of the friction coefficient on channel size is clarified. Moreover, we also discuss the limit of macroscopic hydrodynamic models. From these results, we obtain the basic knowledge about the transport properties of water droplets in the micro-porous layer and the gas diffusion layer.

Considering constant flow, the friction force between a water droplet and a solid wall can be described by a mechanical parameter as

$$F = 2\alpha W_x W_y V_{\text{slip}} + 2\sigma(\cos\theta_b - \cos\theta_a) \quad (1)$$

where α is a friction coefficient between a water droplet and a solid surface, W_x and W_y are the contact lengths in the x and y direction, θ_a and θ_b are the advancing and receding contact angles, V_{slip} is the slip velocity of water on solid walls, σ is the surface tension coefficient, respectively. The important point of this equation is the independence of the friction force on the channel width. Based on this equation, to evaluate the dependence of the friction force, we carried out molecular dynamics simulations of different-sized micro channels as shown in Fig. 3. This model is composed of two alpha graphite-like slabs with honeycomb structure, and the distance between nearest atoms is 3.0 Å. This bond length is determined by adjusting the contact angle of the water droplet on the solid wall. The MPL material used in experiments is highly hydrophobic, and the contact angle is around 145 degree. The macroscopic contact angle derived by the surface tension coefficient between the water droplet and the wall is about 150 degree, which agrees with the experimental value. From the analysis, we found that the friction coefficient decreases with increasing the channel size, while it is constant in hydrodynamics. This difference is due to the contact pressure generated by the surface tension. When the channel size is in a few nm, the pressure difference between liquid phase and vapor phase by the surface tension is in tens of MPa, since this difference is in a few Pa order in case of an mm channel. In the case of nm channel, it can be seen that the effect of the surface tension on the region far from the liquid-vapor interface cannot be ignored.

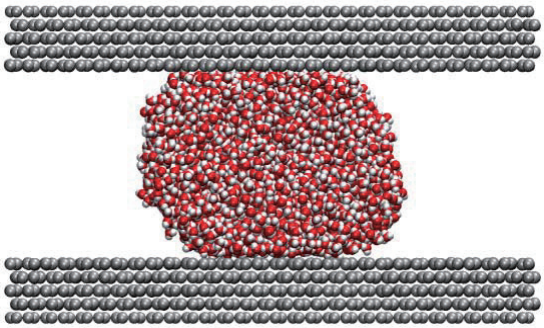

Fig. 3 Schematic diagram of simulation of transport of water droplet in a nano pore

5. Concluding remarks

We performed large scale molecular dynamics simulations to analyze the nanoscale transport phenomena of materials by a supercomputer. Especially, proton and water transport in polymer electrolyte membrane, oxygen permeation through ionomer in cathode catalyst layer, and transport mechanism of water droplet in a nano pore, all of which affects the efficiency of PEFC, were analyzed. From the results of this simulation we have obtained the knowledge about the nanoscale flow phenomena of proton, oxygen and water, which is difficult to analyze from the results by experiment. The knowledge helps us to design the new concept of MEA for higher efficiency and lower cost of PEFC in the future.

Acknowledgements

This work was supported by the New Energy and Industrial Technology Development Organization (NEDO) of Japan and the simulations were mainly performed using the supercomputer of the Institute of Fluid Science (IFS) of Tohoku University.

References

[1] S. Walbran, A.A. Kornyshev, J Chem Phys, **114** (2001) 10039-10048.

Tenth International Conference on Flow Dynamics
November 25-27, 2013, Sendai, Miyagi, Japan

In Situ Analysis of Materials and Reactions in Solid Oxide Fuel Cells

Koji Amezawa[1], Takashi Nakamura[1], Keiji Yashiro[2], Tatsuya Kawada[2], Yuki Orikasa[3], Yoshiharu Uchimoto[3]

[1]Institute of Multidisciplinary Research for Advanced Materials, Tohoku University
2-1-1 Katahira, Aoba-ku, Sendai 980-8577, Japan
[2]Graduate School of Environmental Studies, Tohoku University,
6-6-01 Aoba, Aramaki, Aoba-ku, Sendai 980-8579, Japan
[3]Graduate School of Human and Environmental Studies, Kyoto University,
Yoshida-Nihonmatsu-cho, Sakyo-ku, Kyoto 606-8501, Japan
amezawa@mail.tagen.tohoku.ac.jp.

ABSTRACT

Novel *in situ* analytical techniques using X-ray absorption spectroscopy (XAS) were developed. These techniques enabled us to examine electronic/local structures of SOFC electrode and electrolyte materials at elevated temperatures while controlling atmospheric conditions and passing electric current. We also succeeded to improve the *in situ* XAS techniques with a high position resolution of nm/μm or a high time resolution of 10-100 msec. In this presentation, our recent results on *in situ* analysis of SOFC electrolytes and electrodes by using above-mentioned techniques were reviewed.

1. Introduction

Solid oxide fuel cells (SOFCs), which can convert the chemical energy of fuels directly to electricity, are expected as one of environmental-friendly energy conversion devices in near future. For instance, stationary SOFC systems of a 0.7 kW class have been commercialized in Japan since 2011, and it was proved that the systems principally exhibited high energy conversion efficiency [1]. However, there still exist demands for further wide-spread of SOFCs, *e.g.* improvement of the performance, reduction of the operating temperature, reduction of the fabrication cost and so on. For these purposes, it is indispensable to understand the electrode reactions in SOFCs. Electrode reactions in SOFCs, in general, occur at interfaces consisting of electrode/electrolyte/gas or electrode/gas phases. Thus, it is important to clarify chemical/physical states of the interfaces. However, since SOFCs operate under extremely severe conditions for conventional analytical techniques, *e.g.* high temperature, specific atmosphere and polarization, only a limited number of *in situ* analytical techniques are available. Therefore, chemical/physical states of SOFC electrodes and electrolytes under operation have been poorly understood so far.

Considering such backgrounds, we have established novel *in situ* analytical techniques using X-ray absorption spectroscopy (XAS), which enable us to investigate electronic/local structures of SOFC components at elevated temperatures while controlling atmospheric gas partial pressures and applying electrical voltage. We also improved *in situ* XAS techniques haing a high position resolution of nm/μm or a high time resolution of 10-100 msec. In this presentation, we will overview our recent results obtained with the above-mentioned *in situ* analytical techniques on SOFC electrolytes and electrodes under operation.

2. *In Situ* XAS for SOFCs

Electrode reaction mechanisms on a mixed oxide ion and electron conducting oxide for an SOFC cathode were investigated by the developed *in situ* XAS. Figure 1 shows *in situ* Co *K*-edge XANES spectra observed with a $La_{0.6}Sr_{0.4}CoO_{3-\delta}$ (LSC64) dense thin film electrode on a $Ce_{0.9}Gd_{0.1}O_{1.95}$ electrolyte. The measurements were performed under $p(O_2)$ =0.01 bar at 1073 K under open circuit and polarization. It was clearly seen that the absorption edge shifted toward lower/higher energy as the cathodic/anodic bias was applied, respectively. Such a shift of the absorption edge energy indicated the partial reduction/oxidation of Co ions in the oxide film due to the polarization even under constant $p(O_2)$. In other words, the cathodic/anodic polarization induced the decrease/increase in oxygen chemical potential μ_O in the oxide electrode. The electrode overpotential η at an electrode on an oxide ion conductor can be regarded as a deviation of μ_O at the electrolyte/electrode interface [2]. Amounts of the absorption edge shift could be quantitatively explained

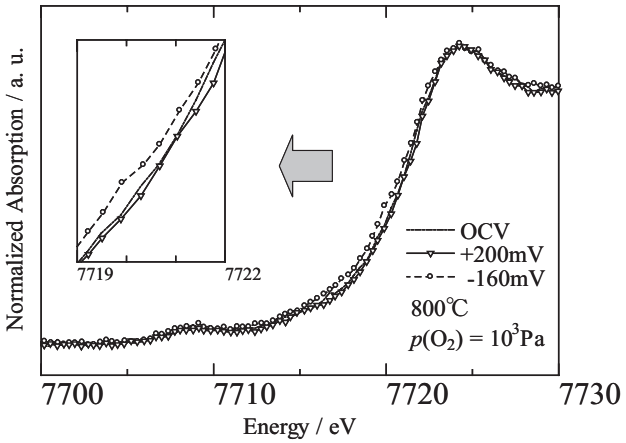

Fig. 1. *In situ* Co *K*-edge XANES spectra of a $La_{0.6}Sr_{0.4}CoO_{3-\delta}$ dense thin film cathode on a $Ce_{0.9}Gd_{0.1}O_{1.95}$ electrolyte under various applied voltages at $p(O_2)$ = 0.01 bar and 1073 K.

by considering the effective oxygen potential change calculated from $\Delta\mu_{O,eff}=2F\eta$. This suggested that the μ_O change due to the polarization was generated dominantly on the electrode surface, and demonstrated that the electrochemical oxygen exchange reaction with the LSC64 dense film electrode was rate-controlled by surface reactions, *i.e.* oxygen adsorption and dissociation.

3. *In Situ* XAS with a high position resolution

Application of a focused X-ray beam makes a high position resolution measurement possible [3]. By using this so-called *in situ* micro XAS technique, we investigated oxygen potential distribution in a porous LSC64 electrode [4]. The oxygen potential distribution evaluated from *in situ* micro XAS is given in Fig. 2 as a function of the distance from the electrode/electrolyte interface. The measurements were carried out at 873 K and $p(O_2)$ = 0.01 bar under cathodic polarization of -0.14 V. As seen in Fig. 2, the cathodic polarization caused the partial reduction of LSC64 in the vicinity of the cathode/electrolyte interface. It was shown that the area within approximately 4μm from the interface was under reduced condition by applying the cathodic voltage. This result suggested that the effective reaction area in the porous LSC64 electrode is around 4 μm from the interface under experiment conditions employed. It was demonstrated that the *in-situ* micro XAS measurement can directly evaluate the distribution of the oxygen chemical potential in a porous SOFC electrode.

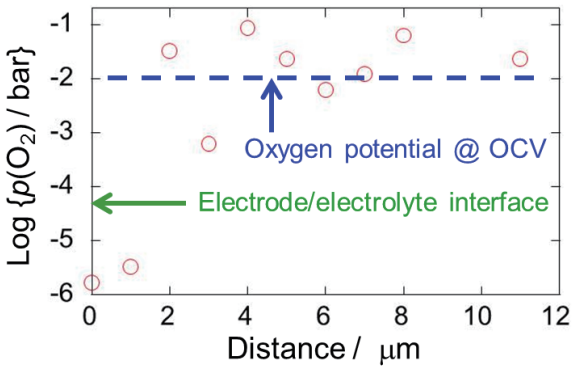

Fig. 2. Distribution of oxygen potential in the porous $La_{0.6}Sr_{0.4}CoO_{3-\delta}$ electrode on a $Ce_{0.9}Gd_{0.1}O_{1.95}$ electrolyte under cathodic overpotential of -0.14 V as a function of the distance from the cathode/electrolyte interface.

4. *In Situ* XAS with a high time resolution

A high time resolution measurement becomes possible by using a high-flux X-ray beam. Time dependence of the oxidation state of an SOFC cathode was investigated with this analytical technique [5]. In Fig. 3, Ni *K*-edge absorption energy observed with the $Nd_2NiO_{4+\delta}$ thin film electrode was plotted as a function of time. In this measurement, XAS spectra were corrected every 500 msec. Under open circuit condition, for the first 10 sec in Fig. 3, the value of the absorption energy seemed independent of time. On the other hand, as soon as a cathodic voltage was applied, the absorption edge shifted toward lower energy and then reached to a constant value. This result suggested that the surface reaction is the rate-controlled step for the oxygen reduction reaction on the $Nd_2NiO_{4+\delta}$ thin film electrode and that the partial reduction of the oxide cathode due to the polarization is relaxed within 20-30 sec. It is supposed that such a slow relaxation of the partial reduction was caused by diffusion of oxide ions in the oxide.

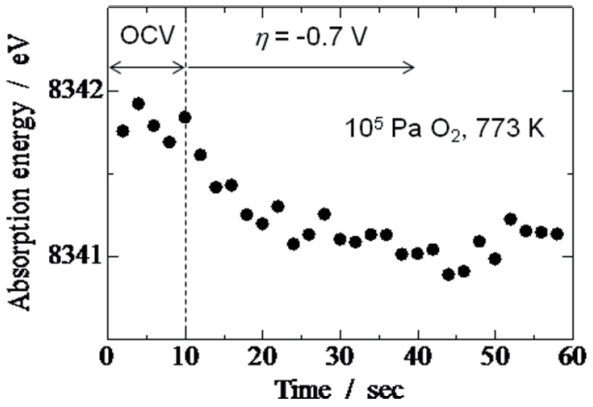

Fig. 3. Time dependence of Ni *K*-edge absorption energy for the $Nd_2NiO_{4+\delta}$ dense thin film electrode on a $Ce_{0.9}Gd_{0.1}O_{1.95}$ electrolyte when a cathodic voltage of -0.7 V was applied in 1 bar of $p(O_2)$ at 773 K.

Acknowledgements

This work was supported by CREST from the Japan Science and Technology Agency (JST) and Grant-in-Aid for Scientific Research of MEXT, Japan.

References

[1] For instance, http://www.noe.jx-group.co.jp/Newsrelease/2011/20110915_01_0950261.html

[2] T. Kawada, *et al.*, *J. Electrochem. Soc.*, **149(7)**, E252 (2002)

[3] K. Amezawa, *et al.*, *Electrochem. Soc. Trans.*, **13(26)**, 161 (2008).

[4] K. Amezawa, *et al.*, *Electrochem. Soc. Trans.*, **25(2)**, 345 (2009).

[5] K. Amezawa, *et al.*, *Extended abstract of the 18th Int. Conf. on Solid State Ionics* (2011).

Tenth International Conference on Flow Dynamics
November 25-27, 2013, Sendai, Miyagi, Japan

All-solid-state Li-ion Battery Research using Epitaxial Thin Films

Taro Hitosugi, Masakazu Haruta and Susumu Shiraki
Advanced Institute for Materials Research (AIMR), Tohoku University, 2-1-1 Katahira, Aoba, Sendai, Japan.
Email: hitosugi@wpi-aimr.tohoku.ac.jp

ABSTRACT

We here demonstrate the fabrication of all-solid-state battery using $LiCoO_2$ epitaxial thin films on Au(110)-2x1 reconstructed surfaces. The epitaxial $LiCoO_2$ thin film consists of three phases with different crystal orientations, all of which have CoO_2-layers tilted with respect to the surface normal. The all-solid-state batteries using the epitaxial $LiCoO_2$ films showed good stability and repeatability during charge and discharge cycles. Further, we discuss on the epitaxial growth of Li-oxides for Li-ion battery, such as, $Li_4Ti_5O_{12}$, $LiTi_2O_4$ and $LiMn_2O_4$.

1. Introduction

All-solid-state lithium-ion battery (LIB) is a promising energy storage system that succeeds the present LIBs based on a liquid organic electrolyte. One of the largest drawbacks that hinder the practical use of all-solid-state LIBs is the low Li-ion conductance at the electrolyte/electrode interface. Recent investigations on the coating of electrodes show an improved conductance at the interfaces by coating electrode materials with other materials [1,2]. However, the mechanism leading to high conductance is still an open question. This is partly because powder samples were used in previous experiments, and thus, interface area, crystal orientations, and structures are not defined, hampering further investigation into the microscopic mechanisms.

Epitaxial thin films offer ideal platform for the study of ionic conduction across the electrolyte/electrode interface. In particular, the abrupt interfaces formed by epitaxial thin films would allow the quantitative analysis of ionic conductivity through ion-conducting channels. Consequently, growth of high-quality Li-oxide is very important for the atomic-level engineering of oxide materials for oxide electronics and LIB research. Epitaxial thin films of electrode materials such as $LiCoO_2$ (LCO) [3, 4, 5, 6], $Li_4Ti_5O_{12}$ [7,8], $LiMn_2O_4$ [9] have been recently reported [10]. No work, however, has been done on the fabrication and evaluation of all-solid-state LIBs containing electrolyte/electrolyte interface composed of epitaxial electrode thin films. Such studies should give further insight into the conduction mechanisms at the interface.

We here report the operation of all-solid-state LIB using epitaxial LCO thin films. We focus on LCO thin films on a reconstructed Au(110)-2x1 substrate surfaces deposited by using pulsed laser deposition (PLD). We evaluated electrochemical properties of the LIB device using the epitaxial LCO film with cyclic voltammetry (CV), demonstrating high mobility at electrolyte/electrode interface. These studies open up the pathways to investigate electrolyte/electrode interface quantitatively, leading to the fundamental understandings of the origin of interface resistance.

2. Method

Since LCO films deposited on as-polished Au(110) surface using PLD showed a variety of thin film orientations owing to the dense scratch on the substrate surface, we prepared the Au(110)-2x1 substrate surfaces with extensive sputtering-annealing cycles in ultra high vacuum (UHV). Surface reconstruction was confirmed with low-energy electron diffraction and reflection high-energy electron diffraction. LCO thin films were deposited by using PLD with a polycrystalline $Li_{1.2}CoO_2$ target (Toshima Manufacturing). A KrF excimer laser (wavelength: 248 nm), with a repetition rate of 5 Hz and a fluence of 1 J/cm^2 at the substrate surface, was used for the deposition. The oxygen partial pressure during the deposition was kept at 1×10^{-6} Torr. The substrate temperature during the deposition was room temperature (RT), and the subsequent annealing was done at 650^{o}C in air. A typical thickness of the LCO films was 200 nm. The crystal structures of the films were characterized with an XRD (NEW D8 Discover, Bruker). The solid electrolyte, lithium phosphorous oxynitride (LiPON), and anode Li thin films were deposited by using RF magnetron sputtering and thermal evaporation, respectively.

3. Results and Discussion

Figure 1 shows an out-of-plane XRD result of the LCO thin film deposited on the Au(110)-2×1 surface. We can clearly see a (104) peak of LCO in addition to a (110) peak from the Au substrate. This indicates the epitaxial growth of LCO thin film with an orientation that c-axis of LCO is tilted by 53.7^o with respect to the surface normal. In addition, we found the growth of small LCO domains with another type of orientation that c-axis of LCO is perpendicular to the {111} micro-facets of the surface reconstruction. Similar tendency was also observed for the LCO thin films deposited on the Pt(110)-2×1 surface. The distance between adjacent CoO_2 planes is slightly longer for LCO on Pt than that on Au. These results suggest that fine structures such as reconstruction on substrate surfaces strongly affect the orientation of the thin films.

We further deposited LiPON and Li thin films on the LCO/Au(110)-2x1 to fabricate thin-film all-solid-state batteries and studied its electrochemical properties by CV. At both positive and negative scans in the CV curves, we found some sharp peaks characteristic to LCO. All the CV curves show good stability and repeatability, which is probably due to smooth transport

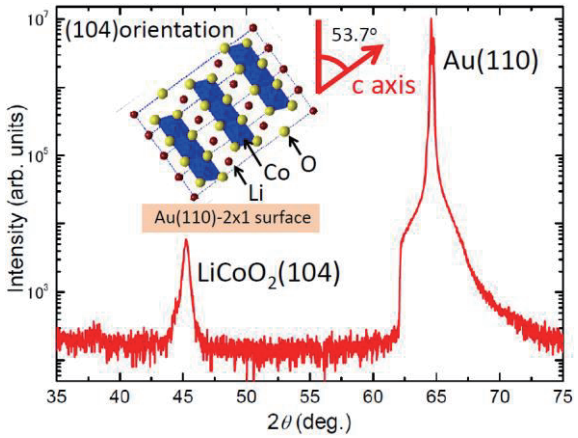

Fig. 1 XRD out-of-plane pattern from the LCO thin film deposited on the Au(110)-2×1 surface.

of Li ions toward in direction perpendicular to the stacking of films.

4. Concluding remarks

We fabricated epitaxial thin films of LCO on the reconstructed Au(110) and Pt(110) surfaces. These films show a mixture orientations that c-axis is tilted with respect to the surface normal. We also fabricated the all-solid-state batteries of Li/LIPON/LCO by stacking those films, showing good CV curves.

5. Acknowledgement

This research was supported by the Japan Society for the Promotion of Science through its Funding Program for World-Leading Innovation R&D on Science and Technology (FIRST Program).

References

[1] N. Ohta1, K. Takada, L. Zhang, R. Ma, M. Osada, T. Sasaki1, Adv. Mater. 18, 2226 (2006).
[2] K. Takada, Acta Mater. 61, 759 (2013).
[3] M. Hirayama, N. Sonoyama, T. Abe, M. Minoura, M. Ito, D. Mori, A. Yamada, R. Kanno, T. Terashima, M. Takano, K. Tamura, M. Junichiro, J. Power Sources 168, 493 (2007).
[4] T. Tsuruhama, T. Hitosugi, H. Oki, Y. Hirose, T. Hasegawa, Appl. Phys. Express 2, 085502 (2009).
[5] H. Moriwake, A. Kuwabara, Craig A. J. Fisher, R. Huang, T. Hitosugi, Y. H. Ikuhara, H. Oki, Y. Ikuhara, Adv. Mater. 25, 618 (2013).
[6] K. Iwaya, T. Ogawa, T. Minato, K. Miyoshi, J. Takeuchi,A. Kuwabara, H. Moriwake, Y. Kim, T. Hitosugi, Phys. Rev. Lett (2013) *in press*.
[7] M. Hirayama, K. Kim, T. Toujigamori, W. Cho, R. Kanno, Dalton Trans. 40, 2882 (2011).
[8] A. Kumatani, T. Ohsawa, R. Shimizu, Y. Takagi, S. Shiraki, T. Hitosugi, Appl. Phys. Lett. 101, 123103 (2012).
[9] N. Sonoyama, K. Iwase, H. Takatsuka, T. Matsumura, N. Imanishi, Y. Takeda, R. Kanno, J. Power Sources 189, 561 (2009).
[10] D. Packwood, S. Shiraki, T. Hitosugi D. Packwood, Phys. Rev. Lett. 111, 036101 (2013).

Tenth International Conference on Flow Dynamics
November 25-27, 2013, Sendai, Miyagi, Japan

A novel nanomaterial design for high energy density lithium ion batteries

Itaru HONMA

Institute of Multidisciplinary Research for Advanced Materials, Tohoku University
2-1-1 Katahira, Aoba-ku Sendai, Miyagi, 980-8577, Japan, i.honma@tagen.tohoku.ac.jp

ABSTRACT

A novel nanomaterials design based on nanocrystalline particles, graphenes, ionic liquids, nano-materials processing such as supercritical fluids have been investigated for the developments of high energy density lithium ion battery, which will be applied to electric vehicles or solar cell back-up electricity storage in the future smart renewable grid systems

Recent surge in demands for large-scale batteries in electric vehicles and "smart grid" applications require development of lithium ion battery (LIB) materials that are low-cost, free of resource restrictions and environmentally friendly. The conventional metal oxide cathodes on the market today falls short for this purpose because they require "rare metals" such as Co, Ni, Mn and their preparation too, involves energy- intensive processes. On the contrary, organic compounds present promising possibilities because they are high energy density, primarily owing to their two-electron redox reactions, in spite of metal-free elements. Figure 1 shows examples of the candidate organic quinone molecules which, theoretically, possess higher specific capacities than that of inorganic cathodes such as $LiFePO_4$. However, they have not been actively pursued due to low cycleability, primarily owing to a dissolution into the electrolyte because discharge products of these organic molecules are highly soluble species of monoanion radical (-) and/or dianion (2-) states. But, we have successfully developed a high energy density all-solid state lithium battery cell with much better cycleability by suppressing the dissolution processes. A novel solid cell design is developed via application of quasi-solid electrolyte at the interface of organic crystalline cathodes, which successfully avoids dissolution of anionic molecular compounds. The cell features totally encapsulated cathode, PEO layer, quasi-solid electrolyte and controlled electrolyte- anode interface that accommodate soluble organic cathodes under charge/discharge cycles. Quasi-solid state electrolyte consists of silica nanoparticles and room temperature ionic liquid (RTIL) were used to stabilize organic cathode interfaces against dissolution. Molecular crystals of tetracyano quinodimethane (TCNQ) possesses two electron redox capacity equivalent of 262 mAh/g with first redox potential plateau at 3.2V (vs. Li/Li^+) and the second at 2.8V, providing apparent two step potential profile in fig.2. Many of such compounds shown in fig.1. have similarly two electron redox capacities exceeding 230 mAh/g; 2,3,5,6-tetrahydroxy benzoquinone (THBQ), 2,3-dichloro-5, 6-dicyano- benzoquinone (DDQ) and 2,5-dihydroxy benzoquinone (DHBQ) are intrinsically possessing higher energy density than that of $LiFePO_4$. The multi-electron capacity at high potential expected in the quinone family of organic cathodes may increase energy densities of the cell although no metallic elements are used in the active materials. If these strategy are successfully implemented in the LIB device, significant reduction of the rare metals can be realized. Figure 3 shows the physical features of bulk organic

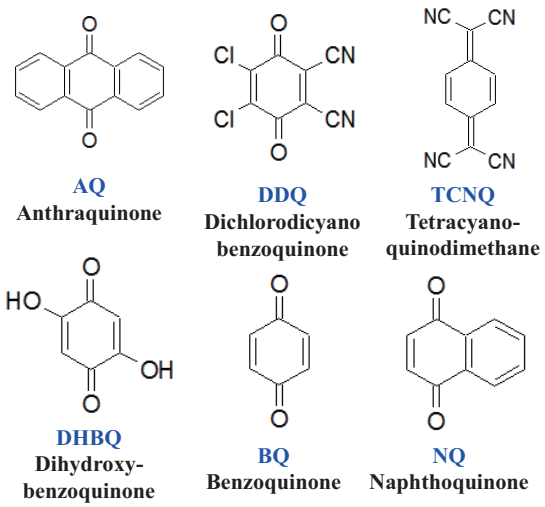

Figure 1.
Families of organic molecular active materials for high capacity electrodes

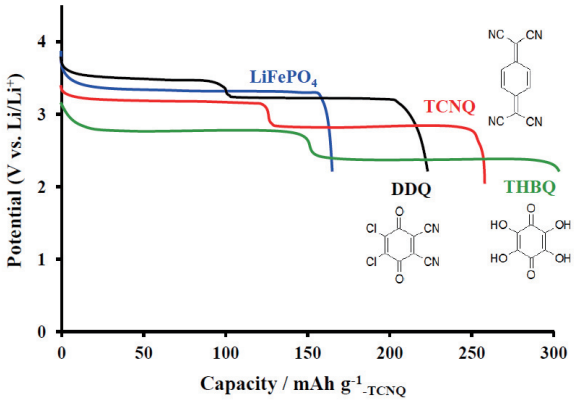

Figure 2.
Discharge profiles of several quinone molecular electrodes. The energy densities of these organic electrodes exceed that of inorganic one, $LiFePO_4$

all-solid lithium cell. A photograph of the actual pellet with a diameter of 10 mm and thickness ~ 1000 μm is shown and the TCNQ cathode paste in the insert. A large (~50 μm) TCNQ crystal is visible, while the solid state cathode contains TCNQ crystals, carbon current collector and room temperature ionic liquids (RTIL). Three layered electrolyte consisting of PEO membrane, silica-RTIL composite quasi-solid state electrolyte and artificial SEI separates the cathode from metallic lithium anode. Figure 4 shows cycle performances of the TCNQ cathodes and favourable capacity retention can be achieved, indicating that, by suppressing molecular dissolution into the electrolyte, organic materials can be used in the secondary battery electrodes under the solid state cell design. A cycleability of TCNQ using [BMP][Tf_2N] ionic liquid in the quasi-solid electrolytes at 0.2 C rate at room temperature has shown that, after extended charge-discharge cycles over 170 times, the capacity was still over 170 mAh/$g_{\text{-TCNQ}}$. The strategy of stabilizing electrode/ electrolyte interface of the organic cathodes have confirmed the possibilities of numerous molecularitic compounds dismissed before due to low cycleability would worth a re-visit under solid state design.

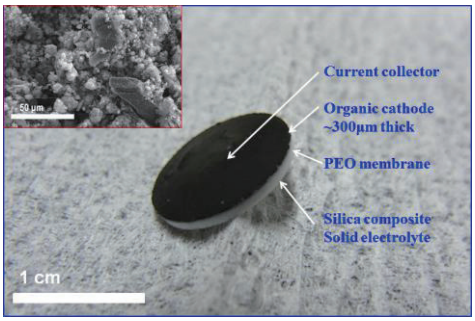

Figure 3.
Solid state lithium ion battery design employing TCNQ crystals (shown in the insert) as cathode enables higher energy storage density against present LIB cells

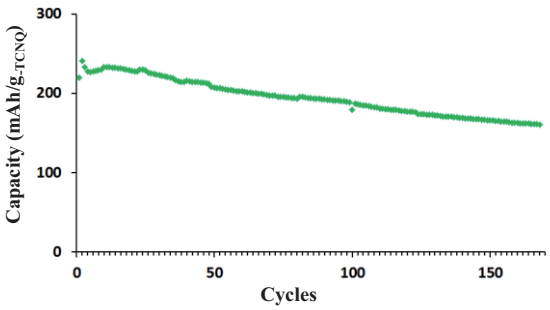

Figure 4.
Cyclic performance of TCNQ cathodes in the solid state cell over 170th times shows favourable capacity retention

References

1. Yuki Hanyu, Yoshiyuki Ganbe and Itaru Honma: Application of quinonic cathode compounds for quasi-solid lithium batteries. ***J. Power Sources***, *221*, 186-190 (2013)
2. Yuki Hanyu and Itaru Honma: Rechargeable quasi-solid state lithium battery with organic crystalline cathode. ***Scientific Reports***, *2*, 453 (2012).
3. Marappan Sathish, Satoshi Mitani, Takaaki Tomai and Itaru Honma: Ultra-thin SnS_2 Nanoparticles on Graphene Nanosheets: Synthesis, Characterization and Li-ion Storage Applications. ***J. Physical Chemistry C***, *116*, 12475 -12481 (2012).
4. Murukanahalli Kempaiah Devaraju, Dinesh Rangappa and Itaru Honma: Controlled Synthesis of Nanocrystalline Li_2MnSiO_4 Particles for High Capacity Cathode Application in Lithium ion Batteries. ***Chemical Communications***, *48*, 2698-2700 (2012).
5. Dinesh Rangappa, Murukanahalli Kempaiah Devaraju, Takaaki Tomai, Atsushi Unemoto and Itaru Honma: Ultra Thin Nanosheets of Li_2MSiO_4 (M= Fe, Mn) as High Capacity Li Ion Battery Electrodes. ***Nano Letters***, *12*, 1146-1151 (2012).
6. Atsushi Unemoto, Yoshiki Iwai, Satoshi Mitani, Seitaro Ito, Takaaki Tomai, Junichi Kawamura and Itaru Honma: Mass transport properties in quasi-solidified lithium-ion conducting ionic liquids at oxide particle surfaces, ***Solid State Ionics***, *225*, 416-419 (2012).
7. Seitaro Ito, Atsushi Unemoto, Hideyuki Ogawa, Takaaki Tomai, and Itaru Honma: Application of quasi-solid-state silica nanoparticles- ionic liquid composite electrolytes to all-solid-state lithium secondary battery. ***J. Power Sources***, *208*, 271-275 (2012)

Tenth International Conference on Flow Dynamics
November 25-27, 2013, Sendai, Miyagi, Japan

High Efficiency Silicon QD Solar Cells Using Bio-template Ultimate Top-down Processes

Seiji Samukawa[1,2,3]
[1] Institute of Fluid Science, Tohoku University, 2-1-1 Katahira, Aoba-ku, Sendai 980-8577, Japan
[2] WPI-AIMR, Tohoku University, Japan
[3] Japan Science and Technology Agency (JST), CREST, Japan
samukawa@ifs.tohoku.ac.jp

ABSTRACT

High density and regularly arranged 2-dimensional array of silicon nanodisk, a sub-10nm-silicon-nano-disk (Si-ND) structure, was fabricated using the bio-template (ϕ7-nm-etching-mask) and damage-free chlorine (Cl) neutral beam (NB) etching. In this structure, the controllable band gap energy (from 2.2eV to 1.4eV) and high photon absorption coefficient (>10^5 cm^{-1}) could be obtained at RT. This structure can be used to develop high efficiency and inexpensive silicon quantum dot solar cells.

1. Introduction

Recently, an all-silicon tandem solar cell comprising a quantum dot superlattice (QDSL) has attracted much attention due to its potential to breakthrough the Shockley-Queisser limit.[1,2] One of the advantages of the QDSL is that the required energy band gap for each cell can be engineered by changing the quantum dot size.[3] Reportedly, the maximum conversion efficiency can be improved up to 47.5% for three-cell tandem stacks.[4] However, not only the uniformity and control of QD size but also of the spacing between QDs are equivalently essential to generate the miniband in the QDSL for carrier transport.[5] The ideal spacing between QDs is approximately 2 nm or less in the SiO_2 matrix.[6] The technique widely used to fabricate the Si quantum dot superlattice is depositing alternately multiple layers of amorphous silicon-rich oxide (SiO_x, x<2) and stoichiometric silicon dioxide (SiO_2) by sputtering or plasma-enhanced chemical vapor deposition followed by annealing at a high temperature.[6] However, the results showed nonuniform dot size and dot spacing.

To address these problems, we have developed a sub-10nm-silicon-nano-disk (Si-ND) structure using the bio-template (ϕ7-nm-etching-mask) and damage-free chlorine (Cl) neutral beam (NB) etching.[7] The fabricated ND had a quantum effect, i.e. Coulomb staircase, at room temperature (RT). Two geometrical parameters of thickness and diameter in Si-ND can be independently controlled. Interestingly, the quantum effect of a single Si-ND is strongly dependent on its thickness, while almost independent of its diameter.[7] In this study, a 2D Si ND array with a high-density and well-ordered arrangement could be fabricated by using bio-template and an etching process combined with nitrogen trifluoride (NF_3) gas/hydrogen radical treatment (NF_3 treatment) and Cl NB etching. In this structure, the controllable band gap energy (from 2.2eV to 1.4eV) and high photon absorption coefficient (>10^5 cm^{-1}) could be obtained at RT by controlling the Si-ND structure.

2. Fabrication of high-density 2D array of Si-ND

The fabrication of a 2D Si-ND array using the bio-template and damage-free NB etching[7] is schematically shown in Fig. 1(a). The steps are as follows: multilayer films of 1.4-nm SiO_2, several nm-thick poly-Si and 3-nm SiO_2 (the 3-nm SiO_2 was fabricated by our developed neutral beam oxidation at a low temperature of 300 ºC and is called NBO SiO_2 hereafter) were sequentially prepared on a Si wafer as shown in Figs. 1(1), (2), and (3), respectively; (4) a 2D array of ferritin molecules (protein including iron oxide core (Fe-core) in the cavity) was placed through directed selforganization on the surface of NBO SiO_2; (5) ferritin protein shells were removed by heat treatment in oxygen atmosphere to obtain 2D Fe-core as a template; (6) etching was carried out using a NF_3 treatment and Cl NB etching to remove NBO SiO_2 and poly-Si, respectively; (7) and finally 2D Fe core was removed by using hydrochloric solution. The sample underwent NF_3 treatment for 30 min to remove NBO SiO_2 and NB etching for 90 seconds to remove 4-nm poly-Si. Figure 2 shows a SEM image of the top view of the sample after etching. We can see that the 2D Si-ND array has a high-density (>7×10^{11} cm^{-2}) and well-ordered arrangement. The 2D array is what remained after etching, proving that a good-quality 2D Si-ND array was successfully fabricated using the bio-template and Cl NB etching with NF_3 treatment. We performed NF_3 treatment to investigate the controllability of the ND diameter, i.e. the spacing between NDs. When the NF_3 treatment times were 15 and 30 min, the average gaps were about 1 and 3 nm (G_{ii} and G_{iii}), and the diameters were about 10 and 8 nm (D_{ii} and D_{iii}), respectively . These results suggest that the spacing between adjacent NDs can be controlled by changing the NF_3 treatment time, which also indicates that the formation of miniband in a 2D Si-ND array can be controlled. Although the spacing control by NF_3 treatment is accompanied by inevitable changes in diameter, the diameter changes do not affect the quantum effect, which was proven in a previous work.[7]

3. Optical Properties of 2D Si-ND array

The absorption properties of the structure were studied by measuring the transmission for samples by

UV-vis-NIR. The absorption coefficient has been calculated in accordance with the equation below

$$T=e^{-\alpha d} \quad (1)$$

α being the absorption coefficient, d the total thickness of the ND thickness and surface oxide thickness (3-nm thick), and T the transmittance of light passing through the structure. Figure 3(a) shows the results of an absorption coefficient of the structure as a function of ND thickness. We found that the absorption spectra strongly depend on the ND thickness and the absorption edge is blue-shifted when the ND thickness decreases due to the quantum size effect. Additionally, the absorption coefficient (>10^5 cm^{-1}) of 2D Si-ND array is extremely high, and therefore it is possible to obtain sufficient absorption if the NDs can be integrated into the 3rd dimension. To determine the optical band gap energy of the structure, the Tauc formula was used:

$$(\alpha h\nu)^{1/2}=A(h\nu-E_g), \quad (2)$$

where A is a constant, h is Planck's constant, ν is frequency, E_g is the band gap energy, and n is 1/2 in the case of indirect allowed and forbidden electronic transitions. The Tauc formulation as a function of ND thickness is plotted in Fig. 3(b). As the ND thickness changes from 2 to 12 nm, the E_g could be controlled from 2.2 to 1.4eV as shown in Fig. 4. From these results, we found that E_g could be certainly controlled by simply changing ND thickness by thin-film deposition in our proposed fabrication. Based on the processes, all-Si tandem solar cells assembled with 3D ND array fabricated by stacking 2D Si-ND array as schematically shown in Fig. 5 could be constructed.

4. Conclusions

We created a 2D Si-ND array with a high-density and well-ordered arrangement using bio-template and an advanced etching process that included NF_3 treatment and damage-free Cl NB etching. The spacing between Si NDs can be controlled in the structure by changing NF_3 treatment time. The E_g can be easily controlled by changing the ND thickness during thin film deposition. The absorption coefficient of single layer 2D Si-ND is comparable to that of 3D QDSL. Our proposed processes for 2D Si-ND array and stacked ND are very feasible for the all-Si tandem solar cells comprising QDSL.

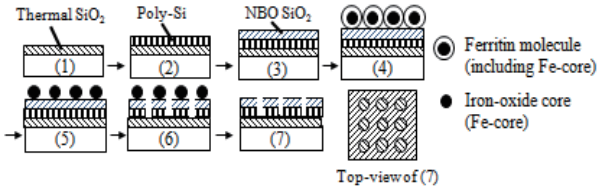

Fig. 1 Fabrication flow of 2 dimensional Si nano-disk array by bio-template and chlorine neutral beam etching.

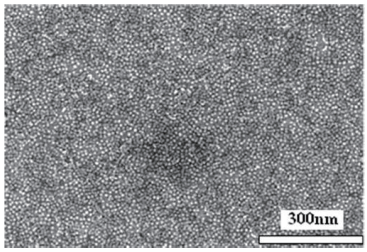

Fig. 2 SEM images of 2 dimensional Si nano-disk array fabricated by Cl neutral beam etching with bio-template.

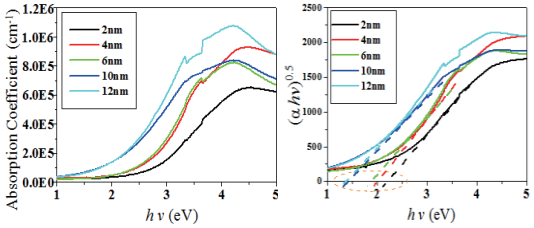

Fig. 3 (a) Absorption coefficient (b) Tauc plot of 2 dimensional Si nano-disk array with different nano-disk thicknesses from 2 nm to 12 nm.

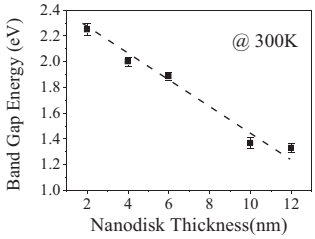

Fig. 4 Band gap energy (E_g) of nano-disk with different Si nano-disk thicknesses by using UV-vis-NIR.

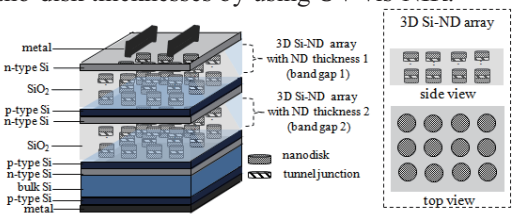

Fig. 5 Scheme of all-silicon tandem solar cell assembled with 3 dimensional Si nano-disk array.

References

[1] W. Shockley and H. J. Queisser, J. Appl. Phys. **32** (1961) 510.

[2] M. A. Green, 20th EU-PVSEC (2005), 1AP.1.1.

[3] A. Kongkanand, K. Tvrdy, K. Takechi, M. Kuno, and P. V. kamat, J. Am. Chem. Soc. **130** (2008) 4007.

[4] G. Conibeer, M. Green, E.-C. Cho, D. Konig, Y.-H. Cho, T. Fangsuwannarak, G. Scardera, E. Pink, Y. Huang, T. Puzzer, S. Huang, D. Song, C. Flynn, S. Park, X. Hao, D. Mansfield, Thin Solid Films **516** (2008) 6748.

[5] A. J. Nozik: Physica E **14** (2002) 115.

[6] Y. Kurokawa , S. Miyajima, A. Yamada, and M. Konagai, Jpn. J. Appl. Phys. **45** (2007) L1064.

[7] S. Samukawa, T. Kubota, C.-H. Huang, T. Hashimoto, M. Igarashi, K. Nishioka1, M. Takeguchi, Y. Uraoka, T. Fuyuki, and I. Yamashita, Appl. Phys. Express **1** (2008) 074002.

Tenth International Conference on Flow Dynamics
November 25-27, 2013, Sendai, Miyagi, Japan

Integration of nanostructures in crystalline silicon solar cells

Noritaka Usami[1], Yusuke Hoshi[1], and Takeshi Tayagaki[2]
[1]Graduate School of Engineering, Nagoya University, Chikusa-ku, Nagoya 464-8603, Japan
[2]Institute for Chemical Research, Kyoto University, Uji, Kyoto 611-0011, Japan
usa@numse.nagoya-u.ac.jp

ABSTRACT

We introduce our recent research activities to integrate nanostructures in crystalline silicon solar cells. Photonic nanostructures coupled with vertically aligned germanium quantum dots are employed for advanced management of photons and carriers. The unique nanostructures are simply fabricated by wet etching without any lithography techniques. Optical properties of nanostructures as well as results of preliminary attempt to integrate photonic nanostructures in crystalline silicon solar cells will be reported.

1. Introduction

Light-trapping structures at the surface are known to be crucial to improve the performance of solar cells through increase of absorptivity and generation of carriers. In crystalline silicon solar cells, surface textures are formed by various techniques including wet etching, reactive ion etching, and so on. The structure of the record crystalline silicon solar cell with a conversion efficiency of 25.0% has inverted pyramids with {111} facets formed by combining photolithography and anisotropic chemical etching [1]. The dimensions of the structures are usually much larger than the wavelength.

In the field of optoelectronics, the structures with the dimensions equivalent with or smaller than the wavelength are intensively studied. For such small structures, coherence and interference phenomena become more important. In fact, photonic nanocrystals to consist of periodic internal region of high and low refractive index [2] are regarded as promising nanostructures to control and manipulate photons. Several attempts have been made to incorporate photonic crystals for management of photons in solar cells [3].

In this contribution, we report on our recent research activities to utilize photonic nanostructures coupled with germanium quantum dots (QDs) to improve performance of crystalline silicon solar cells [4]. We present a simple process to fabricate large-area photonic nanostructures based on wet chemical etching of vertically aligned multiple germanium QDs grown via the Stranski-Krastanov (SK) growth mode. The simple and quick fabrication process has the capability to tune the geometry of the photonic nanostructures by controlling structural parameters and etchant. The effectiveness of the proposed solar cell is demonstrated by increase of quantum efficiency in the entire wavelength.

2. Concept of a solar cell with nanostructures

Figure 1 illustrates the structure of the proposed solar cell to have photonic nanostructures coupled with vertically stacked germanium QDs. The fundamental structure is a single pin junction. There are a number of advantages in the solar cell. The incoming solar light can be diffracted by the photonic nanostructures at the surface, and an interference pattern is formed at the

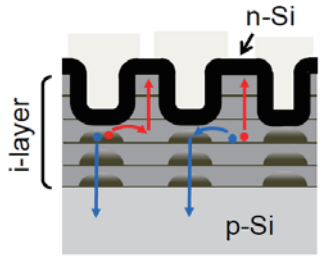

Fig. 1 Schematic illustration of the proposed solar cell with photonic nanostructures

distance of around the wavelength from the surface. We can expect enhanced optical coupling between the solar light and germanium QDs by controlling the geometry of the photonic nanostructures. In addition, infrared light to transmit Si can be absorbed by germanium due to the bandgap smaller than that of silicon. These effects lead to enhanced absorption of photons and generation of carriers around the surface. In addition, type-II band alignment at the germanium/silicon heterointerface is useful to suppress undesirable carrier recombination due to the spatial separation. This would minimize undesirable loss in voltage while having increased photo currents.

3. Fabrication of nanostructures

Since solar cells are large-area devices, fabrication process of photonic nanostructures should be applicable to large-area and cost-effective. Our method is based on wet chemical etching of self-organized semiconductor QDs grown via the SK growth mode.

The SK growth mode occurs as a consequence of minimization of the total free energy in the heteroepitaxy of lattice-mismatched system. The increase of the surface energy due to the formation of QDs can be overcompensated by the energy gain due to

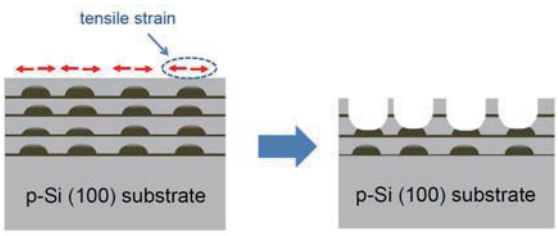

Fig. 2 A simple etching process to fabricate photonic nanostructures coupled with germanium QDs

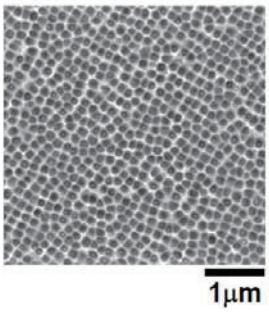

Fig. 3 A typical scanning electron microscope image of photonic nanostructures coupled with germanium QDs

the decrease of the strain energy. As a result, the internal strain is not spatially uniform but spontaneously modulated. We considered that the self-introduced lateral modulation in stain and materials composition will result in spontaneous modulation of the etching rate against a specific chemical solution. Based on this hypothesis, we considered a simple method to fabricate large-area photonic nanostructures as illustrated in Fig.2.

Multiple layers of germanium QDs with silicon spacer layers were grown on silicon (100) substrates by gas source molecular beam epitaxy. The germanium QD layers with coverage 8 monolayers were grown via the SK growth mode. They were separated by silicon spacer layers with a constant nominal thickness. Subsequently, the germanium QDs were chemically etched in a HF/HNO_3 ($HF:HNO_3$=1:100) solution without any mask patterns.

Figure 3 shows a typical scanning electron microscope image of the surface of the etched sample. It is seen that photonic nanostructures are successfully formed without any mask patterns. It should be noted that the geometry of the photonic nanostructures can be flexibly controlled by the structural parameters before the etching or controlling solution for the etching [5].

4. Optical properties and application to solar cells

Figure 4 shows reflectance spectra for photonic nanostructures formed at various etching duration. An abrupt increase in the reflectance around 1100 nm is found for all the samples due to the light reflection from the backside surface based on the onset of the optical transparency. By photonic nanostructure formation, the reflectance is seen to reduce in the entire wavelength.

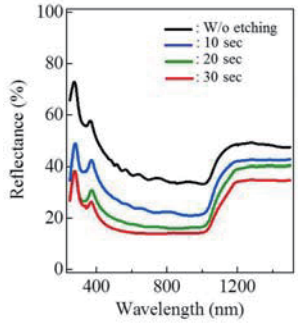

Fig. 4 Reflectance spectra for samples etched with various duration

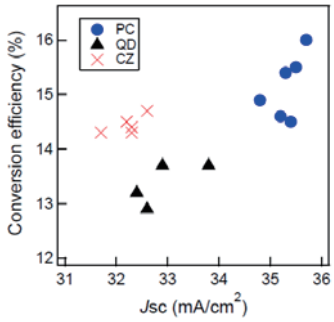

Fig. 5 Conversion efficiency of solar cells with photonic nanostructures (PC), quantum dots without etching (QD) and control silicon (CZ)

This result indicates that the amount of incident photons incorporated in germanium QDs is increased.

To show the effectiveness of the proposed solar cell, we fabricated small-area (~2cm^2) solar cells using samples with and without photonic nanostructures. The n^+ layer was formed by rapid thermal annealing after spinning coating of phosphorus doped glass film. After removal of the residual film by HF, an indium tin oxide film was deposited as an antireflection film by sputtering. The back surface field contact was formed by printing the aluminum-based paste on the backside, and the front electrode was made by firing silver paste through the ITO film.

Figure 5 shows comparison of conversion efficiency of solar cells with and without photonic nanostructures. It is seen that the presence of photonic nanostructures brought increase of the overall conversion efficiency by increasing short-circuit current density. However, it should be noted that the increased photocurrent mainly come from the photonic effect of the nanostructures. Further improvement of solar cells is underway by employing low-temperature fabrication process so that we can improve infrared response.

5. Summary

We introduced our attempt to integrate photonic nanostructures in crystalline silicon solar cells. Photonic nanostructures coupled with vertically aligned germanium quantum dots were fabricated by a simple maskless etching process. Optical properties as well as solar cell performance indicated that photonic nanostructures are promising for high-efficiency crystalline silicon solar cells.

References

[1] J. H. Zhao, A. H. Wang, M. A. Green, and F. Ferrazza, Appl. Phys. Lett. **73**, 1991 (1998).
[2] E. Yablonovitch, Phys. Rev. Lett. **58**, 2059 (1987).
[3] A. Mihi, F. J. Lopez-Alcaraz, and H. Miguez, Appl. Phys. Lett. **88** (2006).
[4] N. Usami, W. Pan, T. Tayagaki, S. T. Chu, J. Li, T. Feng, Y. Hoshi, and T. Kiguchi, Nanotechnology **23**, 185401 (2012)
[5] Y.Hoshi, W.Pan, T.Kiguchi, K.Ooi, T.Tayagaki, N.Usami , Jpn.J.Appl.Phys. **52**, 080202 (2013)

Tenth International Conference on Flow Dynamics
November 25-27, 2013, Sendai, Miyagi, Japan

Multi-Objective Design Exploration and Energy Strategy

Shigeru Obayashi
Institute of Fluid Science, Tohoku University
obayashi@ifs.tohoku.ac.jp

ABSTRACT

This paper gives a brief review of an optimization approach denoted multi-objective design exploration (MODE). MODE is not intended to provide an optimal solution. MODE reveals the structure of the design space from trade-off information and visualizes it as a panorama for a decision maker. The author hopes to apply the same approach to energy systems to be investigated at Innovative Energy Research Center.

1. Introduction

Innovative Energy Research Center at Institute of Fluid Science aims to develop the innovative smart energy supply system, which is materialized by fusion of generation system and accumulation system of electricity in addition to fusion of various electricity generation systems, with the aid of the optimization techniques.

A complex system to be optimized often contains multiple competing objectives. While single objective problems may have a unique optimal solution, multi-objective problems (MOPs) have a set of compromising solutions, largely known as the trade-off surface, Pareto-optimal solutions or non-dominated solutions. These solutions reveal trade-off information among different objectives. They are optimal in the sense that no other solutions in the search space are superior to them when all objectives are taken into consideration. A designer will be able to choose a final design with further considerations.

Multi-objective optimization has the origin in Multiple Criteria Decision Making (MCDM)[1]. MCDM research flourished in 1970's and theoretical foundations were built. During 1980's, emphasis shifted toward capturing decision maker's preferences to support the modeling and structuring of decision problems. Application of Evolutionary algorithms (EAs) [2] to multi-objective optimization has become a very active research area since 1990's. In 2001, the first International Conference on Evolutionary Multi-Criterion Optimization (EMO) was held [3] and the conference has been held every two years since then. Because EAs are suited to finding many Pareto solutions at once, EMO community focuses on generating solutions as closer to the Pareto front and as many as possible. This approach implies that no utility function is necessary. Solutions in the criterion space are presented to the decision makers and they are asked to choose the best one.

This paper introduces an optimization approach based on EMO and shows how a system can be optimized. The author hopes to apply similar approach to energy systems to be investigated at Innovative Energy Research Center.

2. Method

An optimization approach denoted multi-objective design exploration (MODE) was proposed in [4] and is illustrated in Fig. 1. MODE is not intended to provide an optimal solution. MODE reveals the structure of the design space from trade-off information and visualizes it as a panorama for a decision maker.

EAs generally require a large number of function evaluations because EAs are population-based approaches. To alleviate the computational burden, the use of the response surface method (RSM) has been introduced as a surrogate model [5]. The surrogate model used in this study is the Kriging model [6].

The present form of MODE consists of the Kriging model, adaptive range multi-objective genetic algorithms [7], analysis of variance and a self-organizing map (SOM)[8]. SOM divides the design space into clusters. Each cluster represents a set of designs containing specific design features. A designer may find an interesting cluster with good design features. Such design features are composed of a combination of design variables. If a particular combination of design variables is identified as a sufficient condition belonging to a cluster of interest, it can be considered as a design rule. Rough set theory [9] and other data mining techniques have been employed to extract design rules.

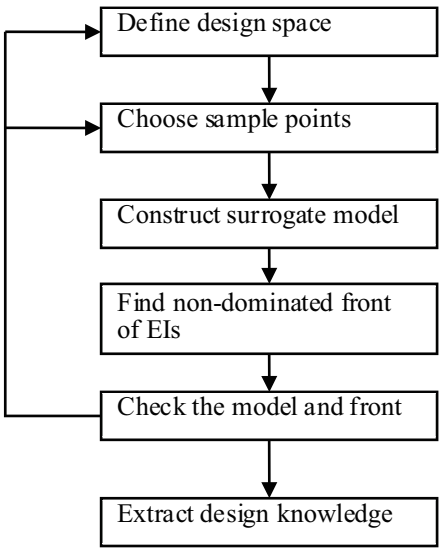

Fig. 1 Flowchart of multi-objective design exploration with component algorithms

3. Results

In Japan, the New Energy and Industrial Technology

Development Organization (NEDO) subsidized the development of an environmentally friendly high performance small jet aircraft. Mitsubishi Heavy Industries, Ltd. (MHI) was the prime contractor for the project. The purpose of this project was to build a prototype aircraft using advanced technologies, such as low-drag wing design, and lightweight composite structures, which were necessary for the reduction of environmental burdens. In March 2008, MHI decided to bring this conceptual aircraft into commercial use. This commercial jet aircraft, named the Mitsubishi Regional Jet (MRJ), has a capacity of about 70-90 passengers. This project focused on environmental issues, such as reduction of exhaust emissions and noise. Moreover, in order to bring the jet to market, lower-cost development methods using computer-aided design were also employed in this project. The application of MODE to MRJ under Tohoku University-Mitsubishi cooperation [10-14] considered the multidisciplinary design optimization (MDO)[15] that optimizes aerodynamic performance and structural weight simultaneously. The following four configurations were investigated: 1. Wing-body configuration, 2. Wing-nacelle-pylon-body configuration, 3. Winglet configuration, 4. Structural design of horizontal tail.

Fig. 2 MRJ(courtesy of Mitsubishi Aircraft Corporation)

4. Concluding remarks

This paper gives a brief review of MODE. Brief history of MCDM is introduced and the development of EMO is discussed. MODE takes one more step to assist real world designs by applying data mining techniques to deign space. MODE reveals the structure of the design space from trade-off information and visualizes it as a panorama for a decision maker. The author hopes to apply similar approach to energy systems to be investigated at Innovative Energy Research Center.

References

[1] Korhonen, Pekka, Herbert Moskowitz, and Jyrki Wallenius. European Journal of Operational Research 63.3 (1992): 361-375.
[2] K.C. Giannakoglou, Progress in Aerospace Sciences, 2002, 38, pp. 43–76.
[3] Zitzler, Eckart. Evolutionary multi-criterion optimization. Berlin, Germany: Springer, 2001.
[4] Obayashi, S., Jeong, S., and Chiba, K., AIAA-2005-4666, 2005.
[5] Alexander I. J. Forrester, Andy J .Keane, Progress in Aerospace Sciences, 2009, 45, 50–79.
[6] Jeong, S. and Obayashi, S., IEEE Congress on Evolutionary Computation, Edinburgh, Scotland., 2005, pp. 2138-2145.
[7] Jones, D. R., Schonlau, M., and Welch, W. J., Journal of Global Optimization, 1998, 13, 455-492.
[8] Kohonen, T., Self-Organizing Maps. Berlin: Springer 1995.
[9] Pawlak, Z., International Journal of Computer & Information Sciences, 1982, 11, 341-356.
[10] Chiba, K., Oyama, A., Obayashi, S., Nakahashi, K., and Morino, H., Journal of Aircraft, 2007, 44, 1100-1112.
[11] Kumano, T., Jeong, S., Obayashi, S., Ito, Y., Hatanaka, K., and Morino, H., 44th AIAA Aerospace Sciences Meeting, Reno, NV., 2006, pp. 11158-11170.
[12] Hatanaka, K., Obayashi, S., and Jeong, S., 25th International Congress of the Aeronautical Sciences, Hamburg, Germany, 2006.
[13] Kumano, T., Jeong, S., Obayashi, S., Ito, Y., Hatanaka, K., and Morino, H., European Conference on Computational Fluid Dynamics (ECCOMAS CFD 2006), Egmond aan Zee, The Netherlands, 2006.
[14] Takenaka, K., Hatanaka, K., Yamazaki, W., and Nakahashi, K., Journal of Aircraft, 2008, 45, 1601-1611.
[15] Simpson, T. W., Toropov, V. and Balabanov, V. and Viana, F. A. C., 12th AIAA/ISSMO Multidisciplinary Analysis and Optimization Conference, Victoria, British Columbia, Canada, September 10-12 2008, AIAA, AIAA-2008-5802.

OS10: Advanced Physical Stimuli and Biological Responses

Tenth International Conference on Flow Dynamics
November 25-27, 2013, Sendai, Miyagi, Japan

Effect on microorganisms by cold atmospheric plasmas

Tetsuji Shimizu[1], Julia L. Zimmermann[1], Gregor E. Morfill[1], Georg Isbary[2], and Wilhelm Stolz[2]
[1]Max-Planck Institute for extraterrestrial physics, Giessenbachstrasse, 85748 Garching, Germany
[2]Department of Dermatology, Allergology and Environmental Medicine, General Hospital Munich Schwabing, Koelner Platz 1, 80804 Munich, Germany
E-mail of corresponding author:tshimizu@mpe.mpg.de

ABSTRACT

In our group, a cold atmospheric plasma using an argon microwave plasma torch demonstrated to reduce the bacterial load on chronic wounds and to alleviate Hailey-Hailey disease. Based on these results, a new plasma device with the ambient air has been developed using Surface Micro-Discharge technique. The plasma chemistry is controllable by changing power input and the experiments with microorganisms showed that the plasma device had a high bactericidal property. Moreover, there is a time window of high germicidal property with no harmful effect on fibroblasts. Using this new device, a clinical study is being planned.

1. Introduction

Cold atmospheric plasmas are of considerable interest in medicine. The plasmas generate reactive species in a wide variation and they are transported onto the biological objects gently. It is possible to make a contact-free treatment and the plasma treatments are waste-free in general. Since the plasma gas is maintained close to room temperature, thermal damage on the objects is negligible. Due to these characteristics, the field of 'plasma medicine' has grown and many studies have been carried out with a wide application spectrum [1-6].

In our group, the cold atmospheric plasma has demonstrated the ability to reduce the bacterial load on chronic wounds [7,8] and to alleviate Hailey-Hailey disease [9] of patients in the phase II clinical study. In this study a microwave plasma torch using argon was used [10]. This system produces an argon plasma in the torch and the plasma gas is transported onto the objects via the applied argon flow.

Based on the encouraging outcomes mentioned above, we developed another cold atmospheric plasma system using the ambient air, the Surface Micro-Discharge (SMD) plasma (one type of surface dielectric barrier discharge) [11]. In this proceeding, a basic characteristic is described and a part of our study is introduced.

2. SMD electrode

The SMD electrode consists of an insulator plate sandwiched by a metal plate and a metal mesh. By applying high AC voltage between the metal plate and mesh, a plasma discharge is formed on the mesh side. The design of this electrode is very simple and robust, so that it is possible to fabricate a complex-shaped electrode. Moreover, the electrode is scalable since the discharge consists of a lot of micro-discharges. A portable device [12] is also possible because it is not necessary to have a gas flow system and a matching unit. For the plasma production, only ambient air is necessary and the frequency range of the applied voltage is around kHz. Typical experimental parameters are shown in Table 1. In many experiments, a closed volume is formed, i.e. no gas exchange between the plasma gas volume and the ambient, since a control of plasma chemistry is easier.

Table 1. Typical experimental parameters for SMD plasma production

Applied voltage	1 ~ 15 kVpp
Power consumption	Max. a few W/cm2
Frequency	50 ~ 100 kHz
Insulator	Glass, ceramic, plastic Typically ~1 mm thick
Mesh grid size	Around 10 mesh/inch

3. SMD plasma chemistry

From the plasma discharge, several kinds of reactive species are produced. Our measurement using FTIR shows that O_3, NO_2, NO, N_2O, N_2O_5, HNO_3 are produced. This is in a good agreement with a computational calculation [13]. Here, a time evolution of ozone is shown because ozone is an important agent to inactivate germs. On the other hand, it is harmful for human health. Figure 1 shows time evolution profiles of ozone density under different power conditions [14]. The ozone density was measured by the absorption spectroscopy using a mercury lamp. When the input was lower than 0.16 W/cm^2, ozone density increased for first tens of seconds and reached a steady state at around one minute. When the input power is over 0.16 W/cm^2, a peak ozone density was observed. Ozone density increased for the first several to ten seconds and a decrease below our detection limit followed. When the power increased further, the period of the ozone presence became shorter and the maximum ozone density decreased.

The quench mechanism of ozone is not yet fully understood, however, we believe that NO plays a major role. Our preliminary calculation shows that there is almost no NO during ozone is present in the plasma gas volume. When the ozone is quenched under the high power input, NO is appeared after the ozone density drops to zero. This means that the control of dominant reactive species is possible between reactive oxygen species like ozone and reactive nitrogen species. For instance, reactive nitrogen species, e.g. NO molecules,

could stimulate wound healing [15]. Reactive oxygen species are known to play a major role to inactivate microorganisms. The observed mode transition could be used to control the plasma effect on biological tissues.

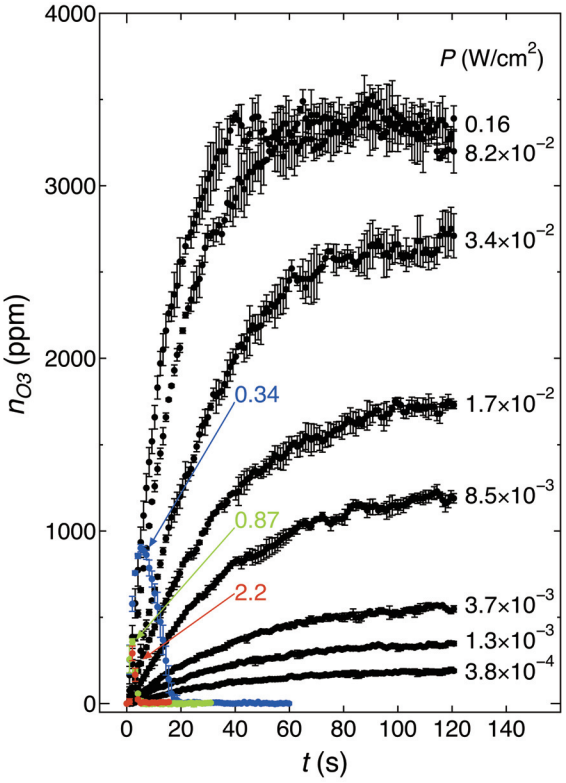

Fig. 1 Time evolution of ozone density under different power input

4. Biological application using SMD plasma

To demonstrate the bactericidal efficacy of the SMD device in vitro, different bacteria on agar were treated. A reduction of 5 log is possible to achieve for all bacteria in 30 s [16]. Experiments with bacteria on ex vivo porcine skin (in order to stimulate in vivo conditions) showed a 3 log reduction in 60 s [12]. Furthermore, tests with Candida albicans on agar, adenoviruses in solution [17] and endospores on metal plates [16] revealed that high log reduction was also possible in several minutes.

In order to demonstrate the safety in the usage of the SMD plasma device, cell culture experiments on fibroblasts were carried out. The test results showed that there was a safe therapeutic window for the plasma treatment, where a high bactericidal property is present with no harmful effect on fibroblasts, up to 30 s. Moreover, plasma treatments up to 4 min did not induce mutagenicity beyond naturally occurring spontaneous mutations.

We are summarizing the above mentioned experimental results for an approval of a clinical phase II study on wounds using the SMD plasma device. Plasma treatments for fungi-related and virus-related disease are also planned.

References

[1] E. Stoffels, Contrib. Plasma Phys., **47** (2007), 40.

[2] G. Fridman, A. B. Shekhter, V. N. Vasilets, G. Friedman, A. Gutsol, and A. Fridman, Plasma Process. Polym., **5** (2008), 503.

[3] M. Laroussi, IEEE Trans. Plasma Sci., **30** (2002), 1409.

[4] E. Stoffels, Y. Sakiyama, and D. B. Graves, IEEE Trans. Plasma Sci., **36** (2008), 1409.

[5] M. G. Kong, G. Kroesen, G. E. Morfill, T. Nosenko, T. Shimizu, J. van Dijk, and J. L. Zimmermann, New J. Phys., **11** (2009), 115012.

[6] K. D. Weltmann, E. Kindel, T. von Woedke, M. Haehnel, M. Stieber, and R. Brandenburg, Pure Appl. Chem., **82** (2010), 1223.

[7] G. Isbary, G. Morfill, H-U. Schmidt, M. Georgi, K. Ramrath, J. Heinlin, S. Karrer, M. Landthaler, T. Shimizu, B. Steffes, W. Bunk, R. Monetti, J. L. Zimmermann, and W. Stolz, Br. J. Dermatol., **163** (2010), 78.

[8] G. Isbary, J. Heinlin, T. Shimizu, J. L. Zimmermann, G. Morfill, H-U. Schmidt, R. Monetti, B. Steffes, W. Bunk, Y. Li, T. Klaempfl, S. Karrer, M. Landthaler, and W. Stolz, Br. J. Dermatol., **167** (2012), 404.

[9] G. Isbary, G. Morfill, J. Zimmermann, T. Shimizu, and W. Stolz, Archives of Dermatology, **147** (2011), 388.

[10] T. Shimizu, B. Steffes, R. Pompl, F. Jamitzky, W. Bunk, K. amrath, M. Georgi, W. Stolz, H-U. Schmidt, T. Urayama, S. Fujii, G. Morfill, Plasma Process. Polym., **5** (2008), 577.

[11] G. Morfill, T. Shimizu, B. Steffes, and H-U. Schmidt, New J. Phys., **11** (2009), 115019.

[12] T. Maisch, T. Shimizu, Y. Li, J. Heinlin, S. Karrer, G. Morfill, and J. L. Zimmermann, PLoS ONE, **7** (2012), e34610.

[13] Y. Sakiyama, D. B. Graves, H-W. Chang, T. Shimizu, and G. E. Morfill, J. Phys. D: Appl. Phys., **45** (2012), 425201.

[14] T. Shimizu, Y, Sakiyama, D. B. Graves, J. L. Zimmermann, and G. E. Morfill, New J. Phys., **14** (2012), 103028.

[15] D. B. Graves, J. Phys. D: Appl. Phys., **45** (2012), 263001.

[16] T. G. Klaempfl, G. Isbary, T. Shimizu, Y. Li, J. L. Zimmermann, W. Stolz, J. Schlegel, G. E. Morfill, and H-U. Schmidt, Appl. Environ. Microbiol., **78** (2012), 5077.

[17] J. L. Zimmermann, K. Dumler, T. Shimizu, G. E. Morfill, a. Wolf, V. Boxhammer, J. Schlegel, B. Gansbacher, and M. Anton, J. Phys. D: Appl. Phys., **44** (2011), 505201.

Tenth International Conference on Flow Dynamics
November 25-27, 2013, Sendai, Miyagi, Japan

Effects of Mechanical Vibration on Cell Proliferation and Differentiation

Toshihiko Shiraishi and Shin Morishita
Graduate School of Environment and Information Sciences
Yokohama National University
79-7 Tokiwadai, Hodogaya-ku, Yokohama 240-8501 Japan
shira@ynu.ac.jp

ABSTRACT

This paper describes effects of mechanical vibration on proliferation and differentiation of osteoblast-like cells derived from mouse bone. The sample cells were cultured under harmonic excitation of 0.5 G and 25 Hz for 24 hours a day during 28 days of culture. The number of cells was counted with a hemocytometer. Gene expression of alkaline phosphatase (ALP) as a osteoblast differentiation marker was measured by a real-time reverse transcription polymerase chain reaction method. As a result, we show that the mechanical vibration increases the cell density and the gene expression of ALP.

1. Introduction

Bone is able to sense and adapt to mechanical stimuli. Examples are the decrease in bone mass of astronauts under zero gravity, the changes that occur during rehabilitation of bone fracture by walking, and the repair of fractures with ultrasound devices [1]. However, there has been little research on effects of mechanical vibration on bone cells [2]. In this study, harmonic inertia force was applied to cultured osteoblast-like cells, MC3T3-E1, and the effects of mechanical vibration on the cell proliferation and differentiation were investigated by measuring the time evolution of the cell density and the gene expression of a protein related to osteoblast differentiation.

2. Materials and Methods

2.1 Cell cultures

MC3T3-E1 (Riken, Tsukuba, Japan) , which is an osteoblast-like cell line derived from mouse calvaria, was cultured in α-MEM (Alpha-Minimum Essential Medium, Gibco, Grand Island, NY, USA) supplemented with 10% FBS (Fetal Bovine Serum, Equitech-Bio, Inc., Kerrville, TX, USA), 50 μg/ml ascorbic acid (Wako Pure Chemical Industries, Ltd., Osaka, Japan) and 2mM β-glycerophosphoric acid disodium salt (NACALAI TESQUE, INC., Kyoto, Japan). Fresh medium was replaced every 3 or 4 days. The cells were maintained at 37°C in a fully humidified atmosphere of 5% CO_2 in air. The cells were used for the experiment after the eighth passage.

2.2 Experimental setup

Figure 1 shows a schematic diagram of the experimental setup. A 24 well culture plate was attached on an aluminum plate which was set on an electromagnetic exciter (Mini-Shaker Type 4809, Brüel & Kjær, Nærum, Denmark). A signal generator (WF 1945B, NF Corporation, Yokohama, Japan) output adjusted harmonic signal to a power amplifier (Power Amplifier Type 2718, Brüel & Kjær) and it was amplified and input to the exciter. The culture plate was excited perpendicular to the cultured plane with cells adhering. Since the first natural frequency of the aluminum plate was approximately 1800 Hz and it had enough stiffness not to resonate with excitation frequency in the range of the experimental condition, mechanical vibration was uniformly applied to all cells and the effect of the vibration on cells can be precisely evaluated.

2.3 Experimental methods

Cells were seeded in culture plates at the density of 8×10^3 cells/ml. After cells were cultured for one day and adhered on the cultured plane, vibration group of the culture plates was set on the aluminum plate of the experimental setup and cultured under harmonic excitation in a CO_2 incubator separated from non-vibration group of the culture plates. The vibration group was excited at the acceleration amplitude of 0.5 G and the frequency of 25 Hz for 24 hours a day.

Time evolution of cell density was obtained by counting the number of cells with a hemocytometer.

In order to investigate whether the cause of the cell number increase could be pile-up of the cells resulting in multilayer in culture, confocal microscopic images of nuclei and actin by immunofluorescence were captured. Cells were fixed with 3% formaldehyde, permeabilized with 0.1% TritonX100 and blocked with 1% bovine serum albumin. Nuclei and actin were fluorescently counterstained with TO-PRO (a dilution of 1:400, Invitrogen, Carlsbad, CA, USA) and Alexa Fluor 488

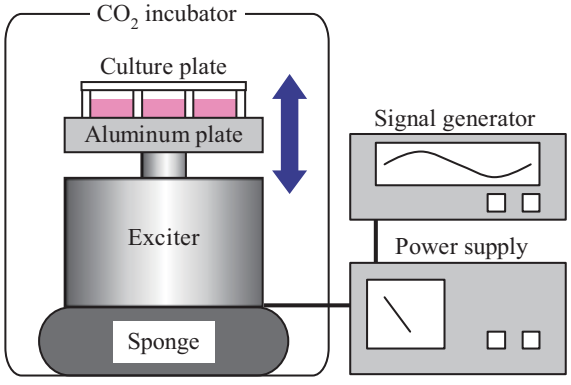

Fig. 1 Schematic diagram of the experimental setup.

Phaloidin (a dilution of 1:100, Invitrogen), respectively. Preparations were examined using a laser-scanning confocal microscope (TE2000 C1 plus, Nikon, Tokyo, Japan).

Gene expression of alkaline phosphatase (ALP) was measured by a real-time reverse transcription polymerase chain reaction (real-time RT-PCR) method. ALP is one of the marker enzymes of bone formation and the mineralization ability of cells can be assessed by measuring it. After the vibration group for the PCR was excited for 7 days, the total RNAs were extracted from 3 wells per sample. After reverse transcription, real-time RT-PCR was performed with a real-time PCR system (Mx3000P, STRATAGENE, La Jolla, CA, USA) using Brilliant SYBR Green QPCR Master Mix (STRATAGENE) and probes (SIGMA-ALDRICH Corporation, St. Louis, MO, USA). Gene expression for ALP and a housekeeping gene (β-actin), which is consistently expressed even during different treatments, was determined simultaneously for each sample in triplicates. ALP gene level in each sample was normalized to the measured β-actin gene levels in case the amount of total RNAs of each sample was different.

3. Results and Discussion

Figure 2 shows the effect of mechanical vibration on cell proliferation. Cell density increased with time and saturated after 11 or 14 days of culture. The statistically significant difference of cell density between the control and vibration groups appeared after 11-day cultivation ($p < 0.01$).

Figure 3 shows cross-sectional confocal microscopic images of nuclei and actin after the significant difference of cell density between the control and vibration groups appeared. We observed that the nuclei piled up and formed multilayers in vibration and that the number of layers in vibration was in the range between one to three layers, whereas that in control was almost one or two layer. Thus, mechanical vibration promoted multilayer of the cells, the reason of which may be higher mobility of the cell by mechanical vibration, resulting in increase of the number of the cells.

Figure 4 shows the effects of mechanical vibration on relative mRNA level of ALP after 7 days of culture. The relative mRNA level of ALP in the vibration group was higher than that in the non-vibration with statistical significance ($p < 0.01$). The experimental result shows that the mechanical vibration promotes osteoblast differentiation.

4. Conclusions

In this study, harmonic inertia force was applied to cultured osteoblast-like cells, MC3T3-E1 and the effects of mechanical vibration on the cell proliferation and differentiation were investigated. As a result, we show that the mechanical vibration increases the cell density and the gene expression of ALP.

References

[1] L. R. Duarte, Arch. Orthop. Trauma Surg., **101** (1983), 153-159.

[2] T. Shikata, T. Shiraishi, S. Morishita, R. Takeuchi and T. Saito, J. Syst. Des. Dyn., **2**-1 (2008), 382-388.

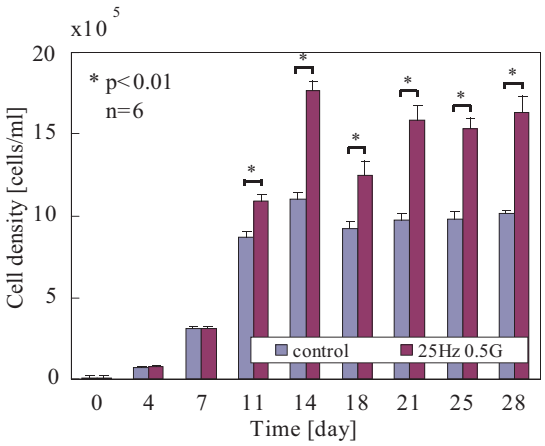

Fig. 2 Time evolution of cell density.

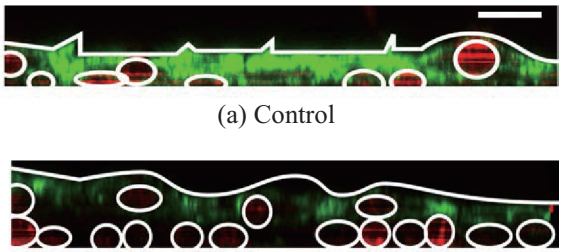

(a) Control

(b) Vibration

Fig. 3 Cross-sectional confocal microscopic images. Nucleus (red) and actin (green). Scale bar, 10 μm.

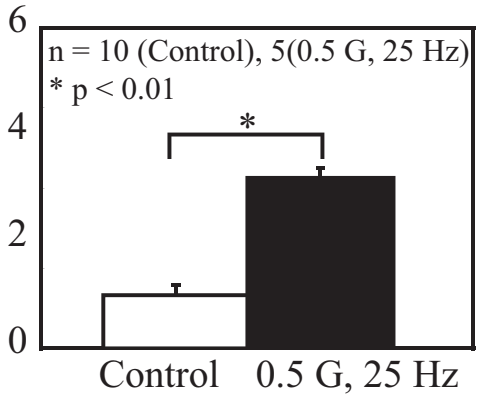

Fig. 4 ALP gene expression after 7 days of culture.

Muscle Contractile Activity and Its Beneficial Effects in Type 2 Diabetes

Makoto Kanzaki
Graduate School of Biomedical Engineering, Tohoku University
6-6-11-901/2 Aoba, Aramaki, Aoba-ku, Sendai, Miyagi, 980-8579, JAPAN
kanzaki@bme.tohoku.ac.jp

ABSTRACT

Physical exercise provokes a highly complex series of interrelated stimuli, including mechanical force and energy expenditure in contracting skeletal muscles. A crucial issue in understanding beneficial effects of exercise is a clarification of the intracellular signaling mechanisms by which muscle cells decipher and response to the highly complex contractile stimulus. Taking advantage of our recent innovation "*in vitro* exercise model", intracellular signaling cascades required for contraction-induced up-regulation of myokines were identified.

1. Introduction

It has become increasing apparent that skeletal muscle functions as an endocrine organ that produces a wide variety of secreting factors including interleukin (IL)-1b, IL-6, IL-8, IL-10, and IL-15. Importantly, physical exercise stimulates secretion of these muscle-derived myokines, which are therefore referred to as "exercise factors". Moreover, regular physical exercise is well known to provide great beneficial effects not only for avoiding disease occurrence of type 2 diabetes, but also for diabetic patients in insulin resistant states. However, there is a relatively paucity of information on the specific molecular mechanisms underlying these beneficial effects of exercise.

Recently, we succeeded in establishing an "Electric Pulse Stimulation (EPS)-evoked myotube contraction culture system" which generates highly developed contractile myotubes similar to *in vivo* skeletal muscle in terms of (1) excitation-induced contractile activity with fully functional sarcomere structure, (2) contraction-induced myokine secretion, (3) higher energy expenditure, and (4) insulin responsiveness [1-4]. In order to explore molecular mechanisms underlying the beneficial effects of muscle contraction, my laboratory has focused especially on intracellular signals directly responsible for the production of these myokines. In the present study, the mechanistic details of the contraction-inducible regulation of two important myokines (CXCL1 and IL-6) were investigated.

2. Method

Cell culture and EPS treatment- A murine skeletal muscle cell line, C2C12 myoblast, was grown on 8-well rectangular plates at a density of 5 x 10^4 cells/well in 3 mL of growth medium, and then they were differentiated into multinuclear myotubes as previously reported [5]. Five to six days after differentiation, electrical pulse stimulation was applied to the C2C12 myotubes using a C-Pace pulse generator [2].

immunoblotting- At various time points of EPS treatment, cells were lysed and total cell lysates were subjected to western blot analysis [6].

ELISA for CXCL1 and IL-6 concentration- Conditioned media were collected and concentrations of various myokines in culture supernatants were measure with ELISA kits [4].

Fluorescent real-time polymerase chain reaction (PCR)- Expression levels of mRNA were evaluated by real-time quantitative PCR using CYBR Green detection kit [7].

Statistical Analysis -Statistical analyses were performed using Student's paired t test for independent samples. Data are expressed as means ± SEM unless otherwise specified.

3. Results and Discussion

CXCL1 production in response to EPS-evoked contraction-

Significant amount of CXCL1 was released immediately after 1h of EPS and its accumulation increased steadily during 24 h EPS, which was dependent on the frequency of EPS. EPS treatments (1 Hz, 2-ms, 40 V/60 mm for 3 h) induced activation of several intracellular signaling cascades as assessed by their phosphorylation status (Fig. 1A). Pharmacological experiments revealed that EPS-induced CXCL1 secretion was significantly inhibited by SP600125, a JNK inhibitor, while neither the Erk1/2 inhibitor nor p38 inhibitor had such inhibitory effect (Fig. 1B & C), suggesting the JNK signaling cascade is predominantly involved in CXCL1 up-regulation in response to 3h of EPS-evoked contractile activity.

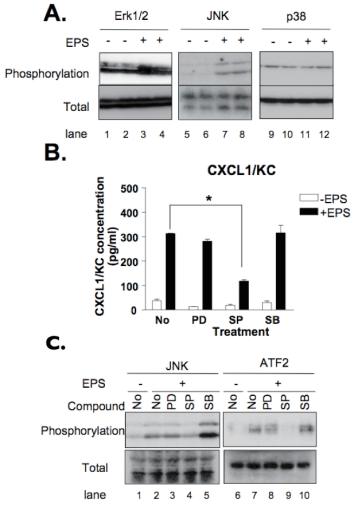

Fig. 1 EPS-stimulated Signaling Cascades (A) and their involvement in the CXCL1 Production (B) in the presence of pharmacological inhibitors (C).

In an attempt to unravel the complexities of contraction stimuli, cyclic longitudinal mechanical stretch, instead of EPS-evoked contraction, was applied to C2C12 myotubes grown in an elastic silicone chamber and measured CXCL1 mRNA level. While CXCL1 expression was immediately detectable in myotubes with EPS-evoked contraction, cyclic stretch (15% at 1 Hz) required 12 h to up-regulate its mRNA level irrespective of the phosphorylation of JNK within just 10-30 min (data not shown) [3]. These data underscore the complexity of stimuli elicited by actual exercise in contracting skeletal muscle cells.

IL-6 production in response to EPS-evoked contraction-

Both secretion and mRNA expression of IL-6 were significantly up-regulated by EPS treatment in contracting myotubes during 24 h period, and the response was blunted by cyclosporine A, a calcineurin inhibitor (Fig. 2A), while the JNK inhibitor had no such inhibitory effect but exhibited even augmenting effect (Fig. 2B). These results indicate that molecular mechanism underlying the EPS-induced up-regulation of CXCL1 and IL-6 can be distinguishable at the level of intracellular signaling cascades (Fig. 2C).

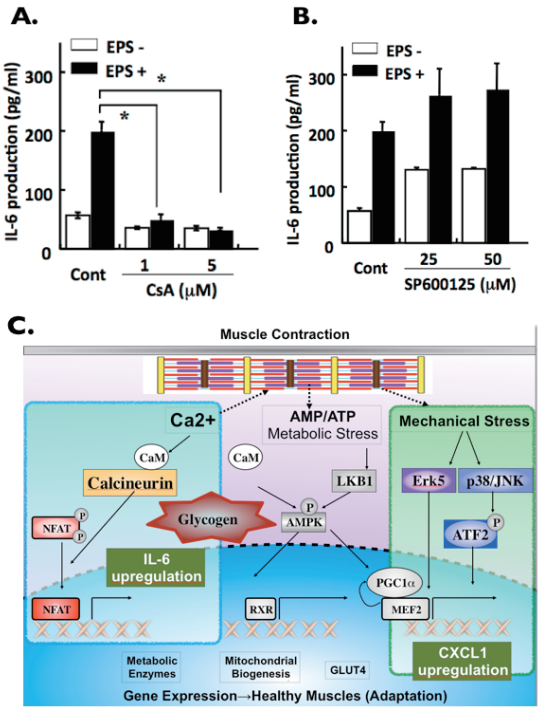

Fig. 2. Characterization of EPS-induced IL-6 Production in the presence of cyclosporin A (CsA) (A) or SP600125 (B), and Schematic Depiction of Intracellular Signals responsible for the Contraction-dependent Up-regulation of these Myokines (C).

In addition, EPS-induced IL-6 production was found to be significantly suppressed in the presence of high concentration of glucose (25 mM), which occurred in concomitant with accumulation of intracellular glycogen contents (data not shown). Importantly, exogenous administration of glucose at a certain EPS period (the last 4h of the EPS treatment) efficiently suppressed IL-6 mRNA expression along with increased glycogen accumulation. However, administration of pyruvate utilized for glycogen synthesis, failed to suppress IL-6 mRNA expression with no glycogen accumulation [4], suggesting that intracellular glycogen accumulation, but not simple energy source supply, is involved in attenuations of contraction-induced IL-6 expression in muscle cells (Fig. 3).

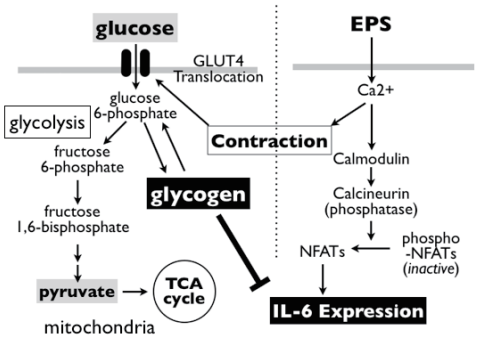

Fig. 3. Schematic depiction of contraction-inducible IL-6 up-regulation mechanism and its suppression with intracellular glycogen accumulation.

4. Concluding remarks

Given the highly complex interrelated stimuli evoked by muscle contractile activity, physiological responses of working muscle to physical exercise have been assessed using animal models and human subjects. The data presented in this study provide important insights into the regulatory mechanism of expression myokines (CXCL1 and IL-6) in response to contractile activity of muscle cells, which is difficult to examine using in vivo experimental techniques. Interrelations/cross-talks between contraction- and energy/energy-source-dependent intracellular signaling cascades have yet to be examined. Further studies will necessary to resolve this important issue for our understanding of precise mechanisms underlying the beneficial effects of exercise.

References

[1] H. Fujita, T. Nedachi, M. Kanzaki, Exp Cell Res, 313 (2007) 1853-1865.
[2] T. Nedachi, H. Fujita, M. Kanzaki, Am J Physiol Endocrinol Metab, 295 (2008) E1191-1204.
[3] T. Nedachi, H. Hatakeyama, T. Kono, M. Sato, M. Kanzaki, Am J Physiol Endocrinol Metab, 297 (2009) E866-878.
[4] A. Farmawati, Y. Kitajima, T. Nedachi, M. Sato, M. Kanzaki, R. Nagatomi, Endocr J, 60 (2013) 137-147.
[5] T. Nedachi, M. Kanzaki, Am J Physiol Endocrinol Metab, 291 (2006) E817-828.
[6] M. Ariga, T. Nedachi, H. Katagiri, M. Kanzaki, J Biol Chem, 283 (2008) 10208-10220.
[7] Y. Tsuchiya, H. Hatakeyama, N. Emoto, F. Wagatsuma, S. Matsushita, M. Kanzaki, J Biol Chem, 285 (2010) 34371-34381.

Pulsed-Liquid Jet Surgical Device: Evolution from Shock Bubble Interaction to Clinical Application

Atsuhiro NAKAGAWA[1], Kiyonobu OHTANI[2], Yoshikazu OGAWA[1],Toshiki ENDO[1], Masaki IWASAKI[1], Kuniyasu NIIZUMA[1], Tatsuhiko ARAFUNE[3], Toshikatsu WASHIO[4] Takashi KATO[5], Daisuke KUDO[6], Takashi IRINODA[6], Chikashi NAKANISHI[7], Tadashi SAKURAI[7], Yoshihiro KAMIYAMA[8], Chiaki SATO[7], Masato YAMADA[7], Toru NAKANO[7], Shinichi YAMASHITA[8], Tomoyuki SUZUKI[9], Yuji TANAKA[10], Naoyuki TAKAGI[11], Yoshimichi IMAI[11], Yoshihiro HAGIWARA[12], Hiroshi KUNIKATA[10], Shunsuke KAWAMOTO[9], Teiji TOMINAGA[1]
[1]Department of Neurosurgery, [6] Critical Care and Emergency Medicine, [7]Division of Advanced Surgical Science and Technology, [8]Urology, [9]Cardiovascular Surgery, [10]Ophthalmology, [11]Plastic Surgery and [12]Orthopaedic Surgery, Tohoku University Graduate School of Medicine, 1-1 Seiryo, Aoba, Sendai 980-8574, Japan
[2]Institute of Fluid Science, Tohoku University, 2-1-1, Katahira, Aoba, Sendai 980-8577, Japan
[3] School of Science and Engineering, Tokyo Denki University, Saitama, 350-0394, Japan
[4]National Institute of Advanced Industrial Science and Technology, 1-2-1, Namiki, Tsukuba, Ibaraki 305-8564, Japan
[5]Graduate school of Engineering, The University of Tokyo, 7-3-1, Hongo, Bunkyo, Tokyo 113-8656, Japan
nakagawa@nsg.med.tohoku.ac.jp

ABSTRACT

The Ho:YAG LILJ system enhances the advantages of commercialized pressure-driven continuous liquid jet instrumentation in terms of small vessel preservation and accessibility in confined spaces. We have shown significant increase of tumor removal rate, reduction of intraoperative blood loss and operation time in difficult lesion in the vicinity of pituitary fossa and now challenging for pharmaceutical approval in neurosurgery, hopefully expanding into multiple medical field. The method for generating pulsed liquid jet is originated from shock/bubble interaction observed during shock wave induced tissue damage. We would like to emphasize the importance of appreciating observation by multidisciplinary teams.

1. Background

Water jet technology, based on conventional pressure-driven continuous [1, 2] or laser [3] /piezo driven pulsed [4] methods, provides an attractive method to dissect tissue. The water jet transmits the kinetic energy to the tissue surface and ejects particles of tissue, creating a corridor through the target tissue, and can also be used for mass reduction. The water jet can selectively dissect tissue under preservation of the blood vessels (minimal diameter is generally 100-200 μm) and nerves, based on the different tensile strengths of tissues against the jet flow [1]. As a result, water jet technology has been applied to the treatment of various organs and has reduced blood loss and parenchymal trauma in liver surgery, which contains an abundant small vessel network, compared to ultrasonic aspiration or blunt dissection [5]. Another notable advantage of this technology is the absence of thermal damage, which is inevitable with other commercialized instruments. The pressure-driven continuous water jet has been used in surgery since the first application to liver surgery in the 1980s. However, excessive water supply, and difficulty in device size reduction for introduction into deep, narrow lesions, as well as endoscopes and catheters, have precluded wider use.

To solve such issues, we have developed pulsed liquid jet generating technology for neurosurgery in the 1990s.

2. Shock/bubble interaction: tissue disruption

Shock waves (SWs) were first applied in medicine as extracorporeal SW lithotripsy for the fragmentation of urinary stones in 1980, and is now accepted widely as minimally invasive treatment. However, diffuse bleeding and intrarenal hematomas have been observed in a restricted area along the high pressure central axis of the SW field. SWs are known to cause cavitation in tissues in vivo. The collapse of the cavitation bubbles is important in the process of tissue damage. The interaction of cavitation bubbles with the primary SW can produce secondary SW and liquid jets, which are considered potential causes of side effects. Shock/bubble interaction has been extensively investigated in the unconstrained free water environment using high speed photography and pressure measurements. The velocity and water hammer pressure of the liquid jet are estimated to exceed 100 m/s and 100 MPa, respectively [6].

3. Shock/bubble interaction: generating pulsed jet

Meticulous investigation of the dynamics of the liquid jet generated by shock/bubble interaction found that the liquid jet can penetrate through the thrombus phantom in a few microseconds, and the penetration depth reached 4 mm using a 1-mm radius bubble [7]. In addition to such direct mechanical revascularization, the effect of fibrinolytic agents might be enhanced by the increase of contact surface area. However, the excellent potential for mechanical destruction of thrombolysis was balanced by the critical drawbacks of the use of gas bubbles and microexplosives, with associated safety and repeatability problems for use in multiple operations.

The Ho:YAG laser is a solid-state laser with a mid-infrared wavelength (2.1 μm) that is close to one of the light-absorption peaks of water at 1.9 μm. Irradiation of water with the Ho:YAG laser is well known to generate laser-induced bubbles, oscillations, and SWs [2]. Therefore, the microexplosive could be substituted with underwater SWs generated by Ho:YAG laser irradiation by using two optical fibers. However, this method has been abandoned due to complexity of controlling the 100-μs interval between the two laser irradiation pulses, and the lack of control of the liquid

jet direction [8].

4. Experimental application of pulsed LILJ

Fortuitously, simple underwater irradiation of the Ho:YAG laser in a tubular structure was found to generate a pulsed liquid jet [2]. Briefly, a laser pulse from the Ho:YAG laser irradiates the interior of the tube, which contains cold lactate Ringer solution supplied via a Y-connector, and forms the transient laser-induced bubble. The three-dimensional expansion of the confined vapor bubble then drives a one-dimensional liquid jet through the nozzle (**Fig. 1, 2**).

The liquid jet was initially generated by inserting an optical fiber (core diameter 600 μm) into a 6F balloon catheter. Laser pulse energy, pulse duration, and nozzle (aspect) ratio are also important factors to control the initial velocity and pressure of the liquid jet [9]. Modification of this LILJ system showed excellent accessibility beyond the tortuous portion of the cavernous sinus, and excellent enhancement of fibrinolytics in vitro [10, 11]. Direct recanalization in Zivin's embolism model using the swine lingual facial artery was also achieved without intimal damage [10]. The temperature remains lower than 41°C, the reported functional threshold of neuronal damage [12]. Significant reduction of liquid supply (less than 2 μl at maximum) [13] may be the most salient difference from the continuous water jet instrument, as well as the potential to preserve small vessels.

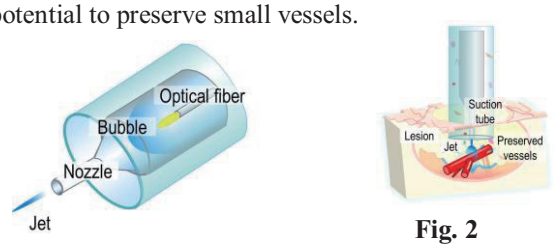

Fig. 2

5. Neurosurgical application of pulsed LILJ

The protocol was initially approved by the internal ethics committees of Kohnan Hospital in 2005, and Tohoku University Hospital in 2007. The LILJ device consists of a catheter incorporating a jet generator formed of stainless tube, and optical quartz fiber, leading into a 19G stainless tube with a metal nozzle, surrounded by a coaxial silicone suction tube (fluorocarbon polymers). The coaxial silicone tube is connected to a conventional aspirating system in the operating theater to remove dissected tissue, and splashed and excess liquid. The distal end of the catheter is sealed with a Y connector to prevent air entering the system. The energy source is a pulsed Ho:YAG laser system (Mid-Infrared Pulse Laser System, model SLS-HO; Sparkling Photon, Inc.) with wavelength of 2.1 μm and pulse duration of 350 μs. The pulsed liquid jet is generated by irradiating the internally supplied lactate Ringer solution (supplied at 4°C) within the stainless tube jet generator.

We have applied the system in patients with malignant glioma, cerebrovascular disease, epilepsy surgery and for lesion in the vicinity of pituitary fossa. Over one hundred patients with skull base tumor were treated through the transsphenoidal approach using the LILJ system at Kohnan Hospital since 2008. The modified LILJ system for the transsphenoidal approach consisted of a bayonet-shaped catheter incorporating a jet generator, leading into a 19G stainless tube with a metal nozzle (20G), surrounded by a coaxial silicone 14 G equivalent suction tube (fluorocarbon polymers, maximal accessible depth 184 mm) (**Fig. 3, 4**). The energy of the laser could be changed between 300 and 500 mJ per pulse at pulse rates of 3 to 5 Hz. The device provided satisfactory accessibility in all cases. Almost all arteries or arterioles (minimum diameter ranging from 100 to 200 μm), and occasional intratumoral veins were preserved. We have shown significant increase of tumor removal rate, decrease of intraoperative blood loss and operation time compared to historical control in complex skull base tumor case through transsphenoidal approach [14]. We have also shown the preservation of visual evoked potential during removal of tumor adjacent to optic nerve using LILJ system [15].

Fig. 3

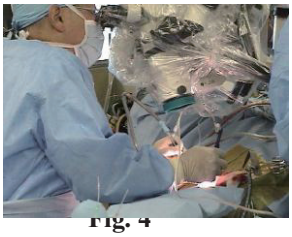

Fig. 4

6. Horizontal expansion of medical application

The system is now under challenge to show proof of concept in preclinical study for partial nephrectomy without temporary occlusion of renal artery in urology, endoscopic submucosal dissection in esophagus, liver dissection in surgery, harvesting vascular graft in cardiovascular surgery, dissection of spinal cord and intrajoint operation in orthopedic surgery, and recanalization of occluded vessels in ophthalmology. We also are making effort to complete the database for material property (breaking strength [16] and Young modulus) to understand the mechanism of tissue dissection by the water jet and creating new application.

References

[1] J. Oertel, Neurosurgery, **52** (2003), 153.
[2] J. Oertel. J Neurosurg, **100** (2004), 498.
[3] T. Hirano, Lasers. Surg. Med, **29**, (2001), 360.
[4] T. Seto, Rev. Sci. Instrum, **82**, (2011), 055105.
[5] H.G. Rau. HPB(Oxford), **10**, (2008), 275.
[6] T. Kodama, Ultrasound. Med. Biol, **24**, (1998), 723.
[7] T. Kodama, Ultrasound. Med. Biol, **25**, (1999), 977.
[8] T. Hirano, Intervent. Neuroradiol, **7(Suppl 1)**, (2001), 35.
[9] A. Nakagawa, Lasers. Surg. Med, **31**, (2002), 129.
[10] Y. Sato, Min. Invas. Neurosurg, **50**, (2007), 212.
[11] T. Hirano, Min. Invas. Neurosurg, **51**, (2008), 324.
[12] T.Hirano,Acta. Neurochir (Wien), **145**, (2002), 401.
[13] T. Ohki, Lasers. Surg. Med, **34**, (2004), 227.
[14] Y.Ogawa, Acta Neurochir (Wien), **153**, (2011), 823.
[15] Y. Ogawa, Acta Neurochir (Wien), (2013, in press).
[16] C. Sato, Dig. Endosc, **25**, (2013), 255.

Tenth International Conference on Flow Dynamics
November 25-27, 2013, Sendai, Miyagi, Japan

Introduction of Medical Plasma Equipment for the Minimally Invasive Treatment

Hajime Sakakita[1,5], Yuzuru Ikehara[2], Jaeho Kim[1], Nobuyuki Shimizu[3], Sanae Ikehara[2],
Hayao Nakanishi[4], Hiromasa Yamada[5], Yusuke Yamagishi[5], Satoru Kiyama[1], Akiko Kubota[1],
Masao Ichinose[6], and Toru Niwa[7]
[1]Innovative Plasma Technologies Group, Energy Technology Research Institute, National Institute of Advanced Industrial Science and Technology (AIST), Tsukuba, Japan
[2]Molecular Medicine Team, Research Center for Medical Glycoscience, National Institute of Advanced Industrial Science and Technology (AIST), Tsukuba, Japan
[3]Sanno Hospital, Tokyo, Japan
[4] Division of Oncological Pathology, Aichi Cancer Center Research Institute, Nagoya, Japan
[5]Department of Engineering Mechanics and Energy, Graduate School of Systems and Information Engineering, University of Tsukuba, Tsukuba Japan
[6]Wakayama Medical University, Wakayama, Japan
[7]Hashimoto Municipal Hospital, Wakayama, Japan
E-mail of corresponding author: h.sakakita@aist.go.jp

ABSTRACT

The medical plasma equipments are categorized in the electrical equipment for the use of medical treatments. At present, internationally, the standardization on the safety of the equipment has been demanded. Therefore, following elemental things on medical plasma equipments have been clarified, such as the electrical safety, performance and plasma characteristics. Namely, the points that required for the clearance of medical plasma equipments for blood coagulation to reduce the invasiveness at the surgical operation have been proposed.

1. Introduction

Plasma, defined as ionized gas, is composed of charged particles (ions and electrons) ionized from atoms or molecules, and excited particles. The main examples of high temperature plasmas are the sun, the aurora, lightning, nuclear fusion plasma and plasma sprays. Low-temperature plasmas have been adopted for manufacturing semiconductors, thin- film solar panels, single-crystal diamond, and fluorescent lamps, for example. Recently, low temperature atmospheric pressure plasmas have been produced by several methods [1-3]. Plasma technologies are already used in medical applications such as for coating a stent with diamond-like carbon, and the modification of biomaterials. A coagulator with a high-temperature argon plasma is used in endoscopic surgery [4]. In this presentation, we introduce minimally invasive plasma as a low-temperature plasma.

2. A medical plasma equipment system for blood coagulation

The equipment is comprised with the control unit, a gas feeding line, power source and the plasma source. Here, a “plasma flare” produced from the plasma source is applied to the bleeding part after cutting out the femoral artery under anesthesia [5]. Coagulation is promptly induced to cover the disrupted blood vessel and stop the bleeding. The surface temperature is less than 40 degree Celsius during the treatment [6]. There is no evidence of burning or tissue damage caused by the heat [7]. Plasma treatments can reduce invasiveness under hemostasis, and reduce risk of postoperative disorders [8].

3. Clinical need for medical plasma equipment in line with progression of minimally invasive surgical procedure

Because minimal invasiveness is one of the ideal conditions that surgeons endeavor to achieve, we have pointed out the issue of burn injury due to cauterization to control the bleeding of capillaries. For example of abdominal surgery, surgeons conventionally control bleeding by methods such as cauterization, clipping, or ligation, depending on the types of blood vessel to do omentectomy. Almost all surgeons have encountered a latent problem caused by the use of high-frequency electronic coagulator, or ultrasound coagulator and its thermal effect, that is, the problem of burn injury. It causes prolonged postoperative disorder and scar tissue formation in the abdominal cavity, which limits adaptability to laparoscopic surgery and the performance of 2nd surgery.

4. Equipment for controlling bleeding from small and capillary vessels

As the basic equipment used to control bleeding from small and capillary vessels, there are high-frequency electrical coagulator, ultrasonic wave equipment, laser, and high-temperature plasma. Operating points for hemostasis can be classified into two categories with or without cauterization. Low-temperature plasma directly accelerates the blood coagulation process, whereas other methods essentially cauterize capillaries, small vessels and veins by heat, ultrasonic vibration and heat, high-frequency current heating. From the viewpoint of the prioritizing the safety of medical electrical equipment, these two types of high and low temperature plasma equipments have not yet been defined by the measurement of output power.

5. Necessity for international standardization of the medical plasma equipment for blood coagulation in medical practice

High-temperature plasma has been used effectively in surgical operation. With the realization of low-temperature and high-reactive atmospheric-pressure plasma that stops bleeding, minimally invasive operations are expected to become the norm in the near future. International standards on the basic performance and safety of medical plasma equipment for blood coagulation will accelerate and extend the possibilities of such equipment. The characteristics of low-temperature and high-reactive atmospheric-pressure plasma strongly depend on the plasma equipment and operation conditions. Therefore, to apply the plasma effectively, safely and reproducibly, it is necessary to clarify the correlation parameters between the plasma components and biological effects. To ensure the safety of medical plasma equipment, specifications such as the output power of the equipment should be measured and evaluated.

By using diagnostic system of specifications, it will become possible to measure the characteristics of a power source and plasma flare. Moreover, the specifications of the equivalent load are also defined.

As a minimum, the following must be defined to establish the specifications: 1) Testing method for the electrical characteristics of medical plasma equipment, 2) Testing procedure, 3) Measurement system, and 4) Criteria.

Acknowledgements

This study was financially supported by International Standardization Project from the Ministry of Economy, Trade and Industry of Japan, and in part by Grants-in-Aid for Scientific Research on Priority Area (21590454, 24590498, and 24108006 to Y. I.) from the Ministry of Education, Culture, Sports, Science and Technology of Japan.

References

[1] Kanazawa S et al 1988 J. Phys. D: Appl. Phys. **21** 838
[2] Stoffels E et al 2006 Plasma Sources Sci. and Tech. **15** S169
[3] Teschke M et al 2005 Proc. 48th Annual Tech. Conf. (Soc. Vac. Coasters) **505/856-7188** 1
[4] Grund K E et al 1994 Endosope Surgery **2** 42
[5] Sakakita H and Ikehara Y 2010 Plasma and Fusin Res. **5** S2117-1
[6] Sakakita H, “Plasma Physics and Its Global Applications”, Material Research Society 2012 Spring Meeting and Exhibition, 2012, April 9 (San Francisco) Tutorial talk, WW-3
[7] Ikehara Y, “PathophysiologicalMeanings of PlasmaTreatment for Blood Bleeding and the Wound Healing Process”, Material Research Society 2012 Spring Meeting and Exhibition, 2012, April 11 (San Francisco) Invited talk
[8] Ikehara Y et al., “Formation of membrane-like structures in clotted blood by mild plasma treatment during hemostasis”, 2013, 26(4), 555-557, Journal of Photopolymer Science and Technology .

Novel Experimental System for Applying Cyclic Tensile Strain and Fluid Shear Stress to Tenocytes

Toshiro Ohashi[1], Yasufumi Hagiwara[2], James HC Wang[3], Eijiro Maeda[1]
1 Laboratory of Micro and Nanomechanics, Faculty of Engineering, Hokkaido University, Sapporo, Hokkaido, Japan
2 Graduate School of Engineering, Hokkaido University, Sapporo, Hokkaido, Japan
3 Department of Orthopaedic Surgery, University of Pittsburgh School of Medicine, Pittsburgh, PA, USA
ohashi@eng.hokudai.ac.jp

ABSTRACT

This study was performed to test a new experimental system, which is suitable for the application of tensile strain and fluid shear stress to tenocytes in vitro. It was confirmed that physiological tensile strain and a wide range of fluid shear stress magnitudes could be applied to the cells. Indeed, it was demonstrated that the combined stimulation of cyclic tensile strain and oscillatory fluid shear stress induced a greater synergetic effect on tenocyte calcium response and significantly increased the percentage of tenocyte exhibiting increases in intracellular Ca^{2+} concentration compared to the solo applications of these two modes of stimulation.

1. Introduction

Most of tendons in the body are subjected to dynamic tensile loading, which imposes cyclic tensile strain on tenocytes. This motivated a number of studies to be performed to evaluate how tenocytes regulate their functions in response to tensile strain [1]. In addition to tensile loading, it has been demonstrated that there is an influx and an outflux of interstitial fluid from tendons when the tissues are loaded and unloaded [2], and the magnitude of fluid shear stress imposed on tenocytes in vivo, due to the interstitial fluid flow, was estimated to be at a level of 0.1 mPa [3]. Accordingly, to obtain a comprehensive understanding of mechano-regulation of tenocyte functions, it is necessary to examine how tenocytes respond to fluid shear stress and cyclic tensile strain, or to a combined stimulus of the two modes of mechanical stress. However, no such attempt has been made due to difficulty of establishing a suitable experimental model.

Therefore, the present study was designed to establish a new experimental system for tenocyte mechanobiology research, enabling the application of fluid shear stress and cyclic tensile strain individually or simultaneously in a controlled manner (Fig. 1a). We have adopted a microgroove structure to align tenocytes and have combined it with a flow unit, both of which are made from polydimethylsiloxane (PDMS). The present study was particularly to investigate the effects of two levels of fluid shear stress; one was at an order of 0.1 mPa that was estimated as a physiological level to tenocytes in vivo [3], and the other was an order of 0.1 Pa, which was demonstrated to induce catabolic gene expression from tenocytes in a monolayer without an elevation of intracellular calcium ion concentration [4]. To date, as far as the authors are aware, no study could apply shear stress as low as 0.1 mPa and observe responses from cells. In the present study, we successfully applied fluid shear stress at the level of 1 mPa to tenocytes, and then examined whether 1 mPa and 0.1 Pa levels of fluid shear stress induced mechano-sensitive responses from tenocytes.

2. Method

The new experimental system - It consists of two components (Fig. 1b): a microgroove substrate and a flow unit were made from PDMS. Fabricated in a rectangular region (10 mm × 15 mm) in the PDMS membrane, the microgrooves have a rectangular profile, with a width of 10 μm, ridge of 10 μm, and depth of 10 μm [5]. The flow unit has a flow path (10 mm in width, 1 mm in height, and 27 mm in length) covering the entire region of the microgrooves. The microgrooves were fabricated through photolithography using a negative photoresist SU-8 3010 and softlithography, and the flow unit was made using a PDMS casting in an aluminum mold. The microgrooves was coated with Pronectin F. These two components were bound following a surface treatment with air plasma.

Flow-field analysis – To estimate the flow field generated within the microgrooves, a CFD domain was created consisting of the flow path as main domain and a microgroove as sub domain. Based on the domain, a finite element model was built. Several flow profiles were applied to the main domain, and a flow field within the microgroove domain was examined using an FEM software ANSYS. To validate estimated flow fields, particle tracking velocimetry (PTV) was performed on a confocal laser scanning microscope. In addition, a finite element model of a whole tenocyte within the microgroove was created based on Z-series images of single tenocytes within the microgrooves that were obtained using confocal microscope, and was integrated within the microgroove domain of the CDF domain. The

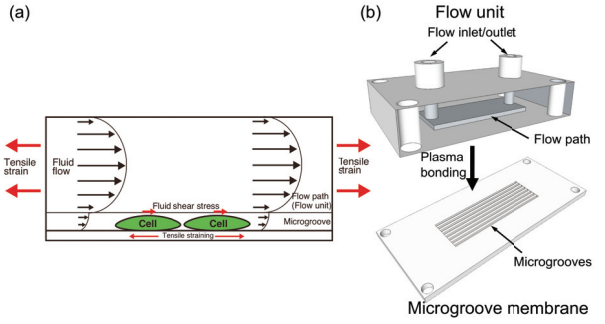

Fig. 1 Schematics of (a) the newly developed device for tenocyte experiment, and (b) mechanical environment of tenocytes within the device.

magnitude of fluid shear stress applied to the cell within the microgroove was estimated under a variety of flow profiles.

Cell experiments – Tenocytes isolated from bovine extensor tendons were loaded into the microgrooves and stained with calcium indicator Fluor-4 AM. To apply fluid shear stress, the flow velocity of 1666 μm/sec and 0.17 μm/sec of oscillatory flow was used. A physiological level of 4% tensile strain was used to apply cyclic tensile strain. Both oscillatory fluid flow and cyclic tensile strain were applied at a frequency of 0.5 Hz for 10 cycles, either individually or simultaneously. Tenocyte calcium responses were observed for 5 minutes following the application of mechanical stimulation. Control data were acquired during 5 minutes prior to the application of mechanical stimuli described above.

3. Results

Calcium experiment – Non-stimulated control data showed no elevation in Ca^{2+} concentration in tenocytes (Fig. 2). The application of mechanical stimulation (oscillatory fluid flow, cyclic tensile strain, and both) induced elevations in fluorescence intensities within a population of tenocytes observed (Fig. 2). The application of oscillatory fluid flow for 10 cycles increased the percentage of cells demonstrating the elevation of Ca^{2+} concentration from the level of pre-stimulated control, although there were no statistically significant increases in either level of fluid flow. The application of 10 cycles of 4% cyclic tensile strain also increased the percentage of tenocytes exhibiting calcium response compared to the pre-stimulated control, although the increase was not statistically significant. On the other hand, the application of combined stimulation of cyclic tensile strain and oscillatory fluid flow at both flow velocities demonstrated synergetic effects on tenocyte calcium response than single-mode applications (Fig. 2). The percentage of cells exhibiting Ca^{2+} responses after the combined stimulation was significantly higher than that of pre-stimulated control samples in the both shear stress levels.

Estimation of the magnitude of fluid shear stress – Flow field within the microgrooves was estimated by CFD analysis and was examined experimentally by PTV. It was observed that the flow velocity obtained by PTV corresponded to the velocity obtained by CFD analysis at 2 μm above the bottom surface of the microgroove. When the flow velocity was at 1666 μm/sec, the estimated magnitude of fluid shear stress applied to tenocytes within the microgrooves was in the range of 0.02 to 0.1 Pa (Fig. 3a). In the case of the flow velocity at 0.17 μm/sec, the estimated magnitude of fluid shear stress was mostly in the range of 1.0 to 2.4 mPa, and approximately 3.0 mPa of shear stress was also estimated in limited regions (Fig. 3b).

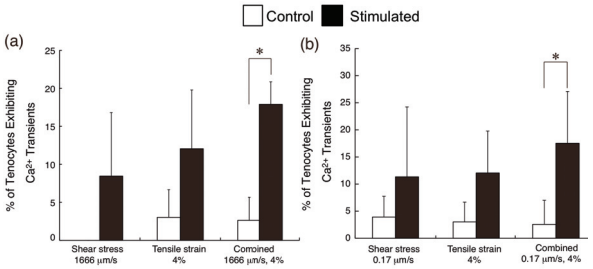

Fig. 2 Percentage of tenocytes exhibiting Ca^{2+} transient responses. (a) Flow velocity of 1666 μm/sec, and (b) flow velocity of 0.17 μm/sec. Control data in the sole application of fluid shear stress (1666 μm/sec) had zero mean value with zero standard deviation. * $p < 0.05$.

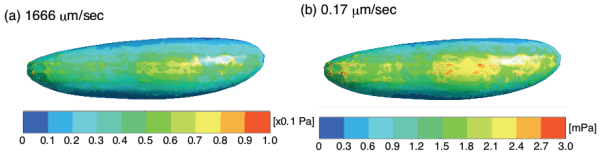

Fig. 3 Shear stress distributions on the upper surface of a finite element model for a single tenocyte. Flow velocity was (a) 1666 μm/sec and (b) 0.17 μm/sec, respectively. The flow was from left to right.

4. Discussion

We have developed a new experimental system with which tenocyte response to fluid shear stress could be examined. Effects of fluid shear stress on tenocyte functionality have not been characterized in detail experimentally, partly due to the lack of an appropriate experimental system. This study shows that the new system was able to apply a broad range of fluid shear stress to tenocytes, including a level close to that was reportedly physiological. Our experimental results also indicate that tenocytes are responsive to fluid shear stress. In addition, synergetic effects of the combined application of cyclic tensile strain and fluid shear stress were clearly demonstrated. These findings imply that shear stress derived from interstitial fluid flow is an important mechanical stimulation in the regulation of tenocyte functions, and shear stress and tensile strain are transduced to biochemical signals in distinct pathways.

Acknowledgements

The present study was supported by JSPS bilateral program (Japan – USA) and Grant-in-Aid for Young Scientists (B, #2370052) from the MEXT, Japan. Technical supports were from OPEN FACILITY, Hokkaido University Sosei Hall and Nikon Imaging Centre at Hokkaido University.

References

[1] J. Wang, J. Biomech., **39** (2006), 1563.
[2] J. Hannafin and S. Arnoczky, J. Orhtop. Res., **12** (1994), 350.
[3] M. Lavagnino et al., Biomech. Model. Mechanobiol. **7** (2008), 405.
[4] A. Archambault et al., J. Biomech., **35** (2002), 303.
[5] J. Wang et al., Ann. Biomed. Eng. **33** (2005), 337.

Tenth International Conference on Flow Dynamics
November 25-27, 2013, Sendai, Miyagi, Japan

Modes of Collective Cell Migration arising from Physical Constraints

Chwee Teck Lim
Mechanobiology Institute, National University of Singapore, Singapore
Department of Bioengineering, National University of Singapore, Singapore
ctlim@nus.edu.sg

ABSTRACT

Collective cell migration plays an important role in regulating various processes such as gastrulation, wound healing and tissue organization. Here, we investigated how physical constraints can modulate collective behavior within epithelial cell sheets. We showed that the geometrical properties of the environment can regulate the formation of collective cell migration patterns through cell-cell and cell-substrate interactions. Using micro patterns to restrict cell migration to well-defined geometries such as circles, we discovered various modes of collective migration in response to such constraints.

1. Introduction

It is a known fact that cells migrating in sheets or large cohorts tend to behave very differently from cells migrating individually [1]. Indeed, the distinctive behavior of cells migrating in a collective manner underlies several important biological processes [2]. Though the factors determining the distinctive migratory characteristics of cells in a cohort is poorly understood; in vitro (e.g. traditional wound healing) and in vivo (e.g. imaging embryos) experiments suggest that intercellular adhesion, guidance from chemical cues and mechanical constraints of the extracellular matrix (ECM) through which cells migrate play an important role. However, in such experiments, it is not only difficult to independently assess the contribution of physical constraints vis-à-vis guidance from chemical cues but also impossible to map the distribution of traction forces exerted by cells on the substrate. Here, we characterized the kinematic behavior of epithelial cell cohorts migrating under well defined geometrical constraints [3]. The geometrical constraints comprised micro-patterned fribronectins in the form of circles.

2. Experimental Methods and Results

Here, we combined microcontact printing with particle image velocimetry (PIV) to investigate the role of cell density ('crowding') and boundary conditions imposed by ECM proteins ('constraints') in regulating collective behavior within MDCK epithelial cell sheets.

We first investigated how cell density regulated the collective behavior of MDCK cells. We first seeded cells at very low density (~800cells/mm^2) on microcontact printed (μCP) circular fibronectin patterns that were about 200 μm in diameter. We then obtained phase contrast images as well as fluorescent images of the nuclei for about 48 hours till the cells reached very high densities (~10,000cells/mm^2). Here, μCP fibronectin patterns restricted cells from migrating out of the pattern thus making it easier to image and analyze the migration behavior. With increasing cell density, we observed distinct phases of cell migration. At very low densities (below confluence), cells were distributed sparsely either as single cells or small clusters and had a tendency to migrate randomly. Once confluence was reached, cells migrated in a synchronized and collective rotation pattern. At higher cell density, collective rotation behavior persisted but the average velocity of the cells was decreased. We then used PIV to quantitatively characterize these phases. The spatial average of all the velocity vectors within the fibronectin pattern (Vavg = <|Vi|>) was computed as a function of cell density. We divided the evolution of the migratory characteristics into three phases. During the first or sub-confluent phase when cell density was about 2000 cells/mm^2, the migration was characterized by a low Vavg and uncorrelated velocity vectors. In the second phase, the onset of collective synchronized rotation of cells and high Vavg (about 25 μm/hr) was observed when a critical density of about 2000 cells/mm^2 was reached. In the third or over-confluent phase, cell densities reach values greater than 4000 cells/mm^2 and Vavg fell below about half its maximum value. These results suggest that collective migration of the monolayer is initiated only after a 'threshold-density' is reached. This 'threshold-density' for monolayer migration and the critical density required for cells to undergo collective rotation on circular patterns is ~2000 cells/mm^2. Furthermore, a decrease in the Vavg to about half of its maximum at cell densities greater than 4000 cells/mm^2 has also been observed in expanding MDCK cell sheets and coincides with their transition into a 'glassy' phase and the inhibition of lamellipodia protrusion [4].

To put our experiments on wt-MDCK in perspective and correlate it with patho-physiological conditions, we studied the migratory behavior of MCF-10A (derived from a benign breast tumor), MCF-7 and MDA-MB-231 cells (derived from a malignant breast tumor) on 200 μm diameter fibronectin pattern. MCF-10A cells were observed to separate frequently from their neighbors, thus suggesting weak cell-cell adhesion. Although the outer cells in contact with the edge of the micropattern exhibited some form of collective rotation at confluence, cells in the centre migrated randomly. This can be explained by the fact that the outer cells are being guided by the edge of the micropattern through a phenomenon known as 'contact guidance'. However, it is likely that synchronized collective rotation of all the cells within the pattern will require mature intercellular adhesion that these MCF-10A cells lack. On the other hand, both MCF-7 and MDA-MB-231 cells showed a

random and chaotic movement with no tendency to undergo collective behavior at any cell density. These results suggest that the loss of collective behavior could be a gradually occurring event during the evolution of cells from normal to a malignant phenotype.

3. Discussion

We performed a systematic and comprehensive study of the influence of cell density and geometrical constraints on collective behavior in epithelial cells by combining μCP and PIV. Our use of micropatterns enables a reproducible platform to characterize the role of cell density, geometric constraints and boundary effects on collective cell behavior. Our results suggest that reaching a critical density (~2,000 cells/mm^2) triggers collective behavior in MDCK cells. This density dependent transition in collective behavior has also been shown in actin filaments [5], keratocytes [6] as well as MDCK cells subjected to traditional scratch wound assays [7]. Although it is still not clear how a synchronized rotation of the cells sheet arises, we postulate that cells on the edge (that experience asymmetric E-cadherin mediated intercellular contacts), polarize along the edge of the fibronectin pattern [8]. This polarization results in an increase of angular velocity which guides the cells along the edge. When confluence is reached, the outer cells will continue to follow this guidance, while their directional migration is transmitted to the inner cells through cell-cell contacts. This rotation of the cell sheet then sets in as cells prefer to orient themselves along the axis of maximal principal stress established by the tangential alignment of the peripheral cells [9]. This phenomenon is not observed below confluence because of the free space available. In fact, this collective rotation behavior is highly reminiscent of the 'coherent angular motion' (CAM) observed in epithelial cells cultured in 3D collagen gels, in which the intercellular contacts induce similar polarization of cells [10].

While cancer cells have a tremendous ability to proliferate, they are unable to organize themselves into higher order tissue structures (e.g. acini in breast tissue). Our results suggest that the inability of cancerous cells to undergo synchronized collective rotation (due to defective cell-cell adhesion as one possible reason) could be partially responsible for preventing them from forming higher order tissue structures. While MCF-10A (benign) showed signs of collective migration along the border of the fibronectin circle (contact-guidance), MCF-7 and MDA-MB-231 (malignant) showed a completely random migratory behavior that was unaffected by cell density and ECM confinement. These results raise the possibility that collective behavior could be gradually lost as cells evolve to become more malignant.

Thus, our system here provides a very simple and easy approach to investigate collective cell migration in health and diseases in a controllable and systematic way.

4. Concluding remarks

We demonstrated that an interplay between cell density, geometrical constraints and intercellular adhesion regulate the synchronized collective rotation behavior observed in epithelial cells. We also validated the use of μCP patterns as a simpler alternative to study collective behavior and 'coherent angular motion' in epithelial cells. The use of such patterns not only provides flexibility in precisely controlling and altering the geometrical constraints but also has all the advantages of imaging such migrations in 2D. Also, other factors such as substrate elasticity and/or chemical gradients could also play a significant role in determining collective cell behavior and this can be easily incorporated into such an assay. Future work can be directed at studying the effects of each of these factors and can help further understand how collective cell behavior is regulated.

References

[1] A. Kabla, Collective Cell Migration: Leadership, Invasion & Segregation, **9** (2012), 3268-3278.

[2] S.R.K. Vedula, A. Ravasio, C.T. Lim, B. Ladoux, Physiology, 2013. (*in press*)

[3] K. Doxzen, S.R.K. Vedula, M.C. Leong, N.S. Gov, A.J. Kabla, B. Ladoux, C.T. Lim, Integrative Biology, **5** (2013), 1026-1035.

[4] D. Gubb, Int J Dev Biol **42** (1998), 369-377.

[5] V. Schaller, C. Weber, C. Semmrich,E. Frey, A.R. Bausch, Nature, **467** (2010), 73-77.

[6] P. Rosen, D.S. Misfeldt, PNAS, **77**, 8 (1980), 4760-4763.

[7] B. Szabo, G.J. Szöllösi, B. Gönci, Z. Jurányi, D. Selmeczi, T. Vicsek, Phys Rev E Stat Nonlin Soft Matter Phys, **74** (2006), 061908.

[8] R.A. Desai, L. Gao, S. Raghavan, W.F. Liu, C.S. Chen, J Cell Sci, **122** (2009), 905-911.

[9] D.T. Tambe, C.C. Hardin, T.E. Angelini, K. Rajendran, C.Y. Park, X. Serra-Picamal, E.H. Zhou, M.H. Zaman, J.P. Butler, D.A. Weitz, J.J. Fredberg, X. Trepat, Nat Mater, **10** (2011), 469-475.

[10] K. Tanner, H. Mori, R. Mroue, A. Bruni-Cardoso, M.J. Bissell1, PNAS, **109** (2012), 1973-1978.

Cold Atmospheric Plasmas in Medicine

Georg Isbary[a], Tetsuji Shimizu[b], Julia Zimmermann[b], Gregor Morfill[b], Wilhelm Stolz[a]
[a]Department of Dermatology, Hospital Schwabing, Munich, Germany
[b]Max Planck Institute for Extraterrestrial Physics, Garching, Germany
dr.isbary@googlemail.com

ABSTRACT

Resistance of microorganisms is one of the big challenges in medicine and hygiene in the 21st century. Cold atmospheric plasma is an innovative promising tool to treat pathogen related skin diseases, regardless of the kind of bacterial species and the resistance level. First clinical trials in patients with chronic infected wounds demonstrated the bactericidal properties in vivo and showed that wound healing can be accelerated. Other studies demonstrated that plasmas could also be designed for other purposes in hygiene and medicine.

1. Main text

Cold atmospheric plasma (CAP) has gained a lot of attention in the scientific community, due to its promising broad antimicrobial features. Already a multitude of publications about the antimicrobial spectrum of CAPs have been published - especially on different pathogens, such as various bacteria including multi-resistant strains, biofilms, spores, fungi and even viruses. First clinical trials in patients had to demonstrate if this innovative technology fulfils the high expectations.

Following preclinical trials first prospective randomized clinical trials were initiated with a CAP-Device – MicroPlaSter alpha (built by ADTEC Plasma Technology Co. Ltd., Hiroshima, Japan). The following setting was chosen for the argon driven device: Microwave 2.46 GHz, 86 W; Ar 2.2 slm; distance to torch 2 cm. In a 5min setting the additional plasma application led to a significant higher germ reduction in plasma treated wounds compared to the controls (291 291 2m1n2s in 38 wounds, 2 1219i1id i 21n1fi2 3s %, 29 f 1nf 211 2 2i1n2 121d s own 1on29oi nd 9111im1d s2 nd 9d 2o2i1 i nd sys21mi1 m1di1 2ionf 291 91du12ion w s found 91g 9di1ss 291 kind nd 291 91sis2 n11 i1m1i of 291 2 1219i f No sid1 1ff112s w191 s11n du1 2o 2 ini1ss 2i sm 291 2m1n2f ku2s1qu1n2 1iini1 i 29i is inm1s2ig 21d 291 1ff112of 2 min s122ing wi29 291 s m1 nd n1x2 g1n19 2ion d1mi11 2212 m19sionn o219 2ing und19 291 s m1 2i sm s122ingf 2g in signifi1 n29ig919 91du12ion 9 21s w191 s11n in 2o29 g9ou2s 2Mi19o2i k219 i29 y 7 291 2m1n2s in 1s 2 2i1n2s, 2 1219i1id i 21n1fi2 s %, 2 9 f 11 Mi19o2i k219 212 y 137 291 2m1n2s in 1 2 2i1n2s, ddi2ion i 2 1219i1id i 1ff112 23f2%, 29 f 1nf 221 2g in 291 2 ini1ss 22ii1 2ion w s f911 of sid1 1ff112sf

We demonstrated that a 2 min and 5 min cold argon plasma treatment led to a significant reduction in bacterial load in chronic wounds of various causes in patients, regardless of the bacterial species. A retrospective study evaluated the effect of CAPs on wound healing purposes. [3] Patients were grouped into three clusters. Group A: Chronic wounds of various types in 70 patients were treated with cold argon atmospheric plasma for 3-7 minutes. Subgroup analyses were performed for all chronic venous ulcers (n=29, Group B) and 5 min plasma treatment of chronic venous ulcers (n=18, Group C). The wound size (length and width) before and after a course of treatment was compared for plasma-treated and control wounds.
Group A revealed a 10.4 % reduction in width of plasma treated wounds compared to 4.2 % in the control (p=0.270). Length reduced by 8.2 % compared to 5.1% respectively (p=0.068). In Group B a significantly greater reduction in width (17.9 %, p=0.03) was measured in plasma-treated ulcers compared to controls (0 %). However changes in length were not significantly different (9.1 % vs. 8.9 %, p=0.46). The Group C sub analysis showed a highly significant reduction in width (14.6 % vs. 0 %, p=0.008) with plasma treatment but not in ulcer length (2.7 % vs. 8.4 %, p=0.352).
This study demonstrated for the first time in a study setting which was primarily not prepared for wound healing purposes, that plasma treatment can accelerate wound healing in a range of chronic wounds in patients, but particularly chronic venous ulcers.

A case report in a patient suffering from a rare disease called Hailey-Hailey disease revealed that CAPs can also be applied on other pathogen related superficial skin diseases. [4] An additional administration of a CAP treatment (Mi19o2i k219 212) resulted in a quick clinical response in therapy resistant lesions, which were secondary infected with *Proteus mirabilis* and the yeast *Candida albicans*.
Another report showed in a patient following surgery of cholesteatoma and subsequent chronic infections (canal including (EPSL+) *E.coli*) of the external auditory, which resulted severe pain, that a plasma treatment can be applied. [5] The application of cold atmospheric plasma (Mi19o2i k219 212) resulted in a significant reduction in pain and clearance of bacterial carriage, allowing antibiotics and analgesics to be ceased.

To assess the efficacy of a CAP treatment (Mi19o2i k219 212) on itching diseases, patients received a 2 min treatment as an add-on therapy. [6] 46 patients with various itching diseases were included. Patients acted as their own control, when the pruritic

disease was treated with placebo (argon gas application alone). A significant reduction of itch was shown in plasma group, but also in control group.

Ongoing studies are investigating the effect of a CAP treatment in patients suffering from shingles/zoster, a *Varicella zoster virus* (VZV) related disease. First results are promising concerning pain reduction in plasma treated patients.

Concluding remarks

First cold atmospheric plasma applications in patients revealed the broad benefits of such a treatment. Future will show whether CAPs will be an established part of medicine, or not.

References

[1] G. Isbary, Brit. J. Dermatol., **163** (2010), 78-82.
[2] G. Isbary, Brit. J. Dermatol., **167** (2012), 404-10.
[3] G. Isbary, Clin. Plasma Med., epub ahead of print
[4] G. Isbary, Arch. Dermatol. **147** (2011), 388-90.
[5] G. Isbary, New Microb. New Infect., submitted
[6] J. Heinlin, J. Eur. Acad. Dermatol., **27**(2013), 324-31.

Tenth International Conference on Flow Dynamics
November 25-27, 2013, Sendai, Miyagi, Japan

The Scaffold-free Cartilage Tissue by Mechanical Stress Loading for Tissue Engineering

Katsuko S Furukawa[1,2*], Masashi Yoshimoto[2], Takashi Ushida[1,2,3]
[1] Department of Bioengineering, School of Engineering, The University of Tokyo, Tokyo 113-8656, Japan
[2] Department of Mechanical Engineering, School of Engineering, The University of Tokyo, Tokyo 113-8656, Japan
[3] Division of Biomedical Materials and Systems, Center for Disease Biology and Integrative Medicine, School of Medicine, The University of Tokyo, Tokyo 113-8656. Japan
E-mail of corresponding author: furukawa@mech.t.u-tokyo.ac.jp

ABSTRACT

Our objective was to investigate the hypothesis that tissue-engineered cartilage with promising biochemical, mechanical properties can be formed by loading mechanical stress under existing cell-cell interactions analogous to those that occur in condensation during embryonic development. By loading dedifferentiated chondrocytes with mechanical stress under existing cell-cell interactions, we could first form a scaffold-free cartilage tissue with arbitrary shapes and a large size with promising biological, mechanical properties. Therefore, our cartilage model loaded mechanical stress based on a mold system may be applicable for tissue-engineered cartilage.

1. Introduction

Cartilage tissue has only a small capacity for self-repair. The avascular nature, the sparse cell population, and the low mitotic activity of the chondrocytes severely limit the natural healing of these cartilage defects. Many patients with damaged cartilage due to trauma or diseases such as osteoarthritis and osteochondrosis dissecans are existing in the world. Current therapies include transplantation of healthy host cartilage or implantation of artificial prosthetic devices. However, problems remained in these treatments. The amount of donor tissue for transplantation is limited, and durability of the prosthetic devices is not good by wear debris or adhesive breakdown at the host/prosthesis interface. For these reasons, there is considerable interest in developing cell therapies and tissue-engineered cartilages to treat damaged cartilage. Still, many problems remain in cartilage tissue engineering using cells. When grown in two-dimensional culture, adult articular chondrocytes are capable of proliferation, promoting researchers to use cultured autologous chondrocytes to accelerate cartilage regeneration. However, the proliferating chondrocytes gradually lose their differentiated phenotyp, as indicated by the loss of synthesis of aggrecan and type II collagen and the increase of synthesis of type I collagen. Therefore, in order to form a tissue-engineered cartilage using proliferated chondrocytes with a dedifferentiated phenotype, it is thought that reexpression of the chondrogenic phenotype should be induced before implantation.

To date, pellet culture systems under static conditions have been reported as a method for preventing and reversing the phenotypic modulation of chondrogenesis *in vitro*. This culture system allows cell-cell interactions analogous to those that occur in condensation during embryonic development. Although the system facilitates chondrogenic differentiation from dedifferentiated chondrocytes or mesenchymal stem cells with high reproducibility, its clinical application to tissue engineering has not been successful thus far. Because the pellet culture system forms only one small cell-aggregate per tube by a centrifugator, it is difficult to yield sufficient numbers of pellets with the differentiated phenotype. Therefore, we tried to form a cartilage tissue with a large size in which cell-cell interactions exist, as in a pellet culture, without using a scaffold for tissue engineering.

In this study, using a high porous simple mold, we tried to fabricate cartilage tissue of arbitrary shapes. Various dynamic stresses such as shear flow, hydrostatic pressure, and direct compression exist in living bodies and are thought to contribute to cartilage formation; the shear flow load on cartilage under a scaffold-free rotational culture provided such a mechanical load in a simple manner. We first demonstrated that a cartilage tissue with a large size and arbitrary shape for tissue engineering could be regenerated without any scaffolds, by making cell-cell interaction and mechanical stress loading for tissue engineering.

2. Method

Bovine articular chondrocytes isolated from the femoropatellar grooves after 2nd passage were inoculated to glass or metal molds. The arbitrary-shaped mold was set on a commercially available culture-insertion film that can diffuse oxygen and nutrition. After 8 hours' inculation of chondrocytes as a cell-culture medium suspension, only chondrocytes were dipped on the membranous surface; then we removed the mold from the membrane. After that, we could observe cell plates with an arbitrary shape on the membrane. After 24 hours, the cell plates were moved to 6-well dishes with 5 ml of differentiation medium, high-glucose (4.5g/l) Dulbecco modified Eagle medium, supplemented with 100nM dexamethasone, 50 μg/ml ascorbic acid 2-phosohate, 100μg/ml sodium pyruvate, 40 μg/ml proline, and ITS-plus (Collaborative Biomedical Products, USA, final concentrations, 6.25 μg/ml bovine insulin, 6.25 μg/ml transferrin, 6.25 μg/ml selenous acid, 5.33 μg/ml linoleic acid, and 1.25 mg/ml bovine serum albumin), penicillin, streptomycin, fungizone and cultured under a dynamic condition of a rotational culture at the speed of 70 rpm. The dishes were placed in a humidified CO_2 incubator. After cultivation for 3 weeks, biological and mechanical examinations of the cartilage tissues were undertaken.

3. Results and Discussion

We tried to form a scaffold-free cartilage tissue utilizing cell-cell interactions like a pellet culture, without any scaffold, for tissue engineering. When a cylindrical glass mold with a diameter of 1 cm was used, dedifferentiated chondrocytes of $1.5x10^7$ cells were inoculated into the mold using a commercially available culture-insertion film with pores of 0.4 μm. Oxygen and nutrition can diffuse from the lower and upper sides of cells. After 8 hours of cell inoculation, the mold was removed from the membranous surface, and cell plates were left on there with the same shape as the mold. After 24 hours' static culture for shape stabilization, scaffold-free tissue was moved to a 6-well culture plate without any shape changing adding 5 ml of differentiation medium, and was begun on rotational culture. In this point, the scaffold-free plate was very fragile; therefore, displacement of the tissue to the rotational culture plate was done with great care. A disk-like cartilage tissue was formed by 3 weeks' culture. When the cartilage plate without any scaffold cultured under shear flow conditions (rotational culture condition) was grasped, the shape of the plate with a disk-like form was maintained. In contrast, the cartilage plates cultured under static conditions changed easily when grasped; often they could not keep their shape for 3 weeks if we changed the medium. Therefore, it was obvious that mechanical conditions played an important role in the mechanical properties of a scaffold-free cartilage tissue(Figure 1). When a square mold was used, a square-shaped cartilage plate was formed under shear flow conditions. The formation of a comparatively large cartilage tissue was also possible. Furthermore, it was possible to form and cut it into spade shapes, i.e., arbitrary shapes, by stamping out with a metal mold

The thickness, diameter, and volume of cartilage tissue formed by a glass mold with a diameter of 1 cm at the start point of culture were measured. The diameter increased for 1 week, then remained the same. The thickness of the cartilage tissue increased rapidly for 1 week, and then continued to increase for the 3-week rotation culture. Similarly, the volume increased rapidly for 1 week, and then continued to increase for the 3-weeks culture. Similar results were obtained in control static culture.

To investigate the existence of proteoglycans, the cartilage tissue with a diameter of 1 cm was stained with safranin-O and toluidine blue. The cartilage tissue cultured under dynamic conditions (rotational culture) for 3 weeks showed strong staining properties compared with that of the static culture. In rotational culture, cells aligned horizontally to the surface were observed. In contrast, cartilage tissue cultured under static conditions did not have such alignment; instead, cells near the surface had a round shape without any orientation. The edge of the cartilage tissue cultured under static conditions was not smooth while that of rotational culture was extremely smooth. In cartilage tissue by rotational culture, there were parts, near the surface, not stained with safranin-O. The results by toluidine blue were similar to the results of safranin-O. The cartilage tissue formed by rotational culture presented metachromasia, and the color was stronger than those of the static cultures. The tendencies of the cell shape and tissue formation were also similar to those of safranin-O.

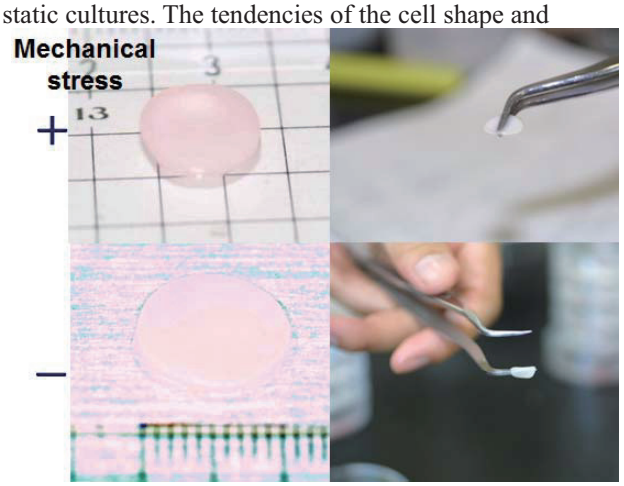

Fig. 1 Scaffold-free cartilage tissues prepared under shear flow conditions.

Immunohistochemical analysis showed that type II collagen protein was abundantly distributed in scaffold-free cartilage tissue cultured by rotational culture. On the other hand, cartilage tissue formed by static culture showed inhomogeneous distribution of type II collagen protein. The cartilage tissue formed by 3 weeks' rotational culture had scarcely any type I collagen protein. In static culture, type I collage protein appeared at the edge of the cartilage tissue as shown in brown color.

The amounts of proteoglycan and total collagen protein secreted were quantitatively investigated. Rotational culture significantly increased the protein production. The rotational culture was-effective in terms of matrix production per DNA contents in the cartilage tissue with a diameter of 1 cm when compared to static culture. There were statistical differences between dynamic and static cultures (PG/DNA; $p<0.05$, CN/DNA; $p<0.01$). The expression levels of mRNA of type II collagen and proteoglycan in cartilage tissue cultured under shear flow conditions were higher than that of static culture. On the other hand, type I collagen mRNA was expressed at a lower level in the cartilage tissue under rotational culture than in static-culture.

To obtain quantitative data of the mechanical properties of the cartilage tissue, a stress-strain curve was obtained using dumbbell-shaped culturing samples prepared by stamping out with a metal mold. The values of rupture strength and Young's modulus significantly increased in cartilage tissue cultured under shear flow conditions. There were statistically significant differences in the values between dynamic and static cultures ($p<0.001$).

4. Concluding remarks

We could first form a scaffold-free cartilage tissue with arbitrary shapes and a large size with promising biological, mechanical properties.

Tenth International Conference on Flow Dynamics
November 25-27, 2013, Sendai, Miyagi, Japan

Optimized Stent

Makoto Ohta*, Hitomi Anzai**, Toshio Nakayama***, Xiaobo Han***, Noriko Tomita*
*Institute of Fluid Science, Tohoku University, 2-1-1 Katahira Aoba-ku Sendai, 980-8577, Japan
**School of Engineering, Tohoku University
***School of Biomedical Engineering, Tohoku University
ohta@biofluid.ifs.tohoku.ac.jp

ABSTRACT

In recent years, they say that intracranial stent called as the flow diverter stent leads to reduce the flow in a cerebral aneurysm and promote thrombosis. However, the recent studies show that thrombosis in the parent artery occurs, because of the material of stent. One of the ways to reduce the materials maintaining the flow reduction may be an optimized design of stent. We introduced the possibility of using Lattice Boltzmann (LB) blood flow simulations in combination with an optimization way in a fully automated way. This method will be also applicable to cell migration by stent strut near future.

1. Introduction

Treatments of cerebral aneurysms using endovascular medical devices have been used widely for last two decades. Coil embolization started on 1994 [1], and intracranial stent was used on 2001. For coil embolization was improved from the viewpoint of fast release (replacement) from the pusher and of fast volume occupancy in the aneurysm using hydrogel or fibers. The volume occupancy will lead the flow reduction into the aneurysm. On the other hand, stent was improved, at first, from the viewpoint of trackability and then of reduction of flow into aneurysm. Therefore, we can say that the endovascular treatment focuses on the flow reduction into aneurysm. The flow reduction in cerebral aneurysms has been examined in several computed fluid dynamics (CFD) studies [2] or experimental study using particle image velocimetry (PIV). PIV system uses a circulation system composed of tubular model made of silicone or PVA-H [3].

Recently, based on suggesting that the porosity, silk and pipeline called as flow diverter stent were released. They have a fine mesh with small diameter struts (around 30 μm) and the mesh covering the neck of aneurysm separates the main flow in parent artery from the flow in aneurysm. However, thrombus in parent artery and rupture of aneurysm after the stent placement were reported. These problems may be caused by increase of the volume of material and the surface area.

To develop a stent design with flow reduction will lead the next generation of stent. Three-dimensional visualization may help to easily specify a inflow zone from the parent artery to the aneurysm and to find the relationship between stent and flow pattern. We introduced and 3-D visualization system to investigate the effect of a stent on flow reduction by visualization of flow structure in 3-D [4]. Each stent was merged on the neck of the aneurysm using 3-D computer aided design (CAD) software. Numerical meshes were generated using a preprocessing software. A steady simulation was performed using a commercial software package. The 3-D visualization of streamlines through the aneurismal neck was performed using Realization workspace (RWS) in Institute of Fluid Science, Tohoku University. As the result of visualization in case of no-stenting aneurysm, a bundle of inflow into the aneurysm (BOI) is observed. After the stenting, the flow pattern changes around the stent and inside of the aneurysm.

In order to find a stent design that reduces the flow in aneurysm effectively, Srinivas et al. applied an optimization procedure to determine the best stent structure across the neck of a 2D aneurysm, by sampling numerical simulations with different designs. This study shows that a better flow reduction is achieved when stent struts are concentrated at the edge of aneurysm neck rather than uniformly along the orifice. Nakayama et al. investigated the size of strut with 80% porosity using a multi-objective genetic algorithm and kriging. Finite volume method (FVM) was used and mesh generation turned out to be a delicate issue.

However, the pre-postprocessing takes long time and the motivation will be reduced. Then we developed an automated simulation for optimal design based on Lattice Boltzmann method [5] and 2D simulation was performed. Then, results show the concept of BOI and the effectiveness of stent struts. In this report, the program was progressed and extended to 3D, to show the relation of the concept of BOI and the optimal design will be described. And in the discussion, an application of the optimization, especially for cell

Fig. 1 First strut placement at the aneurysm in the program

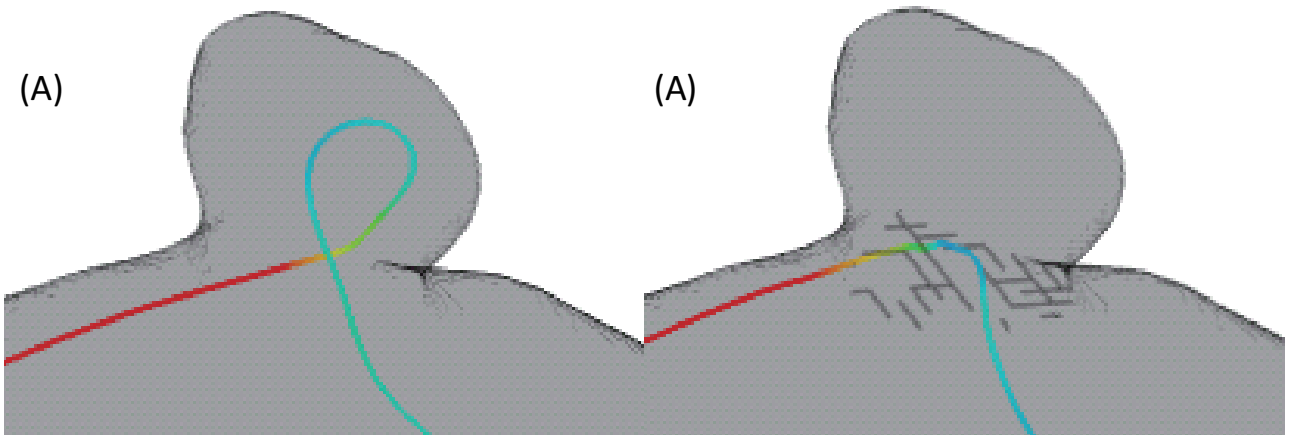

Fig. 2 The effect of optimized stent on flow pattern. (A): Before stent (B): Optimized stent

migration will be discussed.

2. Method

The Lattice Boltzmann (LB) method is an acknowledged alternative to standard computational fluid dynamics (CFD) techniques to solve the Navier–Stokes equations and other partial differential equations. It is described in several textbooks or review papers.

The LB method for hydrodynamics is a mesoscopic approach in which a fluid is described in terms of density distributions of idealized fluid particles moving and colliding on a regular lattice. These fluid particles can only take a finite number of possible velocities such that, in one time step of the dynamics, particles move from one lattice site to another.

Advantages of the LB method over more traditional numerical schemes are its simplicity, its flexibility to describe complex flows and its local nature (no need to solve a Poisson equation). LB solvers can be parallelized very naturally and scale well up to thousands of processors.

Here we perform 3D flow simulations using the standard D2Q9 lattice and the so-called single-time, BGK relaxation method

3. Results and Discussion

3D optimization program is completed. After the finishing program, we analyzed the design of stent after optimization. Then, we reached that our assumption for stent design, “The strut will be placed on the BOI (Bundle of Inflow).” Fig. 1 shows the schematic strut placement. After optimization, the struts are placed such as Fig. 2.

Our primitive results show the Ni-Ti wire under shear stress changes the flow and the WSS. Then the density of cells follows the WSS distribution. Then, the optimization can be applied to cell migration for avoiding damage of cell layer by stent placement.

4. Concluding remarks

Stent struts in BOI have one of role to change the flow direction. 3D Simulation based on LBM with SA show a position of struts in BOI. This finding will be helpful for Stent strut design and the position. An application of the optimization for cell migration is discussed.

Acknowledgements

This project is partially supported by, Collaborative Research Project (IFS, JSPS) and a Global COE Program Grant of the World Center of Education and Research for Trans-disciplinary Flow Dynamics from Tohoku University, and JSPS KAKENHI Grant Number 25282140.

References

[1] Graves V.B., Strother C.M., Rappe A.H., Treatment of experimental canine carotid aneurysms with platinum coils., Am J. Neuroradiol, **14** (1993), 787-793

[2] AENIS M., STANCAMPIANO A.P., WAKHLOO A.K., LIEBER B.B., Modeling of flow in a straight stented and nonstented side wall aneurysm model. J Biomech Eng., **119** (1997), 206-212

[3] M. Ohta, A. Handa, H. Iwata, D. A. Rüfenacht, S. Tsutsumi, Poly-vinyl alcohol hydrogel vascular models for in vitro aneurysm simulations: the key to low friction surfaces, Technology and Health Care, **12** (2004), 225-233

[4] H Anzai, T Nakayama, Y Takeshima, M Ohta, THE EFFECT OF 3D VISUALIZATION ON OPTIMAL DESIGN FOR STRUT POSITION OF INTRACRANIAL STENT, Proc. ASME 2010 FEDSM2010-ICNMM2010, (2010), FEDSM-ICNMM2010-30591

[5] H Anzai, M Ohta, JL Falcone, B Chopard, Optimization of flow diverters for cerebral aneurysms, Journal of Computational Science, **3**, (2012), 1-7

Tenth International Conference on Flow Dynamics
November 25-27, 2013, Sendai, Miyagi, Japan

Computational Fluid Dynamics Modeling of Micro-Vibrating Flow Pumps

Osman Omran Osman and Satoyuki Kawano
Department of Mechanical Science and Bioengineering,
Graduate School of Engineering Science, Osaka University
1-3 Machikaneyama, Toyonaka, Osaka 560-8531, Japan
E-mail: kawano@me.es.osaka-u.ac.jp

ABSTRACT

The aim of this paper is to present the computational model of micro-vibrating flow pump using the immersed boundary method. A novel micropump named micro-vibrating flow pump is developed using microelectromechanical systems technology, where, a cantilever beam is asymmetrically vibrating in a rectangular microchannel filled with liquid inducing a net flow in one direction. A computational model based on the immersed boundary method is used to solve the two dimensional Navier-Stokes equations. Results show the reliability and applicability of the developed model to simulate the micro-vibrating flow pump.

1. Introduction

Fluid-structure interaction is one of the main problems in the fluid mechanics field that gathered a lot of attention in the last few decades [1]. Simulation of fluid-structure interactions problem can be done through two approaches: the fixed mesh method and the moving mesh method. Moving mesh method is facing difficulties when it is applied to structures that induce a large deformation, which requires mesh deformation, causing numerical instabilities. In addition, it is computationally expensive due to the need of large memory and long time to perform the simulation. On the other hand, the fixed mesh methods are more stable and computationally less expensive. One of the approaches based on the fixed mesh method is the immersed boundary method (IBM), which is firstly introduced by C.S. Peskin [2]. In this method, the immersed body is represented by adding a forcing term to the right hand side of Navier-Stokes (N-S) equations. The immersed body exerts a singular force on the surrounding fluid and, at the same time, it reacts and moves at the local fluid velocity. Immersed boundary method can be divided into two categories based on the way the forcing term is represented. The first is called the continuous forcing approach [3], in which the forcing term is added to the N-S equations before discretization. In the contrary, the second approach which is called direct forcing approach [4], the forcing term is added after the N-S equations are discretized.

A novel micropump so called micro-vibrating flow pump (micro-VFP) is developed [5] using microelectromechanical systems (MEMS) technology. Pumping effect is induced by asymmetrically vibrating a cantilever beam in the vicinity of a slit orifice in the rectangular microchannel filled with liquid. Difficulties in the fabrication process and limitation of the experimental device used to actuate the cantilever beam are recognized. They are the main motivation to develop a computational model to simulate the micro-VFP, in order to study the pumping performance at different operation conditions. In addition, the computational model is helpful to obtain the optimum design parameters of the micro-VFP without the need to fabricate a lot of prototypes. Simulation of the cantilever beam motion is performed as large-angle/large-displacement rigid body motion.

The outline of this paper is as follows. The governing equation and the numerical methodology used in the implementation of IBM are discussed in section 2. In section 3 results of the testing cases used to validate the developed code are discussed, in addition, results of micro-VFP simulation will be presented and discussed. Finally, in section 4 concluding remarks are given.

2. Numerical Methods

The numerical scheme used for the solution of the two-dimensional, incompressible, time-dependent N-S equations is based on the fractional step method of Choi and Moin [6], which are discretized in Cartesian coordinates with a staggered grid arrangement of primitive variables [7]. The velocity field is corrected by the pressure Poisson equation (PPE) to satisfy the continuity equation. The convective and diffusion terms are temporally discredited using the explicit Adams Bashforth (AB) method. A second order central difference discretization scheme is used for all of the spatial derivatives.

The discretized form of this scheme is organized in the following sequence of equations:

$$\frac{\mathbf{u}^{*}-\mathbf{u}^{n}}{\Delta t}=-\frac{1}{2}\left(3\nabla\cdot(\mathbf{uu})^{n}-\nabla\cdot(\mathbf{uu})^{n-1}\right) + \frac{1}{2\,\mathrm{Re}}\left(3\Delta(\mathbf{u})^{n}-\Delta(\mathbf{u})^{n-1}\right)-\nabla P^{n}+\mathbf{f}^{n+1} \tag{1}$$

$$\frac{\mathbf{u}^{**}-\mathbf{u}^{*}}{\Delta t}=\nabla P^{n} \tag{2}$$

$$\nabla^{2}\Phi=\frac{1}{\Delta t}(\nabla\cdot\mathbf{u}^{**}) \tag{3}$$

$$\mathbf{u}^{n+1}=\mathbf{u}^{**}-\Delta t\nabla(\Phi) \tag{4}$$

$$P^{n+1}=\Phi \tag{5}$$

Biconjugant gradient stabilized (BI-CGSTAB) iteration method preconditioned with modified incomplete lower-upper decomposition (MILU) is used to solve the PPE in Eq. (3).

Implementation of the IBM is done according to the

method of E. Balaras [8]. In this method, a searching algorithm, based on the method of Udaykumar et al. [9], is used to identify the grid points where the forcing function will be evaluated. A well-defined line normal to the surface of the immersed body boundary is established where a virtual point located on the end of the normal line is used for interpolation. The velocity in the virtual point V_{virtual} is evaluated through bilinear interpolation using grid points (×) surrounding it. Interpolation is performed between the virtual point and point on the immersed body boundary V_{b} to calculate the velocity at the grid point V_{ib} where the forcing function will be calculated as shown in Fig. 1.

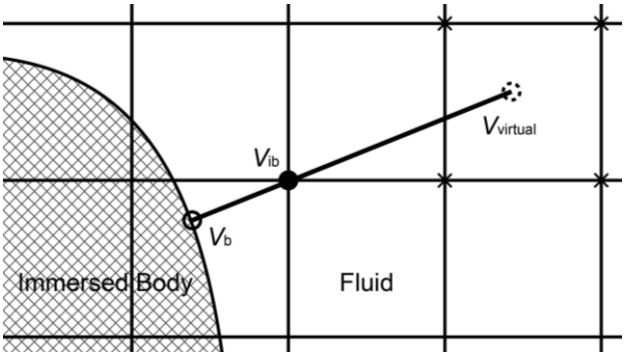

Fig. 1 Schematic drawing of the interpolation procedure for grid point (●) where the forcing function **f** is evaluated

After the velocity V_{ib} is calculated, the forcing function in Eq. (1) is evaluated according to the following equation:

$$\mathbf{f}^{n+1} = \frac{\mathbf{V}_{ib}^{n+1} - \mathbf{u}^{n}}{\Delta t} + \frac{1}{2}\left(3\nabla\cdot(\mathbf{uu})^{n} - \nabla\cdot(\mathbf{uu})^{n-1}\right) - \frac{1}{2\,\mathrm{Re}}\left(3\Delta(\mathbf{u})^{n} - \Delta(\mathbf{u})^{n-1}\right) - \nabla P^{n} \tag{6}$$

3. Results and Discussion

Simulation of a uniform flow past a circular cylinder at Reynolds number (Re) =40 and 185 is performed. Simulation results are compared with the previous established experimental and numerical results. This simulation is used as a validation case for the IBM code we developed. The simulation is performed in a rectangular domain of $l \times h = 45D \times 30D$, where D is the cylinder diameter, which is large enough to minimize the effect of the boundaries. Grid width of $0.05D$ and a Courant Friedrich Lewy (CFL) number of 0.2 are used in the simulation. The drag coefficient C_{d}, lift coefficient C_{l}, length of attached wake L_{w}, separation angel θ_{s}, and Strouhal number are calculated and compared with references data, showing a very good agreement, which proves the reliability and capability of the developed code to be used in micro-VFP simulation.

Immersed boundary method is used to perform a two-dimensional simulation of the micro-VFP. The cantilever beam is simulated as large-angle/large-displacement rigid body motion. Simulation is performed under various operating frequency with zero hydrostatic head H on the outlet. Thus, we can obtain the maximum value of flow rate Q induced by the micro-VFP. Another simulation is performed at various after loads to obtain the H-Q curve. It is found that, by increasing the actuation frequency the volume flow rate generated by the micro-VFP increases; in addition, there is a reasonable agreement between the simulation results and experimental results previously obtained [5]. Results showed that the backward stroke is playing the main role in inducing net flow in comparison with the forward stroke. Although in microfluidic devices the Re is very low, we found that the local Re around the vibrating cantilever is quite high, revealing that fluid inertia has a role in the pumping process.

4. Concluding remarks

The aim of this study is to apply the immersed boundary method for the simulation of two-dimensional viscous incompressible flows interacting with a vibrating cantilever beam. Computations are done on a staggered grid arrangement, using the fractional step scheme, where second-order accurate Adams-Bashforth scheme is used for the temporal discretization, while second-order central difference scheme are used for the spatial discretization. To validate the developed code, simulation of flow past stationary cylinder at Re number of 40 and 185 was performed. Statistical parameters such as drag coefficient, length of attached wake, separation angel, lift coefficient and Strouhal number, obtained from numerical simulation agree well with the previous experimental and numerical results. This benchmark simulation proves the applicability and reliability of the developed code to be used in the simulation of the micro-VFP.

The developed code is used to simulate the micro-VFP. Volume flow rate at various driving frequencies is obtained. In addition, the pumping performance is evaluated by obtaining the H-Q curve at various actuation frequencies. A reasonable agreement between the simulation results and experimental one is found.

References

[1] HJ-P Morand, R Ohayon, CA James, Fluid structure interaction: applied numerical methods. Wiley New York, (1995).
[2] CS Peskin, Annu. Rev. Fluid Mech., **14** (1982), 235.
[3] CS Peskin, Journal of Computational Physics, **25** (1977), 220.
[4] EA Fadlun, R Verzicco, P Orlandi, J Mohd-Yusof, Journal of Computational Physics, **161** (2000), 35.
[5] O Osman, H Shintaku, S Kawano, Microfluidics and Nanofluidics, **13** (2012), 703.
[6] H Choi, P Moin, Journal of Computational Physics, **113** (1994), 1.
[7] FH Harlow, JE Welch, Physics of Fluids, **8** (1965), 2182.
[8] E Balaras, Computers & Fluids, **33** (2004), 375.
[9] HS Udaykumar, R Mittal, W Shyy, Journal of Computational Physics, **153** (1999), 535.

Tenth International Conference on Flow Dynamics
November 25-27, 2013, Sendai, Miyagi, Japan

Sterilization of Bacterial Spores by Atmospheric Pressure Plasma

Kazuhiro Nakamuraya[1], Daisuke Yoshino[2], Tomoki Nakajima[2] and Takehiko Sato[2]
[1] Graduate School of Engineering, Tohoku University, 6-6 Aramakijiaoba, Aoba-ku, Sendai, Miyagi, 980-8579, Japan
[2] Institute of Fluid Science, Tohoku University, 2-1-1 Katahira, Aoba-ku, Sendai, Miyagi, 980-8577, Japan
E-mail: nakamuraya@plasma.ifs.tohoku.ac.jp

ABSTRACT

Medical instruments have been generally sterilized by high pressure steam, ethylene oxide gas (EOG), gamma radiation or electron beam. However, these conventional methods have various drawbacks. Therefore we focus on sterilization using atmospheric pressure plasma. Plasma sterilization can solve problems of conventional sterilization methods. In this study, we developed an effective device for sterilization and discussed a main factor of sterilization by using plasma sterilization device.

1. Introduction

Proper sterilization of used medical instruments is important in clinical site. Medical instruments are generally sterilized by high pressure steam, ethylene oxide gas (EOG), gamma radiation or electron beam. However, high pressure steam needs higher than 121°C and 2 atm, and the EOG has a toxic consequence and takes long time for an operation. The methods using gamma radiation and electron beam have high cost [1] and cause degradation of materials. Therefore, development of a sterilization method with safety, low temperature, short time, and lower cost has been expected. Plasma sterilization method has been considered to be possible to achieve those demands. It has been reported that atmospheric air is one of the good operating gases for the plasma sterilization [2].

In this study, we developed an effective sterilization device and discussed a main factor of sterilization by using low temperature atmospheric pressure plasma sterilization device.

2. Experimental setup

Figure 1 shows a schematic of the developed plasma sterilization device. This device consists of power supply part, discharge chamber, reaction chamber, circulating pump (Nidec, 13H162E030), bubbling chamber and two valves. Plasma was generated between stainless steel needle electrodes in the discharge chamber. In this study, the rectangular-wave voltage of 16 kV_{pp} with a frequency of 3 kHz and duty ratio of 50 % was applied to the electrode. Chemical species generated by the plasma were transported into the reaction chamber and an objective to be sterilized was exposed to these species by using the pump. After the discharge, the generated nitrogen oxide gases were removed by bubbling.

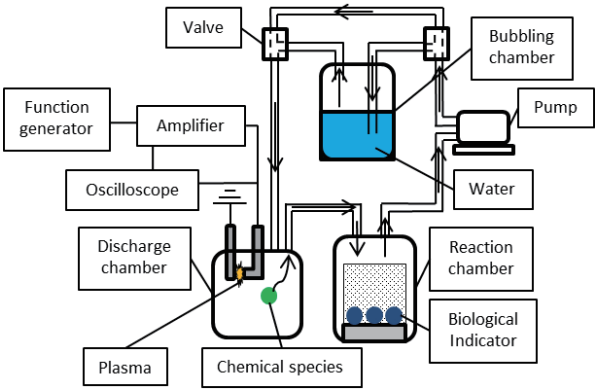

Fig. 1 Schematic of developed plasma sterilization device using circulating flow

To verify the completion of sterilization, we used two kinds of indicator bacterium. One is the Biological Indicator (BI) (3M Healthcare, Attest 1291) using *Geobacillus stearothermophilus* spores (ATCC 7953) for the high pressure steam sterilization. The other is the BI (3M Healthcare, Attest 1294) using *Bacillus atrophaeus* spores (ATCC 9372) for the EOG sterilization. We used three BIs for a trial and conducted three trials. After the end of discharge, we used Auto Reader (3M Healthcare, auto reader 290) to confirm 5 log reductions of the spores. When all BI were sterilized, we determined that the sterilization was complete.

Concentrations of chemical species, i.e. nitrogen oxide (NO_x) and O_3, generated by plasma discharge were measured by using gas detector tubes (GASTEC,

Table 1. Sterilization results of *G. stearothemophilus*

discharge time(min)	results of sterilization		
10	+ + +	+ + +	+ + +
15	- + +	+ + +	+ + +
20	- + -	- - -	- + -
25	- - -	- - -	- - -

Table 2. Sterilization results of *B. atrophaeus*

discharge time(min)	results of sterilization		
5	+ + +		
10	+ + +		
15	+ + +		
20	+ + +		
25	+ + -	- - +	- - -
30	+ - -	- - -	- - -
35	- - -	- - -	- - -

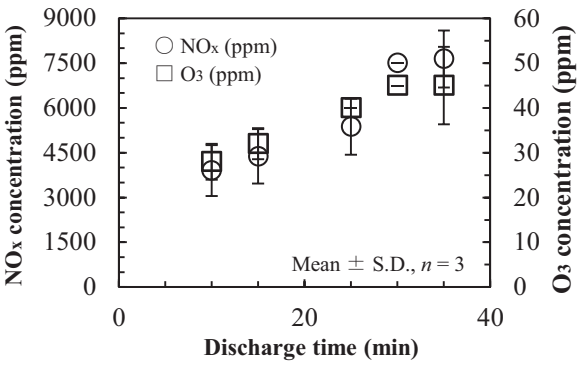

Fig. 2 Changes in concentration of NO_x and O_3 in reaction chamber with increasing discharge time

11HA or 18M) before and after bubbling.

3. Results and Discussion

3. 1 Verification of sterilization

Table 1 and Table 2 show the results of sterilization for *G. stearothemophilus* and *B. atrophaeus*. The spores of *G. stearothemophilus* and *B. atrophaeus* were sterilized in 25 min and 35 min, respectively. There is little change in temperature in the reaction chamber after discharge. These results suggest that the developed device has the potential for sterilization with short time and low temperature.

3. 2 Main factor in sterilization

The concentrations of NO_x and O_3 in the reaction chamber after discharge are presented in Figure 2. NO_x of 7640 ppm and O_3 of 45 ppm were measured for the 35-minutues discharge. It has been reported that UV, etching by reactive chemical species like oxygen atom generated by the discharge and the chemical reaction by NO_2 or H_2O_2 have important roles for plasma sterilization method [3]-[5]. In this study, NO_x and O_3 were mainly generated by discharge under the atmospheric air. In the case of only focusing on O_3, O_3 concentration more than 200 ppm and the exposure time of longer than 100 min were required to sterilize *G. Stearothermophilus* [6]. Therefore, NO_2 is considered to be the main factor of sterilization in this study. After exposing to NO_2 of 8000 ppm for 25 min, *G. Stearothermophilus* could be sterilized. To investigate the effect of NO_2 exposure on bacterial structure, we observed the morphology of spores before and after NO_2 exposure with scanning electron microscope (SEM; KEYENCE, VE-9800). Figure 3 shows SEM images of *G. Stearothermophilus* spores before and after NO_2 exposure. It is confirmed that the spore coat was perforated after treatment. Damage of the spore coat caused by NO_2 exposure may be the main factor in sterilization.

3. 3 Treatment of nitrogen oxide

The concentration of NO_x could reduce down to 41.3 ppm after the bubbling for 40 min. However, it is known that structural and functional changes in trachea or bronchus were caused by exposure of 2 ppm NO_2 for 4

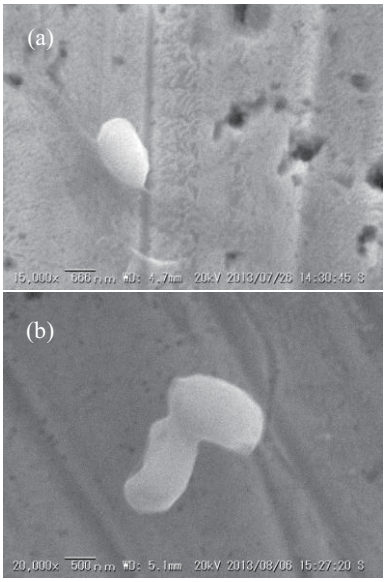

Fig. 3 SEM images of *G. Stearothermophilus* spores before (a) after NO_2 exposure (b)

hours [7]. Furthermore, the pH value of water after bubbling changed to 3.1-3.6. Since the emission standard of pH value is from 5.8 to 8.6, it is also necessary to treat the water after bubbling.

4. Conclusion

In this study, we developed the sterilization device using low temperature atmospheric pressure plasma to improve the performance, and we could realize sterilization in short time and at low temperature. NO_x and O_3 were mainly generated by plasma discharge. As a result of observing the structure of spore coat, it was confirmed that NO_2 is main factor in plasma sterilization method in this study.

Acknowledgements

This study is partly supported by A-STEP, JST, Japan. We thank for Mr. Igarashi, Hirayama Corp. for discussion.

References

[1] M. Nagatsu, J. Plasma Fusion Res., 83 (2007), 601-606.

[2] M. Laroussi, F. Leipold, Int. Journal of Mass Spec., 233 (2004), 81-86.

[3] M. Moisan, J. Barbeau, M. Crevier, J. Pelletier, N. Philip, B. Saoudi, Pure Appl. Chem., 74(2002), 349-358.

[4] T. Namihira, S. Katsuki, R. Hackam, H. Akiyama, K. Okamoto, Proc. of 12th IEEE Int. Pulsed Power Conf., 2(1999), 1313-1316.

[5] R. Burlica, R. G. Grim, K.-Y. Shih, D. Balkwill, B. R. Locke, Plasma Process. Polym., 7 (2010), 640-649.

[6] T. Sato, K. Fujioka, R. Ramasamy, T. Urayama, S. Fujii, IEEE Trans. on Indust. Appli., 42, (2006), 399-404.

[7] Pub. Interest Inc. Foundation JPIC, Poison Information for doctors, [NO_2], Ver. 1.02

Tenth International Conference on Flow Dynamics
November 25-27, 2013, Sendai, Miyagi, Japan

Dynamics and Self-Assembled Pattern Formation of Short DNA Fragments

Kentaro Doi, Ryosuke Nii, Hiroshi Takeuchi and Satoyuki Kawano
Department of Mechanical Science and Bioengineering, Graduate School of Engineering Science, Osaka University
1-3 Machikaneyama, Toyonaka, Osaka 560-8531, Japan
kawano@me.es.osaka-u.ac.jp

ABSTRACT

Self-assembly is one of the most attractive characteristics of deoxyribonucleic acid (DNA). We have also investigated detailed mechanisms of self-assembled pattern formation of 50 base-pairs long poly(dA)·poly(dT) DNA from both experimental and theoretical aspects. Herein, we introduce several methods to elucidate the phenomena associated with short fragments of DNA.

1. Introduction

Deoxyribonucleic acid (DNA) has gathered significant attention due to the capability of its various functions to technological applications. DNA is known to has several characteristics, such as base complementarity, electroconductivity, and self-assembly. According to such striking properties, single-molecule manipulation techniques have also been actively developed [1]. Herein, we especially feature the self-assembly process of DNA. It has already known that DNA tends to form self-assembled peculiar patterns on mica [2], cupper [3], and highly oriented pyrolytic graphite (HOPG) [4–6], which were resulted from atomic force microscopy (AFM) observations. Kawano [2] observed apparent network patterns on mica surfaces and found that segments of the networks gradually grew thicker. Brett et al. [5] and Jiang et al. [6] found out network structures of native calf-thymus double stranded DNA (dsDNA) on HOPG surfaces. On the other hand, details of the nonequilibrium process have not been clarified yet. The behavior of molecules near substrate surfaces is highly complicated due to the presence of various force fields associated with van der Waals interactions, Coulomb interactions, and thermal fluctuations in addition to applied external fields. Such phenomena with respect to biomacromolecules in aqueous solutions cannot be fully described by any simple theoretical model, such as fluid mechanics, molecular dynamics, diffusion, and migration, since their behavior concerns various time and spatial scales.

In our previous studies, we addressed molecular dynamics (MD) simulations of dsDNA aqueous solutions and investigated interactions between such molecules and surrounding environments [7–12]. We could get a better understanding of detailed behavior of the molecules with picosecond time resolution from atomistic point of view. On the other hand, including water molecules, we had to treat about ten thousand atoms and it required very time consuming computations. In particular, Kawano found that self-assembly of DNA took some ten minutes until it got to a stable state [2]. The time scale of this phenomenon quite exceeds the range of atomistic-level MD simulations. In order to treat long-period phenomena, we also developed a coarse-grained bead-spring model of DNA [8]. Applying Langevin dynamics simulations, we succeeded to elucidate electrokinetic transport processes [7] and melting properties [8]. Furthermore, we suggested a heuristic method based on a reaction-diffusion model from a different angle, in which behavior in the mesoscopic model was governed by diffusion coefficients [10]. As a result, the self-assembled pattern formation was replicated in the actual size. It was indicated that the diffusion process seemed to achieve stable conditions within 1 s. In this study, we introduce other methods to investigate intermediate scales of the self-assembly process, comparing the computational results with AFM observations. The difference between simulations and experiments are evaluated from a viewpoint of fractal dimension [2][11].

2. Methods

In experiments, a droplet of DNA solution is placed on a substrate surface of mica and/or HOPG, in which 50 base-pair (bp) poly(dA)·poly(dT) DNA is dissolved in pure water. A 10 μL droplet of a 0.5 μM DNA solution is put on a surface. Both mica and HOPG surfaces are cleaved by using adhesion tape in order to make a naked clean surface, which are known to be a good specimen for AFM observations due to their atomically flat surfaces. In case of HOPG, however, its negatively charged surface should be modified to attract DNA molecules before dropping the DNA solution. Here, we prepare a $MgCl_2$ solution of 40 μM and 100 μM salt concentrations, put the aqueous solution on the surface, and apply an electric potential on it. Using a cathode-side substrate on which Mg^{2+} ions are highly concentrated, the prepared DNA solution is applied.

In theoretical models, we carry out Langevin dynamics simulations to replicate self-assembled patterns, in which 3 bp is replaced by a single bead. The sequentially aligned beads are connected with harmonic springs. A 50 bp-long fragment is represented by 17 beads. In addition, the Morse potential for hydrogen bonds, electrostatic potentials, and Lennard-Jones potentials are taken into account. Simulations are carried out for various number of DNA fragments ranging from 100 to 700 in cylindrical cell whose dimensions are 75 nm radius and 100 nm height. The computations can be performed with time resolution of 10 fs for short range interactions and 100 fs for long range ones. The total computational time reaches a few microseconds. The computational details are also described in Ref. [11].

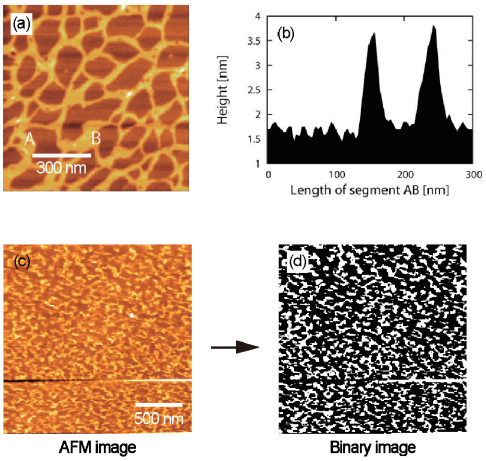

Fig. 1 (a) AFM image of self-assembled pattern of DNA on mica, (b) height profile of line segment AB in (a), (c) AFM image of DNA on HOPG, and (d) binary image of (c).

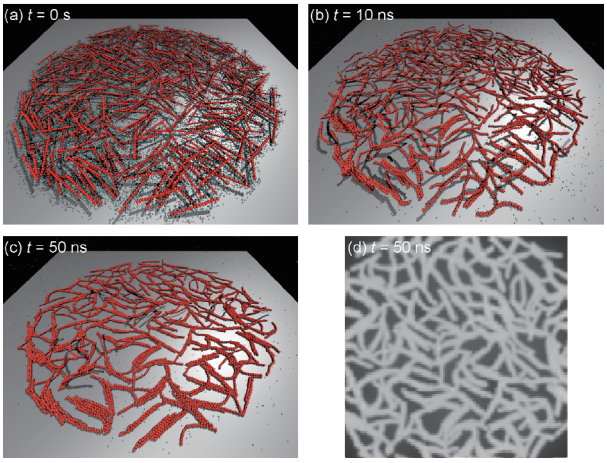

Fig. 2 Snapshots of Langevin dynamics simulation: (a) t = 0 s, (b) t = 10 ns, (c) t = 50 ns, and (d) gray-scaled image of (c).

3. Results and Discussion

Figure 1 shows AFM images of self-assembled patterns of DNA fragments. Figure 1(a) is a network pattern on a mica surface and Fig. 1(b) is the height profile of segment AB in Fig. 1(a), in which sharp peaks corresponding to the diameter of dsDNA can be confirmed. Figure 1(c) is a self-assembled pattern on a modified HOPG surface which was rinsed in 100 μM $MgCl_2$ solution and exposed to a 0.5 μM DNA solution for 20 min. Peculiar structures different from those on mica surface can be observed. In order to analyze the fractal dimension D_f, AFM images are translated to binary images as shown in Fig. 1(d).

Figure 2 presents snapshots of the Langevin dynamics simulation. It is found that short DNA fragments are connected at their ends and make bundles as time progresses. At t = 50 ns as shown in Fig. 2(c), almost all fragments seem to be settled down on the surface. After that, the assembled fragments gradually change to achieve more stable forms. Adsorption due to electrostatic interactions and intermolecular interactions seems to be converged within such a short term. Figure 2(d) presents a gray-scaled picture of Fig. 2(c) in order to clarify its contrast.

To compare the self-assembled patterns obtained from AFM observations and Langevin dynamics simulations, both results are analyzed in terms of D_f:

$$D_f = \lim_{n\to\infty} \frac{\ln N_n}{\ln(1/l_n)}, \quad (1)$$

where N_n is observable elements as the resolution of 1 / l_n [13]. Equation (1) is evaluated by using the box-counting method. The AFM images and simulation results are analysed by using 1 μm × 1 μm and 100 nm × 100 nm areas, respectively. It is found that D_f from both results approaches to 1.9 as the surface density of DNA increases. This means that the patterns resulted from AFM observations and computations are self-similar. In the simulation, we can treat the phenomena governed by molecular interactions and thus, there is a limitation of time scale in a few μs and areas in submicrometers squared. Although these scales are quite different from AFM observations, our results imply that rapid adsorption of DNA fragments to a HOPG surface is related to slow diffusion to form the network structures from a view point of self-similar.

4. Concluding remarks

In this study, we developed a coarse-grained bead-spring model of 50 bp poly(dA)·poly(dT) DNA and carried out Langevin dynamics simulations. The results indicated that DNA fragments were connected with each other via the sticky ends or dissociated ends, aggregated via interactions with Mg^{2+} ions, and at last settled down on a HOPG surface. We could also obtain the self-assembled structures via AFM observations and confirmed that the pattern formation depended on the surface condition of HOPG and immersion time of DNA solution on the surface. Although there was a quite difference in time and spatial scales between the Langevin dynamics simulations and AFM observations, they could be related in terms of fractal dimension.

References

[1] M. Taniguchi and T. Kawai T, Physica E 33 (2006) 1.
[2] S. Kawano, JSME Int. J., Ser. B 48 (2005) 191.
[3] H. Tanaka, T. Nakagawa, and T. Kawai, Surf. Sci. 364 (1996) L575.
[4] S. Tanaka, Y. Maeda, L. Cai, H. Tabata et al., Jpn. J. Appl. Phys. 40 (2001) 4217.
[5] A.M.O. Brett and A.-M. Chiorcea, Electrochem. Commun. 5 (2003) 178.
[6] X. Jiang and X. Lin, Electrochem. Commun. 6 (2004) 873.
[7] S. Nagahiro, S. Kawano, and H. Kotera, Phys. Rev. E. 75 (2007) 011902.
[8] K. Doi, T. Haga, H. Shintaku et al., Philos. Trans. R. Soc. A. 368 (2010) 2615.
[9] S. Uehara, H. Shintaku, and S. Kawano, Trans. ASME., J. Fluids Eng. 133 (2011) 121203.
[10] K. Doi, Y. Toyokita, S. Akamatsu et al., Compt. Method. Biomech. Biomed. Eng. iFirst article (2012) 1.
[11] K. Doi, H. Takeuchi, R. Nii et al., J. Chem. Phys. 139 (2013) 085102.
[12] S. Uehara, M. Tsutsui, K. Doi et al., J. Biomech. Sci. Eng. 8 (2013) 244.
[13] D. Sonrnette Critical Phenomena in Natural Science, 2nd edition, Springer-Verlag, Berlin, (2006) pp.124–125.

OS11: Blood Flow for Medical Equipment

Modeling Thrombosis In Cerebral Aneurysms

Bastien Chopard, Orestis Malaspinas and Jonas Latt
Computer Science Department, University of Geneva, Switzerland
Bastien.Chopard@unige.ch

ABSTRACT

Within the European project THROMBUS (www.thrombus-vph.eu) we study the biological and physical processes that lead to thrombus formation in a cerebral aneurysm. Based on in-vitro experiments, we developed a numerical model that aims at simulating thrombus growth in the aneurysm cavity. Our simulations uses the Lattice Boltzmann method and run on massively parallel computers. Patient specific geometries, with or without flow diverters and physiological flow conditions can be simulated.

1. Introduction

Cerebral aneurysms are bubble-like local deformations of a blood vessel in the brain. Under the action of several physiological factors, some aneurysms may rupture, often causing lethal hemorrhages. Recently, flow diverters have been used in minimally invasive treatments of aneurysms, as an alternative to heavy surgery. Flow diverters are stents made of very thin metal alloys weaved filaments. They are inserted with a guiding catheter into the supporting vessels and deployed right at the aneurysm location in order to reduce the flow in the aneurysm and to induce a clotting process that will fill the cavity, thus healing the patient.

Although it well accepted that hemodynamics plays a central role in the process, little is known about the detailed reasons that make the thrombus grow in the aneurysms cavity. Giant aneurysms are know to sometimes clot spontaneously but never the small ones. Often, stented aneurysms are observed to clot between days or weeks, but other don't. Therefore it is highly desirable that both stent manufacturers and clinicians have a better control of the impact of deploying a flow diverter in a patient.

The THROMBUS European project (www.thrombus-vph.eu) is dedicated to better understand the process of thrombus formation in cerebral aneurysms. It is based on several main components. On the one side, in-vitro experiments are are performed by a team of biologists in order to extract, measure and calibrate the fundamental mechanisms. Second, numerical models are developed to implement, in a computer program, the observed biological scenarios. Third, the predictions of the numerical simulation are compared to the follow up of several patients over several months. These clinical data describe the evolution of the thrombus as a function of time for patients whose aneurysm has been treated with a pipeline flow diverter. Flow properties before and after stenting, as well as blood composition are stored in a data base that are available through the telemedicine framework developed by another partner of the THROMBUS project. Numerical simulations are also compared with in-vitro measurements in flow chambers. The spatial distributions of platelets and red blood cells can be measured in both cases. Another important part of the THROMBUS project is image processing. Two partner teams develop fast algorithms to segment the aneurysm cavity, extract the thrombus, deploy the flow diverter [1], and analyze the movement of the aneurysm wall. All image processing operations can be performed directly from the telemedicine software, as well as to start flow simulations on a parallel computer.

In the rest of this paper we present the numerical approach in more detail and some of our results. Note that the design of optimal flow diverters is also an objective of the THROMBUS project. This will not be discussed here but interesting results can be found in [2,3].

2. Numerical simulations

Within the THROMBUS project, two numerical models are developed. The first one is called the *micro-model* and the second one is the *macro-model*. The first one provides a fully resolved simulation of red blood cells (RCB) and platelets, as deformable suspensions in a fluid flow described by the Lattice Boltzmann (LB) method, using the Palabos software (www.palabos.org). Figure 1 illustrates such a simulation in 2D, in a synthetic side-wall aneurysm. It shows the uneven spatial distribution of the particles [4]. 3D simulations are under development.

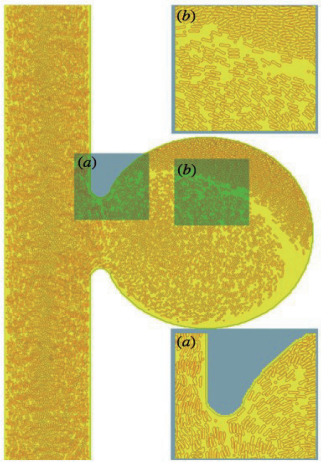

Fig. 1 Fully resolved simulation with RBC ("doughnut" shapes) and platelets (disks) in a 2D synthetic aneurysms (from [4]).

The macro-model developed in THROMBUS is also based on LB simulations with Palabos. It can take

patient specific geometries, physiological flow conditions and can include a fully resolve pipeline stent. Figure 2 shows a snapshot of such a simulation. As the struts of the pipeline flow diverter are of the order of 30 microns and the flow is time dependent, large computing resources are needed. In the present case, to resolve the flow (average Reynolds number of 300), 40 millions of fluid nodes are considered. The simulation of two heart beats took several days on a 120-core parallel machine.

When no flow diverter is deployed in the parent vessel, a coarser spatial an temporal resolution can be used. A thrombosis model can be added on top of the flow dynamics and simulations can be done on a few cores only, within a few hours. The thrombosis model we have implemented is an extension of the models described in [5,6].

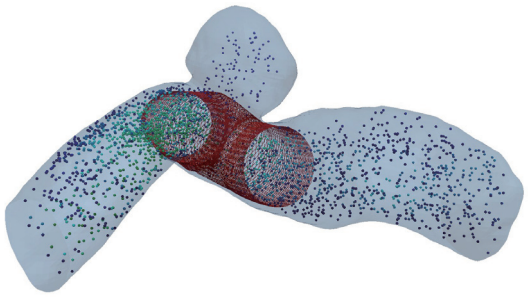

Fig. 2 A patient specific simulation of a stented aneurysms, using the Palabos software. The flow is pulsatile (from left to right) and the particles in suspension are tracers to visualize the flow. Their color is proportional to their velocity.

In short, if the wall shear rate (WSR) at the aneurysm wall is low enough, clotting starts and grows until a higher WSR is reached (which will happen due to the change in geometry resulting from the progressive filling of the aneurysm cavity). The value of the critical WSR has been determined from in-vitro experiment [7]. The material for building the clot is transported by the flow. In the simulation, it is simply represented by advected point particles whose local concentration affects the growth rate. These particles are represented as Lagrangian particles transported in a LB fluid. The so-called “amplification” multiscale technique [8] has been used to accelerate the clotting process which otherwise would take too many heart beats. As already observed in [5,6] for 2D simplified cases, we can have partial or full clotting in the cavity, depending on the simulation parameters. Figure 3 shows the results of the simulation. We can see the progressive growth of the thrombus, from the aneurysm wall to the neck. The validation and calibration of the simulation are currently under investigation.

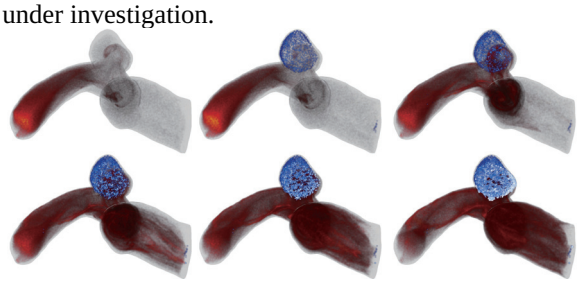

Fig. 3 Snapshots of the simulation of the time evolution (from left to right, top to bottom) of the thrombus (blue dots) in a patient specific geometry, with a physiological flow condition.

4. Concluding remarks

The work of this paper was funded by the European Commission in the Seventh Framework Programme in the area of Virtual Physiological Human (ICT-2009.5.3, project reference 269966).

References

[1] L. Flòrez-Valencia, E. E. Dávila Serrano, J. G. Riveros Reyes, O. Bernard, J. Latt, O. Malaspinas, B. Chopard, G. Courbebaisse and M. Orkisz, MICCAI Conference, 2012

[2] H. Anzai, M. Ohta, J.-L Falcone, B. Chopard. J. of Comp. Sci., vol. 3 pp 1--7, 2012. T. Hayase, M. Ohta,

[3] H.Anzai, B. Chopard and J.-L. Falcone, submitted to Journal of Biomechanical Engineering, 2013

[4] L. Mountrakis, E. Lorenz, E. and A. G- Hoekstra, Interface Focus 3(2), 2013

[5] R. Ouared and B. Chopard, J. Stat. Phys, Vol 121 (1-2), pp. 209--221, 2005.

[6] B. Chopard, R. Ouared, D. A. Ruefenacht and H. Yilmaz. Int. J. Mod. Phys. C, Vol. 18 (4), 712-721, 2007

[7] Karim Zouaoui *et al*. In preparation for Circulation.

[8] A.G. Hoekstra, A. Caiazzo, E.Lorenz, J.-L. Falcone, and B. Chopard. In Modelling Complex Systems by Cellular Automata, chapter 3, Springer Verlag, 2010.

Tenth International Conference on Flow Dynamics
November 25-27, 2013, Sendai, Miyagi, Japan

Stagnant Blood Flow in Intracranial Aneurysms: A Possible Association with Atherosclerosis

Shin-ichiro Sugiyama,[1] Toshio Nakayama,[2] Kenichi Funamoto,[3] Daichi Suzuki,[3] Kuniyasu Niizuma,[1]
Makoto Ohta,[3] and Teiji Tominaga[1]
[1]Department of Neurosurgery, Tohoku University Graduate School of Medicine, 1-1 Seiryo-machi, Aoba-ku, Sendai 980-8574, Japan
[2]Graduate School of Biomedical Engineering, Tohoku University, 2-1 Seiryo-machi, Aoba-ku, Sendai 980-8575
[3]Institute of Fluid Science, Tohoku University, 2-1-1 Katahira, Aoba-ku, Sendai 980-8577, Japan
E-mail of corresponding author: sushi@kohnan-sendai.or.jp

ABSTRACT

This study aimed to investigate hemodynamic characteristics of atherosclerotic legions in intracranial aneurysms. We conducted computational fluid dynamic analyses of 30 aneurysms using patient-derived geometries and inlet flow rates. Among 30 aneurysms, seven atherosclerotic lesions with remarkable yellow lipid deposition were identified in five aneurysms. All seven atherosclerotic lesions were spatially agreed with the area exposed to stagnant blood flow. Statistical analysis revealed that the exposure to stagnant blood flow ($P = 0.024$) are significantly related to atherosclerotic lesion formation on the aneurysmal wall.

1. Introduction

Recently, potentials of computational fluid dynamics (CFD) analysis in predicting natural history of intracranial aneurysms have been reported [1]. However, little work has been done on the atherogenesis in intracranial aneurysms. The purpose of this study was to investigate hemodynamic characteristics of atherosclerotic legions in intracranial aneurysms.

We conducted CFD analysis of 30 unruptured middle cerebral artery (MCA) aneurysms and investigated the relation between the spatial distribution of atherosclerotic lesions on the aneurysm wall and hemodynamic wall parameters including wall shear stress (WSS), oscillatory shear index (OSI), and relative residence time (RRT). WSS is the tangential frictional stress caused by blood flow on the vascular wall. OSI is a dimensionless measure of directional changes in WSS, and used as a marker of oscillatory nature of WSS [2]. RRT demonstrates the residence time of particles near the wall [3], and was used as a marker of stagnant blood flow in this study.

2. Method

This study was granted approval from the ethical committee in Kohnan Hospital. We conducted CFD analysis of 30 MCA aneurysms with atherosclerosis. Data sets of 3D rotational angiography were used to reconstruct accurate geometries of the aneurysms and adjacent arteries. Blood flow was simplified as an incompressible, and laminar Newtonian. Vessel walls were assumed rigid. Therefore, the governing equations of the fluid were the equation of continuity and the Navier-Stokes equation. A commercial software, ANSYS Fluent 12.1 (ANSYS Inc.; Lebanon, NH) based on the finite volume method, was used for numerical simulation. The patient-specific pulsatile flow condition measured by magnetic resonance velocimetry was prescribed at the inlet boundary [4]. Traction free conditions were applied to outlets. The no-slip boundary conditions were applied at the walls. Three pulsatile cycles were simulated to ensure that numeric stability has been reached, and the results from the third cycle were used for analysis.

Wall shear stress refers to the tangential frictional stress caused by the action of blood flow on the vessel wall. For pulsatile flow, the time-averaged wall shear stress was calculated by integrating WSS magnitude over a cardiac cycle for each tetrahedral element:

$$WSS = \frac{1}{T}\int_0^T |\vec{\tau}_w| dt \tag{1}$$

where $\vec{\tau}$ is the instantaneous wall shear stress vector and T is the duration of the cycle.

To describe the temporal disturbance of intra-aneurysm flow, oscillatory shear index (OSI), a dimensionless measure of directional changes in WSS, was calculated using the formula reported by He and Ku [2]:

$$OSI = \frac{1}{2}\left[1 - \frac{\left|\int_0^T \vec{\tau}_w dt\right|}{\int_0^T |\vec{\tau}_w| dt}\right] \tag{2}$$

Note that $0 \leq \mathrm{OSI} < 0.5$, with 0 being completely unidirectional shear and 0.5 being completely oscillatory.

Himburg et al showed that the residence time of particles near the wall is inversely proportional to a combination of WSS and OSI [3].

$$RRT = \frac{1}{(1 - 2 \times OSI) \times WSS} = \frac{1}{\frac{1}{T}\left|\int_0^T \vec{\tau}_i \, dt\right|} \tag{3}$$

Himburg proposed RRT as a robust marker of disturbed blood flow with low and/or oscillatory WSS [3]. However, RRT may serve as a marker of stagnant blood flow, as the prolongation of RRT means the long residence time of particles near the wall.

3. Results and Discussion

Intra-operative video recordings were examined for all 30 cases. Seven atherosclerotic lesions on five aneurysms (5/30, 16.7%) were distinguished by remarkable yellow lipid deposition. All five patients had several vascular atherosclerosis risk factors such as male sex, old age, obesity, smoking history, hypertension, diabetes mellitus, or dyslipidemia.

Among the three hemodynamic variables examined in the current study, only RRT demonstrated qualitative agreement with the spatial distribution of atherosclerosis in all seven lesions as a single metric (Fig.1).

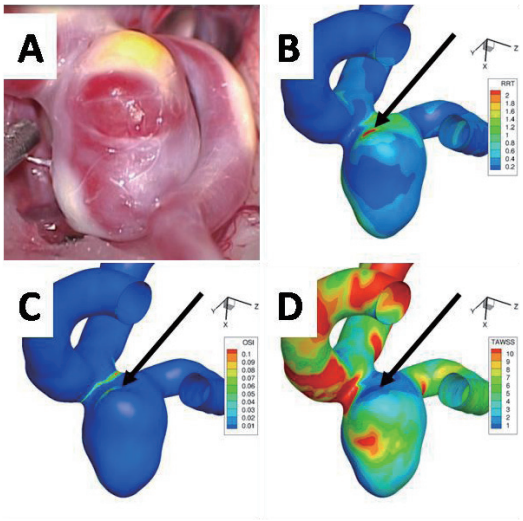

Fig.1 Intraoperative photograph and contour maps of three hemodynamic wall parameters.
A, Intraoperative photograph showing yellowish atherosclerotic legion on the aneurysm wall. **B**, Contour maps of relative residence time (RRT) showing qualitative agreement of the prolonged RRT (arrow) with the spatial distribution of atherosclerosis shown in A. **C, D**, Contour maps of oscillatory shear index (OSI, **C**) and time-averaged wall shear stress (WSS, **D**) from the same viewing angle. The area with prolonged RRT had high OSI value and low WSS magnitude (arrow).

To evaluate the risk factor of atherosclerotic change of the intracranial aneurysms, statistical analyses were performed . Univariate analysis revealed that male (P = 0.031), cigarette smoking (P=0.047) and maximum RRT (P=0.024) are significantly related to atherosclerotic lesion on the intracranial aneurysmal wall. Of those variables that influenced atherosclerotic lesion of the intracranial aneurysmal wall, the variable male (P=0.0046) and maximum RRT (P=0.0037) remained significant in the multivariate regression model ($R2$ =0.52).
Many hemodynamic studies of intracranial aneurysms have reported that low WSS is involved in aneurysm rupture [1, 5], and speculated that low WSS can induce degenerative vascular wall remodeling in intracranial aneurysms that may lead to thinning or rupture of the aneurysm wall. However, the results of our study raise the possibility that an aneurysm wall exposed to low WSS can progress to atherosclerotic remodeling. We consider that low WSS is a risk for aneurysm rupture [5]. However, aneurysms with low WSS accompanied by the stagnation of blood flow indicated by prolonged RRT may be stabilized by atherosclerotic remodeling process. Stagnant blood flow prolongs residence time of atherogenic particles in the blood near aneurysmal wall, thus inducing lipid exchange and recruitment of macrophages, and promoting atherosclerosis [6].

4. Conclusions

The area exposed to stagnant blood flow indicated by prolonged RRT co-localized with atherosclerotic lesions on the aneurysm wall. Male and local stagnant flow were independent risk factors for atherosclerosis in intracranial aneurysms.

Acknowledgement

Part of the work was carried out under the Collaborative Research Project of the Institute of Fluid Science, Tohoku University.

References

[1] Xiang J, Natarajan SK, Tremmel M, Ma D, Mocco J, Hopkins LN, Siddiqui AH, Levy EI, Meng H, Stroke, **42** (2011), p.144-52.
[2] He X, Ku DN, J Biomech Eng, **118** (1996), p.74–82.
[3] Himburg HA, Grzybowski DM, Hazel AL, LaMack JA, Li XM, Friedman MH, Am J Physiol Heart Circ Physiol, **286** (2004), H1916-22.
[4] Sugiyama SI, Meng H, Funamoto K, Inoue T, Fujimura M, Nakayama T, Omodaka S, Shimizu H, Takahashi A, Tominaga T. World Neurosurg, **78** (2012), p.462-68.
[5] Omodaka S, Sugiyama SI, Inoue T, Funamoto K, Fujimura M, Shimizu H, Hayase T, Takahashi A, Tominaga T. Cerebrovasc Dis, **34** (2012), p.121-29.
[6] Sugiyama SI, Niizuma K, Nakayama T, Shimizu H, Endo H, Inoue T, Fujimura M, Ohta M, Takahashi A, Tominaga T. Neurosurgery, *in press*.
(DOI:10.1227/NEU.0000000000000096)

Tenth International Conference on Flow Dynamics
November 25-27, 2013, Sendai, Miyagi, Japan

Investigation of the relationship between hemodynamics and pathology in cerebral aneurysms

Takanobu Yagi, Yuki Iwabuchi, Yasutaka Tobe, Mitsuo Umezu,
TWIns 202 Wakamatsu-cho, Shinjuku-ku, Tokyo, Japan
Yoshifumi Hayashi, Hirota Yoshida, Kazutoshi Nishitani, Yoshifumi Okada, Shigemi Kitahara,
Kitahara International Hospital 1-7-23 Owada-Machi, Hachioji-shi, Tokyo, Japan
takanobu_yagi@aoni.waseda.jp

ABSTRACT

This study examined the hemodynamic index for prediction of thinning area in cerebral aneurysms. 23 cases of cerebral aneurysms were analyzed using computational fluid dynamic analysis and flow pattern was analyzed by diversion of wall shear stress vector. CFD analysis showed that 82% of thinning area contained impinging flow. From the impinging flow point of view, predictability of thinning area was 90% with full-divergence and 67% with partial-divergence. Partial divergence without thinning area was more likely to have adhesion of surrounding tissues than partial divergence with thinning area.

1. Introduction

In recent years, computational fluid dynamic (CFD) analysis technology has made possible to analyze patient specific artery model taken from three dimensional medical images. Relationships of hemodynamic stresses and cerebral aneurysm initiation, growth, and rupture mechanisms have been discussed and studied worldwide. Kitahara International Hospital and Waseda University have been researching on developing the "hemodiagnosis" technology, which quantitatively analyses the blood flow patterns in arteries, by elucidating the cause and effect relationship between hemodynamic stresses and arterial pathologies. The objective of this study is to prove the hypothesis of impingement of blood flow stimulates the wall thinning effect in cerebral aneurysms. Thinning of aneurysm wall, blood blister-like appearance due to transparency of artery wall, are often found characteristics of aneurysm wall. In this study, hemodynamics index for predicting thinning area in cerebral aneurysms were examined to observe the feasibility of CFD analyses for preoperative prediction of thinning area.

2. Method

23 cases of cerebral aneurysms treated under craniotomy from June 2008 to November 2012 that contained thinning area were used for analysis. Each patient's CTA or DSA medical images were used. The resolutions of CTA were in-plane resolution of 0.35-0.48 mm and out-of-plane resolution of 0.63 mm. The resolutions of DSA were in-plane and out-of-plane resolution of 0.2 mm. The three dimensional cerebral artery models were constructed using MIMICS (Materialize). The artery surfaces were extracted using the rendering process. All models were meshed using ICEM (ANSYS) with tetra and prism mesh. The boundary layers were constructed using prism mesh with minimum thickness of 0.015 mm and incrementally increasing as moving away from the artery wall. Artery at inlet and outlet were extended 30 times the equivalent diameter measured at the end surface. CFX (ANSYS) were used for pulsatile simulation with 1 ms time step with second order convection term discretization. Internal carotid artery (ICA) was set as inlet with average flow rate of 330 mL/min. Dynamic coefficient of viscosity ν was set to $\nu=\mu/\rho= 4.57\times10^{-6}$ m^2/s (μ: viscosity coefficient, ρ: density) with Reynolds number of Re=230 at ICA diameter of 5 mm. Flow rates were set to every outlet based on a literature data[1]. This research was accepted by the ethical committee of Waseda University and Kitahara International Hospital.

3. Results and discussion

3.1 Description and categorization of impingement

For defining the presence and level of impingement flow, divergence of wall shear stress (WSS) vector τ was used. Peak divτ values ranged from 1.5 to 2.0, WSS vectors directing in four relative directions, were defined as full-divergence. Divτ values ranged from 0.5 to 1.5, WSS vectors directing in partially relative directions, were defined as partial-divergence (Fig.1). Divτ was defined as shown in equation 1. The WSS τ was defined as a vector projected onto a xy plane of the local coordinate system which was defined by setting the z axis in the normal direction of the surface element.

$$div\tau = \frac{\partial \tau_x}{\partial x} + \frac{\partial \tau_y}{\partial y} \quad (1)$$

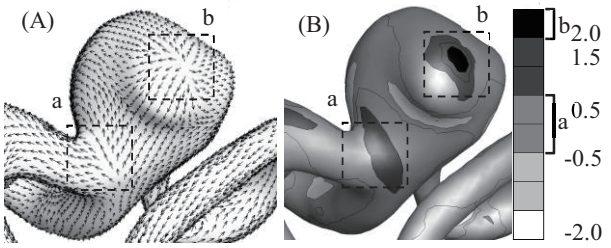

Fig. 1 (A) WSS vector τ (B) div τ mapping of a cerebral aneurysm. Divτ patterns were classified into partial-divergence (a) and full-divergence (b)

3.2Matching rate of impingement at thinning area

The objective of this study is to predict the thinning area of cerebral aneurysm from presence and level of impingement. Fig.2 showed the rate of impingement located at thinning area. From 23 cases, 82% of thinning area matched with impingement of blood flow. This result showed that the thinning of aneurysm wall and impingement is interrelated but further research is required to elucidate the cause and effect relationship of

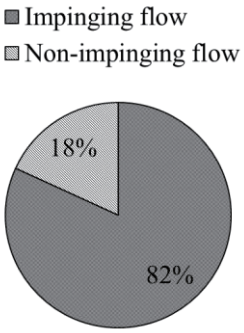

Fig. 2 Characteristics of flow at thinning wall region

wall thinning and impingement of blood. About 20% of thinning area did not match with the impingement. This result implies that the thinning mechanism of cerebral aneurysm involves factors other than mechanical stress from impingement.

3.3 Matching rate of thinning area at impingement

Fig.3 represents the predictability of thinning wall from impinging flow point of view. The impingement was divided into two groups of full-divergence and partial-divergence. The predictability of full-divergence was 90% and partial divergence was 67%. The rate of predictability seems greater on the full-divergence but t-test did not show significant difference between the two types of impingement.

It is known that the endothelial cells sustain the hemostasis of the arteries and they are sensitive to the WSS from blood flow. Tardy et al reported that in in vitro environment, endothelial cells are removed or migrates from the impinging point[2]. Also it may be possible to think that the surrounding environment of cerebral aneurysms affect the regeneration mechanisms of the artery wall. To observe the relationship of wall appearance and surrounding environment, existence of adhesion of surrounding tissues, appearance of the wall, and types of divergence were compared as shown in Table 1. The results showed that thinning area with full-divergence did not have an effect from adhesion of surrounding tissues. For cases with partial divergence, thinning wall was less likely to be seen with cases with adhesion (Fig.4). This result showed that for predicting thinning wall area with partial-divergence flow requires consideration of adhesion of surrounding tissues.

4. Conclusion

This study showed that 82% of thinning area contained impingement flow, 90% of full-divergent flow and 67% of partial-divergent flow matched with thinning area, and areas with partial-divergence with thickened wall contained adhesion of surrounding tissues. This showed the possibility to predict thinning area by the impingement of blood flow. For future study, detection of physical factors of impingement flow which causes wall thinning is required to elucidate the wall thinning mechanisms.

5. Acknowledgement

This research was supported by Health Science Research Grant (H24-IRYOUKIKI-IPAN-006) (23090401) from Ministry of Health, Labor and Welfare, Japan

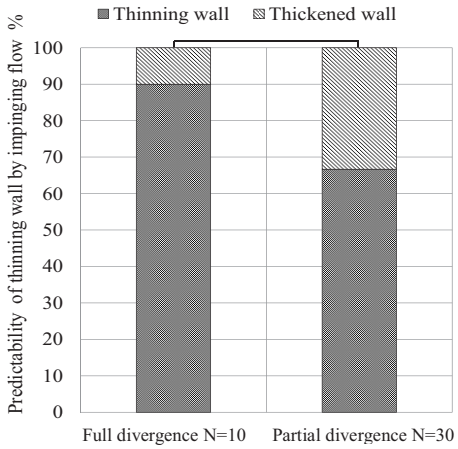

Fig. 3 Predictability of thinning wall by impinging flow

Table 1 Comparison of wall appearance and adhesion

Types of divergence	Wall appearance	adhesion		Total
Full divergence (10)	Thinning wall	With	3	9
		Without	6	
	Thickened wall	With	0	1
		Without	1	
Partial divergence (30)	Thinning wall	With	4	20
		Without	16	
	Thickened wall	With	7	10
		Without	3	

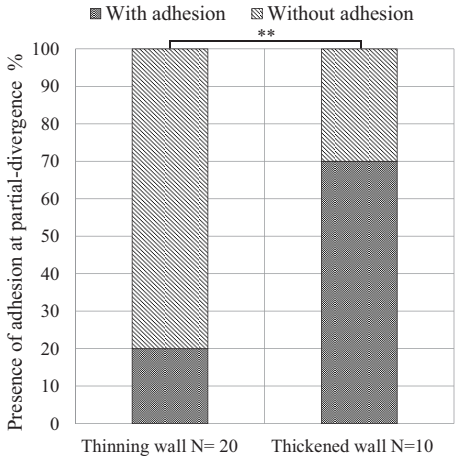

Fig. 4 Presence of adhesion at partial-divergence

References

[1] M.Zhao et al., Regional Cerebral Blood Flow Using Quantitative MR Angiography. AJNR, **28** (2007), pp1470-73

[2] Y. Tardy et al., Shear Stress Gradients Remodel Endothelial Monolayers in Vitro via a Cell Proliferation-Migration-Loss Cycle, Arteriosclerosis Thrombosis Vascular Biology, **17** (1997), pp3102-3106

Tenth International Conference on Flow Dynamics
November 25-27, 2013, Sendai, Miyagi, Japan

Hemodynamic and Clinical Study of Y-stents for Treatment of Cerebral Aneurysms

Kenichi Kono, Tomoaki Terada
Department of Neurosurgery, Wakayama Rosai Hospital
93-1 Kinomoto, Wakayama, 640-8505, Japan
E-mail (K. Kono): vyr01450@gmail.com

ABSTRACT

Y-stent-assisted coil embolization has been performed for wide-necked bifurcation aneurysms. There are two types of stents: open-cell and closed-cell stents. Y-stent with double closed-cell stents causes narrowed structure. In clinical fields, there is controversy whether narrowed structure is beneficial or harmful. To address this issue, we perform computational fluid dynamics (CFD) simulations using a silicone model and Y-stent geometry obtained by micro-computed tomography. In addition, we reviewed four Y-stent cases among 40 consecutive aneurysms treated with stent-assisted coil embolization in our hospital.

1. Introduction

Y-stent-assisted coil embolization has been performed for complex or wide-necked bifurcation aneurysms [1]. There are two types of stents: open-cell and closed-cell stents. In most Y-stent cases, the second stent is deployed through the interstices of the first stent (crossing Y-stent). Use of double closed-cell stents causes narrowing of the second stent through the interstices of the first stent, while using an open-cell stent as the first stent can avoid this effect of narrowing. In our neurosurgical field, there is controversy whether narrowed structure of Y-stents with closed-cell stents is beneficial or harmful. To address this issue, we preformed CFD simulations and reviewed Y-stent cases in our hospital.

2. Method

(a) CFD Simulations

A rigid silicone block model of a bifurcation aneurysm was created based on an asymmetric basilar tip aneurysm in a patient with a maximum diameter of 8 mm (Fig. 1). We deployed closed-cell stents, Enterprise (Cordis Neurovascular, Miami, FL, USA), in the silicone model in the following 7 different configurations: single stent placement from the basilar artery to the right or left posterior communicating artery (PCA), non-overlapping Y-stent, horizontal stent, kissing Y-stent (double stent placement in a parallel fashion), and 2 different crossing Y-stents with a narrowed structure. In one crossing Y-stent, "crossing-Y (R to L)", the first stent was deployed into the right PCA and the second stent was placed into the left PCA through the interstices of the first stent. In another crossing Y-stent, "crossing-Y (L to R)", the order of stent placement was the opposite. Selected configurations of stents are shown in Figure 1.

Stents in the silicone model were scanned by micro-CT. Using an engineering design software, 3-matic (Materialise NV, Leuven, Belgium), we constructed 9 models, including no stent and 8 different configurations of stents (7 stents plus 1 virtual stent): "no-stent", "R-stent", "L-stent", "non-overlapping Y", "virtual-Y", "horizontal", "kissing-Y", "crossing-Y (R to L)", and "crossing-Y (L to R)". We created the "virtual-Y" stent by fusion of 2 single stents, "R-stent" and "L-stent". The "virtual-Y" stent did not have a narrowed structure.

We performed pulsatile CFD simulations in a similar manner as we described previously using ANSYS CFX (ANSYS Inc., Canonsburg, PA, USA) [2]. The fluid domains were meshed to create finite volume tetrahedral elements. The number of elements in each model ranged from approximately 1,800,000 to 2,500,000, which was confirmed to be adequate to calculate the velocity and WSS by creating meshes of finer grid densities.

(b) Clinical Cases

Between July 2010 and October 2012, we treated 40 consecutive aneurysms with stent-assisted coil embolization using Enterprise closed-cell stents in our hospital. There were 36 unruptured aneurysms, four chronic or delayed ruptured aneurysms, and no acute ruptured aneurysms. There were four patients with crossing Y-stent cases that were all treated for basilar tip aneurysms. The rest of the 36 patients were treated with a single stent. Patients were divided into two groups: the single stent group (n=36) and the Y-stent group (n=4).

In the single stent group, patients were pretreated with double antiplatelet agents, 100 mg aspirin and 75 mg clopidogrel, 1 week before the procedure, or were loaded with 300 mg aspirin and 300 mg clopidogrel 4 days before the procedure. In the Y-stent group, patients were pretreated with triple antiplatelet agents, 100 mg aspirin, 75 mg clopidogrel, and 200 mg cilostazol, 1 week before the procedure.

We assessed the following factors for statistical analysis: age, sex, aneurysm location (anterior or posterior circulation), aneurysm shape (saccular or fusiform), aneurysm size, neck size, and maximum and minimum size of parent vessels covered by a stent. Statistical analysis was performed using SPSS version 20 (IBM Corp., Armonk, NY, USA). Fisher's exact test or the Mann–Whitney U test was used. Each hypothesis was tested with a two-tailed analysis. The level of significance was set at $P<0.05$.

3. Results

(a) CFD Simulations

Cycle-averaged velocity and WSS in the aneurysm were reduced because of stent placement in the following order: single stent (19% reduction in

cycle-averaged velocity) < non-overlapping Y-stent (29%) < virtual Y-stent (32%) < horizontal stent (39%) < kissing Y-stent (48%) < crossing Y-stent (54%). Comparing with virtual-Y without narrowed structures, crossing Y-stents with narrowed structures redirected impingement flow into the distal vessels because of lowered porosity of stents (data not shown).

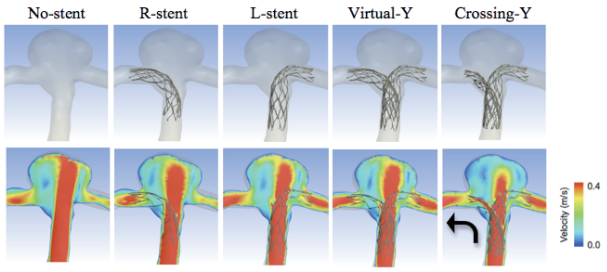

Fig. 1 Contours of flow velocity on coronal sections.

(b) Clinical Cases

There were two cases of symptomatic complications (2/40, 5%) during the peri-procedural and follow-up period: one transient ischemic attacks and one infarction in two patients. Both thromboembolic complications occurred in the Y-stent group, and a Y-stent was the only significant factor for symptomatic or thromboembolic complications (P=0.008; Fisher's exact test) (Table 1). Despite of these complications, the two patients recovered and were discharged without any neurological deficits. All 40 patients were neurologically intact at the mean follow-up periods of 31 months.

Table 1. Thromboembolic complications

	Thromboembolic complications		
	Negative (n=38)	Positive (n=2)	*P*
Age (years)	61±10	62, 70	0.437
Female sex (%)	23 (61)	2 (100)	0.519
Aneurysm location	13/25		0.550
Anterior circulation (%)	13 (34)	0 (0)	
Posterior circulation (%)	25 (66)	2 (100)	
Aneurysm shape			0.533
Saccular (%)	24 (63)	2 (100)	
Fusiform (%)	14 (37)	0 (0)	
Aneurysm size (mm)	10.4±5.3	7.4, 12.3	0.950
Neck size (mm)	8.6±4.5	8.3, 11.9	0.306
Maximum size of parent vessels (mm)	3.7±0.9	2.9, 3.1	0.162
Minimum size of parent vessels (mm)	3.1±0.9	1.4, 2.0	0.181
Stent configurations			**0.008**
Single stent (%)	36 (95)	0 (0)	
Y-stent (%)	2 (5)	2 (100)	

4. Discussion

In the hemodynamic study, while we used vascular-specific conformed stent geometry obtained by micro-CT, in most of the previous studies, stents were virtually conformed to fit into a parent vessel lumen and deployed across an aneurysm neck. Because the geometry and porosity of stents change by the vascular geometry and radius of vessels, virtual deployment is not appropriate for reproducing the real geometry of stents deployed in vessels. Our study shows that changes in porosity of stents are important for hemodynamics due to stent placement. Among the 8 different configurations used in our study, crossing Y-stents showed the strongest reduction in flow because of the narrowed structures, which lowered porosity of stents and redirected flow. The narrowed structures are unique to closed-cell stents. It seems that Y-stents with closed-cell stents may be desirable treatments because it may reduce recanalization rates. However, the CFD simulations provided us only hemodynamic aspects of Y-stents. In clinical cases, we need to consider other aspects such as ease of stent delivery, wall apposition of stents, patient conditions, possible complications, and so on.

In Y-stent cases in our hospital, we experienced significantly higher thromboembolic complication rates even though we used triple antiplatelet agents. This suggests that strong hemodynamic effects of Y-stents with closed-cell stents may increase thromboembolic complications owing to the narrowed structures. Therefore, we cannot simply conclude that Y-stent-assisted coil embolization with closed-cell stents can be the first-line treatment for bifurcation aneurysms from our CFD study. Although, one large-scale study of Y-stent cases (n=183) showed 2.7% peri-procedural complication rates [3], at the moment, we consider that Y-stents with closed-cell stents may be limited to complex or recanalized aneurysms under appropriate use of antiplatelet agents.

5. Concluding remarks

In hemodynamic study by CFD simulations, narrowed structure with closed-cell stents in Y-stents lowered porosity of the stent, which redirected impingement flow into distal vessels. This may be a desirable reconstruction of flow hemodynamics and may decrease recanalization rates. In our clinical Y-stent cases, thromboembolic complications occurred significantly higher than single-stent cases. This may be because of stronger hemodynamic effects. Thromboembolic complication may be reduced with appropriate use of antiplatelet agents. From both CFD and clinical study, we conclude that Y-stent-assisted coil embolization may be an optional treatment for selected cases such as complex or recanalized aneurysms.

References

[1] Fargen KM, Mocco J, Neal D, et al. A Multicenter Study of Stent-assisted Coiling of Cerebral Aneurysms Using a Y-configuration. Neurosurgery. 2013 Jun 14. DOI: 10.1227/NEU.0000000000000015

[2] Kono K, Fujimoto T, Shintani A, Terada T. Hemodynamic characteristics at the rupture site of cerebral aneurysms: a case study. Neurosurgery. 71, E1202-1209, 2012

[3] Yavuz K, Geyik S, Cekirge S, Saatci I. Double Stent-Assisted Coil Embolization Treatment for Bifurcation Aneurysms: Immediate Treatment Results and Long-Term Angiographic Outcome. AJNR Am J Neuroradiol. 2013 May 16.

Tenth International Conference on Flow Dynamics
November 25-27, 2013, Sendai, Miyagi, Japan

Development of a new catheter with innovative concepts for selective venous sampling - preliminary study

Tomo Kinoshita[1)], Kazumasa Seiji[1)], Masashi Otake[2)], Makoto Ohta[2)], Kwon Guiryong[3)]
1) Department of Diagnostic radiology, Tohoku University, School of Medicine
2) Institute of Fluid Science, Tohoku University
3) Terumo clinical supply Co.
E-mail: twilightinupperwest821@gmail.com

ABSTRACT

In selective venous sampling, blood samples are obtained with catheters, but it sometimes happens that blood suction is impossible. The purpose of this study is to search the catheter tip suitable for selective venous sampling. We performed the experiment to evaluate the efficacy of catheter side holes in liquid suction. As a result, two-side-hole catheter was able to suck liquid more rapidly than no-side-hole catheter. This is the first study that proved the efficacy of side holes in liquid suction. Further studies need to be performed to search the catheter side hole suitable for blood suction.

Introduction

Selective venous sampling is essential for diagnosis and localization of some kinds of endocrine tumors as aldosterone producing adenoma, insulinoma, ACTH producing adenoma, and so on.

In selective venous sampling, blood samples are obtained with catheters. For example, adrenal venous sampling is performed as follows. A 6.5 Fr. catheter is inserted from the left femoral vein into the left adrenal vein. Then another 6.5 Fr. catheter is inserted from the right femoral vein into the right adrenal vein. Then microcatheters are inserted into each 3 tributaries of bilateral adrenal vein through 6.5 Fr. catheters by coaxial method and blood samples are obtained by gentle aspiration from both adrenal veins and their tributaries.

In selective venous sampling, it sometimes happens that blood suction is impossible. In such cases, it is suspected that catheter tip hole is occluded by blood vessel wall deformed by suction pressure.

A microcatheter having two side holes on the distal end is commonly used for selective venous sampling. Presumably side holes enhance catheter blood flow and lead to success of blood sampling. However, there is little evidence to support the value of catheter side holes in blood sampling. The purpose of this study is to evaluate the value of catheter side holes in blood sampling by means of comparing the catheter having side holes with the one having no side hole.

Materials and methods

a) Experimental system

The experimental system constructed for this work is shown in Fig.1. We made a suction device which is capable of regulating suction pressure.

Two types of catheters were used for suction; a catheter having two side holes having a semicircular shape on the distal end, and a catheter having no side hole. All catheters were outer 2.2 Fr., 110 cm-long.

Distal end of the catheter was inserted into the blood vessel model and the proximal end was connected to the suction device. Blood vessel model and distal end of the catheter were placed in a laboratory dish filled with the liquid whose viscosity was similar to the blood viscosity. The fluid was a 40 % glycerol aqueous solution with viscosity of 4.0 mPa・s, dynamic viscosity of 3.8 mm^2/s at 20°C. Blood vessel model was made of PVA, 0.6 ml-internal diameter. Blood vessel models were 8 cm in length and each model was cut into two pieces and used.

b) Experimental protocol

Suctions were performed at 10 kPa, 20 kPa, 30 kPa, and 40 kPa for each catheter and the time required for suction of 0.1 ml of fluid at each suction pressure was recorded. In case of not having been sucked 0.1 ml of liquid at 200 sec, suction was terminated and “200 sec“ was recorded as the required time.

Besides, blood vessel model and catheter tip were observed with digital microscope (VHX-2000, KEYENCE, Osaka, Japan) and recorded.

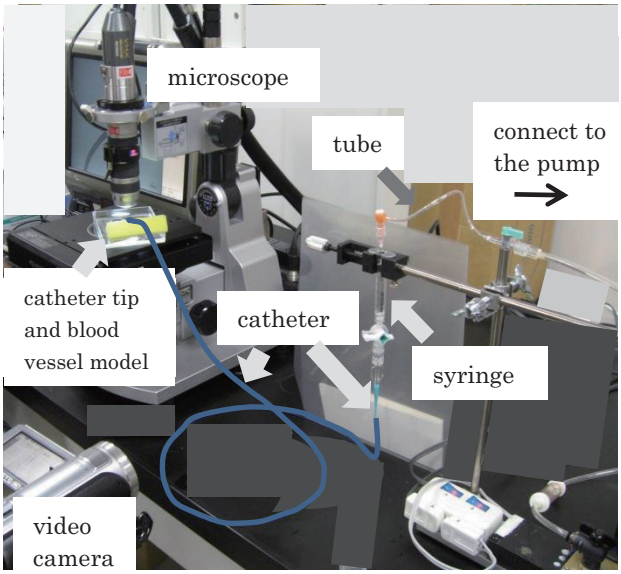

Fig.1 Experimental system

Result

In this experiment, two-side-hole catheter (Table 1) was able to suck liquid more rapidly than no-side-hole catheter (Table 2). Moreover, the time required for

suction became longer as the suction pressure becomes higher in no-side-hole catheter, while two-side-hole catheter could suck fluid at a stable speed even if a suction pressure becomes higher.

Table 1. Time required for suction of 0.1ml of liquid (no-side-hole)

pressure [kPa]	model 1 [sec]	model 2 [sec]	average [sec]	standard deviation
10	14	30	22	8
20	16	23	39	3.5
30	13	200	106.5	93.5
40	200	200	200	0

Table 2. Time required for suction of 0.1ml of liquid (two-side-hole)

pressure [kPa]	model 1 [sec]	model 2 [sec]	average [sec]	standard deviation
10	17	15	16	1
20	9	26	17.5	8.5
30	7	14	10.5	3.5
40	10	18	14	4

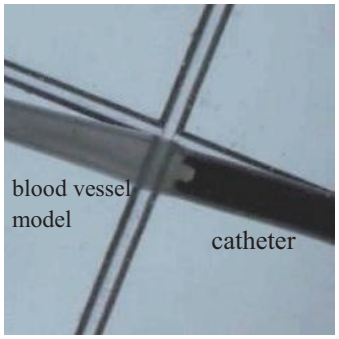

Fig. 4 Suction with two-side-hole catheter
(observed with the stereomicroscope)

Discussion

Little studies concerning about blood sampling catheter have not been conducted. Catheters were originally developed for injection of contrast media or drugs. In blood sampling, we have usually used the catheter developed for injection. This is because there is no catheter which was developed only for suction. The goal of our project is the development of the catheter for selective venous blood sampling. By practical experience, it is presumed that side holes enhance catheter blood flow and lead to success of blood sampling. However, there is little evidence to support the value of catheter side holes in blood sampling. In this study, we compared the catheter having two side holes with the catheter having no side hole at the catheter tip. The purpose of this study was to evaluate the efficacy of side holes of catheters in liquid suction.

As a result, two-side-hole catheter was able to suck liquid more rapidly than no-side-hole catheter. This is the first study that proved the efficacy of catheter side holes in liquid suction. It is assumed that side holes enhance catheter blood flow, and moreover, blood can be sucked through the side hole even if the catheter tip hole is occluded by blood vessel wall.

The standard deviation was relatively large in this study. That is probably derived from small number of experiments and large variation in hardness of blood vessel models.

We are planning further experiments to search the number, shape, size, and location of the side holes suitable for suction of blood. We are also planning to conduct computer simulation of blood flow in catheter suction.

Conclusion

We performed the experiment to evaluate the efficacy of catheter side holes in liquid suction. As a result, two-side-hole catheter was able to suck liquid more rapidly than no-side-hole catheter. It was proved that catheter side holes are effective in blood suction. This is the first study that proved the efficacy of catheter side holes in liquid suction. Further studies are needed for the development of the catheter for selective venous blood sampling.

Acknowledgements

The authors would like to thank KEYENCE CORPORATION for providing the equipment.

Flow Analysis for Coiled Intracranial Aneurysms

Carolina Vallecilla[1], Yu Chen[1], Masanori Kuze[2], Makoto Ohta[3] and Guy Courbebaisse[1]
1: CREATIS; CNRS UMR5220; INSERM U1044; UCBL1; Univ. of Lyon; INSA LYON; 7 Av. J. Capelle, Bat. B. Pascal, 69621 Villeurbanne, France. **2:** Graduate School of Biomedical Engineering, Tohoku Univ., 6-6, Aramaki Aza Aoba, Aoba-ku, Sendai, Japan. **3:** Institute of Fluid Science, Tohoku Univ., 2-1-1, Katahira, Aoba-ku, Sendai, Japan.
E-mail: guy.courbebaisse@insa-lyon.fr

ABSTRACT

A scientific research has been initiated to investigate the behavior of intracranial aneurysms (IA) treated with an endovascular coil. Medical doctors are unable to estimate the ability of a coil in the IA cavity to shape a clot. This is mainly due to the fact that after endovascular treatment, the coil produces medical imaging artifacts. An original way is proposed to quantify blood flow parameters by creating a phantom of the IA and coil. By using medical imaging, image processing, the 3D reconstruction of the coil within the IA is performed, allowing by numerical simulation, a precise hemodynamic study of the considered IA in which a coil is implanted.

1. Introduction

Coiling technique is one of the most common endovascular device used for the treatment of the IA [1][2][3]. Hemodynamic analysis of coiled IA needs means of investigations because neuroradiologists cannot estimate the impact of a coil on the potential clot formation within an IA; this is due to the medical imaging artifacts. The herein work proposes an original way of investigation based on the making of a patient specific transparent model (phantom) mimicking the patient specific IA with the coil. The underlying concept leads to perform experimental measurements and numerical simulation in order to quantify the ability of the treatment for healing the IA.

2. Method

A cerebral aneurysm model was developed using PVA-H (Poly Vinyl Alcohol-Hydrogel) [4][5]. This model or phantom is composed by a transparent and low friction surface to make easy the insertion of medical equipment such as coils. In our work the used coil has been implanted with the standard catheterization techniques [6][7][8]. This phantom is also mounted on a test bench for PIV measurements used for the phase of validation of results.

A technic for the detection of coils once implanted in the model of the patient's aneurysm and its hemodynamic analysis is presented. The methodology consists of coil detection in MRI images (Fig. 1) of the model (IA + coil) by using operators offered by the mathematical morphology [9] and QRS method [10]. By applying the detection on all the MRI images sequence, the 3D reconstruction of the coil is realized (Fig. 2) Then, the flow analysis is performed using CFD [11] based on finite elements method, solving the Navier-Stokes (Newtonian fluid, PISO 2nd order scheme, incompressible Newtonian fluid, density and viscosity of blood are 1060 kg/m3 and 0.0045 Pa-s. An adapted mesh with refinement has been applied to the geometry of the IA and on the reconstructed coil (Fig. 3). The inlet velocity profile is shown on Fig. 4.

By solving the Navier-Stokes equation, the hemodynamics study is performed. Then the Wall Shear Stress (WSS) are calculated without and with the coil; then the modes (Harmonics) of the WSS at selected points are determined by Fourier transform [12].

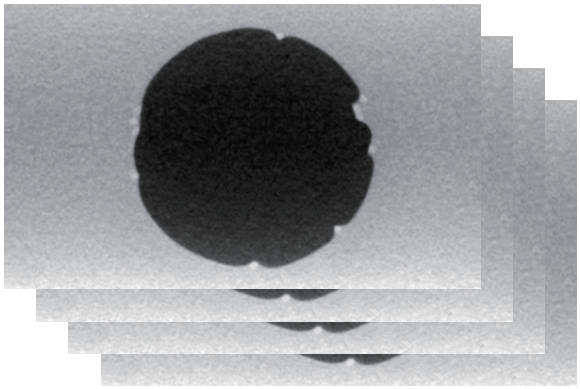

Fig. 1 MRI sequence: IA (black) + coil (white)

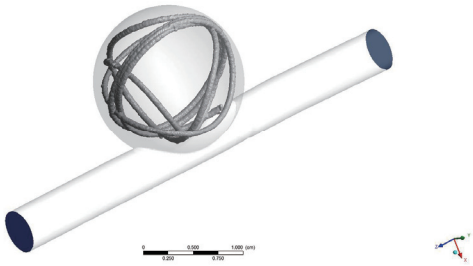

Fig. 2 Aneurysm geometry and 3D reconstructed coil

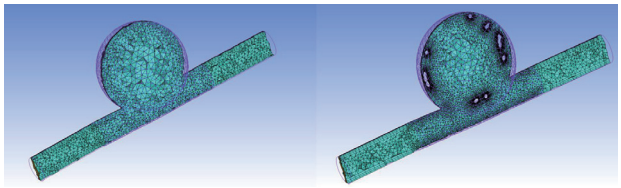

Fig. 3 Mesh of the IA without and with coil

3. Results and Discussion

The numerical simulation provides relevant results; the WSS are quantified on the cavity of the IA without and with coil (Fig. 5), i.e. the WWS are reduced with the coil in points Y1 and Y2 (Fig. 6). Also a complementary way of investigation concerns the calculus of the modes of the WSS [12] in order to estimate if the hemodynamic frequency harmonics play a role in the formation of the clot. As example, in Fig. 7, the odd Fourier modes 1, 3 and 5 are reinforced in Y1 when the coil is present. But

the behavior is totally different in Y2 (Fig.8).

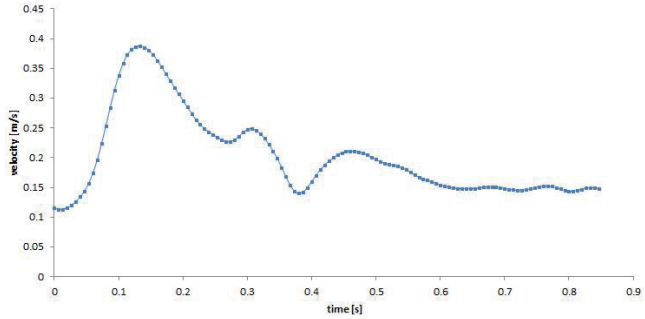

Fig. 4 Inlet Velocity profile (m/s) versus Time (s)

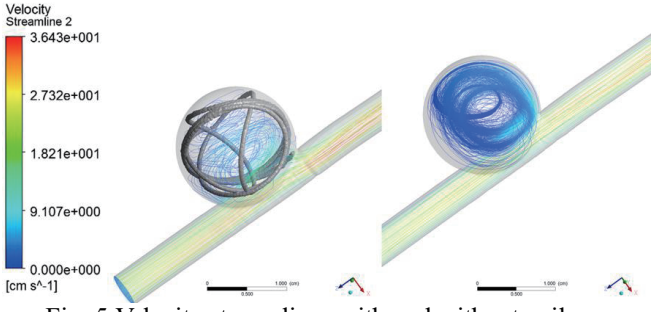

Fig. 5 Velocity streamlines with and without coil

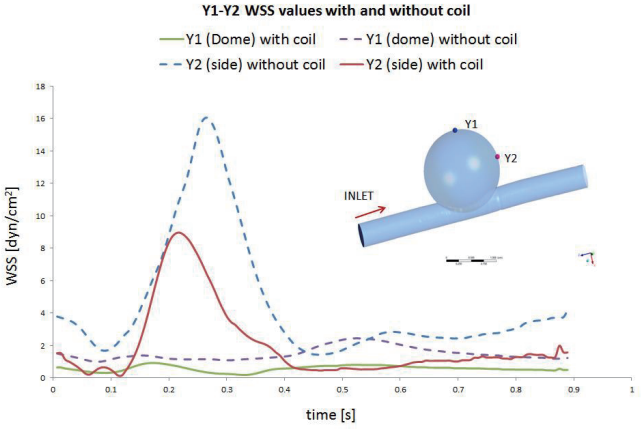

Fig. 6 WSS (Dyn/cm²) versus Time (s.) in Y1 and Y2

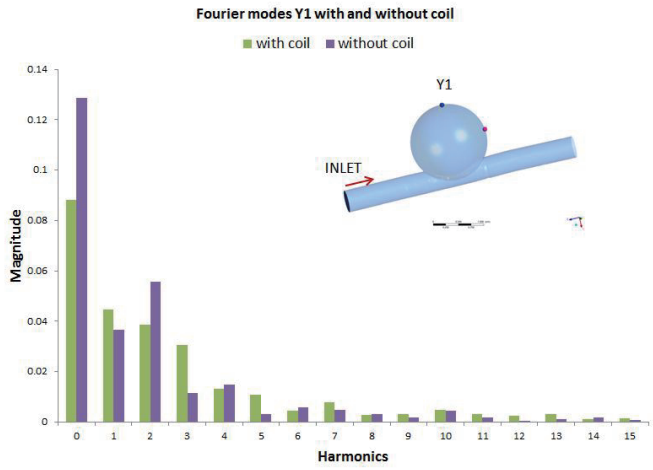

Fig. 7 Fourier modes of the WSS in Y1

This preliminary study within IA by using a reconstructed coil seems to be an approach which will reduce the lack of information when neuroradiologist decides the endovascular treatment of a IA.

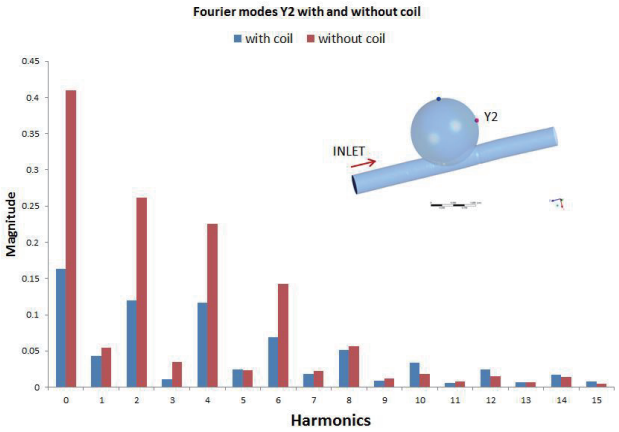

Fig. 8 Fourier modes of the WSS in Y2

4. Concluding remarks

The first results are very promising and the elaborated protocol of experimentation has been validated. Neuroradiologists and endovascular coil manufacturers will be the impacted stakeholders by this research; because a help to medical decision and a way of optimization of the endovascular devices are potentially realizable. Also the results are corroborated by the PIV experiments. This protocol must be now applied to patient specific aneurysms.

Acknowledgement

This study is partially funded by the EC under the 7th FP - THROMBUS project [N° 269966].

References

[1]J. Hop, G. Rinkel, A. Algra, J. van Gijn, Stroke (1997); 28(3): 660-4.

[2]G. Guglielmi, Neurosurgery J., (2009); 111: 1-8.

[3]E.H. Brilstra, G.J. Rinkel, Y. van der Graaf, W.J. van Rooij, A. Algra, Stroke (1999); 30 (2): 470-6.

[4]S. Shida, H. Kosukegawa, M. Ohta, Proc. of the ASME 2011 & Exposition Imece (2011)- 64388.

[5]Y. Shimizu, A. Javadzadegan, T. Hayase, M. Ohta, Technology and Health Care (2013), in press.

[6]M.D. Ford, H.N. Nikolov, JS. Miller, SP. Lownie, EM. Demont, W. Kalata, F. Loth, DW. Holdsworth,DA. Steinman, Journal of Biomechanical Engineering (2008); 130(2):021015.

[7]M. Kuze, M. Ohta, Ninth International Conf. on Flow Dynamics, Sendai, Japan, (2012) 9.19-21, pp.656-657.

[8]R.D.Keane, R.J. Adrian, Applied Scientific Research (1992), 49 (3): 191-215.

[9]G. Matheron, Bulletin of the American Math. Soc. (1975); 81: 844-47.

[10]P.E. Trahanias, IEEE Transactions on Biomedical Engineering (1993), 40: 201-5.

[11]H.S. Byun, K. Rhee, Medical Engineering & Physics (2004), 26 (9), 755-61.

[12]R.E. Feaver, B.D. Gelfand, B.R. Blackman, Nature communication 'ncomms2530', (2013), 4:1525.

Tenth International Conference on Flow Dynamics
November 25-27, 2013, Sendai, Miyagi, Japan

Influence of Ni-Ti Wire under the Shear Stress Environment on Endothelialization

Sho Matsumoto[1], Han Xiaobo[1], Hisatoshi Kobayashi[2], Noriko Tomita[3], Makoto Ohta[3]
[1]Graduate School of Engineering, Tohoku University, 6-6 Aramaki Aza Aoba, Aoba-ku, Sendai, Miyagi, Japan
[2]Biofunctional Materials Group, National Institutes for Materials Science, 1-2-1 Sengen, Tsukuba, Ibaraki, Japan
[3]Institute of Fluid Science, Tohoku University, Tohoku University, 2-1-1 Katahira Aoba-ku, Sendai, Miyagi, Japan
s_matsumoto@biofluid.ifs.tohoku.ac.jp

ABSTRACT

The goal of stent treatment is to cover the layer of endothelial cells (EC) on and around the stent. To investigate the effect of shape and surface treatment of Ni-Ti wire for stent under flow on endothelialization on implanted stent, we measured the density of endothelial cells on and around the wire which was implanted on cultured EC under shear stress (SS) environment. Cross-section shape of the implanted wire effects on the cell density of the area just before the wire and the positions that EC adheres on the wire.

1. Introduction

Atherosclerosis is one of the vascular lesion causing stenosis and ischemic disease. One of the major treatments for stenosis is stent placement for expanding vascular wall at stenosis. However, this treatment has a possibility of causing restenosis through intimal hyperplasia by vessel injury with the implanted stent [1].

Suppression of the restenosis can be performed by EC covering the implanted stent [1]. Thus, the effective condition for progress of endothelialization should be well clarified.

Several researches introduced HMDI for cell adhesion by immobilization of collagen [2, 3]. And the collagen will promote endothelialization. However, SS also affects the endothelialization and several researches pointed the shape of stent will affect the SS.

In this research, we focus the flow influence on the endothelialization using a surface treatment of the stent wire. Square and circle cross-section wires treated with HMDI and collagen were exposed to flow, and then the densities of EC on and around the wire were observed.

2. Method

2.1 Surface treatment

NiTi wire was cleaned by UV ozonization plant (Technovision Inc) for 20 minutes. Then, NiTi wire was agitated in the toluene solution including 0.01 vol% Dibutyltin diraulate and 10 vol% HMDI, for 30 minutes in nitrogen gas atmosphere. Unreacted solution was removed by acetone treatment under nitrogen gas stream, then wire soaked in 8 mg/ml Type I collagen solution(Nitta gelatin) for 3 hours. Unreacted solution was removed by rinsing with 0.01M HCl, PBS(-) and MilQ water, then the wire was dried. On the wire, the link of NiTi-O-CO-NH-$(CH)_2$-NHCO-NH-Collagen combination was achieved.

2.2 Flow exposure

We used a flow exposure circuit (Fig.1). P4~P9 human carotid artery EC (HCtAEC) was cultured in Medium 199 added 20% FBS and penicillin (Proliferative Medium, PM) on the bottom of dish until cells became confluent. This cultured EC was placed at the bottom of the flow circuit. Flow circuit's height is 0.6 mm and width is 1.8 mm. NiTi stent wire was implanted at the center of flow circuit and fixed by two gaskets. Stent wire was provided two cross-section types which are ϕ 3.56 mm circle and 4.57×4.57mm square with three different kinds of surface treatment which is bare wire, treated by HMDI only or HMDI and collagen. This flow circuit was connected in the flow exposure system consisted of roller pump, pulse damper and reservoir. And, PM circulates with 170 ml/min flow rate which made 2 Pa equable SS on the bottom of flow circuit before implanting wire, for 24 hours. The distribution of SS at the bottom of flow circuit after implanting wire and exposing flow was simulated by two-dimensional finite element analysis with COMSOL Multiphysics 4.3a. Fig.2 shows the model of flow circuit with mesh in COMSOL. Inlet was with laminar flow with 2.845×10^{-6} m^3/s flow rate, 0.018 m thickness. Outlet was with 0 Pa pressure and no viscous stress. Mesh consisted of 1572 elements for circuit with no wire, 23500 elements for circuit with square cross-section wires and 25644 elements for circuit with circle cross-section wires.

2.3 Immunofluorescence

After 24 hours exposure, Anti-VE cadherin antibody (abcam) was added to the dish and the wire. And then, cadherin is stained by Alexa488. Moreover, F-actin is stained by Alexa546, and nucleus was stained by DAPI (Thermo). The cell density at the bottom of dish is calculated by counting stained nuclei of ECs in the area that divided every 0.1 mm width along the flow. The cell density on the wire is calculated in the each faces of the wire.

3. Results and Discussion

Fig.3 shows SS on the bottom at dish 3 mm before and 7 mm behind the center of flow circuit and the top of wire after square and circle cross-section wires were implanted. The implanting wires change the distribution of SS, respectively. Fig.4 is immunofluorescent images of ECs on the dish after 24 hours flow exposure. ECs in panel A0 are exposed in flow with 2 Pa SS without NiTi wire. ECs in B1~D1 are exposed in flow with square section wire, and B2~D2 are exposed with circle section wire. In B1 and B2, showing the areas that exposed by around 2 Pa SS, the cell densities are almost the same with in A0. C1 and C2 are before the point that the wire and the dish are attaching. The cell density in C1 is obviously lower than in C2 even though similar SS distribution. This difference is considered to be due to

the wire's cross-section shape. D1 and D2 are around the area showing highest cell density. These areas are nearby specific SS distributions which show significant change between high and low SS. Fig.5 shows immunofluorescent images of ECs on the top of wire. On the both of wires, the cell densities are almost same. However, the positions that ECs are attaching are different. On the circle section wire, ECs uniformly adhere. On the other hand, on the square section wire, ECs tend to adhere upstream on the top of wire.

4. Concluding remarks

Implanted wire's cross-section shape effects on the cell density of the area just before the wire and the position that ECs adhere on the wire. The effects of surface treatment will be discussed on the presentation.

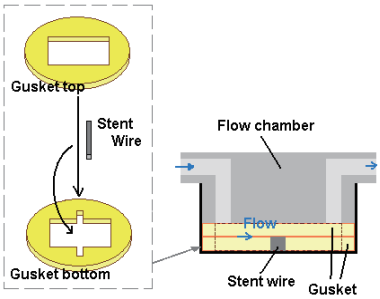

Fig.1 Structure of flow circuit and stent wire

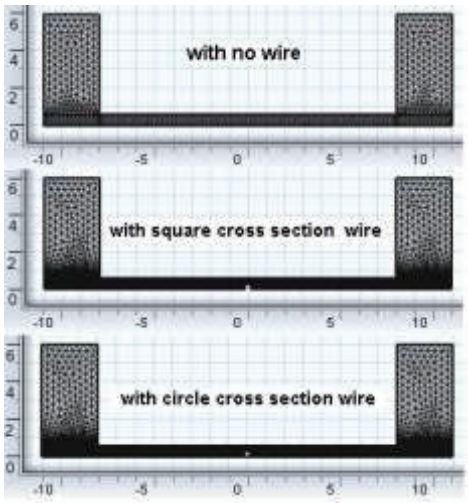

Fig.2 The model of flow circuit with mesh in COMSOL (mm)

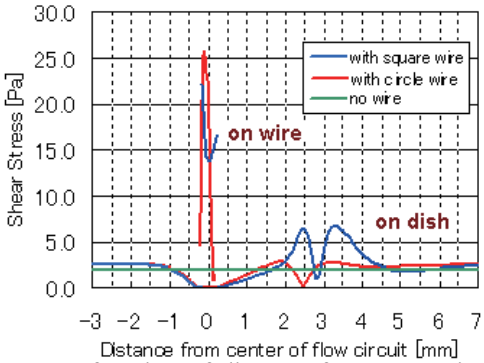

Fig.3 SS as a function of distance from center in flow circuit before and after implanting wire.

References

[1] N. Kipshidze, G. Dangas, M. Tsapenko, J Moses, M B Leon, M Kutryk, P Serruys. J Am Coll Cardiol. 2004; 8; 44(4): 733-9.

[2] H. Kobayashi, Y Ikada. Biomaterials. 1991; 12(8): 747-51.

[3] M.D. Pierschbacher, E Ruoslahti. Nature. 1984; 309; 30-33

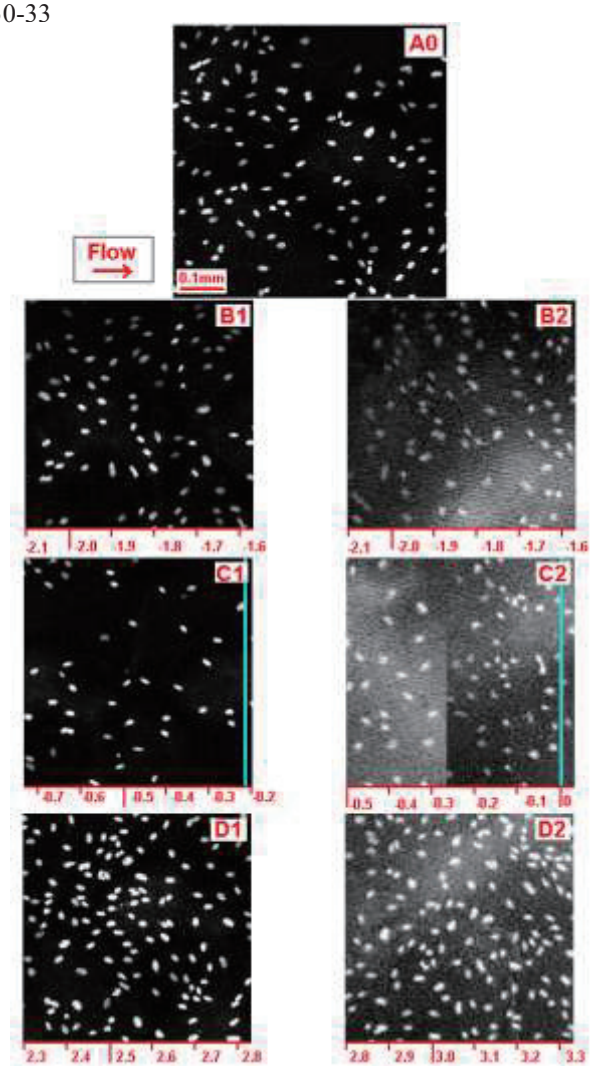

Fig.4 Immunofluorescent images of EC' s nucleus on the dish. (A0: without wire. B1-D1 (left line): with square section wire. B2-D2 (right line): with circle section wire. B area: the area exposed 2 Pa SS. C area: the area just before the wire, blue line is attaching point of wire. D area: the area shows highest cell density.)

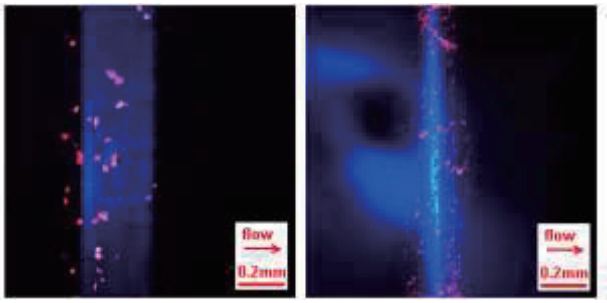

Fig.5 Immunofluorescent images of EC on the top of wire. (left:square section wire, right: circle section wire, blue: stained nucleus, red: stained F-actine, green:cadherin)

Tenth International Conference on Flow Dynamics
November 25-27, 2013, Sendai, Miyagi, Japan

Particle Response in Dielectrophoretic Flow Using CFD

KIM Hyoung June, Masahiro TAKEI
Graduate School of Mechanical Engineering, Artificial System Science Division, Chiba University
Speed-hj@hanmail.net

ABSTRACT

This paper simulates the electrical particle concentration and migration in the small diameter particles in a micro-channel using CFD. This research is a particle concentration and distribution at certain cross-section and between cross section under capacitance sensing. The calculation conditions are Reynolds number influence of electrical power, and cross-section, AC, and frequency. To obtain the high quantitative information of two-phase flow, use Clausius-Mossotti theory, Navier-Stokes and Maxwell equations. As a result, particle is moved in the case of cross-sections. The result is very useful for developing a detector of thrombus in an artificial heart.

1. Introduction

Deielectrophoresis(DEP) is a phenomenon in which a force is exerted on a dielectric particle when it is subjected to a non-uniform electric field. The net force created with DEP generates momentum in the particles. Particle movement towards regions of high electric field intensities is called positive DEP and occurs when the interior of the particle is more permissive to the field. This force does not require the particle to be charged. The DEP force depends on both the gradient of the electric field and electrical properties such as permittivity and conductivity of the particle and medium. It is important to note that the force due to DEP is based on the gradient of electric field and not on the absolute value of electric field at any point. Analysis of movement of the particles in a non-uniform electric field needs an accurate knowledge of the electric field distribution in the system. [1]

Different electrode geometries and arrangements are used to produce non-uniform electric field. The frequency at which the DEP effect changes from positive DEP to negative DEP or negative DEP to positive DEP is called crossover frequency. However, the strength of the force depends strongly on the medium and particles' electrical properties, on the particles' shape and size, as well as on the frequency of the electric field. Consequently, fields of a particular frequency can manipulate particles with great selectivity. This has allowed, for example, the separation of cells or the orientation and manipulation of nanoparticles and nanowires. [2]

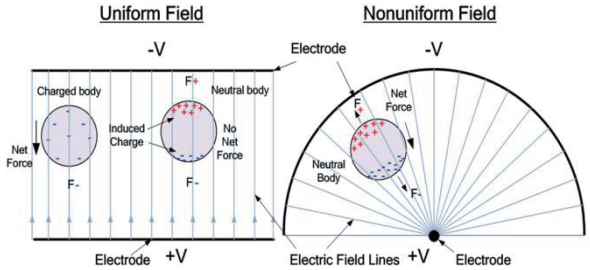

Fig.1 Electric field of Uniform and Non-uniform field

2. Theory

The electric field distribution in the system created by AC signal is described by the Laplace equation.

$$\nabla^2\phi = 0 \tag{1}$$

Where ϕ is the applied electric potential. Solving Eqn.(1) with appropriate boundary conditions will provide the potential distribution in the computational domain. This potential distribution is used to calculate the DEP force acting on particles.

$$F_{DEP} = \frac{\pi r^2 l}{3}\varepsilon_m \mathrm{Re}[K]\nabla\left|\vec{E}\right|^2 \tag{2}$$

The factor in curly brackets is known as the complex Clausius-Mossotti function and contains all the frequency dependence of the DEP force. Where the particle consists of nested spheres - the most common example of which is the approximation of a spherical cell composed of an inner part (the cytoplasm) surrounded by an outer layer (the cell membrane) - then this can be represented by nested expressions for the shells and the way in which they interact, allowing the properties to be elucidated where there are sufficient parameters related to the number of unknowns being sought. [3]

$$K = \frac{\varepsilon_p^* - \varepsilon_m^*}{\varepsilon_p^* + 2\varepsilon_m^*} \tag{3}$$

The complex dielectric constant is ($\varepsilon^* = \varepsilon + \sigma/\, j\, w$) where ε is the dielectric constant, σ is the electrical conductivity, w is the field frequency, and j is the imaginary unit, E is electrical field factor about non-uniform field. this equation is accurate for highly elongated ellipsoids when the electric field gradients are not very large. The equation only takes into account the dipole formed and not higher order polarization. When the electric field gradients are large, higher order terms become relevant, and result in higher forces. To be precise, the time-dependent equation only applies to lossless particles, because loss creates a lag between the field and the induced dipole. When averaged, the effect cancels out and the equation holds true for lost particles as well. DEP can operate directly on native, unlabeled particle, cost, and labor and time for labeling and tagging, as well as development and validation of such labels and tags. [4]

3. Simulation

Both case also calculated by particle size and voltage DEP force is influenced by many factors. Most important things among factors are voltage and size. [5]

At the 0-3 volt, particle size was changed from 1 to

5μm. Diameter of the micro-channel is 40μm and the total length is 600μm. Inlet velocity is set to 0~1μm/s. Model have 4electrode and single section, It calculated 2 kind of force positive DEP force and negative DEP force. Diameter of electrode at the channel is 10μm, and the particles (ρ=1.05kg/m^3, dp=1~3μm) were used as working particles. Using the commercial finite-element method, COMSOL Multi physics, and numerical prediction was performed for the electric current mode. The density of finite element meshes was set to higher at the regions of higher electric fields, i.e. near the electrode edge. The number of elements and the number of degrees of freedom typically considered were 250,000. Computational time of each model required for one frequency value was about 15min with Intel Core i7

4. Results and Discussion

(a) (b)

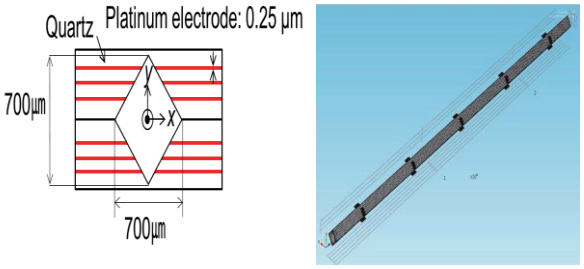

Fig.2 (a) Schematic diagram of micro-channel
(b) Finite element model of micro-channel

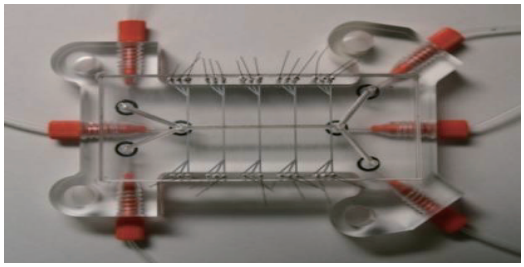

Fig.3 Observation photo 60eletrode of micro-channel

That force moves particle to electrode where is attached wall. But it is not too much different as fundamental case. The reason is that, bulk flow is stronger than DEP force. DEP force has no time to hold the particle because DEP force is weaker than Bulk flow. As shown blow fig.4, compare with fundamental case, mean value of particle concentration is reduced.

Averagely, value of particle concentration is small. But it shows particles move to wall from center. Moreover, near the outlet, particle movement to wall is bigger than before. Reason is that, micro-channel have 5 cross section. Each cross section has electrical force. Each cross section makes particle move to wall. Particles DEP force is more grow up, when near the wall. Particle movement is influenced by DEP force. Because of positive DEP force of particle, Particle is move to wall.

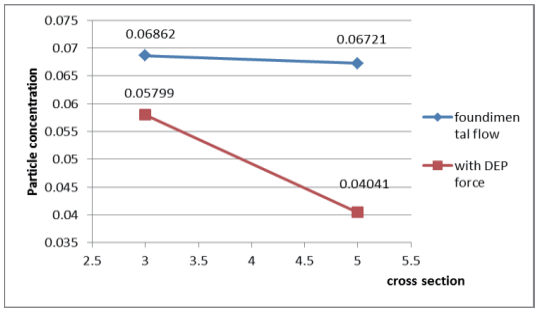

Fig.4 Mean value of particle concentration at cross sections.

5. Conclusion

Calculating about DEP force at this paper is for measurement of fluid using common electrical equipment. For get more high quality data, more force will be considered. To verify the simulation, based on real experimental result was done by micro-CT measurement. Small equipment for experiment must consider about electric field. At the low voltage, frequency influenced particle motion although it is negligible. But especially micro scale like in this paper, it must be considered. It is too small to movement at the macro scale. Highest particle velocity at the changing the particle size case is less than 30 μm/s. At the frequency case, almost does not move. It is less than 10 μm/s. We simulated the behavior under positive DEP force and Negative DEP force conditions for micro sized particle. This result is too small for large scale tomography application such as, ECT or ERT. But micro scale is different as macro scale. At the micro scale, even if particle moved only 1μm. It gives a great influence on result. DEP force and that voltage should be essentially considered for the cases of micro-channel tomography.

References

[1] Naga Siva K. Gunda and Sushanta K. Mitra. Dielectrophoresis for Manipulation of Bioparticles Biomedical Engineering – Frontiers and Challenges, (2011) (Ed.), ISBN : 978-953-307-309-5, InTech

[2] Ali Asgar S. Bhagat el al. Inertial microfluidics for continuous particle filtration and extraction. DOI Microfluid Nanofluid (2009) 7:317-226

[3] Pohl, H. A., Dielectrophoresis the behavior of neutral matter in nonuniform electric fields.(1978) page 233-234

[4] Morgan, H. and Green, N. AC Electrokinetics: Colloids and Nanoparticles(2003),page 113.

[5] Barbaros Çetin, Yuejun Kang, Zhemin Wu and Dongqing Li. Continuous Particle Separation by Size via AC-Dielectrophoresis using a lab-on-a-chip Device with 3-D Electrode. (2009). Volume 30, Issue 5, pages 766–772, March.

OS12: Basic and Applied Research on Membrane Protein for Health Care

Tenth International Conference on Flow Dynamics
November 25-27, 2013, Sendai, Miyagi, Japan

Structure and Mechanism of the Proton Pumping Vacuolar ATPase, a Rotary Motor Enzyme

Stephan Wilkens
Department of Biochemistry & Molecular Biology, The State University of New York Upstate Medical University, Syracuse, NY 13210, USA
wilkenss@upstate.edu

We study the structure and mechanism of the yeast vacuolar ATPase (V-ATPase), a multisubunit rotary motor proton pump that functions to acidify subcellular organelles in all eukaryotic organisms. V-ATPase belongs to the family of rotary motor ATPases, which also includes mitochondrial F_1F_o- and archaeal A_1A_o-ATP synthase. V-ATPase can be divided into a water soluble ATPase sector (V_1) and a membrane embedded proton channel (V_o). Hydrolysis of ATP taking place on the V_1 is coupled to proton translocation across the V_o via a rotating 'central stalk' that serves as axle of the motor. To prevent uncoupling of ATPase motor and proton turbine during rotary catalysis, the complex is stabilized via three peripheral 'stator stalks' that hold the V_1 and V_o in the correct spatial orientation for productive energy coupling to occur. Unlike the related F- and A-ATPase, eukaryotic V-ATPase is regulated by a unique mechanism that involves reversible dissociation into V_1-ATPase and V_o proton channel domains, a process that involves breaking of protein interactions mediated by the three stator stalks, subunit C, and the cytoplasmic domain of V_o subunit '*a*'. To help elucidate the mechanism of reversible dissociation, we have solved crystal structures of a yeast V-ATPase heterotrimeric complex composed of EG heterodimer and the head domain of subunit C. The structural model revealed a number of unusual features in the heterotrimer that point to its function in the intact V-ATPase. The right-handed coiled coil nature of the EG N-terminal domain, a region of partially unfolded secondary structure in the G subunit and the presence of two flexible hinges in the coiled coil are all unique features that have likely evolved to allow flexing of the stator stalks during rotary catalysis. Interestingly, the conformation of the isolated stator stalk as crystallized appears to be different from the conformation of the heterotrimer in the assembled complex and we speculate that the EGC stator stalk is 'spring-loaded' during chaperone mediated enzyme assembly to allow rapid and efficient disassembly of the V-ATPase upon weakening of one (or several) protein-protein interactions in the V_1-V_o interface.

1. Introduction

Vacuolar H^+-ATPases (V-ATPases; V_1V_o-ATPases) are large multi subunit protein complexes that are found in the endomembrane system of eukaryotic organisms where they function to acidify the interior of intracellular organelles [1]. In specialized cells of higher eukaryotes, V-ATPases are also found in the plasma membrane, where the enzyme is pumping protons into the extracellular milieu. V-ATPase is composed of two functional domains, an ATP hydrolyzing V_1-sector containing subunits AB(C)DEFGH in the ratio 3:3:(1):1:3:1:3:1 [2] and a membrane bound proton turbine V_o composed of subunits *acc'c''de* in the presumed ratio of 1:4-5:1:1:1:1 [1]. The three A and B subunits are arranged in an alternating fashion around a central cavity within which are located the N- and C-terminal ends of subunit D [3]. ATP hydrolysis takes place at three catalytic sites located at the interface of the A and B subunits. The proton channel is formed between the ring of the *c* subunits (proteolipid ring) and the C-terminal domain of the *a* subunit [1].

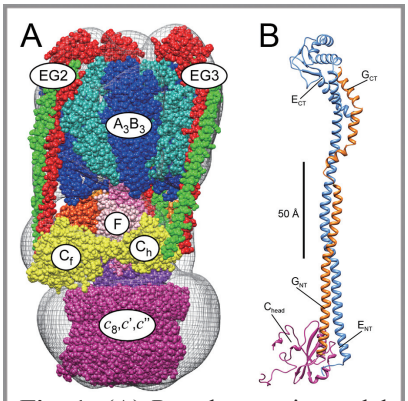

Fig. 1: (A) Pseudo atomic model of the yeast V-ATPase (adapted from [3]). (B) Crystal structure of the yeast V-ATPase EGC_{head} complex [4].

The proton pumping action of the vacuolar ATPase plays a vital role in a large number of intra- and inter-cellular processes [1]. In all eukaryotic cells, these processes include receptor mediated endocytosis, protein trafficking, pH maintenance, storage of metabolites and neurotransmitter release. In polarized cells of higher eukaryotes, a vacuolar type ATPase pumps protons across the plasma membrane leading to extra-cellular acidification. Acidification of the enclosed space between the ruffled membrane of osteoclasts and the bone surface plays an important role in bone resorption and remodeling.

Eukaryotic vacuolar ATPase is regulated by a reversible disassembly and reassembly mechanism that is employed by the organism to modulate the activity of the complex in response to e.g. nutrient availability or developmental state [5]. The mechanism of reversible disassembly has been extensively studied in the yeast system and it is known that V-ATPase dissociation leads to a cytoplasmic V_1 and a membrane bound V_o with the activity of the two domains silenced [1].

Several diseases have been associated with the human vacuolar ATPase [1]. For example, aberrant proton pumping action of the vacuolar ATPase has been identified as being the primary cause of a number of bone-related diseases like osteopetrosis and osteoporosis. Certain cancer cell lines overproduce a vacuolar ATPase in their plasma membranes, possibly for creating the low extracellular pH necessary for activation of proteases that are essential for release of metastatic cells. Renal tubular acidosis is caused by a malfunctioning V-ATPase in kidney tubules and more recently, certain aspects of diabetes have been linked to defective V-ATPase function in insulin secretion. Because the hypo- or hyperactivity of the vacuolar ATPase is in

most cases the direct cause of the disease, the enzyme is a potential target for pharmacological modulators.

To elucidate the mechanism of reversible dissociation, we have recently quantitated some of the interactions at the V_1-V_o interface including interactions of the peripheral stalk proteins EG heterodimer (stator stalk), the N-terminal domain of subunit *a* (a_{NT}) and the C subunit and its foot (C_{foot}) and head (C_{head}) domains [6,7]. Here we have analyzed the interaction of the N-terminal domain of subunit *a* (a_{NT}) and subunit *d* using isothermal titration calorimetry.

2. Methods

Protein Purification — The gene for V-ATPase subunit *d* (Vma6) was PCR amplified from a yeast shuttle vector (pRS316vma6); kindly provided by Dr. Karlett Parra, University of New Mexico) and cloned into pMAL c2E as a N-terminal fusion with *E. coli* maltose binding protein (MBP; Parsons and Wilkens, unpublished). The resulting plasmid was expressed in *E. coli* strain Rosetta at 37 ºC for four hours and the expressed MBP-subunit *d* fusion was purified via amylose affinity chromatography. The fusion was cleaved and subunit *d* was separated from MBP via ion exchange chromatography on a 1 ml Mono-Q column attached to an ÄKTA-FPLC (GE Healthcare). Subunit *d* was further purified by gel permeation chromatography using a Superdex 75 (16/50) column. A slightly longer construct of a_{NT} was cloned (Carroll, Oot and Wilkens, unpublished) and purified as described in [7].

Isothermal Titration Calorimetry — Purified a_{NT} and subunit *d* were dialyzed against 20 mM tris/Cl, pH 7, 0.5 mM EDTA, 1 mM TCEP. Titration calorimetry was performed on a MicroCal VP-ITC (GE Healthcare) with 1.4 ml 25 µM subunit *d* in the sample cell and 300 µl 370 µM a_{NT} in the syringe. Each injection was 10 µl (7% saturation) with a total of 29 injections. The heat generated after each injection was integrated and the data was fitted using Origin VP-ITC software using a single binding site model. Heat of a_{NT} dilution was subtracted from the subunit *d* - a_{NT} titration.

3. Results and Discussion

Subunit *d* and a_{NT} were expressed in *E. coli* and purified to homogeneity (not shown). Both proteins are highly soluble at pH 7 and therefore well suited for binding experiments. Fig. 2 shows isothermal titration calorimetry of 370 µM a_{NT} (in the syringe) with 25 µM subunit *d* in the sample cell. Fitting the data revealed a K_d of 4.7 µM and a ΔG of -6.9 kcal·mol^{-1}.

We have previously shown that the V_1-ATPase - V_o proton channel interface is mediated by one high affinity interaction (EG3-C_{head}; see Fig. 1) as well as several medium to low affinity interactions involving EG2, C_{foot} and a_{NT} [6,7]. The high affinity interaction between EG3 and C_{head} has a K_d of ~40 nM whereas interactions between a_{NT} and EG2 and C_{foot} are 22 and 33 µM, respectively. The here reported medium affinity interaction between a_{NT} and subunit *d* seems counterintuitive since it would link the rotor of the enzyme consisting of V_1 subunits DF and V_o subunits *d* and the *c* subunit (proteolipid) ring. However, we have speculated that the two low affinity interactions involving a_{NT}, EG2 and C_{foot} result in a high avidity four (a_{NT}, E, G and C) subunit junction that would be sufficient to prevent association of a_{NT} with subunit *d* during ATPase driven proton pumping [7]. We further speculate that upon receiving the (hitherto unknown) signal to dissociate, one of three interactions in the high avidity four protein junction would be destabilized, which will result in the release of V_1 from the membrane [4]. At the same time, a_{NT} will now be free to bind subunit *d*, thereby leading to silencing of passive proton translocation. We are now in the process of identifying small molecules that bind subunits at the V_1-V_o interface with high affinity to be able to modulate the assembly state of the enzyme in vivo.

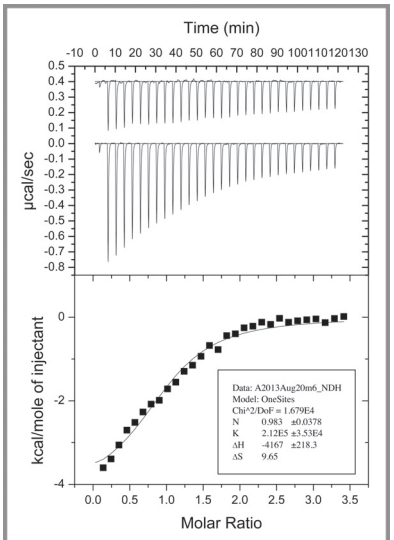

Fig. 2: Titration calorimetry of a_{NT} and subunit *d*.

4. References

[1] Forgac, M. (2007) Vacuolar ATPases: rotary proton pumps in physiology and pathophysiology. *Nat Rev Mol Cell Biol* **8**, 917-929.

[2] Kitagawa, N., Mazon, H., Heck. A.J. and Wilkens, S. (2008) Stoichiometry of the peripheral stalk subunits E and G of Yeast V_1-ATPase determined by mass spectrometry. *J. Biol. Chem*. **283**, 3329-37.

[3] Zhang, Z., Zheng, Y., Mazon, H., Milgrom, E., Kitagawa, N., Kish-Trier, E., Heck, A.J.R., Kane, P.M. and Wilkens, S. (2008) Structure of the Yeast Vacuolar ATPase. *J. Biol. Chem*, **283**, 35983-93.

[4] Oot, R.A., Huang, L.-S., Berry, E.A. and Wilkens, S. (2012) Crystal Structure of the Yeast Vacuolar ATPase Heterotrimeric EGChead Peripheral Stalk Complex. *Structure* **20**, 1881-92.

[5] Kane, P. M. (1995) Disassembly and reassembly of the yeast vacuolar H^+-ATPase *in vivo. J Biol Chem* **270**, 17025-17032.

[6] Oot, R.A. and Wilkens, S. (2012) Subunit interactions at the V_1-V_o interface in the yeast vacuolar ATPase. *J. Biol. Chem*. **287**, 13396-13406.

[7] Oot, R.A. and Wilkens, S. (2010) Yeast V-ATPase subunit C: Domain characterization and interaction with the peripheral stator stalk subunits E and G. *J. Biol Chem*. **285**, 24654-64.

Energy Generation Coupled with Decarboxylation Reactions in Bacteria

Keietsu Abe[1,2] and [3]Kei Nanatani
[1] Department of Microbial Biotechnology, Graduate School of Agricultural Science, Tohoku University
[2] New Industry Creation Hatchery Center (NICHe), Tohoku University
[3] Department of Biomolecular Engineering, Graduate School of Engineering, Tohoku University
1-1 Tsutsumi-dori Amamiya-machi, Aoba-ku, Sendai, 981-8555, Japan
kabe@niche.tohoku.ac.jp.

ABSTRACT

In some strains of the lactic acid bacterium *Tetragenococcus halophilus*, a proton-motive force (PMF) is generated by the combined action of an intracellular L-aspartate decarboxylation reaction, catalyzed by an L-aspartate-4-decarboxylase (AspD), and an electrogenic aspartate^{1-}:alanine^{0} exchange reaction, catalyzed by an aspartate:alanine antiporter (AspT). We purified N-terminal 6 X histidine -tagged AspT (AspT-His6) and characterized its kinetic properties when reconstituted in proteoliposomes. Here we showed that the binding sites of L-aspartate and L-alanine are independently present in AspT by means of the kinetic analyses.

1. Introduction

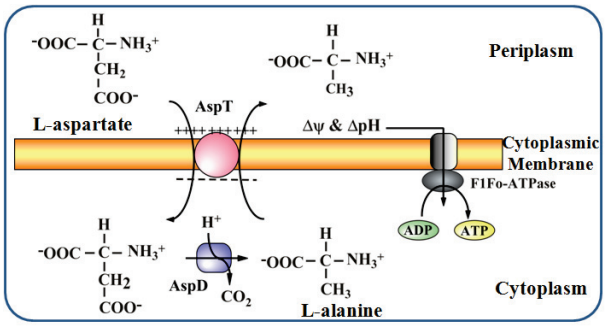

Fig. 1 Energy generation coupled with L-aspartate decarboxylation,

In some strains of the lactic acid bacterium *Tetragenococcus halophilus*, a proton-motive force (PMF) is generated by the combined action of an intracellular L-aspartate decarboxylation reaction, catalyzed by an L-aspartate-4-decarboxylase (AspD, EC 4.1.1.12), and an electrogenic aspartate^{1-}:alanine^{0} exchange reaction, catalyzed by an aspartate:alanine antiporter (AspT, TC# 2.A.81.1.1). The generated PMF is sufficiently high to drive ATP synthesis via the bacterial F_0F_1-ATPase. This combination of PMF and ATP synthesis has been proposed as a proton-motive metabolic cycle (Fig. 1). Such decarboxylation reactions are thought to be advantageous for cells because they generate metabolic energy and regulate intracellular pH [1, 2]. In our previous work with proteoliposomes, we found that the aspartate:alanine exchange catalyzed by AspT is electrogenic [1-3]. AspT is classified as a conventional secondary transport protein and belongs to the newly classified aspartate:alanine exchanger (AAEx) family (TC# 2.A.81) of transporters (http://www.tcdb.org/index.php). AspT is a membrane protein containing 543 amino acids (57.2 kDa). AspT has a unique topology [3] and the transmembrane domain (TM) 3 participates in the formation of a hydrophilic cleft in the membrane, implicating the TM3 in the ligand-induced conformational changes [4]. Previously, we developed a solubilization and purification scheme of AspT by using *n*-dodecyl-β-D-maltoside (DDM) [4]. Here, we characterized, in detail, the kinetic properties of AspT by analyzing the transport kinetics of reconstituted AspT under various conditions. In addition, to reveal the substrate recognition mechanism of AspT, we performed competition analysis with a series of amino acids. The competition analysis suggested that the putative L-aspratate and L-alanine binding sites are independently located in the substrate translocation pathway of AspT.

2. Method

Reconstitution and Transport of Purified AspT-His6

Purified AspT-His6 was reconstituted in a final volume of 1 ml with 800 µl of detergent DDM extracts (10 to 20 µg of purified AspT protein) (or control lipid extract), 130 µl of bath-sonicated liposomes (5.9 mg of *E. coli* phospholipid), and 18 µl of 15% 1-*O*-*n*-Octyl-*β*-D-glucopyranoside, with the balance made up by 50 mM potassium phosphate (pH 7). After incubation for 20 min on ice, proteoliposomes (or control liposomes) were formed at room temperature (RT) by rapid injection of the mixtures into 20 ml of loading buffer containing buffer solution and suitable counter substrate such as 100 mM L-aspartate or L-alanine as the potassium salt for L-aspartate or L-alanine exchange reaction. Buffer components were changed in each experiment. The substrate-loaded proteoliposomes (or liposomes) were kept at RT for 20 min. To assess L-aspartate transport by L-[^{3}H] labeled aspartate or alanine, the substrate-loaded proteoliposomes were diluted 20-fold from the concentrated stock into an appropriate volume of assay buffer (50 mM potassium phosphate [pH 7], 100 mM K_2SO_4). After 1 to 3 min of pre-incubation at 25 °C, L-[^{3}H]aspartate or L-[^{3}H]alanine was added to a final concentration of 100 µM; at various times, 50- to 100-µl aliquots were removed for membrane filtration with 0.22-µm-pore-size GSTF Millipore filter (Millipore Co., Billerica, MA). The membrane filters were washed twice with 5 ml of assay buffer [5].

Filtration Assay of Substrate Transport

Initial rates of L-[^{3}H]aspartate or L-[^{3}H]alanine entry were measured in triplicate at 25 °C by means of a filtration assay [5]. Proteoliposomes were applied

directly to the center of a 0.22-μm pore-size GSTF Millipore filter and washed twice with 5 ml of chilled assay buffer (50 mM potassium phosphate [pH 7], 100 mM K_2SO_4). Upon release of the vacuum, the proteoliposomes were covered with assay buffer that was pre-incubated at 25 °C with 0.1 mM L-[^{3}H]aspartate or L-[^{3}H]alanine, and the reaction was terminated after 10 s by use of filtration and washing.

3. Results and Discussion

Kinetic Analysis of AspT Transport

A kinetic study was undertaken, relying on samples filtered after a 10 s reaction, to estimate the initial velocities of the L-aspartate and L-alanine self-exchange reactions. A Hanes-Woolf plot was used to determine the Michaelis constant (K_m) and the maximum reaction (V_{max}). We found that the L-aspartate self-exchange reaction had a Michaelis constant (K_m) of 0.35 ± 0.03 mM and a maximum velocity of 175 ± 21 μmol min^{-1} mg^{-1} of protein and that the L-alanine self-exchange reaction had a K_m of 26 ± 2 mM and a maximum velocity of 155 ± 9 μmol min^{-1} mg^{-1} of protein (mean ± S.E.). L-Aspartate had a higher affinity than L-alanine for AspT, but the L-aspartate and L-alanine self-exchange reactions had almost the same maximal velocities (V_{max}). Thus, the L-alanine self-exchange reaction showed almost the same transport rate as that of the L-aspartate self-exchange reaction in the presence of sufficiently high concentrations of L-alanine. A kinetic study of D-aspartate and D-alanine self-exchange reactions was also undertaken. D-aspartate and D-alanine showed a higher affinity than L-aspartate and L-alanine, respectively, for AspT. On the other hand, the L-isomers had higher V_{max} values than those of the D-isomers. These results suggest that the D-isomers form a tight and stable complex with AspT, with slow dissociation rates and low V_{max} values.

Substrate Screening of AspT

To examine the substrate specificity of AspT, substrate-competition experiments were performed by measuring the uptake of L-[^{3}H]aspartate and L-[^{3}H]alanine in self-exchange reactions in the presence of 15 mM of various unlabeled amino acids. L-Asparagine, L-cysteine, and D-aspatarate strongly inhibited L-[^{3}H]aspartate uptake. None of the amino acids completely inhibited L-[^{3}H]alanine uptake. L-asparagine, L-serine, and D-alanine considerably inhibited L-[^{3}H]alanine uptake. These results suggest that AspT recognizes as substrates not only L-aspartate, L-alanine, D-aspartate, and D-alanine, but also many other amino acids, such as L-serine and L-cysteine. L-cysteine and L-serine had unique inhibitory effects. L-[^{3}H]aspartate uptake was strongly inhibited by L-cysteine; however, L-[^{3}H]alanine uptake was not inhibited. On the other hand, L-serine apparently inhibited L-[^{3}H]alanine uptake and barely inhibited L-[^{3}H]aspartate uptake.

Inhibitory effect of L-cysteie and L-serine

To evaluate the inhibitory effects of L-cysteine and L-serine, we performed a Dixon-Webb plot analysis of data from samples that were filtered after a 10-s reaction to estimate initial velocities. External substrate concentrations were adjusted to 0.07 mM, 0.35 mM (= K_m value), and 0.7 mM for L-aspartate self-exchange, and 5.8 mM, 26 mM (=K_m value), and 58 mM for L-alanine self-exchange. The three lines in the Dixon plot crossed at one point, demonstrating competitive inhibition of L-aspartate and L-alanine by L-cysteine and L-serine, respectively. The calculated inhibition constant values (K_i) were 2.0 ± 0.2 mM (L-aspartate exchange inhibited by cysteine), 20 ± 2.7 mM (L-alanine exchange inhibited by cysteine), and 5.3 ± 1.7 mM (L-alanine exchange inhibited by serine). The K_i of L-serine for L-aspartate self-exchange was too large to measure, suggesting that serine is a specific inhibitor of alanine self-exchange but not of aspartate self-exchange. These analyses reveal that the mechanism of inhibition of L-aspartate self-exchange and L-alanine self-exchange by L-cysteine and L-serine is competitive inhibition. Because the K_m of L-serine to AspT was larger than the K_m of L-aspartate to AspT but smaller than the K_m of L-alanine to AspT, the apparent selective inhibitory effect of L-serine on L-alanine self-exchange can be explained by the difference in the K_m values of L-serine and L-alanine. However, the K_m of L-cysteine was larger than that of L-aspartate; this cannot explain the apparent selective inhibition of L-aspartate self-exchange with L-cysteine.

4. Concluding remarks

Here we showed that the binding sites of L-aspartate and L-alanine are independently present in AspT by means of the kinetic analyses. We purified AspT-His6 and characterized its kinetic properties when reconstituted in proteoliposomes (Km = 0.35 ± 0.03 mM for L-aspartate, Km = 0.098 ± 0 mM for D-aspartate, Km = 26 ± 2 mM for L-alanine, Km = 3.3 ± 0.2 mM for D-alanine). Competitive inhibition by various amino acids of L-aspartate or L-alanine in self-exchange reactions revealed that L-cysteine selectively inhibited L-aspartate self-exchange but only weakly inhibited L-alanine self-exchange. Additionally, L-serine selectively inhibited L-alanine self-exchange but barely inhibited L-aspartate self-exchange. Taken together, these kinetic data suggest that the putative binding sites of L-aspartate and L-alanine are independently located in the substrate translocation pathway of AspT.

References

[1] K. Abe, H. Hayashi, P.C. Maloney, *J. Biol. Chem.* **271**:3079-84 (1996)

[2] K. Abe, F. Ohnishi, T. Nakajima, , *J. Bacteriol.* **184**: 2906-13 (2002)

[3] K. Nanatani, T. Nakajima, K. Abe, *J. Bacteriol.* **189**: 7089-97 (2007)

[4] K. Nanatani, T. Nakajima, K. Abe, *J. Bacteriol.* **191**: 2122-32 (2009)

[5] A. Sasahara, K. Nanatani K. Abe, *J. Biol. Chem.* **286**: 29044-52 (2011)

Design of Engineered α-Hemolysins for Regulation of Hemolytic Activity by External Stimuli

Kazushi Kinbara[1], Mihoko Ui[1], Kousuke Harima[1], Sumire Endo[1], Kimio Akiyama[1], and Yoshikazu Tanaka[2]
[1]Institute of Multidisciplinary Research for Advanced Materials, Tohoku University, 2-1-1, Katahira, Aoba-ku, Sendai 980-8577, Japan
[2]Creative Research Institution "Sousei," Hokkaido University, North-21, West-10, Kita-ku, Sapporo 001-0021, Japan
kinbara@tagen.tohoku.ac.jp

ABSTRACT
Photoactive Yellow Protein (PYP) is a water-soluble photoreceptor, which undergoes a photocycle accompanying conformational changes due to trans-to-cis photoisomerization of the chromophore. Chimeric proteins *N*-PYP-Hla and *C*-PYP-Hla, consisting of Staphylococcal pore-forming toxin α-Hemolysin (Hla) and PYP, exhibited photoresponsive hemolytic activities, where visible light irradiation gave rise to retardation of hemolysis at 25 °C.

1. Introduction

Optically-controllable proteins provide useful scaffolds for construction of nanodevices to regulate and/or understand the cell systems with high spatiotemporal resolution. We have interests in photocontrollable nano-pore devices that enable small molecules including ions to pass through the cell membrane upon light irradiation. α-Hemolysin (Hla) [1], isolated from Staphylococcus aureus, is a pore-forming toxin that causes lysis of red blood cells. While Hla is secreted as a soluble monomeric protein, it assembles into a cyclic heptamer (Fig. 1) on the surface of the cell membrane. After the formation of the heptameric ring, the stem region forms a β-barrel channel, which penetrates into the membrane to cause lysis of the cell. The pore is inherently stable and acts as a nonspecific ion channel, which is advantageous for various applications. Actually, Hla has been studied for biotechnological applications, including delivery system of small solutes across lipid membranes, bio-sensors for small solutes, and an alternative to conventional device for DNA sequencing.

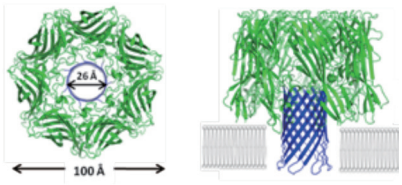

Fig. 1 Schematic image of α-hemolysin.

We have prepared chimeric proteins *N*-PYP-Hla [2] and *C*-PYP-Hla [3], where PYP is connected to the *N*- and *C*-termini of Hla, respectively. We expected that the hemolytic activity of these chimeric proteins could be controlled by visible-light irradiation. Here we report the construction of chimeric proteins *C*-PYP-Hla and *N*-PYP-Hla, and their hemolytic activity in the dark and under irradiation.

2. Method

The PYP units attached to *N*- and *C*-termini of Hla were reconstituted by the reported procedure [4]. To a Tris-HCl buffer (50 mM, pH 8.0, containing 200 mM NaCl) solution of apo-PYP-Hla (3 mg/mL), was added a DMF solution of *p*-coumaric anhydride (10-fold molar excess), and the resulting mixture was stirred overnight at 4 °C. The reaction mixture was filtered to remove insoluble substances, and then subjected to size-exclusion chromatography (HiLoadTM 26/60 Superdex 200, GE Healthcare) to allow isolation of the reconstituted proteins *N*-PYP-Hla and *C*-PYP-Hla. *N*-PYP-Hla and *C*-PYP-Hla were obtained as a monomeric form in Tris-HCl buffer (50 mM, pH 8.0, containing 200 mM NaCl).

UV-Vis spectra were recorded on JASCO V-650 UV-Vis spectrophotometer. Turbidity was recorded on JASCO V-530 UV-Vis spectrophotometer. Irradiation was carried out by a xenon lamp (ASAHI SPECTRA LAX-102).

3. Results and Discussion

The chimeric proteins *N*-PYP-Hla and *C*-PYP-Hla, where PYP is connected to the *N*- and *C*-termini of Hla, respectively, have been prepared according to the conventional procedure. We first obtained apo-proteins without a chromophore at the PYP domain, which was then treated with *p*-coumaric anhydride in DMSO at room temperature to afford desired *N*-PYP-Hla and *C*-PYP-Hla. Successful introduction

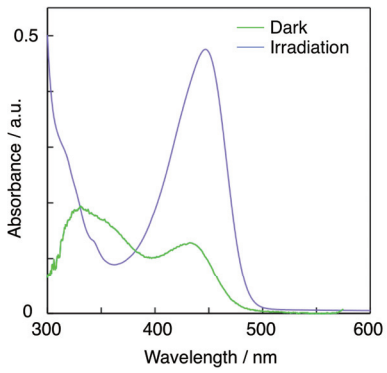

Fig. 2 Electronic absorption spectra of *N*-PYP-Hla in Tris-HCl buffer (50 mM, pH 8.0, containing 200 mM NaCl and 6.25 mM sodium deoxycholate) in the dark (blue) and under irradiation with visible light (green).

of *p*-coumaric acid in these proteins was confirmed by electronic absorption spectroscopy. Indeed, *N*-PYP-Hla and *C*-PYP-Hla displayed an absorption band around 445 nm, as with wild-type PYP in the dark (λ_{max} = 446 nm), indicating the presence of the *p*-coumaric acid moiety attached to PYP via a thioester bond. Irradiation of *N*-PYP-Hla with visible light caused the blue-shifted band at 430 nm with decrease in its intensity, together with an intensified absorption band around 350 nm, similarly to the spectrum of wild-type PYP under irradiation with visible light (Fig. 2). When irradiation is stopped, the spectrum returned to the initial one immediately, suggesting a rapid spontaneous recovery of the trans configuration of the chromophore in the dark. In relation with this, the intensity of absorption at 445 nm reversibly changed in response to visible light irradiation.

Wild-type Hla exists as a monomer in an aqueous buffer solution, which assembles into a heptameric ring upon binding to the cell membranes. This cyclic oligomer formation is also encouraged by sodium deoxycholate micelles even in the absence of lipid membranes. Interestingly, a transmission electron micrograph of *N*-PYP-Hla in a Tris-HCl buffer (50 mM, pH 8.0, containing 200 mM NaCl and 6.25 mM sodium deoxycholate) clearly displayed doughnut-like assemblies consisting of seven monomer units (Fig. 3). Thus, it is likely that *N*-PYP-Hla is able to form a heptameric cyclic assembly on the membrane, like wild-type Hla.

Fig. 3 A transmission electron micrograph of *N*-PYP-Hla in a Tris-HCl buffer (50 mM, pH 8.0, containing 200 mM NaCl and 6.25 mM sodium deoxycholate).

Hemolytic activities of *N*-PYP-Hla and *C*-PYP-Hla were evaluated by adding a phosphate buffered saline (PBS, pH 7.4) solution of each protein (0.18 μM) to a PBS suspension of sheep red blood cells (SRBC), where the progress of hemolysis was monitored by optical density at 700 nm (OD_{700}). Wild-type Hla has strong hemolytic activity and completes hemolysis of SRBC within a few minutes at 25 °C, where 50% of SRBC was lysed at 2 min (t_{50}). Meanwhile, at 25 °C in the dark, *N*-PYP-Hla showed moderate hemolytic activity (t_{50} = 200 min), and the hemolysis finished in ca. 400 min (Fig. 3a, blue line). Interestingly, under irradiation with visible light (λ = 450 ± 10 nm) at 25 °C, the hemolysis has been significantly retarded (t_{50} = 300 min) (Fig. 4a, red line). Thus, the hemolytic activity of *N*-PYP-Hla is controllable by visible light. Likewise, *C*-PYP-Hla also showed photoresponse in its hemolytic activity (Fig. 4b).

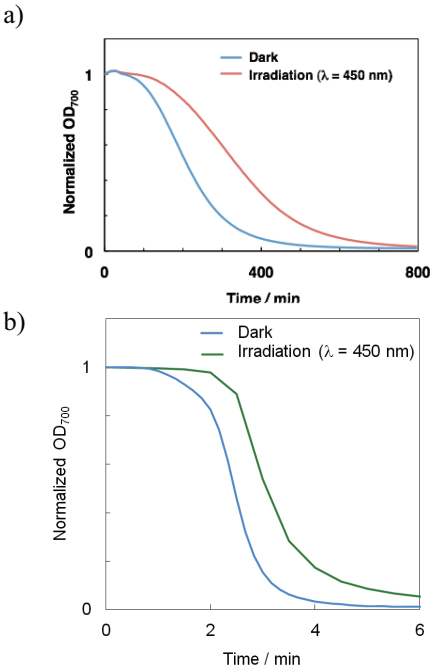

Fig. 4 Time course curves of hemolysis of sheep red blood cells by a) *N*-PYP-Hla and b) *C*-PYP-Hla in PBS in the dark (blue) and under irradiation with visible light (λ = 450 ± 10 nm) (red and green) at 25 °C, monitored by optical density at 700 nm (OD_{700}).

4. Concluding remarks

We found that the chimeric proteins *N*-PYP-Hla and *C*-PYP-Hla showed light-dependent hemolytic activities where the rates of hemolysis under irradiation with visible light (λ = 450 nm) are much slower than those in the dark at 25 °C. The results presented here demonstrate the advantage of a PYP unit as a regulator for protein devices, and would possibly contribute to development of photocontrollable bio-devices.

References

[1] B. Walker, O. Braha, S. Cheley and H. Bayley, Chem. Biol., **2** (1995), 99.
[2] Y. Imamoto, T. Ito, M. Kataoka and F. Tokunaga, FEBS Lett., **374** (1995), 157.
[3] M. Ui, Y. Tanaka, Y. Araki, T. Wada, T. Takei, K. Tsumoto and K. Kinbara, Chem. Commun., **48** (2012), 4737.
[4] M. Ui, Y. Tanaka, Y. Araki, T. Wada, T. Takei, K. Tsumoto and K. Kinbara, J. Photopolym. Sci. Technol., **25** (2012), 655.

Tenth International Conference on Flow Dynamics
November 25-27, 2013, Sendai, Miyagi, Japan

Membrane Channel Dynamics Depended on Lipid Environment

Noriko Tomita[1], Liviu Movileanu[2], Makoto Ohta[1]
1. Institute of Fluid Science, Tohoku University, 2-1-1 Katahira, Aoba-ku, Sendai, Japan
2. Department of Physics, Syracuse University, New York, USA
tomita@biofluid.ifs.tohoku.ac.jp

ABSTRACT

Activities and structures of integral membrane proteins are affected by the lipid bilayer environment. Here we show physical properties of a robust protein nanopore, engineered ferric hydroxamate protein uptake component A (FhuA ΔC/Δ4L) from *Escherichia coli*, on an array of lipid bilayer systems. Remarkably, systematical single-channel analysis revealed conical phospholipids within the bilayer catalyzes the first, stepwise current transition of the FhuA ΔC/Δ4L nanopore to a lower-conductance open state. This study reinforces further developments of FhuA ΔC/Δ4L nanopore in biosensing and molecular biomedical diagnosis.

1. Introduction

Membrane channels are distributed widely from prokaryotic to eukaryotic cell membranes, and are necessary for critical physical processes of the cell activities. Several of them possessing stable and robust structure have been developed as nanopore devices. FhuA (Ferric hydroxamate protein uptake component A) is known well as a ligand-gated channel from the outer membrane of *Escherichia coli*, which is formed monomeric 22-stranded β-barrel protein. Based on the versatile properties of FhuA channel including dynamics, robustness, and thermal stability, its application as a stochastic biosensing element has been focused. Recently, we showed that the removal of four large extracellular loops and the plug domain, produced an unusually stable and quiet nanopore, called FhuA ΔC/Δ4L (Fig.1A). This engineered protein nanopore remained open for long periods under harsh experimental conditions, and exhibits greater conductance of ~4.0 nS in 1M KCl than the conductance values observed with other previously studied FhuA mutants [1]. These structural and biophysical features imply that FhuA ΔC/Δ4L has potential for applications in single-molecule stochastic sensing of nucleic acid and proteins but also in other biotechnological arenas.

Meanwhile, it is already established that the membrane composition, surface charge, the nature of polar headgroup, and the bilayer curvature can play a critical role in promoting the activity, stability, folding, gating and ligand-binding dynamics of the transmembrane proteins [2]. In this study, we pursued any relationship between the membrane lipid composition and electrophysiological properties of the FhuA ΔC/Δ4L protein nanopore by using an array of lipid bilayer system contained charged and uncharged as well as conical and cylindrical lipids. This work provided new insights into the biophysical features of the engineered FhuA ΔC/Δ4L protein nanopore as well as their dependence on the lipid membrane environment.

2. Method

2.1. Preparation on planar lipid bilayers

For the preparation of the planar lipid bilayers, we used five types of phospholipids: 1,2-diphytanoyl-sn-glycerolphosphatidylcholine (DPhPC), 1,2-diphytanoyl-sn-glycero-3-phosphoethanolamine (DPhPE), 1,2-diphytanoyl-sn-glycero-3-phospho-L-serine (DPhPS), N-palmitoyl-D-erythro-sphingosylphosphorylcholine (SM) and E. coli Polar Lipid Extract (ECTPL) containing of phosphatidylethanolamine (PE)/ phosphatidylglycerol (PG)/cardiolipin (CL) in a volume ratio of 6.7:2.3:1.0 (Avanti Polar Lipids, Alabaster, AL).

Powders of lipids were solubilizedwith pentane at a concentration of 10 mg/ml. Phospholipid solutions for bilayer formation were prepared by mixing DPhPE and DPhPC in a volume ratio of 3:7 and 1:1, and by mixing SM and DPhPC in a volume ratio of 1:1.

2.2. Preparation of the FhuA ΔC/Δ4L protein

The protein expression for obtaining the engineered FhuA ΔC/Δ4L protein was described previously [1]. Briefly, 40 μL of His+-tag purified and denatured FhuA ΔC/Δ4L was diluted 50-fold into 1.5% n-Dodecyl-β-d-maltopyranoside (DDM) in Tris buffer, pH 8.0. The protein samples were left overnight at 23 °C for complete refolding of the protein.

2.3. Electrical recordings on planar lipid bilayers

The cis and trans chambers (1.5 ml each) of the apparatus were separated by a 25-μm-thick Teflon septum. An aperture in the septum, 80–120 μm in diameter, was pretreated with hexadecane dissolved in pentane. DPhPE/DPhPC (3:7), DPhPE/DPhPC (1/1), SM/DPhPC (1/1), ECTPL and DPhPS bilayers were formed across the aperture. Single channels of the engineered FhuA ΔC/Δ4L protein were obtained by adding purified and refolded protein to the cis chamber. Single-channel electrical recordings were conducted using an Axon 200B patch-clamp amplifier.The data acquisition and analysis were carried out using pClamp 10.2 (Axon Instruments, Foster City, CA).

3. Results and Discussion

3.1 Geometrical features of the lipids

Fig. 1B and C show various shapes of phospholipids based upon their dimensionless shape parameter, S, which is given by $S=V/a_0l_c$, where a0, lc and V are the optimum area per lipid molecule at the lipid–water interface, the length of the fully extended acyl chain and the molecular volume, respectively [3]. According to the value of S, the lipid can be classified the following: DPhPC is a neutral and cylindrical phospholipid. SM is

also a neutral and truncated, conical phospholipid. PG, CL and DPhPS are cylindrical and negatively charged phospholipids. PE and DPhPE are conical and neutral phospholipids.

3-2 Normalized current step size (NCSS) during the process of closing

As shown in Fig. 2, the open state before closing is termed S1. The following open states are termed Sn (n>1). NCSS was calculated as the change in the single-channel current from C1 to C2, as compared to the current ofthe open state C1:

$$NCSS = (C1\text{-}C2) / C1 \times 100\ \% \qquad (1)$$

Fig. 3 shows the NCSS obtained at the applied transmembrane potential of +180 mV. There is no statistically significant distinction between NCSSs of the protein on the different lipid bilayer systems. The NCSS imply intrinsic structural properties that lead to different closure dynamics. Thus, these systematical single-channel results indicate FhuA ΔC/Δ4L forms similar pores on all types of lipid bilayers.

3-3 Normalized first closure time (NFCT) of the engineered FhuA ΔC/Δ4L protein nanopore is affected by conical phospholipid.

As shown in Fig. 4, the NFCTs of the protein nanopore reconstituted on the SM/DPhPC (1:1) and DPhPS bilayers are significantly greater than those data obtained with the DPhPE/DPhPC (3:7), DPhPE/DPhPC (1:1) and ECTPL bilayers. The voltage-induced sensitivity for the very first closure of the nanopore will be impacted by the dimensionless shape parameter of phospholipid constituents of the lipid bilayer system.

4. Conclusion remarks

We determined that the opening of the FhuA ΔC/Δ4L protein nanopore reconstituted into the cylindrical phospholipid-containing bilayers is maintained for a longer duration compared with the conical phospholipid -containing bilayers at high applied transmembrane potential. These findings suggest that the shape of the phospholipid can alter the stability of the open-state current without any substantial structural change of the engineered FhuA ΔC/Δ4L protein nanopore.

5. Acknowledgements

This work was partly supported by Young Researcher Overseas Visits Program for Vitalizing Brain Circulation (IFS, JSPS). Noriko Tomita is a recipient of a postdoctoral fellowship from JSPS.

References

[1] M.M. Mohammad, R. Lyer, K.R. Howard, M.P. McPike P.N. Borer, L. Movileanu , J. Am. Chem. Soc, **134** (2012), 9521.

[2] R. Phillips, T. Ursell, P. Wiggins, P. Sens, Nature, **459** (2009), 379.

[3] I. van Uitert, S. Le Gac, A. van den Berg, Biochim. Biophys. Acta **1798** (2010), 21.

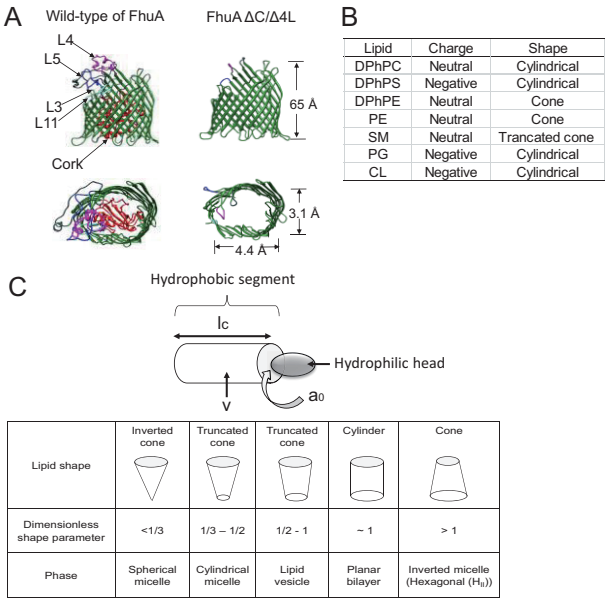

Lipid	Charge	Shape
DPhPC	Neutral	Cylindrical
DPhPS	Negative	Cylindrical
DPhPE	Neutral	Cone
PE	Neutral	Cone
SM	Neutral	Trancated cone
PG	Negative	Cylindrical
CL	Negative	Cylindrical

Fig. 1 The key players in this study: (A) Wild-type FhuA (left) and engineered FhuA ΔC/Δ4L (right), (B) Properties of lipids used in this study, (C) Geometrical shapes of lipids

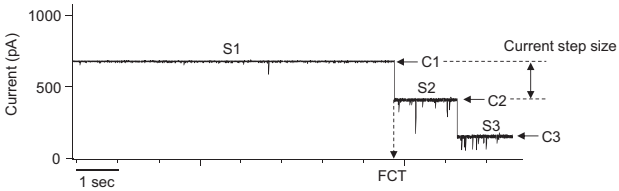

Fig. 2 Representative single-channel electrical recording of the FhuA ΔC/Δ4L at +180 mV.

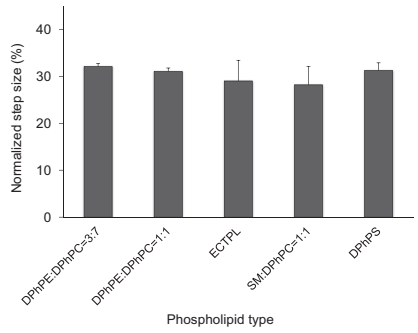

Fig. 3 NCSSs of the FhuA ΔC/Δ4L protein on various lipid bilayer systems.

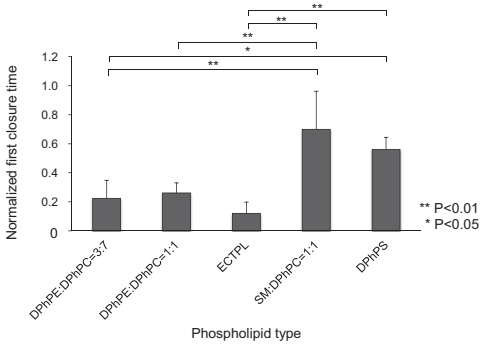

Fig. 4 NFCTs of the FhuA ΔC/Δ4L protein on various lipid bilayer systems.

Structural Aspects of Proteins Modified by Oligosaccharides

Kenji Etchuya and Yuri Mukai
Faculty of Electrical Engineering, Graduate School of Science and Technology,
Meiji University, Kawasaki, Kanagawa 214-8571, Japan
ce21012@meiji.ac.jp

ABSTRACT

A method for discriminating sugar types from protein primary sequences in *O*-glycosylation was developed by alignment position-specific amino acid scoring matrix for the purpose of computational detecting of weak consensus motifs. Fucose and xylose modification sites were discriminated with high accuracies using primary sequences. Position-specific physicochemical properties of each amino acid and protein secondary structures were calculated around *N*-acetylglucosamine and fucose modification sites. Consequently, the characteristics of physicochemical properties and secondary structures were found in each sugar type.

1. Introduction

Most proteins are modified by sugar chains in specific motif sequence due to a function of glycosyltransferase, as a post-translational modification (Figure 1). Sugar modifications play important roles such as a signal transduction systems and enzyme activities in living cells. Therefore, by introducing a suitable kind of sugar chain to the arbitrary positions of target protein, these techniques are expected to be applicable to the technologies in medical and pharmaceutical fields.

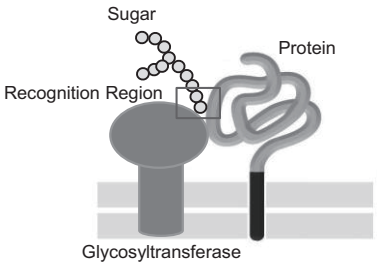

Fig. 1 Glycosylation mechanism;
Sugar chains are attached to motif sequences (Ser/Thr) by glycosyltransferases

Various kinds of sugar types have been discovered in *O*-glycosylation. *O*-glycosylations are known to have motif sequences (Ser/Thr). However even though proteins have a motif sequence, sugar chains are not modified always, the rule of glycosylations has not clarified completely. *O*-glycosylation prediction tools including Oglyc, NetOGlyc and YinOYang were developed and had been opened on the web. In addition, the tools described above were developed for predicting galactose (Gal), *N*-acetylgalactosamine (GalNAc) and *N*-acetylglucosamine (GlcNAc) modifications. Although many sugar types including Gal, GalNAc, GlcNAc, glucose (Glc), fucose (Fuc), xylose (Xyl) and mannose (Man) had been confirmed, the tools can predict modification sites of only 3 sugar types. In this work, Fuc and Xyl modification sites were able to be predicted using the position-specific scoring matrix (PSSM). Moreover, about the sugar types difficult to discriminate by their primary sequences, structural characteristics for sugar type distinction were extracted.

2. Sugar type discrimination in *O*-glycosylation based on protein primary structures

Datasets of *O*-glycosylation modified sequence were obtained from Uniprot KB/Swiss-Prot 2012_06. Each sequence data was 21 amino acid lengths extracted the position between -10 to +10 around sugar modified sites. Representative sequences were extracted from clusters calculated by CD-HIT on the basis of 70% sequence similarity. The data was classified into 4 groups including GlcNAc (57 data), GalNAc (249), Fuc (12) and Xyl (71) according to the annotation of sugar types. Using PSSM calculated by position-specific amino acid propensities, discrimination accuracies of each sugar type in *O*-glycosylation were estimated in table 1.

Table 1. Discrimination accuracy of sugar types of O-glycosylation [1]

Sugar Type	Self-consistency test			5-fold cross-validation test		
	Sens. (%)	Spec. (%)	Success rate	Sens. (%)	Spec. (%)	Success rate
GlcNAc	87.7	53.2	0.683	37.7	34.7	0.355
GalNAc	97.6	83.8	0.904	91	77.2	0.838
Fucose	100	100	1	100	100	1
Xylose	97.2	98.6	0.979	82.2	93.9	0.875

According to Table 1, high accuracies were showed in Fuc and Xyl modification. Fuc modification sites had specific characteristic in amino acid propensities in the fact that there were a number of Cys residues. High propensities of negatively-charged residues were confirmed around Xyl modification sites. Therefore Fuc and Xyl datasets were able to discriminate clearly from other sugars using their primary sequences [2]. GlcNAc modification sites were difficult to discriminate from other sugar types by their primary sequences, especially.

3. Characteristics of protein secondarystructures around glycosylation site

Each glycosyltransferase for modification of each sugar type recognizes the Ser/Thr motifs. However the detail of the recognition mechanism of each glycosyltransferase has not been clarified. Glycosyltransferases are thought to also recognize factors except motif sequences. To clarify glycosylation

mechanism, the analysis taking into consideration the environment around glycosylation sites in addition to the amino acid sequences is required.

Dataset of mammalian proteins including crystal structures were extracted from Uniprot KB/Swiss-Prot 2013_04. Three-dimensional coordinates and secondary structure information of extracted proteins including 21 modification sites obtained from PDB and PDBFINDER2 calculated by DSSP, respectively. The propensities of the secondary structures were calculated based on each sugar type in *O*-glycosylation sites. Physicochemical characteristics of amino acids were classified into 4 groups, and the propensities of 4 groups were calculated based on each sugar type around *O*-glycosylation sites (shown in figure 2).

(a) GlcNAc

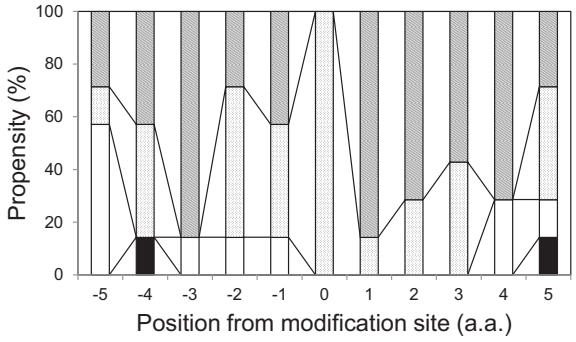

(b) Fuc

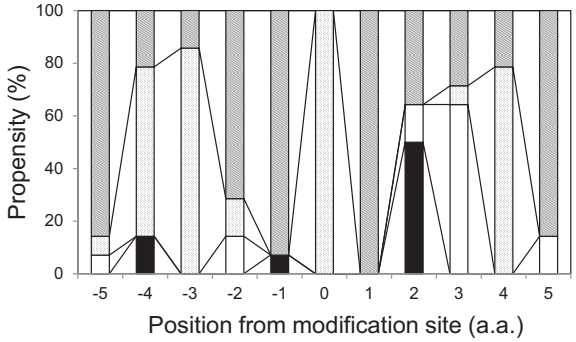

Fig. 2 Propensity of amino acid characteristics around GlcNAc (a) and Fuc (b) modification sites; Black, white, dotted and shaded bars show positively-charged (K, H, R), negatively-charged (D, E), hydrophilic (N, Q, S, T, Y) and hydrophobic residues (A, C, F, G, I, L, M, P, Y, W), respectively.

In figure 2, around GlcNAc modification sites, although many hydrophilic residues were found in the N-terminus side from modification site, hydrophobicity was higher in the C-terminus side from modification site. On the other hand, hydrophobic and hydrophilic residues appeared periodically around Fuc modification sites. Positively- and negatively-charged residues were found significantly in the position +2 and +3 in Fuc modification, respectively.

(a) GlcNAc

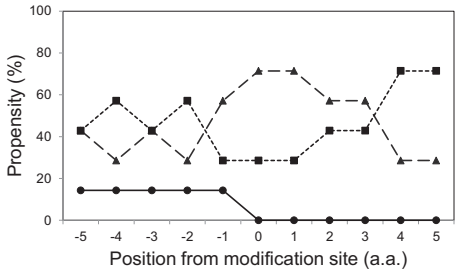

(b) Fuc

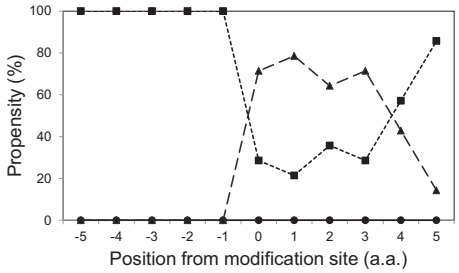

Fig. 3 Propensityof secondary structure around GlcNAc (a) and Fuc (b) modification sites; Circle, square andtrianglesymbols show helix, turn and strand structures, respectively.

Figure 3 shows the propensity of secondary structure around GlcNAc and Fuc modification sites. Strand, turn and small amount of helix structures appeared in front of GlcNAc modification sites. At the modification sites, while strand and turn structures were often observed, helix structures were rarely found. In particular, strand structural specificity was considered at the GlcNAc modification sites. Only turn structures were found before Fuc modification sites. Turn and strand structures were often found at the position 0. Helix structures did not appear around Fuc modification sites at all. Fuc modifications were observed in the region of turn structures connecting the edge of strand structures. The characteristics of secondary structures were found in each sugar type.

4. Concluding remarks

The method in this paper using PSSM could discriminate Fuc and Xyl modification sites with high accuracies. Using physicochemical property and secondary structure, GlcNAc and Fuc modification sites were suggested to be discriminated with higher accuracy.

Acknowledgement

This work was financially supported by KAKENHI Grant-in-Aid for Young Scientists (B) from Japan Society for the Promotion of Science (JSPS).

References

[1] K. Etchuya, Y. Mukai, J. Biomech. Sci. Eng., 8 (2013), 225-232.

[2] K. Etchuya, R. Nambu, Y. Mukai, Chem. Lett., 42 (2013), 1043-1045.

OS13: The Ninth International Students / Young Birds Seminar on Multi-Scale Flow

Tenth International Conference on Flow Dynamics
November 25-27, 2013, Sendai, Miyagi, Japan

Effects of Hydrostatic Pressure on Cell Cycle Progression and Morphology of Endothelial Cells

Kakeru Sato[1], Daisuke Yoshino[2], Takehiko Sato[2]
[1]Graduate School of Engineering, Tohoku University, 2-1-1 Katahira, Aoba, Sendai, Miyagi, 980-8577, Japan
[2]Institute of Fluid Science, Tohoku University, 2-1-1 Katahira, Aoba, Sendai, Miyagi, 980-8577, Japan
satok@plasma.ifs.tohoku.ac.jp

ABSTRACT

Hydrostatic pressure treatment has already been in widespread clinical use for promoting wound healing. Although angiogenesis of blood capillary may become a main factor for promoting wound healing, effects of hydrostatic pressure on angiogenesis are still unclear. In this study, we focus on the cell cycle and morphology of endothelial cells after applying hydrostatic pressure. Endothelial cells were exposed to ±50 mmHg by volume compression and expansion of the media for 6, 12, and 24 hours. The cell cycle was forcibly driven, and the morphology was unaffected by the hydrostatic pressure.

1. Introduction

In case of injuring human body, bleeding is caused by processes of skin laceration, tissue destruction, rapture of blood capillaries. Angiogenesis of capillaries and collagen synthesis by fibroblasts has important role in wound healing. Ubbink *et al*. have reported that wound healing was encouraged by a topical negative pressure (TNP) [1], and TNP has already been used in clinical site. In plastic surgery, it has been reported that binding of an artificial skin to a native skin was enhanced by exposing the grafted area to the negative pressure [2]. In these reports, promotion of capillary angiogenesis is considered to be an important factor in wound healing encouraged by the negative pressure. Although elucidation of the mechanisms of wound healing is required for development of wound healing technology, their details are still unclear.

Vascular endothelial cells (ECs), lining on the luminal wall of a blood vessels, change their morphology and regulate a variety of physiological functions of vessel wall in response to hemodynamic stimuli such as fluid shear stress and hydrostatic pressure in vivo. Although there have been many researches about cellular functions in response to tensile force and shear stress, knowledge of mechanical responses of ECs to hydrostatic pressure is still limited. Baldwin *et al.* have suggested that TNP encouraged proliferation and migration of ECs [3]. It has been reported that ECs were elongated in responses to the hydrostatic pressure, and the hydrostatic pressure suppressed the expression of VE-cadherin, which is known as a cell-cell junction protein [4].

In this study, we aim to reveal the mechanisms of angiogenesis promoted by negative pressure. We developed the a novel hydrostatic pressure exposure system by the liquid compression and expansion, and observed effects of hydrostatic pressure on cell cycle progression and morphological changes.

2. Methods

2.1. Cell culture and experimental setup

Human umbilical vein endothelial cells (HUVECs, Cell Applications) were cultured with M199 (Gibco) containing 20 % heat-inactivated fatal bovine serum (Gibco), 0.1 % Penicillin/Streptomycin (Gibco) and 10 μg/l human basic fibroblast growth factor (AUSTRAL Biologicals). The medium for experiment (EM) consists of Medium199 containing 10 % heat-inactivated fatal bovine serum and 0.1 % Penicillin/Streptomycin. HUVECs from 4th to 8th passages was cultured in 60 mm diameter dish (SUMIRON) pre-coated with 0.1 % bovine gelatin (Sigma-Aldrich), and used for experiments.

ECs were incubated at 37 °C under ±50 mmHg and 0 mmHg (control) by using hydrostatic pressure exposure system (Fig.1) for 6, 12 and 24 hours. The ECs were washed out two times and stationary cultured for an hour with EM to exclude the effect of the growth factor before experiments.

2.2. Cell cycle analysis

After hydrostatic pressure exposure, ECs were harvested from the dish by using 0.05 % Trypsine-EDTA (Gibco), and fixed with ice-cold 70 % ethanol after two times washing with PBS (-). Then the cell concentration of the sample was adjusted to 500 cells/μl. After staining the cells with Guava Cell Cycle Reagent (Millipore) 30 minutes, we analyzed the cell cycle using guava easyCyte^{TM} HT flow cytometer (Millipore).

2.3. Morphological analysis

After hydrostatic pressure exposure, ECs were fixed with methanol and rinsed two times with PBS (-). The ECs were observed with phase contrast inverted microscope (YASHIMA OPTICAL). To evaluate cell morphology, we measured aspect ratios and orientation angle of ECs using ImageJ program (National Institute

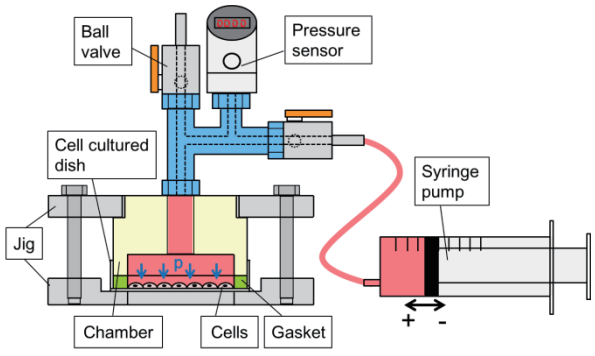

Fig. 1 Hydrostatic pressure exposure system consisting of a hydrostatic pressure chamber, a silicone gasket, cell cultured dish, a pressure sensor, valves, a syringe pump, and jigs

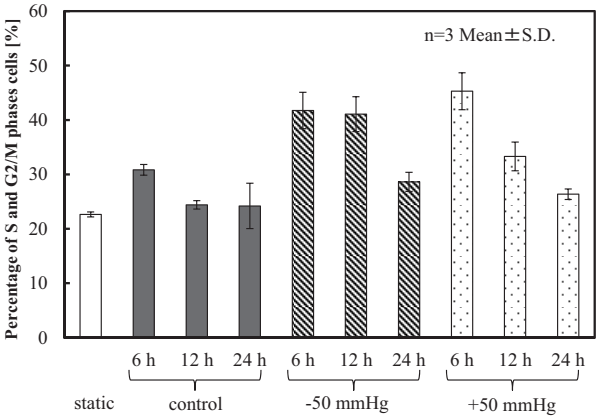

Fig. 2 Percentage of ECs in S and G2/M phases after hydrostatic pressure exposure, and temporal changes in the percentage

of Health). The aspect ratio was defined as the ratio between the minor and major axis of the approximated ellipse. The aspect ratio has a maximum value of 1 for a perfect circle and approaches zero for highly elongated shapes.

3. Results and Discussion

3.1. Effects of hydrostatic pressure on cell cycle progression

Figure 2 shows the percentage of ECs in S and G2/M phases after hydrostatic pressure exposure. The percentage of ECs in S and G2/M phases was 20% under the static condition, and the most of ECs existed in G1 phase. This result is similar to that of the control condition. On the other hand, after exposing ±50 mmHg, more than 40 % of ECs moved to S or G2/M phases after 6-hour pressure exposure. The rate of ECs in S and G2/M phases then decrease.

Cell cycle repeats to go through the phases of G1, S, G2, M. There are some checkpoints in the cell cycle, which monitor whether the cell cycle correctly progress or not. Confluent ECs normally express a growth inhibitory factor. Therefore the most of ECs remains in G1 phase. In this study, we confirmed that the cell cycle of ECs was forcible driven by hydrostatic pressure. Schwartz *et al.* have reported that the rate of HUVECs in S and G2/M phases increased after exposing to hydrostatic pressure of 4 cmH_2O [5]. The results in this study agree with their results. Toby *et al.* have suggested that cell proliferation was enhanced in hypoxia [6]. In this study, dissolved oxygen partial pressure change of EM is negligibly small, so the effects of hypoxia conditions on cell proliferation are negligible.

We confirmed promotion of cell cycle progression under hydrostatic pressure condition. This result suggests that the hydrostatic pressure affects phosphorylation of Rb protein and production of cyclin D1, which are associated with cell cycle progression.

3.2. Effects of hydrostatic pressure on morphology

Table 1 shows the cell aspect ratio and the orientation angle of ECs after exposure to the hydrostatic pressure. ECs maintained a monolayer. The aspect ratio was around 0.6 degree under every condition. Standard deviation of orientation angle was around 45 degrees in every condition. Therefore the cell orientation was random.

Table 1. Aspect ratio and orientation angle of ECs after hydrostatic pressure exposure (n=3, number of cell=75, Mean ± S.D.)

Experimental condition		Aspect ratio	Orientation angle [deg]
static		0.63 ± 0.14	-13.77 ± 49.62
control	6 h	0.63 ± 0.13	0.53 ± 43.60
	12 h	0.57 ± 0.16	0.32 ± 46.98
	24 h	0.66 ± 0.13	-9.00 ± 44.43
-50 mmHg	6 h	0.62 ± 0.15	7.07 ± 46.22
	12 h	0.61 ± 0.16	3.54 ± 41.66
	24 h	0.65 ± 0.10	-1.79 ± 46.63
+50 mmHg	6 h	0.57 ± 0.16	-17.69 ± 42.83
	12 h	0.63 ± 0.16	-5.23 ± 52.56
	24 h	0.60 ± 0.16	-4.52 ± 48.33

Morphological changes in ECs were not observed after exposure to hydrostatic pressure. Acevedo *et al.* have reported that bovine pulmonary artery endothelial cells were randomly oriented after exposure to hydrostatic pressure up to 12 mmHg [7]. The results in this study agree with their results.

4. Summary

In this study, HUVECs were exposed to hydrostatic pressure of ±50 mmHg and we analyzed the effect of hydrostatic pressure on cell cycle progression and morphological changes in ECs. As a result, promotion of the cell cycle progression by exposure to the hydrostatic pressure was confirmed. On the other hand, we confirmed no effect of the hydrostatic pressure on morphological changes in ECs. The results suggested that the hydrostatic pressure affects phosphorylation of Rb protein and production of cyclin D1, which are associated with the cell cycle progression.

References

[1] D.T. Ubbink, *et al*., Brit. J. Surg. **95** (2008), 685-692.
[2] J.A. Molnar, *et al*., Plast. Reconstr. Surg. **113**(5) (2004), 1339-1346.
[3] C. Baldwin, *et al*., Ann. Plast. Surg. **62**, (2007) 92–96.
[4] T. Ohashi, *et al*., J. Biomech. **40** (2007), 2399-2405.
[5] E.A. Schwartz, *et al*., Circ. Res. **84** (1999), 315-322.
[6] I.T. Toby, *et al*., Am. J. Physiol. - Lung Cell. Mol. Physiol. **298** (2010), 600-606.
[7] A.D. Acevedo, *et al*., J. Cell. Physiol. **157** (1993), 603-614.

Tenth International Conference on Flow Dynamics
November 25-27, 2013, Sendai, Miyagi, Japan

Experimental Study on Bubble-Liquid Flow through a Hole at the Bottom of Closed Tank

Takumu Tamaki, Yoshihiro Aoki , Tomonori Kitazume , Eiji Sakamoto and Tameo Nakanishi
Graduate School of Science and Engineering, Yamagata University
4-3-16 Jonan, Yonezawa-shi, Yamagata-ken, Japan
tht77002@st.yamagata-u.ac.jp

ABSTRACT

Experimental investigations on the bubble-liquid flow through a hole at the bottom of a sealed tank were conducted. The flow patterns were classified into three types; (a) single bubble periodically entering the tank without breaking, (b) bubble entering the tank and breaking into pieces, and (c) pattern (b) accompanying with biased instant swirl flow. The characteristics of the flow rate, the bubble volume, and the bubble entering period as to the water head and the hole diameter were disclosed. The flow rate was found slightly decreasing as to increasing water head, and approximately propositional to the cubic of the hole diameter.

1. Introduction

Fuel leakage from a sealed tank undergoing accidental conditions can cause serious pollution problems. Perforation may form on a tank surface being longtime exposed to inferior environment or in a sudden accident during transportation. The liquid inside the tank periodically flows out while the air flows in through the hole which generates intermittent bubble-liquid flow. In disaster prevention engineering, it is very important to understand the characteristics of the intermittent bubble-liquid flow through a hole of a sealed tank. The present study aims to clarify the mechanism of this flow using a transparent acrylic cylindrical sealed tank with bottom plates of different sized center hole.

2. Experimental Method

Figure 1 shows a picture of the experimental setup and its schematics.

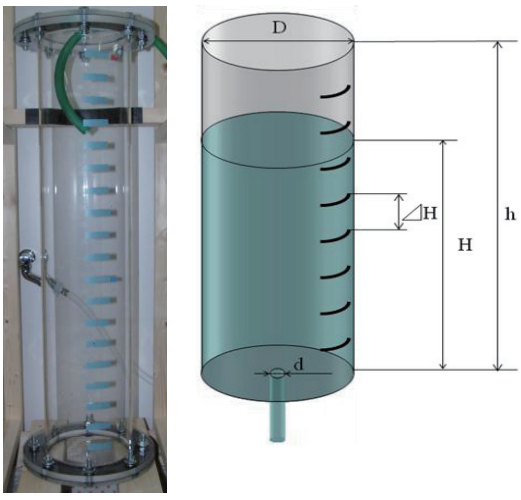

Fig. 1 Left: experimental setup, and Right: schematics

An acrylic cylindrical tank of height of h=1030mm and inner diameter of D=190mm is used. The tank is sealed by a openable top lid. The bottom part of the tank is designed that a circular stainless steel plate of diameter of D=190mm and thickness of 1mm with a center hole of diameter d is supported by a hollow acrylic plate. The heights from the bottom of the tank are marked every 50mm on the tank surface. Given H the water head and $\Delta H = 50$mm the scale, we measure the time ΔT elapsed as water descending one scale from the water head of H. The volume of the tank related to ΔH is $\Delta V = (\pi/4) D^2 \Delta H$.

Although the bubble-liquid flow exhibits an intermittent nature, we define the liquid mean flow rate through the hole by

$$Q = \Delta V / \Delta T \quad (1)$$

Knowing the liquid mean flow rate as a function of the hole diameter (d) and the water head (H) is of most important in an engineering point of view. We further define the mean velocity of the liquid flowing out of the hole by

$$\bar{u} = 4Q / \pi d^2 \quad (2)$$

It should be noted that since the bubble-liquid flow is intermittent and the air bubble can take a large fraction of the cross-sectional area of the hole, the realistic instant velocity of the liquid through the hole is typically much larger than the mean velocity.

By counting the number (n) of bubbles entering the tank from the hole during water descending of every scale from a water head H, the mean bubble entering period (T_b) and the mean bubble volume (V_b) are calculated by

$$T_b = \Delta T / n, \quad V_b = \Delta V / n \quad (3)$$

In the experiment, the tank is firstly fulfilled with water up to H=1100mm while blocking the outlet (i.e. the hole) and then sealed by the top lid. After sufficient rest time, the intermittent bubble-liquid flow is started by opening the outlet. A video camera is used to record the flow. Measurements are made for water head (H) ranging from 950mm to 400mm. The experiment is conducted for the cases of hole diameter of d=10, 12, 15, 20 [mm]. Every experiment is repeated five times. The data are collected for averages of the repeated experiments.

3. Results and Discussions

Fig.2 Typical patterns of intermittent bubble-liquid flow

Figure 2 shows typical patterns of the intermittent

bubble-liquid flow through the hole and inside the tank. The flow patterns may be classified into three types; (a) bubbles periodically entering and rising inside the tank without breaking into pieces, (b) bubbles entering the tank and breaking into pieces while detaching from the hole inside the tank, and (c) flow pattern of (b) accompanying with biased instant swirl flow. Type (a) flow pattern appears when the hole diameter (d) is small (typically $d \leq 12$mm) and the water head (H) is considerably high. Type (b) takes shape when $d > 12$mm and/or the water head becomes low. Type (c) is seen in further larger hole diameter cases.

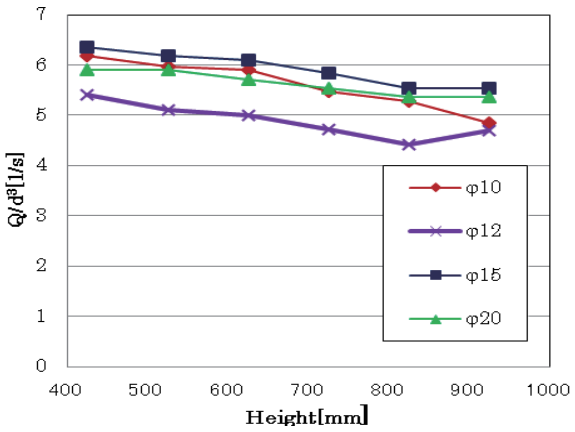

Fig.3 Q/d^3 versus water head H

Figure 3 shows Q/d^3 versus water head H. The flow rate slightly decreases as to increasing water head, which is expected to finally approach a constant. This behavior is completely different from that of the flow from an outlet of an open tank, where the flow rate is propositional to $\sqrt{2gH}$. In the case of an intermittent bubble-liquid flow through a single hole (inlet/outlet) of a sealed tank, the volume of air entering the tank replaces the volume of liquid flowing out of it, which prevents the conversion of the whole water head (H) into the velocity head. The potential head that can be transformed into the velocity head should be approximately the height (h_b) of the bubble rising through the hole. Thus the instant downward velocity of the liquid may be expressed by $u \approx \sqrt{2gh_b}$. The height (h_b) of the bubble depends on the hole diameter (d), the surface tension (σ [N/m]), the oscillation amplitude of the water surface caused by the rupture of bubbles there and thus the water head (H).

Assuming a hemisphere of air volume is about to enter the bottom hole of the tank to replace the liquid volume, the smallest hole diameter ($d_{\min}$) that the bubble can rise through the hole and thus triggers an intermittent bubble-liquid flow is calculated by

$$d_{\min} = 2\sqrt{3\sigma/\rho g} \qquad (4)$$

where ρ is the density of the liquid and $g = 9.8\text{m/s}^2$ is the acceleration of gravity. For the case of water/air system where $\sigma = 72.75$mN/m, we have $d_{\min} = 9.44$mm.

For a hole diameter d slightly larger than $d_{\min}$, we may reasonably assume $h_b = d/2$, which leads to $u \approx \sqrt{gd}$. We then obtain a theoretical estimation for these cases that $Q \propto \sqrt{d} \cdot d^2 = d^{2.5}$. The measured flow rates, however, is more propositional to d^3 than $d^{2.5}$ that Q/d^3 plotted in Fig.3 for different hole diameters except for that of d=12mm possess almost the same value. The disagreement seen in the later case may be caused by some unrevealed flow pattern transition that needs further investigation.

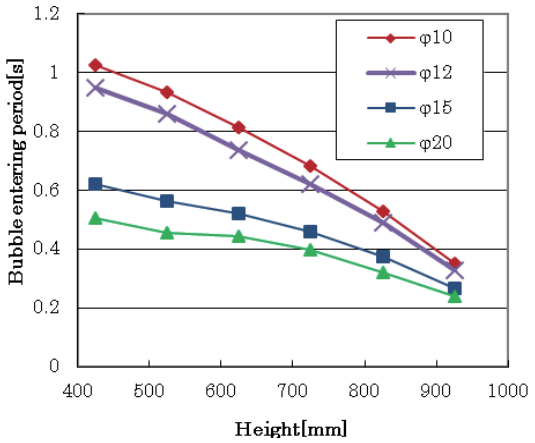

Fig.4 Mean bubble entering period versus water head H

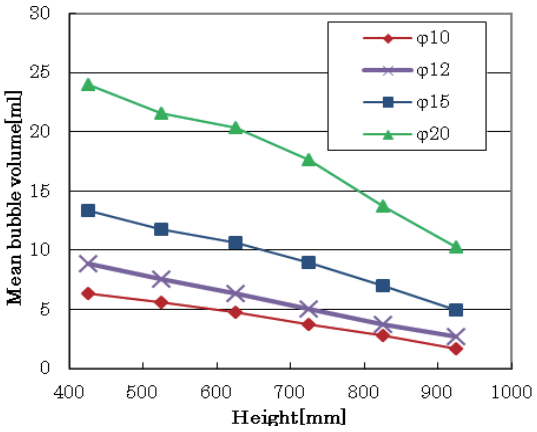

Fig.5 Mean bubble volume versus water head H

Figures 4 and 5 respectively show the mean bubble entering period T_b and the mean bubble volume V_b versus the water head H. Both quantities increase as to decreasing water head. This may be explained like that the oscillation amplitude of the water surface caused by the rupture of bubbles becomes greater at a smaller water head, which leads to a larger bubble volume and a longer bubble entering period. Lastly, mean bubble volume versus water head exhibits an almost linear correlation.

4. Concluding Remarks

The bubble-liquid flow through a hole at the bottom of a sealed tank was investigated. The flow patterns were classified into three types. The characteristics of the flow rate, the bubble volume, and the bubble entering period as to the water head and the hole diameter were disclosed.

Reference

[1] M. I. Kohira, N. Magome, H. Kitahata and K.Yoshikawa (2007) "Plastic Bottle Oscillator: Rhythmicity and Mode Bifurcation of Fluid Flow," *Am. J.phys.* ,75 , pp-893-895

Cavitation Generation near Narrow Container Walls Induced by Underwater Explosion

Taketoshi Koita[1], Mingyu Sun[2]
[1] Graduate School of Engineering, Tohoku University, 6-3 Aoba, Aramaki aza, Aoba-ku, Sendai 980-8578, Japan
[2] Institute of Fluid Science, Tohoku University, 2-1-1 Katahira, Aoba-ku, Sendai 980-8577, Japan
koita@shock.ifs.tohoku.ac.jp

ABSTRACT

The generation of cavitation behind the underwater shock induced by the underwater explosion in a narrow container clamped by the optical acrylic glass was discussed experimentally and theoretically. The propagation of underwater shock wave and cavitation generation were clarified by the visualization from the front and side of the container. The pressure distribution in the container was measured. The displacement of acrylic glass deformation caused by the impact pressure of the shock was estimated with the acoustic riemann solver. Cavitation was generated near the glass wall of container behind the underwater shock wave reflected at the wall.

1. Introduction

In order to simulate numerically the formation of the water jet induced by underwater explosion in a narrow pipe such as a jet knife in the medicine, it is need to calculate the energy conversion rate of the explosion to set up the initial condition. In our previous study of calculation of the conversion rate, cavitation generated after the explosion and after the primary bubble rebound were observed experimentally in a narrow container [1]. Numerical calculations however indicated that the pressure in the region of these cavitation is higher than the saturated vapor pressure [2]. Underwater explosion phenomena in the water tank have been studied [3]. However, these cavitation after the explosion and the bubble rebound have not been reported in the tank.

The purpose of the this study is to investigate the generation of cavitation after the explosion and after the primary bubble rebound in the narrow container. In the narrow container, the underwater shock wave induced by the explosion interacts with container walls because of the small thickness of container. Therefore, in order to clarify the generation of the cavitation, the propagation of underwater shock wave and cavitation phenomena were visualized from the front and side of the container. The pressure distribution of the cavitation zone was measured. The displacement of the wall deformation of the container caused by the impact pressure of the shock was estimated with the acoustic riemann solver. The generation mechanism of the cavitation is discussed experimentally and theoretically.

2. Method

Figure 1 shows a narrow container employed as the test section. Two sides are clamped by two optical windows which are made of 10mm thick acrylic glass. The thickness of container is 5mm. In order to elucidate the behavior of underwater shock wave and cavitation, we visualized these phenomena from the front direction and side direction of the container. Two side walls are made of stainless steel in the visualization from the front direction and that is changed to acrylic glass in the case of it from the side direction. The purified water is filled up the container. The experimental set up and optical arrangement are shown in figure 2. Underwater explosion is created with a high voltage electric discharge. Capacity C is 0.2 μF. The voltages power, V = 4.5kV, is tested and its corresponding energy Ee is 2.25J. When the circuit is triggered manually, the electric discharge is instantly generated, then underwater shock wave is formed. Underwater shock wave and cavitation are visualized by the shadowgraph method. A high-speed video camera, Phantom V7.3, recorded images with 1.0×10^5 frames per second at its exposure time of 2 μsec. The visualized region is 96mm×96mm around the electrode. Pressure is measured by a PVDF needle hydrophone located at 30mm vertically from the electrode in the center of the container.

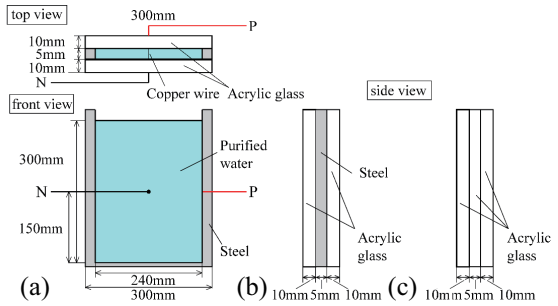

Fig.1 Schematic diagram of the test section, narrow container, (a) the front and top view, (b) the side view at visualization from front direction, (c) the side view at visualization from side direction

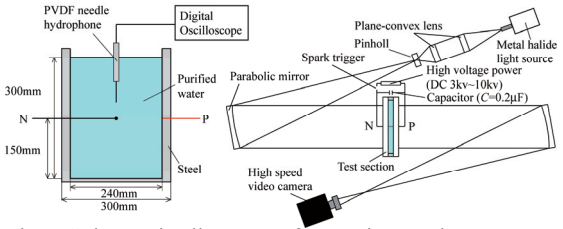

Fig.2 Schematic diagram of experimental arrangement

3. Results and Discussion

Figure 3 presents sequential images visualized from the front direction of the container. The multiple waves propagate due to the reflection of the underwater shock wave (SW) from the glass wall because of the narrow container. In Fig. 3, cavitating bubbles appeared behind the multiple waves at t = 32.67μs and the cavitation zone grows with the passage of the waves. After that, the primary bubble grows, collapses and rebounds. Cavitation also appeared behind the shock wave emitted by the bubble rebound [4]. Figure 4 (a) and (b) show the

pressure histories of the arrival of the shock wave created by the discharge and the shock emitted by the collapse of the primary bubble, respectively. The pressure value in the center of the container at the timing of cavitation generation after the discharge and the bubble rebound is higher than the saturated vapor pressure in Fig. 4(a) and (b). In order to investigate the generation mechanism of these cavitation, we visualized these phenomena from the side direction of the container. Sequential images of the side view are presented in Figure 5. The cavitation is generated near the acrylic glass behind the multiple wave after the discharge in Fig. 5(b). The image after the bubble rebound in Fig. 5(d) also shows that the cavitation appears near the glass wall. The possible reason for the generation of these cavitation is the pressure drop near the glass wall caused by the interaction of the underwater shock wave with the wall. When the underwater shock wave interacts with the acrylic glass wall of the container, the wall is elastically deformed by the impact pressure of the underwater shock wave. Figure 6(a) is the schematic diagram of elastic deformation of the wall. In Fig. 6(a), δ is the displacement of the acrylic glass deformation.

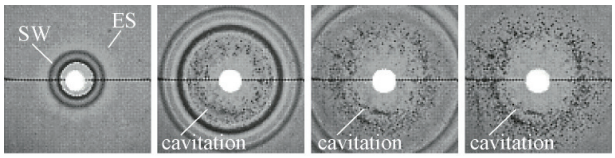

(a)t=12.67μs (b)t=32.67μs (c) t=52.67μs (d) t=72.67μs

Fig.3 Sequential shadow images of underwater shock wave propagation and generation of cavitation after underwater electric discharge at V = 4.5kV.

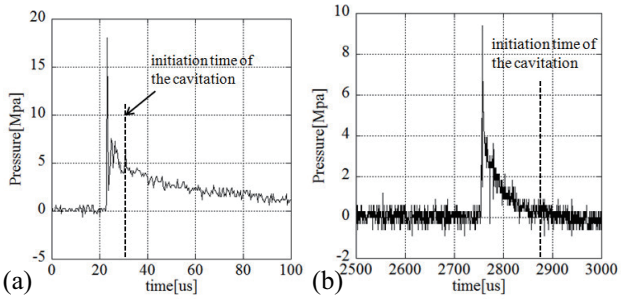

(a) (b)

Fig.4 Pressure histories (a) of shock wave generated by electric discharge, (b) of shock wave generated by the rebound of primary bubble collapse

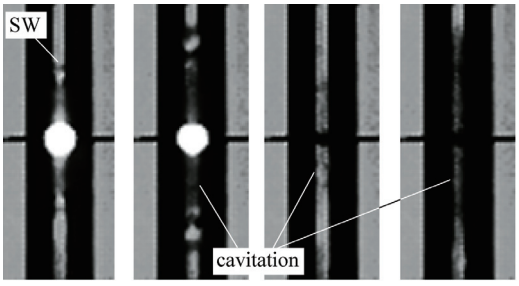

(a) t=26.0μs (b) t=36.0μs (c) t=2.496ms (d) t=2.506ms

Fig.5 Sequential images of the generation of cavitation (a)(b) after the underwater explosion, (c)(d) after the primary bubble rebound at V = 4.5kV.

Pressure of contact surface between the water and the acrylic glass induced by shock wave propagation, P^*, is described by the acoustic linearized riemann solver [5],

$$P^* = P_L - I_L(u_n^* - u_L) \quad (1)$$

$$P^* = P_R - I_R(u_n^* - u_R) \quad (2)$$

where u_n^* is the interface normal velocity and P, I, u represent respectively pressure, acoustic impedance and velocity. Index L and R are the left and right side of the interface as shown in Fig. 6(b). At the interface, u_L = 0 and u_n^* can be approximated as following,

$$u_n^* \sim \delta/\Delta t \quad (3)$$

where Δt is the initiation time of the cavitation. Thus, the displacement of the glass is calculated as following,

$$\delta = \frac{\Delta t}{I_L}(P_L - P^*) \quad (4)$$

By substituting averaged pressure P_L = 5MPa and Δt = 30μs obtained from sequential images in Fig. 3 and pressure histories in Fig.4(a) into the equation (4), when P^* becomes the saturated vapor pressure, δ is 99.95μm. In this study, when the displacement of micro meter order in the acrylic glass wall of the container is formed by the elastic deformation occurred by the interaction of the underwater shock wave, cavitation is generated due to the pressure drop near the wall.

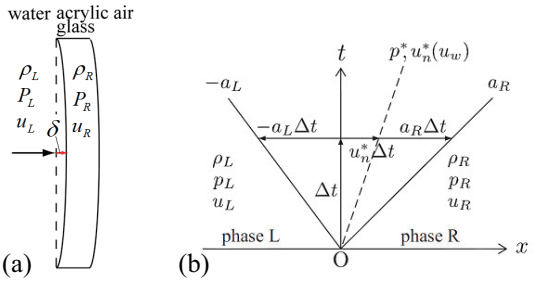

(a) (b)

Fig.6 Schematic diagram of (a) elastic deformation of the acrylic glass wall, (b) calculation of pressure and velocity at interfaces

4. Concluding remarks

The generation of cavitation caused by the underwater explosion in a narrow container was studied experimentally and theoretically. Cavitation appeared near the acrylic glass wall of the container behind the multiple waves after the explosion and the emitted shock wave after the primary bubble rebound.

References

[1] T. Koita, M. Sun, Proc. Japanese Symposium on Shock Waves 2011, (2011), pp. 191-194.

[2] T. Koita, M. Sun, 25th Symposium on CFD, Japan, (2011), **C7-3**.

[3] V. K. Kedrinskii, "Hydrodynamics of Explosion", Springer, (2005).

[4] T. Koita, M. Sun, 29th International Symposium on Shock Waves, (2013), No. **0246-000204**.

[5] R. Saurel, F. Petitpas and R. A. Berry, J. Comput. Phys. **228** (2009), pp. 1678-1712.

Tenth International Conference on Flow Dynamics
November 25-27, 2013, Sendai, Miyagi, Japan

Interaction between Incident Shock Wave and Combustion Downstream of Ramp Injector in Supersonic Flow

Yoshitaka Iwamura, Tatsuya Yamaguchi, Taku Kudo, Akihiro Hayakawa and Hideaki Kobayashi
Institute of Fluid Science, Tohoku University, 2-1-1 Katahira, Aoba-ku, Sendai, Miyagi 980-8577, Japan
iwamura@flame.ifs.tohoku.ac.jp

ABSTRACT

Experiments and numerical simulations were conducted to explore the interaction between an incident shock wave and flames downstream of a ramp injector. The experimental results showed that when incident shock wave is introduced to combustion region, flame-holding region appeared downstream of the incident shock wave. Numerical simulations implied that the mechanism of the observed phenomena lies in the increased reaction rate due to increased static pressure, enhanced mixing due to the strengthened vortices behind the incident shock wave, as well as decreased heat loss to the wall due to an uplift of the jet flow.

1. Introduction

A hypersonic air-breathing propulsion system called SCRAMJET engine enables flight at supersonic speed. This engine will be employed in a single-stage-to-orbit hypersonic vehicle. There are still many problems to be solved. Since the residence time of inlet air in a SCRAMJET combustor is on the order of 1 millisecond, stabilization of flames is difficult. Besides, the existence of many shock waves affects the flow field in a SCRAMJET combustor. In order to realize this engine, efficient fuel injection and mixing are essential. To tackle these problems, various types of fuel injection system have been investigated. Ramp injector is expected to have advantages of the typical fuel injection in parallel and traverse injections toward the mainstream. It strengthens mixing performance by the effect of vertical vortices generated from its leading edge of the ramp without losing total pressure of the mainstream. A schematic of the flow field with an incident shock wave is shown in Fig. 1. The objective of this study was to investigate the interaction between an incident shock wave and the flame holding region in a ramp injector experimentally and numerically.

2. Experimental setup and Procedure

A schematic of the ramp injection device is shown Fig. 1. It has a d = 3.57 mm circular injection hole. The injection surface geometry is 10-mm-square. The most important items in the layout of the ramp injector are ramp angle and geometry of the injection surface. Namely, when the vortex Reynolds number is no less than the order of 10^4, a turbulent mixing region is expected to be formed downstream of the ramp injector [1]. This ramp injector is set in the test section at +2 degrees in the direction of the airstream to prevent boundary layer separation upstream of the ramp. The shock generator was wedge-shaped and its deflection angle was 6 degrees. This was hang on the upside of the test section.

The flow field was visualized by the Schlieren method. When the mach number of the air stream reaches 2.5, fuel rich pre-burnt hydrogen and air mixture was injected from the injection hole. The equivalence ratio was fixed at approximately ϕ = 3.6 for the combustion experiments. The flame-holding regions were identified by a CCD camera.

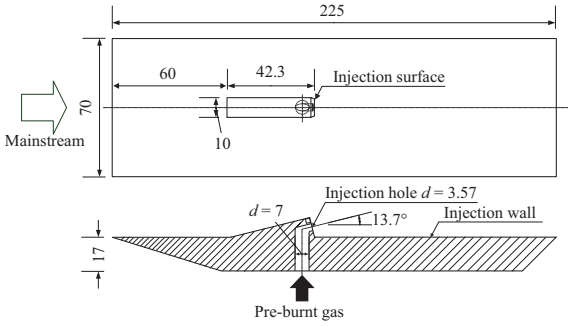

Fig. 1 Schematics of the ramp injector.

3. Method of the numerical simulation

Numerical simulations at uniform condition for a three-dimensional flow field were performed using FLUENT. Three-dimensional compressive Reynolds Averaged Navier-Stokes (RANS) equations were used as governing equations in this study. These equations were solved using the finite volume method. Wilcox's k-ω two-equation turbulence model was used [2]. In order to fit to the actual experimental conditions, the mach number, total pressure and total temperature of the main stream were set to 2.5, 0.5 MPa and 673 K, respectively. High-temperature air as an ideal gas was injected from a ramp injector. The numerical grid was designed in accordance with the actual dimensions of the ramp injector and shock generator. Once the mainstream reaches the mach number at the inlet of numerical region, shock wave is introduced simply because of the generator's deflection angle.

4. Results and Discussion

4.1 Experimental results

Combustion experiments were conducted under three conditions. In order to obtain reference results for experiments with the shock generator, experiments without a shock generator were conducted as shown in Fig. 2 (a). Figure 2 (b) shows the result with the shock generator fixed at the furthest downstream set point, which is located 20 mm downstream of the furthest upstream set point. Figure 2 (c) shows the result with the shock generator fixed at the furthest upstream set point.

In each condition, fuel rich pre-burnt gas of hydrogen and air was injected from the injection hole at the pressure of 0.6 MPa. The equivalence ratio was fixed at approximately ϕ = 3.6. In the result without the shock

wave, no apparent flame-holding region with strong luminescence was observed, while in the results with a shock wave, a flame-holding region was observed immediately downstream of the shock wave. This phenomenon was similarly observed even if the location of shock generator was changed.

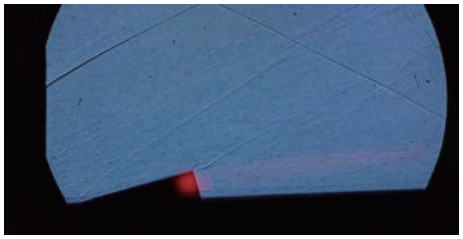

(a) Without shock generator

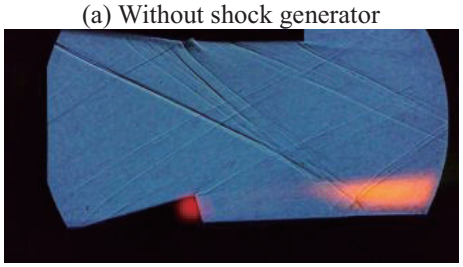

(b) With shock generator at downstream set point

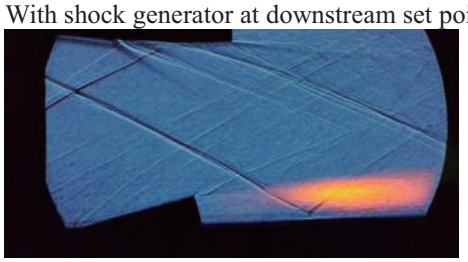

(c) With shock generator at upstream set point

Fig. 2 Flame emission and shock wave images.

4.2 Numerical results

Three-dimensional numerical simulations with an air injection at high-temperature were conducted at uniform condition and the phenomena observed in the experiment were analyzed based on these numerical results in terms of the flow field. A coordinate origin was set at the bottom of the injection surface on the z-centerline. Comparisons were made between the results without a shock wave (a) and those with a shock generator fixed at the furthest upstream set point (b).

Figure 3 shows numerical results of static pressure with streamlines on the x-y surface located on the centerline of the z axis. From Fig. 3, the mainstream is compressed downstream of the shock wave, which is expected to enhance the reaction of injected hydrogen. The pressure gradient was formed downstream of the shock wave in the direction of the y-axis, which induced an uplift effect of the jet flow.

Regardless of the existence of incident shock waves, the streamline was uplifted behind the injection surface, whereas on the plane spacing 15 mm from the centerline, the streamlines lie parallel to the wall. From this numerical result, it is expected that the upward velocity component would be induced due to counter rotating vortex motion formed behind the ramp injector. Besides, in addition to the effect of counter-rotating vortex motion, in the case with an incident shock wave, it is seen that the streamline bends upward due to the pressure gradient behind the shock wave, leading to decreased heat loss of the jet flow to the wall.

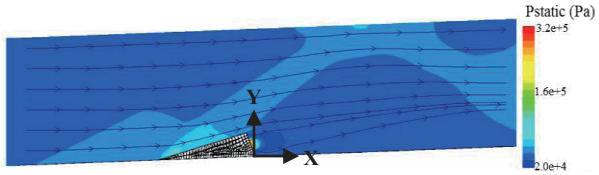

(a)

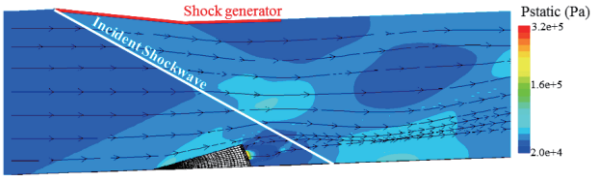

(b)

Fig. 3 Profiles of static pressure with streamlines.

Figure 4 shows x-vortices on the 3 points of contour surface. The shock wave incident point is x = 40 mm. From Fig. 4, it is indicated that vortices were strengthened downstream of the shock wave. It is seen that mixing of the jet flow was strengthened due to vortices generated downstream of the shock wave.

Contour point (x-axis)	Without shock generator	With shock generator
10 mm	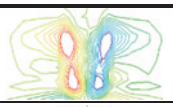	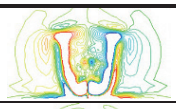
50 mm	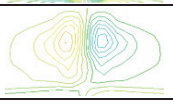	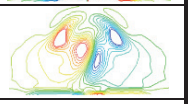
100 mm		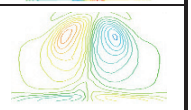

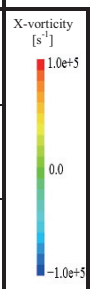

Fig. 4 Profiles of X-vortices.

5. Concluding remarks

In this study, the interaction between the incident shock wave and the flame holding region downstream of a ramp injector was investigated experimentally and numerically. A flame-holding region was observed only downstream of the incident shock wave. From the numerical results, the following mechanisms were expected for enhanced flame-holding; 1) increased reaction rate due to increased static pressure, 2) decreased heat loss to the wall due to an uplift of the jet flow, 3) enhanced mixing due to the strengthened vortices behind the incident shock wave.

References

[1] P. E. Dimotakis, The mixing transition in turbulent flows, J. Fluid Mech. vol. 409(2000) 69-98.

[2] D. C. Wilcox, Turbulence Modeling for CFD, 2nd ed., DCW Industries (1998).

Tenth International Conference on Flow Dynamics
November 25-27, 2013, Sendai, Miyagi, Japan

Status Report on the Development of the 0.3-m Magnetic Suspension and Balance System

Kohei Kakizaki, Daiju Numata and Keisuke Asai
Department of Aerospace Engineering, Graduate School of Engineering, Tohoku University
6-6-01 Aramaki Aza Aoba, Aoba-ku, Sendai, Miyagi, 980-8579 JAPAN
kakizaki.kohei@aero.mech.tohoku.ac.jp

ABSTRACT

The objective of this research is to develop a simulator of the 0.3-m Magnetic Suspension and Balance System (MSBS) in order to apply it to dynamic wind-tunnel testing. We measured internal resistance and inductance of coils and intensity of magnetic fields to understand the specific characteristics of coil systems and use them to develop the simulator. The result of inductance measurement of the lift coil indicates that the response time of current passing through the coil is about 0.12sec. It is necessary to take into account of this response time because it leads to control delay when conducting a dynamic test at this MSBS.

1. Introduction

High-performance aircraft is demanded to achieve severe tasks in a variety of fields. In such a flight, a dynamic effect significantly influences flight condition of the aircrafts. Therefore, it is necessary to develop nonlinear flight dynamics that includes the effects of unsteady aerodynamics. The dynamic wind-tunnel testing (DWT) is a wind tunnel testing method to study nonlinear aerodynamic behavior of the aircraft by oscillating or moving a test model. Currently, DWT uses various types of bulky support system that can bear model weight, inertia force and aerodynamic force. The flow interference between the model and the support significantly degrades the measurement accuracy of DWT.

In order to solve these problems, Magnetic Suspension and Balance System (MSBS) that can support a model in airflow by magnetic force has been conceived [1]. MSBS has several features different from the other support apparatus. The first feature is that MSBS has no support interference. The second feature is that it can measure aerodynamic force acting model from back calculation of current value. The third feature is that it is possible to present a motion, at the maximum, in six degree of freedom.

The objective of this research is to develop a simulator of the 0.3-m MSBS at the Tohoku University in order to apply it to dynamic wind-tunnel testing. Similar work has been done previously [2], but our goal is to create a simulator to understand the behavior of the model under unsteady aerodynamic condition. In this paper, the status of measurement of characteristics of coils and magnetic forces are presented for discussion on the performance of the 0.3-m MSBS for dynamic testing.

2. The 0.3-m MSBS

2.1. Configuration of MSBS

The 0.3m MSBS is designed for use in a low-speed wind tunnel and has a 0.3 m x 0.3 m square test section. This MSBS consists of the following five components.

(1) Levitating model
(2) Coil system
(3) Power unit and amplifier system
(4) Optical sensors
(5) Control system

Figure 1 shows a schematic of coil configuration of the 0.3-m MSBS. The coordinate system of the MSBS is also shown in the same figure. The coil system consists of eight electromagnets and two air-cored coils. The details of the coils are listed in Table 1.

Table 1 The detail of coils

Drag coils (#0, #9)	150 [turns]
Lift coils (#1, #3, #5, #7)	320 [turns]
Side coils (#2,#4, #6, #8)	100 [turns]

The levitating model is a cylinder model weighing 504g. The force and moment act on the magnet of the model in a magnetic field generated by MSBS. The model is suspended against aerodynamic force and moment and gravity force. In order to understand the behavior of a model performing unsteady motion, it is necessary to evaluate parameters for each coil that are required for controlling the model.

2.2. Magnetic force and moment control

Magnetic force, F, and moment, N, acting a model in MSBS can be evaluated by the following expressions, Eq. (1).

$$F = \int_V (M \cdot \nabla) H dV, \qquad N = \int_V M \times H dV, \tag{1}$$

Here, M indicates the magnetic moment of the model and H indicates magnetic-field intensity around the model. By applying current to each coil, magnetic field is created to control position and attitude of the model. For example, lift force is needed to sustain gravity force acting on the model, even at no-wind condition. Lift force F_z is expressed by Eq. (2).

$$F_z = M_x \frac{\partial H_z}{\partial x}, \tag{2}$$

F_z can be controlled by adjusting the derivative of H_z. Currents through #1, #3, #5 and #7 coils are controlled to generate H_z and its x derivative.

3. Description of Experiment

3.1 Measurement of characteristics of coils

The purpose of this test is to measure internal resistance and inductance of each coil and to estimate the response time. The coil circuit of MSBS can be

considered simply as an RC circuit. The internal resistance and inductance was determined by measuring a transfer function of voltage and current in the circuit using an FFT analyzer. The test parameters listed in Table 2.

Table 2 Test parameters

Sweep frequency[Hz]	0.1~50
Input voltage $V_{p\text{-}p}$ [V]	0.2
Sweep time [sec]	10
Average number of FFT [times]	50

3.2 Measurement of magnetic fields

The purpose of this test is to measure the intensity of magnetic fields and to calculate the amount of current necessary to levitate a model. The same current passed through each coil and the magnetic field was formed. To measure magnetic intensity distribution, a Gauss meter was moved by a traverse device ranging $-100 < x < 100$ [mm], every 20 [mm].

4. Result and Discussions

Figure 2 shows the result of internal resistance for each coil. The internal resistance increases non-linearly as the frequency increases. The reason for this is the influence of magnetization of magnetic materials around the coils. The internal resistance of the lift coils (#1, #3, #5, #7) is greater than that of the side and drag coils. This is because the number of turns of the lift coil is greater than that of the side and drag coils.

Figure 3 shows measured inductance of each coil and the inductance are proportional to angular velocity. The internal resistance and inductance of the lift coil are listed in Table 3.

Table 3 Internal resistance and inductance of lift coils

Coil number	#1	#3	#5	#7
Internal resistance [mΩ]	1439.2	1443.3	1410.5	1539.9
Inductance [mH]	38.2	37.6	37.1	38.4

We estimate the response time of current passing through from the result of the lift coils and it is about 0.12 sec. It is necessary to take into this response time when we conduct a dynamic test in this MSBS, because this result introduces control delay.

Figure 4 shows the specific z-components of H per unit lift current (I_{lift}), h_z, vs. x for ten different lift currents. The all data show in fairly good agreement. Since the error becomes larger for smaller current, the data for smaller current do not match with the other results. The x derivatives h_z is independent of I_{lift} and has a constant gradient around the model center. The result show that the amount of current required for levitation of the model is 9.0 A.

4. Concluding remarks

To develop a simulator of the 0.3-m MSBS system for dynamic wind-tunnel testing, we measured parameters of the coil system of the 0.3-m MSBS. We measured internal resistance and inductance of each coil. The response time of the lift coils were estimated to be about 0.12 sec. We also measured the intensity of magnetic field. The result indicates that the amount of a current necessary for levitation of the model is 9.0A.

References

[1] H. Sawada et al., "NAL 60cm Magnetic Suspension and balance System", The 24th international Congress of the Aeronautical Sciences, Yokohama, Japan, 29 August - 3 September, 2004

[2] Dong-Kyu Lee et al., "Status of MSBS Study at KAIST", The 21th International Conference on Magnetically Levitated Systems and Linear Drives, Daejeon, Korea, 10-13 October, 2011

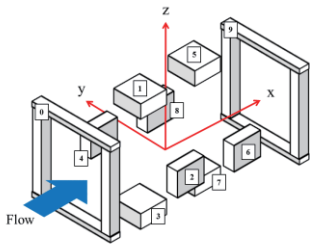

Fig.1 Configuration of coil system

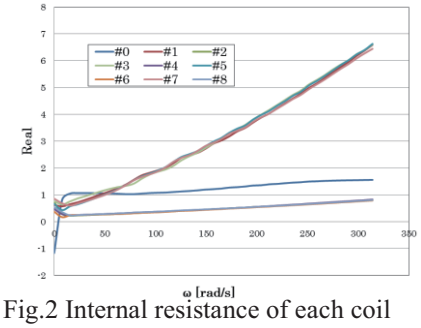

Fig.2 Internal resistance of each coil

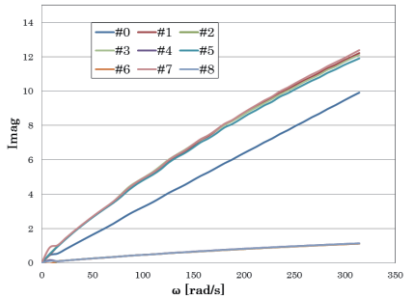

Fig.3 Inductance of each coil

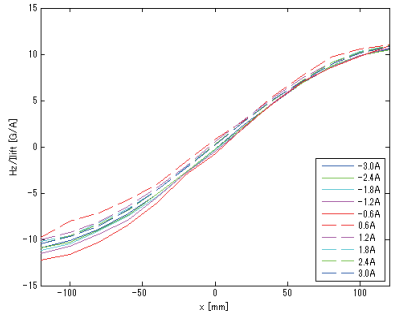

Fig.4 h_z vs. x in lift current change

Tenth International Conference on Flow Dynamics
November 25-27, 2013, Sendai, Miyagi, Japan

SPH Simulation of Liquid Droplet Behavior on a Water-repellent Surface

Masumi Ito, Masaya Shigeta, Seiichiro Izawa and Yu Fukunishi
Department of Mechanical Systems and Design, Graduate School of Engineering, Tohoku University
6-6-01 Aramaki-Aoba, Aoba-ku, Sendai, Miyagi, Japan
masumi@fluid.mech.tohoku.ac.jp.

ABSTRACT

The deformation of a droplet colliding with the wall surface is computed by an incompressible SPH method. The surface tension is modeled by adding attractive forces between both solid and liquid particles. The attractive force depends on spreading coefficient, surface tension coefficient, and the distance between particles. The simulation results appear to be reasonable, in which the droplet behavior strongly depends on the spreading coefficient.

1. Introduction

Smoothed Particle Hydrodynamics (SPH) is a Lagrangian-based method to simulate a fluid motion without a grid. The fluid motion is represented by the behavior of particles that move according to their respective motion equations which include interactions. SPH has several advantages over other grid-based methods, and one of which is the easiness in handling of the deformable free surface of a liquid body.

In a computation of deforming phenomenon of a liquid droplet that touches a solid wall, it is important not only to implement the effect of the surface tension but also to take into account the "wettability" of the material (the spreading character of the liquid on the wall). When the geometry of the liquid body is dynamically changed by the surface tension, the deforming behavior is clearly influenced by the wettability.

In general, the effect of surface tension is implemented into a Lagrangian method by employing a Laplace pressure model or an attractive force model. The former model needs to estimate a curvature of a liquid surface, sacrificing significant amount of computational time. And, this model is not suitable for a liquid-solid contacting phenomena computations, because the curvature is indefinable at the contact line. On the other hand, the latter model is simple, and also can easily compute the surface tension effect which includes the wettability effect.[1]

So, in this study, dynamic deforming phenomena of a droplet that collides against a solid surface are simulated by an incompressible SPH method together with an attractive force model.

2. Numerical Method

2.1 Model Description

In our computation, the mass distribution of each particle is given as a continuous function of Kernel W, so the density distribution at a particle position is expressed as

$$\rho_a = \rho(\boldsymbol{r}_a) = \sum_b m_b W_{ab} = m \sum_b W(|\boldsymbol{r}_b - \boldsymbol{r}_a|), \quad (1)$$

where a and b denote the particle indices, $\boldsymbol{r}$ is the position of a particle, and m is the mass of a particle. Then, the momentum equation is expressed as

$$\frac{\mathrm{D}\boldsymbol{u}_a}{\mathrm{D}t} = -\sum_b \left(\frac{p_a}{{\rho_a}^2} + \frac{p_b}{{\rho_b}^2} \right) m_b \nabla_a W_{ab} + \frac{6\mu}{\lambda_a \rho_a} \sum_b (\boldsymbol{u}_b - \boldsymbol{u}_a) W_{ab} + \frac{\boldsymbol{F}}{m_a}, \quad (2)$$

$$\lambda_a = \sum_b |\boldsymbol{r}_b - \boldsymbol{r}_a|^2 W_{ab}, \quad (3)$$

where $\boldsymbol{u}$ is the velocity, t is the time, p is the pressure, μ is the viscous coefficient, and $\boldsymbol{F}$ is the external driving force. The first term of the right hand side in Eq. (2) represents the pressure gradient. The second term is the same as the Laplacian viscosity model which is normally used in MPS method, which is another particle method. The external force consists of the surface tension and the gravity. The detailed description of the current SPH method can be found in Ref. [2].

2.2 Treatment of Surface Tension

The driving force caused by the surface tension is expressed by adding the attracting force $\boldsymbol{F}^{\mathrm{attract}}$ which includes a weighting function f:

$$\boldsymbol{F}_{ab}^{\mathrm{attract}} = d\alpha \sum_b \Gamma_{ab} f_{ab} \frac{\boldsymbol{r}_b - \boldsymbol{r}_a}{|\boldsymbol{r}_b - \boldsymbol{r}_a|}, \quad (4)$$

$$\Gamma_{ab} = \begin{cases} \gamma \;|_{a \in Liquid \cap b \in Liquid} \\ \gamma S \;|_{a \in Solid \cup b \in Solid} \end{cases}, \quad (5)$$

$$f_{ab} = f(q_{ab}, h) = \begin{cases} q & 0 \le q \le 1 \\ 2 - q & 1 \le q \le 2 \\ 0 & 2 \le q \end{cases}, \quad (6)$$

$$q_{ab} = |\boldsymbol{r}_a - \boldsymbol{r}_b| / h, \quad (7)$$

where γ is the surface tension coefficient, d is the particle diameter, h is the half of influence distance, and S is the spreading coefficient. This force is smoothed afterwards using the kernel functions. The coefficient α depends on the number of the smoothing processes. The smoothing number is 3 and α = 1.2 in this study.

2.3 Computational Condition

Figure 1 shows the initial particle distribution. The blue part is a spherical water droplet with a diameter of 2.7 mm, composed of 12,533 particles. The yellow part is a square solid plate of 10 mm on a side, composed of two-layered 16,150 particles. The particle diameter is

0.1 mm. The physical properties of water at room temperature are given to the liquid particles.

The spreading coefficient S is 0.44 and 0.7 which correspond to the contact angles of 97° and 67°, respectively. The droplet starts to fall from a location 0.5 mm away from the wall, at the initial downward velocity of V = 0.85 m/s,. The time t is reset to 0 when the droplet contacts with the wall. These conditions are similar to those in the experiment.[3]

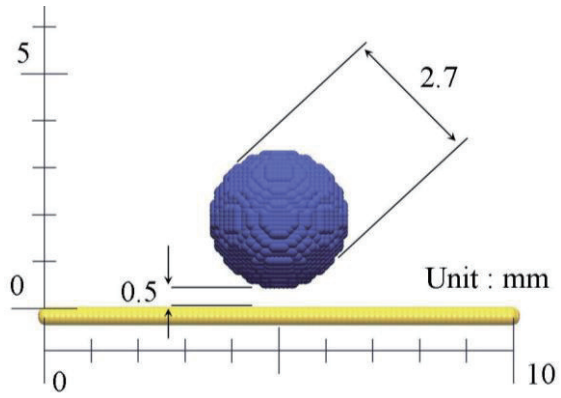

Fig. 1 Initial particle distribution.

3. Results and Discussion

Figure 2 shows the result for the S =0.44 case. After the droplet hits the wall, it crashes into a flat planar snap at t = 5 ms. However, it goes back to a spherical shape and bounce back at t = 23 ms.

When the spreading coefficient becomes higher, S = 0.7, the droplet never detaches from the wall, as shown in Fig. 3.

In both computations, the geometry of a liquid droplet agreed well with that of the experiment.[3]

4. Concluding remarks

SPH method was applied to the simulation of the deforming phenomena of a liquid droplet on a hydrophobic solid surface taking into account the spreading coefficient. The rebounded motion of the droplet was successfully simulated. The results of the simulations were reasonable, compared with the experiment.

References

[1] A. Tartakovsky and P. Meakin,
Modeling of surface tension and contact angles with smoothed particle hydrodynamics,
PHYSICAL REVIEW E, **72** (2005), 026301.
[2] M. Shigeta, T. Watanabe, S. Izawa and Y. Fukunishi,
Incompressible SPH Simulation of Double-Diffusive Convection Phenomena,
International Journal of Emerging Multidisciplinary Fluid Sciences, 1, **1** (2009), 1-18.
[3] T. Mao, D. C. S. Kuhn, and H. Tran,
Spread and Rebound of Liquid Droplets upon Impact on Flat Surfaces,
AIChE Journal 43, **9** (1997), 2169-2179.

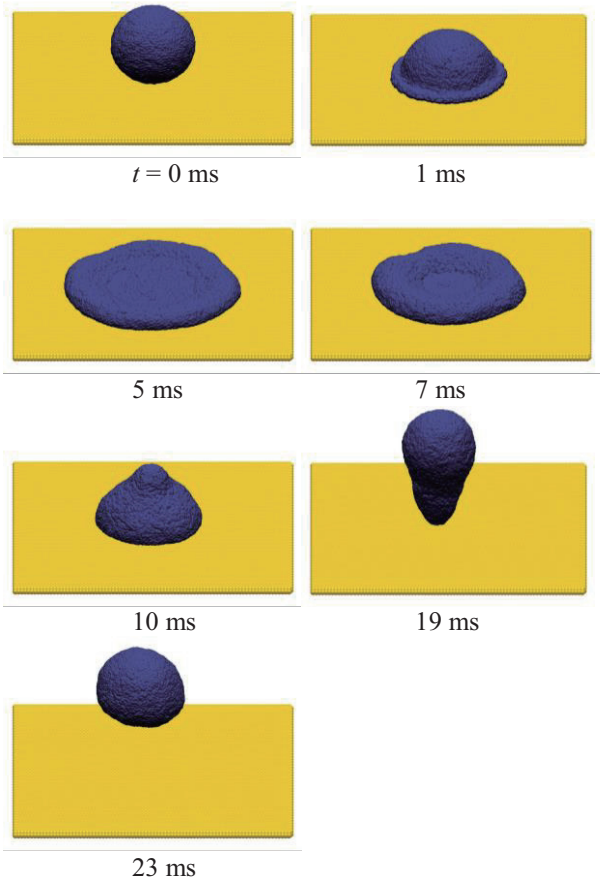

Fig. 2 Bouncing movement of a droplet hitting a hydrophobic surface for S = 0.44 (contact angle: 97°).

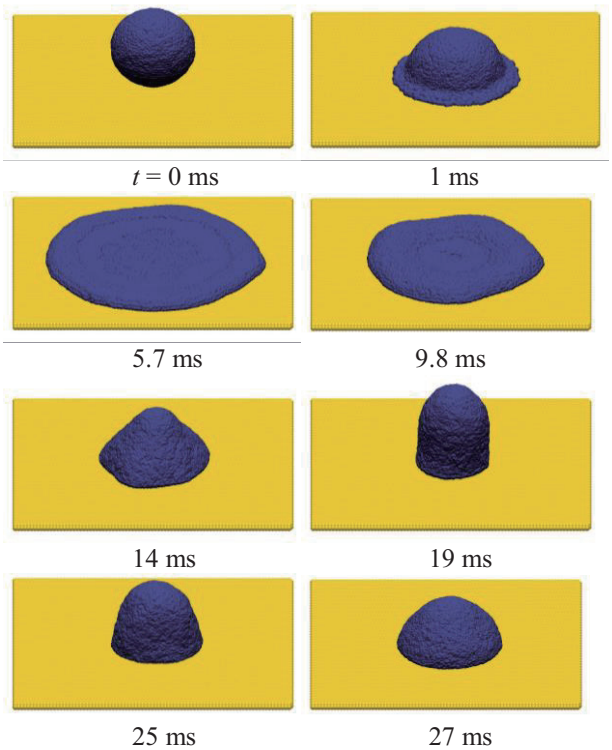

Fig. 3 Deforming sequence of a droplet hitting a wall surface for S = 0.7 (contact angle: 67°).

Tenth International Conference on Flow Dynamics
November 25-27, 2013, Sendai, Miyagi, Japan

Numerical Simulation of Turbulent Spot Generation Process Using Interaction Between Streaky Structure and Jet

Joe Yoshikawa[1], Satoko Komurasaki[2], Masaya Shigeta[3], Seiichiro Izawa[1], Yu Fukunishi[1]
[1] Graduate School of Engineering, Tohoku University
[2] College of Science and Technology, Nihon University
[3] Joining and Welding Research Institute, Osaka University
yoshikawa@fluid.mech.tohoku.ac.jp

ABSTRACT

Numerical simulation is carried out to investigate the destabilizing process of a boundary layer. The boundary layer destabilization is designed to take place by an interaction between streaky structures and a short-duration jet ejection. Although the large deformation of streaky structures takes place when the jet is strong enough, the generation of a turbulent spot cannot be observed in the computation.

1. Introduction

Transition of a flat-plate boundary layer can be categorized into two types. One is initiated by the viscous type instability, which leads to the linear growth of two-dimensional unstable waves, so-called the T-S waves. The other is the bypass transition. The bypass transition takes place when the free stream turbulence intensity is high. Instead of the T-S waves, high and low speed streaks aligned in the spanwise direction appear inside a boundary layer. Then, the velocity fluctuation grows downstream owing to the instability of streaky structures themselves. Finally, the streaky structure break down and a localized turbulent region, i.e. a turbulent spot, is generated in the boundary layer.[1] A turbulent spot can be artificially generated by a spark[2] or by a strong jet ejection. In a natural condition, turbulent spots appear one after another without such strong inputs. So, a turbulent spot should be generated by much weaker inputs, if a proper condition is provided. The goal of this research is to obtain the better understanding of bypass transition by finding the condition which the small flow stimulation can lead to turbulent spot generation. In this study, we try to destabilize a boundary layer by ejecting a jet into the low-speed streaks generated behind small bumps on the flat plate surface.

2. Computational Method

Governing equations are the 3-D incompressible Navier-Stokes equations and the continuity equation.

$$\frac{\partial \boldsymbol{u}}{\partial t} + (\boldsymbol{u}\cdot\nabla)\boldsymbol{u} = -\nabla p + \frac{1}{Re}\nabla^2 \boldsymbol{u}. \quad (1)$$

$$\nabla \cdot \boldsymbol{u} = 0 \quad (2)$$

Each variable is non-dimensionalized using the uniform flow velocity U and the displacement thickness at inlet boundary δ_0^*. MAC method is used. All spatial derivative terms are discretized using a multi-directional difference scheme. The 3rd-order upwind difference scheme is used for the convection term and the 2nd-order central difference scheme is used for the other terms. The 2nd-order Crank-Nicolson method is used for the time integration. In the computations, only the velocity difference from the Blasius profile is computed to deal with the velocity fluctuation with a higher degree of accuracy. The Gauss-Seidel method and the Multi-Grid method are used to solve Poission equation for the pressure.

Figure 1 shows the computational domain. The origin is placed at the center of the inlet, where x, y, and z axes denote the streamwise, wall-normal, and spanwise directions, respectively. The Reynolds number defined as $\mathrm{Re}_{\delta^*} = U\delta_0^*/\nu$ is 530. Computational region is $288\delta_0^* \times 30\delta_0^* \times 40\delta_0^*$. Total grid number is $289 \times 49 \times 41$, where the grids are concentrated near the wall.

The Blasius profile is given as the base flow. Inlet velocity profile is fixed. The non-slip condition is applied to the wall, and the Neumann condition is imposed on the outlet and top boundaries. As for the pressure boundary condition, Neumann condition is used at all boundaries, and the average of the pressure in the computational domain is kept constant, 0, at each timestep. In the spanwise direction, the periodic boundary condition is used.

First, the preliminary calculation is carried out to obtain steady streaky structures by placing small bumps of $2 \times 1.5 \times 3$ at a constant interval in the spanwise direction, z=-20, -10, 0, 10, and 20 at x=20. And then, the jet is intermittently ejected into the boundary layer through a square hole of 3×3, 60 downstream of the bump at z=0. The height of the bumps is approximately a half of the local boundary layer thickness. The duration of jet ejection is 15 (t=0~15), and the jet velocity v_{jet} are 20% or 30% of the free stream velocity.

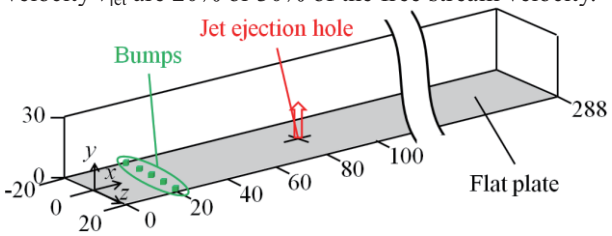

Fig. 1 Computational domain

3. Results and Discussion

Figure 2 shows the streamwise velocity distribution at y=3 before the jet ejection. Low speed regions colored by blue can be observed inside the boundary layer. They

are elongated in the streamwise direction in the wakes of the bumps at x=20.

Figures 3 and 4 show the distribution of spanwise component of "additional" vorticity fluctuation ω_z' in the y=2.25 plane after the jet ejection. Here, "additional" denote the difference from the base flow shown in Figure 2. The stripe pattern is locally distorted and travels downstream. The streaky pattern appears to be more disturbed in the v_{jet}=0.3 case. It should be pointed out that the waviness in the vorticity pattern can be observed upstream of the jet location, which means that the effect of the jet is received at the bumps.

Figures 5 and 6 show the distribution of the spanwise component of additional vorticity fluctuation $\Delta\omega_z'$ in several yz planes at the same instant as the data shown in figures 3 and 4. The additional vorticity fluctuation $\Delta\omega_z'$ decays for the v_{jet}=0.2 case. On the other hand, $\Delta\omega_z'$ value increases during t=180~255 for the v_{jet}=0.3 case. Although the vorticity pattern is largely deformed, generation of a turbulent spot is not observed in this computation.

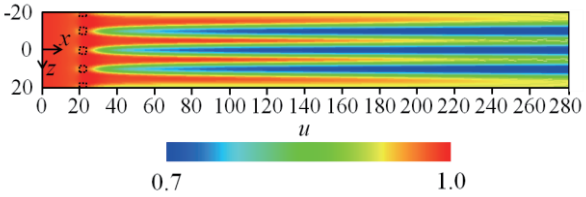

Fig. 2 Streamwise velocity distribution at y=3

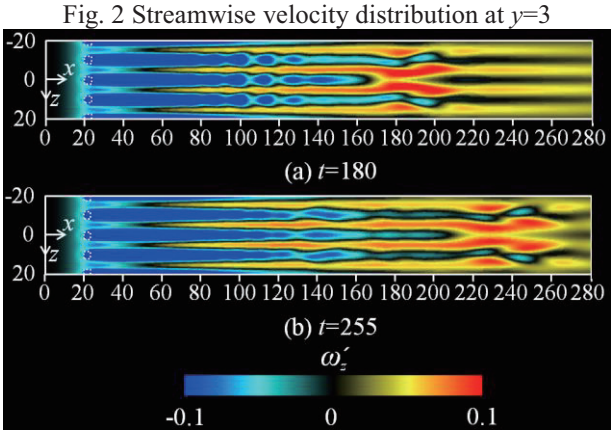

Fig. 3 Spanwise component of vorticity fluctuation at y=2.25 (v_{jet}=0.2)

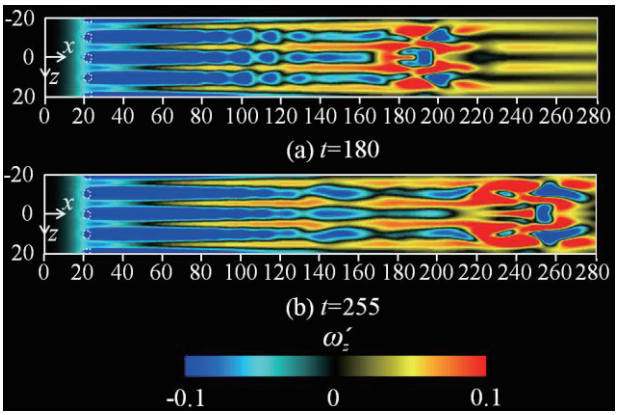

Fig. 4 Spanwise component of vorticity fluctuation at y=2.25 (v_{jet}=0.3)

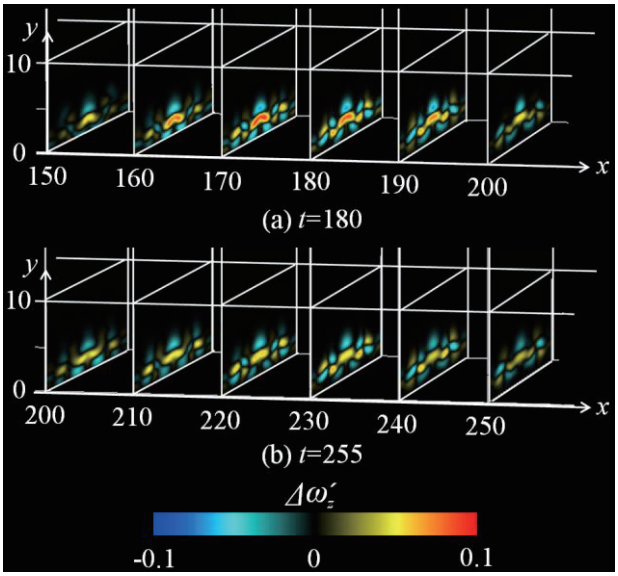

Fig. 5 Spanwise component of vorticity fluctuation. Difference from the no-jet case is shown (v_{jet}=0.2).

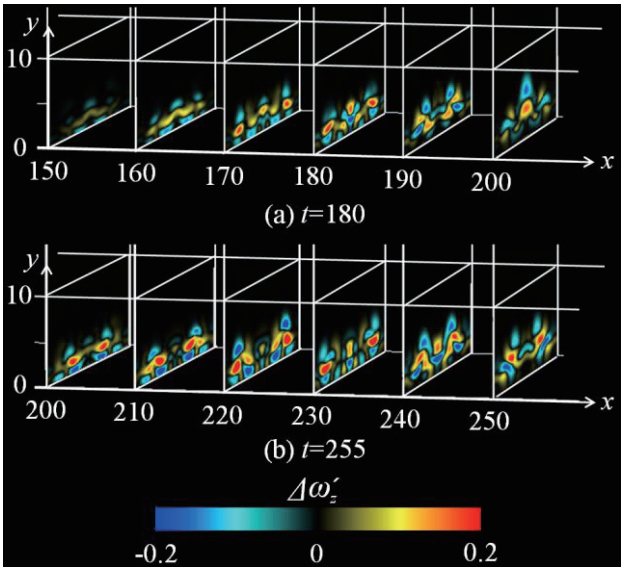

Fig. 6 Spanwise component of vorticity fluctuation. Difference from the no-jet case is shown (v_{jet}=0.3).

4. Concluding remarks

Destabilization of laminar boundary layer was attempted by ejecting a short-duration jet into the low-speed streak region. Although the large deformation of vorticity pattern took place, the onset of turbulence could not be observed.

References

[1] Matsubara, M. and Alfredsson, P. H., Disturbance growth in boundary layers subjected to free-stream turbulence, Journal of Fluid Mechanics, Vol.430 (2001), pp.149-168.

[2] Wygnanski, I., Sokolov, M. and Friedman, D., On a turbulent `spot' in a laminar boundary layer, Journal of Fluid Mechanics, Vol.78 (1976), pp.785-819.

Numerical Analysis of Cryogenic Slush Flow in a Corrugated Pipe (SLUSH-3D)

Yoshiyuki IWAMA, Takumi HOSONO, Katsuhide OHIRA
Institute of Fluid Science, Tohoku University, 2-1-1 Katahira, Aoba, Sendai 980-8577, Japan
iwama@luna.ifs.tohoku.ac.jp

ABSTRACT

Cryogenic slush fluids such as slush hydrogen are two-phase single component fluids containing solid particles in a liquid, which have higher density and refrigerant capacity than those of a single-phase liquid. Flow characteristics of slush flow in a horizontal corrugated pipe which is used to absorb a pipe contraction at cryogenic temperature were numerically analyzed. The results showed that solid particles suppressed the expansion of liquid flow toward the inside of the corrugations and weakened the intensity of liquid vortices within the corrugations, which was one of the main causes of the pressure drop reduction in a corrugated pipe.

1. Introduction

Cryogenic slush fluids are two-phase single component fluids containing solid particles in a liquid. The density and refrigerant heat capacity of slush fluid are higher than those of the liquid. The pressure drop reduction of slush fluids is confirmed in the range of the high Reynolds number [1]. It was also verified that solid particles migrated toward the center of the pipe at high flow velocities served to suppress the turbulence generation on the pipe wall, which caused the pressure drop reduction in a circular pipe. Taking this advantage, the hydrogen energy system is suggested as shown in Fig. 1, where slush hydrogen is transported as an energy source and used as a refrigerant in superconducting power transmission [2]. In this system, a synergic effect can be expected from the simultaneous transportation and storage of fuel and electrical power.

The objective of this study is to investigate flow characteristics and clarify the pressure drop reduction phenomenon of slush fluid in a horizontal corrugated pipe, which is used in order to absorb a pipe contraction at cryogenic temperature. The flow of slush nitrogen is analyzed by using the numerical code “SLUSH-3D”.

2. Numerical method

2.1. Governing equations

In this study, the liquid and solid phases are supposed to be an incompressible continuous Newtonian fluid. Solid phase is consisted of spherical quasi-solid particles. Thermo-physical properties of each phase are the values at the triple point. The Shih’s non-linear k-ε [3] model is used as the turbulence model, which is applied only to the liquid phase. The kinetic theory of granular flow [4] is also adopted to take into account the effect of collisions among solid particles.

Governing equations are based on the Euler-Euler coupling two-fluid model. The continuity equation for the phase φ ($\varphi = l$ for the liquid phase, s for the solid phase) is written as

$$\frac{\partial \alpha_\varphi \rho_\varphi}{\partial t} + \nabla \cdot \left(\alpha_\varphi \rho_\varphi \boldsymbol{U}_\varphi \right) = \dot{m}_\varphi . \tag{1}$$

Where, $\dot{m}_\varphi$ is the mass exchange term between liquid and solid phases. The momentum equation is written as

$$\begin{aligned} &\frac{\partial \alpha_\varphi \rho_\varphi \boldsymbol{U}_\varphi}{\partial t} + \nabla \cdot \left(\alpha_\varphi \rho_\varphi \boldsymbol{U}_\varphi \boldsymbol{U}_\varphi \right) + \nabla \cdot \left(\alpha_\varphi \boldsymbol{\tau}_\varphi \right) + \nabla \cdot \left(\alpha_\varphi \rho_\varphi \boldsymbol{R}_\varphi \right) \\ &\quad = -\alpha_\varphi \nabla P + \alpha_\varphi \rho_\varphi g - \dot{m}_\varphi \boldsymbol{U}_\varphi + \boldsymbol{M}_\varphi . \end{aligned} \tag{2}$$

Where, $\boldsymbol{M}_\varphi$ is the momentum exchange term between solid and liquid phases, and is composed of drag and virtual mass terms. The energy equation is written as

$$\begin{aligned} &C_{p,\varphi} \rho_\varphi \left(\frac{\partial \alpha_\varphi T_\varphi}{\partial t} + \nabla \cdot \left(\alpha_\varphi \boldsymbol{U}_\varphi T_\varphi \right) \right) \\ &\quad = \nabla \cdot \left(\alpha_\varphi \kappa_\varphi^{eff} \nabla T_\varphi \right) + \dot{m}_\varphi h_L + Q_\varphi . \end{aligned} \tag{3}$$

Where, $\boldsymbol{Q}_\varphi$ is the heat exchange term between solid and liquid phases, and is given by the Ranz-Marshall model.

2.2. Numerical Conditions

Figure 2 shows the annular-type corrugated pipe used in the numerical analysis. The flow path length is 300 mm with an inner diameter of 15 mm, a corrugation pitch of 3 mm and a corrugation height of 2.2 mm.

The solid particle diameter d_s is 1.3 mm, which is the same as in the experiment. The solid fractions α_s are 13 and 25 vol.%, and the inlet velocities U_{in} are 1.5-4.0 m/s as the initial conditions.

3. Results and Discussions

Figure 3 shows the pressure drop of slush and liquid nitrogen in a corrugated pipe. At the low inlet velocity, the numerical results of subcooled liquid nitrogen agree well with the experiment. However, at the high inlet velocity, calculation results are smaller than the

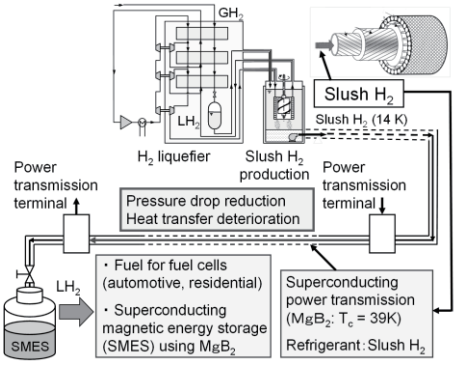

Fig. 1 Hydrogen energy system using slush H_2 [2].

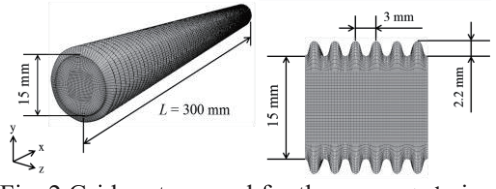

Fig. 2 Grid system used for the corrugated pipe.

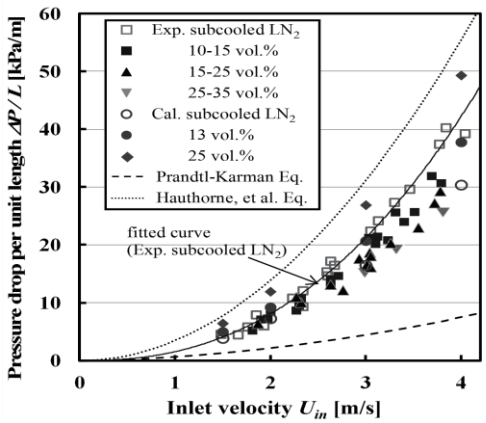

Fig. 3 Pressure drop of liquid and slush nitrogen.

experiments because there is a slight difference between the corrugation shapes of the numerical and experimental pipes.

In the case of slush flow, the experimental result indicates the pressure drop reduction. However, the calculated pressure drop increases with increase in inlet velocity and solid fraction. It is partly because the shear stress among solid particles calculated by the granular flow model might overestimate that of the experiment.

Figure 4 shows the PIV measurement results of the particle path of solid nitrogen particles within the grooves of the grooved rectangular pipe [5]. In Fig. 4 (a) where pressure drop reduction did not occur, the intensity of solid vortices was higher than that in Fig. 4 (b) where pressure drop reduction occurred. It is clear from the experimental result that the intensity of liquid vortices in the case (b) where pressure drop reduction occurs is much less than that in the case (a) where the pressure drop reduction does not occur.

Figure 5 shows the relative velocity contour line of liquid phase in the x direction at the inlet velocity U_{in} = 2 m/s. Subcooled liquid nitrogen expands into the corrugation more than liquid phase flow of slush. Furthermore, there is a negative velocity region within the corrugation in the case of subcooled liquid nitrogen. In the case of slush flow, it is confirmed solid particles migrated toward the center of the pipe contribute to suppress the flow expansion and the recirculation of flow or vortex flow within the corrugations.

Figure 6 shows the streamline and velocity vector of liquid phase for subcooled liquid nitrogen at the inlet velocity U_{in} = 2 m/s, and those of liquid phase and solid particles for slush nitrogen with the initial solid fraction α_s = 13 vol.% and at the inlet velocity U_{in} = 2 m/s. The vortex intensity of subcooled liquid nitrogen is higher than that of liquid phase and solid particles for slush. As mentioned above, subcooled liquid nitrogen expands into the corrugations and generates vortex flow more than the liquid phase flow of slush. In addition, from Fig. 6 (b) and (c), it is found that the solid particles within the corrugation are almost stagnant and the vortex intensity of solid particle is much lower than that of liquid phase of slush.

It is confirmed that these phenomena of less expansion of liquid phase and low vortex intensity of liquid phase and particles cause the pressure drop reduction in a corrugated pipe.

4. Concluding remarks

In this study, slush flow in a horizontal corrugated pipe was numerically analyzed. One of the main causes of the pressure drop reduction for slush flow in a corrugated pipe was clarified. It was confirmed that solid particles suppressed the expansion of liquid phase flow toward the inside of the corrugations and weakened the intensity of liquid vortices within the corrugations.

References

[1] K. Ohira et al., Cryogenics, **51** (2011), 563-574.
[2] K. Ohira, TEION KOGAKU, **41** (2006), 61-72.
[3] T. H. Shih et al., NASA TM -105993, 1993.
[4] D. Gidaspow, "Multiphase flow and fluidization", Academic Press, San Diego, first edition, 1994.
[5] K. Nakagomi, Master thesis, Tohoku Univ., 2011.

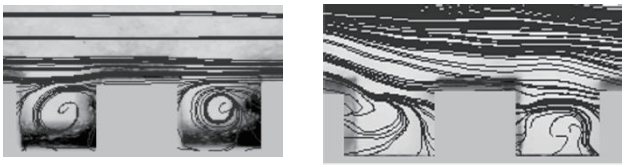

(a) Pressure drop reduction does not occur. (b) Pressure drop reduction occurs.

Fig. 4 Particle path of solid nitrogen particles.

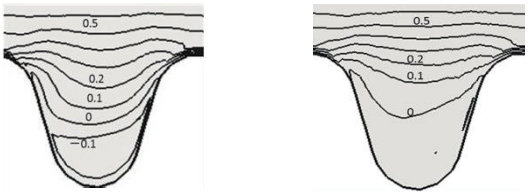

(a) Subcooled liquid nitrogen (b) Slush (α_s = 13 vol.%)

Fig. 5 Relative velocity contour line of liquid phase in the x direction U_l / U_{in} (U_{in} = 2 m/s).

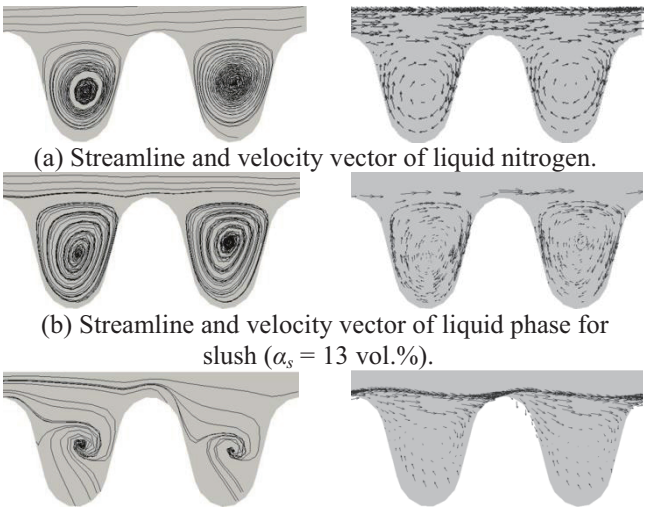

(a) Streamline and velocity vector of liquid nitrogen.

(b) Streamline and velocity vector of liquid phase for slush (α_s = 13 vol.%).

(c) Streamline and velocity vector of solid nitrogen particles for slush (α_s = 13 vol.%).

Fig. 6 Stream line and velocity vector of liquid and solid particles within the corrugations (U_{in} = 2 m/s).

Tenth International Conference on Flow Dynamics
November 25-27, 2013, Sendai, Miyagi, Japan

Molecular Dynamics Study of Oxygen Permeation of the Ionomer on Platinum Catalyst in PEFC Cathode Side

Yuta Sugaya, and Takashi Tokumasu,
Tohoku University, Katahira 2-1-1, Sendai, Miyagi
sugaya@nanoint.ifs.tohoku.ac.jp

ABSTRACT

In Polymer electrolyte fuel cell (PEFC) cathode catalyst layer, an ionomer with which the catalyst is covered is very important on the point of transferring protons to the catalytic surface on the cathode side. On the other hand, it is said that ionomer interferes with oxygen permeation to the catalytic surface. The mechanism of oxygen permeation through the ionomer was not analyzed in detail. In this research, we constructed the system of ionomer on the Pt surface by using molecular dynamics study, and researched about the effect of the water content of the ionomer on the structure of the ionomer and oxygen permeability.

1. Introduction

Polymer electrolyte fuel cell (PEFC) is focused worldwide as the energy conversion device for next generation. However, PEFC is not widespread in general because an actual power generation efficiency is lower than a theoretical power generation efficiency.

PEFC is composed of membrane electrode assemblies (MEAs) that consist of a polymer electrolyte membrane (PEM), catalyst layers (CLs), micro porous layers (MPLs), and gas diffusion layers (GDLs). In CLs, Pt catalyst is the particle whose diameter is 3 ~ 4 nm and it is on a supported carbon. In addition, it is covered with an ionomer because of proton transfer to catalyst surface. The ionomer improves ability of proton transfer but it reduces oxygen permeability to Pt surface and therefore dissociative adsorption reaction becomes slow. It is necessary to research the oxygen permeation and proton transfer in such a situation to raise its efficiency. However, it is difficult to analyze by macroscopic experiment because these phenomena occur in the microscopic structure. For this reason, it is necessary to analyze the oxygen permeation and the proton transfer at the microscopic point of view.

In this research, we constructed the system of ionomer including hydrocarbon membrane, water molecule, oxonium ion and platinum surface by using molecular dynamics study, and researched about the effect of the water content of the ionomer on the structure of the ionomer and oxygen permeability.

2. Method

In this research, we simulated the system of CLs of the cathode side by molecular dynamics simulation. This system includes Pt wall, hydrocarbon membrane, water, oxonium ion and oxygen molecule.

Pt-Pt interactions were represented by spring mass model considering nearest neighbor atom. Hydrocarbon was represented by the flexible model which interaction was expressed by bond, angle, torsion, van der Waals, and coulomb potential. The chemical structure of hydrocarbon is shown in Fig. 1. The F3C model [1] was adopted for water, and for oxonium ion, we selected similar model with four point charges. The Morse potential was used for intramolecular potential of oxygen molecule. The intermolecular potentials between hydrocarbon and water, hydrocarbon and oxonium ion were represented by Lennard Jones (LJ) potential and coulomb interaction. The interaction between Pt and water was represented by Spohr-Heinzinger potential [2] and that between Pt and oxonium ion was represented by the potential that the number of hydrogen atoms changes from two to three. The intermolecular potentials between oxygen and water, oxygen and oxonium ion were represented by LJ potential and Morse potential. The others were connected by LJ potential. In this research, we assumed all permeated oxygen were dissociated at Pt surface and they are used for chemical reaction instantaneously. So, we allowed oxygen molecules to pass through Pt surface by considering only the attractive interaction between Pt-O_2 so that oxygen atoms were not accumulated on the Pt surface.

In this calculation, we considered the periodic boundary condition of x, y direction. The temperature was set at 350 K and the simulation domain was set at 66.5×57.6×150 Å. The platinum surface was placed at the bottom of simulation box and ionomer which was composed of hydrocarbon molecules were placed on the surface. A chain of hydrocarbon was constructed 5 pairs of 1 polar chain and 1 non-polar chain. In this system, 15 hycrocarbon molecules were placed. Moreover, the number of water molecules was determined according to water content. We used velocity verlet and rRESPA [3]. The calculation procedure is described as follows.

Firstly, we made the ionomer without Pt during 800 ps. The temperature was controlled to 350 K by velocity scaling during till first 720 ps. After 800 ps, we attached the ionomer to Pt surface. Then oxygen molecules were introduced. The number of oxygen molecule was set so that the gas phase corresponds to 1 MPa. The number of oxygen in the gas space was constant to keep the pressure in the gas space constant and permeated molecules were returned to gas space. By this procedure, we made the constant oxygen mass flux in the ionomer.

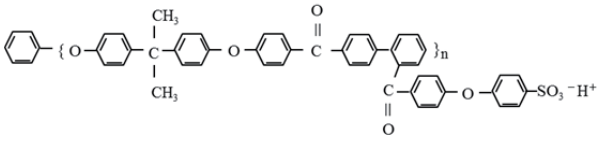

Fig. 1 Chemical structure of hydrocarbon polymer

3. Result and Discussion

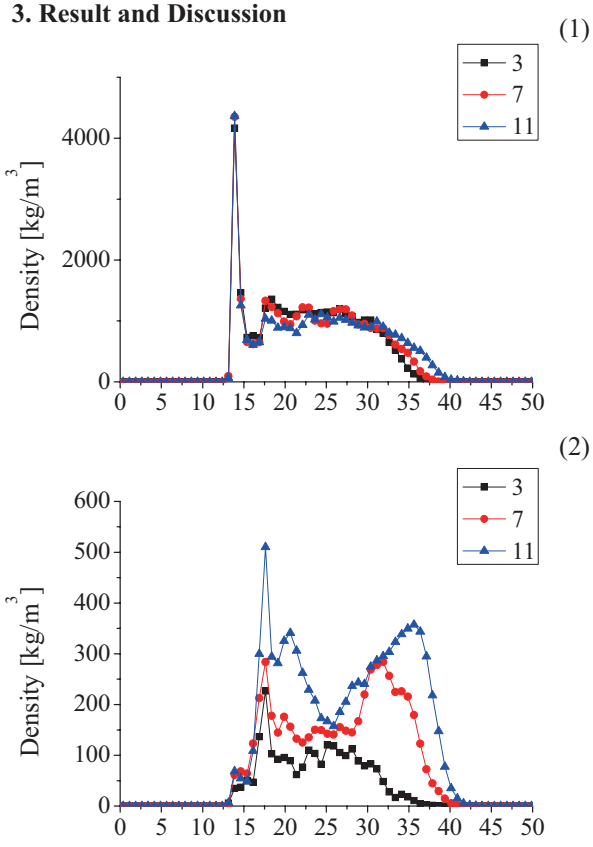

Fig. 2 Density distribution of (1)hydrocarbon molecule, (2)water and oxonium ion along z direction

The density distribution of hydrocarbon and liquid in case of water content λ = 3, 7, 11 are shown in Fig. 2. From Fig. 2 (1), it is said that the hydrocarbon gathers toward the catalyst surface. This phenomenon occurs because Pt strongly attracts the other molecules. From Fig. 2 (2), many water molecules distribute on high density hydrocarbon which are attracted by Pt. The density of water molecules on Pt surface is very low. From Fig. 2 (1) and (2), hydrocarbon molecules absorb Pt surface stronger than water molecule.

Table 1. The number of permeated oxygen molecule

water content λ	3	7	11
No. of permeated O_2	0	1	1

Table 1. shows the number of oxygen molecule which permeated to catalyst surface. From TABLE1, the oxygen permeability in the ionomer composed of hydrocarbon is very low. In order to analyze this reason, we researched paths of oxygen permeation. The results are shown below.

From Fig. 3, many oxygen molecules dissolve in the ionomer in all case. Many dissoloved oxygen molecules are obstructed by high density ionomer at z = 15 Å. For this reason, the oxygen permeability in the ionomer composed of hydrocarbon is very low.

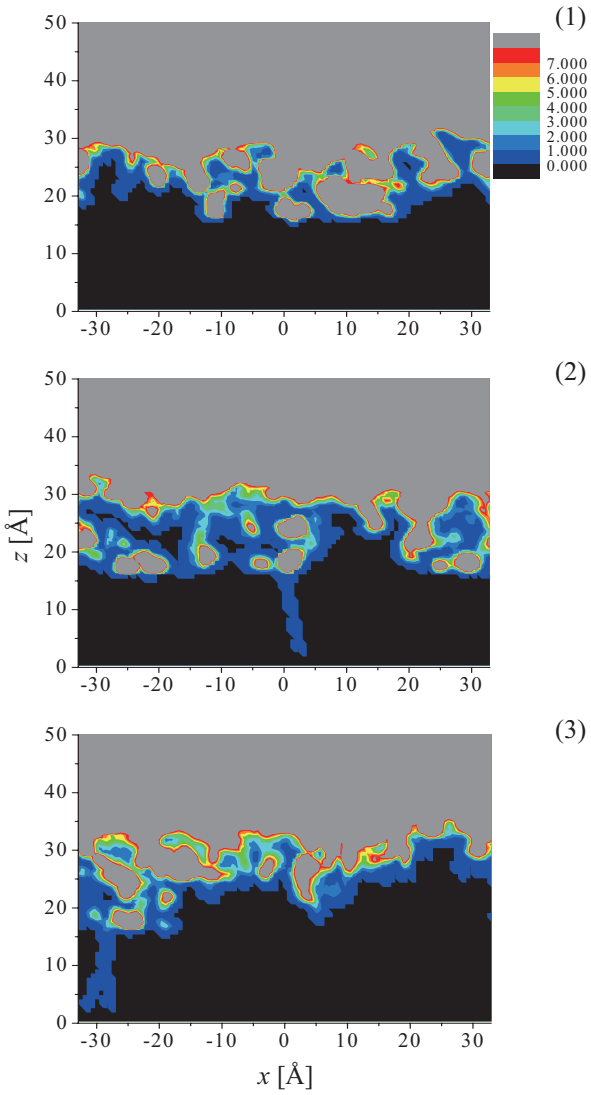

Fig. 3 Density distribution of oxygen molecule in the ionomer composed of hydrocarbon. (1) λ=3, (2) λ=7, and (3) λ=11

4. Conclusion

The oxygen permeability in the ionomer of catalyst surface was examined by using molecular dynamics simulation. In this simulation, we constructed the model of ionomer on the Pt catalyst surface in the PEFC catalyst layer. Hydrocarbon gathers toward the catalyst surface and many water molecules distribute on high density hydrocarbon which are attracted by Pt. We examined the oxygen permeability in the ionomer on the catalyst surface. It is said that the oxygen permeability in the ionomer composed of hydrocarbon is very low. Many dissoloved oxygen molecules are obstructed by high density ionomer.

References

[1] M. Levitt, M. Hirshberg, R. Sharon, K. E. Laidig, and V. Daggett, *J. Phys. Chem.*, **101** (1997), pp. 5051-5061.
[2] E. Spohr, *J. Phys. Chem.*, **93** (1989), pp. 8254-8282.
[3] M Tuckerman, B.J Berne, G.J Martyna, *J. Chem. Phys.*, **97** (1992), pp. 1990-2001.

Tenth International Conference on Flow Dynamics
November 25-27, 2013, Sendai, Miyagi, Japan

Development of Visualization System for Injection Molding by using PVA

Masashi Ohtake[1], Kei Ozawa[2], Ken Nakajima[3], Makoto Ohta[4]
[1] Graduate school of Engineering, Tohoku University, 6-6-01, Aramaki aza aoba, Aoba-ku, Sendai, Japan
[2] Graduate school of Biomedical Engineering, Tohoku University, 6-6-01, Aramaki aza aoba, Aoba-ku, Sendai, Japan
[3] WPI Advanced Institute for Materials Research, Tohoku University, 2-1-1, Katahira, Aoba-ku, Sendai, Japan
[4] Institute of Fluid Science, Tohoku University, 2-1-1, Katahira, Aoba-ku, Sendai, Japan
ohtake@biofluid.ifs.tohoku.ac.jp

ABSTRACT

The injection molding is one of the major methods for fabricating plastic materials. This method is useful for fabricating complex shape and advanced properties of materials. However, the observation of flow during the molding is hard because the molding system is, in general, not to be transparent. To reveal the filling process, we develop a visible system for injection molding, based on PIV method, by using Poly (vinyl alcohol) (PVA) solution with good transparency and capability of changing its viscosity. We found PVA solution is useful for investigation of relationship between flow behavior and viscosity of the material in the injection molding.

1. Introduction

The injection molding is one of the major process methods for fabricating plastic materials. This method is useful for fabricating complex shape and advanced properties of materials widely developed as bone model, recycled plastics or building materials [1-4].

A bone biomodeling requires a realistic mechanical properties and the geometry as use of mechanical tests of medical devices such as bone screw or drill. The development of bone biomodel such as Ozawa et al [5] is also performed with the composite materials and with an injection molding. The mechanical properties of bone biomodeling, such as elastic modulus, strength or fracture toughness have a strong relation not only to the compound condition, but also to the filling process under the injection molding. Therefore, visualization of the flow of materials in the molding is important to grasp the filling process and the microstructure of the model. However, the observation of the flow behavior in the casting process is hard because the injection molding system is, in general, not to be transparent. The injection molding system endures high temperature and pressure in the process of injection molding.

Then Ozawa et al. carried out the observation of flow behavior with tungsten fiber using micro-CT [6]. The orientation and distribution of fibers in materials shows the flow direction. However, the image of micro-CT scanning shows only “a result of the filling process of materials in the injection”.

Therefore, the purpose of present study is to develop a visible system, which reveals the real-time filling process under the injection molding. We develop the visible system by using Poly (vinyl alcohol) (PVA) solution with good transparency and capability of changing its viscosity. Then, PVA solution can be detected by using a camera for analyzing visualization process such as particle image velocimetry (PIV). Viscosity measurement is also performed to research the relationship between flow behavior and viscous property of PVA solution. We found PVA solution is useful for investigation of relationship between flow behavior and viscosity of the material in the injection molding.

2. Material and Methods

2.1. Set up Experimental System for Visualized Injection Molding

The visible system for injection molding is shown in Fig. 1. Injection was performed by using Injection Molding Machine (IMC-18D1, Imoto machinery Co., Ltd.) with dimension of L300 × W400 × H1120 mm and an acrylic transparent mold with inner dimension of 30 × 30 × 30 mm. Poly (vinyl alcohol) (PVA) solution was used as the material for injection with good transparency and capability of changing its viscosity.

2.2. Preparation of PVA solution for Injection Material

PVA powder (JF-17, JAPAN VAM & POVAL Co., Ltd.) was dissolved in distilled water. Concentration, degree of polymerization and saponification value of the PVA was 18 or 25 wt%, 1700 and 99 mol%, respectively. Before dissolution, we added tech polymer cross-linked polystyrene particles (SBX-17, Seikisui Plastics Co., Ltd.) as tracer particles for PIV. For dissolution, the PVA powder in distilled water including the particles was set in HIGH-PRESSURE STEAM STERILIZER (BS-325 TOMY Co., Ltd.) for 15minutes at 120 ˚C. Then PVA solution was cast into the cylinder of the injection molding machine and cooled to 25 ˚C for about 24 hours.

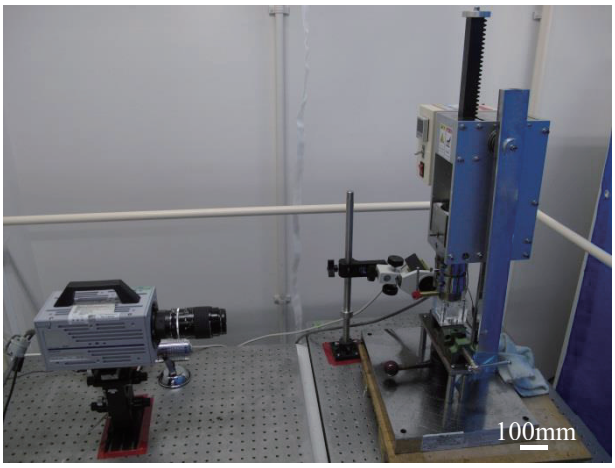

Fig. 1 Visualized system for injection molding

2.3. Casting with Injection Molding

Nd:YAG laser (BWN-532-100E, B&W Tek Inc.) was used with a light source having continuous wave operation. The output wavelength of the laser is 532 nm and the output power is 100 mW. The thickness of the laser sheet is 1 mm. Images of the flow into the mold during casting were taken by a high speed camera (FASTCAM SA3, Photron Limted) with a telescopic micro lens which had 105 mm of focal length and 2.8 of F ratio (Micro-Nikkor, Nikon Co Ltd.). The images (640 × 640 pixels) were saved as 12-bit monochrome BMP images. The flame rate was 1000 fps, and the scale factor was 0.0700 pixels/mm.

2.4. Analysis of viscos property

The viscosity measurement of PVA solution was performed with the rheometer (AR 2000ex, TA instrument). PVA solution, prepared in the above method, was set on a stage controlled at 25°C constantly. The cone plate was used as a test jig, which was connected to the motor for controlling shear stress and rate. The viscosities of PVA solutions with concentration 18 or 25 wt% were measured with shifting the shear rate from 0.1 to1000 s^{-1}.

3. Results and Discussion

The injected PVA solution reaches the bottom of the mold as shown in Fig. 2 (a). Then the solution is coiled up and spread in the mold (Fig. 2 (b)). After the injection, the spreading solution performs relaxation in the mold (Fig. 2 (c)).

The viscous property of the solution can affect the flow behavior in the process of injection molding. The shear rate dependence of viscosity of the PVA solution is shown in Fig. 3. Onogi et al. also reported the shear rate dependence of viscosity of PVA solutions [7]. In comarison between the present study and Onogi's study, the shear rate dependence of viscosity of PVA solution shows the silmilar tendency, while there are difference of the method of viscosity measurement, concentration, degree of polymerization and saponification value of PVA.

4. Concluding remarks

The visualized system for injection molding based on PIV method was developed by using Poly (vinyl alcohol) (PVA) solution as the injection material. The process of the injection molding was observed, injection, coiling, and relaxation. The viscosities of PVA solutions with concentration 18 or 25 wt% were measured with shifting the shear rate. The shear rate dependence of viscosity of the PVA solution shows the silmilar tendency to Onogi's report.

References

[1] S.K Najafi et al., Journal of Applied polymer Science, 100, (2006), 3641-3645.

[2] R. Bouza et al., Journal of Applied polymer Science, 102, (2006), 6028-6036.

[3] N. Sombatsompop et al., Journal of Applied polymer Science, 102, (2006), 1896-1905.

[4] P. Turgut, Building and Environment, 42, (2006), 3801-3807.

[5] K. Ozawa et al., Proceedings of 6th World Congress on Biomechanics, 2010, pp.525.

[6] K. Ozawa et al., Proceedings of 8th International Conference on Fluid Dynamics, 2011, pp.522-523.

[7] Shigeharu Onogi et al., Journal of the Japan Society for Testing Materials 9(79), 245-249, (1960).

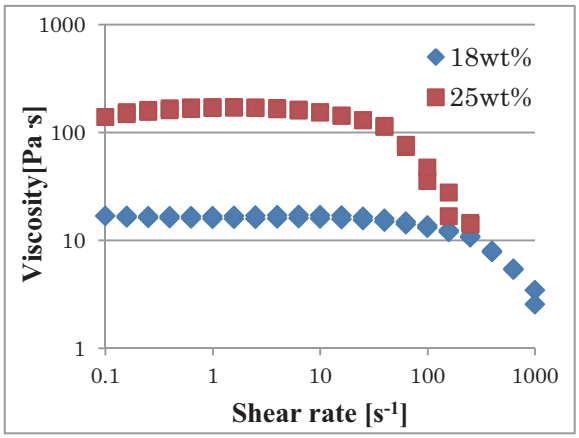

Fig. 3 Viscosity-shear rate of PVA solution

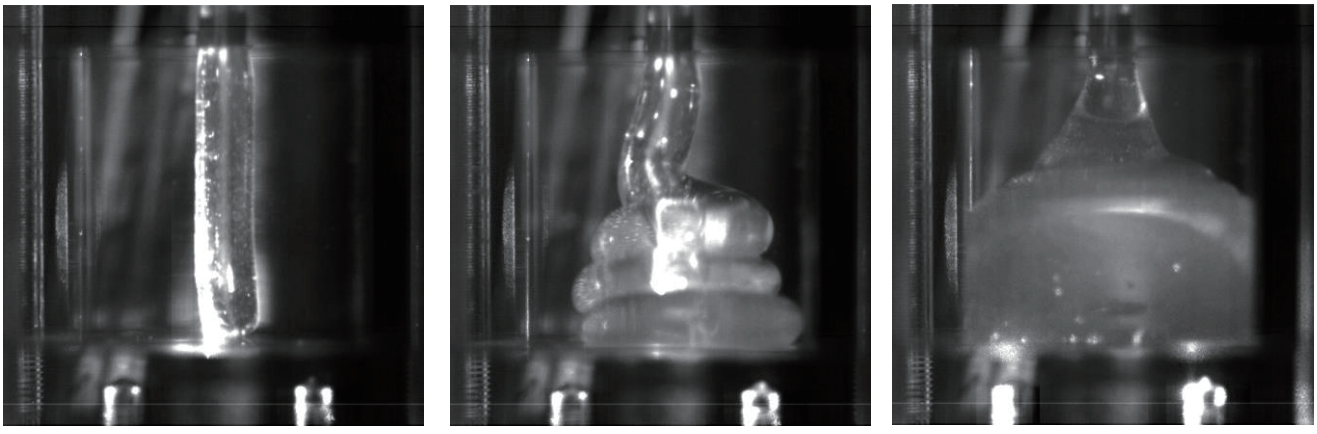

(a) Injecting (b) Coiling (c) Relaxation

Fig. 2 Flow behavior of PVA solution injected into the transparent mold

The Influence of Airflow Uniformity over the Duct Outlet on Cooling Performance of Vehicle Air-condition

Kaiping WEN, Chenguang LAI, and Chao MAN
College of Vehicle Engineering, Chongqing University of Technology, Chongqing, China;
E-mail: chenguanglai@cqut.edu.cn

ABSTRACT

Numerical simulation is performed to simulate different uniformity outflows. It shows that the outflow with higher uniformity is beneficial to cooling performance and thermal comfort by comparing the cooling time and jet range of two different uniformity airflows. It is considered that the lower uniformity outflow have lower boundary velocity and will be attenuated faster in the process of entrainment and admixture. Its center velocity is also attenuated faster and the affected area is smaller than well-distributed outflow so that the amount of the heat exchange is less.

1. Introduction

On the premise of satisfying the demand of occupant thermal comfort, improving the work efficiency of vehicle air-condition is the requirement of energy saving and emission reduction. Moreover, new energy vehicle needs more effective air-condition to match. Outflow uniformity is important for optimum cabin comfort and cooling performance[1]. The objective of this study is to investigate what and how does the uniformity affect the cooling performance and cabin comfort.

2. Model and Mesh

The geometry is modeled in CATIA V5. The engine bay, the trunk and the air leak are ignored. Three outlets are seated on instrument board. Mesh is generated by ANSYS ICEM-CFD. The unstructured mesh on the occupant body and outlet is refined (refer Fig. 1).

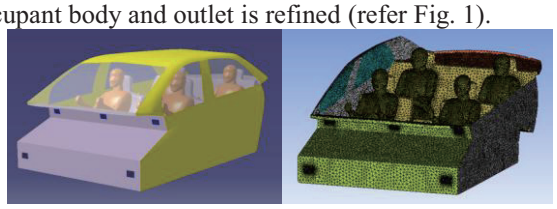

Fig. 1 Model and Mesh

3. Turbulent Model and Radiation Model

The airflow in the cabin is considered as incompressible turbulent flow. The natural convection is simulated by Boussinesq model. The Realizable k-ε turbulent model is chosen for present study because it can give a better jet expansion angle[2]. Considering the solar radiation, DO Irradiation solar radiation model is chosen to simulate the radiation in Chongqing, China. The total radiant intensity is 866.2 W/㎡.

4.Boundary Conditions

The uniformity index can evaluate the flow uniformity, and which is given by:

$$\gamma = 1 - \frac{1}{2A\overline{v_n}} \int \left| v_n - \overline{v_n} \right| dA_n$$

Where γ varies from 0 to 1, corresponding to from completely non-uniform to perfectly uniform flow. A is the cross section area of surface, $\overline{v_n}$ is the mean velocity over the surface, v_n is the velocity on the nth cell face, and dA_n is the cross section area of the nth cell face on respective surface.

Fig. 2 shows two different uniformity index outlets. Both are velocity inlet. (a) is the constant of 3 m/s. Their flux is equal to 0.014 kg/s.

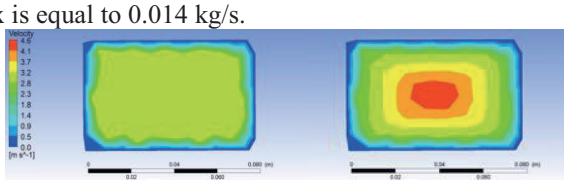

(a) γ=0.87 (b) γ=0.67

Fig. 2 Two different uniformity index outlets

Car body and glasses are heat convection boundary and occupant body is heat flux boundary. The heat rate is 58 W/㎡.

5.Cooling Time

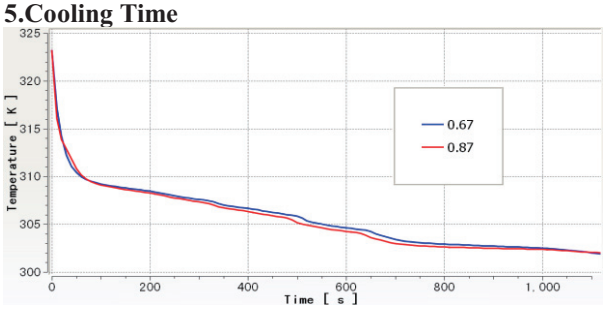

Fig. 3 Cabin Cooling Temperature

Fig. 3 shows the cooling time. The initial cabin temperature is 50 ℃. The time decreasing to 30 ℃ of (a) is 11 min, about 1 min less than (b). After 13 min, the temperature and the tendency are similar.

6. Jet Range

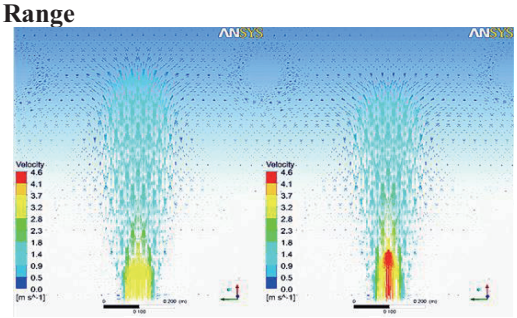

(a) γ=0.87 (b) γ=0.67

Fig. 4 Jet Range

Fig. 4 shows the two outflow ranges. (a) is longer and wider than (b). After the flow jets out, it will draw the static hot air in cabin. As the process going, the

range expends and the center velocity decreases. (b) has lower boundary velocity, so the turbulent fluctuation caused by entrainment and admixture spreads to jet center faster.

The termination of the center velocity represents the end of the jet. Smaller range means fewer amounts of the heat exchange and worse cooling performance.

Fig. 5 shows the cabin temperature distribution at 20 min. The jet on left side is forced submerged jet. It is obvious that (a) affects more room and the temperature area from 25 to 27 ℃ is larger than that of (b).

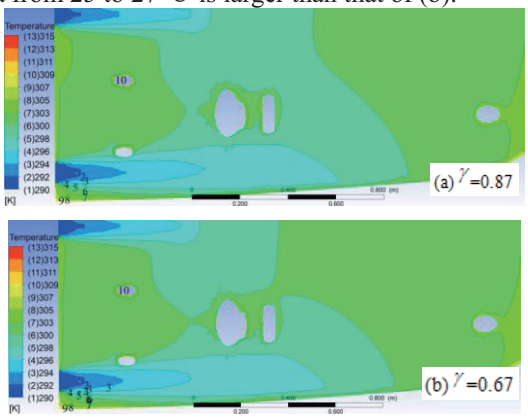

Fig. 5 Temperature distribution of a cross section through the center of the outlet surface

7. Occupant Thermal Comfort

Fig. 6 shows the occupant thermal comfort range and the temperature at the body parts of the back-right row occupant after 20 min[3]. The temperature at almost all parts of the body of (a) is 0.5~1 ℃ lower than that of (b). Comparatively, occupant feels better in the uniform outflow.

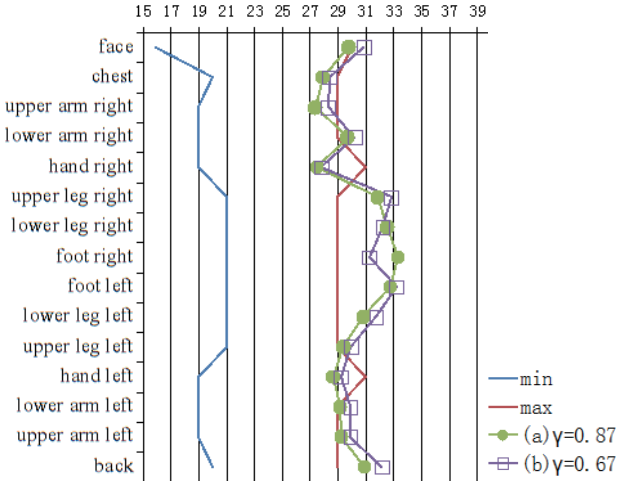

Fig. 6 Occupant thermal comfort range

8. Conclusions

This simulation shows that the outflow with high uniformity is beneficial to the cooling performance and occupant thermal comfort.

The result from the performed study indicates that the reason why uniform outflow cools the cabin more quickly is the longer and wider jet range.

Under the circumstance of energy saving and emission reduction, enhancing the uniformity of outflow is an effective way to improve the utilization coefficient of the engine power.

9. Acknowledgements

This research is supported by Natural Science Foundation Project of CQ CSTC (CSTC, 2011BB6113). Part of the work was carried out under the Collaborative Research Project of the Institute of Fluid Science, Tohoku University.

10. References

[1] A. Patidar, S. Natarajan and M. Panda. CFD Analysis and Validation of an Automotive HVAC System[J]. presented at SAE World Congress, 2009, 1 (0535).

[2] Z. Wen. Fluid Computing Application Tutorial. Tsinghua University press, 2013.

[3] T. Jiang, ZY. Gu,Y. Yang. Influence of solar incidence on thermal comfort of car occupants. presented at Journal of Hefei University of Technology, 2011, 34 (8) : 1137.

Tenth International Conference on Flow Dynamics
November 25-27, 2013, Sendai, Miyagi, Japan

Characteristics of Chemical Species Generated by a Gas-Liquid Plasma Flow Using a Wire Electrode

Masashi HARA[1], Daisuke YOSHINO[2], Tetsuji SHIMIZU[3] and Takehiko SATO[2]
[1]Graduate School of Engineering, Tohoku University, 2-1-1 Katahira, Aoba-ku, Sendai 980-8577, Japan
[2]Institute of Fluid Science, Tohoku University, 2-1-1 Katahira, Aoba-ku, Sendai 980-8577, Japan
[3]Max-Planck Institute for Extraterrestrial Physics, Giessenbachstr., 85748 Garching, Germany
E-mail: hara@plasma.ifs.tohoku.ac.jp

ABSTRACT

Gas-liquid plasma flow has received a great deal of attention because it is easy to make a synergistic effect of chemical reactions in gas phase and gas-liquid interface. As biological applications generally require low temperature and low heat transport, we have developed wire-water discharge system and studied characteristics of transport of heat and chemical species. We focused on temperature rise, pH, conductivity and concentration of ozone.

1. Introduction

Recently, gas-liquid plasma has received much attention[1] because it is well suited for applications of water treatments[2, 3] and a new material process.[4] Because the gas-liquid plasma can easily generate various chemical species and produce synergic effects of chemical reactions in gas phase and gas-liquid interface.

In case these applications of the gas-liquid plasma to physiological tissue, it is required that heat transmission from the plasma to the liquid is low. However, the gas-liquid plasma using a needle electrode, which has been addressed within the most of conventional researches, transport large heat from the plasma to the liquid. On the other hand, plasma generated by dielectric barrier discharge using a wire electrode in atmospheric air could realize low heat transmission.[5] However, knowledge of fundamental characteristics of the gas-liquid plasma using a wire electrode is still unclear.

In this study, we investigate fundamental characteristics of the gas-liquid plasma with a wire electrode focusing on transport and generation of chemical species.

2. Experimental methods

Figure 1 shows schematic diagram of the experimental system for the gas-liquid plasma. The experimental system is composed of a discharge part and a high-voltage power supply part. The discharge part consists of the copper wire electrode covered with polyimide, the ground electrode, and the quartz glass cell filled with pure water. For comparison, a needle electrode was used. The diameter of the wire and needle electrodes is 0.2 mm. The glass cell is 10 mm wide, 10 mm long, and 8 mm depth. The high-voltage power supply part consists of a function generator (NF CORPORATION, WF1976), a high-voltage amplifier (Trek, PD05034), a oscilloscope (LeCroy, WaveSurfer 104MXs) and a current probe (bergoz, FCT-016-125 WB). The rectangular-wave voltage of ± 7.5 kV with a frequency of 5 kHz and duty ratio of 50 % was applied to the two electrodes.

Concentrations of O_3 generated in the air were measured by a gas concentration meter (SEKI Electronics, SOZ-3500). Amounts of chemical species generated in the water were measured by a digital water quality meter (KYORITSU CHEMICAL-CHECK Lab., Corp., DPM-MT) and chemical agents (KYORITSU CHEMICAL-CHECK Lab., Corp., pack test).

3. Results and discussion

3.1 Current-voltage characteristics

Figure 2 shows the wave forms of the applied voltage and discharge current using the wire electrode. On rising and falling edges of the applied voltage, current pulses occurred. The power consumption of plasma discharge was 54.6 W.

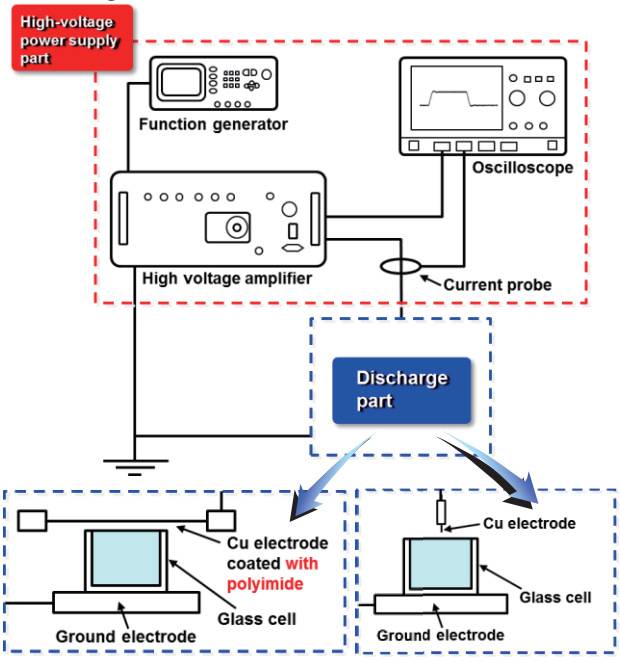

Fig. 1 Schematic diagram of experiment apparatuses

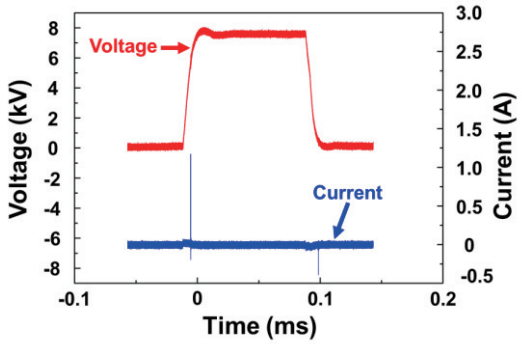

Fig. 2 Waveforms of applied voltage and discharge current

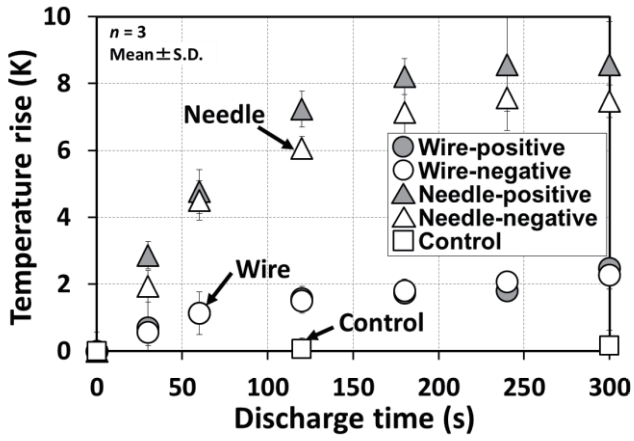

Fig. 3 Change in temperature with discharge time

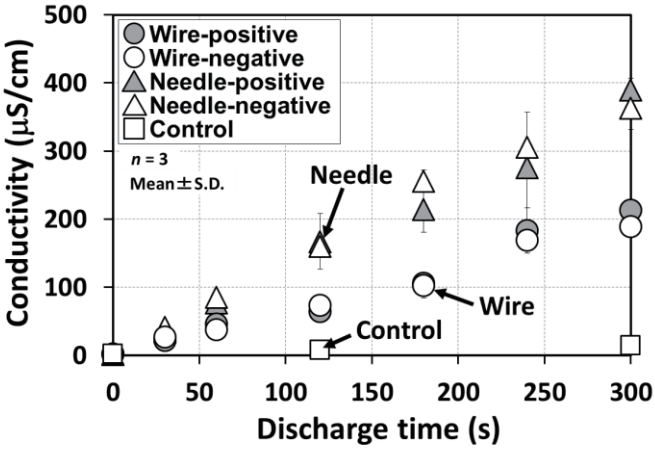

Fig. 5 Variation of conductivity with discharge time

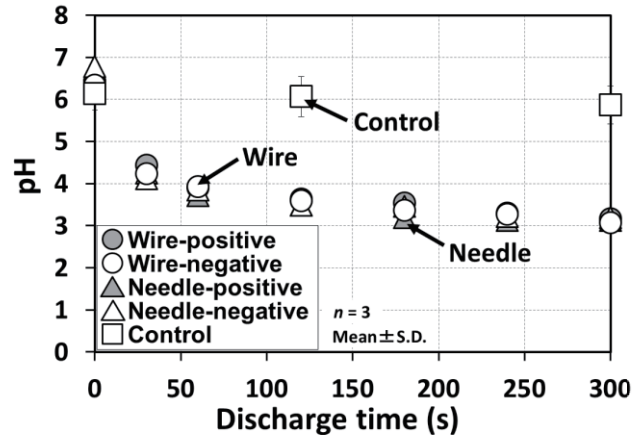

Fig. 4 Change in pH with discharge time

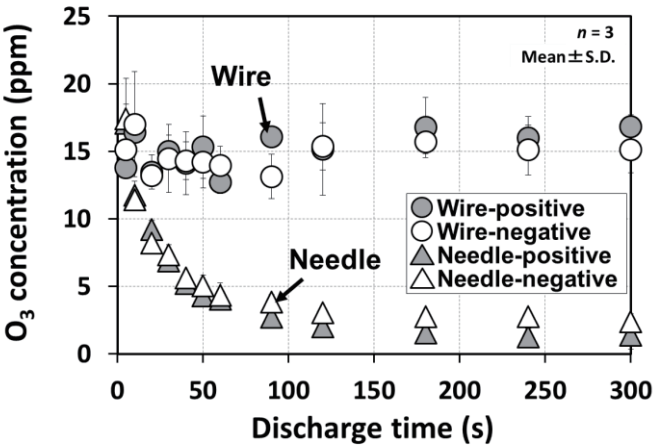

Fig. 6 Variation of ozone with discharge time

3.2 Transport of heat and nitrogen oxide

The temperature rise of the water is shown in Fig. 3. The temperature rise in the case of the wire electrode was lower than that in the case of the needle electrode. The pH of the water changed as shown in Fig. 4. The pH dropped from 6.4 to 4.4 in 60 s, and afterward decreased to 3.2 after 300-second discharge for the both electrodes. The pH variations in the cases of the two electrodes showed the same trend. The conductivity of the water is shown in Fig. 5. The conductivity linearly increased with the discharge time. The inclination of the conductivity using the wire electrode was nearly half of that obtained by using the needle electrode. This result indicates that the concentration of H^+, which plays a role as carrier of charge, using the wire electrode increased nearly half inclination of that using the needle electrode. However, when the concentration of H^+ is considered as pH, the difference is not large

The concentration of O_3 generated in air is shown in Fig. 6. The sampling point was 15 mm distant from the electrodes. The concentration of O_3 generated by the plasma using the wire electrode was constant. On the other hand, the concentration of O_3 with the needle electrode decreased. This result indicates that O_3 can be effectively generated by the plasma discharge using the wire.

4. Conclusion

We investigated fundamental characteristics of gas-liquid plasma with the wire electrode in comparison with the needle electrode, and the results obtained in this study are summarized as follows.

- The amount of heat and nitrogen oxide transported to water using the wire electrode was lower than that with the condition of using the needle electrode. The concentration of O_3 generated in air using the wire electrode was constant.
- The discharge using the wire electrode is low heat transmission. This implies that the plasma using the wire electrode is suitable more for plasma treatment though a control of O_3 and NOx is necessary.

References

[1] P. Bruggeman and C. Leys, Journal of Physics D: Applied Physics, Vol. 42 (2009), 053001.
[2] B. R. Locke et al., Industrial & Engineering Chemistry research, Vol. 45 (2006), pp. 882-905.
[3] M. Sato *et al*., IEEE transactions on Industry Applications, Vol. 44 (2008), pp. 1397-1402.
[4] I. G. Koo et al., Journal of Materials Chemistry, Vol. 15 (2005), pp. 4125-4128.
[5] T. Sato et al., Plasma Processes and Polymers, Vol. 5, (2008), pp. 606-614.

The Effect of Vibration of Ablation Catheter on the Temperature of the Electrode

Kaihong Yu*, Tetsui Yamashita**, Shigeaki Shingyochi***, Makoto Ohta****
*Graduate School of Biomedical Engineering, Tohoku University, 6-6-01, Aobayama, Sendai, 980-8579, Japan
**JMS CO., LTD., 1-13-5, Minamiohi, Shinagawa, Tokyo, 140-0013, Japan
***R&D CENTER, NIDEC COPAL ELECTRONICS CORP., 2188, Akami, Sano, Tochigi, 327-0104, Japan
****Institute of Fluid Science, Tohoku University, 2-1-1, Katahira, Aoba, Sendai, 980-8577, Japan
kaihongmr_yu@biofluid.ifs.tohoku.ac.jp

ABSTRACT

Ablation catheter is widely accepted for treatment of tachycardias. The temperatures of electrode and surface of heart tissue will increase 50°C during ablation and that may lead complications. Then we proposed a new system with electrode vibrating minutely which called vibration ablation catheter for decreasing electrode temperature. We tried to find out the relation by measurements of the temperatures under various frequencies and flow velocities using a new in-vitro system. The cooling effect was increased with increasing frequency. This system has an advantage of decreasing electrode temperature compared to the conventional system.

1. Introduction

Radio-frequency (RF) catheter ablation is a highly effective treatment for many tachycardias such as supraventricular tachycardia, atrial fibrillation, atrial flutter and ventricular fibrillation with a high success rate in excess of 90% [1,2]. During catheter ablation, a catheter with an electrode on the tip is inserted into a blood vessel in the groin and placed at the heart tissue. Then RF energy is introduced through the electrode on the catheter to destroy abnormal heart tissue causing the heart rhythm disorder.

Although the treatment is minimally invasive and curative, problems still remain. A deeper lesion may be necessary for ventricular tachycardia [3]. To ablate deeper tissue, the higher power is needed. However, the high power causes myocardium at interface reaches 100°C which is very dangerous. To prevent that, a temperature sensor inside the electrode and a feedback system inside the RF generator are used to maintain the electrode temperature at a preset level. However, the electrode temperature rises quickly at the preset level, to maintain the electrode temperature output power needs to decrease. As a result, the deeper tissue can't get enough energy to form a lesion. Therefore, it's necessary to make the electrode temperature rising slower under continuous releasing power. To slow the rising speed, cooling for the electrode during ablation becomes necessary. And then irrigation catheter have been developed and widely used.

By releasing saline from the electrode, irrigation catheter can decrease the electrode temperature. However the released saline may increase the burden of heart. And saline can't be used with patients who also have kidney disease. A new cooling mechanism can be used for patients who also have kidney disease is necessary.

We proposed a new system with electrode vibrating minutely which called vibration ablation catheter. However, the effect of frequency of vibration and the flow around the electrode on the temperature are still unclear. The final purpose of this study is to investigate the effects of frequency of vibration and flow velocity on the temperature decrease of electrode. And in this study, we developed an in-vitro system which using PVA-H as ablated tissue and open-channel. Compared to animal myocardium which used in many previous researches, the high transparency makes PVA-H is easily to measure the internal temperature accurately. PVA-H also has dynamic viscoelasticity similar to biological soft tissue [4]. And the catheter can contact with the PVA-H surface in a manner similar to its mode of contact with heart tissue. Using the in-vitro system, we measured the electrode temperature and internal temperature of 2mm depth under various frequencies and flow velocities.

2. Method

2.1 PVA-H preparation

Dimethyl sulfoxide (DMSO, Toray Fine Chemicals Co., Ltd.) and demineralized water were mixed by 80wt% and 20wt% as mixed solvent. PVA powder (JF17, JAPAN VAM & POVAL Co., Ltd.) (99mol% saponification value, 1700 degree of polymerization) of 15 wt% and NaCl of 2 wt% were dissolved into the mixed solvent at 120°C and this temperature was maintained for 2 h. The melted PVA solution was poured into a mold then cooled in a freezer at -20°C for 24 h.

2.2 Open-Channel flow system

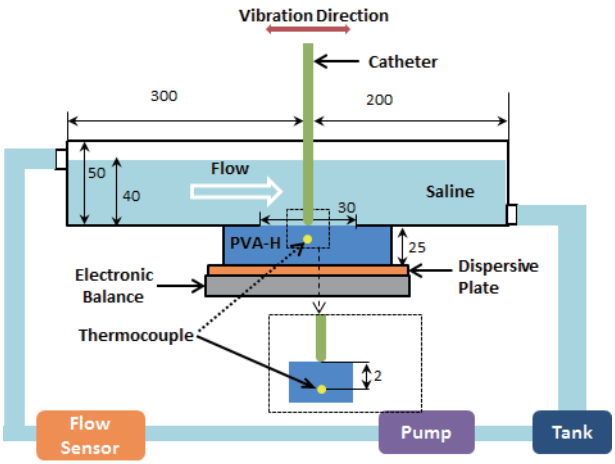

Fig. 1 Schematic diagram of the open-channel flow system. (Unit: mm.)

Figure 1 shows a schematic diagram of the open-channel flow system. The tank was filled with 0.9% saline, and the saline was driven by a magnetic

drive pump (CP20-PPRV-10, Nikkiso Eiko Co., Ltd.). The flow rate was monitored by a capacitance electromagnetic flow sensor (FD-M5AY, Keyence Corporation) at an upstream position. The open channel (500 × 50 × 20 mm) was built using acrylic boards for transparency. A K-type thermocouple (Hayashi Denko Co., Ltd.) with the diameter of 0.5 mm was located at a depth 2 mm from the surface to measure the internal PVA-H temperature. A 7 Fr catheter (Ablaze Single Directional Type, Japan Lifeline Co., Ltd.) with a 4-mm ablation electrode tip was set perpendicular to the PVA-H surface. The catheter axis was placed on the tip of the thermocouple, and the contact weight between the electrode of the catheter and the PVA-H surface was 2.2 gf measured by the electronic balance.

2.3 Temperature measurement

A RF current was introduced into the system at the room temperature. The output power was set at 8W, and the perform time was 60s. Vibrations with amplitude of 0.5 mm and frequencies of 0, 31 Hz and 63 Hz were used. The average flow velocities were: 0, 0.017 m/s, 0.033 m/s. The velocities were calculated from $v=Q/A$, in which v is average velocity of flow, Q is flow rate, A is area of cross section of fluid. The two flow velocities are comparable to blood velocity underneath leaflets [5].

The measurement was carried out three times for each condition. After each measurement, an interval time was set to drop the temperature to the room temperature.

3. Results and Discussion

Figure 2 shows the internal 2mm depth temperature at 60 s under the three flow velocities with vibrations. The temperature at 60 s is the highest temperature during the perform time of 60 s. In case of 0Hz, considering the standard deviations, the 2mm depth under the three flow velocities at 60 s are at the same level of about 51°C. The temperature of internal 2mm depth is maintained when the flow velocity is less than or equal to 0.033 m/s. The output power we used is constant which means the energy delivered to the PVA-H should be constant. And in case of 0Hz, only the flow can reduce the temperature during ablation. However, the flow effect at internal 2mm depth is minor, because the flow doesn't contact to the 2mm directly. That induces the same and the maintained level of temperature in the PVA-H when the flow velocity is less than or equal to 0.033 m/s. In case of 31 Hz vibration, the temperatures are at a same level of 47°C with the standard deviations. And in case of 63 Hz vibration, temperatures are at the level of 45°C. The difference between 0Hz and 63 Hz is only 5°C. Compared to the increased temperature with 0Hz which is 25°C, the difference is small. The cooling effect of vibration on internal 2mm depth is minor.

Figure 3 shows the electrode tip temperature at 60 s under the three flow velocities with vibrations. The temperature of 0Hz decrease as the flow velocity increases. These differences between flow conditions can result from the cooling effect of flow. The 63 Hz vibrations bring the electrode temperatures to a level of about 35°C which is lower than the temperatures with 0Hz. The results could mean that the cooling effect of vibration on electrode is not disappeared by flow velocity. And the effect of 63Hz is stronger than the flow effect under these flow velocities.

The 31 Hz vibrations bring the temperatures to a level of about 42°C under no flow and 0.017 m/s. And under 0.033 m/s, the temperature of 31 Hz is the same as 0Hz. These results could mean that the temperature decrease under low flow velocity depends on the vibration; when the flow velocity gets higher, the temperature decrease depends on the flow. Under 0.017 m/s, the temperature of both 31 Hz and 63 Hz are lower than no vibration, and 63 Hz is lower than 31 Hz. It means that when the cooling effect is depended on vibration, the higher frequency shows the higher cooling effect.

4. Concluding remarks

Vibration ablation catheter can decrease the electrode temperature under the low flow velocity. The cooling effect is increased with increasing frequency. And compared to the conventional system, vibration has an advantage of decreasing electrode temperature without releasing saline.

References

[1] G. Lee, Lancet, **380** (2012), 1509.
[2] F. Morady, NEJM, **340** (1999), 534.
[3] H. Nakagawa, Circulation, **91** (1995), 2264.
[4] H. Kosukegawa, J. Fluid Sci. Tech., **3** (2008), 533.
[5] S. Tungjitkusolmun, IEEE Trans. Biomed. Eng., **48** (2001), 194.

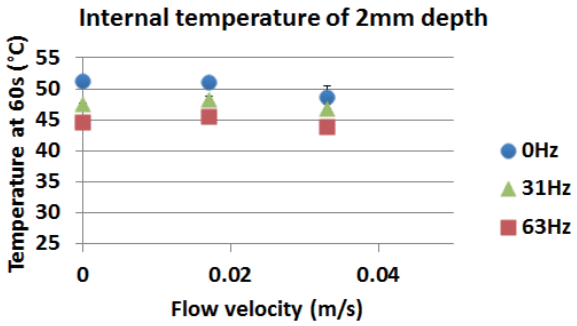

Fig. 2 Internal temperatures of 2mm depth at 60 s under the three flow velocities with vibrations.

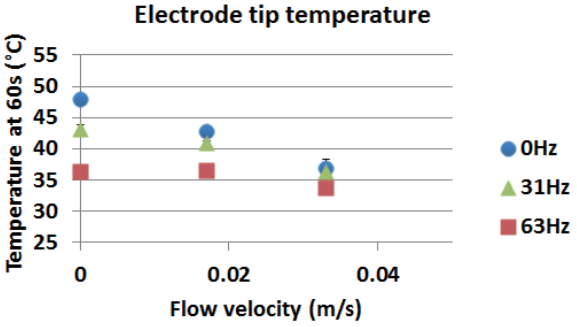

Fig. 3 Electrode tip temperatures at 60 s under the three flow velocities with vibrations.

Tenth International Conference on Flow Dynamics
November 25-27, 2013, Sendai, Miyagi, Japan

Extension of PTV to Three Dimensional Measurement of Velocity Distribution Using Two-Color Intensity Ratio

Hiroshi Isoya, Naoki Shino, Haruko Nagai, Takeshi Yokomori
School of Science for Open and Environmental Systems, Keio University, 3-14-1 Hiyoshi,
Kohoku-ku, Yokohama, Kanagawa 223-8522, Japan
yokomori@mech.keio.ac.jp

ABSTRACT

This study extended PTV to the three dimensional measurement of velocity distribution by using two-color intensity ratio. Particles seeded in a laminar water jet flow were illuminated with two-color laser light, and the scattering light image was taken by a stereo-camera. Three dimensional velocity distribution was estimated from the displacement of the particle spatial position determined with the particle distribution and the two-color intensity ratio. The results proved that this technique can be applicable to measure the three dimensional velocity distribution over a spatially wide area.

1. Introduction

A flow field analysis is important in terms of the fundamental investigation of fluid phenomena. The development of new velocity measurement techniques is required for understanding the flow field in detail.

Particle image velocimetry (PIV) is one of useful techniques for the flow velocity measurement because it provides a non-contact instantaneous velocity distribution measurement. In this technique, the scattering light from particles illuminated with a light sheet is recorded by a camera at two different times, and the displacements of the particles following the flow are determined from those two images. The velocity can be obtained by dividing the displacement distance by the time interval of sequential images.

Many researchers have developed to extend PIV into three dimensional velocimetry. However, those techniques are still not available easily because of a requirement of much analysis time and sensitive optical adjustment.

This study tried to extend PIV to three dimensional measurement of velocity distribution using the two-color intensity ratio. A few researches with the same concept have been reported, and they have only shown the velocity distribution in the quite thin region perpendicular to the image [1]. The purpose of this study was to extend the measurement region perpendicular to the image in this method.

2. Measurement Principle

When two-color laser light is overlapped as shown in Fig. 1, the two-color intensity ratio of scattering light varies depending on the perpendicular position of the particle. The spatial particle positions are determined by the two-color intensity ratio and the particle position in the image plane, and then the velocity distribution can be estimated by the particle tracking in the time series.

3. Experimental set-up

3.1 Optical set-up

The two-color light was obtained from Argon-ion laser (Coherent, Innova 70, 2.3W) as shown in Fig. 2. The wavelengths of 488 nm and 514.5 nm were used. The laser beam was separated into two lights with each wavelength, and then expanded individually in a

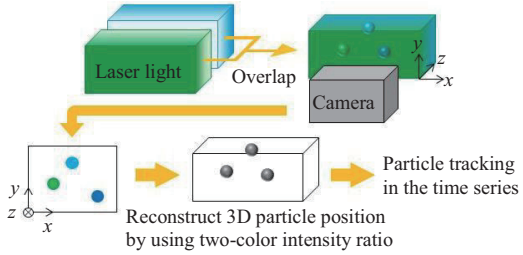

Fig. 1 Schematic diagram of measurement principle.

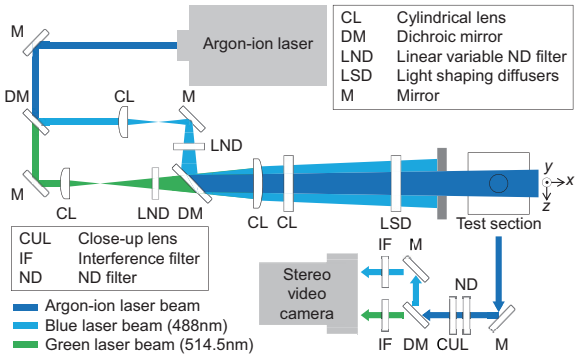

Fig. 2 Schematic diagram of optical set-up.

horizontal direction. Their beams were returned to the same optical path, and finally expanded in a vertical direction. Intensity gradients of the laser light were obtained from a part of a Gaussian distribution and from reforming with a linear variable metallic ND filters (Edmund Optics, NT41-960). The opposite intensity gradients of two lights as shown Fig. 1 were provided by shifting optical paths to the direction perpendicular to the image plane. Light shaping diffusers (Optical Solutions, LSD2PC10-F5) was installed in order to homogenize the small spatial intensity variation of the laser light due to interference of light.

The scattering lights from the particles were recorded by the stereo video camera (JVC, GS-TD1) having twin lenses. The two-color images were taken separately by installing different interference filter in front of each lens.

3.2 Test facility

In this study, the velocity distribution of a laminar water jet ejected from a pipe with 20 mm diameter was measured. Water seeded with tracer particles (Mitsubishi

Chemical, HP20, 200-700 μm) flowed into a rectangular section of 80×80×300 mm^3. The measurement volume was 20×20×20 mm^3 located at 50 mm above the pipe exit. The origin of x, y, and z axes was defined at the center of the pipe exit, and their directions were defined horizontally and vertically parallel, and perpendicular to the image plane, respectively.

An acrylic plate adhered with particles was used for correlating between the two-color intensity ratio and the perpendicular position of the particle. The plate was centered in the measurement volume making an angle of 17° with the image plane. The correlation was investigated by scanning the plate in the perpendicular direction. This scanning was conducted for several regions of image plane because the two-color intensity ratio was not uniform in x-y plane.

3.3 Data processing

This study used particle tracking velocimetry (PTV) which tracks the individual particle in the time series. First, to find x and y positions of each particle in the image plane, the mask correlation method was used [2]. A sub-pixel analysis was also performed by the center of gravity method. Second, the matching of same particles between the two-color images recorded at the same time was performed by using the particle position in the image plane. Third, z position of the particle was obtained from the two-color intensity ratio. Finally, the velocity of a particle was calculated by using the information among four time steps [3].

4. Results and Discussion

An example of the relation between the two-color intensity ratio and the perpendicular position of particle is shown in Fig. 3. The two-color intensity ratio φ is defined as follow equation;

$$\varphi = (I_{488} + I_{514})/(I_{488} - I_{514}). \quad (1)$$

where I is intensity of scattering light and the subscript indicates the wavelength of scattering light. The plots are results obtained from individual particles, and the solid line is the approximate curve. The intensity ratio slightly disperses in the local area because the inhomogenization of the intensity distribution is caused by the interference of the light. The perpendicular particle position (z position) can be obtained by using this relation because the intensity ratio varied only in the perpendicular direction as shown in Fig. 3.

The velocity measurement was demonstrated on the condition of 2.6 mm/s mean jet velocity. Figure 4 shows the velocity vectors averaged over 4×4×4 mm^3, and the region is overlapped 50% with neighbor regions. It is clear from Fig. 4 that the obtained velocity distribution is consistent with the flow qualitatively. However, it was difficult to detect velocities at the end region in the z direction (z ~ -10 mm). The particles are not obtained in the region with the calibration curve as shown in Fig. 3 even if the intensity ratio is small (φ~ -1.0). This can be resolved by adjusting the intensity gradients of the laser light.

The measured velocity distribution is compared with the theoretical velocity distribution of poiseuille flow in Fig.5, where the closed squre is the velocity distribution in the z direction, and the open circle is in the x direction. Both measured velocity distributions are slightly lower than that of poiseuille flow. This is due to the reduction in momentum of the jet and the effect of sedimentation of particle.

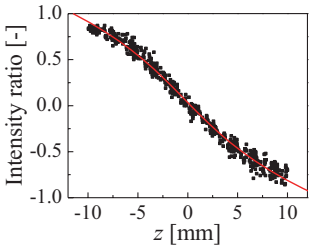

Fig. 3 Relation between two-color intensity ratio and perpendicular position.

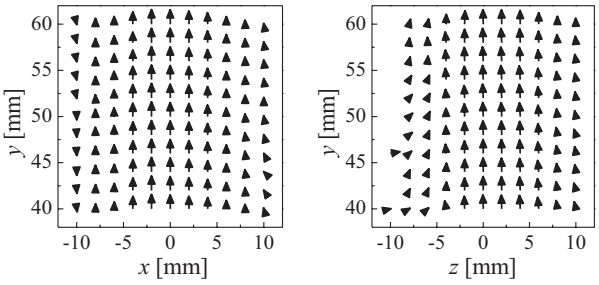

Fig. 4 Two dimensional averaged velocity distribution at (a) z= 0 mm and (b) x= 0 mm.

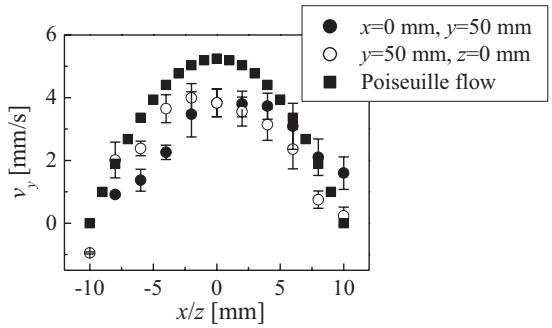

Fig. 5 Comparison with velocity distribution of poiseuille flow and measurement results.

5. Conclusion

This study revealed that two-color intensity ratio PTV could be available to measure the three dimensional velocity distribution, and the measurement region can be expanded widely in the perpendicular direction to the image plane.

References

[1] S. Hosokawa, Multiphase Science and Technology, 19, 3, 269-285, 2007

[2] K. Takehara, T. Etoh, Journal of Visualization, 1, 3, 313-323, 1999

[3] N.A. Malik, et al., Experiments in Fluids, 15, 279-294, 1993

Tenth International Conference on Flow Dynamics
November 25-27, 2013, Sendai, Miyagi, Japan

Application of Paralleling Methods in Solving the Inverse Problem for the Reaction-Diffusion Equations

O. V. Soboleva[1], M. A. Shepelov[1,2]
[1]Institute of Applied Mathematics FEB RAS, 7, Radio St., Vladivostok, 690041, Russia
[2]Far Eastern Federal University, 8, Sukhanova St., Vladivostok, 690950, Russia
soboleva22@mail.ru

ABSTRACT

Inverse extremum problem of identification of the coefficients in an elliptic diffusion-reaction equation is formulated. The solvability of this problem is proved, the application of Lagrange principle is justified and the optimality system is constructed for specific cost functional. The numerical algorithm based on Newton-method of nonlinear optimization and finite-element discretization of linear elliptic problems is developed and programmed on computer. The results of numerical experiments are discussed.

1. Introduction

Modern high-tech manufacturing, medicine, ecology, and other industries require large computing resources and high-tech approach to achieve the best results in its development. Protecting the environment from human impact, and in particular the study of the propagation of the pollutant in water, is one of these areas. Modern computing resources and parallel computing technologies allow highly accurate modeling and statistical analysis of real experimental data in the modeling of mass transfer processes in the study area.

In this work we consider the problem of identification of the coefficients in the differential equation for the mass transfer models using the additional information on the solution of the initial boundary value problem.

The study of this problem can be reduced to the study of the corresponding extremum problem for a certain cost functional. For the theoretical study of inverse extremum problems we use methods of constrained minimization [1-5]. For numerical solution of the inverse problems we use a parallel computing technologies. The application of these technologies enables singles to solve several sub-tasks simultaneously. The application of parallel computing also is caused by processing of a large number of data and solutions of systems of equations with sparse matrices.

The purpose of our work is the theoretical analysis of inverse coefficient extremum problems and creation of efficient numerical algorithms.

We consider the following mass pollutants transfer model:

$$-\operatorname{div}(\lambda\nabla\varphi)+k\varphi=f \quad \text{в} \quad \Omega, \quad \varphi\big|_{\Gamma}=\psi, \qquad (1)$$

considering in a bounded domain Ω of the space R^d, d = 2,3 with Lipschitz boundary Γ.

Here $\lambda\equiv\lambda(\mathbf{x})>0$ is the variable diffusion coefficient, $k=k(\mathbf{x})\geq 0$ is quantity characterizing disintegration of pollutant by chemical reactions, $f=f(\mathbf{x})$ is the volume source density, $\psi=\psi(\mathbf{x})$ is a function given on boundary Γ.

2. Optimal control

The boundary value problem (1) contains a number of parameters that must be given to ensure the uniqueness of the solution. In practice, situations can arise when some of the parameters are unknown. For this reason, we need more information about solution φ of problem (1). As this information we can use, for example, concentration $\varphi_d(\mathbf{x})$ measured in some subdomain $Q\subset\Omega$. Let coefficient k is an unknown function and we must determine this function together with the solution φ of problem (1).

For the study of this identification problem we apply optimization method and reduce solution of this problem to the corresponding extremum problem (see [3-5]). For this purpose we introduce the following cost functional

$$I(\varphi)=\|\varphi-\varphi_d\|_{L^2(Q)}=\int_Q|\varphi-\varphi_d|^2\,dx=\int_\Omega r(\varphi-\varphi_d)^2\,dx$$

Here *r* is the characteristic function of the set *Q*.

Our inverse extremum problem consists of finding a pair of functions (*φ,k*) satisfying the problem (1), and problem of minimizing of the some functional $J: H^1(\Omega)\times L^2_+(\Omega)\to R$:

$$(\lambda\nabla\varphi,\nabla h)+(k\varphi,h)=(f,h) \text{ in } \Omega,\ \varphi\big|_{\Gamma}=\psi, \qquad (2)$$

$$J(\varphi,k)=\frac{\mu_0}{2}\|\varphi-\varphi_d\|^2_{L^2(Q)}+\frac{\mu_1}{2}\|k\|^2_{L^2_+(\Omega)}\to\inf,$$

$$(\varphi,k)\in H^1(\Omega)\times L^2_+(\Omega). \qquad (3)$$

Here (2) is a weak formulation of the direct problem (1), $\mu_0\geq 0$, $\mu_1\geq 0$ are positive constants. Description of the other symbols used can be found, for example, in [3, Chapter 3].

Using the mathematical apparatus of the book [3] we obtained the optimality system. This system has the meaning of the necessary extreme condition of the first-order. The optimality system is essentially used to prove the uniqueness and stability of the solution of the extremum problem and for creation of numerical algorithms. This system consists of the direct problem, adjoint problem and variational inequality, which has the meaning of the minimum principle. The optimality system has the following form:

$$(\lambda\nabla\varphi,\nabla h)+(k\varphi,h)=(f,h)\ \forall h\in\Omega,\ \varphi\big|_{\Gamma}=\psi, \qquad (4)$$

$$(\lambda\nabla\tau,\nabla\eta)+(k\tau,\eta)=(\varphi-\varphi_e,h)_Q\ \eta\big|_{\Gamma}=0, \qquad (5)$$

$$(\mu_1 k+\varphi\eta,\widetilde{k})=0\forall\ k\in L^2_+(\Omega). \qquad (6)$$

3. Numerical experiments

The authors carried out a series of numerical experiments showing the convergence of the developed numerical algorithm based on Newton's method and the efficiency of parallelization techniques for solving inverse problems.

Fig. 1 shows a graph of the restored function k for the case where information about the state of the medium can be described by an analytical function $\varphi_d = (x - x^2)(y - y^2)$, Q coincides with the Ω, λ=0.1, function ψ=0, and our purpose was to recover coefficient k=0.1 sin(πy) when μ_1=10^{-6}.

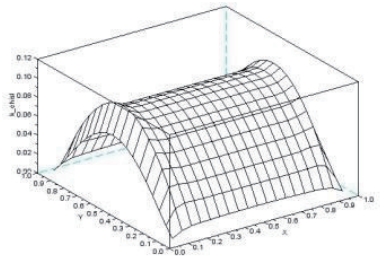

Fig. 1 The restored function k.

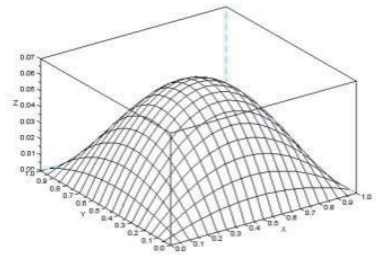

Fig. 2 The restored function φ.

4. Conclusion

In this work the inverse extremum problem was studied for the mass transfer model. Our model has the form of stationary diffusion-reaction equation with variable coefficient of the chemical reactions. This equation is considered in bounded domain under Dirichlet boundary condition. Based on the analysis of optimality system we developed a parallel algorithms for solving of our inverse problems. The testing of our programs has shown the effectiveness of our programs using parallel computing techniques with help a package of computer programs FreeFem++.

Acknowledgments

This work was supported by the Russian Foundation for Basic Research (project nos. 12-01-31288, 13-01-00313), by the Far East Branch of the Russian Academy of Sciences (project no. 12-III-A-01M-002), the Ministry of Education and Sciences (project no. 14.A18.21.0353) and by the Presidium of the Russian Academy of Sciences (basic research program no. 17, project no. 12-1-P17-03).

References

[1] G.I. Marchuk, Mathematical Models in Environmental Problems. Nauka, Moscow, (1982), 319.

[2] A.A. Samarskii and P.N. Vabishevich, Numerical Methods for Inverse Problems in Mathematical Physics (Editorial URSS, Moscow, 2004).

[3] G.V. Alekseev and D.A. Tereshko, Dal'nauka, (2008).

[4] I.S. Vakhitov, Dal'nevost. Mat. Zh., **10** (2010), 93-105.

[5] G.V. Alekseev, I.S. Vakhitov, O.V. Soboleva, Computational Mathematics and Mathematical Physics, **52** (2012), 1635-1649.

[6] A. Murashov, Supercomputers. **1** (2010), 42-45.

[7] E.J. Filatov, Herald ISPU. **3** (2007), 1-4.

Tenth International Conference on Flow Dynamics
November 25-27, 2013, Sendai, Miyagi, Japan

Aerodynamic Influence of a Propeller Wake on NACA0012 Airfoil at Low Reynolds Number

Fumiyasu Makino, Hiroki Nagai
Department of Aerospace Engineering, Graduate School of Engineering, Tohoku University
6-6-01 Aramaki Aza Aoba, Aoba-ku, Sendai, Miyagi, 980-8579 JAPAN
makino.fumiyasu@aero.mech.tohoku.ac.jp

ABSTRACT

The objective of this study is to clarify the effects of the propeller wake on the wing aerodynamics at a low Reynolds number. The experiment was measuring aerodynamic forces of NACA0012 airfoil with and without a propeller and also measuring pressure distributions by pressure taps around the centerline of span direction. Two propeller/wing configurations were studied: pusher and tractor. The tractor propeller wake has an effect to avoid formation of separation bubble and change aerodynamic characteristics. On the other hand, the separation bubble and non-linearity of lift are observed on the pusher propeller configuration.

1. Introduction

The use of airplanes in the exploration of Mars has received much attention because airplane have capabilities of exploring wider area than rover on ground and obtaining higher resolution data than satellite in orbit.

The Mars airplane [1] has propeller propulsion system which needs a large propeller or more numbers of propellers to obtain sufficient thrust in the Martian atmosphere. This is because density of Martian atmosphere is one-hundredth that of the Earth. This results in the problem of a large part of its wing being affected by the propeller-wing interference. Although many studies on the propeller-wing interference of some aircrafts have been reported [2], the case in the Mars airplane is still not clear. Its flight condition becomes low Reynolds number and research of propeller-wing interference in low Reynolds number condition is required.

The objective of this research is to study the effects of the propeller wake on the wing aerodynamics at a low Reynolds number. To clarify this aerodynamic effect, the experiment was measuring aerodynamic forces of NACA0012 airfoil with and without a propeller and also measuring pressure distributions by pressure taps around the centerline of span direction span direction

2. Test models and experimental setup

2.1. Airfoils

The airfoil used in this experiment is NACA0012. Span length of a test model is 300 mm and chord length is 50 mm. To measure characteristics of two-dimensional airfoil, end plates were fitted at both wing tips of the model. The model has five pressure taps around the centerline

2.2. Propeller and motor

The propeller used in this experiment is a thin two-blade propeller for RC model airplanes. It was one of the APC propeller series manufactured by Landing Products. The diameter of the propeller is 8 inches (203.2 mm) and the pitch is 4 inches (106.6 mm). The propeller is driven by a 50 Watts brushless DC motor. The maximum allowable revolution speed of this motor is 10,000 rpm.

2.3. Experimental setup and condition

The experiments were carried out using frontier wind tunnel at the Institute of Fluid Science, Tohoku University. This wind tunnel is open circuit type and test section size is 790 mm by 790 mm square. The aerodynamic force was measured by three-component load cell (Nissho electric works LMC-3531A-5N). The propeller position was set in two cases. First, the propeller was set in front of the airfoil model as a tractor propeller. Second, the propeller was set behind the airfoil model as a pusher propeller. The propeller position was decided so that both center line of propeller and the airfoil model was coincided. The distance between propeller blades and leading edge or trailing edge is 50 mm.

The Reynolds number was set at 40,000 in all experiments. The propeller speed is decided using an advanced ratio *J*. The ratio was defined as follows:

$$J = \frac{U}{nD} \tag{1}$$

where U is flow velocity, n is revolutions per second, and D is the propeller diameter. The propeller was run at J = 0.4, 0.6 and 0.8. The angle of attack was tested from -4 to 20 degrees changed one by one degree in all experiments.

3. Results and Discussion

3.1. Tractor propeller

Figure 1 shows the lift curve of the NACA0012 with the effect of tractor propeller and without the propeller for Re = 40,000. As shown in fig. 1, the stall angle moves to high angle and a maximum lift coefficient increases at J = 0.4 of high rotation speed. However J = 0.6 and 0.8 of low rotation speed, lift coefficient becomes lower compared with a case without the propeller from α = 3 deg to 10deg. When the propeller is run, the lift changes linearly. This is the most important feature of the effect of propeller slipstream. Fig. 2 shows the pressure distribution obtained by pressure taps around the centerline chord. As shown in fig. 2, separation bubble is formed at α = 6 deg in case of without the propeller. On the other hand, separation

bubble is not formed in case of running the propeller. The effect of propeller slipstream is to prevent separation of flow. This effect causes lift curve to change linearly and stall angle to move high angle. The effect of tractor propeller is to make flow on the airfoil as same as flow on the flat plate [3].

3.2. Pusher propeller

Figure 3 shows the lift curve of the NACA0012 with the effect of pusher propeller and without the propeller for Re = 40,000. As shown in Fig. 3, the stall angle moves to high angle and the maximum lift coefficient increases at $J = 0.4$ of high rotation speed as same as the results of tractor propeller. However, overall tendency of the lift coefficient is almost same as the case of without the propeller below $\alpha = 9$ deg. The lift changes non-linearly in all cases. Figure 4 shows the pressure distribution of pressure taps obtained by the centerline chord. As shown in Fig. 4, separation bubble is formed at $\alpha = 6$ deg both in case of with the propeller and without the propeller. The other angle of attack is same as the result of $\alpha = 6$ deg. Those results make lift curve change non-linearity.

4. Conclusions

To study the effects of the propeller slipstream on the wing aerodynamics at a low Reynolds number, the experiment was measuring the aerodynamic force and pressure distribution of NACA0012 with the propeller.

The results of tractor propeller show that the lift coefficient becomes to the linear. This is because the flow separation and bubble formation are prevented by the effect of propeller slipstream. By contrast, the separation bubble is formed in case of pusher propeller. This causes non-linearity of lift curve in all cases of propeller rotation speed.

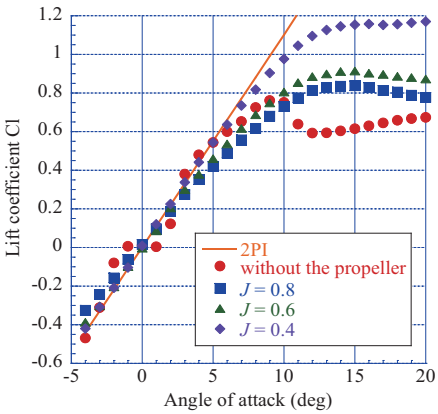

Fig. 1 Lift curve of NACA0012 affected by tractor propeller

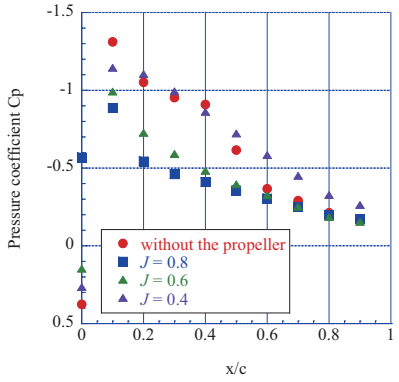

Fig. 2 Pressure distribution in case of tractor propeller at $\alpha = 6$ deg

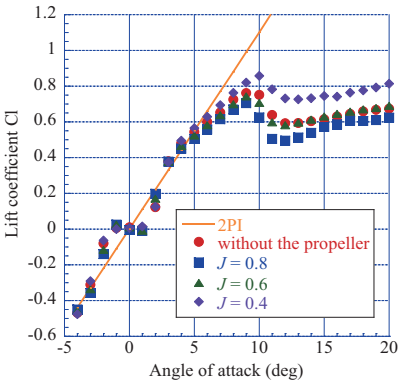

Fig. 3 Lift curve of NACA0012 affected by pusher propeller

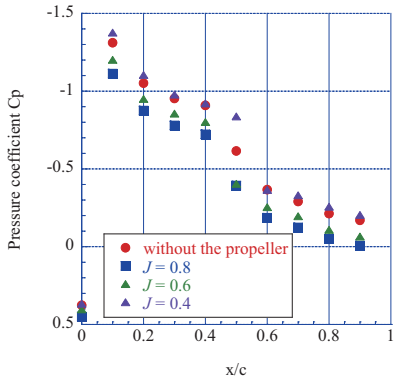

Fig. 4 Pressure distribution in case of pusher propeller at $\alpha = 6$ deg

References

[1] K. Fujita, H. Nagai, K. Asai, "Conceptual Design of a Miniature, Propeller-Driven Airplane for Mars," 50th AIAA Aerospace Sciences Meeting, AIAA 2012-0847, Gaylord Opryland Resort & Convention Center Nashville Tennessee, 9-12 Jan. 2012.

[2] F. M. Catalano, "On the Effects of an Installed Propeller Slipstream on Wing Aerodynamic Characteristics", Acta Polytechnica, Vol. 44, No. 3, 2004.

[3] M. Anyoji, K. Nose, S. Ida, D. Numata, H. Nagai, and K. Asai, "Characteristics of the Mars Wind Tunnel at Tohoku University in CO_2 Operation Mode", 48th AIAA Aerospace Sciences Meeting, Orland, Florida, January 4-7, 2010.

Tenth International Conference on Flow Dynamics
November 25-27, 2013, Sendai, Miyagi, Japan

Pressure Wave Propagation and Unsteady Behavior of Cloud Cavitation in a Cylindrical Convergent-Divergent Nozzle

Shota Hayashi, Keiichi Sato
Graduate School of Kanazawa Institute of Technology, 7-1 Ogigaoka, Nonoichi, Ishikawa 921-8501, Japan
b6101190@planet.kanazawa-it.ac.jp

ABSTRACT

It is well known that cloud cavitation shows periodic unsteady behavior with reentrant motion and shedding motion of clouds on a hydrofoil. In this study, high-speed observation and image analysis were conducted to make clear the mechanism of the unsteady behavior in a cylindrical convergent-divergent nozzle. As a result, it was observed in the nozzle that the periodic unsteady behavior occurs in cloud cavitation and pressure waves form at the collapse of the cloud shed downstream. Also, it was found that the pressure wave plays a role as a trigger mechanism to cause the reentrant motion at the bottom of an attached cavity.

1. Introduction

It is well known that cloud cavitation shows periodic unsteady behavior with growth motion of an attached cavity, reentrant motion and shedding motion of clouds [1-2], and high-intensive impact is caused by collapse of the clouds shed downstream[3]. Also, it has been found that the reentrant motion is closely related to the mechanism of shedding motion of clouds[4].

However, the mechanism of the periodic unsteady behavior remains to be fully elucidated. The authors have studied to make clear the mechanism using a convergent-divergent nozzle with rectangular cross-section. As a result, it has been demonstrated that the reentrant motion is triggered by the pressure wave propagation due to the collapse of the clouds shed downstream[1], and intrusion due to chain-reaction collapse of babble clusters at the nozzle throat has a suppressive action on supply of upstream vorticity[5]. In a cylindrical nozzle with a convergent-divergent part, however, observation of cloud cavitation has scarcely been conducted. The detailed studies of the unsteady behavior are required to apply the high-intensive impact with cloud collapse from an engineering view point.

In this study, high-speed observation technique and image analysis based on a frame difference method were used to analyze and estimate the behavior of cloud cavitation in a cylindrical convergent-divergent nozzle.

2. Experimental Apparatus and Image Analysis Method

Fig. 1 shows the schematic of an apparatus. A high-pressure pump with 3 plungers discharges water, and it is jetted from a submerged nozzle shown in Fig. 2 into water at rest in a large tank. Behavior of cloud cavitation is observed by a high-speed video camera (Photron, FASTCAM SA5, image size of 64×536 pixels at 100,000fps) with a light plane guide set in the water at the opposite side of the camera across the nozzle. The light guide is connected to a light source of 350W with continuous light (NPI, PCS-UMX 350). The nozzle is made of acrylic resin and its flat and smooth outer surface with high transparency allows for obtaining clear images. The nozzle throat is chosen as origin and the flow direction from the origin is defined as x-axis.

A frame difference method is used as image analysis method[6] as shown in Fig. 3. First, an analysis region with 49 pixels of width and 536 pixels of height in images taken by the camera is chosen, where gray level distribution is averaged over 49 pixels in the direction normal to the flow direction. As shown in Fig. 3(a), changes in gray level in the x-direction are obtained over all images. Second, difference values of the averaged gray level are calculated every time interval over a whole time range as shown in Fig. 3(b). Next, the difference values of gray level are colored again based on the definition of gray level map (with n=8 in the present study) as shown in Fig. 3(c), and then the same procedure is applied to all the difference values. Finally, the newly-colored difference values are ordered in time to obtain the contour map of the difference values of averaged gray level, in which the contour map shows relationship between normalized distance x/d and elapsed time t, as shown in Fig. 3(d). In the contour map, white region shows appearance of the cavity and black one shows disappearance of it.

In the paper, p, Fs, β, σ and St denote upstream pressure, frame speed, dissolved oxygen content, cavitation number and Strouhal number, respectively.

$$\sigma = \frac{2(p - p_v)}{\rho u^2} \tag{1}$$

$$St = \frac{lf}{u} \tag{2}$$

where p_v is vapor pressure of water, ρ density of water, u velocity in the throat, l maximum attached cavity length and f the frequency of reentrant motion, respectively.

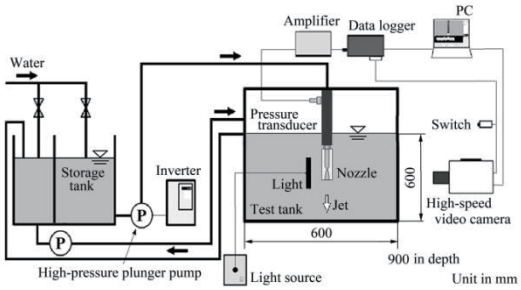

Fig. 1 Schematic of experimental apparatus

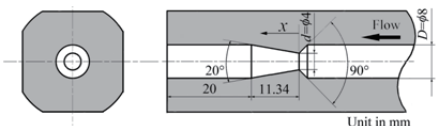

Fig. 2 Transparent convergent-divergent nozzle

3. Experimental Results

Fig. 4(a) shows the successive images of the behavior of cavitation cloud and Fig. 4(b) shows the typical result of the image analysis. As indicated by an arrow A in the figures, a shedding cloud moves downstream, and then it collapses at about t=59.55ms. In Fig. 4(b), chain-reaction collapse of microscopic bubbles corresponding to pressure wave propagation due to the collapse of the cloud is visualized by black lines nearly perpendicular to the time axis, which means that it has very fast speed. From the slope of the black lines, it turns out that the pressure wave labeled P1 propagates at about 250m/s, P2 at 200m/s and P3 at 650m/s, respectively. Since P1 and P2 show propagation within the shedding clouds, their propagation speeds are slower than P3 propagating in the region where a void fraction is considered to be relatively low. When the pressure wave reaches to a growing attached cavity indicated by an arrow B, reentrant motion (arrow C) is triggered and starts along the surface of the divergent part of the nozzle to the throat at speed of about 10m/s while a few rebounds of the cloud occur repeatedly. The attached cavity is separated from the nozzle by the reentrant motion, and moves downstream as the following cloud with large-vortex structure indicated by an arrow D. At the same time, the following attached cavity (arrow E) starts to grow and it moves on to the following cycle. A period of this cycle is estimated to be about 2.1ms and its frequency is approximately 480Hz. Strouhal number St is 0.34±0.02 under σ=2.2.

4. Concluding remarks

Periodic unsteady behavior of cloud cavitation is observed in a cylindrical convergent-divergent nozzle. From image analysis, it is found that cavities behave periodically with 0.34±0.02 of Strouhal number under 2.2 of cavitation number, and pressure wave formation at collapse of clouds shed downstream is considered to be one of trigger mechanisms to cause reentrant motion at the bottom of an attached cavity.

Acknowledgements

We would like to thank Dr. Yasuhiro Sugimoto for his kind and helpful advice on this study.

References

[1] K. Sato, Y. Wada, Y. Noto and Y. Sugimoto, Proc. ASME 2010 3rd Joint Meeting (2010), pp.7-11.

[2] J. P. Franc and J. M. Michel, “Fundamentals of Cavitation,” (2004).

[3] G. E. Reisman, Y. C. Wang and C. E. Brennen, J. Fluid Mech., Vol. 355 (1998), pp. 255-283.

[4] M. Sakoda, R. Yakushiji, M. Maeda and H. Yamaguchi, Proc. 4th Int. Symp. Cav. (2001), pp. 1-8.

[5] K. Sato and S. Shimojo, Proc. 5th Int. Symp. Cav. (2003), pp. 1-7.

[6] K. Sato, Y. Sugimoto and S. Ohjimi, Proc. 7th Int. Symp. Cav., No. 66 (2009), pp. 1-11.

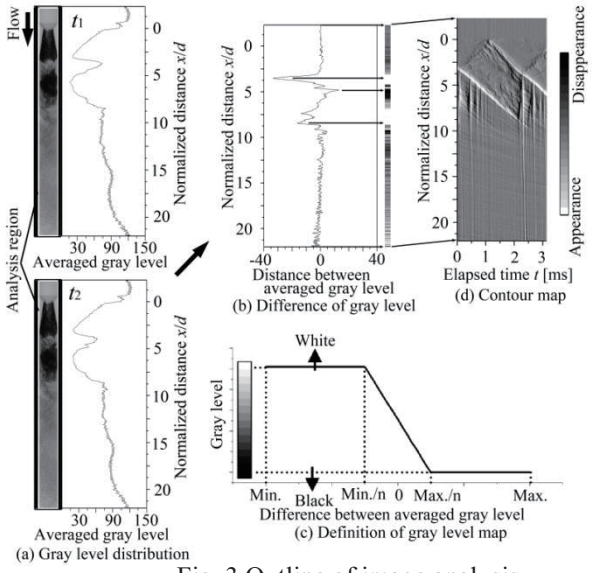

Fig. 3 Outline of image analysis

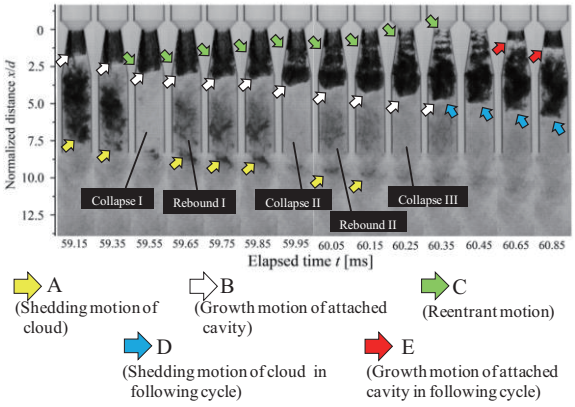

(a) Successive images on unsteady behavior of cavity

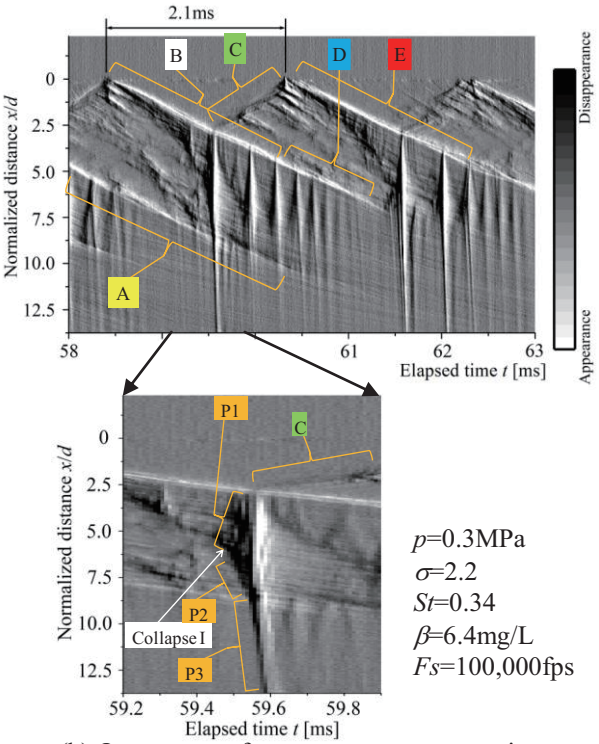

(b) Occurrence of pressure wave propagation

Fig. 4 Periodic behavior of cloud cavitation

Tenth International Conference on Flow Dynamics
November 25-27, 2013, Sendai, Miyagi, Japan

Effect of Impingement Surface Geometry on Erosion in Cavitating Water Jet

Kouhei Yoshihisa, Kazuki Niiyama, Keiichi Sato
Kanazawa Institute of Technology, 7-1 Ogigaoka, Nonoichi, Ishikawa, 921-8501, Japan
kouhei-yoshi@venus.kanazawa-it.ac.jp

ABSTRACT

A high-speed water jet ejected into water forms a cavitating water jet accompanied by cavitation cloud. A powerful impulsive force can be caused when the cavitation cloud collapses. The cavitating water jet produces severe cavitation erosion. However, the detailed mechanism about cavitation erosion have not been fully elucidated. The purpose of this study is to examine the effect of erosion pits on cavitation erosion with the cloud collapses. We focus on cloud collapses in the vicinity of impinging surface of cavitating water jet and discuss a correlation between cavitation erosion and bubble collapses using an image analysis.

1. Introduction

A powerful impulsive force can be caused by collapses of cavitation clouds. Then, the ring-like erosion distribution is often produced on the wall surface when cavitating water jet (CAV-WJ) impinges on the wall surface[1]. The erosion pits are formed by collapses of cavitation clouds[2]. It has been described that the erosion progressed with iteration of these cloud collapses[3] and the impact of cloud collapses converged on the erosion region[4]. The details of interference mechanism, however, have not been fully elucidated.

In the present study, a high speed observation of the behavior of clouds with laser beam was conducted in erosion test. Observation of cloud collapses on the erosion surface was conducted every exposure of CAV-WJ. The correlation between the erosion pits and the cloud collapses was evaluated with an image analysis. We visualized cloud collapses in the vicinity of the impinging surface with a laser sheet and examined the effect of cloud collapses on erosion pits.

2. Experimental Method

2-1 Experimental Apparatus

The experiments were conducted with a convergent-divergent nozzle which has throat diameter of d=0.4mm. Figure 1 indicates a schematic diagram of the test apparatus. Tap-water was ejected to the specimen surface in the test section under the upstream pressure of p_u=10MPa.

A cylindrical specimen of acrylic-resin was used with the diameter in 12mm and thickness in 4mm. The center of the impingement surface was chosen as the origin, the counter direction against the jet direction as the x-axis and the upper side in the direction vertical to x-axis as the y-axis. The z-axis was the perspective direction in Fig.1 (a). Moreover, the stand-off distance from nozzle holder exit to impingement surface was set to X=20mm.

The observation of the Y-Z surface was taken using a high-speed video camera (Photron, Fastcam SA5) with an argon ion laser (SOC, GLS33480B + GLG3482), where the power of the laser was 2W. A sheet laser was made through a cylindrical lens and was irradiated parallel to the Y-Z surface. There was the center of the laser between X=0mm and 2mm so that the cavitation cloud was taken only in the vicinity of the impingement surface. Observation was conducted using a high-speed video camera at frame rate Fs=100000fps, where the observation area was 256×232 pixel (15.1×13.6mm).

Total exposure time of CAV-WJ was t=180min and high-speed observation was conducted every 30min, where high-speed movies were taken three times for 30sec in each period of high-speed observation (the time length of a movie is 64.23ms). Moreover, the exposure of CAV-WJ was halted after each high-speed observation and then the erosion distribution was taken by camera with a metal halide lamp.

2-2 Image Analysis Method

We conducted an image analysis in order to quantitatively estimate a cloud disappearance rate. First, we applied a smoothing filter to the images obtained from the high-speed observation and obtained the difference image GL_i between an image and the next image. Collapses and disappearances of clouds were evaluated by GL_i. Positive values and zero values in GL_i indicate the appearance and the inflow of cloud to the pixel. On the other hand, negative values indicate the collapse, the disappearance and the outflow to the other

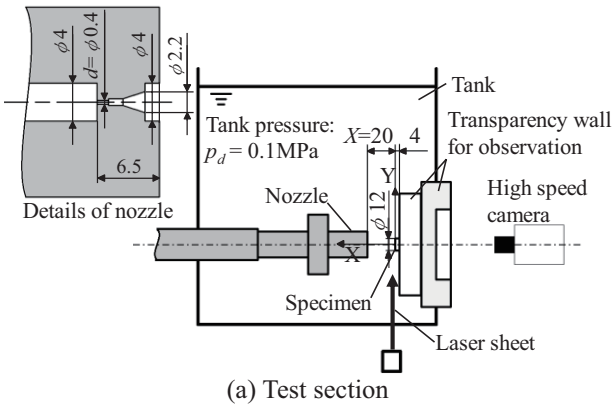

(a) Test section

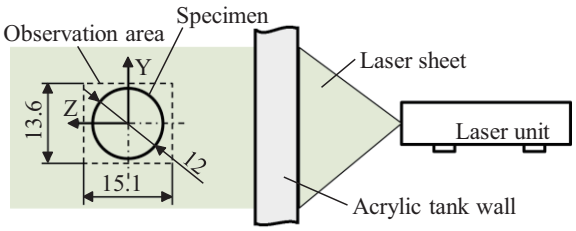

(b) Observation by laser sheet

Fig.1 Schematic diagram of test apparatus

pixel. As a next step, all negative values in GL_i are converted to 1. All positive values and zero values in GL_i are converted to 0. The converted image is called binary image GL_i'.

Second, in order to investigate a collapsing and disappearancing motion in particular, we tried to remove a cloud movement using a filtering process (9×9 pixel). The threshold velocity was set on about 30m/s since typical velocity of movement was estimated to about 20m/s by the experimental observation.

Third, these processings were conducted for all obtained images. Then we calculated disappearance rate D by equation (1).

$$D = \left(\sum_{i=1}^{n} GL_i' \right) \times \frac{100}{n} [\%] \qquad (1)$$

The image analysis was made for three times of observation results, where the number of difference images n per one shoot was n=6422. Thus, the disappearance rates D were shown as the average value of three times together with color bars D in Fig.2 (b).

3. Results and Discussion

Figure 2 (a) shows erosion distributions from the beginning to t=180min. Figure 2 (b) shows the image analysis results. When plenty of clouds were present on the wall surface, the behavior of clouds was observed as an asymmetric form because the laser sheet was prevented by the existence of cavitation clouds. Therefore, in Fig.2 (b), image analysis results show only the irradiated side. Figure 3 shows D_a (averaged disappearance rate) averaged along a circumferential direction in Fig.2 (b).

In Fig.2 (a), the erosion distribution could be observed from t=60min and it became clearer in the course of time. Moreover, the erosion region also expanded. Then, the formed erosion pits were distributed circularly and little erosion pits were observed in the center of jet impingement and the vicinity.

From aspect observation, movements, collapses and disappearances of clouds periodically occurred in the vicinity of the impingement surface. In Fig.2 (b), when CAV-WJ moved from the center of jet impingement to the outer circumference, a part of clouds tended to exist around the center of the jet impingement. Therefore, it is found that D in the vicinity of the jet impingement region (ex. R=2mm) was lower than that of the outer circumference region (R=4mm). However, D_a shown in Fig.3 has an increase trend in erosion region. At t=60min, D_a in the erosion region tended to be higher than the region without erosion. Moreover, at t=120min, D_a was obviously higher in the erosion region. It is considered that the erosion was developed because the collapses and disappearances of clouds were higher in the existing erosion region. Moreover, D was higher than that at the beginning as the erosion developed, especially in the outer region (R=3, 4mm). Consequently, it is presumed that collapses and disappearances of clouds were affected by the formed erosion pits.

In this study, cloud movement could not be removed completely using the present image analysis method. For example, at t=180min, D also appears in the outside of the specimen. Therefore, the image analysis method needs further improvement as a future work.

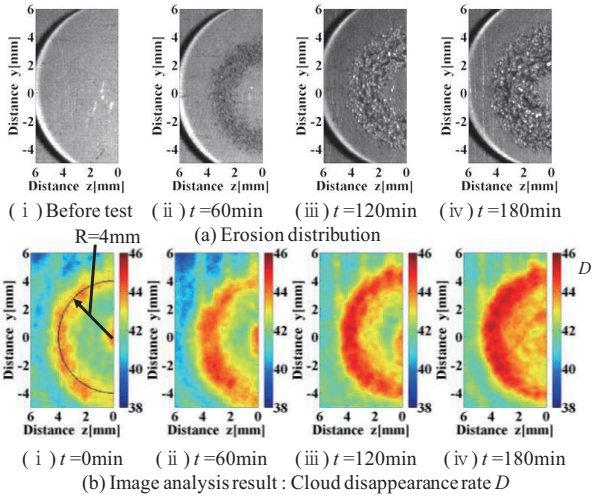

Fig.2 Erosion distribution and cloud disappearance rate against exposure time

4. Concluding remarks

In the present study, the effect of erosion pits on cavitation cloud collapses was experimentally investigated. The main results are summarized as follows.

First, in erosion region, the disappearance rate of cloud increased in the course of time. Second, at the beginning of erosion the disappearance rate in the outer vicinity of the impingement center of CAV-WJ was lower than the other region, though it increased with exposure time.

References

[1] K. Sato, et al., *Proc. The 7th International Symposium on Cavitation CAV2009*, (2009), Paper No.66.

[2] K. Sato, et al., *JSME*, 64-622, B(1998), pp.1683-1688(in Japanese).

[3] Y. Yamauchi, et al., *JSME*, 59-557, B(1993), pp.16-22(in Japanese).

[4] Y. Yamauchi, et al., *JSME*, 60-571, B(1994), pp.736-743(in Japanese).

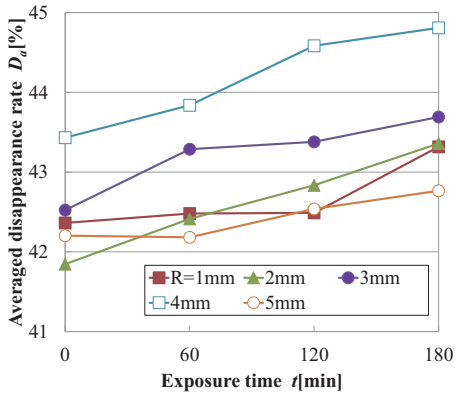

Fig.3 Averaged disappearance rate at several diameters against exposure time

Tenth International Conference on Flow Dynamics
November 25-27, 2013, Sendai, Miyagi, Japan

A Molecular Dynamics Study for Diffusivity of Proton and Water in Nafion Membrane

Takuya Mabuchi[1], and Takashi Tokumasu[2]
[1]Graduate School of Engineering, Tohoku University, Sendai, Miyagi 980-8577 Japan
[2]Institute of Fluid Science, Tohoku University, Sendai, Miyagi 980-8577 Japan
mabuchi@nanoint.ifs.tohoku.ac.jp.

ABSTRACT

We have performed an atomistic analysis of hydronium ions and water molecules transports in the nanostructure of hydrated Nafion membrane using classical molecular dynamics simulations. The new empirical valence bond (EVB) model is developed based on the previous study of EVB model reported by Walbran et al. in order to improve the description of proton mobility in both aqueous and Nafion environments. A large contribution of Grotthuss mechanism for the diffusion of hydronium ions has been found and this implies the important impact of Grotthuss mechanism in the membrane as well as in the bulk aqueous solutions.

1. Introduction

Polymer electrolyte fuel cells (PEFCs) are highly expected as a next-generation power supply system due to the purity of its exhaust gas, its high power density and high efficiency. The heart of PEFCs is polymer electrolyte membrane (PEM) that separated the reactant gases and conducts protons. In the nanoscopic structure of the membrane, ion clusters are formed by water molecules gathered vicinity of sulfonate groups which are hydrophilic parts of Nafion membrane, and protons transport inside of these water aggregations. The molecular level structure and transport mechanism of protons are important factors contributing to dynamic properties of protons in the membrane. Thus, it is critical to understand an important link between Nafion membrane nanostructure and the dynamics of water molecules and hydronium ions to enhance proton transport. In this study, a revised EVB model is developed based on the previous study of EVB model reported by Walbran et al. [1], then we have applied the new EVB model to Nafion system and investigated the impact of the Grotthuss mechanism [2] on the property of hydronium ions transport in the membrane.

2. Method

To reproduce the Grotthuss mechanism in our simulation, a new EVB model is developed. In the EVB model, we employed a function of the proton transfer coordinate, defined as

$$Q \equiv \left|R_{O^*H}\right| - \left|R_{OH}\right| \tag{1}$$

where O* and O are the oxygen of the hydronium ion and water molecule, respectively. Also, the potentialenergy of the Zundel cation V_{ad} uses the following expression:

$$V_{ad} = \frac{\left(V_i + V_f\right) - \sqrt{\left(V_i - V_f\right)^2 + 4\Lambda\left(Q,R\right)^2}}{2} \tag{2}$$

where Λ is a function of Q and R which is the distance between O* and O. V_{ad} is modified by parameterizing the function Λ, to fit it to the curves of the potential energy surface (PES) calculated by ab initio calculation. Fig. 1 shows a comparison between the ab initio data and the results obtained with the EVB model for O*- O separations corresponding to 2.2, 2.4, 2.6, and 2.8 Å, respectively. In all 4 distance cases, the results of EVB model are in good agreement with the corresponding ab initio data.

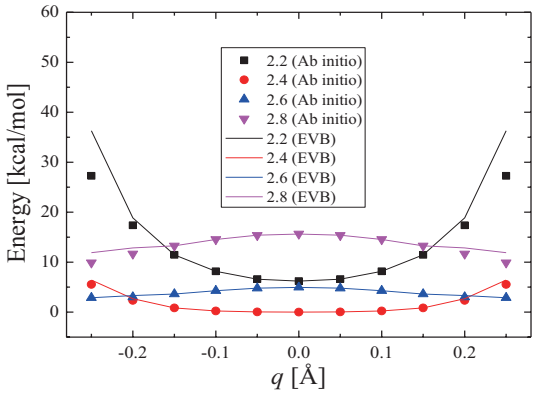

Fig. 1 PES curves for the proton shuttling in the Zundel cation at O*-O distances of 2.2, 2.4, 2.6, and 2.8 Å.

The Nafion membrane was used as PFSA membrane. We generated Nafion by linking the polar monomeric unit (P) to the end of the nonpolar monomeric unit N_7, repeating the procedure 13 times to obtain $(N_7P)_{13}$, in the notation of Jang et al. [3]. The potential model for Nafion was based on the DREIDING force field as referred to previous studies by other authors [3,4]. The aSPC/Fw m model [5] for hydronium ions and water molecule are employed. The initial configurations were generated by randomly placing 25 Nafion chains in a box, $x \times y \times z$ = 200 × 200 × 200 Å^3, with periodic boundary condition in all directions. To ensure charge neutrality, we added a total of 325 hydronium ions and considered water contents of λ = 3, 6, and 12, where the parameter λ indicates the ratio of the number of water molecules to that of SO_3^- ($N_{H2O,\ H3O+}/N_{SO3-}$). After all molecules were added, the annealing procedure was carried out to eliminate initial configuration and orientation of molecules and then to establish equilibrium state. Firstly, the simulation cell was compressed gradually for 50 ps to fit with experimental density [6], and *NPT* MD simulation for 100 ps at 800 K and 100 MPa using the reduced to 1/100 magnitude of L-J

potential parameters, ε, among Nafion atoms [7]. After that, *NPT* MD ensemble for 50 ps with the temperature and pressure gradually decreased from 800 to 300 K and 100MPa to 0 MPa, respectively. In addition, we annealed it in four steps as follows: 1. *NPT* MD simulation for 100ps at 300 K; 2. *NVT* MD simulation for 50 ps with the temperature increased gradually from 300 to 800 K; 3. *NVT* MD simulation for 50 ps at 800 K; 4. *NVT* MD simulation for 50 ps with the temperature decreased gradually from 800 to 300 K. We repeated these four steps four times and the final density was then obtained after *NPT* MD run for 200 ps at 300 K. We used this final structure for the production *NVE* ensemble for 2.4 ns and the trajectory of molecules was collected every 0.2 ps. The temperature was held by the Nosé-Hoover thermostat [8], and the pressure was controlled by the Andersen method [9].

3. Results and discussion

The mobility of the hydronium ions and water molecules was analyzed by calculating the MSDs of the hydronium ions and the water molecules during the simulations. We determined the diffusion coefficients, D, for the hydronium ions and water molecules using MSDs to satisfy the Einstein-Smoluchowski function written as

$$D = \lim_{t\to\infty} \frac{1}{6t} \left\langle \left| r(t) - r(0) \right|^2 \right\rangle \tag{3}$$

where t is the diffusion time, $r(t)$ is the position vector of hydronium ion and water molecule. Fig. 2 shows the diffusion coefficients calculated from the linear regime of their MSD curves and the values from NMR experiment in which the values for hydronium ions are converted from protonic conductivity [10]. The trends of experiment data, the diffusion coefficients of both hydronium ions and water molecule increase with increasing water content, are well reproduced and these results testify the validation of our simulation models. In addition, the diffusion coefficient of hydronium ions for EVB model at $\lambda = 6$ has higher value which is in better agreement with experimental data, than for Vehicle model at $\lambda = 6$ although the diffusion coefficient of water molecules are almost the same for EVB model and Vehicle model. This result is associated with a large contribution of Grotthuss mechanism for the diffusivity of hydronium ions at $\lambda = 6$. However, all diffusion coefficient values from the results obtained with EVB model have slightly lager value than experiment, and this is attributed to the diffusivity of the membrane which is relatively higher in our simulation due to the limitation of chain length compared with that of real polymer chains. In this regard, the use of the membrane with a constraint of its mobility could lead to a more accurate property of solvated molecules transport in the membrane.

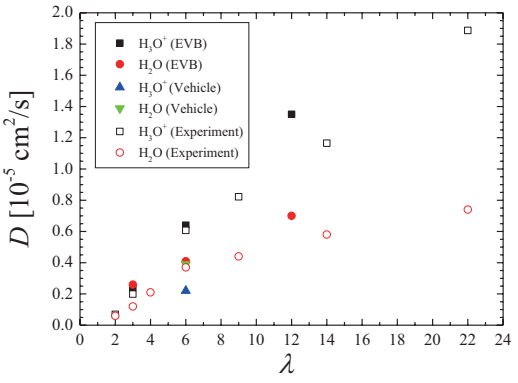

Fig. 2 Diffusion coefficients of hydronium ion and water molecule.

4. Concluding remarks

We have performed an atomistic analysis of hydronium ions and water molecules transports in the nanostructure of hydrated Nafion membrane by systematically changing the hydration level using classical molecular dynamics simulations. The new EVB model is developed to improve the description of proton mobility in the Nafion membrane. We have calculated MSD to determine the diffusion coefficients of hydronium ions and water molecules as a function of hydration level. The results clarified the significant impact of Grotthuss mechanism on the transport property of hydronium ions, and at the same time they testified the validation of our simulation by comparing with the experimental data of diffusion coefficients.

References

[1] S. Walbran, A.A. Kornyshev, J Chem Phys 114 (2001) 10039.
[2] N. Agmon, Chem Phys Lett 244 (1995) 456.
[3] S.S. Jang, V. Molinero, T. Cagin, W.A. Goddard, Journal of Physical Chemistry B 108 (2004) 3149.
[4] T. Li, A. Wlaschin, P.B. Balbuena, Ind Eng Chem Res 40 (2001) 4789.
[5] K. Park, W. Lin, F. Paesani, Journal of Physical Chemistry B 116 (2012) 343.
[6] D.R. Morris, X.D. Sun, J Appl Polym Sci 50 (1993) 1445.
[7] S. Ban, C. Huang, X.Z. Yuan, H.J. Wang, Journal of Physical Chemistry B 115 (2011) 11352.
[8] W.G. Hoover, Phys Rev A 34 (1986) 2499.
[9] H.C. Andersen, J Chem Phys 72 (1980) 2384.
[10] T.A. Zawodzinski, M. Neeman, L.O. Sillerud, S. Gottesfeld, J Phys Chem-Us 95 (1991) 6040.

Tenth International Conference on Flow Dynamics
November 25-27, 2013, Sendai, Miyagi, Japan

Acetic Acid Decomposition by Coaxial Cylinder Type DBD Tube with Mist Flow

Tomohiro Shibata[1] and Hideya Nishiyama[2]
[1]Graduate School of Engineering, Tohoku University, 2-1-1 Katahira Aoba-ku, Sendai 980-8577, Japan
[2]Institute of Fluid Science, Tohoku University, 2-1-1 Katahira Aoba-ku, Sendai 980-8577, Japan
shibata@paris.ifs.tohoku.ac.jp

ABSTRACT

The world has been faced with serious problems of water pollution. The conventional chemical treatment has been replaced by a water treatment system using non-thermal plasma. Because the plasma treatment is environmentally adaptive. In this study, the water treatment method spraying solution into the coaxial cylinder type dielectric barrier discharge (DBD) tube is investigated. Acetic acid, which is one of the Persistent organic carbon, is decomposed about 50 % using coaxial cylinder type DBD tube

1. Introduction

Water pollution is a serious problem in the world. Especially, the persistent organic pollutants (POPs) are one of the most important problems. Various organic compounds are synthesized in industrial processes and used for our convenient living. Since most of them are synthesized in pursuit of stability and do not exist in natural environment, they are resistant to environmental degradations such as chemical, biological and photolytic processes. Because of this, The POPs are accumulated in human and animal tissues through a food chain.

The technology of Non-thermal plasma with liquid have been paid attention because the reactive species such as ozone and OH radical generation. Ozone treatment have been industrially accepted in water treatment applications and conventional waste water treatment e.g., biological and chemical method, has been replaced by a water treatment method using plasma. However the some POPs require higher oxidation potential than that of ozone. Generating plasma near the solution, not only ozone but free radicals which has short life time are utilized for water treatment. Recently, the water treatment method utilizing the discharge in bubble, above water, in water or with mist flow is developed. Furthermore, it is reported that the water treatment method of spraying water into non-thermal plasma shows highest energy efficiency in Malik's paper. The authors also have shown the high energy efficiency of methylene blue decomposition by spraying solution into non-thermal plasma using SMD tube in our earlier study[2].

In this study, water treatment method spraying solution into coaxial cylinder type Dielectric Barrier Discharge (DBD) tube. The target to decompose is acetic acid which require higher oxidation potential than that of ozone. Since the atomized acetic acid solution can interact with plasma directly, acetic acid is decomposed by OH radical. Furthermore, formic acid and oxalic acid are generated as by-products.

2. Experimental setup and procedure

Figure 1 (a) shows the schematics of experimental setup, which mainly consists of an electric power supply, a water tank, an ultrasonic atomizer unit, a DBD tube and a condenser. 9 ℓ/min air is used as a carrier gas. The treatment solution is an acetic acid solution which is diluted 10,000 times in distilled water. The oscillating frequency of the ultrasonic atomizer unit is 2.4 MHz and the electric power is 17 W. The mist density which is calculated by the gas flow rate and treated solution amount is varied from 10 ppm to 100 ppm by changing the water level in the water tank. The mean diameter of droplet D is predicted by equation (1)

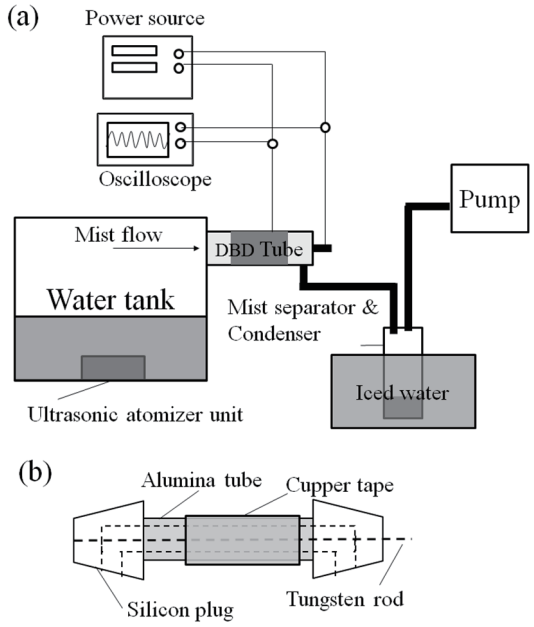

Fig. 1 Schematic illustration of experimental setup (a) and configuration of DBD tube

$$D = 0.34 \times \left(\frac{8\pi\sigma}{\rho F^2}\right)^{\frac{1}{3}} \quad (1)$$

where σ is the surface tension coefficient, ρ is the liquid density and F is sound frequency. The calculated mean diameter is about 2 μm in this condition. The mist density which is calculated by treated amount of solution and air flow rate is varied by changing water level in tank. The atomized mist introduced into DBD tube with carrier gas and pass through only one time. After one pass, the mist is separated by mist separator which has nylon mesh at inlet port, and vaporized mist is condensed because the

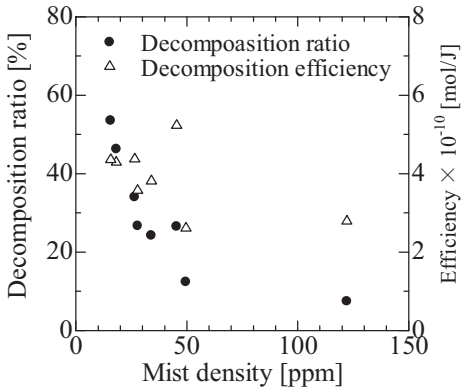

Fig. 2 Acetic acid decomposition ratio and energy efficiency as a function of mist density.

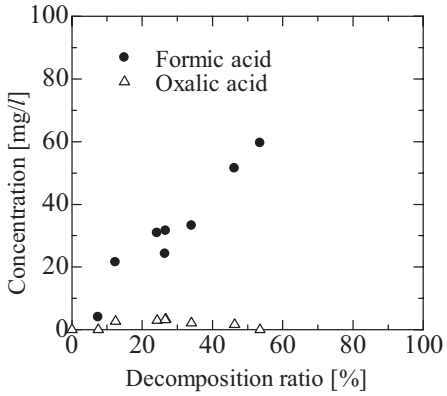

Fig. 3 Formic acid and oxalic acid concentration for acetic acid decomposition ratio

mist separator is cooled by iced water.

The configuration of DBD tube is shown in fig. 1 (b).The DBD tube is made of alumina with 2 mm thickness and 6 mm inner diameter. The DBD tube has inner powered tungsten rod with 3 mm diameter on central axis of tube and has outer cupper tape electrode. The tungsten rod is supported by two silicon plug on both side of the tube.

Ion species in the solution is measured by ion chromatograph. The power consumption is measured by Lisajous figure method. The discharge intensity is calculated by the voltage of an inserted capacitor (0.1 μF). The power consumption is from 4 W to 6 W.

3. Experimental Results and Discussion

Figure 2 shows the acetic acid decomposition ratio and decomposition efficiency. Since acetic acid can not be decomposed by only ozone, it is predicted that acetic acid is decomposed by OH radical in this study. The decomposition ratio exponentially decrease with increase of mist density. Because the energy deposition to the mist is decrease. On the other hand, the decomposition efficiency slightly decrease. Because the water film is formed on the inner surface and the dielectric loss increase when the mist density is high.

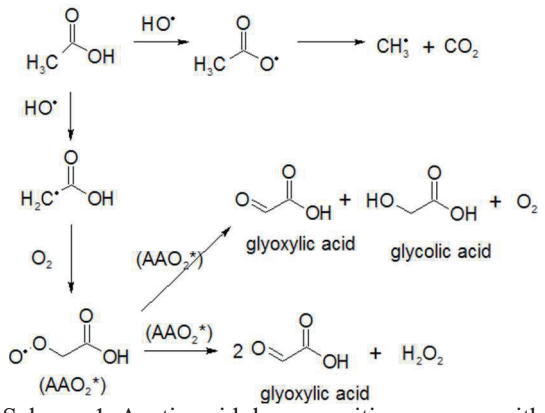

Scheme 1. Acetic acid decomposition process with hydroxyl radical

Figure 3 shows the formic acid and oxalic concentrations in after treatment solution as a function of acetic acid decomposition ratio. Acetic acid and oxalic acid is produced as by-products. The formic acid concentration increase with decomposition increase. Oxalic acid keeps low concentration with decomposition ratio varying.

Acetic acid is decomposed by OH radical as shown in scheme 1. OH radical reacts with acetic acid by H abstraction at the methyl group and by H abstraction at the carboxyl group. CH_2COOH radical and CH_3COO radical are produced respectively. CH_2COOH radical reacts with dissolved O_2 to produce peroxyl radicals (O_2 CH_2COOH). Glyoxylic acid and glycolic acid is produced through the bimolecular reaction of O_2 CH_2COOH. Furthermore, the oxidation of glyoxylic acid and glycolic acid by photolysis of hydrogen peroxide generate the oxalic acid as shown in equation (2),(3).

$$H_2O_2 + 2HOCH_2COOH + O_2 \rightarrow H_2O_2 + 2OHCCOOH + 2H_2O \quad (2)$$

$$H_2O_2 + HOCCOOH \rightarrow HCOOH + CO_2 + H_2O \quad (3)$$

The reaction of glyoxylic with hydrogen peroxide also occurs without UV irradiation and formic acid is produced as shown in following equation (4).

$$H_2O_2 + HOCCOOH \rightarrow HCOOH + CO_2 + H_2O \quad (4)$$

4. Conclusions

The obtained results are summarized as follows.

(1) Acetic acid is decomposed about 50 % in high efficiency (about 5×10^{-10} mol/kJ).

(2) Formic acid and oxalic acid are produced as by-products. It is suggested that the agent of acetic acid oxidation is hydroxyl radical.

Acknowledgment

This work was partly by Grant-in-Aid for Challenging Exploratory Research (24656117) in JSPS and a Grant-in-Aid for JSPS Fellows (24・9008).

References

[1] M. A. Malik, Plasma Chem. Plasma Process, **30** (2011), 21–31.

[2] T. Shibata and H. Nishiyama, Int. J. Plasma Environ. Sci., **6** (2012), 253-259.

Effect of Beam Deflection on Measurement of Boundary Layers Using Phase-shifting Interferometer

Eita Shoji[1], Ryota Nakaoku[1], Atsuki Komiya[2], Junnosuke Okajima[2], Shigenao Maruyama[2]
[1]Graduate School of Engineering, Tohoku University
6-6-04, Aramaki Aza Aoba Aoba-ku, Sendai, Miyagi, 980-8579, Japan
[2]Institute of Fluid Science, Tohoku University
2-1-1 Katahira, Aoba-ku, Sendai, Miyagi, 980-8577, Japan
eita@pixy.ifs.tohoku.ac.jp

ABSTRACT

The effect of beam deflection caused by refractive index gradient on interferometric experiments was estimated by ray tracing method. This study focused on boundary layers of forced convection because the boundary layer thickness is thin and the effect of beam deflection is considered to be large. The calculation results were compared with forced convection experiments. The calculation results show the effect cannot be neglected in experiments using phase-shifting interferometer.

1. Introduction

Many optical techniques in which the density dependence of the refractive index have been developed in the fields of instrumentation engineering[1][2]. The advantage of the methods is that the techniques are non-intrusive experiment. Typical techniques are shadowgraphy, Schlieren method and interferometry. Both the shadowgraphy and Schlieren method provide qualitative information by detecting the beam deflection. On the other hand, interferometry produces phase difference between two beams which is quantitative information.

Generally, interferometry neglects the effect of beam deflection due to the refractive index gradient and the effect could be negligible. However, the beam deflection affects the results in experiments where steep refractive index gradients exist. For example, the effect can be observed in the convection experiments where the boundary layer thickness is thin or the temperature gradient is steep.

Thus, the effect of beam deflection on interferometric experiments was calculated using ray tracing method in this study. Additionally, this paper provides specific example of forced convection experiments conducted by the authors previously.

2. Experimental apparatus and results

Quasi-common-path phase-shifting interferometer has been developed to visualize flow fields quantitatively by the authors. The details of the interferometer were described by Shoji et al.[3][4]. Figure 1 shows the schematic of the interferometer. A non-conventional optical configuration and a phase-shifting technique were introduced to the interferometer. The key points are that it can be integrated with a wind tunnel and can visualize a large area (approximately 200 mm) with high spatial and phase resolution. Thus, this interferometer can visualize temperature fields accurately in various flow fields.

Figure 2 shows the schematic of the flat plate. *z*-axis is the optical axis and wind blows along *x*-axis. The flat plate was heated by the silicon rubber heater and was set at the test section of wind tunnel by using the piano wires. The boundary layer of forced convection over a flat plate was visualized and the steady state temperature distribution was measured by using the interferometer.

Figure 3 shows measured temperature distribution near the flat plate. The measurement data were compared with semi-analytical solution[5]. Here, the surface temperature and the ambient temperature are 22°C and 12°C, respectively. The free stream velocity is 5 m/s and the temperature distribution at 150 mm distance from the leading edge was measured. The spatial resolution and the temperature resolution in the experimental condition are 0.11 mm and 0.025 K, respectively. A good agreement with semi-analytical solution was obtained. The result shows the largest difference between experimental and analytical data is observed in the vicinity of the surface. Since the temperature gradient is the steepest at the points, the effect of beam deflection might affect the measured temperature distribution.

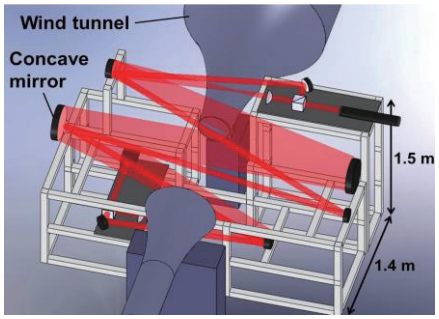

Fig. 1. Schematic of quasi common path phase-shifting interferometer[4].

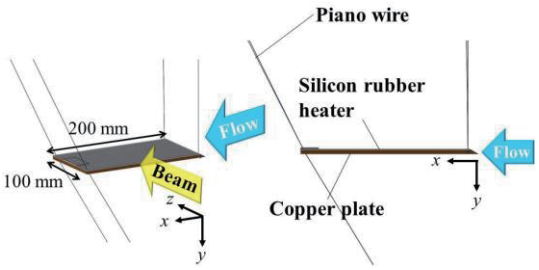

Fig. 2. Schematics of flat plate[4].

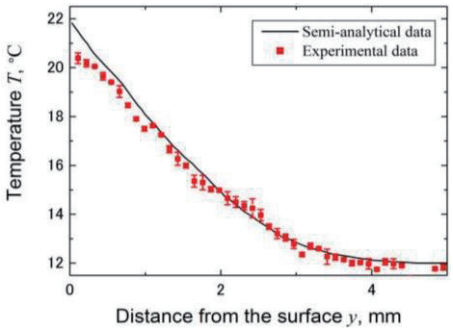

Fig. 3. Comparison of temperature distribution between experimental data and semi-analytical data[4].

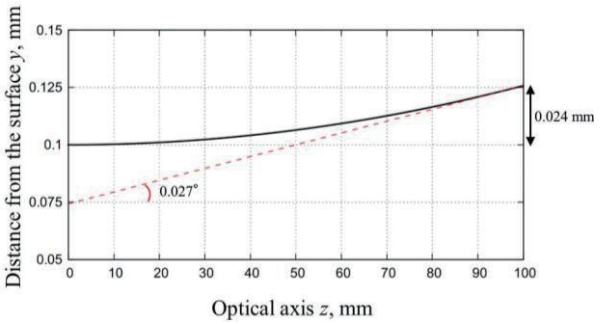

Fig. 4. Ray trajectory in boudnary layer.

Table 1 Beam deflection in boundary layers

ΔT, K	The plate width, mm	Beam deflection, mm
10	100	0.026
10	200	0.101
50	100	0.103
50	200	0.401

3. Ray tracing method

Ray tracing method was used to estimate the beam deflection. The beam deflection caused by refractive index gradient is described by,

$$\frac{d}{ds}\left(n(\boldsymbol{r})\frac{d\boldsymbol{r}}{ds} \right) = \mathrm{grad}(n(\boldsymbol{r})), \tag{1}$$

where $\boldsymbol{r}$ is a position vector of a typical point on a ray, s is an axis of the ray direction, n is refractive index[6].

Nitrogen and oxygen are large percentage composites of air and these gases could be considered non-polar gases. Additionally, air could be assumed to be the ideal gas. Then the refractive index is described by temperature as follow,

$$n = \left[1 + \frac{T_0}{T}\left(\frac{\omega_p^2}{\omega_o^2 - \omega^2} \right) \right], \tag{2}$$

where T is the temperature of air, T_0 is the temperature of air under the standard condition, ω is the beam frequency, ω_p is the plasma frequency, and ω_0 is the eigenfrequency of an air molecule[7]. Here, the temperature distribution over the flat plate was assumed to be the same as semi-analytical solution and a beam deflection occurs due to the temperature distribution.

4. Results and Discussion

Figure 4 shows the ray trajectory in the boundary layer. The position of the incident ray (z = 0 mm) is 0.1 mm distance from the plate surface and the solid line shows the ray. The calculation result shows the beam deflection and the output angle are 0.024 mm and 0.027°, respectively. This deflection is relatively large because the spatial resolution in the experimental condition is 0.11mm. In addition, the ray seems to come from 0.075 mm distance from the plate surface at the incident point because of the output angle as described by the dash line when the x-y plane (z = 0 mm) is focused. As a consequence, the measured temperatures in the vicinity of the plate were underestimated.

Table 1 shows the calculation results of beam deflection in boundary layers. In Table 1, the length of the flat plate along optical axis and the temperature difference were changed. Of course, the beam deflection becomes larger with increasing the length and temperature difference. Besides, the beam deflection is larger than the spatial resolution in four cases.

5. Concluding remarks

In this study, the effect of beam deflection on interferometric experiments was estimated by ray tracing method. The following conclusions were obtained.

1. The beam deflection in boundary layers was calculated by ray tracing method.
2. The beam deflection becomes larger than the spatial resolution of the phase-shifting interferometer when the boundary layer length along optical axis or the temperature difference exceed a certain threshold value.
3. The output angle of the ray also influences the imaging and the measured distribution.
4. The calculation results indicated that the effect of beam deflection affects the experimental results using phase-shifting interferometer.

References

[1] E. R. G. Eckert, R.J. Goldstein, *Measurement in heat transfer*, Hemisphere Publishing Corp., (1976).
[2] W. Merzkirch, *Flow Visualization*, Academic Press, (1987).
[3] E. Shoji, A. Komiya, J. Okajima, S. Maruyama, *Int. J. Heat Mass Trans.*, **55** (2013), 7460–7470.
[4] E. Shoji, R. Nakaoku, A. Komiya, J. Okajima and S. Maruyama, *Proc. ExHFT-8*, (2013), 166.
[5] F.P. Incropera, D.P. De Witt, *Fundamentals of heat and mass transfer*, Wiley, (2001).
[6] M. Born, E. Wolf, *Principle of Optics*, Pergamon Press, (1975).
[7] S. Maruyama, *Light energy engineering*, Yokendo, (2004).

The Effects of Droplet Diameter and Electric Voltage on Droplet Behavior with High Speed Rotary Bell-Cup Atomizer

Tomoyuki Katayama[1], Tatsuya Soma[1], Yasuhiro Saito[1], Yohsuke Matsushita[1], Hideyuki Aoki[1], Toshiki Haneda[2], Yohsuke Hatayama[2], Minori Shirota[2], Takao Inamura[2], Daichi Nakai[3], Genki Kitamura[3], Masanari Miura[3], Takukatsu Asakawa[3], Masatoshi Daikoku[3]
[1]Department of Chemical Engineering, Graduate School of Engineering, Tohoku University, 6-6-07 Aoba, Aramaki, Aoba-ku, Sendai, Miyagi 980-8579, Japan, [2]Department of Intelligent Machines and System Engineering, Faculty of Science and Technology, Hirosaki University,1 Bunkyo-cho, Hirosaki, Aomori 036-8560, Japan, [3]Department of Mechanical Engineering, Faculty of Engineering, Hachinohe Institute of Technology, 88-1 Myo Ohbiraki Hachinohe, Aomori 031-8501, Japan
E-mail: saito@tranpo.che.tohoku.ac.jp

ABSTRACT

The spray flow around a high speed rotary bell-cup atomizer was simulated to investigate the optimal droplet diameter for the maximum transfer efficiency. The monodispersed spray flow was analyzed in electric voltages. The effects of the droplet diameter on the spray behavior were examined, and the transfer efficiency was quantitatively evaluated. As a result, for the case without the electric voltage, the transfer efficiency of the 30 μm droplets showed the maximum value. On the other hand, when the electric voltage is applied, transfer efficiency of the 15 μm droplets showed the maximum value.

1. Introduction

High-speed rotary bell-cup atomizers are widely used in industrial paintings such as automotive painting because of its high productivity and high quality. The bell-cup revolves at a high speed, and sprays paint droplets. The trajectories of the droplets are controlled by the air called shaping air which blows from the rear of the bell-cup and by the electric voltage (EV) which charges droplets. The spray behavior such as a spray angle has been already reported to be affected by the droplet diameter [1, 2]. However, there is little quantitative evaluation for the effect of the droplet diameter on the transfer efficiency (*TE*), which is defined as the ratio of the amount of the injected paint to the amount of the droplets deposited on a target.

In the present study, the monodispersed spray flow on a high-speed rotary bell-cup atomizer was analyzed. The effect of the droplet diameter and EV on the transfer efficiency was discussed. The optimal droplet diameter for the maximum *TE* was investigated.

2. Method

Figure 1 shows a schematic diagram of the computational domain. The division number of the computational domain was 178 × 190 × 5 ($x \times r \times \theta$).

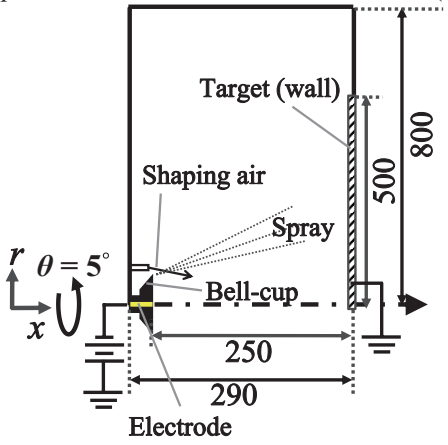

Fig. 1 Computational domain

The bell-cup diameter was 70 mm. The target plane (ϕ1000) was located 250 mm down-stream from the bell-cup. Shaping air was supplied from the inlet of the slit around the bell-cup. The electrode was internally located in the bell-cup. Droplets were located at the edge of the bell-cup, and were injected to the radial direction of the bell-cup by the centrifugal force. In a gas phase, a turbulent flow was described by the standard k-ε two-equation model with the wall function for the boundary condition. The governing equations of a fluid flow were the incompressible Navier-Stokes equations. In the electrostatic field, electrostatic potentials generated by the internal electrode were calculated, and the target was grounded. The governing equation for an electrostatic field was Laplace equation. A spray phase was calculated as rigid particles using a Stochastic Separated Flow (SSF) model. The effect of gas phase turbulent eddies on the droplet motion was estimated using a stochastic approach. Electrostatic force defined as the gradient of the electrostatic potential was applied to the external force term of the droplet equation of motion. Numerical conditions are presented in Table 1. The operating conditions were referred to actual automotive painting conditions. Paint droplets' property was assumed to be the water's one. The transfer efficiency (*TE*) was defined as follows:

$$TE\ [\%] = \frac{\text{Total mass of droplets on the target [kg]}}{\text{Total mass of injected droplets [kg]}} \times 100. \quad (1)$$

Table 1 Numerical conditions

Bell rotational speed	[rpm]	35,000
Liquid flow rate	[mL/min]	200
Particle diameter	[μm]	5, 10, 15, 20, 25, 30
Electric voltage	[kV]	0, -100, -200
Shaping air flow rate	[NL/min]	500

3. Results and Discussion

The calculated transfer efficiency (*TE*) is shown in Figure 2. For the case without the electric voltage (EV), the *TE* increases with an increase in the droplet with diameter of above 10 μm. The maximum *TE*, 69.3 % is

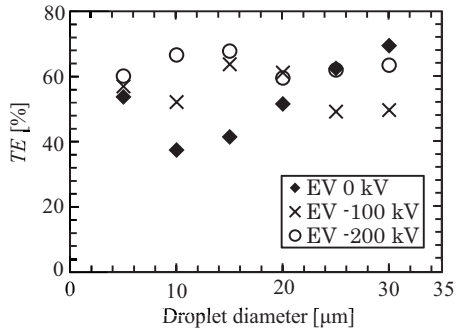

Fig. 2 Calculated transfer efficiency

obtained for the droplets with diameter of 30 μm. Figure 3 shows the distributions of the spray concentration for the small droplets (10 μm) and large ones (30 μm). The small droplets are entrained in the high speed shaping air flow around the center-axis as shown in Figure 4. The large droplets which move radially are entrapped by the shaping air flow. This is because the air around the bell-cup is drawn into the shaping air flow due to the negative pressure generated by the high speed flow in front of the bell-cup. The velocities of the entrained droplets are similar to the velocity of the shaping air flow. Thus, the inertia of the entrained droplets increases with an increase in the droplet diameter. For this reason, the *TE* of the 30 μm droplets shows the maximum value.

When the -100 kV EV is applied, the *TE* of the 15 μm droplets shows the maximum value, 63.6 %. Figure 5 shows the distributions of the spray concentration for the droplets. The droplets with diameter of below 15 μm in diameter are entrained in the shaping air flow. However, the *TE* of the 15 μm droplets is larger than that of the droplets below 15 μm because the inertia of the droplets increases with an increase in the droplet diameter. Although the optimal droplet size is 30 μm in 0 kV, the droplet size is 15 μm in -100 kV. This is because the 30 μm droplets are not entrapped by the shaping air flow, and reach the target. The electrostatic field shown in Figure 6 exerts a force to the droplets along the gradient of the electrostatic potentials. Due to the fact, the 30 μm droplets sprayed radially are pulled toward the target by the electrostatic force without being entrapped by the shaping air flow, and the droplets cannot receive the momentum from the shaping air flow. Thus, the *TE* of the 30 μm droplets is smaller than that of the 15 μm droplets. When the EV is -200 kV, the *TE* of the droplets with diameter of 15 μm also shows the maximum value. This is because the 15 μm droplets are the largest droplets in the ones entrained in the shaping air flow. The *TE* of the droplets shows a trend to increase with increasing the EV independent of the droplet diameter. This results show that the droplets near the target are deposited onto the target with an increase in the electrostatic force.

4. Concluding remarks

In this study, the monodispersed spray flow on a high-speed rotary bell-cup atomizer was analyzed. The effect of the droplet diameter and the electric voltage (EV) on the transfer efficiency (*TE*) was investigated. We obtained the following factors to increase the *TE*.

i) Droplets entrained in the shaping air flow around *x*-axis gain the momentum toward a target.
ii) An electrostatic force make droplets in the vicinity of a target adhere to a target.

As a result, the maximum *TE* 69.3 % for the droplet with diameter of 30 μm in 0 kV, 63.6 % for 15 μm in -100 kV and 67.6 % for 15 μm in -200 kV were obtained.

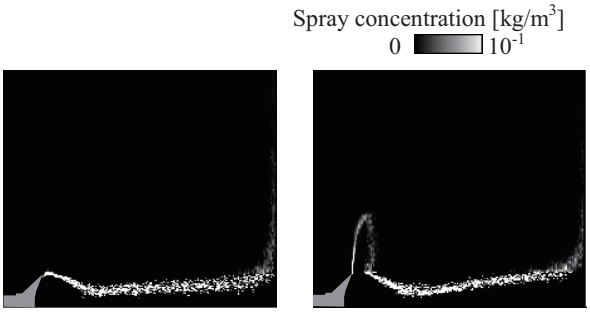

(a) 10 μm in diameter (b) 30 μm in diameter

Fig. 3 Distributions of spray concentration in 0 kV.

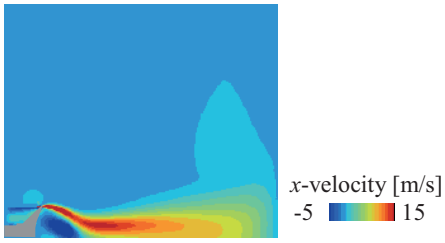

Fig. 4 Contour of the *x*-velocity component.

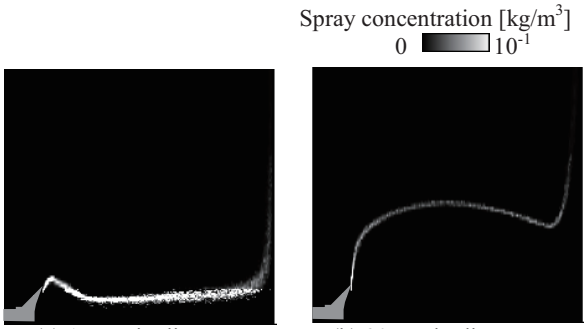

(a) 15 μm in diameter (b) 30 μm in diameter

Fig. 5 Distributions of spray concentration in -100 kV.

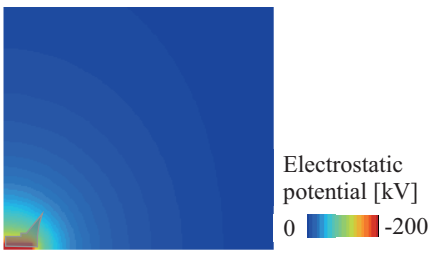

Fig. 6 Electrostatic field.

References

[1] P. L. Corbeels *et al.*, *Atomization and Sprays*, **2** (1992), 87–99.
[2] K. Yasumura *et al.*, Kagaku Kogaku Ronbunsyu, **37** (2011), 251–260.

An Experimental and Computational Study for the Development of High-efficiency Fluidized Bed Solar Reactor

Seung-Jae Lee[a], Atsushi Sakurai[b*], Sho Suzuki[a], So Sakuma[a], Koji Matsubara[b], Nobuyuki Gokon[c] and Tatsuya Kodama[b]
[a] Graduate School of Science and Technology, Niigata University, Niigata 950-2181, Japan
[b]Faculty of Engineering, Niigata University, Niigata 950-2181, Japan
[c]Center for Transdisciplinary Reaserch, Niigata University, Niigata 950-2181, Japan
E-mail: sakurai@eng.niigata-u.ac.jp

ABSTRACT

Solar thermochemical decomposition of water is a promising technology for high efficient mass production of hydrogen. The efficiency can be increased through improving reactor design. However, the design of solar reactor has difficulty due to the complexity of particles movement and temperature distribution. Therefore, we developed the numerical model and compared it with the visualization experiment. These comparisons of the experiment and the simulation help to understand physical insight of the new-type solar reactor.

1. Introduction

Concentrated solar radiation has been received attention due to the application to thermochemical conversion of hydrogen [1]. The internally circulating fluidized bed (ICFB) type solar reactor has been recognized as promising technology for solar energy conversion [2]. In order to develop a high-efficient solar reactor, it is important to control particles movement and temperature distribution; however, it is very complicated to analyze these phenomena, resulting in difficulty on controlling of two-phase flow.

The objective of this study is to develop a fluid dynamic simulation model and collect experimental data for improving of the reactor design. Commercial CFD software (FLUENT ver.13 [3]) is employed to simulate the fluidized bed motions, and Particle Image Velocimetry (PIV) is applied for the visualization. These comparisons of the experiment and the simulation help to understand physical insight of the ICFB type solar reactor.

2. Method

2.1 Experiment

Figure 1 shows the schematic of experimental setup for visualizing the modeled ICFB solar reactor. A twin vessel type solar reactor is modeled. When concentrated solar radiation is collected to metal oxide particles in the left vessel, oxygen is produced in consequence of endothermic reduction reaction, and then the metal oxide particles move into the right vessel, resulting in production of hydrogen.

In the visualization experiment, the front side of vessel is made by acrylic glass, and spherical polystyrene beads were used with particle size distribution between 700-1400μm. Two colors of beads were used to accurately capture the particles movement.

The velocity of particles was analyzed by PIV technique. Particle images were taken at intervals of 5msec for 20sec. by using a high-speed CCD camera (KATOKOKEN). Furthermore, PIV software (FlowExpert2D2C) was used to analyze velocity of particles with the recursive cross-correlation method.

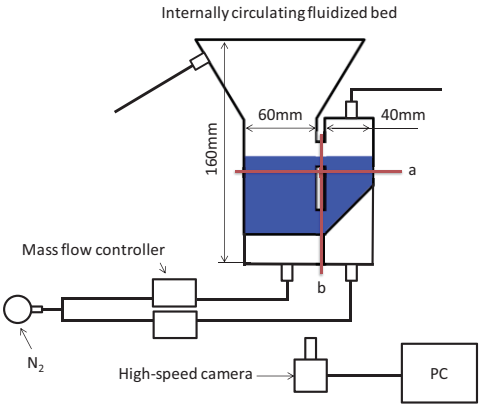

Fig.1Experimental setup

Table 1. Modeling parameters [3]

Drag model	Gidaspow
Solid pressure	Lun
Radial distribution function	Lun
Shear viscosity	Syamlal
Frictional viscosity	Schaeffer
Frictional pressure	Johnson
Granular temperature	Algebraic

Table 2. Physical properties

Gas density	1.225 kg/m^3
Gas viscosity	1.819×10^{-5}kg/m▪s
Particle density	1040kg/m^3
Particle size	1×10^{-3}m
Maximum packing limit	0.63
Friction packing limit	0.5
Angle of internal friction	45°
Restitution coefficient	0.8

2.2 Simulation

The fluidizing regime in a fluidized bed reactor can be simulated by the Eulerian-granular model in FLUENT 13.0. Tables 1 and 2 summarize the modeling parameters and physical properties. The beads are modeled as a solid phase and air is treated as a compressible gas phase. The phases are solved individually using the mass and momentum equations. The phase coupled SIMPLE scheme was used for

pressure velocity coupling and QUICK scheme for the volume fraction and second order upwind for momentum and first order implicit for transient formulation. The inlet velocities for the left vessel and right vessel are set as 0.648 m/s and 0.486 m/s, respectively.

3. Results and discussion

Figure 4 shows the comparison between the experiment and simulation for the snapshots of distribution of particle volume fraction. The instantaneous fields have similar and complex babbly flow structures.

Figures 5 and 6 show the comparison of mean velocity vector profiles between experiment and simulation. These profiles show similar tendency. Due to the bubble assembly, the particles are transported upwards in the center region and move downwards near the walls. Furthermore, it is observed that the particles move into the right vessel, and circulating between the vessels.

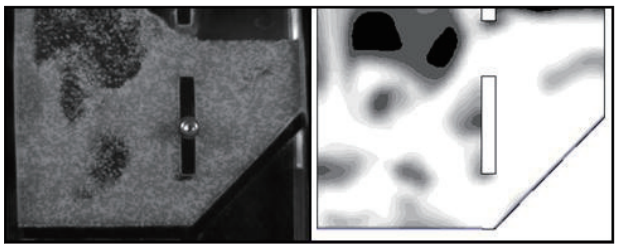

(a) (b)

Fig.4 Instantaneous image in (a) Experiment (b) CFD

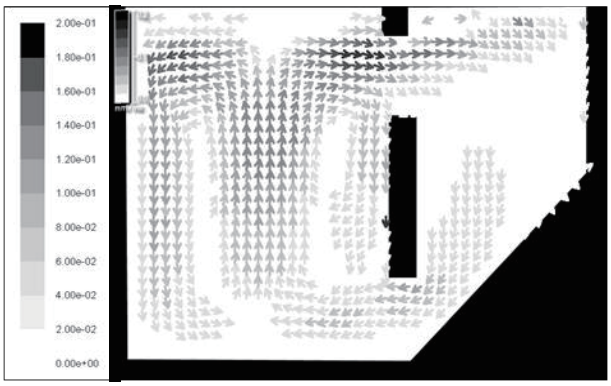

Fig.5 Mean velocity vectors by experiment

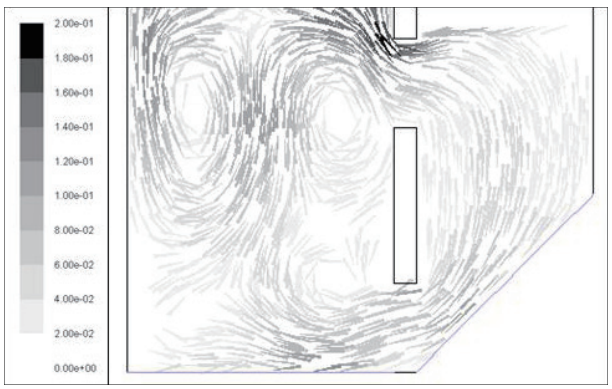

Fig.6 Mean velocity vectors by CFD

Figures 7 and 8 show the comparison of mean x, y directional mean velocities between the experiment and simulation. These results show good agreement, although the simulation results slightly overestimate the experimental one. The discrepancies can be found in the right vessel; however it may be due to the frictional pressure model.

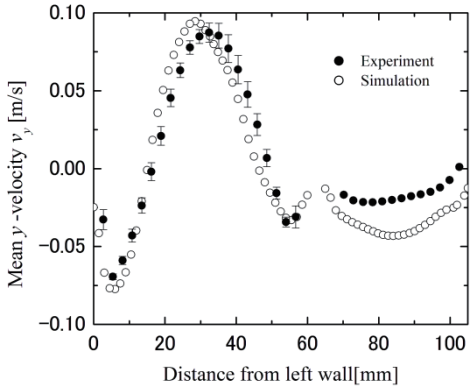

Fig.7 Mean y-velocity distribution at 50mm above from the bottom (Fig.1 – a)

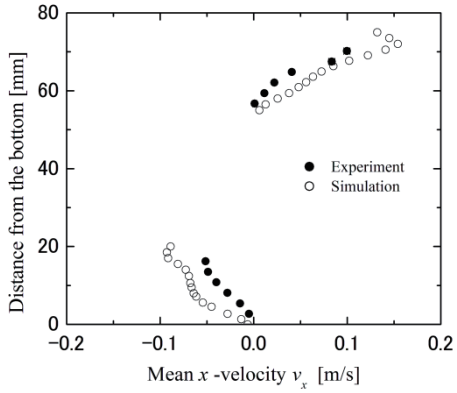

Fig.8 Mean x-velocity distribution at 62.5mm from the left wall (Fig.1 – b)

4. Concluding remarks

Our conclusions are summarized as follows:

1. We developed the numerical simulation model for predicting the flow structures inside the internally circulating fluidized bed solar reactor.
2. The numerical results showed good agreement with the visualization experiment.
3. These comparisons of the experiment and the simulation help to understand flow structures, and are useful for future design of solar reactors.

References

[1] L. Xiao, RENEW.ENERG, 41 (2012), 1-12
[2] N. Gokon , INT.J.HYDROGEN.ENERG, 36 (2011), 4757-4767
[3] ANSYS® Academic Research, Release 13.0 ANSYS Japan User Service Center, ANSYS, Inc

Tenth International Conference on Flow Dynamics
November 25-27, 2013, Sendai, Miyagi, Japan

Multi-Objective Optimization and Data Mining for Process Compressor Design

Ray A. Rockenbach, Koji Shimoyama and Shigeru Obayashi
Tohoku University, Sendai, 980-8577, Japan
rockenbach@edge.ifs.tohoku.ac.jp

ABSTRACT

A design optimization problem of a process compressor, which involves multiple trading-off objectives and many constraints, is solved by a multi-objective genetic algorithm with improved constraint handling. Then, a self-organizing map is applied to the Pareto-optimal solutions for the data mining to extract the design information of maximizing critical speed margin and minimizing shaft power. This information suggests that larger rotation speed and smaller inner diameter leads to smaller critical speed margin due to shaft vibration, while it results in increase of fluid efficiency, which requires smaller shaft power by increasing specific speed.

1. Introduction

A process compressor is one of the turbo fluid machineries mainly operated at a chemical plant to produce high pressure fluid for a chemical reaction. Figure 1 shows the interior of a process compressor. In this machinery, fluid which enters from outside obtains kinetic energy from impellers and the energy is converted to pressure when the fluid goes through diffusers. Usually, multi-stage impellers and diffusers are employed to output sufficient fluid pressure. In the design process of the process compressor, fluid performance, structure strength, and shaft stability are analyzed while the number and size of impellers are adjusted based on the standard impellers with known performance.

In the design case when multiple design objectives conflict with each other, it is desirable to obtain Pareto-optimal solutions, which are the feasible design candidates when no further improvements can be made simultaneously in all objective functions. Multi-Objective Evolutionary Algorithms (MOEAs) are often used to solve multi-objective optimization problems suitably, and the Multi-Objective Genetic Algorithm (MOGA) [1] is typical of MOEAs. However, process compressor design problems have many constraints on, e.g., customer requirements, product safety, and simulation reliability. Unfortunately, conventional MOGAs are still poor in solving such many-constraint optimization problems.

In this research, multi-objective design optimization of a process compressor is conducted using a modified MOGA that handles many constraints suitably. After that, a Self-Organizing Map (SOM) [2] is applied to the obtained Pareto-optimal solutions for the data mining to extract the design knowledge of improving objective functions and satisfying constraints. Finally, the design knowledge is validated based on physical phenomena.

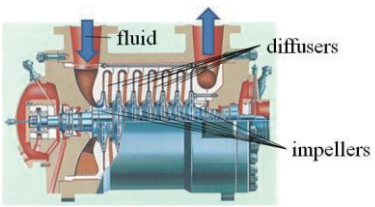

Fig. 1 Interior of a process compressor

2. Multi-Objective Optimization

A multi-objective optimization problem that seeks to minimize all objective functions is expressed as the following equations:

$$\text{Minimize } f_i(x_1,x_2,\cdots,x_n) \quad (i=1,\cdots,p) \qquad (1)$$
$$\text{subject to } g_j(x_1,x_2,\cdots,x_n)\geq 0 \ (j=1,\cdots,q) \qquad (2)$$
$$h_k(x_1,x_2,\cdots,x_n)=0 \ (k=1,\cdots,r) \qquad (3)$$

Equation (1) shows that there are p objective functions f to be minimized corresponding to n design variables. Equations (2) and (3) indicate that there are q inequality constraints g and r equality constraints h. Equation (1) can also be applied to the case of a maximization problem by inverting the plus-minus signs of all objective functions.

In this study, MOGA is applied to the above problem. The genetic algorithm mimics the evolution of organisms, which selects individuals from the current generation as parents, generates new individuals as children by the crossover and mutation of the parents, and inherits better individuals to the next generation. The individuals correspond to the design candidates considered in optimization, and thus MOGA can achieve a global search for Pareto-optimal solutions in a multi-objective optimization problem. In addition, this study adopts the constraint handling technique proposed in [3] to enhance solution search capability in a many-constraint problem. Even if the present MOGA searches for infeasible solutions which do not satisfy at least one of design constraints, these solutions are not forcibly discarded. An infeasible solution that is closer to Pareto-optimal solutions in terms of objective functions has a higher inheritance to the next generations as well as feasible solutions.

3. Data Mining

A Self-Organizing Map (SOM) is a type of artificial neural network that is trained using unsupervised learning. SOMs can be used to visualize the structure of high-dimensional data sets such as Pareto-optimal solutions. As shown in Fig. 2, high-dimensional data vectors are clustered on a two-dimensional plane so that similar data vectors will be located closer to each other (Fig. 2(a)). Data similarity will be measured as the Euclidean distance in the high-dimensional space. After that, the plane is colored by each dimension value (Fig. 2(b)). Thus, SOM is able to visualize high-dimensional data structure in an easy way to understand. This study

uses SOM for effective data mining because the design candidates for the process compressor need to consider many dimensions including objective functions, design variables, and constraint functions.

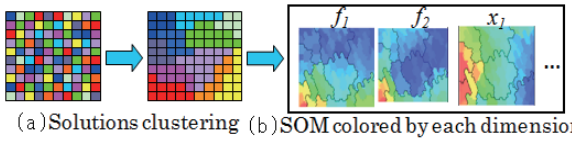

Fig. 2 Concept of SOM

4. Results and Discussion

The present optimization considers 10 design variables, including rotation speed, the outer diameters of the first- and last-stage impellers, and 7 varieties of impellers assigned to each stage, and 2 objective functions, including shaft power (to be minimized) and critical speed margin (to be maximized). In addition, 214 constraints are considered, including discharge coefficient of each impeller etc. The diffuser diameters at all stages are fixed to the same value in the optimization. Population size is set to 100 and the number of generation is set to 150.

After the optimization, SOM is generated for the set of Pareto-optimal solutions based the similarity in 12 dimensions (10design variables + 2 objective functions), as shown in Fig. 3. This is colored by 2 objective functions (Figs. 3(a) and (b)), 3 design variables except the varieties of impellers (Figs. 3(c)-(e)), 2 characteristic parameters (inner diameter of impellers) that are not considered as design variables (Figs. 3(f) and (g)), and 5 constraint functions (Figs. 3(h)-(l)). All these maps indicate larger/smaller values as red/blue colors. In Figs. 3(h)-(l), the maximum/minimum values correspond to the upper/lower limits of the constraints. A same solution is mapped onto the same location of all these maps. A comparison of Figs. 3(a) and (b) observes the trade-off relation between maximizing critical speed margin and minimizing shaft power.

In cluster 1, it is observed that the design candidates have significantly small inner diameters (Figs. 3(f) and (g)), which mean a very small shaft diameter. It leads to a small critical speed margin (Fig. 3(a)).

In clusters 2 and 3, we can observe that a process compressor with a larger critical speed margin has greater shaft power and lower rotation speed (Figs. 3(a)-(c)). Lower rotation speed suppresses shaft vibration, which results in a larger critical speed margin. On the other hand, an increase in shaft power is induced by decrease of fluid efficiency. Specific speed N_s is expressed by Eq. (4).

$$N_S = N\frac{\sqrt{Q}}{H^{3/4}} \tag{4}$$

where N is rotation speed, Q is flow rate, and H is pump head. In this optimization, a change in flow rate and discharge pressure is small and suction pressure is constant, so Q and H are almost constant and thus N_S depends primarily on N. Therefore, lower rotation speed leads to deterioration of fluid efficiency due to smaller specific speed, which requires greater shaft power.

Taking a look at cluster 2, it is observed that the design candidates have much larger rotation speed than those in cluster 3 (Fig. 3(c)). Also, the design candidates have smaller outer diameters compared with those in cluster 3 (Figs. 3(d) and (e)). At the same rotation speed, it is assumed that a smaller outer diameter may lead to decrease of kinetic energy provided from the impellers to fluid. Therefore, to avoid such situation, the rotation speed needs to increase to achieve the same discharge pressure.

Finally, it is suggested that the constraints on the 7th-stage discharge coefficient and discharge pressure are almost at their lower limits(Figs. 3(i) and (l)) and may be important to restrict the Pareto-optimal solutions in this optimization.

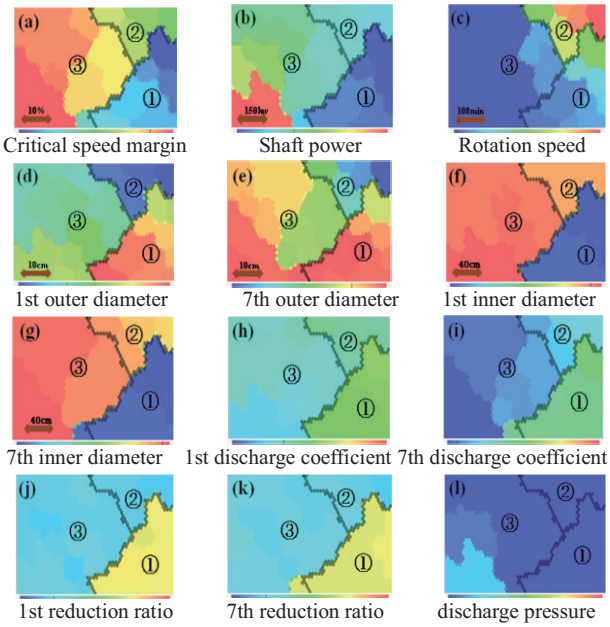

Fig. 3 SOM colored by each dimension

5. Conclusions

The multi-objective many-constraint design optimization of a process compressor was conducted by a multi-objective genetic algorithm with improved constraint handling. Then, a data mining method, SOM, was applied to the Pareto-optimal solutions obtained. It provided the design knowledge, which suggests that larger rotation speed and smaller inner diameters of impellers result in smaller critical speed margin due to shaft vibration. Also larger rotation speed leads to the improvement of fluid efficiency due to larger specific speed, which requires smaller shaft power.

Acknowledgements

We would like to thank Dr. Kazuyuki Sugimura of Hitachi Ltd. for valuable advices on this study.

References

[1]K.Deb, et al., IEEE Trans. Evol. Comput., **6** (2002).
[2]T. Kohonen, "Self-Organizing Maps", Springer, Berlin, Heidelberg (1995).
[3]T. Shimada, et al., Evolutionary Computation Symposium (2011) (in Japanese).

Tenth International Conference on Flow Dynamics
November 25-27, 2013, Sendai, Miyagi, Japan

The Effect of Surface Reactions on Gas-phase Reactions of CH_4/Air Mixture in a Micro Flow Reactor with a Controlled Temperature Profile

Yuta Kizaki, Kenichiro Saruwatari, Hisashi Nakamura, Takuya Tezuka, Susumu Hasegawa and Kaoru Maruta
Institute of Fluid Science, Tohoku University, 2-1-1 Katahira Aoba-ku Sendai Miyagi 980-8577, Japan
kizaki@edyn.ifs.tohoku.ac.jp

ABSTRACT

The effect of radical quenching on gas-phase reactions of CH_4/air flame was investigated using a micro flow reactor with a controlled temperature profile experimentally and numerically. 2-D computations with detailed chemical mechanisms of gas-phase and surface reactions were conducted to examine the effect of radical quenching on gas-phase reactions. By comparing the computation with gas sampling analysis, it was found that the existing surface reaction mechanism for radical quenching overestimate the effect of radical quenching on the gas-phase reaction.

1. Introduction

With the downsizing and technology advance of mobile devices, the demands on micro power source are increasing. Micro combustion systems are expected to be one of the possible power sources having high energy density. Due to large surface-to-volume ratio, heat loss to the wall is increased in micro combustion and it is difficult to maintain a stable combustion. In addition, the effect of radical quenching on the wall surface is not negligible in micro system and it is important to clarify it. However, there are a few experimental and numerical studies on radical quenching [1, 2].

This study focused on a micro flow reactor with a controlled temperature profile [3]. A narrow channel, which inner diameter is smaller than ordinary quenching diameter, was heated by an external heat source and a stationary wall temperature gradient was established. This technique can simulate heat recirculation and enable a stable combustion.

In this study, we applied CH_4 to the micro flow reactor as a fuel. The objective of this study is to examine the quantitative effect of radical quenching on the gas-phase reaction. The flame locations were measured and gas sampling analysis was conducted. The results were compared with two-dimensional computation including detailed gas-phase kinetics with/without radical quenching reaction mechanism.

2. Experimental and computational method

A quartz tube was used as a reactor channel and its inner diameter, d, was chosen to be 1.5 and 2.0 mm in this study. The quartz tube was heated by a H_2/air flat-flame burner to obtain a stationary temperature profile from 300 K to 1300 K along the inner surface of the tube in the axial direction. A stoichiometric CH_4/air mixture was supplied into the tube at atmospheric pressure. Flow rates of CH_4 and air were controlled by mass flow controllers. An inlet mean flow velocity, U, was chosen to be 50 cm/s (for d = 2.0 mm) and 60 cm/s (for d = 1.5 mm) which are near lower limit of the stable planer flame branch. Images of the flame were captured with a digital still camera. The camera was equipped with optical band-pass filters (transparent wavelength: 431.4 nm, half bandwidth: 6.4nm) for better observation of chemiluminecsence from hydrocarbon flames by filtering thermal radiation from the heated tube. The exhaust gas was analyzed by a gas chromatograph with a thermal conductivity detector. Helium was used as a carrier gas. Shincarbon ST was used as a column.

To investigate the experimental result and the effect of radical quenching, 2-D computation was conduct by FLUENT 6.3 with detailed reaction mechanisms. The conservation equations of mass, momentum, energy and species were solved. Because of the symmetry of the cylindrical tube, the computational domain was a half of the tube from central axis (r = 0 mm) to the wall (r = 0.5d mm). As a boundary condition, the wall surface was assumed as non-slip wall and given a stationary wall temperature profile which is the same as the experimental wall temperature profile. GRI3.0 [4] without reactions for N was used to represent the gas-phase reaction. In order to evaluate the effect of radical quenching on the wall, two surface conditions were assumed; (a) inert wall without any surface reaction and (b) quench wall with surface reaction mechanism for radical quenching [1].

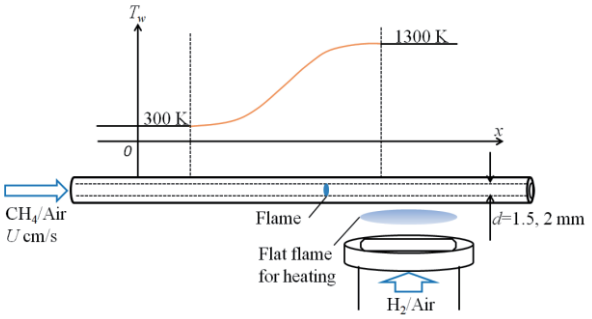

Fig. 1 Schematic of experimental setup and provided wall temperature profile.

3. Results and discussion

Figures 2 and 3 show the computational distributions of CH mass fractions at d = 2.0 and 1.5 mm for (a) inert and (b) quench wall cases. The dashed red lines indicate the experimentally observed flame locations. In both Figs. 2 and 3, there is no significant difference in the flame locations between the inert and quench wall cases. The computational flame locations agree well with the experimental results. These results indicate that there is no significant effect of radical quenching on the flame locations.

Figure 4 shows the mole fraction profile of CO on the axis (r = 0 mm) and the wall (r = 1 mm) for d = 2.0 mm in the inert and quench wall cases. On the axis (r = 0

mm), the CO profile in the inert wall case agrees well with that in the quench wall case at the reaction zone. Behind the reaction zone, however, CO mole fraction in the inert wall case is lower than that in the quench wall case. This tendency can be also seen on the wall (r = 1 mm). The difference in CO mole fractions between the inert and quench wall cases can be seen at the exit of the quartz tube. The flame location was not affected by radical quenching but CO mole fraction behind the reaction zone was significantly affected.

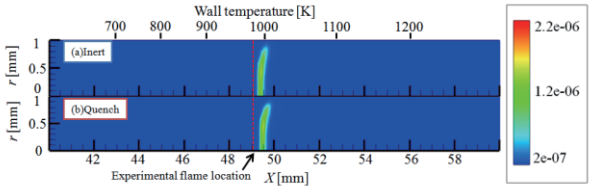

Fig. 2 Distributions of CH mass fractions (d = 2.0 mm; U = 50 cm/s; ϕ = 1.0).

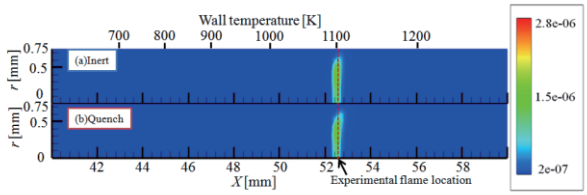

Fig. 3 Distributions of CH mass fractions (d = 1.5 mm; U = 60 cm/s; ϕ = 1.0).

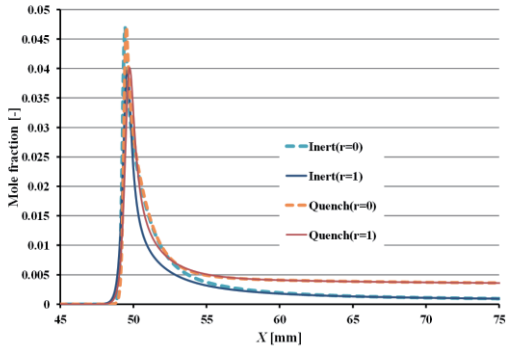

Fig. 4 Profiles of CO mole fraction (d = 2.0 mm; U = 50 cm/s ; ϕ = 1.0).

Figure 5 shows the measured and computational CO mole fractions in burned gas for equivalence ratios, ϕ, from 0.8 to 1.2 at (a) d = 2.0 mm and (b) d = 1.5 mm. At d = 2.0 mm, CO mole fractions in the inert wall case and that of experiments are quite low level at ϕ < 1 and increase with the increase of ϕ when ϕ > 1. At the all equivalence ratios, CO mole fractions for the inert wall case agree well with those for experiments and are much lower than those for the quench wall case. Note that for the inert wall case, CO mole fractions at d = 1.5 mm agree well with those at d = 2.0 mm at the all equivalence ratios. For the quench wall case, CO mole fractions at d = 1.5 mm are higher than those at d = 2.0 mm, due to higher surface-to-volume ratio. However, CO mole fraction of experiments have nearly the same value in the inert wall case. These results indicated that the present surface reaction mechanism overestimated the

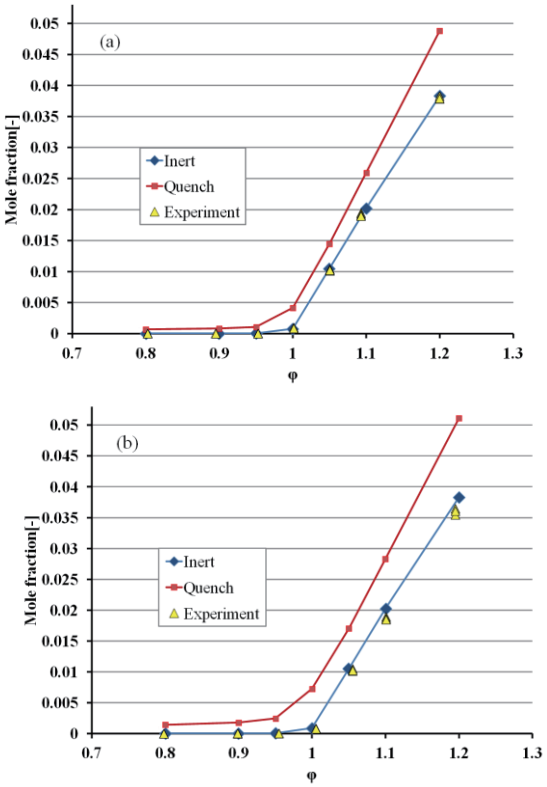

Fig. 5 Equivalence ratio dependence of CO mole fraction of burned gas (a) d = 2.0 mm, (b) d = 1.5 mm.

effect of radical quenching on gas-phase reactions.

4. Conclusions

The effect of radical quenching on gas-phase reactions of a CH_4/air flame was investigated using a micro flow reactor with a controlled temperature profile. There was no significant difference in the flame locations between the inert and quench wall cases. The measured flame locations agreed with the computational flame locations. The effect of radical quenching on the flame locations were neglegible. However, significant difference in CO mole fractions in burned gas between the inert and quench wall cases were observed. The measured CO mole fraction agreed well with the computed CO mole fraction in the inert wall case, i.e., when no radical quenching effect was considered. This indicates that the present radical quenching mechanism overestimates its effect and the effects of surface reactions on gas-phase reactions can be neglected at the conditions addressed in this study.

References

[1] S. Raimondeau, D. Norton, D. G. Vlachos and R. I. Masel, Proc. Combust. Inst. **29** (2002) 901-907.
[2] Y. Saiki, Y. Suzuki, Proc. Combust. Inst.**34**(2013) 3395-3402.
[3] K. Maruta, T. Kataoka, N. I. Kim, S. Minaev and R. Fursenko, Proc. Combust. Inst. **30** (2005) 2429-2436.
[4] G.P. Smith et al., http://www.me.berkeley.edu/gri_mech/.

Tenth International Conference on Flow Dynamics
November 25-27, 2013, Sendai, Miyagi, Japan

Pressure Dependence of n-Butane/Air Weak Flames in a Micro Flow Reactor with a Controlled Temperature Profile

Shogo Kikui, Hisashi Nakamura, Takuya Tezuka, Susumu Hasegawa, Kaoru Maruta.
Institute of Fluid Science, Tohoku University, 2-1-1 Katahira, Aoba-ku, Sendai, Miyagi 980 8577, Japan.
kikui@edyn.ifs.tohoku.ac.jp

ABSTRACT

Weak flames of an *n*-butane/air mixture were investigated using a micro flow reactor with a controlled temperature profile at various pressures. Two luminous zones were observed at 2 atm and three luminous zones were observed at 3-5 atm. 1-D computations were also made to compare the pressure dependence on flame position and flame strength with the experiment. Both experimental and computational results showed the reaction in the low temperature region is important at high pressures.

1. Introduction

For the development of internal combustion engine with higher efficiency, computer simulations of the ignition process is essential and an accurate reaction mechanism is needed. Reaction mechanisms for small hydrocarbons are subset of those for practical large hydrocarbons such as gasoline. Therefore, understanding of the ignition characteristics of small hydrocarbons is very important. Ignition characteristics are mainly studied using rapid compression machines (RCMs) [1]. Studies using RCMs proved that large hydrocarbons have two-stages heat release in the ignition process. However, in the RCM experiments, the effect of heat loss and vortices are not avoidable and the system becomes complicated to further investigate the ignition characteristics precisely.

To investigate in a simpler system, a micro flow reactor with a controlled temperature profile was introduced [2]. A quartz tube with an inner diameter smaller than the quenching diameter is heated by an external heat source providing a stationary temperature gradient. Due to the small inner diameter of the tube, the gas-phase temperature strongly depends on the temperature profile of the inner surface of the tube. As a result, the rapid temperature increase in the gas-phase is suppressed and the reaction is separated into different temperature ranges. Previous studies using the micro flow reactor showed a three-stage heat release in the ignition process.

In this study, *n*-butane was used as a fuel in the micro flow reactor. *n*-Butane is one of the small hydrocarbons which is gas phase at standard condition. *n*-Butane showed a two-stage heat ignition process in the RCM experiments [3], but only single heat release rate peak was observed in the micro flow reactor experiment at atmospheric pressure. Therefore, the micro flow reactor experiments at elevated pressures were conducted to examine the ignition process of *n*-butane. 1-D simulation was also conducted to examine the experiment results in detail.

2. Experimental and computational methods

Figure 1 is a schematic of the experimental setup. A quartz tube with an inner diameter of 1 mm was employed as a reactor and heated using a H_2/air premixed burner to obtain a stationary temperature profile (300–1300 K) in the axial direction. A stoichiometric premixed *n*-butane/air mixture was supplied into the reactor with a mean flow velocity at the inlet of the reactor U = 1 cm/s. The flame images were taken using a digital still camera with a CH filter. The pressure was controlled using a pressure regulator attached at the end of the reactor.

To examine the experimental results, 1-D steady computations were conducted using the PREMIX-based code [2]. Heat convection term between the gas phase and the wall was added to the energy equation. The experimental wall temperature profile was used in the computation. Natural Gas III [4] was employed as a reaction scheme. The same equivalence ratio, φ, and U in the experiment were used in the computation.

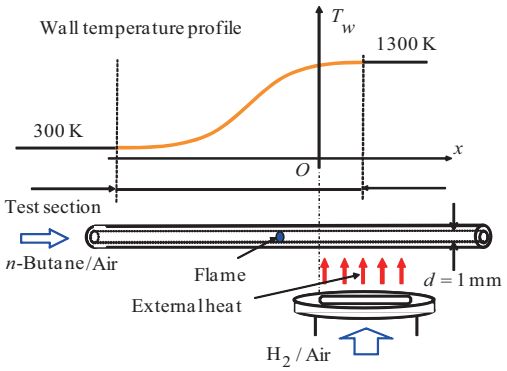

Fig. 1 Schematics of the experimental setup.

3. Results and Discussion

Figure 2 shows the images of *n*-butane/air weak flames at 1-5 atm. At 1 atm, one luminous zone was observed. At 2 atm, two luminous zones were observed. And at 3-5 atm, three luminous zones were observed. The three luminous zones are known as the hot flame, blue flame and cool flame respectively from the high temperature side. Therefore, only the hot flame was observed at 1 atm and only the hot flame and the blue flame were observed at 2 atm. The pressure dependence of *n*-butane/air weak flames of the flame position and the luminosity is discussed. For the hot flame, the flame position shifts toward the lower temperature region from 1-3 atm and then slightly shifts back to the higher temperature region from 3-5 atm. The flame region becomes wider at 4-5 atm compared to 1-3 atm. The luminosity of the flame decreases with the increase of pressure. The blue flame first appears at 2 atm. The flame position shifts toward the lower temperature side

and the luminosity of the flame becomes stronger with the increase of pressure. The cool flame first appears at 3 atm. The flame position stays in the same temperature region and the luminosity becomes slightly stronger with the increase of pressure.

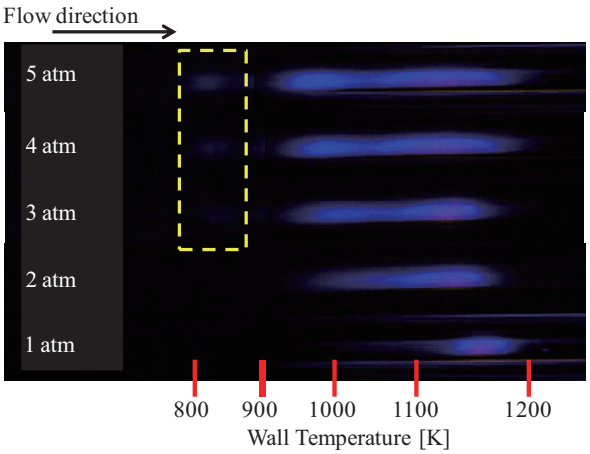

Fig. 2 Weak flame images at p = 1-5 atm.

Figure 3 shows the computational heat release rate (HRR) profiles at 1-5 atm. Strong correlation between HRR and CH profiles was confirmed in our past study, and the CH peak has a strong correlation with the chemi-luminescence observed in the experiments. Therefore, the flame position was defined by the position of the HRR peak in the computation. From Fig. 3, two HRR peaks are seen at 1 atm and three HRR peaks are seen at 2-5 atm. The three HRR peaks correspond to the hot flame, blue flame and the cool flame respectively from the high temperature side. The pressure dependence of the flame position and the position of the HRR peak is examined. For the computational hot flame, the position of the HRR peak shifts to the lower temperature side from 1-2 atm and shifts back to the higher temperature side from 3-5 atm. The peak value of HRR becomes smaller with the increase of pressure. The computational blue flame appears at 2 atm. The flame position shifts to the lower temperature side and the peak value of HRR becomes larger with the increase of pressure. The computational cool flame shifts toward the higher temperature side

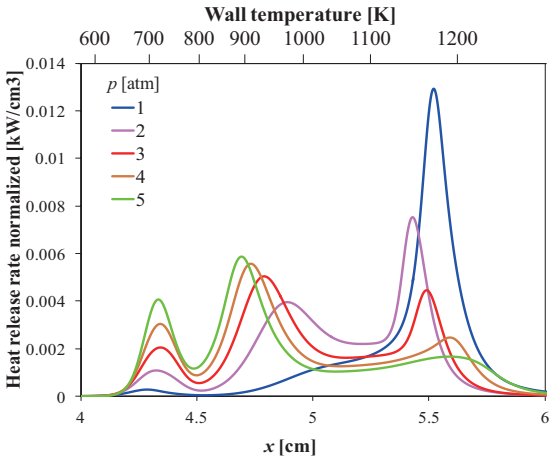

Fig. 3 Computed HRR profiles at p = 1-5 atm.

from 1-4 atm and shifts to the lower temperature side from 4-5 atm. The peak value of HRR becomes larger with the increase of pressure.

Figure 4 shows experimental and computational flame positions at 1-5 atm. The experimental flame position was determined by the wall temperature value at the most luminous point. Although there were differences in the wall temperature at the flame position between experiment and computation, the computation captured the experimental pressure dependence of the flame positions. Comparing the luminosity in the experiment with the HRR in the computation, the tendencies that the hot flame becomes weaker, the blue flame becomes stronger and the cool flame becomes stronger agreed each other. This result indicates that the reaction in the low temperature region becomes important with the increase of pressure.

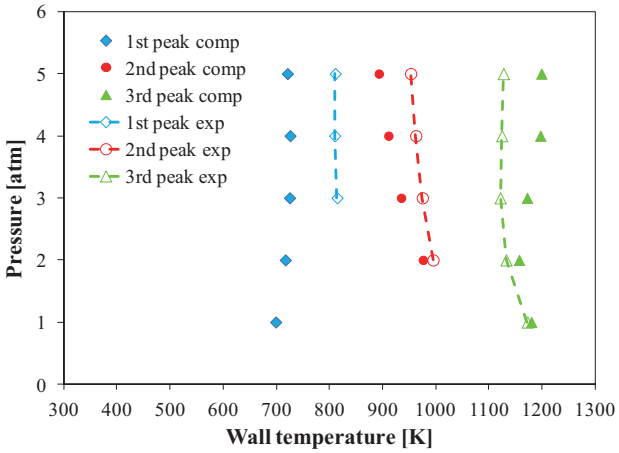

Fig. 4 Wall temperature at flame position in experiment and computation.

4. Concluding remarks

Weak flames of *n*-butane were investigated at various pressures using a micro flow reactor with a controlled temperature profile. The blue flame and the hot flame were observed at 2 atm and the cool flame was also observed at 3-5 atm. The multi-stage ignition process was confirmed at elevated pressures. The pressure dependence of the flame position and the flame strength in the experiment agreed with that in the computation. Both experimental and computational results indicate that the reaction in the low temperature region iis important at elevated pressures.

References

[1] S. Tanaka, F. Ayala, J. C. Keck, *Combust. Flame* **133** (2003) 467-481.

[2] K. Maruta, T. Kataoka, N.I. Kim, S. Minaev and R. Fursenko, *Proc. Combust. Inst.* **30** (2005) 2429-2436.

[3] R. Minetti, M. Ribaucour, M. Carlier, C. Fittschen and L. R. Sochet, *Combust. Flame* **93** (1994) 201-211.

[4] Natural gas III, Combustion Chemistry Centre, National University of Ireland, Galway. http://c3.nuigalway.ie/naturalgas3.html.

Tenth International Conference on Flow Dynamics
November 25-27, 2013, Sendai, Miyagi, Japan

Evaluation of Heat Transfer of Turbulent Natural Convection in Vertical Parallel Plates by Large Eddy Simulation

Takuma Kogawa[1], Junnosuke Okajima[2], Yuka Iga[2], Atsuki Komiya[2], Shigenao Maruyama[2]
[1]Graduate School of Engineering, Tohoku University, [2]Institute of Fluid Science, Tohoku University
E-mail:takuma@pixy.ifs.tohoku.ac.jp

ABSTRACT

In this paper, the turbulent natural convection for parallel plates was calculated by Large Eddy Simulation (LES) in order to evaluate the thermal boundary layer and velocity boundary layer. LES with the dynamic Smagorinsky model was selected for the turbulent model. Velocity and temperature fields of both open and closed condition of parallel plates were compared and the heat transfer rate was analyzed. The location of developing of the turbulent of closed end condition was earlier than that of open end condition and the heat transfer of parallel plates of turbulent region was lower than that of the single plate.

1. Introduction

The natural convection in large scale is essential and fundamental phenomenon in heat transfer engineering. Especially, the characteristics of turbulent natural convection around for the single vertical plate or parallel plate are practically important for such as the cooling system of the power plant and chimney of the factory. Therefore, several researches on the large scale natural convection have been conducted.

Fujii *et al.* conducted the experiment of the turbulent natural around the vertical cylinder and observed the growing of the vortex[1]. In addition, Yan *et al*, conducted the numerical simulation of turbulent natural convection of the single vertical plate by Large Eddy simulation (LES) and clarified the availability of LES for the turbulent natural convection[2]. However, comparing with the case of vertical single plate, the study on the turbulent natural convection in the parallel plate is in sufficient. Therefore, the heat transfer characteristics and structure of turbulent flow in parallel plates have not been investigated adequately.

In this study, in order to clarify the structure of turbulent and evaluate heat transfer characteristic of the turbulent natural convection for parallel plates, the numerical simulation was conducted. The turbulence was modeled by the dynamic Smagorinsky model and the convective boundary condition was adopted as an outlet boundary condition. The temperature field and velocity field were analyzed to investigate the developing of the turbulence in the sides of a plate and heat transfer rate was estimated.

2. Numerical method

Some researches for laminar natural convection of parallel plates have been conducted on both open end and closed end condition. In order to analyze the differences between natural convection and turbulent convection, turbulent natural convection is calculated on both conditions which have the similar configuration to the previous research. Figure 1 shows the calculation condition of this study. As shown in Fig. 1, a working fluid can enter from not only bottom but also the side area in open end condition. On the other hand, the side area of closed end condition consists of adiabatic wall as shown in Fig. 1(b). These parallel plates have 1.5 m long and 2.3×10^{-2} m wide. Additionally, these plates are maintained a constant temperature 320.7 K. The distance of each plate is 4.5×10^{-2} cm. Working fluid on this simulation is water at 305.7 K. The modified Rayleigh number Ra^* of both condition is 1.2×10^{6}.

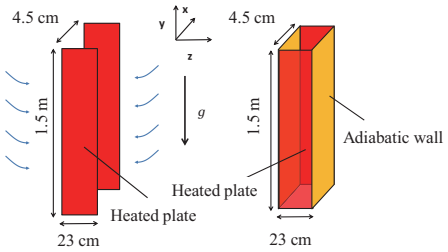

(a) Open end condition **(b) Closed end condition**

Fig. 1 Calculation condition for parallel plates

Filtered Navier-Stokes and energy equation can be described as follows,

$$\frac{\partial \overline{u}_i}{\partial t}+\frac{\partial}{\partial x_i}(\overline{u}_j\overline{u}_i)-\frac{\partial}{\partial x_j}\left\{(\nu_t+\nu_0)\left(\frac{\partial \overline{u}_i}{\partial x_j}+\frac{\partial \overline{u}_j}{\partial x_i}\right)\right\} = -\frac{\partial \overline{p}}{\partial x_i}+g\left[1-\beta\left(\overline{T}-T_0\right)\right], \tag{1}$$

$$\frac{\partial \overline{T}}{\partial t}+\frac{\partial}{\partial x_j}\left(\overline{T}\overline{u}_j\right)-\frac{\partial}{\partial x_k}\left[\left(\frac{\nu_0}{Pr}+\frac{\nu_t}{Pr_t}\right)\frac{\partial \overline{T}}{\partial x_k}\right]=0, \tag{2}$$

where, u_j [m/s] is velocity, ν_0 [m^2/s] and ν_t [m^2/s] kinematic and eddy viscosity, p [m^2/s^2] is modified pressure, g [m/s^2] is acceleration of gravity, β [1/K] is the volumetric thermal expansion coefficient, T [K] is temperature of fluid, T_0 [K] is the temperature of ambient fluid, Pr [-] and Pr_t [-] are Prandtl number of fluid and turbulent-Prandtl number, respectively. The superscripts in each equations show the filtered component parts. Density is calculated by the Boussinesq approximation. The eddy viscosity is calculated by the dynamic Smagorinsky model using Eq. (3)[3]:

$$\nu_t=\frac{\left(\overline{u}_m\overline{u}_n-\overline{u}_m\overline{u}_n\right)\overline{D}_{mn}}{2\left(\tilde{\overline{\Delta}}^2\left|\tilde{\overline{D}}\right|\tilde{\overline{D}}_{kl}-\overline{\Delta}^2\left|\overline{D}\right|\overline{D}_{kl}\right)\overline{D}_{kl}}|D|, \tag{3}$$

where, the Δ [m] is the width of filter and D [1/s] is the strain rate. The width of filter is determined as one third of each grid.

Equations (1) and (2) are discretized using finite volume method. The variables at the cell faces are calculated by the total variation diminishing (TVD) scheme. The computations are explicitly marched. The Poisson equation for pressure derived from continuity equation is solved using conjugate gradient method.

For the flow exiting calculation domain, in order to avoid the numerical reflection, the convective boundary condition[4] is adopted. The used convective boundary condition can be written as,

$$\frac{\partial \vec{V}}{\partial t} + v_{bulk}\frac{\partial \vec{V}}{\partial y} = 0, \tag{4}$$

where, y is the spatial coordinate normal to the outlet, v_{bulk} is the bulk advective velocity which is usually an average value at the outlet boundary. For inlet flow, the total pressure boundary condition is employed.

3. Calculation result

Figure 2 shows the temperature and velocity of x direction on the x-y surface at the center of plates. As shown in temperature fields of Fig. 2(a), the thermal boundary layer of each condition were thin because water has high Prandtl number, however the vortex was growing slightly with y direction. Additionally, as shown in velocity fields of x direction of Fig. 2(b), the velocity has negative value and positive value alternately at the center, this fact shows the vortex was occurred and interaction of each velocity boundary layer which was growing from the plate.

From the temperature fields shown in Fig. 2, the location where the turbulence has developed were determined for both open and closed end conditions. The developing of turbulent in the closed end condition was earlier than that for the open end condition. For the closed end condition, the ambient fluid does not enter from the side area. Because of this reason, the instability of the closed end condition was higher and caused the earlier developing of the turbulent.

In this work, each parallel plates condition has high modified Rayleigh number 1.2×10^6 compared with previous researches for parallel plates. When the modified Rayleigh number is large enough, the flow pattern of laminar region is similar to that of the single plate. To analyze this fact and investigate the difference of flow pattern between parallel plates and the single vertical plate, heat transfer rates were compared.

Figure 3 shows the heat transfer rate of each condition for parallel plates with y direction. Nu_y and Ra_y are defined in Eqs. (5),(6).

$$Nu_y = \frac{\overline{h}y}{k}, \tag{5}$$

$$Ra_y = \frac{g\beta(T_w - T_\infty)y^3}{\nu^2}\cdot Pr. \tag{6}$$

Calculating the heat transfer rate, the temperature gradient was derived from the integral value with the z direction. As shown in Fig. 3, the heat transfer rate of laminar region for each condition was similar to that of the single vertical plate. However, the heat transfer rate of turbulent region for each condition was lower than that of the single vertical plate. This was due to the fact that turbulent boundary layers of parallel plates were interacted each other and streamwise vortices could not exchange the heat easily compared to the single vertical plate case.

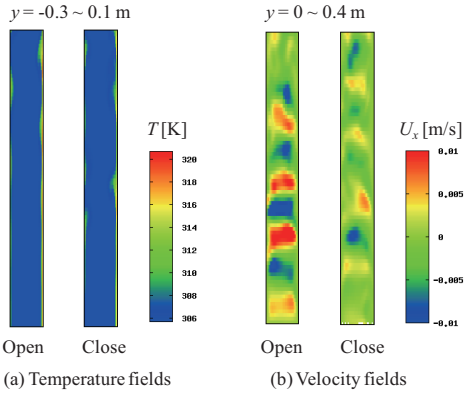

Fig. 2 Temperature and velocity field of each condition

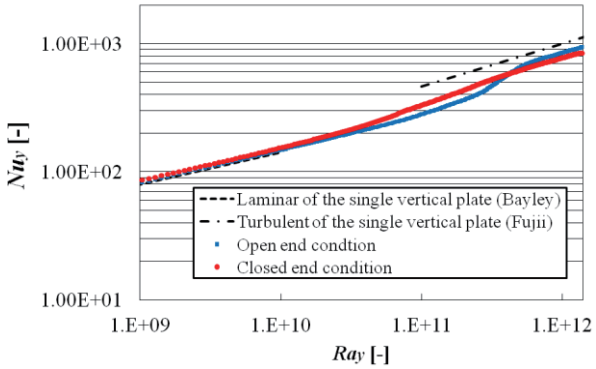

Fig. 3 Comparison of heat transfer rates of each condition for parallel plates

4. Conclusions

Numerical simulation of turbulent natural convection by LES was conducted to analyze the structure of turbulent and heat transfer characteristics. The conclusions are as follows:

1. The transition area of closed end condition was earlier than that of open end condition.
2. The heat transfer of laminar region for parallel plates at high Rayleigh number was similar to the single vertical plate case.
3. The heat transfer of turbulent region for parallel plates was lower than that of the single vertical plate case.

References

[1] T. Fujii *et al.*, Int. J. Heat Mass Transfer. Vol.13, No. 5, pp.753–787, (1970).

[2] Z. H. *et al.*, Heat Mass Transfer. Vol.41, pp.1004–1013, (2005).

[3] Germano P.M *et al.*, Phys. Fluids, Vol.3, No.7, pp.1760-1765, (1991).

[4] Akselvoll K *et al.*, J. Fluid Mech., Vol.315, pp387-411, (1996).

Tenth International Conference on Flow Dynamics
November 25-27, 2013, Sendai, Miyagi, Japan

Experimental Study on Flow and Heat Transfer of Boiling Liquid Nitrogen in a Triangular Pipe

Takuya Morishita*, Ren Sakata*, Katsuhide Ohira*, Kazushi Miyata*, Koichi Takahashi*,
Hiroaki Kobayashi**, Hideyuki Taguchi**, Motoyuki Hongoh** and Takayuki Kojima**
* IFS, Tohoku University, 2-1-1 Katahira, Aoba-ku, Sendai, Miyagi 980-8577, Japan.
** JAXA, 7-44-1, Jindaiji-higashi-machi, Chofu, Tokyo 182-8522, Japan.
+ E-mail:morishita@luna.ifs.tohoku.ac.jp

ABSTRACT

Pressure drop and heat transfer coefficient for boiling two-phase flow of liquid nitrogen in a horizontal triangular pipe are reported in this paper. Experiments were conducted in a horizontal triangular pipe with one side of 20 mm. Six types of flow pattern were observed for a boiling two-phase flow. Pressure drop was measured at heat transfer section and compared with homogeneous and separation flow models. Heat transfer coefficients were evaluated from the wall temperatures measured on the side and bottom surfaces of the heating pipe, and compared with empirical correlations.

1. Introduction

Japan Aerospace Exploration Agency (JAXA) has been promoting the research and development of the hypersonic aircraft since 2004. The key technology of the aircraft which can cruise at Mach 5 is “Pre-cooled turbojet engine”. This engine has a heat exchanger (air pre-cooler) which uses liquid hydrogen fuel (20 K) as coolant for lowering the temperature of incoming air during hypersonic flight. Therefore, it is necessary to obtain the heat transfer and pressure drop of cryogenic fluid. However, because of the difficulty of the handling of the cryogenic fluids, experimental results are not obtained enough.

In this study, liquid nitrogen (77 K) was used for a working fluid. The triangular pipe whose heat transfer area is larger than those of the circular and rectangular pipes with an equivalent hydraulic diameter was used for a test section. The objective of this study is to elucidate the heat transfer and pressure drop of boiling liquid nitrogen flowing in a horizontal triangular pipe.

2. Experimental apparatus

The schematic illustration of the experimental apparatus is shown in Figure 1. The test apparatus consists of a run tank for the storage of liquid nitrogen, a test section and a catch tank. These components are vacuum-insulated for reducing heat inleak. The liquid nitrogen at the temperature of 77 K in the run tank is pressurized by helium gas and transferred into the catch tank by way of the test section. Experimental conditions are shown in Table 1.

Details of the test section are shown in Figure 2. It consists of a heating pipe and a flow visualization pipe with a triangular cross-section of one side 20 mm. An oxygen-free cooper pipe wound around a NiCr wire was installed in the heat transfer section. Total length of the heating pipe is 800mm. Four silicon diode thermometers are used for temperature measurements. Two of them are installed on the side and bottom surfaces of the outer wall of the pipe at the location of 600 mm from the inlet of heating pipe. Other two thermometers are installed inside a stainless steel pipe at locations of 125 mm upstream and 50 mm downstream of the heating pipe to measure the bulk temperatures of liquid nitrogen.

Table 1. Experimental conditions.

Heat flux (q)	5, 10, 20 [kW/m^2]
Run tank pressure	0.10 - 0.13 [MPa]
Mass flux (G)	99 - 1871 [kg/ (m^2・s)]

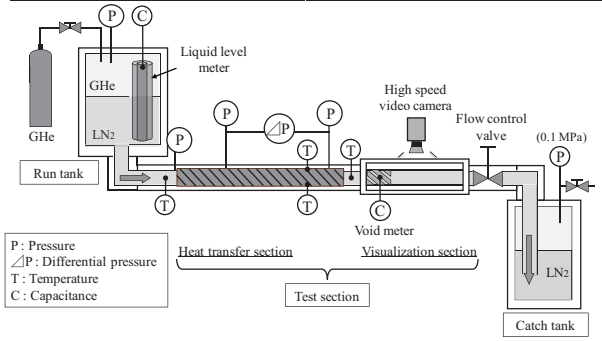

Fig. 1 Experimental apparatus.

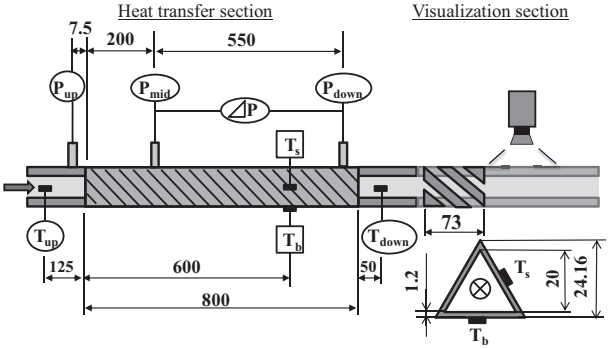

Fig. 2 Details of the test section.

Pressure drop was measured along the 550 mm length of the heat transfer pipe using a differential pressure transducer. The flow visualization pipe is made of polycarbonate resin and equipped with a capacitance-type void-fraction meter. The flow pattern of boiling two-phase flow was observed using a high-speed video camera.

3. Results and Discussion

In this study, six types of steady two-phase flow patterns: bubbly, plug, slug, slug-annular, wavy-annular and wavy flows were observed. Transition flow whose flow patterns emerged cyclically during a short

time-period was also observed.

Figure 3 shows the relationship between the mass flux and the pressure drop per unit length in the case of heat flux 10 kW/m^2. In Figure 3, values calculated by the Blasius equation for the single-phase liquid flow, the homogeneous flow model and the separation flow models [1] are shown by solid and dotted lines. In calculations of the separation flow models, the slip ratios of Khalil, Winterton and Butterworth were used. Mean deviations between the experimental and calculated values by each slip ratio are shown in Table 2. In Figure 3, when flow patterns at the outlet of heating section are slug, slug-annular, wavy-annular and wavy flows, the experimental values are much larger than that of the Blasius equation. The separation flow models have the tendency to agree well with the experimental values. Furthermore, from Table 2, it is confirmed that the separation flow model using the Khalil's slip ratio [2] evaluates the experimental pressure drop with the best accuracy.

Figure 4 shows the relationship between the mass flux and the local heat transfer coefficient in the case of heat flux 10 kW/m^2. In Figure 4, values calculated by the Dittus-Boelter equation, the Gungor-Winterton equation [3] and the Liu-Winterton equation [4] are shown by solid and dotted lines. When flow patterns at the outlet of heating section are slug, slug-annular, wavy-annular and wavy flows, it is found that the Gungor-Winterton equation and the Liu-Winterton equation have the tendency to agree well with the experimental heat transfer coefficients. For the pressure drop and the heat transfer coefficient, it was confirmed that their tendency in the case of 5 and 20 kW/m^2 was similar to those in the case of 10 kW/m^2.

Figure 5 shows the heat transfer coefficient ratio of

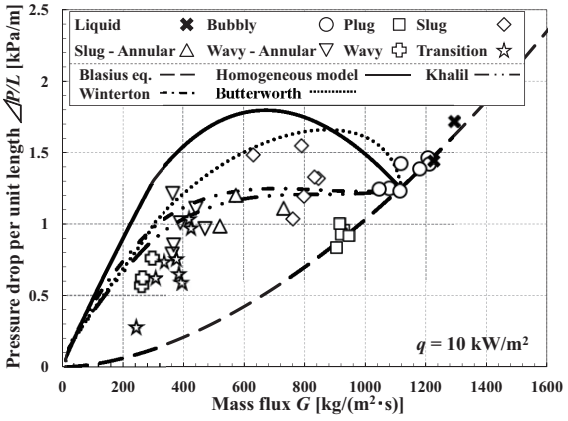

Fig. 3 Relationship between the mass flux and the pressure drop per unit length (q = 10 kW/m^2).

Table 2. Mean deviation between the experimental and calculated values by slip ratio models.

Model	Mean deviation
Homogeneous model	0.513
Khalil	0.343
Winterton	0.379
Butterworth	0.396

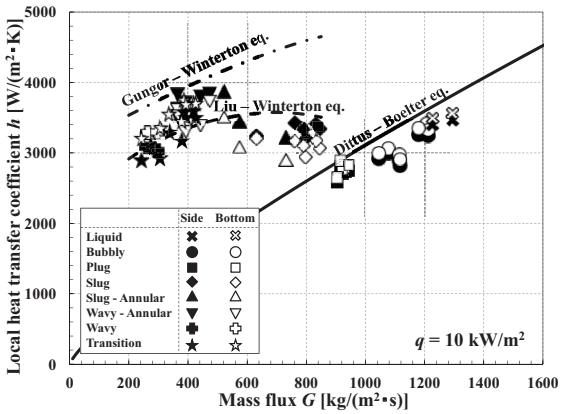

Fig. 4 Relationship between the mass flux and the local heat transfer coefficient (q = 10 kW/m^2).

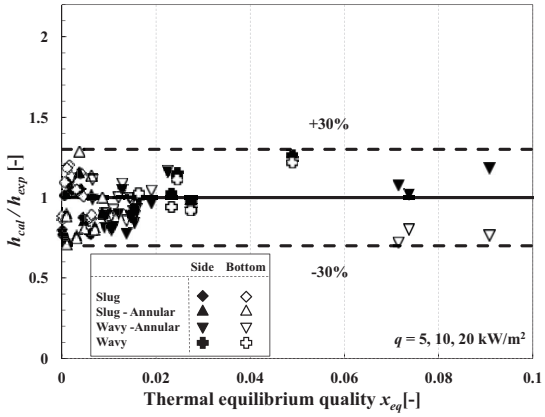

Fig. 5 Comparison of the heat transfer coefficients between experimental data and calculated values by the Liu-Winterton equation.

the values calculated by the Liu-Winterton equation h_{cal} to the experimental values h_{exp} in the region of positive thermal equilibrium quality at the heat flux q = 5, 10 and 20 kW/m^2. Black and white plots are values on the side and bottom surfaces, respectively. From Figure 5, it is confirmed that the Liu-Winterton equation can estimate the heat transfer coefficients within an accuracy of -30% to +30%.

4. Concluding remarks

Pressure drop and heat transfer characteristics for six types of two-phase flow pattern in a horizontal triangular pipe were elucidated by experimental tests.

Acknowledgments

Part of this work was carried out under JAXA-IFS Collaborative Research Project.

References

[1] T. Ueda, In: Gas-Liquid Two Phase Flow, Yokendo Press, Tokyo, Japan, (1981), 34-51 (in Japanese).
[2] A.Khalil et al., Cryogenics, **21**, (1981), 411-414.
[3] K.E.Gungor et al., Chem Eng Res Des, **65**, (1987), 148-56.
[4] Z.Liu et al., Int J Heat Mass Transfer, **34**, (1987), 2759-65.

Tenth International Conference on Flow Dynamics
November 25-27, 2013, Sendai, Miyagi, Japan

Study on Jet Flame Characteristics in High-temperature Oxy-fuel Condition

Takakazu Onishi[1], Li Xing[1], Hisashi Nakamura[1], Takuya Tezuka[1], Susumu Hasegawa[1], Kaoru Maruta[1], Tadariro Araake[2], Susumu Mochida[2]
[1]Institute of fluid science, Tohoku University, 2-1-1 Katahira, Aoba-ku, Sendai, Miyagi 980-8577, Japan
[2]Nippon furnace corporation, 1-53, Shitte 2-chome, Tsurumi-ku, Yokohama, 230-8666, Japan
onishi@edyn.ifs.tohoku.ac.jp

ABSTRACT

Characteristics of coaxial laminar jet diffusion flames in high-temperature oxy-fuel combustion condition were experimentally investigated by changing the CH_4 mole fraction of the fuel stream and oxidizer temperature. Attached flames were observed in the high CH_4 mole fraction while lifted flames were observed in the low CH_4 mole fraction. This tendency was reproduced by two-dimensional computations using detailed reaction scheme.

1. Introduction

Recently, reduction of CO_2 and NOx emissions is very important problem for furnaces. To solve this problem, we proposed high-temperature oxy-fuel combustion technology. This technology is expected to significantly reduce CO_2 and NOx emissions. However, fundamental characteristics of the high-temperature oxy-fuel combustion have not been fully understood yet. In our previous study [1], extinction characteristics were investigated for counterflow diffusion flames in the high-temperature oxy-fuel combustion condition. In the present study, we focused on coaxial laminar jet diffusion flames [2], which is one of the fundamental configurations of furnaces. The objective of this study is to investigate characteristics of coaxial laminar jet diffusion flames in the high-temperature oxy-fuel condition.

2.Experimental and Computational Methods

A jet flame apparatus was used as the experimental setup. Figure 1(a) shows a schematic of the experimental setup. Before jet flame experiments, the honeycomb was heated by a LPG/air flame. After heating of the honeycomb, supply of a LPG/air mixture was stopped and the oxidizer was supplied. High oxidizer temperature was attained by heat transfer with the pre-heated honeycomb. And then, a flame was formed by supplying the fuel stream from the fuel nozzle. Air or an O_2/CO_2 mixture (X_{O2} = 0.4) was used as the oxidizer. X_{O2} = 0.4 was chosen since extinction stretch rate with X_{O2} = 0.4 was comparable to that with air at the oxidizer temperature of 1000 K in our previous study [1]. A CH_4/N_2 mixture or a CH_4/CO_2 mixture was used as the fuel stream. The mean flow velocity of the fuel stream was fixed at 22 m/s and that of the oxidizer was fixed at 1.8 m/s. The inner diameter of the fuel nozzle was 2 mm and that of the outer tube was 94 mm. The oxidizer temperature, T_o, was measured by a K-type thermocouple which was installed near the fuel nozzle. A digital still camera with a CH band pass filter was used to take flame images.

2-D steady computations were conducted by Fluent 6.3.26. An axisymmetric model was employed in the present computation. Figure 1(b) shows tip of the computational domain. The fuel nozzle has 5 mm length and 0.5 mm thickness. The flow velocities of the fuel stream and oxidizers in the experiment were used in the computation. The detailed reaction scheme based on

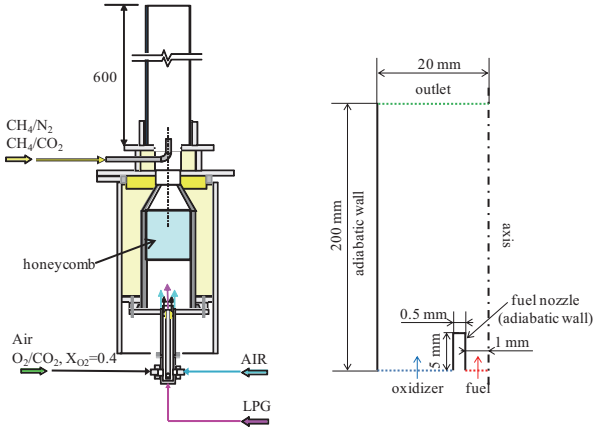

(a) experimental setup (b) computational domain

Fig. 1 Schematic of experimental setup and computational domain

GRI-mech 3.0 [3] (36 species, 219 elementary reactions, NOx reactions removed) were used.

3. Results and Discussion

Figure 2 shows the flame images of CH_4/N_2 versus air (air case) and CH_4/CO_2 versus O_2/CO_2 (oxy-fuel case) at T_o = 1150 K. In low CH_4 mole fraction, lifted flames were observed in both air and oxy-fuel cases. With the increase of the CH_4 mole fraction, the liftoff height decreases and attached flames were observed in a certain CH_4 mole fraction. CH_4 mole fraction of the lifted to attached flame transition in the air case was different from that in the oxy-fuel case. In the air case, the transition occurred at CH_4 mole fraction between 0.15 and 0.2. On the other hand, in the oxy-fuel case, the transition occurred at CH_4 mole fraction between 0.3 and 0.4. The liftoff height in the air case is more sensitive to the CH_4 mole fraction rather than that in the oxy-fuel case. In counterflow diffusion flame, extinction stretch rates in the oxy-fuel condition (X_{O2} = 0.4) were very close to those in air condition at the high oxidizer temperature over a wide range of CH_4 mole fraction [1]. In jet diffusion flames, however, CH_4 mole fraction of the transition in the air case was clearly different from that in the oxy-fuel case. Figure 3 shows regime map of attached and lifted flames in the plane of CH_4 mole fraction and the oxidizer temperature. In the air case, with the increase of the oxidizer temperature, the

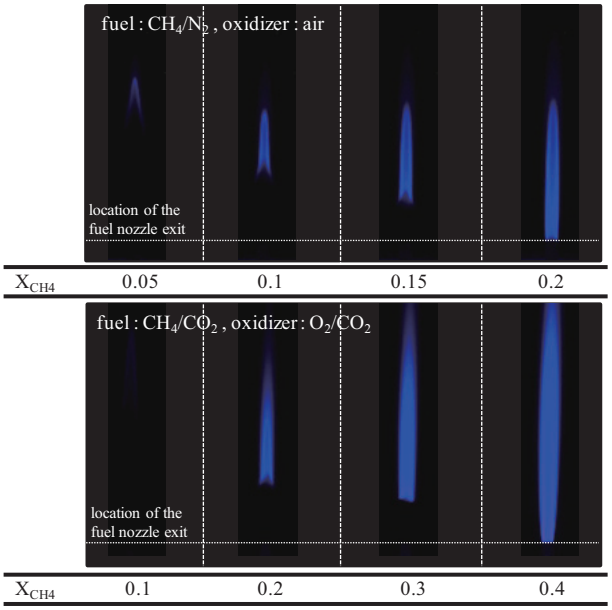

Fig. 2 Flame images with changing CH_4 mole fraction at T_o = 1150 K

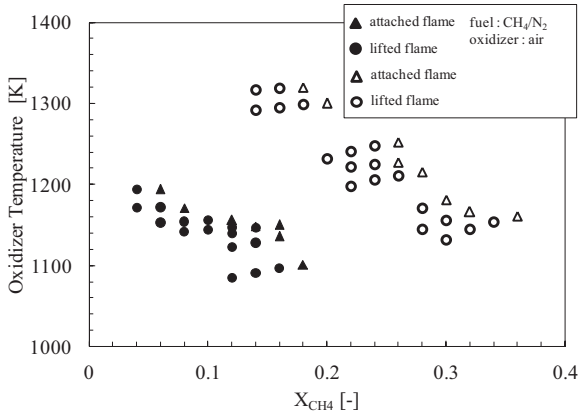

Fig. 3 Regime map of attached and lifted flames in the plane of CH_4 mole fraction and oxidizer temperature

transition point shifted to the region of low CH_4 mole fraction. The same tendency can be observed in the oxy-fuel case.

Figure 4 shows the computational temperature and CH mole fraction in (a) the air case and (b) oxy-fuel case at T_o = 1100 K. With the increase of the CH_4 mole fraction, the liftoff height decreases and attached flames were observed in a certain CH_4 mole fraction. The CH_4 mole fraction of the transition in the air case was different from that in the oxy-fuel case. The liftoff height in the air case is more sensitive to the CH_4 mole fraction rather than that in the oxy-fuel case. These tendencies were observed in experimental results. In both cases, with the increase of the CH_4 mole fraction, The maximum flame temperature, T_{max}, increases with the increase of the CH_4 mole fraction. When CH_4 mole fraction increased, the reactivity of the fuel/oxidizer is expected to be increased due to a large heat release. Thus, when CH_4 mole fraction increased, T_{max} increased. The maximum flame temperature in the air case is more sensitive to the CH_4 mole fraction rather than in the oxy-fuel case.

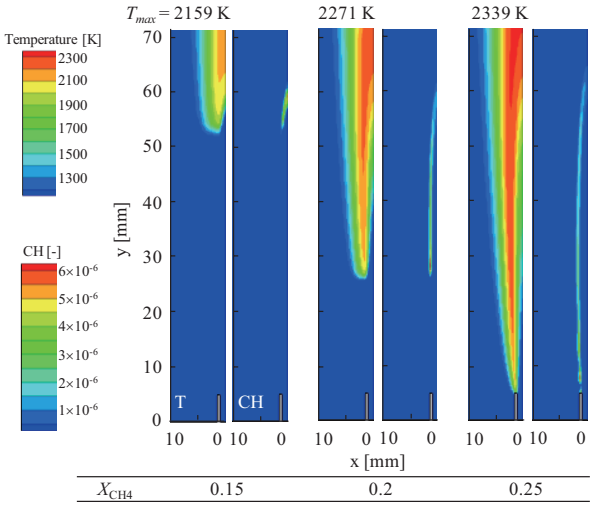

(a) CH_4/N_2 versus air case

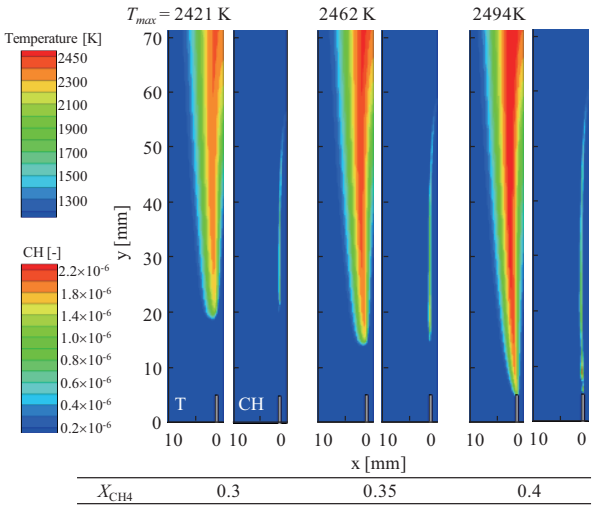

(b) CH_4/CO_2 versus O_2/CO_2 case

Fig. 4 Computational temperature and CH mole fraction at T_o = 1100 K

4. Conclusions

Coaxial laminar jet diffusion flames in the high-temperature air condition and high-temperature oxy-fuel condition were investigated experimentally and computationally.

1. For both air and oxy-fuel cases, lifted flames were observed in low CH_4 mole fraction of the fuel stream while attached flames were observed in high CH_4 mole fraction. CH_4 mole fraction of the transition from lifted flames to attached flames in the air case was lower than that in the oxy-fuel case.
2. In computation, lifted flames were observed in low CH_4 mole fraction of the fuel stream while attached flames were observed in high CH_4 mole fraction. The maximum flame temperature in the air case is more sensitive to the CH_4 mole fraction rather than in the oxy-fuel case.

References

[1] X. Li, et al., 50th Heat Transfer Symposium (2013) 526-527
[2] B. C. Choi, et al, Combust. Flame. 157 (2012)2348-2356
[3] http://www.me.berkeley.edu/gri_mech/

Tenth International Conference on Flow Dynamics
November 25-27, 2013, Sendai, Miyagi, Japan

Characterization of DBD Reactive Air Jet under High Temperature and High Pressure for Combustion Assist

Hikaru Asano[1], Tomoki Nakajima[2], Hidemasa Takana[2], Hideya Nishiyama[2]
[1] *Graduate School Engineering Tohoku University, Sendai, 980-857, Japan*
[2] *Institute of Fluid Science, Tohoku University, Sendai, 980-8577, Japan*
asano@paris.ifs.tohoku.ac.jp

ABSTRACT

Experimental analysis of DBD plasma flow was conducted for plasma assisted combustion in an internal engine under high temperature and high pressure. Fundamental characteristics of discharge such as ozone productions, energy coupling efficiency and ozone production energy for various operating conditions were discussed in detail.

1. Introduction

Recently, plasma has been applied in various fields. Plasma has a multi-functions with high energy density, high controllability by electromagnetic field and chemical high reactivity. In nonequilibrium plasma, active species such as radicals, excited species and charged particles are effectively generated by high energy electron impact reactions. Oxygen radical and ozone in plasma-generated active species have strong oxidation potential and play an important role in combustion enhancement [1]-[5].

However, most of researches on nonequilibrium plasma flow were conducted under atmospheric pressure condition for many applications. Fundamental characteristics of nonequilibrium plasma under high temperature and high pressure condition as in the internal engines have not been clarified in detail.

The purpose of this research is to clarify experimentally the effect of temperature, pressure and applied voltage on radical production in DBD air plasma flow and energy coupling efficiency for plasma assisted combustion in an internal engine.

2. Experimental apparatus and measurement

Figure 1 shows the schematic of experimental apparatus. Experimental device consists of power supplies, plasma torch, gas supply section and chamber. Plasma torch has coaxial annulus geometry. Voltage is applied to the inner electrode and the outer electrode is grounded. The dielectric is attached only inner surface of outer electrode. The inner electrode has diameter of 6.0 mm and the inner diameters and thickness of a dielectric are 7.5 mm and 0.8 mm, respectively. Inner electrode distance is 1.55 mm and the distance between a center electrode and a dielectric is 0.75 mm. Electrode material is copper and dielectric material is quartz, respectively.

Air flow rate introduced to DBD torch is set to 6.0 Sl/min by a massflow controller and air is preheated by a heater. The pressure in the chamber is controlled by adjusting inlet and outlet flow rates in the chamber.

In order to clarify the characteristics of DBD air jet under high temperature and high pressure, current-voltage characteristics were clarified along with the measurements of gas temperature, spectroscopy, and ozone concentration. Ozone concentration was measured using the ultraviolet absorption-type

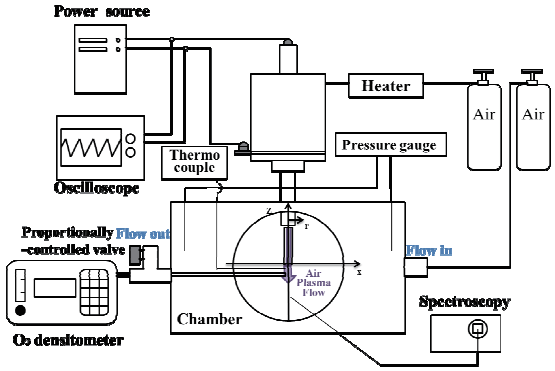

Fig.1 Schematic of experimental apparatus.

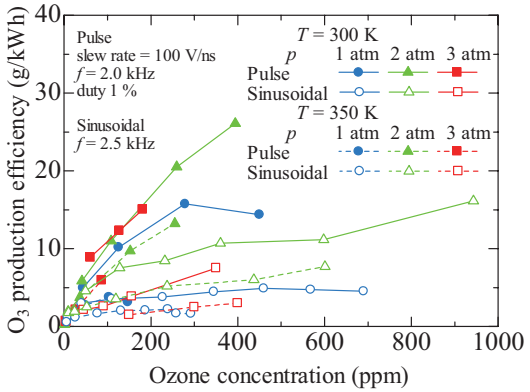

Fig.2 Variation of ozone production efficiency with ozone concentration.

ozone-concentration meter. Additionally, in order to investigate the influence of the voltage wave forms on radical production, the two kinds of power sources are used. One of the power sources can apply the high voltage sinusoidally at 2.5 kHz. The other one can generate positive high voltage pulse up to 2.0 kHz with the slew rate of 100 V/ns at the duty ratio of 1 %. The maximum applied voltages of sinusoidal power source and high voltage pulse generator are 20 kV_{pp} and 13 kV, respectively.

3. Results and Discussion

Figure 2 shows ozone production efficiency versus its concentration at various pressures and temperatures for sinusoidal or pulsed applied voltage. Higher ozone generation efficiency can be obtained under high pressure. On the other hand, the efficiency becomes smaller at high temperature. The production efficiency

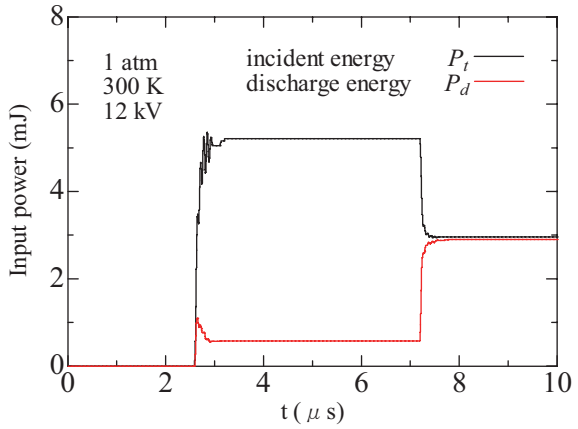

Fig.3 Time integration of incident and discharge energy per one pulse.

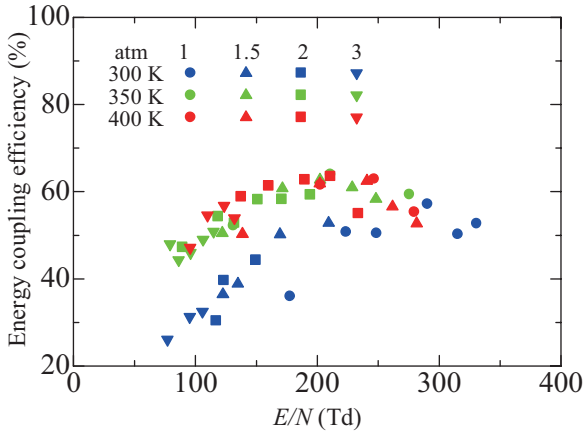

Fig.4 Variation of energy coupling efficiency with *E/N*.

for pulsed applied voltage is higher compared with sinusoidal voltage and it increases with ozone concentration. Although the ozone production efficiency is smaller for sinusoidal applied voltage, the produced ozone concentration is higher than that for pulsed applied voltage.

Figure 3 shows the time integrated incident energy and discharge energy per one pulse at applied voltage of 12 kV at 1 atm and 300 K [6]. Incident energy rises up to 5.2 mJ at 2.6 μs. Total input power drops to 3 mJ at the fall of applied voltage. On the other hands, the discharge energy increases to 0.58 mJ at t = 2.6 μs and to 2.9 mJ at t = 7.2 μs. 3 mJ of energy is input to the discharge for 5.0 μs. Therefore, the energy coupling efficiency η can be defined as the ratio of total discharge input energy to the maximum incident energy to DBD [7] and the energy coupling efficiency is 56 % in this case.

Figure 4 shows the energy coupling efficiency with *E/N* for various operating conditions. There is temperature dependence on energy coupling efficiency strong rather than surrounding pressure. Energy efficiency at 350 K and 400 K is higher than that at 300 K. Moreover, the optimal reduced electric field strength exists for energy coupling efficiency. The highest efficiency of 65 % is obtained at about 200 Td, 350 K and 400 K.

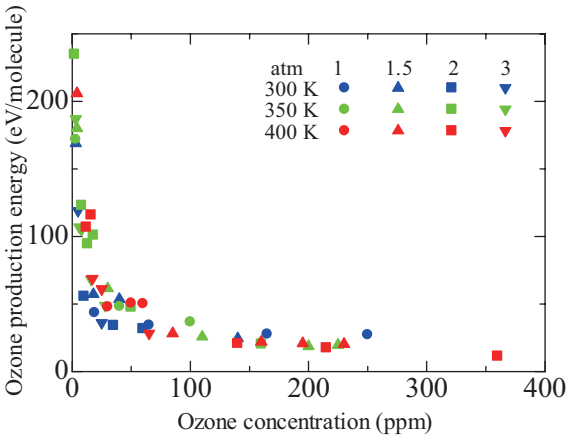

Fig.5 Variation of ozone production energy with ozone concentration.

Figure 5 shows ozone production energy per its concentration at various pressures and temperatures. Ozone production energy decreases inversely for ozone concentration regardless of temperature and pressure. In an ozonizer using air, the theoretical value is 4.46 eV / molecule. Under high ozone concentration, ozone production energy becomes close to a theoretical value. The minimum of 11.3 eV / molecule was obtained at 400 K, 2 atm.

4. Concluding remarks

(1) For sinusoidally applied voltage, higher ozone concentration is produced. For pulsed applied voltage, ozone production efficiency is higher.

(2) Energy coupling efficiency has strong temperature dependence rather than surrounding pressure. Energy efficiency at 350 K and 400 K is higher than that at 300 K. Moreover, the optimal reduced electric field strength exists for energy coupling efficiency. The highest efficiency of 65 % is obtained at about 200 Td, 350 K and 400 K.

(3) Under high ozone concentration, ozone production energy becomes close to a theoretical value. The minimum of 11.3 eV / molecule was obtained at 400 K, 2 atm.

Reference

[1] S. M. Starikovskaia, Journal of Physics D, 39 (2006).
[2] T. Shiraishi, T. Urushihara, M. Gundersen, Journal of Physics D, 42 (2009).
[3] H. Nishiyama, H. Takana, S. Niikura, H. Shimizu, D. Furukawa, T. Nakajima, K. Katagiri and Y. Nakano, IEEE Transactions on Plasma Science, 4, 36 (2008).
[4] H. Nishiyama, H. Takana, H. Shimizu, Y. Iwabuchi and Y. Nakano, International Journal of Emerging Multidisciplinary Fluid Sciences, 1, 2 (2009).
[5] Y. Ikeda, A. Nshiyama, J. Plasma Fusion Res, 89, 4 (2013).
[6] S. Liu and M. Neiger, Journal of Physics D, 36 (2003).
[7] I. V. Adamovich, M. Nishihara, I. Choi, M. Uddi, and W. R. Lempert, Physics of plasmas. 16, 113505 (2009).

Tenth International Conference on Flow Dynamics
November 25-27, 2013, Sendai, Miyagi, Japan

Effect of Nozzle Diameter on NO_X Emission of High-Pressure Pulse Spray Combustion

Satoki Yokoi[1], Shota Sugawara[1], Junichi Tanimoto[1], Ryuichi Sagawa[1], Yasuhiro Saito[1],
Yohsuke Matsushita[1], Hideyuki Aoki[1], Masakazu Shoji[2]
[1]Department of Chemical Engineering, Graduate School of Engineering, Tohoku University,
6-6-07 Aoba, Aramaki, Aoba-ku, Sendai, Miyagi 980-8579, Japan,[2]Shizenkankyosangyo Co. Ltd.,
1-7-21 Hinodemati, Miyagino-ku, Sendai 983-0035, Japan
saito@tranpo.che.tohoku.ac.jp

ABSTRACT

Atomization and combustion experiments of high-pressure pulse sprays were performed to investigate the effect of nozzle diameter on nitrogen oxides (NO_X) emissions from a combustor. Amplitude histograms of liquid fuel concentration at the nozzle diameter of 0.21 and 0.31 mm were obtained in the atomization. Combustion temperatures and NO_X emissions were measured in the combustion experiment. The liquid fuel concentration tended to increase, and the combustion gas temperatures and NO_X emissions were lower with an increase in the nozzle diameter.

1. Introduction

A stationary combustor is widely used in industry. The common rail injection system used in an internal-combustion engine can control the high-pressure fuel injection and intermittent injection to achieve low environmental impact. To develop a low nitrogen oxides (NO_X) combustion system, we apply the injection system to the stationary combustor. In the previous studies, the combustion characteristic of the injection system has been reported for two or three sprays interaction in a small and high-pressure space [1–2]. However, for the steady combustion, not only the spray burns at atmospheric pressure in the large combustion chamber, but also more sprays affect each other. The effect of large space and the sprays interaction on the high-pressure spray combustion is little understood.

In the present study, the liquid fuel concentrations were measured with different nozzle in diameters in atomization. The combustion gas temperatures in a test furnace, and the NO_X emissions were measured in combustion experiments. We investigated the effect of the nozzle diameter of injector on the NO_X emissions of the high-pressure pulse spray combustion.

2. Experiment

2.1 Experimental apparatus for atomization

Figure 1 shows a schematic diagram of experimental apparatus for the spray experiment. The liquid fuel volume at 200 mm downstream from the nozzle tip was measured by the particle size analyzer (Spraytec, Malvern Instruments Ltd) at room temperature and free space. The data were acquired at a 2.5 kHz sampling rate, and time series lasting 0.05 s were obtained. The high-pressure pulse sprays images were taken by the high-speed camera (FASTCAM SA3, PHOTRON LIMITED) with a frame rate of 2.5 kHz. The liquid fuel concentration was determined by the liquid fuel volume and the spray width. The spray width was quantified by the image analyzer software (WinROOF version 6.1.0, MITANI CORPORATION).

2.2 Experimental apparatus for combustion

Figure 2 shows a schematic diagram of experimental apparatus for the spray combustion experiment. The dimensions of the furnace are ϕ312 mm in inner diameter and 1788 mm in length. The furnace has 4 ports for the temperature measurements at 308, 408, 508, 683 mm downstream from the nozzle tip. The combustion gas temperatures were measured by a suction pyrometer. The suction pyrometer consisted of a thermocouple and an alumina tube to minimize radiative heat loss. The NO_X emissions at the outlet of the furnace were measured by the portable gas analyzer (testo350, TESTO, INC.). The combustion gas temperatures and the NO_X emissions were measured for 20 s. The measurement was performed three times in each condition. The measured value of NO_X emissions were translated into NO_X emissions at 0 percent excess air. The maximum values of the three measurement data were averaged.

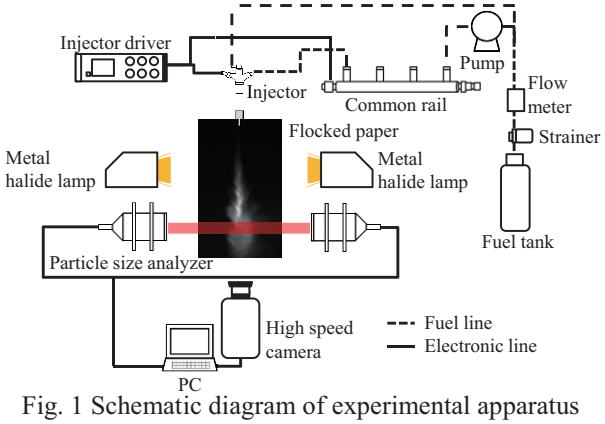

Fig. 1 Schematic diagram of experimental apparatus for the atomization

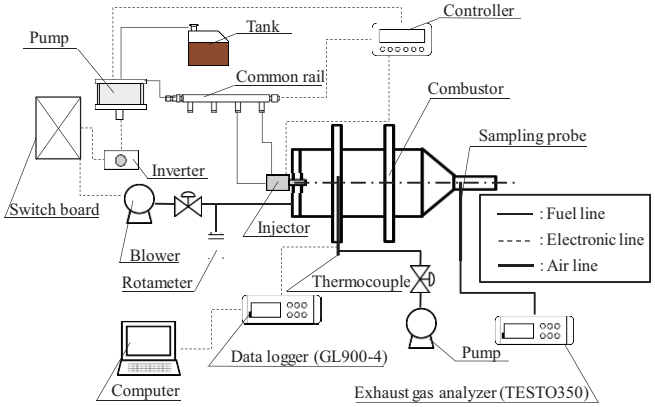

Fig. 2 Schematic diagram of experimental apparatus for the combustion experiment

2.2 Experimental conditions

Table 1 shows experimental conditions. The fuel flow rate was constant for each oscillation frequency. In other words, the higher oscillation frequency is, the lower injection quantity per one spray becomes.

3. Results and discussion

Figure 3 shows the amplitude histogram of the liquid fuel concentration. The increasing nozzle diameter tends to increase the liquid fuel concentration. The reason for the trend is that the injection quantity per the injection time increases with the nozzle diameter. Although this can be caused by the spray evaporation, the amount of spray evaporation is small because the saturated vapor pressure is low at the room temperature. The result suggests that the nozzle diameter affects the concentration of the fuel at a combustion region in a combustor. As to the oscillation frequency, the liquid fuel concentration tends to increase with an increase in the oscillation frequency and the distribution of the concentration narrows. This is because the flow rate of the fuel is constant.

Figure 4 shows the effect of the nozzle diameter on the combustion gas temperatures. Most of them show the maximum value at the 408 mm downstream from the nozzle tip. This means that the fuel is almost burned off from the nozzle tip to 408 mm. The combustion temperatures are lower with the nozzle diameter of 0.31 mm than with that of 0.21 mm. This is because the amount of unburned fuel in the combustion region increases due to the shortage of oxygen owing to the increasing fuel concentration.

The effect of the nozzle diameter on the NO_X emissions is shown in Fig. 5. Because the temperatures shown in Fig. 4 are lower than the temperature at which thermal NO_X is formed, the thermal NO_X is little in the exhaust gas in this work. The NO_X emissions are lower with the nozzle diameter of 0.31 mm than with that of 0.21 mm. This is caused by the liquid fuel concentration increasing at the combustion region because that the formation of prompt NO decreases with increasing the input equivalence ratio from Mori *et al.* [3]. Hence, the liquid fuel concentration increasing with the nozzle diameter reduces the NO_X emissions.

4. Concluding remarks

The effect of the nozzle diameter of injector was investigated in spray and combustion experiments. In the spray experiments, the liquid fuel concentration increased with the nozzle diameter and was described by the injection quantity per the injection time. In the combustion experiments, the liquid fuel concentration at the combustion region affected the combustion temperatures and the NO_X emissions. The present results suggest that the NO_X emissions can be controlled by the nozzle diameter.

Acknowledgements

This work is partly supported by JSPS KAKENHI Grant Number 22360318, JST Research Seeds Quest Program, and Naito Taisyun Science and Technology Foundation.

Table 1 Experimental conditions

Fuel		Diesel			
Fuel flow rate	[l/min]	0.05			
Injection pressure	[MPa]	40			
Nozzle diameter	[mm]	0.21		0.31	
Oscillation frequency	[Hz]	100	250	100	250
Injection time	[ms]	1.32	0.38	0.62	0.36
Air ratio	[–]	1.2			

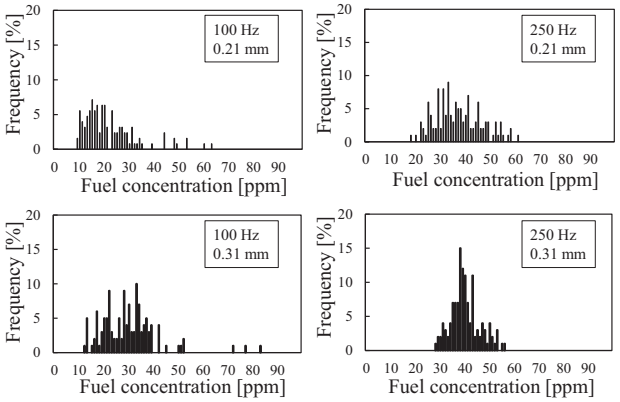

Fig. 3 Liquid fuel concentration at free space

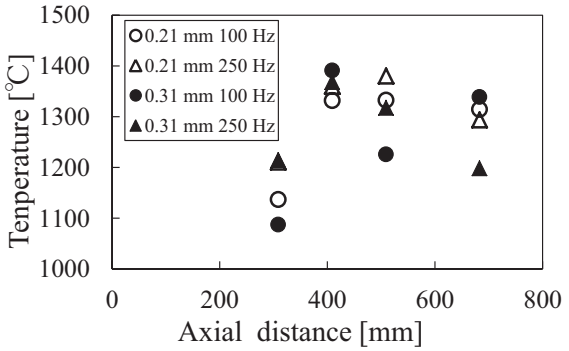

Fig. 4 Combustion gas temperature

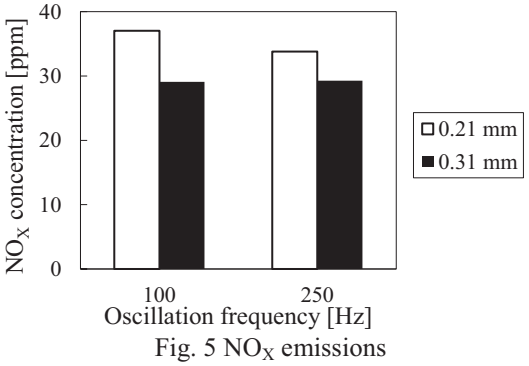

Fig. 5 NO_X emissions

References

[1] G. Zhang *et al.*, *Fuel*, **102** (2012), 666.

[2] M. Zheng, R. Kumar, *International Journal of Thermal Science*, **48** (2009), 1829.

[3] Y. Mori *et al.*, *Transactions of the Japan Society of Mechanical Engineers, Series B*, 42–357(1976), 1511.

Flow and Heat Transfer Characteristics of Slush Nitrogen in a Horizontal Triangular Pipe

Yutaro Saito, Jun Okuyama, Koichi Takahashi, Katsuhide Ohira
Institute of Fluid Science, Tohoku University, 2-1-1 Katahira, Aoba-ku Sendai, Miyagi 980-8577, Japan
saito@luna.ifs.tohoku.ac.jp

ABSTRACT

Cryogenic slush fluids such as slush hydrogen are solid-liquid, two-phase fluids. There are high expectations as a functional thermal fluid. Experiments were performed using slush nitrogen to elucidate pressure drop reduction and heat transfer deterioration in a horizontal triangular pipe flow, while the behavior of solid particles were observed using a high-speed camera and a PIV method. In the tests, the reduction of slush nitrogen emerged in the velocity range of more than 1.8 m/s in the case of non-heated and heated conditions with the heat flux of 10 kW/m^2. The heat transfer deteriorated in the same velocity range where the reduction emerged.

1. Introduction

Cryogenic solid-liquid two-phase slush fluids have superior properties as high-density fluids and refrigerants. Our laboratory has proposed a high-efficiency hydrogen energy system as shown in Fig. 1 [1]-[2]. This system can be expected synergetic effects using slush hydrogen (14K). For development of this system, flow properties of slush fluid in a triangular pipe, which has a larger heat transfer area and a more superior integration than a circular pipe, are important because the pipe will be used as both the hydrogen transport pipe and the refrigerant pipe for superconducting power transmission. In this paper, we report pressure drop reduction, heat transfer deterioration and a result of visualization of slush nitrogen (63K) flow in a horizontal triangular pipe.

2. Experimental apparatus and procedures

Figure 2 shows the test apparatus used in this study. This apparatus is composed of a run tank, a test section and a catch tank. The test section consists of a pressure-drop and heat-transfer measurement section and a visualization section. After slush nitrogen was produced in the run tank, it flows into the test section by pressurization using helium gas. Figure 3 shows details of the heat transfer section. The cross section of the flow channel is equilateral triangular with a side of 20 mm and a wall thickness of 1.2 mm. The pipe is 1025 mm in length and made of oxygen-free copper. The heated section by means of heater wire is 800 mm in length.

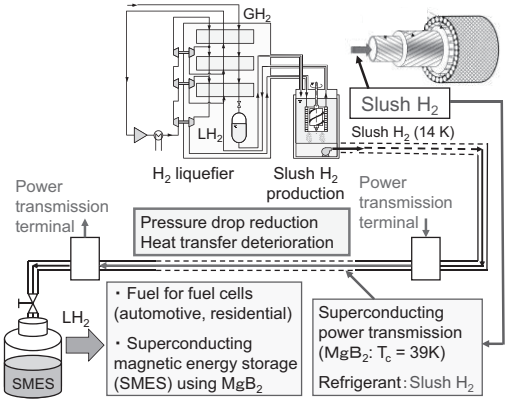

Fig. 1 High-efficiency hydrogen energy system using slush H_2.

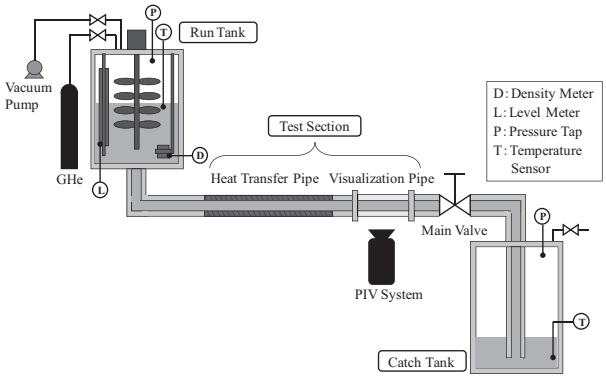

Fig. 2 Experimental apparatus for slush N_2 flow test.

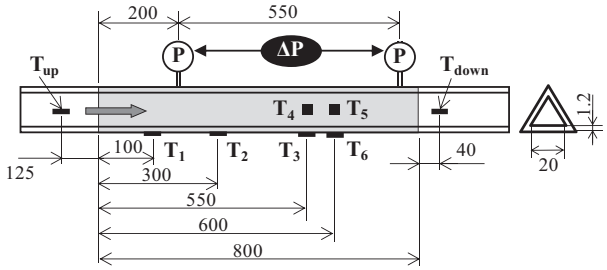

Fig. 3 Details of the heat transfer section.

For the measurement of pressure drop, two pressure taps are installed at the inlet and outlet locations of the 550 mm long measurement section.

Wall and bulk temperatures were measured respectively at six points and two points in the test section for the evaluation of the heat transfer coefficient. In the experiment, liquid nitrogen (63K) flow was also examined for comparison with slush flow. Experimental conditions are as follows: flow velocities 0.6~4.1 m/s, solid fractions 0.4~22 wt.% and heat fluxes 10 and 20 kW/m^2.

3. Results and Discussion

3.1. Non-heated condition

Figure 4 shows the relation between the measured pressure drop versus flow velocity in non-heated conditions. The pressure drop for liquid nitrogen flow shows the same tendency of the Blasius equation.

Pressure drop ratio r_{dp} is plotted against flow

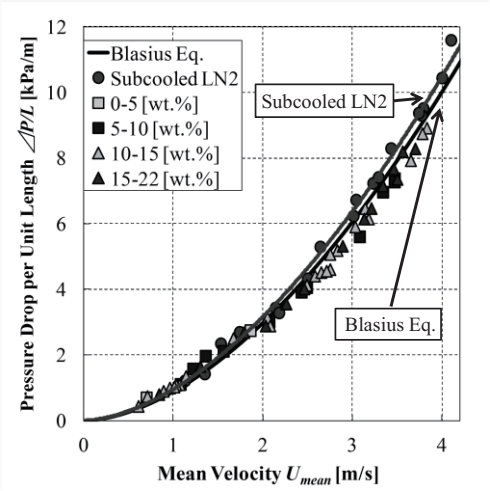

Fig. 4 Pressure drop vs. mean velocity of slush N_2.

velocity in Fig. 5. The pressure drop ratio is defined as

$$r_{dp} = \Delta P_{sl} / \Delta P_{sub} \quad (1)$$

The case where the pressure drop of slush flow is less than that of liquid flow, or $r_{dp} < 1$ shows that the pressure drop reduction emerges. As shown in Fig. 5, the pressure drop ratio decreases with increase in velocity at low velocity region and the ratio falls below unity in the velocity range of over 1.8 m/s. Although the ratio increases gradually with the velocity increase at high velocity region, it never exceeds the unity. Pressure drop reduces up to a maximum of 16 % at around 3.0 m/s. The solid fraction has hardly any effect on the ratio. In low velocity region, by the result of the flow visualization, solid particles settled down and the flow pattern was a sliding flow. In high velocity region, solid particles are uniformly distributed through the pipe cross section and the pattern was a pseudo-homogeneous flow. This phenomenon is also observed in a circular pipe [2]. The pressure drop reduction in the triangular pipe is considered to occur by the same mechanism of the circular pipe. Thus, interference between solid particles and the pipe wall decreases, and solid particles migrated to the pipe center suppress turbulence generation within the liquid layer near the wall.

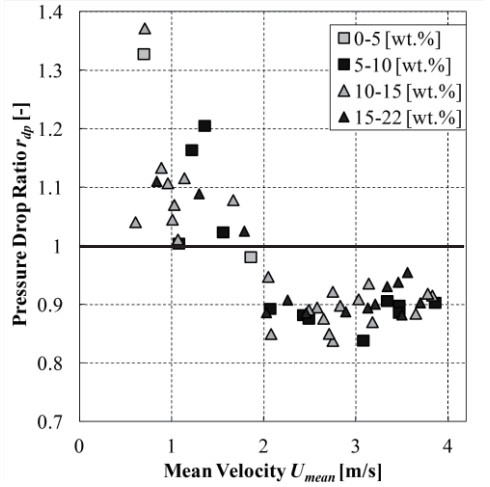

Fig. 5 Pressure drop ratio vs. mean velocity of slush N_2.

3.2. Heated condition

Figure 6 shows the result of pressure drop and local heat transfer coefficient against velocity in heated condition. In the figure, the local heat transfer coefficient measured at the point of the temperature sensor T_3 is shown as an example. The data for 10 kW/m^2 is plotted in the figure. Equation (2) shows the definition of the local heat transfer coefficient.

$$h = q/(T_{wall} - T_{bulk}). \quad (2)$$

In the case of q = 10 kW/m^2, pressure drop reduction appears in the range of over 1.8 m/s. the reduction is a maximum of 18 % and the solid fraction has hardly any influence on the ratio. This tendency is almost the same as the non-heated condition. Thus, the heat transfer to slush nitrogen has little influence on the pressure drop reduction.

Regardless of the magnitude of heat flux, heat transfer coefficient of slush nitrogen is less than that of liquid nitrogen in the range of flow velocity where the pressure drop reduction emerges in the triangular pipe. The maximum heat-transfer deterioration is 15 % for both the heat fluxes. This feature was observed not only at the point of the temperature sensor T_3 but also at the points of all the temperature sensors. As mentioned above, heat transfer deterioration coincided with pressure drop reduction. In this range, solid particles migrated to the pipe center suppress the diffusion of turbulence generated near the pipe wall to the pipe center, as with the reason of the pressure drop reduction.

4. Conclusions

Pressure drop and heat transfer of slush nitrogen flow in a horizontal triangular pipe were examined and clarified in this study. As with a circular pipe, pressure drop reduction and heat transfer deterioration occurred in the case of a triangular pipe.

References

[1] K. Ohira, TEION KOGAKU, **41** (2006), 61-72.
[2] K. Ohira, cryogenics, **51** (2011), 389-396.

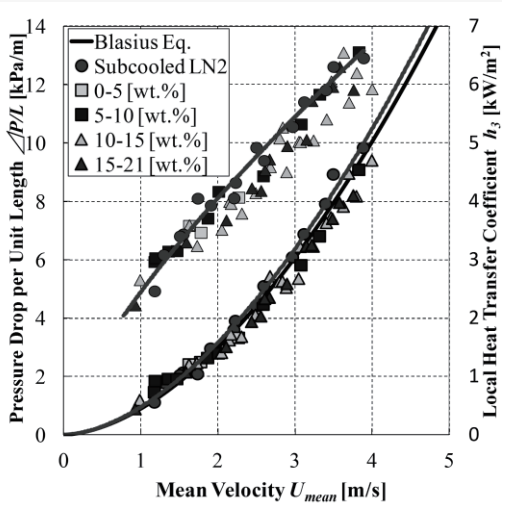

Fig. 6 Pressure drop and local heat transfer coefficient vs. mean velocity of slush N_2. (q = 10 kW/m^2)

Tenth International Conference on Flow Dynamics
November 25-27, 2013, Sendai, Miyagi, Japan

Study on Ignition Characteristics of Syngas in a Micro Flow Reactor with a Controlled Temperature Profile

Hiroki Takahashi, Takuya Tezuka, Susumu Hasegawa, Hisashi Nakamura, Kaoru Maruta
Institute of Fluid Science, Tohoku University
2-1-1 Katahira, Aoba-ku, Sendai, 980-8577, Japan
takahashi@edyn.ifs.tohoku.ac.jp

ABSTRACT

Combustion and ignition characteristics of various compositions of syngas were investigated using a micro flow reactor with a controlled temperature profile. In this study, we focused on weak flames which can be observed at the low flow velocity condition inside a micro flow reactor. Experimental results showed, with an increase of H_2 in CO/H_2 fuel, the weak flame position shifted to the low temperature region, especially noticeable for the lower H_2 concentration. The effects of inert gases (N_2, CO_2 and H_2O) on the weak flame position were investigated numerically and results showed that the H_2O addition chemically decreases the reactivity of syngas.

1. Introduction

Recent years, integrated coal gasification combined cycle technology is paid attention as a new electric power system due to its lower CO_2 emission, energy security superiority and so on. In this system, the syngas which is generated by coal gasification and has CO/H_2 as a main composition is applied to a gas turbine. Since the composition of syngas is varying according to a type of gasification or gasified coals, it is important to understand combustion and ignition characteristics of various compositions of syngas, to combust the syngas safety and low environmental load in a gas turbine combustor.

In this study, we focused on a micro flow reactor with a controlled temperature profile [1] as a method to understand the fundamentals of combustion and ignition characteristics. In this method, a quartz tube whose inner diameter is smaller than quenching diameter of an inlet mixture is used as a reactor. By heating the reactor using an external heat source, a flame is formed inside the reactor. In particular, we can observe the weak flames which are steady and have low intensity of chemiluminescence at the condition of low inlet flow velocity. Focusing on characteristics of the weak flames, several studies have been conducted, such as ignition temperature of methane [2], multi-stage oxidation of DME and *n*-heptane [3,4] and octane number dependence of primary reference fuel and natural gas components [5,6], and they have showed availabilities of the micro flow reactor for understanding the fundamentals of combustion and ignition characteristics.

This work focused on CO/H_2 blends, and investigated effects of CO/H_2 blends ratio and inert gas addition on the weak flames experimentally and numerically.

2. Experimental and computational methods

Schematic of experimental set up is shown in Fig. 1. A quartz tube whose inner diameter is 2 mm was used as a reactor. The reactor was heated by a hydrogen/air premixed flat-flame burner, and a steady wall temperature profile up to 1300 K was given. Each flow rate of CO, H_2, O_2 and N_2 was controlled by a mass flow controller so that equivalence ratio, φ, is 1 and inlet mean flow velocity, U, is 2 cm/s. Each gas was premixed and introduced to the reactor. The introduced mixture was heated by hot wall surface and ignited at a specific location. A digital camera with a band-pass filter was used to observe weak flames. Obtained flame images were image-processed to get a brightness profile of an axial direction. The experimental flame location was defined as a location of a peak of the brightness profile. The wall temperature was measured by a K-type thermocouple. The wall temperature at the flame location was estimated by verifying a location of a peak of brightness profile and measured wall temperature profile. The LPG/air premixed burner was set to prevent a leakage of CO to ambient at the outlet of the reaction.

PREMIX [7] -based one-dimensional steady code was used for the numerical simulation. To simulate the micro flow reactor system, the temperature profile which corresponds to the experimental temperature profile was given. A heat transfer term between a gas phase and a wall surface was added to the gas-phase energy equation. The GRI Mech. 3.0 (53 species, 325 reactions) [8] was used as a detailed reaction mechanism. The computational flame location was defined as a location of a peak of heat release rate. The same conditions with experiment for mixture compositions, inlet flow velocities and pressures were employed in the simulation.

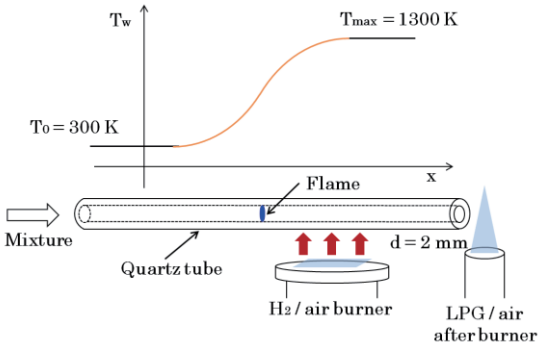

Fig. 1 Schematic of experimental setup

3. Results and discussions

3.1 Weak flame response to CO/H_2 blends ratio

Since H_2 has high laminar burning velocities, inlet mixtures were diluted by N_2 so that O_2:N_2=1:7 in every CO/H_2 blends ratio to prevent a flash back. Experimental flame images of CO/H_2 blends with various blends ratios are shown in Fig. 2. Exposure times of flame images shown in Fig. 2 were 10s for

100%CO and 60s for others. The intensity of chemiluminescence decreased with increase of ratio of H_2 in blended fuels. Only single luminous zone was observed in the flow direction. In the past researches for hydrocarbons [3,4], multiple luminous zones had been observed in the flow direction at low flow velocity conditions. And, from the experimental and computational profile of species, it was identified that these luminous zones corresponded to the process of multi-stage oxidation of fuels. On the other hands, for CO/H_2 blends, since the decomposition of fuel at low temperature doesn't occur, the oxidation process is consisted only of the last stage oxidation which corresponds to the hot flame. This process seems to be observed as a single luminous zone.

As shown in Fig. 2, experimental flame location shifted to the low temperature region with the increase of ratio of H_2 in a fuel. The amount of the shift was greater in the cases of 0-25%H_2 than that in the cases of 25-90%H_2. Figure 3 shows computational flame locations of CO/H_2 blends with various blends ratios. Computational results showed that, with the increase of ratio of H_2 in a fuel, the flame location shifted to the low temperature region (1-25%H_2), and to the high temperature region (25-100%H_2). Both experimental and computational result showed the greater shift of the flame location by H_2 addition in lower ratio of H_2 in a fuel. This trend agrees well with the fact that the rate of CO oxidation is dramatically increased by the addition of even small amounts of hydrogen or hydrogen-containing species, compared with the case that CO reacts only with O atoms [9]. Further discussions are required for the cases of higher ratio of H_2 in a fuel.

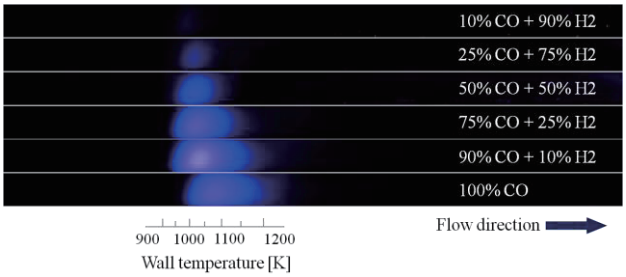

Fig. 2 Weak flame images of CO/H_2 blends with various blends ratios

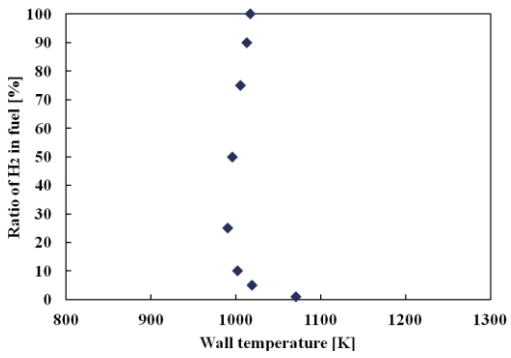

Fig. 3 Computational flame locations of CO/H_2 blends with various blends ratios

3.2 The effect of inert gas addition

The effects of H_2O, N_2 and H_2O additions on combustion and ignition characteristics of the CO/H_2 blends (50%CO+50%H_2) were numerically investigated. For all the cases of inert gases, both the laminar burning velocity and the adiabatic flame temperature decreased with an increase of amount of additional inert gas. On the other hand, the effect of inert gas addition on weak flame locations in a micro flow reactor varied in inert gases, as shown in Fig. 4. With the increase of amount of additional inert gas, the flame location didn't shift significantly in the case of N_2 and CO_2 but shifted to the high temperature region in the case of H_2O. In general, there would be both thermal and chemical effects as the effect of inert gas addition on combustion characteristics. However, since the gas-phase temperature inside a quartz tube is strongly governed by wall temperature in a micro flow reactor, the thermal effect is thought to be small. This implies that the H_2O chemically decreases the reactivity of mixtures.

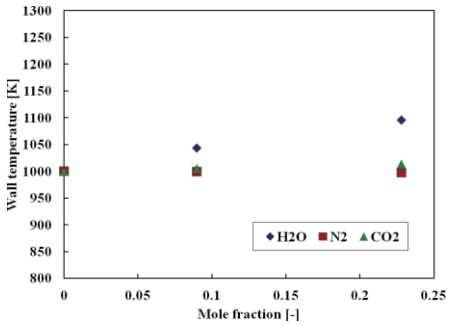

Fig. 4 Effect of additional species on flame location in a micro flow reactor

4. Conclusions

Combustion and ignition characteristics of syngas were investigated using a micro flow reactor with a controlled temperature profile. A single luminous area was observed in every CO/H_2 blends ratio. The flame location shifted to the low temperature region with the increase of ratio of H_2 in a fuel, especially noticeable for lower H_2 ratio condition. Furthermore, the flame location shifted to the high temperature region with the H_2O addition. This implies the chemical effect of H_2O on the ignition is significant.

Reference

[1] K. Maruta et al., Proc. Combust. Inst. 30 (2005) 2429-2436.
[2] Y. Tsuboi et al., Proc. Combust. Inst. 32 (2) (2009) 3075-3081.
[3] H. Oshibe et al., Combust. Flame 157 (8) (2010) 1572-3081.
[4] A. Yamamoto et al., Proc. Combust. Inst. 33 (3) (2011) 3259-3266.
[5] M. Hori et al., Combust. Flame 159 (3) (2012) 959-967.
[6] T. Kamada et al., Tohoku Univ. Master thesis (2013).
[7] R. J. Kee et al., Sandia National Lab. Report (1993).
[8] GRI Mech., http://www.me.berkeley.edu/gri-mech/
[9] T. Lieuwen et al., Synthesis gas combustion (2010).

Filtration Inspiration from Nature

James Herringer †, James G. Mitchell ‡ and Gary Rosengarten †
† School of Aerospace, Mechanical and Manufacturing Engineering, RMIT University, GPO Box 2476, Melbourne, 3000, Victoria, Australia
‡ School of Biological Sciences, Flinders University, GPO Box 2100, Adelaide, 5001, South Australia, Australia
j.herringer@student.rmit.edu.au

ABSTRACT

Diatoms are microscopic, phototrophic, single-celled algae encased in a siliceous, rigid, porous cell wall known as the frustule. They inhabit the zones in bodies of seawater and freshwater in which sunlight penetrates. It has been proposed that the certain species of diatoms use the Brownian ratchet mechanism to sort and separate nutrients and trace elements from harmful particles (i.e. viruses), based on size, through their frustule pores. This study investigates the application of this theory to explain the particle separating capabilities of the frustule by proposing and detailing an experimental and theoretical analysis to be conducted in the near future.

1. Introduction

This investigation will specifically focus on the ocean dwelling, pelagic, centric species of diatom; *T. eccentrica* and *Coscinodiscus sp.* (Fig. 1) [1].

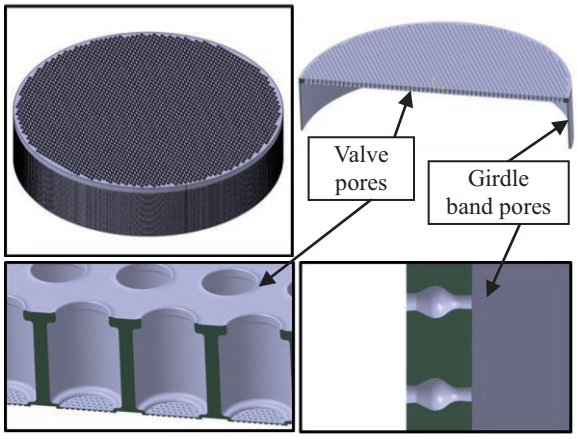

Fig. 1 CATIA [2] image of the siliceous frustule morphology of the centric diatom *T. eccentrica*.

In centric diatom species the frustule structure is composed of two halves (valves) which fit together, akin to two halves of a petri dish, with a mid-section (girdle bands) overlapping that of the top and bottom valve.

Many papers have postulated [3-7] that the porous nature of the diatom frustule is used to passively control their intake of nutrients and essential trace elements to the cell (i.e. HCO_3^-, CO_2, Fe^{2+}, NH_4^+, NO_3^-) [8-10], whilst preventing entry of harmful entities (i.e. viruses and bacteria).

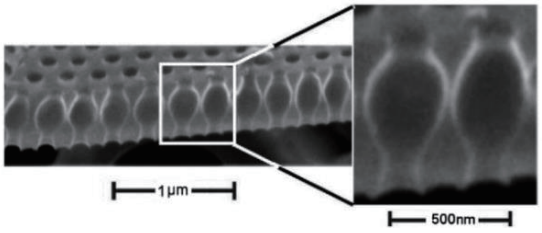

Fig. 2 SEM image of girdle band pore of the diatom *Coscinodiscus sp*. Maximum and minimum pore diameters are 250 nm and 100 nm respectively [3].

Losic, et al. [4] and Losic, et al. [3] highlighted the similarity of the pore structures between a diatom's girdle band in Fig. 2 and the Brownian ratchet membrane investigated by Matthias and Müller [11] in Fig. 3, indicating that the Brownian ratchet concept could be used to explain the size selective transport of solutes and colloids through the girdle bands of centric diatoms.

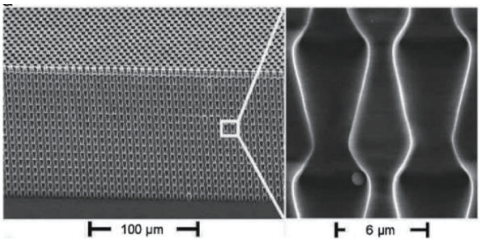

Fig. 3 SEM image of a massively parallel silica membrane with periodic, asymmetric pores [11]. Maximum and minimum pore diameters are 4.8 µm and 2.5 µm respectively.

A Brownian ratchet is a type of Brownian motor generating net transport of particles based on their size, when a symmetric, oscillating driving force is applied with an asymmetric boundary (i.e. pore boundary) [12].

Previous papers [13, 14] have suggested the combination of turbulence in the ocean and active sinking/rotation of a diatom generates oscillating pressure driven flow to act as the ratcheting mechanism in the girdle band pores. Rosengarten [13] estimated the oscillating pressure amplitude and period experienced by a rotating, sinking diatom to be 3.2–60 µPa and 0.5–2 s, respectively.

The Brownian ratchet mechanism studied by Kettner, et al. [15] and Matthias and Müller [11] has not yet been applied to the smaller length scales and amplitudes/frequencies of the periodic pressures experienced by the diatom. After understanding the filtration mechanism, there exists the possible direct or indirect application of it to synthetic filtration systems to improve performance in the future.

This study proposes an experiment to investigate Brownian ratchets and will adapt an analytical method [15-17] to verify the experimental results.

2. Method

Experimental analysis

An experiment was designed to accurately represent the geometry of the girdle band pores as nanochannels in a microfluidic silicon chip in a 2D plane.

A microfluidic chip (Fig. 4) is to be fabricated using planar lithography (microchannels) [18] and focused ion beam (FIB) etching (girdle band channels) [18, 19]. The channels are repeated twice in series to represent the overlapping of the diatom girdle band walls. There are to be 200 channels in parallel.

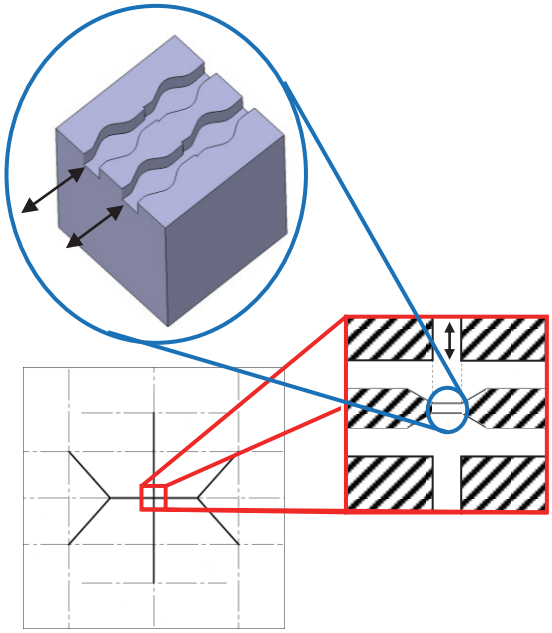

Fig. 4 Schematic diagram of microfluidic chip to be used in experiment, showing two pores in series and two sets in parallel.

Numerical analysis

The axial flow in the channels in the experiment has been theoretically solved (Fig. 5). The next stage involves solving for a rigid sphere's motion in an oscillating flow, taking into account stochastic Brownian motion.

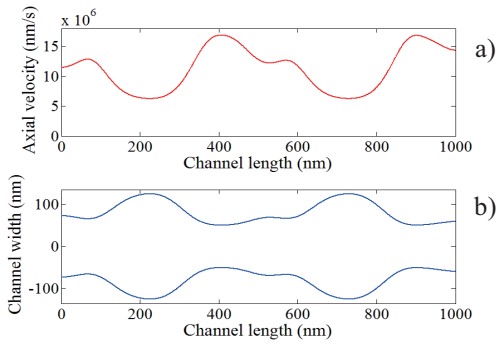

Fig. 5 a) Axial velocity (centerline) b) profile; for channels in the experiment (flow rate of 8.1×10^{10} nm^3/s).

Due to the small scale of a diatom in nature, the corresponding Reynolds numbers are small ($Re<0.1$) which means inertial effects are suppressed and viscous forces dominate the behavior of the flow [20].

3. Concluding remarks

The notion that nature has optimised specific processes over millions of years of evolution (i.e. filter feeding) forms the rationale driving biomimetic research. There are approximately 200 000 species of diatoms, with unique frustule morphology. This variation in frustule shape raises the fundamental questions; if the separation process amongst diatoms is optimised, why are there a plethora of different frustule morphologies across the various species? Are there numerous possible solutions to this problem? Is it competition between different diatom species or does a common feature exist between all species which is yet to be identified [3]?

References

[1] E. V. Armbrust, Nature 459, 185 (2009).
[2] D. Losic, G. Rosengarten, J. G. Mitchell, and N. H. Voelcker, Journal of Nanoscience and Nanotechnology 6, 982 (2006).
[3] Dassault Systemes, (Dassault Systemes, 2011).
[4] D. Losic, J. G. Mitchell, and N. H. Voelcker, Advanced Materials 21, 2947 (2009).
[5] H. Bhatta, J. Enderlein, and G. Rosengarten, Journal of Nanoscience and Nanotechnology 9, 6760 (2009).
[6] H. Bhatta, T. K. Kong, and G. Rosengarten, Journal of Nano Research 7, 69 (2009).
[7] J. G. Mitchell, L. Seuront, M. J. Doubell, D. Losic, N. H. Voelcker, J. Seymour, and R. Lal, PLoS ONE 8, e59548 (2013).
[8] C. M. Boyd and D. Gradmann, Journal of Experimental Botany 50, 461 (1999).
[9] P. D. Tortell, J. R. Reinfelder, and F. M. M. Morel, Nature 390, 243 (1997).
[10] K. Roberts, E. Granum, R. C. Leegood, and J. A. Raven, Photosynthesis Research 93, 79 (2007).
[11] S. Matthias and F. Müller, Nature 424, 53 (2003).
[12] M. Brenk, H. J. Bungartz, M. Mehl, I. L. Muntean, T. Neckel, and T. Weinzierl, SIAM Journal on Scientific Computing 30, 2777 (2008).
[13] G. Rosengarten, in International Conference on Nanochannels, Microchannels and Minichannels (ASME, 2009), p. 1371.
[14] W. Yang, P. J. Lopez, and G. Rosengarten, Analyst 136, 42 (2011).
[15] C. Kettner, P. Reimann, P. Hänggi, and F. Müller, Physical Review E 61, 312 (2000).
[16] E. Lauga, A. D. Stroock, and H. A. Stone, Physics of Fluids 16, 3051 (2004).
[17] T. Li and M. G. Raizen, Annalen der Physik 525, 281 (2013).
[18] M. Madou, Fundamentals of microfabrication: the science of miniaturization (CRC press, 2002).
[19] C. Duan, W. Wang, and Q. Xie, Biomicrofluidics 7 (2013).
[20] H. A. Stone, A. D. Stroock, and A. Ajdari, Annual Review of Fluid Mechanics 36, 381 (2004).

Tenth International Conference on Flow Dynamics
November 25-27, 2013, Sendai, Miyagi, Japan

Variability of Thermal Conductivity Measurement for High-Density Glass Wool by Using Guarded Hot Plate Apparatus Utilizing Peltier Module

Tatsuya Kobari[1], Junnosuke Okajima[2], Atsuki Komiya[2], Shigenao Maruyama[2]
[1] Graduate School of Engineering, Tohoku University, Sendai, 980–8579, Japan
[2] Institute of Fluid Science, Tohoku University, Sendai, 980–8577, Japan
kobari@pixy.ifs.tohoku.ac.jp

ABSTRACT

This paper describes a thermal conductivity measurement of insulation material using guarded hot plate (GHP) apparatus utilizing a Peltier module in order to detect temperature difference between meter plate and guard plate. To evaluate the variability of measurement result, the thermal conductivity measurement of the reference material, high-density glass wool, was conducted and the expanded uncertainty was estimated. The results show that measured thermal conductivity, 0.03807 W/(m·K), was 2.3% larger than the calibrated value, 0.0372 W/(m·K), and the expanded uncertainty was 0.09%.

1. Introduction

Recently, thermal conductivity of insulation material reaches the order of a few 10^{-3} W/(m·K), ten times smaller than conventional insulation material, by the development of vacuum insulation panel (VIP). Especially, because radiative heat transfer decreases in cryogenic region, the thermal conductivity further decreases. While, because it is known that the smaller thermal conductivity, the measurement error becomes significant. The reliability of the existing test method for the ultralow thermal conductivity insulation material has been investigated[1].

Guarded got plate (GHP) method, the most general method to measure thermal conductivity of insulation material, determines thermal conductivity by amount of input heat as described in Fourier's law[2]. The most significant factor of GHP method is conduction heat loss from main heater to guard plate. It has been investigated to estimate the heat loss to put a insulation material with well-known thermal conductivity between main heater and guard plate[3].

In this study, Seebeck effect of Peltier module was utilized in order to detect the temperature difference. The output voltage of Peltier module put between main plate and guard plate was measured and temperature difference was estimated. It has been reported that Peltier module enables to measure heat flux with about ten times larger sensitivity than conventional heat flux sensor[4]. Utilizing a Peltier module GHP apparatus was developed.

In order to evaluate the variability of the measurement result, thermal conductivity measurement of high-density glass wool was conducted as a reference material. Then, the accuracy and the expanded uncertainty of measurement were examined and the availability of the developed GHP apparatus was discussed.

2. Measurement method

2.1 Experimental set-up

Figure 1 shows a schematic of the developed GHP apparatus. It is cylindrical shape and consists of the main plate, guard plate, cold plate, specimen, Peltier module set between the main plate and guard plate and surrounding insulation material.

The main plate and the cold plate are made of aluminum and the guard plate is made of copper. The size of main plate, guard plate and cold plate are respectively 30×ϕ100 mm, 65×ϕ200 mm and 30×ϕ200 mm. A groove with 34×ϕ104 mm of size was fabricated on the center of the guard plate and main plate and Peltier module were put into the groove. To measure the specimen surface temperature, negative temperature coefficient (NTC) thermistors were inserted into a hole and a groove fabricated on the main plate and cold plate, respectively.

The main plate and the guard plate are heated by a main heater and a guard heater, respectively. A main heater with 100 Ω of electric resistance was inserted into the main plate and a guard heater with 56.6 Ω was wrapped around the guard plate. The cold plate is cooled by constant temperature bath.

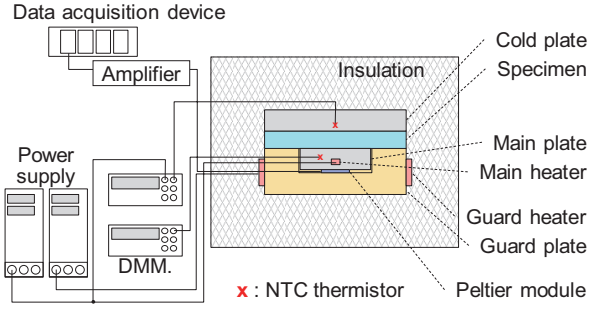

Fig. 1. Schematic of experimental set-up.

2.2 Experiment procedure

The thermal conductivity of insulation material was measured by following procedure. The specimen was put between the main plate and cold plate. The guard and cold plates were preheated and precooled, respectively. Then, the main heater was turned on. The load voltage to main heater was controlled by PID controller, where the process value and set point were the output voltage of Peltier module and 0 V. Since the output voltage is 0 V, it can be thought that the temperature difference between the main plate and guard plate is eliminated. Then, the amount of input heat to the main heater is transferred into only specimen without the conduction heat loss through the contact area between main plate and guard plate. A preliminary calibration of output voltage and temperature deference of Peltier module indicated 4.67 V/K of the sensitivity.

After the temperature and the load voltage condition became steady state, the thermal conductivity was obtained by Fourier's law described as follow equation.

$$k_{\mathrm{SPEC}} = \frac{A_{\mathrm{MN}} L}{Q_{\mathrm{MN,HTR}} dT_{\mathrm{SPEC}}} = \frac{\pi r_{\mathrm{MN}}^2 L}{\frac{V_{\mathrm{MN,HTR}}^2}{R_{\mathrm{MN,HTR}}}(T_{\mathrm{MN}} - T_{\mathrm{PL}})}, \quad (1)$$

where, k_{SPEC} [W/(m·K)], dT_{SPEC} [K] and L [m] are the thermal conductivity, the temperature difference and the thickness of specimen, respectively. A_{MN} [m^2] is the heat transfer area. $Q_{\mathrm{MN,HTR}}$ [W] is the amount of input heat to main heater. r_{MN} [m] is the radius of the main plate. $V_{\mathrm{MN,HTR}}$ [V] and $R_{\mathrm{MN,HTR}}$ [Ω] are the load voltage and the resistance of main heater, respectively. T_{MN} [°C] and T_{PL} [°C] are the specimen surface temperatures.

3. Results and discussions

Using the developed apparatus, the thermal conductivity measurement of the reference material, a high-density glass wool issued by Japan Testing Center for Construction Materials (JTCCM), was conducted. The calibration certificate indicates 24.8 mm of thickness and 0.0372 W/(m·K) of thermal conductivity with 1.6% of expanded uncertainty under the condition that the average temperature was 20.1°C and the temperature difference was 20.2 K. Table 1 shows the specimen surface temperature, the amount of input heat, the estimated temperature difference of Peltier module and the estimated thermal conductivity of the thermal conductivity measurement with difference temperature condition.

Using Peltier module as a temperature difference detector, the high degree of thermal equilibrium between main plate and guard plate could be achieved. The results indicates 0.03807 W/(m·K) of thermal conductivity. It is 2.3% larger than the calibrated value and shows the good agreement with the calibration certificate. Therefore, it can be said that the proposed method is available to measure the thermal conductivity of insulation material.

Table 1. Parameters for the thermal conductivity measurement.

T_{MN}, °C	T_{PL}, °C	$P_{\mathrm{MN,HTR}}$, W	dT_{Peltier}, mK	k_{SPEC}, W/(m·K)
52.16	12.13	0.4763	-0.075–0.049	0.03885
31.47	10.75	0.2416	-0.065–0.074	0.03807

In order to assess the variability of the measurement result, the expanded uncertainty of the measurement was evaluated. The expanded uncertainty characterizes the dispersion of the values attributed to a measured quantity and it is expressed as follow equation.

$$U_k = k_{\mathrm{cf}} \sqrt{\sum_i^n \left(c_i^2 u_i^2\right)}, \quad c_i = \frac{\partial k}{\partial x_i}, \quad (2)$$

where, k [W/(m·K)] is thermal conductivity. u_i and c_i are the standard uncertainty and the sensitivity coefficient of variable x_i, respectively. U_k is the expanded uncertainty with coverage factor $k_{\mathrm{cf}} = 2$ and provides an interval having a level of confidence of approximately 95%. Considering the standard uncertainties of variables in Eq. (1), the expanded uncertainty was evaluated as 0.09%. Table 2 shows the standard uncertainties and the sensitivity coefficients of considered variables. Table 3 shows the comparison of the expanded uncertainty with the GHP apparatus of the international laboratories[5]. It indicates that the developed apparatus enable the high precision thermal conductivity measurement.

Table 2. Sensitivity coefficients and the standard uncertainties of variables considered to evaluate the expanded uncertainty.

	T_{MN}, °C	T_{PL}, °C	$V_{\mathrm{MN,HTR}}$, V	$R_{\mathrm{MN,HTR}}$, Ω	L, m	r_{MN}, m
c_i	0.013	0.013	0.015	3.8×10^{-4}	1.48	1.52
u_i, %	0.003	0.201	0.027	0.010	0.897	0.100

Table 3. Comparison between the expanded uncertainties of GHP apparatus of the international laboratories[5].

	Present	LNE	NIST	NPL	NRCC
U_k, % ($k_{\mathrm{cf}} = 2$)	0.090	1.5	1.0	1.2	1.0

* LNE: Laboratoire National d'Essais, NIST: National Institute of Standatds and Technology, NPL: National Physical Laboratory, NRCC: National Research Council Canada.

4. Conclusions

In this study, a GHP apparatus utilizing Seebeck effect of Peltier module to detect the temperature difference between main plate and guard plate was developed. To assess the variability of the measurement result, the thermal conductivity of the reference material, high-density glass wool, was measured and the accuracy and the precision were discussed. From the results, following conclusions can be obtained.

- Preliminary calibration experiment of output voltage and the temperature difference of Peltier module indicates 4.67 V/K of the temperature difference sensitivity.
- According to the detection of temperature difference by Peltier module, the developed apparatus enables high precision thermal conductivity measurement with 0.09% of the expanded uncertainty.
- The thermal conductivity measurement result of high-density glass wool with 0.0372 W/(m·K) of calibration value shows 0.03807 W/(m·K), which is 2.3% larger than the calibration value.

5. Acknowledgement

T. Kobari was supported by Grand-in-Aid for JSPS Fellows 25·11097.

References

[1] T. Tasaka, M. Akoshima, T. Ohmura, M. Ogawa, T. Fujimoto and Y. Kikuchi, *Proc. 33rd Jpn. Symp. Thermophys. Prop.*, (2012), D106.
[2] JIS A1412-1, "Test method for thermal resistance and related properties of thermal insulations", (1999).
[3] J. Hujino and T. Honda, *Proc. 30th Jpn. Symp. Thermophys. Prop.*, (2009), B204.
[4] T. Haruyama, *Cryogenics*, **41**, (2001), 335–339.
[5] R. R. Zarr and J. J. Filliben, *Insulation materials: Testing and Applications, 4th Volume, ASTM STP 1426*, (2003).

Tenth International Conference on Flow Dynamics
November 25-27, 2013, Sendai, Miyagi, Japan

Influence of Gravity Direction in the Boiling with Impinging Flow Using High-Carbon Alcohol Aqueous Solutions

Hiroshi Ito, Daiki Shimano and Naoki Ono
Shibaura Institute of Technology, 3-7-5, Toyosu, Koto-ku, Tokyo, 135-8548, Japan
naokiono@shibaura-it.ac.jp

ABSTRACT

In recent years, with the technological advance and the downsizing of electronic devices, the thermal efficiency and safety has been more important than ever. We had applied high-carbon alcohol aqueous solution to boiling with impinging flow in mini channel to promote heat transfer and compared with low-carbon alcohol aqueous solution. In addition, we investigated the flow velocity on the bubble and the liquid interface with the numerical model which considered the Marangoni convection. As a result, some relationship about the mechanism indicating maximum of CHF between the experiment and the numerical model was suggested.

1. Introduction

In recent years, the thermal efficiency and safety has been more important than ever with the technological advance and the downsizing of electronic devices. Therefore, we focused on boiling heat transfer and impinging flow which let the fluid collide to heating element as a cooling method. Vochten et al [1] found that aqueous solutions of alcohol with more than four carbon atoms have properties that a value of surface tension turns increase from decrease with temperature, unlike normal solution such as pure water. Due to this specific characteristic, the so-called Marangoni convection occurs in the direction to the heated surface. We predicted that this had good influence on the dryout restraint of the heated surface and the improvement of the heat transfer characteristic.

In this experiment, considering of gravity direction, we applied high-carbon alcohol aqueous solution and low-carbon alcohol aqueous solution to boiling with impinging flow in mini channel and compared the result with each other. Furthermore, using the numerical model which considered the Marangoni convection mechanism, we studied the relationship between results of the experiment and the numerical model.

2. The outline of the experiment

The experimental apparatus and schematic drawing of the test section are shown in Fig.1 and Fig2, respectively. Working fluid in a tank was stirred by a hot stirrer and sent to the pressure tank by a chemical pump. The fluid was heated in the pressure tank with a rod heater and was set to predetermined temperature with a belt heater and a thermoregulator. The fluid which passed the test section was cooled off with a heat exchanger and it was returned in a tank. The test section was composed of PEEK resin which had high adiabatic performance, and PBI resin was used for the vicinity of the heating area which became very high temperature. The test section was assembled with three pieces of boards, and only the middle board is shown in Fig.2. The flow channel was T-junction and the middle board was put with two pieces of boards from both sides with rubber packing. The heated surface of copper block 3mm×10mm was installed in the upper part of the channel center, and three K-type sheathed thermocouples were attached every 4mm from the spot of 4mm in vertical direction on the heated surface.

After confirming that the temperature became steady, the surface temperature was estimated by extrapolating the temperature distribution and the heat flux was determined by the temperature gradient.

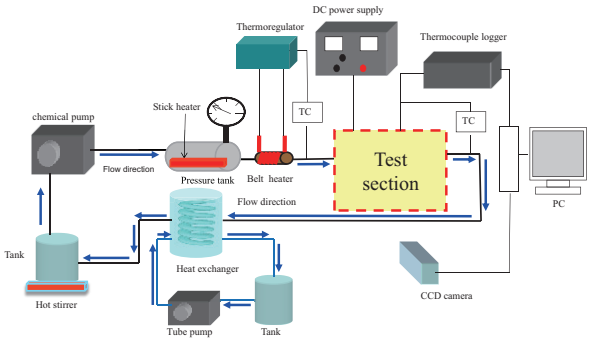

Fig.1 Experimental apparatus

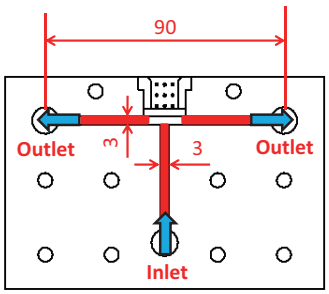

Fig.2 Geometry of test section

3. Numerical model

Using the CFD software PHOENICS[2], we made a simple model to analyze Marangoni convection. In PHOENICS, a calculation is carried out by the finite volume method. On the liquid vapor interface, Marangoni effect was defined as a driving force that was produced by the difference of surface tension and was added to this software. Although the surface tension includes temperature and concentration dependence, the temperature on the liquid-bubble interface should be saturation temperature depending on the concentration and then the temperature dependence was ignored at the liquid-bubble interface. Based on the measured surface tension data, the function of surface tension σ depending on the concentration of butanol aqueous solution was added to the program of the software using the following equation.

$$\sigma = 63 - 44.92(1 - e^{-10.22C_L})^{0.49} \ [\mathrm{mN/m}] \quad (1)$$

Here, C_L is the concentration [wt%] of butanol aqueous solution. The definition of the concentration change owing to the evaporation, was calculated assuming liquid-vapor equilibrium.

4. Results and Discussion

Table1. Experimental conditions

Volume flow rate	40ml/min
Flow velocity	7.4×10^{-2}m/s
Reynolds number	780
Subcooling	20K

Table2. Test fluids

Test fluid	Mass fraction [wt%]
Aqueous solution of 1-butanol	3.0
Aqueous solution of ethanol	15.0

The experimental conditions and test fluids are shown in table 1 and 2, respectively. In addition, in order to investigate the effect of gravity on boiling heat transfer, the experiment was conducted by reversed states of the heating surface by setting it at bottom or at top in the channel of the test section. The boiling curves were shown in Fig.3. In these curves, the comparison was carried out in terms of the direction of the heated surface. The red circled point shows CHF of each alcohol aqueous solution. Both solutions show that CHF of the bottom setting of heating surface was higher than that of the top setting. This result was thought to be because of the influence of the buoyancy. Bubble was seemingly easier to leave from the heated surface at the bottom setting. Furthermore, CHF of the high-carbon alcohol aqueous solution was higher than that of low-carbon.

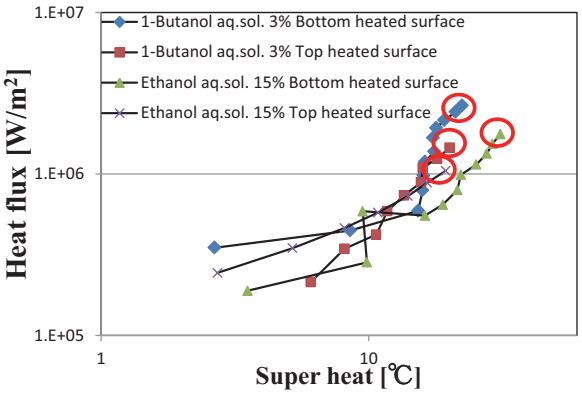

Fig.3 Boiling curves

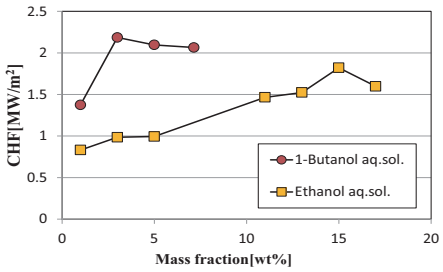

Fig.4 CHF vs. concentration (experiment)

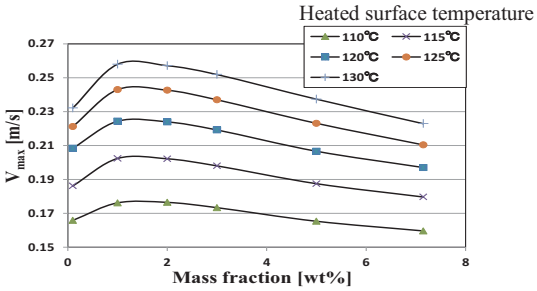

Fig.5 Comparison of the maximum velocity of 1-Butanol aqueous solution (CFD)

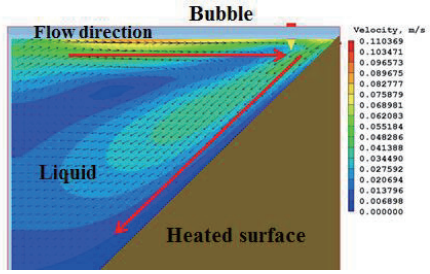

Fig.6 Velocity distribution

CHF of each aqueous solution concentration is shown in Fig.4. This represents that there is the maximum value of CHF depending on the concentration of each fluid. The phenomenon has been reported by some researchers[3][4]. On the other hand, the comparison of the maximum velocity of 1-butanol aqueous solution near the bubble interface was carried out using the CFD model. The result on the condition that changed heated surface temperature from 110 to130 degrees is shown in Fig.5. The velocity distribution at that time is shown in Fig.6. The concentration indicating the maximum value of CHF was 3 wt% for the experiment, and result of CFD represents the maximum value of the velocity for 1 wt%. Though the concentration indicating the maximum value was different for the both cases, we think that the tendency was reproduced in this model and that the model suggested mechanism of the CHF maximum.

5. Concluding remarks

1. From the boiling curve, gravitational direction affected the boiling heat transfer, and it was confirmed that the bottom heating surface had advantage.
2. From the results of experiment and numerical model, the relationship of CHF and the concentration dependency was suggested. We will investigate the influence of gravity direction in detail and will compare with the numerical model in the future.

References

[1] R.Vochten and G.Petre, J.Colloidal Science, **42-2**(1973), pp.320-327.
[2] CHAM Co. (http:// www.cham.co.uk/)
[3] V.P.Carey, Liquid-Vapor Phase-Change Phenomena, second ed, Taylor&Francis, (2008), p.400
[4] K.Suzuki, Microbubble Emission Boiling of Alcohol-Water Mixtures, IASME Transactions, Issue 7, Volume **2**, September (2005), pp.1106-1111

Tenth International Conference on Flow Dynamics
November 25-27, 2013, Sendai, Miyagi, Japan

Development of a New Cooling System Using Phase Change Material for Power Battery Thermal Management of Electric Vehicles

Takuya Ojiro, Keisuke Kanbara, Takashi Yamada and Naoki Ono
Shibaura Institute of Technology
3-7-5, Toyosu, Koto-ku, Tokyo, 135-8548, Japan
naokiono@shibaura-it.ac.jp

ABSTRACT

The performance of lithium-ion power battery suddenly deteriorates when its temperature becomes more than 45℃. In order to increase the life cycle of lithium-ion power battery and to optimize the battery properties, the establishment of a new cooling system for the thermal management is indispensable. This research is aimed for development of a new cooling system using phase change material and heat pipes. Heat pipe can be utilized to delay the finishing of PCM melting. Such a system having PCM and heat pipes can be expected to control the battery temperature to be within desired temperature range.

1. Introduction

In recent years, it is expected that electric vehicles having high performance battery are prevailed. Then the development of lithium-ion battery with increasing power density or higher capacity is going on rapidly. However, the establishment of a new cooling system of the high power thermal management is indispensable for the optimization of its characteristic, long-life and safety improvement. Also the battery cell temperature increases by the generated heat during discharging and charging, which causes degradation of power battery performance and the risk of overheat[1]. The cycle times and the capacity of the battery as a function of temperature is shown in Fig.1. The research shows that the battery temperature above 45℃ will lower the charging efficiency or longevity properties. Therefore, the best range of operating temperature of the battery cell needs to be maintained. The most common method about cooling system includes liquid or air cooling. However, it could not be practical in terms of needed cost and limited space allowed for car batteries.

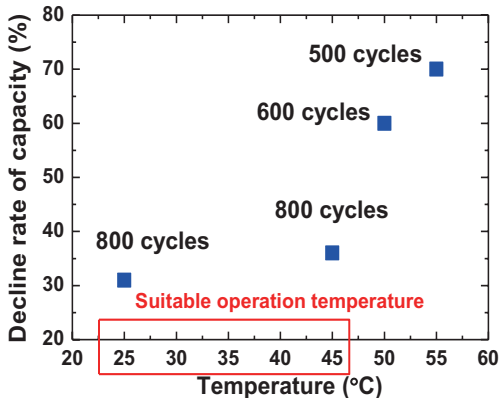

Fig.1 Capacith fade analysis of battery at differnt operation temperatures[1]

In the present study, in order to maintain high performance and long-life of lithium-ion battery, we investigate the most suitable design of a hybrid type thermal management system of power battery, which is based on using phase change material (PCM) [2,3]with heat pipes.

2. The outline of the experiment

Recently the lithium-ion battery used widely in commercial application is cylindrical type $LiFePO_4$ power battery (18 mm in diameter and 65 mm in height). However, laminating type lithium-ion battery is expected in terms of cooling performance in future. Accidents due to the abnormal heat generation of the lithium-ion power battery are actually reported. Thus, this study is focused on laminating type lithium-ion power battery when the battery generates heat in steady driving mode or extraordinary mode about heat transfer. At first, to demonstrate the effectiveness of the heat pipe, in this study we made a simple model as shown in Fig.2.

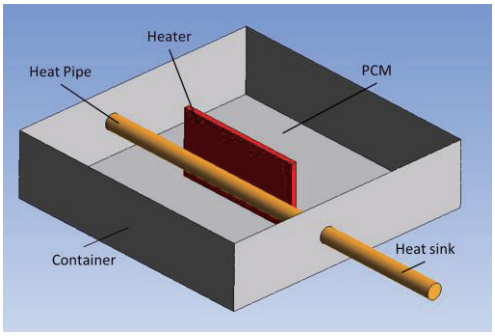

Fig.2 Analysis model

The ceramic heater (50 mm in length, 2 mm in width and 50 mm in height) was located in the middle of the container (100 mm in length, 100 mm in width and 25 mm in height) which was made of aluminum. The heat pipe was made with copper tube with outer diameter of 6 mm, was located in 5 mm apart from the heater. The container was filled with the paraffin, physical property of the material is shown in Table 1.

Table 1. Physical property of the paraffin

Density	880 [kg/m^3]
Heat conductivity	0.2 [W/(m-K)]
Specific heat capacity	2 [kJ/kg-K]
Heat storage capacity	168 [kJ/kg]
Melting temperature	318 [K]

The heat pipe was cooled by iced water (h_{cool} =1000 W/m^{2}K) at the other end of the tube, and the heater input

power was 10 W which can assume the steady driving mode. To be able to simulate the realistic situation, we made the heater of the 1/3 scale (97 mm in height, 72 in length, and 0.2 mm in width) of the lithium-ion power battery, and the heat pipes were located in various places. Generally, the paraffin has low thermal conductivity. Therefore, we need to inspect the difference of the states of the melting using pure paraffin and the PCM with improved thermal conductivity in future.

Temperatures in different locations were measured using K-type thermocouples and the infrared camera. Then we observed the melting and solidification. Furthermore, the experiment was compared with the results of numerical simulation. For the simulation, the CFD software ANSYS Fluent 14.5 was used in the study. The heat pipe was simply modeled by setting its thermal conductivity (h_{HP}=38760 W/m-K) 100 times of that of copper and we did neglect fluid flow.

3. Results and Discussion

Temperature distribution at 30 minutes after the beginning by the simulation and the experimental when the heat pipe was used, is shown in Fig. 3 and Fig. 4. Contour of liquid fraction is shown in Fig. 5. These figures are the result of simple model.

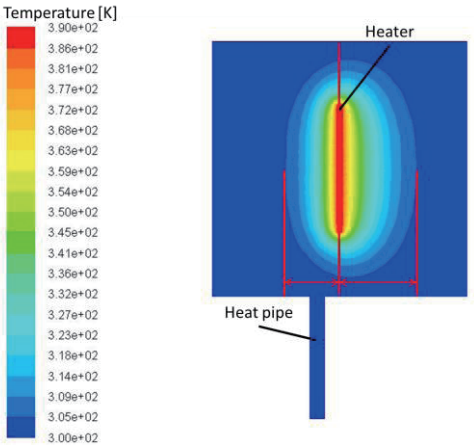

Fig.3 Temperature distribution by simulation (z=25 mm)

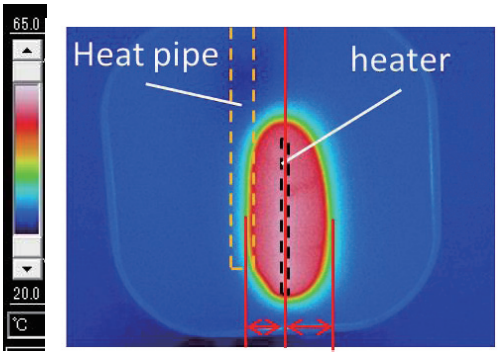

Fig.4 Temperature distribution by experiment

In this figure, the heat pipe was placed at the left side of the heater. Therefore, in the left side, melted area of paraffin was smaller than in the right side. Thus, the heat pipe had ability to delay the melting of PCM. Also it shows the same tendency when we compared the result by the simulation and the experiment. This was because the paraffin stored heat from the ceramic heater using as the form of latent heat and then the heat pipe transported the heat from internal to outside of the paraffin.

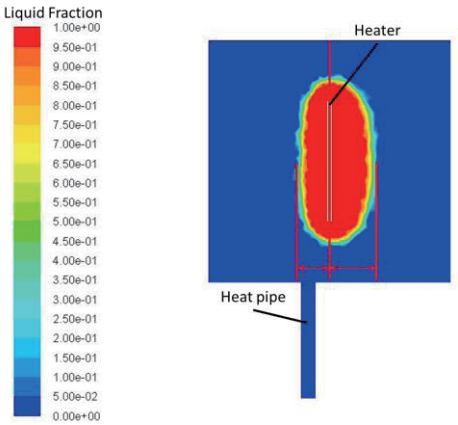

Fig.5 Liquid fraction by simulation (z=25mm)

4. Concluding remarks

This preliminary study confirmed that the heat was at first stored with latent heat of PCM and then the heat pipe transported the heat to the outside heat sink. Such a system having PCM and the heat pipes can be expected to control PCM temperature within desired temperature range, if the system is well designed.

5. Future prospects

We plant to investigate difference in melting state by changing the position of the heat pipe. Also we investigate the heat generation behavior of real electric vehicles and analyze state of PCM melting. We observe melting area of not only laminate type but also cylindrical type. In addition, we need clarify the difference of melting area by water-cooling or air-cooling instead of heat pipes.

Acknowledgement

This research was supported by the strategic international cooperative program of JST in the field of highly-efficient energy utilization.

References

[1] P.Romadass, “Capacity fade of Sony 18650 cells cycled at elevated temperatures”, J.Power Sorces 112(2):614-620 2002.

[2] Zhonghao Rao, Shuangfeng Wang, Maochun Wu, Zirong Lin, Fuhuo Li, “Wxperimental investigation on thermal management of electric vehicle battery with heat pipe”, Energy Conversion and Management 65 (2013), 92-97.

[3] X. Duan, G.F Naterer, “Heat transfer in phase change materials for thermal management of electric vehicle battery modules”, International Journal of Heat and Mass Transfer 53 (2010),5176-5182.

Tenth International Conference on Flow Dynamics
November 25-27, 2013, Sendai, Miyagi, Japan

Comparison of High-pressure Homogenizer and Disc Mill in Microalgae Oil Extraction

Shun Tsutsumi[1], Takehiro Shibuya[2], Kouhei Baisho[1], Yasuhiro Saito[1], Yohsuke Matsushita[1], Hideyuki Aoki[1]
[1]Department of Chemical Engineering, Graduate School of Engineering, Tohoku University, 6-6-07 Aoba, Aramaki, Aoba-ku, Sendai, Miyagi 980-8579, Japan, [2] Department of Chemical Engineering, School of Engineering, Tohoku University, 6-6-07 Aoba, Aramaki, Aoba-ku, Sendai, Miyagi 980-8579, Japan,
E-mail: saito@tranpo.che.tohoku.ac.jp.

ABSTRACT

A high pressure homogenizer and a disc mill as a mechanical oil extraction method from *Botryococcus braunii* were investigated. The power consumption of both instruments was measured by an electrical energy meter, and the treated microalgal cells were observed by optical and fluorescent microscopes to assess disruption degree. The energy consumption of the disc mill was lower than that of the homogenizer. In the microscopic observation, the homogenizer disrupted cells, whereas the disc mill did not.

1. Introduction

Microalgae which produce oil are one of the most promising biomass materials as the non-food crops. Although the microalgae are viable prospects for the next-generation fuel, the practical fuel production system have not been established. The main topic of researches was the attempts to reduce consumption for oil extraction process [1, 2]. To develop an innovative and efficient mechanical extraction method, we have concerned with a high-pressure homogenizer and a disc mill. The high-pressure homogenizer generates shear force and impulse force to working fluid. The disc mill generates shear force. The present study is that the energy consumption of both instruments is compared and treated samples are observed to investigate the difference of energy consumption and the effect of the characteristic of the instruments on microalgal cell aspect.

2. Method

2.1 Microalgae strain and harvesting

Botryococcus braunii BOT 22 strain was used. The cell concentrations were measured gravimetrically by a vacuum drier (AVO-200, Asone, Japan) and an electric balance (MSE225S-000-DU, Sartorius AG, Germany). The temperature was 120 °C and the pressure was gradually reduced from 0.1 MPa to 0 MPa for four hours. The concentration of samples was 1.44 g/L.

2.2 Cell disruption with high-pressure homogenizer

500 ± 60 g of cell suspensions were pumped through a high-pressure homogenizer (APV LAB 2000, SPX, USA) for 1 pass at a selected operating pressure (30, 50 ,80 ± 10 MPa). The weight of treated samples was measured. The test duration was 170 ± 5 s.

2.3 Cell disruption with disc mill

1000 ± 50 g of cell suspensions were thrown in the disc mill (MKZA6-2, Masuko Sangyo Co., Ltd, Japan). The experimental condition is shown on Table 1. To investigate the effect of sample concentration, the centrifuged sample (i.e. 2.47 g/L) was also treated. The centrifugal concentration condition was 10000 rpm in rotation speed, 10 °C in treatment temperature, and 5 min in treatment time. The test duration of the disc mill at 1000 rpm in rotational speed is 100 s, the time at 2000 rpm is 30 s, and the one at 3000 rpm is 5 s. The number of passes for each case is one.

Table 1 Experimental condition by disc mill

Rotation speed	[rpm]	1000		2000	3000
Passes	[pass]	1	2, 3	1	
Concentration	[g/L]	1.44	1.44	1.44	
		2.47			

2.3 Analysis

Power consumptions were measured by an electrical energy meter (HIOKI 3390 POWER ANALYZER, HIOKI E. E. Co., LTD, Japan) until the sampling predetermined suspension weight. Samples were observed by optical and fluorescent microscopic examinations (IX73 and IX3-RFACS, Olympus, Japan). Nile Red was used as fluorescent stain. It colors hydrocarbons produced by *B. braunii* yellow under fluorescence environment (excitation wavelength is 553 nm).

3. Results and Discussion

3.1 Power consumption measurement

Microalgal suspensions were treated through the high-pressure homogenizer and disc mill for oil extraction, and the power consumption during treatment was measured. Fig. 1 shows the power consumption. The power consumption of the homogenizer increased in proportion as pressure. This is because the motor load is increased due to the reinforced plunger load of the homogenizer.

The power consumption of the disc mill was lower than that of the homogenizer. The energy of one pass decreased with rotation speed. In particularly, the power consumption had the smallest value at 2000 rpm. This is because the disc mill is controlled by an inverter, and the inverter frequency is optimized around 2000 rpm. Furthermore, the each experimental condition differs in the residence time, and the residence time of 1000 rpm is longer than that of 2000 and 3000 rpm. Hence, the consumption was inversely proportion to rotation speed and directly proportion to the number of passes. The difference of the power consumption between the non-centrifuged and centrifuged samples was little. This indicates that the centrifugal concentration in this experiment does not influence on the motor load.

3.2 Optical and fluorescent microscopic examination

The optical and fluorescent microscopic images of

samples are shown in Fig. 2. The disruption degree of the homogenizer is compared with that of the disc mill treatments at the smallest and largest energy consumption conditions. Almost all the samples treated by the homogenizer were crushed, and the colonies were also dispersed. The disruption degree of samples was high along with high pressure. In general, *Botryococcus braunii* stores oil between the cells and outside of their cells. Although yellow stains were observed between cells in the raw samples, yellow strains and disrupted cells were entangled in the fluorescent images. This indicates that the oil of outside cells and disrupted cell fractions were mixed by external force of the homogenizer. Microalgal cells treated by the disc mill did not disrupt in all the conditions. There is no difference in the shapes of cells and colonies between raw and treated samples. This is because the disc mill did not have enough force to disrupt cells.

In comparison of two cell disruption methods, the high-pressure homogenizer disrupted cells, but the disc mill did not. The difference between both instruments is the mechanism of cell disruption. The homogenizer generates shear force and impulse force simultaneously during treating samples under high pressure. On the other hand, the disc mill generates only shear force between two grinders under atmospheric pressure.

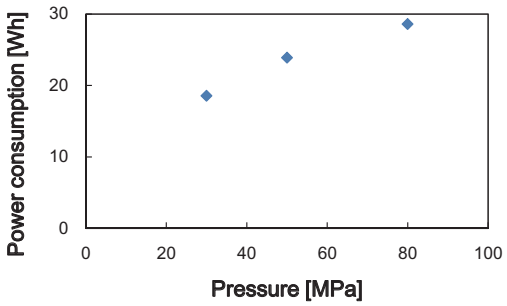

(a) High-pressure homogenizer

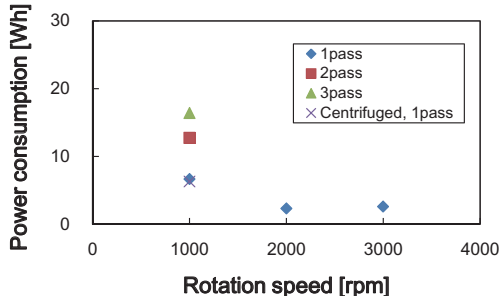

(b) Disc mill

Fig. 1 Power consumption

4. Concluding remarks

The high pressure homogenizer and the disc mill were investigated as a mechanical oil extraction method from *Botryococcus braunii*. The power consumption and disruption degree were compared between both instruments. The difference of the mechanism of cell disruption affects power consumption and disruption degree.

References

[1] L. Xu, *et al.*, *Bioresource technology*, **102** (2011), 5113

[2] A. K. Lee, *et al.*, *Biomass and Bioenergy*, **46** (2012), 89

Acknowledgements

This work was supported by MEXT NET project and the microalgae were offered by Tsukuba University.

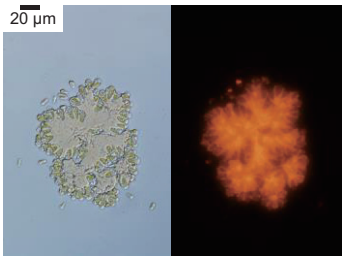

(a) Raw sample

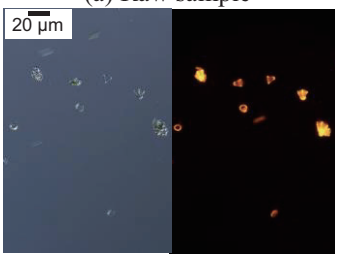

(b) 30 MPa by high-pressure homogenizer

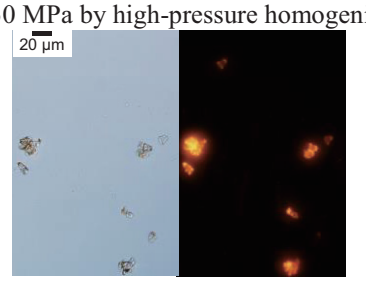

(c) 80 MPa by high-pressure homogenizer

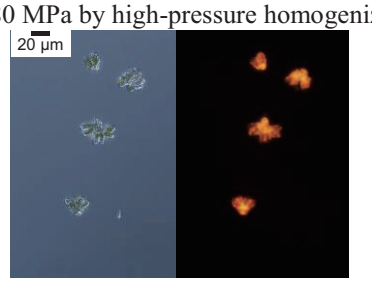

(d) 2000 rpm, 1 pass by disc mill

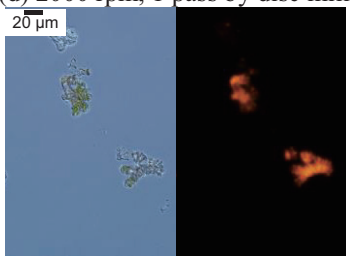

(e) 1000 rpm,3 pass by disc mill

Fig. 2 Microscopic images (left: optical image, right: fluorescent image)

Effect of Secondary Wick on Startup Process of Loop Heat Pipe

Masahiko Taketani, Hiroki Nagai
Department of Aerospace engineering, Tohoku University, Japan
6-6-01 Aramakiazaaoba, Aoba-Ku, Sendai-Shi, Miyagi prefecture, Japan
nagai.hiroki@aero.mech.tohoku.ac.jp

ABSTRACT

Loop Heat Pipe (LHP) is a heat transfer device utilizing a phase change of fluid. It has high thermal performance and robustness for the ambient temperature change. However, LHP has a problem on startup process in low heat load. One of the solutions for this problem is to use a secondary wick. In this study, we studied the effects of secondary wick from the views of heat leak and mass flow rate. Experimental results indicated that the secondary wick improved startup process of LHP by reducing the amount of heat leak to reservoir largely, and effect on mass flow rate was not large.

1. Introduction

Thermal control on the spacecraft is important to operate its equipment surely under strict thermal environment, in which ambient temperatures changes largely. In addition, recent spacecraft need more efficient heat transferring from inside to outside of its structure due to miniaturization. Loop Heat Pipes (LHPs) are promising heat transfer devices that meet these requirements.

However, in certain conditions, LHP has problems on its startup process: unstable behavior and slow startup. The startup process of LHP depends on initial vapor-liquid distribution. If enough amount of liquid is not supplied to evaporator core, the startup process becomes unstable and slow.

One of the solutions for this problem is a method of using a secondary wick. By attaching the secondary wick, enough amount of liquid is supplied to the evaporator core. As a result, the startup process is expected to be stabilized. Nevertheless, effects of secondary wick have not been verified. In this research, we designed a miniature LHP and studied effects of secondary wick on startup process through experiments, especially, in terms of mass flow rate and heat leak.

2. Experimental set up

2.1 Design of miniature LHP

Fig.1 shows a miniature LHP designed for this study. The material for this LHP is stainless.

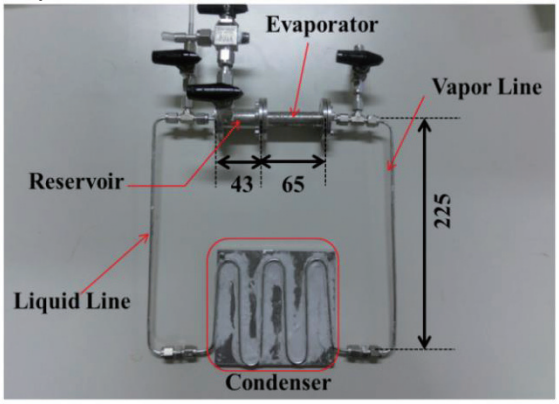

Fig.1 Miniature LHP

2.2 Attaching secondary wick

Fig.2 shows the picture of attached secondary wick. The material is stainless mesh (#300 and #100).

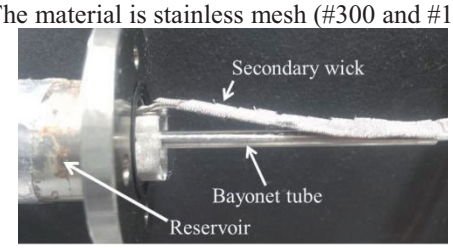

Fig.2 Attachment of secondary wick

2.3 Experimental set up and condition

Temperature data was measured by thermocouples (T-type), and the experimental condition in this study is following:

・Working fluid: Acetone
・Temperature of cooling plate: 10 [deg *C*]
・Heat input: 5, 7 [W] (startup), 10, 20, 30 [W]

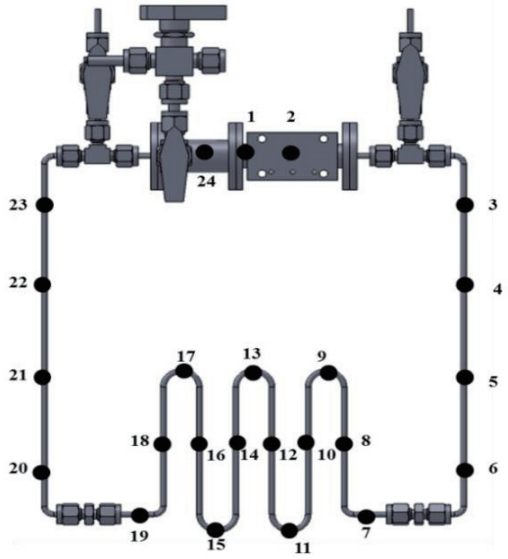

Fig.3 Thermocouple number

3. Result and Discussion

3.1 Case without secondary wick

Fig.4 shows the temperature history at 5 [W] of heat input without secondary wick. In this case, temperature of the evaporator started increasing as soon as heating was started. On the other hand, at the vapor line, time-lag was observed in temperature increasing. In addition, temperatures at the vapor line near the evaporator are different from those near condenser. This result indicates that LHP did not operate at 5 [W] in the case without secondary wick.

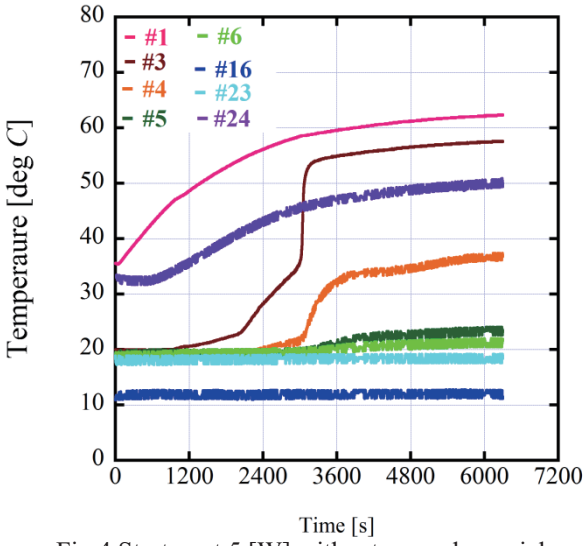

Fig.4 Startup at 5 [W] without secondary wick

3.2 Case with secondary wick

Fig.5 shows the temperature history at 5 [W] of heat input with secondary wick. Compared with the case without secondary wick, the time-lag until temperature increasing at vapor line was reduced drastically, and temperature of the vapor line was nearly constant at any points. Therefore, according to Fig.5, it is indicated that LHP with secondary wick operated.

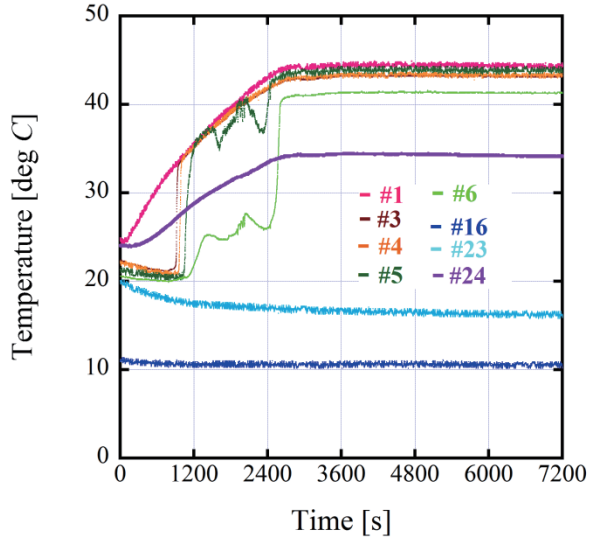

Fig.5 Startup at 5 [W] with secondary wick

3.3 Changes in mass flow rate and heat leak

Fig. 6 shows rate of change in mass flow rate and heat leak to reservoir at steady state. In this study, mass flow rate and heat leak were defined as following:

$$\dot{m} = \dot{Q}/\{L + c(T_{ev} - T_{liq})\} \quad (1)$$

$$L = L_0\left[(1 - T_{r\_ev})/(1 - T_{r0})\right]^{0.38} \quad (2)[1]$$

$$\dot{Q}_{leak} = \dot{m}c(T_{cc} - T_{liq}) \quad (3)$$

$$\Delta\dot{m} = \dot{m}_{with\ SW} - \dot{m}_{without\ SW} \quad (4)$$

$$\Delta Q = Q_{leak\ with\ SW} - Q_{leak\ without\ SW} \quad (5)$$

According to Fig.6, it was found that mass flow rate was a little bit increased while heat leak was decreased drastically by attaching secondary wick at low heat input. Thus, the main reason why secondary wick improved startup process of LHP is considered that attaching secondary wick reduced heat leak to reservoir largely, and sufficient amount of vapor was generated. This effect was caused because sufficient amount of liquid was supplied to the central core of primary wick. However, at high heat input, effects in mass flow rate and heat load were small. This is because sufficient amount of vapor generated, and LHP operated surely without secondary wick

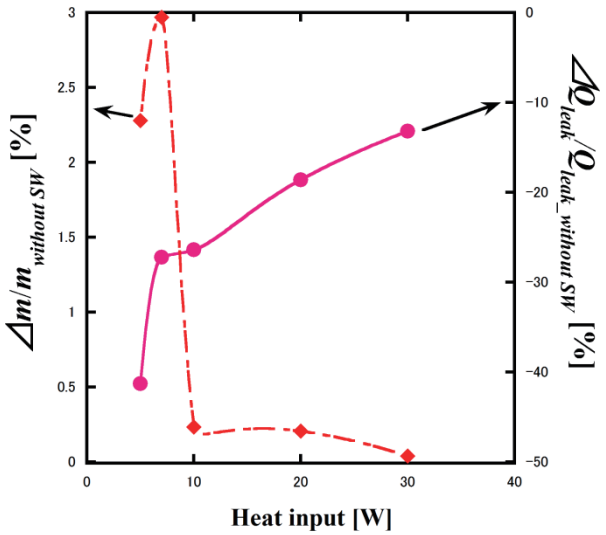

Fig.6 Changes in mass flow rate and heat leak

4. Conclusion

In this study, we designed a miniature LHP and studied effects of secondary wick on startup process through experiments, especially, in terms of mass flow rate and heat leak. Experimental results indicated that secondary wick improved startup process of LHP by reducing the amount of heat leak to reservoir largely, and effect on mass flow rate was not large.

Acknowledgement

This research was conducted as a part of "Study on high performance heat transport control", ISAS/ JAXA in 2012.

References

[1] Oe Shuzo, "Physical properties estimation", pp219

Development of High-performance TSP by Mixing Fine Particle

Takehito Horagiri and Hiroki Nagai
Department of Aerospace Engineering, Tohoku University
6-6-01, Aramaki-Aza-Aoba, Aoba-ku, Sendai 980-8579, JAPAN
horagiri.takehito@aero.mech.tohoku.ac.jp

ABSTRACT

As for designing an atmospheric re-entry of spacecraft, heat flux measurement data are indispensable for designing a heat protection system. To obtain a heat flux data, we utilized Temperature-Sensitive Paint (TSP). While simulating re-entry, shock tubes and shock tunnels were used, but the duration time of the shock tunnels is extremely short. So it is necessary to improve the time response and the luminescent intensity of the TSP for measuring such high-speed phenomena. So, we added two mixtures to the TSP and controlled the mixing ratio ranging from 10% to 90%, and investigated its effects on TSP characteristics.

1. Introduction

Heat flux measurement in a hypersonic wind tunnel is an indispensable requirement for designing a next generation reentry vehicle.

Typically, the method of measurement with a thermocouple is dependent on the model shape and the number of sensors. Thus, we can only get discrete data. In contrast, we can get a full-field image of the temperature distribution on the model surface by using Temperature-Sensitive paint (TSP) [1]. TSP is an optical temperature measurement technique which based on photochemical reaction of luminescent molecules.

Currently, the simulation of a spacecraft re-entry is conducted with a shock tube and a wind tunnel. The duration time of the equipment are extremely short [2], therefore we cannot use standard TSP which does not have enough response time and amount of luminescence. Thus, we need to develop a new TSP to get the temperature and heat flux data by using a wind tunnel with a short test time. Furthermore, a high sampling rate is required to be utilized alongside the high-speed phenomenon. Because of this, we need the exposure time to be very short however this will result in the recorded images becoming too dark. So the TSP with an adequate response time and a large luminescent intensity is required. Then, we developed the new TSP and investigated the luminescent intensity and the response time.

2. Theoretical formula

The response time of the TSP was evaluated by the value of heat flux, q. The value of q is given by the discrete form of the solution of 1-D time-dependent heat conduction equation. The calculation formula of heat flux is expressed by Eq.1 [3].

$$q(t_n)=\frac{k_p(1-\bar{\varepsilon}^2)}{\sqrt{\pi a_p}}\left[\sum_{i=1}^{n}\frac{T(t_i)-T(t_{i-1})}{\sqrt{t_n-t_i}+\sqrt{t_n-t_{i-1}}}\left\{\overline{W}(t_n-t_i)+\overline{W}(t_n-t_{i-1})\right\}\right] \quad (1)$$

where

$$a_p=k_p/\rho_p c_p,\ \varepsilon=\sqrt{\rho_p c_p k_p/\rho_b c_b k_b},\ \bar{\varepsilon}=(1-\varepsilon)/(1+\varepsilon),$$

$$\overline{W}(t,\bar{\varepsilon},L)=\frac{2}{\sqrt{\pi}}\int_0^{\infty}\frac{\exp(-\xi^2)d\xi}{1+\bar{\varepsilon}^2-2\bar{\varepsilon}\cos(2L_p\xi/\sqrt{a_p t})}$$

The parameter t is the time, T is the surface temperature of the substrate, ρ, c and k are the density, specific heat and heat conductivity of the model, respectively. The subscript p and b indicate the TSP layer and the model substrate, respectively. L_p is the TSP layer thickness and W is the error function. We normalized $q(t_n)$ with the maximum heat flux in the calculation. Then, we assumed the experimental curve as a single exponential function and determined the time constant by fitting the estimated curve with the experimental curve.

3. Experimental Setup

In this experiment, we evaluated the TSP response time with a CO_2 laser to simulate the short test time in wind tunnels. We assumed that the heating time of the CO_2 laser is the test time of the wind tunnels. Test parameters are shown in Table 1. In this test, a ceramic model of 50 mm × 50 mm and the thickness is 10 mm which was half coated with the TSP. A ceramics (Macor@) model, which is well insulated, was used for this test in one-dimensional heat conduction [4]. The output of the CO_2 laser was set at 40 J /s. The model was pulse heated with the laser. Figure 1 shows the experimental setup for the response time evaluation test. The excitation light is Blue LED which excitation peak wavelength is 470 nm. A 12bit high-speed video camera was used to take images of the luminescence from the TSP. The frame rate of the camera was set at 20000 fps. In this study, Ru (phen) $_3^{2+}$ is used as the reference TSP. Ru (phen) $_3^{2+}$ is known to have high temperature sensitivity at approximately room temperature (about 2.0 %/K). The absorption peaks of this TSP are at a wavelength of approximately 260 nm, 430 to 450 nm and the emission peak is 610 nm. Calcium silicate which has low conductivity is used as mixture.

Table 1. Test parameters

Mixing ratio m [%]	0	10	30	50
TSP thickness L [μm]	1		10	
Heating time t_h [ms]	0.3	0.7	1.7	

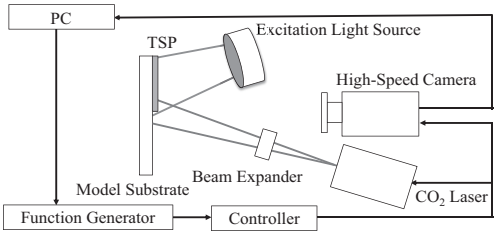

Fig. 1 Setup of response time experiment

4. Results and Discussion

Figure 2 shows the heat flux histories at the center of the heating spot at t_h = 1.7 ms. The heat flux is calculated by Eq.1. The vertical axis is normalized heat flux calculated. In the case of t_h = 1.7 ms and L = 1 μm, there is a period in which the heat flux is constant (from 0.9 to 1.7 ms). Hence, we considered that the heat capacity of TSP layer would be saturated at 0.9 ms. On the other hand, in the case of L = 10 μm, there is no period of constant heat flux, and the maximum value of heat flux results at the end of the pulse heating. We considered that the heat capacity of the TSP is larger, thus the amount of heat provided is lower than the heat capacity of the TSP at 10 μm. For this reason, the relation of heating time and heat permeability in the TSP layer is an important factor in which the heat is unable to be conducted throughout the TSP layer when the TSP layer is too thick. The change ratio of the heat flux at the leading edge is increasing as the mixing ratio is increased. However it has no effect on the arrival time of the constant heat flux. In this experiment we decreased the thermal effusivity of the TSP by adding in a mixture which has a low thermal conductivity, thermal capacity and density compared to Ru (phen) $_3^{2+}$. Because of this, the heat could not effectively spread throughout the TSP layer and it tends to accumulate on the TSP surface. Therefore the value of the heat flux rose rapidly compared to the non-mixture at the leading edge. In the case of t_h = 0.3 ms, there is no constant heat flux period and there are minimal effects in relation to the mixing ratio and TSP film thickness. For this reason, the effect of thermo-osmosis is insignificant when the heating time is short.

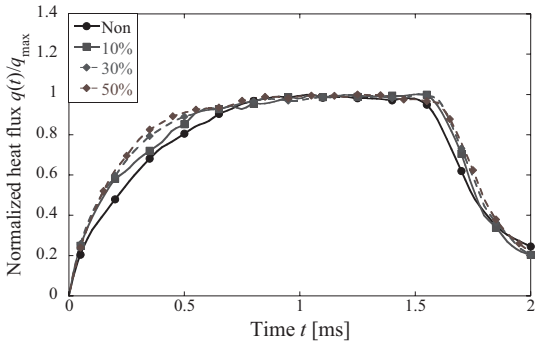

(a) L = 1 μm, t_h = 1.7 ms

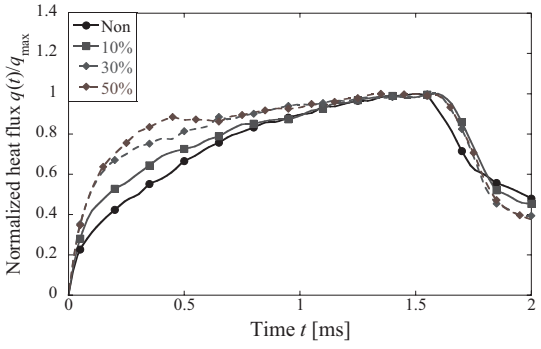

(b) L = 10 μm, t_h =1.7 ms

Fig. 2 Heat flux histories

We calculated the time constant from the results of heat flux histories. First of all, we assumed that acquired normalized heat flux data are a first-order exponential function. Next, we fitted calculated wave to the experimental data. Finally we determined the time constant. Figure 3 shows the relation of the thermal diffusivity and the time constant. From the results of fitting, the time constant is decreased as the thermal diffusivity increased. In the case of 50% mixing, the time constant is 0.205 ms, which is 0.69 times as that of Ru (phen) $_3^{2+}$.

A heat penetration time of TSP is proportional to the square of the TSP film thickness and inversely proportional to the TSP thermal diffusivity. The experimental results are well accorded with this theory.

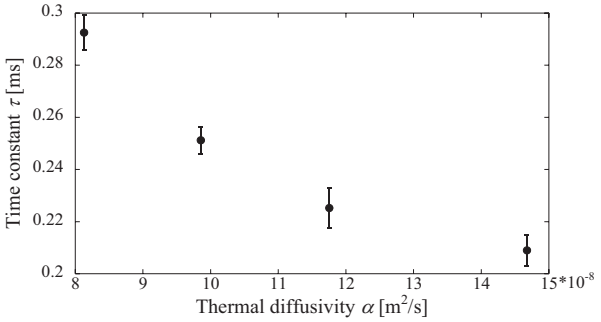

Fig. 3 Time constant

5. Conclusion

In this study, a TSP with high performance and high responsivity to be applied to a short-time wind tunnel was developed. As for the luminescent intensity, at a mixture content of 50%, increased nearly twofold when compared to Ru (phen) $_3^{2+}$. As for the response time evaluation test, we showed the efficacy of evaluation method using heat flux history. The effect of thermal diffusivity for the time constant was clear. The time constant of new TSP is 0.69 times as that of original one. Then we indicated possibility of new TSP for hypersonic wind tunnel test.

References

[1] T. Liu, J. P. Sullivan, “Pressure and Temperature Sensitive Paints”, Springer, Berlin, 2005.

[2] K.Itoh, S.Ueda, H.Tanno, T.Komuro, K. Sato, Hypersonic aerothermodynamic and scramjet research using high enthalpy shock tunnel, Shock Waves (2002) 12: 93–98

[3] Tianshu Liu, Zemin Cai, Jianhuang Lai, “Analytical Methods for Determination of Heat Transfer. Fields from Temperature Sensitive Paint Measurements in Hypersonic Tunnels”, AIAA 2009-736, (2009).

[4] NAGAI, H. , OHMI, S. , ASAI, K. , NAKAKITA, K. , “Effect of Temperature-Sensitive Paint Thickness on Global Heat Transfer Measurement in Hypersonic Flow”, Journal of Thermophysics and Heat Transfer, Vol. 22, No. 3, pp373-381, (2008).

Experimental and Numerical Determination of Radiative Properties of CeO_2 Packed Bed

Kyohei Ogino[1], Atsushi Sakurai[2], Hiroki Gonome[3], and Shigenao Maruyama[4]
[1]Graduate School of Science and Technology, Niigata University, Niigata 950-2181, Japan
[2]Department of Mechanical and Production Engineering, Niigata University, Niigata950-2181, Japan
[3]School of Engineering, Tohoku University, Sendai 980-8579, Japan
[4]Institute of Fluid Science, Tohoku University, Sendai 980-8577, Japan
ogikyo.syukatsu@gmail.com

ABSTRACT

CeO_2 packed bed has been received attention as promising catalyst for solar energy conversion. The accumulated knowledge is insufficient. We measured hemispherical reflectance and hemispherical transmittance in the wavelength range of 0.22-0.85μm by the ultra-violet and visible spectrophotometer. Radiation Element Method by Ray Emission Model (REM^2) is employed to analyze radiative transfer in the ceria packed bed. The calculated results showed similar tendency with the measured one. To evaluate particle size and scattering effect of nonspherical particles will be necessary in our future work.

1. Introduction

Concentrated solar radiation has been received attention due to the application to thermochemical conversion of hydrogen [1]. Recently, CeO_2 (ceria) particles have been recognized as promising catalyst for solar energy conversion. In order to develop a high-efficient solar reactor, radiative heat transfer analyzes are more important in high temperature field. In these analyzes, accurate optical properties of ceria are necessary. Lipinski et al. [2-3] has been investigated the optical properties of ceria packed bed by the experimental measurement and Monte Carlo method.

However, accumulated knowledge regarding optical properties of ceria packed bed is insufficient. Therefore, the objective of this study is to provide these optical properties by experimental spectroscopic measurement. Furthermore, the Radiation Element Method by Ray Emission Model (REM^2) is employed to analyze radiative transfer in the ceria packed bed. These comparisons of the experiment and the simulation help to understand physical insight of the radiative transfer in a ceria packed bed.

2. Method

2.1 Experiment

Hemispherical reflectance and transmittance of ceria packed bed was measured using the ultraviolet and visible spectrophotometer (Shimadzu UV-2450) [4]. The ceria particles were packed in a rectangular sample holder made by quartz. The thickness of sample is 0.5 mm. The mass of packed bed was measured, and the volume fraction can be estimated as 0.437. The hemispherical reflectance and transmittance were measured in the spectral range 0.22-0.85μm measured with spectral resolution of 0.5 nm.

Fig. 1 shows the schematic of experimental setup for hemispherical transmittance and reflectance using integrating sphere. In the sphere, reference beam and sample beam enters. The former is 0 degree, the latter are 8 degrees of incidence angles. Reference reflection is barium sulfate. (a) In the measurement of hemispherical reflectance, the sample installed in the reflection surface of the sample beam side. (b) In the measurement of hemispherical transmittance, the sample is installed in the entrance of the sample beam side and empty cell installed in entrance of the reference beam side. Both of reflection surfaces are reference reflection.

2.2 Simulation

In order to calculate the hemispherical reflectance and transmittance in a participating medium, it is necessary to solve a radiative transfer equation. The ceria packed bed can be dealt with a one-dimensional plane parallel system. In the present study, the Radiation Element Method by Ray Emission Model (REM^2) is employed [4-5]. REM^2 is a generalized numerical method for analyzing radiative heat transfer in participating media and between specular and/or diffuse surface with arbitrary configurations and thermal conditions. REM^2 has been also applied to the spectral selective pigmented coating[4], atmospheric radiative transfer problem [5].

An analysis model is shown in Fig. 2.A radiation element exists from 1 to *N*. The element *N* is assumed air. The refractive index of ceria can be obtained from the reference [2], and the particles are assumed to be monodispersed. Although the results are not shown here, it was observed that the ceria particles are nonspherical by SEM. Furthermore, it is difficult to determine the size of nonspherical ceria particles. Therefore, parametric study for different size of particles is performed in the range 50-200μm. The extinction, absorption, scattering coefficient are calculated by the Mie scattering theory.

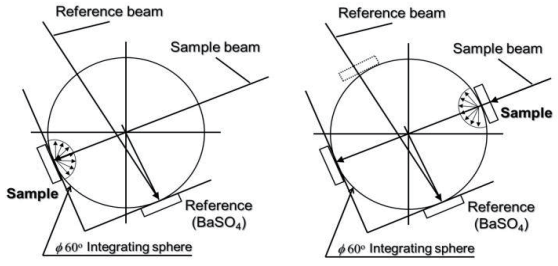

(a) reflectance (b) transmittance

Fig.1 Experimental set-up

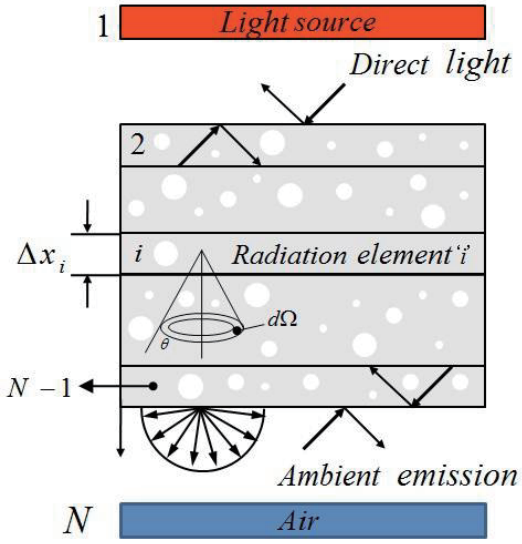

Fig.2 Analysis model

Table 1.Computational condition

Parameter	Value
Radiation Elements	102
Wavelength range, λ [μm]	0.3-2.0
Light path length, t [mm]	0.5
Volume fraction, f_v [-]	0.437
Particle diameter, d [μm]	50, 100, 150, 200

3. Results and Discussion

Fig. 3 shows the results of calculated and measured hemispherical reflectance. The calculated results are shown with varying diameters. The reflectance increases as the diameter decreases because of back scattering effect by smaller particles. Although there is difference of sharp change in wavelength between measurement and calculation, the tendency is similar.

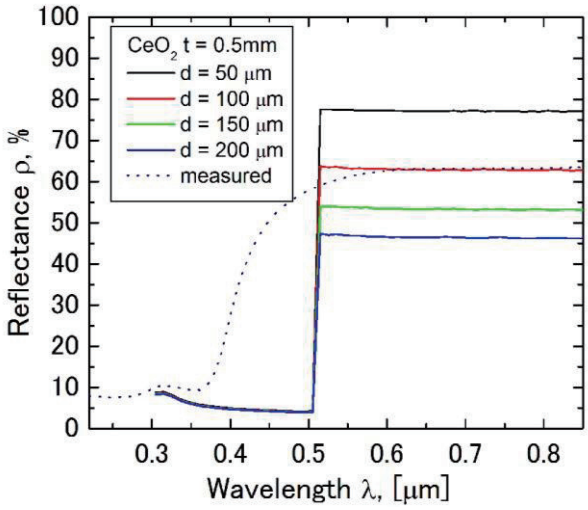

Fig.3 Hemispherical reflectance of CeO_2 packed bed

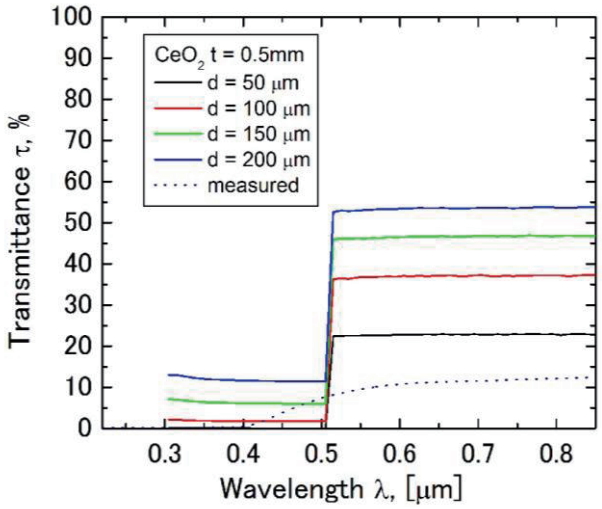

Fig.4 Hemispherical transmittance of CeO_2 packed bed

Ceria has a large imaginary part of refractive index in the shortwave length region, therefore the reflectance is small. The calculated result with the diameter of 100μm shows good agreement with the experimental result.

Fig. 4 shows the results of calculated and measured hemispherical transmittance. The transmittance decreases as the diameter increases because of forward scattering effect by larger particles. The calculated results overestimate the measured result because it is difficult to determine the characteristic cross section of ceria particles, and to evaluate the scattering effect of nonspherical particles by Mie scattering theory.

4. Conclusion

The obtained results are as follows:

1. The hemispherical transmittance and reflectance of ceria packed bed were measured by the ultraviolet and visible spectrophotometer, furthermore, these measured results were compared with the calculated one by the REM[2].
2. The calculated results with varying particle diameter showed similar tendency with the measured results. In our future work, it is necessary to appropriately evaluate particle size and scattering effect of nonspherical particles.

References

[1] A.Steinfeld, Solar Energy, **78** (2005) 603-615.
[2] K.Ganesan, W. Lipinski, Infrared Physics & Technology, **57**(2013)101-109.
[3] W. Lipinski et al, Experimental Heat Transfer, **24**(2011) 285-299.
[4] H. Gonome, S. Maruyama et al, Journal of Thermal Science and Technology, **7**(2012)364-378.
[5] S. Maruyama, Y. Mori et al, Journal of Quantitative Spectroscopy & Radiative Transfer, **83**(2004)361-375.

Tenth International Conference on Flow Dynamics
November 25-27, 2013, Sendai, Miyagi, Japan

Preliminary Experiment of Supersonic Micro-channel Gas Flow Visualization by Using Interferometer

Yuya Takahashi[1], Junnosuke Okajima[2], Yuka Iga[2], Atsuki Komiya[2], Shigenao Maruyama[2]
[1]Graduate School of Eng., Tohoku Univ., Sendai, 980-8579
[2]Institute of Fluid Science, Tohoku Univ., Sendai, 980-8577
yuya@pixy.ifs.tohoku.ac.jp

ABSTRACT

In this study, micro scale cooling device using supersonic flow was studied. Preliminary experiment of supersonic micro-channel single phase gas flow visualization by using interferometer was conducted. The micro-channel was placed in 20×20 mm^2 Si plate. The channel size is about 200 μm in width, 500 μm in depth, 6,000 μm in length. The phase-shifted data at inlet and outlet were recorded in the experiment by using a phase-shifting interferometer. From the recorded phase-shifted data, the refraction field of supersonic micro-channel gas flow was evaluated.

1. Introduction

In recent years, the power density of integrated circuit such as CPU comes up 1 MW/m^2 with the increase of components per chip. It causes rise of energy consumption to cool for example the datacenters and its cost becoming significant issue[1]. Thus several researches about coolant, such as liquid, gas[2] and two-phase[1,3] flow have been conducted to improve cooling ability. However, these on-chip cooling systems are not enough to cool CPU, so in the present state, these are used with air conditioner and the integration degree is suppressed.

In the previous study[4], in order to decrease the driving energy, air flow which has low viscosity was used as the working fluid. In addition, air cooling can use the temperature drop due to an adiabatic expansion and the supersonic flow can be generated under relatively low pressure. In the previous study[4], it is revealed that supersonic micro-channel has great cooling ability by the numerical calculation. However, there are few experimental studies of the micro-channel gas flow visualization because of its small scale.

There are many experimental methods for the visualization and measurement of the flow field. In those methods, the Mach-Zehnder interferometry is widely used because of its non-intrusive and quantitative nature. Generally, it is difficult to measure the supersonic flow in the micro-channel because it is hard to take enough length of optical path, and its low spatial resolution for the measurement of refractive index. However, phase-shifting technique[5] make it possible to improve the phase resolution. The phase-shifting technique is an image processing technique, which is used three interferogram in different polarization angle. Every pixels of CCD camera could have a value in the phase-shifting interferometer as against the general interferometer could have a value only on the fringe. So, this phase-shifting interferometer is available for the micro-channel gas flow, which has short optical path length.

In order to develop an effective air cooling device, it is needed to understand of the phenomenon of the supersonic flow in the micro-channel. The objective of this study is the visualization and the measurement of the supersonic flow in the micro-channel by using the phase-shifting interferometer.

2. Flow condition in micro-channel

Figure 1 shows the schematic diagram of the experimental apparatus. The light source is He-Ne laser, which is 632.8 nm in wave length. The photograph of the micro-channel is shown in Fig. 2. This is a preliminary experiment, so the flow in a micro-channel was subsonic in this study. The entire size of this device is 20×20 mm^2. The length, wide, and depth of the channel are 6,000 μm, 235 μm, and 500 μm, respectively. This channel depth corresponds to the optical path in the experiment. This micro-channel was made by using the Micro Electro Mechanical System (MEMS) techniques. However, it is difficult to make a deep micro-channel, which can be visualized. Hence,

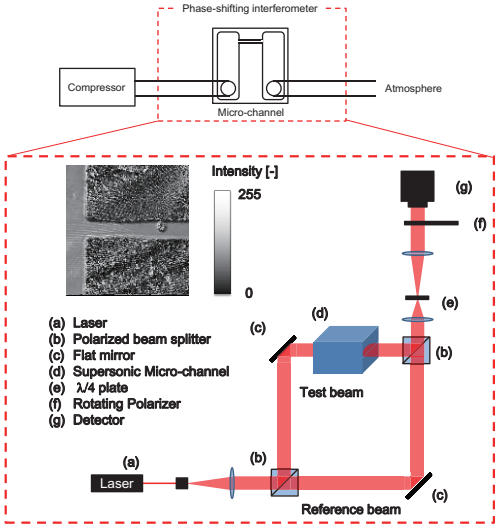

Fig. 1 Schematic diagram of the experimental apparatus.

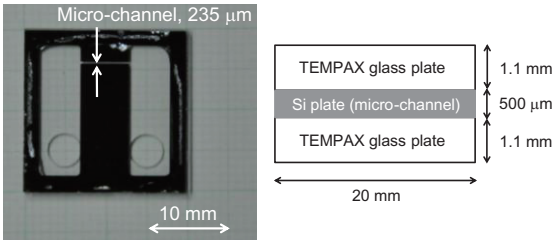

Fig. 2 Photograph of the micro-channel.

this depth was decided on the predicted fringe number (≈ 0.5) from the calculation results[4]. This device is consisted from three plates, Si plate, which includes the micro-channel is sandwiched by two TEMPAX glass plates. The Si plate is processed by deep reactive ion etching (D-RIE) and bonded with TEMPAX plates by anodic bonding.

3. Results and Discussion

Before the experiment, the flow rate of the micro-channel was measured and compared with the calculated results[4]. The total pressure of the compressor and the pressure at the end of the flow path are 0.7 MPa and 0.1 MPa, respectively. The calculated and measured values of the flow rate are 141.12 mL/s and 142.95 mL/s, respectively. There is good agreement between the calculated results[4] and the measured values. The slight difference between these values is caused by some conditions, which is depended on the accuracy of the MEMS technology and pipe laying (channel width and total pressure).

This experiment was conducted in room temperature. Figures 3 and 4 show the phase-shifted data at the inlet and the outlet of the micro-channel, respectively. As shown in Fig.3, refractive index distribution, which is caused by the pressure drop in the micro-channel is observed in gray scale. The right side shows an inlet reservoir. In Fig. 4, the free jet stream could be observed at the end of the channel. Then, flow density and temperature would be decreased because of the flow expansion. There are several fringe caused by the flow expansion.

The brightness distributions at the channel center, which is shown in Figs. 3 and 4 as red lines are evaluated. The results are shown in Figs. 5 and 6, respectively. At the inlet of the channel, the brightness rapidly decreased. In a channel, the values were decreasing by the pressure loss. At the end of the channel, the brightness decrease sharply. This drop-off

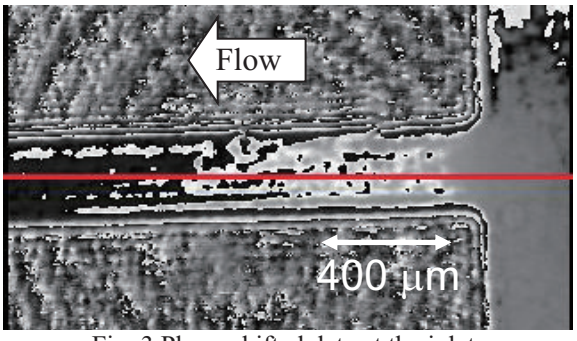

Fig. 3 Phase-shifted data at the inlet.

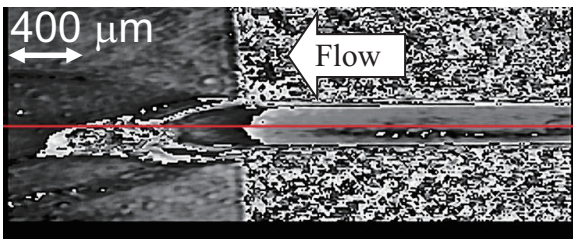

Fig. 4 Phase-shifted data at the outlet.

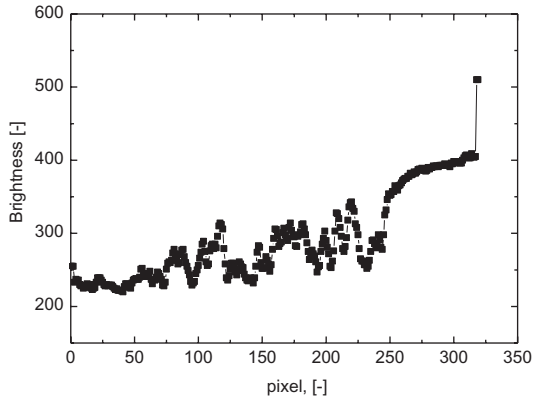

Fig. 5 Brightness distribution at the inlet.

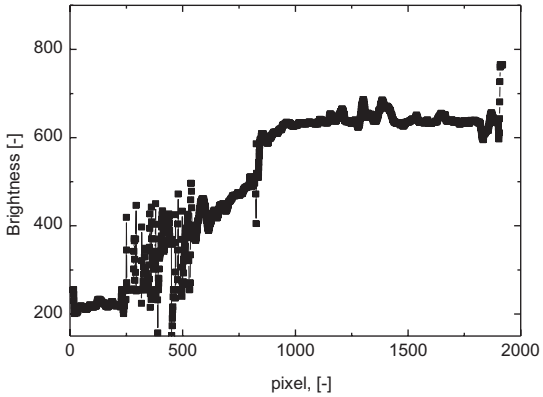

Fig. 6 Brightness distribution at the outlet.

was caused by the flow expansion. As shown in Fig. 5, this measurement could catch the brightness data despite the fringe number was less than one. However, there are many fluctuations especially in the region, which has a large density change. This problem should be improved in the future work.

4. Concluding remarks

In this study, preliminary experiment was performed for the visualization and the measurement of the supersonic flow in the micro-channel. The following conclusions were obtained.

(1) From the phase-shifted data, the refractive index fields in the subsonic micro-channel with 235 μm in width were evaluated.

(2) The results showed the possibility of the measurement of the supersonic micro-channel flow. However, the data of the refractive index has fluctuation and the improvement is future work.

References

[1] J. B. Marcinichen et al., Appl. Therm. Eng., (2012), pp. 1–16.

[2] C. Hong et al., Int. J. Therm. Sci., 46, (2007), pp. 1153–1162.

[3] J. Xu et al., Int. J. Multiphase Flow., 35, (2009), pp. 773–790.

[4] Y. Takahashi et al., Proc. 11th ICNMM, (2013), ICNMM2013-73134.

[5] S. Maruyama et al., Exp. Therm. Fluid Sci., Vol. 19, (1999), pp. 34–48.

Tenth International Conference on Flow Dynamics
November 25-27, 2013, Sendai, Miyagi, Japan

Explosion Venting of Porous Walls Gas Storage

Taisia Miroshnichenko, Nickolay Belyakov, Nickolay Lutsenko, Sergey Minaev
FEFU, School of Engineering Sciences, Vladivostok, Russia
E-mail of corresponding author: tmi.malle@gmail.com

ABSTRACT

The gas outflow process from the storage is considered. The process begins due to the gas ignition. The one-dimensional problem is solved numerically. The maximum gas pressure into the storage depending on the medium permeability is analyzed. The discharge time is investigated.

1. Introduction

Gas combustion problem in the closed vessel is one of the fundamental problems of combustion theory. Its solution is important for many of practical applications related with the risk of fire and explosion of industrial units, description of combustion processes in engines, measurement of normal flame velocity etc [1]. Another essential problem for practical applications is the gas combustion problem in a semi closed vessel with the hole from which the gas flows out [2, 3]. In this paper the problem when combustion takes place in the closed vessel with porous walls is considered. Such situation can be realized, for example, when the gas is burned in the underground storage and the ground can be considered as a permeable porous medium. The aim of this paper is investigation of the pressure change processes in the storage and porous medium and the features of gas flow in the porous medium.

2. Mathematical model

Gas parameters in the storage don't depend on the x-coordinate. They are calculated depending on the flame front location from the next conditions:

$$\frac{1}{\gamma}\frac{d\hat{p}}{d\hat{t}} = \frac{T_r M}{h_0}\hat{p}^{\gamma} - \frac{\hat{\upsilon}_{out}}{h_0}\hat{p}, \qquad (1)$$

$$\frac{d\hat{x}_f}{d\hat{t}} = -\frac{1}{\gamma}\frac{d\hat{p}}{d\hat{t}}\frac{\hat{x}_f}{\hat{p}} + T_r M\hat{p}^{\gamma-1} + M \quad \text{when} \quad -h_0 \le \hat{x}_f \le 0$$

$$\frac{d\hat{\rho}}{d\hat{t}} = -\frac{a}{\gamma h_0}\hat{\rho}\hat{\upsilon} \quad \text{when} \quad \hat{x}_f = 0$$

The conservation laws in view of the heterogeneous are true. Gas is supposed perfect and the porous medium is fixed and homogeneous.

$$\frac{\partial\hat{\rho}}{\partial\hat{t}} + \frac{\partial\hat{\rho}\hat{\upsilon}}{\partial\hat{x}} = 0,$$

$$\hat{\rho}\left(\frac{\partial\hat{\upsilon}}{\partial\hat{t}} + \hat{\upsilon}\frac{\partial\hat{\upsilon}}{\partial\hat{x}}\right) = -\frac{1}{\gamma}\frac{\partial\hat{p}}{\partial\hat{x}} - \hat{F}\hat{\upsilon}, \qquad (2)$$

$$\hat{\rho}\left(\frac{\partial\hat{T}}{\partial\hat{t}} + \hat{\upsilon}\frac{\partial\hat{T}}{\partial\hat{x}}\right) = \hat{A}\left(1-\hat{T}\right) + \frac{\gamma-1}{\gamma}\left(\frac{\partial\hat{p}}{\partial\hat{t}} + \hat{\upsilon}\frac{\partial\hat{p}}{\partial\hat{x}}\right) + (\gamma-1)\hat{\upsilon}\hat{F},$$

$$\hat{p} = \hat{\rho}\hat{T}.$$

Here $\hat{p} = p/p_0, \hat{\rho} = \rho/\rho_0, \hat{T} = T/T_0$ are the scaled pressure, density and temperature in units of the initial ones. $\hat{\upsilon} = \upsilon/c$ is the scaled gas velocity in units of the sonic velocity. υ_{out} is the gas velocity on the output of the storage. x_f is the x-coordinate of the flame location. h_0 is the scaled storage height in units of the height of the porous layer. γ is the adiabatic exponent. $T_r, \mathrm{M}, \hat{\mathrm{A}}, \hat{\mathrm{F}}$ are the constants.

Let's write the boundary conditions. On the lowest wall of the storage:

$$\hat{x} = -h_0: \quad \hat{\upsilon} = 0, \frac{d\hat{p}}{d\hat{x}} = 0.$$

On the exit of the porous medium: (3)

$$\hat{x} = 1: \quad \hat{p} = 1:$$

Furthermore the conditions on the boundary of the storage and the porous medium are needed to introduce. Let's denote the variables related to the storage the "1" index and its related to the porous medium the "2" index.

$$\hat{\rho}_1\hat{\upsilon}_1 = a\hat{\rho}_2\hat{\upsilon}_2,$$

$$\hat{\upsilon}_1^2 - \hat{\upsilon}_2^2 = \frac{2}{\gamma-1}\left(\hat{T}_2 - \hat{T}_1\right), \qquad (4)$$

$$\frac{\hat{T}_2}{\hat{T}_1} = \left(\frac{\hat{p}_2}{\hat{p}_1}\right)^{\frac{\gamma-1}{\gamma}}$$

To calculate this problem the Flux-Corrected Transport (FCT) numerical algorithm was used. The finite-difference grid is regular and it was broken up on 600 parts. It was supposed that the height of the porous medium in 10 times more than the height of the storage.

3. Results and Discussion

The gas pressure in the storage for the media with different permeability and in the closed vessel are illustrated on the fig. 1. As it was expected the largest extremum of the gas pressure depends on the medium permeability strongly. The fast pressure rise doesn't lead to the formation of the shock wave in the porous medium and the pressure profiles are monotonically decreasing functions of the x-coordinate (see fig. 2).

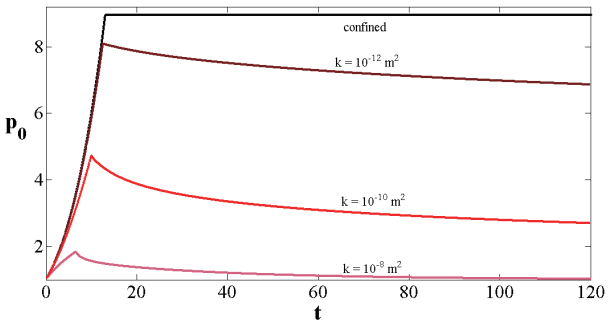

Fig. 1 The gas pressure in the storage.

The pressure distributions at different times after explosion initiated in the storage are shown on the fig. 2. They were calculated with the permeability coefficient k = 10^{-8} m^2. Maximum of the gas pressure in the storage is reached at the moment when all gas volume is burned in it. It is assumed that the gas combustion stops at the moment when the flame coming closer to the porous wall of the storage. The pressure decreases rapidly after that.

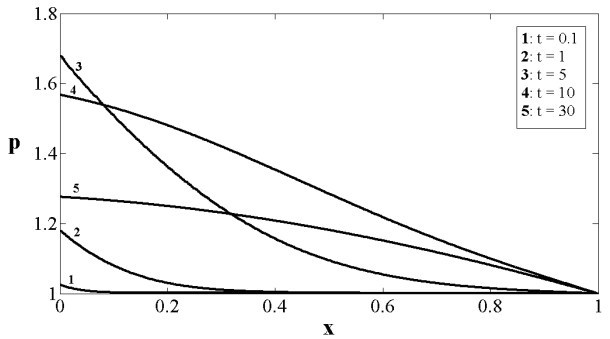

Fig. 2 Gas pressure in the porous medium at different times with k = 10^{-8} m^2.

On the fig. 3 you can see when the combustion front reaches the porous layer.

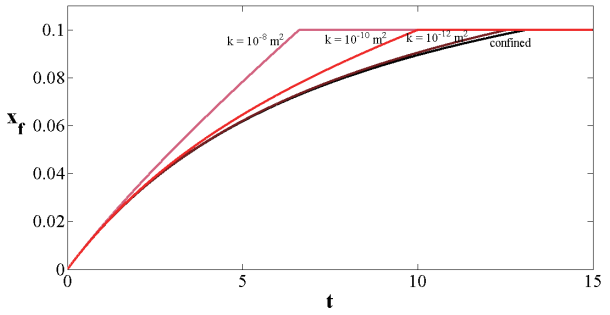

Fig. 3 Coordinate of the combustion front.

Dynamics of relative gas mass changes moved through the lower and upper boundaries of the porous layer are shown on the fig. 4. They are drawn for the medium with the same permeability. The output time only of the main gas mass is shown on the grid. Filtration of the rest part of gas (about 10%) is the exhaustive process and it can proceed for the long time.

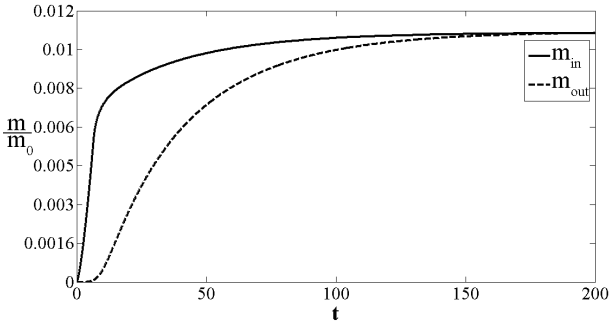

Fig. 4 The gas mass moving through the lower and upper boundaries of the porous layer.

4. Concluding remarks

One-dimensional problem of the gas outflow from underground storage where combustion wave appears at initial time was considered. The problem was solved numerically using finite-difference method.

Changes of the gas dynamic parameters in the storage and porous medium were investigated. Dependencies of maximum gas pressure in the storage and the discharge time of the gas pressure on the medium permeability and the height of the porous layer were got.

Acknowledgements

This work was supported by RFBR-FEFU grant No.12-08-13007, Integration project SB – FEB RAS No.38 and FEFU scientific research programs.

References

[1] Zeldovich, Ya.B., Barenblatt, G., Librovich, V.B., Makhviladze, G.M. 1985. The Mathematical Theory of Combustion and Explosions. Translated by McNeil, D. New York: Plenum.

[2] Bradley, D. & Mitcheson, A. 1978b. The venting of gaseous explosions in spherical vessels.II-Theory and experiment. Combustion and Flame, 32, 237-255.

[3] Molkov, V.V. 1995. Theoretical Generalization of International Experimental data on Vented Gas Explosion Dynamics. Physics of Combustion and Explosions, 165-181.

Tenth International Conference on Flow Dynamics
November 25-27, 2013, Sendai, Miyagi, Japan

Modeling Mass and Heat Transfer in Geothermal Reservoirs Using Fractional Differential Equations

Anna Suzuki, Yuichi Niibori, Sergei A. Fomin, Vladimir A. Chugunov, Toshiyuki Hashida
Graduate School of Environmental Studies, Tohoku University,
6-6-11-707 Aramaki-aza-Aoba, Aoba-ku, Sendai, Miyagi, 9808579, Japan
anna.suzuki@rift.mech.tohoku.ac.jp

ABSTRACT

Mass and heat transfer equations based on fractional derivatives have been proposed to evaluate the effect of cold water injection into a geothermal reservoir. Numerical simulations are conducted to investigate tracer responses and temperature profiles due to dispersion into the surrounding rocks with varying permeability distribution. The calculated tracer responses exhibit apparent long tails, which are characterized by the mass transport model based on a fractional derivative. The heat transfer model using the fractional derivative is also in a good agreement with the calculated temperature profile.

1. Introduction

A major problem for geothermal reservoir engineers is to prevent thermal breakthrough due to water injection in a geothermal reservoir. Tracer tests have been used to characterize flow of injected water and can provide useful information for design injection operation. In order to represent tracer responses obtained from complex fractured reservoirs, a mass transport model, which is called fractional advection dispersion equation (fADE), has been developed [1]. The advantage of using fADE is its ability to describe fluid flow conditions in a geothermal field with great spatial and temporal heterogeneities, based on a mathematical description of the fundamental physical processes in the reservoir. It is reasonable to suppose that a heat transfer model based on a fractional derivative could also describe the effect of heat transfer into the surrounding rocks. This paper shows the applicability of fADE and and the heat transfer equation based on fractional derivatives to evaluate the effect of water injection into a complex reservoir.

2. Mathematical model

We consider a fractured reservoir as illustrated in Fig. 1. Detailed descriptions to derive the mass transport model are available in Fomin et al. [1]. The fractional advection dispersion equation (fADE) and fractional heat transfer equation (fHTE) can be described as follows:

$$\frac{\partial C}{\partial \tau} + b_3 \frac{\partial^{\gamma} C}{\partial \tau^{\gamma}} + b_1 \frac{\partial^{\beta} C}{\partial \tau^{\beta}} = \frac{1}{Pe}\frac{\partial}{\partial X}\left(p\frac{\partial^{\alpha} C}{\partial X^{\alpha}} + (1-p)\frac{\partial^{\alpha} C}{\partial (-X)^{\alpha}} \right) - \frac{\partial C}{\partial X} \quad (1)$$

$$\frac{\partial \mathrm{T}}{\partial \tau_h} + e_3 \frac{\partial^{\gamma'} \mathrm{T}}{\partial \tau_h^{\gamma'}} + e_1 \frac{\partial^{\beta'} \mathrm{T}}{\partial \tau_h^{\beta'}} = -\frac{\partial \mathrm{T}}{\partial X} \quad (2)$$

where C, T, and X are concentration, temperature and distance, which are normalized with respect to each representative value. The representative concentration is the injected concentration at the inlet point. τ and τ_h are representative time of mass transport and heat transfer, respectively. The velocity in Eq. (1) makes a correlation between the representative time and distance. b_1, b_3, e_1, and e_3 are the retardation coefficient and Pe is Péclet number. p ($0 \le p \le 1$) the skew parameter that controls the bias of the dispersion. α ($0< \alpha \le 1$) is the order of fractional spatial derivative. β, β', γ, and γ' are the order of fractional temporal derivatives, values of which are between 1/2 and 1. Here, the first terms on the left side of Eqs. (1) and (2) are the accumulation term, and the second terms on the left side of Eqs. (1) and (2) model the retardation processes associated with dispersion into secondary branched fractures with respect to mass and heat transfer, respectively. The third term on the left side is the process of vertical dispersion into surrounding rock masses with respect to mass and heat transfer, respectively. The first and second terms on the right side of Eq. (1) express dispersion within the fractured reservoir, and the third term is the advection term. The right side term of Eq. (2) represents convection term. In this study, a finite difference approach is used to solve the Eqs. (1) and (2) [2].

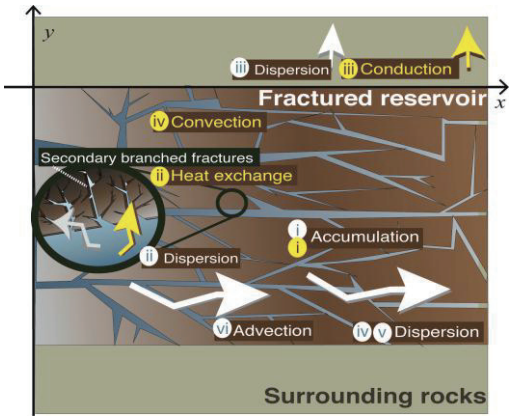

Fig. 1 Schematic of a fractured reservoir

3. Numerical simulation methods

A reservoir simulator TOUGH2 [3] was used to evaluate the effect of cold water injection on reservoir performance. Fluid, mass, and heat flow are numerically simulated in a two-dimensional reservoir model. The numerical properties are summarized in Table 1.

The injection takes place along the entire left side of the domain, and the extraction is performed on the right side. The tracer is injected at 0.2 kg/s for one day, after

which the injection switches to fresh water.

The non-Fickian behavior occurs due to the geological structures and dispersivities are considered to be fractal [1]. In this study, the permeability of the surrounding rock, K_s is defined as a function of power law.

4. Results and Discussion

Numerical tracer results obtained using TOUGH2 shows the dependence of the permeability of the surrounding rocks. When the flow was controlled only by advection in the reservoir, the tracer response exhibited a Gaussian curve. In contrast, a response curve for a spatially varying permeability distribution of the surrounding rocks produced a heavy tail and gradual decrease in breakthrough curve.

In the case of impermeable surrounding rocks, both fADE and classical ADE were in a good agreement with the tracer response. The long tail behavior in the tracer response of permeable surrounding rocks can be calculated by fADE, the third term on the left hand side of which expresses the effect of dispersion into surrounding rocks. Figure 2 shows the best-fit of fADE onto the calculated tracer responses for spatially varying permeability of the surrounding rocks. The higher permeability of surrounding rocks resulted in an increase in retardation parameter in fADE as shown in Table 2. For the constant permeability of surrounding rocks, the order of temporal fractional derivative in fADE was shown to be constant. On the other hand, for a spatially varying permeability, the order was dependent on the change in permeability.

The solutions of the fHTE are in a good agreement with the calculated temperature profiles as shown in Fig. 3. The curve fittings on the temperature profile using the fHTE suggested that the order of the fractional derivative in the heat transfer equation was close to that in fADE (Table 2). However, the retardation factor in the heat transfer model differed from the factor in the fADE.

5. Concluding remarks

The simulation of water injection into fractured reservoirs revealed the interplay of different permeability distributions in the surrounding rocks. The calculated tracer responses for the permeable surrounding rocks produced a heavy tail, which can be characterized by the fADE solution. The fADE parameters show relations with the permeability of surrounding rocks. The curve fittings on the temperature profile using the fHTE suggested that the order of the fractional derivative in fHTE was close to that in fADE. However, the retardation factor in the heat transfer model differed from the factor in the fADE.

References

[1] S. Fomin, V. Chugunov and T. Hashida, Adv. Water Resour, **34** (2011), 205–214.

[2] M. Meerschaert and C. Tadjeran, Appl. Numer. Math, **56** (2006), 80-90.

[3] K. Pruess, C. Oldenburg and G. Moridis, LBL Report, LBNL-43134.

Table 1 Summary of the reservoir and numerical properties

Property	
Calculation domain	80 m× 20 m
Element size	1m×1m×1m
Thickness of reservoir	2m
Permeabilities:	
Reservoir	1.0×10^{-13} m^2
Surrounding rock	$0-1\times10^{-14}$ m^2
Porosity	0.1
Rock density	2600 kg/m^3
Rock heat capacity	1 kJ/kg°C
Thermal conductivity	0 W/m°C
Initial pressure	10 MPa
Initial temperature	175°C
Injection temperature	35°C
Productivity Index	1×10^{-8}m^3
Production pressure	9 MPa

Table 2 Estimated parameters of ADE, fADE and fHTE for spatially varying permeability of the surrounding rocks $Ks(y) = y^{-\theta} \times 10^{-13}$

Ks	ADE	fADE		fHTE	
	b_1	b_1	β	e_1	B'
1.5	0.7	1.5	0.1	2.9	0.1
1.8	0.5	0.8	0.2	2.3	0.2
2	0.2	0.3	0.3	1.9	0.5
2.5	0.1	0	1.0	1.6	0.7

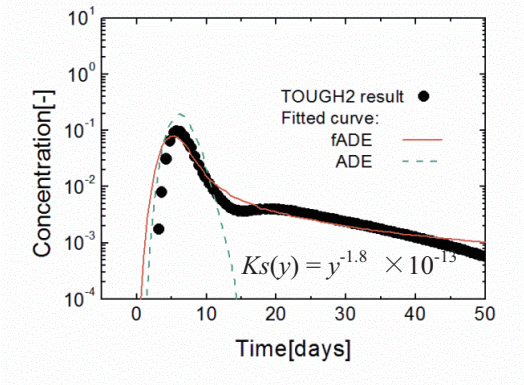

Fig. 2 Simulated tracer responses by TOUGH2 and best fits with fADE and ADE

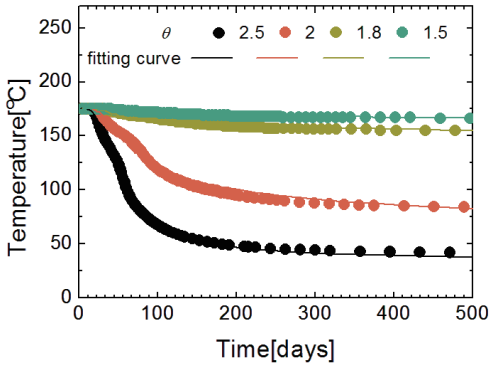

Fig. 3 Simulated temperature profiles using TOUGH2 and the fitting curve of fHTE

Tenth International Conference on Flow Dynamics
November 25-27, 2013, Sendai, Miyagi, Japan

Effects of Ambient Pressure on Liquid Sheet Breakup of Airblast Atomizer

Kodai Kato[1], Soichiro Suzuki[1], Taku Kudo[1], Soichiro Kato[2], Mitsunori Itoh[2], Akihiro Hayakawa[1], Hideaki Kobayashi[1]
[1]Institute of Fluid Science, Tohoku University, 2-1-1 Katahira, Aoba-ku, Sendai,
Miyagi 980-8577, Japan
[2]IHI Corporation, 1 Shin-nakahara-cho, Isogo-ku, Yokohama,
Kanagawa 235-8501, Japan
kodai.kato@flame.ifs.tohoku.ac.jp

ABSTRACT

The effects of ambient pressure on liquid sheet breakup of an airblast atomizer were experimentally investigated. Two-dimensional atomizer and high-speed back light imaging were used to study liquid sheet breakup mechanism at high pressure. In addition, the effects of ambient pressure on droplet formation in the secondary atomization region were investigated by using PDPA. The results indicated that the structure of airflow changed and the droplets became small near the nozzle edge with increasing pressure. However, in the secondary atomization region, droplets became large presumably due to collision of droplets with high number density.

1. Introduction

Recently, the reduction of emissions produced by power plants and aircraft engines has been required. Several concepts are suggested to reduce NO_x emissions, requiring high degree of homogeneity and quick mixing of fuel and air in a chamber at the same time. These depend on atomization of liquid fuel.

Airblast atomizer has been widely used as fuel injector of gas turbines for industry and aircraft. This atomizer has several advantages including high degree of homogeneity, relatively little change in performance over the wide operation range and rapid mixing of fuel and air [1]. However, the mechanism of the atomization using airblast atomizer and the influence of ambient pressure on atomization are not well clarified. Ishikawa et al. observed inhomogeneous profiles and unsteadiness of atomization at high number of mass air fuel ratio, AFR [2]. It is important that revealing these leads to utilize the high performance of the atomizer. In this study, therefore, the effects of ambient pressure on the liquid sheet breakup of the airblast atomizer and particle diameters in the secondary atomization region were investigated using a two-dimensional atomizer simulating the airblast atomizer for gas turbine.

2. Experimental method

In this study, a two-dimensional atomizer simulating an airblast atomizer was produced as shown in Fig. 1, which enables observations of liquid sheet breakup process at the nozzle edge. Liquid sheet is ejected between two co-flowing airstreams at the nozzle edge and break the liquid sheet into droplets.

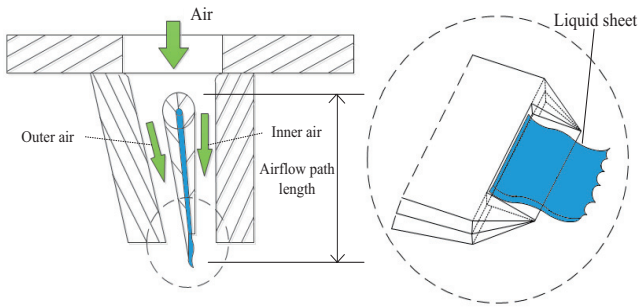

Fig. 1 Schematic of the two-dimensional atomizer

The high-speed back light imaging was used to observe behavior of the liquid sheet breakup operated at high pressure. In addition, Phase Doppler Particle Analyzer, PDPA was used to measure particle size and velocity.

In the present experiment, air and water were introduced to the atomizer as an oxidizer and a fuel, respectively. Air flow velocity, U_A, was 70 m/s and AFRs were 10 and 40, respectively. The ambient pressure in the chamber, Pc, was set to 0.1, 0.3, 0.5, and 0.7 MPa.

3. Results and Discussion

3.1 Effects of pressure on liquid sheet formation

High-speed back light imaging of the longitudinal liquid sheet breakup is performed in the condition that the co-flowing air velocity, U_A, is 70 m/s and ambient pressure, P_C, are 0.1 MPa and 0.7 MPa and they are shown in Figs. 2 (a) and (b), respectively. At the atmospheric pressure, the liquid sheet is ejected through narrow region of the nozzle edge and forms long ligaments. These ligaments are stretched and broke into large size droplets. When the pressure is increased to 0.7 MPa, the liquid sheet widely spread in the nozzle edge and it rapidly broke into small size droplets. The liquid sheet spread in the nozzle edge and long ligaments disappeared with increasing pressure. This means that change of the phenomena caused by various factors, such as the velocity boundary layer thickness in the air flow pass is thinned and the momentum of airstream is increased due to increasing air density.

Figures 3 (a) and (b) show high-speed back light images in the conditions of U_A = 70 m/ and AFR = 40 at P_C = 0.1 and 0.7 MPa. At atmospheric pressure, a liquid sheet is ejected the from the region of nozzle edge that is narrower than that of AFR = 10 (Fig. 2 (a)). Also, liquid sheet is ejected from narrow region like that of P_C = 0.1 MPa. For high number of AFR, liquid mass flow rate is low and agglutinate characteristics of liquid is strongly shown. Therefore, liquid sheet is ejected from narrow region for high number of AFR and inhomogeneous profiles and unsteadiness of atomization is occurred in a practical airblast atomizer [2].

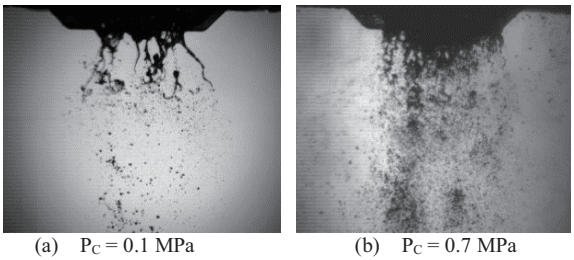

(a) P_C = 0.1 MPa (b) P_C = 0.7 MPa

Fig. 2 High-speed back light images (U_A= 70 m/s, AFR = 10)

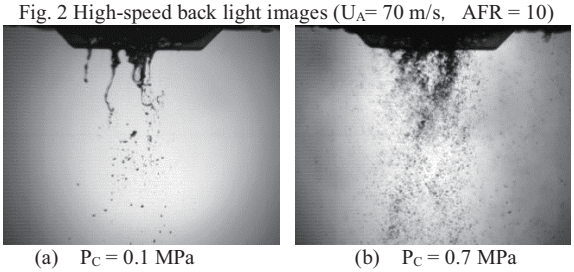

(a) P_C = 0.1 MPa (b) P_C = 0.7 MPa

Fig. 3 High-speed back light images (U_A = 70 m/s, AFR = 40)

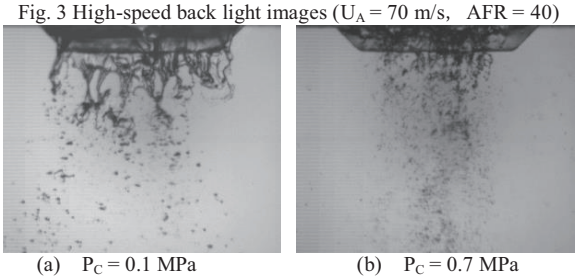

(a) P_C = 0.1 MPa (b) P_C = 0.7 MPa

Fig. 4 High-speed back light images (U_A = 70 m/s, Q_w = 76 ml/m)

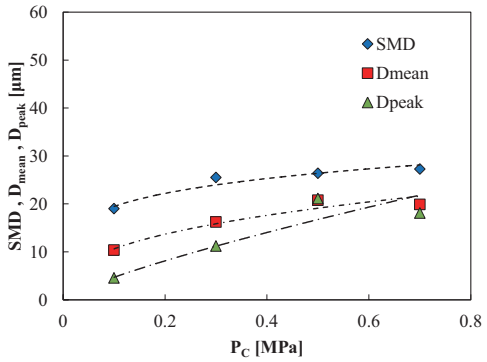

Fig. 5 Pressure dependence of particle diameter (U_A = 70 m/s, AFR =10)

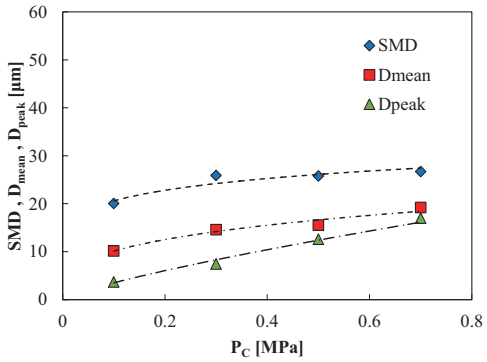

Fig. 6 Pressure dependence of particle diameter (U_A = 70 m/s, Q_w =76 ml/m)

To understand the effects of pressure on liquid sheet details, experiments are performed in the conditions of U_A = 70 m/s, liquid volume rate, Q_W = 76 ml/min and P_C = 0.1 and 0.7 MPa. Figures 4 (a) and (b) show high-speed back light images in above-mentioned conditions. At atmospheric pressure, the liquid sheet is ejected and breaks into droplets. On the other hand, liquid sheet is not seen and small droplets or ligaments is ejected at P_C = 0.7 MPa. Figure 4 (b) shows that airstream affects liquid sheet is formed close to the exit and droplets and ligaments break into smaller droplets. Also, this result indicates that the structure of flow is obviously changed and liquid sheet breaks rapidly into small droplets with increasing pressure.

3.2 Effects of pressure on particle diameters

In this study, arithmetic mean diameter, D_{mean}, peak diameter, D_{peak}, and Sauter Mean Diameter, SMD, were calculated from measured particle diameter profiles.

Figures 5 and 6 show relationships between ambient pressure and above-mentioned particle diameters measured at the secondary atomization region in the condition of U_A = 70 m/s for AFR = 10 and U_A = 70 m/s for Q_W = 76 ml/min, respectively. In Fig. 5, it is seen that these diameters become larger with increasing pressure. It is indicated that the velocity of liquid becomes faster with increasing pressure, while the velocity of air does not change because AFR is constant and the velocity difference between gas and liquid becomes small, meaning that the atomization is suppressed under high pressure. In addition, the collision frequency of the droplets is increased because liquid flow rate, thus droplet number density, increased with increasing pressure. Therefore, it is presumed that these diameters become large. However, in Fig. 6, also, these diameters become large with increasing pressure. In this condition that liquid flow rate is constant, it is expected that particle diameters are constant because velocity of the liquid and the collision frequency of the droplets do not change. In the lateral direction, it was observed that small droplets are wedged between two co-flowing airstream and do not spread widely downstream. At high pressure, small droplets are generated near the nozzle edge, which flow with airstream. In addition, droplets do not have an enough penetrating power through the airstream because the momentum of airstream is much larger than those of droplets. Therefore, collision frequency of the droplets increase and particle diameter became large at high pressure.

4. Concluding remarks

1. The structure of airflow changes and liquid sheet breaks rapidly into small droplets with increasing pressure.
2. At high pressure, particle diameter formed at nozzle edge is small, while droplets can not spread widely into downstream because the momentum of airstream is large. Therefore, collision frequency of the droplets increase and thus droplets diameter becomes large.

References

[1] S. Gepperth, ILASS Europe, 23th, (2010).
[2] S. Ishikawa, Proc. 50th Symp. Combust. Japan, 384-385 (2012).

Evaluation of CO_2/Water/Rock Interactions for CO_2 Geological Sequestration: Experimental Study of CO_2 Storage Capacity Using a Manometric Method

Kaori Endo[1], Koyo Ryu[1], Takashi Fujii[2], Toshiyuki Hashida[1]
[1]Fracture and Reliability Research Institute, University of Tohoku, 6-6-11-707, Aza-Aoba, Aramaki, Aoba-ku, Sendai, Miyagi 980-8579, Japan
[2]Institute for Geo-Resources and Environment, National Institute of Advanced Industrial Science and Technology, Tsukuba, Central 7, Higashi 1-1-1, Tsukuba, Ibaraki 305-8567, Japan
E-mail: kaori.endo@rift.mech.tohoku.ac.jp

ABSTRACT

For the evaluation of CO_2 storage capacity of deep saline aquifers, it is of crucial importance to understand the CO_2/water/rock interactions. The purpose of this study is to measure the CO_2 storage capacity for four types of rocks using a manometric method under air-dry and wet conditions at 50 °C and pressures of up to 20 MPa. The results showed that the two types of sandstone gave CO_2 storage capacity which was close to the model prediction: the pore-filling model which assumes that the pore volume is replaced with CO_2. The two types of sandstone exhibited a maximum CO_2 storage capacity of 1.8 mmol/g at 50 °C and 20 MPa.

1. Introduction

For recent decades, because of the large-scale industrial activities, concentration of the atmospheric greenhouse gas has been continuing to increase. Especially, the large amount of CO_2 emission which is considered to be one of the major causes for the global warming is the pressing problem. The CO_2 capture and storage technology which entails CO_2 capture from large emission sources and injection into deep saline aquifer (water-filled reservoir rocks) is practiced as one of the CO_2 reduction technology.

It is envisaged in general that CO_2 injected into deep saline aquifers stays in the injection zone for a geologic time, eventually dissolves in the formation brine and remains trapped by mineralization. However, a great part of the injected CO_2 has been demonstrated to remain as immiscible state in the aquifer. Consequently, within the aquifer, the CO_2 may dominantly occur in the two forms: (i) a CO_2 rich dense phase that may contain some water and (ii) an aqueous phase that either CO_2 dissolves into the formation water or CO_2 reacting with minerals in rocks. From the above backgrounds, to make reliable and accurate estimation of CO_2 storage potential in deep saline aquifers, it should be an important step to better understand the effect of water saturation state on CO_2/water/rock interactions during CO_2 injection [1].

In this study, we measured CO_2 storage capacity for four types of rocks using a manometric method under air-dry and wet conditions at 50 °C and pressures of up to 20 MPa.

2. Method

Rock samples used were Kimachi sandstone (KS), Berea sandstone (BS), Nachiguro mudstone (NM) and Iidate granite (IG). Bulk density and porosity for the rock samples were measured based on the principle of Archimedes method [2], and these properties were listed in Table 1. The dimensions of core specimens are each about 60 mm in diameter and about 72 mm in length. All the cut samples were washed with distilled water. In the case of the experiment under air-dry condition, core specimens were dried at 105 ˚C, whereas the samples tested under water-saturated condition were placed into a sealed desiccator containing distilled water and were degased in vacuum using a rotary pump.

Table 1. Rock properties of each specimen in this study.

	KS	BS	NM	IG
Bulk density [Mg/m^3]	1.98	2.12	2.70	2.62
Porosity [vol. %]	20.1	20.2	1.5	1.1

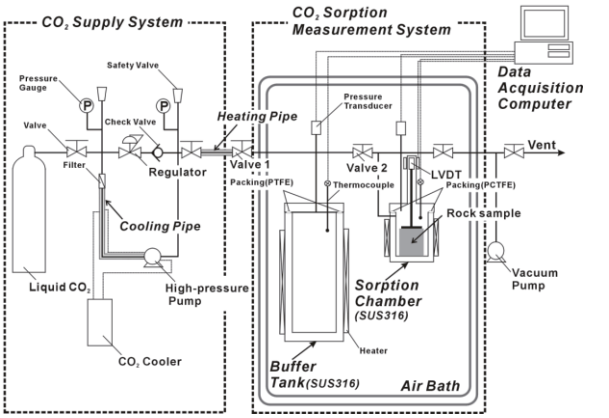

Fig. 1 Schematic diagram of CO_2 storage capacity measurement system.

Our experimental technique employs a manometric method. Figure 1 shows a schematic diagram of the experimental apparatus.

The CO_2 storage capacity was determined by the following equation:

$$n^{ex} = \left[\left\{\rho_b(P_i,T) - \rho_b(P_f,T)\right\}\cdot V_b - \rho_s(P_f,T)\cdot V_d\right] / M_{CO_2} \quad (1)$$

where $\rho_b(P,T)$ and $\rho_s(P,T)$ are the density of CO_2 in the buffer tank and the sorption chamber at pressure, P, and temperature, T, respectively. V_b is volume of the buffer tank, V_d the dead volume which is subtracted the sample volume from the calibrated volume of the sorption chamber based on the helium expansion method. M_{CO_2} is a molecular mass of CO_2. i and f represent initial and final stages, respectively.

In addition, we attempt to compare the calculated storage capacity by employing Equation (1) with theoretical values based on the two models: the solubility model (SM) and the pore-filling model (PM). In the former model, the CO_2 solubility in pore water, n_w, is

determined by assuming that CO_2 dissolved completely in the entire pore water of the sample and is given as:

$$n_w = V_r \cdot \phi_r \cdot \rho_w \cdot \chi_{CO_2} / M_{CO_2} \quad (2)$$

where V_r and ϕ_r are volume and porosity of the sample, respectively. ρ_w is density value of pore water under the liquid state (1000 kg/m^3), χ_{CO_2} CO_2 solubility of distilled water, and the dissolution amount of CO_2 is calculated using the literature data based on Wiebe and Gaddy [3]. In the latter model, the CO_2 storage capacity of the rock mass, n_p, is assumed to be equal to the amount of CO_2 required for filling the entire pore volume of the sample and is given as:

$$n_p = V_r \cdot \phi_r \cdot \rho_{CO_2} \cdot (1 - S_w) / M_{CO_2} \quad (3)$$

where ρ_{CO_2} and S_w are the density of CO_2 fluid and water saturation of the sample, respectively.

3. Results and Discussion

The CO_2 storage capacity had the tendency to depend on water content of samples. Figure 2 shows a comparison of the CO_2 storage capacity on air-dry conditions for KS (Figure 2(a)) and BS (Figure 2(b)) with the theoretical values calculated from the pore-filling model. The experimental results show that the two types of sandstone gave CO_2 storage capacity which was close to the pore-filling model. In the case of the air-dry conditions, the two types of sandstone exhibited a maximum CO_2 storage capacity of 1.8 mmol/g at 50 °C and 20 MPa. Cyclic pressure tests using the manometric method have shown that the CO_2 storage behavior was approximately reversible, suggesting the occurrence of a physical pore-filling process (rather than sorption) as the mechanism for the CO_2 storage.

On the other hand, Figure 3 shows a comparison of the CO_2 storage capacity on wet conditions for KS (a) and BS (b) with the theoretical values calculated from the solubility and pore-filling models. The CO_2 storage capacity on wet conditions was dependent on water content after the experiment.

As shown in Figure 3, the experimental results showed that the two types of sandstone gave CO_2 storage capacity which was close to the theoretical values. Furthermore, the wet samples of BS have larger storage capacity than the wet samples of KS. This is attributed to the differences of mineral surfaces and pore size between two types of sandstone.

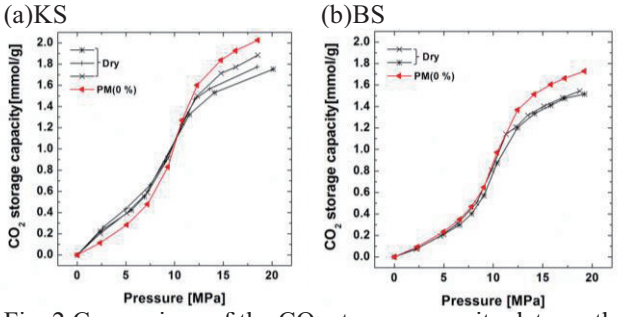

Fig. 2 Comparison of the CO_2 storage capacity data on the air-dry samples for KS(a) and BS(b) with theoretical values calculated from the pore-filling model. Water contents are shown in parentheses.

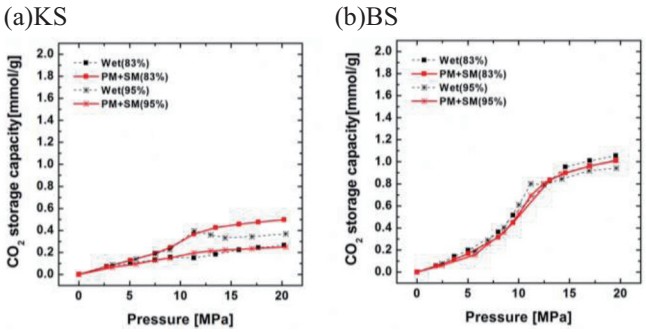

Fig. 3 Comparison of the CO_2 storage capacity data on the wet samples for KS(a) and BS(b) with theoretical values calculated from the solubility and pore-filling models. Water contents are shown in parentheses.

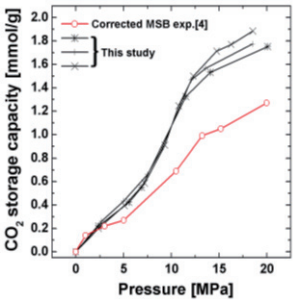

Fig. 4 Comparison of the CO_2 storage capacity data obtained from the manometric method on the air-dry samples for KS with the corrected CO_2 storage capacity obtained from the MSB measurement.

Therefore, it is important to understand the characteristics of reservoir rocks such as pore microstructure and wettability for the evaluation of the CO_2 storage capacity.

As can be seen in Figure 4, the validity of the experimental results was verified by comparison with the CO_2 storage capacity obtained from the MSB measurement [4].

4. Concluding remarks

In order to evaluate CO_2/water/rock interactions for rocks of assuming deep saline aquifers, CO_2 storage capacity measurements for four types of rocks were performed at 50 °C and pressures of up to 20 MPa for air-dry and wet conditions using a manometric method. In cases of air-dry conditions, the results showed that the two types of sandstone gave CO_2 storage capacity which was close to the model prediction. Even in cases of wet conditions, the results showed the same tendency.

The present study indicates that the CO_2 storage capacity in the reservoir was comparable with the pore filling model.

References

[1] T. Fujii et al., Natural Resources, **3** (2012), 48-55.
[2] ASTM C 20-80a, Annual Book of ASTM Standards, (1981).
[3] R. Wiebe and V. L. Gaddy, Journal of the American Chemical Society, **61** (1939), 315-318.
[4] T. Fujii et al., Journal of MMIJ, **126** (2010), 84-94.

Tenth International Conference on Flow Dynamics
November 25-27, 2013, Sendai, Miyagi, Japan

Characterization of Gas Permeability in Rock for the Development of CO_2 Geological Storage Technology

Koyo Ryu[1], Kaori Endo[1], Takashi Fujii[2], and Toshiyuki Hashida[1]
[1]Fracture and Reliability Research Institute, Graduate School of Engineering Tohoku University, 6-6-11-707 Aoba, Aramaki, Aoba-ku, Sendai, 980-8579, Japan
[2]National Institute of Advanced Industrial Science and Technology, Institute for Geo-Resources and Environment, 1-1-1, Higashi, Tsukuba, 305-8567, Japan
koyo.ryu@rift.mech.tohoku.ac.jp

ABSTRACT

CO_2 geological storage is a promising technology that may contribute to significant reduction of CO_2 emission. In this study, the pressure dependence of gas permeability was evaluated by using N_2 gas and CO_2 gas. The confining pressure was 10MPa.The inlet pressure and outlet pressure were controlled to examine the pressure effect of permeability. Our results show that pressure dependence of permeability can be described by Klinkenberg effect in relatively low pressure region($P_m \leq$ 2MPa), and the absolute permeability obtained by extrapolating the experimental data can be used in analysis of the flow behavior for CO_2 injection.

1. Introduction

In recent years, because of the large-scale industrial activities, the amount of greenhouse gas emissions continues to increase [1]. Especially, the increase in CO_2 gas emission can negatively impact the environment, such as the destruction of an ecosystem or the climate change. From the view point of the environmental conservation, the reduction of CO_2 gas emission is one of the upmost urgent and important issues.CO_2 geological storage is a promising technology that may contribute to significant reduction of CO_2 emission, and allow the development of sustainable energy production systems [2]. A schematic illustration of CO_2 geological storage is shown in Fig.1. CO_2 emitted from large sources is caught and then injected into brine aquifer. So, for the development of CO_2 geological storage technology, we need to accurately understand the flow of CO_2 injected into brine aquifer, which is usually characterized by Darcy's law. Therefore, it is necessary to investigate the pressure dependence of the CO_2 permeability in order to design and determine the CO_2 injection conditions. In this study, we evaluated the pressure dependence of gas permeability for dry Kimachi sandstone by using CO_2 gas and N_2 gas.

2. Material and methods

2.1 Sample preparation

In this study, Kimachi sandstone was used. The rock samples tested in this study were 39mm diameter cylinders, with length of 80mm.The average porosity is 20.1 vol.% and the bulk density is 1.97 Mg/m^3. All samples were washed with distilled water and ethanol. After washing, in order to conduct experiment on the air-dry basis, core samples were dried under vacuum in an oven equipped with a rotary vacuum pump at 105° C for at least 24 hours.

2.2 Permeability measurement

The experimental setup is shown in Fig.2. The experimental setup is mainly composed of a gas-supply system, a pressure control system, a high pressure core holder, and a flowmeter system. To mimic reservoir conditions, The experiments were conducted at 45° C, and the confining pressure was 10 MPa. The inlet and outlet pressure were controlled to examine the pressure effect of permeability. The inlet pressure is from 1 MPa up to 7 MPa, and outlet pressure is from 0 MPa up to 6 MPa. The permeability is calculated using the following equation.

$$K_g = \frac{2P_{out}\mu LQ \times 10^{-2}}{A(P_{in}^2 - P_{out}^2)} \quad (1)$$

where, K_g is gas permeability (md), A is cross section area of the rock sample (cm^2), P_{in} is inlet pressure (MPa), P_{out} is outlet pressure (MPa), μ is viscosity (mPa・s), L is length of the rock sample (cm), Q is gas flow rate (cm^3/s). This equation can be applied only when the flow is laminar flow.

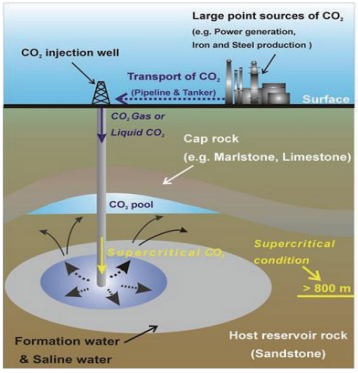

Fig. 1 Schematic illustration of CO_2 geological storage.

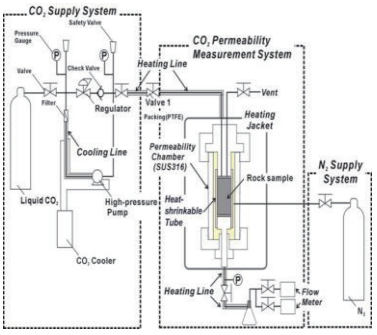

Fig.2 Schematic diagram of experimental setup for gas permeability measurement.

Pressure dependence was investigated by Klinkenberg equation

$$K_g = K_l\left(1+\frac{b}{P_m}\right) \quad (2)$$

where, K_g is gas permeability (md), K_l is liquid permeability (md), b is Klinkenberg constant (Pa). P_m =1/2(P_{in}+P_{out}) is average pore pressure (MPa).

3. Results and Discussion

The pressure dependences of gas permeability are shown in Fig.3 and Fig.4 for dry Kimachi sandstone obtained by N_2 gas and CO_2 gas, respectively. It is seen that the relationship between the permeability K_g and the inverse of average pore pressure 1/P_m can devided into two regions; Region1 and 2.In region1 (P_m ≤2MPa), the permeability is inversely proportioned to the average pore pressure and the pressure dependence can be described by Klinkenberg effect. Klinkenberg effect is the phenomenon that gas permeability is higher than liquid permeability, which is attributed to slip flow between gas molecules and walls[3]. For Region (P_m ≥ 2 MPa), the measured permeability has been shown to increase with increasing pressure, deviating from the trend of Klinkenberg effect. The increasing trend in the permeability may be possibly explained either by volume expansion of flow path due to the reduction of effective confining pressure or by the transition from laminar flow to turbulent flow. In actual CO_2 injection sites(~1km),the estimated injection pressure is in the range of about 10 MPa-20 MPa. The pressure condition at real field is shown in a shaded area of Fig.5. Our results indicate that it is reasonable to extrapolate the experimental data (Region 1) to the pressure condition at actual fields. This result suggests that the absolute permeability gives an appropriate value for the actual field conditions. Based on this method, we can estimate absolute permeability of Kimachi sandstone. The absolute permeability obtained by CO_2 gas is 0.0442md, and 0.0444md, N_2 gas. As you can see from this result, absolute permeability obtained by CO_2 gas and N_2 gas was almost the same.

4. Concluding remarks

In this study, in order to better understand the flow of injected CO_2, the pressure dependence of gas permeability for dry Kimachi sandstone was evaluated by controlling inlet pressure and outlet pressure. The results show that pressure dependence of permeability exhibits two trends. The pressure dependence in the relatively low pressure region(P_m ≤ 2MPa) can be explained by Klinkenberg effect, and the permeability in higher pressure region(P_m ≥ 2MPa) increases with increasing pressure. The absolute permeability obtained by extrapolating the pressure dependence in Region1 may provide an appropriate value for the analysis of CO_2 injection. Moreover, the absolute of CO_2 gas permeability calculated based on this method was almost the same as N_2 gas.

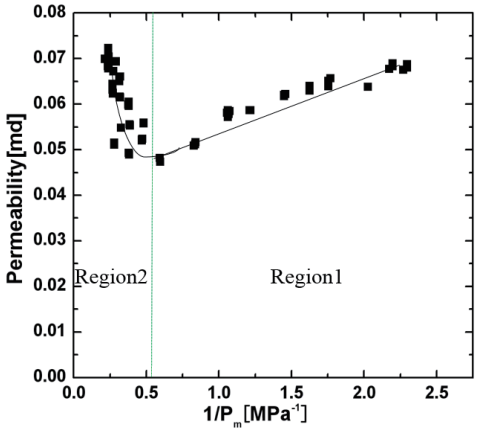

Fig.3 Relationship between CO_2 permeability and inverse of average pore pressure.

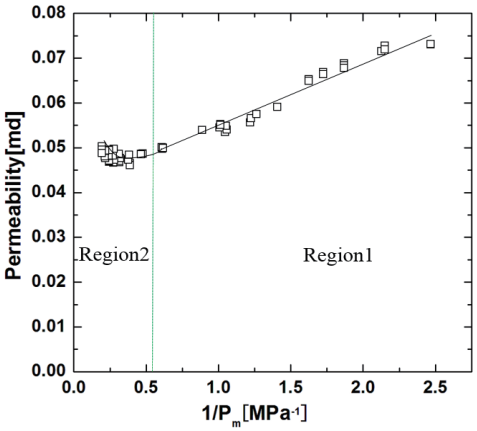

Fig.4 Relationship between N_2 permeability and inverse of average pore pressure.

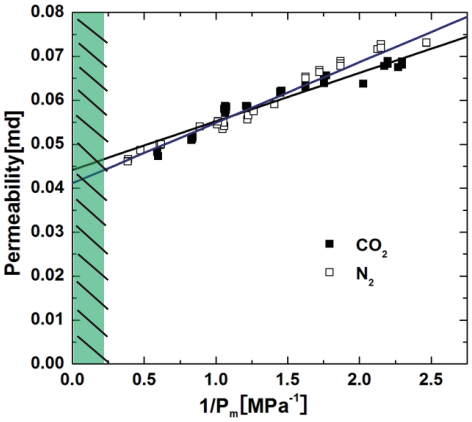

Fig.5 Comparison of experimental data and assumed actual filed conditions.

References

[1] IPCC, “Introduction (Chapter 1), Special Report on Carbon Dioxide Capture and Storage”, (2005), 53-72.
[2] S.Bachu, CO_2 storage in geological media : “Role, means, status, and barriers to deployment” Progress in Energy and Combustion Science,.34,(2008), 254-273.
[3]Tanikawa *et al*., “Klinkenberg effect for gas permeability and its comparison to water permeability for porous sedimentary rocks” Hydrology and Earth System Science Discussion 3, (2006), 1315-1338

Tenth International Conference on Flow Dynamics
November 25-27, 2013, Sendai, Miyagi, Japan

Numerical Modeling of ECT Signals for Fatigue Crack

Hao Feng[1], Ryoichi Urayama[2], Shejuan Xie[2], Tetsuya Uchimoto[2] and Toshiyuki Takagi[2,*]
[1]Graduate School of Engineering, Tohoku University, Japan
[2]Institute of Fluid Science, Tohoku University, Japan
[*]Corresponding author, Toshiyuki Takagi, E-mail: takagi@ifs.tohoku.ac.jp

ABSTRACT

This study evaluates the numerical modeling of fatigue cracks from the viewpoint of eddy current simulations. Three fatigue cracks are artificially introduced into austenitic stainless steel plate measuring 19mm in thickness using a four-point bending method, and then eddy current inspections are conducted to gather eddy current signals. Subsequent numerical simulations model each crack as an elliptical region with a fixed width and the region is surrounded by a rectangular magnetic layer which simulates the martensite transformation effect due to the bending moment.

1. Introduction

In this paper, we discussed the cyclic stress effect on the permeability of specimen which is made of austenitic stainless steel by the crack formation process using a four point bending method. The bending moment tortures fatigue crack section, and martensite transformation may occur in vicinity of crack region [1], this transformation increases the permeability in the vicinity of crack section. The martensite transformation also can be reversed by heating the specimen, so the permeability may decrease to normal. The fatigue crack is modeled as an insulating wall [2], which is validated in part by several groups reporting success in sizing fatigue cracks appearing in a thin structure [3].

The objective of this paper is, firstly to confirm the martensite transformation, secondly to get the equivalent widths of the crack and martensite layer around the crack, and lastly to get the relative permeability of martensite layer.

2. Specimen and Method

2.1 Preparation of specimens

The material of the specimen is AISI316 and the shape is rectangular with length 300mm, width 75mm, and thickness 20mm. The four point bending fatigue experiment was performed on the fatigue test equipment of INSTRON 8802. Three specimens with 3 different cracks were prepared. After that each specimen was heated in electric furnace with temperature 600 Celsius for 24 hours.

2.2 Eddy current inspection and destructive test

Before and after heat treatment, eddy current inspection was conducted with self-inductance and self-comparison pancake-type probe respectively. The outer diameter of probe is 5mm, inner diameter 2mm, and height 3mm. The frequency used in experiment is 50 kHz. The scanning line was perpendicular to the crack in the middle as shown in Fig.1. Destructive test was performed to evaluate the depth of the cracks. The depth and length of the cracks was shown in Table 1.

Table1. Depth and length of cracks.

	Depth	Length
No.1	4.1mm	10.5mm
No.2	2.5mm	9.3mm
No.3	0.9mm	8.3mm

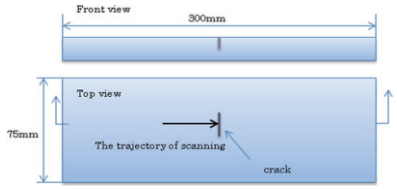

Fig.1. Diagraph of model used in the simulation and trajectory of scanning

2.3 Numerical simulation

Numerical simulations were carried out to evaluate the equivalent width of cracks and permeability change in the vicinity of the crack qualitatively. The code employed in the simulation is based on finite element method using A_r formulation [4]. The number of element in the simulation is 22,750. In the simulation model, the crack region was discretized with zigzagged shape similar to an ellipse. The trajectory of scanning is a line perpendicular to the length of the crack as shown in Fig.1. The conductivity of specimen in the simulation was 1.35×10^6 S/m and relative permeability was 1. The region modeling a crack with an insulating wall which has no conductivity has a constant width, and the region of martensite transformation is modeled by a magnetic layer surrounded the crack with fixed width. The relative permeability of the layer is changed in the range of 1.0, 1.05, 1.1, 1.15, 1.2, 1.25, 1.3, 1.35, and 1.4.

The equivalent widths of crack and magnetic layer used in the simulation model are shown in Table 2.Through fixing the equivalent width of crack and magnetic layer we can evaluate the permeability of magnetic layer to confirm the occurrence of martensite transformation. Whereas numerical simulations using the code considered only these parameters, subsequent numerical evaluation finds the difference between the permeability of magnetic layer before and after the heating process.

Table2. Equivalent width of cracks and magnetic layers.

	Equivalent width of crack	Equivalent width of magnetic layer
No.1	0.1mm	0.5mm
No.2	0.08mm	0.4mm
No.3	0.06mm	0.3mm

3. Results and Discussion

The signals obtained in the experiment and simulations are shown in the Figs.2, 3 and 4. The signals were calibrated using the same amplitude expansion factor and the phase rotation angle. The factor and the angle were decided by the comparison between calibration slit signals and numerical simulation results. The two slits used in this calibration were 0.5mm in width, and 1mm and 2mm in depth respectively. The frequency was set as 50 kHz.

In Fig.2 the experimental result of after heating process is approximately matched the simulation result of relative permeability equaling 1. While the result of before heating process is matched with simulation result of relative permeability equaling 1.2. This result is also similarly got from the Fig.3 and Fig.4 about the signal of crack No.2 and No.3 respectively. Before the heating process the value of permeability of magnetic layer is larger than the one after heating which approximately equal 1, the No.1 crack is about 1.2, No.2 crack is 1.25, No.3 crack is 1.15. These results shows that in the process of four-point bending experiment, the cyclic stress has the effect to cause the occurrence of the martensite transformation in the vicinity of crack. From the results, we can also find that the experiment value was a little lower than the simulation one. We assume that the crack region which was simulated by an insulating wall may have certain conductivity because a little fraction of the crack region was attached with each other, so the impedance change is a little lower than the simulation results.

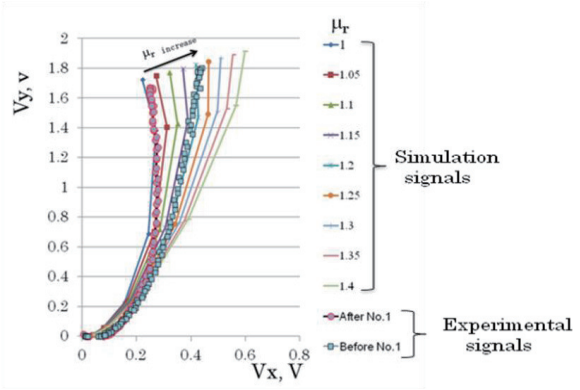

Fig.2. Eddy current signals in the experiment and simulation of No.1 crack.

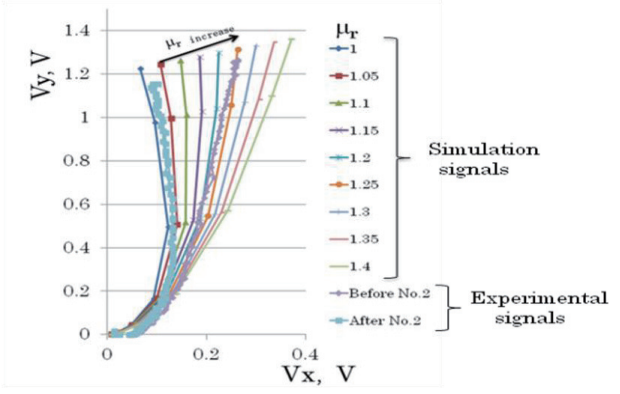

Fig.3. Eddy current signals in the experiment and simulation of No.2 crack.

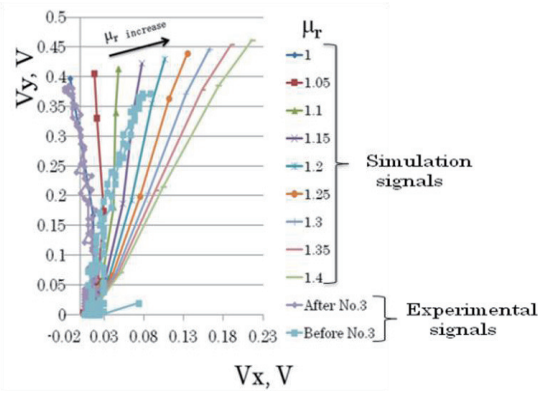

Fig.4. Eddy current signals in the experiment and simulation of No.3 crack.

4. Summary

This study evaluated cyclic stress effect on martensite transformation in the vicinity of crack during the formation process of fatigue crack from the viewpoint of eddy current simulation. From the comparison of experiment and simulation results the occurrence of martensite transformation surrounding the crack region is verified. However, it is difficult to evaluate the exact effect of the martensite transformation quantitatively because the relationship between the width and relative permeability of martensite layer is not determined. In order to get more information about the influence of conductivity and relative permeability of the crack region to eddy current signals, more studies are needed in the future.

5. Acknowledgement

This work was partly supported by the JSPS Core-to-Core Program, A. Advanced Research Networks, “International research core on smart layered materials and structures for energy saving”.

References

[1]T. Uchimoto, T. Takagi, K. Ohtaki, Y. Takeda and A. Kawakami. International Journal of Applied Electromagnetics and Mechanics Vol. 39, 2012, pp. 261–268.

[2]N. Yusa, S. Perrin, K. Mizuno, K. Miya. NDT&E Int Vol. 40, 2007, pp. 577-83.

[3]N. Yusa, L Janousek, M. Rebican, Z. Chen, K. Miya, N. Chigusa, H. Ito. Mucl EngDes Vol. 236, 2006, pp. 1852-9.

[4]T. Takagi, M. Hashimoto, H. Fukutomi, M. Kurokawa, K. Miya, H. Tsuboi, M. Tanaka, J. Tani, T. Serizawa, Y. Harada, E. Okano and R. Murakami. Int. J. of Applied Electromgnetics in Materials, vol. 5, pp.149-162, 1994.

Tenth International Conference on Flow Dynamics
November 25-27, 2013, Sendai, Miyagi, Japan

Gravity Assists and Associated Phase-Space Flows in Space Mission Design

Kenta Oshima, Tomohiro Yanao
Graduate School of Fundamental Science and Engineering, Waseda University, Tokyo 169-8555, Japan.
kenta-oshima@akane.waseda.jp

ABSTRACT

In recent space missions, design of low-cost trajectories has increased its importance. Gravity assist is one of the most effective techniques to achieve low-cost transfers of spacecrafts by harnessing the gravity of celestial bodies in multi-body dynamics. While recent studies have exploited gravity assists in the three-body problem to construct low-cost trajectories, the present study proposes a novel type of gravity assist in the four-body problem. Using this technique, we extract transfer trajectories connecting unstable periodic orbits of different energies based on the analysis of phase-space flows. We discuss their possible use in real space missions.

1. Introduction

Design of low-cost trajectories has been one of the central issues in recent space missions. The circular restricted three-body problem (CR3BP) is often used to find nominal reference trajectories. By virtue of the autonomous nature of the CR3BP, one can exploit useful dynamical objects such as invariant manifolds to design mission trajectories in the CR3BP [1].

Not only invariant manifolds, but also gravity assists provide another option for the design of low-cost transfer trajectories. Many recent studies have investigated gravity assists in the CR3BP and proven their usefulness in real space missions [2].

In the present study, on the other hand, we explore gravity assists in the four-body problem and suggest novel effects that are hardly achieved in the CR3BP. Although the non-autonomous nature of the four-body problem poses novel challenges, we make use of this non-autonomous nature in turn to change the spacecraft's energy.

2. Gravity Assist in the Four-Body Problem

Throughout this study, we work on the Sun-Earth-Moon-spacecraft four-body system modeled by the bicircular model (BCM) [1]. Fig. 1 shows the schematic of the BCM in the Sun-Earth rotating frame.

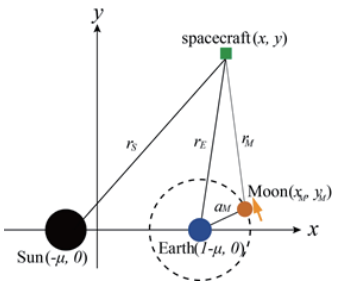

Fig. 1. Configuration of the BCM in the Sun-Earth rotating frame.

The difficulty arises from the fact that the BCM is a non-autonomous system. For example, energy of the spacecraft can be expressed as

$$E_{BCM} = \frac{1}{2}(\dot{x}^2+\dot{y}^2) - \frac{1}{2}(x^2+y^2) - \frac{1-\mu}{r_S} - \frac{\mu}{r_E} - \frac{m_M}{r_M}, \quad (1)$$

where r_M is the distance between the spacecraft and the Moon, which makes the energy time-dependent.

Indeed, this time-dependent nature due to the Moon's motion can be harnessed to change the energy of the spacecraft, which is the key idea for the gravity assists in the present four-body problem. Fig. 2(a) shows an example trajectory that receives gravity assist by the Moon. This trajectory starts from the Earth (blue point), approaches the Moon's orbit (pink), receives the gravity assist by the Moon, and leaves the Moon's vicinity. Fig. 2(b) shows the time evolution of the spacecraft's energy along the trajectory in (a). The red curve shows the energy defined in Eq. (1), and the blue curve shows the energy of the Sun-Earth-spacecraft CR3BP. Note that this energy, which never changes in the CR3BP alone, has changed (increased) by the Moon's perturbation. This is a novel effect obtained by working in the four-body problem.

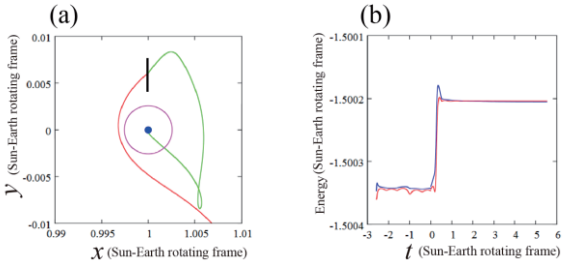

Fig. 2. (a) An example trajectory receiving gravity assist by the Moon. (b) Change in energy along the trajectory in (a). The time origin, t=0, is set at the time when the spacecraft crosses the thick black line in (a).

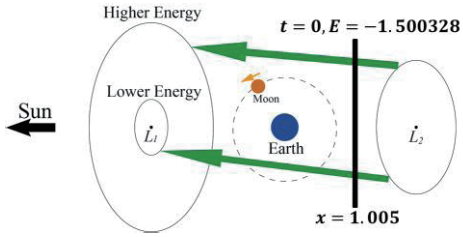

Fig. 3. Poincaré section (thick black line) that captures phase-space flows between unstable periodic orbits of different energies.

3. Transfer between Orbits of Different Energies

As a practical application of the above framework of gravity assist, we construct transfer trajectories connecting unstable periodic orbits of different energies in the BCM. The method uses the Poincaré section as schematically shown in Fig. 3: There exist families of unstable periodic orbits around the Sun-Earth Lagrange points, L_1 and L_2. We call these periodic orbits "L_1 Lyapunov orbits" (left) and "L_2 Lyapunov orbits"

(right) respectively. Koon *et al.* [1] investigated transfers between such unstable periodic orbits of the same energies. Recently, Davis *et al.* [3] investigated transfers between unstable periodic orbits of different energies using fuel consumption. As a next step to these studies, we explore here nominal transfers between the Lyapunov orbits of different energies by harnessing gravity assists by the Moon without fuel consumption.

Fig. 4 shows the phase-space flows of the BCM extracted on the Poincaré section introduced in Fig. 3. The green points correspond to the trajectories that pass through the L_2 Lyapunov orbit upon backward propagation from the Poincaré section. The red points correspond to the trajectories that pass through L_1 Lyapunov orbits upon forward propagation from the Poincaré section. The black/blue points are parts of the red points corresponding to the trajectories resulted in large increase/decrease in energy.

Due to the asymptotic nature of the unstable and stable manifolds of the Lyapunov orbits, the boundaries of the green/red regions are asymptotic to the L_2/L_1 Lyapunov orbits. Thus, the intersections of the boundaries of green, red, black/blue regions should correspond to the heteroclinic connections between Lyapunov orbits of largely different energies. We investigated such intersections in Fig. 4 and obtained transfer trajectories from the L_2 Lyapunov orbit to L_1 Lyapunov orbits harnessing Moon's gravity assists as shown in Fig. 5. Note that different sizes of the Lyapunov orbits indicate different energies.

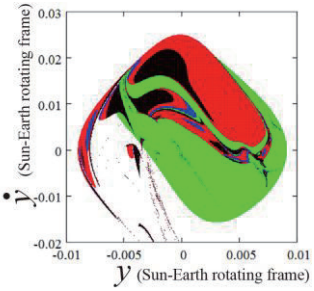

Fig. 4. Poincaré section introduced in Fig. 3, visualizing phase-space flows from the L_2 Lyapunov orbit to the L_1 Lyapunov orbit.

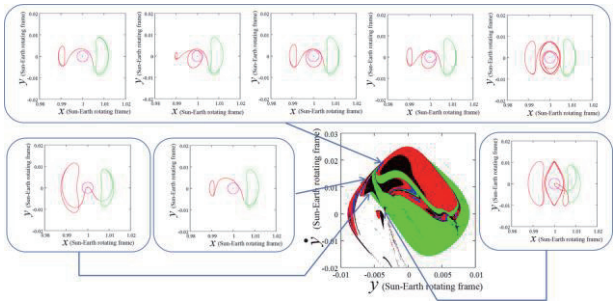

Fig. 5. Heteroclinic connections between Lyapunov orbits of different energies. The trajectories are integrated forward (red) and backward (green) from the Poincaré section.

A similar method can be adopted to find homoclinic connections. Fig. 6 shows the phase-space flows on the same Poincaré section introduced in Fig. 3, which visualizes the phase-space flows from L_2 to L_2 Lyapunov orbits. Fig. 6 also shows the extracted transfer trajectories connecting L_2 Lyapunov orbits of largely different energies by harnessing Moon's gravity assists. The green points correspond to the trajectories that pass through the L_2 Lyapunov orbit upon backward propagation. The red points correspond to the trajectories that pass through L_2 Lyapunov orbits upon forward propagation. The black/blue points are parts of the red points corresponding to the trajectories resulted in large increase/decrease in energy.

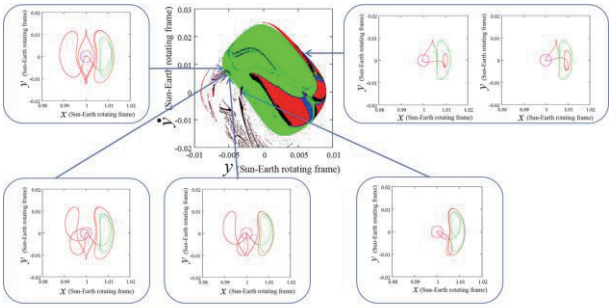

Fig. 6 Homoclinic connections between Lyapunov orbits of different energies. The trajectories are integrated forward (red) and backward (green) from the Poincaré section. There are apparent intersections of boundaries that belong to the region that trajectories cannot exist energetically.

4. Concluding Remarks

This study has explored gravity assists in the Sun-Earth-Moon-spacecraft four-body system on the basis of the bicircular model. We have shown that the Moon's perturbation can be harnessed to change the spacecraft's energy, which can hardly change in the Sun-Earth-spacecraft CR3BP alone.

As applications, we have proposed a method of finding nominal transfer trajectories connecting unstable periodic orbits of different energies. We have found both the heteroclinic and homoclinic connections by visualizing phase-space flows on the Poincaré section. These transfer trajectories would broaden our options in real space missions. We also expect that these transfer trajectories could be useful in rescue missions from, for example, a failure in the main engine of a spacecraft.

Finally, we plan to find out essential phase-space structures that mediate gravity assists in the four-body problem. Recently, it has been shown that resonance transition plays a dominant role in the gravity assists in the CR3BP [4]. Such fundamental mechanism could contribute to the efficient design of gravity assists.

References

[1] W. S. Koon, M. W. Lo, J. E. Marsden, S. D. Ross, Dynamical Systems, the Three-Body Problem and Space Mission Design, (2008).

[2] S. D. Ross, D. J. Scheeres, SIAM J. Applied Dynamical Systems, **6** (2007), pp. 576-596.

[3] K. E. Davis, R. L. Anderson, D. J. Sheeres, G. H. Born, Celest. Mech. Dyn. Astr., **107** (2010), pp. 471-485.

[4] R. L. Anderson, M. W. Lo, 21st AAS/AIAA Space Flight Mechanics Meeting (2011), pp. 11-125.

Tenth International Conference on Flow Dynamics
November 25-27, 2013, Sendai, Miyagi, Japan

Flutter Analysis of Deployable Wing using Multibody Dynamics

Hiroki Sakiyama and Kanjuro Makihara
Department of Aerospace Engineering, Tohoku University, Sendai, Japan
sakiyama@ssl.mech.tohoku.ac.jp

ABSTRACT

Absolute nodal coordinate formulation (ANCF) is widely used in flexible multibody dynamics. This paper proposes the application of ANCF to the subsonic aeroelastic analysis of an imaginary flat plate wing. The wing is modeled as a flexible beam at its elastic axis which undergoes torsional deformation around the elastic axis. Beside the bending of the beam in ANCF, we added one more degree of freedom to each node to represent torsional angle. Two-dimensional unsteady aerodynamics is adapted to represent the lift and pitching moment of the oscillating wing section. It is found that such formulation was successful.

1. Introduction

DARPA and NASA are developing concepts of morphing wings in order to improve flight performance and extend flight envelop (ref.[1]). One example of morphing wing is a deployable wing, as shown in Fig 1, whose span consists of several "smaller" wings that can be folded into a compact size, and then stretched out in a full-span wing. Although several efforts have been made to develop tools to analyze aeroelastic problems of morphing wings, it is still not adequate (ref.[1]).

Multibody dynamics is computational tool to solve dynamics of a system that consists of several flexible and rigid bodies, hence may be suitable for dynamic analysis of a deployable wing.

This report aims to analyze subsonic aeroelastic problem that may occur on aluminum flat plate wing in morphing from state (a) to state (b) as shown in Fig. 1. For this purpose, the application of absolute nodal coordinate formulation, which is the major method in flexible multibody dynamics, to aeroelastic analysis of a flat plate wing is presented in this report.

2. Absolute Nodal Coordinate Formulation

Fundamental concept of using absolute nodal coordinate systems is to represent the location of an arbitrary point on the deformed beam element directly by inertial coordinate system. In Fig. 2, coordinate system *O-XY* is the absolute coordinate system or inertial coordinate system, and a beam element is shown. The beam element has two nodes, A and B. Each node has four degrees of freedom, making 8×1 generalized coordinate vector **e** in one element as below.

$$\mathbf{e}=\begin{bmatrix}e_1 & e_2 & e_3 & e_4 & e_5 & e_6 & e_7 & e_8\end{bmatrix}^{\mathrm{T}}$$

e_1 and e_2 are *X*- and *Y*-coordinates of point A in *O-XY* system, respectively, and e_3 and e_4 are their derivatives by element's local coordinate system *x*. e_5 to e_8 are those of point B. Let 2×8 **S** be a shape matrix, then the position vector **r** of arbitrary point P on the deformed beam is interpolated as **r**=**Se** (ref.[2]). **S** is independent of time *t*, while **e** is dependent on *t*.

Defining *T* as kinetic energy of the beam element and *U* as elastic energy due to stretching and bending, the equation of motion is obtained using Lagrangean method as

$$\frac{d}{dt}\frac{\partial T}{\partial\dot{\mathbf{e}}}=\mathbf{M}\ddot{\mathbf{e}},\ \mathbf{Q}_k\equiv\frac{\partial U}{\partial\mathbf{e}}\ \therefore\mathbf{M}\ddot{\mathbf{e}}=\mathbf{Q}_g-\mathbf{Q}_k(\mathbf{e}). \quad (1)$$

The mass matrix **M** is a constant matrix, while the elastic force $\mathbf{Q}_k$ is a highly nonlinear function of **e**. This is because, in Fig. 2, the beam's local *x*-axis is defined by generalized coordinates **e**, thus tangential deflection u_t and longitudinal displacement u_l of point P in the local frame are also functions of **e**. Despite its complexity, $\mathbf{Q}_k$ is valid in both small and large deformation problems of beam in large translational and rotation motion. Moreover, if we assume that deflection is small and stretching is negligible, the elastic force can be expressed by the product of a constant stiffness matrix **K** and **e** as $\mathbf{Q}_k$=**Ke**. $\mathbf{Q}_g$ is the generalized external force vector.

In multibody dynamics, constraints among bodies or boundary conditions are collected into constraint vector equation as $\mathbf{\Phi}=\mathbf{0}$. Using Langrange multiplier method, the constraint equation and Eq. 1 are integrated into the following differential algebraic equation (DAE).

$$\begin{pmatrix}\mathbf{M} & \mathbf{\Phi}_{\mathbf{q}}^{\mathrm{T}}\\ \mathbf{\Phi}_{\mathbf{q}} & \mathbf{0}\end{pmatrix}\begin{bmatrix}\ddot{\mathbf{q}}\\ \boldsymbol{\lambda}\end{bmatrix}=\begin{bmatrix}\mathbf{Q}_g-\mathbf{Q}_k\\ \boldsymbol{\gamma}\end{bmatrix}. \quad (2)$$

Here, $\boldsymbol{\lambda}$ is lagrange's multiplier and $\boldsymbol{\gamma}$ is the vector obtained by differentiating $\mathbf{\Phi}=\mathbf{0}$ twice by time *t*.

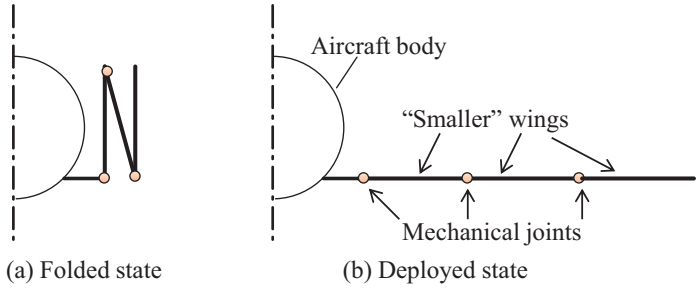

Fig. 1 Deployable wing

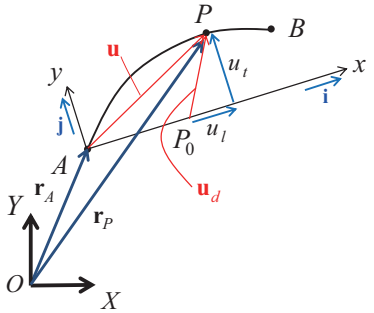

Fig. 2 Beam element in ANCF

3. Proposal of Application of ANCF to Aeroelastic Analysis

ANCF introduced above is used to describe the bending motion of a root-fixed slender wing. The slender wing is considered as a small-deformation beam which undergoes torsional deformation around its elastic axis, i.e., the center of rotation.

In order to handle torsion, we need to add one more degree of freedom to each node to represent torsional angle at the node. In Fig. 2, e_9 is added as torsional angle at point A and e_{10} at point B. Torsional angle at arbitrary point on the beam element is interpolated by first order polynomials as $\phi = \mathbf{S}_t[\phi_9 \quad \phi_{10}]^{\mathrm{T}}$ where $\mathbf{S}_t$ is the shape matrix. Mass matrix and stiffness matrix of torsional motion is given by

$$\mathbf{M}_t \equiv \int_0^L J\mathbf{S}_t^{\mathrm{T}}\mathbf{S}_t dx,\ \mathbf{K}_t \equiv \int_0^L GK\left(\frac{\partial \mathbf{S}_t}{\partial x}\right)^{\mathrm{T}}\left(\frac{\partial \mathbf{S}_t}{\partial x}\right)dx$$

Here, J is the mass moment of inertia around the elastic axis per unit length, and GK the torsional stiffness. Both $\mathbf{M}_t$ and $\mathbf{K}_t$ are constant matrices. Those matrices and e_9 and e_{10} are added to Eq. 1 in suitable manner.

From unsteady aerodynamics of a two-dimensional oscillating wing, when harmonic oscillation is assumed, lift L and pitching moment M around center of rotation is written as (ref. [3])

$$L \equiv qc(L_h h + L_\alpha \alpha),\ M \equiv qc^2(M_h h + M_\alpha \alpha),$$

where h is the height of heaving motion, α the angle of attack, q the dynamic pressure and c the chord length. L_h, L_α, M_h and M_α are complex functions of reduce frequency k, containing Theodorsen function. In the slender wing problem now being considered, L and M are supposed to act on the beam element as in Fig. 3, where θ_0 is the angle between the beam's local x-axis and inertial X-axis. From geometric relationships, generalized aerodynamic force is obtained as

$$\mathbf{Q}_g = \int_0^L \mathbf{S}_{\mathrm{total}}{}^{\mathrm{T}}\begin{bmatrix} q_x \\ q_Y \\ q_T \end{bmatrix} dx = q\mathbf{Q}_{aero}(k,\mathbf{e})\mathbf{e},$$

$$\begin{bmatrix} q_X(x) \\ q_Y(x) \\ q_T(x) \end{bmatrix} = \begin{bmatrix} -L\sin\theta_0 \\ L\cos\theta_0 \\ M_T \end{bmatrix} - qc\begin{bmatrix} 0 & -L_h\sin\theta_0 & -L_\alpha\sin\theta_0 \\ 0 & L_h\cos_0 & L_\alpha\cos\theta_0 \\ 0 & cM_h & cM_\alpha \end{bmatrix}\begin{bmatrix} u_l \\ u_t \\ \phi \end{bmatrix}.$$

Here, $\mathbf{S}_{total}$ is the total shape matrix, and $\mathbf{Q}_{aero}$ is called aerodynamic transfer matrix. Total equation of motion is finnaly obtained as

$$\mathbf{M}\ddot{\mathbf{e}} + \mathbf{K}\mathbf{e} = q\mathbf{Q}_{aero}(k,\mathbf{e})\mathbf{e}\,. \tag{3}$$

Since harmonic motion $\mathbf{e} = \hat{\mathbf{e}}e^{i\omega t}$ is assumed in the unsteady aerodynamics, substituting this relationship to above equation of motion results in

$$\left[-k^2\left(\frac{U}{b}\right)^2\mathbf{M} + \mathbf{K} - q\mathbf{Q}_{aero}(k,\mathbf{e})\right]\hat{\mathbf{e}} = \mathbf{0}\,. \tag{4}$$

This is expressed in frequency domain, and at the moment for one-body root fixed wing now considered, p-k method is used instead.

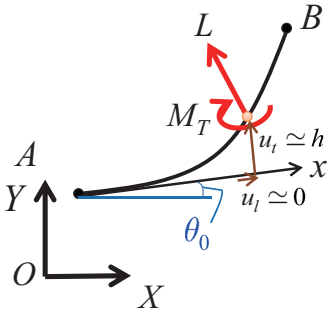

Fig. 3 Aerodynamic force acting on a beam element

4. Simulation result

The wing to be considered is flat aluminum plate wing with a thickness of 1.0 cm, a chord of 0.5m, a half span of 2.0m, Young's modulus of 70GPa and Poisson ratio of 0.3.

Figure 4 shows the result of p-k method of the flat wing problem. $\hat{p}$ is plotted on Gaussian plane. In this plane, the negative real part of $\hat{p}$ shows aerodynamic damping, and the positive means divergence of oscillation or flutter. When a line crosses the imaginary axis, this point is considered as a starting point of flutter. The calculated result of this point is k=0.053 and U=79.4m/s. This corresponds to an angular frequency of ω =16.9Hz, and the eigenmode shows the first bending mode with some torsional displacements.

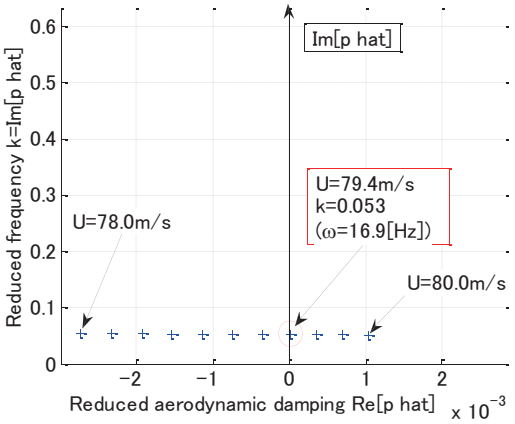

Fig. 4 $\hat{p}$ on Gussian plane

5. Conclusions

Application of absolute nodal coordinate formulation with an additional degree of freedom for torsional deformation to subsonic flutter analysis is shown, and calculation was done successfully for the case of one-body wing. Further development of the flutter analysis of multibody wing motion is in progress.

References

[1] D.D. Lu et al., RTO-MP-AVT-168 Morphing Vehicle April 2009, pp.(26-1)–(26-27)

[2] A. Shabana, Dynamics Of Multibody System, 2005

[3] D. Borglund, D. Eller, Aeroelasticity of Slender Wing Structures in Low-Speed Airflow, 2012

Tenth International Conference on Flow Dynamics
November 25-27, 2013, Sendai, Miyagi, Japan

Study on the Reduction of Wind Pressure of Solar Panels

Yusuke Sato, Mingyu Sun
School of Aerospace Engineering, Institute of Fluid Science,
Tohoku University, 2-1-1 Katahira, Aoba-ku, Sendai,980-8577 Japan
sato@shock.ifs.tohoku.ac.jp

ABSTRACT

This study is for researching and designing the new models of solar panels which reduces wind pressure. This short paper shows two dimensional researches of wind pressure about three solar array on the ground using CFD software Fluent. The three solar array are board type, box type, and box with round-top type. We confirm that a top end of arrays have more wind pressure than other part.

1. Introduction

Recently, natural energy occupies the interest of provisions about environmental problems. Especially, solar power generation attracts people's attention from a point of view about easy maintenance and no restriction on places. So, large scale solar power generation called mega solar power plants are under constructions all around the world.

However, those constructions are not easy because it need rigid frameworks in order to resist wind pressure. Naturally the construction costs are high and this fact prevents mega solar plants from being built.

For the above reasons, this study aims at researching characteristic of wind pressure on solar panels or arrays, and designing epoch-making models of solar power form. Successes of coordination between reduction of wind pressure and electrical efficiency contribute to the development of solar power generation and environmental problems.

This paper picks up two dimensional problems. We suppose that solar arrays are located on the ground and front flow and back flow run into there. In fluid dynamics, a streamline shape reduces air resistance. Therefore we simulate wind pressure on generic solar array form and find strong pressure point from the simulation. Then we compare generic solar array form and experimental form making strong pressure point into round shape in a point of view about minimization of wind pressure.

2. Method

In this research, we made three models for Fluent. Figure 1 shows mesh models of three array or panel.

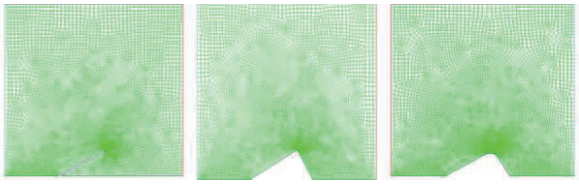

(a) board (b) box (c) round-top
Fig.1 Three mesh models of solar array

The number of grids is about 7000 to 9000 according to mesh type. In Fluent simulation, front flow and back flow which is ideal flows of 30 m/s (reference wind speed of Sendai [1]) run into these mesh models. In above pictures front flow run from left and back flow is the opposite. The angle of Front board is 30 degrees in fig. 1, and back side's is 120 degrees in fig. 1(b)(c).

Wind pressure P_w is in proportional to dynamic head [2].

$$P_w \propto \frac{1}{2}\rho v^2 \qquad (1)$$

Hence, contours of dynamic head are useful for finding strong wind pressure zones. We get contours of dynamic head about three mesh types for two cases which is front and back flow.

3. Results and Discussion

First, Figure 2 shows contour of dynamic head about board type.

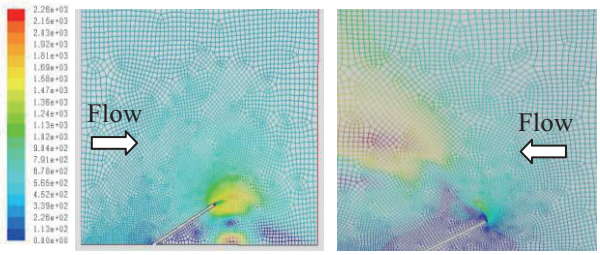

(a) front flow (b) back flow
Fig. 2 Contour of dynamic head about board type

In front flow case, the top end has more dynamic head than other parts. In back flow case, the flow exfoliates and becomes instable.

Second, Figure 3 shows contour of dynamic head about box type.

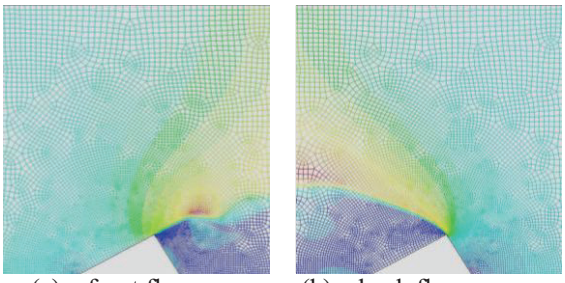

(a) front flow (b) back flow
Fig. 3 Contour of dynamic head about box type

In the both cases, the top end has more dynamic head and the flow is stable. The flow goes upwards through box face. So, this type may also reduce wind pressure of the back row arrays in solar plant situation.

From fig.2 and fig.3, we found that strong wind pressure point is the top end of solar arrays. Therefore, we make the top end of box model into streamline shape, that is box with round top model. A curvature of this type's roundness is chosen suitably.

Figure 4 shows contour of dynamic head about box with round top type.

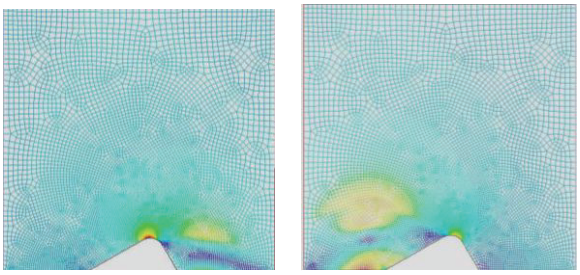

(a) front flow (b) back flow

Fig. 4 Contour of dynamic head about round top type

In front and back flow cases, there is strong wind pressure point locally. An area of zones of high dynamic head looks smaller than other types. However, the flow's exfoliation shifts backwards, then backwards flow goes down and may have an impact on the back row arrays.

Table 1 shows values of dynamic head at the top end about all types and all cases.

Table 1: Dynamic head at the top end

	Board	Box	Round top
Front flow	2139.9	1076.9	2643.0
Back flow	509.07	995.82	1847.3

Dynamic head: [Pa]

Round top type has the strongest point of dynamic head and the weakest is box type in front flow case. In back flow case, board type has the weakest dynamic head of the top end and the strongest is round top.

But table 1 is for the values of local point. We couldn't decide the better model from table 1. Moreover, all types show vortexes in the backwards flow. In order to find a new model which reduces wind pressure, we need to know effects of vortex behavior on wind pressure [3].

4. Concluding remarks

In this research, we picked up two dimensional problems about wind pressure on the three models of solar panels or arrays using CFD software Fluent.

Then the following conclusions were made based on the numerical simulation presented here.

1) Board type array made the flow instable, but in back flow case, the top end point recorded minimum dynamic head which is in proportional to wind pressure.

2) Box type array made the flow stable, and the dynamic head is small relatively, furthermore, this type may reduce wind pressure of the back row arrays because the flow goes upwards through surface.

3) Box with round-top type recorded maximum dynamic head, but this is local point. The area of zones of high dynamic head is the smallest by an estimate. An adaption of round top type needs rational of fluid dynamics.

4) All contours of dynamic head showed vortexes in backwards flow. There is a need to research how the vortexes have an influence on array's surface or wind pressure.

This study is for designing a new model of solar array which reduces wind pressure. However, it is difficult to get idea about new model from this paper's result.

As future works, we should approach detailed simulation by Fluent, and get to know characteristics between wind pressure and solar array form. After that, we continue to challenge this problems expanding up to three dimensions.

References

[1] JIS C 8955, Design guide on structures for photovoltaic array, (2011)

[2] N. Takizawa, N. Okada, A. Iwasaki, Wind-tunnel Investigation of the Pressure Distribution and Deduced Characteristics of Semi-Circular Cylinder in the Vicinity of Critical Reynolds Number, Technical Report of National Aerospace Laboratory, TR-871(1985)

[3] T. Jimbo, D. Biswas, T. Nimoto, Wind Flow Simulation around Mega Solar Power Generation System Arrays to Predict Flow-Induced Lift Force Based on High-Order LES Turbulence Model, TOSHIBA Special Report , Vol.67 No.7, (2012)

Observation of Heat and Fluid Flow in the Cooling of Phase Change Material for Power Battery Thermal Management of Electric Vehicles

Kosuke Nonaka, Kazuhiro Kudo, Takashi Yamada and Naoki Ono
Shibaura Institute of Technology
3-7-5, Toyosu, Koto-ku, Tokyo, 135-8548, Japan
naokiono@shibaura-it.ac.jp

ABSTRACT

In lithium ion battery used for an electric vehicle, battery deterioration and possible thermal runaway by temperature rise of the battery cell, and drop of the battery output in low temperature are considered to be a big problem. This study is aimed at the development of the heat control technology that can keep the temperature of the battery cell at the most suitable temperature by using PCM(Phase change material) and heat pipes. We need to investigate the size, form, position and the number of most suitable heat pipes. We here report the fundamental results by performing the model experiment simulating lithium ion battery using a heater, and by observing the melting of PCM.

1.Introduction

In late years electric vehicles are in practical usage for high energy efficiency. The electric vehicle can be driven with the electric power from a variety of energy sources such as new energy. In addition, by saving electricity as chemical energy of the batteries at night, we can perform a peak shift of the electricity use. Therefore, the electric vehicle can utilize energy efficiently from the viewpoint of new energy and energy saving. In a battery used for an electric vehicle, the lithium ion battery is now used by many electric vehicles and attracts attention because it has the high electric capacity and the high output. However, in the case of electric charge and the discharge of the battery, the battery cell becomes hot, and the battery deterioration by the temperature rise is considered to be a big problem[1]. On the other hand, the battery output decreases when used at low temperature. Furthermore, by the temperature rise of the battery cell, there is a problem of the risk of the explosion of the battery cell in worst case. The temperature change of the battery cell and the efficiency of the battery by the cycle number of times are shown in Fig.1.

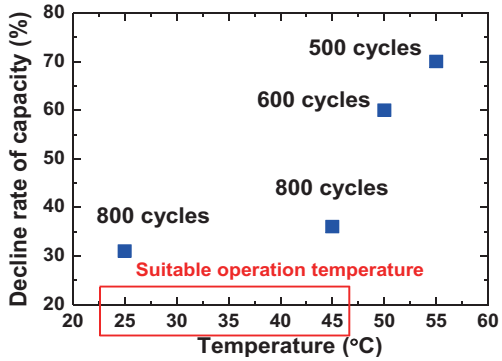

Fig.1 Capacity fade analysis of battery at different operation temperature[1]

For these problems, it is thought that the battery heat control technology is necessary, and that a battery cell can have longer life and safety by controlling a battery cell at the most suitable temperature.

This study is aimed at the development of the heat control technology that can keep the temperature of the battery cell at the most suitable temperature by using PCM (Phase change material)[2,3] as a thermal buffer and heat pipes for heat transport. By this heat transfer system, the heat of the battery cell is absorbed by latent heat of PCM and it is transported to heat sink by heat pipes and is radiated to the heat sink. By this heat control technology, we will develop an electric module which has high efficiency, safety, compactness and reduced cost. By the experiment, we will inspect the size, form, position and the number of most suitable heat pipes by making the heat transfer measuring equipment which simulated a battery module, and by performing the heat transfer measurement.

2. The outline of the experiment

As fundamental experiment here, the temperature change of PCM was observed using a ceramic heater. The paraffin which has thermal conductivity 0.2 W/(m・K) in melting point 49 degrees was used as PCM and the heat pipe which had 6mm of diameter and 200 mm of the lengths was used. In addition, an infrared camera and a K type sheath thermocouple were used for thermometry. The temperature distribution of the PCM surface was measured by the infrared camera. Temperature in PCM of the position of 5 mm, 11 mm, 15 mm, 20 mm and 25 mm from the heater was measured by the thermocouple. Under the conditions, the melting of PCM with or without heat pipe and the cooling methods of the heat pipe were compared. The experiment situation is shown in Fig.2.

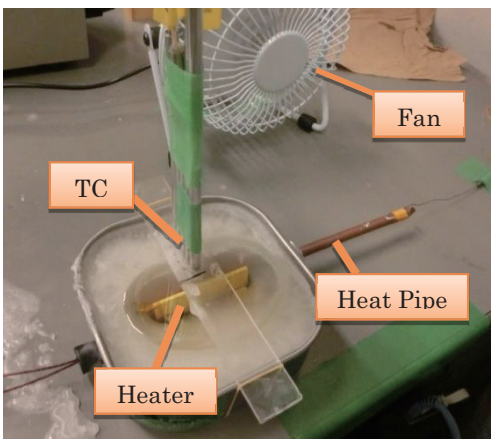

Fig.2 Experimental apparatus

The experiments were done with the electric heater of the similar size and shape of real lithium ion battery. Cylinder type lithium ion battery 18650 was simulated by covering a cartridge heater which has 16mm of diameter and 60 mm of the lengths, with aluminum of thickness 1 mm. In addition, laminating type lithium ion battery (290mm ×216mm) was simulated by covering a polyimide heater (97mm×72mm) of the size of 1/9 with aluminum of thickness 1mm. The heat release extent with the heat pipe was measured by a temperature change of the water of the heat sink. In this experimental device, the melting situations of PCM by changing the size, form, position and the number of the heat pipes were compared.

3. Results and Discussion

In the fundamental experiment using the ceramic heater, the images by the infrared camera of the surface temperature of PCM after 60 minutes from the start of heating is shown in Fig.3. Fig.3 shows three results of (a) when a heat pipe was not used, (b) when a heat pipe was used and it was cooled by air forced convection at the other end, (c) when a heat pipe was used and it was cooled by iced water at the other end.

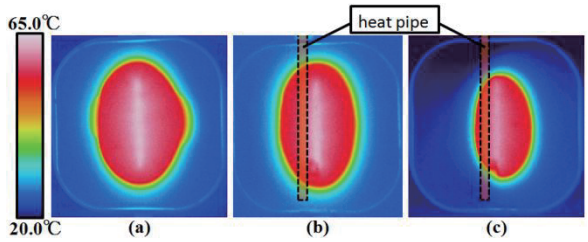

Fig.3 surface temperature of PCM after 60 minutes from heating

It was understood that the area where PCM was melted became larger in the order of (c), (b), (a). In addition, it was found that PCM of the same side of the heat pipe was hard to be melted.

Temperature for the time change in each position in PCM is shown in Fig.4 and Fig.5. Fig.4 shows the result when a heat pipe was not used and Fig.5 shows that when a heat pipe was used and it was cooled by air forced convection at the other end of the pipe.

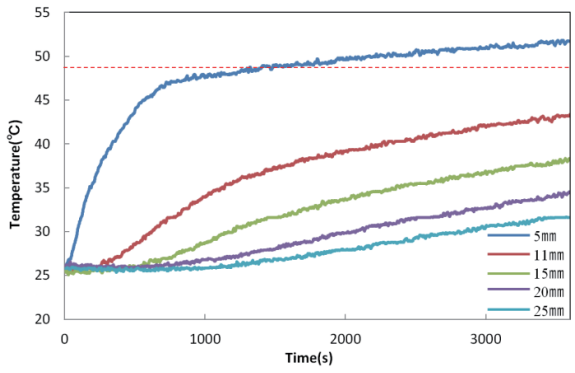

Fig.4 Temperature change in each position in PCM (heat pipe was not used)

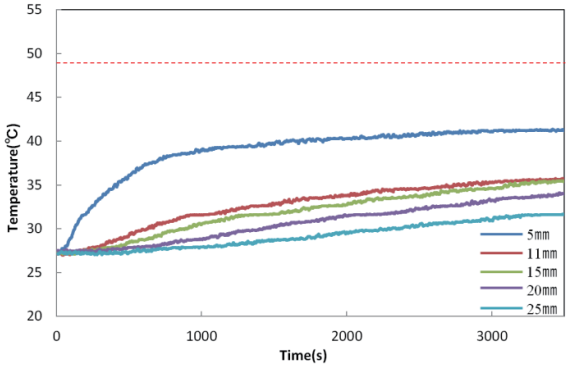

Fig.5 Temperature change in each position in PCM (a heat pipe was used and it was cooled by air forced convection at the other end)

When a heat pipe was used, the temperature rise was low and did not exceed a melting point in all positions. However, the temperature rise was remarkable and exceeded a melting point at a 5mm spot when a heat pipe was not used.

From these results, the PCM was cooled and delayed melting by inserting a heat pipe. Furthermore, it was confirmed that the melting of PCM when the heat pipe was cooled off in iced water than when it was cooled by air forced convection at the other end of the heat pipe.

4.Concluding remarks

(1)It was confirmed that the melting of PCM was restrained by using a heat pipe.
(2)It was suggested that the melting of PCM would be greatly affected by size, form, position and the number of the heat pipe and heat sink.

5.Future plans

(1) We will compare the results of using pure PCM (pure paraffin) and of using high heat conductivity PCM composite and so on.
(2)We will simulate practical situations of the lithium ion battery in detail to reproduce actual vehicle driving.
(3)We will make a heat pipe with glass and observe the internal flow when the heat pipe functions in PCM.

Acknowledgement

This research was supported by the strategic international cooperative program of JST in the field of highly-efficient energy utilization.

References

[1] P.Romadass “Capacity fade of Sony 18650 cells cycled at elevated temperatures” J.Power Sorces 112(2):614-620 2002.
[2] Guoqing Zhang, Yunyun Zhang, Zhonghao Rao “Phase Change Materials Coupled with Copper Foam for thermal Management of Lithium-Ion Battery” Advanced Science, Engineering and Medicine Vol.4 484-487 2012.
[3] X.Duan G.F.Naterer, Heat transfer in phase change materials for thermal management of electric vehicle battery modules, International Journal of Heat and Mass Transfer 53(2010), 5176-5182.

Prototype Experiment and Numerical Analysis of Processing a Thin Plate from the Molten Metal

Mitsutaka Umeta, Naoki Kondo and Naoki Ono
Shibaura Institute of Technology
3-7-5, Toyosu, Koto-ku, Tokyo, 135-8548, Japan
naokiono@shibaura-it.ac.jp

ABSTRACT

Silicon plate of 100μm thickness can be bent flexibly, which becomes valuable characteristic for practical usage. However, production of plate with less than 100μm has been difficult by conventional methods. In this study, we investigated a new horizontal pulling method using surface tension. We draw solidified thin plate from a slit of the crucible. This experiment is a prototype experiment using the metal with low melting temperature. We succeeded in obtaining minimum thickness of 100μm, although the process was not stable. We then mainly studied solid-liquid interface position and temperature control to obtain the process stability.

1.Introduction

Solar energy is one of the important sources as De-fossil fuel. Most of the solar batteries are made with silicon crystal plates, but the classical ribbon growth method provides plates with more than 200μm thickness [1]. Silicon plate with less than 100μm thickness can lead to flexible solar cells. Very thin solar cell can be installed on complex shape geometry. Our major objective in this study is to produce plate with less than 100μm thickness by a new method using surface tension.

2.Experiment method and apparatus

The seed was dipped into liquid metal in the crucible, and pulled horizontally. The liquid metal attaching to the seed was cooled down and was solidified in the air during the pulling. Heating at the top and cooling at the bottom of the crucible were imposed to restrain the buoyant convection and to control the melt temperature. We measured and recorded temperature of the molten metal by thermocouple. Crucible material was polyester putty because it is heat resistant and easy to give shape. We performed model experiment using low melting point (= 60 ℃) alloy because the melting point of silicon is as high as 1400 ℃. We illustrate the crucible and cooling unit in Fig.1 and the drawer unit in Fig.2 [2].

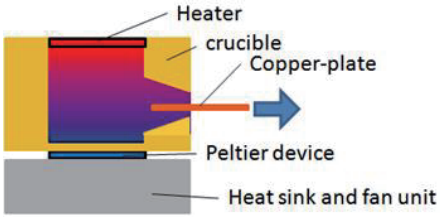

Fig.1 Crucible and cooling unit

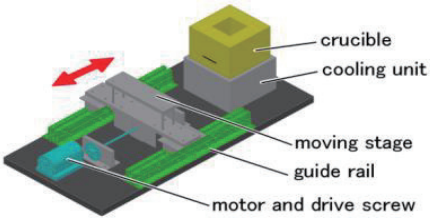

Fig.2 Drawer unit

3. Results and Disccusion

We did experiment using a crucible with a slit of 0.2mm thickness and were able to produce a metal plate of minimum thickness 0.1mm.We show the metal plate in Fig.3.

Fig.3 Produced metal plate (0.2mm slit)

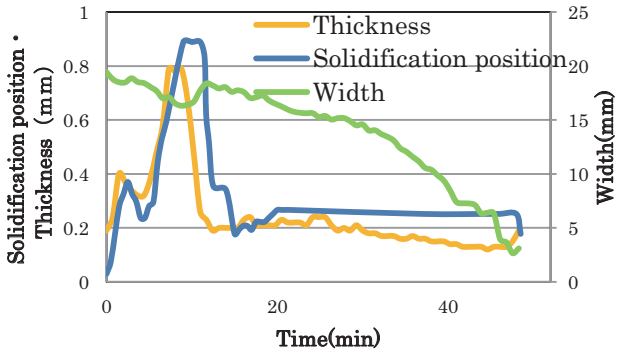

Fig.4 Time –Solidification position・Thickness・Width

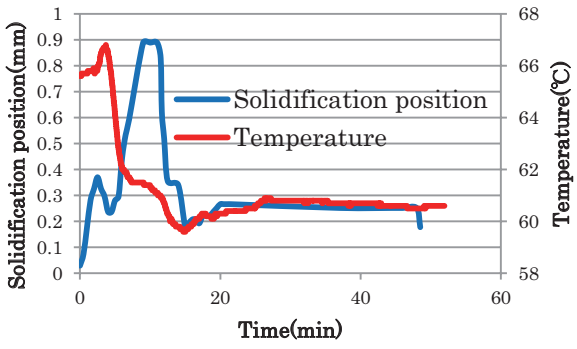

Fig.5 Time- Solidification position・Temperature

Fig.4 shows the relationship of the metal plate thickness (thickness of the left end of the plate), the width and the solidification position (distance from the slit to the position of solidification). Fig.5 shows the relationship of the solidification position and the temperature at the slit.

Plate thickness was quite stable while the position of solidification was constant, but it slightly decreased as shown in Fig.4. This was caused by the decrease of static pressure (weight of the liquid above the slit position). When static pressure decreased, liquid metal outflow decreased. Thus, liquid metal surface was desired to stay at the slit position. After liquid metal surface gradually decreased, metal plate width also decreased. This was also caused by the decrease in liquid outflow from a slit. Thus, we thought that improvement would be possible by feeding material metal into the container to keep the liquid level. Experiment of material feeding is described below.

Solidification position changed with temperature as shown in Fig.5. Solidification depends on liquid metal temperature at the slit, room temperature and drawer velocity. Room temperature and drawer velocity was decided to be fixed values in the beginning of the experiment, but the temperature at the slit cannot be decided beforehand because it has to be regulated by changing the heater power. Thus, we adopted the following procedure to decide the temperature at the slit in the beginning of the experiment. Firstly, the relation of room temperature and drawer velocity was estimated by an analytical one-dimensional solution [3,4]. Thus, the velocity variation per 1 ℃ change of room temperature was understood. Secondly, the relation of temperature at the slit and the drawer velocity was estimated. Thirdly, by using the estimation, the temperature at the slit was deduced which can be changed depending on the actual change of the drawer velocity.

4.The outline of the experiment

We produced a setup to supply material metal with the same rate with the solidification, for the purpose of stabilizing metal plate width. Moreover, metal plate could be provided continuously for a long time by feeding material metal. Fig.7 shows the relationship of the metal plate width and the temperature at the slit.

Metal plate width was more stable than when the material was not supplied. Thus, the decrease of the metal plate width was suppressed by the feeding and it became almost constant.

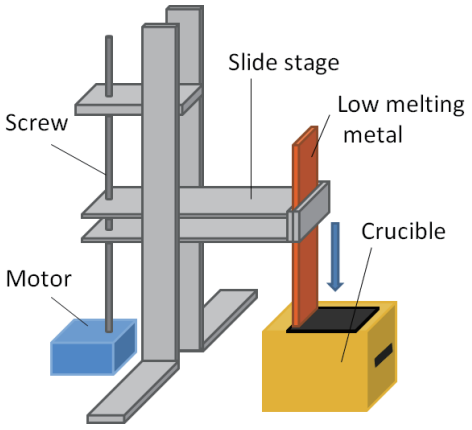

Fig.6 Feed unit

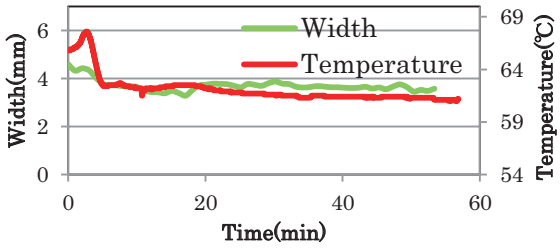

Fig.7 Time- Width・Temperature

5. Concluding remarks

By this new method, we were able to achieve minimum thickness of 100 μm by using low melting point (= 60 ℃) metal alloy. We understood that generation of constant thickness metal plate was possible by keeping a fixed solidification position. Moreover, we found the feeding of the material metal was useful for obtaining long and constant width plate with small thickness.

6.Future plans

1) We introduce a position sensor to control the metal liquid level and then prevent the increase of plate thickness.
2) We perform a new experiment with two times larger width of plate, and a comparative study of the temperature, velocity, metal plate thickness, and solidification position.
3) We predict the state when we use silicon by using software because our experiment was a model experiment with low melting point metal.
4) We will explore an idea about adding magnetic pressure by alternating magnetic field from top and bottom like in Fig.8 because a thinner metal plate and a flatter surface might be obtained.

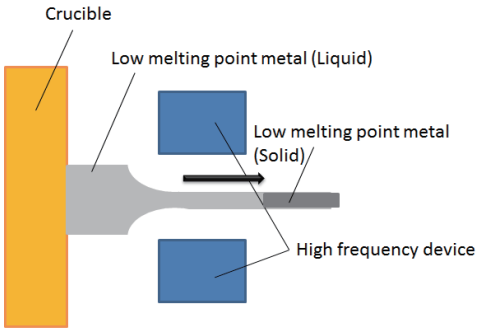

Fig.8 Magnetic pressure device

References

[1] K.Nakajima and N.Usami, Crystal Growth of Si for solar cells, (2009), p.96-117, Spring-Verlag
[2] K.Matsumura, graduation thesis, Shibaura Institute of Technology, (2011)
[3] Y.Mitsuhashi, M.Umeta, T.Yamada and N.Ono, JSME Thermal Engineering Conference 2012, Proceeding Paper No. G131, p215-216.
[4] Y.Mitsuhashi, master degree thesis, Shibaura Institute of Technology, (2013)

Tenth International Conference on Flow Dynamics
November 25-27, 2013, Sendai, Miyagi, Japan

Flow-Coupled Multibody Dynamics Simulation for an Aerial Deployment of a Folded Wing

Koji Fujita[1)], Toshikazu Motoda[2)], Hiroki Nagai[1)]
[1)]Department of Aerospace Engineering, Tohoku University,
6-6-01 Aramaki Aza Aoba, Aoba-ku, Sendai, Miyagi, 980-8579 Japan
[2)]Japan Aerospace Exploration Agency,
6-13-1 Osawa, Mitaka, Tokyo, 181-0015 Japan
fujita.koji@aero.mech.tohoku.ac.jp

ABSTRACT

An airplane has been expected as a new method for Mars exploration. An aerial deployment technique is required for the mission to get a large wing area and compactness. Dynamic behavior at aerial deployment was simulated using the theory of the multibody dynamics to assess safety. An effect of the asymmetric motion of the wing deployment was evaluated.

1. Introduction

Application of an airplane for Mars exploration has been considered as an exploration method [1,2]. Airplanes can fly over several hundreds to thousands of kilometers and get higher resolution data than satellites.

One of the challenges of an airplane for Mars is the aerial deployment mechanism. The airplane needs both a larger wing to fly in low density air and compactness to be packed into the aeroshell. Consequently, the airplane would require deployment mechanisms. In addition, aerial deployment technique can be suitable because it allows for elimination of a take-off system and for using the initial altitude to its advantage. Because of these reasons, several design concepts of the Mars airplane have been planned to deploy in the air [2,3].

Folding type is well known as a deployment mechanism [4]. This type uses hinges. Because the folding type has a simple structure, this type is lightweight and has a high reliability.

However, aerial deployment of the folded wing has a risk for instability due to aerodynamic and inertial forces during deployment. To assess safety before the flight, a multibody dynamics simulation was performed and the dynamic behavior of the Mars airplane with folded-wing deployment was investigated.

In case where the right and left wing are folded at the same position, the aerial deployment motion has to be asymmetry to avoid contacting each wing. This could lead the instable motion. Therefore the effect of the asymmetrical deployment motion was evaluated.

2. Method

Figure 1 shows model geometry. The model consists of three rigid bodies: center, right wing, and left wing. These bodies are described as rigid body A, B, and C in this paper. The center consists of a center wing, a fuselage, and a tail. The right and left wings are assumed as a flat plate. Each body is connected by hinges. The hinge axes are parallel to the X axis. The hinge has a spring to help deploying. Figure 2 shows a deployment process. At first, the right and left wings are folded under the fuselage. Then both wings are rotated around the hinges. The rotation stops when the wings align with the center. Specifications of the three rigid bodies are defined as shown in table 1.

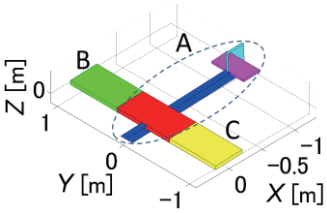

Fig. 1 Model geometry.

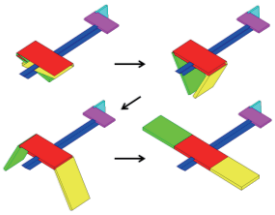

Fig. 2 Deployment process.

Table 1. Specifications of the rigid bodies.

Name		Center	Right and Left wings	Unit
Mass		4.5	0.1	kg
Wing area		0.41	0.41	m^2
Chord length		0.51	0.51	m
Span length		0.80	0.80	m
C.G.	X_{CG}	40	40	%c
	Y_{CG}	0	0	m
	Z_{CG}	0	0	m
Inertia matrix	I_{XX}	0.23	0.0054	kg・m^2
	I_{YY}	1.10	0.0021	kg・m^2
	I_{ZZ}	1.34	0.0075	kg・m^2
	I_{XZ}	0.088	0	kg・m^2

The equation of motion for this multibody system was reported in a previous paper [5]. External forces are aerodynamic force, hinge torque, and gravity. Therefore the motion is affected by the aerodynamic force. However, the aerodynamic force is a function of the relative velocity between rigid body and air. Hence the aerodynamic force is also affected by the motion.

Longitudinal aerodynamic characteristics of the right and left wings are given as a flat plate [6]. Lateral aerodynamic characteristics are assumed using the paper [7]. Longitudinal and lateral aerodynamic characteristics of the center body are based on the experimental data of the deployed state scale model [8]. The effect of the right and left wing are subtracted. All control surfaces are fixed to study the motion of the airplane itself. The effect of the flow interference is ignored in this paper.

A hinge moment is set to depend on the deployment angle θ_{dep} [5]. The deployment angle is defined to be 0 and 180 degrees at folded and deployed state.

4th order Runge-Kutta method is applied as a numerical integration method. A time interval is set to a 0.005 seconds. Atmospheric density and acceleration

due to gravity are fixed at the value of 32,500 m height for simplicity. An initial condition is set to an equilibrium gliding condition. Here, the true air speed is set to 98 m/s. A termination condition is based on the deployment angle θ_{dep}. Finishing deployment is detected using the following inequalities.

$$\theta_{dep} > 175[\mathrm{deg}] \quad \& \quad \left|\dot{\theta}_{dep}\right| < 20[\mathrm{deg/s}] \qquad (1)$$

The simulation is terminated 5 seconds after the finishing deployment.

Parameter of this simulation is the deployment starting time for the right wing T_s to evaluate the effect of the asymmetrical motion. This value is set to 0 and 0.2 seconds, respectively.

3. Results and Discussion

Figure 3 shows the time history of the deployment angle at T_S = 0.2 [s]. The deployment angle of the left wing was near 90 degrees at the time when the right wing starts deployment. The left wing was finished deploying at 0.5 seconds. Figure 4 shows the time history of the angle of attack of each body at T_S = 0.2 [s]. At the beginning, the angle of attack of the right and left wings were opposite in sign to that of the center body, because wings were folded as shown in fig. 2. Each angle of attack history was different due to its attitude and motion. Therefore aerodynamic force and moment were different. Figure 5 shows the comparison of the roll rate P of the center body. When T_S = 0 [s], i.e. motion was symmetric, the roll rate was near 0. When T_S = 0.2 [s], i.e. motion was asymmetric, the roll oscillation was generated by the lift of the left wing. The mechanism is shown in Fig. 6. This result suggests that the symmetricity is one of the important parameter of the aerial deployment technique.

4. Concluding remarks

The flow-coupled multibody dynamics simulation was performed to investigate the aerial deployment motion of the Mars airplane. The asymmetric motion of wing deployment has an effect on the roll motion due to the lift.

Acknowledgments

This work was supported by JSPS KAKENHI, Grant-in-Aid for JSPS Fellows (Number 25-4187).

References

[1] T. Kubota, Proc. of the 2nd Annu. Symp. on Planetary Exploration, 2010.
[2] A. Oyama, 21st Workshop on Astrodynamics and Flight Mechanics, 2011.
[3] H. S. Wright, et al., AIAA 2003-6577, 2003.
[4] J. D. Jacob, et al., AIAA 2009-1291, 2009.
[5] K. Fujita, et al., 29th ISTS, 2013-k-07, 2013.
[6] M. Okamoto, et al., AIAA J., Vol.49, No.6, 2011.
[7] S. F. Horner, et al., *Fluid-dynamic Lift*, 1975.
[8] M. Anyoji, et al., JSASS-2012-4359, 2012.

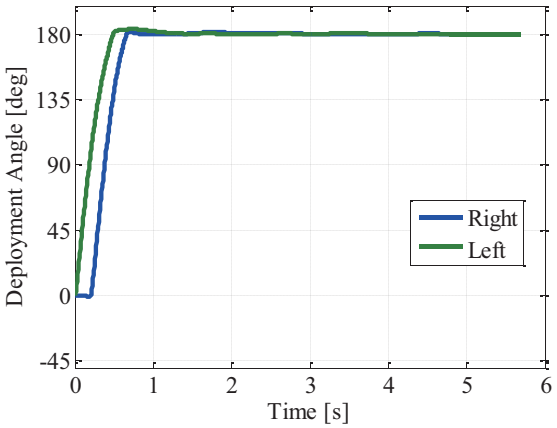

Fig. 3 Deployment angle vs. time at T_S = 0.2 [s].

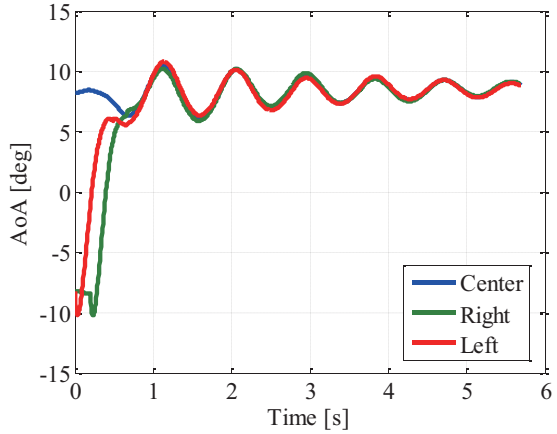

Fig. 4 Angle of attack of the each body vs. time at T_S = 0.2 [s].

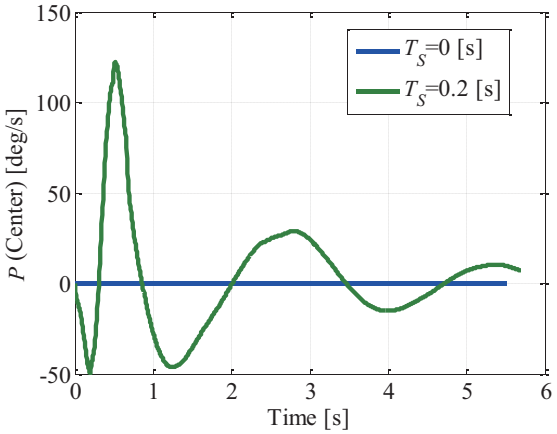

Fig. 5 Comparison of the roll rate P of the center body.

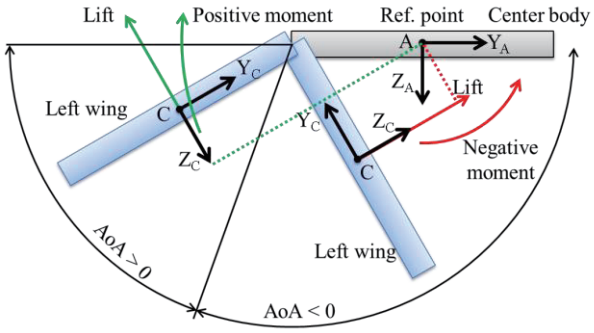

Fig. 6 Mechanism of roll moment generation.

Tenth International Conference on Flow Dynamics
November 25-27, 2013, Sendai, Miyagi, Japan

Experimental Evaluation of the Applicability of a Sided-incidence Microwave Probe for a Microwave Nondestructive Testing Method

Kota Sasaki, Noritaka Yusa, Hidetoshi Hashizume
Department of Quantum Science and Energy Engineering, Graduate School of Engineering, Tohoku University,
6-6-01-2, Aramali Aza Aoba, Aoba-ku, Sendai, Miyagi 980-8579, Japan
ksasa@karma.qse.tohoku.ac.jp

ABSTRACT

This study reports the development of a new microwave incidence probe connected to pipe sided wall for the nondestructive evaluation of pipe wall thinning inside a pipe so that a microwave nondestructive testing method is applicable to pipe without open end. Three-dimensional finite element simulations are carried out to evaluate effects of geometric conditions of the probe. The simulation results show that reflected signals of the sided-incidence probe with the bended coaxial cable and outer conductor is relatively better than the conventional probe connected to open end of the pipe in wider frequency range.

1. Introduction

Maintenance of piping system is one of the most important matters in many industries such as nuclear power plants [1]. However, present major inspection methods such as ultrasonic and eddy current testing have a long inspection time and a lot of costs. Thus nondestructive testing method using microwaves has been developed as a new technique that enables to detect pipe wall thinning defects in long distance piping systems quickly [2]. Earlier studies have demonstrated that this method can detect pipe wall thinning conditions based on evaluating the transmitted and reflected microwave signals propagating inside a metal pipe [1].

However, most of previous studies only focused on microwave probe connecting to an open end of the pipe, did not deal with pipes without an open end. Because pipes without an open end are the most general case in industries, developments for them are necessary to put this method to practical use.

Therefore, in this research, we focus on developing a novel sided-incidence microwave probe that can be attached to the side-wall of a pipe as much as the dedicated port of this proposed probe is required. A previous study has revealed that the probe profile has significant effect on the microwave signals propagating inside a pipe [4]. Hence, we carry out detailed three-dimensional numerical analyses about the profile of a probe to design a novel sided-incidence microwave probe. In addition, experimental evaluations based on the results of numerical simulations are performed to validate simulations and evaluate its applicability.

2. Numerical simulation

One of the numerical configurations is illustrated in Fig. 1. The connection part of the coaxial cable and pipe wall is modeled to evaluate the dependency of the reflection characteristics of microwaves propagating inside pipe at the connection. The core wire is inserted perpendicularly and bended to have better directional characteristics because the core wire set along axis of pipe showed better signals than that of non-axial case in our previous simulations [4]. The outer conductor of the coaxial cable is also modeled. The curvature radius of bended portion is 6.5 mm, which is the minimum endurable radius of the actual coaxial cable.

All of the geometric parameters are shown in Fig. 1, where "L" is the length of the coaxial cable's core wire protruding into pipe. The absorbing boundary condition, perfectly matched layer (PML), is set at both pipe ends, and thus reflections due to the pipe ends do not arise and the model equals a sufficiently long pipe. In the simulations, all of metallic surface are considered as a perfect conductors and TEM mode is excited at the start port of a coaxial cable. To simulate actual Anritsu K118 coaxial cable, Teflon with relative permittivity and permeability of 1.687 and 1, respectively, is defined as the dielectric. The second order tetrahedral elements are used for discretization. Considering the memory consumption, the frequency range is set to be 12 ~ 30 GHz with frequency step of 1 GHz. However, in this numerical configuration, the practical cut-off frequency of TM_{01} mode which is the lowest order TM mode is 12.08 GHz.

The three-dimensional finite element simulations are carried out using commercial software, COMSOL Multiphisics and its RF Module (version 4.3b). The governing equations of the simulations are

$$\nabla \times \mu_{\mathrm{r}}^{-1}\left(\nabla \times \boldsymbol{E}\right) - k_0^2[\varepsilon_{\mathrm{r}} - \mathrm{j}\sigma/(\omega\varepsilon_0)]\boldsymbol{E} = \boldsymbol{0} \quad (1),$$

$$k_0 = \omega\sqrt{\varepsilon_0\mu_0} \quad (2)$$

where $\boldsymbol{E}$ denotes the electric field, ε_0 and μ_0 are the permittivity and permeability in vacuum, and ε_{r} and μ_{r} are the relative permittivity and permeability, respectively; σ is the electrical conductivity, ω is the angular frequency, and j is imaginary unit.

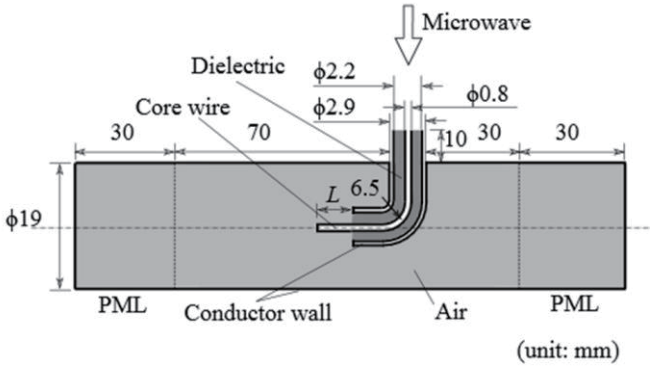

Fig. 1 Numerical configuration and geometric parameters

3. Results and Discussions

Fig. 2 shows the three-dimensional simulation results of the reflection characteristics as a function of exciting frequency. The figure presents results of reflection characteristics of the conventional method (i.e., the microwave probe connected to open end of the pipe.) used in our previous study and the sided-incidence method. To detect pipe wall thinning in high accuracy, exciting more obvious pulse in the time domain is desirable. To that end, small amplitude change of reflection signals in wide frequency range and small dependence on frequency are preferable.

The reflected microwaves of the sided-incidence method have a relatively large dependence of exciting frequency and periodical peaks when the frequency increases. As large reflection peaks means that signals are reflected back instead of transmitting, it shows that the transmission characteristics of some frequency ranges are much better than others.

In addition, comparing conventional and new methods reveals that the propagating characteristics of microwaves along the frequency range in the sided-incidence method is better (i.e., a wider frequency range of microwave signals can propagate) than that of the conventional method. As the conventional method can detect pipe wall thinning, it should be more preferable to apply this new probe to the inspection.

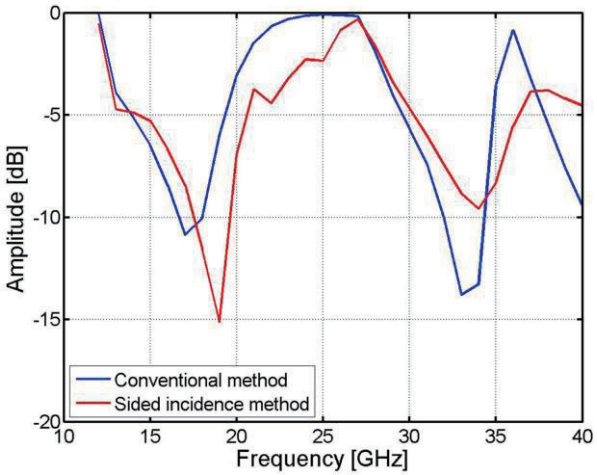

Fig. 2 Reflection characteristics of the conventional method and the sided-incidence microwave method (L = 5 mm)

4. Concluding remarks

This study evaluated the novel sided-incidence microwave probe used for nondestructive testing using microwave. The simulation results showed applicability of a new profile of microwave probe by calculating reflection characteristics significantly depending on their profiles. Based on the numerical simulation results, the experimental verification and further evaluations of pipe wall thinning defects using a sided-incidence probe are performed and will be presented at the conference.

References

[1] I, Nishiguchi et al., E-jounal of advanced Maintenance, 2 (2010)9, 14-24.
[2] H. Hashizume, T. Shibata, K. Yuki, Int. J. Appl. Electromag. Mech., **20** (2004), 171-178.
[3] Y. Sakai, N. Yusa, H. Hashizume, Nondestr. Test. Eval, **27** (2012), 171-184.
[4] K. Sasaki, L. Liu, N. Yusa, H. Hashizume, Proc. 18th Int. Workship on Electromag. Nondesr. Eval., (2013) 30-33

Tenth International Conference on Flow Dynamics
November 25-27, 2013, Sendai, Miyagi, Japan

The Effect of Size of Caking Coal and Low-quality Coal on the Tensile Strength of Coke

Shohei MATSUO[1], Tetsuya KANAI[1], Ayuko TOISHI[1], Yasuhiro SAITO[1], Yohsuke MATSUSHITA[1], Hideyuki AOKI[1], Seiji NOMURA[2], and Shigeto MIYASHITA[3]
[1]Department of Chemical Engineering, Graduate School of Engineering, Tohoku University, 6-6-07 Aoba, Aramaki, Aoba-ku, Sendai, 980-857
[2]Process Research Laboratories, Nippon Steel & Sumitomo Metal Corp., 20-1 Shintomi, Futtsu, 293-8511
[3]KASHIMA WORKS, Nippon Steel & Sumitomo Metal Corp., 3 Hikari, Kashima, 314-0014
saito@tranpo.che.tohoku.ac.jp

ABSTRACT

The effects of size of caking coal and low-quality coal on the tensile strength of coke were investigated. The tensile strength of coke was measured by a diametral-compression test, and the cross-section of coke was observed by scanning electron microscopy. As a results, small low-quality coals form large and complex non-adhesion grain boundaries, and decrease the tensile strength of coke. In addition, small caking coals prevent small low-quality coals from forming non-adhesion grain boundaries, and improve the strength of coke.

1. Introduction

Coke used as a reducing agent is mainly made from caking coal, and high strength coke is desired in the blast-furnace. Recently, there is a need to use low-quality coals such as non- or slightly- caking coal as raw materials to use the coal resource effectively. However, the strength of coke made from low-quality coal is lower than that of coke made from caking coal due to non-adhesion grain boundaries. Non-adhesion grain boundaries do not adhere to another coal in the carbonization process, and result in large defects in coke[1]. To use the coke made from large quantity of low-quality coal, it is necessary to clarify the factor in forming non-adhesion grain boundaries and the effect of non-adhesion grain boundaries with coke strength quantitatively.

From a stand point of the blending ratio of low-quality coal, Kanai *et al.*[2] reported that the grain boundaries increased with the blending ratio of low-quality coal and just a few non-adhesion grain boundaries decrease the tensile strength of coke drastically. From a stand point of the grain size of coal, Arima[3] reported that a drum index was increased by refining the grain of caking coal and non-adhesion grain boundary could affect the coke strength. However, the relationship between the grain size and the coke strength is not revealed quantitatively.

In this study, the effect of size of caking coal grains and low-quality coal grains on the coke strength were investigated by a diametral-compression test for coke specimens made from graded coal grains. In addition, to observe the non-adhesion grain boundaries, the fracture cross-section of coke was observed by using scanning electron microscopy (SEM).

2. Method

2.1 Specimen making

The characteristic of the coals is shown in Table 1. To consider the effect of coal grains size, some graded coal grains were used. Coking coals and low-quality coals were separately crushed into <3mm 75%, and these were graded <3mm and <1mm using sieve. Fig. 1 shows grain size distribution of each grade. Table 2 shows manufacturing conditions. The coal was charged in a both sides heating oven whose size was 40 mm × 60 mm × 60 mm, and heated with 3K/min to 1273K and kept for 30 min. Coke taken out from the oven was drilled and sliced off to the discs whose size was 10 mm in diameter and length.

Table 1 Characterization of coal

	C [mass%] (daf basis)	H	O	Ro [%]	MF [ddpm]	TD [%]
Coal A (caking coal)	81.4	4.7	11.5	1.2	2.61	78
Coal B (low-quality coal)	78.6	5.2	13.9	0.69	0.90	1

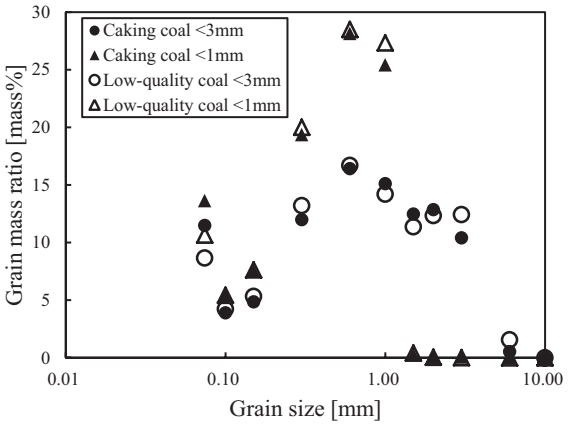

Fig. 1 Grain size distribution

Table 2 Manufacturing conditions

Sample No.	Size of caking coal	Size of low-quality coal	Density [dry-g/cm^3]
1	< 3 mm	< 3 mm	0.8
2	< 3 mm	< 1 mm	0.8
3	< 1 mm	< 3 mm	0.8
4	< 1 mm	< 1 mm	0.8

2.2 Diametral-compression test

Tensile strength of coke was measured with a diametral-compression test using universal testing machine (Shimadzu Co., Autograph AG-150 kN). The loading rate was 2 mm/min. Tensile strength was

calculated from Eq.(1):

$$\sigma = \frac{2P}{\pi dl}, \qquad (1)$$

where d and l are a diameter and a length of specimen respectively, and P is the maximum load when coke fractures. In order to evaluate tensile strength statistically, tensile strength was evaluated with Weibull plot. A Weibull distribution function is represented as Eq.(2):

$$\log_e \log_e \frac{1}{1-P_f(\sigma_t)} = m\log_e \sigma_t - m\log_e \xi, \qquad (2)$$

where P_f is cumulative failure probability, m is the Weibull slope, ξ is scale parameter, and σ_t is tensile strength. Scale parameter means the tensile strength when cumulative failure probability reaches 63 % median rank method.

2.3 Observation of fracture cross-sections

Scanning electron micrographs on fracture cross-section of coke were captured using SEM (KEYENCE Co., VE8800). Accelerating voltage was set to 1.7kV. Fracture cross-section of coke consists pore, pore wall, fractured coke matrix and non-adhesion grain boundary.

3. Result and Discussion

Figure 2 shows the tensile strength of the diametral-compressive test. Specimens made from <3mm caking coals were compared. The tensile strength of sample 2 was lower than that of sample 1. This is because that the <1mm low-quality coal grains decrease the strength of coke. Fig. 3 (a) shows fractured surface of sample 2. In sample 2, it was observed that small low-quality coal grains filled void between caking coal grains and formed non-adhesion grain boundaries. Results of tensile strength and micrograph suggest that small low-quality coal grains form large and complex non-adhesion grain boundaries, while the non-adhesion grain boundaries decrease the strength of coke. In addition, specimens made from <1mm low-quality coals were compared. The tensile strength of sample 4 was higher than that of sample 2. This is because that <1mm caking coal grains improve strength of coke made from <1mm low-quality coal grains. Fig. 3 (b) shows fractured surface of sample 4. In sample 4, small caking coal grains filled void between low-quality coal grains, and bonded these grains. From Fig. 2 and Fig. 3 (b), caking coal grains which are as small as low-quality coal grains can prevent fine low-quality coal grains from forming non-adhesion grain boundaries, and improve the coke strength. Furthermore, specimens made from <3mm low-quality coals were compared. The tensile strength of sample 1 and 3 are almost the same. This is because that the size effect of caking coals does not contribute improvement of coke strength. It is suggested that quantity of caking coals which can fill void between caking coals do not increase by refining caking coals under 3 mm.

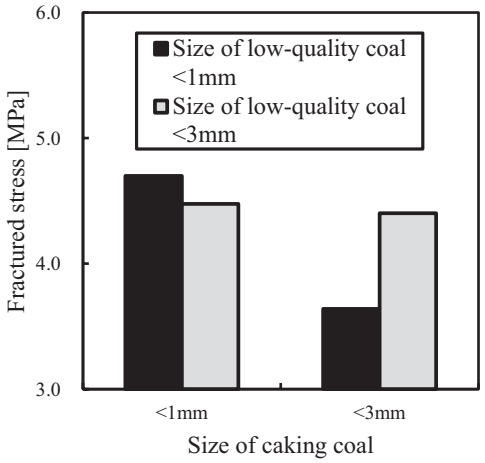

Fig. 2 Effect of coal size on tensile strength

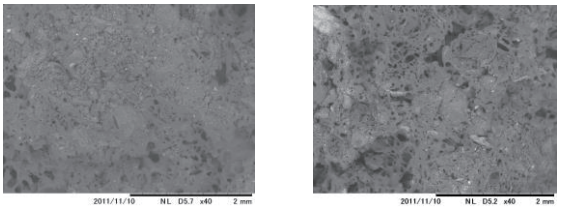

(a) Sample 2 (b) Sample 4

Fig. 3 Micrographs of fracture cross-section of coke

4. Concluding remarks

In this study, the effect of size of caking coal and low-quality coal on the tensile strength of coke was investigated by the diametral-compression test and the observation of fracture cross-sections of coke. As a results,

(1) Low-quality coals which are smaller than caking coals decrease the tensile strength of coke because small low-quality coals form large and complex non-adhesion grain boundaries.
(2) Caking coals which are as small as low-quality coals improve strength of coke made from small low-quality coals because caking coals prevent low-quality coals from forming non-adhesion grain boundaries.

Nomenclature

d : diameter of specimen [m], l : length of specimen [m], m : Weibull slope [-], P : load[N], P_f : cumulative failure probability, σ : tensile stress [MPa], σ_f : tensile strength [MPa], ξ : scale parameter [MPa]

Acknowledgements

This work has been done in “Cokemaking Technology for Low-quality and Unused Carbon Resources” (The chief examiner: Prof. H. Aoki, Tohoku Univ.). The authors would like to acknowledge the research group members gratefully.

References

[1] T. Arima : Tetsu-to- *Hagané*, **87** (2001), 274
[2] T. Kanai *et al.* : *Journal of Thermal Science and Technology,* **7** (2012), 351
[3] T. Arima : Japanese Patent Disclosure 2002-121566 (2002)

Effect of Cation Substitution on Chemical Stability and Transport Properties of $Ba_{0.5}Sr_{0.5}Co_{0.8}Fe_{0.2}O_{3-\delta}$-based Mixed Conductors

Fang Wang,[1] Takashi Nakamura,[1] Keiji Yashiro,[2] Junichiro Mizusaki,[1] Koji Amezawa[1]
[1]Institute of Multidisciplinary Research for Advanced Materials, Tohoku University
2-1-1 Katahira, Aoba-ku, Sendai 980-8577, Japan
[2]Graduate School of Environmental Studies, Tohoku University,
6-6-01 Aoba, Aramaki, Aoba-ku, Sendai 980-8579, Japan
f-wang@mail.tagen.tohoku.ac.jp.

ABSTRACT

The chemical stability of $Ba_{0.5}Sr_{0.5}Co_{0.8}Fe_{0.2}O_{3-\delta}$ (BSCF)-based mixed conductors were evaluated by *in situ* HT-XRD as a function of temperature and oxygen partial pressure, $p(O_2)$. The stability boundary for the oxidation of $Ba_{0.5}Sr_{0.5}Co_{0.8}Fe_{0.1}Nb_{0.1}O_{3-\delta}$ (BSCFN) obviously shifted to relatively higher $p(O_2)$ range than that of BSCF. This result suggested that the Nb substitution effectively improved the chemical stability under high oxidation condition and the cubic perovskite phase of BSCF could be stabilized by lowering the Co mean valence through doping high valence cation on B-site.

1. Introduction

BSCF was found to exhibit excellent performance as a cathode for intermediate temperature solid oxide fuel cells (IT-SOFCs) [1], owing to be a good ionic and electronic conduction. However, the severe performance degradation was reported with BSCF cathodes [2-4]. This might be caused by the instability of BSCF at intermediate temperature range. More recently, attentions have been paid on the relationship between the performance degradation and the crystal structure transition of BSCF. The crystal structure of BSCF was well studied at intermediate temperature range in air atmosphere [5-8]. Svarcova *et al.* found the formation of the hexagonal and cubic polymorphs after long time annealing at 1073 K [5]. D. N. Müller *et al.* indicated phase equilibrium between hexagonal and cubic perovskite phase at 1073 K by a combined study with XRD and electron microscopy [6]. P. Müller observed a trigonal phase besides the hexagonal and the cubic phases by TEM analysis on a bulk BSCF sample [7]. All of these results indicated the complicated decomposition of cubic BSCF at intermediate temperature range in air. However, there is no systemic study on the effect of $p(O_2)$ on the chemical stability of BSCF in the wide temperature range. In our recent work [8], the chemical stability map of BSCF was proposed in wide ranges of $p(O_2)$ (1 to 10^{-22} bar) and temperature (300 to 1373 K) based on the results by *in situ* HT-XRD, HT-gravimetry and coulometric titration, as shown in Fig.1. The decomposition of the cubic perovskite phase of BSCF was confirmed in connection with the oxidation/reduction of Co ions due to the oxygen nonstoichiometry (δ) change. We found the cubic perovskite phase of BSCF decomposed when cobalt ions were oxidized to higher oxidation state than trivalence in high $p(O_2)$ or were reduced to lower oxidation state than divalence in low $p(O_2)$ condition. The results suggest the cubic perovskite phase of BSCF can be stabilized by lowering the Co mean valence in high $p(O_2)$ condition. Therefore, B-site cation substitution by higher valence cation Nb^{5+} was studied in this work. The effect of the Nb substitution on the chemical stability under high $p(O_2)$ atmospheres was investigated by *in situ* HT-XRD.

2. Method

$Ba_{0.5}Sr_{0.5}Co_{0.8}Fe_{0.2}O_{3-\delta}$ (BSCF) was synthesized by the Pechini method [9]. $Ba_{0.5}Sr_{0.5}Co_{0.8}Fe_{0.1}Nb_{0.1}O_{3-\delta}$ (BSCFN) was synthesized by solid state reactions [9]. The obtained powders were analyzed by X-ray diffraction (Phase D2, Bruker), and were confirmed to have the single-phase perovskite.

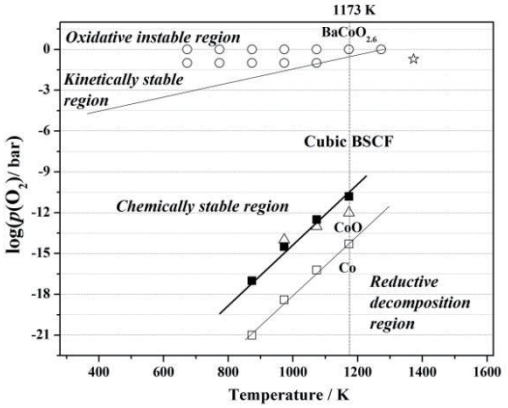

Fig. 1. Chemical stability diagram of $Ba_{0.5}Sr_{0.5}Co_{0.8}Fe_{0.2}O_{3-\delta}$ based on analysis of structure and oxygen nonstoichiometry [8].

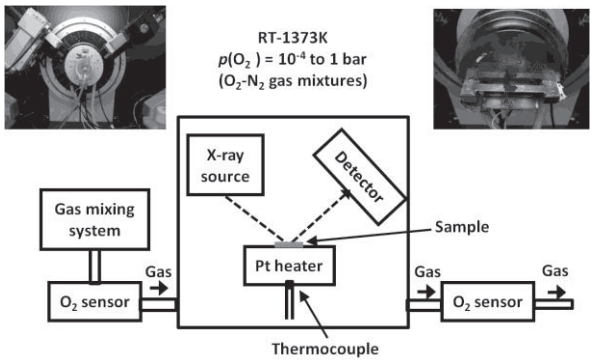

Fig. 2. Schematic illustrations of experimental setup for high-temperature X-ray diffraction measurements.

X-ray diffractometer (D8 Advance with LYNXEYE™ Super Speed Detector, Bruker AXS, and CuKα

radiation), shown in Fig.2, was used for the *in situ* HT-XRD measurement as a function of oxygen partial pressure $p(O_2)$, temperature and annealing time. The BSCF powder was set on a platinum heater inside the XRD chamber. In order to investigate the chemical stability, the XRD patterns were measured in the $p(O_2)$ = 1 bar. The $p(O_2)$ was monitored at the inlet and the outlet of the XRD chamber by two zirconia sensors.

3. Results

Fig.3 shows the HT-XRD patterns of BSCFN in pure O_2 during cooling from 1373 K to 673 K. It was found that BSCFN remained as the cubic perovskite phase at temperatures above 1173 K. In our previous work [8], HT-XRD results of BSCF in pure O_2 showed an impurity phase below 1373 K. Comparing HT-XRD results with BSCF and BSCFN, it seemed BSCFN exhibited better structural stability in pure O_2 gas. However, the cubic phase of BSCFN started to decompose at 1173 K. A small impurity phase appeared although most of the cubic phase of BSCFN remained as it was even after the 5 hours annealing.

Fig.4 shows the stable boundaries for the oxidation of BSCF and BSCFN evaluated from HT-XRD results. The stable boundary of BSCFN was obviously shifted to relatively high oxidation condition (relatively high $p(O_2)$) comparing with the oxidation boundary of BSCF. It indicated the BSCFN had better chemical stability than BSCF in high oxidation atmosphere. This result suggests the doping higher valence cations stabilized the cubic perovskite phase of BSCF in relatively high oxidation condition.

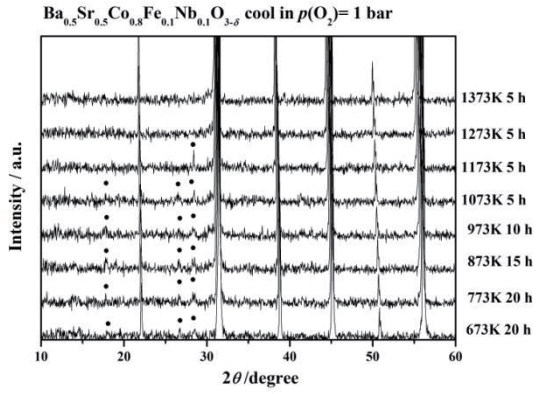

Fig. 3. HT-XRD patterns of BSCFN powder in 100% O_2 during cooling from 1373 K to 673 K. The circles express peaks of the impurity phase. [9]

4. Concluding remarks

The *in situ* HT-XRD measurements were employed for the chemical stability analysis of BSCF-based materials. Compared with BSCF, BSCFN exhibited better chemical stability under high $p(O_2)$ at temperatures higher than 1173 K. Nb-doping into the B-site was effective to stabilize the perovskite structure of BSCF under SOFC operating conditions.

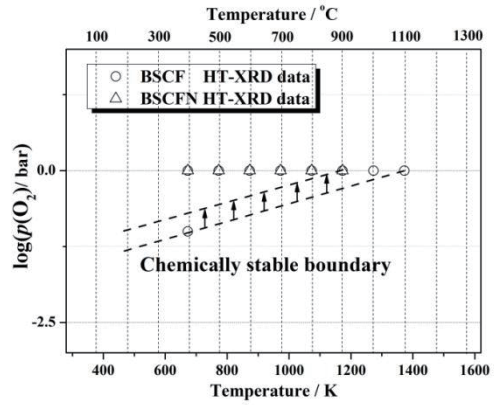

Fig. 4. Chemical stability map of $Ba_{0.5}Sr_{0.5}Co_{0.8}Fe_{0.2}O_{3-\delta}$ and $Ba_{0.5}Sr_{0.5}Co_{0.8}Fe_{0.1}Nb_{0.1}O_{3-\delta}$ in high oxidation atmosphere. Open circles and triangles indicated decomposition conditions of BSCF and BSCFN, respectively. Dash lines demonstrated the chemically stable boundaries.

Acknowledgements

This work was supported by CREST from the Japan Science and Technology Agency (JST) and Grant-in-Aid for Scientific Research of MEXT, Japan.

References

[1]Z.P. Shao, S.M. Haile, *Nature* **431**,170 (2004)

[2]W. Zhou, R. Ran, Z.P. Shao, *J. Power Sources* **192**, 231 (2009)

[3]A. Yan, M. Cheng, Y. L. Dong, W. S. Yang, V. Maragou, S. Q. Song and P. Tsiakaras, *App. Catalysis B-Environmental* **66**, 64 (2006)..

[4]Z.P. Shao, W.S. Yang, Y. Cong, H. Dong, J.H. Tong, G.X. Xiong, *J. Membrane Science* **172**, 177 (2000) .

[5]S. Svarcova, K. Wiik , J. Tolchard , H. J.M. Bouwmeester, T. Grande, *Solid State Ionics* **178**, 1787 (2008).

[6]D. N. Mueller, R. A. D. Souza, T.E. Weirich, D. Roehrens, J. Mayer, M. Martin, *Phys. Chem. Chem. Phys.*, **12**, 10320 (2010).

[7]P. Müller, H. Störmer, L. Dieterle, C. Niedrig, E. Ivers-Tiffée b, D. Gerthsen, *Solid State Ionics* **206**, 57 (2012).

[8]F. Wang, T. Nakamura, K. Yashiro, J. Mizusaki, K. Amezawa, to be submitted.

[9]F. Wang, T. Nakamura, K. Yashiro, J. Mizusaki, K. Amezawa, *ECS Trans.*, (2013), in press.

Tenth International Conference on Flow Dynamics
November 25-27, 2013, Sendai, Miyagi, Japan

Evaluation of Fatigue Process of Molybdenum-containing Diamond-like Carbon Coatings for Sensor Application

Mami Takahashi[1], Hiroyuki Miki[2], Takanori Takeno[1], Toshiyuki Takagi[3]
[1]Graduate School of Engineering, Tohoku University, Aoba 6-6-1, Aramaki, Aoba-ku, Sendai 980-8579, Japan
[2] FRIS, Tohoku University, Aramaki aza Aoba 6-3, Aoba-ku, Sendai, 980-8578, Japan
[3]Institute of Fluid Science, Tohoku University, Katahira 2-1-1, Aoba-ku, Sendai 980-8577, Japan
takagi@ifs.tohoku.ac.jp

ABSTRACT

We propose the new concept of fatigue sensor using metal-containing diamond like carbon(DLC) film. After the vibration test, we measured structure of Me-DLC and pure-DLC by using Raman spectroscopy. We found that the carbon bonding of the DLC matrix has changed by doping metal cluster and the carbon bonding in Me-DLC films change sp^2 to sp^3 due to the cyclic bending.

1. Introduction

Deformation and vibration of the structure of bridges and ships become the factor for cracking and structural fatigue. To prevent serious accidents of these structures, the development of monitoring techniques for evaluating the fatigue state is required. In the public constructs, it is difficult to supply the power to sensors at all time from the viewpoint of cost and complexity. The sensors, furthermore, might be exposed to humidity environment even more corrosive environment. Therefore, for monitoring sensors used in such structures, the availability with no power supply and good corrosion resistance is required.

Diamond-like carbon (DLC) coatings are widely used in industrial field because of their excellent mechanical properties such as high hardness, low friction, insulation and chemical stability. Therefore, DLC coatings can be used in extreme environmental conditions such as a corrosive environment because of their chemical stability. Recently, many attempts have been done to fabricate a smart sensor having good mechanical functionality by using DLC coatings [1].

Recently we proposed Molybdenum-containing DLC (Mo-DLC) as a fatigue sensor, which its electric resistance increases in accordance with number of cycles, especially in high cyclic region [2]. Although it indicated the possibility to use metal-containing DLC as a fatigue sensor, it is still not clear whether electric resistance is an optimum parameter for output of fatigue sensor. To use Mo-DLC as a fatigue sensor, we should figure out how fatigue develops. We investigate the structure change of Mo-DLC in accordance with cyclic stress by Raman spectroscopy to understand the mechanism of fatigue process of Mo-DLC film.

2. Method

Ceraflex (ZrO_2) was used for substrate of DLC coating. Ceraflex has high elastic deformation property. The size of substrate is $7\times4\times0.1$ [mm^3]. Samples of Mo-DLC were prepared by the combined technique of chemical vapor deposition (CVD) and DC sputtering of molybdenum target. Pure-DLC, defined as DLC film without any kinds of metal elements, was prepared by only CVD method [3]. Methane gas was used for CVD process. The parameters used for the deposition in this study are listed in Table 1. The metal content of Mo-DLC was 41.2 at.% and film thickness was 1μm.

Table 1. Parameters of the deposition

	CVD+spattering	CVD
Substrate	ZrO_2	ZrO_2
DC generator	200 W	-
Deposition pressure	1.3 ~ 1.6 Pa	13 Pa
Bias voltage	- 400 V	- 600 V
Target material	Molybdenum	-
Ar flow	7.5 ccm	0.0 ccm
CH_4 flow	6.0 ccm	10.0 ccm
Deposition time	30 min.	25 min.

Fatigue process was applied by using a vibration testing device. Figure 1 shows a schematic illustration of the experimental setup in this study. Test samples were bonded on the cantilever beam with glue.

Dynamic strain was applied using an electromagnet with an AC input. The strain applied to Mo-DLC was measured using a strain gauge attached on the backside of the sample. The displacement of beam was measured by using a laser displacement sensor. In this study, the resonance frequency of cantilever was set from 80 to 100 Hz.

The film structure of DLC coatings was measured by Raman spectroscopy analysis with steps of number of bending cycles in the order of 10^i ($i = 0, 1, \cdots 7$). The maximum bending strain applied to the beam of sample was ±250 μ.

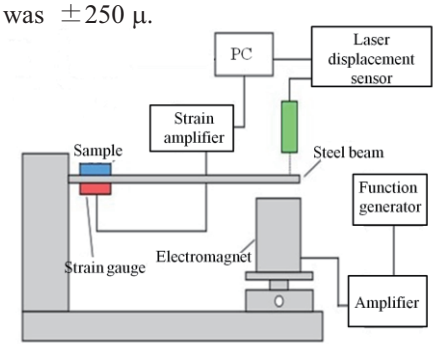

Fig. 1 Experimental setup of vibration test.

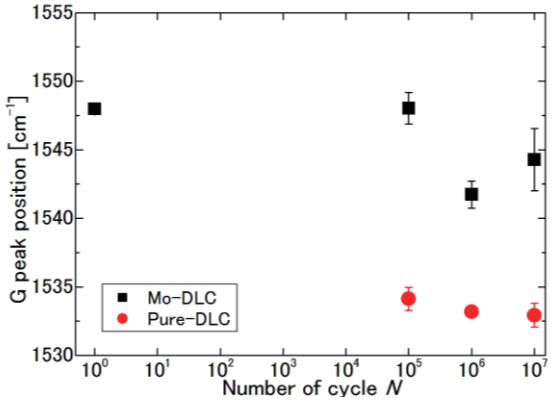

Fig. 2 G peak position in Raman spectra and number of cycles.

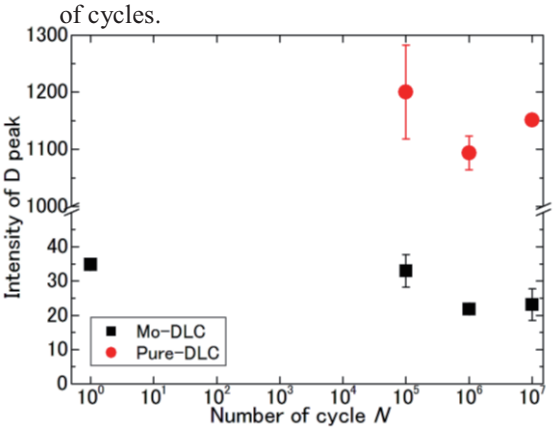

Fig. 3 Variation of intensity of D peak and number of cycles.

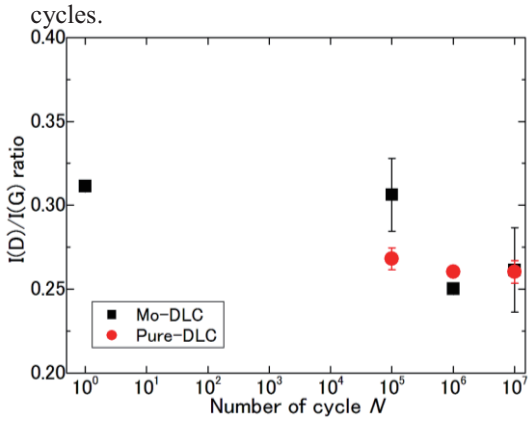

Fig. 4 Variation of intensity ratio and number of cycles.

The specimen with number of cycles (1×10^0, 10^5, 10^6, 10^7) were analyzed by Raman spectroscopy. We used the green light of 532 nm for the Raman spectroscopy using the NRS-5100(JASCO). Raman spectra were fitted using the convoluted BWF function to the G peak, the Lorentz function to the D peak.

3. Results and Discussion

Figure 2 shows the G peak position of Raman spectrum plotted against number of cycles. G peak position of Mo-DLC film was higher than pure-DLC. The G peak position, however, shifted over 10^6 cycles. According to Robertson[4], hydrogen in the DLC film converts sp^2C=C bonds into sp^3C-H binds. There is also a down-shift of the G peak position because of formation of polyacetylene-like H bonded chains. Therefore, G peak position shifts downward with increase of sp^3 content in a-C:H [4].

By taking into account Robertson's suggestion, Mo cluster may make sp^2 bonds unstable, and the sp^2 bonds change to sp^3 bonds by applying the cyclic bending. Furthermore, Fig. 3 shows that the intensity of D peak decrease on Mo-DLC over 10^6 cycles. It is known that lower intensity of D peak suggested less crystallinity of sp^3C-C bonds.

Figure 4 shows the variation of intensity ratio of D peak, I(D), and G peak, I(G), against the number of cycles. Intensity ratio of Mo-DLC was decreased over 10^6 cycles, whereas intensity ratio of pure-DLC was not largely change. According to Tamor, I(D)/I(G) is related to the content of sp^3 bonds, in other words, the higher the intensity ratio means the lower content of sp^3 bonds[5].

These data indicate that the state of carbon bonds in Mo-DLC films change sp^2 to sp^3 due to the cyclic strain derived from metal doping to the DLC host matrix.

4. Summary

In this study, we investigated the mechanisms on change in the film structure with the fatigue cyclic loading. We summarize this study as follows:

- G peak position is increased by including of metal and decreased over 10^6 cycles.
- In Mo-DLC, intensity of D peak decreases over 10^6 cycles by the cyclic bending.
- In the Mo-DLC film, I(D)//I(G) decreases with increase of cycles by cyclic bending.

From the above results, content of sp^2C=C bonds in Mo-DLC film is higher than pure-DLC matrix. Because this sp^2 bond may be unstable, hydrogen may convert sp^2C=C bond to sp^3C-H bond by cyclic bending.

Acknowledgements

This work was partly supported by a Grant-in-Aid for Scientific Research (A) (23240638), the JSPS Core-to-Core Program, A. Advanced Research Networks, "International research core on smart layered materials and structures for energy saving" and the Promoted Research program from the Frontier research Institute for Interdisciplinary Science, Tohoku University. The authors express their appreciation to Mr. Takeshi Sato from the Institute of Fluid Science at Tohoku University for his technical assistance.

References

[1] E. Peiner et al., *Sensors and Actuators A – Physical,* 130, (2006), pp. 75-82.

[2] M. Takahashi et al., *The Ninth International Conference on Flow Dynamics*, (2012), pp. 610-611.

[3] T. Takeno et al., *Diamond and Related Materials*, 17 (2008), pp. 713-716.

[4] J. Robertson, Diamond-like amorphous carbon, *Material Science and Engineering R,* **37**, (2002), pp.129-281.

[5] M. A. Tomor et al., *Journal of Applied Physics,* 76, (1994), pp. 3823-3830.

Study on Micro-/Nanoscale Gas-Film Lubrication of Sliding Surface with Three-Dimensional Structure

Yoshiaki Kawagoe[1], Shigeru Yonemura[2], Susumu Isono[1], Takanori Takeno[1], Hiroyuki Miki[3] and Toshiyuki Takagi[2]
[1]Tohoku University, JAPAN
[2]Tohoku University, IFS, JAPAN
[3]Tohoku University, FRIS, JAPAN
kawagoe@chapman.ifs.tohoku.ac.jp

ABSTRACT

Nakamori et al. found experimentally that the friction between a partly polished diamond-coated surface and a metal surface was drastically reduced to zero as relative speed increased to a few m/s, and it seems that the diamond-coated surface took off the counter surface and the sliding mechanism was the gas film lubrication. In this study, to investigate the role of the gas flow for this phenomenon, we reproduce the complicated structure of the diamond-coated surface in the computational domain by using the data measured by Atomic Force Microscope (AFM), and perform numerical simulations of three dimensional micro-/nanoscale gas flows.

1. Introduction

Recently, Chemical Vapor Deposition (CVD) has made progress, so that it has become possible to manufacture of diamond thin film. Diamond-coated sliding surface is promising for gas bearing because it produces very low friction in the boundary lubrication. Nakamori et al. [1] found experimentally that the friction between a diamond-coated surface and a metal surface was drastically reduced to zero as relative speed increased. Their experimental results are shown in Fig. 1. In their experiment, sliding became noiseless. This indicates the sliding mechanism is not the boundary lubrication, but would be the molecular gas film lubrication after the substrate with diamond coating takes off the counter surface. In the previous work, to investigate the floating mechanism, we performed numerical simulations of micro-/nanoscale gas flow in two dimensional space by using very simplified surface structure[2]. However, the real diamond coated surface has very complicated configuration and therefore the gas flow between sliding surfaces is not simple. In this study, we reproduce the complicated structure of the diamond-coated surface in three dimensional space by using the data measured by AFM. The reproduced surface is shown in Fig. 2. We investigate the gas flow between the two sliding surfaces by performing numerical simulations.

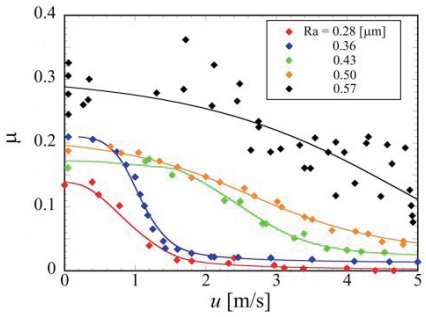

Fig. 1 Experimental results of the relation between the friction coefficient and the relative speed.

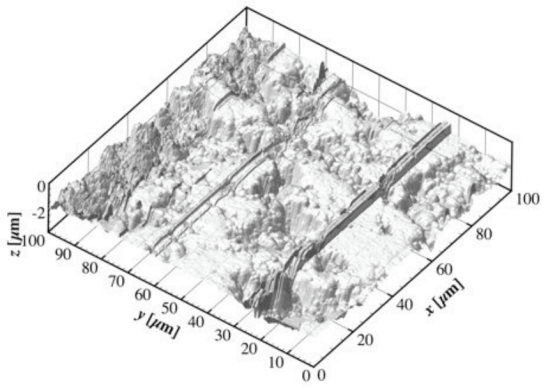

Fig. 2 The diamond-coated surface reproduced from the measured data by using Marching Cubes Method.

2. Method

Gas flows between two sliding surfaces cannot be treated as a continuum. The mean free path λ of atmospheric molecules is estimated at 0.065 μm, while the surface roughness of the diamond coated substrates is from 0.28 μm to 0.57 μm. The distance between two sliding surfaces will be in the order of surface roughness or smaller. Therefore, Knudsen number $Kn(=\lambda/L)$ will be larger than 0.1, where L is the characteristic length of the flow. Such kind of microscale gas flow, which is called 'high Knudsen number flow', is in nonequilibrium due to the lack of intermolecular collisions and is not governed by Navier-Stokes equations but by Boltzmann equation. To simulate this flow, we use the direct simulation Monte Carlo (DSMC) method [3], which is the stochastic solution of Boltzmann equation.

We reproduce the diamond-coated surface by using Marching Cubes method[4]. The computational domain is the region surrounded by the red lines as shown in Fig.3. In Fig. 3, the lower surface imitates the diamond-coated surface and the upper surface imitates the counter surface. The counter surface is treated as the flat plate in the present simulation. The lower surface moves in the x direction at relative speed u. The length $h_{\min}$ represents the minimum distance between two

surfaces. The computational region surrounded by the red lines is symmetry with respect to $x = l/2$, where l is the length of the computational domain. We treat the boundaries in the x direction as periodic and the boundaries in the y direction as specular.

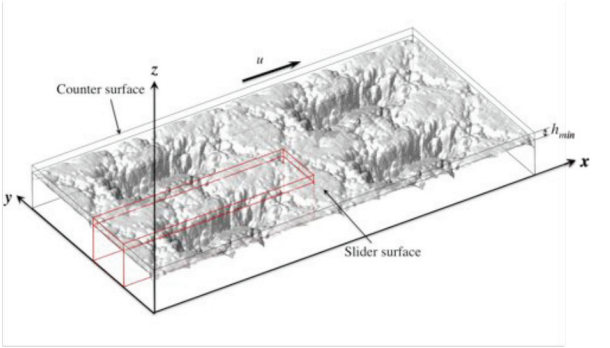

Fig. 3 Conputational domain.

The flow field and molecular motions are treated as three-dimensional. The motions and collisions of molecules are traced and, hence, time evolution of the flow field is simulated. The computational domain is divided into cells. Intermolecular collisions in the same cell are calculated stochastically by using the maximal collision number method. The gas is atmospheric air with the room temperature, T_g=300 K. The wall temperature is also set at the room temperature T_g=300K. The hard sphere model is used for collision calculation. The molecular diameter is 0.37 nm. Since the mean free time of molecule is 1.4×10^{-10} s, the time step of simulated molecule is set at 1.4×10^{-11} s. The velocities of the molecules reflected by the solid surface are determined by using the diffuse reflection model with the wall temperature.

3. Results and Discussion

Figure 4 shows the pressure distribution obtained in the DSMC simulation. In the case of Fig. 4, the surface roughness R_a of the diamond-coated substrates is 0.21μm, h_{min} is 0.028 μm and the average distance from the counter surface to diamond-coated surface h_{ave} is 0.28μm. The pressure distribution shows that the gauge pressure of 2.33×10^3 Pa acts on the diamond coated surface. While in the experiment, the slider used in the experiment of Nakamori et al. has a weight of 280 gf and an area of 1960 mm^2. Hence, the gauge pressure of 1.4×10^3 Pa (=2.74 N) is required to float the slider. Therefore, the lift force obtained in the present simulation is large enough to suspend the slider.

Figure 5 shows the effect of the relative speed u on the lift force. The lift force increases as the relative speed increases.

4. Concluding remarks

In this study, we reproduced the diamond-coated surface in the computational space by using the data measured by the AFM. To investigate the effect of micro/nanoscale gas flow between two sliding surfaces, we performed numerical simulations. In the DSMC simulation, we obtained the lift force of 2.33×10^3Pa, which is large enough to suspend the slider used in the experiment. The simulation results shows that the lift force increases as the relative speed increases.

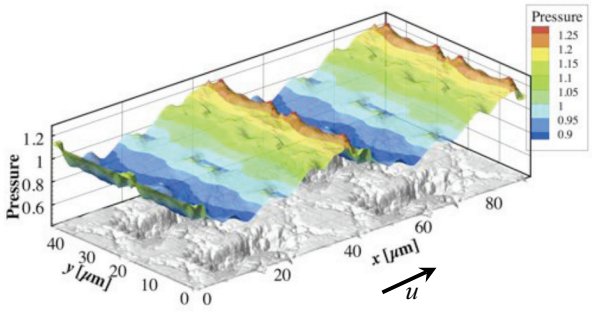

Fig. 4 Pressure distribution(u=10 m/s, R_a=0.21 μm, h_{min}=0.028 μm).

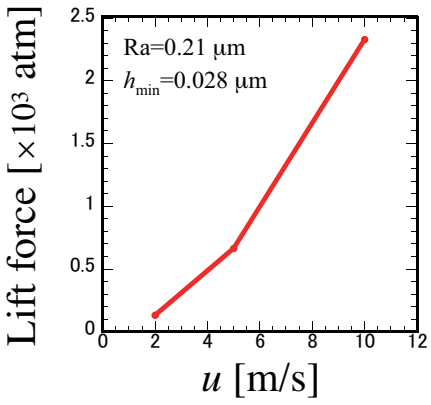

Fig. 5 The effect of the relative speed u on the lift force.

References

[1] Nakamori, I. et al., *Diamond Relat Mater,* Vol. 14, (2005), pp. 2122-2126.

[2] Yonemura, S. et al., *AIP Conf Proc,* Vol. 1084, (2008), pp. 1153-1157.

[3] Bird, G. A., *Molecular Gas Dynamics and the Direct Simulation of Gas Flows,* (1994), Clarendon, Oxford.

[4] Lorensen, W. E. and Cline, H. E., *Computer Graphics,* Vol. 21, (1987), pp. 163-169.

Tenth International Conference on Flow Dynamics
November 25-27, 2013, Sendai, Miyagi, Japan

Lubrications of MoS_2 Dispersed Ti based Composite Materials Formed by the Compression Shearing Method at Room Temperature

Sho Takeda[1], Noboru Nakayama[2], Hiroyuki Miki[3], Hiroyuku Takeishi[4], Toshiyuki Takagi[5]
[1]Graduate school of Engineering, Tohoku University, 6-6 Aramaki aza Aoba, Aoba-ku, Sendai, 980-8579, Japan
[2]Shinshu University, 4-17-1 Wakasato, Nagano, 380-8553, Japan
[3]FRIS, Tohoku University, 6-3 Aramaki aza Aoba, Aoba-ku, Sendai, 980-8578, Japan
[4]Chiba Institute of Technology, 2-17-1 Tsudanuma, Narashino, 275-0016, Japan
[5]Institute of Fluid Science, Tohoku University, 2-1-1 Katahira, Aoba-ku, Sendai, 980-8577, Japan
*Corresponding author: takagi@ifs.tohoku.ac.jp

ABSTRACT

To improve friction characteristics of Ti, MoS_2 powder was dispersed in Ti matrix. Ti/MoS_2 composite plates were formed by the compression shearing method at room temperature (COSME-RT). The samples with five different MoS_2 content ratios between 0 to 2.0 vol.% were prepared. In comparison with a rolled Ti, the friction characteristics of the Ti/MoS_2 formed by COSME-RT were improved due to the reason that the tensile strength was increased. The tensile strength of Ti/MoS_2 was 2.3 times larger than rolled Ti and the abrasion resistances were improved. In addition, the coefficients of friction of the Ti/MoS_2 become high in some samples.

1. Introduction

Titanium (Ti) and its alloy are lightweight and have high strength, and these are widely used in many fields. However, their adhesions are too low to use as slide members. If Ti has a self-lubricating property by distributing a solid lubricant, it can be adapted as a slide member to reduce weight especially for the space equipments.

Molybdenum disulfide (MoS_2) is known as a representative of the solid lubricant. It is used in the same way of lubricant oil and grease in many fields. In addition, MoS_2 shows very low friction in the vacuum. For these reason, the development of composite material of Ti and MoS_2 has been investigated.

The powder metallurgy is one of the typical forming methods of composite materials from powder material. However, since the sintering temperature of Ti is higher than the oxidization temperature of MoS_2 (623K), the friction characteristic of the composite material become worse under the conventional powder metallurgy technique. Thus, the new method for forming composite materials which prevent oxidation process of MoS_2 is required.

The compression shearing method at room temperature (COSME-RT) is a method for forming a thin metal plate by applying a shearing strain and a compression stress to a metal powder simultaneously at room temperature and in the atmosphere[1]. By using this method, it is expected that Ti/MoS_2 thin plates show self-lubricating property. In fact, the study by Miki et al.[2] indicated that Al-Si-Cu-Mg/MoS_2 composite material formed by COSME-RT has excellent friction characteristic.

In this study, Ti/MoS_2 composite materials are formed by COSME-RT, and lubrications of them are investigated.

2. Method

2.1 Materials

The materials used in this study were powder of 99.65% purity Ti and 98.00% purity MoS_2. Fig. 1 shows scanning electron microscopy (SEM) images of the pure Ti and MoS_2 powders. The average particle size of the Ti and MoS_2 were 45 and 6 μm, respectively. Ti powder was manufactured by a hydrogenation-dehydrogenation process, and its shape was non-spherical.

2.2 Mixed conditions

Ti and MoS_2 powders were mixed by a triaxial milling machine. The powders were mechanically mixed at 300 r/min and in Ar atmosphere, and milling time was 480 min. MoS_2 content ratio r was varied to 0, 0.5, 1.0, 1.5, and 2.0 vol.%.

2.3 Forming conditions

Fig. 2 shows a schematic illustration of solidification process of COSME-RT. First, Ti/MoS_2 mixed powder is placed between the stationary plate and the moving plate, and the compression stress σ_N is applied to the moving plate and maintained during forming process. Then, the shearing strain γ is added to a mixed powder by displacing the moving plate, and a metal plate sample is solidified. The shearing strain was determined from $\gamma = L_S / t_P$, where L_S is the shearing distance (L_S = 4 mm) and t_P is the sample thickness (t_P = 0.25 mm). The net weight of a mixed powder was 0.45 g, the target size was 20 × 20 × 0.25 (mm), σ_N = 1250 MPa, γ = 20, and the shear rate was 5 mm/min. All samples were formed at room temperature and in the atmosphere.

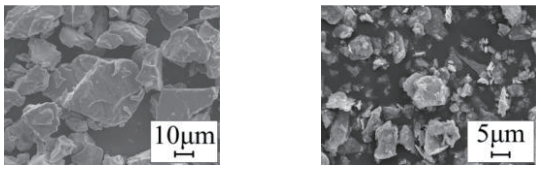

(a) Pure Ti powder (b) MoS_2 powder

Fig. 1 SEM images of the Ti and MoS_2 powders.

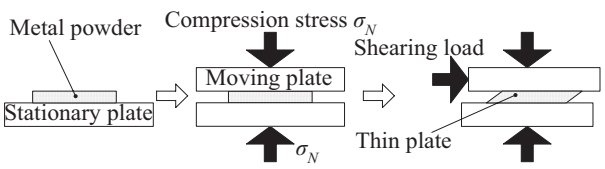

Fig. 2 Schematic illustration of COSME-RT.

3. Results and Discussion

To investigate the mechanical strength of the samples, a tensile test was carried out by using a table-top type universal testing machine. The test was carried out for r = 0, 1.0, 2.0 vol.% samples, and the rolled Ti for comparison with crosshead speed set to 0.5 mm/min. Fig. 3 shows the relationship between MoS_2 content ratio and the tensile strength of the samples. It shows the tensile strengths of the samples formed by COSME-RT were 2.3 times larger than those of the rolled Ti.

To investigate the friction characteristics of the samples, friction test was carried out using a ball-on-disk type tribometer. The test was also carried out for the rolled Ti samples for comparison. The normal load, the sliding distance, and the sliding velocity were 1 N, 130 m, and 12 mm/s, respectively. A Si_3N_4 ball with a diameter of 6 mm was used for the test, and the test was carried out at room temperature and in the atmosphere. Fig. 4 shows the relationship between the sliding distance L and the coefficients of friction of r = 1.0 vol.% samples. It shows that the coefficients of friction of the samples were approximately 0.4 and frictional behavior were unstable at first. However, if the coefficient of friction of the sample after running-in was approximately 0.2 even if it was high at first, frictional behavior was stable.

The average values of the coefficients of friction were calculated by averaging the values of coefficients of friction from L = 100 to 130 m in each sample. Fig. 5 shows the relationship between MoS_2 content ratio and the average coefficients of friction of the samples. In the low friction cases, the coefficients of friction of the samples formed by COSME-RT were 0.2, and these were approximately 60% lower than the rolled Ti. On the other hand, in the high friction cases, the coefficients of friction of the samples formed by COSME-RT were as high as those of the rolled Ti samples. In addition, there was no correlation between MoS_2 content ratio and the coefficient of friction of the sample. However, although the coefficients of friction of r = 0 vol.% samples were constantly low, those of r = 2.0 vol.% samples were constantly high. From these results, it seems that there is upper limit of MoS_2 content ratio.

To investigate the effects of MoS_2 on the bonding strength of the samples, the fracture surfaces were observed. Fig. 6 shows SEM image of fracture surface of r = 2.0 vol.% sample. It indicated that MoS_2 is likely to drop out, and separate Ti and MoS_2 regions exist. These results suggest that MoS_2 prevents bonds of Ti powder particles.

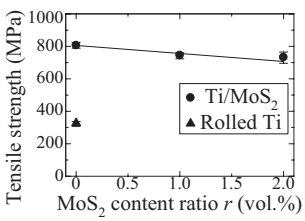

Fig. 3 Relasionship between MoS_2 content ratio and the tensile strength of the samples.

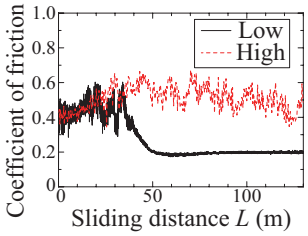

Fig. 4 Relationship between sliding distance L and coefficient of friction of r = 1.0 vol.% samples.

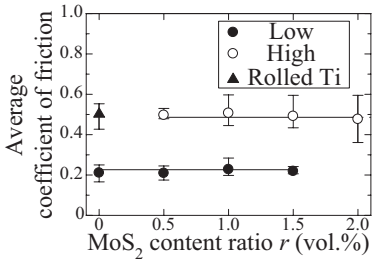

Fig. 5 Relationship between MoS_2 content ratio and average coefficient of friction of the samples.

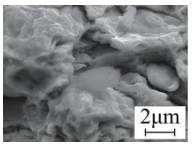

Fig. 6 SEM image of the fracture surface of r = 2.0 vol.% sample.

4. Concluding remarks

In this study, Ti/MoS_2 composite materials were formed by COSME-RT, and lubrications of them were investigated. The results were as follows.

1) The friction characteristics of the samples were improved because of the strengthened tensile strengths of the samples formed by COSME-RT. Those were 2.3 times larger than rolled Ti and the abrasion resistances of the samples were improved.
2) Since MoS_2 prevents bonds of Ti powder particles, the coefficients of friction of the Ti/MoS_2 composite plates become high in some samples.

As a result, the Ti thin plate formed by COSME-RT has more excellent friction charactaristics than the rolled Ti and Ti/MoS_2 in the atmosphere. In addition, it became clear that change of the crystal structure due to the dispersion of MoS_2 is the factor of stability of frictional behavior of the Ti/MoS_2 composite plates.

Acknowledgement

Part of this work was carried out under the Collaborative Research Project (J13066) of the Institute of Fluid Science, Tohoku University, Japan and the Promoted Research program from the Frontier research Institute for Interdisciplinary Science, Tohoku University, Japan.

References

[1] H. Takeishi, N. Nakayama, H. Miki, J.Soc. Mat. Sci., Japan, 54-3 (2005), 233-238.

[2] H. Miki, N. Nakayama, H. Takeishi, T. Takagi, 38th Leeds-Lyon Symposium on Tribology, Lyon, France, (2011).

Development of Phosphor-TSP for High-Temperature Distribution Measurement

Akiho Ishida and Hiroki Nagai
Department of Aerospace Engineering, Tohoku University
6-6-01, Aramaki-Aza-Aoba, Aoba-ku, Sendai 980-8579, JAPAN
ishida.akiho@aero.mech.tohoku.ac.jp

ABSTRACT

Temperature-Sensitive-Paint (TSP) is known as the temperature sensor can provide a full-field image of the temperature distribution on a model surface. However, TSP has a limit for temperature sensitivity. In this research, we studied Phosphor-TSP for high temperature region. We clarified temperature characteristics of some Phosphor-TSP and measured temperature distribution.

1. Introduction

Temperature-Sensitive Paint (TSP) is generally used for thermal analysis of model surface. Usual TSP is made of organic compound, but they decompose thermally at temperatures greater than about 100 °C. So, these days TSP using phosphor has been studied [1]. Phosphor is an inorganic powder, and has high thermal tolerance.

However, the temperature characteristics of Phosphor have not been clarified in detail.

In this study, we conducted experiments to clarify the temperature characteristics of some Phosphor. Moreover, we make Phosphor-TSP and paint to the model to measure the temperature distribution.

2. Phosphor-TSP

In this study, we focused on the characteristics of four Phosphors: Y_2O_3:Eu^{3+} , YAG:Dy^{3+} , $LaPO_4$:Ce^{3+},Tb^{3+} and $BaMgAl_{10}O_{17}$:Eu^{3+}. These Phosphors have different emission wavelength (Fig.1).The colloidal-silica was chosen as a binder.

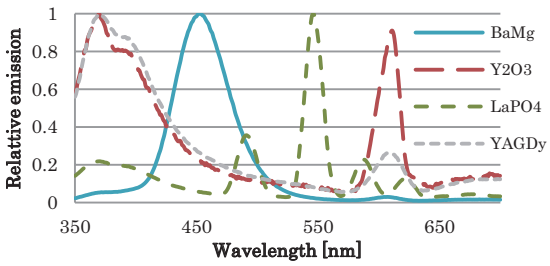

Fig.1 Emission Wavelength

3. Temperature Characteristics Tests

3-1 Setup

In this study, three kinds of tests were conducted.

- Test1: temperature sensitivity test
- Test2: durability for heating time test
- Test3: heat cycling test

Fig.2 shows the image of the setup for these tests. Phosphor was heated by heating-stage. The pictures of heated Phosphor were taken by 16 bit Cooled CCD camera with band-pass-filter. Additionally, we used spectroscope to measure the emission spectrum. Hg-Xe lamp was used as the excitation light.

The range of testing temperature was decided by expected temperature sensitivity of Phosphor[1]. We took pictures of Phosphor luminescent every 50 °C with excitation light and without it to cut off the influence of the infrared radiation emitted by the heating-stage in high temperature.

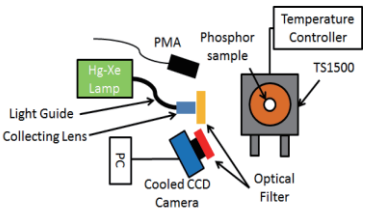

Fig.2 Setup of temperature characteristics tests

3-2 Results of Temperature Characteristics Tests

Fig.3 shows the result of Test.1. The emission intensity and the condition are expressed by *I* and *ref*, respectively. The reerence condition is the emission at 20 °C (I/I_{ref}=1). According to Fig.3, each Phosphor has different temperature sensitivity. Y_2O_3:Eu^{3+} and $LaPO_4$:Ce^{3+},Tb^{3+} have two points which have the same value of I/I_{ref}. Thus, it is necessary to decide the temperature range for getting reliable temperature distribution data with these Phosphors. YAG:Dy^{3+} can be used at narrow temperature range at higher temperature. $BaMgAl_{10}O_{17}$:Eu^{3+} has good sensitivity under 750 °C.

As the result of Test1, suitable temperature rage for each Phosphor and maximum sensitivity is clarified in Table.1.

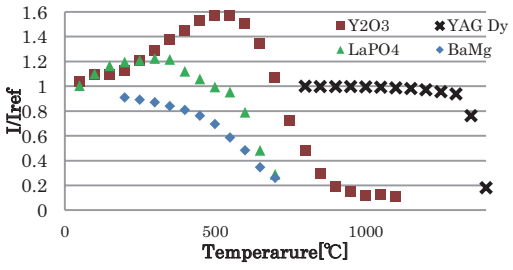

Fig.3 Temperature sensitivity curb

Table.1 Characteristics of sensitivity

Phosphor	Range [°C]	Sensitivity[%/K]
Y_2O_3:Eu^{3+}	200～550 550～1000	0.51
YAG:Dy^{3+}	1300～1400	2.3
$LaPO_4$:Ce^{3+},Tb^{3+}	400～700	0.38
$BaMgAl_{10}O_{17}$:Eu^{3+}	200～700	0.30

Fig.4 shows the result of Test2. The reference condition is the emission at 0 min after heating. The emission intensity of Y_2O_3:Eu^{3+} and $LaPO_4$:Ce^{3+},Tb^{3+} decreased as time running. Thus, these two Phosphors are inadequate to use in long time heating tests. Especially, the emission of $LaPO_4$:Ce^{3+},Tb^{3+} decreases largely within first 5 min.

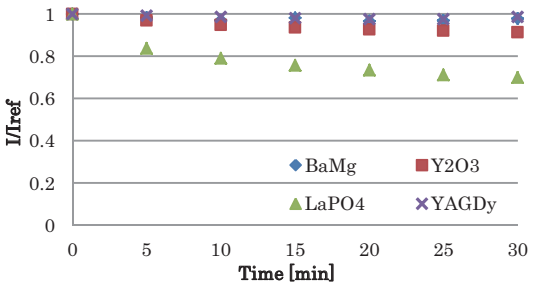

Fig.4 Characteristics of durability

Fig.5 shows the result of Test3. In this test, we set the minimum and maximum temperature in Table.2. At first, all phosphors were heated to maximum temperature (Cycle1). After that, Phosphors were cooled to minimum temperature and heated again (Cycle2). The reference condition was the emission of Cycle1.

The emission intensity of $LaPO_4$:Ce^{3+},Tb^{3+} decreased at both temperature. This decreasing caused by deterioration of $LaPO_4$:Ce^{3+},Tb^{3+} in heat cycle. On the other hand, the emission of YAG:Dy^{3+} and $BaMgAl_{10}O_{17}$:Eu^{3+} were decreased a little only at minimum temperature. It is considered that these decreases were caused by inaccurate control of minimum temperature.

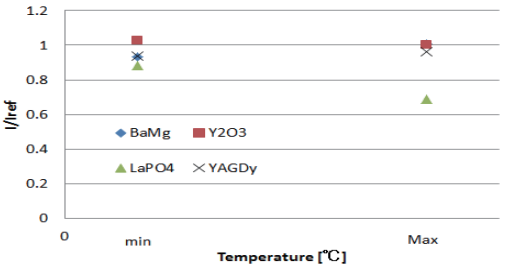

Fig.5 Characteristics of Cycling

Table.2 minimum and maximum temperature

Phosphor	min [℃]	max [℃]
Y_2O_3:Eu^{3+}	200	850
YAG:Dy^{3+}	800	1350
$LaPO_4$:Ce^{3+},Tb^{3+}	200	700
$BaMgAl_{10}O_{17}$:Eu^{3+}	200	700

4. Temperature Distribution Test

4-1 Setup

Fig.6 shows the image of the setup. Testing plate was heated by a non-flame torch. The temperature was controlled by voltage and the maximum temperature was set to about 550 ℃. The pictures of heated Phosphor were taken by high speed CCD camera with band-pass-filter. $BaMgAl_{10}O_{17}$:Eu^{3+} was chosen as based on the result of temperature characteristics tests and the maximum temperature of the torch. The half of the plate was painted with $BaMgAl_{10}O_{17}$:Eu^{3+} Phosphor-TSP.

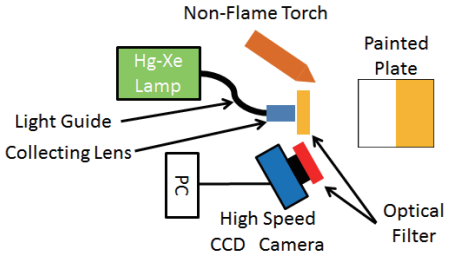

Fig.6 Set-up of temperature distribution test

4-2 Results of Temperature Distribution Test

Fig.7 shows temperature distribution image of the surface. Time history of temperature at heating point is shown in Fig.8. From Fig.7, it was found that temperature changes resulted in heat conduction were measured by using Phosphor-TSP even though temperature images were rough a little. This roughness was caused by the bigness of $BaMgAl_{10}O_{17}$:Eu^{3+} particle.

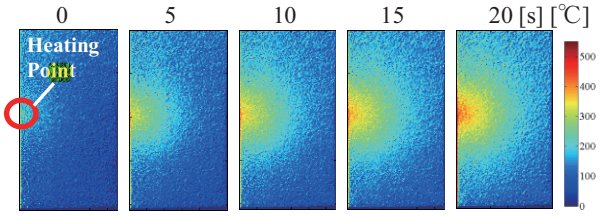

Fig.7 Time history of the temperature distribution

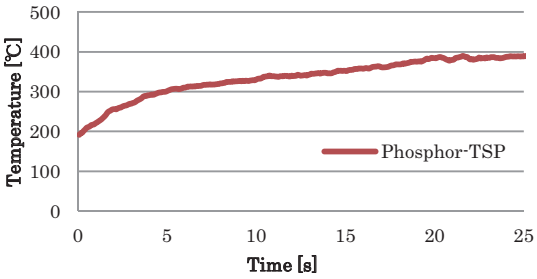

Fig.8 Time history of the temperature at heating point

5. Conclusion

In this study, the temperature characteristics of four kinds of Phosphors were investigated and measured the temperature distribution by heating on the model.

Through temperature characteristics tests, we chose $BaMgAl_{10}O_{17}$:Eu^{3+} for the temperature distribution test and, we could get good temperature distribution images and time history of temperature. Thus, the Phosphor-TSP can be used in high temperature distribution measurement.

6. Reference

[1]*S. W. Allison*
Rev. Sci. Instrum.,Vol.68, No.7, pp.2623-2624 *1997*

Mechanical Properties and Martensitic Transformation of Ni-Mn-In Based Magnetic Shape Memory Alloy Films

Koki Tsuchiya[1], Makoto Ohtsuka[2], Hiroyuki Miki[3] and Toshiyuki Takagi[4,*]
[1]Graduate school of Engineering, Tohoku University, Aramaki aza Aoba 6-6, Aoba-ku, Sendai 980-8579, Japan
[2]IMRAM, Tohoku University, Katahira 2-1-1, Aoba-ku, Sendai 980-8577, Japan
[3]FRIS, Tohoku University, Aramaki aza Aoba 6-3, Aoba-ku, Sendai, 980-8578, Japan
[4]IFS, Tohoku University, Katahira 2-1-1, Aoba-ku, Sendai 980-8577, Japan
*Corresponding author: takagi@wert.ifs.tohoku.ac.jp

ABSTRACT

The mechanical properties of Ni-Mn-In films containing Co were measured by a nanoindentation method. The films were deposited by a dual magnetron sputtering apparatus using $Ni_{45}Mn_{40}In_{15}$ and Co targets. The crystal structures of the Ni-Mn-In films were changed by the Co concentration. The martensitic transformation temperature decreased with increasing Co concentration. After heat-treatment, the films showed the good crystalline order and both the hardness and the elastic modulus decreased by changes in microstructure. The relative decreasing elastic modulus was observed with increasing Co concentration.

1. Introduction

Ferromagnetic shape memory alloys (FSMAs) show the martensitic transformation (MT) induced not only by temperature and stress but also by magnetic field. Therefore, FSMAs have been expected to be applied to a magnetic driven actuator material which may enable quick response and remote control [1]. Recently, Ni-Mn-*X* (*X* = In, Sn) type FSMAs have been found and their MT has been observed from ferromagnetic austenitic (A) phase to antiferromagnetic or paramagnetic martensitic (M) phase [2]. It was reported for Ni-Mn-In bulk samples that the MT temperature decreases by a magnetic field [3]. In the same way, this fact suggests the magnetic induced meta-magnetic phase transition (reverse MT). Therefore these alloys are expected to exhibit the shape memory effect (SME) associated with the reverse MT induced by a magnetic field. Additionally, it was reported for Ni-Mn-In bulk samples contained Co that the MT temperature (M_s) decreases while Curie temperature (T_C) increases with increasing Co concentration [2].

In this study, the Ni-Mn-In FSMA films with various Co concentrations are prepared by sputtering method. The crystal structure and mechanical properties of these films are investigated.

2. Experimental procedure

The Ni-Mn-In films containing cobalt were deposited using the dual magnetron sputtering apparatus which has radio-frequency (RF) and direct current (DC) power sources. The RF power for Ni-Mn-In target was kept at 200 W and the DC power for Co target was changed from 0 to 15 W. The nominal composition of Ni-Mn-In target is $Ni_{45}Mn_{40}In_{15}$. The thickness of the films was kept at about 1 μm. After deposition, the films were heat-treated (HT) at 1123 K for 3.6 ks. The crystal structures of the films were investigated at room temperature (RT) using an X-ray diffraction (XRD) equipment (D8 DISCOVER, Bluker). The concentrations of the films were determined by an inductively coupled plasma (ICP) spectrometry apparatus (SPECTRO ARCOS, AMETEK). For mechanical properties, hardness and elastic modulus were measured by the nanoindentation apparatus (ENT-1100a, ERIONIX) with triangular-base Berkovich indenter (a face angle of 65.03°) in reference to ISO14577-1 [4]. In the case of indentation test for thin film, the effects of substrate and interface are considered to be negligible if penetration depth is kept to less than one-tenth of the film thickness [5]. Therefore maximum indentation load, F_{max}, was varied from 0.1 to 1.0 mN in ten steps so that the maximum indentation depth, $h_{max,}$ be within 0.015 ~ 0.10 μm. In regard to nanoindentation testing, the projected area of contact, $A_p(h_C)$, is found from a determination of the contact depth, h_C, and the known geometry of the indenter. The elastic modulus of the film, E_{IT}, is determined from the slope of the unloading curve at maximum load (contact stiffness), S,

$$E_{IT} = \left\{1-(\nu_S)^2\right\} \Bigg/ \left\{ \frac{2\sqrt{A_p(h_C)}}{\sqrt{\pi}S} - \frac{1-(\nu_i)^2}{E_i} \right\}. \qquad (1)$$

Here, ν_S is Poisson's ratio for the specimen, and ν_i and E_i are Poisson's ratio and the elastic modulus of the indenter.

Furthermore, hardness of the film, H_{IT}, is defined as

$$H_{IT} = F_{max} / A_p(h_C). \qquad (2)$$

3. Results and Discussion

3.1 Concentration of Ni-Mn-In alloy films

Table 1 shows the concentration of the as-deposited films. Co concentration of the films increased in proportion to DC sputtering power, W_{DC}, for Co target. In this paper, the prepared films are expressed as *x*Co through each Co concentration (*x* mol%Co).

Table 1 Concentration of the Ni-Mn-In sputtered films containing Co.

Sample	W_{RF} /W	W_{DC} /W	Concentration of films mol%Ni	mol%Mn	mol%In	mol%Co
0Co	200	0	49.7	38.0	12.3	0
2.3Co	200	5	50.1	35.1	12.5	2.3
3.4Co	200	8	49.7	34.5	12.4	3.4
4.4Co	200	10	49.1	34.2	12.3	4.4
6.4Co	200	15	48.0	33.5	12.1	6.4

3.2 Structures

Fig. 1 shows the XRD profiles at RT for *x*Co (x = 0, 2.3, 3.4, 4.4, 6.4) HT films and 3.4Co as-deposited film after separating a substrate. For the 3.4Co as-deposited film, the weak diffraction peaks were observed. After heat-treatment, the XRD pattern of *x*Co (x = 0 ~ 6.4) HT films showed the distinct diffraction peaks due to good crystalline order. The diffraction peaks from M phase were observed for *x*Co (x = 0 ~ 4.4) HT films in Fig. 1. The diffraction peak from A phase was also appeared at around 43° of 2θ for the 4.4Co HT film. It indicates that two phases may coexist at RT for the 4.4Co HT film. For the 6.4Co HT film, the diffraction peaks from M phase became smaller and those from A phase enlarged. These results show that M_s of the Ni-Mn-In HT films decrease with increasing Co concentration.

3.3 Load - displacement curves

Fig. 2 shows the typical load - displacement curves obtained by indentation testing. There were differences in the maximum indentation depth and the slope of the unloading curve for the as-deposited and the HT films in Fig. 2. This difference suggests that the mechanical properties of the films were changed by heat-treatment. As shown in Fig. 2, load - displacement curves seemed to be not dependent on Co concentration.

3.4 Hardness

After heat-treatment, the hardness of films decreased from about 9 GPa to about 5 GPa regardless of Co concentration. This decrease of hardness with heat-treatment is attributed to grain coarsening and decreasing compressive stress in the film due to a peening effect during sputtering.

3.5 Elastic modulus

The elastic modulus of films decreased from about 170 GPa to about 140 GPa after heat-treatment. This decrease of elastic modulus is assumed to be due to waning of a peening effect during sputtering. As for the each film which has the different phase states at RT according to Co concentration, the change of elastic modulus could not be confirmed. In general, in regard to SMA bulk samples, elastic modulus of A phase is considered to be larger than that of M phase because of the difference in crystal structure. For Ni-Ti type SMA as practical use (e.g. KSM-SM Alloy, Nippon Steel & Sumitomo Metal Corporation), the elastic modulus changes from 15 ~ 30 GPa (M phase) to 50 ~ 70 GPa (A phase) with phase transition [6]. In this research, there was little difference in elastic modulus between M phase (0 ~ 3.4 Co) and A phase (6.4Co). It indicates relative decreasing elastic modulus for 6.4Co (A phase). In the future, temperature dependence of the mechanical properties will be evaluated for each phase.

4. Summary

In this study, for Ni-Mn-In alloy films containing Co prepared by co-sputtering method, the concentration and crystal structure were investigated. The diffraction peaks

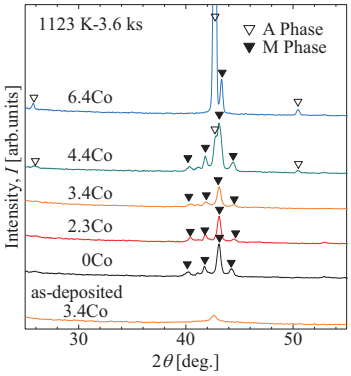

Fig. 1 Effect of Co addition on the XRD profiles of Ni-Mn-In films.

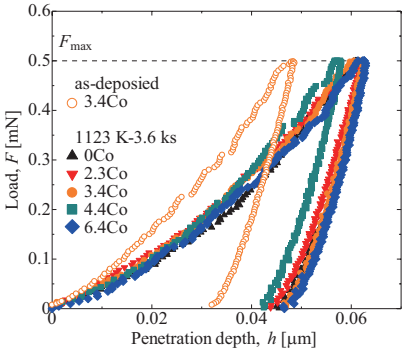

Fig. 2 Load - displacement curves for the 3.4Co as-deposited film and the *x*Co (x = 0 ~ 6.4) HT films on Al_2O_3 substrate.

from A phase appeared and were enlarged with increasing Co concentration. The mechanical properties of the films were evaluated by nanoindentation methods. The hardness and the elastic modulus of the HT films are lower than those of as-deposited films. For the HT films, the elastic modulus gradually decreases with increasing Co concentration. These results indicate that the ductility of the films may be improved by heat-treatment, and the obtainable strain associated with the shape recovery is expected to be larger.

Acknowledgement

This work was partially supported by the Promoted Research program from the Frontier research Institute for Interdisciplinary Science, Tohoku University and the JSPS Core-to-Core Program, A. Advanced Research Networks, "International research core on smart layered materials and structures for energy saving".

References

[1] M. Matsumoto *et al.*, J. JSAEM, **8** (2000), 445.
[2] Y. Sutou *et al.*, Appl. Phys. Lett., **85** (2004), 4358.
[3] K. Oikawa *et al.*, Appl. Phys. Lett., **88** (2006), 122507.
[4] ISO14577-1, "*Metallic Materials-instrumented Indentation Test for Hardness and Materials Parameters-Part 1*": Test Method, 2002.
[5] M. F. Doerner *et al.*, J. Mater. Res., **1** (1986), 845.
[6] Nippon Steel & Sumitomo Metal Corporation. "*Shape-memory alloys*", <http://www.nssmc.com/en/product/railway-automotive-machinery-parts/keijou/>.

Studies of Transport Mechanism of The Bacterial Aspartate : Alanine Antiporter (AspT). Functional Analysis of The Amino Acid Residues in The Transmembrane Domain 3 of AspT.

Satomi Suzuki,[1] Takuya Kimura,[1] Ayako Sasahara,[1] Kei Nanatani,[2] Keietsu Abe[1,3]
1 ; Tohoku Univ., Agr.
2 ; Department of Biomolecular Engineering, Graduate School of Engineering, Tohoku University
3 ; Tohoku Univ., New Industry Creation Hatchery Center (NICHe).
1-1 Tsutsumi-dori Amamiya-machi, Aoba-ku, Sendai, 981-8555, Japan
kabe@niche.tohoku.ac.jp

ABSTRACT

The secondary transporter AspT of the lactic acid bacterium *Tetragenococcus halophilus* catalyzes the electrogenic exchange of L-Aspartate^{1-} (L-Asp) with L-Alanine^{0} (L-Ala). In our previous studies, we found AspT has two substrate binding sites and binding conformations for L-Asp and L-Ala. To elucidate the substrate transport mechanism of AspT, we focused on transmembrane domain (TM) 3 which is one of TMs forming the putative substrate translocation pathway. Consequently, a unique amino acid sequence, GxxxG, located at the center of TM3 was experimentally demonstrated to be involved in the maintenance of transport ability of AspT.

1. Introduction

In some strains of the lactic acid bacterium *Tetragenococcus halophilus*, a proton-motive force (pmf) is generated by the combined action of the intracellular L-Aspartate decarboxylation reaction, catalyzed by an L-Aspartate-4-decarboxylase (AspD), and an electrogenic L-Asp^{1-} : L-Ala^{0} exchange reaction, catalyzed by an L-Asp : L-Ala antiporter (AspT)[1]. The generated pmf is sufficiently high to drive ATP synthesis via the bacterial F1Fo-ATPase. This combination of pmf and ATP synthesis has been proposed as a proton motive metabolic cycle.

AspT is classified as a conventional secondary transport protein and belongs to the newly classified Aspartate : Alanien Exchanger (AAEx) family (TC number 2. A. 81) of transporters in the Membrane Transport Proteins Classification system developed by Saier *et al* (http://www.tcdb.org/index.php). Some industrially important transporters including succinate transporter SucE1 are categorized in this family. In the physiological viewpoints, AspT is one of transporters possessing high transport rates, and forms an energy production system with cytoplasmic AspD as previously described[1]. These properties are useful for fermentation industry.

In our previous work, we reported that AspT has two different substrates binding sites[2] and binding conformations for L-Asp and L-Ala by means of the kinetic studies of competitive inhibition and the Oregon Green Maleimide (OGM) labeling assays. In addition, we found that AspT consists of ten transmembrane (TM) helices[3] and TM3 forms a putative substrate translocation pathway[4]. To reveal the substrate transport mechanism of AspT, we focused on the TM3 and analyzed L-Asp or L-Ala self exchange activities of TM3 single-cysteine variants.

2. Method

Purification of AspT-His[2]

Histidine (His)-tagged AspT (Cysteine-less or TM3 single-cysteine variants) was expressed in *Escherichia coli*. Each AspT-His variant solubilized from the cell membranes with DDM was trapped with a Co^{2+} resin column. Then AspT-His was purified by elution buffer containing 250 mM Imidazole.

Reconstitution into proteoliposomes and transport assay of AspT-His variants

Purified AspT-His was reconstituted in a final volume of 1 ml with 800 µl of detergent extracts (5 µg of protein or control lipid extract), 130 µl of bath-sonicated liposomes (6.5 mg of *E. coli* phospholipid), and 18 µl of 15% OG, with the balance made up by 100 mM potassium phosphate (pH 7). After incubation for 20 min on ice, proteoliposomes (or control liposomes) were formed at room temperature (RT) by rapid injection of the mixtures into 20 ml of loading buffer containing buffer solution and suitable counter substrate such as 100 mM L-Asp or 100 mM L-Ala as the potassium salt for L-Asp or L-Ala exchange reaction respectively. The substrate-loaded proteoliposomes (or liposomes) were kept at RT for 20 min. To assess L-Asp or L-Ala transport by L-[2,3-^{3}H]Asp or L-[2,3-^{3}H]Ala-loaded particles, proteoliposomes were suspended in 300 µl of assay buffer (50 mM potassium phosphate [pH 7], 100 mM K_2SO_4 or 50 mM potassium phosphate [pH 7], 50 mM K_2SO_4 for L-Asp or L-Ala exchange reaction respectively).

Aliquots (6 µl) of reconstituted proteoliposomes (or liposomes) were mixed with assay buffer and pre-incubated at 25°C. After 3 min of pre-incubation, L-[2,3-^{3}H]Asp or L-[2,3-^{3}H]Ala was added to a final concentration of 0.039 mM or 2.9 mM respectively, Aliquots (50 µl) were removed for membrane filtration with 0.22-µm-pore-size GSTF Millipore filter (Millipore Co., Billerica, MA). After 1 min at 25°C of L-[2,3-^{3}H]Asp or L-[2,3-^{3}H]Ala entry to proteoliposomes (or liposomes), the membrane filters were washed twice with 3 ml of assay buffer and stopped transport reaction.

3. Results and Discussion

TM3 is predicted to form a putative substrate translocation pathway and separated into the following three parts; a hydrophobic core, GxxxG motif, and a cytoplasmic hydrophilic cavity[4]. However, the

function of each part of TM3 for transport remains unclear. To investigate the transport function of TM3, we purified AspT-His TM3 single-cysteine variants and performed transport assay. The result was shown in Fig. 1.

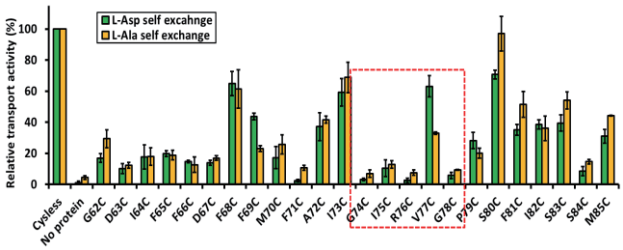

Fig. 1 Relative transport activity of TM3 variants

Initial transport rates of AspT-His variants for L-Asp and L-Ala are shown as green and orange bars, respectively. A vertical axis shows the transport amount of substance of each variant (μmol/mg protein) when Cysteine-less AspT is made into 100%.

The transport activities of the single-cysteine variants in the GxxxG motif located at the center of TM3 were markedly lower than those of variants in other regions. Because GxxxG motif is generally known to be involved in helix-helix interaction in a protein molecule or between protein molecules, the result suggests that the active structure of AspT was collapsed due to the single-cysteine substitution in the motif. We predicted that this motif is one of the important parts required for maintaining the function of AspT.

4. Concluding remarks

We clarified that GxxxG is involved in the stabilization of active structure of AspT. In our future work, we will identify other TMs that interact with this TM3's GxxxG.

References

[1] Abe K., Hayashi H., Maloney PC., J. Biol. Chem. 271:3079-84 (1996)
[2] Sasahara A., Nanatani K., Enomoto M., Kuwahara S., Abe K., J. Biol. Chem. 286:29044-29052 (2011)
[3] Nananatani K., Fujiki T., Kanou K., Takeda-Shitaka M, Umeyama H., Ye L, X Wang, Nakajima T., Uchida T., Maloney PC., Abe K., J. Bacteriol. 189:7089-7097 (2007)
[4] Nanatani K., Maloney PC., Abe K., J. Bacteriol. 191:2122-2132 (2009)

Quantitative Evaluation of Residual Strain in Carbon Steels by Magnetic Incremental Permeability Method

Seiya SATO[1], Tetsuya UCHIMOTO[2], Toshiyuki TAKAGI[2], Shejuan XIE[2], Ryoichi URAYAMA[2], Takeshi SATO[2], Zhenmao CHEN[3], Yasuhiko YOSHIDA[4]
[1]Graduate School of Engineering, Tohoku University, Japan
[2]Institute of Fluid Science, Tohoku University, 2-1-1 Katahira Aoba-ku, Sendai, Miyagi 980-8577, Japan
[3]State Key Laboratory for Strength and Vibration of Mechanical Structures, Xi'an Jiaotong University, Xi'an, China
[4]The Kansai Electric Power Company, Inc., Japan
Email: uchimoto@ifs.tohoku.ac.jp

ABSTRACT

In this study, quantitative evaluation of small amount of residual strain in carbon steels JIS SS400 are investigated by applying magnetic incremental permeability (MIP) method. There are two parameters to evaluate residual strain. First, peak-to-peak distance of incremental permeability has a good correlation with residual strain and there is almost no dependence on the rolling direction. Second, maximum permeability value takes almost constant for different residual strain but it is larger when tensile direction is parallel to the rolling direction than when it is perpendicular.

1. Introduction

When large amount of seismic load is exerted to components in nuclear power plants like the Great East Japan Earthquake, structural integrity evaluation is required [1, 2]. Currently, it is expected to establish nondestructive evaluation techniques that are more reliable and convenient. Electromagnetic method is promising since magnetic properties are sensitive to the microstructure changes due to plastic deformation. In order to put these techniques into practical, it is necessary to figure out the quantitative relationship between residual strain and electromagnetic properties.

In this study, nondestructive methods are investigated to evaluate small amount of residual strain of structural components in nuclear power plants due to seismic loading, focusing on the change of electromagnetic properties. Carbon steels JIS SS400 are discussed as target materials. Uniaxial tensile tests are carried out and electromagnetic nondestructive evaluation method, specifically magnetic incremental permeability (MIP) method is applied.

2. Specimen

Specimens were cut out by machining from plates with thickness of 4mm. Fig. 1 shows the schematic drawing of tensile specimens. Tensile tests were carried out using INSTRON5582 and 10 specimens with residual strains from 1% to 6.7% were prepared. Table 1 shows residual strain values together with resulting thickness of the specimens after tensile tests. Tensile direction of A specimens is perpendicular to the rolling direction and tensile direction of B specimens is parallel to the rolling direction.

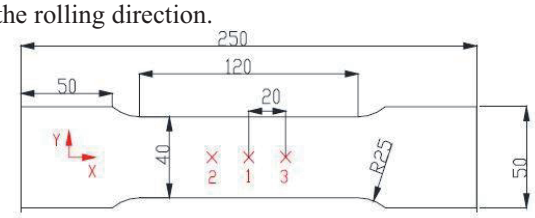

Fig. 1 Schematic drawing of tensile specimens.

Table 1. Results of tensile test.

No.		Rolling direction	Residual strain [%]	Thickness [mm]
A	0	perpendicular	0	3.97
	1		1.1	3.85
	2		2.7	3.89
	3		4.7	3.85
	4		6.7	3.81
B	0	parallel	0	3.86
	1		1.3	3.83
	2		2.9	3.84
	3		4.7	3.80
	4		6.7	3.74

3. MIP

MIP method is to evaluate the magnetic field dependence of the incremental permeability. Fig. 2 shows measurement system of MIP. Sinusoidal magnetic field is applied to the specimen by the excitation coil with the york. Probe has two coils and a hall sensor. Eddy current signal and tangential magnetic field are measured by the probe at the same time, and then incremental permeability can be evaluated by the voltage of the eddy current probe. Fig. 3 shows an example of the tangential magnetic field measured by the hall sensor. Fig. 4 shows eddy current signal amplitude as function of applied magnetic field. There are various parameters which characterize this butterfly shape figure [3]. In this study, peak-to-peak distance and magnitude of eddy current signal are extracted as parameters. Peak-to-peak distance is the magnetic field value between the maximum eddy current signals in the butterfly shape figure. Magnitude of eddy current signal is the difference between the maximum and minimum eddy current signals. Excitation frequency is 0.5Hz and frequency of eddy current test is 50kHz. To keep the magnitude of magnetic field in the specimen constant, applied voltage to excitation coil is adjusted.

4. Results and Discussion

Fig. 5 shows relationship between peak-to-peak distance and residual strain and Fig. 6 shows relationship between magnitude of eddy current signal

and residual strain. While peak-to-peak distance and residual strain showed good correlation, magnitude of the eddy current signal takes almost constant value for the residual strain. The reason of the peak-to-peak distance change is considered that coercivities of pearlite phase and ferrite phase are changing complicated by residual strain [3]. Tendency of A and B specimens are almost same, which implies that the peak-to-peak distance is independent from rolling direction. But the magnitude of the eddy current signal has larger value when tensile direction is parallel to the rolling direction than when it is perpendicular.

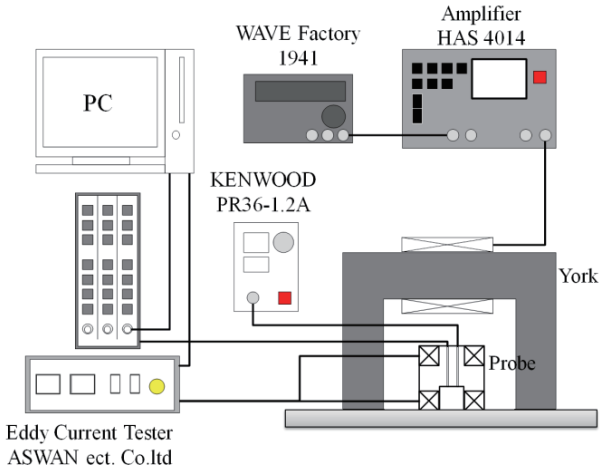

Fig. 2 Measurement system for incremental permeability.

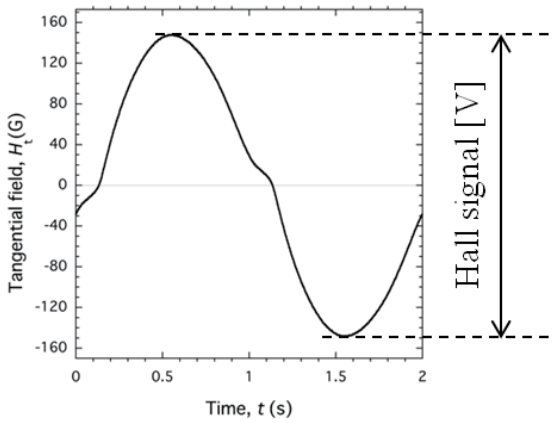

Fig. 3 Figure of hall signal.

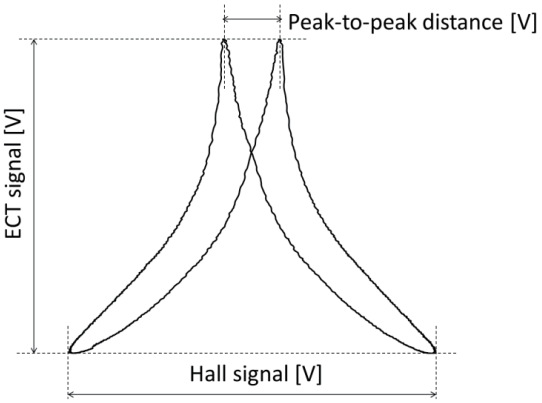

Fig. 4 Parameter of incremental permeability.

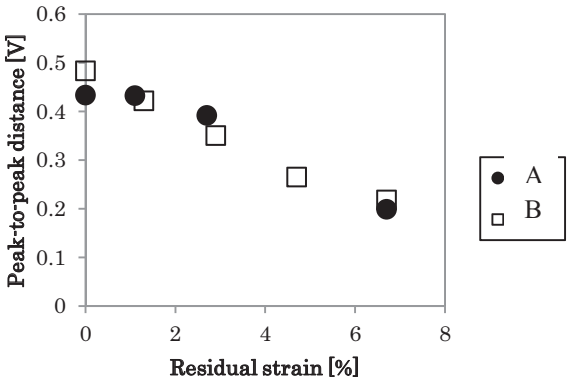

Fig. 5 Relationship between peak-to-peak distance and residual strain.

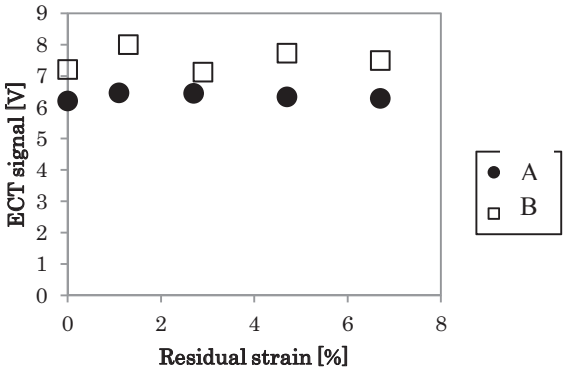

Fig. 6 Relationship between magnitude of the eddy current signal and residual strain.

5. Summary

In this study, MIP method is applied to evaluate up to about 5% residual strain in carbon steels quantitatively. Relationship between peak-to-peak distance and residual strain shows good correlation and there is possibility to evaluate small amount of residual strain quantitatively. From now on, it should be revealed that mechanism of incremental permeability changes due to variations of microstructures.

Acknowledgment

The authors thank the JSPS Core-to-Core Program, A. Advanced Research Networks, "International research core on smart layered materials and structures for energy saving". The authors express our appreciation for technical advice to Mr. G. Dobmann of Fraunhofer Institute for Nondestructive Testing IZFP, and for making specimens, equipments and their technical assistances to Mr. K. Kuroki and Mr. S. Onuma of Institute of Fluid Science, Tohoku University.

References

[1] M. Kamaya, *INSS Journal*, **16** (2009), pp.179-188.
[2] M. Kawakubo *et al.*, *Transactions of the Atomic Energy Society of Japan*, **9** (2010), pp.166-173.
[3] I. Altpeter *et al.*, *Inverse Problems*, **18** (2002), pp.1907-1921.

Tenth International Conference on Flow Dynamics
November 25-27, 2013, Sendai, Miyagi, Japan

Mixed-Lubrication of Fine Textured Polycrystalline CVD Diamond Surface

Kyohei Naito[1], Hiroyuki Miki[2], Michel Belin[3], Toshiyuki Takagi[4]
1) Graduate School of Engineering, Tohoku University, Aramaki aza Aoba 6-6, Aoba-ku, Sendai, 980-8579, Japan
2) Frontier Research Institute for Interdisciplinary Sciences, Tohoku University, Aramaki aza Aoba 6-3, Aoba-ku, Sendai, 980-8578, Japan
3) Laboratoire de Tribologie et Dynamique des Systemes, UMR5513, 36 avenue Guy de Collongue, Ecully 69134, Ecole Centrale de Lyon, France
4) Institute of Fluid Science, Tohoku University, 2-1-1 Katahira, Aoba-ku, Sendai, 980-8577, Japan
E-mail: takagi@ifs.tohoku.ac.jp

ABSTRACT

The partially polished diamond film shows good frictional properties at high sliding speed. Previous reports indicated that coefficient of friction (CoF) is reduced as sliding speed becomes fast because lift-off force occurs in the concave part of diamond coated substrate. However, the detailed relationship between the surface geometry of diamond film and lift-off parameters is still unclear. In this report, we carried out a pin-on-disk friction test for partially polished diamond films which have different surface geometries in order to investigate the relationship between the surface geometry and lift-off phenomenon of diamond film.

1. Introduction

Partially polished diamond film is expected to be applied for solid lubricant film because it has good frictional properties at high sliding speed without lubricant oil. Nakamori[1] and Yonemura[2] described that the drop-off of coefficient of friction (CoF) on diamond film is caused by "lift-off" due to increase of lift force generated by the pressure change between partially polished diamond film and counter material. In addition, Miki *et al*. [3.4] found that CoF and drop-off threshold on CoF of partially polished diamond film is reduced as arithmetic average surface roughness (*Ra*) of the film decreases. However, the detailed relationship between the surface geometry of polished diamond film and lift-off phenomenon is still unclear.

In this study, we carry out pin-on-disk friction test for partially polished diamond films that have different surface geometry to investigate the relationship between the surface geometry of diamond film, frictional properties and lift-off phenomenon.

2. Experiment

In this experiment, diamond film was deposited by a hot-filament chemical vapor deposition (HFCVD) method. HFCVD is the method that excites hydrocarbon gas by electrical heating of filaments to deposit carbon elements onto a substrate. We used tungsten filament with a diameter of 0.3 mm. The substrate is SiC disk (ϕ50 mm ×3 mm). Deposition parameter of HFCVD process is shown in Table 1.

After the deposition, the diamond film was polished by a diamond coated whetstone. The polishing parameters are shown in Table 2. The optical photos of the surface of polished diamond film were obtained by using an optical microscope (BX51M, OLYMPUS). With those photos, we calculated the ratio of the polished area of diamond film by using a software package (Image J, National institute of Health).

To evaluate friction properties of diamond coated substrate, a pin-on-disk friction test was carried out. The used pin is AISI440C, and the dimensions are ϕ10 mm×7 mm. The surface of the pin was polished up to about *Ra* = 0.08 μm. The pin was contacted on the surface of diamond film, and was subjected to the normal load of 50 mN. The tests were performed after 6,000 cycles sliding to avoid the primary instability of sliding surface. The test performed at atmospheric pressure, room temperature, and humidity of 60-63 RH%. The friction tests were carried out with sliding speed from 0.06 m/s to 1.2 m/s.

3. Results and Discussion

Fig. 1 shows that the result of the partially polished diamond film. According to this result, the CoF of diamond film is clearly reduced as the *Ra* of the film decreases. In addition, the inflection point at where CoF starts to decrease rapidly is observed in all samples.

Table 1 Deposition parameter of HFCVD

H_2 flow	100 ml/min
CH_4 flow	2.3 ml/min
Total gas pressure	8.0 kPa
Deposition time	5 hours
Filament temperature	2000 K

Table 2 Polishing condition of samples

	Ra[μm]	Polished area ratio [-]
A	0.39	0.106
B	0.14	0.190
C	0.07	0.414
D	0.06	0.462

It indicates that the influence of lift-off related to the surface geometry of diamond film remarkably appears at this point. We define this sliding speed at the inflection point of CoF as "lift-off" speed, V_L.

Fig. 2 exhibits the relationship between V_L and the polished area ratio and the relationship between V_L and *Ra* of diamond film is shown in Fig. 3. These two relationships have clearly different tendency.

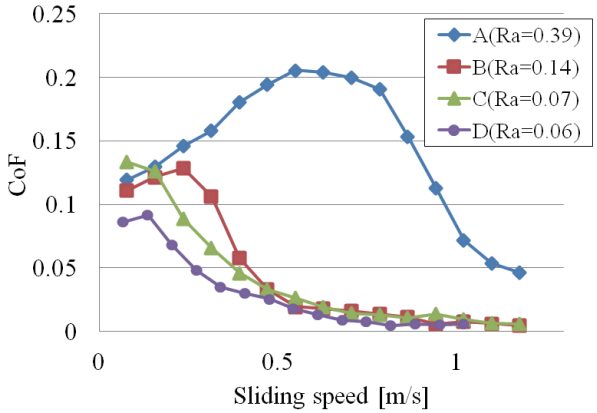

Fig. 1 Relationship between CoF and sliding speed

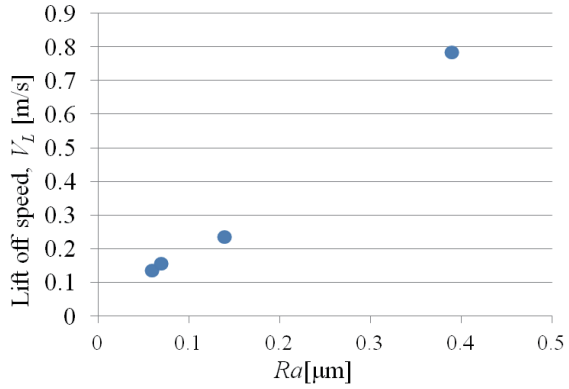

Fig. 2 Relationship between V_L and *Ra*

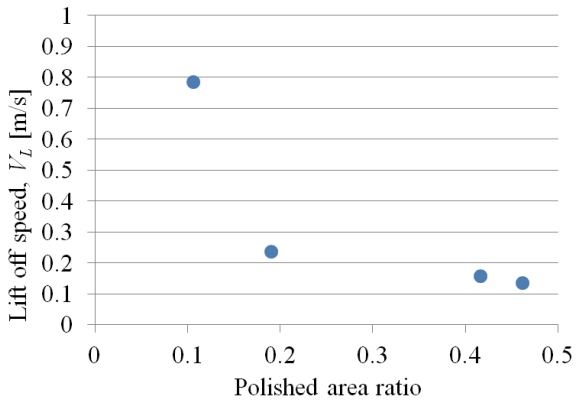

Fig. 3 Relationship between V_L and polished area ratio

Concerning the relationship between V_L and the polished area ratio, V_L decreases rapidly in the range of polished area ratio from 0.10 to 0.20. After that, V_L continues to reduce. This relationship shows a distinct different tendency from *Ra* of polished diamond film.

To explain the influence of *Ra* and polished area ratio on reducing friction and lift-off, we consider some reports describing friction of a surface textured by laser surface texturing (LST). For example, the friction behavior of textured ceramic substrate with dimples at equal intervals by LST[5]. In their report, the CoF is reduced as the diameter of dimples or distances between neighboring dimples becomes large. Based on these tendencies, even though the geometries are different between substrate prepared by LST and partially polished diamond, we assume that the polished area ratio of diamond film is important parameter which may decide to lift-off parameter of diamond film.

4. Summary

We evaluated the relationship between friction properties and surface geometry of partially polished diamond film. We obtained the following conclusions:

1) The CoF of diamond film is reduced as *Ra* decreases.
2) As *Ra* becomes smaller, V_L shifts down and the lift-off starts at lower sliding speed.
3) The polishing area ratio is also an important parameter that may decide to the lift-off parameter of diamond film.

Acknowledgements

This work was partially supported by the Asahi Glass Foundation in Japan, Grant-in-Aid for Challenging Exploratory Research (23656113, 25630032) of Japan Society for the Promotion of Science (JSPS) and the JSPS Core-to-Core Program, A. Advanced Research Networks, "International research core on smart layered materials and structures for energy saving". Authors are thankful to Mr. Takeshi Sato from the Institute of Fluid Science, Tohoku University, Japan, for his technical assistance.

References

[1] I.Nakamori, T.Takagi, T.Takeno, T.Abe, T.Uchimoto, Y.Kohama, Diamond and Related Materials **14** (2005) 2122-2126.

[2] S.Yonemura, M.Yamaguchi, T. Takeno, H. Miki, T.Takagi, AIP Conf. Proc. **1084** (2008), 1153-1157.

[3] H. Miki, A. Tsutsui, T. Takeno, T. Takagi, Diamond and Related Materials **17** (2009), 868-872.

[4] H.Miki, A.Tsusui, T.Takeno, T.Takagi, Diamond and Related Materials **24** (2012) 167-170.

[5] H.Yamakiri, S.Sasaki, T.Kurita, N.Kasashima, Tribology International **44** (2011), 579-584

Tenth International Conference on Flow Dynamics
November 25-27, 2013, Sendai, Miyagi, Japan

Development of High Temperature Electromagnetic Acoustic Transducer for Monitoring of Metal Processing

Shohei Ogata[1], Tetsuya Uchimoto[2], Toshiyuki Takagi[2], Toshiaki Ichihara[2], Gerd Dobmann[3]
1) Graduate School of Engineering, Tohoku University, 6-6 Aramaki Aza Aoba, Aoba-ku, Sendai, Miyagi, Japan
2) Institute of Fluid Science, Tohoku University, 2-1-1 Katahira, Aoba-ku, Sendai, Miyagi, Japan
3) Fraunhofer IZFP, Fraunhofer-Gesellschaft zur Förderung der angewandten Forschung e.V.Postfach 20 07 33
80007 München, Germany
E-mail: uchimoto@ifs.tohoku.ac.jp

ABSTRACT

Understanding of the metal solidification is a key issue to increase the reliability of the metal processing, and the sensors for monitoring such process at high temperature are highly required. EMAT (Electromagnetic Acoustic Transducer) provides non-contact measurements, and it is suitable for measurements in high temperature. This paper proposes to use air-cored coil as the bias magnetic source of EMAT. The pulse-echo waveforms of an aluminum specimen are measured by the present EMAT and shear wave velocity of the specimen at each temperature is evaluated. Back-echo signals can be identified at the range of temperature from RT to 460℃.

1. Introduction

To evaluate solidification of metals during casting or welding process, it is highly required to develop a high temperature ultrasonic transducer. Electromagnetic Acoustic Transducer (EMAT) can provide non-contact measurements, and it is suitable for measurements in high temperature [1]. Conventional EMAT uses rare-earth based magnets such as Nd or Sm-Co base ones for its bias magnetic sources, but the operation temperature of these types of magnets are limited by their Curie points. Recently, pulsed electromagnet EMAT which use iron yoke is developed [2, 3]. It is confirmed that this EMAT can be used at 600℃. However, to use it in higher temperature, it is supposed that the Curie point of iron yoke becomes a problem. To overcome this limitation, we suggest applying an air-cored coil for bias magnet of EMAT. The purpose of this study is to evaluate performance of the pulsed electromagnet EMAT with air-cored coil and final goal is to develop EMAT which can be used over 1000℃.

In this paper, we design the air-cored electromagnet which can apply sufficient magnetic field, and EMAT testing under room temperature is conducted. After that, EMAT is fabricated using high temperature materials, and performance of the present EMAT under high temperatures is evaluated.

2. Experiments

The pulsed electromagnet EMAT proposed in this study consists of an air-cored solenoid coil providing bias magnetic field and RF coil inducing eddy current in the specimen. Pulsed current is fed to the air-cored coil and bias magnetic field is generated, and simultaneously RF coil which is located between bias electromagnet and specimen induces eddy current in the specimen. Interaction between the eddy current and the bias magnetic field makes Lorentz force and the oscillation propagates into specimen as ultrasonic wave. When the reflected wave reaches near the surface, it is measured by the RF coil.

The schematic of experimental equipments are shown in Fig.1. Pulsed current generator which can provide the maximum current of 2000A drives the electromagnet and it also produces a trigger signal for the pulser/receiver system. The trigger signal is adjusted so that pulse-echo signals can be acquired when the magnetic field becomes maximum. The center frequency is set to 3MHz.

A multilayered solenoid coil is used for pulsed electromagnet. In order to overcome the coil's insulation constraints at high temperatures, a copper wire (ϕ1.0mm) is wound leaving behind a uniform gap in between the turns, and it is stabilized and insulated by magnesia-based ceramic adhesive. The number of turns is 100 and inner diameter, outer diameter, length are 25mm, 53mm and 25mm, respectively. To make peak of the magnetic field broad, the coil is connected to another coil in series to increase the inductance. The current waveforms of bias magnet coil are shown in Fig.2. Inductance value increases from 290μH to 1446μH, and the pulse width increases 1ms. When the supply voltage is set to 1000V, the maximum magnetic flux density is 372mT. The race track shape RF coil is wound by a copper wire coated by Polyamide-Imide (ϕ0.1mm). The wire is wound 30 turns leaving uniform gaps. Direction of generated Lorentz force is parallel to surface of the specimen, therefore, shear wave is generated and propagate to the vertical direction of the surface.

The EMAT is placed on an aluminum specimen which has the thickness of 20mm. They are set in an electric furnace and heated up to the target temperature, and, back echo signals were measured at every 40℃. The signals are averaged 8 times to remove the noise.

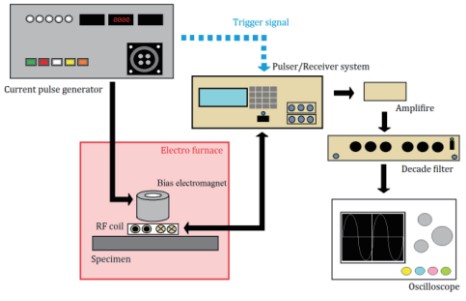

Fig.1 Experimental setup

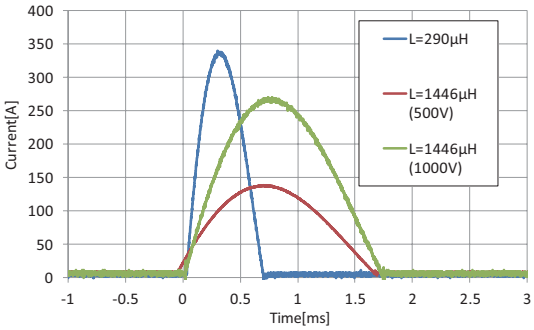

Fig.2 Current waveforms

3. Results

The obtained pulsed-echo signals are shown in Figs. 3 and 4. Clear echo signals were confirmed at the range of temperatures from 18℃ to 300℃. Decreasing of the signal amplitudes with temperature rise due to the reduction of output of pulser/receiver was confirmed. By keeping the output voltage constant, echo signals at 340℃ to 460℃ are successfully obtained.

Shear wave velocities at each temperatures are calculated by using the time of flight of echoes and the thickness of specimen. To consider the thermal expansion in high temperatures, the thickness of specimen is calculated by

$$L = L_o[1 + \alpha(T - T_o)], \qquad (1)$$

where, L_o, α and T-T_o are the thickness of specimen at RT, the expansion coefficient of aluminum and temperature changes from RT, respectively. The estimated wave velocity as function of temperature is shown in Fig.5. The shear wave velocity decreases with temperature rise. Generally, the elastic coefficient decreases with temperature rise, which leads decrease of the shear wave velocity. This result supports that the measurement by the present EMAT at elevated temperature was conducted properly.

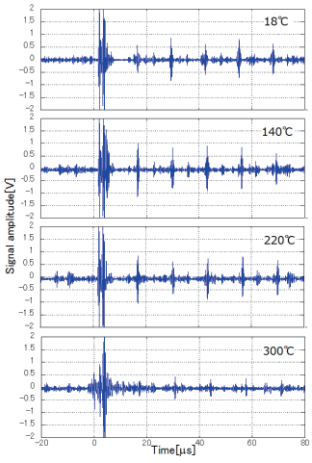

Fig.3 Pulse-echo waveforms at a range of temperatures from RT to 300℃

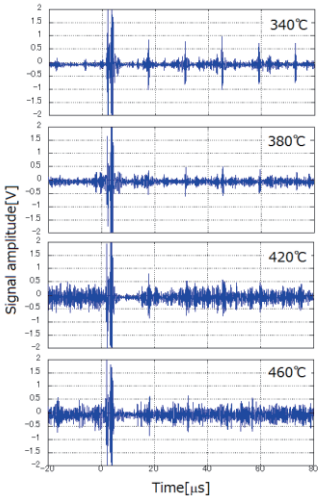

Fig.4 Pulse-echo waveforms at a range of temperatures from 340℃ to 460℃

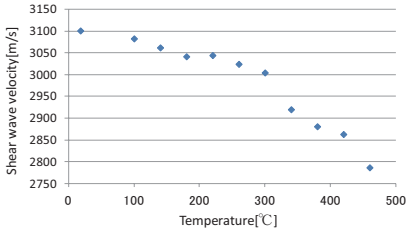

Fig.5 Shear wave velocity as function of temperatures

4. Summary

In this study, we designed the pulsed electromagnet EMAT with air-cored solenoid coil for utilize at high temperatures up to 1000℃.The bias coil is fabricated with copper wire and high temperature ceramic adhesive. Measurement of back echo signals of aluminum specimen at elevated temperatures was conducted. As a result, the echo signals are successfully obtained from RT to 460℃, and the decrease of shear wave velocity with temperature rise is confirmed. We are going to improve the cable in the electro furnace, and increase the number of averaging of signal. If the high temperature noise is removed by these method, it can be expected that the echo signals are observed at 500℃ or higher.

Acknowledgements

This study is supported by the Grant-in-Aid for Challenging Exploratory Research (24656080) of Japan Society for the Promotion of Science (JSPS), and the JSPS Core-to-Core Program, A. Advanced Research Networks, “International research core on smart layered materials and structures for energy saving”.

References

[1]R. Murayama, Non-destructive inspection, Vol.51, No.2, pp.62-67 (2002).

[2]F. Hernandez-valle and S Dixon, NDT&E International, Vol.43, No.2, pp.171-175 (2010).

[3]F. Hernandez-valle and S. Dixon, Insight, Vol.43, No.2, pp.96-99 (2011).

Tenth International Conference on Flow Dynamics
November 25-27, 2013, Sendai, Miyagi, Japan

Anomalous Behaviors of Ultra-High Molecular Weight Polyethylene Processed by Sintering

Tiana Deplancke[1*], Olivier Lame[1], François Rousset[2], Roland Seguela[1] and Gérard Vigier[1]
[1]Université de Lyon, CNRS, INSA-Lyon, MATEIS, UMR5510, F-69621, Villeurbanne, France
[2] Université de Lyon, CNRS, INSA-Lyon, CETHIL, UMR5008, F-69621, Villeurbanne, France
tiana.deplancke@insa-lyon.fr,

ABSTRACT

One of the main issues of ultra-high-molecular-weight polyethylene (UHMWPE) is its very high viscosity. Sintering of these polymers is then often required instead of injection or extrusion. Sintering mechanisms remains partially understood. Indeed, the two main mechanisms generally mentioned for interparticle welding, i.e. re-entanglement and cocrystallization, can hardly be observed separately. Fortunately, due to its very high molecular weight, UHMWPE exhibits an exceptionally broad rubbery plateau so that mechanical tensile tests can be easily performed both below and above the melting point.

1. Introduction

Processing UHMWPE is problematic due to its very high viscosity that prevents processing by conventional means such as extrusion or injection molding. Therefore processes inspired from powder metallurgy such as sintering have been developed. However, the sintering mechanisms remain incompletely understood.

Sintering is a diffusive process analogous to the diffusion of long polymer chains across interfaces in the case of welding. The sintering phenomenon is generally modeled by the reptation theory [1,2]. The mechanical characteristics are generally supposed to mainly depend on the interpenetration distance in the interfacial region [3]. It is even often assumed that the bulk mechanical properties only depend on the interpenetration distance [2,3]. Moreover, in the case of semi-crystalline polymers, the interfacial strength also depends on the occurrence of cocrystallization [4].

In the present work a sintering procedure has been developed. Two methods are proposed to evaluate the influence of sintering parameters (temperature and time) and of molecular weight in the range of $0.6.10^6$ g.mol^{-1} to 10.5. 10^6 g.mol^{-1}, on the mechanical properties of the material. New features of the sintering mechanisms are discussed.

2. Method

The sintering process is often described by two steps [3]. In a first time the densification stage corresponds to the wetting of the surfaces between the powder grains. In a second time the interface consolidation takes place via chain diffusion. This second step is the most influential in the completion of sintering.

In order to discriminate these two main stages the forming has been done in two steps. First, densification was carried out under vacuum. The temperature was kept below the melting temperature so as to neglect diffusion of chains across the interface. This procedure was the same for all samples.

The density after this first step is approximately 0.95g.cm^{-3}. Considering that crystallinity is about 60%, according to DSC measurement, this result confirms the hypothesis that densification and wetting have been correctly achieved.

During the sintering step two variable parameters have been studied: time and temperature (Fig. 3). The pressure cycle is the same for all samples: 5MPa during sintering and 20MPa during subsequent cooling in order to prevent shrinkage cavities upon crystallization.

Cylinders having 2 mm in length and 25 mm of diameter have been prepared.

A nascent GUR powder supplied by Ticona (Oberhausen, Germany) was used to produce sintered parts. The average grain size is 150µm.

This material was chosen because of its very high viscosity in the melt that results in an extremely broad rubbery plateau as can be seen on the shear modulus versus temperature plot displayed on Fig. 1. This exceptional property enables to perform tensile drawing experiments below as well as above the melting point. This enables to split the studies of the two main mechanisms of sintering, i.e. chain re-entanglement and cocrystallization.

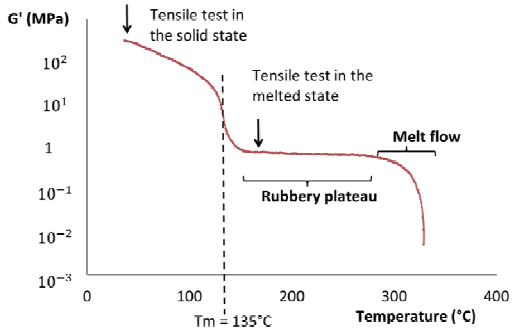

Fig. 1 Elastic shear modulus of UHMWPE versus temperature (f = 1 Hz)

The DSC curves displayed on of Fig. 2 show the melting endotherm of the nascent powder and that of the re-crystallized material following the first heating run. The much higher crystallinity and melting point of the nascent powder are characteristic of UHMWPE nascent reactor powders [5], and has been assigned to *non-equilibrium* chain conformations - but the actual origin is not clearly understood. In the present study of sintering of UHMWPE nascent powders, the DSC curves of Fig. 2 clearly indicate the predominance of *non-equilibrium* crystals likely to undergo *melting explosion* [6]. In these circumstances, the first step of chain interdiffusion across interfaces would occur in a

time scale much shorter than predicted from a reptation regime.

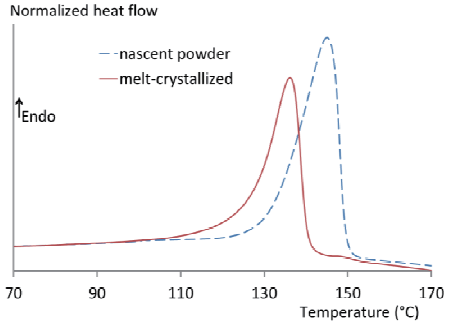

Fig. 2 DSC curves of the nascent powder and the melt-crystallized material (Perkin Elmer Pyris - heating rate 10°C/min)

3. Results and Discussion

The case presented here is that of a molecular weight of 4.10^6 g.mol^{-1} (the same work was done for masses of 0.6. 10^6 g.mol^{-1}, $6.8.10^6$ g.mol^{-1} and $10.5.10^6$ g.mol^{-1}).

The tensile test at 150°C permits to focusing on the re-entanglement because at this temperature all crystallites have melted.

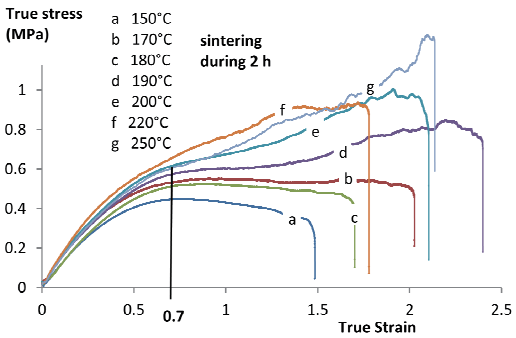

Fig. 3 True stress-strain tensile curves at room temperature for a sintering time 2 h at different sintering temperatures given in the legend.

The tensile curves display two different behaviors:

- Without strain hardening for sintering performed below 190°C
- With strain hardening for sintering performed above 190°C

This is a piece of evidence that re-entanglement increases with temperature of sintering.

The stress at strain 0.7 in the pseudo-plateau region (σ_{pp}) has been chosen for comparison of different sintering treatments. As expected in the reptation theory, the evolution of this parameter with temperature and sintering time are power laws. The evolution of σ_{pp} with sintering time is very weak as compared to the evolution with sintering temperature, the exponent of the power law being about 10^2 times lower.

Mechanical tests of the solid sintered materials give information on the strength of the particles interface including the contributions of both the interdiffusion of the chains emanating from the jointing particles and the cocrystallization of these chains. Even though a major role is attributed to cocrystallization on the welding efficiency [4,7], it is to be noticed that very few direct experimental evidences have been provided.

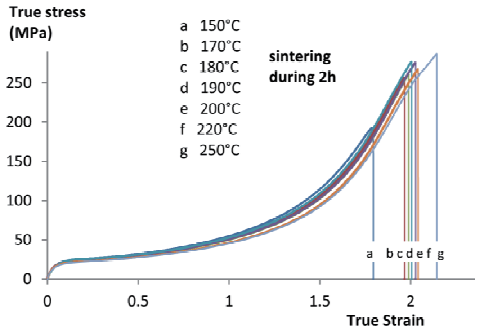

Fig. 4 True stress-strain tensile curves at room temperature for a sintering time 2 h at different sintering temperatures given in the legend.

The stress-strain curves at room temperature (Fig. 4) show that cocrystallization ensures a good interparticle cohesion. It is worth noticing that the tensile modulus and the yield stress are very similar for all samples regardless of the type of sintering.

4. Concluding remarks

A sintering protocol was developed that involves both time and temperature as variable parameters of sintering. The samples were then tested at room temperature and in the rubbery region, which allows following the evolution of re-entanglement and cocrystallization.

The very weak influence of sintering time compared to that of sintering temperature gave evidence that chain interdiffusion was not governed by a reptation mechanism. The entropy-driven *melting explosion* of the *non-equilibrium* crystals in the nascent powder is suggested to be the main mechanism of the fast chain re-entanglement and subsequent particle welding. Cocrystallization is so much efficient in the interface consolidation in the solid state that it significantly hides the temperature-governed kinetics of chain intertwining that occurred in the melt. The same trends are observed for all the materials having molecular mass in the range of 0.6 10^6 - 10.5 10^6 g.mol^{-1}.

References

[1] P.-G. de Gennes, J. Chem. Phys. 1971, **55,** 572-579.
[2] M. Bousmina *et al.*, Macromolecules 1998, **31**, 8273-8280.
[3] Y.H. Kim, R. Wool, Macromolecules 1983, 16, 1115-1120.
[4] Y.Q Xue, T.A Tervoort, S. Rastogi, P.J. Lemstra, Macromolecules 2000, 33, 7084-7087.
[5] H.D. Chanzy, E. Bonjour, R.H. Marchessault, Colloid Polym. Sci. 1974, 22,523-531.
[6] Y.Q. Xue, T.A. Tervoort, P.J. Lemstra, Macromolecules 1998, 31, 3075-3080.
[7] A.N. Gent, E.-G. Kim, J. Polym. Sci., Polym. Phys., 1997, 35,615-622.

Tenth International Conference on Flow Dynamics
November 25-27, 2013, Sendai, Miyagi, Japan

Effect Of Adhesive Forces On The Prediction Of Cold Spray Process

Paul Profizi, Alain Combescure
LaMCoS, INSA
18-20, rue des Sciences
F69621 VILLEURBANNE CEDEX
FRANCE
paul.profizi@insa-lyon.fr

ABSTRACT

The impact of a solid particle on a substrate and the effect of surface adhesion on the final state of the particle – stuck or rebounding – is studied and analyzed in the context of the Cold Spray Coating process. Geometry is simplified and temperature, strain rate effect and plasticity are taken into account in an axisymmetric finite element model. The adhesion process is modeled with a cohesive law. The experimental phenomenon of an impact velocity range for the sticking of the particle is retrieved numerically and conclusions are made on the scale effect and the influence of the different adhesion parameters involved.

1. Introduction

The Cold Spray Coating process consists in the spraying of particles of the desired coating material on the surface to be coated, and this at high speed and a relatively low temperature compared to other coating processes. In a certain velocity range the particles stick to the surface and create a very homogeneous coating of good quality.

The physical reasons of the sticking of the particles are not very well known yet and efforts are made toward a better understanding of the physics involved. This study focuses on the influence of solid surface energy and adhesion forces.

2. Method

A numerical 2D axisymmetric model is implemented using the finite element method.

The geometry of the sphere on plane impact is simplified to avoid Hertz law computation by using an energetically equivalent cylinder on cylinder impact.
The height of the cylinder is chosen so that the initial kinetic energy is the same in the two geometries.

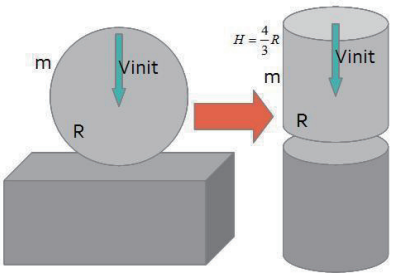

Fig. 1 Simplified geometry of the model

The Johnson-Cook law is chosen as a material law, so as to take into account plastic deformations, strain rate effects and temperature dependency.

$$\sigma = [A + B(\varepsilon^p)^N][1 + C\log(\dot{\varepsilon}^p)][1 - \hat{\theta}^M] \quad (1)$$

With
$$\hat{\theta} = \frac{T_{end} - T_{ref}}{T_{melt} - T_{ref}} \quad (2)$$

Where A, B, N, M, p, C, T_{melt} and T_{ref} are known for a given material.

An adiabatic heating of the material proportional to 80% of the plastic work is used for the temperature variation:

$$dT = \frac{0.8\, dw^{plast}}{k\rho} \quad (3)$$

Since the goal is to study the influence of adhesion, an adhesive law is added to the model.
The adhesion/interface energy G_c is given for each couple of materials. It is the energy per square meter that is required to break the interface between the two materials. This energy has to be dissipated for the bond to break.

The energy required to break the bond depends on the current interface surface, which is computed with the current radius R_{bott}^{parti} of the bottom of the particle:

$$W_{adhesion} = G_c\pi\left(R_{bott}^{parti}\right)^2 \quad (4)$$

G_c being the critical adhesion energy. This energy is dissipated by an adhesion stress working with a critical opening distance.

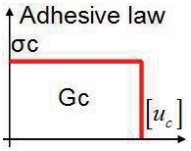

Fig. 2 Adhesive energy representation

The critical stress is chosen in such a way it will always be less than the minimum yield stress in the particle and the substrate, so that the adhesive bond will not cause a breaking or excessive plastic deformation in neither two pieces:

$$\sigma_c = 0.8Min\left(\sigma_y^{subs}(0.8T_{melt}^{subs}), \sigma_y^{part}(0.8T_{melt}^{part})\right) \quad (5)$$

An adhesion force can then be computed and applied to the nodes in contact:

$$F_{adhesion} = -\sigma_c\pi\left(R_{bott}^{parti}\right)^2 \quad (6)$$

The critical opening is then obtained:

$$[u]_c = \frac{G_c}{\sigma_c} \tag{7}$$

Impedance is put at the bottom of the substrate as an axial boundary condition to model the non-reflection of elastic waves.

$$F_{impedance} = -\pi\left(R_{bott}^{subs}\right)^2 \sqrt{E_{subs}\rho_{subs}}\,\dot{u}_{bott}^{subs} \tag{8}$$

With E_{subs} being the Young modulus of the substrate, ρ_{subs} its density and $\dot{u}_{bott}^{subs}$ the speed at the bottom.

The particle is considered to be stuck if the final remaining energy (elastic and kinetic) is less than the non-dissipated adhesion energy.

3. Results and Discussion

The model is used to simulate the impact of an aluminum particle on an aluminum substrate.

The particle is given different initial velocities and the final state of the particle after impact (flying away or stuck on the substrate) is observed for different particle radiuses.

The material data used for aluminum is:

Table 1. Material data used for the Al/Al impact

G (GPa)	ρ (kg/m²)	A, σ_y (MPa)	B (MPa)	C	N
27	2700	148.4	245.5	0.001	0.183
M	T_{ref} (°K)	T_{melt} (°K)	k (J/kg/°K)	G_c (J/m²)	σ_c (MPa)
0.895	300	916	904	10	10.7

Table 2. Simulation results for the Al/Al impact

Particle state after impact			
	r_0 (µm)		
v_0 (m/s)	5	12,5	125
30	stuck	stuck	Stuck
40			flying
50		flying	
100			
150		stuck	
500			
600		flying	

The particle always sticks at very low velocity because non reflective boundaries absorb enough energy for the adhesion to maintain the particle in contact.

When the particle is large enough (here R>12.5µm) and above a certain velocity (here v_0 > 45m/s), the kinetic energy becomes high enough to enable the rebounding of the particle after energy has been dissipated by the boundary conditions and adhesion forces. When impact velocity is still increased (here v_0 > 125m/s) the particles deformations are large enough to activate again the gluing of the particle on the substrate. This gluing phase is valid until here 500m/s. At higher impact velocity the particle rebounds. For larger sizes, e.g. R=125µm, there is no sticking because the surface energy is not large enough compared to the initial kinetic energy.

Simulation results show a clear scale effect in the sticking of the particle, as is observed in experiments.

There is for each couple of materials a maximum particle radius above which the particle will never stick to the substrate without melting. This maximum particle radius usually never exceeds a hundred microns.

4. Concluding remarks

This model reproduces, qualitatively, scale effects observed experimentally in the Cold Spray process.

A “sticking zone” is observed between two “rebounding zones” for particles with a radius of some tens of microns.

A maximum radius value can be found for different couples of material, above which the particle will never stick to the substrate.

The addition of an adhesion law in the impact model is the reason for retrieving experimental phenomena and leads to more complex studies with implementation of an adhesion law in explicit dynamic finite-element software and the use of solid-SPH for simulating the particle, the goal being to have quantitative results on the velocity range for the sticking.

This will eventually lead to a better understanding of the real sticking phenomenon and improvement of the Cold Spray technology.

Tenth International Conference on Flow Dynamics
November 25-27, 2013, Sendai, Miyagi, Japan

Tribological Characteristics of Cu-DLC Under Micro-vibration

Kosuke Ito[a], Dongkelong Ai[a,*], Takuma Ohnishi[a], Takanori Takeno[b], Hiroyuki Miki[c], Toshiyuki Takagi[c]
a: College of Engineering, Nihon University, Fukushima, Japan
b: School of Mechanical Engineering, Tohoku University, Sendai, Japan
c: Institute of Fluid Science, Tohoku University, Sendai, Japan
* E-mail of corresponding author: ceto13001@g.nihon-u.ac.jp

ABSTRACT

Tribological characteristics of Cu-DLC were investigated. Tests were performed under micro-vibration conditions. The normal load was 2N. The frequencies of vibration were 60 or 100 Hz. The number of cycles was 300, 1000 or 10000 cycles. Under these conditions, (1) the apparent coefficient of friction under the vibration of 100 Hz was nearly 0.2, while that under 60 Hz was nearly 0.15. (2) With the increase in the number of cycles, the area of wear track on the plates increased under 100 Hz, while it remains unchanged under 60 Hz.

1. Introduction

Diamond-like carbon (DLC) coatings have unique properties such as low friction, high wear resistance, chemical inertness, and high electrical resistivity. DLCs have been used in various industrial fields. However, they have not been used for electrical components because of their high electrical resistivity. Takeno et al. have developed a hybrid deposition method by combining CVD and PVD, which enabled simultaneous deposition of nano-sized metal particles and DLC as metal-containing DLC (Me-DLC) [1][2]. Me-DLCs can be electrically conductive. Their applications for sliding electrical contacts in automobiles, space applications, etc. are expected. On the other hand, it has been reported that micro-vibration significantly affected tribological characteristics of electrical contacts [3].

The objective of this presentation is to clarify the effects of frequency and number of cycles on tribological characteristics of Cu-DLC under micro-vibration.

2. Experimental Conditions

In this study, copper is selected as the metal species for Me-DLC (i.e. Cu-DLC) because of its high conductivity. The Cu-DLC films were deposited on Si wafers by a hybrid process of plasma-enhanced chemical vapor deposition (RF-PECVD) and DC magnetron co-sputtering of copper. The deposition parameters are summarized in Table 1. The mating specimen was a JIS SUJ2 bearing steel ball with the diameter of 8 mm.

Micro-vibration tests were performed at room temperature using a reciprocating type ball-on-plate micro-vibration tribo-tester (see Fig. 1). Cu-DLC plate was vibrated in horizontal direction by a vibrator (Asahi-Seisakusho WaveMaker05). Tangential force and normal load were measured by load cells (Kistler 9217A and Kyowa LMB-A-50N, respectively). All the data were recoded simultaneously by a data logger (Keyence NR-600).

Experimental conditions were summarized in Table 2. The load of 1 N was applied by pressing down the upper arm and then 1 N was added by a dead weight, which resulted in the total load of 2 N. The apparent coefficient of friction (μ_a) was calculated by the tangential force divided by the normal load. Tangential force is defined as the total of the friction and the inertia forces.

Due to the influence of the leaf spring, the vertical inertia force is also acted to the upper specimen, which resulted in the variation of the normal load.

After the tests, wear tracks were observed by an optical microscope (Keyence VHX-1000).

Table 1. Film Deposition conditions

C_2H_2 flow rate	0.9 sccm
DC Power	100 W
Time of deposition	30 min.
Cu content	85at%
Film thickness	400 to 500 nm
Substrate	Si-wafer

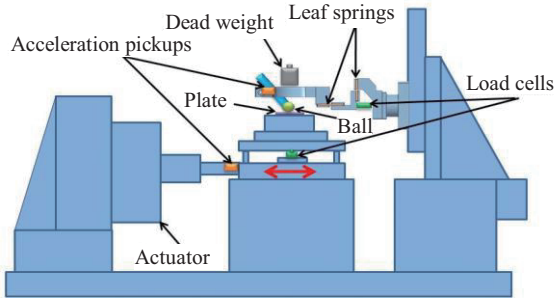

Fig. 1 Schematic representation of the reciprocating type ball-on-plate micro-vibration tribo-tester

Table 2. Experimental conditions

	T60HZ	T100HZ
Frequency of vibration (Hz)	60	100
Vibration amplitude (μm)	40±5	30±5
Normal load (N)	2	
Number of cycle (cycles)	300, 1000, 10000	
Room temprature (℃)	24.5±0.5	
Relative humidity (%)	64±1	

3. Results and Discussions

The apparent coefficient of friction curves of each test are shown in Fig. 2. Generally speaking, the apparent coefficient of friction is higher under 100 Hz (T100HZ, see Table 2.) than that under 60 Hz (T60HZ, see Table

2.).

In the tests under the T60HZ, the apparent coefficient of friction ranges from 0.07 to 0.08 at 300 cycle test, from 0.14 to 0.21 at 1000 cycle test, from 0.14 to 0.18 at 10000 cycle test. In the tests under the T100HZ, the apparent coefficient of friction ranges from 0.17 to 0.20 at 300 cycle test, from 0.19 to 0.22 at 1000 cycles, from 0.17 to 0.26 at 10000 cycle test.

Fig. 3 shows optical images of wear tracks on Cu-DLC plates. In Fig. 3(a), the plate was slightly discolored. In Fig. 3(b), (c), and (d), the plates partially discolored. In Fig. 3(e) and (f), the Cu-DLC coating on the plate almost completely discolored.

Fig. 4 is optical images of wear tracks on SUJ2 balls. In Fig. 4(a), the wear track was hardly visible. In Fig. 4(b), (c), and (d), small areas were discolored. The color of the areas was like copper. In Fig. 4(e) and (f), greater areas were discolored. The color of the areas was also like copper.

The discolored area increases as number of cycles under the T100HZ. On the other hand, the discolored area remained unchanged regardless of the test cycles under the T60HZ. The shape of discolored area on a plate (See Fig. 3) and that on a ball (See Fig. 4) are similar in each test. Their shapes almost match each other. Probably, the Cu-DLC coating on the plates was delaminated, and transferred to the SUJ2 balls.

As mentioned above, the apparent coefficient of friction under the T100HZ was higher than that under the T60HZ, which might have been caused by the delaminating of Cu-DLC. The correlation between their apparent coefficient of friction and their wear track discoloration was seen. The discoloration of the plate and the increase in apparent coefficient of friction might have caused by the adhesion and transfer of Cu-DLC layer to the ball. In Fig. 3(b), a little delamination was seen. An abrupt increase in the apparent coefficient of friction from approximately 0.18 to 0.20 occurred at around 800 cycles. The delamination might have happened at around 800 cycles.

4. Conclusions

Micro-vibration friction and wear properties of Cu-DLC coating films against SUJ2 ball were investigated and summarized as follows:

(1) The apparent coefficient of friction under the vibration of 100 Hz was nearly 0.2, while that under 60 Hz was nearly 0.15.

(2) With the increase in the number of cycles, the area of wear track on the plates increased under the vibration of 100 Hz, while it remains unchanged under the vibration of 60 Hz.

(3) The correlation between the apparent coefficient of friction and the delamination of Cu-DLC was suggested.

References

[1] T. Takeno, Diamond Relat. Mater., **17** (2008), 713.
[2] T. Takeno, Diamond Relat. Mater., **15** (2006), 1902.
[3] J. Higaki, IEICE, **12** (2008), 1578

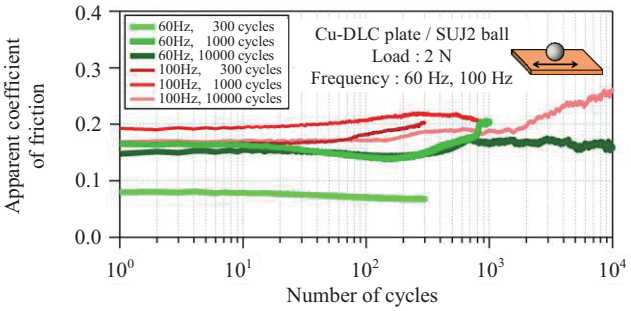

Fig. 2 Apparent coefficient of friction curves of each test

Number of cycles	T60HZ	T100HZ
300	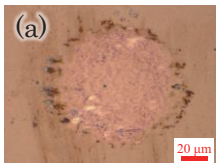	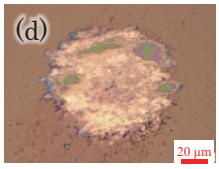
1000	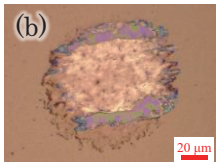	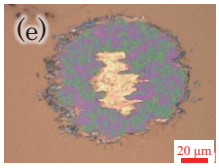
10000	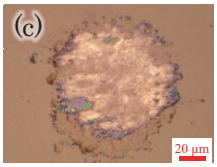	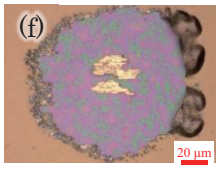

Fig. 3 Optical images of wear tracks on Cu-DLC plates.

Number of cycles	T60HZ	T100HZ
300	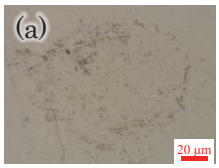	
1000	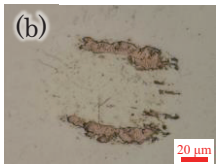	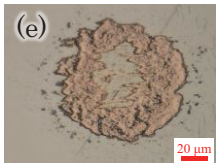
10000	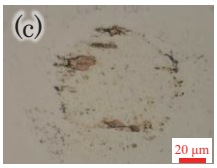	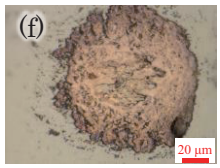

Fig. 4 Optical images of wear tracks on SUJ2 balls.

PS1: IFS Collaborative Research Forum

For details, please refer to separate proceedings

PS2: Young Researcher Overseas Visits Program Research Forum

For details, please refer to separate proceedings

Author Index

Author Index